AGARD-CP-536

AGARD-CP-536

AGARD

ADVISORY GROUP FOR AEROSPACE RESEARCH & DEVELOPMENT
7 RUE ANCELLE 92200 NEUILLY SUR SEINE FRANCE

AGARD CONFERENCE PROCEEDINGS 536

Fuels and Combustion Technology for Advanced Aircraft Engines

(Les Propergols et les Systèmes de Combustion pour les Moteurs d'Aéronefs)

Papers presented at the Propulsion and Energetics Panel 81st Symposium held in Fiuggi, Italy, 10th—14th May 1993.

NORTH ATLANTIC TREATY ORGANIZATION

Published September 1993

Distribution and Availability on Back Cover

AGARD

ADVISORY GROUP FOR AEROSPACE RESEARCH & DEVELOPMENT

7 RUE ANCELLE 92200 NEUILLY SUR SEINE FRANCE

AGARD CONFERENCE PROCEEDINGS 536

Fuels and Combustion Technology for Advanced Aircraft Engines

(Les Propergols et les Systèmes de Combustion pour les Moteurs d'Aéronefs)

Papers presented at the Propulsion and Energetics Panel 81st Symposium held in Fiuggi, Italy, 10th—14th May 1993.

North Atlantic Treaty Organization
Organisation du Traité de l'Atlantique Nord

The Mission of AGARD

According to its Charter, the mission of AGARD is to bring together the leading personalities of the NATO nations in the fields of science and technology relating to aerospace for the following purposes:

- Recommending effective ways for the member nations to use their research and development capabilities for the common benefit of the NATO community;
- Providing scientific and technical advice and assistance to the Military Committee in the field of aerospace research and development (with particular regard to its military application);
- Continuously stimulating advances in the aerospace sciences relevant to strengthening the common defence posture;
- Improving the co-operation among member nations in aerospace research and development;
- Exchange of scientific and technical information;
- Providing assistance to member nations for the purpose of increasing their scientific and technical potential;
- Rendering scientific and technical assistance, as requested, to other NATO bodies and to member nations in connection with research and development problems in the aerospace field.

The highest authority within AGARD is the National Delegates Board consisting of officially appointed senior representatives from each member nation. The mission of AGARD is carried out through the Panels which are composed of experts appointed by the National Delegates, the Consultant and Exchange Programme and the Aerospace Applications Studies Programme. The results of AGARD work are reported to the member nations and the NATO Authorities through the AGARD series of publications of which this is one.

Participation in AGARD activities is by invitation only and is normally limited to citizens of the NATO nations.

Published September 1993

ISBN 92-835-0719-3

Printed by Specialised Printing Services Limited
40 Chigwell Lane, Loughton, Essex IG10 3TZ

Recent Publications of the Propulsion and Energetics Panel

CONFERENCE PROCEEDINGS (CP)

Smokeless Propellants
AGARD CP 391, January 1986

Interior Ballistics of Guns
AGARD CP 392, January 1986

Advanced Instrumentation for Aero Engine Components
AGARD CP 399, November 1986

Engine Response to Distorted Inflow Conditions
AGARD CP 400, March 1987

Transonic and Supersonic Phenomena in Turbomachines
AGARD CP 401, March 1987

Advanced Technology for Aero Engine Components
AGARD CP 421, September 1987

Combustion and Fuels in Gas Turbine Engines
AGARD CP 422, June 1988

Engine Condition Monitoring – Technology and Experience
AGARD CP 448, October 1988

Application of Advanced Material for Turbomachinery and Rocket Propulsion
AGARD CP 449, March 1989

Combustion Instabilities in Liquid-Fuelled Propulsion Systems
AGARD CP 450, April 1989

Aircraft Fire Safety
AGARD CP 467, October 1989

Unsteady Aerodynamic Phenomena in Turbomachines
AGARD CP 468, February 1990

Secondary Flows in Turbomachines
AGARD CP 469, February 1990

Hypersonic Combined Cycle Propulsion
AGARD CP 479, December 1990

Low Temperature Environment Operations of Turboengines (Design and User's Problems)
AGARD CP 480, May 1991

CFD Techniques for Propulsion Applications
AGARD CP 510, February 1992

Insensitive Munitions
AGARD CP 511, July 1992

Combat Aircraft Noise
AGARD CP 512, April 1992

Airbreathing Propulsion for Missiles and Projectiles
AGARD CP 526, September 1992

Heat Transfer and Cooling in Gas Turbines
AGARD CP 527, February 1993

Fuels and Combustion Technology for Advanced Aircraft Engines
AGARD CP 536, September 1993

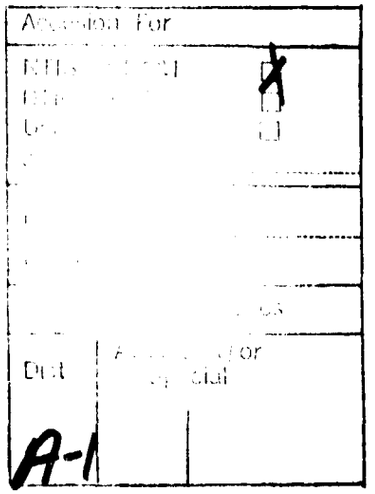

ADVISORY REPORTS (AR)

Suitable Averaging Techniques in Non-Uniform Internal Flows *(Results of Working Group 14)*
AGARD AR 182 (in English and French), June/August 1983

Producibility and Cost Studies of Aviation Kerosines *(Results of Working Group 16)*
AGARD AR 227, June 1985

Performance of Rocket Motors with Metallized Propellants *(Results of Working Group 17)*
AGARD AR 230, September 1986

Recommended Practices for Measurement of Gas Path Pressures and Temperatures for Performance Assessment of Aircraft Turbine Engines and Components *(Results of Working Group 19)*
AGARD AR 245, June 1990

The Uniform Engine Test Programme *(Results of Working Group 15)*
AGARD AR 248, February 1990

Test Cases for Computation of Internal Flows in Aero Engine Components *(Results of Working Group 18)*
AGARD AR 275, July 1990

Test Cases for Engine Life Assessment Technology *(Results of Working Group 20)*
AGARD AR 308, September 1992

Terminology and Assessment Methods of Solid Propellant Rocket Exhaust Signatures *(Results of Working Group 21)*
AGARD AR 287, February 1993

LECTURE SERIES (LS)

3-D Computation Techniques Applied to Internal Flows in Propulsion Systems
AGARD LS 140, June 1985

Engine Airframe Integration for Rotorcraft
AGARD LS 148, June 1986

Design Methods Used in Solid Rocket Motors
AGARD LS 150, April 1987
AGARD LS 150 (Revised), April 1988

Blading Design for Axial Turbomachines
AGARD LS 167, June 1989

Comparative Engine Performance Measurements
AGARD LS 169, May 1990

Combustion of Solid Propellants
AGARD LS 180, July 1991

Steady and Transient Performance Prediction of Gas Turbine Engines
AGARD LS 183, May 1992

Rocket Motor Plume Technology
AGARD LS 188, June 1993

AGARDOGRAPHS (AG)

Measurement Uncertainty within the Uniform Engine Test Programme
AGARD AG 307, May 1989

Hazard Studies for Solid Propellant Rocket Motors
AGARD AG 316, September 1990

Advanced Methods for Cascade Testing
AGARD AG 328, August 1993

REPORTS (R)

Application of Modified Loss and Deviation Correlations to Transonic Axial Compressors
AGARD R 745, November 1987

Rotorcraft Drivetrain Life Safety and Reliability
AGARD R 775, June 1990

Theme

New technologies for low-NOx combustors and advanced high-pressure/high-temperature cycle engines result in unique problems in design and performance. There have been significant advances in modelling and diagnostics to aid the development of these technologies.

The purpose of this Symposium is to bring together experts from industry, research establishments, and universities to discuss fundamental and applied research in combustion, diagnostics, and modelling as relevant to the development of advanced gas turbine engines, to exchange practical experience, and discuss the state of the art.

The Symposium focusses on high temperature fuel systems, atomization and mixing, emissions, and combustor design and performance.

Thème

Les nouvelles technologies pour chambres de combustion à faible dégagement de NOx et moteurs avancés à cycles haute pression/haute température soulèvent des problèmes particuliers de conception et de performances. Les progrès considerables réalisés dans les domaines de la modélisation et du diagnostic représentent une aide appréciable au développement de ces technologies.

L'objet de ce symposium est de réunir des experts de l'industrie, des établissements de recherche et des universités pour discuter des aspects de la recherche fondamentale et appliquée en combustion, diagnostic, et modélisation qui sont appropriés au développement des turbomoteurs avancés, pour échanger leur expérience pratique et pour discuter de l'état de l'art dans ce domaine.

Le symposium met l'accent sur les dispositifs d'alimentation haute température, la vaporisation et le mélange, les émissions, la conception des chambres de combustion et les performances.

Propulsion and Energetics Panel

Chairman: Prof. Dr Ahmet Üçer
Middle East Technical University
O D T Ü
Makina Müh. Bölümü
06531 Ankara
Turkey

Deputy Chairman: Mr Robert E. Henderson
Acting Chief
Advanced Propulsion Division
WL/POT
Wright Patterson Air Force Base
Ohio 45433-6563
United States

PROGRAMME COMMITTEE

Dr Clifford A. Moses (Chairman)
South West Research Institute
P.O. Box 28510
San Antonio, TX 78228-0510
United States

Prof. M. Bardon
Royal Military College of Canada
(RMC) Dept of Mechanical Engineering
Kingston, Ontario, K7K 5L0
Canada

Prof. Corrado Casci
Dipartimento di Energetica
Politecnico di Milano
Piazza Leonardo da Vinci 32
20133 Milano
Italy

I.A. Louis de Chanterac
DRET/Service des Recherches
Groupe 7
Chef de la Division Machines Thermiques
26 Boulevard Victor
004600 Armées
France

Prof. Ronald S. Fletcher
Pro Vice Chancellor of Cranfield
Institute of Technology
Cranfield, Bedford MK43 0AL
United Kingdom

Prof. Dr Dietmar K. Hennecke
Fachgebiet Flugantriebe
Technische Hochschule Darmstadt
Petersenstrasse 30
W-6100 Darmstadt
Germany

Prof. Dr Petros Kotsiopoulos
Hellenic Air Force Academy
Chair of Propulsion Systems
Dekelia, Attaki
Greece

Prof. Mario N.R. Nina
CTAMFUL
Instituto Superior Tecnico
Avenida Rovisco Pais
1096 Lisboa Codex
Portugal

Professor Carlos Sanchez Tarifa
Sener
Ingenieria y Sistemas S.A.
Pza. Manuel Gomez Moreno
Edificio Bronce
28020 Madrid
Spain

HOST NATION COORDINATOR

Mr Bruno della Vecchia

PANEL EXECUTIVE

Dr Ing. E. Riester

Mail from Europe:
AGARD—OTAN
Attn: PEP Executive
7, rue Ancelle
F-92200 Neuilly-sur-Seine
France

Mail from US and Canada:
AGARD—NATO
Attn: PEP Executive
Unit 21551
APO AE 09777

Tel: 33(1)47 38 57 85
Telex: 610176F
Telefax: 33 (1) 47 38 57 99

ACKNOWLEDGEMENT

The Propulsion and Energetics Panel wishes to express its thanks to the National Authorities from Italy for the invitation to hold this meeting in Fiuggi, Italy, and for the facilities and personnel which made this meeting possible.

Contents

* Paper available and distributed but not presented at the Symposium.

"Easy access to advanced knowledge and technical information on COMPACT DISK. . . . "

The new "NATO DISK"

The NATO-PCO DATABASE *and* the AGARD AEROSPACE DATABASE on CD-ROM

2 important databases of interest to scientists and engineers working in universities, research institutes and industry

We are pleased to announce that the enhanced version of the "NATO DISK", i.e. the computer-readable COMPACT DISK (CD-ROM) has just become available. It contains the first major update of the NATO-PCO DATABASE with its 40.000 bibliographical records referring to non-military scientific/technical literature generated with the sponsorship of the NATO Science Committee, and - for the first time - a special version of the AGARD AEROSPACE DATABASE providing access to the aerospace literature resulting from the programmes of NATO's Advisory Group for Aerospace Research and Development.

With the easy-to-follow menu options of the retrieval software, access to data is simple and fast! The data is well-structured and the presentation is pleasant while functional. The software CD-ANSWER - (c) Copyright DATAWARE Technologies Inc. - which comes with the CD-ROM, received the prize for "The Best CD-ROM Retrieval Software of 1990". It functions in ENGLISH, FRENCH and GERMAN. *There is no need to learn a complex search language.*

The CD-ROM can be used with standard Personal Computer equipment (PC XT/AT or 100% compatible, minimum 512 KByte RAM and with MS-DOS/PC-DOS version 3.0 and above) including a CD-ROM drive.

The NATO-PCO DATABASE

The NATO-PCO DATABASE -(c) Copyright WTV GmbH, Germany - is a reference database. It covers more than 20 years of non-military scientific/technical meetings and publications in the NATO ASI SERIES, sponsored by the NATO Science Committee. The NATO ASI SERIES - which is the official vehicle for publication of the results of NATO Advanced Study Institutes, NATO Advanced Research Workshops and other high-level scientific/technical meetings - is published by KLUWER ACADEMIC PUBLISHERS (The Netherlands), PLENUM PUBLISHING Corporation (USA) and SPRINGER-VERLAG (Germany)

The NATO-PCO DATABASE contains full references (with keywords and/or abstracts) to more than 40.000 contributions from international scientists of high repute.

The database covers a broad spectrum of scientific disciplines: *LIFE SCIENCES, ECOLOGY, MEDICINE, CHEMISTRY, GEOSCIENCES, ASTRONOMY, MATHEMATICAL AND PHYSICAL SCIENCES, BEHAVIOURAL SCIENCES, MATERIALS SCIENCES, ENGINEERING, SYSTEMS and COMPUTER SCIENCES.*

The AGARD AEROSPACE DATABASE

This bibliographic database generated by PCO in co-operation with NASA (USA) and AGARD (France) provides information on thousands of AGARD-sponsored publications - conference proceedings, AGARDographs (major works of long-lasting interest), lecture series, reports and advisory reports - published from about 1960 to 1991. As is the case for the NATO-PCO DATABASE, the AGARD AEROSPACE DATABASE includes details not only of the complete publications but also of the papers contained in them (up to 40 or more in a conference proceedings).

AGARD (The Advisory Group for Aerospace Research and Development) is an agency of NATO based in Paris. Its mission is essentially to interchange information about R&D in aerospace within and between the NATO nations. AGARD's areas of activity cover: *AEROSPACE MEDICINE, AVIONICS, FLIGHT MECHANICS, ELECTROMAGNETIC WAVE PROPAGATION, FLUID DYNAMICS, GUIDANCE AND CONTROL, PROPULSION AND ENERGETICS, STRUCTURES AND MATERIALS, and TECHNICAL INFORMATION.*

The price for the CD-ROM containing both databases is DM 1.140.-- or USD 790.00 (excluding tax).
Updates are planned to appear on a yearly basis.

The "NATO DISK" is available from:

NATO ASI SERIES Publication Coordination Office (PCO),
(Information Office of WTV GmbH, Germany)
Elcerlyclaan 2, B-3090 Overijse / BELGIUM
Tel. +32-2-687.66.36 Fax. +32-2-687.98.82

en français au verso

Le nouveau "DISQUE SCIENCE & TECHNOLOGIE OTAN"

La base de données du Bureau de coordination des publications (PCO) de l'OTAN et la Base de donneés aérospatiales de l'AGARD mises sur disque compact (CD-ROM):

Ces deux bases de donneés importantes présentent un très grand intérêt pour les scientifiques et les ingénieurs qui travaillent dans les universités, les instituts de recherche et l'industrie.

Nous avons le plaisir d'annoncer que la version améliorée du "Disque Science & Technologie OTAN"; c'est à dire le disque optique compact (CD-ROM) lisible par ordinateur, est disponible depuis peu. Il contient la première mise à jour importante de LA BASE DE DONNÉES DU BUREAU DE COORDINATION DES PUBLICATIONS DE L'OTAN (NATO-PCO) avec ses 40.000 entrées bibliographiques renvoyant à la littérature scientifique non militaire produite sous l'égide du Comité Scientifique de l'OTAN et, pour la première fois, une version spéciale de la "BASE DE DONNÉES AÉROSPATIALES" de l'AGARD donnant accès à la littérature aérospatiale qui découle des programmes du Groupe consultatif pour la recherche et les réalisations aérospatiales (AGARD) de l'OTAN.

Grace à la facilité d'exploitation offerte par les options sur menu du logiciel d'extraction, l'accès aux données est simple et rapide! La structure de ces données est excellente et leur présentation agréable tout en étant fonctionelle. Le logiciel CD-ANSWER - (c) Copyright DATAWARE Technologies Inc. - , qui accompagne le disque compact a reçu le prix du "Meilleur logiciel d'extraction de disque compact CD-ROM" pour 1990. Il fonctionne en ANGLAIS, en FRANÇAIS et en ALLEMAND. *Il n'impose pas l'apprentissage d'un langage de recherche compliqué.*
Le disque optique peut être utilisé avec un ordinateur personnel standard (PC XT/AT 100 % compatible, avec RAM de 512 kilo-octets minimum et MS DOS/PC DOS version 3.0 minimum), comportant un lecteur de disque optique.

BASE DE DONNÉES (NATO-PCO)

La BASE DE DONNÉES NATO-PCO, dont les droits d'auteur sont détenus par la société allemande WTV GmbH, est un outil de référence. Elle couvre plus de vingt années de réunions et de publications scientifiques et techniques non militaires de la série ASI de l'OTAN, tenues ou émises sous l'égide du Comité Scientifique de l'OTAN. Cette série, véhicule officiel de publication des résultats des instituts d'études avancées et des ateliers de recherche de pointe de l'OTAN et autres réunions scientifiques et techniques de haut niveau, est publiée par les maisons d'édition KLUWER ACADEMIC PUBLISHERS des Pays-Bas, PLENUM PUBLISHING Corporation des États-Unis et SPRINGER-VERLAG d'Allemagne.

La BASE DE DONNÉES NATO-PCO contient les références intégrales (y compris les mots clés/résumés) concernant plus de 40.000 articles rédigés par des scientifiques internationaux de haut niveau.

La base de données couvre un large éventail de disciplines scientifiques: *SCIENCES DE LA VIE, ECOLOGIE, MEDECINE, CHIMIE, SCIENCES DE LA TERRE, ASTRONOMIE, SCIENCES MATHEMATIQUES ET PHYSIQUES, SCIENCES DU COMPORTEMENT, SCIENCES DES MATERIAUX, TECHNOLOGIE, SCIENCES DES SYSTEMES ET DE L'INFORMATIQUE.*

BASE DE DONNÉES AÉROSPATIALES DE L'AGARD

Cette base de données bibliographique créée par le Bureau de coordination des publications (PCO) en coopération avec la NASA (États-Unis) et l'AGARD (France) fournit des informations sur des milliers de publications réalisées sous l'égide de l'AGARD et éditées entre 1960 et 1991 environ: procès verbaux de conférence, AGARDographies (travaux importants présentant un intérêt sur une longue période), cycles de conférences, comptes rendus et rapports consultatifs. Comme dans le cas de la BASE DE DONNÉES NATO-PCO, la BASE DE DONNÉES AÉROSPATIALES DE L'AGARD inclut le détail non seulement des publications complètes, mais aussi des communications qu'elles renferment (jusqu'à 40 ou plus dans un procès verbal de conférence).

L'AGARD (Groupe consultatif pour la recherche et les réalisations aérospatiales) est une agence de l'OTAN dont le siège est à Paris. Sa mission consiste essentiellement à échanger des informations de R et D dans le domaine aérospatial tant à l'intérieur des pays de l'OTAN qu'entre eux. Ses secteurs d'activité couvrent:
LA MEDECINE AEROSPATIALE, AVIONIQUE, LA MECANIQUE DU VOL, LA PROPAGATION DES ONDES ELECTROMAGNETIQUES, LA DYNAMIQUE DES FLUIDES, LE GUIDAGE ET LE PILOTAGE, LA PROPULSION ET L'ENERGETIQUE, LES STRUCTURES ET LES MATERIAUX ET L'INFORMATION TECHNIQUE

Le prix hors taxe du CD-ROM contenant les deux bases de données est de 1140 DM ou 790 $ US (soit environ 4000FF).
Il est prévu de procéder à une mise à jour annuelle.

Il est possible de se procurer le "DISQUE SCIENCE & TECHNOLOGIE OTAN" auprès du:

NATO ASI SERIES Publication Coordination Office (PCO),
(Bureau d'information de la société WTV GmbH, Allemagne)
Elcerlyclaan 2, B-3090 Overijse / BELGIQUE
Tel. +32-2-687.66.36 Fax. +32-2-687.98.82

English version overleaf

Technical Evaluation Report

by

George Opdyke Jr
Dykewood Enterprises
5 Lordship Road
Stratford
Connecticut 06497
United States

1. INTRODUCTION

There has been little fundamental change in the challenges in gas turbine combustor design since the AGARD Symposium on Combustion and Fuels in Gas Turbine Engines held in Chania, Crete, Greece in 1987, and reported in AGARD Conference Proceedings 422. However, the understanding of the nature of the combustor design challenges has improved in the intervening years, as well as the quality of the design and development tools. There have also been some demonstrations of possible design solutions for problems.

The papers presented in this 81st AGARD Symposium include a discussion of design goals and objectives, reviews of analytical and physical design tools and techniques, descriptions of new demonstration test rigs, and explanations of solutions for some combustor design problems. This symposium volume will be a significant addition to the gas turbine combustion literature, and some concepts described herein can be of immediate practical use.

The papers in this Symposium can be divided into five categories:

- Design Goals and Technology Overview
- Pollutant Formation and Emissions
- High Temperature Fuel and Fuel Systems
- Fuel Atomization
- Combustor Research — Modelling, Design and Operation.

This is a somewhat different category selection than in the table of contents of this volume, and it provides an additional way of referring to the subject matter. Each subject is discussed in Sections 2 through 6, in order, and they are tabulated, with indications of their major content, in Tables I to V. The author referred to in the charts and in the text of this report is the first author listed on the paper, not necessarily the first author listed in the Table of Contents.

2. DESIGN GOALS AND TECHNOLOGY OVERVIEW

Schumann, in his Keynote Address, provided considerable hard data about the impact of gas turbine emissions on various portions of the atmosphere. While absolute quantities of emissions from air traffic are small, their impact is significant. Nitric oxide emissions reduce ozone levels above the tropopause (approx. 12-14 km, or 35-40 thousand feet), but increase ozone levels below that altitude. The future strong increase in air traffic will further increase NOx and water vapour in the stratosphere, even though the total fleet fuel consumption will increase only moderately because of the projected increase in propulsive efficiency. There must be a significant decrease in engine NOx emissions, particularly at high altitudes, in order to counteract the effect of increased fuel usage. While some reduction of the harmful impact of aircraft emissions on the stratosphere could conceivably be obtained by appropriate air traffic control, the bulk of the reduction is the responsibility of the gas turbine combustor designer. Since the contribution from military aircraft is not large, probably less than 25% of the aircraft total, and since much of the military aircraft operation is below the troposphere, a decrease in emissions from this source has a small impact. This leaves the major emission reduction effort on the shoulders of the designers of engines for high flying, long range, commercial aircraft.

Clouser (Paper 1) pointed out that because military aircraft procurement is declining, both commercial and military technology development is being aimed at dual use. The military programmes for high technology demonstrator engines and advanced component and materials development continue to be funded in the United States by the Integrated High Performance Turbine Engine Technology (IHPTET) programme, which requires significant financial contribution from industry. The major goal has remained constant from the programme's inception several years ago: to double gas turbine performance in a 15 to 18 year period. Combustor design goals are based on near stoichiometric operation at high combustor inlet temperature, with a 50% reduction in weight, and with no loss in other significant operating parameters. While low emissions are not at the top of the priority list (and low NOx is not compatible with the high reaction temperatures associated with stoichiometric combustion), the technology required by the IHPTET goals is readily adaptable to low emission combustor designs, and this adaptability will be a requirement for the survival of gas turbine engine manufacturers in the 21st century.

In his discussion of the combustor design requirements for the next generation of supersonic civil aircraft, Lowrie (Paper 2) emphasized that the high combustor inlet temperatures at supersonic cruise conditions create difficult targets for combustor hardware life and for low emissions. This temperature would be approximately 950K (1250 F), and would be maintained for the major part of the engine operation. While the stator exit temperature would not be abnormally high, about 1650K (2510 F), the reaction temperature of a diffusion flame combustor is clearly unacceptably high for the ultra low NOx emissions required for operation in the stratosphere. Lowrie recommends that the NOx target should be less than an Emission Index of 5g/kg, and suggests that the probable combustor solution would be a lean, premixed, staged combustor design, with ceramic matrix composite walls, operating at an equivalence ratio of near 0.3.

Presented at an AGARD Meeting on 'Fuels and Combustion Technology for Advanced Aircraft Engines', May 1993.

Biddle (Paper 16) summarized the high temperature fuel and fuel system problem very nicely by evaluating the heat load of advanced fighter airframes. They concluded that both a high temperature fuel (about 650 K capability) and a fuel recirculation system will be required. Supersonic flight conditions were covered.

These four papers, which are listed in Table I, very nicely summarize the design requirements for future aircraft gas turbine combustors. Since some requirements are incompatible, combustor designs must be tailored for the specific application, but the technology required has very much in common.

The technology objectives include:

- Low emissions, particularly ultra low NOx
- Combustor inlet temperature of 950K
- Fuel bulk temperatures up to 750K (900 F) at the fuel injector
- Equivalence ratios from lean to near stoichiometric
- Short, light long life combustor liners with minimum cooling air and advanced materials
- Little or no reduction in other performance requirements like cold day or high altitude ignition or combustor stability
- Low pattern factor at the turbine inlet

All this is to be done in the face of declining development funding, so the combustor design has to be close to right the first time. The papers in the following sections help to explain how these very difficult goals might be met, at least in part.

3. POLLUTANT FORMATION AND EMISSIONS

The first series of papers on this subject dealt with modelling of pollutant formation and consisted of four papers. Investigators at Leeds University (Paper 3) showed that under lean premixed flame conditions where thermal NOx does not form, small amounts of prompt NOx will form, either as hydrocarbon prompt NOx or via the nitrous oxide route. The coherent flamelet model, tested by investigators at the Ecole Central Paris (Paper 4), gave only fair quantitative predictions of CO, and needs further improvement. The flamelet model evaluated by Alizadeh and Moss (Paper 7) gave NO and temperature predictions qualitatively similar to those obtained with equilibrium predictions. Soot predictions were uncertain, although the predictions of the spatial distributions of soot compared reasonably with measurements in the test combustor. They show that soot formation can extend into the intermediate zone between the primary jets, where the local temperatures can quickly drop to levels which result in slow carbon oxidation rates. Carvalho (Paper 8) evaluated three soot formation and oxidation models and concluded that none were good enough if quantitative results were desired.

There were seven papers dealing with emissions, but having a point of view which is readily applicable to combustors. Drennan (Paper 28) has set up a test rig at Irvine where a simplified, but realistic, combustor can be operated at practical gas turbine conditions, and baseline emission data has been taken which is representative of typical current combustors. The data show that the effluent from the primary zone forced between the primary jets is a source of hydrocarbon and CO reaction quenching at low inlet temperatures and NOx production at high inlet temperatures, somewhat similar to the observation of Alizadeh and Moss relative to soot formation and quenching. Increased atomizing air was shown to decrease NOx, while a larger SMD was observed to increase NOx, even though there is no obvious reason for this latter effect.

Segalman (Paper 29) reviewed the status of the fuel staged combustor being developed for the V2500 engine by Pratt and Whitney. The staging is done axially with airblast injectors used in both the pilot and the main stages. The NASTAR computer code was used in support of a test rig programme to determine aerodynamic influences within the combustor and to predict temperature distributions. While this code could not directly determine emissions, it was possible to make educated inferences concerning combustion characteristics and low emissions potential, thus saving considerable development time. The result was good altitude relight, combustor efficiencies above 99.9% over the operating range, and satisfactory radial and circumferential temperature distributions. At take off, NOx was reduced by half, compared to the conventional combustor, and engine tests proved that the engine EPAP NOx is only half of the current ICAO requirements. The tests also showed the NOx reduction potential of fuel staging even though main stage premixing was not used.

At SNECMA, Meunier and others (Paper 30) ran tests on a five injector annular sector combustor using variable swirlers to adjust the primary airflow. This method was used to tailor the primary zone equivalence ratio and hold it between 0.6 and 1.0 over the operating range, thereby assuring low smoke, good stability and relight, while making it possible to reduce NOx. Diluent holes were eliminated, the liner length was reduced 20%, and it was noted that primary holes which were only ½ an annulus height downstream of the swirlers gave a wider stability range than holes at a location further downstream.

Tilston and others, at Pyestock (Paper 32), tested three very short (primary zone) combustors, modified to thirty different configurations, which were fuelled with air assist atomizers. They concluded that regardless of the primary zone equivalence ratio NOx is formed only at a local equivalence ratio close to stoichiometric, and the thermal NOx reduction that occurs when the overall equivalence ratio is leaned is caused by reduced residence time, not by a substantial reduction in reaction temperature. There was no evidence that any combustion took place at mixtures leaner than 0.90 equivalence ratio. They conclude that for a diffusion flame combustor with a primary zone equivalence ratio reduced from near stoichiometric to about 0.5, a 30% to 40% NOx reduction is possible. This is somewhat less than that demonstrated by the Pratt and Whitney staged combustor.

Salvá and López (Paper 33) tested the interesting concept of injection of hydrogen into a conventional diffusion flame can combustor, fuelled with a simplex injector, with the primary equivalence ratio leaned to 0.5 or less. Without hydrogen injection, NOx would decrease, particularly if the reference velocity was increased, but CO would increase to unacceptably high values. With the addition of about 2% hydrogen premixed into the primary zone airflow, the combustor efficiency improves, while NOx is increased very little. The largest part of this decrease in CO is caused by an improvement in chemical kinetics. This concept could be very effectively combined with a variable area primary zone.

Another experimental programme, this one at The University of Leeds, reported by Andrews (Paper 24), showed that swirler and fuel injector designs which gave low NOx in a research combustor with gaseous fuel could also give low NOx with kerosene fuel. In one instance, liquid kerosene gave lower NOx than natural gas. One key is to insert the fuel into the combustor at the point where turbulence dissipation is greatest, i.e., in shear layers. This can mean that CFD modell-

ing can be misleading if precise fuel placement is important and this boundary condition is not properly accounted for in the calculation. Also, it appears that for a lean burn combustor, backside impingement cooling may be sufficient to cool the liner walls. Andrews suggested that equivalence ratios of 0.4 and 0.5 be considered for lean burn combustor styles. Santavicca (Paper 22) presented an interesting paper describing an experimental study to determine the lean limit and emissions of a simple kerosene fuelled, prevaporized, premixed combustor. They found that the NOx emissions were the same whether the fuel and air were well mixed or poorly mixed, but the well mixed case had the better lean limit. A phenomenological explanation of this anomaly, based on combustion of "pockets", was given.

4. HIGH TEMPERATURE FUELS AND FUEL SYSTEMS

There were a total of seven papers which addressed the problem of high temperatures in the fuel delivery system, a problem solvable either with fuels that do not break down at temperatures up to 750K, or by fuel systems so thermally isolated from the combustor inlet air or from other heat sources that a lower temperature capability fuel can be used. Obviously, a combination of both approaches is possible. These papers are listed in Table III.

Ianovski (Paper 44) proposed that endothermic fuels can be a solution for the cooling of elements of hypersonic vehicles, and the resultant gaseous products of the decomposed liquid fuels, which consist primarily of hydrogen and light hydrocarbons, will improve the combustor stability, thereby permitting satisfactory lean burn operation. Appropriate catalysts can markedly improve the fuel decomposition rate, and the cooling capability of the fuel is thereby doubled at temperature levels near 1200K.

Peloche and Asensio (Paper 17) pointed out that fuel thermal instability is caused by compounds in the fuel which can be reduced or eliminated by percolation of the fuel through an absorbent clay. The best clays tested were able to increase the fuel break point by about 50 degrees C. Edwards (Paper 18) reviewed results of tests at the USAF Wright Laboratory designed to reach a better understanding of fuel instability. It appears that a fuel's tendency to oxidise is often inversely proportional to its tendency to form deposits, but additional work is needed to complete this programme. However, it appears possible to develop an additive package to increase the thermal stability of JP-8 by 55 degrees C.

Katta, et al. (Paper 19) reported on the development of two global chemistry models for fuel stability, and noted that the models are not yet sufficient to predict fuel oxidation and deposition rates simultaneously, but the global chemistry model shows promise. For a fuel to be thermally stable at 750K, it appears that all oxygen must be removed from the fuel, and the research is not far enough along to know if it can be done with additives.

Stickles, et al. (Paper 20) reported on The U.S. Navy High Temperature Fuel Nozzle Program which was aimed at a fuel injector design which would operate satisfactorily at a combustor inlet air temperature of 1144K and a fuel temperature of 450K. JP-5 fuel was used as the test fuel. Although much care was taken to shield the dual orifice injector from the hot air, and the fuel wetted surfaces were polished to minimize coke deposition, the result was disappointing. Apparently coke had formed in the fuel itself, had not deposited on the passage walls, but then accumulated in the swirl slots, which had not been redesigned.

Some of the advantages of the use of CFD in the detailed design of airblast injectors, particularly those for small engine combustors, was described by McCaldon (Paper 21). The airflow distortions approaching and within the injector swirlers plus in the flow field within the combustor resulting from the swirlers can both be useful in design. Pratt and Whitney Canada has been successful in avoiding significant clogging of fuel metering orifices with linear dimensions as small as 200 microns by keeping wetted wall temperatures below 480K.

5. FUEL ATOMIZATION

There were five papers in this group, four dealing with spray modelling and experiments, plus one paper describing a new type of fuel injector.

Tests at Imperial College, reported by Perez-Ortiz, et al., in Paper 34, involved observations of flames stabilized by various flameholders in a duct, fuelled by premixed methane plus atomized kerosene injected at several locations, both at uniform and pulsed flow rates. The most important conclusion was that pulsed kerosene injection can induce large amplitude combustion oscillations in normally smooth burning flames and damp large amplitude oscillations at rough burning conditions. Not much effort has yet been expended to model the flame characteristics observed. Mularz (Paper 35) described experiments done at NASA, Lewis, to measure spray characteristics, and described details of the CFD code under development to predict these characteristics. Code validation with the experimental data has yet to be done. The code is named ALLSPD, and is a variant of TEACH, and a two dimensional version should be available during the summer of 1993.

Hebrard (Paper 36) reported on the development of a similar code at ONERA, and showed a good correlation between prediction and measurement of drop trajectories from an air blast injector. Data was taken with a high speed video camera. A Weber number relationship was given to predict whether a droplet will bounce or film when hitting a wall, and it was also observed that droplets burn singly, in groups, or en masse.

Another code for modelling turbulent, evaporating sprays has been developed at University Karlsruhe (Paper 36), and it was reported that it agrees well with experiments measuring droplet diameter and drop concentrations. The code is Eulerian and contains transport equations for droplet heating and evaporation and can handle recirculating flows. It gives good agreement with Lagranglan calculations, and can be readily incorporated into existing codes.

Whitlow (Paper 38) described recent experimental studies on effervescent atomizers. These atomizers produce a fine spray over a wider range of flows than either a pressure atomizer or an air blast atomizer because both liquid and air are ejected through the same exit, and the atomization is a function of both the liquid flow and the air flow. Tests were run on two basic designs: plain orifice and conical sheet atomizers. In both cases, the Sauter Mean Diameter decreases with an increase in either the air/liquid ratio or the operating pressure. Both designs had a wide spray angle. A variety of design parameters were varied and their effects on SMD and drop size distribution were measured.

These papers are listed in Table IV.

6. COMBUSTOR RESEARCH – MODELLING, DESIGN AND OPERATION

This category of papers is the largest of the Symposium, and contains reviews of investigations of methods to handle the design of a combustor or a portion thereof. There are 13 papers in this group and they are listed in Table V.

Maidhof and Janicka (Paper 10) described the calculation of the flow and scalar fields of an axisymmetric non-premixed combustor. The code includes a radiation model, a diffusion flame combustion model using either chemical equilibrium or laminar flamelet schemes, a NOx model, which includes the effect of radiation on NOx, and a turbulence model, where Reynold's stress was found to be superior to eddy viscosity closure. The non linear equation system is solved by a time marching iteration, which converges in about 400 iterations.

Martino et al. (Paper 11) describe a method of calculating steady, 3D, two phase turbulent reacting flows with irregular boundaries, and they compare the calculated results with measurements from a reverse flow annular vaporizing combustor. The agreement was fair to good, and they feel that the code can be used with confidence for the design and development of combustors. There is no calculation of wall temperatures or for soot or gaseous emissions, however.

Mongia reviewed in Paper 12 the 23 combustors which he and his colleagues have designed in the past two decades using some form of numerical combustor modelling. He concludes that second order closure models, while useful in understanding many combustion phenomena, are not sufficiently accurate for quantitative design. He recommends a hybrid technique where empirical, semi-analytical and quasi 1-D analyses are used in conjunction with 2-D and 3-D computational models, and then use the best of both types to go from preliminary design and through development to the final combustor design. This permits all aspects of combustor design to be approached in a consistent manner, and builds a useful design data base.

Hu and Prociw (Paper 14) described the usefulness of a 3-D computer code to predict the flow field of a real combustor, and feel that despite some shortcomings it is a valuable tool for combustor design. It can be reasonably accurate, at least for predicting details of the flow field. Several practical design problems are shown which are amenable to solution. At SNECMA, a 3-D code named DIAMANT was successfully used in the design of a fairly conventional afterburner, according to Dejeu, et al. (Paper 15). The model consisted of 60,000 nodes, and the code included droplet Sauter Mean Diameter and velocity, turbulence, eddy breakup and PDF elements.

Ballal described in Paper 23 a study intended to predict the lean limit of a practical gas turbine combustor by using test data from a simplified research combustor, and several combustion models were compared for accuracy of their prediction of lean blowout. While lean blowout was correlated with partially stirred reactor theory, and Swithenbank's dissipation gradient approach offered a possibility of an a priori calculation for the research combustor, it was found that the flame characteristic at lean blowout in the research combustor was different than that in the engine combustor, making a general prediction "challenging".

An experimental study with a small can combustor has been conducted by Dini (Paper 25) to assess the advantages of the use of hydrogen as a fuel for small gas turbines. These could be used in automobiles, helicopters and even turboramjets. His tests included the use of hydrogen and air, hydrogen, oxygen and steam, and hydrogen, natural gas and air. The first combination results in higher NOx unless run lean, the second gives no NOx, and the third, called "Hythane", produces low NOx. When steam is used, a closed cycle is preferred, and the hydrogen and oxygen should be stored in liquid form.

Two papers discussed the absolute necessity of combustor test rigs.

Rosfjord (Paper 26) described a unique test facility to assess the tolerance of a fuel staged combustor to rapid changes in air and fuel flows, with the resultant fuel flow redistribution which occurs in the system. Both slow and snap accelerations and decelerations plus cyclic operation can be programmed by the control computer. Sectors of operating annular combustors, of fuel systems or of combustor components can be tested.

Afterburner test rigs at Fiat, discussed by Riccardi et al. (Paper 27), demonstrated that where very high gas temperatures may cause important mechanical integrity problems, analytical computer codes are not completely satisfactory, making development test rigs mandatory. Well defined design practices are also not sufficient. Fiat has found (as have other companies) that water analogue test rigs are inexpensive, very fast and easy to use, and will give at least a qualitative description of the flow patterns within the test unit. The same perspex models used in the water rig can be used in a simple airflow rig to measure pressure drops and flow coefficients. Fiat also uses sector combustion rigs for measurement of altitude performance, and then finally uses full scale afterburner test rigs prior to engine testing. They claim that these rigs give reliable results at lower cost than the detailed CFD codes required plus the powerful computers needed to operate them.

Doerr and Hennecke (Paper 39) reported on a very nice experimental programme to determine the best way to mix in the quench zone of a Rich-Quick Quench-Lean combustor design. The major conclusions were that there is an optimum momentum flux ratio, and opposing jets should not impact on one another. The spacing/hole diameter ratio should be small, and it is best if the jets are staggered. Increasing pressure drop does not necessarily help much. The programme is now being enlarged to include the effects of orifice size, shape and number. Hassa (Paper 41) measured droplet and gas velocities in a cylindrical combustor fed by an airblast atomizer with a corotating swirl. He showed a high speed video which illustrated that the flame was intermittent and ragged, even at stoichiometric. In this combustor, a considerable amount of drop vaporization occurred before combustion, with about 85% evaporating within 45mm, before luminous flames could be seen. The SMD of the spray tended to increase with distance downstream, since the smaller droplets evaporate so quickly.

Jeckel and Wittig (Paper 42) described the research combustor installed at Karlsruhe for extended benchmark measurements. It is a jet stabilized combustor, and measurements of time averaged velocity, temperature and species show that the three dimensional effects caused by the turbulence in this combustor are of major significance. A different type of research combustor was described by Vermeulen (Paper 43), in which primary air jets were acoustically controlled to increase mixing. The pattern factor was thereby improved by up to 20%, without an appreciable change in

pressure loss. The major reason for the improvement was increased flow blockage caused by the acoustically increased jet penetration. At higher load levels there was a lesser, unfortunately unexplained, pattern factor improvement.

7. CONCLUSIONS AND EVALUATION OF THE MEETING

The 81st PEP Symposium and the coincident panel meetings were attended by 116 delegates from 13 NATO countries and from three non-NATO countries. This is a decrease from the last Combustion Symposium (PEP 70) held in Crete, apparently caused by the depressed economic condition in much of the world. Nonetheless, the papers were of good quality and elicited considerable discussion, both formal and informal. The resulting information exchange among the combustion experts at the Symposium added significantly to its value. The papers contained considerable new information and some authors pointed out failures and shortcomings in their investigations, plus limitations inherent in their results, demonstrating a frankness which added greatly to the understanding of the subjects. It is clear that we are far from being able to design a satisfactory combustor without a development programme, but that programme can be shorter now than two decades ago, when combustor modelling was in its infancy.

The subjects covered in the Symposium were planned to help combustor designers understand the combustion phenomena which will occur under future engine operating conditions, and to suggest approaches to overcome the many design difficulties which are being and will be encountered. The Symposium met its objective of reviewing progress made in modelling pollutant formation and combustor performance and design, high temperature fuel systems and fuel atomization, and combustor research on phases of combustor operation. The questions and discussions on these subjects were a significant addition to the papers themselves, and these questions are included in this Symposium volume. The delegates appreciated the coordination of the meeting by the Propulsion and Energetics Panel, and by the Programme Committee and the AGARD staff.

8. RECOMMENDATIONS FOR FUTURE MEETINGS

Future combustion Symposia should primarily feature subjects connected with emissions reduction, particularly for aircraft operation at high altitude, at high flight Mach numbers, and with advanced, high pressure ratio engines. These should include both advancements in emissions modelling and in understanding of the combustion and post combustion reactions involved, as well as descriptions of low and ultra low NOx combustor designs, both successful and unsuccessful, particularly if combustor models have been used effectively in their designs. Staged combustors would be of particular interest. Secondly, subjects dealing with advanced, high pressure, high temperature rise combustors should be featured, including the performance of fuel injection systems using hot fuel. This should also include advanced ignition and wall cooling techniques plus experience gained with advanced high temperature combustor materials. In short, reports on progress in meeting the combustor design and performance goals described in this Symposium should be the subjects for the next Symposium.

Table I
Major subjects contained in the category
Design goals and technology overview

No.	Authors	Major subject
Keynote	Schumann	Gas turbine emission data — atmospheric effects Emission reduction objectives — some approaches
1.	Clouser, Kamin	Military (IHPTET) combustor objectives. Status. Review of design difficulties and possibilities
2.	Lowrie	Emission, noise, durability needs for advanced SST
16.	Biddle, Croswell	Goals for high temperature fuel and fuel system development for advanced fighter aircraft

Table II
Major subjects in the category
Pollutant formation and emissions

No.	Authors	Emissions	Pollutant formation	Models, analysis	Bench tests	Comb tests
3.	Dupont, et al.		x	x	x	
4.	Djavdan, et al.		x	x		
7.	Alizadeh, Moss		x	x		
8.	Carvalho, et al.		x	x		
22.	Santavicca, et al.	x		x		x
24.	Andrews, et al.	x		x		x
28.	Drennan, et al.	x				x
29.	Segalman, et al.	x		x		x
30.	Meunier, et al.	x				x
32.	Tilston, et al.	x	x	x	x	
33.	Salvá, López	x	x			x

Table III
Major subjects in the category
High temperature fuel and fuel systems

No.	Authors	Fuels	Fuel Systems	Models	Tests	Hardware
17.	Peloche, Asensio	x			x	
18.	Edwards, et al.	x			x	
19.	Katta, et al.	x		x	x	
20.	Stickles, et al.		x		x	x
21.	McCaldon, et al.			x		x
44.	Ianovsky	x	x		x	

Table IV
Major subjects in the category
Fuel atomization

No.	Authors	Sprays, Models	Sprays, Tests	Injector Design	Injector Tests
34.	Perez-Ortiz, et al.		x		
35.	Mularz, et al.	x	x		
36.	Hebrard, et al.	x	x		x
37.	Wittig, Hallmann	x	x		
38.	Whitlow, Lefebvre			x	x

Table V
Major subjects in the category
Combustor research — modelling, design and operation

No.	Authors	Combustor Models	Combustor Design	Combustor Perf.	Combustor Tests	Combustor Test rigs
10.	Maidhof, Janicka	x				
11.	Di Martino, et al.	x				
12.	Mongia	x	x	x		
14.	Hu, Prociw	x			x	
15.	Dejeu, et al.	x				
23.	Ballal, et al.	x	x	x	x	
25.	Dini		x	x	x	
26.	Rosfjord, Cohen		x		x	x
27.	Riccardi, et al.		x			x
39.	Doerr, Hennecke		x	x		
41.	Hassa, et al.		x	x	x	
42.	Jeckel, Wittig			x	x	
43.	Vermeulen, et al.		x	x	x	

ON THE EFFECT OF EMISSIONS FROM AIRCRAFT ENGINES ON THE STATE OF THE ATMOSPHERE

U. Schumann

Deutsche Forschungsanstalt für Luft- und Raumfahrt (DLR)
Institut für Physik der Atmosphäre
D-8031 Oberpfaffenhofen, Germany

ABSTRACT

Emissions from aircraft engines include carbon dioxide, water vapour, nitrogen oxides, sulphur components and various other gases and particles. Such emissions from high-flying global civil subsonic airtraffic contribute to anthropogenic climate changes by increase of ozone and cloudiness in the upper troposphere, and by enhanced greenhouse effect. The absolute emissions by airtraffic are small (a few percent of total) in comparison to surface emissions. However, the greenhouse effect of emitted water and of nitrogen oxides at cruise altitude is large in comparison to that of the same emissions near the earth's surface because of relatively large residence times at flight altitudes, low background concentrations, low temperature, and large radiative efficiency. At present, it appears that the emissions of nitrogen oxides have changed the background concentration in the upper troposphere in between 40°N and 60°N by 100 %, causing an increase of ozone by about 20 %. Regionally the observed annual mean change in cloudiness is of order 0.4 %. The resultant greenhouse effect of changes in ozone and thin cirrus cloud cover causes a climatic surface temperature change of the order 0.01 to 0.1 K. These temperature changes are small in comparison to the natural variability. Recent research indicates that the emissions at cruise altitude may increase the amount of stratospheric aerosols and polar stratospheric clouds and thereby may have an impact on the atmospheric environment, to an yet unknown degree. Airtraffic is increasing by about 5 to 6 % per year, fuel consumption grows by about 3 % per year. Moreover, the climatic changes due to airtraffic enhance other environmental problems originating, e.g., from anthropogenic carbon dioxide or methane emissions. Hence, airtraffic induced emissions are of growing importance. This calls for the development of efficient and low-emission propulsion systems and other means to reduce the emissions. This paper surveys the state of knowledge and describes several items of results from recent and ongoing research.

1. Introduction

Until fairly recently, the environmental effects resulting from aircraft exhaust emissions have been a minor item in the general debate on the environment. However, the growing awareness on global climate changes has brought about a discussion, especially in Europe and North America, and aircraft emissions are now perceived as a far more relevant issue than a decade ago (CAEP 1991). Because of the large residence time, low background concentrations and large radiative sensitivity, the main concern comes from the present airtraffic near and above the tropopause, polewards of 40° latitude. The most important emissions are those of nitrogen oxide, water vapour, and sulphur dioxide. In particular, emissions of nitrogen oxides at high altitudes are considered to have possibly marked effects on the formation or destruction of ozone, depending on deposition altitude. Also discussed are the contributions from water vapour emissions on cloudiness and climate change. More recently, in view of our understanding of the origin of the Antarctic "ozone hole" (WMO, 1991), the potential effect of chemical reactions on the surface of particles (heterogeneous reactions) originating from water, sulphur or soot emissions are gaining increasing attention.

In the early 1970s, concern about the potential effects of emissions from a proposed fleet of supersonic transport (Johnston 1971, Crutzen 1972) caused an extensive study (CIAP 1975). Partly because of the outcome of this study but mainly because of economical reasons it was decided at that time that such a fleet of SST should not be built. Recently there has been renewed interest in the development of faster aircraft for international passenger flight. The question how far such a system is environmentally acceptable triggered a High-Speed Research Program by NASA in 1990 (Watson et al. 1990, Johnston et al. 1991, Douglass et al. 1991, Prather et al. 1992). In Germany, the environmental impact of a hypersonic space transport system SÄNGER was investigated and shown to be small by Brühl et al. (1991) and Graßl et al. (1991). In 1990, an international Colloquium provided an overview on the state of knowledge with respect to the impact of global airtraffic on the atmosphere (Schumann 1990). Since then, several related research programs have been initiated in Europe (see Dunker, 1993). This paper surveys the knowledge in this quickly evolving research area.

Nitrogen oxide NO_x ($NO + NO_2$) plays a major role in the chemistry of tropospheric ozone. In regions of high NO_x concentrations, a photochemical sequence initiated by the reaction of methane (CH_4) and carbon monoxide (CO) with hydroxyl (OH) leads to ozone (O_3) production while in regions of low NO_x concentrations, such as over ocean areas, the reaction of CH_4 and CO with OH initiates a sequence that destroys O_3 (Isaksen and Hov 1987; Crutzen 1988). Hence, added NO_x enhances ozone in the free troposphere. In the stratosphere, NO_x as HO_x and in particular ClO, tend to deplete ozone. As shown by Hidalgo and Crutzen (1977), Johnston et al. (1989) and others, using 1D models, NO_x emissions enhance ozone depletion above about 12 to 14 km but produces ozone below that level, see Fig. 1 (Douglass et al. 1991).

Presented at an AGARD Meeting on 'Fuels and Combustion Technology for Advanced Aircraft Engines', May 1993.

Injection of NO_x by airtraffic in the stratosphere may reduce the efficiency of the HO_x and ClO_x catalytic cycles by the homogeneous formation of HNO_3 and $ClONO_2$. Hence, emissions of nitrogen oxide from airtraffic has the potential to reduce ozone destruction caused by increasing levels of chlorofluorocarbons, but Johnston et al. (1989) found that this effect is small for present levels of ClO. However, the previous models ignored the potential impact of heterogeneous reactions on the surface of stratospheric aerosols and polar stratospheric clouds (PSCs) (Crutzen and Arnold 1986, Brasseur et al. 1990, Brasseur 1992, Granier and Brasseur 1992, McElroy et al. 1992).

The stratospheric aerosol layer contains droplets of aqueous sulphuric acid solution (about 75 weight % H_2SO_4). In the absence of sunlight, NO_x gets converted into the reservoir gas N_2O_5. The heterogeneous reaction

$$N_2O_5 \text{ (gas)} + H_2O \text{ (liquid)} \rightarrow 2\,HNO_3 \text{ (gas)} \qquad (1)$$

on the sulphate aerosol surface converts N_2O_5 and thereby NO_x into the less reactive nitric acid. Hence, this reaction is likely to reduce the ozone depletion effect of NO_x-emissions from high flying airtraffic (Rodriguez et al. 1991, Kinnison and Wuebbles 1991, Bekki et al. 1991, Weisenstein et al. 1991)

Polar stratospheric clouds (PSCs) are believed to consist of either H_2O-ice or HNO_3 (NAT = nitric acid trihydrate or metastable nitric acid dihydrate) or H_2O particles, Type I and Type II PSCs, respectively (Hanson and Mauersberger 1988, Hanson 1992). Type I PSCs can form at higher temperature than Type II PSCs. The threshold temperature, T(NAT), below which NAT Aerosols can exist (in equilibrium) ranges from about 206 K at 10 km altitude to about 191 K at 25 km (Schlager et al. 1990). Because T(NAT) is markedly larger than the threshold temperature of water ice existence (by about 1 K at 10 km altitude and by about 12 K near 25 km altitude), Type II PSCs are more prevalant and thus can have a greater effect on the atmosphere. Heterogeneous reactions on the surface of such PSCs may convert $ClONO_2$ and HCl to reactive ClO_x which possibly destroys ozone. PSCs also form a sink for NO_y which otherwise moderates the ozone destruction cycles.

The region where NAT particles can be formed increases with decreasing temperature, increasing humidity and increasing concentration of HNO_3 (Peter et al. 1991, Hofmann and Oltmans 1992, Arnold et al. 1992). Increases in CO_2 concentrations may cause cooling of the lower stratosphere and more PSCs and hence more ozone depletion, in the Antarctic and eventually also in the Arctic (Austin et al. 1992). Hence, aircraft emissions may also enforce ozone destruction in the coldest regions of the stratosphere. The overall consequences of such heterogeneous reactions have not yet been investigated in detail with respect to emissions from present subsonic airtraffic.

Over the industrialized continents, one has observed a strong increase of tropospheric ozone by about 2 %/yr, see e.g. Fig. 2 and Wege (1992). Volz and Kley (1988) deduced more than a doubling in comparison to the preindustrial era. This trend is consistent with increases of nitrogen oxide (Logan 1985; Brühl and Crutzen 1988). In the stratosphere, Fig. 2 shows a reduction of ozone of about 0.5 %/yr (Wege 1992). Also

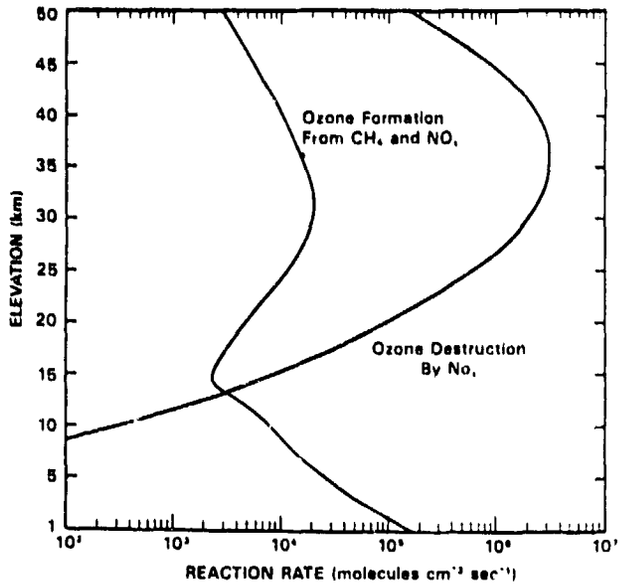

Fig. 1. Ozone formation from the smog reactions based on methane and nitrogen oxides (45° latitude, spring) (Douglass et al. 1991).

satellite measurements of total column amount of ozone show a decrease of stratospheric ozone by about 0.5 to 0.8 %/yr near 50°N (Stolarski et al. 1991).

The changes in the ozone concentration have environmental effects because ozone is a greenhouse gas (Lacis et al. 1990) and is important for the production of OH which is responsible for the removal of greenhouse gases (e.g., methane) and other pollutants (Crutzen and Zimmermann 1991). Moreover, the ozone layer protects

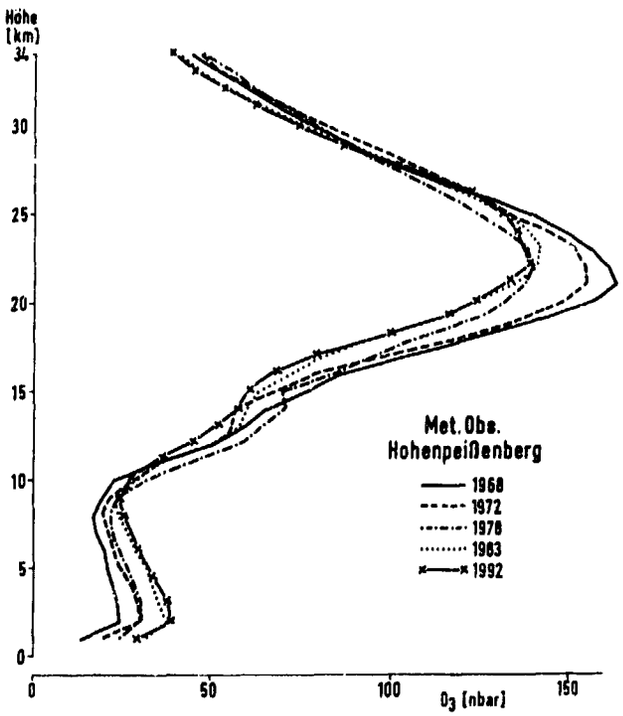

Fig. 2. Annual mean profiles of ozone partial pressure in nbar versus altitude in km for the years 1968 to 1992 at Hohenpeißenberg, Southern Germany, (provided by Meterol. Observatory Hohenpeißenberg, see also Wege 1992).

the biosphere from the UV radiation, but increased tropospheric ozone may also cause damage to both animal and plant life.

The other potentially important emission is that of water vapour, mainly because of its direct or indirect (by cloud forming processes) impact on the radiation budget of the atmosphere. It is known that thin cirrus clouds of large ice particles in the upper troposphere at low and mid latitudes act to enhance the "greenhouse effect." An increase in cirrus cloud coverage by a few percent might have the same effect as a doubling of the amount of CO_2 (Liou 1986; Liou et al. 1990). Contrails from aircraft enhance the appearance of high-level clouds (Schumann and Wendling 1990).

The purpose of this paper, which evolved from that presented by Schumann and Reinhardt (1991), is to review the present knowledge on the impact of high-flying civil subsonic airtraffic on the atmosphere in terms of environmental and climatic aspects. The paper excludes effects of airtraffic in the vicinity of airports.

2. Airtraffic and emissions

Global airtraffic of scheduled services has grown from $940 \cdot 10^9$ passenger-km in 1978 to almost $1700 \cdot 10^9$ passenger-km in 1988, 45 % of the total being international traffic (Nüßer and Schmitt 1990). The non-scheduled traffic adds about $170 \cdot 10^9$ passenger-km for the year 1988. The annual growth rate in the decade between 1978 and 1988 was 6.1 %. ICAO expects presently an increase of worldwide scheduled passenger traffic at an annual growth rate of about 4 % for domestic traffic and 6 % for international traffic in the years until 2001, with the strongest increase (up to 8.5 %/yr) for international traffic in the Asia/Pacific region.

Data by the International Energy Agency of 1991, see Fig. 3, show that the world demand of aviation fuel increased from 117 Mt (Million tons) in the year 1977 to 167 Mt in the year 1989, i.e. by about 3 % per year. Hence, the increase rate in terms of fuel consumption is roughly half the rate of passenger transport performance. Egli (1990) estimated 176 Mt for 1990. Kavanaugh (1988) estimates that commercial jets burn about 70 % of all jet fuel, military jets consume 24 % and business and turbu-props the remainder 6 %. These numbers are roughly consistent with information from G. J. Bishop, Shell International Petroleum Co., London (personal communication 1991), reporting jet fuel consumption by civil airlines in the western world in 1990 of approximately 125 Mt and estimating an additional military part of 25 % of the civil volume. No reliable figures exist for the former eastern bloc countries. For the future, Kavanaugh (1988) estimates the jet fuel use to grow by 2.2 % annually from the year 1990 to 2025 in a "low fuel estimate" scenario, but to grow 3.6 % per year from 1990 to 2000 and then moderates to 2.9 % in a "high fuel estimate," depending on various assumptions. These estimates imply increases by a factor of 1.4 to 1.6 in 2005 and by 2.1 to 2.9 in the year 2025 relative to 1990.

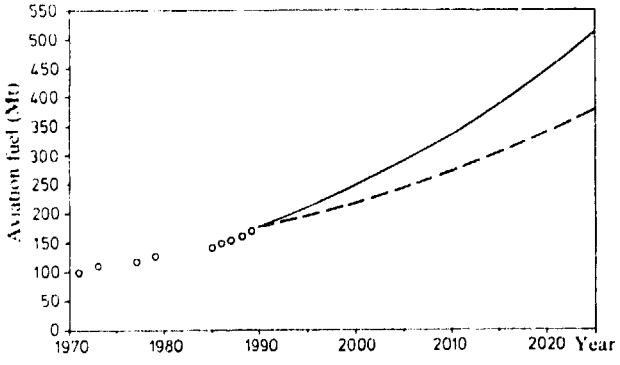

Fig. 3. Aviation fuel versus time. Data up to 1989 from the International Energy Agency (1991). Extrapolations according to Kavanaugh (1988) with 2.2 % per year in a low fuel scenario and with 3.6 % up to 2000 and 2.9 % thereafter in a high fuel scenario.

Hence, although airtraffic will increase strongly, a doubling in fuel consumption should not be expected before 20 years from now. However, it appears reasonable that most of the increase will be related to high flying long-distance traffic. The lower increase of fuel consumption when compared to the increase in the number of passenger-kms is related to increases in the fuel efficiency of aircraft. Within the last 30 years, the specific fuel consumption per passenger-km decreased by about 45 % (Simon 1988).

When the fuel is burned with air in the jet engines, the exhaust gases cause emissions into the atmosphere. For complete combustion, the emissions would contain mainly carbon dioxide (CO_2) and water vapour (H_2O). The emission index (emitted mass of pollutant per unit mass of fuel) for these emissions depend solely on the stoichiochemical composition of the kerosine fuel. The carbon content is about 86 % by mass. The mean molecular weight is 164 (Prather et al., 1992, p. 98). Other emissions of much smaller amount are nitrogen oxides (NO_x) of varying composition (NO_2 fraction decreasing from 18 % at idle to less than 5 % at more than 30 % engine power setting, according to Spicer et al. 1990), carbon monoxide (CO), hydrocarbons (HC), and soot particles (mainly carbon) and other particles acting as condensation nucleus (CN) for cloud formation. One distinguishes between CN and CCN (cloud condensation nuclei), where the latter form cloud nuclei at small supersaturation (less than 1 %), whereas CN require large supersaturation. Pitchford et al. (1991) measured large concentrations of CN of up to 300.000 cm^{-3} in the exhaust plume of a Sabreliner, with an emission index of soot in between 0.001 and 0.03 g(soot)/kg(fuel). They found, moreover, that background particles are much more active as CCN than exhaust particles of the same size (ratio of CCN to CN less than 1 %), but Whitefield et al. (1993) found that 30 to 40 % of the combustion aerosols generated in laboratory burners can be considered as CCN. Most of the aerosols in jet exhausts are found to have diameters in between 0.01 and 0.1 µm (Pitchford et al. 1991; Hagen et al. 1992).

As a minor emission, the exhaust contains sulphur dioxide (SO_2) because aviation fuel is allowed to contain up to 0.3 weight percent (wt%) of sulphur (IATA Guidance material for aviation turbine fuels, Amendment No. 1, 14 Nov. 1988, International Air Transport Association, Montreal, Canada). According to Shell, London (personal communication 1991), fuels can vary from very

low sulphur contents (< 0.01 wt%), if they have been manufactured by a hydroprocessing route, to levels around 0.2 wt% if they have been chemically processed. From 1978 to 1991, the average sulphur content in fuel samples was in between 0.050 and 0.055 wt% (Dickson et al. 1989, 1992) with very few samples exceeding 0.1 wt%. In an analysis of 53 Jet-A fuel samples the average sulphur content was 0.042 wt% (Prather et al. 1992). As confirmed by Shell, the average sulphur content of jet fuel worldwide is around 0.04 to 0.05 wt%; resulting in 0.8 to 1 g SO_2 per kg burned fuel.

Very little information exists on the composition of the HC. The standard method of exhaust analysis for organic compounds is only a measure of "total unburned hydrocarbons" as measured by a flame ionization detector. The specific compounds are of interest because the exhaust organics vary substantially in their chemistry. Such organic compounds may be important in converting NO, into reservoir gases, and in contribution to ozone formation, in particular in the stratosphere. Any technical development leading to reduced NO, emissions might lead to increasing amounts of unburned hydrocarbons. Spicer et al. (1990) review earlier investigations and report about measurements in the exhaust of two military engines, the F101, used on B-1B aircraft, and the F110, used for F-16C and F16D aircraft. They found that much of the HC consists of methane, part of which enters the engine with the combusted air, in particular for low power settings. The content of NMHC (non-methane hydrocarbons within the HC), mainly alkanes, decreases with the load factor of the engine. The organic compounds in the two engines reached up to 1.44 g/kg fuel in the idle state and decreased below 0.2 g/kg fuel at power settings above 63 %.

For NO_x, published emission indices vary considerably. This is mainly due to the fact that measured emission indices are obtained for surface pressure conditions while the emissions at cruise height are much smaller. Presently, measurements in altitude test chambers are underway to determine these differences. Given values of the emission index in g(NO_2)/kg(fuel) are 10.9 (Kavanaugh 1988), 9.3 around 8 km and 14.4 for long-range cruise at altitude between 10 and 11 km (Ko et al. 1992; the differences reflect different mixes of aircraft), 11.6 (Johnson et al. 1992, McInnes and Walker 1992), 15 (Reichow 1990), and 18 (Egli 1990, Beck et al. 1992) based on the data compiled by Lecht et al. (1986). Even larger variations are found with respect to emission indices for CO: 14.6 (Johnson and Henshaw 1391), 4 (Reichow 1990), and 0.7 to 2.5 (Nüßer and Schmitt 1990), based on Lufthansa estimates. For HC the variations are 0.05 to 0.7 (Nüßer and Schmitt 1990), 1.5 (Reichow 1990), and 2.6 (Johnson and Henshaw 1991). With respect to soot the numbers are 0.007 to 0.03 (Nüßer and Schmitt 1991) and 0.014 (Reichow 1990).

Deidewig (1992) evaluated the emissions for the aircraft types B737-300, B737-500, A310-300 and B747-400, propelled by the engines CFM56-3 and CF6-80C2. For various typical missions, he computed the emissions of NO_x, CO, and HC in the atmosphere along the flight route. For the B747-400, his results are repeated in Figs. 4 and 5. We see that the emission indices of NO, vary in between 8 and 12 at cruise, where in between 31 % and

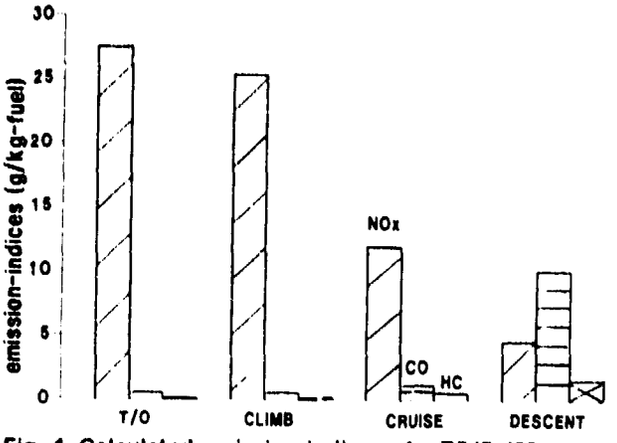

Fig. 4. Calculated emission indices of a B747-400 with a CF6 engine at take/off (T/O), during climb, cruise and descent, for NO_x, CO, and HC (from Deidewig, 1992).

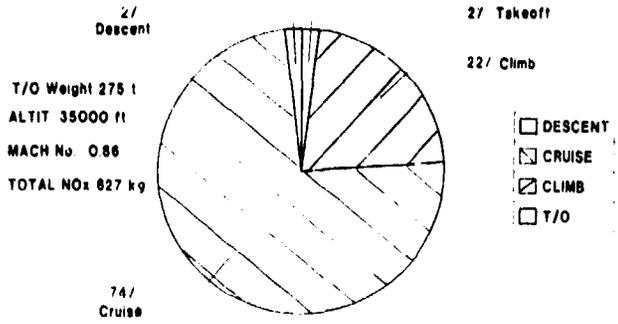

Fig. 5. Percentage NO_x emissions of a B747-400 with a CF6 engine during take/off (T/O), climb, cruise and descent (from Deidewig, 1992).

74 % of the total NO, emissions take place. Larger specific emissions occur in the other parts of the routes, which are important in particular for short range missions. Note that this analysis applies to a specific set of engines with NO, emission indices that are lower than average.

Hoinka et al. (1993) recently analysed the traffic over the North Atlantic in the region shown in Fig. 6, i.e. between 10°W and 60°W and 45°N and 65°N. Based on data of the Civil Aviation Authority (CAA), they found

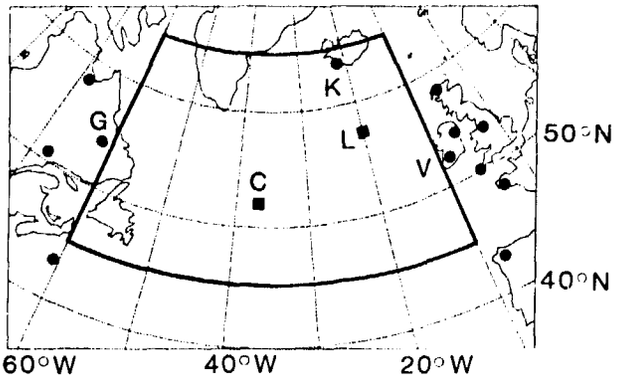

Fig. 6. Map of the Northern Atlantic showing the area for which Hoinka et al. (1993) performed an analysis of traffic and tropopause statistics. The dots (squares) indicate land (ship) stations where radiosondes are launched twice a day.

that on average 512 aircraft per day (sum of both directions) passed that region during the period from 1989 to 1991. Based on the fleet composition as given by the CAA and estimates for the individual engines used (from Lecht et al. 1986), they determine the total emissions and fuel consumptions from which one obtains the following average emission indices for the whole fleet: 17.5 for NO_x, 0.6 for HC, and 1.5 for CO. The amount of fuel used by the average aircraft in that region, with an average flight path length of 2730 km, amounts to 32.4 t.

Based on the various sources and arguments, Table 1 contains what we believe are best estimates of emission indices. They are meant to apply for long-distance cruise conditions. The table also contains an estimate of present (as of 1990) emissions from airtraffic. In this table, the most important uncertainty is that of NO_x emissions (which are quantified as if all emissions were NO_2), for which we have selected the upper bound of the various estimates.

With respect to the spatial distribution of the emissions, previous estimates have been compiled in Schumann and Reinhardt (1991), Ko et al. (1992) and Beck et al. (1992). These data are not repeated here, because several studies are in progress with the objective to produce a refined data base.

As a preliminary result from these studies, a 3D data base of emissions has been provided by McInnes and Walker (1992). These data still contain considerable uncertainty because the data are based on a traffic statistics for scheduled flights and cargo only. Hence, the resultant fuel consumption accounts for only about 50 % of the total fuel consumption. The results have been scaled by the factor 2 to get an estimate of the total emissions. This inventory is presently used as test input for 3D atmospheric computations within the project AERONOX (Dunker, 1993). For illustration purpose, Fig. 7 shows the distribution of the source of NO_x-emissions per unit volume and unit time at an altitude of about 12 km (190 hPa). We see clearly that the sources at this altitude are large in particular along the main flight corridors between the northern continents with peaks over North America, Europe and the North Atlantic.

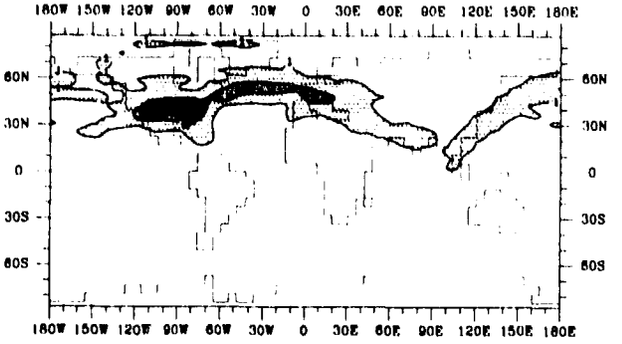

Fig. 7. Source of NO_x due to air traffic emissions at an altitude of about 12 km (at pressure level 190 hPa) in the T21 grid version of the ECHAM code (I. Köhler, DLR). The contours correspond to emissions of 1, 5 and 10 in units of 10^{-9} kg(NO_2)/(kg(air) s). The emissions exceed 10 such units within the black areas.

3. Some relevant properties of the atmosphere

The concentrations which result from the emissions are the larger the larger the product of emission rate and residence time and the smaller the mass of atmosphere over which the emissions get dispersed. (Mass specific concentrations are converted to volume specific concentrations by multiplication with the molecular weights M_i = 44, 18, 46, 18, 64, and 29, of the individual gases CO_2, H_2O, NO_2, CO, SO_2, and air, respectively). Hence, the concentration change can be estimated from

$$\text{volumetric concentration change} = \frac{\text{emission rate} \cdot \text{residence time} \cdot M_{air}}{\text{mass of atmosphere} \cdot M_i} \qquad (2)$$

The residence time and the relevant mass of atmosphere depend strongly on the emission altitude and on the manner by which the emitted quantities get mixed and removed from the atmosphere.

As described in Brasseur and Solomon (1986), Fabian (1992) and others, the atmosphere is structured into various layers. The lower troposphere contains roughly 80 % of the mass of the atmosphere. In the troposphere, the temperature decreases with height (the potential

Emission	Emission index (g pollutant per kg fuel)	Emission rate 1990 in Mt/yr	Comparable emissions in Mt/yr	Comparable emissions source	Reference
Fuel	1000	176	3140	Total consumption of petrol	1
CO_2	3150	554	20900	Burning of fossil fuels	2
H_2O	1260	222	45	Methane oxidation in the stratosphere	3
			525000	Evaporation from earth surface	4
NO_x (as NO_2)	18 (7-20)	3.2	2.9 ± 1.4	Flux from stratosphere	5
			90 ± 35	All anthropogenic sources	5
CO	1.5 (1.5-10)	0.26	600 ± 300	CH_4 oxidation	6
			1490	All anthropogenic sources	7
HC	0.6 (0.2-3)	0.1	90	Anthropogenic emissions at the earth's surface	8
Soot (C)	0.015 ± 0.014	0.0025			
SO_2	1 (0.02-6)	0.176	0.0625	Rate required to sustain background aerosol in the lower stratosphere	9
			134	Total from fossil fuel combustion	10

Table 1. Estimated emission rates and comparison. Best estimate emission indices are listed together with the present range of uncertainty in brackets. The corresponding emissions are given in units of Mt/yr (10^{12}g yr^{-1}). References for comparable emissions: (1): International Energy Agency (extrapolated from 3095 Mt/yr for 1989). (2): German Bundestag (1991), p. 151 ($5.7 \cdot 10^9$ t C /yr in 1987 from anthropogenic sources). (3): German Bundestag (1991), p. 156, (4): p. 147, (5): p. 170, (6): p. 168, (7): p. 168. (8): Hough (1991). (9): Hofmann (1991). (10): Hameed and Dignon (1992).

temperature increases slightly) so that this layer is only weakly stably stratified. In this range, vertical mixing is quite strong and cloud systems contribute to deposition of soluble quantities. Above the troposphere, i.e. above the tropopause, within the stratosphere, the temperature increases with height. Therefore, this layer is stably stratified with much weaker vertical mixing. As a consequence of these properties and of the conversion into soluble forms, nitrogen oxides have a residence time of the order of 1 to 4 days in the troposphere. For inert tracers emitted into the stratosphere, the residence time quickly increases with height above the tropopause and reaches values in excess of one year (Fabian 1992). For the present airtraffic at altitudes below 13 km, the residence time is probably below 6 months (see Fig. 8, taken from Brühl et al. 1991). The altitude of the tropopause is highly variable from day to day and from season to season (Hoerling et al. 1993, Hoinka et al. 1993). It amounts on average to about 8 km over the polar regions and to about 16 km at the equator. Hence, the residence times of aircraft emissions depend strongly on whether the aircraft flies above or below the tropopause.

The residence time depends also strongly on the latitude because the lower stratosphere exhibits mean rising motion near the equator and, to first approximation, mean sinking motion elsewhere (Plumb and Mahlman 1987), and because of strong tropospheric-stratospheric exchange at mid-latitudes (Vaughan 1988, Ebel 1991, Appenzeller and Davies 1992, Rood et al. 1992, Hoerling et al. 1993). The polar jet stream is important because of sinking motion (of order 50 to 500 m per day) near or poleward of its core and rising motion on its equatorward side (Mahlman 1973, Schoeberl et al. 1992). Hoerling et al. (1993) diagnose the cross-tropopause mass flux globally for January 1979. They find that the mass flux from the troposphere to the stratosphere in between 50°N-70°N is as intense as that over the tropics, while the same flux is rather small over the poles. This suggests that material deposited in the stratosphere or near the tropopause poleward of the jet core would have shorter residence time than material injected equatorward of the jet core.

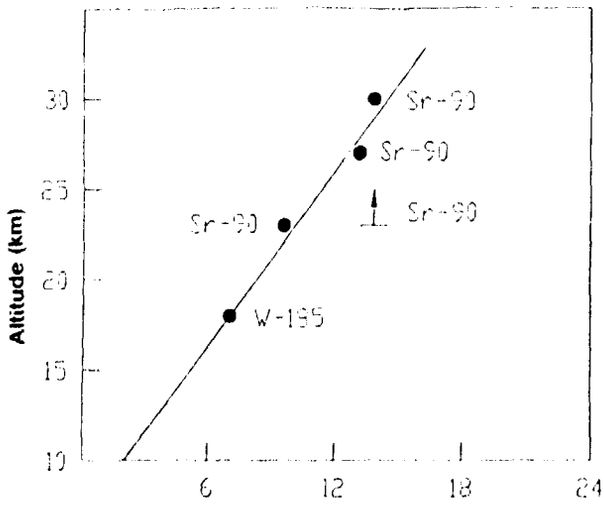

Fig. 8. Height-dependend residence time in the stratosphere in units of months, deduced from radioactive tracers (from Brühl et al. 1991)

Jackman et al. (1991) show that ozone depletion from NO_x injections of stratospheric supersonic aircraft, as computed in 2D models, depends strongly on the stratospheric/tropospheric exchange rate by the mean circulation. The computed ozone loss gets reduced when the exchange rate is increased.

Reichow (1990) estimates that Lufthansa consumes about 17 to 20 % of the fuel above the tropopause. However details of this estimate have not been published. Havlik (1988) analyzed radiosonde data for the year 1970 for 00 and 12 UTC. He determined the height of the tropopause (i.e. the lowest altitude above which the vertical temperature gradient was above -2 K/km over an interval of at least 2 km). From his data one can determine how often an aircraft at 250 hPa or about 33000 ft (10.8 km) flies above the tropopause. We found that most of the flights north of 50°N occur within the stratosphere according to these data. Ko et al. (1992) use zonally averaged climatologies and estimated the fuel use in the stratosphere for the 1987 subsonic fleet assuming an average flight altitude of 37000 ft. They conclude that 48 % of the 1987 northern hemisphere fuel burn occurs in the stratosphere and 52 % in the troposphere, with strong seasonal variations. These numbers are likely to change when more accurate emission inventories become available (see also Hoinka et al. 1993, and chapter 5).

4. Global concentration changes due to present aircraft emissions

Table 1 lists the emitted masses of various pollutants and gives other emission rates for comparisons. We see that nearly 6 % of all petrol is used for aviation. This is quite a large number. However, because of many other sources, it contributes only 2.6 % of all CO_2 from burning of fossil fuels. The water vapour emission rate from aircraft is very small (0.04 %) in comparison to the amount of water which gets evaporated from the surface. However, it represents a large source when compared to the amount of water vapour released into the stratosphere by methane oxidation.

Table 2 gives an overview on various sources of NO_x. Aircraft cause the only direct anthropogenic emissions in the upper troposphere. Here other sources are those from lightning and stratospheric downward flux. Note that there is much disagreement regarding the source of NO_x from lightning (Jacob 1991), and this represents an important uncertainty (Beck et al. 1992). The upward flux from surface emissions will be large only over the continents, in cyclones, and in the tropics where strong convective events transport the pollutants from the surface quickly up into the upper troposphere (Ehhalt and Drummond 1988). The aviation emissions are large in comparison to the flux of NO_x from the stratosphere into the troposphere.

The aviation contribution to all anthropogenic NO_x sources is about 3 %. The emissions from airtraffic grow faster than the other anthropogenic emissions which increases the relative importance of emissions from airtraffic. For example, the global emissions of nitrogen from fossil fuel combustion increased from 18 Mt N/yr

Emission	Ehhalt and Drummond (1988)	Penner et al. (1991)	Hough (1991)	German Bundestag (1991), p. 170.
Fossil fuel burning	13.1 to 28.9	22.4	21	20 ± 7
Biomass burning	5.6 to 16.7	5.8	8	7 ± 3
Soil microbial activity	1 to 10	10	5	12 ± 6
NH_3 oxidation	1.2 to 4.9			3 ± 2
Lightning discharges	2 to 8	3	8	5 ± 3
Flux from stratosphere	0.3 to 0.9	1.0		1.0 ± 0.5

Table 2. Global sources of nitrogen oxide and their strengths. In units of Mt (N)/yr (10^{12}g N yr^{-1}). 14 kg N ≅ 46 kg NO_2. For 1986, Hameed and Dignon (1992) estimate the total emissions from fossil fuel combustion to be 24 Mt (N)/yr.

in 1970 to 24 Mt/yr in 1986, i.e. at a rate of 1.8 %/yr (Hameed and Dignon, 1992). Obviously, various reduction measures with respect to emissions at the earth surface (e.g. from car traffic) become effective (Amann 1990).

The amount of emitted HC appears to be small in comparison to anthropogenic sources. Also the CO contributed from aviation is very small in comparison to the budget of CO. It reaches only 0.03 % of all anthropogenic sources. The CO concentration may get reduced in spite of the aircraft emissions; this is caused by a greater oxidation of CO due to enhanced concentrations of OH as shown by Beck et al. (1992).

The absolute amount of soot induced by aircraft into the atmosphere is certainly much smaller than those from other sources. Moreover, this class of emissions has been reduced already considerably in the past. However, soot contributes significantly to the CN concentration in the lower stratosphere (Pitchford et al. 1991).

The emission of sulphur from aviation is much smaller than from surface emissions and negligible in terms of the resultant acid rain or so but may be important if emitted at high altitudes. Hofmann (1991) reported observations which indicate an increase of non-volcanic stratospheric sulphate aerosol of about 5 % per year. He suggests that if about 1/6 of the Northern Hemisphere airtraffic takes place directly in the stratosphere and if a small fraction of other emissions above 9 km would enter the stratosphere through dynamical processes then the jet fleet appears to represent a large enough source to explain the observed increase. He calls for the use of aviation fuel which is essentially sulphur free. On the other hand, Bekki and Pyle (1992) conclude from a model study that although aircraft may represent a substantial source of sulphate below 20 km, the rise in airtraffic is insufficient to account for the observed 60 % increase in large stratospheric aerosol

Emission product	Residence time	Emission rate in Mt/yr	Mean concentration increase	Background conc. at 14 km
CO_2	10 yr	111	1.4 ppmv	354 ppmv
H_2O	0.5 yr	44	0.07 ppmv	5 - 20 ppmv
NO_x	0.5 yr	0.63	0.4 ppbv	0.2-0.5 ppbv
SO_2	0.5 yr	0.035	16 pptv	20-100 pptv

Table 3. Concentration increases due to aviation emissions mixed over the northern stratosphere.

Emission product	Residence time	Emission rate in Mt/yr	Mean concentration increase	Background conc. at 8 km
CO_2	10 yr	443	0.7 ppmv	354 ppmv
H_2O	9 d	177	0.002 ppmv	20-400 ppmv
NO_x	4 d	2.5	4.1 pptv	10-50 pptv
SO_2	5 d	0.14	0.21 pptv	30-150 pptv

Table 4. Concentration increases due to aviation emissions mixed over the whole troposphere.

particles over the 1979-1990 period. Sulphate particles generated from SO_2 may also contribute to nucleation particles (Arnold et al. 1992). Whitefield et al. (1993) find a positive correlation between sulphur content and CCN efficiency of particles formed in jet engine combustion.

Tables 3 and 4 show equilibrium concentrations which are computed using Eq. (2). Here, we follow Fabian (1990) who presented similar estimates. Note that these computations neglect any chemical transformations. In Table 3, we present an update of such computations for the stratosphere assuming that 1/5 of the fuel (total 176Mt/yr) is burned within 1/10 (i.e. only the northern stratosphere) of the atmosphere's mass of $53 \cdot 10^6$ Mt total (Fabian 1990). The residence times and background concentrations are as estimated in Schumann and Reinhardt (1991). For the troposphere, Table 4, it is assumed that 80 % of all fuel is burned and distributed over 4/5 of the atmosphere's mass (i.e. below 200 hpa).

The contributions of emissions from airtraffic are obviously significant with respect to NO_x. The changes may reach 10 to 100 % of the background concentrations both in the upper troposphere and also in the lower stratosphere, even when the emissions are assumed to be mixed over such large volumes. Also, the contribution of airtraffic to SO_2 is significant in this global mixing analysis, in particular in the lower stratosphere. On the other hand, such calculations show a rather small effect from emitted water vapour. Larger effects are to be expected regionally.

5. Traffic, dispersion and concentration changes over the Northern Atlantic

Duclos et al. (1991) recently reported a North Atlantic traffic analysis using actual traffic data as provided by the CAA, and presented forecasts for the years up to 2010. Fig. 9 shows the annual number of aircraft movements over the North Atlantic in the past and as estimated for the future. We see that these numbers increased from 120000 in the year 1976 up to 206100 in 1990 and the study predicts about 356000 movements in the year 2005. This corresponds to about 560 aircraft movements per day at present increasing to nearly 1000 in 2005.

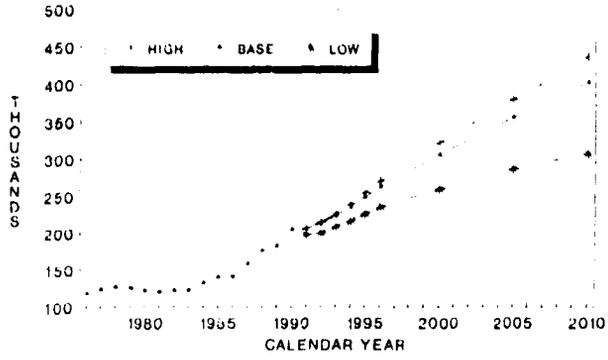

Fig. 9. From Duclos et al. (1991): North Atlantic traffic forecasts showing aircraft movements 1976 to 2010. The extrapolations apply for various traffic scenarios.

As mentioned before, Hoinka et al. (1993) also analysed the traffic in the region depicted in Fig. 6. In addition they determined the height of the tropopause from weather analysis data as provided by the European Centre for Medium Range Weather Forecasts (ECMWF) in Reading. By correlating both data sets, they found that about 44 % of all fuel is burned above the tropopause in the stratosphere, and 56 % in the troposphere in that region. In February, the stratospheric part reaches about 75 %.

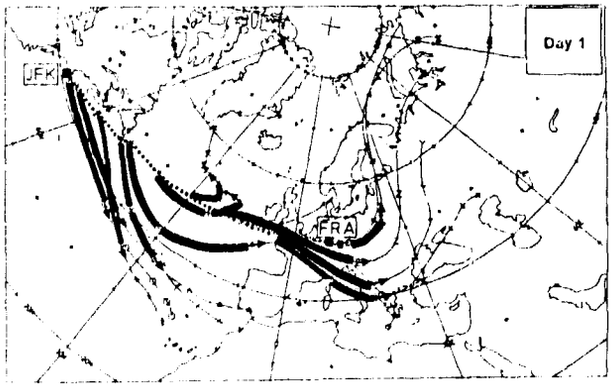

Fig. 10 Forward trajectories of emission products along a North Atlantic eastbound jet aircraft track from New York (JFK) to Frankfurt (FRA) on June 20, 1991 at flight level 10 km. Dotted line = flight track, thick arrowed curves = horizontal trajectory for 24 hours, for day 1 after release. The thin trajectory curves extend up to three days. The symbols at the trajectories mark time intervals of 12 hours. Computed with the Europa model of the DWD (German Weather Service). (Schumann and Reinhardt 1991).

Schumann and Reinhardt (1991) reported about trajectory analysis of emissions which are emitted along the path of an airliner, according to Lufthansa flight dispatch data and meteorological data from the German Weather Service, see Fig. 10 for example. A statistical analysis of the results, see Fig. 11 (D. Heimann, DLR, personal comm., 1991), shows that the standard deviation σ in the vertical amounts to 0.729 km at time of tracer release (due to variation in flight altitudes), 0.860 km after 12 hours, 1.014 km after one day and 1.194 km after 2 days. The north-south standard deviations are 496, 638, 854, 1303 km after 0, 12, 24 and 48 hours, respectively. This corresponds to mean diffusion coefficients $K = 0.5\partial\sigma^2/\partial t$ of 2.8 m^2s^{-1} in the vertical, and 4.6 km^2s^{-1} in north-south direction. The related vertical dispersion extends from about 9 to 11 km within the first day, i.e. over about 2 km. Hence, the emissions from this and the other flights at the same day, which take various routes staggered over about 500 to 800 km (at 20°W) in north-south direction (Schumann and Reinhardt 1991), become distributed over the flight corridor with a typical cross-section of about 1000 to 1500 km in latitude and about 2 km in height along a distance of order 5000 km. The tracer results indicate also that residence times in excess of several days are unlikely for emissions near the tropopause.

Based on these analysis, the mean concentration increase is estimated, see Table 5, assuming an air volume of 1000 km x 5000 km x 2 km with an air density of 0.35 kgm^{-3}, and a residence time of 1 day for all emissions which come from 500 aircraft consuming 60 t of fuel each in this corridor. The latter number corresponds to the previously given mean fuel consumption per distance as estimated by Hoinka et al. (1993).

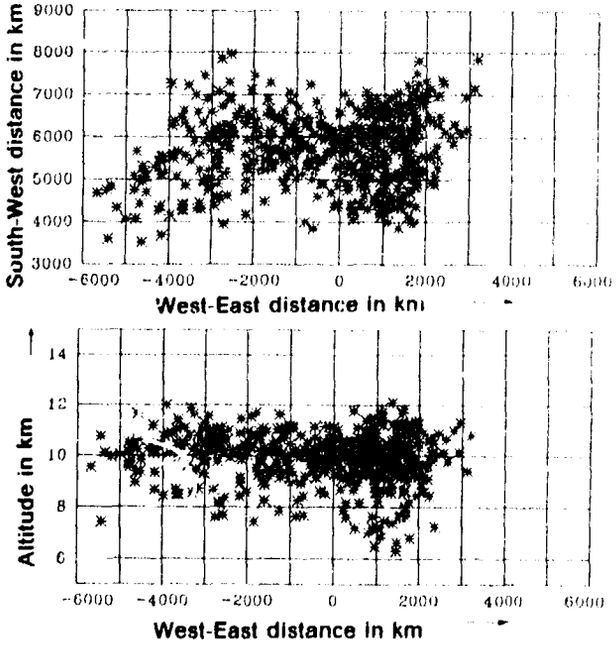

Fig. 11. Particle positions as released along the 40 aircraft tracks in June 1991 after 24 hours dispersion along the trajectories, computed using the Europa model of the DWD. The plots show the distribution in a horizontal plane (upper panels) and a vertical west-east plane (lower panels) (D. Heimann, DLR, 1991).

(Schumann and Reinhardt (1991) assumed 100 t of fuel per 5000 km, and obtained larger concentrations, therefore.)

Emission product	Mean concentration increase	Background conc. at 8 km
CO_2	0.02 ppmv	354 ppmv
H_2O	0.02 ppmv	20-400 ppmv
NO_x	97 pptv	10-50 pptv
SO_2	4 pptv	30-150 pptv

Table 5. Concentration surplus in the North Atlantic flight corridor due to air traffic exhaust emissions from 500 aircraft consuming 60 t of fuel per 5000 km mixed over a corridor cross-section of 1000 km width and 2 km height. (Assumed residence time = 1 day within corridor for all emitted gases.)

One finds that the concentration change of NO_x in the flight corridor can be considerably larger than the background concentration value. The mean concentration increase in SO_2 is still appreciable. On the other hand, the effect from emitted water vapour is small. These emissions may become important only for flight corridors with long residence times in the lower stratosphere where the background concentration can be as small as 3 ppmv.

Fig. 12 snows the increase in NO_x as computed with the global circulation climate model ECHAM (Cubasch et al., 1992) using the NO_x source distribution as illustrated in Fig. 7, and a sink corresponding to a residence time of 5 days (I. Köhler, DLR, personal comm., 1993). It should be stressed that these results are preliminary and are used here for illustration purpose only. The picture shows a zonal cross-section along 45°W, i.e. through the Northern Atlantic flight corridor. The maximum concentration computed in this plane amounts to 150 pptm = 95 pptv. In view of the various assumptions, this value is surprisingly close to the simple corridor estimate given in Table 5. The simulations show that the emissions from the flight corridors over the North Atlantic are mixed rather quickly downwards into the mid-troposphere. There is relatively little transport

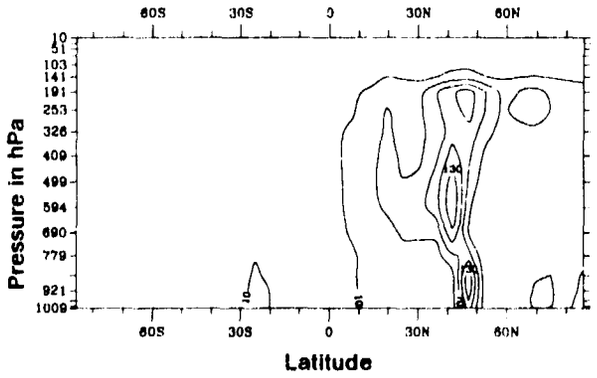

Fig. 12. Increase of NO_x due to air traffic emissions as computed by the ECHAM-T21-model in a zonal plane at 45°W as a function of latitude and height (in pressure units). The contours range from 10 to 130 with intervals of 30 in units of 10^{-12} kg(NO_2)/kg (air). (From I. Köhler, DLR, 1993).

upwards but some transport northwards into the lower stratosphere over the Arctic. In the troposphere one finds some mixing in north-south direction. The direct impact of airtraffic emissions to nitrogen oxides in the Southern Atlantic appears to be very small. More refined simulations are under progress.

The simple corridor estimate is also approximately consistent with the analysis of Ehhalt et al. (1992) who used a 2D model to study the zonal distribution of NO_x. The model includes vertical transport in the form of eddy diffusivity and deep convection, zonal transport by a uniform mean wind, and a simplified chemistry of NO, NO_2, and HNO_3. The model distinguishes between the contributions from various emissions sources and is applied to the latitude band of 40°N to 50°N during the month of July. The model predictions of NO compare quite well with experimental observations. Ehhalt et al. (1992) conclude that aircraft emissions contribute on average 30% to NO_x concentration in the upper troposphere. The contribution is high in particular over the North Atlantic, see Fig. 13. Table 5 suggests an even larger percentage contribution which might be caused by differences in the assumed rate of emissions.

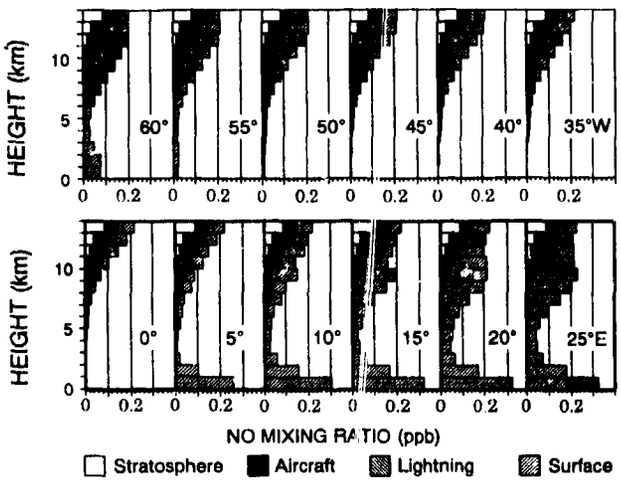

Fig. 13. Vertical mixing ratio profiles of NO over the western North Atlantic (top) and over continental Europe (bottom). The different shadings indicate the contributions from the individual sources. The black part defines the contribution from aircraft emissions. From Ehhalt et al. (1992).

6. Concentration change in the wake of an airliner

The processes in the aircraft wake control the formation of contrails, the formation of soot and sulphur particles, and determine the composition of emissions as becoming effective for the global scale.

The aircraft wake can be conveniently subdivided into three regimes (CIAP 1975): the jet, the vortex, and the dispersion regimes. These regimes correspond to the flow dynamics that control the structure and growth of the wakes in the subsequent time interval. In the jet regime, the engine effluents are initially confined to individual exhaust jets. At the end of the jet regime, the jets merge and are entrained in the roll-up vortex. The following vortex regime persists until the vortices get unstable (Crow 1970) and brake up into a less ordered configuration. Thereafter, the dispersion regime follows,

in which further mixing is influenced by atmospheric shear motions and turbulence. Also buoyancy from the jet exhaust heat or from differential heating by radiation in contrails may contribute to this mixing.

Using simple analytical models (Miake-Lye 1993), for a B-747, Gerz (DLR, personal comm., 1993) estimates that in the jet regime the effective cross-section of mixing grows within 10 s from about 3 m^2 near the four engine exits to about 3600 to 5400 m^2 at the end of the jet regime. In the following vortex regime, which lasts for about 2 to 3 minutes, the cross section of the trailing vortex pair grows to about 21000 to 52000 m^2. The lift of the aircraft causes downward motion of the double vortex structure at about 2.3 ± 0.2 ms^{-1}. The theory of the Crow (1970) instability predicts a wavelength of the most unstable mode of approximately 400 m. The distance between the cores of the two trailing vortices (for an elliptical wing) amounts to about 46 m. However, very little data are available to verify these estimates.

In order to estimate the vertical motion and lateral dimensions of the vortex structure behind an aircraft, Baumann et al. (1993) measured the structure of contrails during the vortex regime as produced by a civil airliner. The measurements have been made by remote sensing from the Falcon research aircraft of the DLR flying about 1200 m above and behind civil airliners at cruise altitude. Due to its lower speed, the horizontal distance between the observed aircraft and the Falcon increases with time. The actual distance has been estimated from Radar observations and the time of measurement. The contrail is observed from above by a Lidar system and by a video camera. The Lidar emits laser light pulses, determines the distance of the backscattering contrails and the amount of light backscattered from the particles within the contrails. Using data on the actual position of the Falcon, these lidar signals are used to determine the altitude and lateral structure of the contrails.

Fig. 14 shows the measured altitude of a contrail versus the distance behind the airliner. In this case the contrail was induced by a B 747-200, flying at about 10.65 km altitude and a true airspeed of about 225 ms^{-1} over Southern Germany (49°N, 12°E), on 12:24:40 to 12:30:08 UTC April 9, 1991, heading 310°. The contrail was clearly visible for a distance of more than 15 km behind the aircraft. At a distance of about 7 km, the contrail becomes unstable by showing oscillating motions. These observations are documented by a video in addition to the Lidar data. Fig. 14 shows that the contrail sinks at an average speed of 2.4 ± 0.6 ms^{-1}, amounting to about 120 m over a distance of 11.2 km, in ideal agreement with the above mentioned theoretical estimate. Virtually the same values (120 m over 12 km distance) have been observed for the contrail of a DC-10.

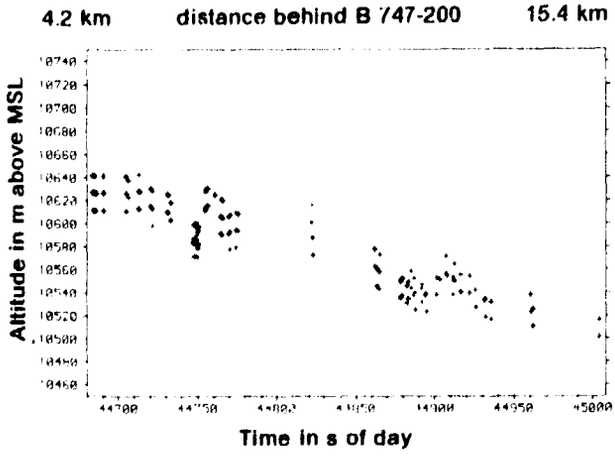

Fig. 14. Altitude of contrail of a B 747-200 versus distance (approximately proportional to time of measurement), from Baumann et al. (1993).

Fig. 15 shows the integrated backscatter signal, as a function of the cross-track coordinate, 4.4 km behind the B 747-200. The lateral distance between the two vortex cores of the contrail is indicated by the distance between the two backscatter maxima. It amounts to 42 m in this figure. The diameter of each of the two vortex cores forming the contrail is defined by the distance between the positions where the backscatter signal reaches 50 % of the maximum value, giving 14 m (left) and 11.5 m (right) for this case. Table 6 lists the results for various distances behind the airliner. Again the measurements are in close agreement with the analytical estimate of 46 m. Table 6 shows that the lateral distance between the vortex cores is close to constant until about 5.7 km behind the B 747, but then starts to oscillate at a wavelength of the order 400 m, as expected for the Crow instability.

distance behind aircraft (km)	plume age (s)	lateral distance (m)	diameter of left contrail (m)	diameter of right contrail (m)
4.4	19.6	42	14	11.5
4.8	21.3	44	12.5	11
5.2	23.1	41	15.5	14
5.7	25.3	44	12	11
7.0	31.1	36	10	9
7.2	32.0	51	10	14

Table 6. Measured scales of a contrail of a B 747-200.

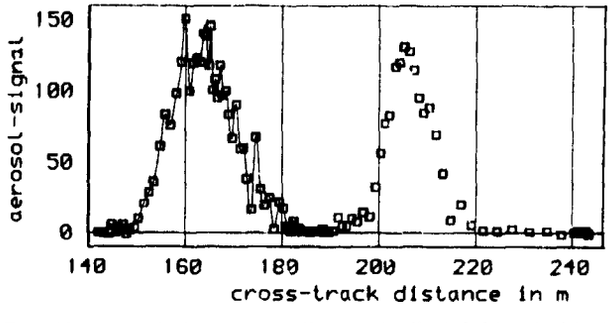

Fig. 15. Lateral structure of the contrail at 4.4 km behind a B 747-200, as indicated by the integrated backscatter signal per Laser shot versus cross-track position in m, from Baumann et al. (1993).

Emission product	Concentration increase	Background concentration at 8 km
CO_2	14 ppmv	354 ppmv
H_2O	14 ppmv	20-400 ppmv
NO_x (NO_2)	78 ppbv	0.01-0.05 ppbv
CO	17 ppbv	40-100 ppbv
SO_2	3.1 ppbv	0.03-0.15 ppbv

Table 7. Mean concentration increases in trail after airliner jet.

Table 7 presents mean concentrations in the wake in the young vortex regime. The computation assumes that the airliner consumes 60 t fuel per 5000 km or 12 g/m and that the emission indices are as given in Table 1. The resultant emissions are assumed to be evenly distributed over 5000 m², as estimated above for the end of the jet regime behind a B 747. The density of the environmental air is taken as 0.35 kg/m³. The table gives the resultant concentration increases and provides typical order of magnitudes of environmental data for comparison. All the listed concentration changes are of measurable magnitude. Again we find the largest effect with respect to NO_x and SO_2. The change in water vapour concentration is rather small and does not explain why large contrails are observed rather often (Schumann and Reinhardt 1991).

In cooperation with MPI Heidelberg (F. Arnold et al.) and DLR (H. Schlager et al.), measurements have been performed using the DLR research aircraft Falcon which flew into several trails of commercial aircraft at flight altitude. The dusty plume was clearly visible and the wake turbulence of the airliners was still very notable, so that one was sure to measure inside the plume. This is corroborated by high resolution humidity and temperature signals (R. Busen, DLR, personal comm., 1993). Measurements on the abundances of the odd-nitrogen gases NO, NO_2, HNO_2 and HNO_3 in the young trail (trail age $t_p \approx 9$ s corresponding to a distance of about 2 km) of a DC-9 airliner at 9.5 km altitude are reported in Arnold et al. (1992), as obtained using a novel aircraft borne automatic mass spectrometer (AAMAS). Simultaneously, AAMAS measured SO_2 and H_2SO_4 (Arnold et al. 1993).

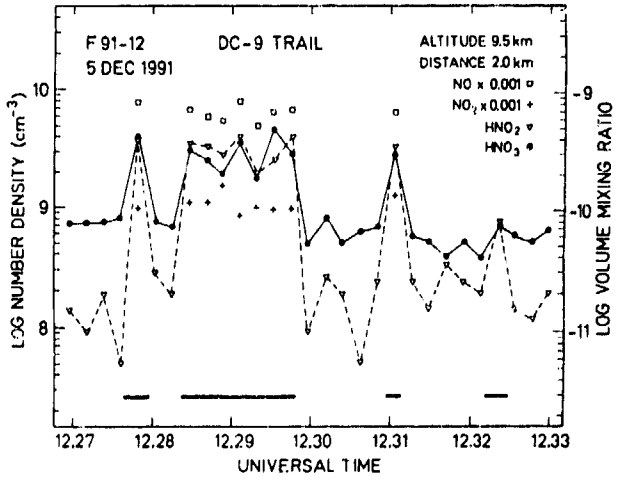

Fig. 16. Time plot of nitrous acid (HNO_2) and nitric acid (HNO_3) abundances measured during chase of a DC-9 airliner at 9.5 km altitude and a distance of 2 km. Periods when the research aircraft was inside the exhaust-trail of the DC-9 are marked by bars. For these periods NO and NO_2 abundances are also given (from Arnold et al. 1992).

Fig. 16 shows for example the result from a measurement of the odd-nitrogen abundances. The HNO_2 abundances increased from about a background value of 5 pptv to a maximum of 520 pptv. Nitric acid is closely correlated with nitrous acid and reaches a maximum abundance of 460 pptv in the trail which exceeds the background abundance (about 40 pptv) by a factor of 10.

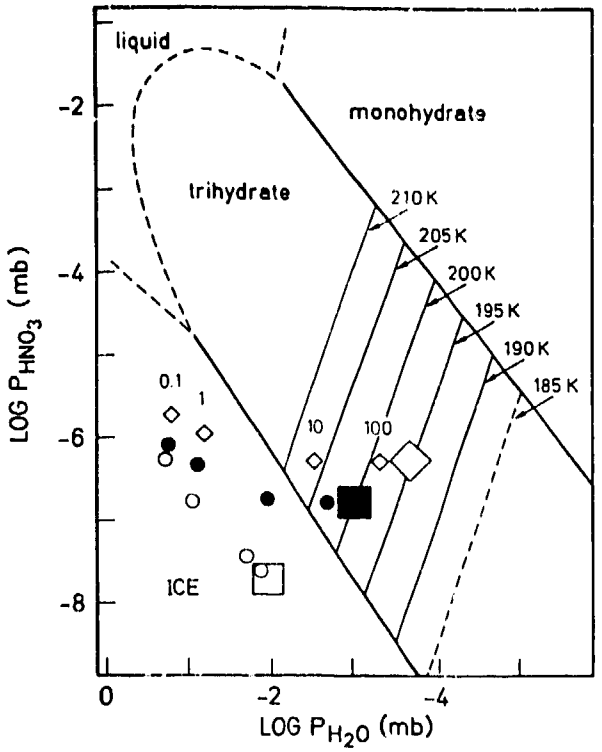

◇ stratosphere at 20 km altitude

● lower stratosphere

○ upper troposphere

Fig. 17. Phase diagram of the HNO_3-H_2O system as obtained from laboratory measurements of Hanson and Mauersberger (1988), with symbols indicating typical conditions in the aircraft plume at various plume ages (from 0.1 to 100 s) (small symbols) and in the environment (large symbols). The water vapour concentration increases from right to left. The diagram shows that the atmosphere tends to form ice particles in the troposphere, but NAT particles (nitric acid trihydrate) in the lower stratosphere and even more in the middle stratosphere, provided the temperature is as low as indicated. Within the aged plumes, the NAT particles may form at higher temperature than in the environment. For ambient temperatures which allow the existence of NAT particles, the plumes may provide the supersaturated conditions which are expected to be required for the initial NAT particle formation. Hence, PSC formation is more likely in the plume of stratospheric aircraft than in the undisturbed environment, mainly because of the higher water vapour concentration in the plume. From Arnold et al. (1992).

Within the exhaust plume of the DC-9, the figure shows NO and NO_2 abundances up to 750 and 150 ppbv, respectively. These values are considerably higher than estimated from Table 7, which is presumably explainable by the different mixing properties in the wake of the DC-9. At this distance, more than 80 % of the NO_x emissions are composed by NO, and less than 0.05 % of the NO_x emissions have the photochemically less reactive form of HNO_3. Also, the rather low values would hardly favour the formation of NAT particles. However, as explained by Fig. 17, Arnold et al. (1992) point out that the emitted water vapour causes supersaturated conditions in the plume of an aircraft and hence may initiate NAT particle formations. The formation of NAT particles may contribute to ozone destruction.

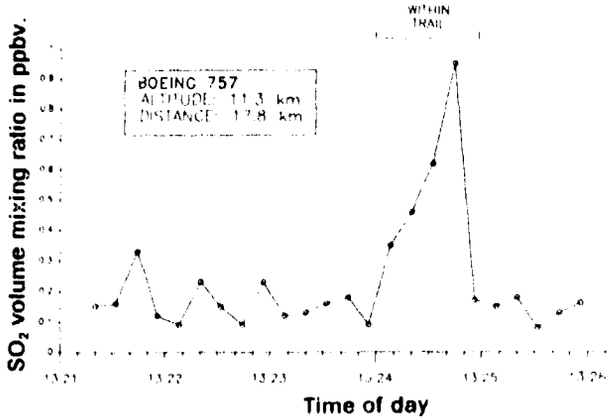

Fig. 18. SO_2 mixing ratio in the wake (trail) of a B 757 aircraft (Arnold, Schlager et al. 1991, personal communication).

Measurements of SO_2 have been performed in the same wake and in addition in several further cases. Fig. 18 shows, for example, the results obtained behind a B757 aircraft at a distance of 17.8 km and at an altitude of 11.3 km. The concentration reaches a maximum value of about 1 ppbv. The measured background concentration of 100 pptv corresponds to previous findings (Georgii and Meixner 1980). The value is smaller than estimated in Table 7, which is presumably caused by a larger area of mixing at this distance. Moreover, the measurements show that a large portion (of the order 20 %) of the sulphur is converted into H_2SO_4. This is an important finding. It suggests that jet aircraft may form contrails composed of sulphuric acid aerosols. These aerosols do not evaporate after plume dissipation because the background atmosphere, around 10 km, is supersaturated with respect to liquid H_2SO_4-H_2O. The aerosol may provide CCN and sites for heterogeneous chemical reactions of trace gases. Thereby they may have an impact on the atmospheric environment (Arnold et al. 1993).

These are the first direct measurements of the chemical compositions in the wake of an airliner at cruise altitude. Douglass et al. (1991) presented measurements showing peaks in NO_2 and NO_y but were not sure that these peaks result from aircraft emissions.

7. Effects of emitted nitrogen oxide

Only a few studies of the effects of impact of aircraft emissions on air chemistry are known. Most studies concentrated on the effects from high speed airtraffic in the stratosphere (e.g. Johnston et al. 1989, Jackman et al. 1991). Early exceptions are Isaksen (1980) and Derwent (1982) who investigated the potential effects of airtraffic operations in the troposphere using a 2D (latitude-altitude) transport-kinetics model. Their investigations were recently refined by Johnson et al. (1992). Similar investigations have been performed by Wuebbles and Kinnison (1990), Crutzen and Brühl (1990) and Beck et al. (1992). Up to present, all studies neglected the impact of heterogeneous chemistry for subsonic airtraffic. For illustration, we include Figs. 19 and 20 as published by Beck et al. (1992). The computations show that aviation emissions cause an increase of NO_x of more than 100 % near the tropopause. This supports the above given corridor estimate according to Table 5. The resultant ozone changes are of order 12 % slightly below the tropopause, and positive everywhere.

These studies are not quite consistent because of different models and different emission rates. However, the studies agree in the general conclusion that the

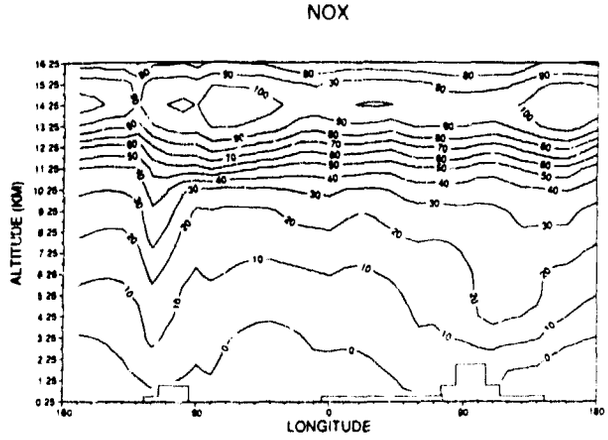

Fig. 19. The percentage change in the NO_x concentration relative to a standard run without aircraft emissions due to the 1987 civil aircraft emissions, for April conditions, from Beck et al. (1992).

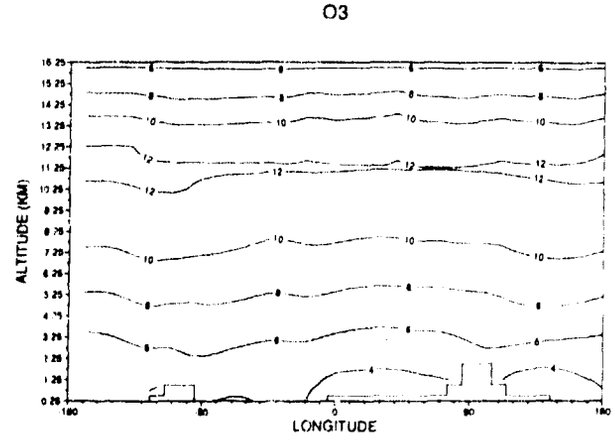

Fig. 20. Same as Fig. 19 for O_3 changes. From Beck et al. (1992).

present emission rate of emissions from aircraft causes a notable increase in ozone in the upper troposphere, ranging from 4 % (Derwent 1982), 7 % (Johnson and Henshaw 1991), 12 % (Beck et al. 1992), to 15 % (Isaksen 1980). Significant changes to ozone occur in regions with low background values of nitrogen oxide. Hence, Johnson et al. (1992) find the largest changes in ozone concentration to occur in the southern hemisphere. For the future, using various assumptions on extrapolated emissions, the ozone change may reach an order 20 to 30 % locally in the troposphere (Beck et al. 1992). Beck et al. (1992) suggest that most of the presently observed ozone increase, see Fig. 2, in the upper troposphere is likely be caused by NO_x emissions from airtraffic.

The other emissions have a much smaller effect on ozone in these calculations. Beck et al. (1992) and Johnson and Henshaw (1991) show that the ozone changes are virtually independent of the HC and CO emissions. Hence, the uncertainty in their emission factors is of minor importance, at least with respect to global ozone chemistry.

The above mentioned studies concentrated on the global impact of NO_x. The chemistry in the immediate wake of aircraft has been studied recently by Weibrink and Zellner (1991), Danilin et al. (1992) and Miake-Lye et al. (1993). Since most of the NO_x emissions have the form of NO, a rapid but local destruction of ozone is to be expected. The effects depend strongly on the rate of mixing of the exhaust plume with the environmental air. Danilin et al. (1992) have also considered the heterogeneous reaction $N_2O_5 + H_2C \rightarrow 2HNO_3$, but found that this reaction does not play an important role at a time scale of up to one hour in the wake. But this reaction can increase the HNO_3 in a plume near the tropopause by a factor of two per week approximately, causing a reduced effectivity of the ozone depletion potential.

With respect to the global warming effect from aircraft NO_x emissions, it is found that their specific effect is considerably larger (about thirty times according to Johnson et al. 1992) than for man-made emissions of NO_x at the surface. This comes from the larger changes in ozone and the larger radiative effects of ozone near the tropopause. These differences occur because the tropopause is cold so that greenhouse gases have the strongest effect there and that the lifetime of NO_x is rather large and because the background concentration of NO_x is low at this altitude so that the photochemical effect of added NO_x is large. Lacis et al. (1990) use a one-dimensional radiative-convective equilibrium model and show that the surface temperature should warm in response to both decreases in ozone above 30 km and increases in ozone below 30 km. Observed ozone trends suggest a cooling of the surface temperature of order 0.05 °C. However, ozone changes due to NO_x emissions from subsonic airtraffic cause a heating effect. The absolute warming effect from present aircraft emissions is of order 0.02 K (Johnson and Henshaw 1991), a number which is about consistent with the findings of Lacis et al. (1990), and might reach a value of order 0.2 K by the year 2050 (Brühl and Crutzen 1988). However, these results are obtained for fixed cloud amounts, and without accounting for heterogeneous chemistry on sulphuric acid aerosols, PSCs or ice clouds.

The increase in tropospheric ozone may offset the decrease in stratospheric ozone due to release of chlorofluorocarbons (Derwent 1982) and even reduce the solar UV-B radiation at the earth surface in the industrialized northern hemisphere, in particular in summer (Brühl and Crutzen 1989).

8. Effects of emitted water vapour and cloud formation

Water vapour is by itself one of the most important greenhouse gases. In a warmer world, an increase of water vapour is expected which may about triple the greenhouse effect of carbon dioxide. The greenhouse effect of added water vapour (or any other infrared absorber) is strongest when added near the tropopause because shielding of radiation to space is most pronounced if the absorber is cold (Graßl 1990, Lacis et al. 1990). As an absorber of terrestrial radiation in the stratosphere, a water vapour molecule is up to 200 times more effective than a CO_2 molecule (Graßl et al. 1991).

As shown by simple radiation transfer calculations (Schumann and Wendling 1990), an increase in water vapour concentration from its standard value to saturation in (an arbitrarily selected) altitude range 9 to 14 km causes changes in the local heating rate of order 1 K/h which is about 100 times larger than the effect of doubling CO_2. Although such a drastic change in water vapour concentration will not occur globally, it nevertheless demonstrates the strong radiative sensitivity of the atmosphere with respect to water vapour concentrations. A similar computation has been reported by Shine and Sinha (1991), who find that the sensitivity of the surface temperature to a fixed absolute increase in water vapour mixing ratio in individual global 40-hPa slabs is largest when the increase occurs in a slab at altitudes with pressure in between 400 and 100 hPa. In absolute terms, the increase in surface temperature is of the order 0.02 K for an increase of 0.001 g per kg in such a 50 hPa-slab.

Tables 3 and 4 indicate that the global contribution of water vapour emissions is small in comparison to the background state. However, the emissions add to the expected increases in water vapour concentrations due to the warming of the troposphere, and add to stratospheric water vapour from the increasing rate of methane oxidation.

Even larger changes occur if the water condenses and forms thin ice clouds (Liou 1986). Such ice clouds have a strong greenhouse effect if their albedo is low but the emissivity is large which is the case for thin clouds with large (order 0.3μm in radius or larger) particle sizes (Stephens and Webster 1981; Stephens et al. 1990). Liou et al. (1990) computed from a 2D model an increase in surface temperature of 1 K for a 5 % increase of high cirrus clouds (increase of total coverage by high clouds by about 1 %) between 20N and 70N. Recently, Strauß and Wendling (DLR, personal comm., 1992) applied Liou's model in a regionalized version to the spacific climatic conditions in Southern Germany. They find that the surface temperature increases about linearly with cloud cover due to contrails, see Fig. 21. For 0.4 % additional cloud coverage by contrails, which is the presently observed value (Schumann & Wendling 1990), the model predicts an increase in surface tem-

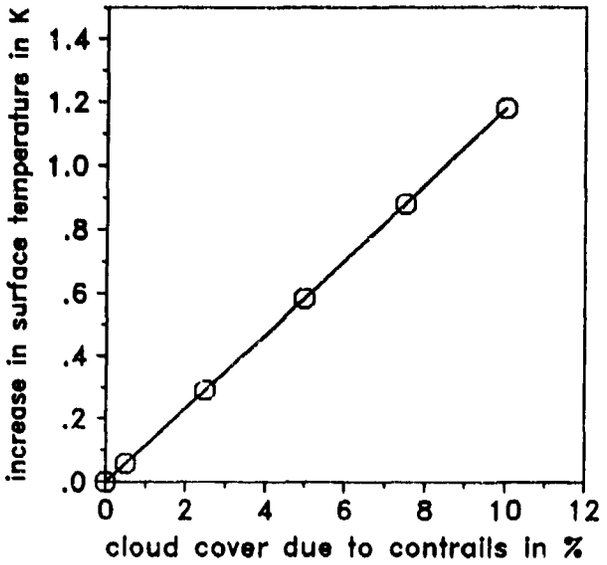

Fig. 21. Increase in surface temperature as a function of percentage cloud cover due to contrails. This is the result from a cloud radiation model which is adjusted to the local climatic conditions of South Germany. From Strauß and Wendling, DLR (1992).

perature by about 0.05 K. The regional effect is smaller because some of the feedback effects used by Liou (e.g. polar albedo change) are unimportant in this regional analysis.

Contrails emerge in particular at temperatures below -40°C (Appleman 1953). Such low temperatures prevail at the tropopause, where temperatures in the range -50° to -70°C are typical for extratropical regions. Miake-Lye et al. (1993) have applied the analysis of Appleman (1953) to the standard atmosphere as a function of altitude and latitude. The result, see Fig. 22, shows regions labelled with ALWAYS corresponding to regions with temperature low enough so that contrails form even in dry air. The region labelled NEVER corresponds to warmer parts where contrails would not form even in a saturated atmosphere. By inspection we see that much of the high-flying airtraffic takes place at altitudes where the formation of contrails is very likely, in particular in the northern winter hemisphere. A small reduction of global mean temperature near and above the tropopause by, say, 2 K would strongly increase the region in which contrails have to be expected. Note that this analysis only considers the formation process of contrails. The residence time of such contrails depends strongly on the relative humidity of the environmental air and the amount of mixing with the contrail. The relative humidity is lower in the stratosphere but the mixing will be more rapid in the troposphere. Since very long living contrails will occur only at high relative humidity, the upper troposphere is more likely covered by large amounts of cirrus clouds induced by aircraft than the lower stratosphere.

Contrail observations from satellite data, Lidar measurements, and climatological observations of cloud cover changes have been described in Schumann and Wendling (1990). Large (1 to 10 km wide and more than 100 km long) contrails are observed regionally on about a quarter of all days within one year, but the average contrail coverage is only about 0.4 % in mid Europe.

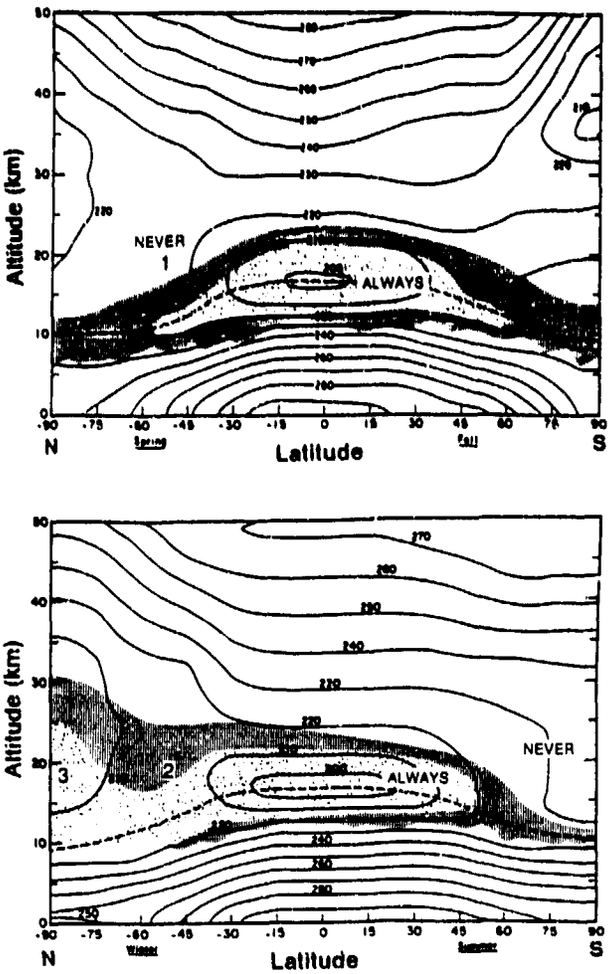

Fig. 22. Map versus latitude from pole to pole and altitude from surface to 50 km showing shaded regions where contrails form ALWAYS, eventually, or NEVER, assuming a standard atmosphere and contrails in local equilibrium after complete mixing. Contours represent constant temperature at increments of 10 K. Top: for March 22, bottom: for Jan. 15. From Miake-Lye et al. (1993).

Fig. 23 shows a further example of Lidar observation of contrails formed by airtraffic. The Lidar observations have been taken on board of the Falcon aircraft at an altitude of about 12 km looking downward and passing over the airway G104 in southern Germany on Nov. 7, 1990, 15:20 local time. The plot shows the backscatter signal which indicates a rather young contrail on the right and two older contrails at the left side. The thickness of the contrails is of order 1.5 km with a core of 300 m. The width shown reaches 10 km but is actually smaller by a factor of 0.64 because the Falcon did cross the airway at an angle of about 40°. The core of the contrail with strong backscatter signals indicates high concentrations of small particles. Below that core we see the trace of sedimented larger particles with motions which are obviously affected by wind shear.

The Lidar observations show that the contrails may become more than 1 km thick. Such big contrails cannot be explained by the amount of water which is emitted by the aircraft. Obviously, the large contrails form by triggering ice formation in air which is subsaturated with

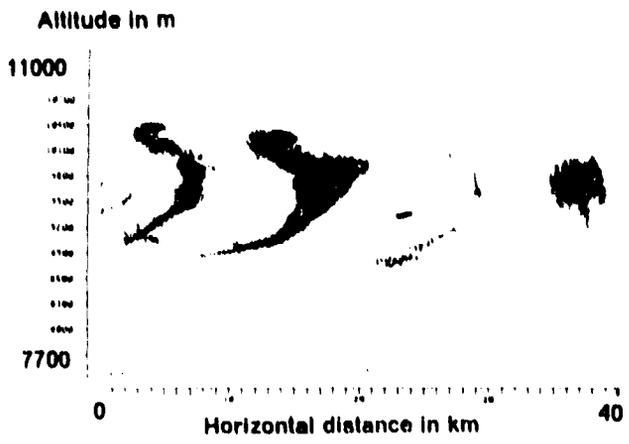

Fig. 23. Vertical cross-section with contrails. The grey tones represent the backscatter signal amplitude as obtained from a Lidar sounding on board of the Falcon (flying from left to right) at 12 km altitude on Nov. 7, 1990, 14.20 UTC (Schumann and Reinhardt, 1991).

respect to liquid water but supersaturated with respect to the ice phase. Also the emitted sulphur particles may trigger such ice clouds in supersaturated regions. Hence, the largest artificial contrails are to be expected in regions where the water vapour concentration is above saturation with respect to the ice phase but below the saturation with respect to water. Unfortunately, the present data on water vapour concentrations from the global operational observation system are too inaccurate to determine these regions.

9. Summary

This survey reveals that high-flying subsonic airtraffic affects the present state of the atmosphere mainly by its emissions of NO_x at high altitudes. As shown by simple estimates of mean concentration changes, the increase in NO_x exceeds previous estimates of 30 % and may even exceed 100 % in particular in the flight corridors over the North Atlantic. Such changes are causing about 20 % change for ozone in the upper troposphere. It appears as if the present airtraffic is responsible for most of the observed ozone increase in the upper troposphere (Beck et al. 1992). The greenhouse effect of this change is estimated to be of the order 0.01 to 0.02 K (Johnson et al. 1992).

With respect to additional cloud cover the estimates are very uncertain. Regional changes in between a fraction of a percent and 2 % appear to be possible. Analyses of satellite data for one year over central Europe indicate 0.4 % additional cirrus clouds from contrails. Lidar observations show that very large contrails may be formed with small particles which grow and sediment quickly. Hence, the additional cloudiness induced by contrails can be much larger than that to be expected from the added water vapour (which is small) because of ice nucleation triggered by the contrails in air supersaturated with respect to ice. Very thin ice clouds will cause warming while thicker clouds cause cooling. It is not absolutely sure at present that the warming dominates but this is what actual models predict. Quantitatively, the computed warming effect at the surface is not very large (of order 0.01 to 0.05 K) but it is not clear whether this is the most meaningful impact indicator.

With respect to SO_x the results suggest that airtraffic increase the aerosol concentration in the lower stratosphere and upper troposphere. The aerosol may provide cloud condensation nuclei and sites for heterogeneous chemical reactions of trace gases. Thereby they may have an impact on the atmospheric environment. The increased concentrations of water vapour may also increase the amount of PSCs with possible negative effects on the ozone layer. However, these effects cannot yet be quantified.

For the future, the strong increase in airtraffic will be accompanied by a weaker but still important increase of about 3 to 4 % in fuel consumption per year, meaning a doubling within the next 20 years or so. The climate changes induced by these emissions enhance the problems from other sources (e.g. reduced stratospheric temperature due to CO_2 increases or increased water vapour concentration due to increased methane concentrations, and related increase in PSCs and reduced ozone).

Many open questions have been identified which require further research. The most important ones are: What are the effective emission rates from present and future traffic at all levels of the atmosphere? How is the 3-D dispersion and conversion from jet exit and flight corridors to global distribution? What are the chemical conversions, ozone generation, heterogeneous reactions on PSCs, ice crystals and aerosols? How large is the global area where the water vapour concentration is above saturation with respect to the ice phase but below the saturation with respect to water, i.e. where large contrails may be formed? What are the climatic and environmental effects of the atmospheric changes for the living conditions on earth?

Corresponding 3D global circulation models including a sufficiently complete chemical cycle and radiation scheme for both the troposphere and the stratosphere are still under development (Dameris 1993). Much more basic work is required to provide suitable models for the heterogeneous reactions. The 3D models are extremely computer time consuming because of the large number of chemical components and reactions to be treated. Moreover, the models have to provide sufficient resolution in particular near the tropopause. Model validation studies are needed, in particular to verify the correct treatment of the interaction between stratosphere and troposphere. Also, the models need reliable estimates on natural emissions and background concentrations as input, which are not readily available. Of an utmost importance are observational programs to see whether the essential effects are included in the models, and data to verify the model predictions. The North Atlantic flight corridor appears to be particularly suited for such validation measurements because the impact of airtraffic emissions should be of measurable magnitude in this region and clearly distinguishable from other causes.

Several research projects have been started (Dunker 1993) to resolve the list of open questions. However, long-term research is still to promote, in particular to obtain the required observational data in the polluted

atmosphere at cruise altitude and to develop and verify according models.

Certainly, the list of uncertainties is long. Some of the effects of emissions on environment and climate may be small or even may mitigate the impact of other, more important disturbances to ozone layer and greenhouse effects. Nevertheless, the potential of aviation emissions to cause serious changes to climate and ozone layer exists, and limitations of the emissions from airtraffic may become necessary sooner or later. Therefore, efficient means have to be developed to reduce the specific emissions from airtraffic, in particular with respect to NO, but also with respect to H_2O and SO_2.

In order to reduce the emissions of nitrogen oxide, new propulsion systems should be developed. This requires extensive research and developments on the technological side (Dunker 1993). Other means (like better traffic control etc.) should be also considered. These means have to be developed and installed at sufficient speed to compete with the growth rate of airtraffic.

Acknowledgement. The author is grateful to F. Arnold (Max-Planck Institut für Kernphysik, Heidelberg), D. Ehhalt (Forschungszentrum Jülich), B. Fay (Deutscher Wetterdienst Offenbach), Lufthansa Frankfurt, R. C. Miake-Lye (Aerodyne Research Inc., USA), K. Wege (DWD Hohenpeißenberg), and to several colleagues in DLR, for providing unpublished research results and support. The author also gratefully acknowledges the support by the Deutsche Forschungsgemeinschaft (DFG), the Bundesministerium für Forschung und Technologie (BMFT), and the Commission of the European Community.

References

Amann, M., 1990: Recent and future development of emissions of nitrogen oxides in Europe. Atmos. Environm. 24A, 2759-2764.

Appenzeller, C. and H.C. Davies, 1992: Structure of stratospheric intrusions into the troposphere. Nature 358, 570-572.

Appleman, H., 1953: The formation of exhaust condensation trails by jet aircraft. Bull. Amer. Meteorol. Soc., 34, 14-20.

Arnold, F., J. Scheidt, T. Stilp, H. Schlager and M.E. Reinhardt, 1992 Measurements of jet aircraft emissions at cruise altitude I: The odd-nitrogen gases NO, NO_2, HNO_2 and HNO_3. Geophys. Res Lett. 12 (1992) 2421-2424.

Arnold, F., J. Scheidt, T. Stilp, H. Schlager and M.E. Reinhardt, 1993 Sulphuric acid emission by jet aircraft. subm. to Nature.

Austin, J., N. Butchart and K.P. Shine, 1992: Possibility of an Arctic ozone hole in a doubled-CO_2 climate. Nature 360, 221-225.

Baumann, R., R. Busen and H.P. Fimpel, 1993: Measurements on contrails of commercial aircraft. Proc. 8th Symp. Meteorol. Obs. and Instrum., Amer. Met. Soc., Boston, p. 484-489.

Beck, J. P., C. E. Reeves, F. A. A. M. de Leeuw and S. A. Penkett, 1992: The effect of airtraffic emissions on tropospheric ozone in the nothern hemisphere. Atmospheric Environment 26A, 17-29.

Bekki, S., R. Toumi, J.A. Pyle and A.E. Jones, 1991: Future aircraft and global ozone. Nature 354, 193-194.

Bekki, S. and J.A. Pyle, 1992: Two-dimensional assessment of the impact of aircraft sulphur emissions on the stratospheric sulphate aerosol layer. J. Geophys. Res. 97, 15839-15847.

Brasseur, G., 1992: Natural and anthropogenic perturbations of the stratospheric ozone layer. Planet. Space Sci. 40, 403-412.

Brasseur, G. and S. Solomon, 1986: Aeronomy of the Middle Atmosphere. Second Ed., D. Reidel, Dordrecht, pp. 452.

Brasseur, G., C. Granier and S. Walters, 1990: Future changes in stratospheric ozone and the role of heterogeneous chemistry. Nature 348, 626-628.

Brühl, C. and P.J. Crutzen, 1988: Scenarios of possible changes in atmospheric temperatures and ozone concentrations due to man's activities, estimated with a one-dimensional coupled photochemical climate model. Climate Dynamics, 2, 173-203.

Brühl, C. and P.J. Crutzen, 1989: On the disproportionate role of tropospheric ozone as a filter against solar UV-B radiation. Geophys. Res. Let. 16, 703-706.

Brühl, C., P. Crutzen, E.F. Danielsen, H. Graßl, H.-D. Hollweg and D. Kley, 1991: Umweltverträglichkeitsstudie für das Raumtransportsystem SÄNGER. Teil 1, Unterstufe. Studie im Auftrag des BMFT, Bonn, Mai 1991.

CAEP, 1991: Committee on Aviation Environmental Protection (CAEP/2), Second Meeting, ICAO, Montreal, Report CAEP/2-DP/5 10/12/91, pp 28.

CIAP, 1975: Final Report, Department of Transportation, Climatic Impact Assessment Program, DOT-TST-75-51 and ff. (8 vols.).

Crow, S.C., 1970: Stability theory for a pair of traveling vortices. AIAA Journal, 8, 2172-2179.

Crutzen, P.J., 1972: SST's - a threat to the earth's ozone shield. Ambio, April 1972, 41-51.

Crutzen, P.J., 1988: Tropospheric ozone: an overview. In I.S.A. Isaksen (ed.): Tropospheric Ozone, D. Reidel Publ., 3-32.

Crutzen, P.J. and F. Arnold, 1986: Nitric acid cloud formation in the cold Antarctic stratosphere: a major cause for the springtime "ozone hole". Nature 324, 651-655.

Crutzen, P.J. and C. Brühl, 1990: The atmospheric chemical effects of aircraft operations. In: U. Schumann (ed.): Air-Traffic and the Environment. Lect. Notes in Engrg., Vol 60, Springer-V., Berlin, p. 96-106.

Crutzen, P.J. and P.H. Zimmermann, 1991: The changing photochemistry of the troposphere. Tellus 43AB, 136-151.

Cubasch, U., K. Hasselmann, E. Maier-Reimer and R. Sausen, 1992: Time-dependent greenhouse warming computations with a coupled ocean-atmosphere model. Climate Dyn. 8, 55-69.

Dameris, M., 1993: Zusammenstellung und Bewertung von numerischen Modellen im Hinblick auf Untersuchungen zum Thema Schadstoffe in der Luftfahrt. DLR, Institut für Physik der Atmosphäre, Oberpfaffenhofen, DLR-Mitt., in press.

Danilin, M.Yu., B.C. Krüger and A. Ebel, 1992: Short-term atmospheric effects of high-altitude aircraft emissions. Ann. Geophys. 10, 904-911.

Deidewig, F., 1992: Schadstoffemissionen ziviler Flugtriebwerke. DGLR-Report 92-03-084. Deutsche Gesellschaft für Luft- und Raumfahrt, Bonn, pp. 10.

Derwent, R.G., 1982: Two-dimensional model studies of the impact of airtraffic exhaust emissions on tropospheric ozone. Atmos. Environm. 16, 1997-2007.

Dickson, C.L. et al., 1989: Aviation turbine fuels, 1988, Report No. NIPER-159 PPS, National Institute for Petroleum and Energy Research, Bartlesville, OK.

Dickson, C.L. et al., 1992: Aviation turbine fuels, 1991, Report No. NIPER-174 PPS, National Institute for Petroleum and Energy Research, Bartlesville, OK.

Douglass, A.R., M.A. Carroll, W.B. DeMore, J.R. Holton, I.S.A. Isaksen, H.S. Johnston and M.K.W. Ko, 1991: The atmospheric effects of stratospheric aircraft: a current consensus. NASA Refer. Publ. 1251, 39 p.

Duclos, R.M., R.L. Bowles, M. Manarte, M.J. Ellis, A. Potter, 1991: North Atlantic air traffic forecasts for the years 1991-1996, 2000, 2005 and 2010. Report of: The North Atlantic Traffic Forecasting Group, 25th Meeting, 10 June - 19 June, 1991, ICAO Regional Office, Paris.

Dunker, R. (ed.), 1993: Understanding the Atmospheric Impact of Aircraft Emissions. Report of the APARTE Group, Comm. of the European Comm., DGXII-F & DGXII-D, in preparation.

Ebel, A., H. Hass, H.J. Jakobs, M. Memmersheim, M. Laube, A. Oberreuter, H. Geiss and Y.-H. Kuo, 1991: Simulation of ozone intrusion caused by a tropopause fold and cut-off low. Atmospheric Environm., 25A, 2131-2144.

Egli, R.A., 1990 Nitrogen oxide emissions from air traffic. Chimia 44, 369-371.

Ehhalt, D.H. and Drummond, J.W., 1988: NO_x sources and the tropospharic distribution of NO_x during Stratoz III. In: I. S. A. Isaksen (ed.), Tropospheric Ozone, D. Reidel Publ. Co., 217-237.

Ehhalt, D.H., F. Rohrer and A. Wahner, 1992: Sources and distribution of NO_x in the upper troposphere at northern mid-latitudes. J. Geophys. Res. 97, 3725-3738.

Fabian, P., 1990: Constituents and transport properties of the atmosphere above and below the tropopause. In: U. Schumann (ed.): Air Traffic and the Environment. Lect. Notes in Engrg., Vol 60, Springer-V., Berlin, p. 84-95.

Fabian, P., 1992: Atmosphäre und Umwelt. 4th. revised ed., Springer-V., Berlin, pp. 144.

German Bundestag (ed.), 1991: Protection of the Earth. A Status Report with Recommendations for a New Energy Policy. Vol. 1, Deutscher Bundestag, Referat Öffentlichkeitsarbeit, Bonn, ISBN 3-924521-71-9, pp. 672. Economia Verlag, Bonn.

Georgii, H.W. and F.X. Meixner, 1980: Measurements of the tropospheric and stratospheric SO_2 distribution. J. Geophys. Res. 85, 7433-7438.

Granier, C. and G. Brasseur, 1992: Impact of heterogeneous chemistry on model predictions of ozone changes. J. Geophys. Res. 97, 18015-18033.

Graßl, H., 1990: Possible climatic effects of contrails and additional water vapor. In: U. Schumann (ed.): Air Traffic and the Environment. Lect. Notes in Engrg., Vol 60, Springer-V., Berlin, p. 124-137.

Graßl, H., C. Brühl, P. Crutzen, E. Danielsen, H.-D. Hollweg, D. Kley, 1991: The possible environmental impact of hypersonic transport systems. 42nd Congr. Intern. Astron. Feder., October 5-11, 1991, Montreal, Canada, Paper no. IAA-91-735, 7 p.

Grieb, H. and B. Simon, 1990: Pollutant emissions of existing and future engines for commercial aircraft. In: U. Schumann (ed.): Air Traffic and the Environment. Lect. Notes in Engrg., Vol 60, Springer-V., Berlin, p. 43-83.

Hagen, D.E., M.B. Trueblood and P.D. Whitefield, 1992: A field sampling of jet exhaust aerosols. Particulate Sci. & Techn. 10, 53-63.

Hameed, S. and J. Dignon, 1992: Global emissions of nitrogen and sulfur oxides in fossil fuel combustion 1970-1986. J. Air Waste Manage. Assoc. 42, 159-163.

Hanson, D. and K. Mauersberger, 1988: Laboratory studies of the nitric acid trihydrate: Implications for the southpolar stratosphere. Geophys. Res. Lett. 19, 2063-2066.

Hanson, D.R., 1992: The uptake of HNO_3 onto ice, NAT, and frozen sulfuric acid. Geophys. Res. Lett. 19, 2063-2066.

Havlik, D., 1989: Die Höhenlage atmosphärischer Niveaus entlang von Flugrouten. Geographisches Institut der RWTH Aachen.

Hidalgo, H. and P.J. Crutzen, 1977: The tropospheric and stratospheric composition perturbed by NO_x emissions of high-altitude aircraft. J. Geophys. Res. 82, 5833-5866.

Hoerling, M.P., T.K. Schaack and A.J. Lenzen, 1993: A global analysis of stratospheric-tropospheric exchange during northern winter. Mon. Weather Rev. 121, 162-172.

Hofmann, D.J., 1991: Aircraft sulphur emissions. Nature 349, 659.

Hofmann, D.J. and S.J. Oltmans, 1992: The effect of stratospheric water vapor on the heterogeneous reaction rate of $ClONO_2$ and H_2O for sulfuric acid aerosol. Geophys. Res. Lett. 19, 2211-2214.

Hoinka, K.P., M.E. Reinhardt and W. Metz, 1993: North Atlantic air traffic within the lower stratosphere: Cruising times and corresponding emissions. Subm. to J. Geophys. Res.

Hough, A.M., 1991: Development of a two-dimensional global tropospheric model: Model chemistry. J. Geophys. Res. 96, 7325-7362.

Isaksen, I.S.A., 1980: The tropospheric ozone budget and possible man made effects. Proc. Quadrennial Ozone Symposium, WMO, Boulder, 4-9 August 1980, p. 845-852.

Isaksen, I.S.A. and O. Hov, 1987: Calculation of trends in the tropospheric concentration of O_3, OH, CO, CH_4 and NO_x. Tellus 39B, 271-285.

Jackman, C.H., A.D. Douglass, K.F. Brueske and S.A. Klein, 1991: The influence of dynamics on two-dimensional model results: Simulations of ^{14}C and stratospheric NO_x injections. J. Geophys. Res. 96, 22559-22572.

Jacob, D.J., 1991: Tropospheric chemistry: 4 years of U.S. research, Rev. Geophys., Suppl., 2-11. (U.S. National Report to Intern. Union of Geodesy and Geophysics 1987-1990).

Johnson, C.E. and J. Henshaw, 1991: The impact of NO_x emissions from tropospheric aircraft. Harwell Lab., Oxon, UK, Report AEA-EE-0127.

Johnson, C., J. Henshaw and G. McInnes, 1992: Impact of aircraft and surface emissions of nitrogen oxides on tropospheric ozone and global warming. Nature 355, 69-71.

Johnston, H.S., 1971: Reduction of stratospheric ozone by nitrogen oxide catalysts from supersonic transport exhaust, Science, 173, 517-522.

Johnston, H.S., D.S. Kinnison and D.J. Wuebbles, 1989: Nitrogen oxides from high altitude aircraft: An update of potential effects on ozone. J. Geophys. Res., 94, 16351-16363.

Johnston, H.S., M.J. Prather and R.T. Watson, 1991: The atmospheric effects of stratospheric aircraft: A topical review. NASA Refer. Public. 1250, 28 p.

Kavanaugh, M., 1988: New estimates of NO_x from aircraft: 1975-2025. Proc. 81st Annual Meeting of APCA (Air Pollution Control Association), Dallas, Texas, June 19-14, paper 88-66.10, 15 pp.

Kinnison, D.E. and D.J. Wuebbles, 1991: Future aircraft and potential effects on stratospheric ozone and climate. Paper no. IAA-91-736, 42nd Congr. of the Intern. Astron. Federation, October 5-11, 1991, Montreal, Canada, 12 p.

Ko, M.K.W., D. Kley, S. Wofsy and E. Zhadin, 1992: Pre-

dicted aircraft effects on stratospheric ozone. Chapter 9 in WMO: Scientific Assessment of Ozone Depletion: 1991, WMO Geneva: Global Ozone Research and Monitoring Project - Report No. 25, pp. 9.1-9.17.

Lacis, A.A., D.J. Wuebbles and J.A. Logan, 1990: Radiative forcing of climate by changes in the vertical distribution of ozone. J. Geophys. Res. 95, 9971-9981.

Lecht, M., P. Schimming and G. Winterfeld, 1986: Ermittlung der Emissionen ziviler Triebwerkstypen im Teillastbereich. DFVLR-IB-325-12/86, DLR Cologne.

Liou, K.-N., 1986: Influence of cirrus clouds on weather and climate processes: A global perspective. Mon. Wea. Rev. 114, 1167-1199.

Liou, K.-N., S.-C. Ou and G. Koenig, 1990: An investigation of the climatic effect of contrail cirrus. In: U. Schumann (ed.): Air Traffic and the Environment. Lect. Notes in Engrg., Vol 60, Springer-V., Berlin, p. 154-169.

Logan, J.A., 1985: Tropospheric ozone: seasonal behavior, trends, and anthropogenic influence. J. Geophys. Res. 90, 10463-82.

Mahlman, J.D., 1973: On the maintenance of the polar front jet stream. J. Atmos. Sci. 30, 544- 557.

McElroy, M.B., R.J. Salawitch and K. Minschwaner, 1992: The changing stratosphere. Planet. Space Sci. 40, 373-401.

McInnes, G. and C.T. Walker, 1992: The global distribution of aircraft air pollution emissions. Warren Spring Lab , Report No. LR 872 (AP).

Miake-Lye, R.C., M. Martinez-Sanchez, R.C. Brown and C.E. Kolb, 1993: Plume and wake dynamics, mixing, and chemistry. AIAA paper No. 91-3158, J. Aircraft, in press.

Nüßer, H.-G. and A. Schmitt, 1990: The global distribution of air traffic at high altitudes, related fuel consumption and trends. In: U. Schumann (ed.): Air Traffic and the Environment. Lect. Notes in Engrg., Vol 60, Springer-V . Berlin, p. 1-11.

Penner, J.E., C.S. Atherton, J. Dignon, S.J. Ghan and J.J. Walton, 1991: Tropospheric nitrogen: A three-dimensional study of sources, distributions, and deposition. J. Geophys. Res. 96, 959-990.

Pitchford, M., J.G Hudson and J. Hallet, 1991: Size and critical supersaturation for condensation of jet engine exhaust particles. J. Geophys. Res. 96, 20787-20793.

Peter, T., C. Brühl and P.J. Crutzen, 1991: Increase in the PSC-formation probability caused by high-flying aircraft. Geophys. Res. Let. 18, 1465-1468.

Plumb, R.A. and J.D. Mahlman, 1987: The zonally averaged transport characteristics of the GFDL general circulation/transport model. J. Atmos. Sci. 44, 298-324.

Prather M.J., H.L. Wesoky, R.C. Miake-Lye, A.R. Douglass, R.P. Turco, D.J. Wuebbles, M.K.M. Ko, A.L. Schmeltekopf, 1992: The atmospheric effects of stratospheric aircraft: A first program report. NASA Ref. Publ. 1272, pp. 233.

Reichow, H.-P., 1990. Fuel consumption and emissions of air traffic. In: U. Schumann (ed.): Air Traffic and the Environment. Lect. Notes in Engrg., Vol 60, Springer-V., Berlin, p. 12-22.

Rodriguez, J.M., M.K.W. Ko and N.-D. Sze, 1991: Role of heterogeneous conversion of N_2O_5 on sulphate aerosols in global ozone losses. Nature 352, 134-137.

Rood, R., A. Douglas and C. Weaver, 1992: Tracer exchange between tropics and middle latitudes. Geophys. Res. Lett. 19, 805-808.

Schlager, H., F. Arnold, D. Hofmann and T. Deshler, 1990: Geophys. Res. Lett. 17, 1275-1278.

Schoeberl, M.R., L.R. Lait, P.A. Newman and J.E. Rosenfield, 1992: The structure of the polar vortex. J. Geophys. Res. 97, 7859-7882.

Schumann, U. (Ed.), 1990: Air Traffic and the Environment - Background, Tendencies and Potential Global Atmospheric Effects. Proc. of a DLR Intern. Coll., Bonn, Nov. 15/16, 1990, Lecture Notes in Engrg., Vol. 60, Springer-V., Berlin, pp. 170.

Schumann, U. and M.E. Reinhardt, 1991: Studies on the effect of high-flying air-traffic on the atmosphere. 42nd Congr. Intern. Astron. Feder., October 5-11, 1991, Montreal, Canada, Paper no. IAA-91-737, 11 p.

Schumann, U. and P. Wendling, 1990: Determination of contrails from satellite data and observational results. In: U. Schumann (ed.): Air Traffic and the Environment. Lect. Notes in Engrg., Vol 60, Springer-V., Berlin, p. 138-153.

Shine, K.P. and A. Sinha, 1991: Sensitivity of the earth's climate to height-dependent changes in the water vapour mixing ration. Nature 354, 382-384.

Simon, B., 1988: Umweltaspekte bei der Entwicklung von Flugtriebwerken. Vortragsmanuskript, Luftfahrt-Städtebau-Umwelt, Haus der Technik Essen, 6./7.12.88.

Spicer, C.W., M.W. Holdren, D.L. Smith, D.P. Hughes, and M.D. Smith, 1990: Chemical composition of exhaust from aircraft turbine engines. ASME-paper 90-GT-34, 7 p.

Stephens, G.L. and P.J. Webster, 1981: Clouds and climate: Sensitivity of simple systems. J. Atmos. Sci., 38, 235-247.

Stephens, G.L., S.-C. Tsay, P.W. Stackhouse and P. Flatau, 1990: The relevance of the microphysical and radiative properties of cirrus clouds to climate and climatic feedback. J. Atmos. Sci. 47, 1742-1753.

Stolarski, R.S., P. Bloomfield and R.D. McPeters, 1991: Total ozone trends deduced from Nimbus 7 TOMS data. Geophys. Res. Lett. 18, 1015-1018.

Vaughan, G., 1988: Stratosphere-troposphere exchange of ozone. In: I. S. A Isaksen (ed.), Tropospheric Ozone, D. Reidel Publ. Co., 125-135.

Volz, A. and D. Kley, 1988: Evaluation of the Montsouris series of ozone measurements made in the nineteenth century. Nature 332, 240.

Watson, R.T., M.J. Kurylo, M.J. Prather and F.M. Ormond, 1990: Present state of knowledge of the upper atmosphere 1990: An assessment report. NASA Ref. Publ. 1242, p. 123-136.

Wege, K., 1992: Die Ozontrends am Hohenpeißenberg. Meteorol. Zeitschrift N.F. 1, 260-262.

Weibrink, G. and R. Zellner, 1991: Modelling of plume chemistry of high flying aircraft with H_2 combustion engines. Proc. of 3rd Aerospace Symposium (H. Oertel, Jr., ed.), Springer-Verlag, Berlin, in press.

Weisenstein, D.K., M.K.W. Ko, J.M. Rodriguez and N.-D. Sze, 1991: Impact of heterogeneous chemistry on model-calculated ozone change due to high speed civil transport aircraft. Geophys. Res. Lett. 19, 1991-1994.

Whitefield, P.D., M.B. Trueblood, and D.E. Hagen, 1993: Size and hydration characteristics of laboratory simulated jet engine combustion aerosols. Particulate Sci. & Techn., in press.

WMO, 1991: Scientific Assessment of Ozone Depletion: 1991. World Meteorological Organization, Global Ozone Research and Monitoring Project - Report No. 25. WMO, Casa Postale No. 5, CH-1211 Geneva 20, Switzerland.

Wuebbles, D.J. and D.E. Kinnison, 1990: Sensitivity of stratospheric ozone to present and possible future aircraft emissions. In: U. Schumann (ed.): Air Traffic and the Environment. Lect. Notes in Engrg., Vol 60, Springer-V., Berlin, p. 107-123.

Discussion

Question 1. Clare Eatock
Was the final temperature effect of 0.01 to 0.1K a global or a Northern Europe effect?

Author's Reply
This is an order of magnitude effect with respect to the greenhouse gases, ozone and water vapour. It is meant as a global estimate. The contrail impact is of the order of 0.05K regionally.

Question 2. Leonhard Fottner
Could you please comment on the contribution of military aircraft?

Author's Reply
The amount of fuel consumed by military aviation is roughly 25% of all aviation fuel consumption. About 5% of all traffic over the North Atlantic is identified as being military type aircraft. Estimates for Germany show that most of the military traffic occurs below 8 km. altitude. I do not know about military flights in the stratosphere, but I expect that this contributes less than 25% of all aviation in the stratosphere.

Question 3. Dilip Ballal
Is there much turbulent diffusion in the atmosphere at altitudes at which aircraft emissions are significant? What effect would this have on the dispersion of pollutants?

Author's Reply
Turbulence near the tropopause is highly intermittent with long periods of no turbulence, and short periods of intense turbulence due to breaking gravity waves or Kelvin-Hemholtz instabilities. Such turbulence occurs more frequently over land than over the oceans. The mean vertical diffusivity in the lower atmosphere is estimated to be of the order of 0.2 square metres/sec. Mixing is important for all nonlinear processes, like particle and contrail formation.

Question 4. N.H. Pratt
Have you assessed the potential impact of nitrous oxide, which is likely to increase with emphasis on lean burn, on processes in the upper atmosphere?

Author's Reply
The emission of nitrous oxide from aircraft could be of climatic relevance because N_2O has a lifetime in the atmosphere of about 100 years, and is an efficient greenhouse gas. Since it is long living, its emission from aircraft has to be compared directly with other sources. As best I can remember, about 10 to 20 Mt of N_2O are emitted annually from the earth's surface. The amount of fuel burned is about 200 Mt/yr. Hence N_2O would be an important emission from aircraft if the emission would be about 1g/Kg or higher. As far as I know, the emission index is much smaller, however.

Question 5. Dr Gordon Andrews
You mentioned that a reduction in aviation fuel sulphur levels may be required to limit sulphur dioxide and suphuric acid emissions in the upper atmosphere. What level of fuel sulphur do you think might be required? Will the reduction of sulphur levels in diesel fuel to below 0.05% in Europe, USA and Japan have an associated benefit of reduced aviation fuel sulphur? Sweden has legislated a diesel fuel limit of 0.001% S. Is this the level that might be required for future aviation fuels?

Author's Reply
The present level of sulphur content in kerosene varies considerably but is of the order of 0.05% by weight. The present knowledge is still uncertain but suggests a reduction by about a factor of ten in order to make sure that the sulphur emissions in the lower stratosphere are small in comparison with other sources.

Question 6. Dr Gordon Andrews
What is known about the concentrations of radicals like OH, O, H, HO_2, H_2O_2, etc. at the exit plane of modern jet engines burning kerosene? Both model and measurements are of interest because OH, although having very low concentration in the atmosphere, is responsible for most oxidation processes.

Author's Reply
Emissions of radicals from gas turbines are at a very low level. Essentially, the exhaust will have equilibrium levels of radicals which are in the 10^{-7} to 10^{-8} mole fraction range for the radicals you mentioned. I know of no measurements of these radicals in engine exhausts, but I would be interested to know what emission levels might be of significance in terms of upper atmosphere chemistry.

COMBUSTION TECHNOLOGY NEEDS FOR ADVANCED HIGH PRESSURE CYCLE ENGINES

Stephen D. Clouser and Richard A. Kamin
Naval Air Warfare Center Aircraft Division
P.O. Box 7176
Trenton, New Jersey 08628-0176
USA

ABSTRACT

The challenges in designing high performance aircraft combustion systems have not changed significantly over the years, but the approach has shifted towards a more sophisticated analytical process. Initially an overview of the U.S. Navy's component technology development procedure is presented to show how technology development is still tied into mission requirements. A more technical discussion on combustion technology status and needs will show that the classic impediments that have hampered progress towards near-stoichiometric combustion still exist. Temperature rise, mixing, liner cooling, stability, fuel effects, temperature profile control and emissions continue to confront the aerodynamic and mechanical designers with a plethora of engineering dilemmas and trade-offs. In addition, new materials such as ceramic matrix composites (CMC) and intermetallics like titanium aluminides (TiAl) are now being incorporated into every advanced design. The process of combustion design has taken on a new meaning over the past several years as three dimensional codes and other advanced design and validation tools have finally changed the approach from a "cut and burn" technique to a much more analytical process. All of these new aspects are now integral elements of the new equation for advanced combustion design that must be fully understood and utilized. Only then will the operable, high temperature capable combustion systems needed for future military aircraft be developed.

INTRODUCTION

The purpose of this paper is to review the progress and look into the future of combustion and fuel system development from a government point of view. In the propulsion technology area, most government sponsors do not conduct the actual research, but take an active part in technically managing the programs. They rely mostly on the engine manufacturers who have the facilities, resources and experience to provide the solutions and develop the hardware. From this perspective, the government sponsors have a unique vantage point to observe all of the ongoing efforts across the industry and are able to assess their relative position as they compete for resources.

Over the years, the seven U.S. engine manufacturers have flourished under the Department of Defense and Navy funding as they strove to stay ahead in the Cold War. Then our once reliable enemy became our sometimes reliable ally and the race for the peace dividend was on. Now these same companies are in a race to downsize their organizations in light of stronger international competition, recent budget cuts and economic recession. They are getting back to their core profit centers and becoming much more responsive to customer requirements.

So where does that leave the industry? From a technical perspective, the larger companies command more resources for luxuries such as high powered computer systems, testing facilities and generic research. However, future engines are becoming so sophisticated and expensive that it is not cost effective to maintain complete research and development (R&D) organizations. More than ever, cost is the new driving force in terms of R&D. Company controlled, government sponsored independent R&D (IR&D) has been severely reduced reflecting the declining purchases of military engines and spare parts. Along with government support, subcontractors are now being utilized much more for their technical expertise and to share in the developmental expenses. This is especially true in the materials world where fiber is the life blood of the composite industry. There are relatively few manufacturers who now produce it and they are dictating their terms to the engine industry with little rebuttal. Many engine company executives are now suggesting that more active cooperation amongst all the participating sectors of the aerospace industry is necessary in order to survive.

With this in mind, combustion system designers have many things to consider, not least of which are the technical challenges ahead. As part of the development process of military gas turbine technology, it is very important to understand the genesis of the goals and how they impact the evolution of military propulsion.

ORIGIN OF GOALS

Aircraft combustion needs are well defined and have been under continuous development for many years by both military and civilian organizations. The military approach towards meeting the combustion and fuel challenges begins with a top-down understanding of the hierarchy of system requirements, starting with aircraft missions. There are a variety of missions utilized by the United States Navy which periodically change as prevailing international conditions evolve. Perennial members include projection-of-power, fleet defense, air superiority, sea control, electronic warfare, surveillance, command, control and communication (C^3) and the newest member, littoral warfare. Improving upon mission effectiveness is an ongoing process and the Navy is continually investigating methods to enhance component and engine performance as well as life and durability.

Presented at an AGARD Meeting on 'Fuels and Combustion Technology for Advanced Aircraft Engines', May 1993.

For fighter/attack style aircraft (F-14/A-6), the Navy is historically attracted to engine cycles that provide transonic/supersonic capability for combat, but exhibit good specific fuel consumption characteristics (SFC) at subsonic cruise speeds to meet long over-water flight requirements. This multimission requirement imposes a wide variety of diverging needs upon the combustion system. Included are smoke free, high temperature capability, combined with good lightoff and lean blow-out characteristics while maintaining adequate durability and life.

The pure subsonic engines for patrol/transport style aircraft and helicopters (P-3/SH-60) are not as temperature dependant as fighter/attack engines but require shorter, lightweight designs with relatively low pressure loss that operate at much higher engine pressure ratios for enhanced SFC. Operability, durability and life are again major factors in their designs.

The procedure to improve an engine's performance is basically an analytical exercise which breaks down the engine performance by component and seeks to find the proper combination of advanced technologies that may be incorporated to provide the best performing engine. First, the aircraft mission parameters such as Mach number, altitude, time-on-station, range and payload are delineated. Since the engine design and the component configurations are known, the component performance parameters such as speeds, pressures, temperatures and efficiencies can be identified throughout the mission. Then the performance characteristics of the existing components are compared to the performance of the most advanced technology components. Consideration must be given to the fact that optimum engine performance can only be achieved by incorporating the correct balance of component technologies. The engine must then be reassessed to determine the performance improvements and to evaluate the benefits based on mission requirements (Fig 1). Through this cyclical process, combustion system and other component advancements are continually compared against higher order mission requisites in an attempt to provide an endless supply of options to improve engine performance for the ultimate customer, the aviator.

TECHNOLOGY BASE DEVELOPMENT

Maintaining an engine technology base is a critical part of the military engine development process. It allows the customer to have many options to chose from in order to meet system/mission requirements. In the United States, the advanced technology engines and exploratory development component programs are being addressed under the Integrated High Performance Turbine Engine Technology (IHPTET) Initiative. This is a three phase effort that incorporates all three military services, the National Aeronautics and Space Administration (NASA), the Advanced Research Projects Agency (ARPA) and the seven major engine manufacturers. The purpose of IHPTET is to develop a united approach towards significantly improving engine performance levels in order to double the thrust/weight ratio of future gas turbine engines by the year 2000. More specifically, these goals apply to manned and

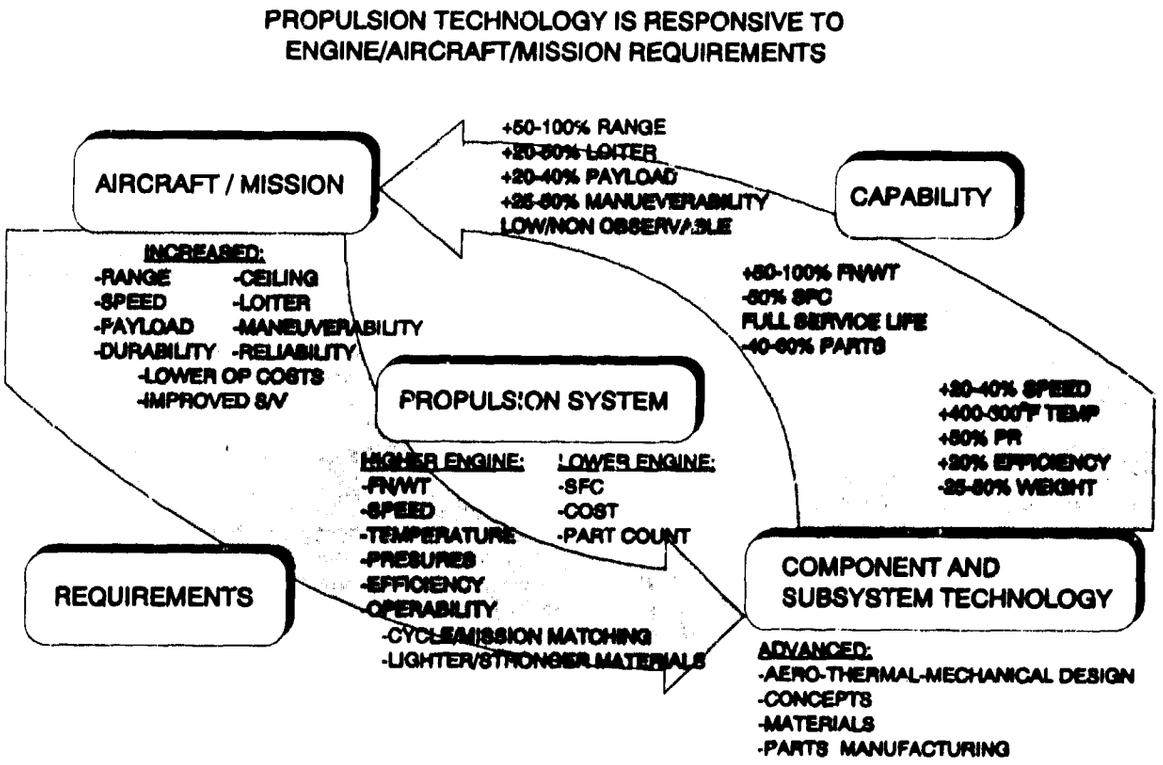

Fig 1: Developing Component Requirements

unmanned turbofan/turbojet engines while turboprop/turboshaft engine goals require 120% improvement in power/weight. In addition, there are aggressive fuel consumption goals for the initiative, while life and durability goals will also be incorporated into each engine design.

Each phase addresses material, component and demonstrator engine development and operation in which the majority of the efforts are sponsored by the three services and conducted at the engine manufacturers' facilities. The components and engine performance are measured giving an accurate assessment of the overall engine thrust class while the engine weights are calculated. Usually, advanced materials are not incorporated throughout every section of the engine. However, selective placement of key materials in critical areas of the engine allow a realistic assessment of their ability to survive in an engine environment.

There are six component areas (compression, combustion, turbines, mechanical systems, controls and exhaust nozzles) which have sequenced design goals in each of the three phases. In addition, there are structures, materials and computational fluid dynamics (CFD) disciplines which are all aligned with the component areas to manifest themselves into the demonstrator engine performance. The demonstrator engine goal substantiation is the ultimate test for the component design whereby all the components are integrated into an operating system that provides the most extensive verification short of actual aircraft operation.

The combustion system goals for IHPTET have been identified to provide near-stoichiometric operation combined with a 50% reduction in weight over the entire system by Phase III. Life and operability goals such as lean blowout, relight and turndown ratio have also been established to ensure a complete combustion system design.

CURRENT ISSUES

The past is full of significant accomplishments, however the challenges for future combustion system designs are also apparent. If we follow the progress of certain parameters over the past 35 years such as combustor exit temperature (CET), combustor size (length/diameter), fuel/air ratio (FAR) and pattern factor as outlined by Cifone and Krueger [1], notable progress has been made and yet the future requirements are still more challenging. Hopefully the successes of the past will provide some insight into future solutions.

TEMPERATURE CAPABILITY

In reaction to the demand for higher engine thrust levels, higher CET has always been the major focus in the design process. An increase in CET is often the first choice in upgrading an engine's thrust. Usually the increase is at the expense of the liner and the turbine nozzle which must improve their cooling effectiveness or suffer a life penalty. CET is often recognized as a barometer for combustion technology and a direct measure of the capacity of the design. As seen in Fig 2, the CET trend has been a long and steady rise towards stoichiometric temperatures. Over the years, a wide variety of designs have been tested to improve temperature levels such as the complex Pratt & Whitney Vorbix combustor, and the simple General Electric F101 combustor (Fig 3). Although the designs are radically

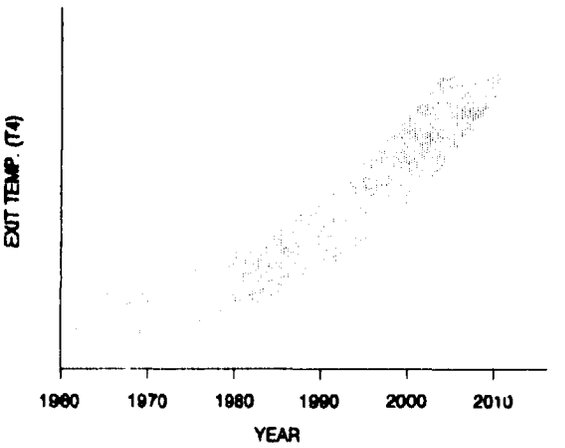

Fig 2: CET Trend

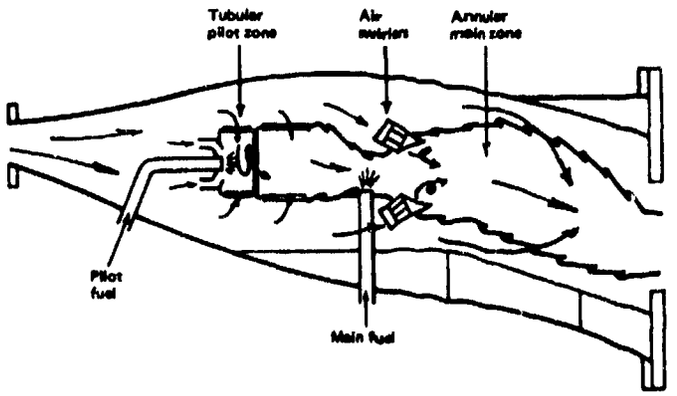

Vorbix Combustor (Courtesy Pratt & Whitney)

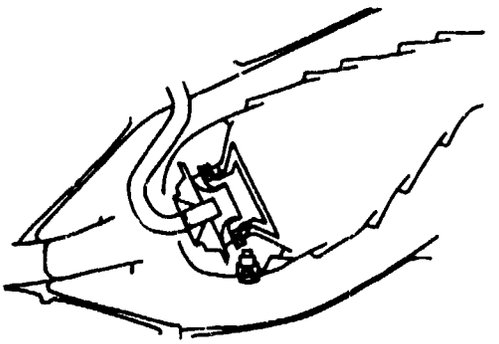

F101 Combustor (Courtesy General Electric)

Fig 3: Contrast in Style

different, the focus is the same; a combustor designed to withstand the highest possible temperature limit that the materials, fuel injection system and liner designs can support. To that end, conventional materials such as Hastelloy X, HS188 and Inconel 718 have been pushed to their limits. Innovative liner cooling schemes such as Floatwall, Multihole, Lamilloy and Lycolite have been developed utilizing every type of heat transfer mechanism available to dissipate the temperature and maintain material integrity. Hundreds of fuel injector designs have also been developed investigating any means to push a sufficient amount of fuel and still maintain some level of operability. The influence that CET has had on the other parameters in the design has been quite significant. So much so, that innovations in operability and durability are constantly responding to higher CET in order to support improvements in engine thrust levels.

CFD and ANALYTICAL TOOLS

CFD codes are in the unenviable position of defining the interactions of three dimensional, multiphase, turbulent, reacting flows that reside inside a combustor. Further they must accurately predict those same flows after changes are made to the configuration or harder yet, predict flows of a new design. The current models are just beginning to provide a return on their investment after many years of development. Initially, CFD codes were very cumbersome and required a substantial amount of empiricism and correlations on the part of the designers in order to complete the total picture. The overall accuracy of the models suffered since the turbulence and chemistry models could not be coupled with the transport equations in an efficient manner. Another limitation of the codes was their necessity to be operated on expensive mainframe computers. Today more powerful computers are allowing designers to invest more time into modifying the codes and validating the analyses through actual testing. Now, after many years of validation testing, CFD codes are becoming more reliable and predictive.

DIFFUSERS

The diffuser section has quite an impact on combustion performance. It must reduce the compressor velocity and minimize flow perturbations in a controlled manner in order to provide a uniform flow that does not tax the pressure rise accomplished by the compressor. Expanding the divergence angle and/or shortening the system to improve static pressure recovery has been a topic of many research efforts. A variety of different vortex generators and vortex controlled designs have been used in an attempt to delay the onset of flow separation by modifying the boundary layer characteristics. Vortex generators though, have an inherent shortcoming. While they are effective in improving pressure recovery with a developed profile incorporating substantial boundary layer thickness, they provide a substantial pressure loss for flows with minimal boundary thickness. Vortex controlled designs which bleed a small portion of air have been successful in providing adequate pressure recovery at larger area ratios, however, turbulence, system complexity and excess weight often overshadow the benefits.

COMBUSTOR SIZE

Reductions in combustor size are difficult to achieve due to the demands for higher CET and the need to maintain

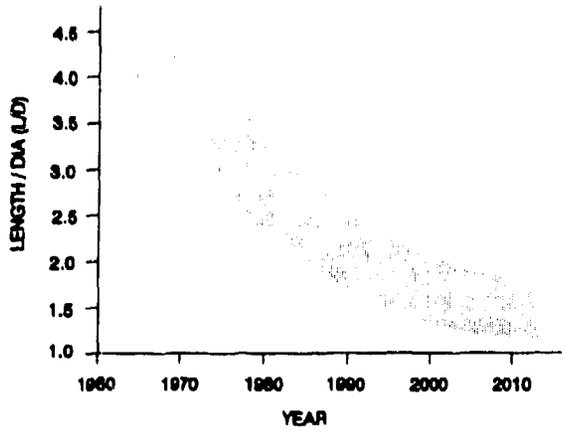

Fig 4: Size Trend

acceptable operability. Combustor L/D is gradually being reduced in order to meet weight goals (Fig 4). Older designs which had the luxury of an intermediate zone must now cope with the fact that modern combustion designs have eliminated this section while raising temperature levels. This requires the primary zone aerodynamics and the fuel injection system to be more efficient in mixing a higher volume of fuel in a reduced axial distance. The impact is a reduction in time for the primary zone to complete burning and the dilution zone to provide an even temperature profile at the turbine nozzle inlet.

Current designs are transitioning to multiple dome configurations to support staggered fuel injection systems which have a tendency to swell the dome area. This gives the appearance of a shorter L/D without an actual reduction in liner length.

LINER DESIGN

In order to improve combustor temperature rise, there is a need to burn a larger percentage of the air entering the combustor (Fig 7). This trend detracts from the air available for exit temperature control, as well as liner cooling, and places more of a burden on the cooling system effectiveness. Due to higher temperature levels, rolled sheet metal liners have been supplanted by machined ring and shingle style liners in most production designs. These configurations have successfully operated at fleet engine temperature levels for many years, albeit many liners need ceramic thermal barrier coatings for protection against hot spots caused by variances in manufacturing and general wear. Now more recently, advances in manufacturing processes have allowed laser drilled effusion cooled liners to become state-of-the-art due to their effectiveness, simplicity and weight savings. The shaped holes in these liner designs are a by-product of the drilling process and have improved the cooling effectiveness by assisting to develop a regenerating film of cooling air along the liner. This type of liner cooling configuration uses less air and allows more air to be available for dilution control.

As shown in Fig 5, pattern factor has made significant improvements over the years. Combined with profile factor, these two measurands are a critical gauge of exit temperature profile which the turbine cooling system is designed around. A major reason for the improvements in pattern factor has

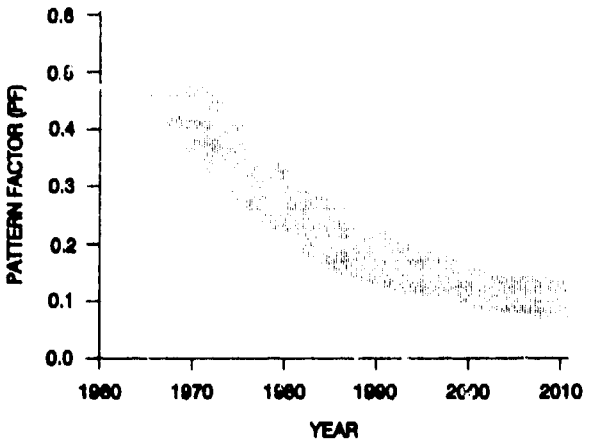

Fig 5: Pattern Factor Trend

been the increased use of CFD throughout the design process. This allows designers the ability to easily visualize the temperature gradients and effectively tailor the dilution air with greater precision than ever before.

FUELS AND FUEL DELIVERY SYSTEMS

Fuel delivery systems have been a major consideration in combustor designs for many years. Many attempts have been made to expand the upper and lower fuel flow limits in preparation for the demand of higher exit temperatures. These include many different types of injectors and even variable geometry swirlers. However, simple pressure and airblast atomizers in conjunction with their swirler packages are near their practical limits in terms of providing a full range of fuel distribution capability. Current fuel nozzles designed for higher fuel flows at max power do not provide good low power performance in regard to lean blow-out and relight. Due to requirements for greater FAR range (Fig 6), fuel and air staging, which adds weight and complexity to the engine, is necessary to maintain good operability characteristics. This is a vital aspect for Navy aircraft which need good low power stability especially during landing on an aircraft carrier and quick response time to max power during a possible aborted landing.

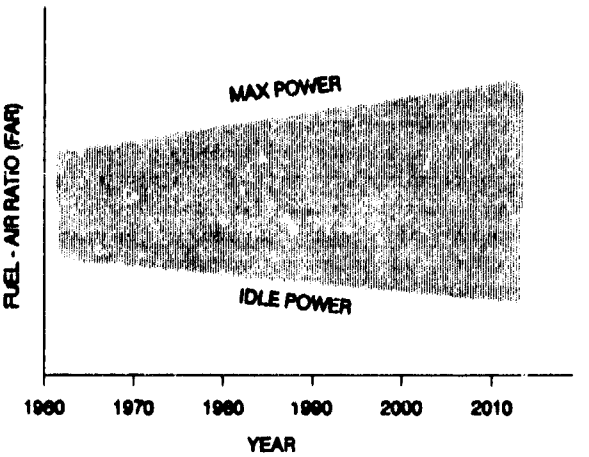

Fig 6: FAR Trend

Fuel operating temperature is a growing concern as engine cycle temperatures continue to rise. Increased heat rejection into the fuel by the various aircraft subsystems will significantly increase the fuel's potential to undergo thermal oxidation degradation reactions. This degradation leads to carbon deposition around the outside tip and in the interior passages of the fuel injector. Poor fuel quality and hot spots on the fuel injector have been factors in many instances where coke formation has deteriorated fuel injector performance. This leads to hot spots in the combustor and turbine nozzle and a subsequent reduction in life of the components. The Navy has a particular concern in the this area due to its unique problem with decreased shipboard thermal oxidation stability of its fuel caused by the deleterious effects of the copper-nickel piping in its shipboard aviation fuel delivery systems. Current design practice to reduce fuel temperatures and therefore the potential for carbon deposition is to recirculate the fuel through fuel-air heat exchangers. This method of thermal management does however impose a penalty on the aircraft by increasing system complexity, weight and drag. Other concerns are increased carbon content in the fuel which leads to a higher smoke number and reduced life, while higher viscosity and lower volatility have a negative effect on atomization and operability.

In summary of the current issues, conventional approaches that have been employed by the industry for many years will no longer suffice in meeting the needs of the next generation of combustor designs. For example, the temperature limits of conventional materials such as HS188 and Hastelloy X have been met and many of the new innovative liner cooling configurations designed by the engine manufacturers are struggling to meet their temperature requirements. Traditional fuel distribution techniques are not adequate to meet the ever increasing demand for higher fuel flows for increased engine thrust in combination with the lower fuel flows needed for good low power stability. Combined with the fact that most CFD analyses are not totally predictive but usually postdictive, the industry must now head into more unfamiliar territory.

THE FUTURE

The future for high performance combustion systems will be an interesting time as new laboratory tools are employed to validate innovative analytical designs incorporating composite materials which will produce the most advanced combustion system designs to date. As seen by the trend charts, there is significant progress yet to be accomplished in many areas. The most predominant goal is still CET. The following sections are written with CET in mind as the major challenge ahead.

CFD and ANALYTICAL TOOLS

In the analytical area, supercomputers such as the CRAY and most recently the high powered work stations which are networked together to provide supercomputer capability, have allowed designers to delve into many areas that several years ago were still an enigma. Today, 3D CFD codes utilize body fitting orthogonal grid generators to map complex shapes in order to predict velocity and temperature profiles. Enhanced graphics packages allow these gradients to be viewed from any angle giving the designer access to any trouble spot. Using these elaborate codes that effectively link cooling, turbulence and reacting models, an accurate prediction of combustor trends is now possible to analyze before a piece of metal is

ever cut or a section of CMC sent to the autoclave.

In the experimental and validation areas, cold flow visualization tests and 2D sector tests are becoming very proficient in validating initial designs. Tools such as laser doppler velocimetry, Schlieren visualization, CARS and Raman spectroscopy are used to validate turbulence levels, species concentration, and velocity and temperature profiles. Now, the results of most sector tests provide enough reliable data to proceed to the full annular design. This in itself is a significant feat since manufacturing costs of high temperature composites are still exorbitant and programs can not afford to make multiple sets of hardware to cover several design iterations.

MATERIALS

Advanced non-metallic materials development will be the pacing item in the combustion systems of the future due to their unfamiliar characteristics and high cost. Current designs are now attempting to incorporate both monolithic ceramics and ceramic matrix composites into basic metal liner designs in order to increase the temperature capability. The only drawback is that the temperature limit of CMC is approximately 3000 °F which is still far short of the goal needed to achieve near-stoichiometric operation. Carbon/Carbon which was the one material that was envisioned to provide uncooled capability has been a great disappointment and now most efforts have been suspended due to the lack of a durable oxidation coating and general brittleness of the material.

Currently, monolithic ceramics do not to have the strength nor the durability to survive the harsh combustor environment without some sort of metallic structure for support. Most of these designs have evolved into configurations that were not feasible for production. Other designs employed monolithic tiles as heat shields for their primarily metallic designs. Most designers have now abandoned the monolithic area and switched to primarily CMC for their applications. After several years of experimentation to develop some sort of familiarity with the material, attempts are currently being made to build and test one piece CMC liners. There have been numerous growing pains throughout this process as many different configurations involving 2D and 3D weaving and braiding of the matrix fibers have been investigated. Ineffective densification, oxidation and poor thermal conductivity, which causes damaging temperature gradients, have left most designers lacking any confidence that CMC will meet temperature and life requirements. Therefore, most composite designs have been categorized for unmanned engine applications which can accept higher levels of risk. Other problems still exist in the interface areas between the metallic dome sections and the composite liners. Uneven thermal expansion, sealing and attachments are all new problem areas that are still being addressed.

Our knowledge of producing nonmetallic parts is basically limited to simple shapes. Only in the last few years have combustor designers and material manufacturers working closely together, developed the processes necessary to manufacture a more intricate piece such as a liner. The time is coming whereby more complex shapes such as the dome shroud and swirlers must be manufactured. Effective densification of these complex shapes is the next step to producing a full nonmetallic combustor in order to realize the full potential of these lightweight, high temperature capable materials.

FUEL DISTRIBUTION AND FUELS

This is probably the most heavily researched portion of combustion system development since it is well recognized as the most rewarding area in terms of total payoff. As mentioned before, the need for increased temperature capability is the driving force of most design efforts. Fig 7 shows the distribution of air as a function of temperature rise. In the past, approximately 30% of the available air was used for combustion, the remainder was split between cooling (40%) and dilution (30%). Over the past five years, gradual improvements have been made to increase the amount of available combustion air. However, in order to provide near-stoichiometric combustion, higher flow fuel distribution systems that can accommodate the increasing max power fuel requirements are being developed for the new, shorter, high temperature combustors. The traditional airblast fuel injector and the accompanying high shear swirler systems that are utilized in current systems will not be able to accommodate the higher fuel flows of future engines and also maintain good operability characteristics. Innovative fuel delivery and atomization techniques are being investigated, although it is highly unlikely that they alone will provide the necessary improvements to meet future requirements.

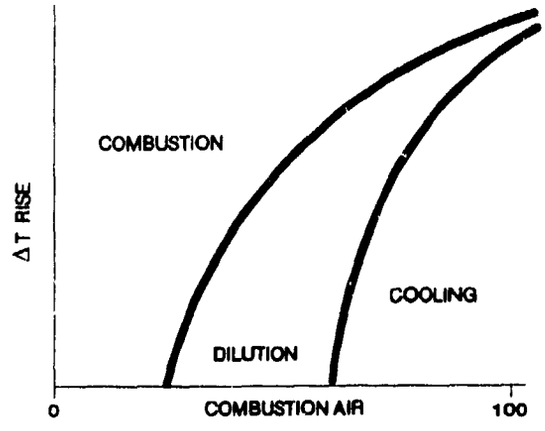

Fig 7: Air Distribution Trend

Future fighter/attack aircraft will rely more on the engine fuel system as a heat sink to cool electronics, oil and turbine cooling air (Fig 8). This will further raise the bulk fuel temperature causing coking throughout the fuel system. These projections have increased efforts to develop a cost effective high thermally stable aviation fuel. Although increased refinery processing or a specialty fuel like JP-7 would provide the desired increased stability, its cost would be prohibitive. Current efforts are extensively investigating the use of additives to provide the increased stability. The goal of these programs is to increase the maximum fuel operating temperatures at the injector nozzle by 100° F from the current design limits. Some additives have been developed to raise the thermal stability limits, but they have other side effects. Endothermic and slurry fuels have been tested over the years, but it will be a long time before they are introduced as viable alternatives due to their unique handling needs and corrosive nature.

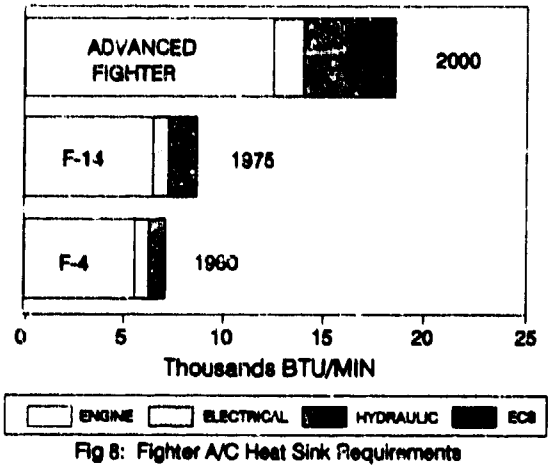

Fig 8: Fighter A/C Heat Sink Requirements

IGNITION SYSTEMS

Innovative ignition concepts such as radiative ignition designs which incorporate infrared and ultra violet lasers and microwave systems are being developed. These systems are desirable from the standpoint that they provide extremely intense, localized ignition sources that can be strategically placed to contain the reactive combustion area to the primary zone, thus shortening the combustor. These approaches are quite different from the previous plasma ignitor designs which needed an inert gas source and a large cumbersome power supply to operate. Advances in electronics have miniaturized power supplies to the point that they can be used on an aircraft engine. In addition, the plasma medium or inert gas is not required in the recent designs. Other benefits of this technology may include the capacity to accept higher compressor exit Mach numbers. The ability to accept higher velocity flowstreams would be quite significant to both component areas in terms of weight and system complexity if these types of ignition systems were successful. Initial laboratory tests have also shown that these systems would also expand the lightoff and relight capability of current combustors without fuel staging.

DIFFUSERS

The advanced diffusers of tomorrow will be encumbered by the complexities of the future combustor dome configurations. Since many combustor designs are investigating multiple dome configurations, diffuser designs must be capable of introducing separate flowstreams which are balanced through several passages to accommodate multiple fuel injection planes. This must be accomplished without significant amounts of turbulence and without a great weight penalty. A complex design of this nature must utilize lightweight materials such as TiAl in order to be practical. TiAl development is being focused towards this need as well as other areas, but problems in casting a one piece diffuser have not been overcome.

Dump diffusers have recently demonstrated good performance in short axial distances. In some designs, the dome and the case area are also used as secondary dump areas to continue the pressure recovery process. Future diffuser designs may be aided by the fact that new ignition systems may allow higher velocity flows to enter the combustor, thereby off loading the responsibilities of the diffuser. Hopefully, the complications caused by the increased compressor exit velocities will not outweigh the benefits.

EMISSIONS

In order to survive in the markets of the 21st century, engine manufacturers must now design military engines that are also adaptable to the civilian sector needs. From a combustion viewpoint, that translates to lower emissions. Many countries in Europe have already legislated strict laws governing engine emissions. The United States has also passed regulatory laws, however the military is still exempt from complying with them. Included in the restrictions are smoke, unburned hydrocarbons, carbon monoxide and especially NOx. As combustor temperatures continue to rise so do the NOx levels. This will be a huge design consideration in the future because of the diverging requirements of higher temperatures versus lower emissions. Advanced combustor flowpaths must be designed to be smokeless at high FAR's required for the military yet have low NOx emissions at the lower max power FAR's necessary for commercial designs.

SUMMARY

Technically speaking, the goals are apparent. Higher CET is the predominant intent of the combustion world for both military and commercial applications. The tools required to meet that intent are becoming more useful and the materials more familiar. As usual, a balancing act is necessary to meet all the goals and the solution is never easy.

The future for military aviation will be focused towards a peace time operation and will no longer be the bountiful market that it was for the past 50 years. The long term contracts for thousands of aircraft and engines will no longer be the focus of military services around the world. Dual use technology and technology transition is now the "mode of operation" amongst both government and industry. In the military, more emphasis will be on derivative and growth programs with only a few new center line "silver bullet" production efforts. In the short term, the commercial sector will now be incumbent to provide the resources for future engine development programs. Military budgets will be declining for several more years, although high technology is supposedly safe from the budget knife.

In the combustion world, perseverance is the key to continuing to meet the technical goals in spite of the other distractions. The combustion system of the future may look quite different than the current designs. A complete non-metallic design with a unique multipoint fuel injection system and a radiative ignitor may be the ultimate configuration of the future. Sooner or later the inventions will be developed to allow the goals to be reached. As mentioned above, there are many new ideas coming to address old problems. The future is full of promise as the 21st century approaches.

REFERENCES

1. Cifone, A., and Krueger, E., "Combustion Technology, A Navy Perspective", 1985 AIAA Paper No. 85-1400.

ACKNOWLEDGEMENTS

The authors would like to thank Anthony Cifone of the Naval Air Warfare Center, Charles Graves of Pratt & Whitney and John Sanborn of AlliedSignal Propulsion Engines for their insightful technical comments on this effort.

Discussion

Question 1. L. Fottner
Could you comment on the trend of combustor exit temperature with time? Will there be a limit on this temperature? When will it be reached?

Author's Reply
There are two major limiting factors to the maximum achievable exit temperature. One is material temperature and the other is the fuel chemistry of current kesosene based gas turbine fuels. Fuel chemistry will probably remain constant, therefore the maximum temperature is approximately 4,100 degrees F. Material temperature capability is limited to approximately 3,000 degrees F using ceramic matrix composites. Carbon/carbon material is the only known candidate that has the capability to reach 4,100 degrees F. The major problem is the inability to develop an oxidation coating that has a life of more than 10 to 20 hours. Our plans for stoichiometric combustion have slipped by at least 10 years because of the lack of a suitable material.

Question 2. T. Rosfjord
Can you expand your comments on innovative ignition system needs?

Author's Reply
Ignition system involvement in current combustion systems is currently limited to initial lightoff and to help prevent blowout during transient operation. Radiative ignition systems could change the method by which ignition systems are utilized. A radiative system could be used in a continuous manner to burn in an unstable flowfield, eliminating heavy two stage fuel delivery systems and possibly shortening the combustor's axial length. Initial tests have shown that microwave and ultraviolet systems have this capability.

Combustion for future Supersonic Transport Propulsion

Dr B W Lowrie
Chief of Powerplant Engineering - Military

Rolls-Royce plc
PO Box 3
Filton
Bristol
BS12 7QE
England

SUMMARY

Even with it's marginal performance, Concorde has demonstrated that Supersonic Civil Aircraft are a practical proposition.

A second generation machine will need sufficiently good performance for a robust operating system that can provide reliable frequent service with competitive economics. Additionally the propulsion system must be acceptable environmentally. That is it must create acceptable noise levels around airports and have acceptable emissions throughout its mission including cruise.

Whatever devices may be used to improve the acceptability at subsonic flight conditions, the high operating temperatures at cruise can create difficult targets for the operation of the combustion system both mechanically and in the combustion process itself.

While the driving force is ever better fuel consumption and weight to achieve economic viability, a future supersonic transport engine will have cycle temperatures limited only by the mechanical integrity of the major components. The environment of the major components in modern gas turbine engines is dominated by the air delivered by the compressor system. Consequently the maximum compression temperature is governed by materials available for the turbine and compressor discs.

The continued improvement of the disc materials leads to combustion inlet temperatures beyond today's experience and sets difficult targets for combustion system emissions. This is worsened by the requirement being at cruise and therefore maintained for the major part of the mission. Problems such as creep and oxidation of metallic parts are also considered.

INTRODUCTION

The history of air travel has been one of increasing speed, efficiency and reliability. A speed plateau of jet engine powered aircraft carrying people and goods at Mach numbers in the range .8 to .85, was first reached in the 1950's and has remained to the current day, see Figure 1.

Higher speeds are perfectly feasible as experimental, military and civil aircraft have shown. Both Concorde and the Russian TU144 entered service in the mid 1970's and Concorde is still in service today. However, no-one would argue that Concorde's costs, reliability and environmental impact would be acceptable with a large fleet.

This paper reviews the improvements in technology that are available and would be required for future supersonic transport propulsion and identifies the technology improvements which must be pursued to this end with particular reference to combustion.

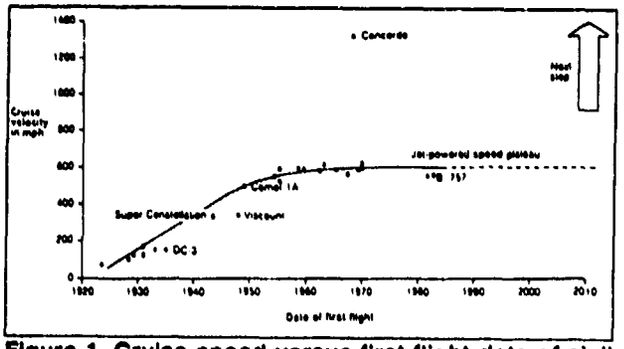

Figure 1 Cruise speed versus first flight date of civil aircraft in western world

Supersonic Flight Requirements

A dominant feature of the practicality of supersonic cruising flight is the necessity for good fuel consumption. As in subsonic aircraft jet engines improvements have taken advantage of better materials, cooling system technologies, component efficiencies and the balance between these technologies at any particular time. The most fundamental difference with the propulsion systems for supersonic flight is the increase in temperature of the air entering the main turbomachinery components of the engine. This high temperature, due to the high relative speed of the aircraft, brings with it high pressure. That is a substantial part of the compression required in the engine is actually carried out by the intake. Furthermore because this compression has already occurred prior to any rotating machinery being involved there is apparently potential to carry out compression to pressure ratios beyond that achieved in typical subsonic propulsion units by this additional compression in a large variable geometry intake. The consequence of this is that temperature becomes the limiting feature at cruise on a supersonic engine, Figure 2, whilst it is not on a subsonic engine.

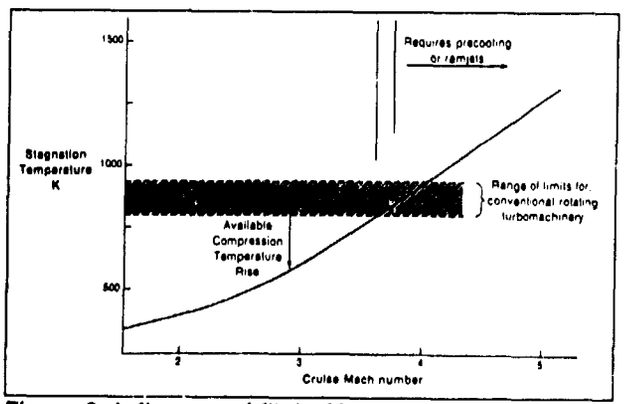

Figure 2 Influence of flight Mach number on engine cycle

Presented at an AGARD Meeting on 'Fuels and Combustion Technology for Advanced Aircraft Engines', May 1993.

Of course the temperature limit also applies to subsonic engines but this normally limits the pressure ratio achievable during the take off or climb phases of flight. The increased ratio of cruise thrust to take off thrust that supersonic aircraft require, due primarily to the poorer system lift/drag ratio at cruise, see Figure 3, also contributes to this change in critical condition.

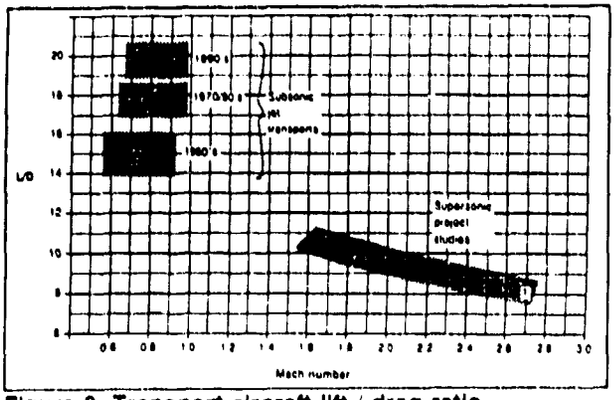

Figure 3 Transport aircraft lift / drag ratio

This then highlights the major differences in engine operation for supersonic cruise compared with subsonic cruise, that is the core of the engine is operating at high temperatures at cruise and additionally all the sources of air available to it are relatively hot. (Recall that on Concorde the external skin of the aeroplane is at temperatures up to that of boiling water).

For essentially the same reason (good fuel consumption) good installed propulsion efficiency is required. Because axial flow turbomachinery systems operate efficiently with subsonic axial flow, supersonic propulsion systems require a large diffuser intake, usually of variable geometry and similarly a large variable nozzle system to re-accelerate the flow. Both these components have a large size and weight and add significantly to the drag. This is particularly true of the intake system, see Figure 4 which illustrates the Concorde installation.

This extra penalty of the intake and nozzle system over and above the installation requirements for subsonic operation leads to an optimum propulsion system of very much higher specific thrust. Such systems are very noisy during subsonic operation near airports as has been demonstrated by Concorde.

The efficiency of a propulsion system at cruise can be broken out into those inefficiencies due to the thermal limits of the cycle, the component efficiencies of the engine, and the propulsion efficiency. See Figure 5.

For bypass engines (as most modern jet engines are) it is convenient to be able to control the propulsive efficiency by changes to the LP system design only and this uncouples this particular aspect from the major

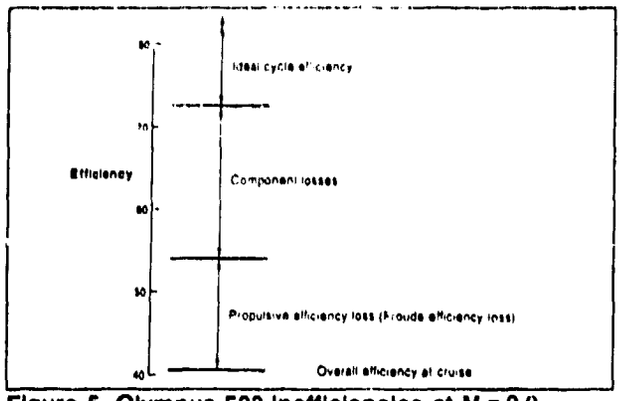

Figure 5 Olympus 593 inefficiencies at M = 2.0 cruise

design parameters of the core engine. Consequently it is convenient here to regard the design and technology requirements on the LP system as a subject that can be dealt with elsewhere as indeed it is in for instance references 1 & 2 and concentrate solely on the core engine parameters required to improve the thermal efficiency of the system.

Specific Performance Targets for Advanced Supersonic Transport Propulsion

Concorde is the only example of continuous effective operation at supersonic cruise conditions within the normal constraints of airline operation. Even though with a range of some 3,400 nautical miles, it only operates regularly across the Atlantic, it has demonstrated many times that it can operate using normal facilities to almost any international airport in the world.

While this range met the design intent of the aircraft, Figure 6 shows a future aircraft would need a significant increase in its capability to a range of at least 10,000 km for regular worldwide operation. Thus a second generation supersonic transport requires an increase in range of around 50% to which the propulsion system will need to contribute a significant proportion.

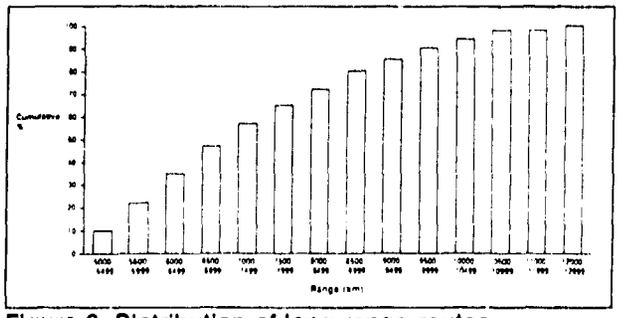

Figure 6 Distribution of long range routes

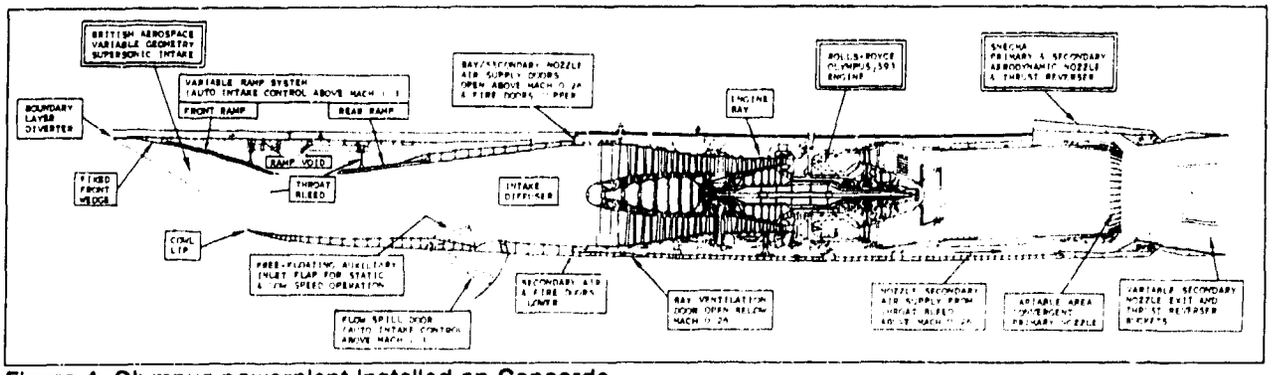

Figure 4 Olympus powerplant installed on Concorde

Figure 3 has shown that the typical lift / drag ratios proposed for supersonic transports are only some 30-35% better than Concorde. This means that the propulsion system must achieve at least another 10% in improved fuel consumption beyond that of the Olympus.

Practical Limits on Thermal Performance

The history of improved jet engine performance is tied very closely to the availability of improved temperature capability of the materials used for some of the major components. High speed rotating components such as compressor drums and turbine discs must sustain high levels of stress at the highest pressure parts of the cycle where the only convenient heat sink is the air delivered by the compressor system. Thus the temperature at compressor exit is governed by the material temperature capability for these components and Figure 7 illustrates the materials available and the projections in the next five to ten years.

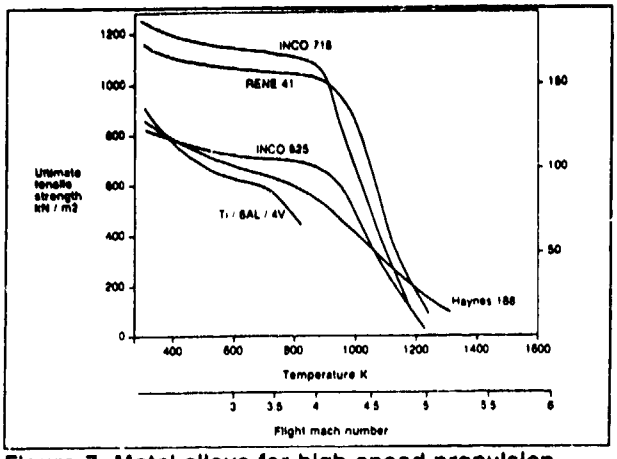

Figure 7 Metal alloys for high speed propulsion systems

From this picture it is quite clear that it is unlikely that we will have materials with good mechanical properties beyond a temperature of around 670-700°C. This can be translated into a temperature limit of 950K.

Nearly as important as the compressor exit temperature is the stator exit temperature of the first HP turbine stage in the jet engine since this is the temperature of the gas stream in which the highly stressed HP turbine blade needs to operate. The sustainable temperature here can only be established as the result of a compromise between available material properties, acceptable turbine blade life (recall that the blade is operating hot at cruise unlike a subsonic engine) the cooling technology and airflow available, and the efficiency and the specific power output of the core. Preliminary assessments within Rolls-Royce and SNECMA* of likely acceptable stator outlet temperatures indicate that 1650K could give a reasonable balance between life, specific power output, and therefore size and weight of the core engine. Furthermore as shown in Figure 8, this limit of 1650K at Mach 2 is a little beyond the optimum sfc point, ie is also a good compromise between thermal efficiency and weight of the core engine.

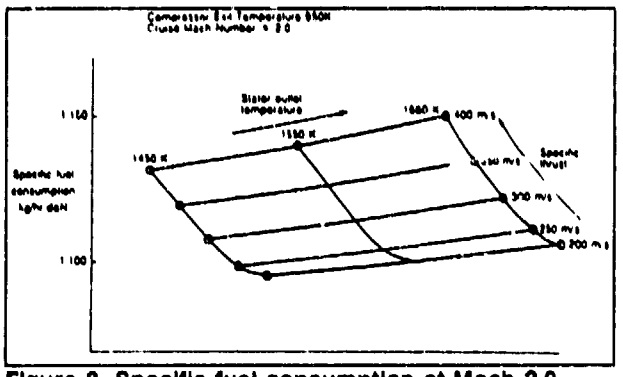

Figure 8 Specific fuel consumption at Mach 2.0

Combustion System Mechanical Considerations

While the stator outlet temperature 1650K derived as recounted above does not seem an outstanding temperature since many engines, civil and military, run to these temperatures today, the compressor exit temperature of 950K is rather more significant. Within Rolls-Royce over the years our experience has built up with increasing compressor delivery and HP turbine rotor entry temperatures as illustrated in Figure 9, and the introduction of improved cooling techniques and improved alloys, (we have moved from wrought to cast), have allowed us to continue this process as we project into the future.

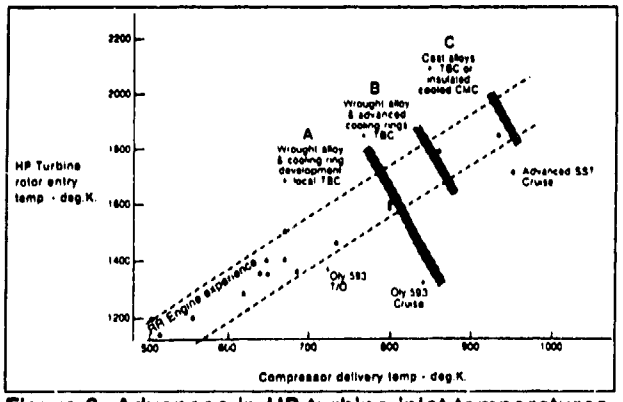

Figure 9 Advances in HP turbine inlet temperatures

Indeed this cruise requirement of compressor exit temperature of 950K combined with a turbine rotor entry temperature of 1650K is somewhat less arduous than existing advanced projects are already experiencing. There is a difference of course in the time for which these temperatures have to be sustained but as the major problems in combustion systems are associated more with cyclic behaviour rather than being time dependent then one does not observe a fundamental problem.

However, weight is an ever present enemy and as will be argued in the following sections of this paper a double annular combustion system is perceived as being a likely requirement. Some preliminary assessments have been carried out of combustion chamber weight and the influence of the construction type and the materials used is simply summarised in Figure 10 where the relative weights of different construction systems are compared.

Footnote: * Rolls-Royce and SNECMA are partners in Propulsion studies for future Supersonic Transports.

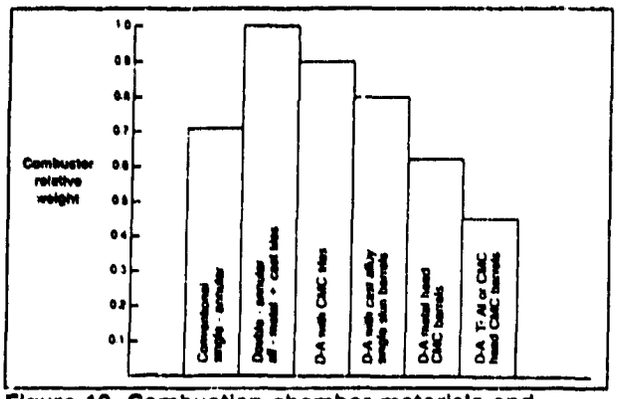

Figure 10 Combustion chamber materials and constructions

The figure uses a double annular system with cast metal tiles as a datum. Today's conventional single annular system developed as shown on the previous figure is only 70% of this weight. Changing the tiles to ceramic matrix composite would it is believed save some 10% of the weight. A lighter alternative would be to use existing construction systems but using ceramic matrix composites for the barrel. Making the head also in ceramic composite potentially could produce a system with a better weight than today's conventional single annular system. Thus even though demonstrated technologysuggests that the temperature being required in the combustion system are within our capability we find that with the imposition of stringent emissions restrictions some considerable advances in technology of construction and the materials used will be needed to reduce the weight.

Atmospheric Contamination

There are already regulations that restrict the amount of carbon monoxide and unburnt hydrocarbons that aircraft engines can discharge in the vicinity of airports. There are ICAO recommended proposals for restricting NOx generation and although the effectiveness of these measures is open to dispute, they are already applied in some countries, and provide an Industry Standard.

At this time there are very serious discussions about the impact that emissions from jet engines can have in the higher atmosphere and particularly in the stratosphere, for example Ref 3. Figure 11 gives a pictorial illustration of the regions of the atmosphere and the effect of industry and transport systems on the contaminants which are introduced by aircraft engines.

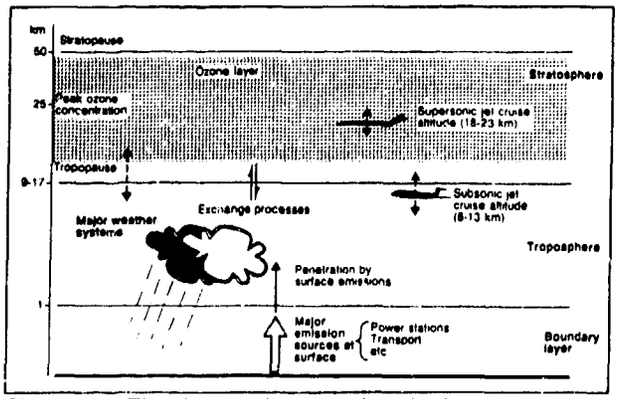

Figure 11 The Atmosphere and emissions

Up to 1 kilometre altitude there is a boundary layer of the atmosphere to which numerous sources contribute with a very small amount from aircraft. Above that boundary layer there is a migration through natural atmospheric processes, sometimes violent, to the level of the tropopause. Above the tropopause in the stratosphere the exchange is a much slower process. The altitude of the tropopause varies and is somewhere in the range 9-17 kilometres, a usual standard is 11 kilometres and most long range subsonic aircraft fly high enough to achieve the smooth conditions in the vicinity and above the tropopause and thus are usually in the range of altitude 8 kilometres to 13 kilometres for long range flights.

Supersonic transport aircraft on the other hand will cruise in the range 15-20 or even 25 kilometres altitude, that is in the regions of the so-called ozone layer where the ozone concentrations are sufficiently high to act as ultra-violet absorbers and protect the lower altitudes.

Indeed in the early days of Concorde there was concern that the aircraft would be flying in a region of higher ultra-violet with potential dangers for crew and passengers, but as the windows on Concorde absorb sufficient of the ultra-violet, this has not proved to be a major problem.

Supersonic transport aircraft cruising typically at 18 kilometres where the ozone concentration is important, therefore need to keep NOx emissions somewhat lower than those for subsonic aircraft, engines and this is compounded by the fact that the supersonic transport engine combustor operates at temperatures substantially higher at cruise than the subsonic engines.

Whilst there is not sufficient understanding or data available to deduce hard and fast rules, considerations such as these have lead to a target being set to reduce the EI NOx from SST combustion systems to 5g/kg fuel. Figure 12 summarises the approach as proposed by NASA, Ref 4 and Figure 13 illustrates the improvement in Technology required compared to conventional systems and the advanced proposals for subsonic aircraft. Clearly a considerable step change in technology will be required.

- Aircraft will cruise in the stratospheric ozone layer
- Improved combustion technology required for acceptable emissions (ie 5 EI)
- Current environmental assessment from NASA Atmospheric Effects of Stratospheric Aircraft (AESA) programme
  - 1% ozone depletion predicted for homogeneous chemistry only
  - Initial results including heterogeneous chemistry show 0.2% ozone depletion

  (Scenario : at northern mid - latitudes, 600 aircraft cruising below 20km, EI = 5g / kg)

Figure 12 Environmental impact of HSCT - current status

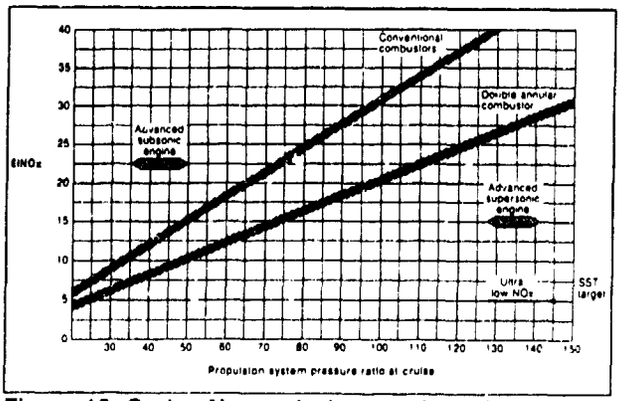

Figure 13 Cruise Nox emissions and combustor technology

Low NOx Combustors

Various approaches have been made to solve the problem of how to reduce NOx formation and yet allow the mean operating temperature to increase. Figure 14 illustrates the way the NOx production rate varies as the local fuel air ratio increases and produces higher local temperatures. The maximum rate occurs where the fuel air ratio is stoichiometric and the maximum flame temperature of around 3,000° is experienced locally.

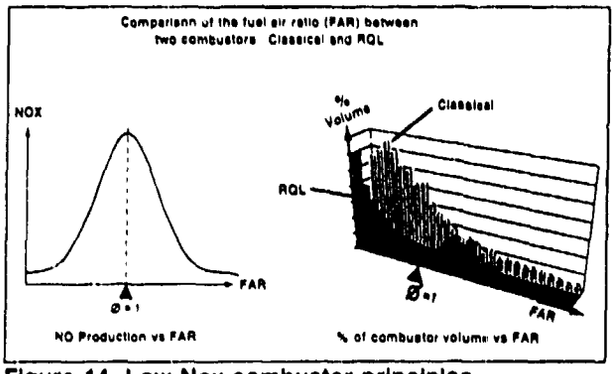

Figure 14 Low Nox combustor principles

As the fuel air ratio differs from the stoichiometric value, either greater or smaller, the temperature following combustion and therefore the NOx production will locally decrease. Obviously a combustion system which avoids having near stoichiometric mixtures anywhere within the burning zone stands the best change of achieving low rates of NOx production.

This can either be done by having a very uniform mixture of fuel and air and always keeping well away from the maximum temperatures of stoichiometric mixtures, or alternatively having locally very rich (over stoichiometric) zones where the initial burning takes place followed by the rapid mixing to a lean fuel air ratio condition for the remainder of the burning. The region where the mixing takes place being traversed rapidly in a minimum time. These two approaches are described as the premixed, pre-vaporised (uniform mixing) system and the rich burn-quick quench-lean burn system, respectively.

Yet a third possibility is to premix the fuel and air and allow the reaction to take place stably in contact with a catalytic device. These three systems are illustrated in basic terms by the three diagrams in Figure 15.

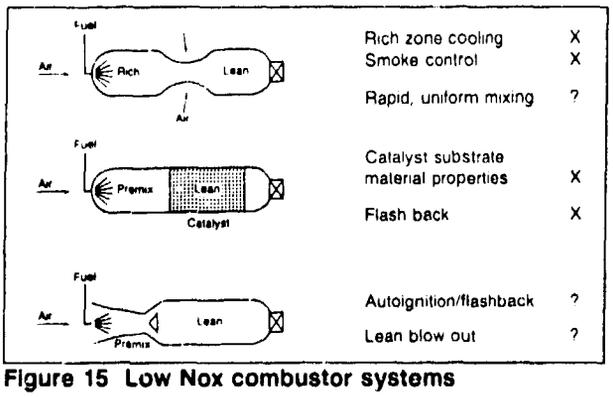

Figure 15 Low Nox combustor systems

Experience has shown that it is very difficult to identify suitable catalysts which can survive the very high temperatures and high gas flow erosion conditions that exist in gas turbine combustor systems for aircraft engines, consequently this style of control is not favoured. Note the alternative use of catalysts to 'clean up' the gas at exit from the turbine system (paralleling automobile systems) would give larger volumes and/or high losses unacceptable to high speed aircraft installations.

The rich-burn-quick-quench-lean-burn system can suffer by producing carbon in the rich burning process which it is difficult to subsequently burn in the cooler temperatures of the lean burn phase without fairly long lengths or large dimensions of that part of the combustor system. While these problems may be soluble with more research the presently favoured approach is to have a pre-vaporised fuel premixed to provide a nearly uniform lean burning system, Ref 5.

Attempts to develop lean premixed designs during the 1970's encountered serious problems due to auto-ignition, ignition and flashback resulting in mechanical failure. In some cases inadequate premixing still resulted in high NOx emissions. Research is in hand at Rolls-Royce, SNECMA and elsewhere to develop suitable premixers for high power operation. Early indications from low pressure testing are encouraging but much work remains to be done before a design can be committed to an SST engine project. The resulting combustor will need to operate at both low and high power conditions. The aim is to produce a high power premixer which gives acceptable performance with regard to relighting efficiency and stability at low power settings. If successful this would lead to the simplest possible combustor design. However, it is almost certain that fuel staging will be required to achieve acceptable fuel air ratios in the premixer ducts at all engine power settings. More probably separate low power operation fuel/air modules may be required which do not employ premixing. These would not yield low NOx emissions at high power conditions and so would have to be turned off. In this case the module air would have to be diverted into the high power premixers for NOx control and hence mechanical variables or flow diverters would be required. Thus the resultant developed combustor for a future SST aircraft engine could have both staged fuel and staged air to meet both ultra low NOx at cruise and low power engine operating requirements.

CONCLUDING REMARKS

In this paper we have reviewed briefly the reasons why the propulsion system for a supersonic transport aircraft needs to operate with high temperatures in the combustor system and the significance of those conditions to the design and operation of the combustor. Whilst the need to operate with temperatures of nearly 1,000°K at inlet to the combustor and some 16-1700°K at entry to the turbine rotor does not in itself pose particular mechanical problems on the design of the combustor. The combination of these temperatures and the need to save weight in a staged (double annular) combustion system would be greatly benefited by the use of ceramic matrix composite materials. The complementary requirement for ultra low NOx in the exhaust gases from the combustor whilst pushing beyond what has been achieved is nevertheless seen as a possible development provided that technologies associated with maintaining suitable fuel air mixture preparation over the full power range whilst also controlling the flame to avoid ignition flashback can be developed. Research towards these objectives is in hand in many parts of the world at this time, including activities with which Rolls-Royce is closely associated.

ACKNOWLEDGEMENTS

This paper has been assembled with the support and cooperation of the Advanced Design Engineering and Combustion Engineering departments in Rolls-Royce and that support is gratefully acknowledged. As is the permission of the Directors of Rolls-Royce for permission to publish the paper.

REFERENCES

1. Lowrie, B W & Portejoie E
   Two Variable Engine Cycle Concepts for Second Generation Supersonic Transport
   Paper No 901892presented at SAE AeroTech '90, Long Beach, California, Oct 1990

2. Champagne, F G; Allen G E ; Palmieri M; Adler RM
   Low noise propulsion concept for the supersonic transport
   SAE Paper 91-GT 397 presented at Int'l GT and Aeroengine congress Orlando FL USA June 1991

3. Prather M J et al
   The Atmospheric Effects of Stratospheric Aircraft: A First Programme Report, NASA RP-1272 January 1992

4. Wesoky H
   High Speed Research Programme Overview, 2nd Annual Meeting of the HSRP/AESA Virginia Beach, VA, 17-21 May 1992

5. Jones B
   Core Engine Emissions Control Technology for an HSST Combined Cycle Turbo-Ramjet Engine, International Symposium on Japan's National Project for a Super/Hypersonic Transport Propulsion System, Tokyo, 28-29 October 1992

PREDICTION OF PROMPT NOx IN HYDROCARBON AIR FLAMES

V. Dupont, M. Pourkashanian, A. Williams

Department of Fuel and Energy,
Leeds University,
Leeds, LS2 9JT, UK

1. INTRODUCTION

The gas turbine industry is directing particular attention tc very low-NOx combustors, whether for aircraft or land-based CCGT systems. These low-NOx combustors frequently use liquid fuels or natural gas burning under very lean premixed conditions with air or under rich-lean conditions, although only the first case is studied here. In land based systems, diluted steam or nitrogen are sometimes injected into the combustion chambers to reduce flame temperature. The NOx emissions from such systems are the product of three chemical mechanisms which are interrelated: the hydrocarbon prompt-NO, the thermal-NO (extended Zeldovich mechanism) and the nitrous oxide route to NO. Formation of NO_2 from NO also occur, as well as emission of carbon monoxide and unburnt hydrocarbons. When the fuel-oxidant proportion decreases towards leaner conditions, flame temperatures are lowered, resulting in the total NO being reduced and the thermal-NO contribution greatly diminished to the benefit of the remaining two mechanisms of NO formation. Whilst knowledge of the elementary reactions and their chemical kinetics concerning methane and simple hydrocarbons combustion exists now for a number of years, its use for computer modelling is limited to simple flow dynamics configurations. Nevertheless, understanding of such combusting flows under a wide range of experimental conditions allows for analogies or speculations with more complex actual systems. Such understanding can be achieved by means of 1-D laminar premixed flame modelling, with a full chemical mechanism which incorporates the three routes of NO formation, like that proposed by Miller and Bowman (1). Complementary to this understanding is the modelling of the actual combustion system using a full description of the fluid dynamics coupled with a reduced chemical scheme, which is then compared against the first model.

The object of this investigation is to evaluate the relative importance of the three mechanisms of NO formation in lean premixed methane-air combustion with increasing pressure using the 1-D plug flow package PREMIX, and to test the validity of a 3-D model with a global chemical mechanism against the 1-D model in the atmospheric pressure case. Methane is chosen because it is the only mechanism which is reasonably well known and is a good guide to the behaviour of other hydrocarbons. The mixture ratio chosen is richer than that in lean gas turbines, but the combustion of this mixture with the low preheat gives realistic gas turbine final flame temperatures. Conditions of NO_2 formation are also analysed in the 1-D model and results extrapolated to the case of gas turbines.

2. THE CHEMICAL MODELS USED IN THE 1-D MODEL AND THE 3-D MODEL

In order to predict NOx formation it is necessary to describe the fluid flow and chemical reactions. It is possible to set up these equations in a comprehensive way for 1-D combustion including NOx prediction by using PREMIX as in the next section. The limitations of current computers preclude the use of such extensive chemical mechanisms in complex flow systems unless cost is not of significance. In this section, the

Presented at an AGARD Meeting on 'Fuels and Combustion Technology for Advanced Aircraft Engines', May 1993.

chemical model used in the Sandia PREMIX is discussed, and the simplified mechanism of methane combustion together with the derivation of the global equations of prompt and thermal-NO utilised in the post-processor of NOx in the CFD package presented subsequently.

The chemical mechanism chosen in the 1-D model of a laminar premixed methane-air flame at different pressures is that of Miller and Bowman (1) from which the most insignificant species were eliminated. It modelled the evolution of 24 species (CH_4, CH_3, CH_2, CH, CH_2O, HCO, CO_2, CO, H_2, H, O_2, O, OH, HO_2, H_2O, N_2, N, NO, HCN, NCO, NH, CN, N_2O, NO_2) using 79 reactions and their corresponding reverse reactions throughout the same length of domain of 10 cm. Two modes of burning were computed of which the first one was the freely propagating adiabatic flame, which calculates the temperature rise and the adiabatic flame temperature, the burning velocity and the concentrations of the above species as functions of distance. The second mode was the plug flow flame to which a chosen temperature profile and an incoming flow rate of reactant mixture are imposed, bearing in mind the resulting computed burning velocity cannot exceed the adiabatic one. In this case, the temperature profile imposed was taken from the prediction of the 3-D model at the location of the highest temperature, and the mass flow rate of reactants chosen to produce a burning velocity equal to the adiabatic one.

An additional mechanism suggested by Michaud et al (2) was employed in the same conditions as before and also in the modelling of a plug-flow flame of fuel-air equivalence ratio 0.77 (5) and at atmospheric pressure. This mechanism, based on the Miller and Bowman one, indicated a greater role of the NO formed by oxidation of N_2O especially through an excited state of O atom (O^1D) which displays faster kinetics than the O atom in its ground state. This mechanism included the species CH_3O, H_2O_2 and O^1D in addition to the above mentioned species, and was defined by 96 reactions.

In the following is the approach taken in the 3-D model using the FLUENT version 3.03 CFD package by means of reduced mechanisms and global equations for methane combustion and NO formation in the atmospheric pressure case. A global reaction for methane oxidation can be used but this approach gives no information on the important intermediate, CO, nor can it predict the flame temperatures correctly. This can be partially circumvented by using a two-step reaction scheme based on the reactions

$$CH_4 + 1.5\ O_2 \xrightarrow{1} CO + 2H_2O \qquad (1)$$

or in the case of higher hydrocarbons

$$C_xH_y + (x/2 + y/4)O_2 \longrightarrow xCO + y/2\ H_2O \qquad (1a)$$

followed by

$$CO + 0.5\ O_2 \xrightarrow{2} CO_2 \qquad (2)$$

which have been used by a number of researchers, e.g. Dryer and Glassman (3) and Dupont et al (4, 5).

Reaction (1) effectively incorporates the two steps

$$CH_4 + O_2 \rightarrow CO + H_2O + H_2 \qquad (1a)$$

$$H_2 + 0.5\ O_2 \rightarrow H_2O \qquad (1b)$$

which in turn include all the elementary reactions. Reaction (2) truncates the CO plus hydroxyl chemistry and as such the CO concentration can be used if necessary as an indicator of the degree of radical overshoot; in particular it can be used to calculate oxygen atom concentration. We then couple this two-step mechanism with a post-processing computational stage for NOx prediction. NOx can be formed by both the thermal route (including O atom overshoot) or by the prompt-NO route involving hydrocarbon radicals reacting directly with N_2 and to a lesser extent via a nitrous oxide intermediate. As

the flame temperature is reduced the prompt route dominates and that is the case in the present investigation.

The thermal-NOx formation mechanism is fairly well understood but the difficulty is applying it with precision. The reactions involved are:

$$O + N_2 \overset{k_3}{\rightleftharpoons} NO + N \qquad (3)$$

$$N + O_2 \overset{k_4}{\rightleftharpoons} NO + O \qquad (4)$$

$$N + OH \overset{k_5}{\rightleftharpoons} NO + H \qquad (5)$$

Thus in stoichiometric and lean flames the thermal-NO formation rate may be expressed by the equation:

$$\frac{d[NO]_T}{dt} = 2k_3\,[O]\,[N_2] \left\{ \frac{1-[NO]^2/K[O_2][N_2]}{1+k_{-3}[NO]/k_4[O_2]+k_5[OH]} \right\} \qquad (i)$$

where $K = (k_3/k_{-3})(k_4/k_{-4})$ and $k_3 = 1.8\times10^{14}\exp(-38{,}370/T)$ cm^3 mol^{-1} s^{-1}. Equation (i) assumes that the NO formation rate will be dependent on the local stable (i.e. O_2, N_2) and unstable (i.e. OH and O) species. Thus thermal NOx can be modelled with an accuracy of ± 35% given the information on the actual oxygen atom and OH radical from a library data function of the O_2 concentration. The effect of pressure is that the rate of formation of NO_T varies as the square root of the total pressure. This is the relationship commonly assumed to predict the pressure dependence of NOx in gas turbines.

NO can also be formed by the prompt-NO route involving the sequence:

$$CH + N_2 \rightleftharpoons HCN + N \qquad (6)$$

followed by reaction (4) and the oxidation of HCN subsequently leading to NO and N_2, the latter predominating under these lean reaction conditions.

If the reaction rate is controlled by equation (6) then the concentration of prompt-NO, $[NO]_{Pr}$, is given by

$$\frac{d[NO]_{Pr}}{dt} = C_0\,k_6\,[CH]\,[N_2] \qquad (ii)$$

where $C_0 = 2$ in very lean flames when both the HCN and N can form NO. In stoichiometric and rich mixtures it takes a value between 1 and 2.

If [CH] is formed by the steps

$$CH_4+OH \rightleftharpoons CH_3+H_2O \text{ etc.} \longrightarrow\longrightarrow CH \qquad (7,8,9)$$

and if the following reactions

$$OH + OH \rightleftharpoons H_2O + O \qquad (10)$$

and

$$O_2 \rightleftharpoons 2O \qquad (11)$$

are in partial equilibrium, then it can be shown that

$$\frac{d[NO]_{Pr}}{dt} \propto \frac{k_6\,K_7\,K_8\,K_9\,K_{11}^{3/4}}{K_{10}^{3/2}\,[H_2O]^{3/2}}\,[N_2][CH_4] \qquad (iii)$$

There are a number of uncertainties: firstly whether radical equilibrium is maintained, secondly the conversion efficiency of HCN to NO and thirdly the value of k_6. There are considerable doubts about k_6 and recent estimates cover a relatively wide range of values (see ref. 5), at a temperature of 1300 K, this implies relative rates of 1, 3 and 7 for these rate expressions respectively. The form of equation (iii) is that the rate of formation of NO_{Pr} is proportional to total pressure.

Equation (iii) is similar to the expression obtained experimentally by De Soete (6) and with the same pressure dependence. We have modified this to the form given below for methane as fuel reactant, namely

$$\frac{d[NO]_{Pr}}{dt} = 6.4\times10^6\,f\,[O_2]^{\alpha}[N_2][CH_4]^{\beta} \times \exp(-Ea/RT) \qquad (iv)$$

However equation (iv) only applies to high temperature flames and a modification of this, based on reaction orders calculated from experimental composition data, must be applied in the lower temperature slower reacting regime.

The overall activation, Ea, in equation (iv), can take two values corresponding to a low temperature range and a high temperature one, namely for T < 1920 K Ea = 177.7 kJ/mol, and for T > 1920 K Ea = 303.1 kJ/mol. Such values of Ea are based on experimental data as described in (5).

The value of the factor f for aliphatic fuels is given by $f = 4.75 + C1\ n - C2\ \phi + C3\ \phi^2 - C4\ \phi^3$ where C1 to C4 are constants, n is the number of carbon atoms in the hydrocarbon fuel and ϕ the fuel/air equivalence ratio. The values of C1 to C4 are 8.19 x 10-2, 23.2, 32 and 12.2 respectively. These values are valid for aliphatic alkane hydrocarbon fuels and for ϕ between 0.62 - 1.43 and possibly for even leaner mixtures.

In practice the methane (or other hydrocarbon) and oxygen exponents are variable. α and β, the reaction orders, can take values respectively from 0 to 1 for O_2, and 0.2 to 1 for CH_4. At low temperatures (i.e. < 1000 K) the reactivity of CH_4 with O_2 is very low and the reaction order of O_2 is taken to be 0. As T increases the reaction order for O_2 increases also. α is a function of the concentration of O_2 and an average local temperature. β was taken to be 1 because of the low temperatures involved in the present case. In the case of turbulent combustion a joint variable pdf treatment using the variables ($\tilde{T}$, $[O_2]$) for thermal-NOx and (T, $[CH_4]$) for prompt-NOx was used to determine the NO concentration field.

The third route (7) leading to NO involves the formation of N_2O as an intermediate via the reaction:

$$O + N_2 + M = N_2O + M \qquad (12)$$

where M is mainly N_2, and is followed by

$$N_2O + O = 2NO \qquad (13)$$

If the rate of NO is controlled by reaction (12) then we can set

$$\frac{d[NO]}{dt} = k[O]\ [N_2][M] \qquad (v)$$

where [O] is the actual oxygen atom concentration but can approximately be made equal to $[O_2]^{0.5}$. On this basis the pressure dependence of d[NO]/dt is $(\text{pressure})^{1.5}$.

Both the thermal route and the N_2O prompt route are subject to uncertainties not only in kinetic data but in the actual reactions involved.

Since the rate of prompt-NO formation was empirically derived with respect to the low activation energy found, and knowing that the experimental concentration of NO used for its calculation included the N_2O-route of NO formation, it is justified to say that the N_2O route to NO was included in the prompt-NO equation through the value of the activation energy. The term of CH_4 concentration not directly responsible for the N_2O route to NO as the hydrocarbon prompt-NO is, accounts for the life duration of the N_2O - NO mechanism. A future improvement of the mechanism is to incorporate a separate global equation for the N_2O route to NO. However, since the 3-D model was only run for atmospheric pressure, it is necessary to study the effect of pressure in the 1-D cases for the equivalence ratio of 0.65 and the results of this study are presented in the next section.

3. FULL COMPUTATION OF NOX FORMATION IN ATMOSPHERIC AND ELEVATED PRESSURE FLAMES

Computations were undertaken using PREMIX for the combustion of methane at 1, 5, 10 and 20 atm for the fuel-air equivalence ratio 0.65. Two burning modes were studied : the freely propagating adiabatic flame and the

plug flow flame to which the adiabatic burning velocity and an imposed temperature profile reaching the maximum temperatures of 1350 K and 1500 K were applied. Furthermore, the mechanism of Miller and Bowman (1) and its modification by Westmoreland and co-workers (2) were compared. Results from the former mechanism are initially discussed and those from the latter commented upon subsequently. The computed adiabatic flame temperature remained unchanged at 1751 K at the different pressures. The effects of increasing pressure on the freely propagating adiabatic flames were that the temperature gradients were increased, the burning velocity diminished as an effect of increasing density. This had the effect of extending the reaction time for a same length of domain. Also, the thickness of the radical overshoot zone was reduced but the time of appearance of the radical pool was affected differently with increasing pressure. With increasing pressure from 1 to 5 atm, the radicals O, OH, H and HO_2 appeared sooner and moved the flame front upstream considerably. However, when increasing from 5 to 20 atm, the radical appearance was slightly moved downstream even though their gradient was more pronounced. The peak value of these radicals was maximum at atmospheric pressure. The effects of increasing pressure on NO formation in the radical overshoot region - which is usually taken to be the prompt-NO formation zone- are shown in Fig. 1 for the freely propagating adiabatic flames at 1, 5, 10 and 20 atm. In this region, the maximum NO was found to be equal at 10 atm and 20 atm but at a value of only 4.8 ppm for the original Bowman and Miller mechanism. When eliminating the species HCN and CN responsible for hydrocarbon prompt-NO, the total NO formed in this early region was diminished by a maximum of 30% for atmospheric flame and 55% for the 20 atm flame. However, as the reaction time increased and the radicals reached their equilibrium values, the NO increased linearly with time in a more pronounced way as pressure increased. The prompt-NO was in no way responsible for this increase as demonstrated in Fig. 2. This displays the matching curves of NO as a function of reaction time using the mechanism without N_2O and the thermal-NO mechanism only for 20 atm. The NO formed when the species N_2O was eliminated from the mechanism in the 20 atm flame showed it was entirely due to the thermal route. The formation of N_2O and NO_2 throughout the combustion domain is shown in Fig. 3. From this plot, the equilibrium values of N_2O increasing with pressure indicated the N_2O route was not responsible for the increase in NO in the radical equilibrium region, and that the maximum values of N_2O matched those of NO in the radical overshoot zone. It also indicated that N_2O formation preceded that of NO in time. Like NO, equilibrium values of N_2O were increased by high pressure when the thermal-NOx mechanism was active, which was always the case for adiabatic flames. The species NO_2 remained in small quantities (less than 1 ppm) but increased also with reaction time in the radical equilibrium zone and increasingly with pressure.

At the end of the domain the relative contributions of hydrocarbon prompt-NO and thermal-NO were respectively 7.2% and 59.1% for 1 atm, and 1.5% and 70.9% for 20 atm. Analysis of the results obtained for the atmospheric case using the modified mechanism (2) (see Figs. 1 and 2) showed that the total-NO obtained was increased by 16% and that the corresponding final thermal contribution was 67%. Therefore, the overall effect of the modified mechanism was due to (a) increasing the total-NO, (b) increasing the thermal-NO and (c) decreasing the final proportion of the thermal contribution while increasing the remaining two.

Figures 4 and 5 illustrate the evolution of the main parameters of NO formation (temperature, CH_4, NO, N_2O, O, OH and H) at 1 and 20 atm for the plug flow mode; in the same figures are also plotted the NO and N_2O predictions using the modified chemical mechanism. The same temperature input was used for the two flames and showed that these parameters start to change once the maximum temperature of 1500 K had been

reached. Comparison of the two figures lead to interesting discoveries. In the first place, the total-NO found for 20 atm was nearly the same as for 1 atm, at 0.5 ppm using the unmodified mechanism. The value obtained with the modified mechanism was similar at 1 atm (0.6 ppm) but doubled at 20 atm (1.2 ppm). These small values are consistent with the freely propagating adiabatic values of NO in the prompt-NO zone, taking into account that the temperature was 250 K smaller in the plug flow case. The same low value of maximum temperature was responsible for the quasi- elimination of thermal-NO formation in the radical equilibrium region. Explanation of the shapes of NO and N_2O at 20 atm and 1 atm for the unmodified mechanism is found in the effect of pressure on the hydrocarbon attack by free radicals. Many recombination reactions involving H, OH and O were speeded up by increasing pressure, in a larger extent than the chain branching reactions. This phenomenon was even more pronounced for low temperatures since the reactions concerned have a zero activation energy and a negative exponential term on temperature. Hence, the plug flow high pressure flames, at a lower temperature than the adiabatic ones, displayed a slowing down in the usual build-up in radical concentrations as soon as they reach a minimum sufficient for the recombination reactions to occur. The ultimate effect of this on NO, N_2O, H, OH, and O was that their rate of formation and removal were increased. However H, OH and O were more heavily affected by their rate of removal, thus their equilibrium more rapidly reached generally after a smaller superequilibrium value . The species N_2O followed the opposite trend as its rate of formation was increased by pressure due to a faster third-body recombination reaction $H+O_2+M=HO_2+M$ and the reaction $N_2+HO_2=N_2O+OH$. Therefore the peak concentration of N_2O was higher for 20 atm (6ppm) than for 1 atm (0.5ppm). NO formation which was on one hand slowed down by a reduction in O and OH at high pressures, was on the other hand accelerated by an increase in N_2O through the reaction $N_2O+O=2NO$, ending in similar values of NO at 20 atm and 1 atm. The modified mechanism which includes two additional third body reactions of formation and removal of NO by N_2O and by NO_2 leads to a higher peak in N_2O at 20 atm and a higher equilibrium value of NO. The slowing down of the rates of formation of the radicals also extended the duration of methane oxidation. Naturally this has to be placed in the context of actual turbulent flames where the maximum temperatures reached fluctuate around an average of 1500 K locally, due to imperfect mixing, hence variations of stoichiometry. Similar runs of plug flow flame using the CFD 3-D prediction of maximum temperature of 1360 K lead to difficulties in achieving the burning of the methane in the 20 atm case, extending the distance of CH_4 decay over 10 cm. This result seemed to show that the mechanism or the kinetic data used were no longer valid, and indeed it is not recommended in such extreme conditions of pressure and temperature. In this run, the equilibrium values of the radicals O, H and OH were even more rapidly reached without displaying the superequilibrium characteristics, leading to even lower NOx than in the 1500 K case. From these observations, the predicted average turbulent maximum temperature of 1360 K was probably underestimated in the CFD calculation and the equivalence ratio of 0.65 of the primary mixture to the limits of flammability hence the results displayed for 1500 K only.

3.1 Application to a Full CFD Computation

In order to test the use of the prompt-NOx equation together with thermal NOx prediction, a very lean combustor which produces very low levels of NOx was modelled. It is similar to a gas turbine chamber in its design, hence its usefulness in making the comparison with the formation of NOx in gas turbines. The burner, shown in Fig. 6, consists of a planar enclosure followed by a divergent section in which the flame sits. A long planar duct comes next, ending in a short convergent section from which emerge the hot mixture of air and combustion gases. Only the parts of the burner where the flame develops have been modelled, the

remaining sections being of little interest from the point of view of NOx formation.

A section of the burner is drawn in Fig. 7a and the finite volume grid of the model is given as front and enlarged top views in Fig. 7b. The 3-D model took advantage of the multiple planes of symmetry of the burner. The choice of keeping to minimum the number of cells in the z direction (7 cells) to allow larger numbers in the main directions of the flow in x and y (71 and 50 cells) was made. The size of the domain in respectively x, y, and z directions was 0.142, 0.05 and 0.00635 m.

The geometry of the burner head played a crucial part in the flow pattern and in the stability of the flame. The velocity field and the mixing of the primary fuel-air mixture and secondary air were highly dependent on the balance of pressures at their release in the burner head. It was their influence which ensured that (a) the primary methane-air mixture distributed in a balanced way between the two first and the third rows of holes, and (b) the secondary air flow was sufficiently large to entrain the fuel-air mixture toward the divergent section, but low enough to let the feed gas emerge from the two first rows of holes.

Figure 8 shows the temperature field for the equivalence ratios 0.77 (left) and 0.65 (right). Calculated prompt-NO concentrations at = 0.77 and 0.65 are plotted in Fig. 9. no thermal-NO was formed in either cases due to the low temperatures involved. Experimental results for the equivalence ratio 0.77 agreed well with the predictions considering measurements of NOx could not appreciate tenth of ppms. These results are summarised in Table 1.

Table 1

ϕ = 0.77			
	Min Thermal Input	Max Thermal Input	CFD
CH_4 (m^3/s)	$4.73 \cdot 10^{-3}$	$3.42 \cdot 10^{-2}$	$8.93 \cdot 10^{-3}$
T (K)	1383	1453	1230
NO (ppm)	0	2	0.2
NO_2 (ppm)	0	0	0
CO (ppm)	53	302	215
O_2 (%)	12	10.4	12
CO_2 (%)	4.6	5.9	3.8

Table 2 displays comparative results obtained by the CFD model and the PREMIX at atmospheric pressure and fuel-air equivalence ratios 0.77 and 0.65.

Figure 10 shows the contours of rate of NO formation for ϕ = 0.77 and ϕ = 0.65. Fig. 11 gives the streamlines, similar at ϕ = 0.77 and ϕ = 0.65.

Table 2

		Total NO (ppm)		% Contributions		
	Mechanism	at T_{max}	at 10 cm	hc prompt	N_2O prompt	Thermal
ϕ = 0.77 T = 1541K 1 atm						
PREMIX	M & B W	0.5 0.6	0.67 0.9	61-52 29-21	33-38 64-70	6-10 7-9
CFD	Global	2		100		0
ϕ = 0.65 T = 1500K 1 atm						
PREMIX	M&B W	0.36 0.6	0.56 1.2	55-37 -	40.7-56 -	4.3-7 3.7-6
CFD	Global	0.24		100		0

4. CONCLUSIONS

High pressures in the case of very lean methane-air premixed laminar flames were found to have different effects in the two main zones of the flame. In the radical overshoot region, the unmodified mechanism showed NO increasing parameters such as temperature and N_2O to NO third body reactions competing against NO reducing factors such as lower O and OH superequilibrium values due to faster recombination reactions. The modified mechanism emphasized the third body reactions forming NO. In this region, pressure was not found to affect the relative contributions of the three mechanisms of NO formation: hydrocarbon prompt was around 35% - 55% depending on temperature, thermal was from 5% - 20% and the rest was due to N_2O-prompt.

In the radical equilibrium zone, the dominant parameter in NO and NO_2 formation was temperature. Thus in the adiabatic case, since the temperature was high enough for the thermal-NO to occur, high pressures increased the level of NO to few a tens of ppm. The other two mechanisms of NO formation were inactive in that region. In the plug flow case where temperatures did not allow thermal NO formation (1500 K), the nitrogen oxides remained approximately at the values reached in the radical overshoot region; with respectively the N_2O intermediate route to NO and the hydrocarbon prompt-NO as the highest contributors at high pressure and at atmospheric pressure. The CFD 3-D model succeeded in predicting similar levels of NO as the full chemical laminar 1-D model in the atmospheric case, although the N_2O-prompt route to NO was not explicitly included. Nitrogen dioxide, which forms mainly through the reaction NO + HO_2, was also increased by high pressures in the adiabatic case, although of two orders of magnitude smaller than NO. This reaction is greatly accelerated at low temperatures and all NO present would eventually convert to NO_2 if the radical HO_2 is present, that is if H radicals and O_2 are present. This situation can arise when exhausts containing NO are injected into a cold air stream where H atoms from the flame react with O_2. We have undertaken studies which show that in such cases the $[NO_2]/[NOx]$ ratio varies with the cold air stream temperature, details of this work will be published later.

ACKNOWLEDGEMENTS

Valerie Dupont wishes to thank British Gas plc for a SERC CASE studentship.

REFERENCES

1. Miller, J.A. and Bowman, C.T. Prog. Energy Comb. Sci. 15, 287 (1989).

2. Michaud, M.G., Westmoreland, P.R. and Feitelberg, A.S. Twenty-fourth Symposium (International) on Combustion, The Combustion Institute. To be published.

3. Dryer, F.L. and Glassman, I. Fourteenth Symposium (International) on Combustion, The Combustion Institute, p. 987 (1973).

4. Dupont, V., Pourkashanian, M., Williams, A. Proceedings of the Tenth Members Conference, IFRF (1992).

5. Dupont, V., Pourkashanian, M., Williams, A. J.Inst.E. To be published (1993).

6. De Soete, G.G. Fifteenth Symposium (International) on Combustion, The Combustion Institute, p. 1093 (1974).

7. Corr, R.A. , Malte, P.C. and Marinor, N.M. J. Engineering for Gas Turbines and Power, 114, 425 (1992).

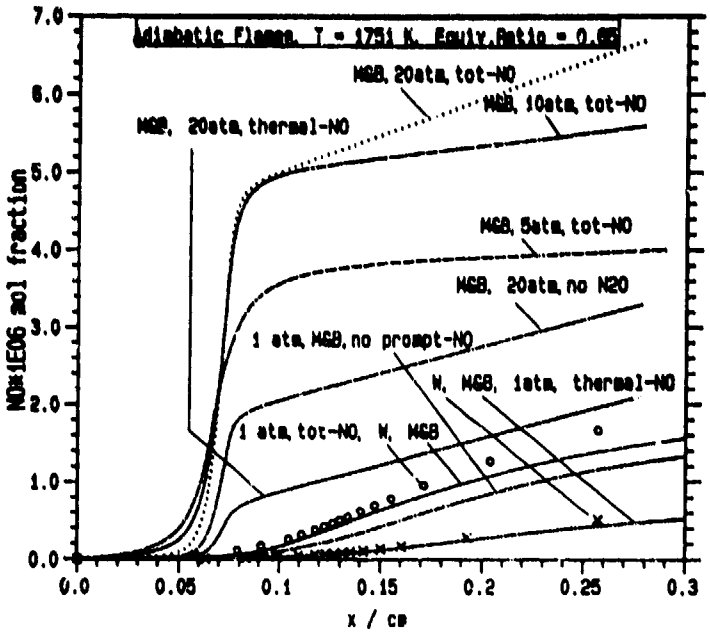

Fig. 1 NO concentrations in radical overshoot region for various pressures of freely propagating adiabatic flames, ϕ = 0.65. M&B: Miller and Bowman mechanism, W: Westmoreland mechanism.

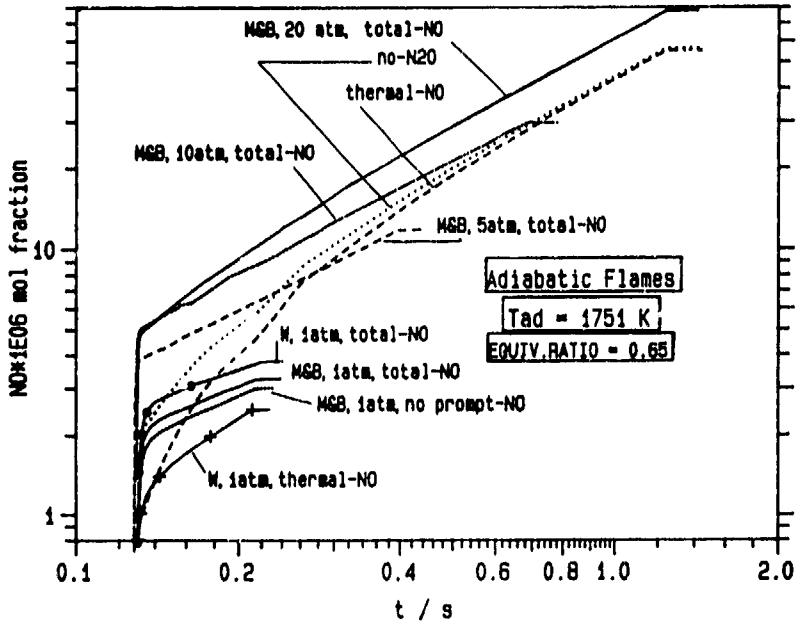

Fig. 2 NO concentrations in radical equilibrium zone for various pressures of freely propagating adiabatic flame, ϕ = 0.65. M&B: Miller and Bowman mechanism, W: Westmoreland mechanism.

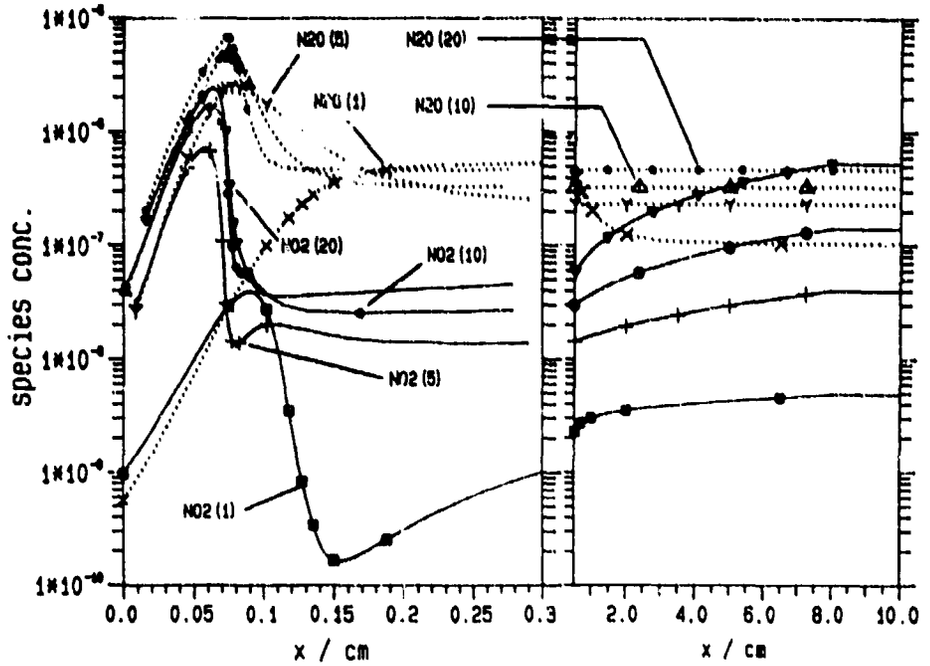

Fig. 3 N_2O and NO_2 concentrations in radical overshoot zone and in radical equilibrium zone at various pressures of freely propagating adiabatic flame, $\phi = 0.65$. Only Miller and Bowman mechanism.

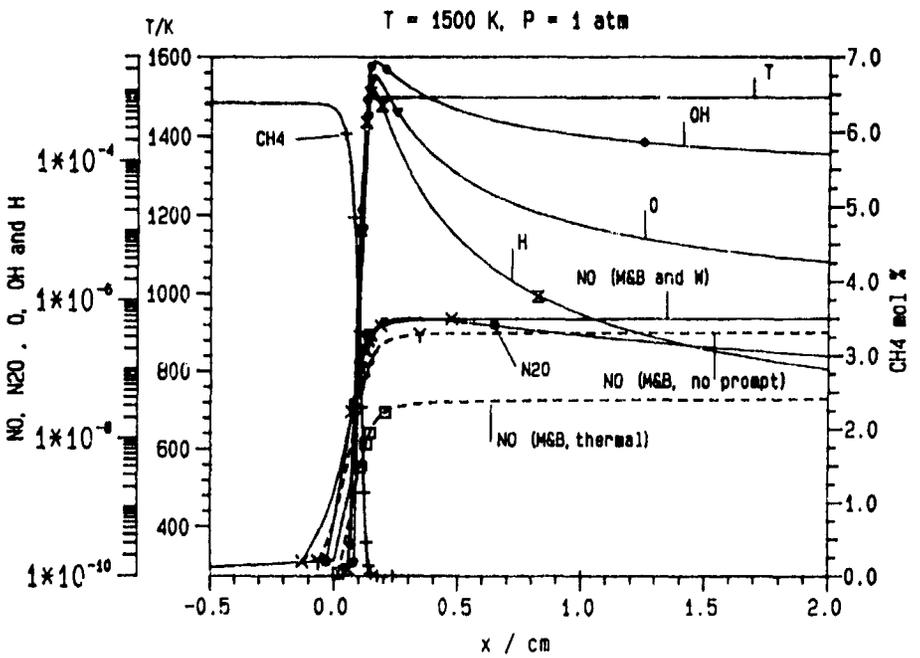

Fig. 4 Plug flow flame at 1 atm. Radicals, CH_4, NO and N_2O concentrations for T = 1500K for various mechanisms. (M&B: Miller and Bowman mechanism, W: Westmoreland mechanism, no prompt-NO mechanism without HCN and CN, thermal-NO mechanism without HCN, CN and N_2O).

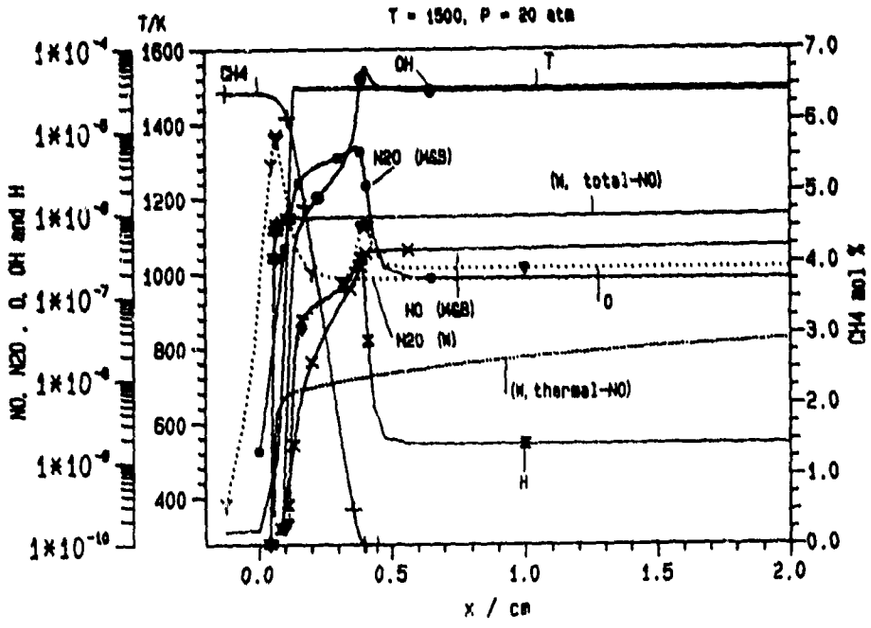

Fig. 5 Plug flow flame at 20 atm. Radicals, CH_4, NO and N_2O concentrations for T = 1500K for various mechanisms. (M&B: Miller and Bowman mechanism, W: Westmoreland mechanism, no prompt-NO mechanism without HCN and CN, thermal-NO mechanism without HCN, CN and N_2O).

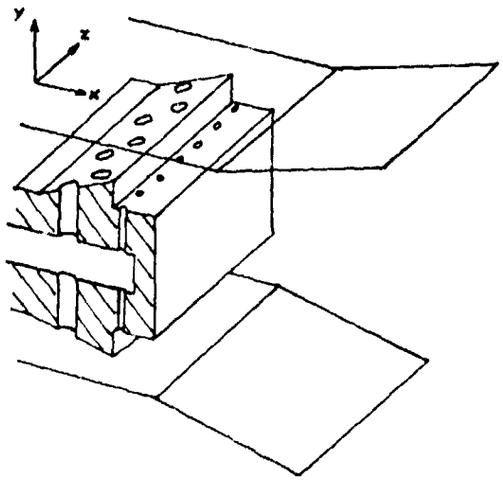

Fig. 6 Burner section.

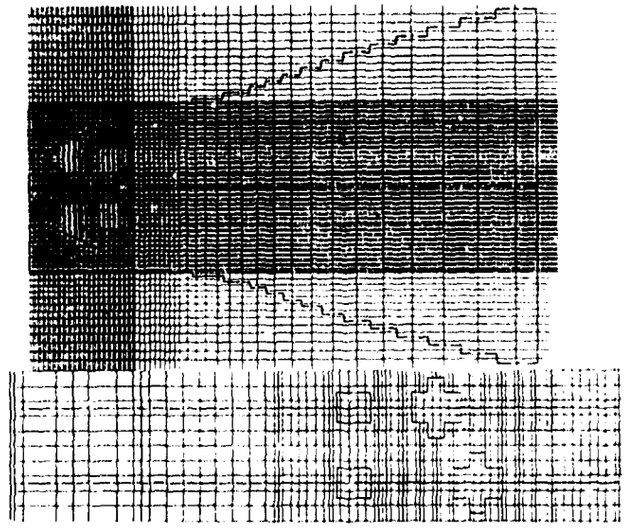

Fig. 7 (a) Front view of finite volume model.
(b) Top view (enlarged) of finite volume model.

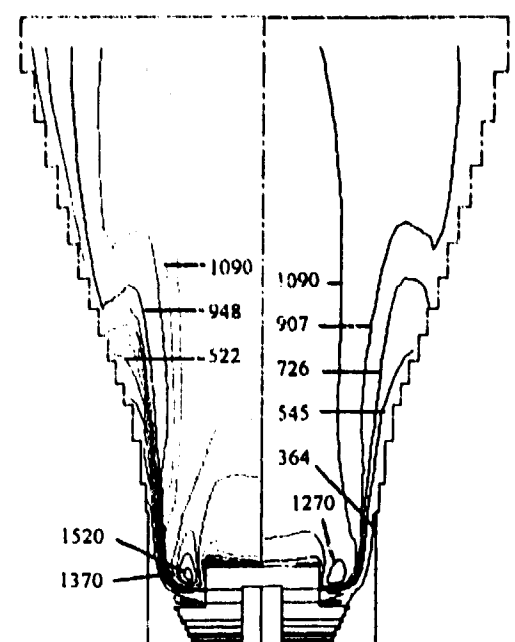

Fig. 8 (a) Temperature contours for $\phi = 0.77$
(b) Temperature contours for $\phi = 0.65$

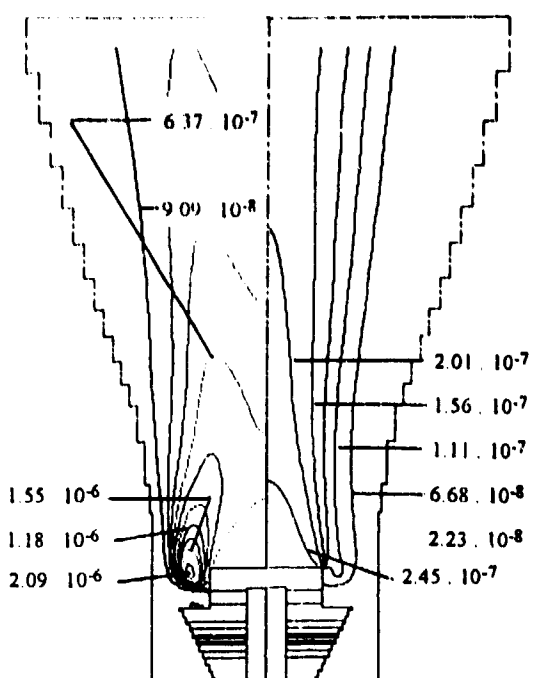

Fig. 9 (a) Prompt-NO contours for $\phi = 0.77$
(b) Prompt-NO contours for $\phi = 0.65$

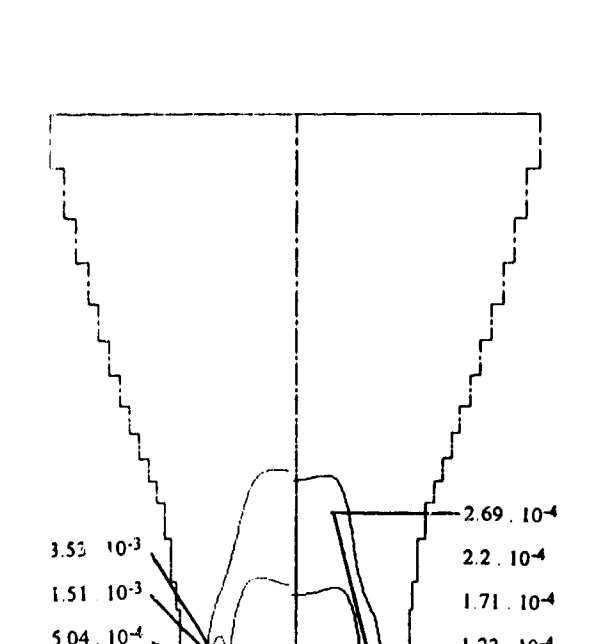

Fig. 10 Rates of NO formation for $\phi = 0.77$ and $\phi = 0.65$.

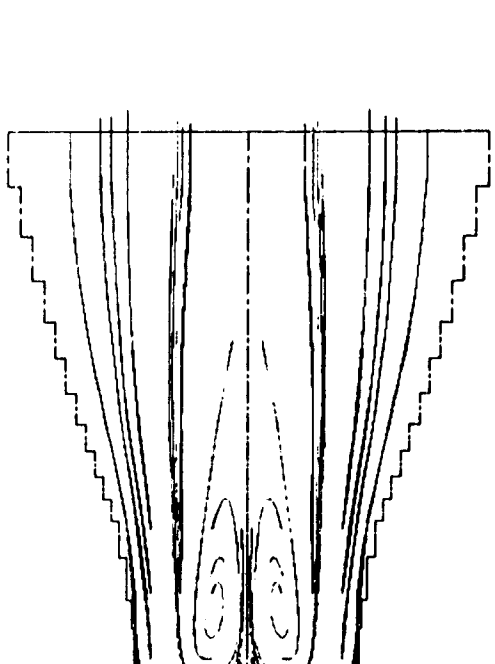

Fig. 11 Streamlines showing recirculation zones.

SIMULATION OF POLLUTANT FORMATION IN TURBULENT COMBUSTORS USING AN EXTENDED COHERENT FLAME MODEL

E. Djavdan[‡], D. Veynante, J. M. Duclos and S. Candel

Laboratoire EM2C, CNRS, Ecole Centrale Paris, 92295 Chatenay-Malabry, France

An extension of a flame surface density model, combining flamelet concepts and homogeneous reactor combustion is proposed to predict NO and CO formation. Results for CO in propane-air premixed flames for different equivalence ratios are compared to available experimental measurements. The agreement is good but the model is sensitive to the determination of the flamelet model parameters such as those governing the effective strain rate.

Cet article présente une extension du modèle de flamme cohérente à l'analyse de la formation de polluants comme CO et NO. Le nouveau modèle combine une description de type flammelette avec une représentation de la combustion à l'aide de réacteurs homogènes. Les résultats obtenus pour CO dans le cas de flammes turbulentes stabilisées dans un canal, sont comparés à des mesures. L'accord entre les calculs et les expériences est encourageant mais les résultas dépendent sensiblement des hypothéses utilisées pour la détermination du taux d'étirement efficace.

1. INTRODUCTION

Prediction of pollutants like carbone monoxide or nitrogen oxide constitutes an important issue if one wishes to improve combustion performance and more generally to decrease the impact of hydrocarbon combustion on the environment. This problem also poses a scientific challenge because the standard fast reaction assumption (short chemical time compared to turbulent time) generally made in turbulent combustion modeliing, is no longer valid for pollutant prediction.
It is known for example that carbon monoxide oxidation into carbon dioxide or nitrogen oxide formation requires longer residence times than the initial reaction of hydrocarbon combustion. This situation is analogous to that encountered in supersonic combustion, for scramjet applications. In this case, due to the high flow velocities, the mechanical time is noticeably decreased and becomes comparable to chemical times. Classical turbulent combustion models of premixed turbulent combustion, such as the well known Eddy Break Up approach or those based on the "flamelet" concept assume a thin reaction zone between fresh and burnt gases with a single very fast global reaction :

$$F + O \longrightarrow P$$

where the global reaction rate is mainly governed by turbulent flow characteristics. Chemical effects are only included in the determination of the local laminar rate of consumption and in the calculation of extinction conditions which results for example from excessively high strain rates.
A new formulation is necessary to take into account species such as CO or NO because the caracteristic chemical time of oxidation of these species is longer than the one of hydrocarbon oxidation and the hypothesis of a thin reaction zone becomes inadequate. In fact, the CO oxidation takes place in hot gases, mainly through reactions like :

$$CO + OH \longrightarrow CO_2 + H$$

where the OH radicals are also products of the first hydrocarbon oxidation.
The approach proposed in this work is to extend a flame surface density model designated as the "Coherent Flame Model" (CFM) to the analysis of the pollutant formation. The original CFM was derived by Marble and Broadwell (1977) for non premixed turbulent combustion and it has since then been used, tested and extended for premixed turbulent combustion by Candel *et al.* (1982), Darabiha (1984), Candel *et al.* (1991), Maistret (1991), Veynante *et al.* (1991) and Boudier *et al.* (1992). The extension of such a model for pollutant prediction is based on the assumption that the fuel oxidation mechanism mainly takes place is a thin reaction zone and is governed by a flamelet regime whereas the oxydation mechanism of intermediate species such as CO and NO is modeled by a classical well stirred reactor approach (i.e., the chemical time of oxidation of these species is assumed to be longer than the local turbulent time). This oxidation takes place and involves species originating from the flamelet reaction inside the hot gases. One may note that such a general idea has been already suggested by Bray (1979). According to this author, pollutant formation could be analysed in terms of two kinetic reactions occuring sequentially so that the first one is assumed to be complete before the next reaction begins. Accordingly, two progress variables and probability density functions are required (one per reaction) if one wishes to exploit this analysis with a pdf approach. Broadwell and Breidenthal (1982) have also proposed to decouple chemical reactions in a mixing layer in two parts one corresponds to a strained laminar flame sheet (i.e., flamelets) in the vortex braids, the other in a well stirred reactor in the vortex core. Such an analysis has been used for NO prediction by Dibble *et al.* (1989) and extended by Miller *et al.* (1989) for supersonic combustion. Nevertheless, to our knowledge, these approaches have only been exploited

[‡] Present adress : Centre de Recherche Claude-Delorme, Air Liquide, 78350 Jouy en Josas, France

Presented at an AGARD Meeting on 'Fuels and Combustion Technology for Advanced Aircraft Engines', May 1993.

to obtain simple analytical relations for specific flows and not for numerical simulation of a complete turbulent reacting flow field. For hydrogen/air combustion, Janicka and Kollman (1982) have suggested a splitting of the reaction scheme in two parts. The first reactions are assumed to have reached an equilibrium state whereas the recombination reaction are treated with a finite reaction rate. In the particular case of the scheme considered, due to equilibrium expressions and conservation of atomic element, a complete determination of the chemical state is made through a "combined variable" (a linear combination of reaction rate of each reaction) and a passive scalar. Only a single variable have to be modeled. Nevertheless, this interesting idea is only applicable when the chemical scheme is not too large and the problem may be reduced to the determination of two variables by making use of a sufficient number of atomic conservation relations and equilibrium assumptions.

The present article comprises four sections. Section 2,summarizes the main elements of the Coherent Flame Model, used to describe fuel oxidation in the flamelets. The complete formulation for pollutant formation is then given in section 3. Numerical simulations and available experimental data are presented and discussed in section 4.

2. REVIEW OF THE COHERENT FLAMELET MODEL

In this section we will briefly present the basic element of the coherent flame model for premixed turbulent combustion. Further details may be found in previous articles, for example in Candel *et al.* (1991) or Veynante *et al.* (1991). A block diagram of the model is shown in Fig. 1. One assumes that the turbulent flame may be viewed as a collection of thin flame elements between fresh and hot gases. These elements are convected and distorted by the turbulent flow motion but keep an identifiable structure and, in this sense, remain coherent. This analysis is valid if the thickness of the reactive sheet, δ_r, is sufficiently small compared to the typical length scales l_t of the turbulent motion. Some authors believe that δ_r should be less than the smaller turbulent scale contained in the flow, the Kolmogorov scale. But recent results obtained from direct numerical simulation (Poinsot et al. 1990) or by flame vortex interaction experiments (Roberts and Driscoll, 1991) indicate that fluctations with a length scale smaller than a certain cut-off scale are unable to interact with the flame. Such a phenomenon has been already pointed out by Peters (1986) who proposes a "Gibson scale" for this cut-off but the value of this Gibson scale does not generally correspond to that found by direct simulation. It is now probable that the flame thickness δ_r may exceed the Kolmogorov scale and the "flamelet domain" of premixed turbulent combustion is more important than generally believed.

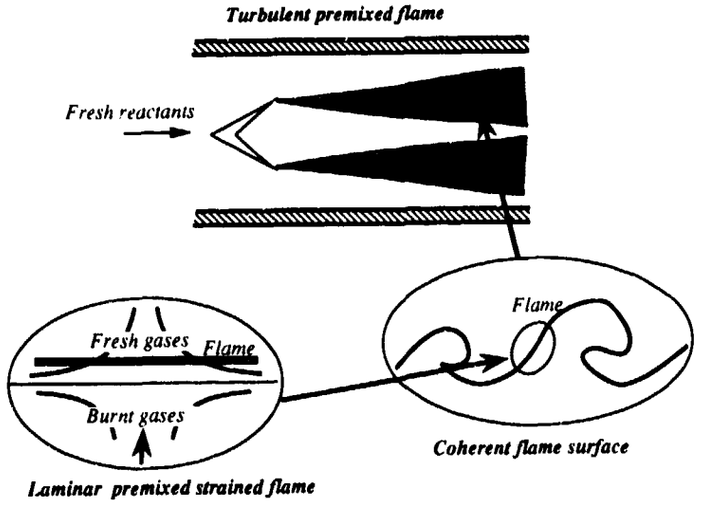

Figure 1. Description of premixed turbulent combustion using flamelet concepts.

Each flamelet element is mainly affected by the local strain rate which acts in the plane of the flame, modifies its structure and changes the local reaction rate. As a consequence, the local reation rate per unit of flame area may be determined by the analysis of a laminar strained flame. This simple geometry is adopted in many studies for detailed calculations of the local reaction rate, including complex chemistry features and multicomponent transport properties (see for example Darabiha *et al.*, 1988 or Rogg *et al.*, 1986). Experimental data are also available for a variety of strained flames.

Following this analysis, the global reaction rate of each species i, $\dot{W}_i$, may be written as the product of the local reaction rate per unit of flame area, ω_i by the available flame surface density per unit volume Σ :

$$\dot{W}_i = \omega_i \Sigma$$

The flame surface density has now to be determined. The central idea originating from Marble and Broadwell is to use a transport equation for the density of flame surface. This equation may be derived from the transport equation for a

material surface in a turbulent flow (see the derivation of Candel and Poinsot, 1990). The strain rate imposed by the turbulent motion change the local reaction rate of the flame but also has the effect of increasing the available reaction area. This production process is also balanced by various destruction mechanisms (not existing for a material surface) : flame shortening (mutual interaction of adjacent flame front and consumption of the intervening reactants), flame quenching under excessively high strain rates.

To summarize, the coherent flame model combines the three following elements : (1) A model for the turbulent flow, including a standard set of Reynolds or mass average dynamic equations and a turbulent closure model. (2) A local model for the laminar strained elements providing the consumption rates per unit of flame area. This model, combining complex chemistry kinetics and detailed molecular transport, is essentially decoupled from the turbulent flow description. In pratical computations, this model is implemented as a flamelet library, providing the local reaction rate as a function of various parameters (local strain rate, equivalence ratio, pressure, fresh gases temperature, ...). No local computations are carried-out during turbulent flow numerical simulations. (3) A balance equation for flame surface density accounting for transport, diffusion, production and destruction of flame area. A schematic representation of the model is given in Fig. 2. The main advantage of this analysis is that it decouples complex chemistry from the turbulent flow computation.

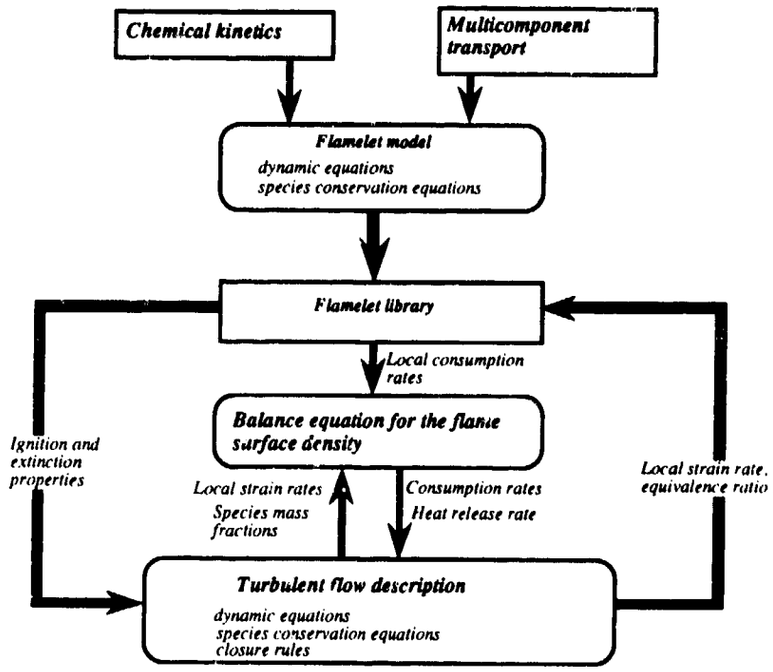

Figure 2. Block diagram of the coherent flame model

An important ingredient of the model is the modeling of the strain rate used both for local reaction rate determination and in the source term of the balance equation for flame surface density. In the simplest case of a two dimensional mixing layer, this strain rate ϵ_s may be deduced from the transverse gradient of the mean axial velocity. In more complex situations, it may be evaluated in terms of the turbulent kinetic energy k and dissipation ϵ as :

$$\epsilon_s = \alpha\epsilon/k$$

A more complex approach, based on direct numerical simulations carried out by Poinsot *et al.* (1990), have been proposed by Meneveau and Poinsot (1991) : the Intermittent Net Flame Stretch model (ITNFS). An effective strain rate is introduced in the production term of the flame surface which only takes into account the length scales that actually affect the flame front. Flame front thickness δ_l and laminar flame speed u_l are respectively compared to the turbulent integral length scale l_t and to the turbulent velocity fluctuations u' to determine the effective flame strain rate :

$$\epsilon_s = \Gamma_k(l_t/\delta_l, u'/u_l)$$

where Γ_k is a function provided by the authors.

Models based on an equation for the flame surface density are now being explored by many groups (for example Cant *et al.* 1990, Mantel and Borghi, 1991, Cheng and Diringer, 1991, Rogg, 1989, ...). A summary of their models is given in Duclos *et al.* (1993) together with an analysis in the case of turbulent flame propagation in one dimension and a comparison

with experimental data. It is interesting to note that whatever the derivation of the flame surface equation, the source and destruction terms of the balance equation for flame surface density proposed in each case have much in common. The differences mainly come from the closure assumptions used for the modeling of the effective strain rate.
To end this brief survey of the coherent flame model, one may note that extensions have been proposed for non uniformly premixed reactants (Veynante *et al.*, 1989), for situations including both premixed and non-premixed flames elements such as those encountered in transient ignition of a non premixed turbulent devices (Veynante *et al.*, 1991, Fichot *et al* , 1991) or in Diesel engines, taking into account the vaporization of a fuel spray (Dillies *et al.* 1993).

3. AN EXTENDED FLAMELET MODEL FORMULATION

To extend the flame surface density model to the prediction of pollutant formation, we assume that the combustion mechanism of hydrocarbons takes place in two submechanisms. The first one, the oxidation of fuel producing intermediate species (mechanism called $M1$) is typically very fast compared to the other caracteristic times. This oxidation is supposed to take place in a flamelet. The second mechanism (CO_2 and NO formation), called $M2$, with a longer chemical time, takes place in high temperature regions where the fluctuations are relatively less important and where one may consider that the corresponding kinetics are best represented by homogeneous reactor conditions.
The source term of the conservation transport equation of species k may be formally written as

$$\Lambda(\overline{Y_k}) = \sum_{i=1}^{R} \nu_{ki} \overline{\omega_i(T, [Y_1], ..., [Y_K])} \tag{1}$$

where $\overline{\omega}_i$ is the mean mass reaction rate of reaction i, R is the number of chemical reactions and ν_{ki} the stoichiometric coefficients of species k in reaction i.
Under the previous assumptions, this source term may be expressed as :

$$\Lambda(\overline{Y_k}) = \omega_k \Sigma + \sum_{i=1}^{R2} \nu_{ki} \omega_i(\overline{T}^b, \overline{[Y_1]}^b, ..., \overline{[Y_K]}^b)$$

where the first right hand term is the reaction rate of specie k due to the flamelet reaction, ω_k is the local reaction rate per unit of flame area of specie k. The second term, for the $R2$ reactions of mechanism $M2$, expresses the consumption rate for a well stirred reactor in the hot gases.
For clarity, the proposed model, combining the flamelet assumption and a well stirred reactor analysis is now presented in the particular case of a propane/air premixed flame. The kinetic scheme used has the form :

$$C_3H_8 + \frac{3}{2}O_2 \longrightarrow 3CO + 4H_2 \tag{I}$$

$$H_2 + \frac{1}{2}O_2 \Longleftrightarrow H_2O \tag{II}$$

$$CO + H_2O \Longleftrightarrow CO_2 + H_2 \tag{III}$$

$$N_2 + O_2 \Longleftrightarrow 2NO \tag{IV}$$

The first three reactions and their kinetic constants come from the work of Jones and Linsted (1988), the last one is a simplified Zeldovich mechanism for thermal NO formation (De Soete, 1989).
An order of magnitude analysis of the reaction constants indicates that the caracteristic chemical time of the first reaction is small compared to the time of the three others. As a consequence, the first reaction (i.e. the fuel oxidation mechanism) is assumed to take place in an infinitely zone and, accordingly, a flamelet formulation, such as the so called "coherent flame model" is retained for this reaction. The three other reactions (oxidation of H_2, CO and N_2) are assumed to take place in the reacted gases of the previous reaction as in a well stirred reactor.
The available flame surface density is provided by a classical transport equation, where the source term is given by :

$$\Lambda(\Sigma) = \alpha \epsilon_s \Sigma - \beta \frac{\dot{\hat{W}}_{C_3H_8}}{\hat{Y}_{C_3H_8}} \Sigma^2 \tag{2}$$

Where $\dot{\hat{W}}_{C_3H_8}$ is the consumption rate of propane per unit of flame area and Σ designates the mean flame surface density (i.e. the available flame area per unit volume). The first term expresses the production of flame area under the strain rate ϵ_s imposed by the turbulent flow. This term incorporates results from direct numerical simulations to take into account turbulence/combustion interaction. The second term models the annihilation of flame surface by consumption of the intervening reactant. In the present formulation, only lean combustion is being considered.
For the chemical scheme (I - IV), the reaction rate of each species may be written as :

$$\Lambda(\tilde{Y}_{C_3H_8}) = -\omega_{C_3H_8}\Sigma$$

$$\Lambda(\tilde{Y}_{O_2}) = -\frac{3}{2}\frac{M_{O_2}}{M_{C_3H_8}}\omega_{C_3H_8}\Sigma - \frac{1}{2}\frac{M_{O_2}}{M_{H_2O}}\omega^{II}_{H_2O} - \frac{1}{2}\frac{M_{O_2}}{M_{NO}}\omega^{IV}_{NO}$$

$$\Lambda(\dot{Y}_{CO}) = 3\frac{M_{CO}}{M_{C_3H_8}}\omega_{C_3H_8}\Sigma - \frac{M_{CO}}{M_{CO_2}}\omega^{III}_{CO_2}$$

$$\Lambda(\dot{Y}_{H_2}) = 4\frac{M_{H_2}}{M_{C_3H_8}}\omega_{C_3H_8}\Sigma - \frac{M_{H_2}}{M_{H_2O}}\omega^{II}_{H_2O} + \frac{M_{H_2}}{M_{CO_2}}\omega^{III}_{CO_2}$$

$$\Lambda(\dot{Y}_{H_2O}) = \omega^{II}_{H_2O} - \frac{M_{H_2O}}{M_{CO_2}}\omega^{III}_{CO_2}$$

$$\Lambda(\dot{Y}_{CO_2}) = \omega^{III}_{CO_2}$$

$$\Lambda(\dot{Y}_{NO}) = \omega^{IV}_{NO}$$

where $\omega_{C_3H_8}$ is the propane consumption rate per unit of flame area (flamelet model), M_k designates the molar mass of species k. The reaction rate ω^i_k of equation i for species k is determined from standard homogeneous reactor expressions (i.e. standard Arrhenius law, without turbulence interactions). For example, the reaction rate of carbon dioxide CO_2 in reaction III comes from :

$$\omega^{III}_{CO_2} = M_{CO_2}\left(k_{3f}(T_b)\frac{\bar{\rho}_b\tilde{Y}^b_{CO}}{M_{CO}}\frac{\bar{\rho}_b\tilde{Y}^b_{H_2O}}{M_{H_2O}} - k_{3r}(T_b)\frac{\bar{\rho}_b\tilde{Y}^b_{CO_2}}{M_{CO_2}}\frac{\bar{\rho}_b\tilde{Y}^b_{H_2}}{M_{H_2}}\right) \quad (3)$$

where $\tilde{Y}^b_k$ is the mass fraction of species k in the hot gases, $\bar{\rho}_b$ and T_b are the density and the temperature of the hot gases, k_{3f} and k_{3r} are the forward and backward reaction constants.

4. NUMERICAL RESULTS

The proposed model is now tested by numerically simulating a ducted turbulent premixed propane-air flame stabilized behind a V gutter flame holder (Fig. 3). The combustor is 32.5 cm long and 5 cm high. The channel width is 8 cm so that the mean flow is nearly two dimensional. The blocage ratio is 50 %. The lateral walls are made of Vycor (artificial quartz) allowing flow visualization and radical emission measurements. The air mass flow rate may vary between 30 and 120 g/s

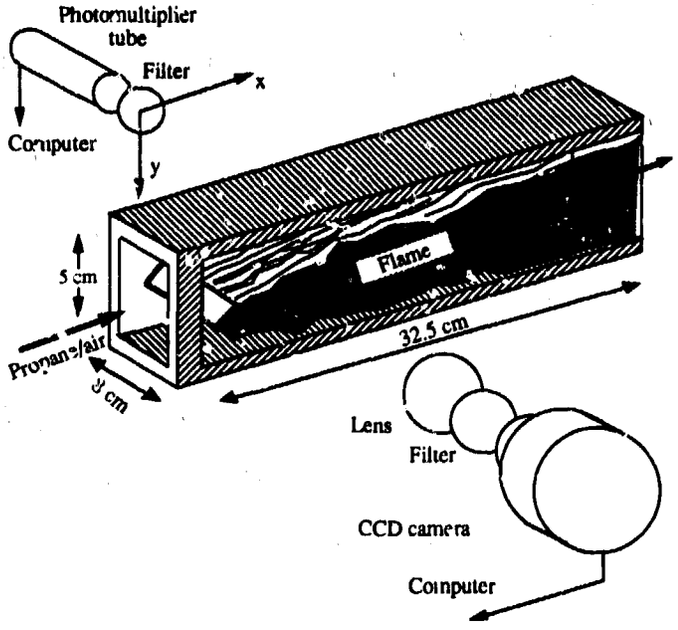

Figure 3. Premixed propane-air flame stabilized behind a V gutter flame holder. The flames spread in a rectangular channel equipped with transparent side walls. Light radiation from free radicals is monitored with a moving photomultiplier and a CCD camera.

and the equivalence ratio takes values in a range extending from 0.6 to 1.2. Available experimental data comprise radical emission images and gas analysis. The light emitted by free radicals like CH and C_2 is measured to determine the regions of heat release. It has been shown that for a given equivalence ratio, this light emission is nearly proportional to the local mean reaction rate. Light emission is collected by a photomultiplier or a CCD camera through a narrow band pass filter. Gas analysis is carried out with a sampling probe and classical gas analyzers for CO, CO_2, O_2 and unburnt hydrocarbons (CH_x). Due to the size of the cooling sampling probe, gas analysis results are only available in the exit plane of the burner. In this work, two experimental conditions are studied. The air mass flow rate $\dot{m}_a$ is fixed at 75 g/s and the equivalence ratio ϕ takes values of 0.75 and 0.65.

Results corresponding to the first case ($\dot{m}_a = 75g/s, \phi = 0.75$) are displayed in Fig. 4. Fields of temperature, mass fractions of propane, carbon monoxide CO, hydrogen, flame surface, effective strain rate (provided by the ITNFS model) and local reaction rate are shown in this figure. For comparison, the experimental reaction rate obtained from CH light

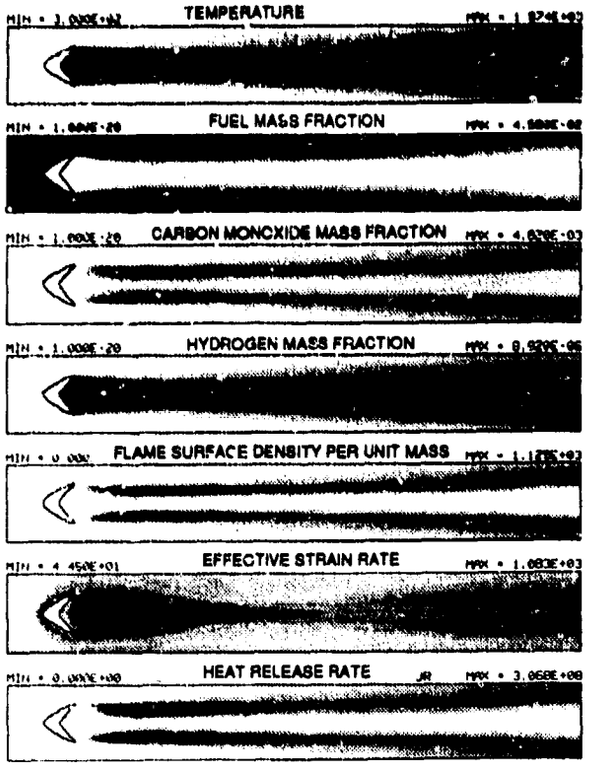

Figure 4. Results of calculation corresponding to the first case ($\dot{m}_a = 75g/s, \phi = 0.75$). Fields of temperature, mass fractions of propane, carbon monoxide CO, hydrogen H_2, flame surface density Σ, effective strain rate (provided by the ITNFS model) and local reaction rate are displayed in this figure on a scale of grey levels.

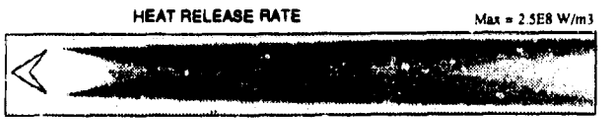

Figure 5. Experimental reaction rate deduced from CH light emission measurement. $\dot{m}_a = 75g/s, \phi = 0.75$.

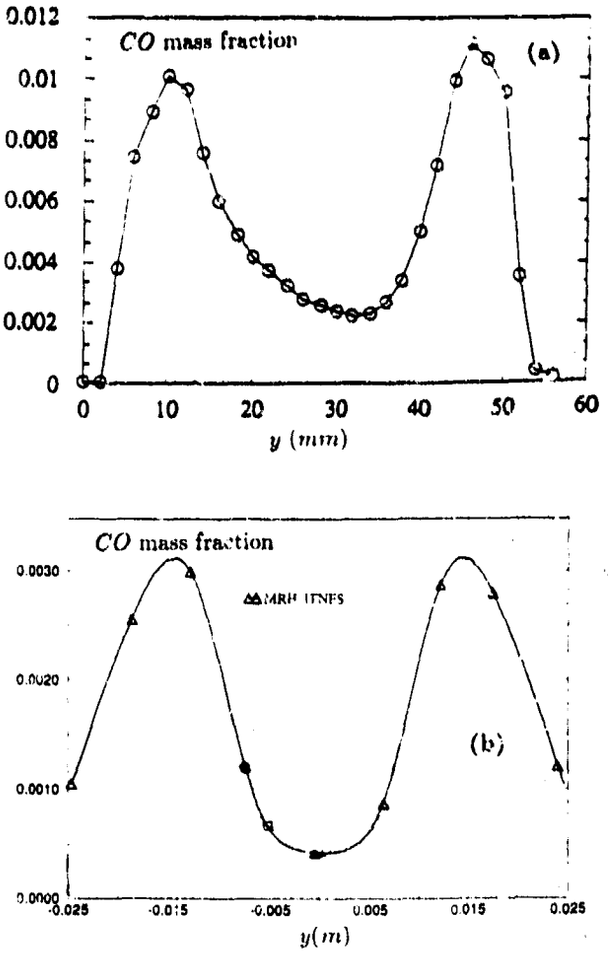

Figure 6. Profile of CO mass fraction in the combustor exit plane. (a) Experimental profile, (b) Computed profile. $\dot{m}_a = 75g/s, \phi = 0.75$.

emission is presented in Fig. 5. Two flame regions, separated by a stream of burnt gases, appear on the downstream flow from the flame holder. Combustion is incomplete inside the chamber and the flame extends beyond the combustor exhaust plane. Numerical simulations of the reaction rate are in qualitative agreement with the available experimental data (the scale of light emission is arbitrary) and the flame spreading is well simulated by computations (Maistret, 1991). Light emission measurements may be calibrated to give the local mean heat release rate. Values obtained from the experiment and the model are also in good agreement. The experimental CO mass fraction is only available in the exit plane of the burner. Comparisons with numerical computations are carried out in Fig. 6. Calculated profiles are reasonably close to the experimental ones but the computation underestimates the maximum value of CO mass fraction by a factor of about 3.

Numerical simulations corresponding to the second test case ($\dot{m}_a = 75g/s, \phi = 0.65$) are shown in Fig. 7. One may note that when the equivalence ratio is decreased, the maximum temperature is also decreased but the mass fraction of carbon monoxide, CO, is increased. Once more, the CO mass fraction is qualitatively well reproduced (Fig. 8) but the peak values are slightly underestimated.

Computations taking into account the thermal NO formation are shown in Fig. 9 ($\dot{m}_a = 75g/s, \phi = 0.75$) and Fig. 10 ($\dot{m}_a = 75g/s, \phi = 0.65$). No experimental data are available in this case but the calculation indicates that NO is mainly formed in the burnt gases and reaches near equilibrium values in the hot gas stream. As expected, the maximum mass fraction of NO decreases when the equivalence ratio is decreased.

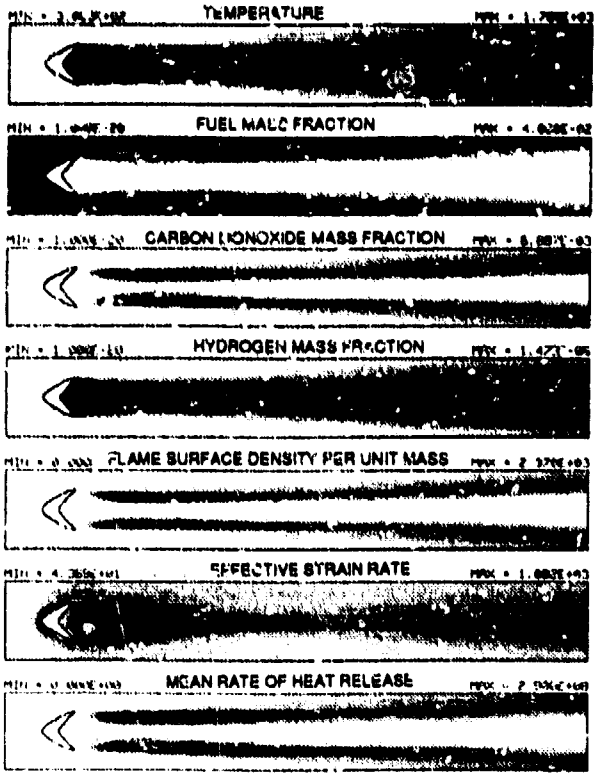

Figure 7. Results of calculation corresponding to the first case ($\dot{m}_a = 75g/s, \phi = 0.65$). Fields of temperature, mass fractions of propane, carbon monoxide CO, hydrogen H_2, flame surface density Σ, effective strain rate (provided by the ITNFS model) and local reaction rate are displayed in this figure on a scale of grey levels.

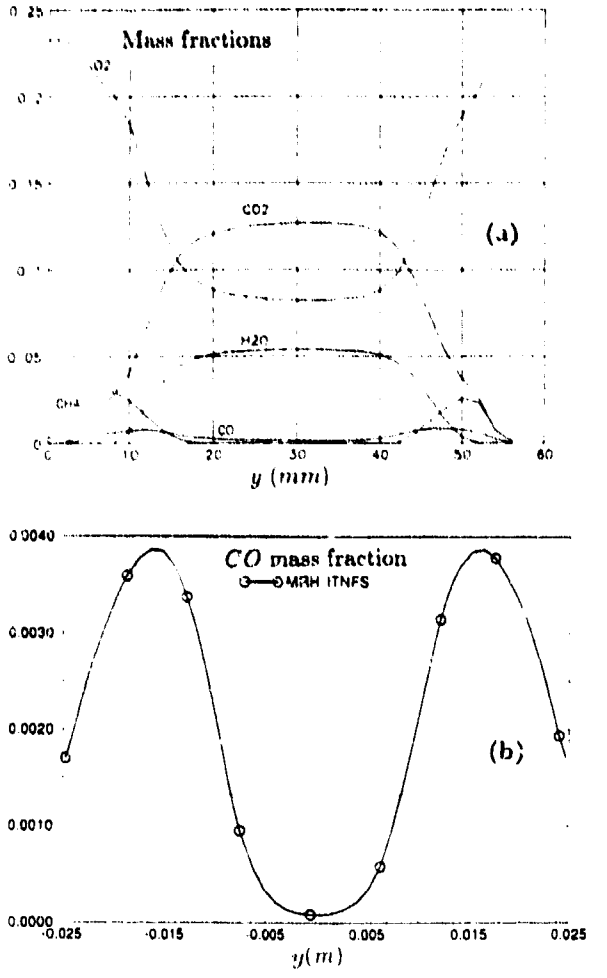

Figure 8. Profile of CO mass fraction in the combustor exit plane. (a) Experimental profile, (b) Computed profile. $\dot{m}_a = 75g/s, \phi = 0.65$.

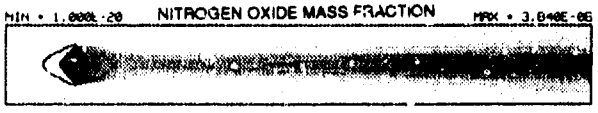

Figure 9. Results of calculations including thermal NO formation. ($\dot{m}_a = 75g/s, \phi = 0.75$).

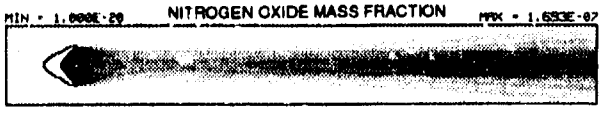

Figure 10. Results of calculations including thermal NO formation. ($\dot{m}_a = 75g/s, \phi = 0.65$).

CONCLUSION

A new model combining flamelet concept and homogeneous reactor combustion is proposed in order to calculate the formation of pollutants such as CO and NO in turbulent combustors. Calculations, based on a semi-global kinetic scheme and a flamelet formulation combined with a well stirred reactor analysis of the burnt gases are carried out for premixed propane-air flames for two different equivalence ratios. Comparison with experimental measurements shows that the model provides reasonably accurate values of CO.The study also proves that taking into account the kinetics of pollutant formation may influence the global description of the flow field. For example, the maximum reaction rate is decreased in the more detailed analysis including CO and NO formation. The calculations are sensitive to the determination of the flamelet model parameters and specifically to the effective strain rate. Further progress in the development of predictive methodologies will require improvements of the model and will allow quantitatively precise numerical simulation of pollutants mass fractions.

ACKNOWLEDGEMENTS

This work was supported in part by SNECMA

REFERENCES

Boudier, P., Henriot, S., Poinsot, T. and Baritaud, T., *24th Symposium (International) on Combustion*, pp 503-510, The Combustion Institute, Pittsburg (1992).
Bray, K.N.C., *17th Symposium (International) on Combustion*, The Combustion Institute, Pittsburgh, pp 223-233 (1979).
Broadwel, J.E. and Breidenthal, R.E., *Journal of Fluid Mechanics* 125, pp 397-410 (1982).
Candel, S., Darabiha, N. and Esposito, E., *AIAA 18th Joint Propulsion Conference, Cleveland*, AIAA Paper 82-1261 (1982).
Candel, S. M. and Poinsot, T., *Combustion Science and Technology* 70, pp 1-15 (1990).
Candel, S.M., Maistret, E., Veynante, D., Lacas, F., Darabiha, N. and Poinsot, T., *In Recent Advances in Combustion Modelling, B. Larrouturou Ed., Series on advances in mathematics for applied sciences*, World Scientific, Singapore, pp 19-64 (1991).
Cant, R.S., Pope, S.B. and Bray, K.N.C., *23rd Symposium (Int.) on Combustion* , The Combustion Institute, Pittsburgh, pp 809 - 815 (1990).
Cheng, W.K. and Diringer, J.A., *International Congress and Exposition* , SAE Technical Paper 91-0268 (1991).
Darabiha, N., *PhD Thesis, Ecole Centrale Paris*, Chatenay-Malabry, France (1984).
Darabiha, N., Giovangigli, V., Candel, S. M. and Smooke, M. D., *Combustion Science and Technology*, 60, pp 267-285 (1988).
Dillies, B., Marx, K.D. and Veynante, D., *14th ICDERS*, Coimbra, Portugal (1993).
De Soete, G.G., *Revue Générale de Thermique*, 330, pp 353-373 (1989)
Dibble, R.W., Broadwell, J.E., Lutz, A.E. and Kee, R.J., *Central States Combustion Institute Meeting* (1989).
Duclos, J.M., Veynante, D. and Poinsot, T., *Accepted, Combustion and Flame* (1993).
Fichot, F., Schreiber, D., Lacas, F., Veynante, D. and Yip, B., 13th ICDERS, Nagoya (1991).
Fichot, F., Lacas, F., Veynante, D. and Candel, S.M., *Combustion Science and Technology*,90, p 35 (1993).
Janicka, J. and Kollman, W., *Combustion and Flame*, 44, pp 319-336 (1982).
Jones, W.P. and Lindstedt, R.P., *Combustion Science and Technology* , 73, p 233 (1988).
Maistret, E.,*Ph D thesis*, Ecole Centrale Paris, Chatenay-Malabry, France (1991).
Mantel, T. and Borghi, R., *13th ICDERS* (1991).
Meneveau, C. and Poinsot, T., *Combustion and Flame*, 86, pp 311-332 (1991)
Miller, M.F., Bowman, C.T., Miller, J.A. and Kee, R.J., *Western States Section of the Combustion Institute Fall Meeting* (1989).
Peters N., *21st Symposium (International) on Combustion*, The Combustion Institute, Pittsburgh (1986)
Poinsot, T., Veynante, D. and Candel, S. M., *23rd Symposium (International) on Combustion*, The Combustion Institute, Pittsburgh, pp 613-619 (1990).
Poinsot, T., Veynante, D. and Candel, S. M., *Journal of Fluid Mechanics*, 228, pp 561-606 (1991).
Roberts, W.L. and Driscoll, J.F., *Combustion and Flame*, 87, pp 245-256 (1991).
Rogg, B., Behrendt, F. and Warnatz, J., *21st Symposium (International) on Combustion*, The Combustion Institute, Pittsburgh, pp 1533-1541 (1986).
Rogg, B., *7th Symposium on Turbulent Shear Flows*, Stanford, p 26-1.1 (1989).
Veynante, D., Lacas, F., Maistret, E. and Candel, S., *7th Symposium on Turbulent Shear Flows*, Stanford, p 26-2.1 (1989).
Veynante, D., Lacas, F., Boudier, P., Dillies, B., Samaniego, J.M., Poinsot, T. and Candel S. *Agard Conference Proceedings CP 510*, pp 40.1-40.14 (1991).
Veynante, D., Lacas, F. and Candel, S.M., *AIAA Journal*, 29, 5, pp 848 - 851 (1991).

FLOWFIELD PREDICTION OF NO_x AND SMOKE PRODUCTION IN AIRCRAFT ENGINES

by

S. Alizadeh and J.B. Moss
School of Mechanical Engineering
Cranfield Institute of Technology
Bedford MK43 0AL
United Kingdom

SUMMARY

CFD predictions of nitric oxide and smoke production in a tubular combustor are described for a range of inlet temperature and pressure conditions up to 800K and 8 bar, chosen to distinguish the effects of both state properties and turbulence on formation rates. Combustion models based on both laminar flamelet and chemical equilibrium representations are contrasted and compared with measurements in the literature. Whilst uncertainties persist in respect of the detailed mechanisms, notably for soot formation, a strategy is identified which extends the role of mixture fraction in the calculation of the influence of turbulent scalar fluctuations on emissions prediction.

INTRODUCTION

Detailed combustor flowfield predictions play an increasingly important role in the process of engine design analysis and evaluation. Challenging goals have been set for advanced combustor design in relation to pollutant emissions levels in addition to the more traditional concerns for exit temperature traverse quality and liner wall temperatures. Numerical simulation is then a key component of "right-first-time" strategies designed to reduce the cost and timescale of advanced combustor development. Whilst CFD techniques have proved effective in reproducing the principal features of combustor flowfields, the more recent emphasis on combustion chemistry, relative to emissions performance, presents significant additional challenges. The present paper will focus on the prediction of two distinctive scalars, the concentrations of nitric oxide and particulate soot - species of direct interest which also exhibit a different range of flowfield interactions and modelling demands.

The combustion process in the present generation of gas turbine combustors is essentially non-premixed and can be conveniently characterised by the distribution of local mixture fraction, ξ, (or local air-fuel ratio $\xi = (1 + AFR)^{-1}$). As a conserved property - free from the direct influence of highly non-linear chemistry - the statistics of mixture fraction, typically the Favre meand and variance, $\tilde{\xi}$ and $\widetilde{\xi''^2}$ be computed comparatively readily. In this way the turbulent mixing field can be comprehensively mapped. The modelling strategy customarily adopted for combustion is therefore to assume that the chemistry is fast, relative to this rate controlling turbulent mixing, and that the accompanying scalars may be inferred simply from state relationships. The particular advantage of this approach is evidently the limited number of scalar variables introduced which require the solution of additional balance equations. Despite enhanced computer capabilities this remains a critical concern for reacting flows in complex 3-D combustor geometries.

The fast chemistry assumption may be conveniently implemented in two forms; local state relationships

$$\phi = \phi(\xi)$$

established from either complete chemical equilibrium or from laminar flamelets. Laminar diffusion flame calculations can be performed exactly, within the constraints of our understanding of the detailed chemistry, and economically in a one-dimensional counter-flow configuration, for example. The microscopic structures represented by these relationships differ in a number of ways. Reaction intermediates - whether quasi-stable, as in the case of CO, or highly reactive, as with radical species such as OH, O and H - are found in steady-state concentrations far removed from chemical equilibrium. Whilst such differences may have little influence on gross flow patterns, their implications for trace species chemistry can be very large indeed.

Pollutant emissions, with the contentious exception of CO_2, essentially result from chemical non-equilibrium - mean formation and destruction rates which are not fast by comparison with flow processes. This makes their prediction difficult within the framework of the simplified description of combustion chemistry outlined earlier. Where the effects of finite rate chemistry are thermally insignificant - as in the case of nitric oxide - the computation of pollutant species concentration can be undertaken as a post-process super-imposing the

Presented at an AGARD Meeting on 'Fuels and Combustion Technology for Advanced Aircraft Engines', May 1993.

production mechanism on an established flowfield. The influence of turbulent fluctuations in trace species composition must be accommodated in this mechanism, however, in addition to the fluctuating temperature field. The single scalar probability density function - that for mixture fraction, $P(\xi)$ - is therefore a constraining factor in even the simplest representations of pollutant chemistry, for example that for NO formation by the Zeldovich mechanism.

These issues are examined here within the framework of detailed calculations for NO and smoke production in a representative tubular combustor for a range of inlet temperatures and pressures. The choice of a tubular combustor geometry reflects the dearth of detailed experimental data on distributions of velocity and scalar properties within combustor liners more generally, as distinct from nozzle exit conditions. Experimental measurements for purposes of comparison with prediction are therefore drawn from families of related experiments reported in the literature.

Combustor Flowfield

Isothermal and combusting flow experiments are reported in model tubo-annular combustors of essentially similar design by Heitor and Whitelaw (1986), Bicen et al (1989) and (1990). The basic primary and dilution zone architecture of this combustor has been reproduced computationally in the present study. Given the focus on emissions chemistry modelling, the configuration has been simply modelled in polar co-ordinates with the injector and hemispherical head section simulated using blockages as furnished by the general purpose CFD package, PHOENICS. The disposition of six primary and dilution holes in the liner suggest that cyclic symmetry may be exploited. A 60° sector has been modelled with bounding planes which bisect two adjacent primary holes as shown in fig. 1. The computational mesh comprises 20 x 16 x 45 nodes, in the r, θ and z directions respectively, reflecting a compromise between geometrical fidelity and grid independent solutions.

The laser Doppler anemometry and flow visualisation studies on a plexiglass model of this combustor reported by Bicen et al (1989) recommend a flow split between swirler, primary and dilution holes of 17%, 33% and 50% respectively to reproduce the principal internal flow features of the combusting flow experiments of Heitor and Whitelaw (1986) and Bicen et al (1990). These values have been adopted in the present computations with an overall air-fuel ratio of 57.

In the experiments, gaseous propane was introduced through ten 1.7mm diameter jets uniformly spaced around the circumference of a cone located at the centre of a 45° swirler. The experimentally-determined swirl number of 0.6 was incorporated in a uniform representation of the air flow across the complete swirler face. Partial cell blockaging was used to reproduce the injector geometry whilst the aerodynamic blockage introduced by the swirler vanes was incorporated in the specification of annulus area.

Although the flowfield detail is not our primary concern here, isothermal model calculations have been performed for the steady, time-averaged balance equations for mass and momentum, closed through a two-equation k-ε turbulence model in the standard form within the PHOENICS package. In particular, the system of equations comprises

$$\frac{\partial}{\partial x_j}(\rho \bar{u}_j) = 0 \qquad (1)$$

$$\frac{\partial}{\partial x_j}(\rho \bar{u}_i \bar{u}_j) = -\frac{dp}{dx_i} - \frac{\partial}{\partial x_j}\overline{(\rho u_i' u_j')} \qquad (2)$$

incorporating the turbulence model

$$-\rho \overline{u_i' u_j'} = \mu_t \left\{ \frac{\partial \bar{u}_i}{\partial x_j} + \frac{\partial \bar{u}_j}{\partial x_i} \right\} - \frac{2}{3}\delta_{ij}\rho k \qquad (3)$$

$$\mu_t = C_\mu \rho k^2/\varepsilon \qquad (4)$$

and

$$\frac{\partial}{\partial x_j}(\rho \bar{u}_j k) - \frac{\partial}{\partial x_j}\left(\frac{\mu_t}{\sigma_k}\frac{\partial k}{\partial x_j}\right) = -\rho \overline{u_i' u_j'} \frac{\partial \bar{u}_i}{\partial x_j} - \rho\varepsilon \qquad (5)$$

$$\frac{\partial}{\partial x_j}(\rho \bar{u}_j \varepsilon) - \frac{\partial}{\partial x_j}\left(\frac{\mu_t}{\sigma_\varepsilon}\frac{\partial \varepsilon}{\partial x_j}\right) = -C_1 \frac{\varepsilon}{k}\rho \overline{u_i'' u_j''}\frac{\partial \bar{u}_i}{\partial x_j} - C_2 \rho \varepsilon^2/k \quad (6)$$

with the model constants $C_\mu = 0.09$, $C_1 = 1.44$, $C_2 = 1.92$ and Prandtl-Schmidt numbers

$$\sigma_k = 1.0,\ \sigma_\varepsilon = 1.3$$

The flow split recommended from the water analogy studies generates the flowfield predictions illustrated in fig. 2. The key features of the flowfield observed experimentally are clearly reproduced, although significant quantitative differences exist in relation to the strength and 'eye' location of the primary zone vortex (Alizadeh (1993)). These discrepancies appear to emanate from the primary jet impingement zones where spatial property gradients are large and the k-ε turbulence model is perhaps least able to accommodate the accompanying anisotropy. The predicted mean axial and swirl velocities are compared with reported laser Doppler anemometry measurements at axial stations z = 40, 50 and 60mm, spanning the primary jet, in fig. 3.

Combustion Model

A fast chemistry, conserved scalar approach is adopted to describe the combustion process. The balance equations (1) - (6), interpreted in terms of Favre-averaged quantities.

$$\tilde{\phi} = \overline{\rho\phi} / \bar{\rho},$$

are supplemented by equations for the mixture fraction Favre mean and variance, specifically,

$$\frac{\partial}{\partial x_j}(\bar{\rho} \bar{u}_j \tilde{\xi}) - \frac{\partial}{\partial x_j}\left(\frac{\mu_t}{\sigma_\xi}\frac{\partial \tilde{\xi}}{\partial x_j}\right) = 0 \quad (7)$$

and

$$\frac{\partial}{\partial x_j}(\bar{\rho} \bar{u}_j \widetilde{\xi''^2}) - \frac{\partial}{\partial x_j}\left(\frac{\mu_t}{\sigma_g}\frac{\partial \widetilde{\xi''^2}}{\partial x_j}\right) = C_{g1}\,\mu_t\left(\frac{\partial \tilde{\xi}}{\partial x_j}\right)^2 - C_{g2}\,\bar{\rho}\varepsilon\widetilde{\xi''^2}/k \quad (8)$$

The probability density function for mixture fraction, P(ξ), is assumed to take the general form of a beta function, whose detailed shape is determined from the calculated first and second moments, $\tilde{\xi}$ and $\widetilde{\xi''^2}$. The mean mixture density, $\bar{\rho}$, is inferred from an instantaneous state relationship

$$\rho = \rho(\xi)$$

and evaluated by quadrature,

$$\bar{\rho}^{-1} = \int_0^1 \rho^{-1} \tilde{P}(\xi)\, d\xi \quad (9)$$

State relationships are most readily determined under the assumption of complete chemical equilibrium or for laminar flamelet burning. Both are employed in comparisons reported here and the strategy is extended to the complete range of scalars, including in particular - relative to the emissions focus - the temperature, the unburnt fuel and molecular oxygen concentrations and that of oxygen atoms.

The equilibrium calculations are performed using the program of Gordon and McBride (1971) and the state relationships defined by curve fitting.

Laminar flamelet calculations have been carried out in a one-dimensional counter-flow geometry, employing a code developed by Warnatz and co-workers (cf. Warnatz (1982)). Detailed chemical reaction mechanisms for propane-air are well-established and that employed here comprised 52 chemical reactions and 40 species with rate data drawn from Leung et al (1991). The present calculations have been performed over a range of inlet air temperatures and pressures up to 800K and 8 bar. The local hydrodynamic strain rate is a prescribed parameter in such calculations. In the absence of strain rate information in a practical combustor, a single comparatively benign level of 150 s^{-1} has been adopted throughout. Illustrative

profiles are presented in fig. 4 of the instantaneous state relationships for adiabatic temperature and oxygen atom mole fraction emerging from such flamelet calculations.

The implications of these relationships for turbulent combustor predictions are discussed in later sections.

Nitric Oxide Formation

The principal mechanism of NO formation in the current generation of gas turbine combustors is that identified by Zeldovich

$$N_2 + O \underset{k_{-1}}{\overset{k_1}{\rightleftharpoons}} NO + N$$

$$N + O_2 \underset{k_{-2}}{\overset{k_2}{\rightleftharpoons}} NO + O \qquad (10)$$

supplemented by the further step

$$N + OH \underset{k_{-3}}{\overset{k_3}{\rightleftharpoons}} NO + H$$

The molar rate of NO formation can therefore be identified as

$$\frac{d}{dt}[NO] = 2k_1 [N_2][O] \times \left\{ \frac{1 - K[NO]^2/[N_2][O_2]}{1 + k_{-1}[NO]/(k_2[O_2] + k_3[OH])} \right\} \qquad (11)$$

on the assumption that the N-atom concentration remains in steady state. For trace concentrations of NO, far removed for equilibrium, eq (11) may be further simplified to

$$\frac{d}{dt}[NO] = 2k_1 [N_2][O] \qquad (12)$$

where the rate constant, k_1, takes the form

$$k_1 = 1.36 \times 10^{11} \exp(-37750/T). \qquad (13)$$
$$[m^3/kmol.s]$$

For combustion in air the rate of NO formation is thus primarily determined by local temperature and O-atom concentration. The flamelet levels of the latter, as illustrated in fig. 4b, are appreciably in excess of equilibrium - at 800K, 8 bar;

$$X_{O_{max,f}} = 1.0 \times 10^{-3}, \quad X_{O_{max,eq}} = 0.6 \times 10^{-3}$$

- and will enhance formation rates accordingly.

Since NO production is insignificant thermally, we may super-impose the calculation for NO mass fraction onto the existing flowfield solution. In particular, we introduce

$$\frac{\partial}{\partial x_j}(\bar{\rho}\tilde{u}_j\tilde{f}_{NO}) - \frac{\partial}{\partial x_j}\left(\frac{\mu_t}{\sigma_\xi}\frac{\partial \tilde{f}_{NO}}{\partial x_j}\right) = \overline{\dot{\omega}_{NO}} \qquad (14)$$

where $\dot{\omega}_{NO} = \dot{\omega}_{NO}(\xi)$

$$= 2\frac{W_{NO}}{\bar{W}^2}\rho^2(\xi)\, k_1(\xi)\, X_{N_2}(\xi)\, X_o(\xi)$$

and $$\overline{\dot{\omega}_{NO}} = \bar{\rho}\int_0^1 \frac{\dot{\omega}_{NO}}{\rho}\tilde{P}(\xi)\, d\xi \qquad (15)$$

Smoke Production

By comparison with oxides of nitrogen the underlying mechanisms of soot formation and burn-out remain quite poorly understood. Fuel pyrolysis mechanisms are inevitably complex, whilst the heterogeneous processes of surface growth and oxidation introduce interaction with incompletely specified physical properties, for example particle size and surface condition. Progress has been reported however in relation to extending the flamelet approach to encompass simplified representations of sooting processes in terms of two additional variables, the soot particle number density, n, and volume fraction, f_v, (Moss et al (1988), Young et al (1991)).

Source terms for these variables, incorporating representations of the processes of nucleation, surface growth and coagulation, take the form

$$\frac{d}{dt}\left(\frac{n}{N_o}\right) = \alpha - \beta\left(\frac{n}{N_o}\right)^2 \qquad (16)$$

$$\frac{d}{dt}\left(\rho_s f_v\right) = \gamma n + \delta \qquad (17)$$

where N_o denotes Avogadro's number (6×10^{26}/kmol), ρ_s is the particulate soot density (1800 kg m^{-3}) and the individual processes are described by

nucleation

$$\alpha = C_\alpha \rho^2 T^{1/2} X_F \exp\left(-T_\alpha/T\right)$$

$$\delta = C_\delta \alpha$$

coagulation

$$\beta = C_\beta T^{1/2} \qquad (18)$$

surface growth

$$\gamma = C_\gamma \rho T^{1/2} X_F \exp\left(-T_\gamma/T\right)$$

The model parameters $C_{\alpha,\beta,\gamma,\delta}$ are determined from detailed comparison between prediction and experiment in laminar diffusion flames. The parameter values employed here are taken from the ethylene flame study reported by Young et al (1991),

$$C_\alpha = 1.7 \times 10^8 \ (m^3 kg^{-2} K^{-1/2} s^{-1}),$$
$$C_\beta = 9 \times 10^{19} \ (m^3 K^{1/2} s^{-1})$$

$$C_\gamma = 1.26 \times 10^{-11} \ (m^3 K^{-1/2} s^{-1}),$$
$$C_\delta = 144,$$

$$T_\alpha = 46.1 \times 10^3 \ (K)$$

$$T_\gamma = 12.6 \times 10^3 \ (K)$$

Soot oxidation is introduced through the mechanism of Nagle and Strickland-Constable (1961)

$$\dot{\omega}_{ox} = 120 \times \left\{\left(\frac{k_A p_{o2}}{1 + k_z p_{o2}}\right) x + k_B p_{o2} (1-x)\right\} \qquad (19)$$

where the rate constants distinguish surface sites of different reactivity and

$$k_A = 20 \exp\left(-30{,}000/RT\right),$$
$$k_B = 4.46 \times 10^{-3} \exp\left(-15{,}200/RT\right)$$

$$k_z = 21.3 \exp\left(4100/RT\right),$$
$$k_T = 1.51 \times 10^5 \exp\left(-97000/RT\right)$$

$$x = \left(1 + \frac{k_T}{k_B p_{o2}}\right)^{-1}$$

Eq (19) is surface area specific and that of the soot particle aerosol is determined from the gross properties number density and volume fraction. An average particle size, D, may be estimated from

$$f_v = \frac{\pi}{6} n D^3$$

The incorporation of such a mechanism into combustor predictions raises a number of modelling issues.

Following the flamelet approach outlined earlier, those aspects of these source terms dependent on gas phase properties, for example temperature and composition, may be characterised by further state relationships and averaged over the computed mixture fraction field. The correlation between soot properties, n and f_v, and mixture fraction is however inaccessible and has been neglected in present computations. Specifically, therefore, we consider

$$\overline{\dot{\omega}}_{soot} = \int_0^1 \dot{\omega}_{soot}\left(\bar{n}, \bar{f}_v, \xi\right) \tilde{P}(\xi)\, d\xi \qquad (20)$$

In order to reconcile the Favre-averaged flowfield model and soot properties, the latter are

incorporated into the turbulent calculation in the form

$$\phi_n = \frac{n}{\rho N_o} \quad \text{and} \quad \phi_f = \frac{\rho_s f_v}{\rho} \qquad (21)$$

Two additional balance equations are thereby introduced into the equation set described earlier,

$$\frac{\partial}{\partial x_j}(\bar{\rho}\tilde{u}_j\tilde{\phi}_n) - \frac{\partial}{\partial x_j}\left(\frac{\mu_t}{\sigma_\phi}\frac{\partial\tilde{\phi}_n}{\partial x_j}\right) \qquad (22)$$

$$= \bar{\alpha} - \bar{\rho}^2\,\bar{\beta}\,\tilde{\phi}_n^2 - N_o^{1/3}\,\bar{\rho}\,\overline{\dot{\omega}_{ox}}\,\tilde{\phi}_n^{4/3}\,\tilde{\phi}_f^{-1/3}$$

and $$\frac{\partial}{\partial x_j}(\bar{\rho}\tilde{u}_j\tilde{\phi}_f) - \frac{\partial}{\partial x_j}\left(\frac{\mu_t}{\sigma_\phi}\frac{\partial\tilde{\phi}_f}{\partial x_j}\right) \qquad (23)$$

$$= \bar{\delta} + N_o\bar{\rho}\bar{\gamma}\tilde{\phi}_n - N_o^{1/3}\,\bar{\rho}\overline{\dot{\omega}_{ox}}\,\tilde{\phi}_n^{1/3}\,\tilde{\phi}_f^{2/3}$$

The simplest approach to the incorporation of this model into the combustor calculations is again to post-process the solution for ϕ_n and ϕ_f after the manner of the NO prediction. Some calculations of this kind will be presented later. However, two of the conditions underlying this approximation will not generally be satisfied in rich burning primary zones. In post-processing the calculation we imply that the additionally computed scalars exert little influence on the pre-determined flowfield. Unlike NO formation, soot production may influence the temperature field significantly through enhanced radiative loss and the mixture fraction field through its action as a sink for carbon, since this is generally a less reactive state than the gas phase.

The latter problem has been addressed by Young et al (1991) who decomposed the mixture fraction into two contributions, one derived from the gas phase and the other from the mass concentration of soot. The gas phase field is locally leaner in the presence of solid carbon in consequence and a modified gaseous composition is inferred from the reduced gas phase mixture fraction through the state relationships.

A fully-coupled calculation incorporating both a detailed soot formation mechanism and radiative loss is under development but has not been incorporated into 3-D combustor calculations. The predictions reported here therefore consider the temperature field to be adiabatic.

Prediction and Experiment

The detailed property maps on tubular combustors reported in the literature (Heitor and Whitelaw (1986), Bicen et al (1990)) have been obtained over a limited range of inlet air temperatures and atmospheric pressure operation. These studies did not include measurements of particulate soot. Some indication of the general level of the latter can be inferred from the laser extinction measurements reported by Moss et al (1992) on a model tubular combustor fuelled by kerosine at pressures up to 4 bar.

Calculations are presented here spanning three operating conditions - 300K inlet air temperature and 1 bar pressure; 800K inlet and 1 bar; 800K inlet and 8 bar. The flow split inferred from the isothermal study has been employed throughout and the mass flows scaled according to a fixed normalised mass flow $(\dot{m}\sqrt{T}/P)$ from the 1 bar experiment. The pollutant production processes being modelled are strongly temperature and pressure dependent and the range of conditions examined were chosen to reveal such behaviour.

Illustrative profiles of distributions over the liner primary and dilution zones are shown in fig. 5 for mean mixture fraction, temperature, oxygen atom mole fraction and the mass rate of nitric oxide formation. The state relationships underlying these predictions are derived from flamelet calculations. The influence of mixture fraction is evident throughout these different property maps, as might be expected, but the detailed non-linearity of the NO production source term is apparent in the comparison of figs 5 (c)-(e).

A more detailed comparison of prediction and experiment is provided by fig. 6 for planes bisecting the primary $(\theta = 0°)$ and dilution holes $(\theta = 30°)$. Both distributions and absolute temperature levels are plausibly reproduced. The computed primary zone profiles indicate slightly lower temperatures than measured on the combustor centre-line and suggest less rapid

mixing of the fuel jet initially. This is believed to reflect the limited resolution of the injector geometry. The radial penetration of the dilution jet also appears slightly less than is observed experimentally and is more persistent in the axial direction in consequence. The general level of quantitative agreement however is good and provides an encouraging basis for emissions prediction.

Computed distributions of mean NO mass fraction down the liner are shown in fig. 7 for the three operating points. The NO - source term illustrated in fig. 5(e) reveals limited production in the primary zone in comparison with that adjacent to the wall between the primary and dilution zones influenced by both higher temperatures and O-atom concentrations. This region is sharply terminated by the dilution jet in the plane $\theta = 30^{\circ}$ although further production is evident in the lee of the jet, particularly at the higher pressure. Broadly similar distributions are evident under all the conditions investigated. Predicted NO levels are very low (< 5 ppm) throughout the combustor under 300K inlet air and atmospheric pressure conditions. Profound increases however accompany both increasing air temperature and pressure.

Whilst the model combustor investigated by Heitor and Whitelaw (1986) is similar to that subsequently mapped by Bicen et al (1990), modifications were made to both the swirler and dilution hole flows. The primary zone flow predicted here is therefore richer than that studied by Heitor and Whitelaw but, in the absence of NO data from the later study, fig. 8 illustrates their measured distributions at an AFR of 52 for 318K inlet air and 1 bar conditions. Beyond the leaner, higher temperature primary zone the measured NO levels are comparable with those predicted here despite the implied differences in the patterns of production. Limited exit plane measurements at 750K air inlet temperature are also reported in this study, indicating levels in excess of 50 ppm (cf. fig. 7(c), (d)).

Increasing the operating pressure to 8 bar produces further enhanced NO levels approaching an order of magnitude larger. The simplified source term representation of eq. (12) has been retained for comparison purposes here although the levels now begin to more nearly approach local equilibrium values in the intermediate zone of the combustor and the more complete representation of eq. (11) would be more appropriate. In this simpler formulation NO, once generated, can only be reduced by dilution. The peak level attained, 1230 ppm, is approximately 30% of the stoichiometric equilibrium value. The roughly linearly increased NO levels accompanying the higher pressure - rather than the $\sqrt{P}$-dependence which might be expected from the O-atom partial pressure (cf. fig. 4(b)) - arises from compensatory effects of increased peak temperatures ($\tilde{}$ 200K, cf. fig. 4(a)) together with reduced scalar fluctuation levels and slightly increased residence times in the intermediate zone of the combustor.

The predictions illustrated thus far are based on an underlying laminar flamelet model but it is instructive to compare such calculations with those of the fast chemistry - equilibrium limit, often employed in combustors. Fig. 9 therefore compares mean temperature and NO predictions in the $\theta = 0^{\circ}$ plane for 800K inlet, 1 bar conditions employing both flamelet and full equilibrium state relationships. Whilst the peak equilibrium temperatures are higher than those based on the laminar flamelet, they are spatially less extensive and the NO-production term is generally lower than its flamelet counterpart for mixtures leaner than ξ<0.05 reflecting the super-equilibrium O-atom concentration. Despite their differing historie the 'exit' levels are quite comparable. A more detailed discussion of these modelling issues is given by Alizadeh (1993).

The foregoing predictions emphasise the sensitivity of NO-production to temperature variations at the level > 100K and must therefore raise doubts concerning the robustness of the assumption that the flowfield is also adiabatic. Radiative heat transfer will be locally re-distributive at such levels, particularly in richer regions, even if the combustor is near-adiabatic overall. Soot formation within the combustor is therefore of interest not only as an exhaust pollutant in its own right but, through its effect on the temperature field, also as a factor influencing NO formation.

Predictions of the distribution of soot volume fraction within the liner for the three operating conditions are illustrated in fig. 10. Broadly similar structure is predicted over this range of temperature and pressure with the highest levels of soot volume fraction in the intermediate zone, punctured in the plane $\theta = 0^{\circ}$ by the primary jet and terminated in the 30° plane by the dilution jet. The distributions are essentially annular, with low levels on the cooler, leaner combustor centre-line (cf. fig. 6), similar to the extinction measurements reported by Moss et al (1992) also in a tubular combustor.

Soot production is moderately enhanced by increased temperature levels but more dramatically by increased pressure. For the same mass fraction $(\rho_g \bar{f}_v / \bar{\rho})$, the volume fraction will increase linearly with pressure, however the predicted changes suggest growth αp^2. This sensitivity is significantly greater than that observed by Moss et al (1989) and Young et al (1993) from measurements in laminar and turbulent non-premixed flames respectively. The preferential enhancement with increased pressure of particle nucleation rate, relative to surface growth, implied by eq. (18), generally lies outside the range of detailed experimental studies of laminar flames against which simplified mechanisms have been calibrated.

There is little overlap between soot formation and oxidation regimes (cf. fig. 11). Peak formation is predicted to occur between adjacent primary holes in the circumferential direction ($\theta \approx 30°$) but in their vicinity axially. Peak oxidation occurs in similar circumstances in the neighbourhood of the dilution jets. These jets effectively terminate further oxidation downstream once the mean temperature falls below ~ 1800K. Peak local mass fractions, $\rho_g \bar{f}_v / \bar{\rho}$, approach 5% at 8 bar pressure - mass concentration of $50gm^{-3}$ - and imply conversion rates for locally available carbon approaching 75%. Evidently not a small perturbation to the underlying composition field which can be simply accommodated by post processing.

Figure 12 illustrates the effect of incorporating carbon mass loss to the solid phase on the calculation of local mixture fraction. In comparison with Fig. 11(a), the reduced gas phase component of the mixture fraction restricts soot formation to the more immediate neighbourhood of the injector, inhibiting its production in leaner regions adjacent to the primary jets. Peak volume fraction levels are roughly halved.

A number of uncertainties surround this model of soot formation and oxidation, both in respect of the simplified mechanisms employed and in the treatment of turbulence interaction. The difficulty of evaluation is compounded by the limited data base, even in simpler combustor configurations. However these predictions do provide an encouraging framework within which to undertake a design assessment and demonstrate the potential of currently accessible CFD techniques in relation to species controlled by finite rate chemistry.

Acknowledgement

The authors are pleased to acknowledge the support of the Science and Engineering Research Council in the form of a research studentship to S Alizadeh.

References

Alizadeh, S. (1993)
Computational Prediction of Pollutant Emissions from Gas Turbine Combustors. Ph.D. Thesis, Cranfield Institute of Technology, 1993 (in preparation).

Bicen, A.F. McGuirk, J.J. and Palma J.M.L.M. (1989)
Gas Turbine Combustor Flow Fields in Isothermal Flow Experiments. Proc. Instn. Mech. Engrs. Vol. 203, 113.

Bicen, A.F. Tse, D.G.N. and Whitelaw, J.H. (1990)
Combustion Characteristics of a Model Can-Type Combustor. Comb. and Flame, 80, 111.

Gordon, S. and McBride, B. (1971)
Computer Program for Calculation of Complex Chemical Equilibrium Compositions, Rocket Performance, Incident and Reflected Shocks, and Chapman-Jouget Detonations. NASA SP-273.

Heitor, M.V. and Whitelaw, J.H. (1986)
Velocity, Temperature and Species Characteristics of the Flow in a Gas Turbine Combustor. Comb. and Flame, 64, 1.

Leung, K.M. Lindstedt, R.P. and Jones, W.P. (1991)
A Simplified Reaction Mechanism for Soot Formation in Non premixed Flames. Comb. and Flame 87, 289.

Moss, J.B. Stewart, C.D. and Syed, K.J. (1989)
Flowfield Modelling of Soot Formation at Elevated Pressure. Twenty-second Symp. (Int.) on Combustion, Combustion Institute, p. 413.

Nagle, J. and Strickland-Constable, R.F. (1961)
Oxidation of Carbon between 1000-2000°C. Proc. Fifth Conf. on Carbon, Pergamon, p. 154.

Warnatz, J. (1982)
Numerical Methods in Laminar Flame Propagation. Friedr. Vieweg & Sohn, Braunschweig/Wiesbaden.

Young. K.J. Stewart, C.D. Syed, K.J. and Moss, J.B. (1991)
Soot Formation in Confined Turbulent Flames Fuelled by Pre-vaporised Kerosine and by Ethylene Proc. Tenth Int. Symp. on Air-Breathing Engines (ISABE), AIAA, p. 239.

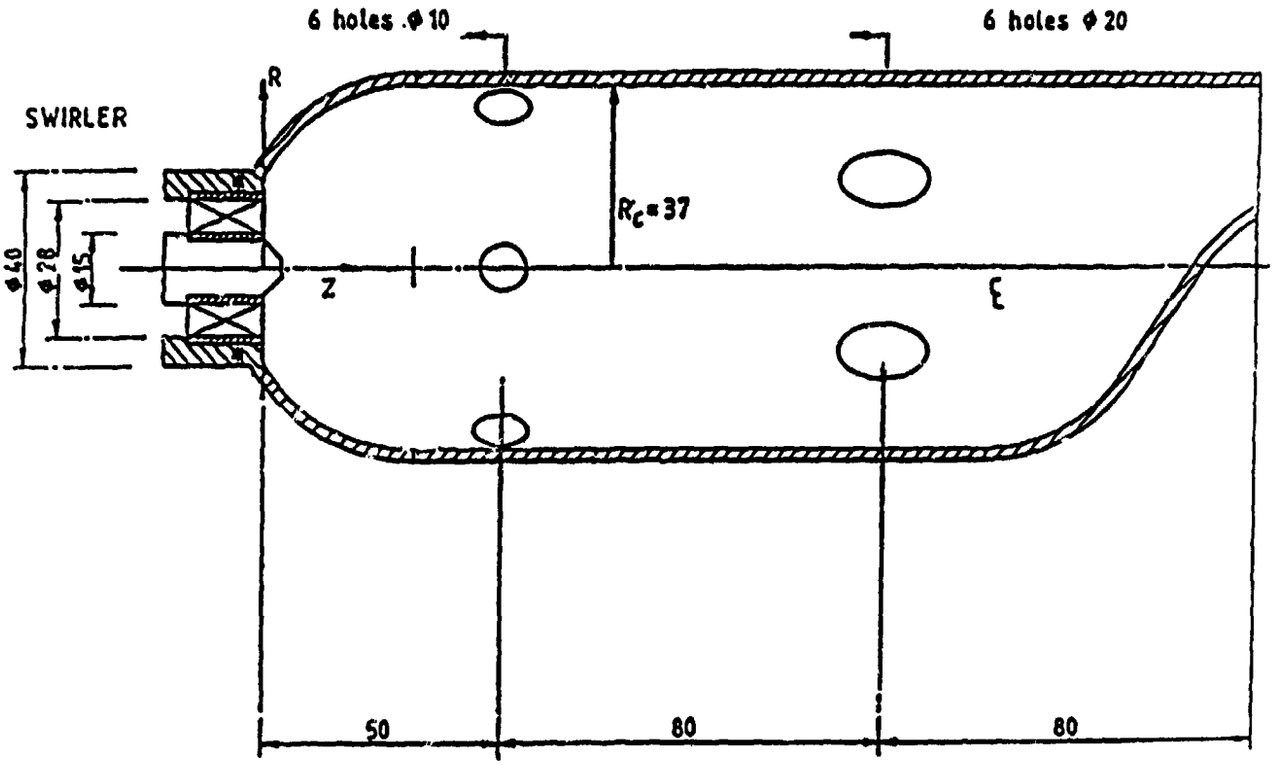

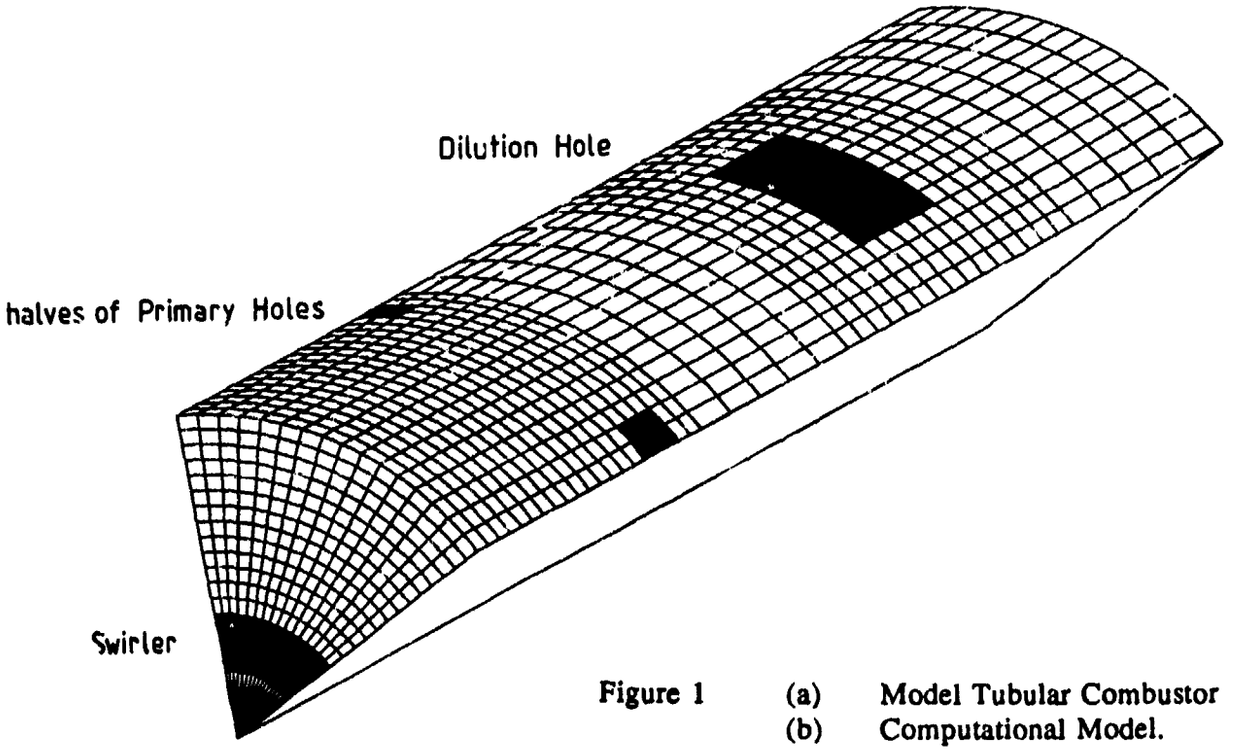

Figure 1 (a) Model Tubular Combustor
(b) Computational Model.

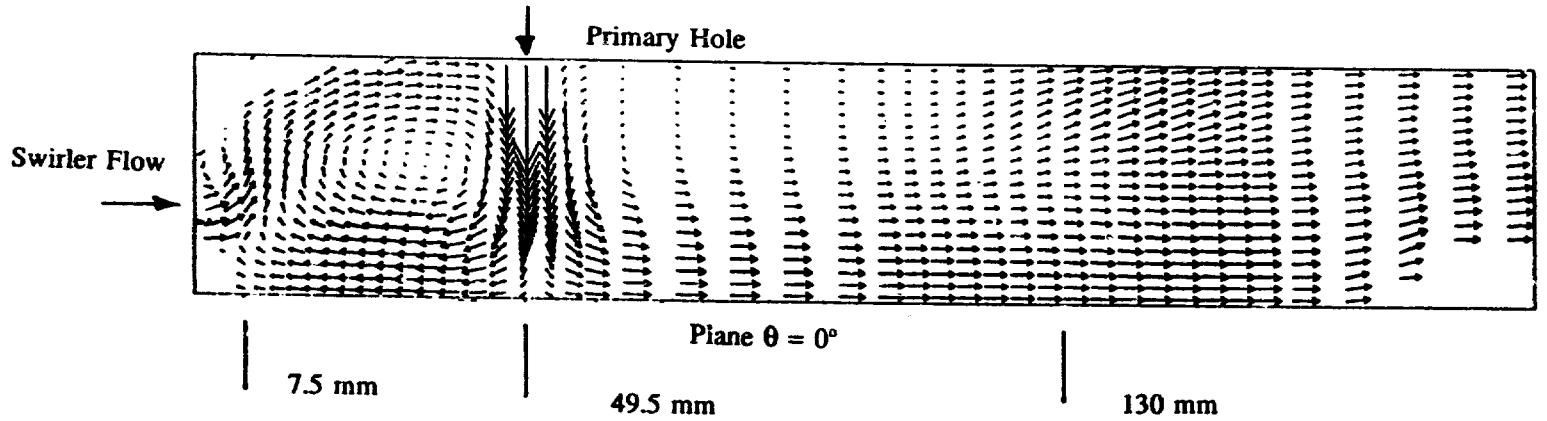

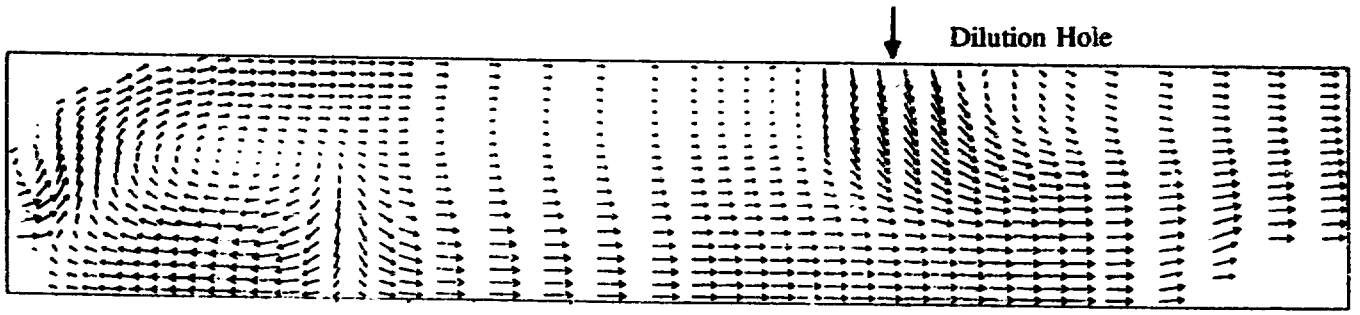

Figure 2 Predicted Isothermal Flowfield

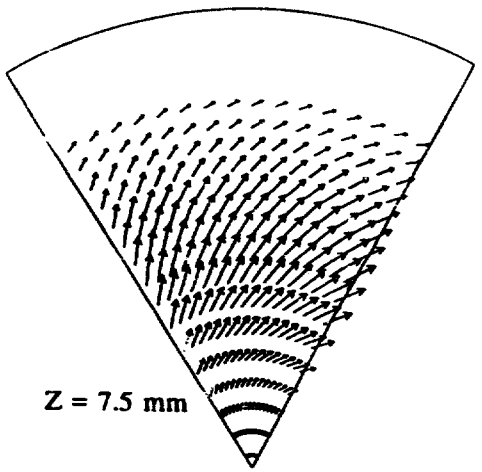

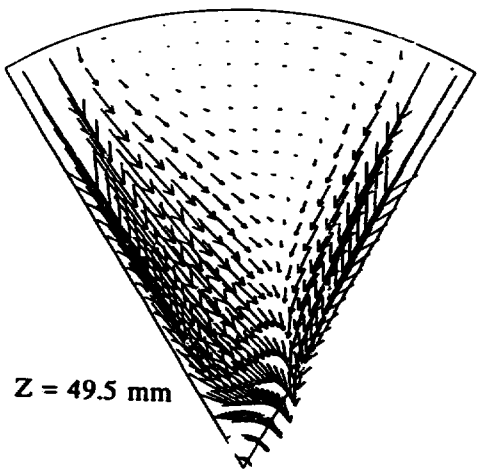

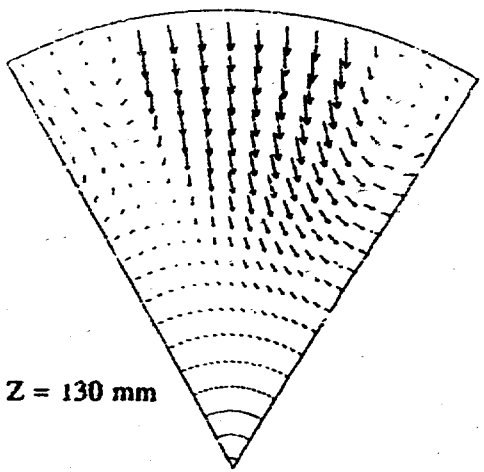

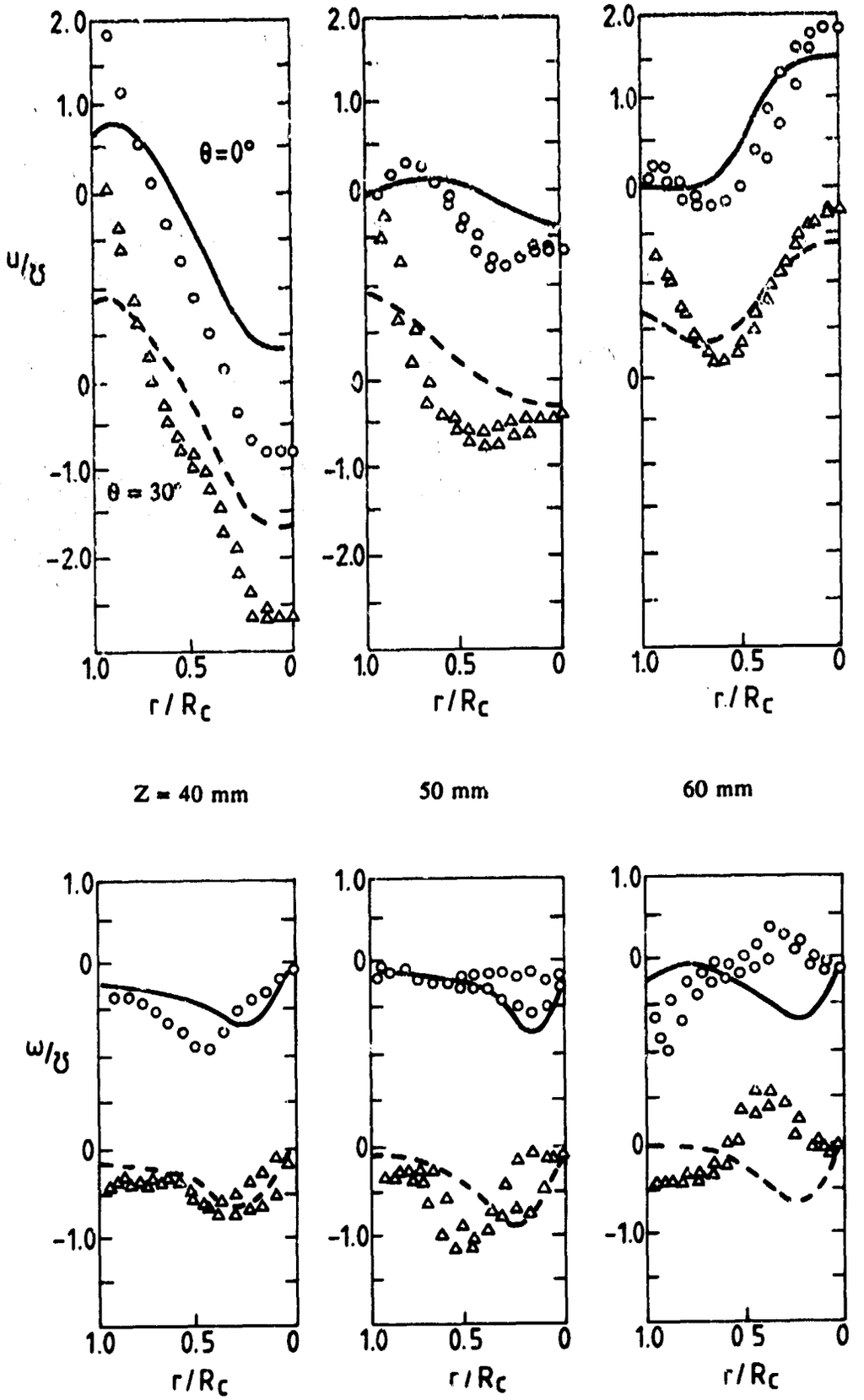

Figure 3 Radial Distributions of Axial (u) and Swirl Velocity (w) at Stations Z = 40, 50 and 60 mm along The Combustor in the Planes θ = 0° and 30°.

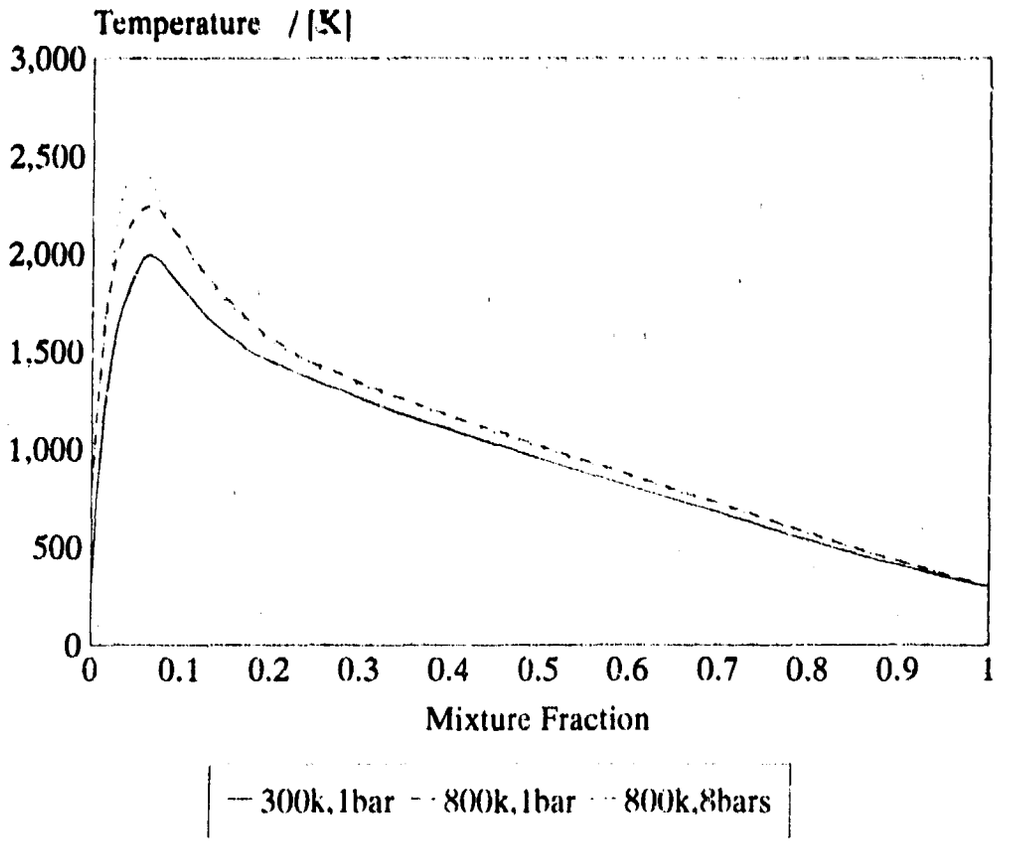

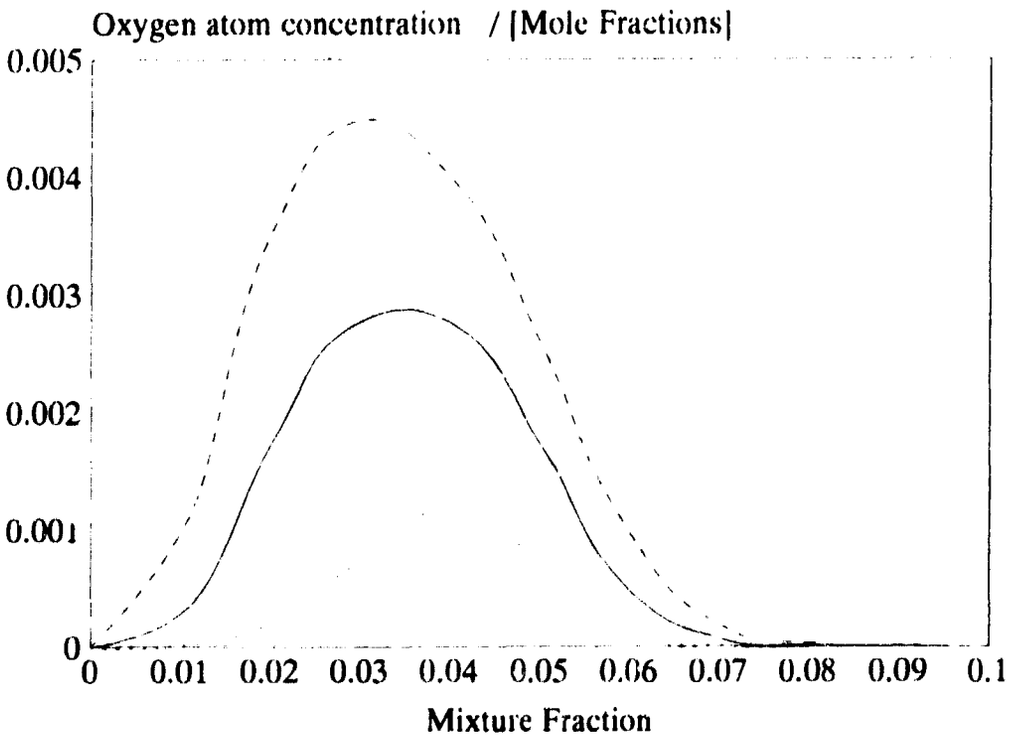

Figure 4 **Computed Laminar Flamelet Relationships for Non-premixed Propane-Air Combustion.**

(a) Mean Mixture Fraction (Plane θ = 0°)

(b) Mean Mixture Fraction (Plane θ = 30°)

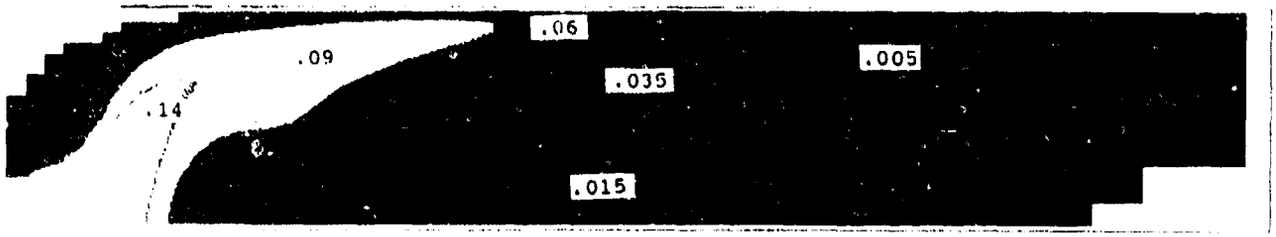

(c) Mean Temperature [K] (Plane θ = 0°)

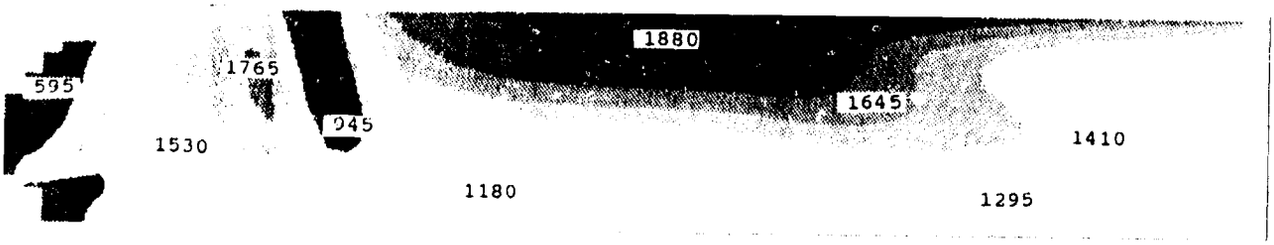

(d) Mean O-Atom Mole Fraction (Plane θ = 0°)

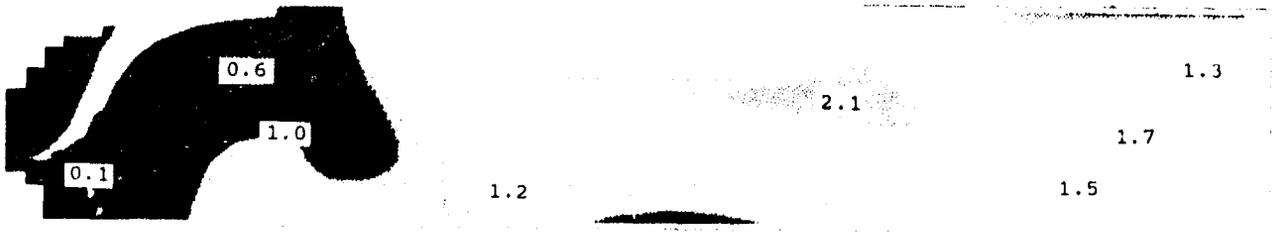

(e) Mean Mass Rate of NO Formation [10^{-4} kg m^{-3}s^{-1}]

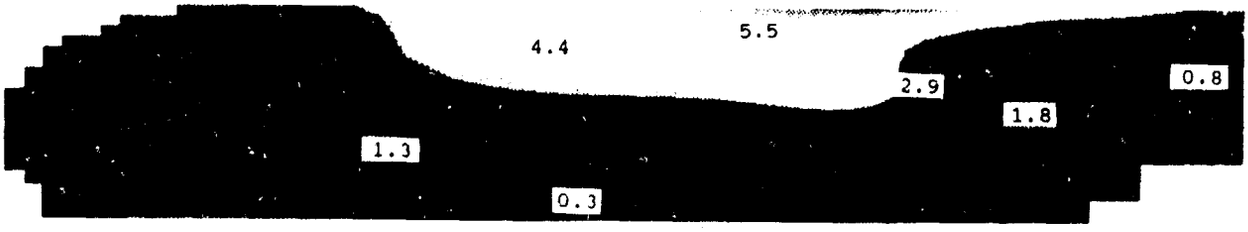

Figure 5 Predicted Property Maps for 300K inlet, 1 bar Conditions.

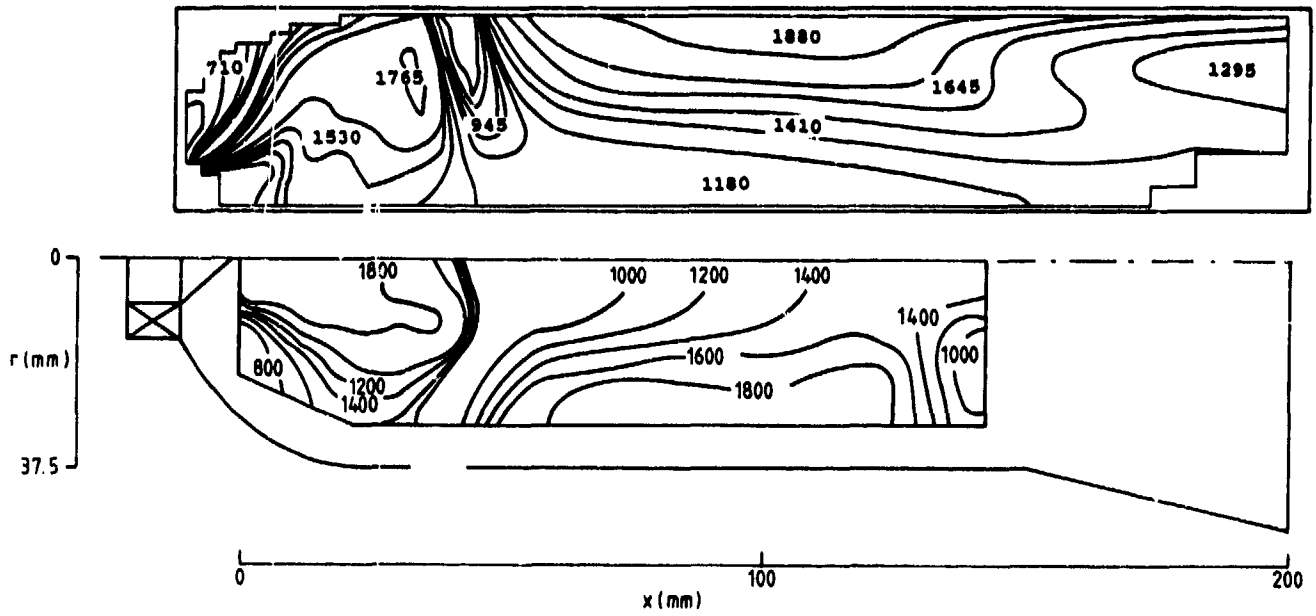

(a) Inlet Temperature 300K, Pressure 1 bar,
Plane θ = 0°.

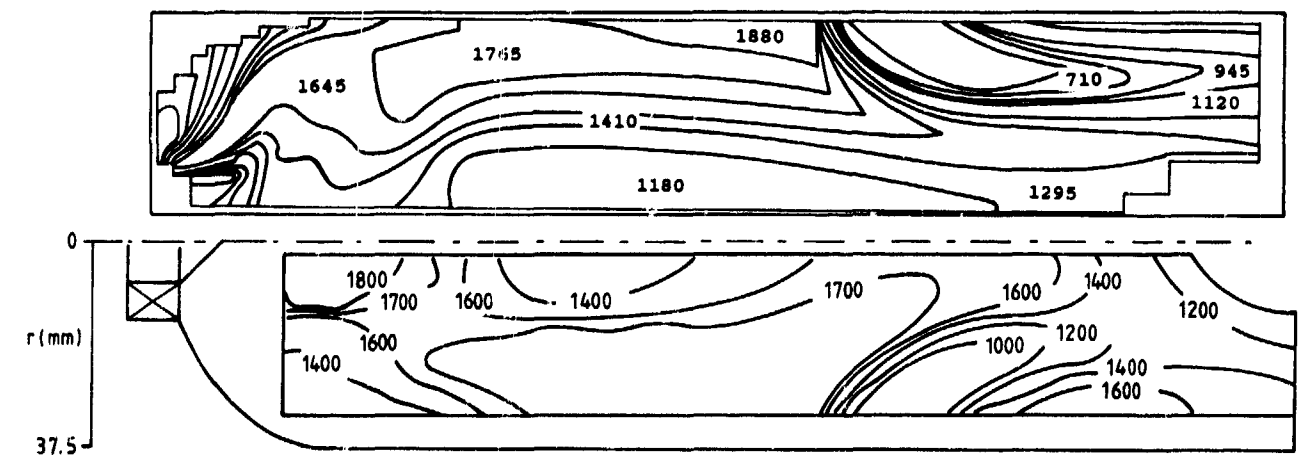

(b) Inlet Temperature 300K, Pressure 1 bar,
Plane θ = 30°.

Figure 6 Mean Temperature [K] : Prediction and Experiment
(Bicen et al, 1990)

(a) 300K, 1 bar, θ = 0°

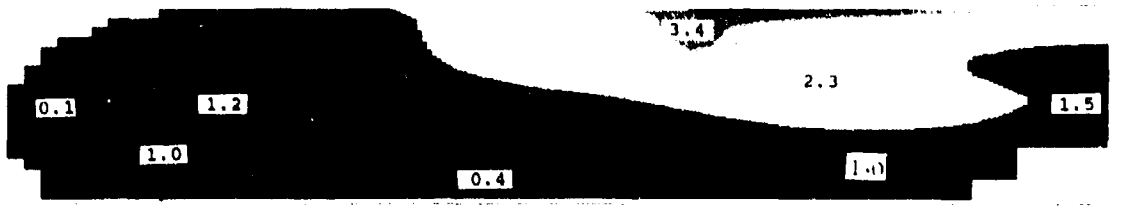

(b) 300K, 1 bar, θ = 30°

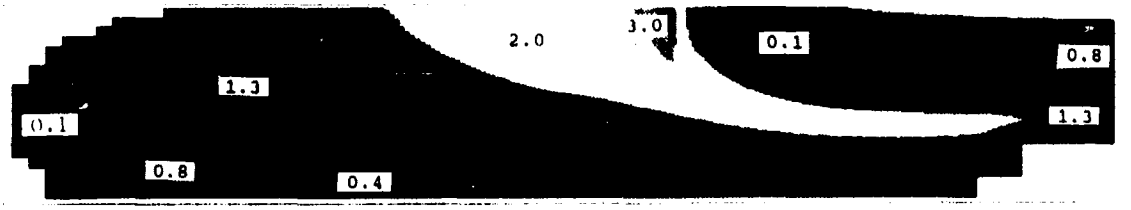

(c) 800K, 1 bar, θ = 0°

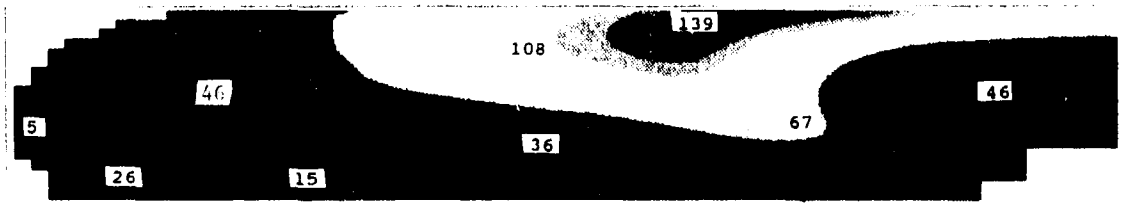

(d) 800K, 1 bar, θ = 30°

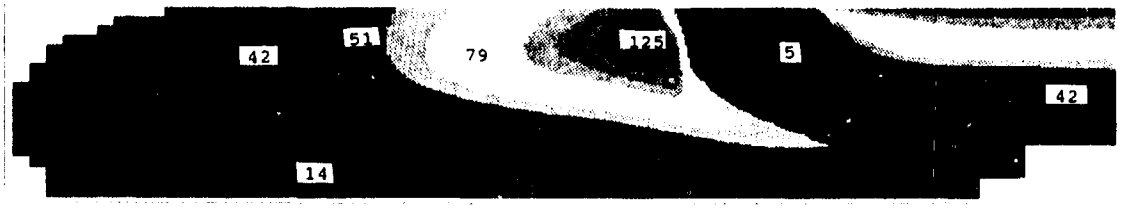

(e) 800K, 8 bar, θ = 0°

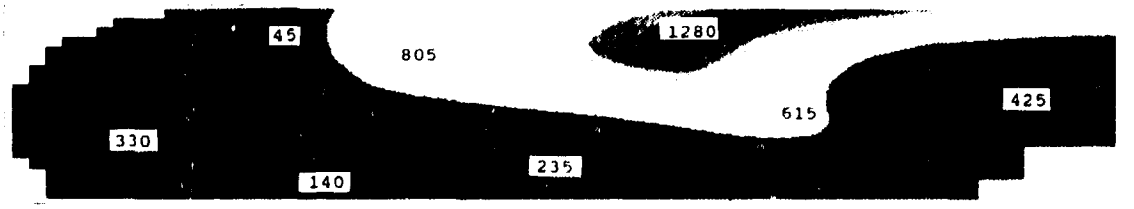

(f) 800K, 8 bar, θ = 30°

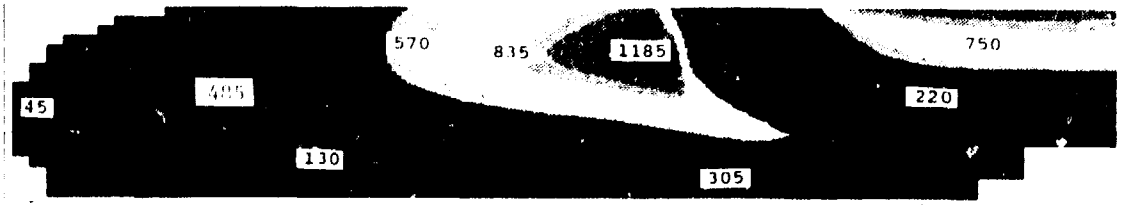

Figure 7 Predicted Mean NO Mole Fraction [ppm]

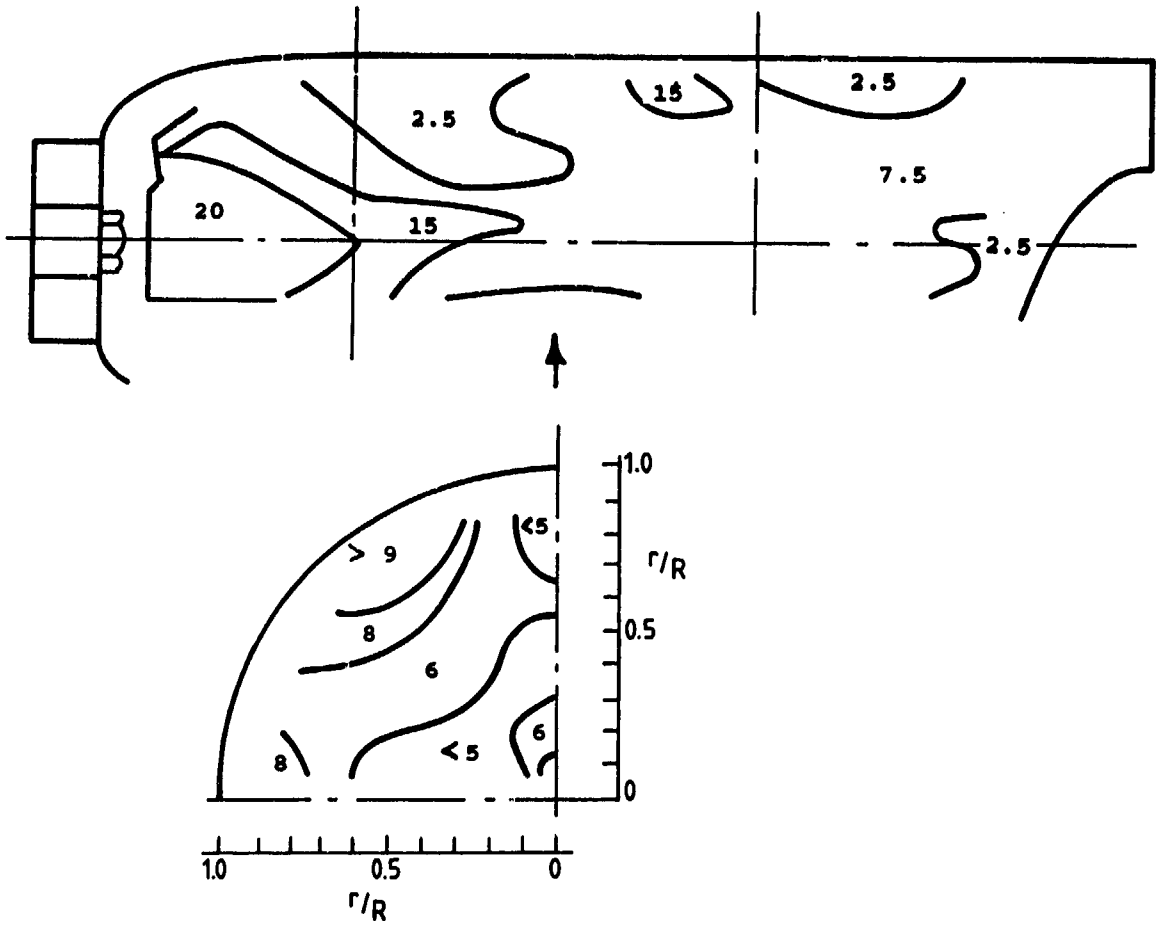

Figure 8 Measured NO Mole Fraction [ppm] ;
300K, 1 bar (Heitor and Whitelaw (1986)).

(a) Flamelet-based Temperature [K]

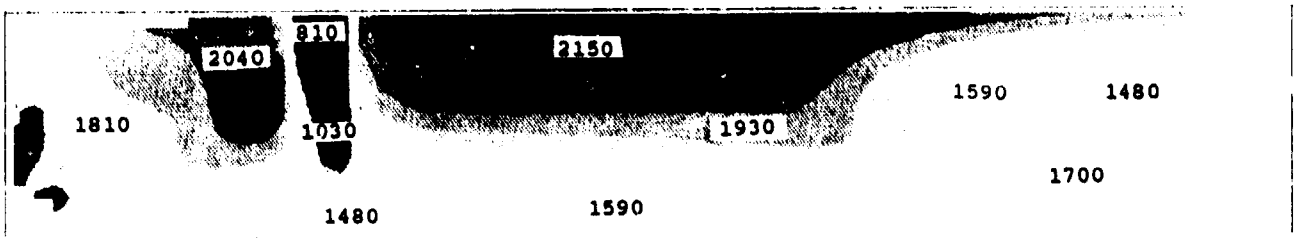

(b) Equilibrium-based Temperature [K]

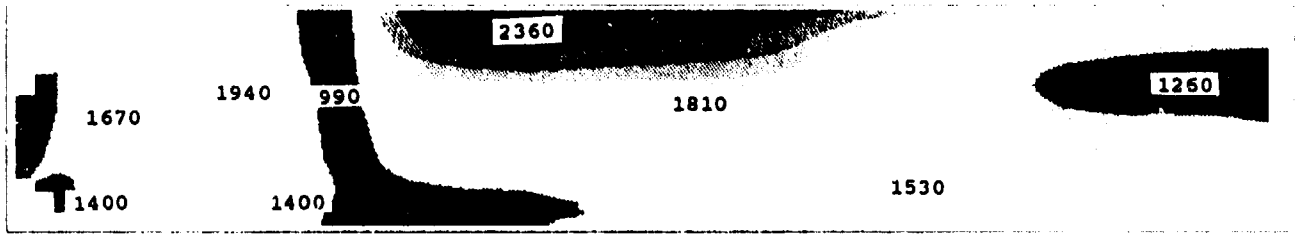

(c) Flamelet-based NO Mole .ion [ppm]

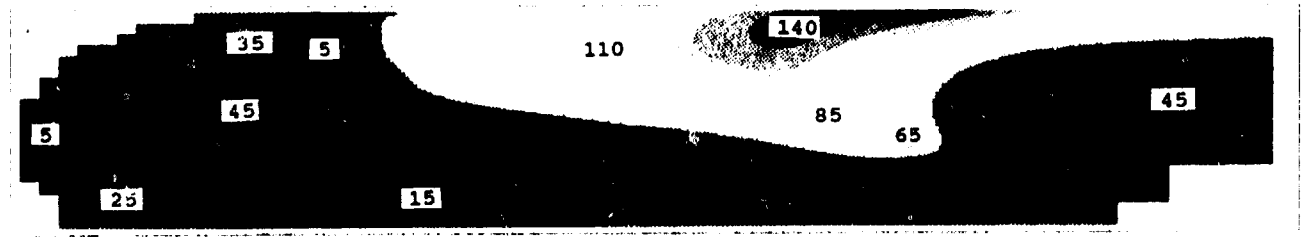

(d) Equilibrium-based NO Mole Faction [ppm]

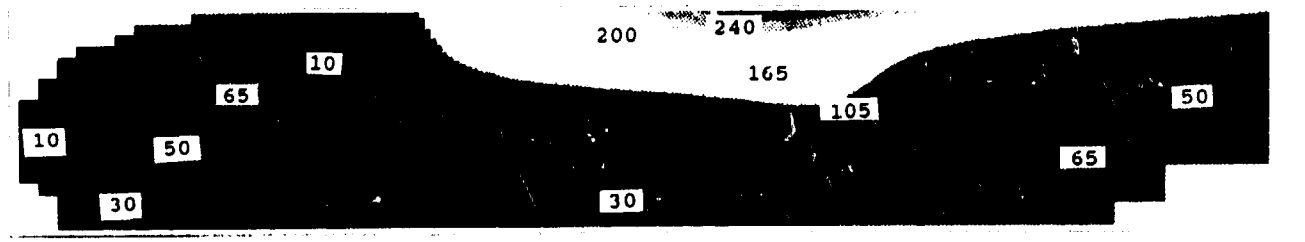

Figure 9 Comparison between Flamelet and Equilibrium Predictions for Mean Temperature and NO Mole Fraction ; $\theta = 0°$, 800K, 1 bar.

(a) 300K, 1 bar, $\theta = 0°$

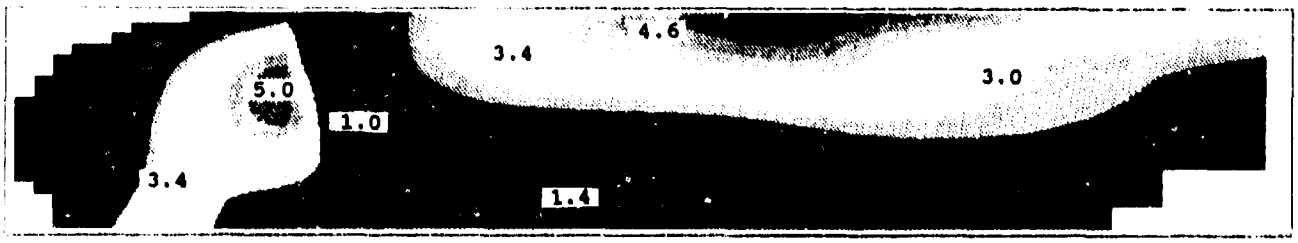

(b) 300K, 1 bar, $\theta = 30°$

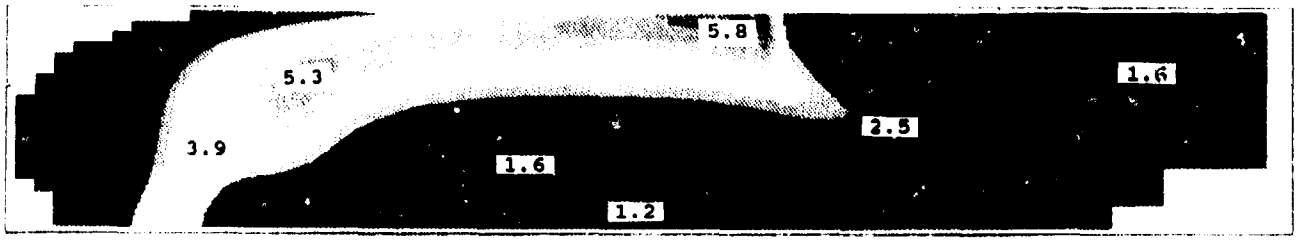

(c) 800K, 1 bar, $\theta = 30°$

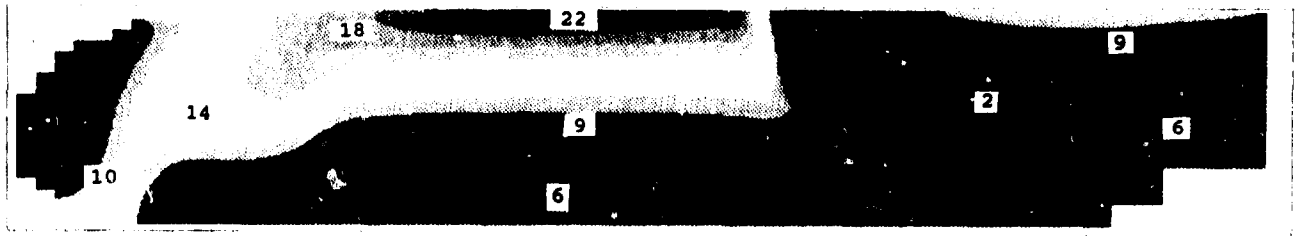

(d) 800K, 8 bar, $\theta = 30°$

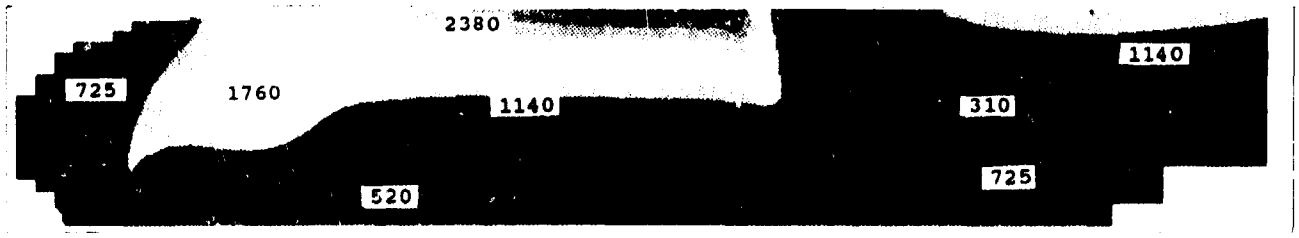

Figure 10 Predicted Distributions for Mean Soot Volume Fraction [$f_v \times 10^6$]

(a) Soot Formation Rate [kg $m^{-3}s^{-1}$]

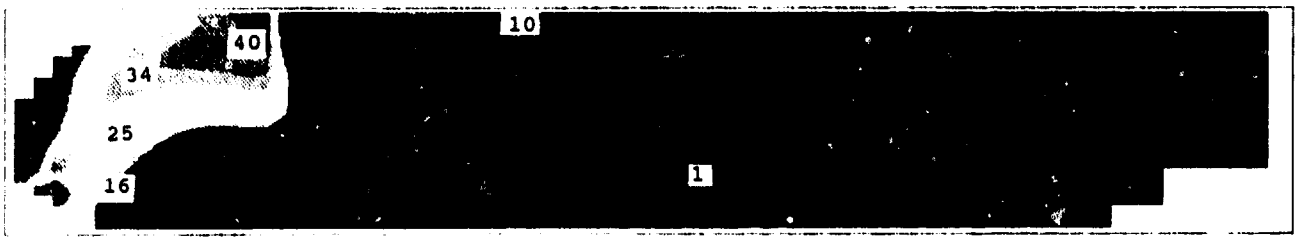

(b) Mass Oxidation Rate [$kgm^{-3}s^{-1}$]

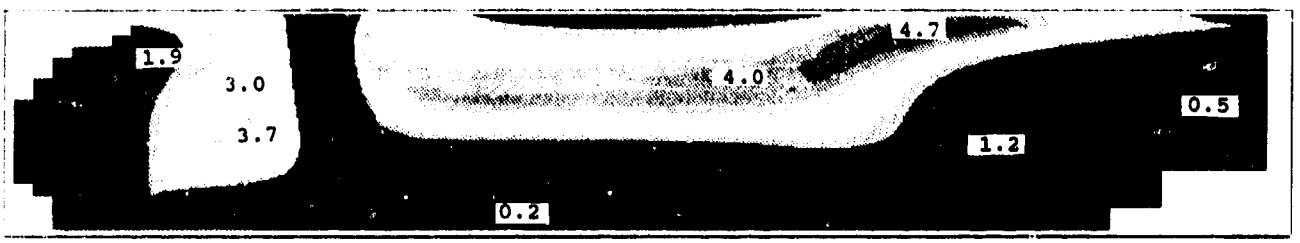

Figure 11 Predicted Distributions for Soot Formation and Oxidation at 800K Inlet Air Temperature and 8 bar Pressure. (Plane $\theta = 0°$)

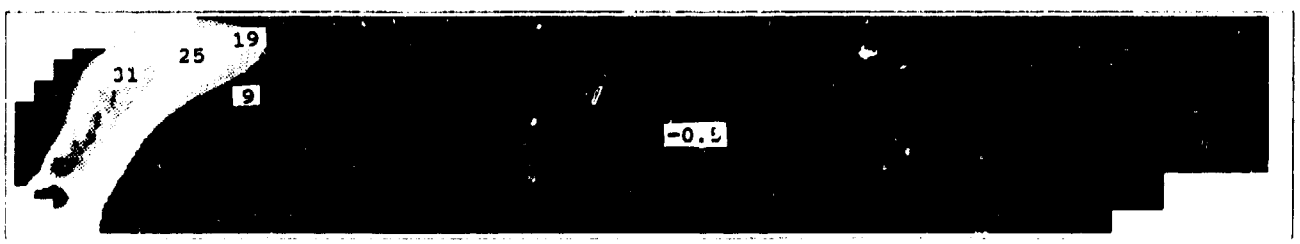

Figure 12 Predicted Distribution of Soot Production Source Term for 800K, 8 bar conditions (Plane $\theta = 0°$) incorporating the "Carbon Feedback" Mechanism [$kgm^{-3}s^{-1}$]

Discussion

Question 1. R. Parmesani
How many cells were used in the computational mesh? How much time did the calculation take and on what kind of a machine?

Author's Reply
The computational mesh illustrated in Figure 1 comprised approximately 15,000 cells (20 × 16 × 45 in the x, e, z directions respectively) distributed within a 60 degree sector incorporating cyclic boundaries. Each iteration sweep required approximately 5 minutes of CPU time on a SUN SPARC 1+ work station. Convergence of the reacting flows was achieved in approximately 2,000 sweeps.

Question 2. J.R. Tilston
I find the NOx pressure dependence very surprising. Was the combustor run at a constant flow function at the two pressure conditions?

Author's Reply
The pressure dependence of NOx production implied by these predictions is greater than expected. Although the calculations were performed at a fixed flow function ($\dot{m}\sqrt{T}/P$), differences in key flow field properties were predicted in relation to both peak temperature and fluctuation levels. Their influence on the highly non-linear rate expression is then predicted to mask the pressure dependence anticipated from 0 — atom equilibrium. The lengthy burning zones exhibited in Figure 6 (a, b) are perhaps untypical and exaggerate these effects.

Question 3. T. Rosfjord
Experimental evidence for a can combustor containing a single pressure atomizing injector/swirler configuration indicated a reduction in soot mass fraction (soot loading) by 100. Do your results also show a strong consumption of soot?

Author's Reply
The integrated mass fractions at planes along the combustor, necessary to address this question fully, have not been computed, but the predicted effect of oxidation is here generally less dramatic than the quoted value suggests. The reduction in soot mass concentration does not exceed a factor of 10.

More specifically, the predicted soot formation zones are not compact but extend into the intermediate zone between the primary jets, changing the balance between the competing processes. While the dilution jets do bring about a composition field favouring oxidation, the accompanying temperature falls rapidly to levels at which the Nagle and Strickland-Constable mechanism employed here is comparatively ineffective. Recent studies, however, have suggested an important enhanced role for oxidation via OH, rather than O_2, in combustion zones. Uncertainties over soot particle size, and therefore the effective aerosol surface area, further compound the problem.

Optical measurements of soot volume fraction in a model tubular combustor at Cranfield do not suggest quite such a large disparity in formation and oxidation rates, albeit at modest pressures and air preheat. There is clearly a need for more detailed in-situ soot measurements at realistic combustor operating conditions to refine the discussion of such issues.

NUMERICAL PREDICTION OF TURBULENT SOOTING DIFFUSION FLAMES

P.J. Coelho, T.L. Farias, J.C.F. Pereira and M.G. Carvalho
Mechanical Engineering Department
Instituto Superior Técnico, Technical University of Lisbon
Av. Rovisco Pais, 1096 Lisboa Codex. Portugal

SUMMARY

Soot formation is an important but poorly understood subject. Although significant advances have been made in the last few years, soot formation models for numerical calculation still present recognised shortcomings. The objective of this paper is to compare different soot formation models in the calculation of a propane turbulent diffusion flame and to investigate the influence of soot agglomeration and refractive index on soot volume fraction values inferred from extinction measurements. The time-averaged equations governing conservation of mass and momentum are closed by the k-ε eddy viscosity/diffusivity model and combustion is modelled using the laminar flamelet approach. Soot prediction involves the solution of transport equations for soot particle number density and soot mass fraction. The uncertainties of soot volume fractions obtained from extinction measurements due to agglomeration and the value of the complex refractive index were studied. Results using Rayleigh approximation were compared with predictions using the model presented by Iskander et al. for scattering and extinction of light by an ensemble of spherical particles.

LIST OF SYMBOLS

A	—	constant in Magnussen et al model (see eq. 11)
C_2	—	constant in transport equation for ε
C_α, C_β, C_γ, M_α, M_γ, T_α, T_γ	—	constants in Stewart, Syed and Moss model (see eqs. 5-9)
C_d	—	constant in Lee et al model (see eq. 12)
C_{ext}, Q_{ext}	—	extinction cross section and efficiency
C_f, n	—	constants in Khan and Greeves model (see eq. 3)
E	—	activation energy
$E_{i,\ inc,\ sca}$	—	electric field of the ith particle, incident and scattered respectively
$\hat{e}_0$, E_0	—	unit vector in the direction of the incident electric field; intensity of incident electric field.
f	—	mixture fraction
f_v	—	soot volume fraction [m^3/m^3]
Io, I	—	entering and leaving intensity of laser beam crossing the flame
k	—	imaginary part of soot refractive index
k	—	wave number [m^{-1}]
k, ε	—	turbulent kinetic energy and its dissipation rate
K_A, K_B, K_T, K_Z	—	constants in Nagle et al model (see eq. 13-14)
k_{ext}	—	extinction coefficient [m^{-1}]
L	—	path length.
m	—	soot refractive index (m=n+ik)
N	—	number of primary particles in the agglomerate
n	—	real part of soot refractive index
N_o	—	Avogadro number
n_p	—	soot particle number density
p_i	—	partial pressure of species i
R	—	gas constant; radius of a spherical primary particle.
(R, θ, ϕ)	—	coordinates of the centre of the ith sphere.
S	—	source term of the transport equations
s_i	—	self interaction term (see eq. 19)
s	—	stoichiometric oxygen requirement for fuel combustion
s_s	—	stoichiometric oxygen requirement for soot combustion
T	—	temperature
T_{ij}	—	3x3 matrix in terms of spherical Bessel functions and associated Legendre functions.
$\overline{w}$	—	oxidation rate [g cm^{-2} s^{-1}]
X	—	mole fraction
x	—	primary particle size parameter $\left(x = \frac{2\pi R}{\lambda}\right)$
α,δ	—	nucleation rate
β	—	coagulation rate
ε	—	dielectric constant
ϕ	—	equivalence ratio
γ	—	surface growth rate
λ	—	wavelength [m]
ρ	—	density

Superscripts

* — conjugate
¯ — mean value
^ — vector

Subscripts

s	—	soot
O_2	—	oxygen
fu	—	fuel
f	—	formation
d	—	oxidation

1. INTRODUCTION

The problem of soot formation and oxidation has received significant attention due to its practical importance in combustion equipment. However, the complexity of the soot formation mechanisms has prevented the development of reliable modelling approaches. The evaluation of soot formation and oxidation models is generally accomplished by means of comparison of predicted soot concentration with available measurements. Experimental values of soot concentration are

Presented at an AGARD Meeting on 'Fuels and Combustion Technology for Advanced Aircraft Engines', May 1993.

often deduced from extinction measurements, assuming that soot particles are spherical and small compared to the wavelength. However, this assumption is questionable due to soot agglomeration and to uncertainties regarding the soot refractive index.

The purpose of the present paper is twofold. First, to compare several soot formation and oxidation models by means of comparison of their ability in predicting soot concentration in a propane turbulent diffusion flame for which measurements are available. Second, to investigate the influence of soot agglomeration and soot refractive index on the values of soot volume fraction inferred from extinction measurements.

1.1 Modelling of Sooting Diffusion Flames

Soot formation models are generally based either on one-step kinetic mechanisms or two-step mechanisms. A review of one-step kinetic mechanisms was presented by Mullins et al. (Ref. 1). A simple kinetic expression often used in calculations in furnaces and boilers is due to Khan and Greeves (Ref. 2), although it was originally developed for Diesel engines. Tesner et al. (Ref. 3) proposed a two-step mechanism where the first stage represents formation of radical nuclei, involving fuel cracking, branching and coagulation steps, and the second stage describes formation of soot particles from the radical nuclei. This model was applied to turbulent acetylene-air flames (Ref. 4) and to propane turbulent jet flames (Ref. 5).

The laminar flamelet approach has been the basis of recently developed soot formation models. A straightforward extension of the flamelet concept to soot volume fractions is not possible. Gore et al. (Ref. 6) have shown that calculations based on a relationship between soot volume fraction and mixture fraction yield reasonable predictions in the overfire region. A similar approach was followed by Kent et al. (Ref. 7) who established the relationship between instantaneous soot volume fraction and mixture fraction from measurements in turbulent flames. They concluded that in the lower parts of the flame this formulation is not adequate and a finite chemical rate model is needed. The maximum soot concentrations further up the flame are less dependent on residence time and a mixture fraction approach may be useful there.

Moss and coworkers (Ref. 8, 9) presented a model based on the solution of transport equations for the soot particle number density and soot mass fraction and accounting for the processes of nucleation, coagulation and surface growth. The rates of these processes are expressed as functions of mixture fraction. The constants of the model were determined from numerical experiments to optimize the predictions of a laminar diffusion flame of ethylene. A modification of the surface growth term was later proposed to cope with experimental evidence in methane and pre-vaporized kerosene flames (Ref. 10, 11). A similar model was suggested by Kennedy et al. (Ref. 12, 13) who prescribed the soot particle number density, based on experimental data, rather than solving a transport equation for this quantity.

Leung et al. (Ref. 14) and Fairweather et al. (Ref. 15, 16) proposed a model based on the solution of the same transport equations and on the simulation of the same physical phenomena of Moss and coworkers model. However, they assume that nucleation and surface growth rates are related to the concentration of a characteristic pyrolysis product, taken as acetylene, rather than the concentration of fuel. The model was successfully applied to counterflow diffusion flames of ethylene and propane, a turbulent natural gas jet in a cross-wind and to a turbulent diffusion propane flame.

Most of the works mentioned above include a model of soot oxidation. The semi-empirical formula of Nagle and Strickland-Constable (Ref. 17) was used by Syed et al. (Ref. 10) in their predictions of thermal radiation in buoyant turbulent diffusion flames. The oxidation rate expression due to chemical kinetics and proposed by Lee et al. (Ref. 18) was incorporated in the model of Leung, Fairweather and co-workers. Magnussen et al. (Ref. 4) used their own oxidation model which is based on the assumption that the oxidation rate is controlled by the mixing rate of air and fuel. More recently, several authors have pointed out that molecular oxygen is not necessarily the only species responsible for soot oxidation and the role of OH radicals may be significant (Ref. 19, 20).

In this work the soot formation models of Ref. 2 and 11 are applied to the propane turbulent diffusion flame studied experimentally by Nishida et al. (Ref. 21) and which was modelled recently by Fairweather et al (Ref. 15). The soot oxidation models of ref. 4, 17 and 18 are employed.

1.2. Soot volume fractions inferred from extinction measurements

Extinction measurements have been extensively used to measure the rates of soot formation and soot concentration for various different types of flames and fuels (see Ref.1, 8, 22, 23 and references therein). Based on extinction measurements soot volume fractions, among other properties, can be inferred by using an appropriate method capable of predicting the extinction efficiencies of the soot particles encountered in the zone of the flame in study. The method most commonly used to relate the extinction measurements to soot volume fractions is based on the assumption that soot particles are spherical and small compared to the wavelength (size parameter, x, much smaller than unit). The one term Rayleigh limit expression for computing the extinction efficiencies is used and the following expressions are obtained:

$$f_v = \frac{k_{ext} \cdot \lambda}{36\pi}\left[\frac{(n^2-k^2-2)^2+4n^2k^2}{nk}\right] \quad (1)$$

$$k_{ext}=\frac{\ln(I_o/I)}{L} \quad (2)$$

where n an k denote the real and complex parts of the soot refractive index; λ, the wavelength of the laser beam; Io and I, the entering and leaving intensity of the beam crossing the flame and k_{ext} the extinction coefficient.

As it has been stated by several authors (Ref. 22-26) soot particles in flames generally possess two basic morphological forms. In its early stage of formation soot particles are approximately spherical in shape and present mean diameters between 10 and 60 nm (Ref. 22). These sphere-like primary units clearly satisfy the Rayleigh limit and soot volume fraction can therefore be obtained using equations 1 and 2. Nevertheless, these primary particles, beyond a certain stage in their evolution, tend to group by agglomeration, forming chain-like clusters composed of these primary units. While the primary particles are reasonably small, the aggregates may consist of a wide range of primary particles leading to an equivalent size parameter that most frequently exceeds one. The applicability of the Rayleigh approximation can and should therefore be questioned.

Besides assuming a specific morphology for soot the complex refractive index (m=n+ik) used in equation 1 is a parameter that has to be selected before calculating soot volume fractions from the attenuation of the intensity of a laser beam. A wide variety of values for m can be found in the literature. Depending on the experimental or theoretical method used, as well as the type of flame and fuel, the real part of the refractive index obtained by different authors varies between 1.4 and 2 while the values of the imaginary part may fall in the range of 0.4 to 1.(Ref. 26).

The purpose of the second part of this study is to investigate the influence of soot agglomeration and soot refractive index on the values of soot volume fractions obtained for an extinction coefficient. For a reference extinction measurement where I/Io, λ and L are pre-established (see equation 2), soot volume fractions obtained for different types of soot morphology and covering the soot refractive index range are calculated. The influence of these two parameters is then analysed.

The mathematical models used in this study are described in the next section. Then, the results obtained are presented and discussed. The main conclusions achieved are summarized in the last section.

2. MATHEMATICAL MODELS

2.1 Governing Equations, Turbulence and Combustion Models

The model employed to calculate the velocity and temperature fields and the species concentrations distributions is based on the numerical solution of the density-weighted average form of the equations governing conservation of mass and momentum and transport equations of scalar quantities.

The k-ε eddy viscosity/diffusivity model was employed to close these equations. Standard values were used for all the constants except for constant C_2 in the transport equation for the dissipation rate of turbulent kinetic energy. The configuration of the flame studied in this work is similar to a round jet whose spreading rate is overestimated by first and second moment closures. Several modifications of the k-ε model have been proposed to overcome this problem in isothermal round jets (see, e.g., Ref. 27). Here, we have simply reduced C_2 to 1.65, as discussed in the following section. A reduction of the standard value of C_2 was also the solution of Fairweather et al. (Ref. 15), who employed a second moment closure, to bring the predicted flame spreading rate into agreement with measurements.

Combustion was modelled using the conserved scalar/prescribed pdf formalism. The mixture fraction was the scalar chosen and a clipped gaussian shape was assumed for the probability density function of mixture fraction. The laminar flamelet model was used to relate temperature and species concentrations to mixture fraction. The resultant relation between temperature and mixture fraction is valid for an adiabatic flame, but does not hold for a sooting flame due to the radiative heat loss. Therefore, a method has to be devised to relate temperature to mixture fraction accounting for heat losses.

It is possible to use a model to calculate soot concentration and to estimate the radiative heat transfer. Then, an energy equation may be solved and a relationship between enthalpy and mixture fraction assumed to compute flame temperature taking into account the radiative heat loss. However, this procedure is not recommended when the soot formation or oxidation models are evaluated by comparing predicted soot concentration with available measurements. In fact, soot formation and oxidation are strongly dependent on temperature. Therefore, temperature and soot distributions both depend one on the other. Soot concentration influences radiation which influences enthalpy and, therefore, temperature and soot concentration. Supposing that soot formation and oxidation models are accurate enough to provide a correct distribution of soot concentration, it may happen that modelling assumptions concerning the influence of turbulence/ radiation interaction or enthalpy/mixture fraction relationship yield an inaccurate temperature field. In such a case, predicted soot concentration would be poorly predicted because the temperature field was not correct. Consequently, it is better to decouple soot from temperature predictions if attention is focused on evaluation of soot formation models.

A simple method suggested in ref. 28 was used to adjust flamelet temperatures as a function of mixture fraction such that peak mean temperatures are in agreement with the measurements. The same procedure was used, among others, in ref. 10, 14, 15 and 16.

The governing equations are discretized using a finite volume/finite differences method and solved using the SIMPLE method. The results obtained are used as input data for the subsequent solution of transport equations for the soot particle number density, when the soot formation model involves this quantity, and soot mass fraction. The soot formation and oxidation models employed in this work are described below.

2.2 Soot formation models

(i) Khan and Greeves (Ref. 2)

This model uses a simple kinetic rate expression to model soot formation. The source term of the transport equation for soot mass fraction is given by:

$$S_f(m_s) = C_f\, p_{fu}\, \phi^n \exp(-E/RT) \qquad (3)$$

where C_f and n are constants of the model. The equivalence ratio, ϕ, the fuel partial pressure, p_{fu}, and the temperature, T, may be related to mixture fraction and the mean value of the source term is computed by integration:

$$\bar{S}_f = \bar{\rho} \int_0^1 \frac{S_f}{\rho}\, p(f)\, df \qquad (4)$$

Soot formation occurs only for values of ϕ in the range $\phi_{min} \le \phi \le \phi_{max}$, where ϕ_{min} stands for the incipient sooting limit and ϕ_{max} is a value above which soot formation becomes negligible.

(ii) Stewart, Syed and Moss (Ref. 11)

This model solves transport equations for the soot particle number density, n_p, and soot mass fraction, m_s, whose source terms are calculated as follows:

$$S_f\left(\frac{n_p}{\rho N_o}\right) = \alpha - \beta \left(\frac{n_p}{N_o}\right)^2 \qquad (5)$$

$$S_f(m_s) = \gamma f_v^{2/3} n_p^{1/3} + \delta \qquad (6)$$

$$\alpha = C_\alpha \rho^2 T^{1/2} X_{fu}^{M\alpha} \exp(-T_\alpha/T) \qquad (7)$$

$$\beta = C_\beta T^{1/2} \qquad (8)$$

$$\gamma = C_\gamma \rho T^{1/2} X_{fu}^{M\gamma} (-T_\gamma/T) \qquad (9)$$

$$\delta = 144\, \alpha \qquad (10)$$

where C_α, C_β, C_γ, M_α, M_γ, T_α and T_γ are constants of the model. The two terms in the second member of equation (5) describe the processes of nucleation and coagulation, respectively, and the two terms in the second member of equation (6) represent the contributions of surface growth and nucleation. Equation (4) is employed to calculate the mean values of the source terms.

2.3 Soot oxidation models

(iii) Magnussen and Hjertager (Ref. 4)

This model assumes that turbulence decay controls the rate of soot oxidation. The source term is computed as the minimum of two expressions, one appropriate in regions where the local mean soot concentration is low compared to the oxygen concentration and the other applicable to regions where oxygen concentration is low and limits the oxidation rate:

$$S_d = \min\left\{ A\, m_s\, \rho\, \frac{\varepsilon}{k},\ A\, \frac{m_{O2}}{s_s}\, \frac{m_s s_s}{m_s s_s + m_{fu} s}\, \rho\, \frac{\varepsilon}{k} \right\} \qquad (11)$$

where A is a constant of the model.

(iv) Lee, Thring and Beer (Ref. 18)

This model estimates the rate of soot oxidation using a simple kinetic rate expression:

$$S_d = C_d\, m_s\, \frac{p_{O2}}{\sqrt{T}} \exp(-E/RT) \qquad (12)$$

where C_d is a constant of the model.

(v) Nagle and Strickland - Constable (Ref. 17)

The rate of oxidation of soot particles (g cm^{-2} s^{-1}) is given by:

$$\bar{w} = 12\left[\left(\frac{K_A p_{O2}}{1+K_Z p_{O2}}\right) x + K_B p_{O2}(1-x)\right] \qquad (13)$$

where

$$x = \left(1 + \frac{K_T}{p_{O2} K_B}\right)^{-1} \qquad (14)$$

and K_A, K_B, K_T and K_Z are rate constants given in ref. 17. The source terms of the transport equations for soot particle number density and soot mass fraction may be obtained from equation (13) (see Ref. 10).

2.4 Soot volume fractions inferred from extinction measurements

Soot volume fraction, f_v, and particle number density, n_p, based on extinction measurement are calculated from the following expressions:

$$n_p = \frac{k_{ext}}{C_{ext}}$$

$$f_v = V_{soot} \cdot n_p$$

where k_{ext} is a direct output of the experimental measurements, and C_{ext} is the extinction cross section, a value that strongly depends on the shape, size and refractive index of the soot particles.

Soot Extinction Cross Section of Primary Particles - Rayleigh Limit Approximation

The approximate expressions used for the extinction cross sections of small spheres were the one and three term series presented in ref. 29 depending on the size parameter and refractive index chosen for the soot particles. The three-term expression can be expressed as follows:

$$C_{ext} = Q_{ext} \cdot \pi R^2 \qquad (15)$$

where Q_{ext} is obtained from:

$$Q_{ext} = \left\{ \frac{4}{15} + \frac{20}{3z_2} + \frac{4.8}{z_1^2}\left[7(n^2+k^2)^2 + 4(n^2-k^2-5)\right] \right\} nkx^3$$

$$+ \frac{8}{3z_1^2}\left\{ \left[(n^2+k^2)^2 + n^2 - k^2 - 2\right]^2 - 36n^2k^2 \right\} x^4 + \frac{24nk}{z_1} x \ ,$$

$$z_1 = 4(n^2+k^2)^2 + 12(n^2-k^2) + 4,$$

$$z_2 = 4(n^2+k^2)^2 + 12(n^2-k^2) + 9 \qquad (16)$$

For the one-term expression both the x^3 and x^4 terms are neglected. As mentioned by Ku and Felske (Ref. 30), less than one percent error in using Rayleigh expressions compared to the exact Mie calculations can be obtained with the one term approximation when

$$x \le 0.238 |m|^{-5/3} \qquad (17)$$

while for the three term approximation the inequality to be satisfied is less restrictive and given by:

$$x \le 0.386 |m|^{-1.09} \qquad (18)$$

For each Rayleigh calculation performed in this paper these two inequalities were tested and depending on the results the one term or the three term expression was used.

Extinction Cross Section of Soot Agglomerates

An extensive comparison of three different solution methods for calculating the extinction cross section of soot agglomerates consisting of assemblies of primary particles in the Rayleigh approximation was presented by Ku and Shim (Ref. 31), namely the Iskander et al method (Ref. 32), the Purcell and Pennypacker model (Ref.33) and the Jones solutions (Ref.34, 35). Although different in their mathematical approaches these three methods involve the solution of an identical system of linear equations with slightly different coefficients. The main differences between the three approaches reside in the fact that Jones solution includes multiple scattering terms up to the second order whereas the others include terms up to the third order. The Iskander et al method (which, for abbreviation, will be addressed to as ICP) is the only one that includes a self-interaction term when calculating the electric field induced in each particle. The major conclusions achieved by the authors mentioned above were the following: according to the level of accuracy and range of applicability the ICP solution is the best, followed by the Purcell and Pennypacker and Jones; for the range of validity of the methods (according to the size parameter of the primary particles and absolute value of the refractive index) the ICP method outscores once again its competitors. Since all the three methods require approximately the same amount of computational time and storage, the ICP solution should therefore be used exclusively. Following these conclusions the ICP method was adopted in the present work for the calculations of extinction cross sections of the agglomerates.

Following ref. 31, Jones nomenclature and formulation were adopted to describe the ICP method. The solution of the scattering of an electromagnetic wave by an agglomerate of N spheres starts by obtaining the internal electric field of each primary particle in the agglomerate due to the incident field, the secondary fields of all the particles surrounding the particle in study and the field of the particle itself. The internal field E_i of the ith particle can be obtained by solving a linear system of 3Nx3N equations of the form:

$$E_i = \left(\frac{3}{\epsilon+2}\right) E_{inc,i} + \frac{i}{3}\left(\frac{\epsilon-1}{\epsilon+2}\right) \sum_{\substack{j=1 \\ j \neq i}}^{N} x_j^3 \bar{T}_{ij} E_j + s_i E_i \ ; \ i = 1, 2.., N \qquad (19)$$

According to ref. 31, the value of the primary particle size parameter should not exceed $0.8\left[m^2+5\right)/(2m^2+1)\right]$ for a <10% error on extinction cross sections.

Once the electric fields inside each primary particle are known the solution for the scattered wave at any point (R, θ, ϕ) in the far field for an agglomerate of particles can be given by (see Ref. 31,34,35):

$$E_{sca}(\hat{r}) = \frac{\exp(ikr)}{-ikr} F(\hat{r}), \qquad (20)$$

where $F(\hat{r}) = (-i)\left(\frac{\epsilon-1}{3}\right) \sum_{i=1}^{N} x_i^3 \exp(-ikr_i \cos\beta_i)\left(\Theta_i \hat{\theta} + \Phi_i \hat{\phi}\right)$

and $\cos\beta_i = \cos\theta_i \cos\theta + \sin\theta_i \sin\theta \cos(\phi_i - \phi)$. (R, θ, ϕ) are the coordinates of the centre of the ith sphere, θ_i and Φ_i the components of the internal electric field in the θ and Φ directions, given by:

$$\Theta_i = \cos\theta \cos\phi E_{x,i} + \cos\theta \sin\phi E_{y,i} - \sin\theta E_{z,i},$$

$$\Phi_i = -\sin\phi E_{x,i} + \cos\phi E_{y,i}, \qquad (21)$$

The extinction cross section can be derived from the following expression (Ref. 36):

$$C_{ext} = 4\pi k^{-2} \mathrm{Re}\left[E_0^* \hat{e}_0^* \cdot F_{\theta=\phi=0}\right], \qquad (22)$$

where Re denotes the real part of the complex quantity and the superscript * refers to the complex conjugate. $\hat{e}_0$ is a unit vector in the direction of the incident field with intensity E_0. For agglomerates of uniform sized particles the resulting extinction cross section equation is:

$$C_{ext} = \frac{4\pi}{3} kR^3 \mathrm{Im}\left[(\epsilon-1)\sum_{i=1}^{N} \exp(-ikz_i) E_0^* \hat{e}_0^* \cdot E_i\right] \qquad (23)$$

A more detailed description of the present formulation can be found elsewhere (Ref. 31-37).

3. RESULTS AND DISCUSSION

This chapter is dedicated to the presentation and discussion of the results. The first part deals with the prediction of soot concentration in a turbulent diffusion flame and the second part analyses the uncertainties arising in the inference of soot concentration from extinction measurements.

3.1. Calculation of a turbulent sooting diffusion flame

The propane/air turbulent diffusion flame analysed experimentally by Nishida and Mukohara (Ref.21) is considered here as a basis for comparison of the soot formation and oxidation models described in the previous section. The results

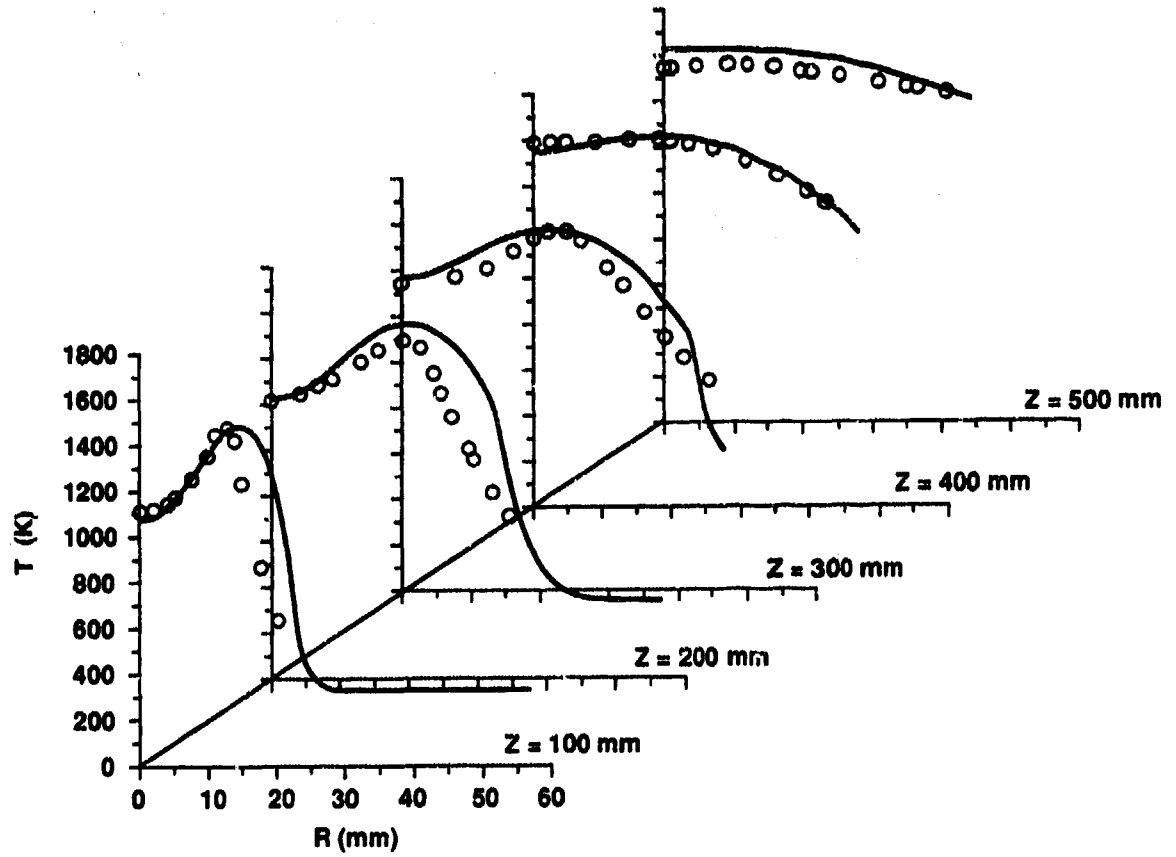

Figure 1 — Predicted and measured radial temperature profiles (solid line: predictions; symbols: measurements of Nishida and Mukohara, 1982).

may also be compared with the predictions of Fairweather et al. (Ref. 15) who recently studied this flame. Propane at ambient temperature is introduced in the combustion chamber through a nozzle of inner diameter 2.0 mm at an average velocity of 30m/s. Air is supplied through an annulus surrounding this pipe with an average velocity of 0.4 m/s and at a temperature of 50°C. The combustion chamber has an internal diameter of 115 mm.

Temperature and Species Concentration

In the soot formation and oxidation models evaluated in this work the source terms are dependent on the temperature, density, oxygen and fuel concentrations. Therefore, it is important to investigate how accurate the predictions of these quantities are.

The predicted radial temperature profiles are compared with the measurements in fig. 1. It can be seen that the flame width is slightly overpredicted. In fact, the peak temperature at z = 100 mm occurs at a larger distance from the centreline. The reduction of constant C_2 of the turbulence model yields an increase of the dissipation rate of turbulent kinetic energy and a decrease of the turbulent viscosity. Consequently, the diffusion is smaller and larger temperature gradients occur. Hence, a smaller value of C_2 would improve the predictions at the outer flame edge but at the expense of a decrease of the centreline temperature. It was found that C_2 = 1.65 is the best compromise between the predictions of centreline temperature and flame width. At z = 200 mm the temperature is again overpredicted at the outer flame edge but a good agreement with the data was obtained farther downstream. Fairweather et al. (Ref. 15) predicted well the flame width but they overestimated the centreline temperatures at z = 200 mm and z = 300 mm. As in their calculations, we have also overpredicted the centreline temperature at axial stations beyond 0.5 m (not shown here). This has been attributed to the radiative heat loss treatment (Ref. 15).

The computed fuel and oxygen mole fractions at axial stations z = 100 mm and z = 300 mm are compared in fig. 2 with the available data. The mole fraction of oxygen is reasonably well predicted but, contrary to the calculations, small amounts of oxygen were measured within the flame region. A similar behaviour was found in the model of Fairweather et al (Ref. 15). The model overestimates the centreline fuel mole fraction. This is a consequence of the reduction of C_2 constant and it is the price to pay for a reasonable prediction of the flame width. Nevertheless, the concentration gradient in the flame zone closely follows the data.

On the whole, the predictions of temperature, oxygen and fuel concentration are satisfactory and sufficiently close to the data to allow the comparison of the soot formation and oxidation models presented below.

Soot Formation Model of Khan and Greeves (Ref. 2)

A sensitivity study of Khan and Greeves (Ref. 2) soot formation model is shown in fig. 3. The soot oxidation model of Magnussen et al. (Ref. 4) was used in all the test cases reported in fig. 3. The value C_f = 0.468 kg N^{-1} m^{-1} s^{-1} employed by Khan et al. in the calculation of soot formation in a Diesel engine, neglecting soot combustion, tends to underestimate soot concentration except along the centreline at axial locations near the burner exit. In the work of Khan and Greeves C_f was increased to 1.376 kg N^{-1} m^{-1} s^{-1} when soot combustion was accounted for. This value is similar to the one employed in ref. 38, C_f = 1.5 kg N^{-1} m^{-1} s^{-1}. Calculations using this value perform much better, although they overestimate soot concentration up to z = 300 mm. An intermediate value, C_f = 0.84 kg N^{-1} m^{-1} s^{-1}, tuned by Abbas to fit the experimental data of Dalzell et al. (Ref. 39), was also tried.

In a later work Abbas et al. (Ref. 40) suggested that C_f is proportional to Richardson number and took the numerically

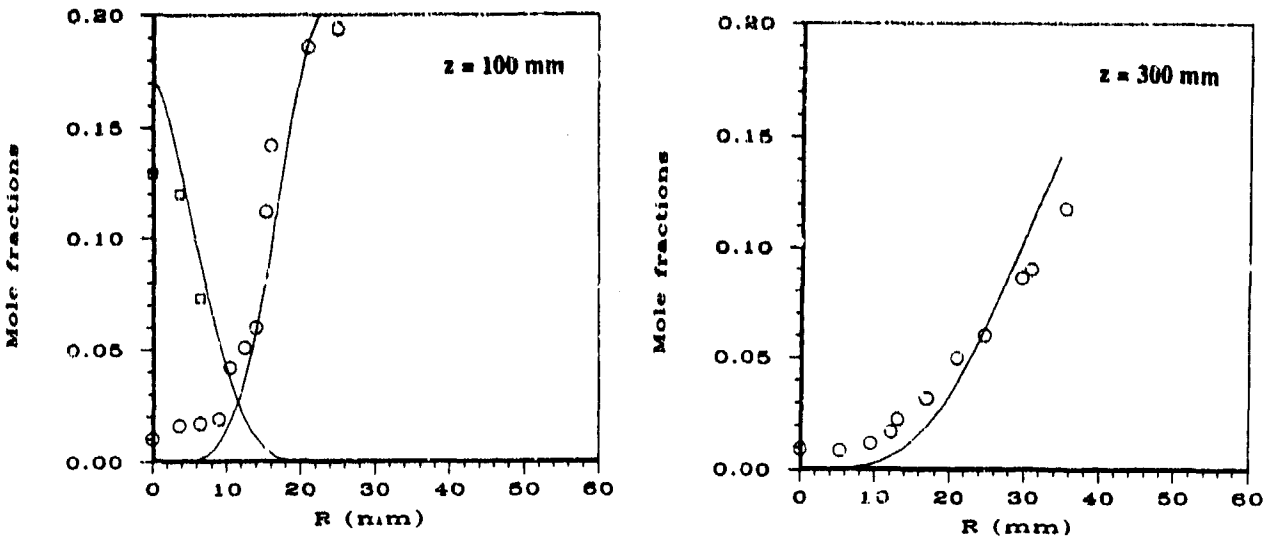

Figure 2 — Predicted and measured radial mole fraction profiles (solid lines: predictions; O: measured O_2 mole fraction; □ : measured C_3H_8 mole fraction).

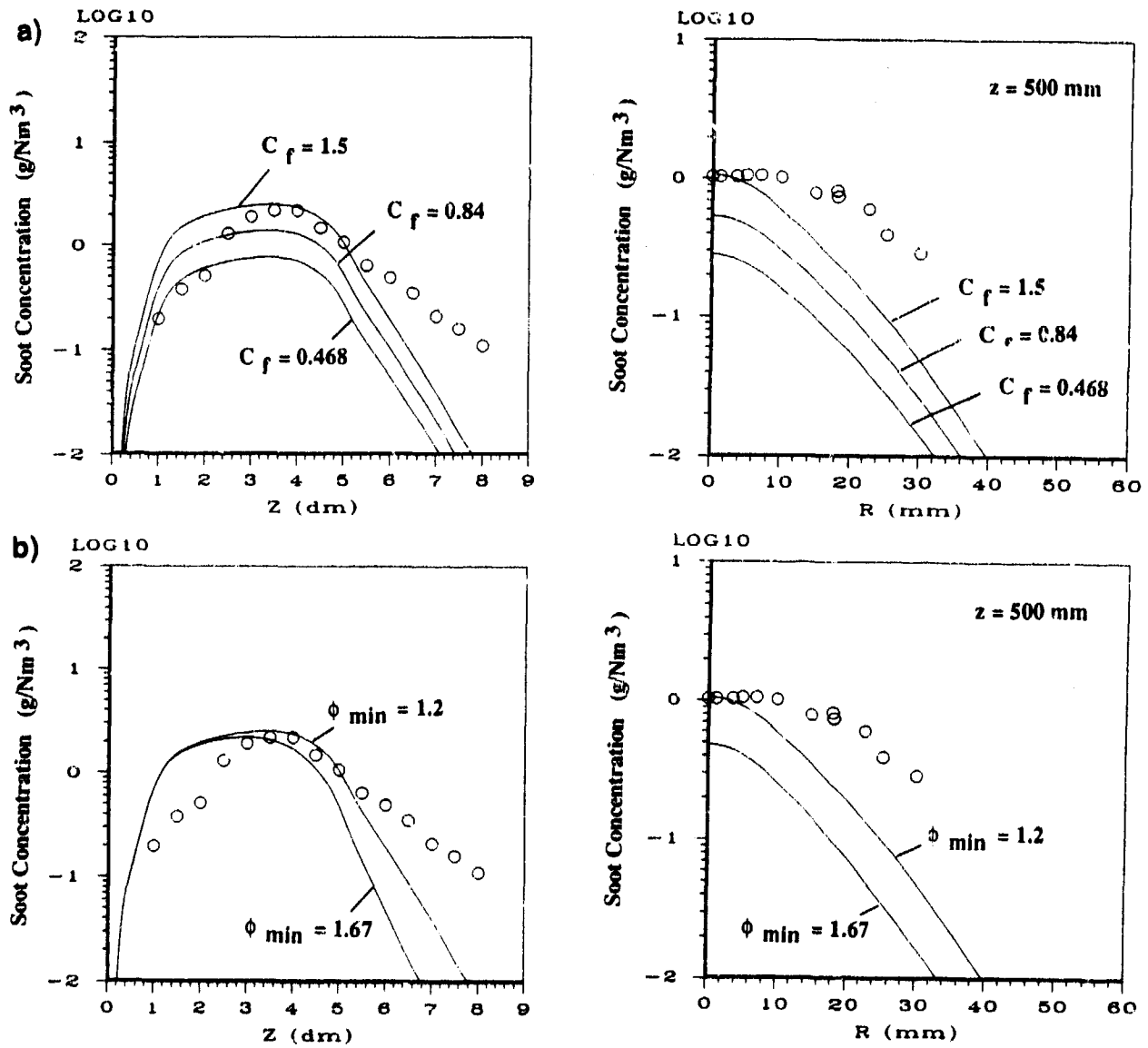

Figure 3 — Influence of constants C_f (kg N^{-1} m^{-1} s^{-1}) and ϕ_{min} of Khan and Greeves model on the predicted soot concentration (g/Nm^3).

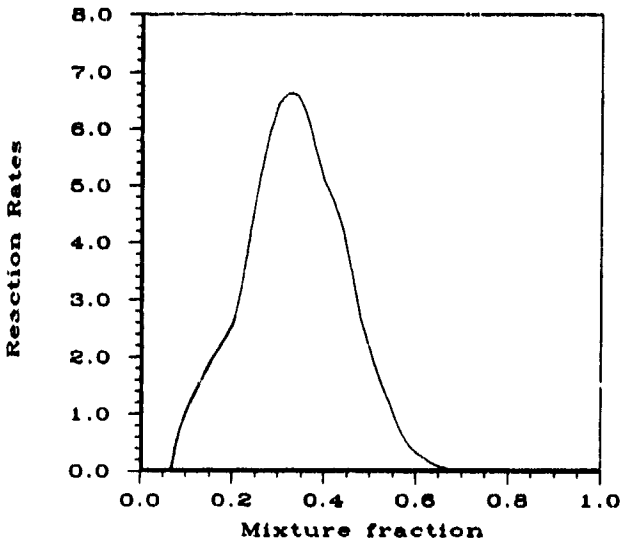

Figure 4 — Instantaneous soot formation rate (10^{-2} kg m^{-3} s^{-1}) as a function of mixture fraction according to Khan and Greeves model.

optimized proportionality constant equal to 2.54×10^6 kg N^{-1} m^{-1} s^{-1}. This yields C_f values higher than the previously mentioned ones overpredicting significantly soot concentration for the propane flame considered here. This may be due to the fact that this proportionality constant was chosen to fit the measurements of Kent and Bastin (Ref. 41) in acetylene flames whose soot propensity is greater than in propane flames. However, it is important to point out that the variation of C_f has only a quantitative influence on the computed profiles whose shape remains qualitatively similar. The value $C_f = 1.5$ kg N^{-1} m^{-1} s^{-1}, was selected and used in all the following calculations.

The influence of the value of ϕ_{min} is analysed in fig. 3b). The incipient sooting limit for propane is about C/O = 0.5 (see, e.g., Ref. 24), that is, an equivalence ratio of 1.67. This value is close to $\phi_{min} = 2$, employed by Abbas (Ref. 38), but much higher than $\phi_{min} = 0.5$, reported in ref. 40. We have compared the predictions obtained using $\phi_{min} = 1.67$ and $\phi_{min} = 1.2$ (a value below which fuel concentration is so small that yields a negligible soot formation rate). Fig. 3b) shows that an improvement of the results is achieved when $\phi_{min} = 1.2$ and, therefore, this value was selected for further calculations. The value $\phi_{max} = 8$ was also increased but it was found that is does not influence the results.

No attempt was made to change the constant n = 3 and the activation energy E/R = 20 000 K which have been employed in all previous studies. However, the instantaneous soot formation rate displayed in fig. 4 as a function of mixture fraction suggests that the exponent n = 3 is too high. The peak of soot formation occurs at f = 0.32 and this is responsible for the prediction of a faster increase of soot concentration near the burner exit when compared with the measurements.

Fig. 5 shows a comparison between the predictions of soot concentration (mass per unit volume at N.T.P.) using the soot formation model of Khan and Greeves with the set of constants selected above and three different soot oxidation models (Ref. 4, 17 and 18). The main features of the predictions are only marginally influenced by the soot oxidation model chosen. On the whole, regarding the simplicity of the soot formation model and the complexity of soot formation processes, the agreement between the predictions and the measurements may be considered good. However, there are several features of the data that are not reproduced by the predictions.

As stated above, the rate of increase of soot concentration along the centreline in the initial regions of the flow is overestimated. On another hand, the soot concentration along the centreline is underpredicted beyond z = 0.6 m, suggesting a too fast soot burn-out rate. However, this is the expected behaviour given that the temperature was overpredicted in this region. Hence, it is not possible to judge the performance of the soot oxidation models at these locations. The measured increase in radial soot concentration from the centreline to the reaction zone at axial stations z = 100 mm and z = 200 mm is not well predicted. Moreover, all the oxidation models tend to underestimate the soot burnout rate at the outer flame edge in the axial stations near the burner exit, particularly at z = 200 mm and z = 300 mm. Farther downstream (z = 400 mm, z = 500 mm) the predicted rate follows the measurements.

The comparison between the three different oxidation models shows that Magnussen et al and Lee et al models display rather similar qualitative behaviour, with a faster oxidation rate predicted by Magnussen et al model, except beyond z = 0.6 m, where the oxidation rate given by Lee et al model becomes higher. Although the predictions obtained using Nagle et al model are not significantly different from the others, this model gives a higher soot oxidation near the centreline and a smaller oxidation rate far from the centreline (see, e.g., the profile z = 400 mm).

With the available data it is not possible to decide which oxidation model is performing better because, for example, an underprediction of soot concentration may be either due to an overestimated soot oxidation rate or an underestimated soot formation rate. However, the predictions do show that for this flame, at the locations where measurements are available, the different oxidation models broadly yield qualitatively similar results.

Soot Formation Model of Moss, Syed and Stewart (Ref. 10,11)

The soot formation model of Moss and co-workers was evaluated next. The set of constants optimized by Stewart et al. in their predictions of a laminar diffusion pre-vaporised kerosene flame and the set of constant used earlier by Syed et al. in a buoyant turbulent diffusion flame of methane were tried. In both cases the model fails to predict peak soot concentration levels by at least two orders of magnitude. Soot concentration is overpredicted in the first case and underpredicted in the second one. This shows that the model is highly dependent on the constants and this is an undesirable feature if the model is to be applied to a new situation. To apply the model to the flame studied here several numerical experiments were carried out with different constants and the selected set was the following:

$C_\alpha = 10^4$ m^3 K$^{-1/2}$ kg^{-2} s^{-1}, $C_\beta = 6 \times 10^3$ m^3 K$^{-1/2}$ s^{-1}, $C_\gamma = 1$ mK$^{-1/2}$ s^{-1},

$T_\alpha = 21\,000$ K, $T_\gamma = 12\,600$ K, $M_\alpha = M_\gamma = 1$

The activation temperature for nucleation, T_α, and surface growth, T_γ are the same employed in ref. 11 and are very close to those used in ref. 15. The nucleation and surface growth rates were assumed to be linearly related to fuel mole fraction, contrary to the assumption of Stewart et al. (Ref. 10) but in agreement with Syed et al. (Ref. 11).

The motivation of Stewart et al. to increase the exponents M_α and M_γ was to displace the maximum source strength to richer mixtures, as if the reaction rates were dependent on an intermediate species rather than the parent fuel. For example, the peak of surface growth rate is shifted from f = 0.10 to f=0.34 using $M_\gamma = 3$ and to f = 0.46 using $M_\gamma = 5$. This is consistent with Khan and Greeves model which exhibits a peak of soot formation at f = 0.32 and depends on the third power of the equivalence ratio. However, if M_α or M_γ are increased, the rate of increase of soot concentration along the centreline in the neighbourhood of the burner is overestimated, as it was using Khan and Greeves soot formation model. This does not occur when $M_\alpha = M_\gamma = 1$. Moreover, Fairweather et al. (Ref. 15, 16), who have assumed that the reaction rates are linearly related to an intermediate species, acetylene, have found that the peaks in nucleation and surface growth rates occur at a mixture fraction

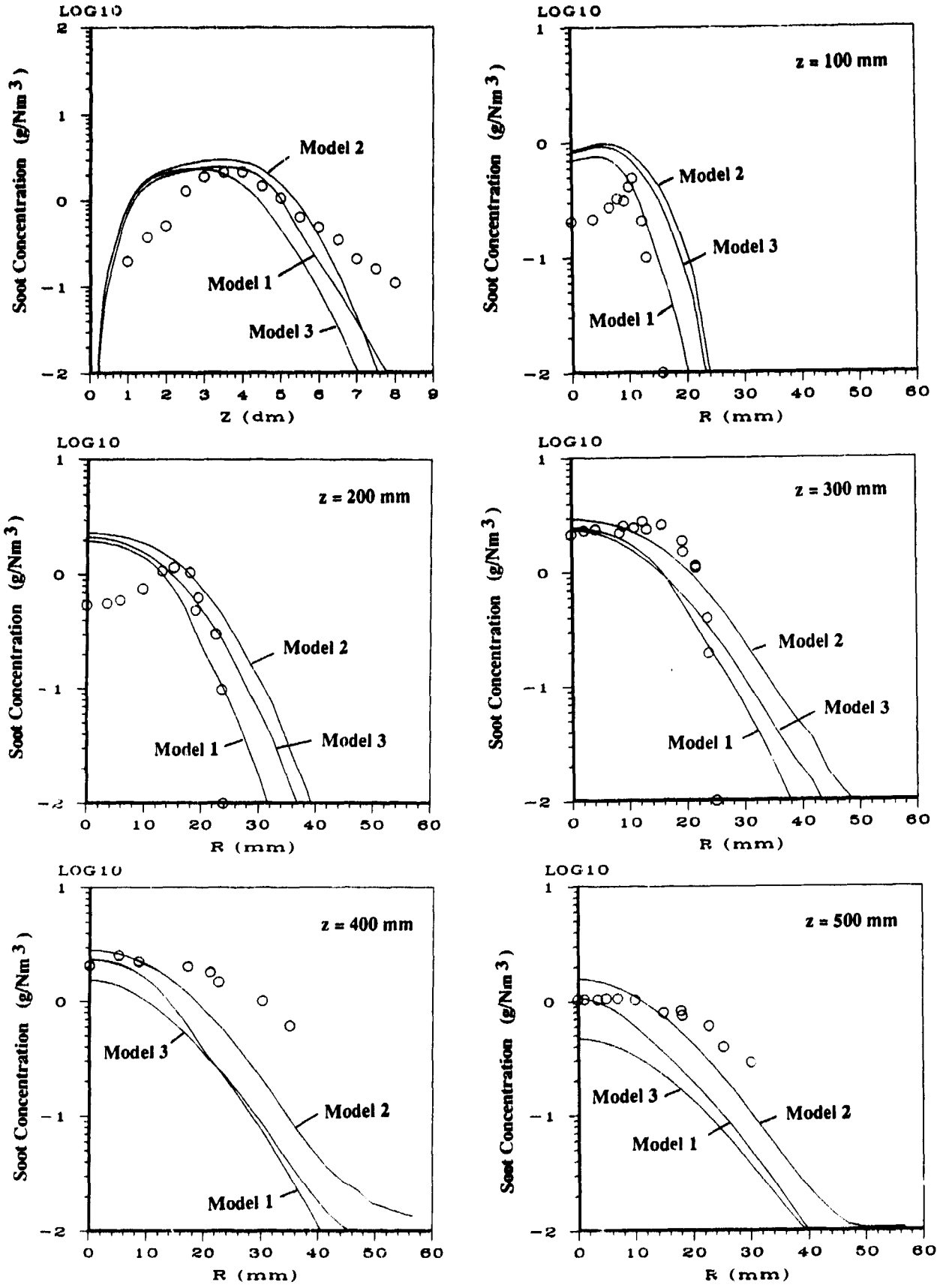

Figure 5 — Predicted and measured soot concentration (g/Nm ^{3}) profiles (solid line: predictions; symbols: measurements).
Model 1 — Soot formation: Khan et. al.; soot oxidation: Magnussen et al.
Model 2 — Soot formation: Khan et. al.; soot oxidation: Lee et al.
Model 3 — Soot formation: Khan et. al.; soot oxidation: Nagle et al.

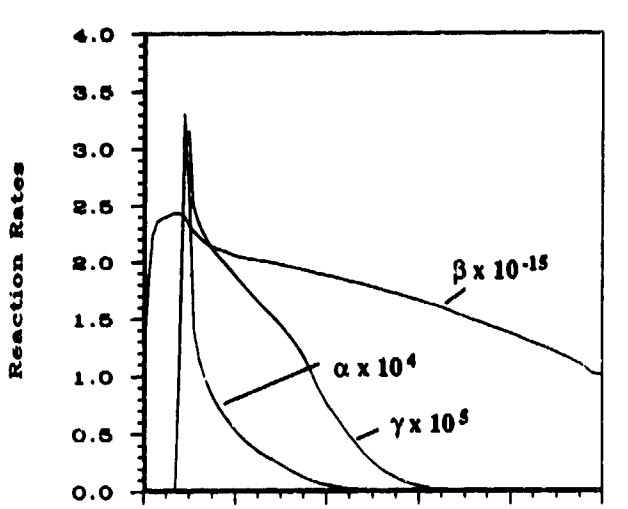

Figure 6 — Instantaneous nucleation ($\alpha x10^4$ m^{-3}s^{-1}), coagulation ($\beta x10^{-15}$m^3 s^{-1}) and surface growth ($\gamma x10^5$ kg m^{-2} s^{-1}) rate terms used in soot mass fraction and particle number density equations.

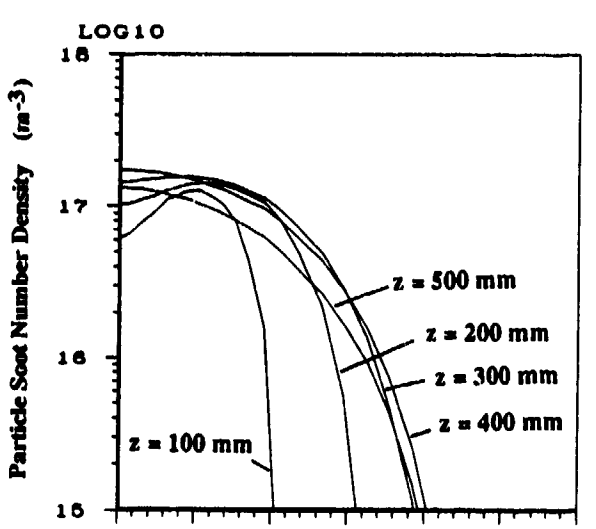

Figure 7 — Predicted radial profiles of particle soot number density (m^{-3}).

of about 0.10 (see Ref. 16).Their predicted variation of instantaneous rate terms with mixture fraction is very similar to our prediction, displayed in fig. 6.

Constants C_α and C_β were adjusted coherently to give peak values of soot particle number density of the order of 10^{17} m^{-3}. Values of this order of magnitude are generally found in the measurements available in the literature (see, e.g., Ref. 11 and 42). This observation is the basis for the prescription of an average number density in Kennedy et al. model (Ref. 12, 13). The predicted radial profiles of soot particle number density are shown in fig. 7.

Constant C_γ was tuned together with C_α and C_β to give soot concentration profiles close to the measurements and to provide a dominance of surface growth relative to nucleation, as occurs throughout most laminar diffusion flames (Ref. 43). The source terms of the soot mass fraction transport equation due to surface growth and nucleation rates are displayed in fig. 8. The peak of surface growth rate is three times larger than the peak of nucleation rate. The surface growth rate prevails over the nucleation rate except near the flame front. Both rates increase up to z = 400 mm and decrease farther downstream. These evolutions are consistent with those calculated be Stewart et al. (Ref. 11).

The computed soot concentration profiles are presented along with the measurements in fig. 9. The three oxidation models mentioned above were used again. It is evident from the figures that, after tuning the constants appropriately, the soot formation model of Moss and co-workers yields better predictions than Khan's model. This is not surprising since the physical processes embodied in Moss et al. model are a much better description of reality than the simple kinetic expression used in Khan's model.

Fig. 9 shows that the rate of increase of soot concentration along the centreline closely follows the measurements in the initial flow region and the radial increase of soot concentration at z = 100 mm is also predicted reasonably well. Nevertheless, the rate of soot oxidation in the post-flame region remains underpredicted at z = 200 mm and z = 300 mm. It may happen that the oxidation due to OH radicals, as suggested for example, in Ref. 20, plays an important role here. This would explain why none of the oxidation models employed follows the measured trend. The relative behaviour of the oxidation models is similar to that analysed earlier together with Khan and Greeves soot formation model.

Comparison of Soot Formation Models

Finally, a comparison of three different soot formation models is illustrated in fig. 10. The soot formation models of Khan and Greeves (Ref. 2) and Stewart et al. (Ref. 11), coupled with the oxidation model of Magnussen et al. (Ref. 4), are compared with the predictions of Fairweather et al. (Ref. 15) using their own soot formation model along with the soot oxidation model of Lee et al. (Ref. 18). Fairweather's model had been applied previously to laminar counterflow ethylene and propane flames (Ref. 14) and it was applied almost in the same form to the propane flame of Nishida et al. (Ref. 21) considered here. Only the oxidation rate constant was modified. The agreement between Fairweather's model predictions and the measurements (Ref. 21) suggests that the model is much less sensitive to different flames and conditions than Moss and co-workers model.

Fairweather's soot formation model significantly underestimates soot concentration in the flow region near the burner (see the radial profile z = 100 mm in fig. 10) but it performs as well as the other models or even better farther downstream. Indeed, the radial decrease of soot concentration at z = 400 mm and z = 500 mm is simulated more accurately using Fairweather's model. This model, like the others, underestimates soot oxidation at z = 200 mm and z = 300 mm, supporting the hypothesis of the influence of a physical phenomenon not taken into account or not modelled correctly. This may be the soot oxidation due to OH radicals.

3.2. Prediction of Soot Concentration from extinction measurements

Soot concentration measurements of Nishida et al (Ref. 21) were obtained using a soot sampling probe. However, in many experiments soot concentration is determined from extinction measurements assuming a spherical particle shape with a size parameter satisfying the Rayleigh limit as mentioned in the introduction (e.g., Ref. 1, 8). This assumption and the influence of the refractive index are analysed below.

The present section is divided in two parts: in the first one the influence of agglomeration on soot volume fraction predictions based on extinction measurements is studied. The size of the

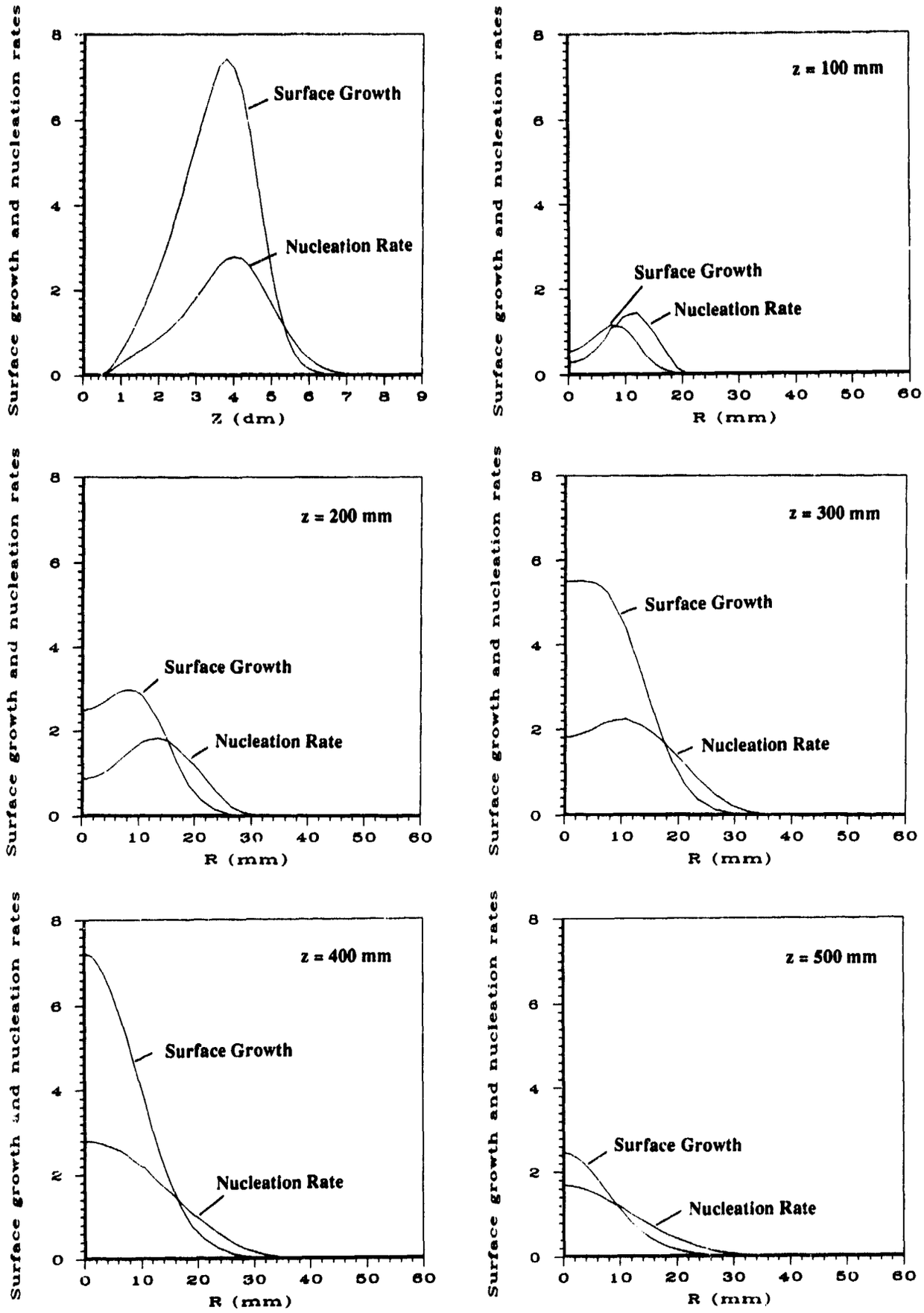

Figure 8 — Source terms for surface growth and nucleation (kg m^{-3} s^{-1}).

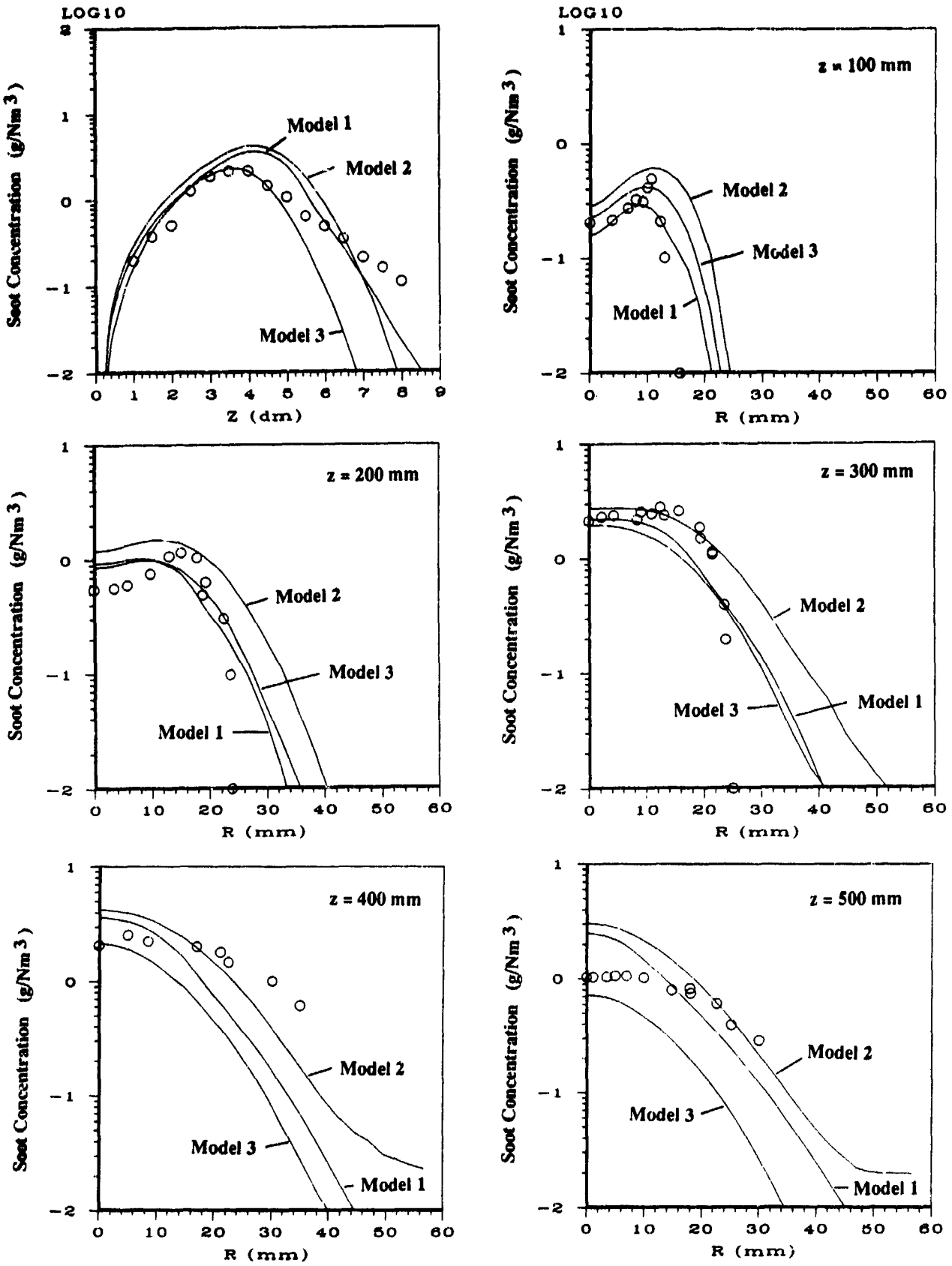

Figure 9 — Predicted and measured soot concentration (g/N m ^{3}) profiles (solid lines: predictions; symbols: measurements).
Model 1 — Soot formation: Moss et. al.; soot oxidation: Magnussen et al.
Model 2 — Soot formation: Moss et. al.; soot oxidation: Lee et al.
Model 3 — Soot formation: Moss et. al.; soot oxidation: Nagle et al.

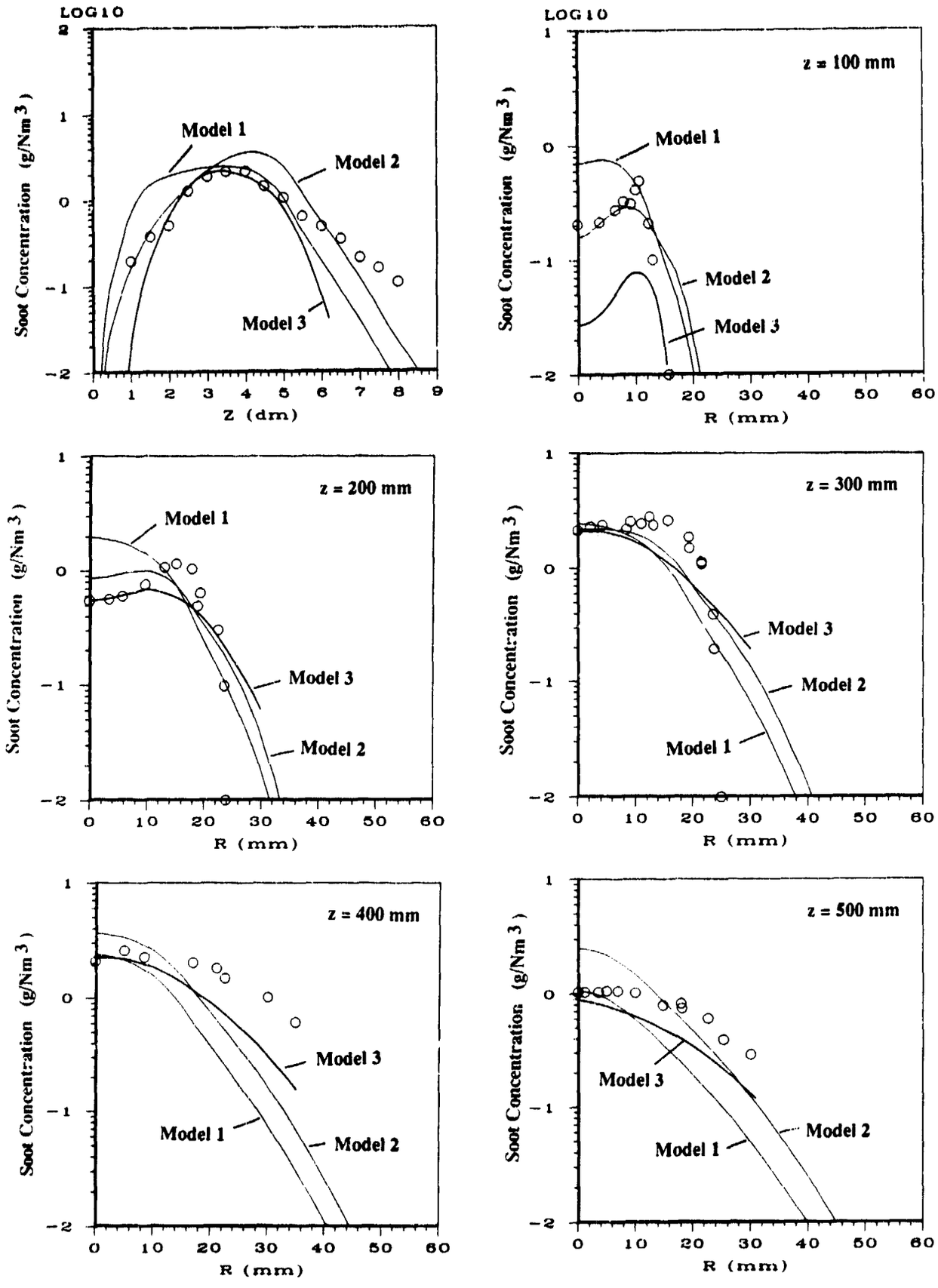

Figure 10 — Predicted and measured soot concentration (g/N m ^{3}) profiles (solid lines: predictions; symbols: measurements).
Model 1 — Soot formation: Khan et. al.; soot oxidation: Magnussen et al.
Model 2 — Soot formation: Moss et. al.; soot oxidation: Magnussen et al.
Model 3 — Predictions of Fairweather et al. (1992).

agglomerates, the dimension of the primary particles, the fractal number of the agglomerates generated and the homogeneity or heterogeneity of the sample studied are taken into consideration. The second part deals with the influence of the real and imaginary parts of the soot refractive index both when soot particles are considered to be small and spherical (Rayleigh limit approximation) and when agglomeration is assumed (ICP calculations).

Preliminary Considerations

To create soot agglomerates a computer code was developed capable of generating different agglomerates randomly. The size of the sample to be created (number of agglomerates to be generated) is introduced and the number of particles of each agglomerate and the respective diameter can be chosen following log-normal and normal pdfs respectively (see Ref. 22). Mean values and standard deviations both for the number of particles and diameters are introduced and the upper and lower limits for the fractal dimension of the agglomerate may be selected by the user.

For soot volume fraction calculations an extinction coefficient of $1m^{-1}$ was assumed. The reference values used for the primary particle size parameter, wavelength, geometric mean value of number of primary particles and refractive index are 0.19, 488 nm, 50 and 1.72+i0.62 respectively (the later was taken from the expressions presented by Chang and Charalampopoulos, Ref. 44). Concerning the fractal dimension values of 1.7 and 1.8 were assigned for the lower and upper limits, respectively. For each soot agglomerate studied results were calculated for 20 different orientations in space. An increase in the number of directions would not change the soot volume fraction predictions in more than one percent. The orientations were selected to equally cover the entire 4π solid angle.

Influence of Agglomeration on Soot Volume Fraction Predictions

Several test were performed to analyse the influence of considering the sample of agglomerates as homogeneous or heterogeneous. For that purpose the number of particles of each agglomerate was chosen to match a log-normal pdf with a geometric mean value and standard deviation varying from 10 to 100 and 1 to 3 respectively. For the cases where the standard deviation was greater than one 20 agglomerates were created to cover the log-normal pdf curve. Typical mean diameters of soot primary particles were studied (primary particle size parameter between 0.01 and 0.5). The reference values presented above were adopted for the complex refractive index, the fractal dimension and the extinction coefficient. The differences found in the results obtained never exceeded 5% and for that reason only the calculations for homogeneous samples are shown in fig. 11 and 12.

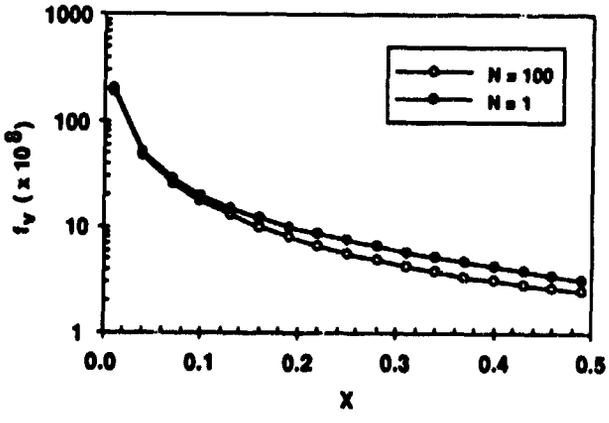

Figure 11 — Volume fraction (m_s^3/m^3) dependency on soot primary particle size parameter and agglomeration.

Fig. 11 shows the influence of the primary particle size parameter and the size of the agglomerates on the soot volume fraction predictions. It can be concluded that for typical values of the primary particle size parameter (between 0.01 and 0.3) soot volume fractions may change by a factor of more than 10. In the range where Rayleigh calculation are acceptable, results obtained with this approximation always overpredict the ICP calculations.

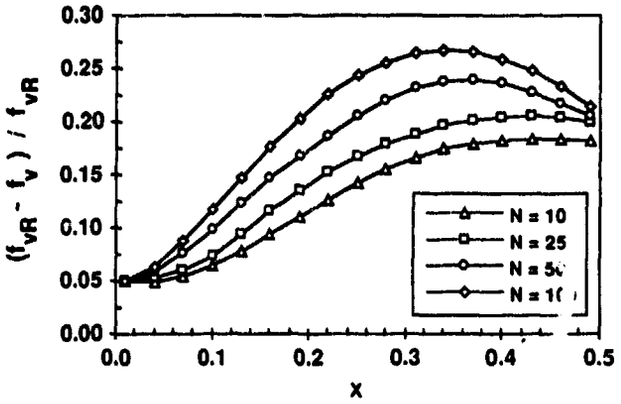

Figure 12 — Influence of agglomeration on soot volume fraction (m_s^3/m^3) calculations for different size parameters: f_{vR} — Rayleigh calculations; f_v — ICP calculations.

Relative differences between Rayleigh and ICP results are depicted in fig. 12. For small size parameters ($x<0.01$) neglecting agglomerations yields deviations lower than 5%. Nevertheless, with the increase of the size parameter, this deviation tends to become more notorious, especially for larger agglomerates. Results shown in fig. 12 for $x>0.3$ should not be considered valid as Rayleigh calculations are no longer acceptable. According to equation 1, soot volume fraction calculations based on Rayleigh approximation are independent of the size of the particle. Therefore, in order to reduce the influence of agglomeration on volume fraction calculations it is preferable, when possible, to use high values of wavelengths in extinction experiments. This way an increase in the size parameter can be avoided.

Influence of Refractive Index on Soot Volume Fraction Predictions

The influence of the refractive index on volume fraction when considering soot particles as small spheres can be seen in fig. 13a). The reference values required to evaluate soot volume fractions were the ones mentioned above — correcting present results to any new values appropriate to a specific extinction measurement (namely wavelength and extinction coefficient) only involves a simple ratio. Fig. 13a) illustrates that the soot volume fractions are more sensitive to variations in the imaginary part of the refractive index. While covering the range of values studied for k, soot volume fractions may change by a factor greater than 2. The influence of the real part, n, on soot volume fraction is not so significant but it should not be neglected — results may vary in the range of 0.5 to 0.8 These conclusions (in agreement with the ones reported in ref. 45) will be helpful when analysing and comparing similar results for soot agglomerates.

In fig. 13b) the same calculations are shown, but taking agglomeration into account. For conciseness only the results for a 50 particle agglomerate are shown. The very strong dependency of f_v on the real and especially the imaginary part of the refractive index becomes less notorious when agglomeration is considered. This can also be confirmed by the results shown in fig. 14 where the relative difference between the maximum and the minimum values of f_v are depicted. It is also interesting to notice that the influence of agglomeration on the calculation of soot volume fractions becomes small (less than 10% for

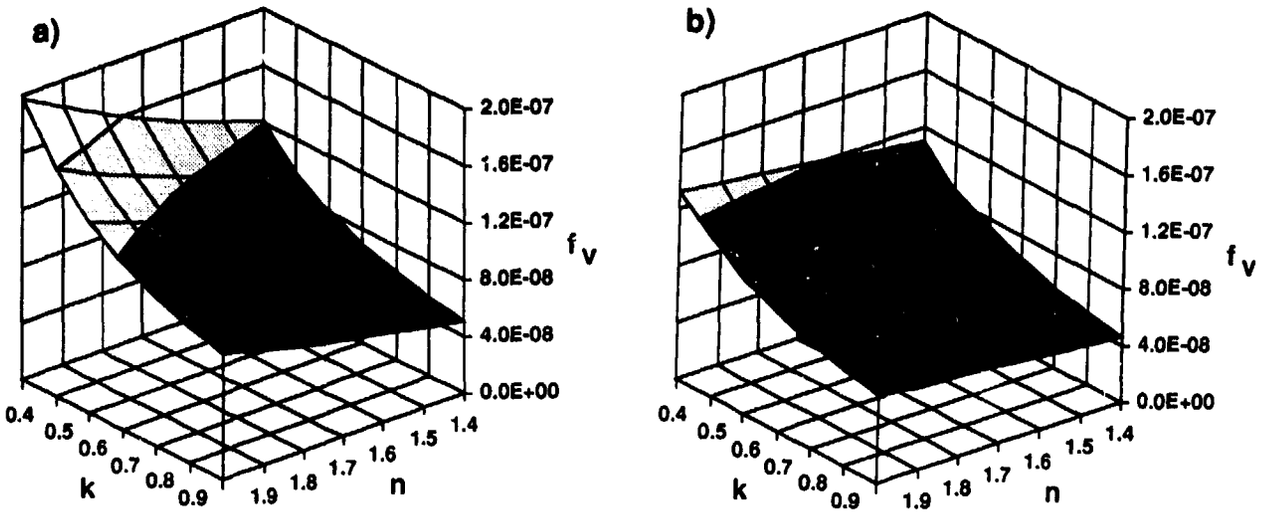

Figure 13 — Influence of the complex refractive index on soot volume fraction (m_s^3/m^3)calculations: a) spherical particles (Rayleigh approximation); b) aggregates of 50 spherical primary particles (ICP method).

agglomerates up to 100 particles) for low values of the real part of the refractive index, independently of the imaginary part. This suggests that special care should be taken when selecting the imaginary part of the refractive index. As for the real part, it is preferable to adopt a low value. This way Rayleigh results become closer to ICP, the latter ones being less dependent on the real part of refractive index.

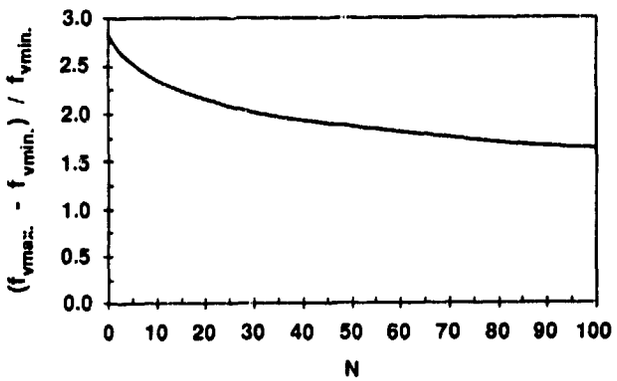

Figure 14 — Maximum relative deviations of soot volume fractions for the range of the real and imaginary parts of the refractive index studied.

4. CONCLUSIONS

Several soot formation and oxidation models were applied to the calculation of a turbulent propane diffusion flame and the results were compared with experimental values of soot concentration.

From the analysis carried out it may be concluded that caution should be taken if Moss and co-workers soot formation model is to be applied to a new situation, due to its strong dependence on the set of constants. Khan and Greeves soot formation model, despite its simplicity and more limited physical basis, is not so much influenced by the constants and it seems to yield the correct orders of magnitude, although it is not adequate if reasonably good quantitative predictions are sought. The soot formation model of Fairweather et al. appears to be much less sensitive to the constants than Moss and co-workers model and, given its better physical basis, it seems to have a good potential for application to new situations. Nevertheless, we believe that there is still a lot of work to do before soot formation and oxidation models have achieved a level of accuracy and reliability comparable with presently available turbulence and combustion models.

The influence of soot agglomeration and soot refractive index on the values of soot volume fraction obtained from extinction measurements was analysed. For low values of the primary particle size parameter ($x<0.01$) agglomeration may be neglected. Nevertheless, with the increase of the size parameter, the deviations between calculations assuming soot particles to be spherical and taking agglomeration into consideration might increase up to 25 %, for the range of aggregates studied.

Although agglomeration influences the calculations of soot volume fractions, it is the refractive index that contributes to the larger uncertainties. When agglomeration is neglected, and covering the typical values for the real and imaginary parts of the refractive index, results may change by a factor greater than 3. Nevertheless, with agglomeration this strong dependency tends to decrease. Additionally, for low values of the real part of the refractive index, the influence of agglomeration becomes less notorious. This suggest that, when agglomeration is not taken into account, the value of the imaginary part of the refractive index should be selected carefully, while the real part should stay closer to the lower values studied.

ACKNOWLEDGMENTS

The authors acknowledge the Ph. D. scholarship BD/860/90-IB of CIENCIA Program - JNICT.

REFERENCES

1. Mullins, J., Simmons, B. and Williams, A., "Rates of Formation of Soot from Hydrocarbon Flames and its Destruction", AGARD CP-422, 1987, paper 23.
2. Khan, I.M. and Greeves, G., "A Method for Calculating the Formation and Combustion of Soot in Diesel Engines" in "Heat Transfer in Flames", Afgan, N.H. and Beer, J.M. (Ed.), Scripta Book Co., Chapter 25, 1974.
3. Tesner, P.A., Snegiriova, T.D. and Knorre, V.G., "Kinetics of Dispersed Carbon Formation", Combustion and Flame, 17, 1971, pp. 253-260.
4. Magnussen, B.F., Hjertager, B.H., "On Mathematical Modelling of Turbulent Combustion with Special Emphasis on Soot Formation and Combustion", 16th Symp. (Int.) on Combustion, The Combustion Institute, 1977, pp. 719-728.

5. Ahmad, T., Plee, S.L. and Myers, "Computation of Nitric Oxide and Soot Emissions from Turbulent Diffusion Flames", J. Eng. Gas Turbines and Power, *107*, January 1985, pp. 48-53.
6. Gore, J.P. and Faeth, G.M., "Structure and Spectral Radiation Properties of Turbulent Ethylene /Air Diffusion Flames", 21st Symp. (Int.) on Combustion, The Combustion Institute, Pittsburgh, 1986, pp. 1521-1531.
7. Kent, J.H. and Honnery, D., "Soot and Mixture Fraction in Turbulent Diffusion Flames", Combust. Sci. and Technol., *54*, 1987, pp. 383-397.
8. Moss, J.B., Stewart, C.D. and Syed, K.J., "Flamelet Chemistry Modelling of Soot Formation for Radiation Prediction in Combustor Flow Fields", AGARD CP-422, 1987, paper 18.
9. Moss, J.B., Stewart, C.D. and Syed, K.J., "Flowfield Modelling of Soot Formation at Elevated Pressure", 22nd Symp. (Int.) on Combustion, The Combustion Institute, 1988, pp. 413-423.
10. Syed, K.J., Stewart, C.D. and Moss, J.B., "Modelling Soot Formation and Thermal Radiation in Buoyant Turbulent Flames", 23rd Symp. (Int.) on Combustion, The Combustion Institute, 1990, pp. 1533-1541.
11. Stewart, C.D., Syed, K.J. and Moss, J.B., "Modelling Soot Formation in Non-Premixed Kerosene-Air Flames", Combust. Sci. and Technol., *75*, 1991, pp. 211-226.
12. Kennedy, I., Kollmann, W. and Chen, J.-Y., "A Model for Soot Formation in a Laminar Diffusion Flame", Combustion and Flame, *81*, 1990, pp. 73-85.
13. Kennedy, I., Kollmann, W. and Chen, J.-Y., "Predictions of Soot in Laminar Diffusion Flames", AIAA J., *29*, 9, September 1991, pp. 1452-1457.
14. Leung, K.M., Lindstedt, R.P. and Jones, W.P., "A Simplified Reaction Mechanism for Soot Formation in Non-Premixed Flames", Combustion and Flame, 87, 1991, pp. 289-305.
15. Fairweather, M., Jones, W.P., Ledin, H.S. and Lindstedt, R.P., "Predictions of Soot Formation in Turbulent, Non-Premixed Propane Flames", 24th Symp. (Int.) on Combustion, 1992.
16. Fairweather, M., Jones, W.P. and Lindstedt, R.P., "Predictions of Radiative Transfer From a Turbulent Reacting Jet in a Cross-Wind", Combustion and Flame, *89*, 1992, pp. 45-63.
17. Nagle, J. and Strickland-Constable, R.F., "Oxidation of Carbon Between 1000°-2000°C", Proc. 5th Conference on Carbon, Pergamon, *1*, 1961, p. 154.
18. Lee, K.B., Thring, M.W. and Beer, J.M., "On the Rate of Combustion of Soot in a Laminar Soot Flame", Combustion and Flame, *6*, 1962, pp. 137-145.
19. Neoh, K.G., Howard, J.B. and Sarofim, A.F., "Soot Oxidation in Flames", in "Particulate Carbon Formation During Combustion", Siegla, D.C. and Smith, G.W. (Eds), Plenum Press, 1981.
20. Garo, A., Prado, G. and Lahaye, J., "Chemical Aspects of Soot Particles Oxidation in a Laminar Methane-Air Diffusion Flame", Combustion and Flame, *79*, 1990, pp. 226-233.
21. Nishida, O. and Mukohara, S., "Characteristics of Soot Formation and Decomposition in Turbulent Diffusion Flames", Combustion and Flame, *47*, 1982, pp. 269-279.
22. Köylü, U.O. and Faeth, G.M., "Structure of Overfire Soot in Buoyant Turbulent Diffusion Flames at Long Residence Times", Combust. Flame, *89*, 1992, pp. 140-156.
23. Köylü, U.O, "Emission Structure and Optical Properties of Overfire Soot From Buoyant Turbulent Diffusion Flames", Ph.D. Thesis, The University of Michigan, Ann Arbor, Michigan, 1992.
24. Wagner, H., "Soot Formation in Combustion", 17th Symp. (Int.) on Combustion, The Combustion Institute, 1979, pp. 3-19.
25. Dobbins, R.A. and Megaridis, C.M., "Absorption and Scattering of Light by Polydisperse Aggregates", Appl. Optics, *30*, 1992, pp. 4747-4754.
26. Felske, J.D., Hsu, P.F., and Ku, J.C., "The Effect of Soot Particle Optical Inhomogeneity and Agglomeration on the Analysis of Light Scattering Measurements in Flames", J. Quant. Spectrosc. Radiat. Trans., *35*, 1986, pp. 447.
27. Pope, S.B., "An Explanation of the Turbulent Round-Jet/Plane-Jet Anomaly", AIAA J., *16*, 3, March 1978, pp 279-291.
28. Crauford, N.L., Liew, S.K. and Moss, J.B., "Experimental and Numerical Simulation of a Buoyant Fire", Combustion and Flame, *61*, 1985, pp. 63-77.
29. Penndorf, R.B., J. Opt., Soc. Am., *52*,1962, 896.
30. Ku, J.C. and Felske, J.D., J. Quant. Spect. Rad. Transf., *31*, 6, 1984, pp. 569-574.
31. Ku, J.C. and Shim, K.H., "Optical Diagnostics and Radiative Properties of Simulated Soot Agglomerates", J. Heat Trans., *113*, 1992, pp. 953-958.
32. Iskander, M.F., Chen, H.J. and Pemier J.E., App. Opt., *28*, 1989, pp. 3083-3091.
33. Purcel, E. M. and Pennypacker, C. R., Astrophysics J., *186*, 1973, p. 705.
34. Jones, A.R., "Electromagnetic Wave Scattering by Assemblies of Particles in the Rayleigh Approximation", Proc. R. Soc. London A *366*, 1979, pp. 111-127.
35. Jones, A.R., "Scattering Efficiency Factors for Agglomerates of Small Spheres", J. Phys. D: Appl. Phys., *12*, 1979, pp. 1661-1672.
36. Ku, J.C., J. Phys. D: Appl. Phys., *24*, 1991, pp.71-75.
37. Drolen, B.L. and Tien, C.L., "Absorption and Scattering of Agglomerated Soot Particulate", J. Quant. Spectrosc. Radiat. Transfer, *37*, 5, 1987, pp. 433-448.
38. Abbas, A.S., "The Prediction of the Performance of Heavy Oil-Fired Combustors", Ph.D Thesis, University of London, 1982.
39. Dalzell, W.D., Williams, G.C. and Hottel, H.C., "A Light-Scattering Method for Soot Concentration Measurements", Combustion and Flame, *14*, 1970, pp. 161-170.
40. Abbas, A.S. and Lockwood, F.C., "Prediction of Soot Concentration in Turbulent Diffusion Flames", J. Institute of Energy, September 1985, pp. 112-115.
41. Kent, J.H. and Bastin, S.J., "Parametric Effects on Sooting in Turbulent Acetylene Diffusion Flames", Combustion and Flame, *56*, 1984, pp. 29-42.
42. Vandsburger, U., Kennedy, I.M. and Glassman, I., "Sooting Counterflow Diffusion Flames with Varying Oxygen Index", Combust. Sci. Technol., *39*, 1984, pp. 263-285.
43. Glassman, I., "Soot Formation in Combustion Processes", The Combustion Institute, 22nd Symp. (Int.) on Combustion, The Combustion Institute, 1988, pp. 295-311.
44. Chang, H., and Charalampopoulos, T.T., "Determination of the Wavelength Dependence of Refractive Indices of Flames Soot", Proc. R. Soc. London A., *430*, 1990, pp. 577-591.
45. Charalampoppoulos, T.T., "Morphology and Dynamics of Agglomerated Particulates in Combustion Systems using Light Scattering Techniques", Prog. Energy Combust. Science, *18*, 1992, pp. 13-45.

Discussion

Question 1. U. Schumann
What is the size of the soot being formed, and what are its properties with respect to cloud condensation nuclei? These properties are of environmental importance.

Author's Reply
These properties cannot be predicted by the models considered in this study. Moreover, the authors are not aware of any theoretical model that can predict such properties. This also applies to the size of the soot particles.

As stated in the paper, experiments have shown that in the early stages of formation soot particles are approximately spherical and have mean diameters between 10 and 60 nanometres (see Ref. 22). These particles tend to agglomerate during their evolution forming chain-like clusters whose equivalent size parameter most frequently exceeds one. Such information cannot be theoretically predicted at present.

NUMERICAL MODELLING OF TURBINE COMBUSTION CHAMBERS

by

S. Maidhof and J. Janicka
Institut für Energie- und Kraftwerkstechnik
Technische Hochschule Darmstadt
Petersenstrasse 30
6100 Darmstadt
Germany

SUMMARY

The Paper focuses on the calculation of the flow and scalar fields of axisymmetric gas turbine combustion chambers with non-premixed combustion. Modelling of the turbulent swirling flow is carried out both by eddy viscosity and Reynolds stress closure. It is the intention to specify the shortcomings as well as the potential of the different schemes with regard to prediction capabilities, numerical performance and economic worth. The various aspects of modelling are discussed. A short description of the governing transport equations as well as the turbulence closure is given. An equilbrium chemistry model is compared to a laminar flamelet model, both schemes applied in conjunction with a probability density formulation for scalar properties. Numerical results of velocities and temperature in model gas turbine combustion chambers are compared with experimental results. Probable reasons for deviations are deduced and some prospects for possible future development of numerical simulation of gas turbine combustion are given.

NOMENCLATURE

C_{1-4}, C_ϵ	turbul. model consts.
B	Arrhenius factor
D	diffusion coefficient
E	activation energy
f	mixture fraction
k	turbulence kinetic energy
P	static pressure
$P(f)$	probab. density function
r	radius
S_Φ	source term of variable Φ
$\tilde{U}_i$	cartesian mean velocity
u_i''	fluctuating cartesian velocity
$\tilde{U}, \tilde{V}, \tilde{W}$	mean velocities
u'', v'', w''	fluctuating velocities
x	mass fraction
x_i	cartesian coordinates
Γ	diffusion coefficient
δ_{ij}	Kronecker symbol
ϵ	turb. kin. energy dissipation
ϵ_Φ	scalar dissipation rate
Φ	any variable, scalar or velocity
$\Phi_{ij}, \Phi_{i,c}$	pressure strain interaction
ρ	density

superscripts

$\tilde{}$	density aver. mean quantity
$''$	density aver. fluct. quantity
$\bar{}$	time aver. mean quantity
$'$	time aver. fluct. quantity

subscripts

i, j, k, l	vector components
c	scalar
ij	tensor component
i, c	scalar flux
n	normal

1 INTRODUCTION

Gas turbine chambers are a typical example for common engineering practice: while the overall perfor-

Presented at an AGARD Meeting on 'Fuels and Combustion Technology for Advanced Aircraft Engines', May 1993.

mance is well understood and the period of successfull operation has been lasting since many years, the detailed computer simulation ist just beginning to be no longer in its infancy. The present state of knowledge however shows the perspective of a rapid evolution towards computing tools which allow for a real prediction. This is not yet reality, many questions still remaining unanswered, but there exists a clear list of research tasks to be attacked. It is the distinct need for a high level simulation by specific questions such as nitric oxide formation, turbine charge by peak temperatures or sedimentations of carbon. Simulation of physical processes usually comprise several models each covering a specific aspect. The quality of the overall model performance is restricted by the quality of the weakest sub model. Therefore it is evident that a balance of features between the models has to be maintained in order to guarantee a progressing general result. The various aspects of modelling shall be discussed in greater detail in the next section. Examples of computations are provided afterwards. Model development, testing and validation can best be performed in simple 2d geometries, excluding numerical uncertainties and keeping computing time within realistic boundaries. This demand is in good agreement with experimental work which certainly is most reliable under simple conditions. However there is also the need for developing computer code for complex 3d flow surroundings, based upon lower models, but ready to adopt higher ones as soon as those are approved.

2 MODELLING ASPECTS

2.1 Radiation Model

Radiative temperature loss with respect to adiabatic burning temperature is roughly directly proportional to the combustion chamber volume divided by the total mass flux. The ratio chamber volume to mass flux is for gas turbine combustors usually smaller than for any other industrial furnaces and therefore radiation seems to be negligible. But, as will be pointed out below, there is the need for a detailed radiation model, as the nitric oxide formation is extremely sensitive to heat loss by radiation The potential for developing a complete radiation model is large, but the task is more than complex. In a finite volume environment flux models show the best relation between quality and computational effort. It is not only the radiation model itself which is complicated, but also the question how to use the additional information. A pdf formulation for scalars must then be expanded to a 4 parameter model (mixture fraction, enthalpy and their variances). Employing a laminar flamelet model introduces the local strain rate as an additional argument.

As long as those fundamental problems have not been solved sufficiently, the effort from consideration of radiation in a gas turbine combustor is uncertain.

2.2 Combustion Model

Attention shall be restricted to gas diffusion flames. This environment is the simplest compared to premixed flames or spray flames and thus offers the opportunity of emphasising the study of turbulence models in reactive systems without having to pay too much attention to reaction kinetics or two phase problems. Two approaches treating chemical reactions are most frequently applied to non-premixed flames: the chemical equlibrium assumption [3] and the laminar flamelet model [10]. Both schemes relate all scalar quantities as temperature, density, molecular viscosity and extinction coefficients to a conserved scalar variable, the mixture fraction, which can be interpreted as the conservation of the number of atoms despite chemical reaction. The second quantity the scalars depend on is the degree of radiation, varying from adiabatic conditions to a state when all heat is emitted. Applying a laminar flamelet model to a system considering radiation raises the question how enthalpy in addition to mixture fraction and a strain parameter can be integrated into the derivation of the scalar quantities.

2.3 NO_x Model

Whatever model for chemical reactions and for nitric oxide in diffusion flames is employed, three statements are always valid

- only a small percentage of the combustor volume (or the computing grid points) produce nearly the total amount of NO
- the typical length scale associated with NO formation is far below the smallest possible numerical grid spacing
- NO formation is highly sensitive to radiative heat loss

All three points can be visualized with a 3dimensional graphics showing the NO source term as a function of mixture fraction and radiation degree.

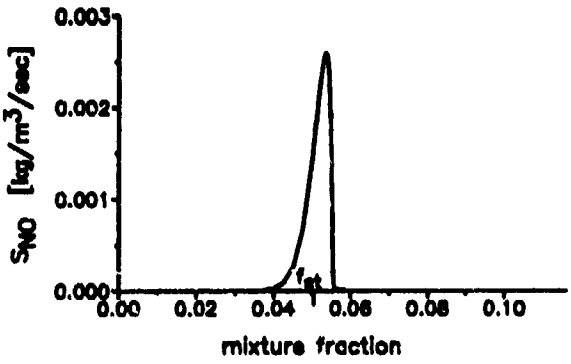

Fig. 1 NO source term for CH_4 at radiation degree zero

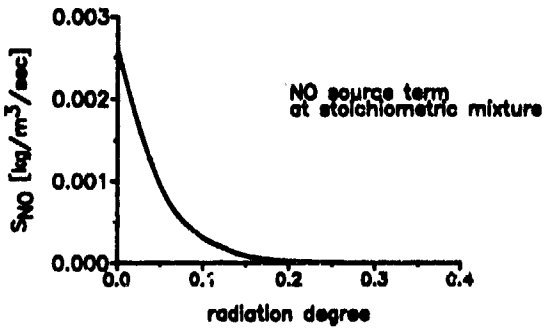

Fig. 2 NO source term for CH_4 at stoichiometric mixture

Starting point for nitric oxide emissions computations is the transport equation for NO

$$\overline{\rho}\frac{\partial \widetilde{x}_{NO}}{\partial t} + \overline{\rho}\widetilde{u}_j\frac{\partial \widetilde{x_{NO}}}{\partial x_j} = \frac{\partial}{\partial x_j}\left(\overline{\rho}D\frac{\partial \widetilde{x}_{NO}}{\partial x_j} - \overline{\rho}\widetilde{x''_{NO}u''_j}\right) + \widetilde{S}_{NO} \qquad (1)$$

Integrated over the whole furnace yields

$$\int_{A_{outlet}} \overline{\rho}\widetilde{U_n}\widetilde{x}_{NO}\,dA = \int_{Vol} \widetilde{S}_{NO}\,dVol \qquad (2)$$

This means, the amount of NO which is transported out of the chamber is equal to the volume integral over the NO source term. The task is to determine the source term. Peters [14] derives a formation rate from the Zeldovich mechanism under the assumption of stationarity of N radicals and of equilibrium between O and O_2

$$\rho\frac{\partial x_{NO}}{\partial t} = \rho B\frac{M_{NO}}{M_{N_2}}x_{N_2}\sqrt{x_{O_2}}\sqrt{\frac{\rho}{M_{O_2}}}$$
$$exp(-\frac{E}{T}),\ B = 5.74\ 10^{14}(cm^3/mole)^{0.5}/sec$$
$$E = 66900K \qquad (3)$$

This expression contains the mass concentrations of nitrogen and oxygen, temperature and density, all of which are functions of mixture fraction and radiation degree. It can therefore be computed in advance and stored as a database. Coupling of NO balance equation and all the other equations is only very weak. The nitric oxide calculations are thus restricted to the mere integration of the source term once the flowfield has reached a converged state. Advising a NO source term to the grid points of the numerical mesh according to their respective mixture fraction and radiation degree and integrating over the control volume will lead to a rather arbitrary result. Recalling into mind the second statement at the beginning of this section makes this evident. If a point of stoichiometric conditions exists between two grid points, it remains undetected while the grid point values are counted, which do not necessarily make a considerable contribution to NO. This effect is partially compensated by another wrong assumption, which takes the source term at the grid point as constant throughout the control volume. Finite volume theory does not at all apply to nitric oxide calculations. A solution of this dilemma may be found introducing a mathematical substitution. For a single control volume this means

$$\int_{y_1}^{y_2}\int_{x_1}^{x_2}\widetilde{S}_{NO}(f(x,y))\,dx\,dy = \int_{y_1}^{y_2}\int_{f(x_1)}^{f(x_2)}\widetilde{S}_{NO}(f(x,y))\frac{\partial x}{\partial f}\,df\,dy \qquad (4)$$

The summation of all control volumes finally makes the NO output. The value at the control volume centre is regarded as a representative for the whole control volume and is multiplied by the axial dimension Δ x. This procedure is valid as long as the flame has an axial long shape. At the end of the flame this does not longer apply. Therefore the substitution is performed either in axial or radial direction depending on the bigger of the two derivatives $\frac{\partial \widetilde{f}}{\partial x}$ and $\frac{\partial \widetilde{f}}{\partial r}$. The method explained above contains several uncertainties, among which the interaction between radiation and NO formation is the most serious. It is therefore not able to predict a distinct NO emission, but can certainly serve as an assessment tool for parameter variations.

2.4 Turbulence Model

Technical combustors usually are operated with mass flow rates far too big for the flow to remain laminar. Operationally this does not make problems, the enforced mixing is even appreciated in most cases. But the turbulent random variation of the velocities affects all flow variables and causes unknown correlations when transport equations are statistically averaged. The most prominent of the new unknowns is the Reynolds stress tensor whose modelling is performed on various levels of sophistication. Most common is the k-ϵ model, a variant of a model family solving equations for turbulent kinetic energy and an integral length scale. This model stands out by its numerical stability and its broad palette of applications to many types of flows [1], there evidently exist limits of validity. One of those is the presence of swirl which cannot be simulated without ad hoc modifications whose physical rationale is vague. The more complex Reynolds stress models have not yet attained a wide propagation into fluid dynamic computer programs. They are predominantly restricted to research codes. The superior qualities of the second moment models lie in their ability to reflect any flow mechanism like production, transport and dissipation directly to the Reynolds stress tensor. Any terms stemming from a coordinate transformation, e. g. into axisymmetric coordinates, directly appear in the equations. Critical voices against Reynolds stress models often are based on two arguments: first, the augmented computing time. This is undoubtedly true and can hardly be attenuated. In the computations which will be presented here the additional time effort for the Reynolds stress equations is in all cases more than a hundred percent of the k-ϵ time. Taking into account the individually augmented time until a converged solution has been reached, a constant ratio cannot be given. The second argument postulates, that the problem of turbulence, the assumptions about unknowns, is only distributed onto more free parameters which can more easily be adjusted to a better representation of experimental results. Table 1 lists equations and the number of respective constants for both the k-ϵ and the Reynolds stress model (RST).

Table 1
velocity field turbulence constants

equation	RST	k-ϵ
k	-	2
$\tilde{\epsilon}$	4	3
$u_i" u_j"$	5	-
Σ	9	5

Of the five constants in the RS equations, one belongs to a diffusive term modelling the third order correlations of velocities

$$\frac{\partial}{\partial x_k}(\widetilde{u_i'' u_j'' u_k''}) = \frac{\partial}{\partial x_k}\left(C_s \bar{\rho} \widetilde{u_k'' u_l''} \frac{\tilde{k}}{\tilde{\epsilon}} \frac{\partial \widetilde{u_i'' u_j''}}{\partial x_l}\right). \quad (5)$$

Here the gradient model of Daly and Harlow [9] is adopted. The remaining four constants come up from the pressure rate of strain correlation.

$$\Phi_{ij,1} = -C_1 \frac{2\tilde{\epsilon}}{q^2}(\widetilde{u_i'' u_j''} - \frac{1}{3}\delta_{ij}\widetilde{u_k'' u_k''}) \quad (6)$$

$$\Phi_{ij,2} = C_3(\widetilde{u_i'' u_l''}\frac{\partial \widetilde{U_j}}{\partial x_l} + \widetilde{u_j'' u_l''}\frac{\partial \widetilde{U_i}}{\partial x_l})$$
$$+C_2\delta_{ij}\widetilde{u_l'' u_m''}\frac{\partial \widetilde{U_l}}{\partial x_m} + C_4(\frac{\partial \widetilde{U_i}}{\partial x_j} + \frac{\partial \widetilde{U_j}}{\partial x_i})\tilde{k}$$
$$-(3/2C_2 + C_3)(\widetilde{u_i'' u_j''}\frac{\partial \widetilde{U_l}}{\partial x_i} + \widetilde{u_i'' u_i''}\frac{\partial \widetilde{U_l}}{\partial x_j}). \quad (7)$$

The formulation of equations [7] and [8] is solely based on tensorial arguments. The determination of the constants is not carried out, examining complex flow experiments in order to produce good agreement, but it is performed on two rather simple turbulent flows. The constants are then taken over to complex flow conditions without modification indicating universality of both the model and the related parameters. For C_1, known as the return to isotropy constant [1], experiments on decaying anisotropic turbulence in the absence of mean strain are evaluated [8], leading to a value of 1.5 which makes the best average performance on all available data. The constants C_2, C_3 and C_4, which are associated with mean strain can be determined from homogeneous shear experiments [11] to C_2 = -0.53, C_3 = 0.67 and C_4 = -0.12. When involving chemical reaction, additional equations have to be solved for the mean scalar, the scalar fluxes and for the scalar variance. Neglecting pressure-driven production of Reynolds stress $\overline{u_i"}\,\partial\bar{p}/\partial x_i$ and employing a simple algebraic model for the scalar dissipation the model constants are

Table 2
scalar field turbulence constants

equation	SFT	k-ϵ
$\tilde{f}$	1	1
$\widetilde{f"^2}$	1	1
$\tilde{\epsilon}_f$	1	1
$u_i" f"$	5	1
Σ	8	4

Here 5 constants arise from the scalar flux transport modelling (SFT) opposing one turbulent Prandtl number in the case of a k-ϵ model. Again the constants of the second moment closure are deduced from experiments in simple turbulent flows and taken over unchanged to any type of flow. [11]

3 PRESENT MODEL

The computations provided in the following section are basing on a system of transport equations for mass, mean momentum and mean scalar. Turbulence modelling is carried out either by a standard k-ϵ model or a Reynolds stress model [11]. The set of equations is descritised by a finite volume method using a staggered grid for the variables [5]. The nonlinear equation system is solved by a time-marching iteration. Any scalar variables as density or temperature is calculated in the framework of non-premixed flames by a beta probability density function constructed from mixture fraction and its variance.

4 RESULTS OF COMPUTATIONS

4.1 Non-reacting flow

Enclosed non-reacting combustor flows do not possess great practical relevance, but are very important for the validation of turbulence models. Apart from uncertainties about radiation, wall heat transfer and chemistry modelling, also the turbulence modelling is much more unambiguous. When reaction is taking place, correlations of fluctuating density and other variables usually are avoided by application of a density-weighted averaging [7] leaving the problem of comparing the Favre averages to conventionally time averaged experimental values. At the moment there is also no reasonable explanation why modelling assumptions of cold flows are taken to reacting flows without modifications. There are important arguments for cold flow studies from the experimenters point of view as well. Hot wire probes can be used in regions not accessible for LDV, but even the whole chamber can be made of glass for the convenience of LDV work.

The first example (Fig. 3)is a combustor flow with counterswirl conditions examined by Vu and Gouldin [15]. The second case under examination is a cold combustion chamber flow investigated by Wilhelmi [12] at Imperial College. Relevant data for both experiments are tabulated in table 3.

The first measurements show a large deceleration of the inner jet and the formation of a small recirculation bubble with low swirl velocities. Positive swirl momentum of the inner jet gradually diffuses outward getting absorbed by the outer flow swirling in the opposite way. The superiority of the Reynolds stress simulation is evident. The k-ϵ model without modifications accounting for swirl is not able to describe the measured swirl distribution.

Figure 4 shows mean axial and circumferential velocities of the second case. Again the tendency of the k-ϵ model to predict swirling fluid motion as a solid body rotation is visible. The extension and magnitude of the recirculation zone is not registered by either model.

4.2 Reacting Flow

Two computations of combustion chambers with the non-premixed burning of propane are presented. The first is the already introduced combustor of Wilhelmi, the second was operated by Owen et al. [13]. Table 4 gives the most important information about both cases. In the first two sets of drawings (Figs. 5 and 6) the normalized axial velocity and the tangential velocity as well as temperatures at several locations x/D are given. In the near inlet plane x/D=0.1 both models detect the corner and central recirculation, but cannot simulate the radial extension of the latter. This becomes even more obvious in the second picture. The axial recirculation also diminishes too early, already at x/D=0.8 the simulations show uniform axial velocity direction. Further downstream the velocity increase, indicating continuing reaction with density loss can be determined. The movement of the axial component towards the wall is predicted too weak, accordingly the $\widetilde{W}$ component is too high, resulting in a conserved swirl momentum flux. The rankine vortex shape of the circumferential velocity with a steep gradient near the axis is somewhat better represented by RST. Nonetheless also the k-ϵ model shows clearly a free vortex component in the reacting case too.

Temperature is gained via mixture fraction, mixture fraction variance and a pdf integration. All scalar quantities with steep gradients in diffusion flames are highly sensitive to the fluid field. Fig 7 shows calculations with a laminar flamelet dataset in comparison with an equilibrium dataset, both computations based on a RST model.

The nitric oxide calculations result in an estimated output of 150 mg NO per m^3 at standard conditions reduced to 3 % O_2 in the exhaust gases.

The last example (Fig 8) shows a velocity and temperature contour plot of Owen's combustor. Regarding the axial iso-velocity lines, the computed contours show a good qualitative picture of the experiment but the values are generally too large, indicating distinct difference in temperature and accordingly in density. The central recirculation zone was estimated correctly in its axial and radial extensions. However it is located too far downstream and the maximal backflow velocity of 6 m/sec is predicted too low.

From the temperature plot the extension of the annular flame front can be determined from the maximum isoline which is fairly consistent with experimental results. The temperature as mentioned before, is generally estimated much higher than measured. Especially in the region of x/D=1 to x/D=2 the strong acceleration of the fluid is now explicable when looking at the temperature contours. The calculated 2200-K-isoline is almost located at the same position as the

measured 1600-K-line. A possible explanation for the deviations might be found in the neglected radiative flame cooling and heat exchange with the wall. It is also probable that the departure from chemical equilibrium at the near inlet region contributes to the discrepancy between calculations and experiment. For this combustion chamber an NO output of 192 mg/m^3 was computed.

5 Résumé and Prospect

The calculation of axisymmetric model combustors relevant to gas turbine combustion has been presented. Reynolds stress models have so far not been widely used in computational fluid dynamics but are superior to eddy viscosity turbulence closures. Any further development in statistical description of turbulence can only be based upon second moment closure. In this context the consideration of the spectral behaviour of turbulence or the inclusion of multiple length scales models has to mentioned. Prior to model development is the urgent need for experiments in both reacting and non-reacting combustion chambers. As computational simulation is highly sensitive to starting conditions these measurements must include a full dataset for all variables.

References

[1] ROTTA, J.C.: Statistische Theorie nichthomogener Turbulenz, Zeitschrift für Physik 129 (1951), 547-572.

[2] LAUNDER, B. E., SPALDING, D. B.: The numerical computation of turbulent flows, Computer Methods in Applied Mechanics and Engineering 3 (1974), 269-289.

[3] GORDON, S. and MCBRIDE, B. J.: NASA SP-273 (1971).

[4] JONES, W. P. and WILHELMI, J.: Velocity, temperature and composition measurements in a confined swirl driven recirculating flow, Comb. Sci.Tech. 63 (1989), 13-31.

[5] HARLOW, F. H. and WELCH, J. E.: Numerical computation of time-dependent viscous incompressible flow of fluid with free surface, Phys. Fluids, 8 (1965), 2182-2189.

[6] Wilhelmi, J.; *Axissymetric swirl stabilited combustion*, PhD Thesis.
University of London, 1984

[7] Favre, A.; *The Equations of Compressible Gases.*
USAF Contract AF61 (052)-772, 1965, AD 622097

[8] Launder, B.E., Reece, G.J. und Rodi, W.; *Progress in the development of a Reynolds stress tubulence closure.*
Journal of Fluid Mechanics, 1975, **68**, 537–566

[9] Daly, B.J. und Harlow, F.H.; *Transport equations of turbulence.*
Physics of Fluids, 1970, **13**, 2634-2649

[10] Jones, W.P. und Lindstedt, R.P.; *Global reaction schemes for hydrocarbon combustion.*
Combustion and Flame, 1988, **73**, 233–249

[11] JONES, W. P. and MUSONGE, P.: Phys. Fluids 31, p. 3589, 1988.

[12] JONES, W. P. and WILHELMI, J.: Comb. Sci. Tech. 63, p. 13, 1989.

[13] OWEN, F. K. SPADACCINI, L. J. and BOWMAN, C. T.: Sixteenth Symposium (International) on Combustion, p. 105, The Combustion Institute, 1977.

[14] Peters, N.:
An Asymptotic Analysis of Nitric Oxide Formation in Turbulent Diffusion Flames
Comb. Sci. Tech., Vol. 19, 1978, pp. 39 - 49

[15] Vu, B. T. and Gouldin, F. C.:
Flow Measurements in a Model Swirl Combustor
AIAA Journal, Vol. 20, No. 5, 1982, pp. 642 - 651

Table 3
Cold Combustor Flows

experiment	$\dot{m}[\frac{kg}{sec}]$	$l[m]$	$d[m]$	S	$T[K]$
Wilhelmi	0.035	0.3	0.1	0.73	313
Gouldin/Vu	1.45	0.65	0.29	0.49/-0.51	298

Table 4
Hot Combustor Flows

experiment	$\dot{m}_{air}[\frac{kg}{sec}]$	$\dot{m}_{fuel}[\frac{kg}{sec}]$	Φ	$l[m]$	$d[m]$	S	$T_{air}[K]$	$T_{fuel}[K]$
Wilhelmi	0.0304	0.0013	0.55	0.3	0.1	0.71	313	294
Owen	0.137	0.0072	0.5	1700	0.122	0.8	750	356

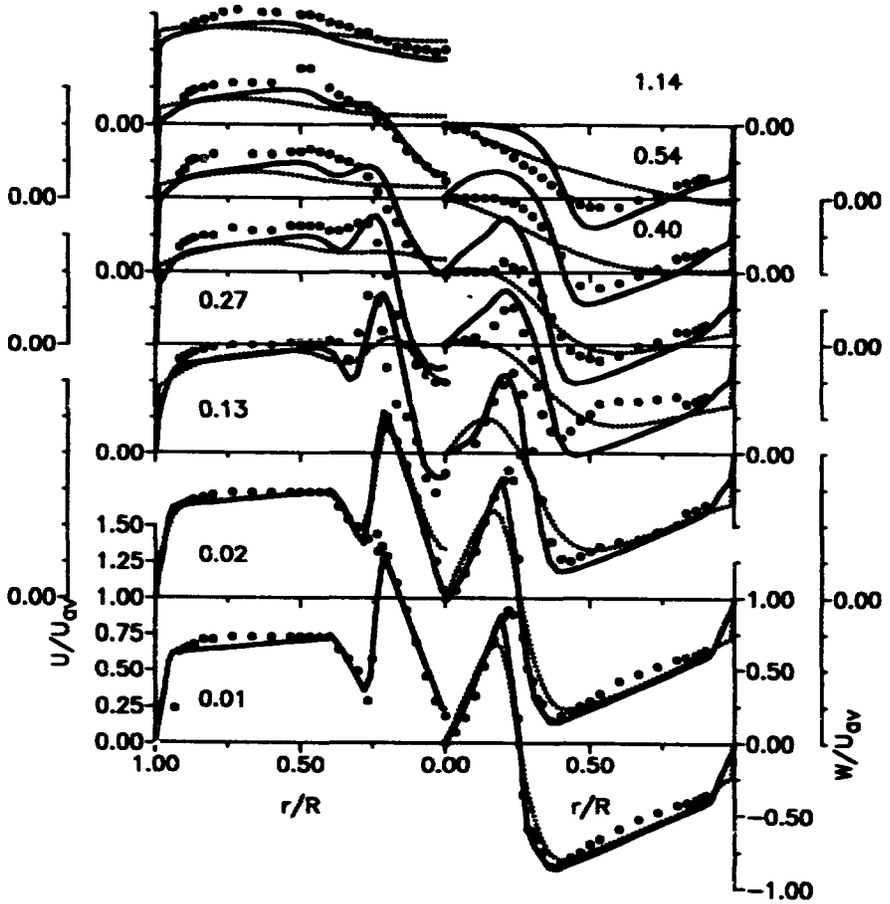

Figure 3: Axial and tang. velocities for the first cold combustor $U_{av} = 30.3$ m/sec, — RST, ····· k-ϵ, • measurement

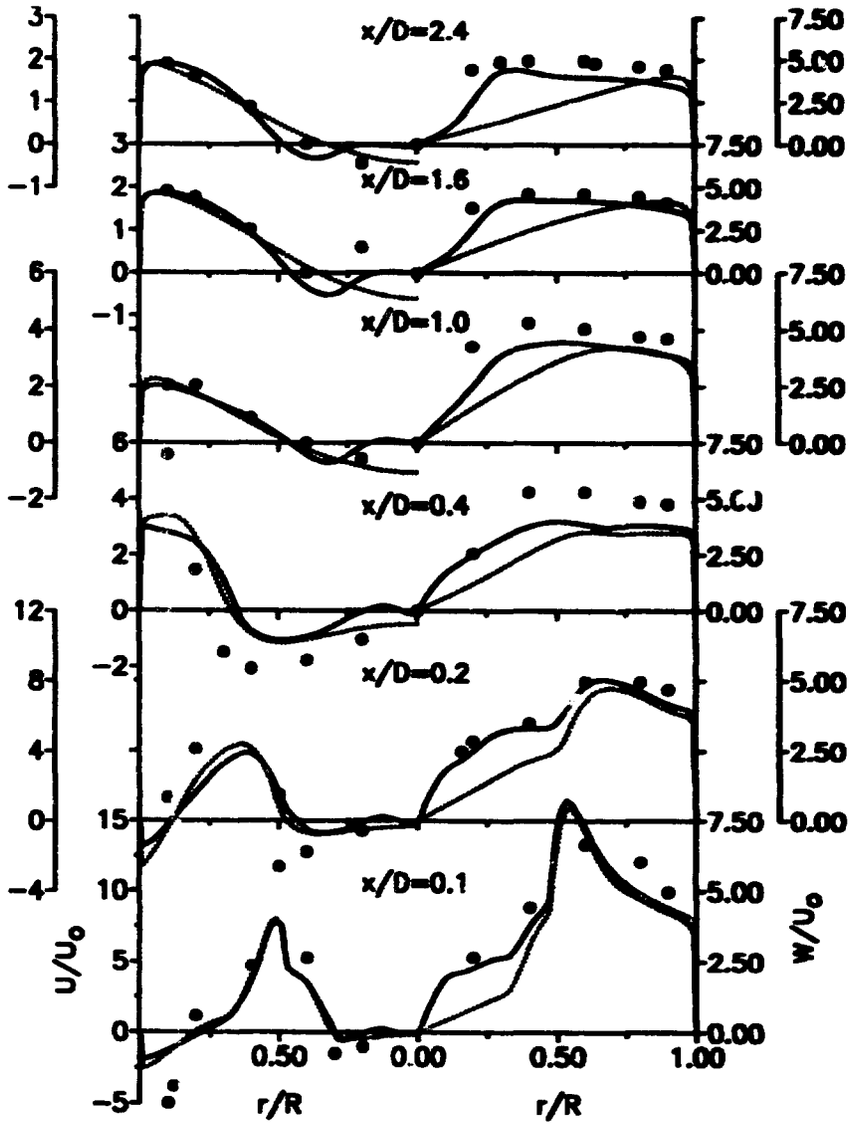

Figure 4: Axial and tang. velocities for the second cold combustor $U_o = 3.45$ m/sec, — RST, ····· k-ϵ, • measurement

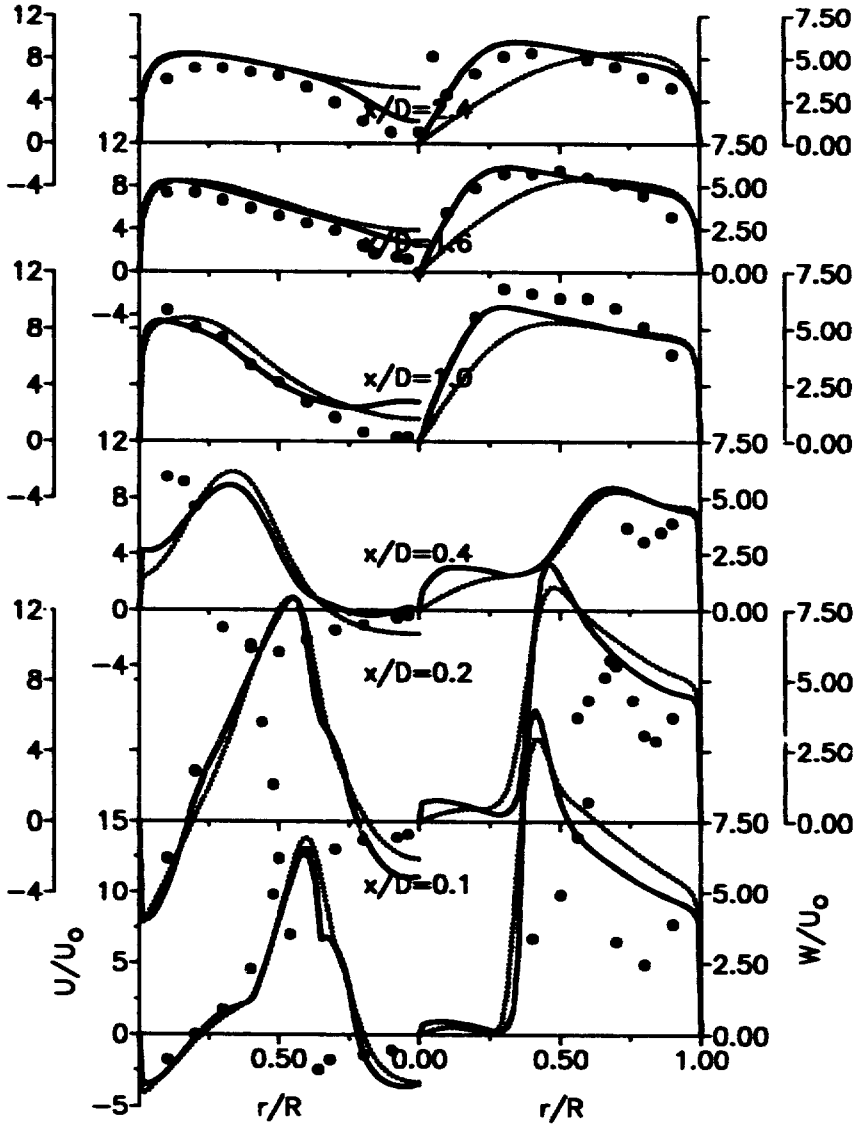

Figure 5: Axial and tang. velocities for the first hot combustor $U_{av} = 3.45$ m/sec, — RST, ····· k-ϵ, • measurement

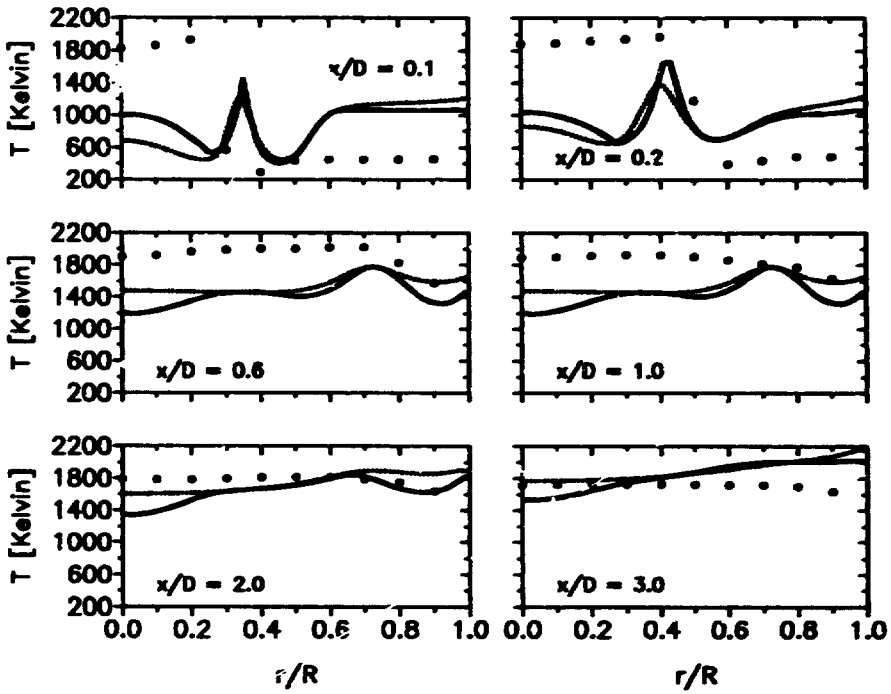

Figure 6: Temperatures for the first hot combustor — RST, ····· k-ϵ, • measurement

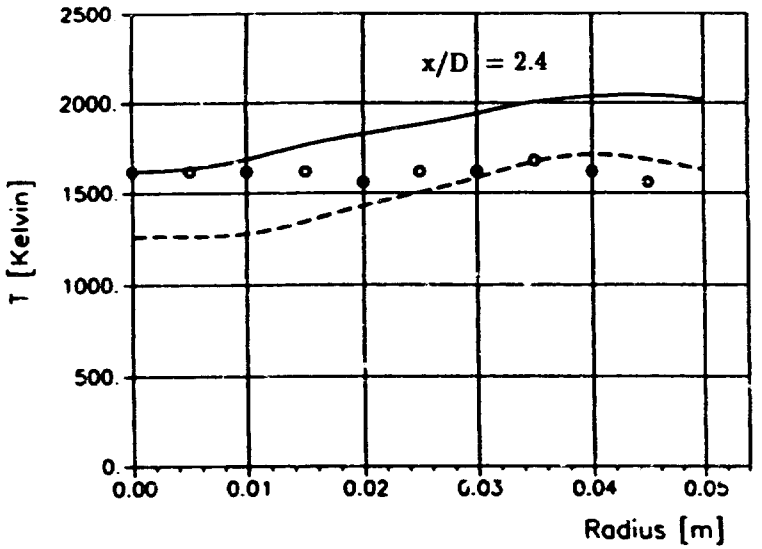

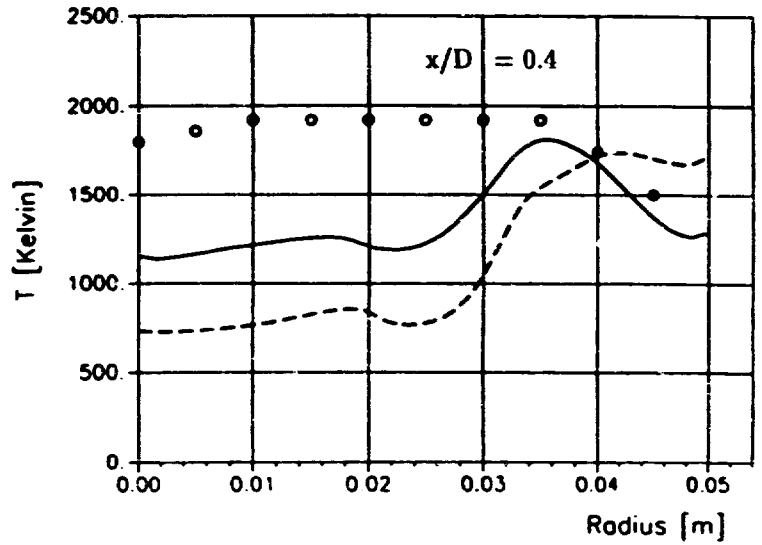

Figure 7. Temperatures for the first hot combustor, — laminar flamelet ····· chemical equilibrium , • experiment

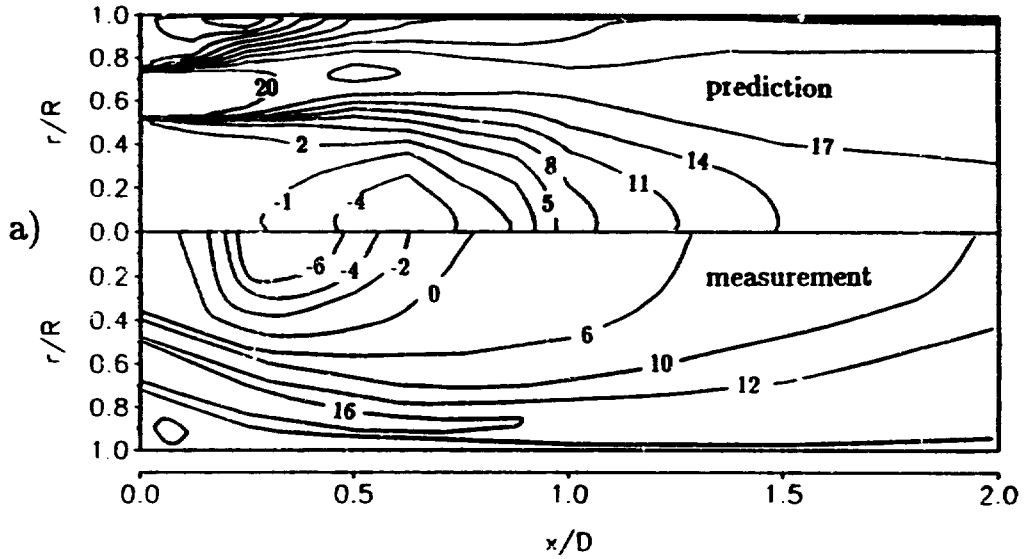

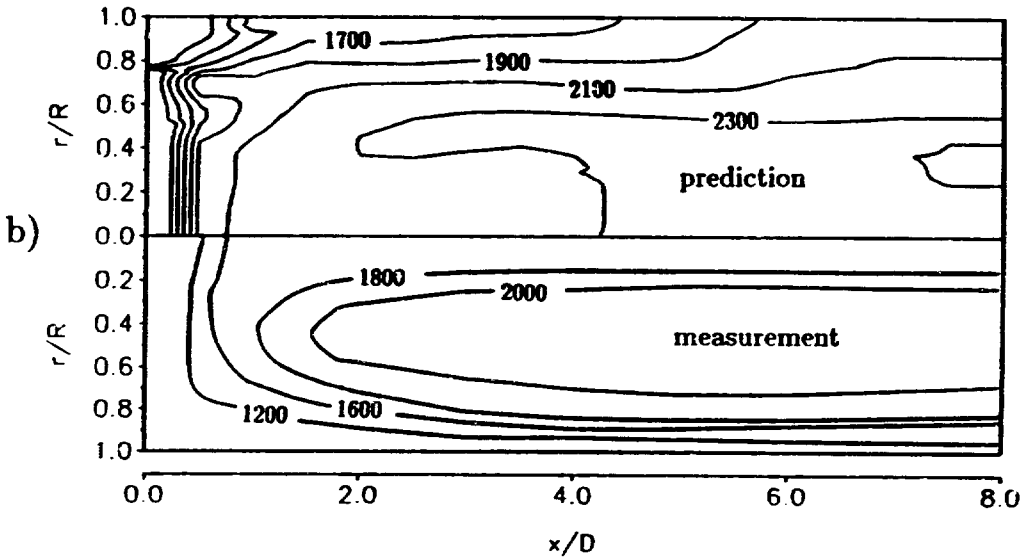

Figure 8. a) Axial velocity contours (m/sec) for the second hot combustor
b) Temperature contours (K) for the second hot combustor

Discussion

Question 1. J. Tilston
You pointed out the differences between the prediction of axial velocity and the measurements (Fig. 8): however, it appears from the illustration that much of this "error" could originate in a poor definition of the boundary conditions. The entering flow (measured) is clearly at an angle to the longitudinal axis.

Author's Reply
Figure 8 does not show streamlines but iso-velocity lines of axial velocity. You cannot directly conclude from the shape of these lines how the other velocity components behave. The experiment does not show that a radial entry velocity exists.

NUMERICAL SIMULATION OF AEROTHERMAL CHARACTERISTICS IN GAS TURBINE COMBUSTORS WITH COMPLEX GEOMETRIES

P. Di Martino, G. Cinque and C. Paduano
Research and Development Department
Alfa Romeo Avio S.A.p.A.
80038 Pomigliano d'Arco (NA), ITALY

SUMMARY

A method is presented for calculating steady three-dimensional two-phase turbulent reactive flows with curved irregular boundaries. The gas phase equations are solved in an Eulerian frame of reference by a numerical technique based on the finite volume approach, while the equations describing droplet motion, evaporation and burning are treated in a Lagrangian frame of reference.
Turbulent transport is described by the standard k-ε model. The combustion model utilizes a conserved scalar formulation and an assumed shape probability density function to account for chemistry-turbulence interaction. The numerical scheme employs structured non-orthogonal grids, node-centered variable arrangement and Cartesian velocity components. A special interpolation procedure is used to avoid checkerboard oscillations due to pressure-velocity coupling and a low diffusive and bounded scheme is introduced to approximate the convective terms in the transport equations.

The capabilities of the numerical procedure are demonstrated by simulating an annular combustion chamber for which experimental results were available. The agreement between calculation and experiments ranges from fair to good.

LIST OF SYMBOLS

a	exponent of beta-function
a_i	coefficients of discretized equations
b	exponent of beta-function
C_p	specific heat at constant pressure
C_μ	constant of turbulence model
D_s	additional diffusion source term
f	mixture fraction
g	variance of mixture fraction
h	stagnation enthalpy
h_p	heat transfer coefficient
H_i	coefficient of interpolation
k	kinetic energy of turbulence
J	Jacobian
L	Latent heat of vaporization
M_j	molar mass of species j
p	pressure
$P(f)$	probability density function
q_{ij}	geometric coefficient of equations
R	universal gas constant
S	source term
S_1	constant part of S
S_2	coefficient of dependent variable in the linear expression for S
T	gas temperature
T_r	reference temperature
u	velocity component along x-direction
U	contravariant velocity component along ξ-direction
v	velocity component along y-direction
V	contravariant velocity component along η-direction
w	velocity component along z-direction
W	contravariant velocity component along ζ-direction
x	Cartesian coordinate
y	Cartesian coordinate
Y_j	mass fraction of species j
z	Cartesian coordinate

Greek symbols

α_u	relaxation coefficient
Γ_ϕ	transport property in equation (1)
ε	dissipation rate of k
ζ	curvilinear coordinate
η	curvilinear coordinate
μ_g	gas laminar viscosity
μ_t	turbulent viscosity
ξ	curvilinear coordinate
ρ	gas density
ρ_p	liquid density
ϕ	generalized dependent variable

Superscripts

e	equilibrium value
$\circ$	value at the previous iteration
$-$	linear average

Presented at an AGARD Meeting on 'Fuels and Combustion Technology for Advanced Aircraft Engines', May 1993.

Subscripts

d	downward cell interface
D	downward grid-point
e	eastern cell interface
E	eastern grid-point
g	gas-phase
n	northern cell interface
N	northern grid-point
P	grid-point under consideration
p	liquid-phase
s	southern cell interface
S	southern grid-point
u	upward cell interface
U	upward grid-point
w	western cell interface
W	western grid-point
fu	fuel

INTRODUCTION

The role of computational methods in the design and development of gas turbine combustors has become more pronounced in recent years due to influences from a number of sources. From a computational viewpoint, the availability of more powerful computer hardware has enabled the calculation of complex flowfields with a predictive capability improved through the use of more accurate numerical schemes and physical models. In addition, the pressures to design combustion chambers exhibiting, for example, improved durability and reduced pollutant emissions, has made the task of the combustion engineer more challenging, necessitating a move away from the traditional 'cut and try' approach or the use of empirical correlations based on previous results. Consequently, advanced computational fluid dynamics techniques are now an essential tool for use in the design and development processes.

Finite-volume methods have been widely applied to problems with regular geometries where the boundaries happen to coincide with the coordinate lines of an analytic orthogonal coordinate system. But this approach is quite unsatisfactory for many problems of practical interest involving complex irregular boundaries since prescription of conditions at boundaries not conforming to the coordinate lines is difficult and near-wall regions with steep gradients are no easy to resolve accurately. Further, most commonly used solution algorithms converge rather slowly, which poses limitations on grid refinement, particularly for three-dimensional situations.

In this paper an efficient finite-volume method using body-conforming non-orthogonal but structured grids for three dimensional turbulent reactive flows has been derived. The main issues addressed are the accurate modelling of the two-phase 3-D flow phenomena, the influence of turbulence on chemical kinetics and the higher-order discretization of the convective terms. The calculation and comparison with experiments demonstrate the performance of the method with respect to numerical accuracy, computational efficiency and flexibility in handling complex geometries.

GAS-PHASE GOVERNING EQUATIONS

Steady fully elliptic density-weighted Navier-Stokes equations describing gas phase, under low Mach number approximation, coupled to the energy and momentum balance equations for the liquid phase, are considered [1]. The standard k-ε model provides for turbulence closure along with the wall function treatment for the near-wall regions. The conservation equations solved for the gas phase are those for momentum, mass, kinetic energy of turbulence and its dissipation. The general form of these equations, written in cartesian coordinates, is:

$$\left[\frac{\partial}{\partial x}(\rho u\phi) + \frac{\partial}{\partial y}(\rho v\phi) + \frac{\partial}{\partial z}(\rho w\phi)\right] = \left[\frac{\partial}{\partial x}\left(\Gamma_\phi\frac{\partial\phi}{\partial x}\right) + \frac{\partial}{\partial y}\left(\Gamma_\phi\frac{\partial\phi}{\partial y}\right) + \frac{\partial}{\partial z}\left(\Gamma_\phi\frac{\partial\phi}{\partial z}\right)\right] + S_\phi + S_d \qquad (1)$$

All terms which arise in addition to convection and diffusion are grouped in the source-term S_ϕ for the gas-phase, while S_d accounts for liquid droplets.

In order to fit the very complex geometries encountered in industrial applications, a body conforming system of coordinates is used. The latter can be obtained by mapping the arbitrarily shaped physical domain into a rectangular parallelopiped (fig. 1) through a transformation such as:

$$\xi=\xi(x,y,z)\ ,\ \eta=\eta(x,y,z)\ ,\ \zeta=\zeta(x,y,z) \qquad (2)$$

The equations (2) provide the relationships between cartesian x,y,z and curvilinear ξ,η,ζ coordinates. By using

(2) the transport equation (1) can therefore be transformed in a formally analogous one in curvilinear coordinates, with convective, diffusive and source terms clearly distinguishable [2]:

$$\frac{\partial}{\partial\xi}(\rho U\phi)+\frac{\partial}{\partial\eta}(\rho V\phi)+\frac{\partial}{\partial\zeta}(\rho W\phi)=$$
$$\frac{\partial}{\partial\xi}\left(\frac{\Gamma}{J}q_{11}\frac{\partial\phi}{\partial\xi}\right)+\frac{\partial}{\partial\eta}\left(\frac{\Gamma}{J}q_{12}\frac{\partial\phi}{\partial\eta}\right)+\frac{\partial}{\partial\zeta}\left(\frac{\Gamma}{J}q_{13}\frac{\partial\phi}{\partial\zeta}\right)+$$
$$\frac{\partial}{\partial\xi}\left[\frac{\Gamma}{J}\left(q_{12}\frac{\partial\phi}{\partial\eta}+q_{13}\frac{\partial\phi}{\partial\zeta}\right)\right]+\frac{\partial}{\partial\eta}\left[\frac{\Gamma}{J}\left(q_{21}\frac{\partial\phi}{\partial\xi}+q_{23}\frac{\partial\phi}{\partial\zeta}\right)\right]+ \quad (3)$$
$$\frac{\partial}{\partial\zeta}\left[\frac{\Gamma}{J}\left(q_{31}\frac{\partial\phi}{\partial\xi}+q_{32}\frac{\partial\phi}{\partial\eta}\right)\right]+JS(\xi,\eta,\zeta)$$

In the foregoing mathematical expression U,V,W are the so-called contravariant velocity components, J is the Jacobian of the coordinate transformation, q_{ij} are metric quantities, terms with i≠j accounting for grid distortion.

The distribution of the turbulent viscosity is provided by the turbulence characteristics, namely k, the kinetic energy of the fluctuating motion and its dissipation rate ε.
The turbulent viscosity is related to k and ε by dimensional arguments in the following way:

$$\mu_t = C_\mu\rho\left(\frac{k^2}{\epsilon}\right) \quad (4)$$

The additional conservation equations required for a chemically reacting system are those for stagnation enthalpy and chemical species mass fractions. The definition of stagnation enthalpy is:

$$h = \int_{T_0}^{T} C_p dT + Y_{fu}\cdot\Delta H + \frac{1}{2}(u^2+v^2+w^2) \quad (5)$$

and it is used to calculate the temperature T. In this equation ΔH is the heat of combustion. The dependence of the specific heat of the mixture on temperature and composition is considered.

In the case of a practical gas turbine combustor, since fuel and air enter the combustion system via separate streams, the combustion model used is one appropriate to so-called non-premixed flames. The reasonable assumptions of negligible heat loss due to radiation and equality of all diffusive transport coefficients, allow all thermochemical state variables to be expressed in terms of any conserved scalar, which is chosen to be the mixture fraction f [3]. Further, if recognition is taken of the fact that combustors operate predominantly at high inlet temperatures and pressures, then it may be assumed that the chemical reactions have time scales very short compared to those characteristic of the transport processes. This leads to the "fast chemistry" approximation implying that it is admissible to assume (instantaneous) chemical equilibrium appropriate to the local mixture fraction value. Modelling the consequences of turbulent fluctuations on the chemical composition is then reduced to describing the fluctuations of the mixture fraction. This is done via the introduction of the probability density function (pdf) of the conserved scalar f. The shape of the pdf is presumed, in terms of the local mean and variance of the mixture fraction, the values of which are obtained from the solution of the modelled partial differential equations. Thus the local pdf at each point is convoluted with the corresponding equilibrium vector to generate required quantities and the mean values of temperature, density and chemical species mass fraction can be evaluated from:

$$\phi = \int_0^1 \phi^e(f)P(f)df \quad (6)$$

$$\rho = \left[\int_0^1 \frac{P(f)}{\rho(f)}df\right]^{-1} \quad (7)$$

where $\phi^e(f)$ is the chemical equilibrium value of ϕ as a function of f and P(f) is the density weighted p.d.f. for the scalar f. The function chosen was the two-parameter β-probability density function [3]:

$$P(f)=\frac{f^{a-1}(1-f)^{b-1}}{\int_0^1 f^{a-1}(1-f)^{b-1}df} \quad (8)$$

where a and b are given by:

$$a = f\left[\frac{(1-f)}{g}f\right] \quad , \quad b = \frac{(1-f)}{f}a \quad (9)$$

The density is provided by the equation of state:

$$\rho = \frac{p}{\left[RT\sum_j\left(\frac{Y_j}{M_j}\right)\right]} \quad (10)$$

LIQUID-PHASE MODEL

This model assumes that the fuel is injected into the combustion chamber as a fully atomized spray which consists of spherical droplets. The liquid-phase equations are based on the Lagrangian formulation of the droplet trajectory, transient heating and vaporization. The entire fuel spray is constructed using a finite number of size ranges obeying a two parameter droplet size distribution, which is assumed to be of Rosin-Rammler type. The equations of motion for each of the droplets, representing the size groups which constitute the spray, are based on the concept of relaxation time:

$$\frac{d\vec{V}_p}{dt} = \frac{\vec{V}_g - \vec{V}_p}{\tau_d} \tag{11}$$

where

$\vec{V}_p$ = *velocity vector of droplet*

$\vec{V}_g$ = *velocity vector of continuous gas phase*

τ_d = *dynamic relaxation time of droplet*

The dynamic relaxation time of droplet, τ_d, is defined as:

$$\tau_d = \frac{4}{3}\left(\frac{\rho_p D^2}{\mu_g}\right)\left(\frac{1}{C_D Re}\right) \tag{12}$$

The particle Reynolds number is defined as:

$$Re = \frac{\rho_g |\vec{V}_g - \vec{V}_p| D}{\mu_g} \tag{13}$$

An important quantity is the drag coefficient C_D. There are several expressions available in the literature, each of which has an experimental basis. In this study C_D is taken from [4]:

$$C_D = \frac{24}{Re}(1 + 0.15Re^{0.687}), \qquad Re<10^3$$
$$C_D = 0.44, \qquad Re>10^3 \tag{14}$$

The description of droplet heating and evaporation is added to the computational model using two equations which are solved separately. The former, which accounts for energy balance, is given by:

$$\frac{dT_p}{dt} = 6h_p\left(\frac{T - T_p}{\rho_p D^2 C_p L}\right) \tag{15}$$

and is solved only during the preheating period until the droplet temperature reaches the boiling point, at constant diameter. Subsequently the droplet temperature remains constant and the decrease in diameter occurs. This is described by the second equation:

$$\frac{dD}{dt} = -\frac{C_b}{2D}(1 + 0.28Re^{0.5}) \tag{16}$$

where C_b is the vaporization rate constant whose value depends on the physical properties of the surrounding medium as well as fuel itself.

The liquid-phase equations are coupled to the equations describing gas-phase through the droplet source term, which are obtained by calculating what is lost or gained in terms of mass, momentum and energy as the droplets enter and leave volume elements. The set of simultaneous ordinary equations for liquid phase are solved by the fourth order Runge-Kutta method at suitable intervals within the iterative procedure (see next section). The time step is dynamically adjusted based on droplet velocity and grid cell size. At this level the effects of turbulence on the droplet motion are neglected.

FINITE VOLUME METHOD

Control Volume and Variable Arrangement. Figure 1 shows the kind of control volume and the variable arrangement used in the present method. The grid generation procedure calculates the coordinates of the control volume vertices which are simply joined by linear segments to form the same. All the variables are stored at the geometric center P of the control volume. The six

neighboring control volume centers are indicated by N, S, E, W, U and D for the north, south, east, west, up and down neighbors. The face center points n, s, e, w, u and d are located at the intersection of the lines joining the midpoint of the opposite edge. These points are used for locating the variables and their gradients on the control volume faces.

Flux Balance Equations. The partial differential equations previously described have been transformed into difference equations by integrating over each control volume with the aid of Gauss theorem.

Thus, the volume integral of the terms under the differential operator on the left hand side of the transport equation (3) may be converted to surface integrals (fluxes) over the six different faces of the control volume. The resulting balance equation for each control volume and variable ϕ may the be expressed as follows:

$$I_e - I_w + I_n - I_s + I_u - I_d = \iiint S_\phi dV \quad (17)$$

where I_e, for example, represents the total flux of ϕ across the face e. Each of the surface fluxes is made of three distinct part, namely a convective contribution I^C, a normal diffusive contribution I^{DN} and a cross-derivative diffusive part I^{DC} arising from the coordinate transformation. Equation (17) involves no approximation and represents the finite volume analog of the differential equation (3).

The diffusive terms I^{DN} were replaced by their central difference analogs, while a higher order upwind scheme was used for convective terms I^C. It is well known that first-order upwinding fails to give accurate solutions at high Reynolds numbers. For recirculating flows weaker vortices and sometimes incorrect flow fields are predicted. In this study we have chosen the QUICK differencing along with a boundedness criterion to avoid numerical oscillations.

The cross-derivative diffusive part I^{DC} is included in the source term, which may be expressed as follows:

$$D_s + \iiint J \cdot S(\xi,\eta,\zeta) d\xi d\eta d\zeta = S_1 + S_2 \phi_P \quad (18)$$

where D_s is the term involving the cross derivatives.

Replacing the expressions for convective and diffusive face fluxes and the corresponding source terms, a set of algebraic equations is obtained which can always be cast in the following linearized form:

$$a_P \phi_P = a_E \phi_E + a_W \phi_W + a_N \phi_N + a_S \phi_S + a_U \phi_U + a_D \phi_D + S_1 \quad (19)$$

with

$$a_P = a_E + a_W + a_N + a_S + a_U + a_D - S_2 \quad (20)$$

where the A's are the coefficients which contain the contributions from the convective and diffusive fluxes, and S_1 and S_2 are the components of the linearized source terms.

Momentum Interpolation for Calculation of Pressure Field. Storing the variables at the geometrical center of the control volume coupled with the use of linear interpolation for internodal variation usually leads to non-physical oscillations or the so-called red-black checker-board splitting of the pressure field and the associated difficulties in obtaining a converged solution. To avoid this problem, a special interpolation suggested by Rhie and Chow, termed as momentum interpolation [2], has been adopted to evaluate cell face variables from the node centered quantities. For 3-D flows, the discretized momentum equations for the node centered u velocity, using underrelaxation parameter α_u, are:

$$u_P = \alpha_u [H_p + D_{1p}(p_U - p_e) + D_{2p}(p_s - p_n) + D_{3p}(p_d - p_u)] + (1-\alpha_u) u_P^o \quad (21)$$

where u_p° is the value of u_P at the previous iteration and D_{ip} are geometrical quantities.

The discretized momentum equations for the node centered velocities show that each velocity component at the node center consists of two contributions, namely the convective and diffusive transport from neighboring control volumes and the pressure difference. The momentum interpolation procedure assumes a linear variation for the first contribution whereas no interpolation is needed for pressure which is available right at the nodes (for example at P and W for the face w). Accordingly the west face velocity u_w, with proper underrelaxation, may be expressed as:

$$u_w = \alpha_u [\overline{H_w + D_{2w}(p_s - p_n) + D_{3w}(p_d - p_u)} + \overline{D_{1w}}\,(p_W - p_P)] + (1-\alpha_u) u_w^o \quad (22)$$

where the expression with overbar represents the linear average of the same quantities evaluated at the points P and W adjacent to the face w.
In this study the well established SIMPLEC [5] method was used to handle the velocity-pressure coupling and the solution of the individual equations sets was obtained by TDMA (tridiagonal matrix algorithm) based iterative solvers.

Boundary Conditions. One of the most important aspects in numerical modelling of internal flows lies in the formulation and implementation of appropriate boundary conditions (BC). Unless there is mass injection involved in treating solid surfaces, the no-slip (u=0) and no throughflow (v=0, w=0) conditions are imposed. To avoid the need for detailed calculations in the near-wall regions, algebraic relations, termed wall functions [1], are derived so as to reproduce identically the implications of the "logarithmic profiles", with uniform shear stress prevailing up to the near wall grid node and generation and dissipation of turbulent kinetic energy locally in balance.

The wall is adiabatic, as a consequence of the hypotheses on the energy loss. No surface BC on either pressure or density are required. However values of both need to be calculated at the surface in order to solve the numerical central difference scheme ($\partial p/\partial n = 0$.) The same condition is valid for f and g, except where air (f=0, g=0) or fuel (f=1, g=0) inlets are present.

At the outflow boundary, a zero gradient of the contravariant velocity components is specified from which the cartesian components are derived. For all the other scalar variables the same gradient condition is fulfilled. The above argument is based on the Peclet number being sufficiently large: since the boundary points are downstream of the calculation domain, they do not influence the solution. The assumption of large Peclet number is a slight distortion of reality but is also what we must resort to if we are to get meaningful solutions in the absence of any further information about the outflow boundary. The resulting inaccuracy, if there is any at all, is the price we pay for the freedom to isolate the calculation domain from the universe that lies downstream of the outflow boundary. In order to avoid recirculation across the outflow boundary, we made the grid mesh a little bit longer along the streamwise direction. It is only a numerical requirement and this is the reason why it was not represented in the plot (62 points instead of 81).

RESULTS

The calculation procedure described in the foregoing sections was used to analyze the internal reactive flowfield of the GEM-60 annular combustion chamber, for which experimental results were available [6]. The geometry of the combustor is shown in fig. 2. It consists of five film-cooling slots, a set of five primary holes located on the lower wall (two of which are in line with the vaporizer exit), and two sets of dilutions holes staggered by a half-pitch with respect to the primary holes. Natural gas (94% CH_4) was used as fuel and delivered to the T-vaporizer at flow rate which led to air-fuel ratio of 29, corresponding to the take-off condition. The inlet air flow temperature was 515 K. As gaseous fuel was used, in this calculation the liquid phase model was not activated. It is only mentioned to illustrate the capabilities of the model. A future investigation on liquid fuel combustors is planned.
A 3-D view of the curvilinear grid mesh used for calculation is plotted in fig. 3. After 600 iterations the maximum residual of mass is lower then 10^{-5} (log values reported in fig. 4), thus showing that the solution has reached a reasonable convergence at this point.

The predicted velocity field in three vertical planes is shown in fig. 5. For clarity the vectors are plotted every other one. The primary jet has an almost vertical trajectory and limits the extent of the primary zone vortex which is mainly driven by the film cooling flow. The eye of the primary vortex is shifted toward the upper wall in regions close to the primary jets. The downstream dilution jets, which are directly opposed, show a larger penetration of the upper jet. It is in this region where the largest changes in flow pattern occur. This is indicated even more clearly by the transverse section particle tracks shown in fig. 6. Very different and complex secondary flows are displayed.

Horizontal cross-stream distributions of longitudinal mean velocity, obtained in the primary zone, are presented in fig.7. The agreement with experiments is considered good.

The temperature field in the same planes as fig. 5 is plotted in fig. 8 along with experimental measurements. The maximum temperatures occur in the upper half of the primary and intermediate zones and are in line with the vaporizer exits, as it can be seen in fig. 9, where cross-plane distributions of temperature are reported. This general pattern has been maintained at the exit plane with a slight shift in the high temperature regions. The trend is qualitatively and in some cases even quantitatively well predicted.

Figure 10 shows the main chemical species mass fractions (%) in a vertical plane. Relatively high values of unburned fuel observed in presence of O_2 below the midplane in the primary zone indicate that the reactions have not proceeded to equilibrium and the global fuel breakdown has been inhibited in very fuel rich regions close to the lower wall. Oxygen levels are underpredicted in the primary zone while unburned fuel is overpredicted in the intermediate zone. The reasons for that are believed to be the simplified reaction mechanism used. Further improvements which

account for finite rate chemistry effects are under way.

Finally the exit plane temperatures distributions measured at different values of y-coordinate are represented in fig. 11. The root mean square (RMS) of relative error between theoretical and experimental results is indicated in each diagram. The trend is fairly well predicted.

CONCLUSIONS

A general finite-volume method has been described for calculating 3-D, turbulent, combusting flows with complex geometries and its application to gas turbine combustion chambers has been shown.

The agreement with experimental data used to validate the model ranged from fair to good. These results illustrate that, while much work remain to be done in improving physical models, the techniques outlined here have reached a sufficient state of maturity to be used with confidence in the design and development stages for gas turbine combustors.

REFERENCES

[1] A. K. Gupta and D. G. Lilley, Flowfield Modeling and Diagnostic, Abacus Press, 1985.

[2] W. Rodi, S. Majiumdar and B. Schonung, Finite-Volume Methods for Two-dimensional Incompressible Flows with Complex Boundaries, 8th International Conference on Computing Methods in Applied Sciences and Engineering, Versailles, 1987.

[3] W. P. Jones and J. H. Whitelaw, Calculation Methods for Turbulent Reacting Flows: a Review, Comb. Flame, Vol. 48, 1982, pp. 1-26.

[4] K. K. Kuo, Principles of Combustion, John Wiley and Sons, 1986

[5] S. V. Patankar, Numerical Heat Transfer and Fluid Flow, Hemisphere Publishing Co., New York,1980.

[6] A. F. Bicen, D. Tse and J. H. Whitelaw, Flow and Combustion Characteristics of an Annular Combustor, Combustion and Flame Vol. 72, pp 175-192, 1988.

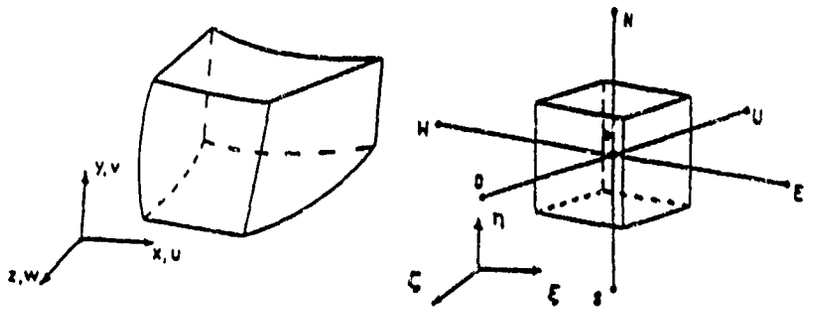

Fig. 1. Control volume in physical and computational space.

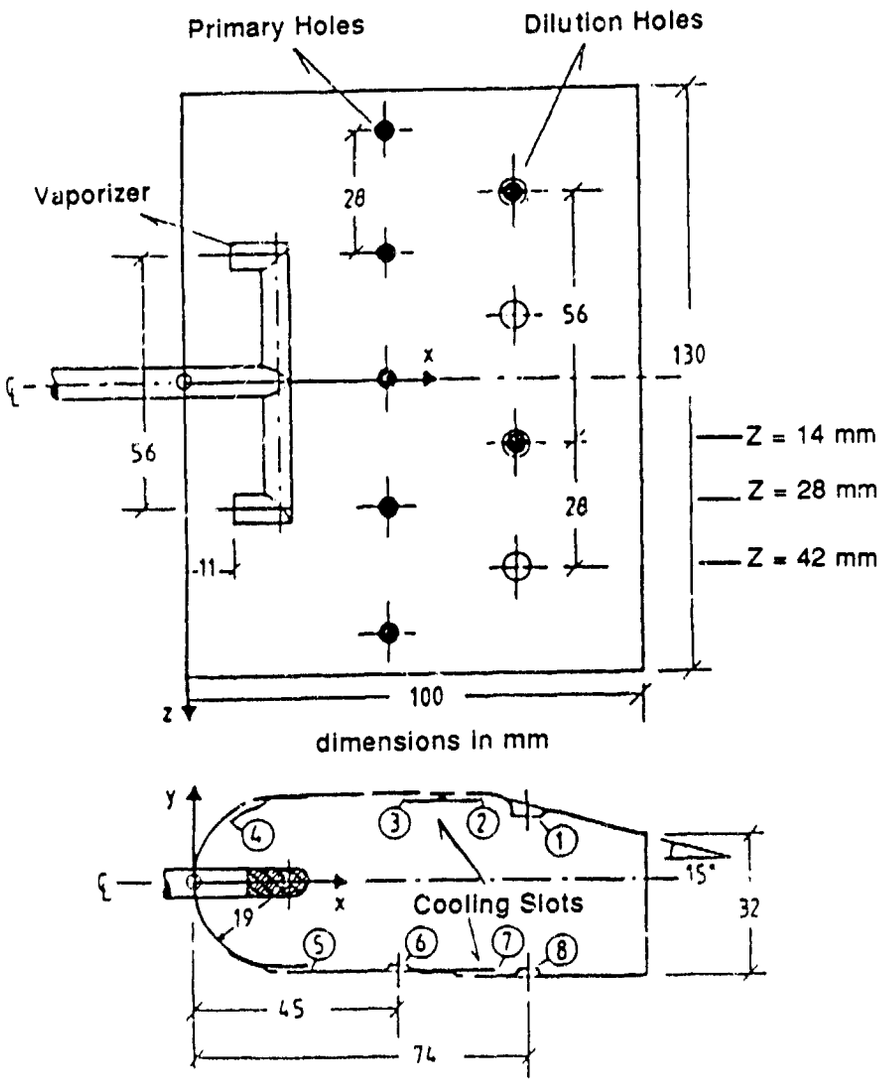

Fig. 2. Combustor geometry.

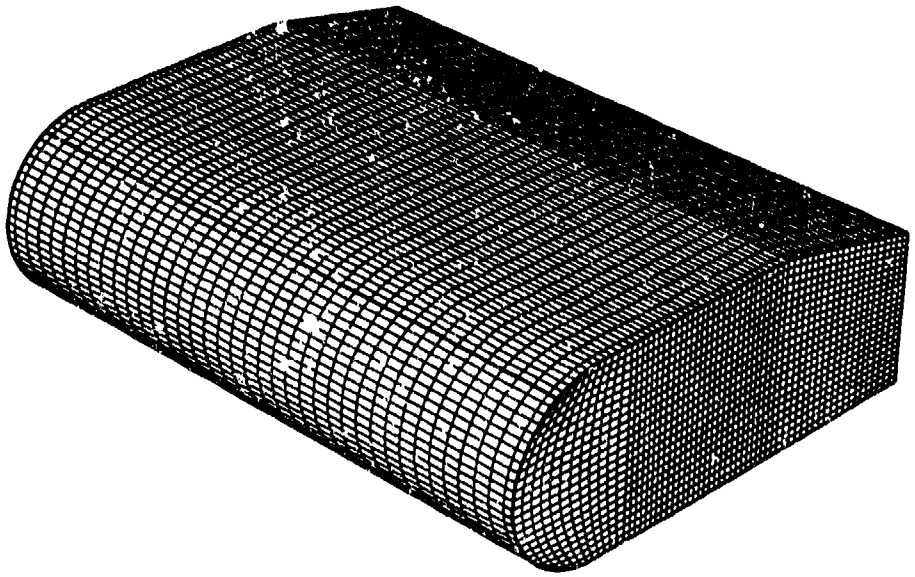

Fig. 3 Model Grid Mesh 81x25x39.

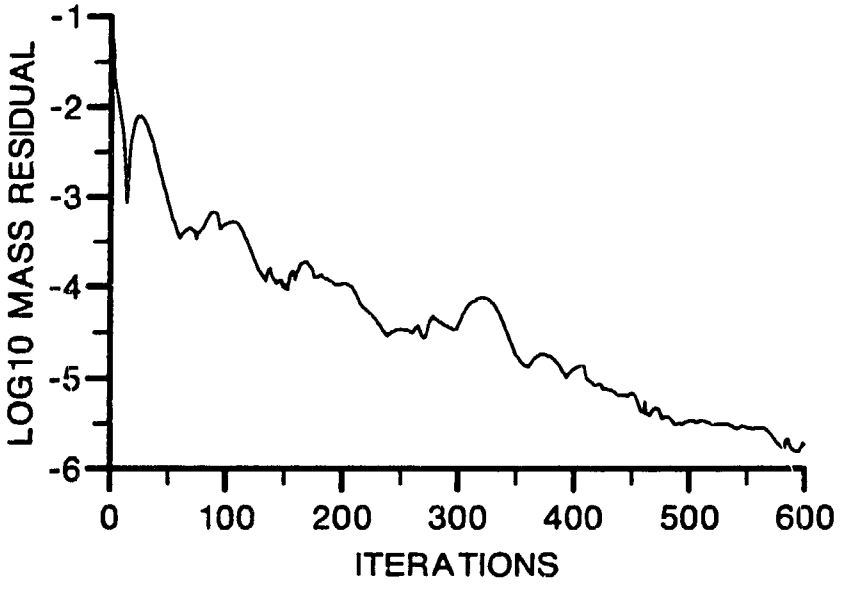

Fig. 4 Convergence history.

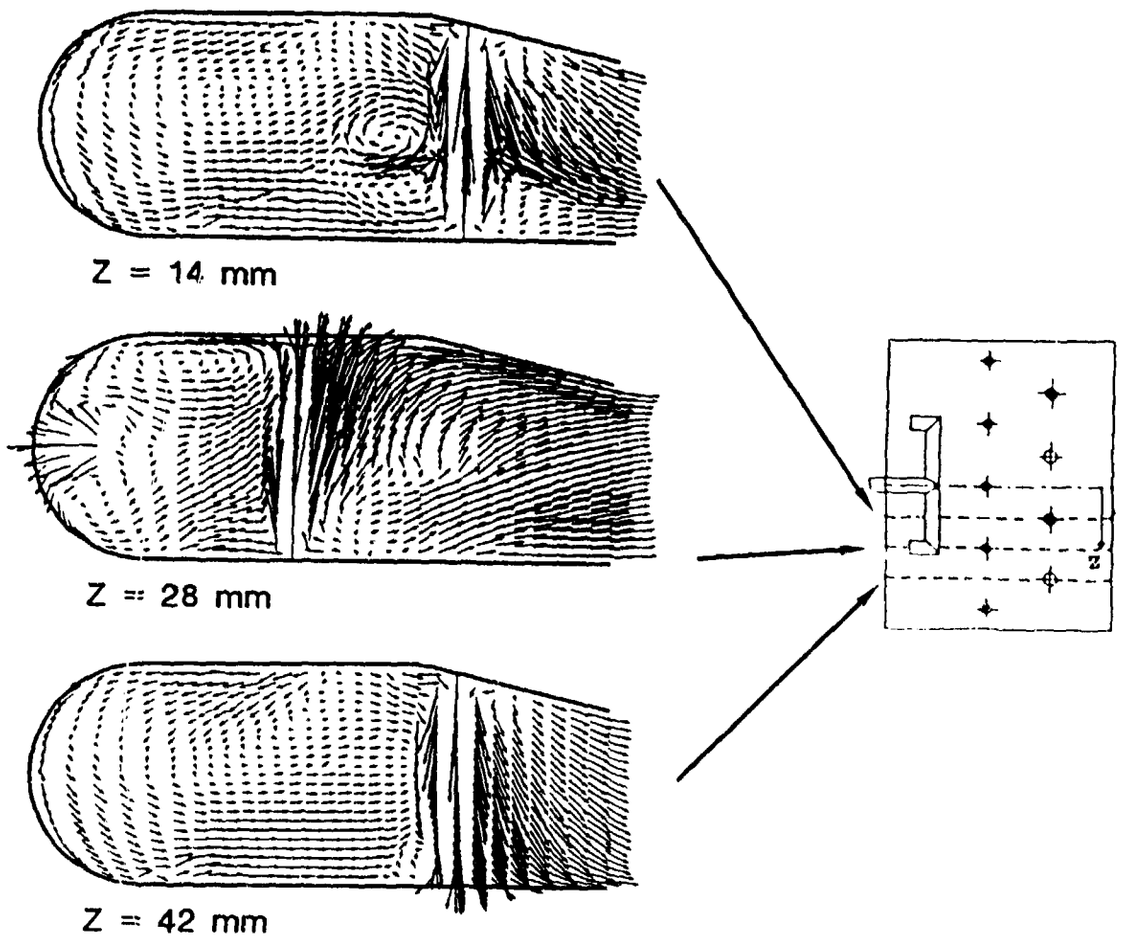

Fig. 5. Calculated velocity field in various vertical planes: Z=14 mm; Z=28 mm; Z = 42 mm.

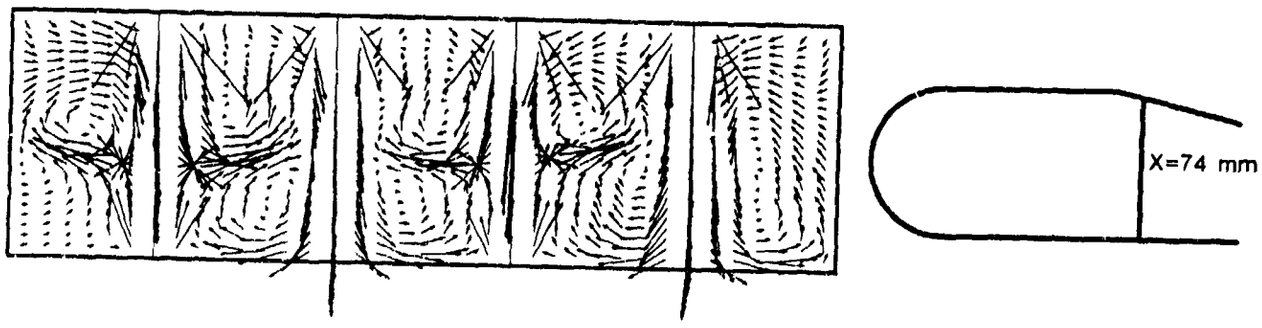

Fig. 6. Cross-plane calculated velocity field (dilution holes X=74 mm).

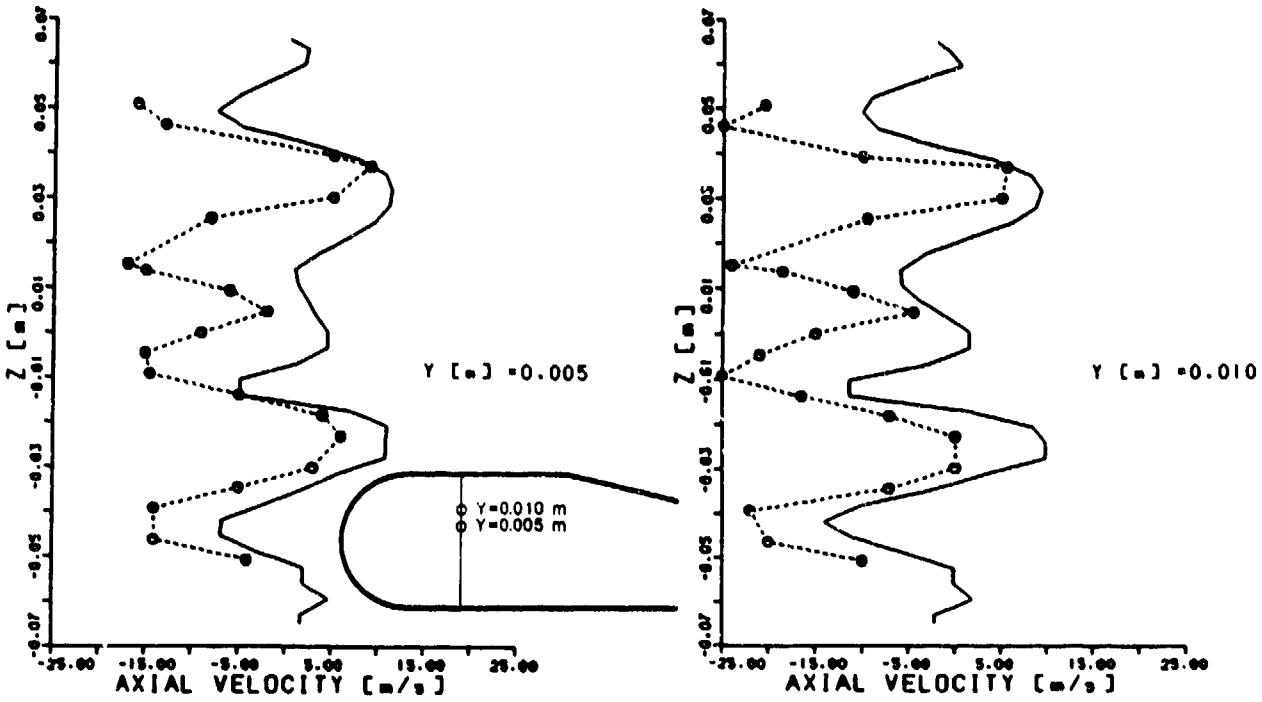

Fig. 7. Distributions of longitudinal mean velocity in primary zone at two values of y-coordinate. (— model, –°– experiments)

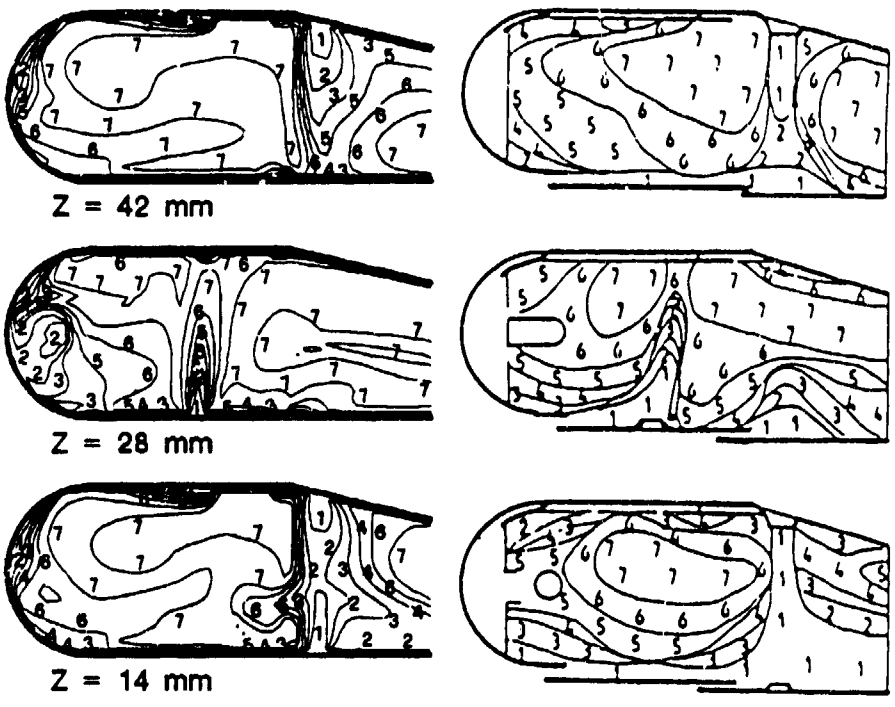

7	>1700
6	1500-1700
5	1300-1500
4	1100-1300
3	900-1100
2	700-900
1	<700

Fig. 8. Distribution of mean temperature (K) in various vertical planes: Z=14 mm; Z=28 mm; Z=42 mm (A = model; B = experiments).

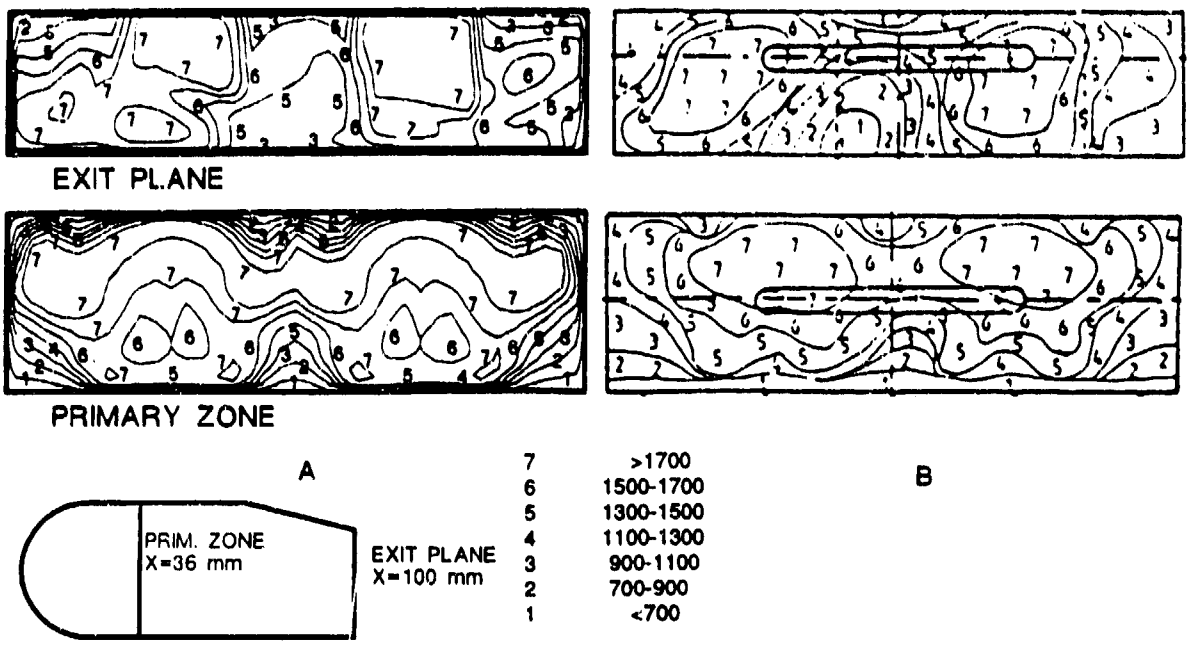

Fig. 9. Cross-plane distributions of mean temperature (K): (A = model; B = experiments).

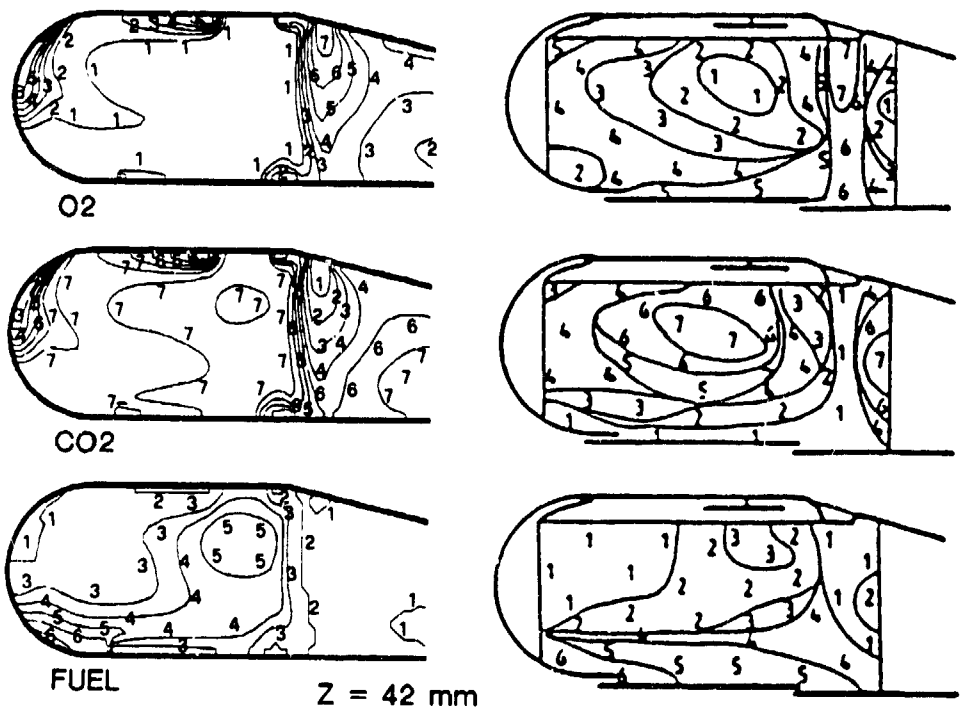

A	CO_2(%)	O2(%)	FUEL(%)	B
7	>9.0	>18.	>18.	
6	7.5-9.0	15.-18.	12.-18.	
5	6.0-7.5	12.-15.	6.0-12.	
4	4.5-6.0	9.0-12.	3.0-6.0	
3	3.0-4.5	6.0-9.0	1.5-3.0	
2	1.5-3.0	3.0-6.0	0.3-1.5	
1	<1.5	<3.0	<0.3	

Fig. 10. Mass fractions of chemical species in a vertical plane: Z = 42 mm; (A = model; B = experiments).

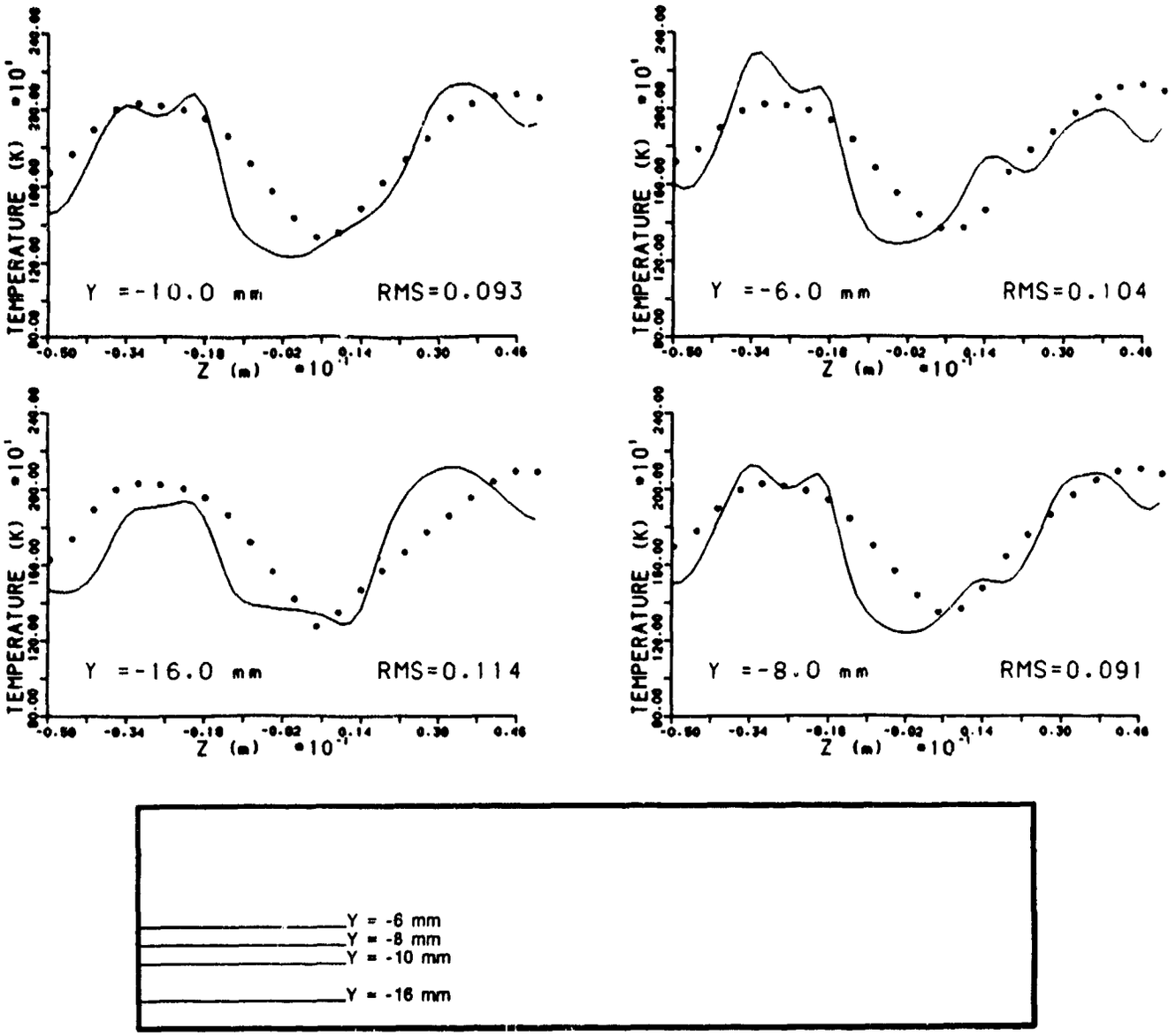

Fig. 11. Comparison of measured (°) vs. calculated (—) exit plane temperatures distribution at different values of y-coordinate.

Discussion

Question 1. S. Maldhof
You showed a line drawing with the development of residuals. These curves end at iteration no. 600. Is the solution then already in a converged state? Do you perform any other tests to prove convergence?

Author's Reply
Yes, the solution is already converged after about 400 iterations. For the convergence we control the maximum mass residual and the difference of pressure between the inlet and the exist of the combustor. The former has to be less than a specified value, and the latter has to become constant. We can also control the history of convergence of specific points within the combustor by plotting the temperature, total enthalpy, mixture fraction and its fluctuations. All these tests showed convergence of the calculation.

Question 2. Dr G. Andrews
Will you please outline how the film cooling air was modelled, as it does not seem to form part of the mesh geometry in Figure 3. Also, what boundary conditions were ued for the airflow distribution and hole velocity profiles at the inlet?

Author's Reply
In our code we can model the film cooling in two ways. Either the film cooling is considered as a flow entering the boundary, or it is considered as an injection or air with a given mass flow, momentum and enthalpy in the near wall mode corresponding to the film cooling slot. In the present calculation the latter method was used which permits an easier shape of the mesh. The boundary conditions in the holes are: temperature, pressure, mass flow of the entering flow and the effective area of the holes.

APPLICATION OF CFD IN COMBUSTOR DESIGN TECHNOLOGY

by

Hukam C. Mongia
Allison Gas Turbine Division
General Motors Corporation
P.O. Box 420, Speed Code T-14
Indianapolis, Indiana 46206-0420, USA

ABSTRACT

Multidimensional computational combustion dynamics has been used over the last twenty years by Mongia and his co-workers to provide improved insight during gas turbine combustor design and development processes. The empirical/analytical combustor design methodology that was first demonstrated under the Army sponsored Combustor Design Criteria Validation program conducted during 1974-1978 has been used in the design and demonstration of 15 advanced rig combustors, four technology demonstrator engine combustors, three engine combustors and one small turbine augmentor. Recognizing the limitations of turbulent combustion models, numerics and the assumptions required to fully specify the boundary conditions for practical gas turbine combustion systems, a new technique that combines state-of-the-art turbulent combustion models with "consistent" macro-volume expressions ("hybrid combustor modeling") was proposed by Rizk and Mongia (1986). This hybrid modeling approach has been calibrated with combustors that include diffusion flame, lean premix/prevaporized, or rich-lean types of combustion processes. The hybrid modeling technique gives good "quantitative" agreement with measured data on gaseous emissions, smoke, combustion efficiency, lean blowout fuel-air ratio, pattern factor, liner wall temperature levels and gradients of a number of combustors.

I. INTRODUCTION

Conventional combustor design techniques make extensive use of empirical design data based on proven gas turbine combustion systems, empirical and semi-empirical design correlations, simplified calculation methods (mostly quasi-one-dimensional), innovative intuitions based on the fundamentals of turbulent combustion, element test rigs coupled with bench-scale and sector test rigs to complete preliminary and detail design of "near next-generation" combustion systems. This is followed by a protracted combustor development process that uses full-scale test rigs, development engines and lead-the-fleet field demonstration engines. This empirical combustor design technique has been quite successful, and significant advances in the combustor technology and design concepts have been made during the last thirty years.

The limitations of empirical combustor design techniques are well-known. Multidimensional computational combustion dynamics (CCD) has therefore been used by many to help provide insight during combustor design process as summarized in Section II. An empirical/analytical design methodology was proposed and demonstrated[1-2] for two small reverse-flow annular combustors. Subsequently, this methodology has been used by Mongia and co-workers for a number of gas turbine combustors as described briefly in Section III. The limitations associated with multidimensional turbulent combustion models and their application to gas turbine combustion analysis are outlined in Section IV. Consequently, a new technique [3] called hybrid modeling has evolved over the last seven years (Section V) that gives "bottom-line" output for gaseous emissions, smoke, combustion efficiency, lean blowout, burner exit pattern factor, liner wall temperature levels and gradients.

II. USE OF CCD FOR IMPROVING UNDERSTANDING

A number of significant improvements have been made over the last thirty years in our ability to calculate complex turbulent combustion flows relevant to gas turbine combustors[4]. Mongia and his colleagues have conducted research in the areas of numerics[5-11], spray dynamics[12-16], fuel nozzle modeling[17-19], jet mixing[2, 20-22], swirling flows[2, 23-30] and combustor-diffuser interaction[31]. We have been using two-and three-dimensional reacting flow programs for improving our basic understanding in engine combustors since 1974 starting with the smoke and lean blowout trade-off studies conducted for the TFE-731. Other applications included the following:

- wall-carboning issues on the TPE 331-10
- fuel spray and flow interaction in the ATF-3 combustor
- cold start and excessive hot wall temperature concerns on the recuperative engine GT601
- primary orifice placement optimization study on the TPE 331-14/15
- development of a low-smoke combustor for the TFE 731
- root cause for the durability distress on the 501-K34 convective/film cooled combustor liner
- low-smoke 570 combustor flow configurations

Presented at an AGARD Meeting on 'Fuels and Combustion Technology for Advanced Aircraft Engines', May 1993.

- T56-A427
- T406/GMA 2100 combustors
- GMA 3007 combustor

A typical illustration is given in the following paragraphs on how 3-D combustor calculations have been used to achieve trade-off between smoke, lean blowout, and pattern factor.

The baseline 570 combustor was discretized into an x-y-z grid network of approximately 70,000 nodes. The baseline design does not have any swirler dome; whereas the final low-smoke combustor used an optimum swirler design that reduced the maximum SAE smoke number (of the baseline) from 38.0 to 11.0.

From predicted profiles of fuel-air ratios, gas temperatures and turbulence kinetic energy of these two combustors, as shown in Figures 1, 2 and 3 from Rizk and Mongia[60], one could convince oneself with the basic explanation for achieving a three-fold reduction in exhaust smoke emissions.

Similarly, over the years, a number of researchers have reported[(32-34)] that 3-D reacting flow models provide an improved understanding in gas turbine combustion processes. Therefore, the use of CCD to provide an improved insight during the combustor design and development process has become a common practice in many gas turbine companies.

III. USE OF EMPIRICAL/ANALYTICAL DESIGN METHODOLOGY

The first application of the empirical/analytical design methodology was the design and development of two small reverse-flow annular combustors[(1-2)] as shown in Figure 4. These two combustors were unique and as such there was hardly any significant experience data base available to provide empirical design guidance. The Army Combustor Design Criteria Concept I (ACDCI) uses ten discrete dome swirlers and ten radially inserted air-assist airblast nozzles which inject the fuel (JP-4 or JP-5) upstream toward the dome with analytically optimized down and back angles. It has a single row of 20 primary orifices on the outer wall at the location marked 2 in Figure 4. Two geometrically opposed rows of intermediate orifices are located at 4 and 11, respectively. Finally, dilution orifices are at locations 6 and 13. Figure 4 lists the design point combustor air flow rate ($Wa_{3.1}$), inlet pressure (P_3) and temperature (T_3), corrected airflow rate (W_c), combustor fuel/air ratio (F/A) and exit temperature (T_4), the liner outer wall diameter (OD), combustor channel height (H), liner length (L) and heat release rate (HRR, MBTU/ft^3 hr atm) for Concept I (i.e. ACDC I).

The Army Design Criteria Concept II (ACDC II) has a single-sided primary zone flow pattern established by discrete slot air injection (with a 30 deg angle to the outer wall toward the combustor dome) at two axial locations marked 2 and 3. The single-sided primary zone flow pattern is further strengthened by thirty radial entry jets at location 1. The primary zone is terminated by thirty radial primary jets at location 10. The dilution orifices are located at stations marked 5 and 12. ACDC II combustor liner length was 4.27 in. and the corresponding HRR was 6.0 MBTu/ft^3 hr atm.

Both combustor concepts used the same set of fuel nozzles to minimize fabrication cost. Both the combustor liner and the outer transition liner used a low-cost, relatively inefficient "English" louver film cooling technique as shown in Figure 4.

Table I shows comparison between Concepts I and II (ACDC I and ACDC II) in regard to total cooling air, dilution air, and the aerothermal performance achieved with the baseline Concept I and Concept II after one modification. Both combustors met or exceeded design goals.

In a follow-on effort, the baseline Combustor Concept I was analytically assessed for increasing the burner temperature rise to 2200°F. The modified combustor as shown in Figure 5 is identical to the baseline combustor Concept I except for the thirty primary orifices added to the ID wall. This combustor achieved performance goals without requiring any further hardware refinement.

A low-NOx fuel-staged reverse-flow annular combustor evolved through a systematic design, rig testing, and development process under the NASA sponsored Pollution Reduction Technology Program[37]. This combustor that originally started as a premix/prevaporizing combustion concept was developed by using the empirical/analytical design methodology[37, 38]. A number of combustor configurations were tested in this program which provided us with an extensive data base to calibrate the design methodology.

The Phase II combustor[37] Concept 3 as shown in Figure 6 used an annular pilot zone fueled by 20 piloted airblast nozzles. Forty simplex pressure atomizers surrounded by air chutes that inject approximately 22% W_{a3} were used for the main combustion zone. Compared to build-of-material engine combustor, Concept 3 achieved approximately 70% reduction in the take-off NOx emission index (NOxEI), and the idle unburned hydrocarbon and CO emission indices (HCEI and COEI) reductions were 97% and 70%, respectively.

The first ceramic engine demonstration program under the sponsorship of DARPA/NAVSEA required the development of a reverse-flow annular combustion system that exhibits

soft-ignition and "uniform" wall temperature characteristics[39] with attendant beneficial impact on the survivability of monolithic ceramics. The empirical/analytical design approach was used to analyze a number of combustor configurations leading to the definition of the baseline system as shown in Figure 7. The corrected flow rate (W_c) of this combustor is 1.03 PPS compared to 0.4 PPS in the Army Concept (Figure 4) and 3.3 PPS in the NASA Concept 3 (Figure 6). The combustor liner, the outer and inner transition liners comprise of fifteen ceramic rings and a metallic dome. The combustion system achieved superior aerothermal performance, exhibited soft ignition and extremely uniform temperature levels on the outer wall. Although the inner wall temperature gradients were less than half of those on the conventional combustors (typically 500°F/in.), further development work was considered necessary for the ceramic rings to survive the planned cyclic testing.

A unique reverse-flow annular combustion system for high altitude propulsion engine application as shown schematically in Figure 8, was designed analytically[40]. This rig combustor was to operate over a very wide operational envelope with the corresponding range of inlet pressure (P_3) and temperature (T_3) as listed. The ratio of the maximum to minimum fuel flow rates was 1600, and the corresponding ratio of the fuel/air ratio was 20. The corrected burner reference velocity range (V_ρ) was between 1.6 and 3600 fps. The minimum wind-mill ignition pressure was 2.0 psia and the corresponding goal for lean blowout fuel/air ratio was 0.004. Because a state-of-the-art cooling technique (stacked ring film-cooled with thermal barrier coating) was used for the combustor liner, and the outer and inner transition liners, we had to achieve low pattern factor without any dilution air. As shown in Figure 8, the baseline combustor met or exceeded all design goals and exhibited extremely uniform wall temperature distribution and pattern factor of 0.11.

A unique stoichiometric in-line annular combustor (Figure 9) was analytically designed[41] that demonstrated very soft ignition and lean blowout characteristics in addition to achieving essentially uniform wall temperature levels, high combustion efficiency and low smoke[42] at the fuel/air ratio of 0.053. Its dome design consists of twelve high-flow (24.3%) dual-spray piloted airblast nozzles surrounded by high-flow (26.2%) counter-rotating swirlers. Because the combustor was designed for stoichiometric operation, it used 76.8% Wa3 in the primary zone and no dilution air. The basic combustor with minor modifications met or exceeded design requirements.

A counter-flow convection-cooled reverse-flow annular combustor (Figure 10) was designed[43] for rig testing at the NASA Lewis Research Center to demonstrate its aerothermal performance and cooling effectiveness. To fully utilize the effectiveness potential of offset-fin extended-surface geometry with double-wall construction, it is essential that the combustor walls be designed to give essentially uniform temperature. This was achieved by analytically optimizing the airflow distribution around the combustor liner. The baseline combustor testing at NASA showed that all design goals were met and the maximum wall temperature levels were more than 300°F lower than those of another combustor that used conventional slot film cooling technique.

The design of ceramic ultra low emission combustor for regenerative automotive gas turbine is quite challenging. A systematic empirical/analytical design and proof-of-concept demonstration was undertaken by Sanborn, Mongia and Kidwell[44]. The basic combustion concept as shown schematically in Figure 11 comprises of a unique pure airblast nozzle that can translate axially to vary the effective area of an optimized radial inflow swirler. Two types of swirlers, namely radial inflow swirler and an axial swirler located on the backward facing step, were tested in a flame tube test rig. With a suitable fuel nozzle and swirler arrangement, it is possible to achieve an effective internal fuel-air mixing region so that the NOx emissions can be minimized over the entire automotive driving cycle. However, for the dome designs that do not create the required internal premixing region, one should expect high NOx emissions because of the high combustor inlet temperature levels (typically 1670-1940°F) in addition to the high degree of unmixedness.

As shown in Figure 11, when we used the half-area radial swirler with the full-area axial swirler (configuration 3), the flame tube rig testing at the simulated max and max-max power points produced NOx emissions index of 65.0 and 103 gm/kg fuel, respectively. However, the corresponding NOx EIs with the full-area (optimum) radial swirler (configuration 1) were 2.0 and 1.8. This translates into a 98.0 percent reduction in NOx emission index at the max-max engine power point.

The main combustor empirical/analytical design methodology was modified for application in the design and testing of a small turbine augmentor[45]. This augmentor design (Figure 12) evolved after analytically assessing (by means of two-and three-dimensional reacting flow programs) a number of parametric variations involving flame tube diameter, flameholder geometries, spray injection devices, etc. The 3-D predicted profiles of fuel-air ratio, combustion efficiency, temperature and axial velocity are shown in Figure 12 for an axial plane 8.1 in. downstream from the flameholder. The two most promising flameholder designs were fabricated and tested in an augmentor test rig. Both configurations easily met the design objectives.

Two reverse-flow annular combustors (Figures 13 and 14) were designed for potential application in future advanced helicopter engines. Because of the high surface to volume ratios of small reverse-flow annular combustors, two ad-

vanced cooling schemes, namely Lamilloy®* and effusion[76], were used in this effort. The primary zone airflow distribution, fuel nozzles, dome swirlers, the geometrical dimensions of the barrel, outer and inner transition liners were identical for both combustors. Therefore, it was a good back-to-back comparison between the two cooling schemes in regard to the total cooling air requirement. The maximum liner wall temperature exhibited by both the Lamilloy and effusion combustors at the conclusion of a limited rig development effort as 1670°F. The amount of total cooling air used by Lamilloy and effusion combustion systems were 34.7% and 49.1%, respectively. In other words, the Lamilloy cooling scheme for this application required approximately 30% less cooling air than the effusion cooling.

Advanced cooling schemes need to be developed for application in high temperature-rise, small reverse-flow annular combustors so that the durability objectives can be met with acceptable levels of cooling air requirement. One of the most promising cooling schemes is the compliant-matrix cooling technique[46] as illustrated in Figure 15. This cooling scheme, which reduces the cooling air requirement by 75 percent compared to that of film-cooled combustor was demonstrated on a reverse-flow annular combustor (OD = 13.48 in.) with the design inlet pressure ($P_{3.1}$), temperature ($T_{3.1}$), air flow rate ($Wa_{3.1}$), corrected airflow rate (Wc) and burner outlet temperature (T_4) of 272 psia, 1355°R, 7.24 lb/s, 0.69 lb/s and 3460°R, respectively. The total amount of cooling air used for this combustion system is approximately 23% compared to 30.8% used in the counter-flow film-cooled combustor (shown previously in Figure 10) designed for the lower $P_{3.1}$ and T_4 levels, namely 235 psia and 2960°R.

The rig testing including the simulated cyclic tests has been completed recently[47]. Acceptable wall temperature levels and aerothermal performance were demonstrated with the baseline combustor. Measured idle efficiency, lean blowout fuel/air ratio, pattern factor and maximum SAE smoke number were 99.1%, less than 0.005, 0.15 and less than 10, respectively.

A short, high-temperature-rise, reverse-flow annular combustor (liner length L = 3.2 in., combustor liner OD = 13.6 in., channel height H = 1.98 in.), sponsored by the Army, was designed by using the empirical/analytical design methodology. The main objective of this combustor, as shown in Figure 16, is to demonstrate low pattern factor of 0.15. The design conditions of this combustor should be compared with other small combustors discussed in this section, e.g. Figures 4, 5, 7, 10, and 13 through 15. The LPF combustor uses an effusion cooling scheme with thermal barrier coating. The baseline combustor with the cooling air modification has achieved 0.12 PF (2000°F temperature-rise with depressed combustor inlet temperature) along with acceptable idle efficiency, CO, unburned hydrocarbon and lean blowout fuel/air ratio of 99%, 22.2 gm/kg, 3.3 gm/kg and 0.006, respectively.

A near-stoichiometric in-line annular combustor (liner OD = 11.8 in., channel height H = 3.0 and length L = 6.9 in.) as shown in Figure 17, was designed to operate over a broad operating envelope from the simulated sea-level idle to max-power at sea-level flight Mach number of 1.2. This combustor was intended to run in a simulated engine environment behind a centrifugal compressor as shown in Figure 17. The placement of the combustor liner relative to the discharge plane of the diffuser was quite critical to ensure uniform pressure distribution in the combustor annulii. An earlier version of the 2-D combustor-diffuser interaction (CDI) model described in Reference 31 was used to optimize the flow-field characteristic around the combustor liner. A number of computer runs were made using the CDI and 3-D reacting flow programs to define the final combustor configuration.

The baseline combustor with one modification met all design objectives including high combustion efficiency at near-stoichiometric fuel-air ratio and essentially zero smoke number. This combustor used eight pure airblast nozzles, the primary zone air was 58.4% Wa_3, and the dilution air was approximately 10%.

A unique nonmetallic in-line annular combustion system, as shown in Figure 18 was designed by using the empirical/analytical design methodology. This combustor used sixteen pre-chamber cups fueled by 16 piloted premix fuel injectors. As shown, each cup used three swirlers, namely fuel nozzle swirler, primary and secondary swirlers. The OD and ID liner walls employed a total of eight silicon carbide composite ceramic rings. The basic design of the combustion system was optimized in regard to the airflow distribution through the three swirlers (and swirl angles and relative rotation, i.e., clockwise or counter clockwise), primary orifices and the cooling flows with assumed spray quality.

The first rig test with simulated metallic hardware showed a severe hot-streaking characteristics caused by the poorly performing fuel nozzles. A programmatic decision was therefore made to abandon this prechamber dome design and pursue the future test program by adopting the nonmetallic rings to the XTC 16/1 dome design, that is discussed later in this section.

The first application of the empirical/analytical design methodology for a demonstrator engine combustor was quite challenging[36] in that a small channel height (1.32 in.) reverse-flow annular combustor with stacked ring film cooled structure was to be designed to burn JP-10 fuel with low exhaust smoke. This combustor, as shown in Figure 19, with a 5.3 ms residence time, pure airblast noz-

* Lamilloy is a trademark of the General Motors Corporation.

zles, 7.8×10^6 BTu/ft^3-hr-atm heat release rate, produced low pattern factor (less than 0.2) and very uniform liner wall temperature levels as determined from a temperature-sensitive paint run at P_3=196 psia, T_3 = 750°F and T_4 = 2300°F. The baseline combustor with a half-area swirler successfully concluded the engine demonstration program without encountering any combustor related problems.

A high temperature-rise, reverse-flow annular combustor with stacked ring film-cooled structure with thermal barrier coating was analytically designed (Figure 20) and tested in an advanced gas generator[35, 36]. In spite of the short combustor length (L = 1.6 H), high heat release rate (8×10^6 BTU/hr-ft^3-atm), zero dilution air, the burner exit pattern factor was less than 0.15. Even though the primary zone equivalence ratio was close to unity at the design point with attendant SAE smoke number less than 10, its sea-level idle lean blowout fuel/air ratio of 0.005 was achieved without any fuel-staging. In addition, the maximum wall temperature levels did not exceed 1500°F and the maximum temperature gradients were significantly lower than 500°F/in.

The same combustor liner barrel that was used for the AF High Temperature Limited Life Turbine (Figure 17) was expected to be used in the AF Expandable Turbine Engine Component (ETEC) program. The ETEC demonstrator engine was required to operate successfully from the sea-level static operation to 3.5 Mach number at 90,000 ft altitude. Therefore, in addition to the challenges posed by the near-stoichiometric combustion operation, we had to design the combustion system for wide variations in the reference velocity, residence time, and loading. In addition, the fuel injection device was required to operate with the unheated as well as super-critically heated JP-10 fuel.

An innovative fuel nozzle as shown in Figure 21 was used in this program. Because of the excess cooling air requirement due to high T_3, and high dome flow with attendant 58.7% primary zone air flow, no dilution air was left for controlling the burner exit radial profile. The baseline combustor met or exceeded all design requirements from sea-level static to 3.5 Mach number, 90,000 ft altitude. The engine exhaust SAE smoke number was less than 10.0.

An innovative combustion system (Figure 22) was designed for the Generation 6 Build 1 ATEGG demonstrator XTC 16/1. The advanced multiswirl fuel nozzles when combined with optimum dome swirlers, and two closely spaced rows of primary orifices gave excellent aerothermal performance in regard to high-power near-stoichiometric combustion efficiency, liner wall temperature levels and gradients, and maximum SAE smoke number less than 10.0. In spite of short combustor volume and residence time (mean dia = 18.72 in., L = 6.62 in., H = 3.72 in.) and high primary zone air, the engine ignition characteristics were excellent, and we achieved acceptable lean blowout characteristics without requiring fuel staging.

The first application of the empirical/analytical combustor design method for a full-scale engine design and development effort was for the F109 turbo propulsion engine[48].

A compact reverse-flow annular combustion system (Figure 23) with stacked ring liner wall and thermal barrier coating along with 12 piloted airblast nozzles evolved based upon a number of 3-D reacting flow calculations and systematic combustor rig and engine development effort. This small combustor with 0.8 PPS corrected inlet airflow, 3.5% system pressure drop, 40% cooling air and 12.5% dilution air met or exceeded all design objectives including start envelope to 25,000 ft, less than 0.2 pattern factor, 0.005 lean blowout fuel/air ratio and 1500° maximum lines wall temperature.

An advanced turbofan inline annular combustor placed behind an axial-centrifugal compression system was designed by using empirical design data base, 2-D combustor-diffuser and 3-D reacting flow programs[49] as shown in Figure 24. The placement of the combustor liner relative to the prediffuser exit and the dome cowling design were optimized by a 2-D combustor-diffuser interaction model similar to the technique used in limited-life turbine rig combustor (Figure 17) discussed previously. The 3-D combustor model along with minimal combustor development testing gave an optimum liner airflow distribution as shown in Figure 24. The combustion system met all design objectives as summarized.

The last and perhaps the most convincing illustration on the application of the empirical/analytical combustor design methodology is by Roesler, Mongia and Stocker[50]. Because of limited time schedule and resources, no combustion development testing on the test rigs or the engine was planned. In other words, the basic combustion system was intended to meet all design objectives without any hardware modifications. Many of the combustors discussed in this section did not require any modifications, and the remaining needed only minor hardware changes to meet the requirements. However, the test rigs available for these combustors were used to investigate parametric effects of important variables. In many cases, the testing in conjunction with detailed modeling efforts were conducted to determine the limitations of the combustion concepts as well as the design methodology. Typical examples for these types of activities are reported in References 2, 37, 39, 40 and 44.

The annular combustion system for a low-cost expandable engine (Model 150) application (Figure 25) used ten vaporizer tubes for fuel injection. This engine is a 11.6 in. diameter, 500-lb thrust class turbojet for tactical missile applications. The engine was designed for a maximum flight Mach number of 0.8 and a peak altitude of 10,000 ft along with the wind-mill ignition capability over its operational envelope. The engine is to use JP-10 or JP 4. The sea-level design conditions are listed in Figure 25 along with

combustor length (L), channel height (H), reference velocity (V_r), residence time (τ) and the final design liner airflow distribution, which was determined based upon 3-D modeling that used 45x21x25 control volumes. Figure 25 also shows predicted flow field including U-V velocity vectors, profiles of fuel-air ratios and outer liner wall isothermal lines. The baseline combustor met or exceeded all design requirements.

IV. LIMITATIONS OF EMPIRICAL/ANALYTICAL DESIGN METHODOLOGY

Even though the empirical/analytical methodology has been successfully used in the design and development process of 22 combustion systems described in Section III, and CCD has provided insight for a number of production engine combustors (Section II), the basic limitations associated with turbulent combustion models are primarily responsible for our failure to make quantitatively accurate predictions even for an "average" fuel nozzle combustor sector. Over the years, significant progress has been made in the theories of turbulent combustion and the submodels of turbulence, kinetic, radiation, spray, soot, etc. A number of interesting and very important observations, milestones, and conclusions have been achieved.

For example, Frenklach, Wang and Rabinowitz[57] maintain that "it is hard to expect that a reaction mechanism composed from first principles will possess the high degree of numerical accuracy required for combustion modeling." The application of their solution mapping method to optimize the rate constants of a detailed 149-step methane-air combustion should be extended to include NOx chemistry in addition to other required extensions, e.g., higher molecular weight fuels.

Similarly, alot more work needs to be done in turbulence, radiation, nozzle modeling, spray, soot and radiation in addition to advanced numerics, body conforming grids, etc., to achieve a quantitatively accurate turbulent combustion model. Our work on advanced numerics[5-11], spray transport[12-16, 29], fuel nozzle modeling[17-19], jet mixing[20-22], swirling flows[21, 23-30] and excellent research conducted by others has convinced us that conventional second-order closure models might not give us the level of accuracy required for making quantitatively reliable analytical predictions for gas turbine combustors.

The scalar and joint PDF transport models look promising[51-54] but their application to practical gas turbine combustors as design tools is many years away.

Many of the challenging combustor performance characteristics (e.g. pattern factor, liner hot spots) cannot be modeled mechanistically. Similarly, the mechanistic reacting flow models have not provided definite guidance in carrying out the tradeoffs between conflicting design requirements, e.g., low smoke versus flame stability and relight; high-power NOx versus low-power CO and unburned hydrocarbons.

Another area of significant weakness is the fuel nozzle modeling because in many combustion development activities, the lack of detailed information on fuel nozzle performance (e.g., radial and circumferential fuel distribution) can lead to serious design deficiencies including start, lean blowout, and hot-streaking.

The modeling of fuel nozzle processes should include the filming, ligament formation, primary and secondary breakup. The undesirable spray impingement on the nozzle shroud can adversely affect combustor performance and cause severe liner hot streaks as encountered in the Non-metallic Combustor (Figure 18).

Multidimensional modeling attempts for radiation, gaseous, and smoke emissions have been less than satisfactory[55, 56].

Figure 26 is from a smoke-reduction program on a turbofan engine[35]. The predicted flowfield for the engine (baseline) combustor shows that the primary zone has quiescent regions for flame stabilization, and that the primary jet air is not recirculating. The predicted fuel-air ratio profiles, which are not shown here, indicated the existence of fuel-rich pockets indicating the root cause for high smoke emissions. By changing the air flow distribution, we were able to identify a compromise combustor configuration (identified as Mod V) wherein we could maintain selectively the fuel rich pockets (for flame stability) and simultaneously get improved mixing and more agitated primary zone flow field as shown in Figure 23. Therefore, we intuitively expected Mod V to have lower exhaust smoke emission than the baseline. We did not expect any deterioration in the lean flame stability characteristics. However, the rig testing showed no smoke reduction.

In summary, the empirical/analytical method cannot be easily extended to provide quantitatively accurate results. Mechanistic models based on second-order closures are limited in scope. Liner hot spots, pattern factor, lean blowout, gaseous, and smoke emissions cannot be predicted due to the inaccuracies involved with the physico chemical models, numerics and the specification of the boundary conditions.

V. HYBRID ANALYTICAL DESIGN METHODOLOGY

Prompted by the limitations of current turbulent combustion models, the lack of well-defined boundary conditions in engine combustors, and routine successful application of simple correlations in combustor design and development process, Rizk and Mongia proposed a hybrid modeling technique[3] that combines analytical model predictions with physically realistic macro-volume expressions to es-

timate combustion efficiency, lean blowout, pattern factor, wall temperature, gaseous and smoke emissions.

The usefulness of the hybrid design methodology (when fully calibrated) over the empirical/analytical design approach can be illustrated by referring back to the smoke reduction program for the Model 570 engine. Although the 3-D model calculations were made during the smoke reduction program, these could only provide qualitative guidance as to how much smoke reduction the planned modification would result in. As shown previously in Figures 1-3, one could tentatively infer from the calculations that the final low-smoke configuration (with dome swirlers) should produce lower levels of exhaust smoke than the baseline. The hybrid modeling (Figure 27) approach not only gave good agreement with measured smoke emissions, it also provided further insight by identifying the regions of soot formation and oxidation. In all four of the modifications (namely Mod I, Mod II, Mod III, and the final low-smoke configuration), we predict significant reduction in the soot formation rates. However, the difference between the mods is quite small. On the other hand, these modifications show that their soot oxidation characteristics are quite different. Consequently, the net difference between soot formation and oxidation reveals that the low-smoke final combustor gives the lowest exhaust SAE smoke number of 11.0.

Round I activities were completed by 1990 as described in References (3, 58-62). We were able to calibrate the hybrid modeling approach with measured data on smoke, pattern factor, lean blowout fuel-air ratio, gaseous emissions, and combustion efficiency for ten different diffusion flame combustors by using the macro volume expressions shown in Table 2. Some limited model calibration was done with the measured liner wall temperature levels. The comparison between predictions and measurements[60] as shown in Figures 28 and 29 is with a fixed set of empirical constants A_1 through A_{10}, which are 0.0093, 3.85, 15.0, 0.1773, 0.042, 0.07, 1.71, 1500, 0.0095, and 98,000, respectively.

The hybrid modeling approach gave good agreement with NOx data from rich-quench-lean[61], Figure 30, and lean premix/prevap[62], Figure 31, combustors.

The main objective of Round 2 hybrid modeling formulation/calibration activities[63-71] is to develop a self-consistent set of macro-volume expressions for NOx, CO, and unburned hydrocarbons so that the procedure can provide uniformly good agreement with data on a number of gas turbine combustors of diffusion, lean premix/prevap, lean direct injection, and rich-lean combustion types. Typical example for diffusion flame type combustors is shown in Figure 32.

The calibration of the Round 2 hybrid modeling approach is essentially complete. Its application in the design and development testing of ultra low NOx combustors is planned for the middle of 1993.

The Round 3 hybrid modeling effort will incorporate improved expressions for jet mixing, liner cooling, smoke formation/oxidation, and hybrid nozzle model[72-75].

VI. SUMMARY

The empirical/analytical combustor design approach of Mongia and co-workers has been successfully applied to 22 gas turbine combustors and one small turbine augmentor. Its limitations for providing quantitative design guidance are due to the inaccuracies of the state-of-the-art turbulent combustion models, numerics, grid resolution and boundary conditions. Next generation turbulent combustion models[51-54] are expected to give improved predictive capability.

Hybrid analytical design methodology of Rizk and Mongia[3, 58-71] has been calibrated with an existing combustor design data base. This technique is expected to provide quantitatively accurate estimates of combustion efficiency, lean blowout, pattern factor, wall temperatures, gaseous and smoke emissions.

REFERENCES

1. Mongia, H.C. and Smith, K.F., "An Empirical/Analytical Design Methodology for Gas Turbine Combustors," AIAA Paper 78-998, 1978.

2. Mongia, H.C., Reynolds, R.S., Coleman, E. and Bruce, T.W., "Combustor Design Criteria Validation, Volumes I, II and III," USARTL-TR-78-55 A, B and C, (AD-A0-67657, 67689 and 66793), 1979.

3. Rizk, N.K. and Mongia, H.C., "Gas Turbine Combustor Design Methodology," AIAA Paper 86-1531, 1986.

4. Borghi, R. and Murthy, S.N.B., (Eds), "Turbulent Reactive Flows, Lecture Notes in Engineering, 40," Springer-Verlag, Berlin, 1989.

5. Runchal, A.K., Anand, M.S. and Mongia, H.C., "An Unconditionally Stable Centeral Differencing Scheme for High Reynolds Number Flows," AIAA Paper 87-0060, 1987.

6. Patankar, S.V., Karki, K.C. and Mongia, H.C., "Development and Evaluation of Improved Numerical Schemes for Recirculating Flows," AIAA Paper 87-0061, 1961.

7. Karki, K.C., Patankar, S.V., Runchal, A.K. and Mongia, H.C., "Improved Numerical Methods for Turbulent Viscous Recirculating Flows Aerothermal Modeling Phase II, Final Report," NASA CR-182169, June 1988.

8. Karki, K., Vanka, P. and Mongia, H.C., "Fluid Flow Calculations Using a Multigrid Method and an Improved Discretization Scheme," AIAA Paper 89-0483, 1989; also Numerical Heat Transfer, Part B, V16, pp. 143-159.

9. Karki, K., Patankar, S. and Mongia, H.C., "Solution of Three-Dimensional Flow Problems Using a Flux-Spline Scheme," AIAA Paper 89-0687, 1989; also AIAA J. V28, n4, pp. 631-634.

10. Karki, K. and Mongia, H.C., "Recent Development in Computational Combustion Dynamics," AIAA Paper 89-2808, 1989.

11. Karki, K.C. and Mongia, H.C., "Evaluation of a Coupled Solution Approach for Fluid Flow Calculations in Body Fitted Coordinates," Int. J. Numerical Methods in Fluids, V11, pp. 1-28, 1990.

12. Mostafa, A.A. and Mongia, H.C., "On the Turbulence-Particle Interaction in Turbulent Two-Phase Flows," AIAA Paper 86-0215, 1986; also Int. J. HMT, V31, n10, pp. 2063-2075, 1988.

13. Mostafa, A.A. and Mongia, H.C., "Eulerian and Lagrangian Predictions of Turbulent Evaporating Sprays," AIAA Paper 86-0452, 1986; also Int. J. HMT, V30, n12, pp. 2583-2593, 1987.

14. Mostafa, A.A. et al., "On the Evolution of Particle-Laden Jet Flows: A Theoretical and Experimental Study," AIAA Paper 87-2181, 1987; also AIAA J., V27, n2, pp. 167-173, 1989.

15. Mostafa, A.A. et al., "On the Evolution of Particle-Laden Coaxial Jet Flows: A Theoretical and Experimental Study," AIAA Paper 88-0239, 1988; also Int. J. Heat and Fluid Flow, V11, n2, pp. 90-97, 1990.

16. Nikjooy, M. et al., "Calculations of Particle-Laden Flows by Second Moment Closures," AIAA Paper 91-0082.

17. Sultanian, B.K. and Mongia, H.C., "Fuel Nozzle Air Flow Modeling," AIAA Paper 86-1667, 1986.

18. Rizk, N.K., Mostafa, A.A. and Mongia, H.C., "Modeling of Gas Turbine Fuel Nozzles," ASME Publication AMD-Vol. 81, pp. 91-106, Dec. 1986, also Atomization and Spray Tech., V3, pp. 241-260, 1987.

19. Rizk, N.K. and Mongia, H.C., "A Model for Airblast Atomization," AIAA Paper 89-2321, 1989.

20. Srinivasan, R., Berenfeld, A. and Mongia, H.C., "Dilution Jet Mixing Program Phase I Report," NASA CR-168031, November 1982.

21. Srinivasan, R. et al., "Aerothermal Modeling Program Phase I - Final Report," NASA CR-168243, August 1983.

22. Oechsle, V.L., Mongia, H.C. and Holdeman, J.E., "A Parametric Numerical Study of Mixing in a Cylindrical Duct," AIAA Paper 92-3088, 1992.

23. Srinivasan, R. and Mongia, H.C., "Numerical Computations of Swirling Recirculating Flow - Final Report," NASA CR-165196, September, 1980.

24. So, R.M.C., Ahmed, S.A. and Mongia, H.C., "An Experimental Investigation of Gas Jets in Confined Swirling Air Flows," NASA CR-3832, September, 1984.

25. So, R.M.C., Ahmed, S.A. and Mongia, H.C., "Jet Characteristics in Confined Swirling Flow," Exp. Fluids, V3, pp. 221-230, 1985.

26. So, R.M.C., Ahmed, S.A. and Mongia, H.C., "Density Effects on Jet Characteristics in Confined Swirling Flow," Exp. Fluids, V3, pp. 231-238, 1985.

27. Nikjooy, M., Mongia, H.C. and Samuelsen, G.S., "Calculations of Recirculating Flows Using Second Moment Closure," AIAA Paper 89-0484.

28. Nikjooy, M. et al, "A Numerical and Experimental Study of Confined Swirling Jets," AIAA Paper 89-2898, 1989.

29. Nikjooy, M., Mongia, H.C., McDonell, V.G. and Samuelsen, G.S., "Fuel Injector-Air Swirl Characterization Aerothermal Modeling Phase II - Final Report," NASA CR-189193, September 1992.

30. Nikjooy, M., Mongia, H.C., Sullivan, J. and Murthy, S.N.B., "Flow Interaction Experiments Aerothermal Modeling Phase II - Final Report," NASA CR-189192, 1993.

31. Karki, K.C., Oechsle, V.L. and Mongia, H.C., "A Computational Procedure for Diffuser-Combustor Flow Interaction," ASME Paper 90-GT-87; also J. Eng. Gas Turbines and Power, V114, pp. 1-7, 1992.

32. Turan, A. et al., "Three-Dimensional Modeling of Reacting Flows in Horse-Shoe Vortex Combustors," ASME Paper 84-GT-170, 1984.

33. Burrus, D.L., Shyy, W. and Braatan, M.E., "Numerical Models for Analytical Predictions of Combustor Aerothermal Performance Characteristics," Combustion and Fuels in Gas Turbine Engines, AGARD-CP-422, October 1987.

34. Huebner, S. and Exley, T., "Numerical Analysis of the Flows in Annular Slinger Combustors," AIAA Paper 90-2164, 1990.

35. Mongia, H.C., Reynolds, R.S. and Srinivasan, R., "Multidimensional Turbulent Combustion: Analysis, Applications and Limitations," AIAA Paper 84-0477.

36. Mongia, H.C., "Application of Multidimensional Modeling Techniques to the Design and Development Testing of Gas Turbine Combustors," Invited Speaker at the 1982 AFOSR Annual Contractor's Meeting.

37. Bruce, T.W., Davis, F.G., Kuhn, T.E. and Mongia, H.C., "Pollution Reduction Technology Program Small Jet Aircraft Engines, Phase I, II and III Final Reports," NASA CR-135214, 159415 and 165386, September, 1977, September, 1978 and December, 1981.

38. Reynolds, R.S., Kuhn, T.E. and Mongia, H.C., "Advanced Combustor Analytical Design Procedure and its Application in the Design and Development Testing of a Premix/Prevaporized Combustion System," presented at the 1977 Central States Combustion Institute Meeting.

39. Johansen, K.M., Johnston, B.H., Mongia, H.C. and Sanborn, J.W., "Combustion Process Testing for Reduced Wall-Temperature Gradients," Proceedings 1977 DARPA/NAVSEA Ceramic Gas Turbine Demonstrator Engine Program Review.

40. Mongia, H.C., Coleman, E.B. and Bruce, T.W., "Design and Testing of Two Variable-Geometry Combustors for High-Altitude Propulsion Engines," AIAA Paper 81-1389, 1981.

41. Dins, C.R., Eversmed, R.J., Mongia, H.C. and Wimmer, J., "Advanced Material Segmented Combustor Phase II Interim Report," AFAPL-TR-80-2065, July, 1980.

42. Johnson, K.P. et al., "Advanced Material Segmented Combustor Program," AFWAL-TR-83-2036, March, 1983.

43. Mongia, H.C. and Brandes, D.J., "Design Documentation Report Counter-Flow Film-Cooled Combustor Program," NASA CR-167922, June, 1982.

44. Sanborn, J.W., Mongia, H.C. and Kidwell, J.R., "Design of a Low-Emission Combustor for an Automotive Gas Turbine," AIAA Paper 83-0338, 1983.

45. Kuhn, T.E., Mongia, H.C., Bruce, T.W. and Buchanan, E., "Small Gas Turbine Augmentor Design Methodology," AIAA Paper 82-1179, 1982.

46. Paskin, M.D., Ross, P.T., Mongia, H.C. and Acosta, W., "Composite Matrix Cooling Scheme Small Gas Turbine Combustors," AIAA Paper 90-2158, 1990.

47. Paskin, M.D., Mongia, H.C. and Acosta, W., "An Efficient Liner Cooling Scheme for Advanced Small Gas Turbine Combustors," AIAA Paper 93-1763, 1993.

48. Maertins, H.F.W. and Bruce, T.W. (1990), "The F109-GA-100 Engine Designed Specifically for Trainer Use," ASME Paper 90-GT-167.

49. Sanborn, J.W., Lenertz, J.E. and Johnson, J.D., "Design and Test Verification of a Combustion System for an Advanced Turbofan Engine," AIAA Paper 87-1826, 1987.

50. Roesler, T.C., Mongia, H.C. and Stocker, H.L., "Analytical Design and Demonstration of a Low-Cost Expendable Turbine Engine Combustor," AIAA Paper 92-3754, 1992.

51. Anand, M.S., Pope, S.B. and Mongia, H.C., "A PDF Method for Turbulent Recirculating Flows," Turbulent Reactive Flows, Lecture Notes in Eng., 40, Springer-Verlag, Berlin, 672, 1989.

52. Anand, M.S., Pope, S.B. and Mongia, H.C., "Calculations of Axisymmetric Turbulent Jets by the PDF Method," 7th Symp. Turbulent Shear Flows, p. 3.3, 1989.

53. Anand, M.S., Pope, S.B. and Mongia, H.C., "Pressure Algorithm for Elliptic Flow Calculations with the PDF Method," NASA CP-3078, 347, 1990.

54. Anand, M.S., Pope, S.B. and Mongia, H.C., "PDF Calculations for Swirling Flows," AIAA Paper 93-0106, 1993.

55. Sanborn, J.W., Reynolds, R.S. and Mongia, H.C., "A Quasi-Three-Dimensional Calculation Procedure for Predicting the Performance and Gaseous Emissions of Gas Turbine Combustors," AIAA Paper 76-682, 1976.

56. Srivatsa, S.K., "Computations of Soot and NOx Emissions from Gas Turbine Combustors," NASA CR-167930, 1982.

57. Frenklach, M., Wang,H. and Rabinowitz, M.J., "Optimization and Analysis of Large Chemical Kinetic Mechanisms Using the Solution Mapping Method - Combustion of Methane," Prog. Energy Comb. Sci., Vol. 18, pp. 47-73, 1992.

58. Rizk, N.K., Oechsle, V.L., Ross, P.T. and Mongia, H.C., "High Density Fuel Effects," AFWAL-TR-88-2046, August, 1988.

59. Rizk, N.K. and Mongia, H.C., "A 3-D Combustor Performance with High Density Fuels," AIAA Paper 89-0219, also J. Propulsion and Power, V6, n6, pp. 660-667, 1990.

60. Rizk, N.K. and Mongia, H.C., "A 3-D Analysis of Gas Turbine Combustors," AIAA Paper 89-2888, also J. Propulsion and Power, V7, n3, pp. 445-451, 1991.

61. Rizk, N.K. and Mongia H.C., "Ultra-Low NOx Rich-Lean Combustion," ASME Paper 90-GT-87, 1990.

62. Rizk, N.K. and Mongia, H.C., "Lean Low NOx Combustion Concept Evaluation," 23rd Int. Comb. Symp., pp. 1063-1070, 1990.

63. Rizk, N.K. and Mongia, H.C., "Gas Turbine Combustor Performance Evaluation," AIAA Paper 91-0640, 1991.

64. Rizk, N.K. and Mongia, H.C., "Low NOx Rich-Lean Combustion Concept Application," AIAA Paper 91-1962, 1991.

65. Rizk, N.K. and Mongia, H.C., "Three-Dimensional Gas Turbine Combustor Emissions Modeling," ASME Paper 92-GT-129, 1990.

66. Rizk, N.K. and Mongia, H.C., "Semianalytical Correlations for NOx, CO and UHC Emissions," ASME Paper 92-GT-130, 1990.

67. Rizk, N.K. and Mongia, H.C., "NOx Model for Lean Combustion Concept," AIAA Paper 92-3341, 1992.

68. Rizk, N.K. and Mongia, H.C., "Three-Dimensional NOx Model for Rich/Lean Combustors," AIAA Paper 93-0251, 1993.

69. Rizk, N.K. and Mongia, H.C., "A Semianalytical Emission Model for Diffusion Flame, Rich/Lean, and Premixed Lean Combustors," ASME Paper 93-GT , 1993.

70. Rizk, N.K. and Mongia, H.C., "Evaluation of Emission Model for Diffusion Flame, Rich/Lean, and Premixed Lean Combustors," ASME Paper 93-GT- , 1993.

71. Rizk, N.K. and Mongia, H.C., "Three-Dimensional Emission Modeling for Diffusion Flame, Rich/Lean, and Lean Gas Turbine Combustors," AIAA Paper 93-2338, 1993.

72. Rizk, N.K. and Mongia, H.C., "Semianalytical Fuel Injector Performance Correlation Approach," AIAA Paper 89-2902, 1989.

73. Rizk, N.K. and Mongia, H.C., "A Semianalytical Approach Validation for Airblast Atomizers," AIAA Paper 90-0361, 1990.

74. Rizk, N.K. and Mongia, H.C., "Further Validation of a Semianalytical Approach for Fuel Injectors of Different Concepts," AIAA Paper 90-2190, 1990.

75. Rizk, N.K. and Mongia, H.C., "Calculation Approach Validation for Airblast Atomizers," ASME Paper GT-91-305, also J. Eng. Gas Turbine and Power, V114, pp. 386-393, April, 1992.

76. Nealy, D.A., Reider, S.B., and Mongia, H.C., "Alternate Cooling Configurations for Gas Turbine Combustion Systems," AGARD-CP-390, pp. 25-1 to 25-15, 1985.

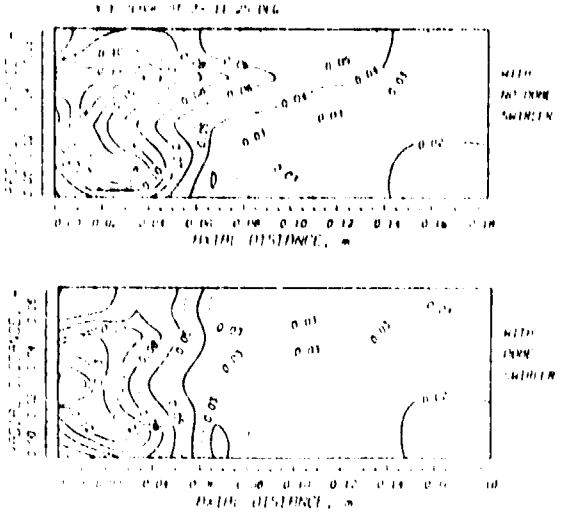

Figure 1. Effect of dome design on fuel/air ratio distribution.

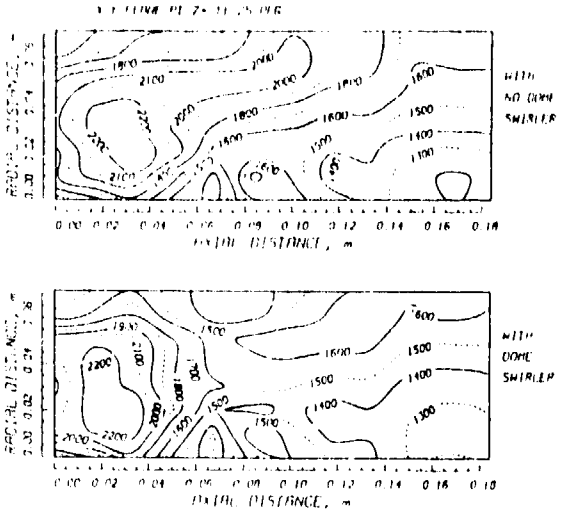

Figure 2. Influence of dome swirler on gas temperature pattern, K.

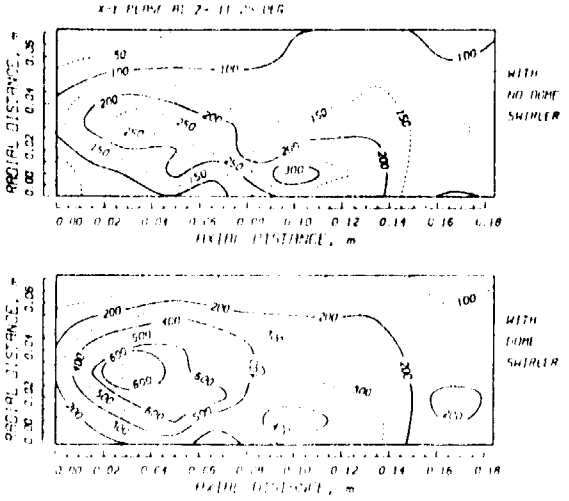

Figure 3. Kinetic energy of turbulence pattern for both combustor designs, m2s2.

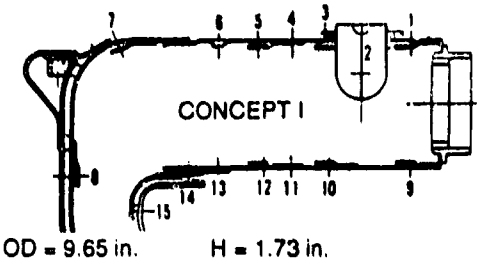

OD = 9.65 in. H = 1.73 in.
L = 3.8 in. HRR = 6.42 MBTU/ft^3-hr-atm

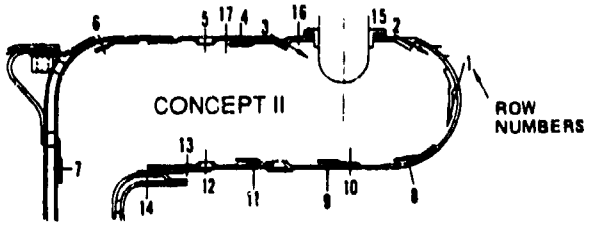

L = 4.27 in. HRR = 6.0 MBTU/ft^3-hr-atm
$W_{a3\text{-}1}$ = 2.7 PPS P_3 = 147 psia T_3 = 665°F
W_c = 0.397 PPS F/A = 0.0268 T_4 = 2300°F

Figure 4. Two small annular combustors met program goals with one modification.

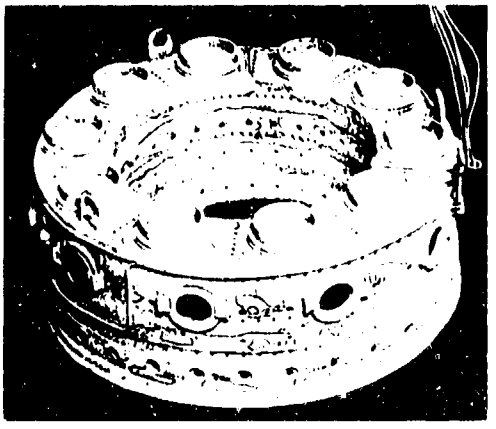

ΔT = 2200°F T_4 = 2850°F
LBO F/A < 0.005 $T_{wall, max}$ = 1600°F

Figure 5. Army Design Criteria Concept I modified for 2200°F DT gave good aerothermal performance.

Table I.

Cooling air , % W_A	51.09	25.01
Dilution air , % W_A	13.65	21.14
Pressure drop, % P_3	2.5	1.7
Pattern factor	0.17	0.22
Idle efficiency	98.08	99.57
Lean blowout	0.003	0.003
SAE smoke No.	0	8.5
Max wall temp, °F	1425	1600
Cooling flux, PPS/in.^{2}	0.0052	0.003

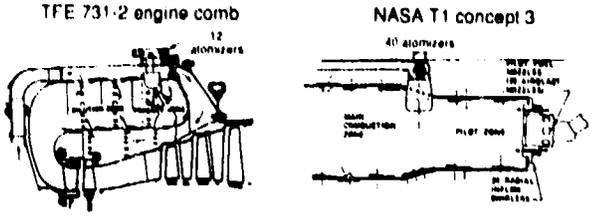

W_{a3} = 29.5 PPS P_3 = 200 psi T_3 = 743°F
W_c = 3.3 PPS T_4 = 1753°F OD = 21.1 in.
ID = 15.43 in. L = 7.2 in.

Emissions levels, emissions index

	Engine comb	Concept 3
Takeoff NOx	11.5	3.6
Idle HC	20.6	0.7
Idle CO	58.8	17.9

Figure 6. NASA T1 Concept 3 fuel-staging concept.

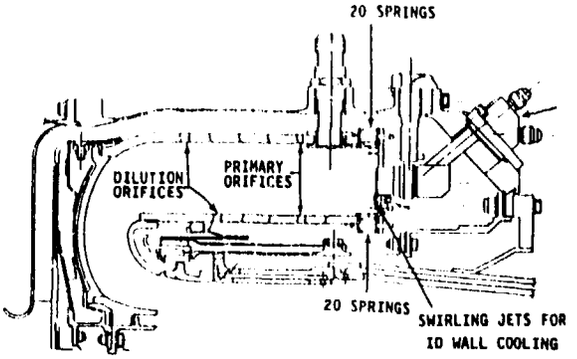

$W_{a3\text{-}1}$ = 6.16 PPS P_3 = 125 psi T_3 = 600°F
W_c = 1.03 PPS T_4 = 2200°F
OD = 14.16 in. H = 1.69 in. L = 4.5 in.

Figure 7. DARPA/NAVSEA reverse-flow annular ceramic rig combustor designed for "uniform" wall temperature levels and soft ignition.

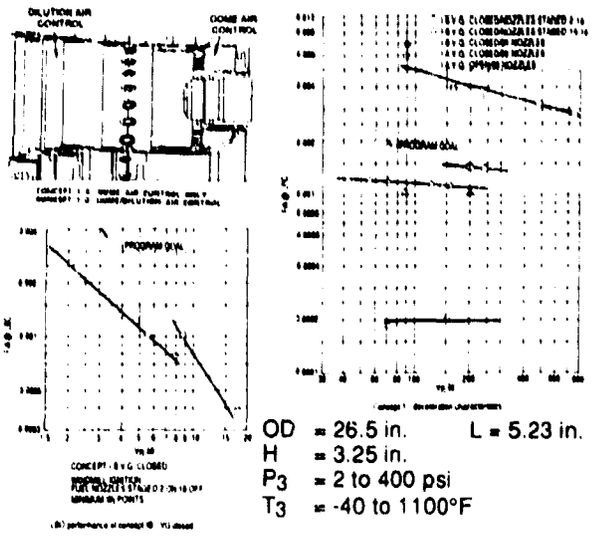

OD = 26.5 in. L = 5.23 in.
H = 3.25 in.
P_3 = 2 to 400 psi
T_3 = -40 to 1100°F

Max temp rise = 2400°F
Max to min fuel flow rate = 1600
Max to min F/A ratio = 20
Corrected reference velocity = 1.6-3600 fps
Minimum wind-mill ignition P_3 = 2.0 psi
Primary zone air = 74.2% w/ VG open
= 11.8% w/ VG closed

Figure 8. AF variable geometry reverse-flow annular combustor designed for high-altitude ignition and enhanced stability.

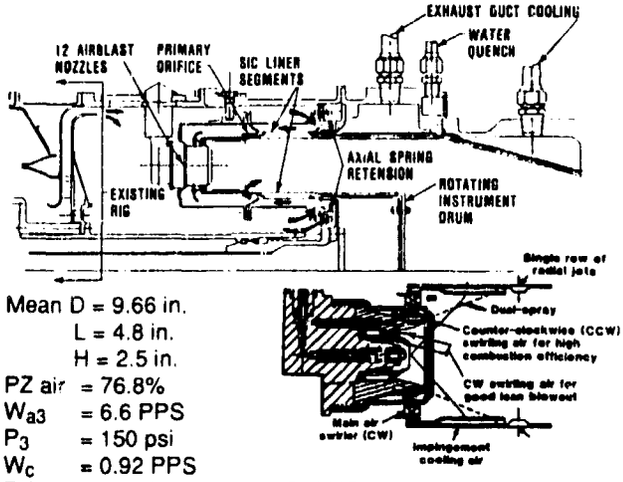

Mean D = 9.66 in.
L = 4.8 in.
H = 2.5 in.
PZ air = 76.8%
W_{a3} = 6.6 PPS
P_3 = 150 psi
W_c = 0.92 PPS
F/A = 0.053 T_4 = 3530°F Comb eff. = 99.06%
HRR = 13.7 MBTU/ft^3-hr-atm

Figure 9. AF segmented ceramic annular combustor designed for soft ignition and uniform wall temperature levels.

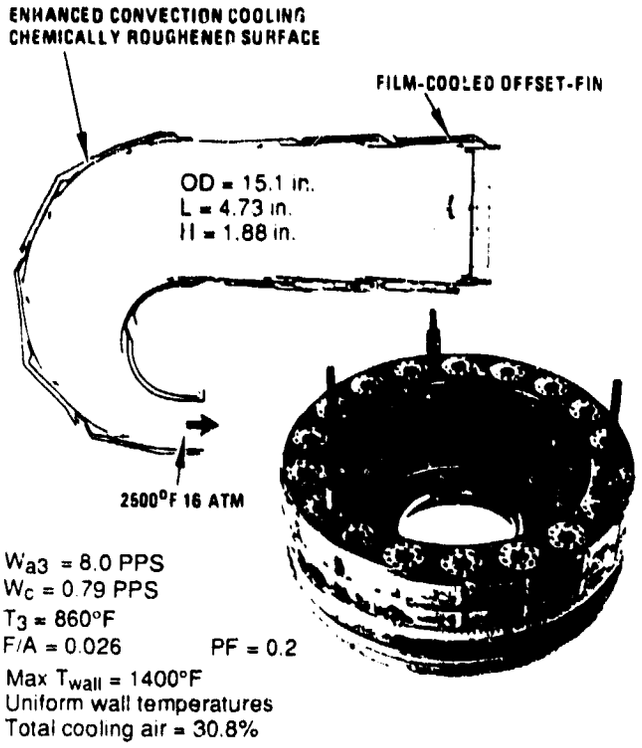

Figure 10. Counter-flow convection film cooled reverse flow annular combustor tested at NASA Lewis Research Center.

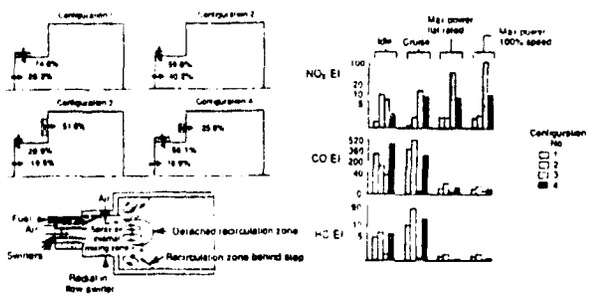

Figure 11. Variable geometry regenerative automatic gas turbine combustor can be designed with 98% reduction in NOx emission.

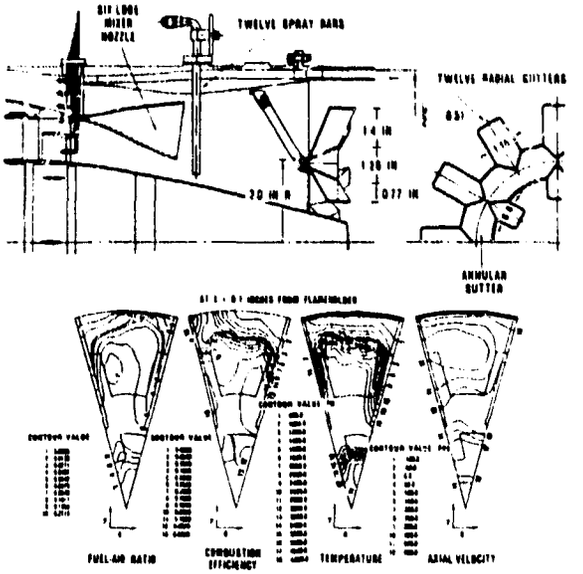

Figure 12. AF small turbine engine augmentor designed with empirical/analytical methodology met all aerothermal performance goals.

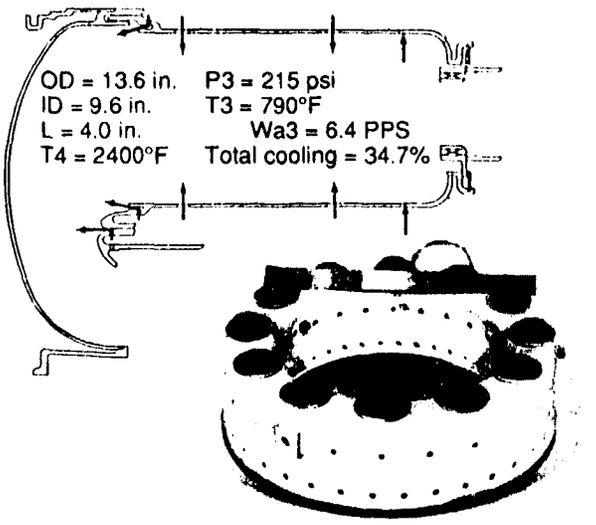

Figure 13. A reverse-flow annular combustor designed with Lamilloy cooling scheme.

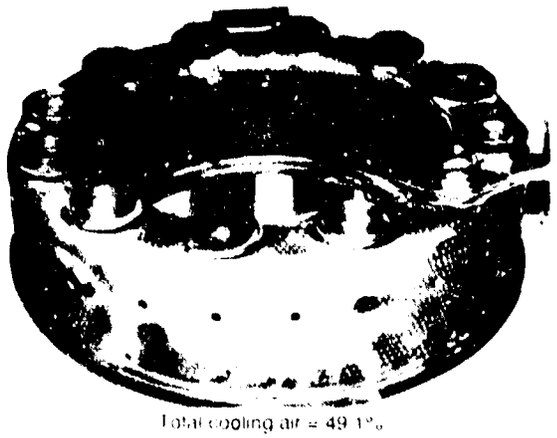

Total cooling air = 49.1%

Figure 14. Effusion cooled reverse flow annular combustor, dimensions, and design conditions as given in Figure 13.

SHORT REVERSE FLOW LINER (L/H = 1.6) WITH EFFICIENT TBC EFFUSION COOLING

SIMPLEX PURE AIRBLAST NOZZLE WITH CONCENTRIC SWIRLERS

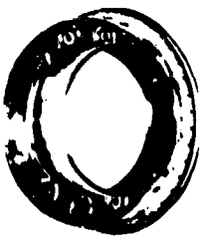

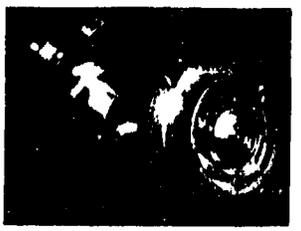

OD = 13.6 in. L = 3.19 in. H = 1.98 in. P_3 = 367 psi
W_{a3-1} = 10 PPS T_3 = 1000°F T_4 = 3000°F
Total cooling air = 38.3% PF = 0.12 (with depressed T_3)

Figure 16. Army low pattern factor reverse flow combustor.

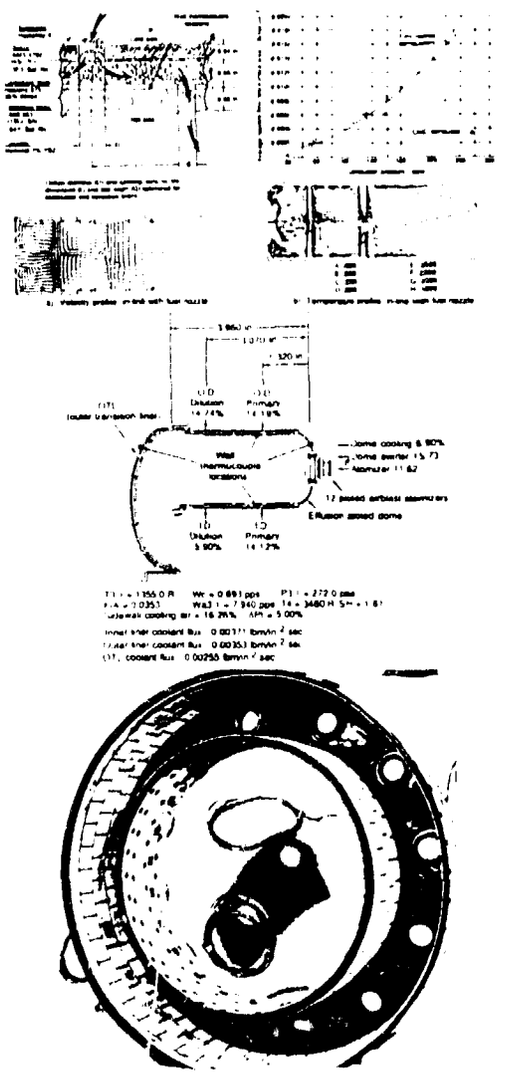

Figure 15. NAS/Army compliant matrix cooled combustor.

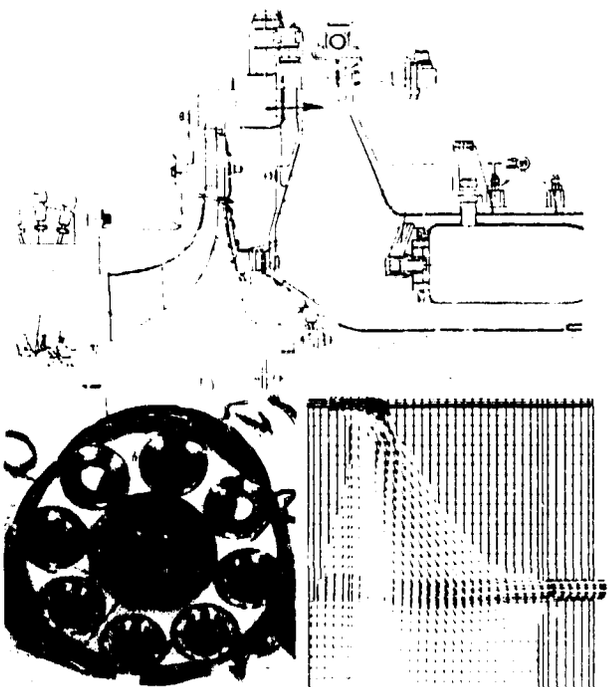

OD = 11.8 in.
L = 6.9 in.
H = 3.0 in
Leq = 6.5 in.
PZ air = 58.4% Dil air = 10.0%
8 pure airblast nozzles

Figure 17. AF high temperature limited life turbine combustor for near-stoichiometric operation.

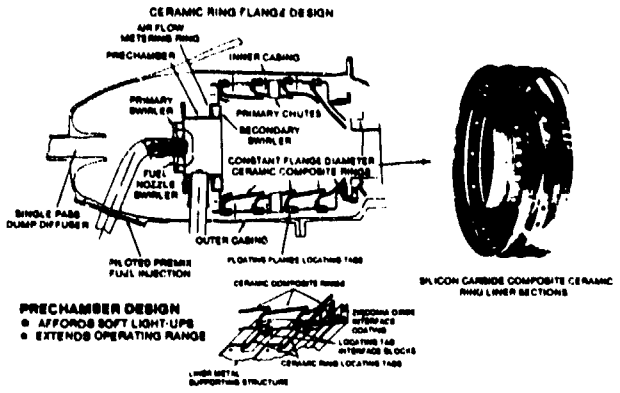

Figure 18. AF nonmetallic combustor.

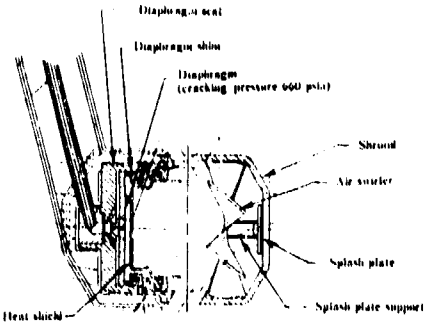

Wide operating envelope
SL static to 90,000 feet
Altitude 3.5 flight mach number

Figure 21. AF ETEC combustor burned supercritically heated JP-10 fuel; combustor liner dimensions identical to Figure 17.

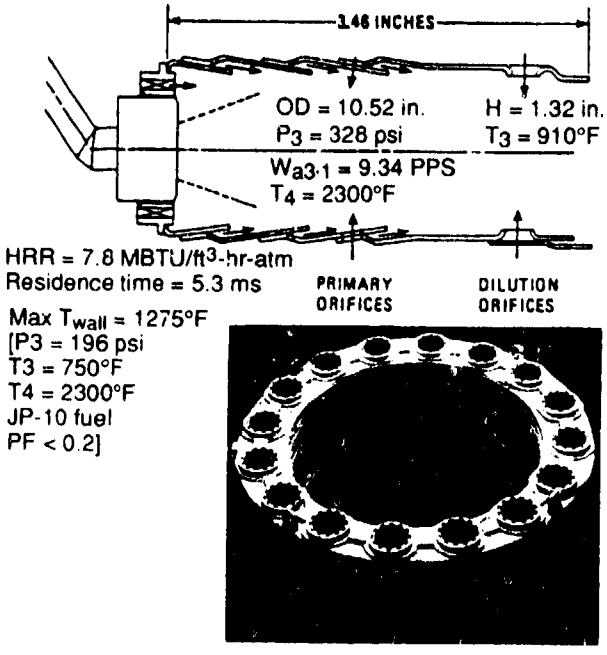

Figure 19. ETF 1050 demonstrator engine reverse-flow annular combustor.

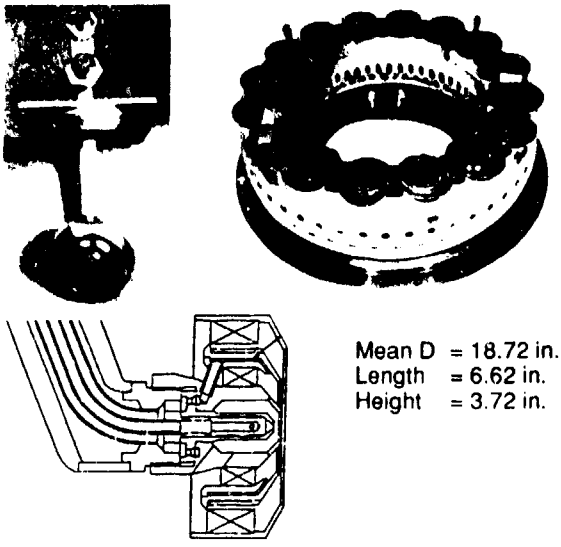

Mean D = 18.72 in.
Length = 6.62 in.
Height = 3.72 in.

Figure 22. XTC 16/1 demonstrator combustor successfully completed near-stoichiometric test program.

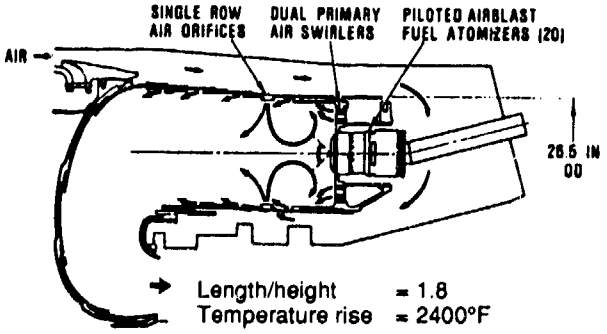

Length/height = 1.8
Temperature rise = 2400°F
Heat-release rate = 8.0 MBTU/ft3-hr-atm
PZ air = 65.7% PF < 0.15 SL idle LBO F/A = 0.005
Maximum wall temperature = 1500°F

Figure 20. Advanced gas generator reverse flow annular combustor.

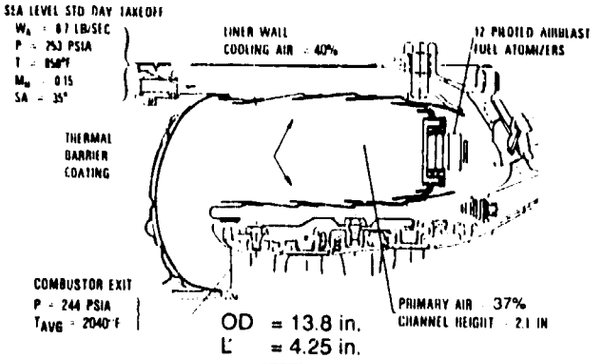

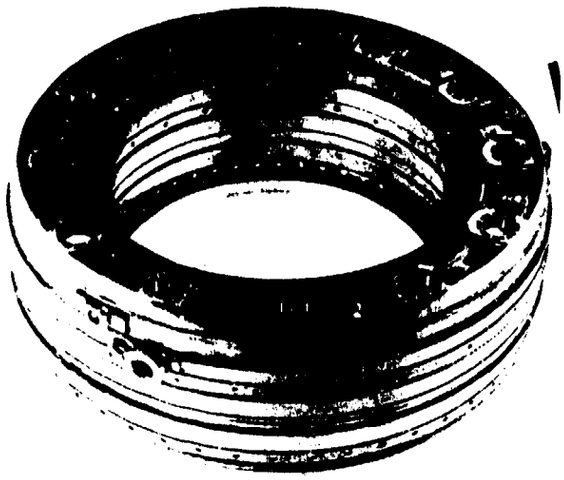

Figure 23. First application of empirical/analytical methodology for reverse flow annular combustor of a turbopropulsion engine.

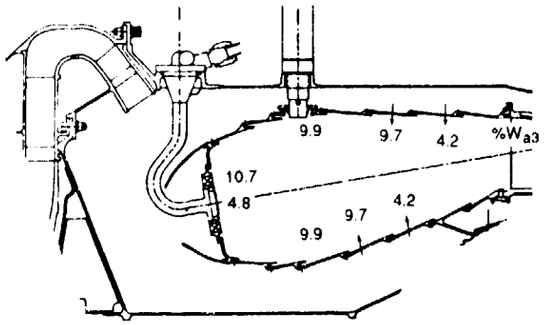

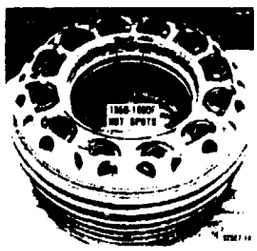

L/H = 2.1
V_R = 68 fps
HRR = 6.2 MBTU/ft^3-hr-atm
ΔT = 1300°F
ΔP = 5.7%
LBO F/A < 0.005
Max T_{wall} = 1600°F

Figure 24. First application of empirical/analytical methodology to inline annular combustor of a turbofan engine.

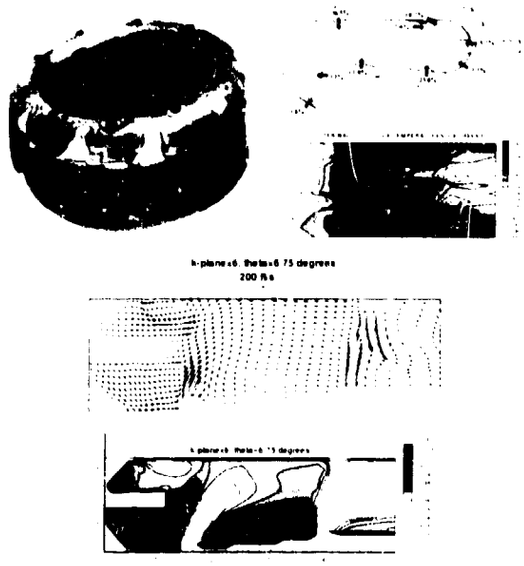

Engine diameter = 11.6 in. L = 4.5 in. H = 1.74 in.
P_3 = 83.3 psi T_3 = 490°F F/A = 0.0254 V_R = 74 fps
τ = 7 ms 10 vaporizer tubes inject JP-4 or JP-10

Figure 25. Baseline combustor met or exceeded all requirements of Model 150 engine.

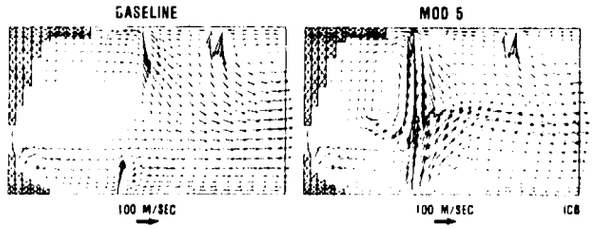

Figure 26. Mechanistic flow concentrations can mislead on smoke-reduction potential.

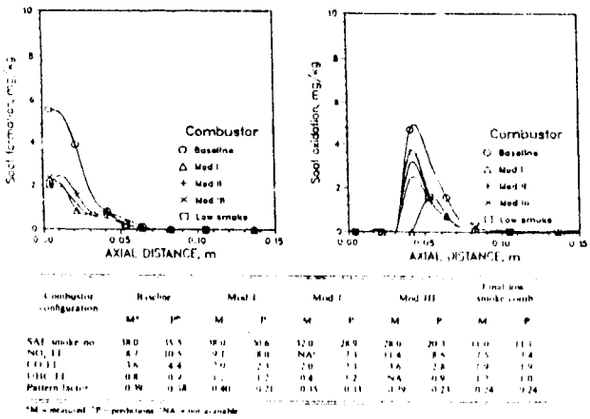

Figure 27. Good comparison between measured and hybrid modeling smoke predictions.

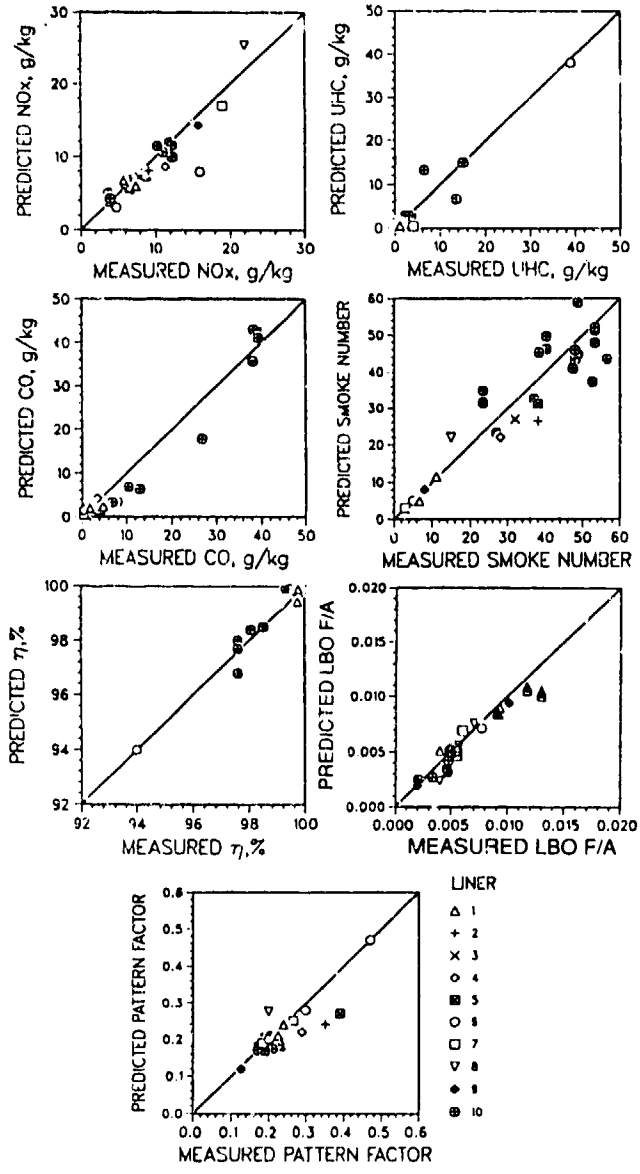

Figure 28. Hybrid modeling calibrated with ten different combustors.

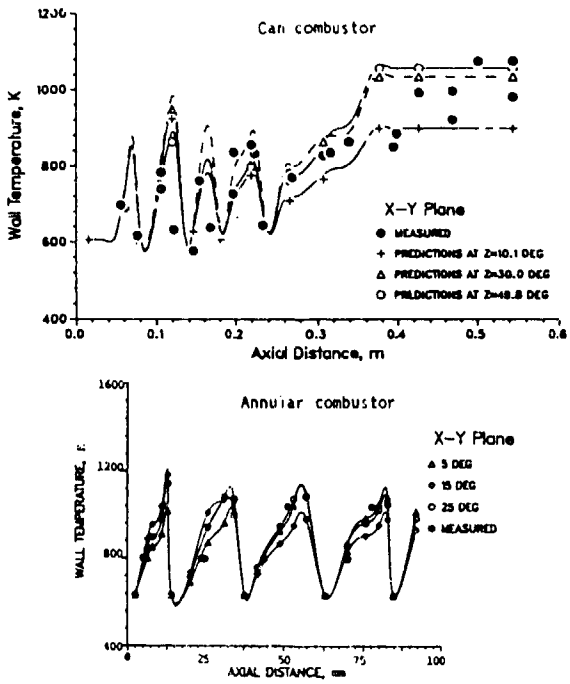

Figure 29. Comparison between predicted and measured wall temperatures.

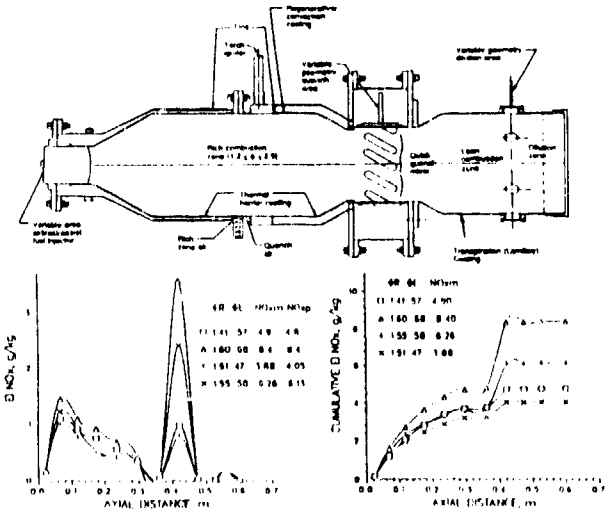

Figure 30. Hybrid modeling calibrated with a rich-quench-lean combustor.

Table 2.

$$CO(g/kg) = \frac{A_1}{P_3^{1.5}}\left[\frac{m_A m_B T e^{-0.0023T}}{V(1 - m_{ev}/m_F)T_u^{0.5}}\right]_{ijk}$$

$$UHC(g/kg) = \frac{A_2}{P_3^{2.5}}\left[\frac{m_A m_B T e^{-0.0025T}}{V(1 - m_{ev}/m_F)T_u^{0.5}}\right]_{ijk}$$

$$NO_x(g/kg) = A_3 P_3^{1.25}\left[\frac{V m_B \ell^{0.003T}}{T m_A}\right]_{ijk}$$

$$S_F(mg/kg) = A_4 P_3^2 (18 - H)^{1.5}\left[\frac{(F/A)m_B}{T m_A T_u^{0.25}}\right]_{ijk}$$

$$S_o(mg/kg) = A_5 \frac{P_3^2}{V}\left(\frac{F/A}{T}\right)_{pz}\left[\frac{Ve^{0.00117}}{m_A(F/A)}\right]_{ijk}(18 - H)^{1.5}$$

$$\eta_c = \eta_r \eta_{ev} \eta_{mix}$$

where

$$\eta_r = 1 - \exp\left(-A_6 P_3^{1.3}\left[\frac{V m_B \ell^{T/400}}{m_A}\right]_{ijk}\right)$$

$$\eta_{ev} = 1 - \exp\left(-A_7\left[\frac{m_F m_B}{m_A}\right]_{ijk}\right)$$

$$\eta_{mix} = 1 - \exp\left(-\frac{A_8}{V}\left[T_u^{0.5} V\right]_{ijk}\right)$$

$$PF = 1 - \exp - A_9 / \left(\frac{L_L - L_{ev}}{D_L V}\left[T_u^{0.5} V\right]_{ijk}\right)$$

$$LBO\ F/A = \frac{A_{10}}{LHV} P_{3des}\left(\frac{FW_{a3} t_r}{P_3^{1.3} e^{T/300}}\right)\left[\frac{m_{ev} m_B}{T m_A m_F}\right]_{ijk}$$

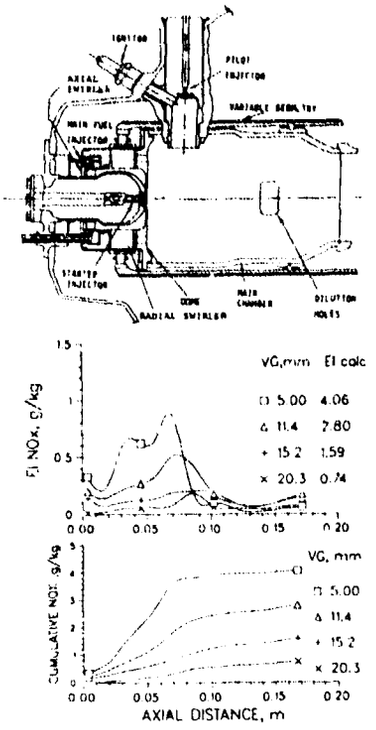

Figure 31. Hybrid modeling calibrated with a premix/prevaporized regenerative cycle combustor.

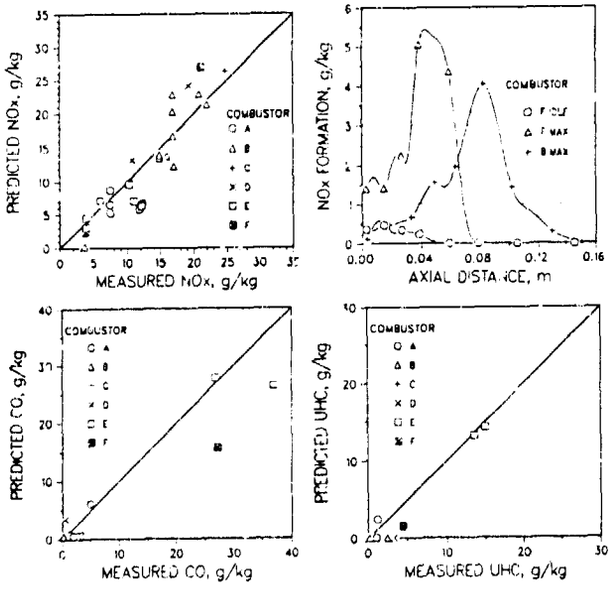

Figure 32. Hybrid modeling based on comprehensive kinetic scheme is being calibrated with diffusion flame, lean PM/PV and rich-lean combustion systems.

Recent CFD Applications in Small Gas Turbine Combustion Systems Development

T. C. J. Hu and L. A. Prociw
Pratt & Whitney Canada Inc.
A Division of the United Technologies Corporation
6375 Dixie Road, Mississauga, Ontario, Canada L5T 2E7

1. SUMMARY

A typical small gas turbine combustor is modelled using CFD and the numerical results compared with LDV measured data. The predicted flow characteristics are in excellent agreement with the measurements. Some aspects of CFD application in combustor design are discussed. CFD can be used as a tool in studying the flowfield development, in the optimization of location, size and quantity of flow devices, in monitoring flow performances and in correlating important design parameters. Use of CFD can significantly reduce lapse time and development cost of gas turbine combustors.

2. INTRODUCTION

Gas turbine combustor design has historically depended on the use of empirical correlations and trial and error approaches. The time and cost involved in the development of gas turbine components in this traditional way is considerable. Laser diagnostic techniques allowing detailed and simultaneous measurements of important flow properties in complex flows have become possible, and have encouraged the collection of benchmark quality database available for combustor designs, and for calibration of numerical analysis tools. Recent advances in combustor technology enabled numerical simulation of complex flowfields of the type seen typically in gas turbine combustors.

Computational fluid dynamic (CFD) is showing great potential as a design tool for combustion systems. Advances in computers allow the use of detailed numerical algorithms and physical models for more accurate predictions of complex flows. The recent global demand for reduced pollutant emissions and improved fuel efficiency have made the design of combustion system very challenging. A design tool that can predict the flowfield and be used for optimization of the design becomes essential.

Experimental measurements of flow properties in real combustor geometries have been very limited. This is mainly due to the highly hostile environment and the difficulties of accessing the complex flowfield with diagnostic probes or optical instrumentation. However, CFD can be used to simulate the combustor geometry and flowfield. The numerical solution can provide detail information of all flow properties being modelled across the entire flowfield, whereas experimental measurements can only provide flow properties being measured in the region of the flowfield where a test is performed. Because of the limitations of experimental measurements, validated CFD codes become the prime choice of design tools for the analysis of a complex combustor flowfield.

The complex flowfield in an annular combustor is typically three-dimensional, turbulent, recirculating, chemically reacting, and confined by complicated louvre and liner geometries. Very limited experimental data is available on real combustor geometries as reviewed recently by Heitor [1] and as such, Pratt & Whitney Canada Inc. (PWC) initiated a joint research program with the University of Toronto, Institute for Aerospace Studies (UTIAS) to investigate the complex flowfield of a practical combustor of current design.

The present paper shows the prediction capability of CFD for combustion systems by comparing numerical solutions with measurements which employed advanced nonintrusive diagnostic techniques. Some examples of CFD application to combustion system design are also illustrated.

3. SECTOR COMBUSTOR MEASUREMENTS

The experimental data used for comparison of CFD results was measured by Hu et al. [2,3] using laser Doppler velocimetry (LDV). These measurements were obtained from a straightened 90° sector of a toroidal-vortex reverse-flow annular combustor of Pratt & Whitney Canada PW209 engine. The sector combustor investigated represents a three nozzle combustor segment. The cross-section of the sector combustor is shown in Fig. 1. There were a total of 3 different sets of jets and nine sets of wall louvres. Two inclined side quartz windows were mounted flush to the combustor ends to simulate the flow volume of a quarter of a full combustor. They also allowed optical access to the combustor flowfield for LDV. In both the cold and hot flow experiments, only one of the three fuel nozzle positions was used. A Parker-Hannifin pure air-blast fuel nozzle was mounted at the centerline of the sector. The experiments were conducted at a constant 204 mm (8 inches) of water differential pressure drop across the combustor in ambient conditions representing normal combustor operating condition (Q_1 simulation). Commercial grade methane gas of 96% purity was employed as fuel. A lean fuel-air ratio of 0.004 was used for the test to avoid the flame from scavenging the side quartz windows.

The $\overline{u}$ and $\overline{v}$ components of the mean velocity and the corresponding turbulence intensities $\overline{u'^2}$, $\overline{v'^2}$ and $\overline{u'v'}$ were mapped in detail for cold and hot flows with a two-component argon-ion laser Doppler velocimeter operated in dual-beam forward scatter mode.

Presented at an AGARD Meeting on 'Fuels and Combustion Technology for Advanced Aircraft Engines', May 1993.

4. NUMERICAL SIMULATION

The numerical simulation of the combustor described here was initiated following the experimental measurements to validate the prediction of the CFD code and its applicability as a design tool for combustion systems.

A mesh system comprising 53 x 22 x 130 grid lines (151 580 grid points in total) along the axial, radial and tangential directions was generated for the sector geometry.

The number of grid points used was kept to this size so that a quick turn around was possible with a workstation. Several views of the grid system are illustrated in Fig. 2. The model contained 13 and 14 circular dilution jet holes on the outer and inner liners, respectively. Each of these circular holes was represented by a 4 x 6 grid mesh. There were also 21 circular primary jet holes on the inner liner in the primary zone.Because of the large number of these primary jets, each of them was only represented by a 4 x 4 grid mesh. There were 7 and 4 film cooling slots on the outer and inner liners, respectively. Each slot was represented by 4 grid lines, of which 3 were for the slot opening. A 5 x 12 grid mesh was used to model the injector inlet which had the effective flow area of the actual hardware. The igniter mounted on the front dome was not simulated since its influence on the flowfield was minimum, as observed in the LDV measurements.

Boundary conditions for the CFD runs were provided in the following fashion. The air mass flow rate through the inlet slots and jet orifices were computed using a one-dimensional flow distribution program by iterating the flow splits until the specified pressure drop across the combustor was achieved. Fuel injection at the fuel nozzle was assumed to be premixed and the methane gas mass flow rate used was based on actual test data. The cold and hot flows were computed using the TASCflow [4] Navier-Stokes fluid flow prediction software, Version 2.1, on an IBM RS6000 workstation.

5. NUMERICAL RESULTS AND COMPARISONS

In the cold flow experiment, only the centerline plane of the combustor was mapped. The measured velocity vectors are shown in Fig. 3. In general, the characteristics of this complex flowfield are well predicted. The computed cold flow velocity vectors are shown in Fig. 4. In the primary zone, the primary vortex is found above the fuel jet as a weak vortical flow near the outer liner and the front dome. The fuel jet is injected into the flow domain with a small cone and swirl as shown by the velocity vector at the fuel nozzle exit face. The entrainment of the surrounding flow into the fuel jet is clearly seen around this jet inlet. The dominant feature is the high momentum fuel jet penetrating right across the primary zone at a trajectory of 45° to the axial direction and striking the inner liner of the front dome. This splashing of the fuel jet on the front dome creates a small curling up of the flow towards the front dome louvre. A strong sidewash in the tangential directions, and a vortex which extracts energy from the film cooling louvre flow adjacent to the inner liner wall and the near vertical primary jets are also created. The low pressure created by the high momentum fuel jet attracts the primary jets to flow upward towards the nozzle. Consequently, a large secondary recirculating flow is formed. The predicted primary jet is found not spreading downstream as much as in the measurement. This is most likely due to the underprediction of the turbulence viscosity by the turbulence model. Less flow from the primary zone is seen entering the secondary zone in this plane. The crossflow and entrainment of the surrounding flow into the high momentum outer dilution jet are also observed. This dilution jet penetrates across the flow domain and splashes onto the inner liner. A wake just downstream of the dilution jet is predicted, but the measurement indicated that the dilution jet diffuses faster and the interaction of the two sets of opposing staggered dilution jets is stronger than predicted. The slight differences in the secondary zone are largely due to the diffusion rate of the free jets, which may be caused by the underprediction of the turbulence parameters in the k-ε turbulence model and the lack of refinement of the grid around the dilution jets.

The contour of the velocity magnitude of $\bar{u}$ and $\bar{v}$ in the centerline plane as measured and computed for the cold flow are shown in Fig. 5 and 6, respectively. A film cooling flow of less than 10 m/s is seen along the liner in the front dome. Toward the primary vortex, the velocity magnitude drops to just a few meters per second. The dominating feature in the primary zone is the fuel jet. The core velocity of this jet is seen decaying quite rapidly as it cuts across the combustor and splashes on the bottom liner with velocities of less than 10 m/s. The spread of the fuel jet near the nozzle exit towards the front dome is more pronounced in the measurement. The minimum velocity magnitude between the interaction of the fuel jet and the primary jet is predicted slightly higher in magnitude and in radial location. The spread of the primary jet is seen as very limited. Hence the velocity magnitude in the primary jet and the secondary recirculation zone are not quite as well predicted. The outer dilution jet is seen decaying slowly along its trajectory from the outer liner to the inner liner. Because these dilution jets are also underpredicted in their diffusion rate, the interaction between the two sets of opposing dilution jets are not obvious in this plane.

In the hot flow experiment, three planes were measured. The measured velocity vector plot of the hot flow experiment at the centerline plane is shown in Fig. 7. The computed velocity plot at the centerline plane is shown in Fig. 8. In the measured data, the center of the primary vortex is much better defined and it is located closer to the front dome and the outer liner than in the cold flow. This same flow behaviour is also found in the predicted results. A wake flow on the upstream of the fuel nozzle is predicted though this is not found in the measurement. This may be due to the fuel jet and the primary jet both diffusing at a slower rate than in reality, and thus a large wake region is created on the front face of the fuel nozzle as the primary jet flows across the nozzle body and the fuel jet entrains the surrounding flow into the jet. In comparison with the cold flow, the fuel jet penetrates across the primary zone with higher momentum and splashes onto the front dome inner liner with higher velocity. The curling up of the fuel jet towards the front dome louvre is much stronger. The roll up of the fuel jet on the inner liner is also found much stronger with the center lying closer to the liner wall. The primary jet is predicted to have diffused more than in the cold flow. Hence the secondary recirculation is much better predicted. More of the primary jet flow is seen going

downstream toward the dilution zone. The flow reversal observed downstream of the outer dilution jet is a combination of the wake flow and the interaction of the outer and inner dilution jets. The flow interaction between the two sets of opposing staggered dilution jets is found at a higher radial location than in the measured data. This may be due to the coarseness of the grids in the dilution zone which does not allow the detail of the flow to be resolved properly.

The second plane measured for the hot flow is at the edge of the fuel nozzle body, which is 0.007m away from the centerline. The measured velocity vector plot and the corresponding computed velocity vector are shown in Figs. 9 and 10, respectively. The primary vortex is similar to that of the centerline plane with the center close to the outer liner and the front dome. The spray cone of the fuel nozzle is seen merging into this plane slightly below the outer liner in the primary zone. This fuel jet and the vortices it creates from splashing onto the front dome inner liner are still the dominating features in the primary zone. The roll up of the fuel jet vortex towards the front dome is not quite clearly defined in the predicted flow. This may be due to the coarseness of the grid in that region, and the wall function may not be appropriate for jet impingement on the wall type of flow prediction. The LDV data in the centerline plane indicated that the impinging flow is tripped by the incoming flow of the dome louvre and curled up into a vortex with the primary vortex strengthening it. The vortex on the downstream of the fuel jet is very well predicted. This is because this vortex is being driven by three flows, namely the fuel jet, the film cooling louvre flow and the primary jet flow. The primary jet flow that reaches the outer liner and then turns toward the front-end is not seen in the measurement. This may be attributed to the same amount of mass flow specified to all of the primary jet holes at the boundary. But in the actual flow, less mass goes through the hole in regions where the gas temperature is high due to combustion. The primary jet flow that reaches the dilution zone close to the outer liner and the secondary recirculation zone that was generated in its wake are very well predicted. The penetration, the spreading and the wake region of the inner dilution jet are also in very good agreement with the measured data. The interaction of the two sets of opposing dilution jets in this section is not obvious in the predicted flow.

The third plane measured in the hot flow is 0.04 m away from the centerline plane. Figure 11 shows the measured velocity vector in this plane and the predicted velocity vector plot in Fig. 12. Because this plane is located far away from the fuel injector, the entire flow picture appears significantly different from the two previous sections. The fuel jet and its affiliated roll up vortices have completely disappeared from the primary zone. The dominating feature here is the primary vortex which has increased in size from the centerline plane to this plane. The center of this primary vortex is predicted further away from the front dome than in the measured data. Part of the flow in the primary zone recirculated back into the front dome and the rest flowed into the dilution zone. Even though no primary jet inlet exists in this plane, the influence of primary jet flow from the neighbouring plane is seen here. It is bent over by the oncoming flow from the primary vortex. The secondary recirculation zone has decreased drastically in size in the measured data and the predicted flow shows the same characteristic downstream of the primary jet. The inner dilution jet is seen penetrating halfway across the combustor and then turning downstream approaching the exhaust. Lower velocity flow in the wake of the inner dilution jet is well predicted. Flow from the primary zone is seen pushed by the inner dilution jet toward the outer liner before leaving the dilution zone in this plane.

Overall, the computer code has predicted all of the flow characteristics of a complex flowfield inside a real practical combustor reasonably well. Although the k-ε turbulence model does not predict exactly the turbulence quantities in parts of the flow and underestimates the diffusion rate of free jets, it does help provide physically realistic flow characteristics and velocities. Because the computed results provide valuable detailed flow parameters of the flowfield, they allow an insight into the physics of the flow. In practical usage, CFD can be employed for parametric studies and optimization of a particular flow feature and has become a valuable tool at PWC for the design of combustors.

6. OTHER APPLICATIONS OF CFD IN COMBUSTOR DESIGN & DEVELOPMENT

The advent of 3D CFD into industrial design has opened several new application possibilities. The previous example has reaffirmed that CFD, even in its crudest coarse mesh form, is capable of describing the physics of flow with fairly good accuracy. This is especially remarkable when compared to how those descriptions were expressed when CFD was not so readily available just a few years ago. When asked the appropriate questions, CFD can reveal a wealth of information and can confirm or deny a variety of notions regarding the nature of a specific flow configuration. It is useful for estimating pressure losses in a wide range of unusual regions as well as those which are physically difficult to access; it can provide heat transfer correlations for geometries not found in any literature; it is useful as a diagnostic tool in explaining unusual data, investigating the feasibility of certain flow devices or modifications to hardware; and it is most useful for exploring scaling laws under a variety of physical conditions which would not be realistically attainable through experimental techniques. A major asset is its power to provide insight into the physics of a given practical situation through visualization of the phenomena in question. This is particularly true in the field of combustor design, where many options and solutions are available to the designer.

One of the main concerns in combustor design is the component durability in the hot-end of the engine. Advancements in material technology have allowed engines to operate at higher pressure ratios and temperatures. Properly controlled exit temperature profile of the combustor is vital to the life of turbine vanes, blades and disks of the turbine. Traditional way of tailoring the Temperature Distribution Factor (TDF) by trail and error involves high cost and long development time.

Temperature prediction by combustion models has lagged other parameters due to the simplified models of the turbulence quantities and the dependency of the chemical reaction rates on such parameters. However, CFD can play a very useful role in combustor development. Every

flow device in a combustor can be traced with a non-reactive scalar. By tracking the flow paths and concentrations of such scalars, the mechanisms of their mixing and degree of mixedness can be studied. In the sector combustor CFD discussed above, a dye is injected into each louvre and jet with a concentration value of one at the inlet. It is expected that the film cooling provided by the louvres in the front-end is already well mixed by the time it reaches the exhaust plane of the sector combustor. This is illustrated by the contour of the dye concentration from the front dome louvre in Fig. 13(a). The concentration of this louvre flow has typically mixed to below 0.07 in the center region of the exhaust plane. Higher concentrations on both sides are due to the wall effect of the liners and side windows. Because of a tangential thumbnail louvre on the outer liner, the flow is not symmetrical. At the same exhaust plane, the outer dilution jets have shown a much higher concentration of about 0.10 to 0.26 in the center region as shown in Fig. 13(b). This is due to the high mass flow rate from the outer dilution jets, and the jets have not yet fully mixed with the surrounding flow. Feasibility and optimization of these flow devices in terms of their locations, sizes, and quantities can be accessed through parametric studies and by monitoring their changes in terms of their concentration at a fixed reference plane.

An example of using scalar concentration to optimize combustor flow is the positioning and sizing of the primary and dilution jets in the combustor where the fuel nozzles are located at the top corner of the front dome. The interaction of the fuel jet with the primary jets and the two sets of opposing dilution jets was investigated with the simulation of a typical sector of the combustor using CFD. The solution indicated that a streak from the fuel jet escapes from the primary zone by means of the primary jets, as shown in Fig. 14, and not through the gap in between the primary jets as one might suspect. As a portion of the fuel finds its way to the jets inside the primary vortex, the lifting effect of these primary jets drags the fuel up towards the outer liner and out of the primary zone. The number of primary jet holes and the mass flow rate through them can determine how the fuel streaks out of the primary zone. The placement of the outer and inner dilution jets is also crucial in the breaking up of such streaks before they reach the exhaust duct, which if not properly dealt with would appear as hot spots in the TDF. The final optimized configuration had the fuel nozzle aligned with one of the primary jets and one of the dilution jets with the two opposing dilution jets staggered in order to minimize the extend of the fuel streak.

Another application of CFD in combustion systems is the study of the interaction between the diffuser pipes and the fuel nozzles, when the number of diffuser pipes is not a multiple of the number of fuel nozzles. A sector of such a combustor outer annulus was modelled from the root of the diffuser pipe to the beginning of the small entry duct. The mesh system consisted of an outerannulus with a common plenum attached to the base of the fuel nozzles. An isometric view of the mesh for the three diffuser pipes and the two fuel nozzles modelled are shown in Fig. 15. The outer annulus flow was enclosed by the gas generator case on the larger radius and the combustor outer liner on the small radius. The exit pressure profile and direction of a diffuser pipe measured in rig tests was converted to velocity profile and was given as the inlet boundary condition at the exit plane of these three diffuser pipes. The sheath and window of the fuel nozzles, and the nozzle boss were modelled precisely. The stem of the fuel nozzles was omitted in the model. At the base of each fuel nozzle, the flow area decreased gradually down to its effective exit flow area. It was then attached to a plenum for the simulation of the air flow through the fuel nozzles.

A section of the computed velocity field is shown in Fig. 16. Diffuser pipes normally produce an exit velocity profile with two counter-rotating vortices on both sides of the pipe, leaving a low velocity zone near the center. In this figure, as viewed from the top, high exit velocity is seen skewed to both sides and low velocity is seen at the center of the pipe. The fuel nozzle on the left is located midway between two diffuser pipes, whereas the fuel nozzle on the right is located near the center of a diffuser pipe. Due to the nonuniform exit pressure profile of the diffuser pipes and the relative location of these diffuser pipes with the fuel nozzles, 4.2% more of the total fuel nozzle air mass flow goes through the left fuel nozzle. Moreover, a large wake is found immediately downstream of this left fuel nozzle. Backside cooling is thus reduced because the velocity in this wake flow is low. Only a very small wake flow is found downstream of the right fuel nozzle. Most of the diffuser pipe flow goes around this right fuel nozzle and does not separate. This type of flow interaction is atypical and it is difficult to predict a prior without CFD. Such computer simulation benefits both combustion and compressor designers and helps in understanding the effects of diffuser exit profile on combustion system performance. CFD is also useful in determining the discharge coefficient (Cd) of holes in areas where the flow is difficult to predict. For example, the outer dilution holes of this model are located immediately downstream of the diffuser pipes, where some of the flow must reverse in direction. Where the flow splits and reverses direction and determining the flow conditions around the holes are difficult to assess without CFD.

The impact of fuel spray on the combustion systems has included ignition, starting, flame stability, TDF, smoke and emissions, fuel consumption rate, and hot-end durability. Hence, the design of the fuel nozzle is really critical. CFD is valuable in modelling the small flow passages that often have a swirler and operated under very high pressure. Several grid meshes are shown in Figs 17 and 18 illustrating the complexity of the components and flow paths inside fuel injectors.

More applications of CFD in the design and studies of fuel injectors for small gas turbine engines are also discussed by McCaldon et al. [5].

Up to now, much of the activity in combustor design has been built on empirical correlations based on experience. CFD is valuable in providing detail information and flow visualisation of the flowfield. Many empirical correlations can now be verified by CFD. Together, these tools are powerful both in monitoring each other's performance and in making up each other's weaknesses. The ability to work with well defined physical parameters will dispel the black art image that is sometimes associated with combustor designed in the engine community.

Despite the capabilities and wide usages of CFD in the

gas turbine combustion systems, there remains much room for improvement in the mathematical methodology and physical modelling for turbulent reactive recirculating combustor flows. The goal for CFD in the future is to become an every day design tool, which is capable of accurately predicting crucial parameters for the combustion systems under both steady and unsteady state operating conditions, and reduce the lengthy and costly rig testings in the development stage. CFD will play an ever increasing role both in quantifying the design rules established in combustor design practice and in allowing the exploration of the boundaries to which these rules apply to future designs.

7. CONCLUDING REMARKS

The numerical modelling of the sector combustor as presented here showed that the characteristics of the complex flowfield of a practical combustor with complicated geometry is very well predicted even with a coarse mesh. Although most of the mathematical models and numerical algorithms have room to improve, CFD in its present state is capable of being used with confidence as a tool in the design and development of gas turbine combustion systems. Since CFD is capable of providing physically realistic solutions, it becomes feasible to be used in areas where experimental testing may be too costly or impossible for diagnostic tools to access. It is best employed as a tool to provide detailed information in understanding, optimizing, monitoring, parameterizing and correlating the intrinsic flow and physical parameters that governs the complex flowfields in combustion systems.

8. REFERENCES

[1] Heitor, M.V., 1989, "Velocity and Scalar Measurements in Model and Real Gas Turbine Combustors," in Instrumentation for Combustor and Flow in Engines, (ed. Durão D.F.G. et. al), Kluwer Academic Pub., pp. 1-44.

[2] Hu, T.C.J., Cusworth, R.A. and Sislian, J.P., 1989, "Laser Doppler, Velocimetry Investigation and Numerical Prediction of the Flowfield in a Practical Annular Reverse-Flow Combustor," Proc. 9th Intl. Symp. on Air Breathing Engines, Athens, Greece.

[3] Hu, T.C.J., Cusworth, R.A. and Sislian, J.P., 1990, "An Experimental and Computational Investigation of an Annular Reverse-Flow Combustor", UTIAS Report No. 338, University of Toronto Institute for Aerospace Studies, Toronto, Canada.

[4] TASCflow is a registered trademark of Advanced Scientific Computing Ltd., Waterloo, Canada.

[5] McCaldon, K., Prociw, L.A. and Sampath, P., 1993, "Fuel Injection Design Constraints for Small Aircraft Gas Turbine Application," Proc. 81st Symp. Propulsion & Energetic Panel on Fuels & Combustion Tech. for Advanced Aircraft Engines, AGARD Conf., Rome, Italy.

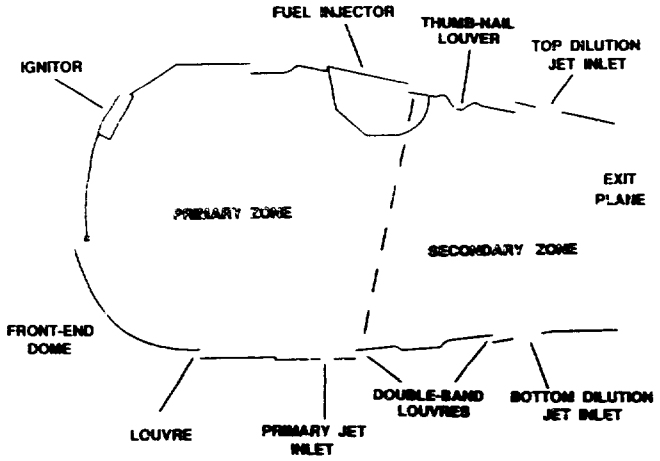

Fig. 1: Schematic diagram of the cross-section of the PW209 sector combustor

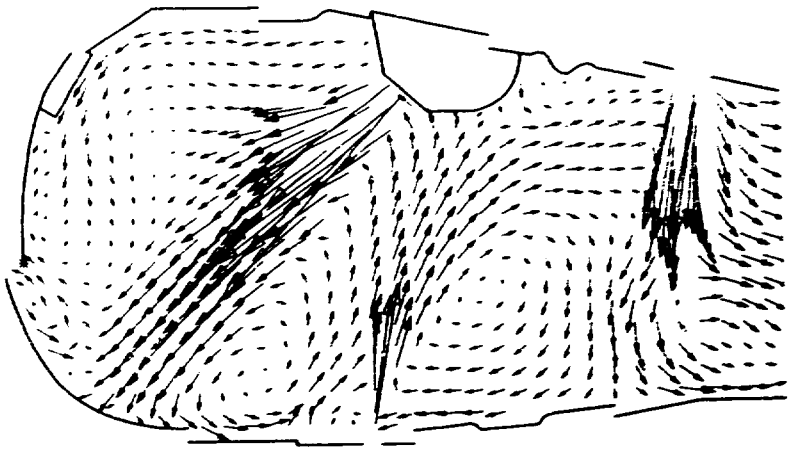

Fig. 3: Velocity vector plot in the centerline plane (z = 0.0 m) of the cold flow experiment [Ref. 2, 3)

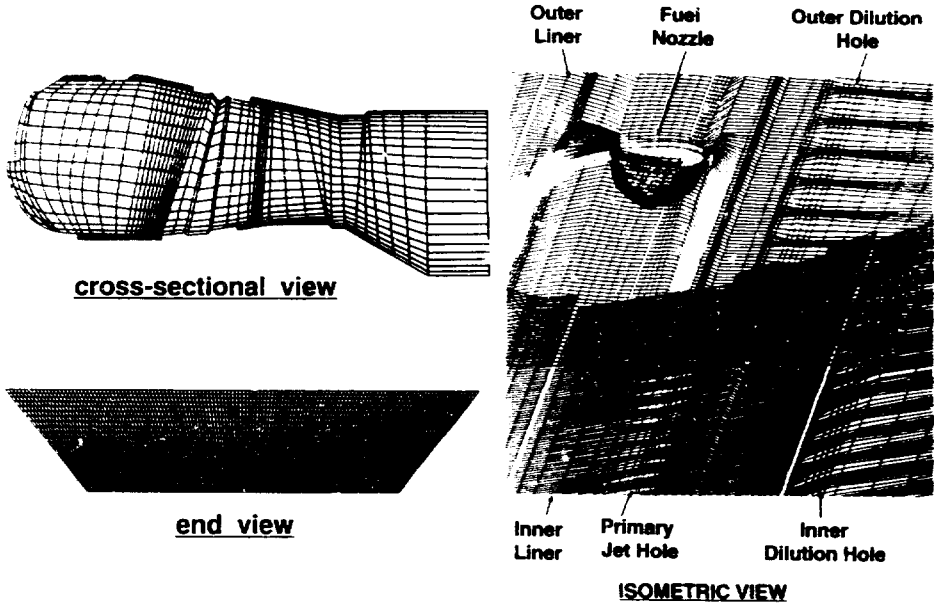

Fig. 2: Representative views of the modelled geometry and curvilinear grid mesh

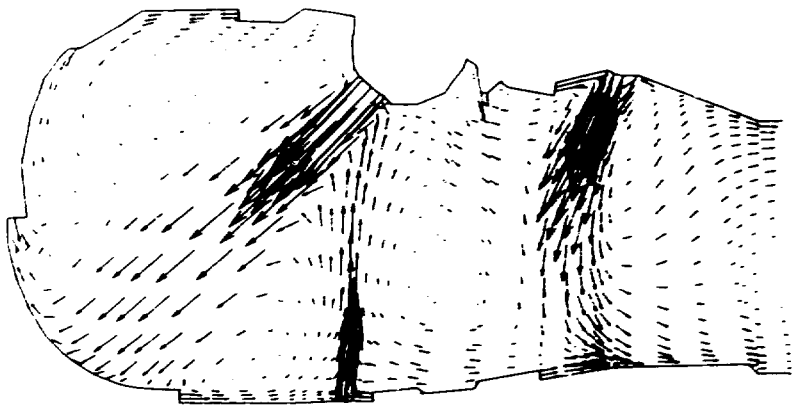

Fig. 4: Computed velocity vector in the centerline plane (z = 0.0 m) of the cold flow

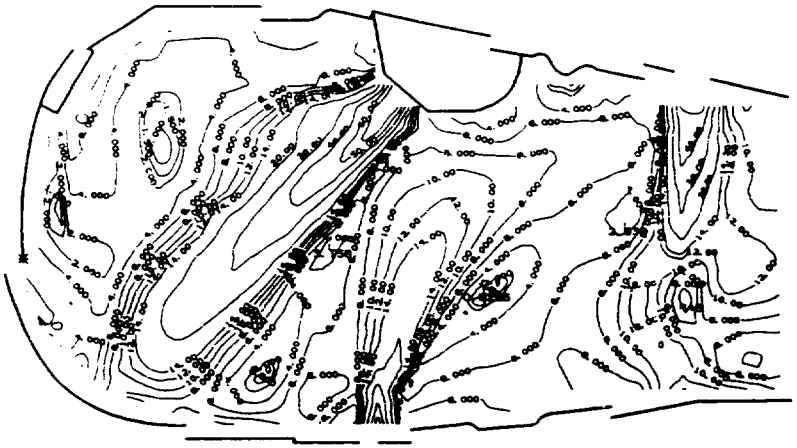

Fig. 5: Contours of the measured velocity magnitude [m/s] in the centerline plane (z = 0.0 m) of the cold flow experiment [Ref. 2, 3]

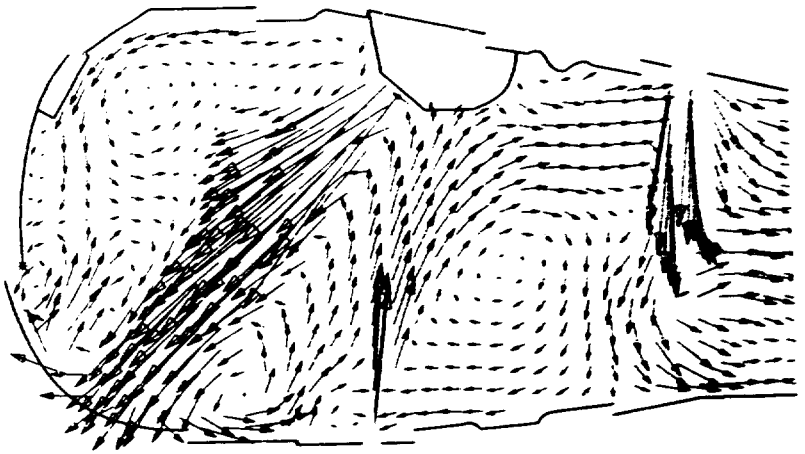

Fig. 7: Velocity vector plot in the centerline plane (z = 0.0 m) of the hot flow experiment [Ref. 2, 3]

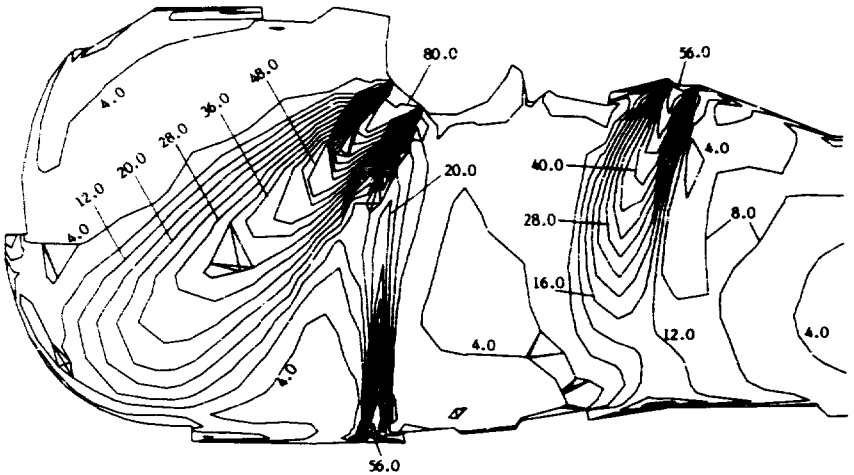

Fig. 6: Contours of the computed velocity magnitude [m/s] in the centerline plane (z = 0.0 m) of the cold flow

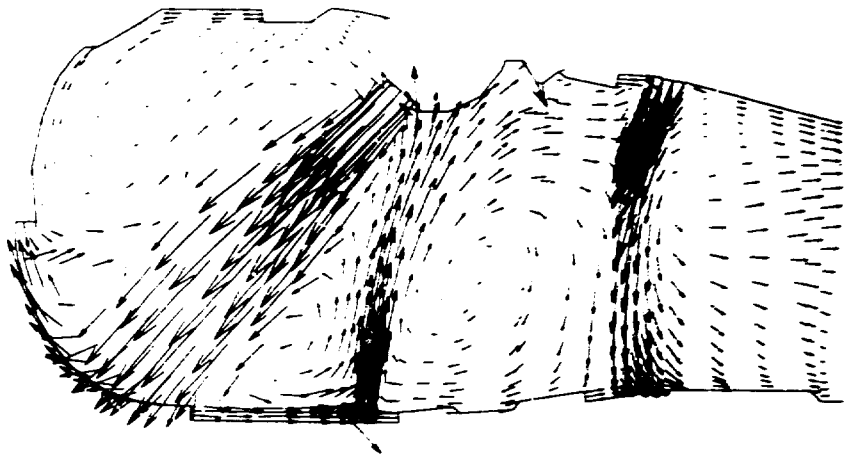

Fig 8: Computed velocity vector plot in the centerline plane (z = 0.0 m) of the hot flow

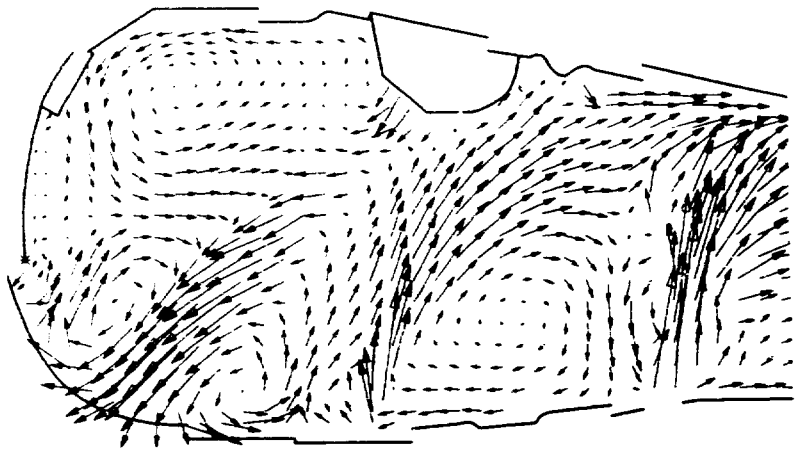

Fig. 9: Velocity vector plot in the second plane (z = 0.007 m) of the hot flow experiment [Ref. 2, 3]

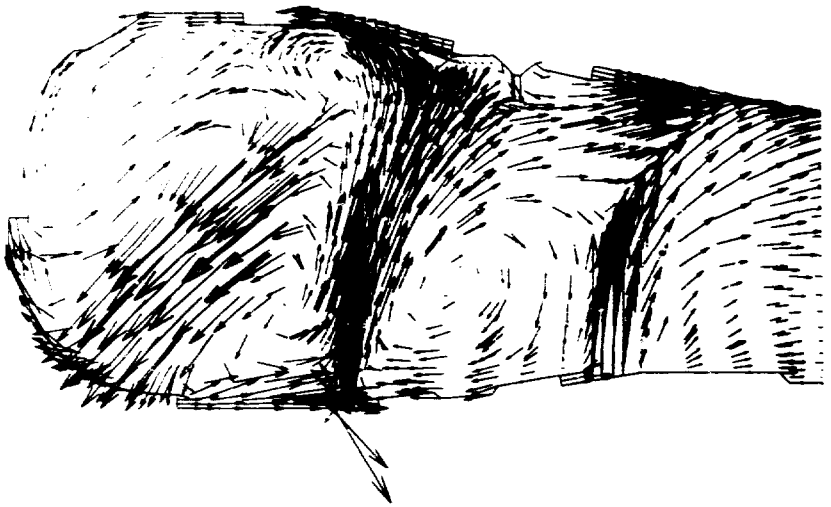

Fig. 10: Computed velocity vector plot in the second plane (z = 0.007 m) of the hot flow

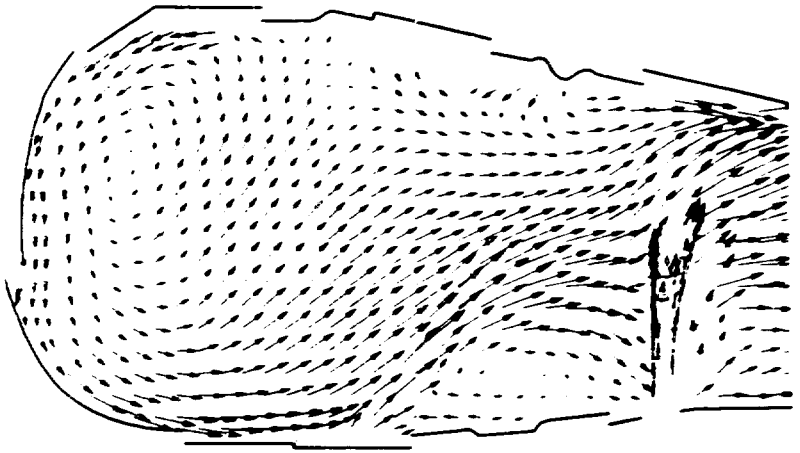

Fig. 11: Velocity vector plot in the third plane (z = 0.04) of the hot flow experiment [Ref. 2, 3]

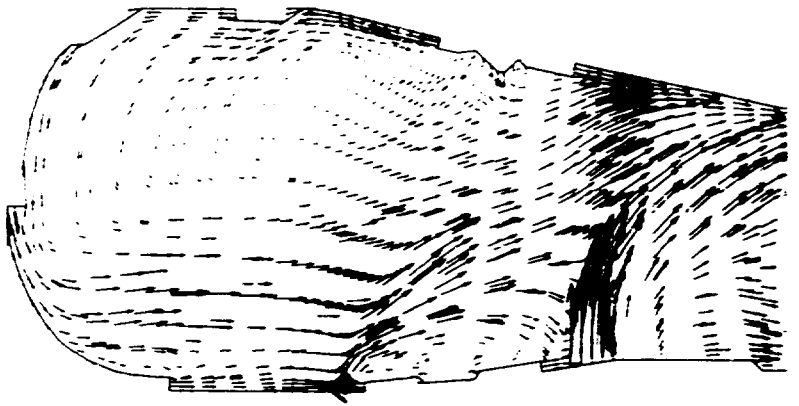

Fig. 12: Computed velocity vector plot of the hot flow in the z = 0.04 m plane

(a)

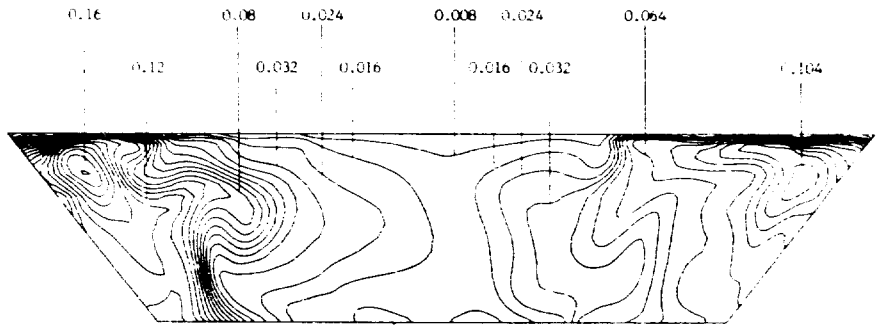

(b)

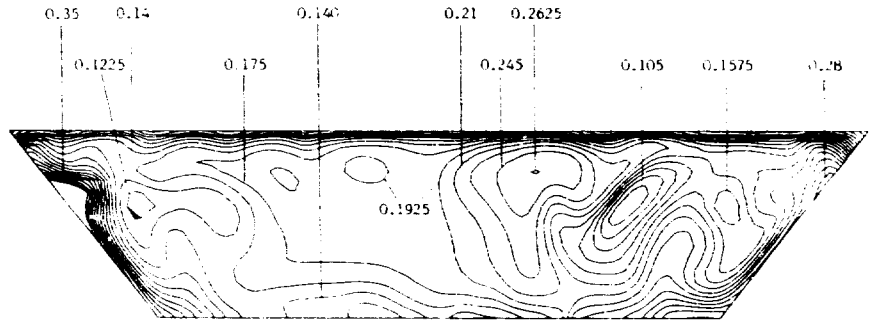

Fig. 13: Contours of the dye concentration at the exhaust plane from:
(a) front dome louvre and
(b) outer dilution jets

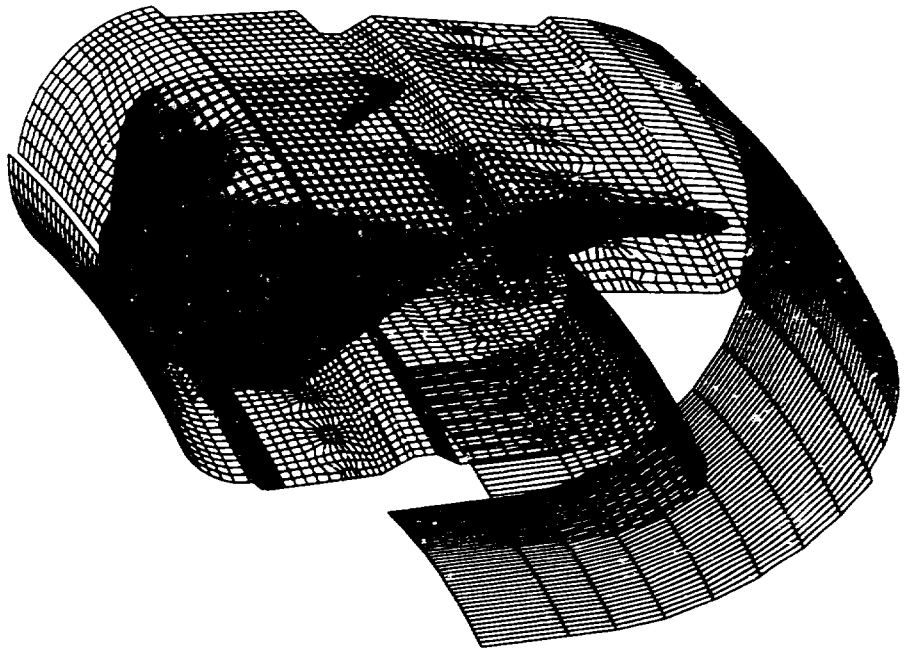

Fig. 14 A streak from the fuel jet escapes the primary zone

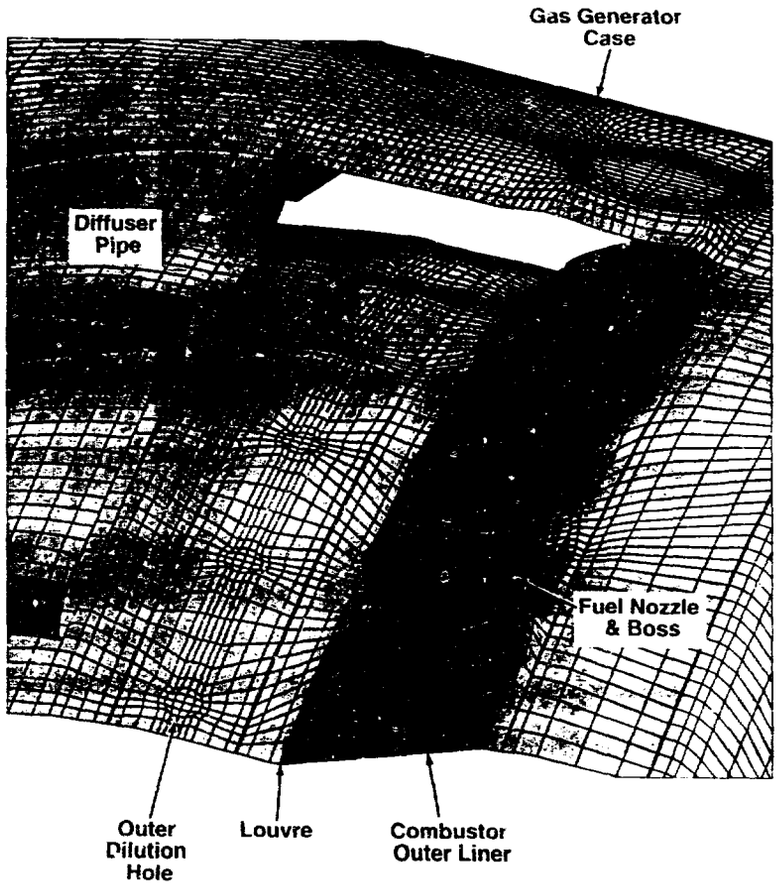

Fig. 15: A combustor outer annulus model for the study of flow interaction

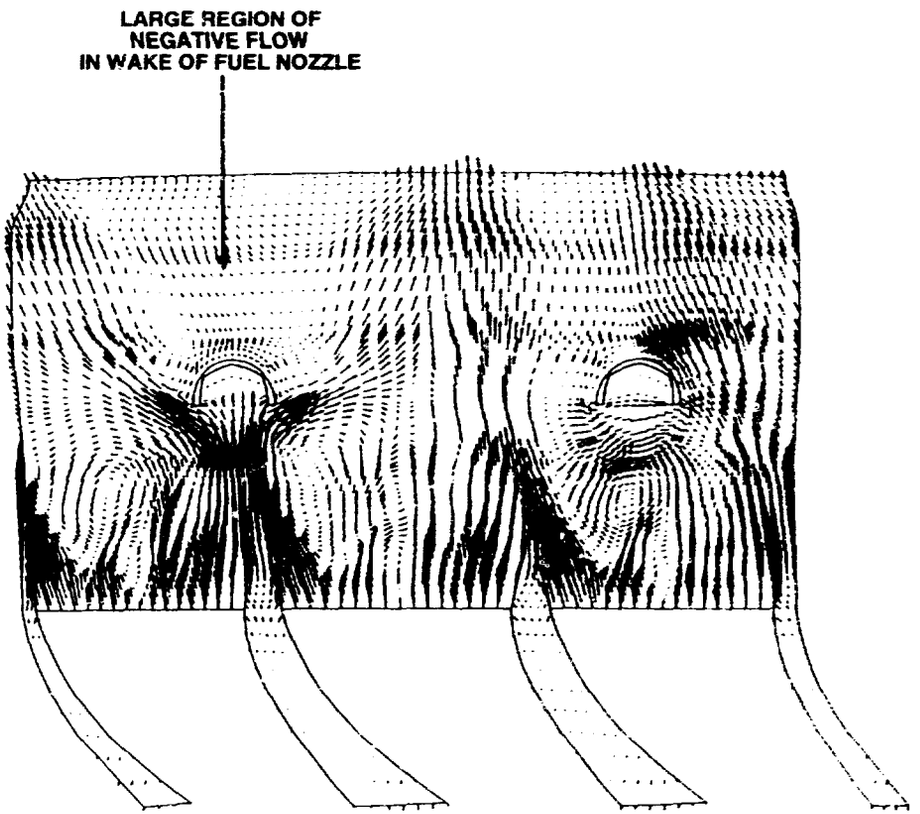

Fig. 16: Predicted velocity field of the interaction between diffuser pipe and fuel nozzle flows

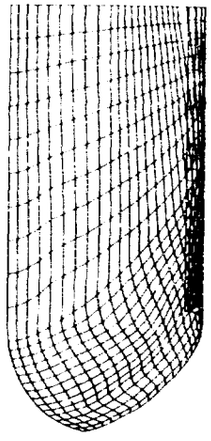

SHEATH

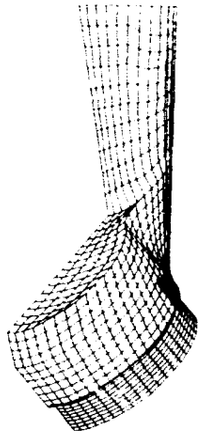

STEM

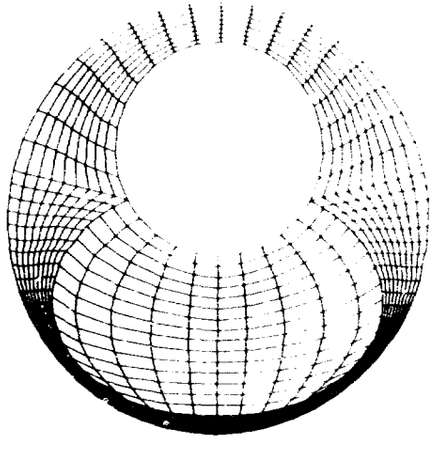

A SECTION OF THE
FLOW ANNULUS

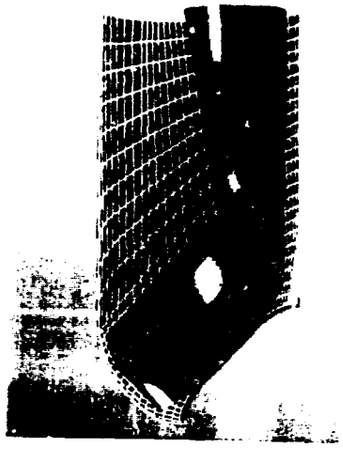

A SECTIONAL VIEW OF THE
ASSEMBLED FUEL NOZZLE

Fig. 17: A grid mesh modeling the annulus flow between the sheath and the stem of a fuel nozzle

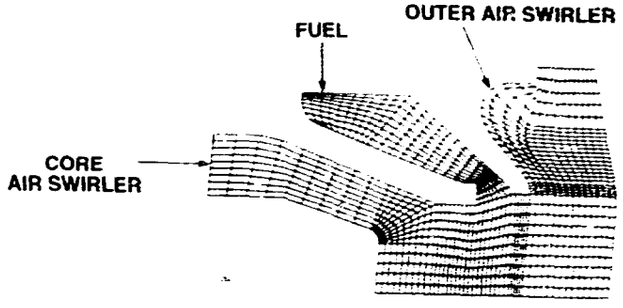

ENLARGE VIEW OF THE GRID
AT THE FUEL NOZZLE TIP

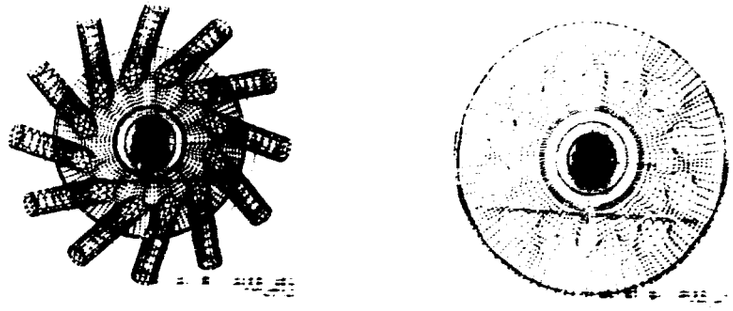

GRIDS FOR THE OUTER AIR SWIRLER

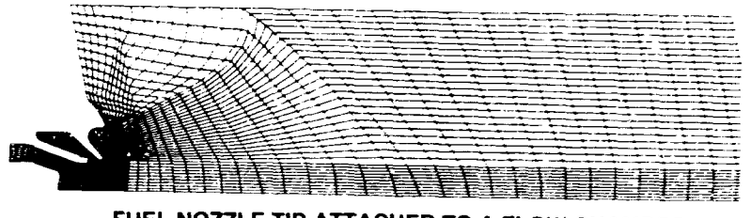

FUEL NOZZLE TIP ATTACHED TO A FLOW CHAMBER

Fig. 18: A grid mesh modeling the detail design of a fuel nozzle tip

Discussion

Question 1. Dr Gordon E. Andrews
You have given examples of CFD computations of combustor external flow and internal flow. Do you have experience in combined external/internal flow computations that avoid the need to specify an airflow distribution and inlet hole velocity profiles if any internal predictions are made? Are there any additional problems, such as convergence, in combined flow predictions?

Author's Reply
The combustor external flow is normally computed separately from the internal flow. The results from the external flow computation are used to provide inlet boundary conditions for the internal flow. Combined 3-D external and internal flow computations have not been attempted seriously, largely due to the limitations of the grid size the current computer workstation can handle. However, the attachment feature has been used to couple the fuel nozzle to the combustor to allow flow development inside the fuel nozzle before injection into the combustor.

Question 2. P.J. Coelho
Could you provide some details of the model, namely the physical submodels and numerical techniques?

Author's Reply
The solver used is the TASC code, trade marked by Advanced Scientific Computing Ltd., Waterloo, Ontario, Canada.

The code uses a fully general non-orthogonal and logically Cartesian grid. It is based on a conservative finite volume approach with all variables stored at the same grid location. The Mass Weighted Discretization Scheme and the Physical Advection Connection terms in all transport equations except $k-\epsilon$ were used. The turbulence model is the standard $k-\epsilon$ model with wall functions where τ_{wall} is proportional to the turbulent kinetic energy.

The fluid mixtures consisted of 4 separate physical components, namely O_2, N_2, fuel and products. The Multi-Component Fluid Model takes into account the component properties and the proportion of each component present in the control volume.

For combustion, the simple Eddy Break Up Model, which is based on the concept that the chemical reaction is fast relative to the transport processes in the flow, is used. The EBU model requires that fuel, oxidant, and products be available in a control volume before reaction may occur. The minimum concentration of these three components, together with a turbulent mixing rate ϵ/k are used to calculate the reaction rate of fuel.

CALCULS AEROTHERMOCHIMIQUES DANS LES FOYERS DE RECHAUFFE

C. DEJEU, J.L. SCHULTZ, S. MEUNIER

Snecma Villaroche
Département Combustion
77550 MOISSY-CRAMAYEL
FRANCE

RESUME
L'étude détaillée de l'aérodynamique et de la thermique des systèmes est aujourd'hui un des points importants rentrant dans le processus de dimensionnement et d'optimisation des foyers de réchauffe des turboréacteurs modernes.

Dans ce contexte, l'article présente deux exemples de géométries et de résultats récents tirés de cas concrets et montre par quels moyens le recours au calcul numérique peut permettre d'aider le concepteur dans son étude.

Le code aérothermochimique qui a été utilisé a été développé par l'ONERA dans le cadre de l'Action Concertée pour les Chambres de Combustion (A3C).Il est basé sur une technique de type volumes finis avec un maillage tridimensionnel structuré adapté aux parois.Le modèle de combustion utilisé de type "Eddy Break Up" généralisé fait l'objet d'une présentation plus détaillée.

1. GENERALITES

De nombreux progrès ont déjà été obtenus dans le domaine de l'amélioration des performances des foyers de turboréacteurs. Ces progrès qui sont dûs en grande partie à des technologies nouvelles ont permis jusqu'à présent de répondre aux problèmes posés par l'élargissement constant du domaine de fonctionnement des moteurs.

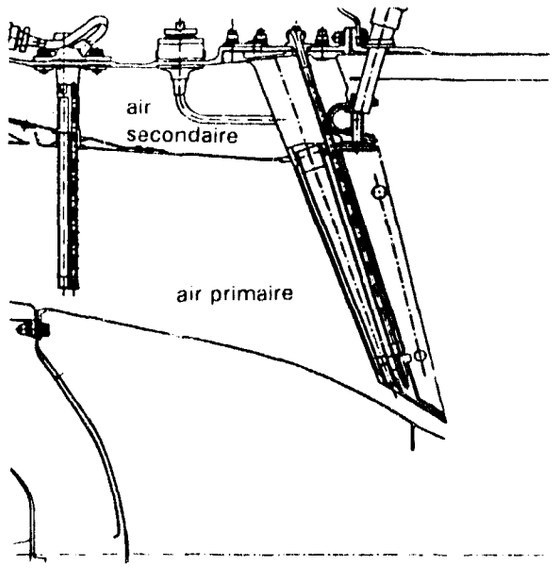

Fig 1a Vue schématique du système accroche-flammes dans le canal de post-combustion.

Plus particulièrement dans le domaine des foyers de réchauffe, les développements qui ont été faits dans le domaine des systèmes de refroidissement ou de mélange et les travaux concernant les nouveaux concepts de stabilisateurs de combustion ont contribué d'une façon significative à repousser les limites des performances.

Dans le passé, le développement de ces systèmes reposait essentiellement sur une approche empirique basée, d'une part sur une modélisation simplifiée reproduisant le comportement global d'un système complet et d'autre part, sur une exploration systématique à l'aide d'essais partiels permettant de mettre au point les différents composants. Une expérimentation globale du dispositif devant a posteriori vérifier le bon fonctionnement dans l'ensemble du domaine de vol. Aujourd'hui, l'évolution vers des systèmes de plus en plus complexes et performants, aux paramètres de contrôle nombreux, limite les marges de progrès et rend le recours à un empirisme systématique hasardeux. De plus, la nécessité pour des raisons de compétitivité, de réduire les coûts et les délais de développement conduit à rechercher des moyens qui permettront de prévoir dès le stade du dimensionnement le comportement local d'un ensemble.

Ce but ne peut être atteint que par la description quantitative de l'aérothermodynamique au moyen de codes prenant en compte et décrivant localement l'ensemble des phénomènes mis en jeu. Dans ce contexte, le recours au calcul numérique a deux objectifs, d'une part, l'aide au dimensionnement a priori, et d'autre part l'orientation des expérimentations dont le nombre, grâce à un choix mieux justifié, pourra être grandement réduit.

Fig 1b Système accroche-flammes-Vue arrière

L'article que nous présentons permet d'illustrer par un exemple l'application de cette méthodologie chez Snecma, dans le domaine de l'étude du foyer de réchauffe d'un turboréacteur (ref 1,2,3).

2. INTRODUCTION

Dans le cas de beaucoup de turboréacteurs militaires modernes et de quelques moteurs civils, il peut être nécessaire d'obtenir ponctuellement un surcroît important de poussée. Ceci peut être obtenu en carburant à nouveau l'air vicié issu du moteur. En effet, la combustion dans la chambre principale ne consommant pas tout l'oxygène disponible, il est possible d'assurer une nouvelle combustion. Cette post-combustion permet ainsi d'élever fortement la température des gaz d'éjection et augmente par là même la poussée du moteur. Dans ce foyer de réchauffe, il est nécessaire d'injecter le carburant liquide d'une façon relativement homogène, puis de fixer la combustion au moyen d'un dispositif "accroche-flammes" permettant de produire le temps de séjour suffisant pour stabiliser la combustion. La figure 1 représente la schématisation d'un système de réchauffe type d'un turboréacteur militaire moderne. L'injection de carburant est ici assurée en particulier, au moyen de crayons disposés radialement en amont du système accroche-flammes qui lui est mixte annulaire et radial.

La mise au point, de ce type de systèmes "injection de carburant/accroche flammes" est un des éléments essentiels rentrant en jeu lors de la conception du foyer de réchauffe.

Parmi les paramètres d'optimisation recherchés, celui de la poussée est bien entendu un des plus importants. Ainsi, pour une longueur de canal la plus courte possible, minimisant donc la masse, le concepteur cherchera à obtenir la température la plus élevée et la plus homogène possible maximisant ainsi la poussée. Un autre paramètre d'optimisation est celui de la perte de charge. En effet, à débit donné en fonctionnement en rechauffe ou non, la poussée est également conditionnée par le niveau de pression à la sortie de la tuyère qu'il est donc nécessaire de garder le plus élevé possible.

On voit déjà apparaître ici une difficulté majeure puisque ces deux critères peuvent être contradictoires. En effet, si la multiplication des points d'injection et des systèmes d'homogénéisation serait tout à fait favorable à l'obtention d'une température élevée et homogène, elle conduirait évidemment à un niveau de perte de charge important. "Température homogène à perte de charge réduite" est ainsi un exemple de compromis à réaliser lors de la conception des foyers de rechauffe. Il en est bien évidemment beaucoup d'autres liés à la tenue thermique ou mécanique, la stabilité de combustion ou encore les instabilités acoustiques, par exemple.

On voit donc que la multiplicité des critères d'optimisation ainsi que le nombre important de degrés de liberté à la disposition du concepteur (position, débit des injecteurs, des stabilisateurs, forme de la veine, systèmes de refroidissement ...) rend très délicate la tâche de conception de ces systèmes particulièrement complexes. Dans ce contexte, la méthodologie développée par Snecma met en oeuvre plusieurs codes de calcul aérothermique ou thermique 2D et 3D dont la combinaison permet d'assister le concepteur dans son dimensionnement.

Ainsi, l'article est centré plus particulièrement sur un des outils numériques utilisés aujourd'hui chez Snecma. Dans une première partie, nous décrirons d'une façon relativement détaillée le code de calcul DIAMANT, en insistant plus particulièrement sur le modèle de combustion utilisé actuellement. La deuxième partie présentera deux calculs réalisés récemment, illustrant d'une part les possibilités du code et d'autre part l'apport des méthodes numériques en général dans le développement des foyers modernes de turboréacteurs.

3. Le code DIAMANT

Le code DIAMANT a été développé par l'ONERA dans le cadre de l'opération A3C (ref 9). Cette action met à contribution la plupart des pôles de compétences importants en France dans le domaine de l'aérothermochimie et a pour but d'une part, de développer les nouveaux modèles physiques avancés qui seront nécessaires pour la description plus précise des écoulements dans les chambres de combustion et d'autre part, de construire le code numérique capable de les acceuillir. L'introduction de ces nouveaux modèles est en cours de réalisation. Le code DIAMANT (ref 4,5,6) qui est présenté dans cet article est la version de base munie de modèles classiques. Il est employé chez Snecma depuis 1991 et commence maintenant à être utilisé d'une façon relativement courante pour la réalisation des problèmes de conception.

Le code est basé sur la résolution des équations de Navier-Stokes moyennées dans une approximation compressible subsonique. La turbulence est simulée par un modèle à deux équations et la combustion par un modèle de type "Edoy Break Up" généralisé complété par une Pdf présumée. La méthode numérique repose sur un schéma semi-implicite et une résolution à pas fractionnaires. La discrétisation est de type volumes finis strictement conservative. En tridimensionnel, le réseau de maillage est constitué par des empilements adjacents d'hexaèdres dont la forme et l'agencement peuvent être quelconques. Ce type de maillage, s'il reste structuré, permet dans une certaine mesure de représenter des géométries relativement complexes avec des obstacles internes sans amener des déformations de mailles trop importantes (fig 3).

3.1 Les équations d'évolution

Les équations instantanées d'évolution sont obtenues à partir des principes fondamentaux de conservation de la masse, de la quantité de mouvement, de l'énergie et des espèces. Un traitement statistique classique est appliqué à ces équations pour tenir compte du caractère turbulent des écoulements considérés. Le système complet des équations s'exprime de la façon suivante:

$$\partial\bar{\rho}/\partial t + \nabla.(\bar{\rho}\tilde{U}) = 0$$

$$\partial\bar{\rho}\tilde{U}/\partial t + \nabla.(\bar{\rho}\tilde{U}.\tilde{U}+\bar{\rho}\widetilde{u'u'}+\bar{\tau}) + \nabla\bar{P} = 0$$

$$\partial\bar{\rho}\tilde{H}/\partial t + \nabla.(\bar{\rho}\tilde{U}.\tilde{H}+\bar{\rho}\widetilde{u'h'}+\bar{J}_h) = \partial\bar{P}/\partial t + \bar{\rho}\tilde{W}\Delta H$$

$$\partial\bar{\rho}\tilde{G}/\partial t + \nabla.(\bar{\rho}\tilde{U}.\tilde{G}+\bar{\rho}\widetilde{u'g'}+\bar{J}_g) = \bar{S}_g$$

où $\tilde{G}$ représente l'une quelconque des grandeurs scalaires qui sont calculées, à savoir k,ε, ou la fraction massique d'une espèce $\tilde{Y}_i$. Le tenseur $\bar{\tau}$ et les vecteurs $\bar{J}_i$ représentent la contrainte visqueuse et les flux de diffusion laminaires. Les flux turbulents $\widetilde{u'u'}$, $\widetilde{u'h'}$ et $\widetilde{u'g'}$ sont donnés par un modèle de turbulence classique de type k,ε. $\tilde{H}$ représente ici l'enthalpie sensible totale massique et $\bar{P}$ la pression statique qui se déduit de $\bar{\rho}$, $\tilde{H}$, et $\tilde{U}^2$ par une équation d'état. Enfin, $\tilde{W}$ représente le taux de réaction moyen et est donné par le modèle de combustion qui sera décrit plus loin.

Sur les parois, les contraintes pariétales sont modélisées, soit par un modèle algébrique basé sur l'approximation de Couette, soit sur un modèle reposant sur les lois logarithmiques classiques. Dans les sections d'entrée du domaine de calcul, toutes les variables sont specifiées sauf la pression. Dans les sections de sortie, seule la pression statique est imposée.

3.2 Traitement numérique

Les équations de bilan sont discrétisées sur chaque cellule suivant la technique des volumes finis, assurant ainsi une conservativité totale. Le système à résoudre se résume simplement à:

$$\delta f/\delta t = S(f)$$

où f représente le vecteur des inconnues du problème:

$$f = (\bar{\rho}\ ,\ \bar{\rho}\tilde{U}\ ,\ \bar{\rho}\tilde{h}\ ,\ \bar{\rho}\tilde{g})$$

Elles sont calculées au centre de chaque maille. Les flux à travers les interfaces sont exprimés en fonction de l'état de l'écoulement au centre de chaque face de part et d'autre de l'interface. En fonction des caractéristiques locales, un décentrement plus ou moins important peut être appliqué pour obtenir la valeur finale du flux à l'interface. Une discrétisation temporelle semi-implicite est appliquée et le système global s'écrit alors:

$$(I - A\alpha\Delta t)\delta f = S(f^n)$$

avec $$\delta f = (f^{n+1}-f^n)/\Delta t$$

et où A est la matrice jacobienne de S: $A=\partial S/\partial f$

et α est le paramètre d'implicitation.

Le système d'équations linéaires résultant est encore factorisé suivant les trois directions du maillage et le système consiste finalement à résoudre successivement trois séries de systèmes tridiagonaux par blocs. D'une façon pratique, seules les variables aérodynamiques ($\rho,\rho\tilde{U},\rho\tilde{H}$) sont fortement couplées. Les grandeurs scalaires ($k,\varepsilon,\tilde{Y}_i$) sont découplées et calculées de façon indépendante. Les systèmes linéaires correspondants à une direction donnée sont indépendants les uns des autres. Ils sont donc classés suivant leur taille puis traités par lots, ce qui permet une vectorisation poussée de l'ensemble de l'algorithme.

3.3 Le modèle de combustion turbulente

Le modèle que nous utilisons est basé sur la notion classique d' "Eddy Break Up" généralisé aux écoulements non homogènes (ref 7,8). Une seule réaction globale d'oxydation d'un carburant est utilisée. Elle peut s'écrire sous forme massique:

$$F + s (O + \beta D) \dashrightarrow (1+s) P + s\beta D$$

où F représente le carburant, O l'oxygène, D le diluant (typiquement l'azote) et P globalement les produits de combustion sans distinction de composition. s est le rapport stoechiométrique massique et β le rapport massique diluant/oxygène. Si l'on fait l'hypothèse que le comburant est toujours de l'air pour lequel le rapport β est constant, le problème peut se résumer à la connaissance de seulement deux inconnues indépendantes. Nous avons choisi de conserver $\tilde{Y}_F$, la fraction massique de carburant et $\tilde{Z}_F$ le traceur de carburant total. Les autres fractions massiques se déduisent de ces deux valeurs par des relations algébriques. Les deux inconnues $\tilde{Y}_F$ et $\tilde{Z}_F$ sont données par des équations de bilan classique du type:

$$L(\tilde{Y}_F)=-\tilde{W}_F \quad \text{et} \quad L(\tilde{Z}_F)=0$$

Le problème revient maintenant à calculer le taux moyen de disparition du carburant $\tilde{W}_F$. Le modèle est basé sur l'hypothèse de réaction infiniment rapide. L'expression du taux de réaction moyen va dépendre de la situation des particules fluides dans le plan des phases (Y_F,Z_F).

Le domaine possible dans ce plan est limité par l'intérieur du triangle ABC (fig 2). L'hypothèse de chimie infiniment rapide limite encore le domaine aux seules frontières. Le segment AB correspond aux particules qui se mélangent sans brûler et la ligne ACB aux particules entièrement brûlées. Sur ACB, AC représente une combustion complète en sous-stoechiométrique pour laquelle $Y_F=0$ tandis que CB correspond à une combustion sur-stoechiométrique pour laquelle $Y_O=0$. Lors du processus de combustion, le point représentatif d'une particule se déplace instantanément, à Z_F constant du segment AB vers un des segments AC ou CB. D'une façon générale, la ligne ACB est une ligne théorique qui correspond à une combustion complète.

Par la suite, elle sera remplacée par une courbe plus précise représentant l'état d'équilibre pour lequel on notera:

$$Y_F=Y_L(Z_F)$$

Cette dernière courbe est obtenue par un programme classique de calcul de l'équilibre chimique et permet de tenir compte de l'effet des radicaux et également des limites d'extinction pauvre et riche le cas échéant.

Pour introduire le taux de réaction, nous utilisons le modèle IEM dérivé du génie chimique (ref 8). Les équations de bilan instantanées lagrangiennes de chaque particule (Y_F,Z_F) sont alors:

$$dY_F/dt = (\tilde{Y}_F - Y_F)/\tau - \dot{W}_F$$

et

$$dZ_F/dt = (\tilde{Z}_F - Z_F)/\tau$$

où τ représente un temps caractéristique d'échange que nous prenons ici proportionnel à k/ε. Lorsque la particule n'a pas brûlé, W_F est,par définition, nul. Par contre, à l'issue de la réaction chimique, la fraction massique de carburant est stationnaire et donc $dY_F/dt=0$. On a donc:

$$\text{sur AB} \quad W_F=0$$

$$\text{sur ACB} \quad W_F=(\tilde{Y}_F-Y_L(Z_F))/\tau$$

La valeur moyenne $\tilde{W}_F$ s'obtient en moyennant le taux de réaction sur toutes les particules possibles. On obtient alors:

$$\tilde{W}_F = \int_0^1 \alpha(\tilde{Y}_F-Y_L(Z_F))/\tau . P(Z_F)dZ_F$$

où α est la probabilité qu'une particule fluide se trouve sur ACB et $P(Z_F)$ est la fonction densité de probabilité de Z_F. Pour simplifier, α est supposé indépendant de Z_F. Il est possible de déterminer α en calculant Y_F de la même manière que W_F, soit:

$$\tilde{Y}_F = (1-\alpha)\tilde{Z}_F + \alpha\int_0^1 Y_L(Z_F).P(Z_F)dZ_F$$

Le taux de réaction moyen s'écrit alors finalement:

$$\tilde{W}_F = 1/\tau.(\tilde{Z}_F-\tilde{Y}_F).(\tilde{Y}_F-\tilde{Y}_L)/(\tilde{Z}_F-\tilde{Y}_L)$$

avec

$$\tilde{Y}_L = \int_0^1 Y_L(Z_F).P(Z_F)dZ_F$$

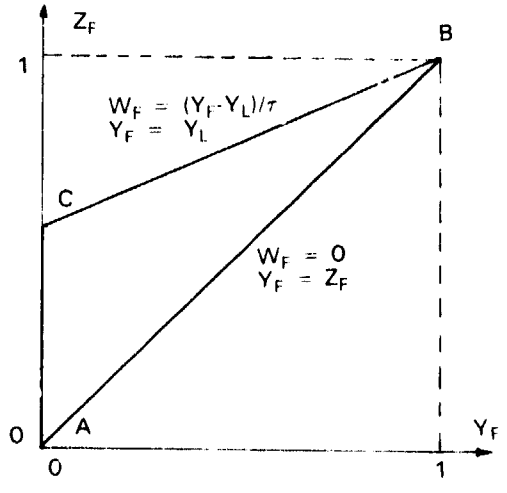

Fig 2 Plan des phases (Y_F,Z_F)

Cette formulation est valable pour toutes les richesses, aussi bien en sous-stoechiométrique qu'en sur-stoechiométrique. D'une façon générale, $Y_i(Z_F)$ est approximé soit par une fonction linéaire par morceaux, soit calculé à l'aide d'un programme annexe de calcul d'équilibre thermodynamique. La fonction densité de probabilité $P(Z_F)$ est modélisée à l'aide d'une forme présumée en fonction créneau ou béta. Elle est alors calculée à l'aide de la valeur moyenne locale $\widetilde{Z}_F$ et de sa variance $\widetilde{Z_F''^2}$ donnée par une équation de bilan supplémentaire.

4. UTILISATION INDUSTRIELLE

Le code de calcul décrit dans les paragraphes précédents a été utilisé sur de nombreuses configurations de foyers de turboréacteurs et en particulier pour les foyers de réchauffe.Comme il a déjà été montré dans l'introduction, la méthodologie développée mise sur les possibilités numériques mais joue également sur la complémentarité entre les essais et les études théoriques.En effet, les foyers de réchauffe sont des systèmes complexes qui rassemblent un grand nombre de phénomènes physiques souvent très différents. Le concepteur est alors amené à isoler les problèmes et à mettre au point séparément chaque élément.
Le système d'injection et d'accroche-flammes au niveau de la confluence des flux est un de ces systèmes élémentaires. Pour son étude, une maquette simulant une portion de secteur du canal entier a été construite. Ceci permet la mise au point sur le plan expérimental. Toutefois, plusieurs calculs complets ont été effectués sur cette géométrie ce qui a permis par une visualisation fine et complète de mieux comprendre toute la complexité des écoulements et des phénomènes mis en jeu. Un exemple des calculs effectués sur cette maquette est présenté dans la première partie du paragraphe.

Ce type de calculs et ces expérimentations permettent de mettre au point des systèmes partiels qui sont ensuite intégrés dans l'ensemble. Des essais sur le système complet sont ensuite réalisés permettant de juger des qualités globales du foyer. Là encore des études numériques contribuent à ce travail. Un calcul sur un foyer de réchauffe complet est ainsi présenté dans la deuxième partie du paragraphe.

4.1 Maquette carrée 2D/2F

Une représentation du maillage utilisé est donné figure 3. Il comprend environ 60000 noeuds. On simule ici la moitié de la maquette qui est symétrique par rapport à un plan méridien et qui représente une portion redressée d'un secteur annulaire complet. Le système accroche-flammes est constitué dans ce cas de bras radiaux disposés dans le flux primaire et d'un anneau en forme de gouttière dans le flux secondaire. la carburation est effectuée dans le flux primaire, d'une part par un crayon radial en amont du bras et d'autre part par une carburation directement dans le bras accroche-flammes. Le flux secondaire est carburé par une injection dans l'anneau accroche-flammes. Outre la compréhension fine des phénomènes, la détermination d'une carburation optimale vis à vis du rendement de combustion est, bien entendu, un des objectifs de l'étude.

Les figures 4 donnent d'une façon détaillée les champs de fraction massique de carburant total (ie. $\widetilde{Z}_F$) et montrent comment la carburation s'effectue. On voit bien en particulier sur les figures 4a,4b et 4c les sillages du bras, du crayon et de l'anneau. Dans l'anneau le carburant est injecté pur dans la recirculation (fig 4e) ce qui produit une zone relativement étendue à forte richesse. Par contre dans le bras, le carburant est, à l'aide d'un dispositif annexe, méiangé à de l'air et l'injection dans le flux principal se fait ainsi à une richesse moindre. On observe tout de même à l'aval une zone à richesse moyenne coïncidant avec la zone de recirculation produite par le sillage du bras. Enfin, le crayon est un injecteur de carburant pur mais qui ne produit pas de recirculation importante. le carburant pur est ainsi rapidement convecté vers l'aval et dilué par le flux primaire.

Ce genre de système produit une carburation en aval relativement homogène comme on peut le voir sur la figure 4.d. Les sillages des bras, crayons et anneau sont bien alimentés en carburant. On observe toutefois, du coté de la paroi latérale une zone à richesse quasi nulle. Il apparaît ici qu'à défaut d'une carburation directe en amont, la turbulence produite par le bras n'est pas suffisante sur une telle distance pour amener le carburant dans cette portion de domaine. D'autre part, une zone à forte richesse se crée à la confluence du sillage du crayon et de l'anneau. cette surrichesse contribue à alimenter le sillage du bras par l'intermédiaire d'un jeu assez complexe de recirculations qui prend place juste au niveau de la confluence. De la même manière, cet écoulement complexe est également responsable du creusement du champ de richesse au niveau du sillage de l'anneau au droit du bras. Cette recirculation très caractéristique qui a tendance à "remonter" du fluide du flux secondaire vers le primaire (fig 4e) en aval du bras et à le "ramener" vers le bas le long du bras est sans doute un élément important pour le mélange et l'homogénéisation tridimensionnelle. Son étude détaillée et son contrôle doivent aider à l'optimisation de ce système. Des études numériques sont en cours dans ce sens.

Cette carburation relativement homogène devrait laisser espérer une combustion là encore homogène et donc un champ de température calqué sur la carburation. Ce n'est pas le cas du tout. L'allumage a été effectué juste en aval du bras en maintenant artificiellement la fraction massique du carburant à sa valeur brûlée pendant quelques itérations. La convergence est ensuite poursuivie sans autre intervention. On s'aperçoit ainsi que la combustion a bien lieu en aval du bras et de l'anneau (fig 5a,5b) et que la zone de combustion a tendance à

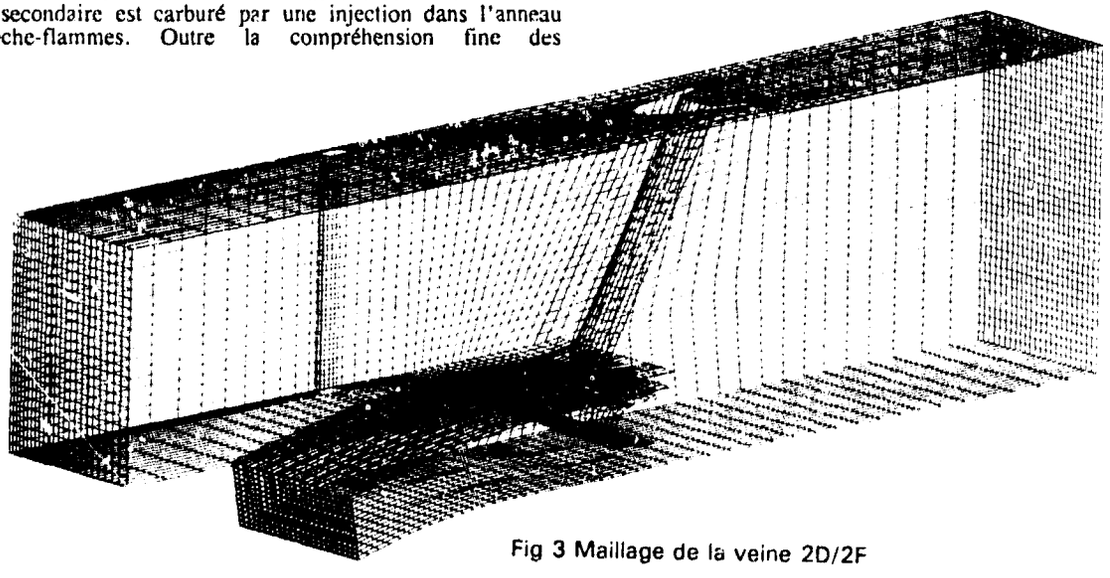

Fig 3 Maillage de la veine 2D/2F

Fig 4a Champ de $\mathcal{Z}_F$ - Plan des bras

Fig 4b Champ de $\mathcal{Z}_F$ - Plan des crayons

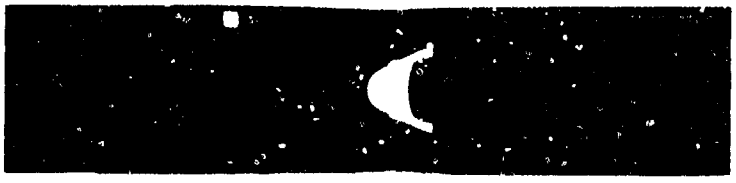

Fig 4c Champ de $\mathcal{Z}_F$ - Coupe des bras

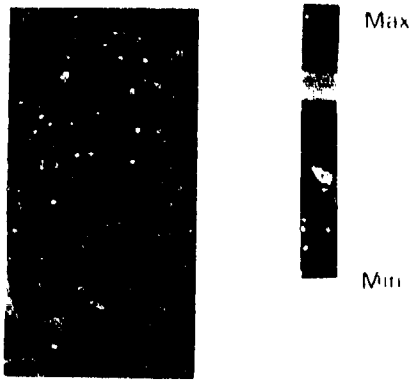

Fig 4d Champ de $\mathcal{Z}_F$ - Sortie de la veine

Fig 5a Champ de température - Plan des bras

Fig 5b Champ de température - Plan des crayons

Fig 5c Champ de température - Coupe du bras

Fig 5e Champ de température aval du bras

Fig 5f Champ de température sortie de la veine

s'élargir vers le haut à cause d'une convection dans ce sens comme il a été vu précédemment. Par contre, si l'on compare les figures 4d et 5f on voit nettement que la partie carburée en aval des crayons n'est pas une zone de réaction et que le carburant bien que présent ne brûle pas. La même constatation peut se faire en comparant les figures 4c et 5c. A cette distance en aval seul le carburant issu du bras participe à la combustion. Il est probable que plus loin à l'aval le carburant issu des crayons rentrera dans la zone d'influence du bras et ainsi pourra éventuellement commencer à alimenter la combustion. Même en initiant la combustion par un allumage derrière le crayon la flamme est très rapidement convectée vers l'aval. Il s'avére en fait que le crayon n'est destiné qu'à l'injection de carburant et non pas à produire suffisamment de perte de charge et de recirculation pour stabiliser une flamme immédiatement en aval (fig 7a et 7b).

Les figures 6 et particulièrement 6b sont significatives. Elles représentent l'inverse d'un temps caractéristique de la turbulence, soit ε/k directement proportionnel à la vitesse de flamme dans notre modèle (paragraphe 3). On s'aperçoit sur cette figure que le sillage des ailes du bras sont le lieu d'un cisaillement important ce qui produit donc un étirement ε/k important. Derrière les bras cette zone de forte réaction est très étendue et avoisine une zone de recirculation où les termes de convection sont faibles. Ceci permet d'initier et de stabiliser la flamme. Au contraire, dans le sillage du crayon, si le cisaillement est important il n'est pas très étendu et se produit dans une zone où la convection est forte. La vitesse s'accélère même encore à cause du blocage des bras. Ainsi, l'étirement important causé par le crayon diminue très rapidement et le soufflage augmente encore ce qui laisse peu de chance à la combustion de se stabiliser.

Ce type d'analyse permet déjà de comprendre un peu mieux les phénomènes complexes qui se produisent dans ces systèmes. Des études numériques de ce type, peu coûteuses au demeurant au regard d'un essai équivalent, sont maintenant utilisées d'une façon qualitative voire quantitative pour de nombreuses applications. Dans ce cas précis on peut par exemple penser que la position des crayons ou la disposition des bras peuvent être optimisées afin d'obtenir un résultat plus satisfaisant.

4.2 Foyer de rechauffe

Le même outil et la même analyse sont utilisés pour l'étude de foyers complets du type de celui représenté sur les figures 8.

Le maillage sur la figure 8a comprend environ 120000 noeuds et simule un secteur d'un canal de post-combustion complet d'un turboréacteur militaire moderne. Comme pour le cas précédent, un des principaux résultats recherchés est l'évolution de la température dans le canal. Ce premier résultat permet d'abord d'accéder à la charge thermique des matériaux par rayonnement et transfert conducto-convectif. On a ainsi la possibilité d'optimiser au mieux leur refroidissement. D'autre part, le niveau de température et son homogénéité à la sortie du canal conditionne directement la poussée.

On montre sur les figures 8b et 8c l'évolution du champ de température depuis l'immédiat aval du bras jusqu'à la sortie du canal. Le même type de phénomènes s'observe que sur la maquette partielle précédente, à savoir la forte influence du bras qui favorise dans son sillage la dilution du flux primaire avec le flux secondaire. On remarque que bien qu'étant déjà assez éloignée de l'injection l'homogénéité n'est pas très bonne et semble encore pouvoir être améliorée par l'optimisation des paramètres d'injection par exemple.

5. CONCLUSION

Le but de l'article a été de montrer par des exemples concrets comment l'utilisation d'une méthode de calcul peut contribuer à une meilleure définition des systèmes de post-combustion.

Cette méthode est maintenant utilisée relativement fréquemment pour l'étude des chambres de combustion en général et des foyers de réchauffe en particulier. Elle est intégrée avec d'autres méthodes 2D et 3D chez Snecma dans la méthodologie de mise au point de tels foyers. Ceci permet déjà en combinaison avec un nombre réduit d'études expérimentales de diminuer d'une façon sensible les délais de développement.

Le code de calcul aérothermochimique utilisé a été développé à l'origine par l'ONERA. Il est basé sur une technique de volumes finis et repose sur un maillage structuré adapté aux parois. Un des points essentiels de la méthode numérique est la modélisation du taux de réaction. Le modèle est basé sur une technique de type Eddy Break Up dont la principale hypothèse est de considérer la chimie infiniment rapide et de supposer la vitesse de flamme seulement conditionnée par le mélange turbulent. La prise en compte au moins partielle d'un effet de cinétique chimique est une des voies d'amélioration possible. Ce thème est actuellement en cours de développement chez Snecma et à l'ONERA.

REFERENCES

1. Cazalens M., Meunier S. Desaulty M. Dimensionnement des foyers de turboréacteurs à performances élevées. 77eme symp. AGARD (PEP) Mai 1991 San Antonio,EU

2. Karadimas G. Application of computationnal systems to aircraft engine components development. 9th ISABE Sept. 1989 Athens,Greece

3. Desaulty M., Meunier S., Heat transferts predictions in aircraft engines combustors and reheats. 17th Eurotherm Seminar, Heat Transfert in Radiating and Combustion Systems. Oct. 1990 Cascais, Portugal.

4. Caillau P., Dupoirieux F. Calculs d'écoulements turbulents réactifs dans les foyers aéronautiques. 80eme symp. AGARD (PEP) Oct 1992 Antalya,Turquie

5. Pit F., Maistret E., Dupoirieux F. Développement du code DIAMANT dans le cadre de l'opération A3C. Rapport technique ONERA 5/4386EY Mars 1990

6. Pit F. Modèle Probabilistique Eulerien Lagrangien (PEUL) de combustion turbulente. Rapport technique ONERA 8/4386EY Août 1991

7. Dupoirieux F. Calcul numérique d'écoulements turbulents réactifs et comparaison avec des résultats expérimentaux. La Recherche Aérospatiale n°6 pp443-453 1986

8. Pourbaix E. Prédiction numérique des écoulements turbulents multiréactifs par une méthode Eulerienne-Lagrangienne, Thése à Poitiers, France Fev. 1983

9. Dupoirieux F.,Firsinger F. Modélisation des chambres de combustion. Opération A3C. 3rd European Propulsion Forum, Cologne 1990

Fig 6a Champ de $1/r$ - Plan du bras

Fig 6b Champ de $1/r$ - Coupe du bras

Fig 7a Champ de pression - Plan du bras

Fig 7b Champ de pression - Coupe du bras

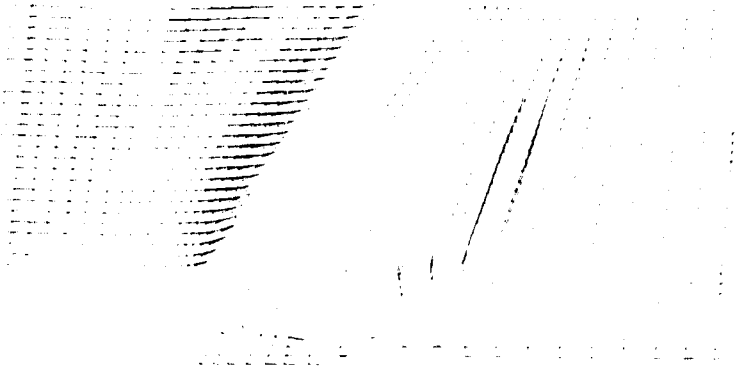

Fig 4e Vecteurs vitesse - plan des bras

Fig 8c Canal de post-combustion
Evolution de temperature

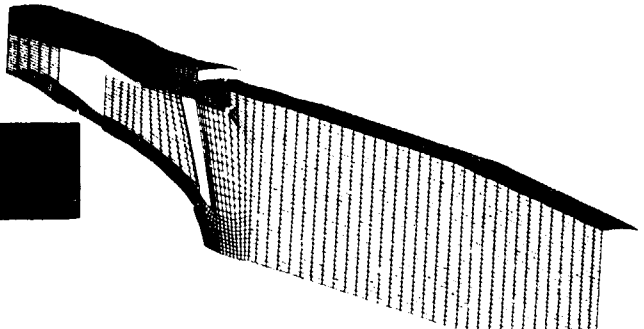

Fig 8a Canal de post-combustion
Maillage

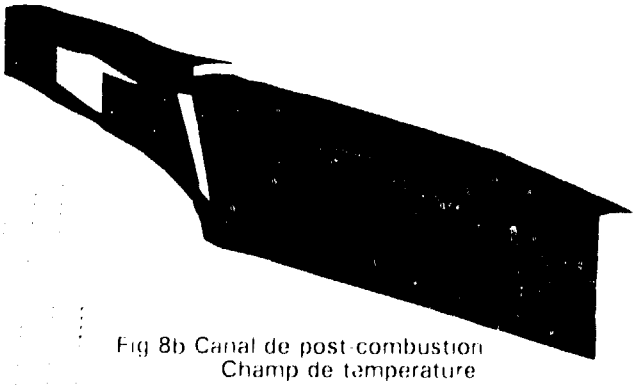

Fig 8b Canal de post-combustion
Champ de temperature

Discussion

Question 1. L. de Chanterac
How long does one calculation case of about 60,000 cells take to run, and on which computer? What is the contribution of the combustion and diphasic models to the time?

Author's Reply
The time calculation of one case is about 8 hours on a Cray computer. The contribution of the combustion model is not important since it needs only two additional transport equations. The time needed by the diphasic model depends on how detailed the boundary conditions are (number of droplets . . .).

Question 2 T. Rosfjord
I assume that the fuel is liquid. How is it modelled? Are droplet sizes and initial velocities specified? What is the basis of the velocity values?

Author's Reply
Droplet sizes and initial velocities are specified. These values are obtained from 1-D calculations and from measurements.

Question 3. A. Trovati
In your presentation the simulation of the combustion region is shown. Have you simulated the effects of liner cooling flows on the temperature profile and on the linear temperature?

Author's Reply
Yes. The linear cooling flow has been taken into account as a boundary condition for the complete 3-D calculation of the reheat system.

HIGH TEMPERATURE FUEL REQUIREMENTS AND PAYOFFS

Tedd B. Biddle and Bennett M Croswell
Fuels and Lubricants Group, M/S 722-04
Pratt & Whitney
P.O. Box 109600
West Palm Beach, FL 33410-9600 USA

1.0 SUMMARY

This paper describes a study performed under contract to Air Force Wright Laboratory, Wright-Patterson Air Force Base, Dayton, OH in association with the Naval Air Propulsion Laboratory, Trenton, NJ. The study projected fuel temperature capability requirements for future tactical fighter applications and the payoffs that would be realized by achieving these capabilities. The study was approached on the basis of the maximum benefit that might be realized through the use of high temperature fuels, i.e. elimination of the recirculation system. Heat loads were projected for different missions spanning IHPTET technology phases I, II, and III at different flight conditions. Fuel temperatures across fuel system components were calculated at these heat loads. Shortfalls of the current 163°C fuel capability were shown and minimum fuel temperature requirements defined. The study concluded that elimination of the recirculation system is not feasible but shows how high temperature fuel capability can minimize the weight penalty associated with fuel recirculation. In this way, potential payoffs for high temperature fuel development were shown in the form of reduced weight penalties that would normally be encountered as larger and larger recirculation systems are required to accommodate the increasing heat loads projected for advanced aircraft.

2.0 INTRODUCTION

The Integrated High Performance Turbine Engine Technology (IHPTET) initiative is a joint Department of Defense/NASA/industry effort to develop and demonstrate revolutionary and innovative technologies that will double propulsion system capability. The technologies which result from this initiative will allow future gas turbine engines to operate at much higher temperatures, pressures and rotational speeds. As a result, the next generation of propulsion systems will exhibit vastly improved levels of engine thrust-to-weight and fuel burned. These increased propulsion system capabilities will translate into significantly improved aircraft system performance including missions with long range, high speed cruise capabilities.

Improvements in both the propulsion and aircraft systems will place a much greater requirement on the fuel which will act as the primary heat sink for both the airframe and engine. Under Air Force contract, P&W conducted analytical studies to establish the temperature capability that would be required of advanced JP fuels for each IHPTET technology phase. In addition, the study quantified payoffs associated with high temperature fuel capability and showed that development of these fuels is critical to the IHPTET initiative. High temperature fluid development goals established by P&W for each IHPTET Phase are shown in Table 1.

For missions with very severe operating environments such as those associated with very high speed flight, defining the requirement for high temperature fuels is fairly straightforward. Heat sink capacity is a barrier for flight speeds above Mach 5. Without advanced fuels like endothermic or cryogenic fuels, these systems cannot

TABLE 1 -- P&W high temperature fluid development goals

	Base	IHPTET Phase I	IHPTET Phase II	IHPTET Phase III
Liquid Lubricants (°C)	163	204	329	371
Fuels (°C), JP-4/JP-8	163	218	288	371
JP-7	288			

Presented at an AGARD Meeting on 'Fuels and Combustion Technology for Advanced Aircraft Engines', May 1993.

achieve their missions. For more traditional missions, the use of existing JP fuels, while requiring some design compromises, would not likely restrict the engine flight envelope. This has been demonstrated on several weapon systems which are currently in or are nearing service. An example is the Advanced Tactical Fighter (ATF) aircraft which uses a fuel recirculation system to provide sufficient heat sink for the airframe and engine. This approach could continue to be used for future weapon systems but with an increasing penalty as the heat generation of both the airframe and engines become greater. For this reason, high temperature fuel requirements will be dependent on what is an acceptable recirculation system size and weight for future aircraft.

3.0 APPROACH

Selected missions spanning IHPTET technology phases I, II, and III were investigated. These missions determined the engine operating environment and power levels. Following selection of a propulsion system concept, engine performance was modeled to establish engine internal gaspath temperatures, pressures and flows, as well as the levels of engine fuel flow. This information was used to conceptually design the engine flowpath and to determine rotor speeds. This is also where configuration issues such as rotor support arrangement were determined. All of this information along with assumed airframe heat loads were used in the development and exercise of fuel system thermal management models. These models established recirculation flow requirements and temperatures throughout the fuel system. With the fuel heat sink requirements determined, relative sizing of the fuel system components was performed to establish payoffs in terms of reduced weight that would be realized with high temperature fuel development.

It should be noted that there is little definitive information relative to the future levels of airframe heat loads. Consequently, projections were made based on heat loads near the levels projected for the prototype of the next generation of tactical fighter aircraft. Only JP fuels were considered in this study. Endothermic fuels were not addressed. Missions investigated were limited to the more conventional advanced military tactical missions. Special missions with very high speed requirements (greater than Mach 3.0) were not considered. Although P&W's technology plan calls for the development and demonstration of magnetic bearings in IHPTET Phase III, in this study high temperature liquid lubricants and conventional high speed bearings were assumed.

3.1 Advanced Applications / Missions

The significant propulsion system improvements realized from the IHPTET initiative will result in lighter weight, smaller diameter engines and lower takeoff gross weight (TOGW) aircraft. Reduced drag associated with these smaller aircraft will allow sustained flight at much higher speeds and require future aircraft and propulsion systems to operate in much harsher thermal environments. To determine the impact of these environments on required fuel temperature capability, this study evaluated the advanced missions shown in Table 2.

4.0 FACTORS INFLUENCING FUEL TEMPERATURE REQUIREMENTS

4.1 Airframe Heat Loads

The levels of heat loads generated by future aircraft are unclear at this time but an extrapolation of operational systems indicates that the fuel will be required to absorb much greater thermal loads. Figure 1 shows the historical trend of airframe heat load for typical two-engine Air Force fighters as well as projections for the ATF. The increasing levels of heat generated can be attributed to a number of factors. These include more stringent missions which results in higher airframe skin temperatures, the increased hydraulic system requirements associated with large control surfaces, and

TABLE 2 -- Advanced missions selected for study

	IHPTET Technology Phase		
	I	II	III
Advanced Tactical Fighter (ATF)	X		
Advanced Navy Fighter (ANF)		X	
Mach 2.5 Air Superiority Fighter (ASF)		X	X
Mach 1.5 Lightweight Fighter (LWF)		X	X

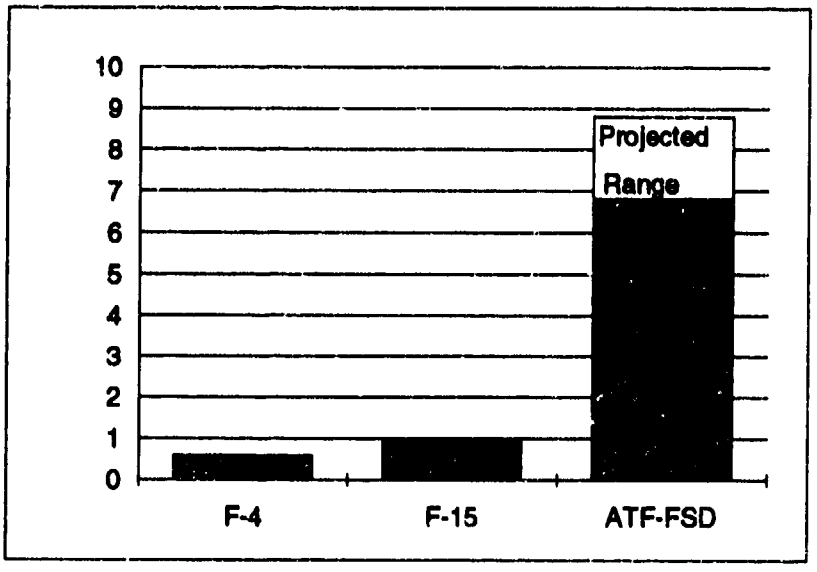

FIG. 1 -- Historical trend of airframe heat load (per engine)

the requirement to provide cooling for environmental control systems and advanced airframe avionics.

4.2 Propulsion System Heat Loads

The propulsion system cycles used in this study reflect the IHPTET trend of increased capability through higher operating speeds, pressures and temperatures. These cycles have been optimized to meet the individual requirements of each mission. For example, the ASF and LWF missions require propulsion systems with high specific thrust (thrust-per-pound of airflow). Accordingly, these engines have high fan pressure ratios (6.0-8.0) and low bypass ratios (0.1-0.3). The engine operating pressure ratios for the ASF engines are lower than those for the LWF. This reflects the requirement to avoid compressor discharge temperature limits at the higher cruise Mach numbers of that mission. The propulsion systems for both of these missions will have turbine temperatures which are 316 to 371°C higher than current engines. In addition, the engine rotational speeds for the Phase II propulsion systems are approximately 5% higher than current engines while the Phase III speeds are 12% to 20% greater.

The mission for the ANF application includes an extended loiter requirement. A major goal of advanced Navy systems will be to extend the time-on-station capability at the loiter condition. This requirement places a premium on propulsion systems with reduced fuel consumption. As a result, the engine has a higher operating pressure ratio and more moderate bypass ratio than the cycles selected for the ASF and LWF. While the rotational speeds for the engine will be similar to the ASF and LWF, turbine temperatures for this application are 149°C lower.

The higher rotor speeds, internal gas path pressures and temperatures of the propulsion system cycles just described are the primary factors effecting engine heat generation. Increased speeds will translate to higher tangential velocity and friction between moving components like gears, seals and bearings. Lubrication system heat generation will also be higher due to increased lubricant shear and churning. The result will be higher lubricant temperatures and a requirement for greater fuel heat sink capacity.

5.0 THERMAL MANAGEMENT MODELS

5.1 Overview

The propulsion system heat loads, as well as the fuel, lube oil and hydraulic fluid temperatures are determined and maintained within design limits by the Integrated Thermal Management System. The model uses system requirements and operating limits determined by aircraft operations, engine/airframe equipment and the physical and chemical properties of the system fluids. Aircraft operations take into account the flight envelope and aircraft mission. Engine equipment includes the bearings, seals, gearbox mechanical requirements, fuel/oil/hydraulic pumps and engine controls. Airframe equipment affecting system requirements include avionics, the cockpit environmental control system and the flight control surface hydraulic system.

Engine fuel is the principal heat rejection medium. In addition to the heat generated by the fuel system components, heat is transferred to and from the fuel by a complex system incorporating fuel/oil and fuel/air heat exchangers. In the systems studied, heat rejected to the fuel is either burned or recirculated back to the airframe fuel tank after passing through an airframe mounted fuel/air heat exchanger.

The key assumptions made in the generation of this model include:

- Temperature of the fuel in the tank is 43°C. The study assumes that future systems with higher Mach number cruise requirements will have increased insulation to maintain this fuel temperature in the tank.
- Increased temperature capable oil and hydraulic fluids will be available for use with the higher temperature capable fuel.
- The fuel system components in this study, e.g. fuel lines, fuel pumps, heat exchanger components and fuel nozzles, have all been assumed to have adequate temperature capability.
- Fuel will be used as the engine hydraulic fluid which eliminates the need for an engine fuel/hydraulic fluid heat exchanger.
- For the IHPTET Phase I system studied, airframe heat loads in the range of 3,000 to 3,700 Btu/minute per engine were assumed depending on the flight condition. For the IHPTET Phase II and III systems, an airframe heat load of 4,000 Btu/minute per engine was assumed at all flight conditions.

5.2 Fuel Recirculation System

The fuel recirculation system assumed in this study is very similar to systems used in the latest generation of tactical fighter aircraft. A sensor indicates when fuel temperature limits are being reached and a fuel recirculation valve opens. Fuel in greater amounts than is required for operation of the engine is routed through the fuel system to provide a sufficient heat sink for the airframe and engine. The hot fuel not used for engine combustion is routed through the recirculation valve to a fuel/air heat exchanger before being reintroduced into the tank. While this cooling does not reduce the returned fuel to the same temperature as the fuel in the tank, the system does minimize the heat-up of the tank. Air for the heat exchanger is brought in through an inlet on the aircraft. For static conditions such as ground idle where recirculation is required, a flow inducing device is used to bring airflow into the system.

The majority of the fuel recirculation system design responsibility falls to the airframer. Based on an industry survey, baseline fuel recirculation system weights were estimated for the purpose of calculating potential payoffs for advanced fuels development. These estimated weights are shown in Table 3.

Development of high temperature fuel capability would realize it's greatest payoff if sufficient heat sink capacity could be generated without a fuel recirculation system. For the next generation of tactical fighters, elimination of this system would save approximately 200 lb of weight in the airframe and engine. As heat sink requirements increase in the future, these systems will likely weigh even more. With this in mind, the first approach taken in this study was to identify the fuel temperature capability required to eliminate the recirculation system.

TABLE 3 -- Estimated fuel recirculation system component weights

Component	Weight
Fuel/Air Heat Exchanger (one per engine)	30 lb
Fuel Recirculation Valve (one per engine)	10 lb
Ram Circuit (Inlet, Flow inducer)	100 lb
Plumbing, Lines, etc.	20 lb
Total (single engine aircraft)	160 lb
Total (twin engine aircraft)	200 lb

6.0 FLIGHT CONDITIONS AND MISSIONS

The following five flight conditions were considered when determining maximum fuel temperature requirements for selected IHPTET missions:

1.) Ground Idle
2.) Subsonic Cruise
3.) Supersonic Cruise
4.) Idle Descent
5.) Loiter

Ground idle and loiter were selected because these are conditions where the engine operates at very low levels of fuel flow and require high levels of recirculation flow or high fuel temperature capability to achieve the necessary heat sink. The high flight speeds associated with supersonic cruise, while providing a higher level of fuel flow to act as the heat sink, also result in more stringent operating temperatures for the fuel system. Somewhere in between these two extremes are the subsonic cruise flight points that combine moderate levels of fuel flow and operating temperatures.

The final flight condition considered was idle descent. This occurs when the pilot, in order to reduce flight speed and altitude, cuts engine power to an idle setting. When this happens after a supersonic flight point, the worst case combination of low fuel flow and high operating temperatures is encountered. These are transient conditions since the thermal environment becomes less severe as flight speed decreases. The thermal management models used in this study are steady state models and do not handle conditions such as these in a transient manner. The idle descent points were still felt to be critical to defining fuel temperature requirements and for this study were investigated using the steady state models. Estimated maximum fuel temperatures determined at these flight conditions may be somewhat higher than if transient models had been available for use.

The five flight conditions described previously were investigated for the following three missions:

1.) IHPTET Phase I Advanced Tactical Fighter
2.) IHPTET Phase II Air Superiority Fighter
3.) IHPTET Phase II Lightweight Fighter

Results of the first phase of this study indicated idle descent was the flight condition where maximum fuel temperatures were encountered. Ground idle was also considered to be a critical condition since this is the sizing point for the recirculation system. Consequently, only these two flight points were considered for the final three missions studied:

4.) IHPTET Phase II Advanced Navy Fighter
5.) IHPTET Phase II Lightweight Fighter
6.) IHPTET Phase III Air Superiority Fighter

In the study results which follow, maximum fuel temperatures were established for systems without fuel recirculation. Airframe heat loads in the range of 3,000 to 4,000 Btu/min were used because they are in the range anticipated for the prototype of the next generation of tactical fighter aircraft. Table 4, for example, shows the sources and levels of heat that the fuel must absorb at the supercruise flight condition.

TABLE 4 -- Summary of fuel heat loads (Btu/min) for Supercruise flight condition

	IHPTET Phase/Mission		
	I/ATF	II/ASF	III/LWF
Hydraulic System	1253	1061	156
Main Fuel Pump	4466	1959	3055
Airframe	3650	4000	4000
Bearing Lube System	4319	5130	8534
Misc.	1053	954	672
Total	14741	13104	16417

7.0 STUDY RESULTS

Fuel requirements for the missions discussed in the following paragraphs are based on fixed airframe heat loads and no recirculation system.

7.1 IHPTET Phase I Advanced Tactical Fighter Mission

For an IHPTET Phase I propulsion system in an ATF mission, Figure 2 shows that without recirculation, current fuels (JP-4, JP-8) with 163°C capability would have insufficient heat sink at all flight conditions except supersonic cruise. Fuel temperature capability was then allowed to vary until sufficient heat sink capacity was provided. Table 5 indicates a fuel temperature capability of approximately 346°C would be necessary to provide the heat sink needed for the idle descent flight condition.

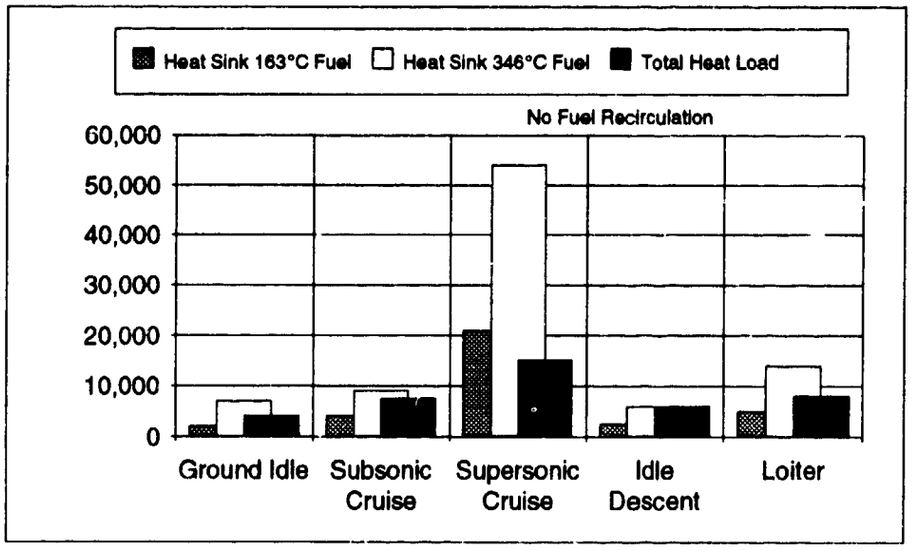

FIG. 2 -- IHPTET Phase I ATF Mission - heat load vs. heat sink

This capability would result in an excess heat sink capacity for all other flight conditions, although the margin is relatively small at subsonic cruise conditions. Fuel with this capability would, however, require a bearing lubrication fluid capability of approximately 349°C.

Table 5 shows that maximum fuel temperatures are encountered at the gas generator inlet for all flight conditions except supersonic cruise. For this high speed flight point, the increased actuator adiabatic wall temperature results in a heat gain for the fuel and a maximum fuel temperature in the hydraulic system loop. Conversely, the low speed, subsonic flight points have an adiabatic wall temperature lower than the fuel temperature, resulting in a fuel temperature drop across the hydraulic system. Simply put, at the low speed flight conditions, the hydraulic system actuators act as a fuel/air heat exchanger.

7.2 IHPTET Phase II Air Superiority Fighter (ASF) Mission

As with the ATF mission, the ASF mission exhibits maximum fuel temperatures at the gas generator inlet for all flight conditions except supersonic cruise. At this high speed flight point, fuel in the actuators is absorbing heat because of the high ambient wall temperatures. As a result, maximum fuel temperatures during supersonic cruise are encountered in the hydraulic loop.

Fuel temperatures were determined at the boost pump, main fuel pump, gas generator and hydraulic system return for the five flight conditions studied. The maximum fuel temperature was 340°C at the gas generator during the idle descent flight condition. Figure 3 shows that at an IHPTET Phase II engine technology level, current fuels would be unable to provide the required heat sink at all ASF mission flight conditions investigated. For this mission, the requirement for a Mach 2.5 descent at idle power sets the need for a 340°C capable fuel if the required heat sink is to be provided without recirculation. This is by far the most difficult condition in this mission and requires fuel temperature capability over 38°C higher than the other flight points. This is reflected by the excess heat sink capacity which results when a 340°C fuel is used at the other flight conditions.

TABLE 5 -- IHPTET Phase I Advanced Tactical Fighter Mission - fuel and oil temperatures without fuel recirculation

	Temperature, °C				
Component	Ground Idle	Subsonic Cruise	Supersonic Cruise	Idle Descent	Loiter
Boost pump in	197	178	67	226	124
Boost pump out	207	193	71	244	133
Main pump in	219	230	84	293	167
Main pump out	239	263	107	324	190
Fuel to GG	238	287	130	346*	214
Hyd system return	223	256	148	317	207
Oil in	237	302	156	347	227
Oil out	239	294	127	340	215

* Maximum fuel temperature

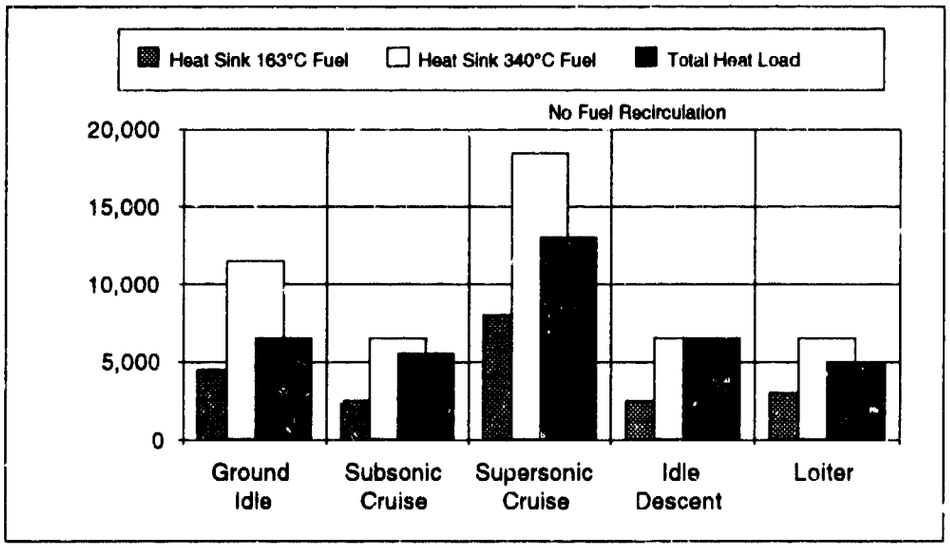

FIG. 3 -- IHPTET Phase II ASF Mission - heat load vs. heat sink

7.3 IHPTET Phase III Lightweight Fighter (LWF) Mission

For a LWF mission using IHPTET Phase III technology level engines, Figure 4 indicates inadequate heat sink capacity at all flight points in the mission except supersonic cruise. Idle descent is again the flight condition which sets the maximum fuel temperature requirement. In this case, an 449°C capable fuel would be necessary to provide the heat sink capacity without recirculation.

A significant difference between the LWF and the ASF application is that maximum fuel temperature is encountered not at the gas generator inlet, but instead at the exit of the fuel boost pump. This occurs because of the lower engine cycle overall pressure ratio selected for the LWF. Engines operating at altitude idle flight conditions often must run at higher idle power settings than is necessary for the mission. This is required so the engine can provide sufficient engine bleed air pressure to meet airframe power requirements. The ASF engines have lower engine pressure ratios than the LWF engines. As a result, the ASF engines must run to higher idle power settings to meet this bleed pressure requirement.

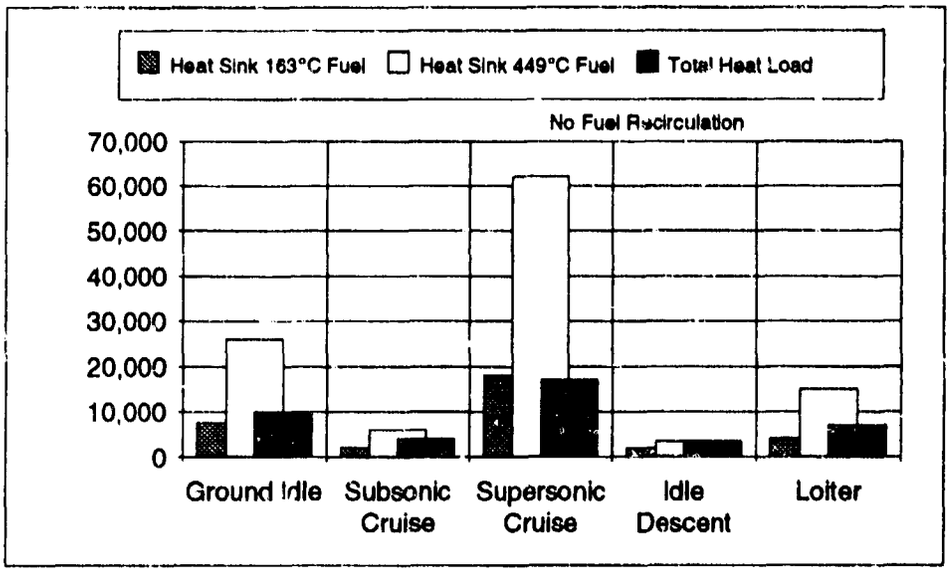

FIG. 4 -- IHPTET Phase III LWF Mission - heat load vs. heat sink

Because of this, the ASF propulsion systems have approximately twice the fuel flow to absorb the same 4000 Btu/min airframe heat load as do the LWF engines. Consequently, the fuel entering the LWF engines, following heat pickup from the airframe, is at a significantly higher temperature than the ASF mission. In fact, the boost pump fuel temperatures for the idle descent and subsonic cruise flight conditions are such that the remainder of the fuel system has a net heat loss. This is again the result of heat being lost from the fuel in the hydraulic system loop.

7.4 Other Missions Investigated

For the final three missions studied, only the idle descent and ground idle flight conditions were investigated. Table 6 summarizes the fuel temperatures at idle descent for all the missions investigated. Out of all of the missions investigated, the Advanced Navy Fighter (ANF) exhibited the highest maximum fuel temperature (466°C). Like the LWF mission, this can be traced to the optimum propulsion system cycle that has a high operating pressure ratio (OPR) for good fuel consumption characteristics. This cycle allows the engine to run to very low idle fuel flows and as a result,

TABLE 6 -- Fuel temperatures for Idle Descent without fuel recirculation

	IHPTET Phase/Mission					
Temperature, °C	I	II	II	II	III	III
Component	ATF	ANF	ASF	LWF	ASF	LWF
Boost pump in	226	412	223	387	238	421
Boost pump out	244	466*	252	437*	254	449*
Main pump in	293	303	295	291	318	335
Main pump out	324	313	312	299	341	349
Fuel to GG	346*	322	341*	311	376*	365
Hyd. sys. return	317	259	313	249	341	304
Oil in	347	326	362	317	399	374
Oil out	341	323	343	312	379	372

* Maximum fuel temperature

creates very high fuel temperatures when absorbing the airframe heat load. Similar to the LWF mission, the remainder of the fuel system has a net heat loss. Here again, the actuators are acting as a fuel/air heat exchanger with the fuel showing a significant reduction in temperature across the hydraulic system loop.

TABLE 7 -- Fuel temperatures for Ground Idle without fuel recirculation

	IHPTET Phase/Mission					
Temperature, °C	I	II	II	II	III	III
Component	ATF	ANF	ASF	LWF	ASF	LWF
Boost pump in	197	196	149	106	158	113
Boost pump out	207	221	167	116	168	118
Main pump in	219	213	172	131	187	147
Main pump out	239*	221	180	138	198	161
Fuel to GG	238	233*	200*	161*	222*	193*
Hyd. sys. return	223	206	176	154	201	184
Oil in	237	245	227	206	247	237
Oil out	239	236	207	176	226	203

* Maximum fuel temperature

Comparison of predicted temperatures for the Phase II and III ASF and LWF yielded expected results. The higher speeds and lower fuel flows of the Phase III propulsion systems result in increased fuel temperatures. The differences are not large since the same mission profile and airframe heat loads were considered in both phases.

The results for ground idle are shown in Table 7. While this flight condition has significantly lower fuel temperatures than idle descent, it is critical for sizing the recirculation system. These results provided a baseline for the next phase of the study which focused on fuel recirculation requirements in a parametric manner.

7.5 Feasibility Of Eliminating The Recirculation System

Table 8 shows the maximum fuel temperatures encountered with no fuel recirculation for each mission studied. These are compared to the IHPTET goals for high temperature fluid development presented earlier in Table 1. Realization of technologies to reach these fuel temperature capabilities will still probably not allow future tactical fighters to eliminate the recirculation system. This is because a number of factors are likely to drive heat loads up even further and because several other factors will limit the usable fuel temperature capability:

- Future levels of airframe heat load can only be roughly approximated based on little definite information. New trending indicates that future heat loads will significantly exceed the 3,000 to 4,000 Btu/min used in the first phase of this study. This means that without recirculation, even higher fuel temperatures than were projected in this study could result.

- For a twin-engine aircraft, some kind of contingency plan for a one-engine out situation needs to be considered. This situation would require the fuel system of the remaining operational engine to handle the entire airframe heat load. Recirculation provides a way to handle this type of situation.

- No matter how much fuel capability is increased, fuel temperature will still have to be kept at a lower level than oil and hydraulic fluids to insure outflow of heat from these systems. For this reason, any fuel temperature capability above the development goals for these other fluids will not be usable in a conventional tactical fighter fuel system.

- Considerable technology development in the area of fuel system components is required. A prime example is the fuel pump. A survey indicated

current pumps can handle maximum fuel temperatures slightly above 116°C. The first phase of this study indicated fuel pump temperatures of up to 449°C for some of the missions investigated. This would require a significant increase in pump material temperature capability as well as pump designs to preclude cavitation at these elevated fuel temperatures.

TABLE 8 -- Maximum fuel temperatures relative to P&W IHPTET fluid development goals

	IHPTET Phase/Mission					
	IHPTET Phase I	IHPTET Phase II			IHPTET Phase III	
	ATF	ANF	ASF	LWF	ASF	LWF
Max Fuel Temperature With No Recirculation, °C	346	466	340	437	376	449
Fluid Development Goals						
Fuel, °C	218		288			371
Liquid Lubricant, °C	204		329			371

7.6 Payoff For High Temperature Fuel Development

The first phase of this study indicates that elimination of the fuel recirculation system may not be feasible. The second phase of the study, however, shows how high fuel temperature capability can minimize the weight penalty associated with fuel recirculation. Since future levels of airframe heat load are unclear, a parametric study for each of the missions of interest was performed. The parametric looked at fuel recirculation requirements for different levels of fuel temperature capability and airframe heat load.

A second parametric was performed to show the potential weight payoff for reducing recirculation flow. The results of the first parametric were used in the second parametric to do a relative sizing of a fuel recirculation system component. The recirculation system component selected was the fuel/air heat exchanger. Since ground idle is the critical flight condition for sizing the fuel recirculation system, the parametrics were performed at that condition. It should be emphasized that the fuel/air heat exchanger is the design responsibility of the airframer and the estimates made here by P&W are used to show relative component weight improvements.

Fuel recirculation requirements as a function of maximum fuel temperature and airframe heat load for the IHPTET Phase II ASF mission at a ground idle flight condition is shown in Figure 5. Table 9 summaries the results of this parametric study for six missions spanning IHPTET Phases I, II, and III using the P&W fuel temperature goals and a best guess of airframe heat loads for future tactical fighters. The airframe heat loads shown in Table 9 reflect new trending which indicates that future heat loads will significantly exceed the 3,000 to 4,000 Btu/min used in the first phase of this study. The new values are a best guess and are considered extremely conservative.

Table 9 suggests that achievement of P&W's fuel development goals will allow the system to operate with significantly reduced or with no fuel recirculation at ground idle. Earlier results indicated that fuel recirculation would be required at the idle descent flight condition even with high temperature fuel capability. Again, the explanation for this may be that the idle descent requirements identified earlier are estimates of transient conditions using a steady state model. As a result, the estimated idle descent fuel heat sink requirements may be too high. Despite this, the trend established here of significantly reduced recirculation flow should apply at both flight conditions.

8.0 CONCLUSIONS

Based on this investigation, the following conclusions can be made:

- Payoff studies, the projection of future fuel system capabilities and the temperature development goals for other fluids indicate that the following

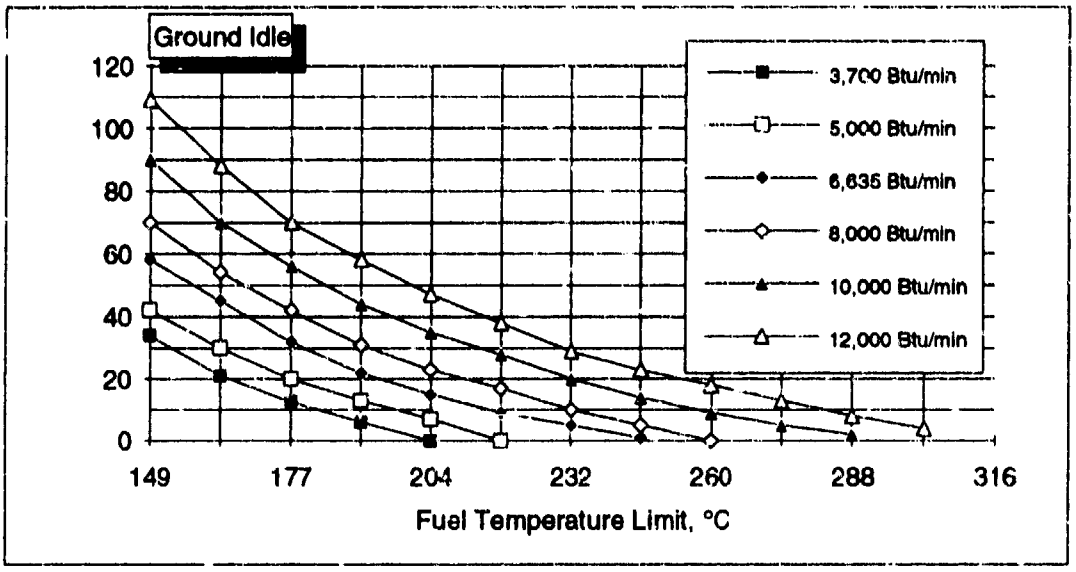

FIG. 5 -- Fuel recirculation requirements for IHPTET Phase II ASF Fighter Mission

TABLE 9 -- Summary of recirculation flow requirements at ground idle

IHPTET Phase	Mission	*Fuel Capability (°C)	Airframe Heat Load (Btu/min)	Fuel Recirculation (lb/min)
I	Advanced Tactical Fighter	163 218	5,000	62 20
II	Air Superiority Fighter	163 288	8,000	55 00
II	Advanced Navy Fighter	163 288	8,000	55 07
II	Lightweight Fighter	163 288	8,000	31 00
III	Air Superiority Fighter	163 371	10,000	78 00
III	Lightweignt Fighter	163 371	10,000	69 00

* Values shown are current capability followed by development goal for each phase

are reasonable advanced JP fuel development goals:

	Max Fuel Temperature At the Nozzle, °C
IHPTET Phase I	218
IHPTET Phase II	288
IHPTET Phase III	371

- Achievement of these goals will not likely eliminate the requirement for a fuel recirculation system for future tactical fighters.
- Achievement of these goals will permit a significant reduction in the size and weight of the fuel recirculation system.

- Increasing heat loads on the fuel and the desire to minimize the penalty associated with the recirculation system demands that higher fuel temperature capability be developed. While the engine itself will realize little weight savings, the benefit to the total airframe and propulsion system would be significant. The fact that fuel is a critical component to gas turbine operation makes the IHPTET initiative a logical vehicle for the development of advanced fuels.

Discussion

Question 1. W. Dodds
You talked about higher temperature fuels. What is your measure of fuel stability — JFTOT?

Author's Reply
Candidate thermal stability improving additives are added to a reference fuel. The thermal stability properties of the candidate formulations are compared to that of the JP-Thermally Stable fuel in a variety of experimental static and dynamic tests. JP-Thermally Stable fuel was selected as the target because it is the fuel used in the U-2. In the U-2, it is subjected to temperatures in excess of 425 degrees F without exhibiting fouling or coking. Therefore, if an additive formulation can duplicate the thermal stability characteristics of JP-Thermally Stable, then we can say that we have a 425 degree F formulation.

HIGH TEMPERATURE RESISTANT JET FUELS

by

Luis M. Peloche and Santiago Asensio
Propulsion and Energy Division
Fuels and Lubricants Laboratory
INTA
Torrejon de Ardoz
28850 Madrid
Spain

ABSTRACT

The thermal stability of the aviation fuels is evaluated according to the ASTM D 2341 method. This characteristic is linked to the presence of the generators of instability, mainly diolephins and N and S derivates.

The objects of the present work are: the obtention in laboratory of kerosene which is thermally stable, the isolation and identification of the generators of instability and the regeneration of the thermally unstable kerosenes.

Keywords: Kerosene, thermal stability, percolation and break point.

1. INTRODUCTION

The fuels used in aviation are a mixture of hydrocarbons obtained by distillation of petroleum crudes followed by refinement. In addition to the mentioned products and during the distillation phase related to the kerosene (2nd lateral current, 150 to 260ºC.), other types of compounds appear whose presence is due to either their existence in the oil or to contamination by slops. The said compounds are mainly derivatives of sulphur, nitrogen and oxygen.

These compounds, together with diolephines and polynuclear aromatics, are those which create the thermal instability problems.

The chemical reactions contributing to the decomposition of the fuel have been widely studied. Generally, these reactions occur through oxidization processes forming hydroperoxides and peroxides. There is a nucleation process followed by growth of deposits and gums which create obstruction problems in filters and injectors.

The principal test for determining this property of aviation fuels is the thermal stability test (ASTM D 2341). It consists of passing kerosene, during 150 minutes and with a flow rate of 3 mL/min., first through an aluminum heating tube and after through a stainless steel filter with a porosity of 17µm, where the fuels deterioration products are deposited.
The test is carried out at 260ºC. and shows the tendency of reactor fuels to deposit deterioration products in the engine supply system.

2. OBTENTION OF KEROSENES OF HIGH THERMAL STABILITY

With this purpose in mind, we took as starting point a kerosene which we called A, hydrogened but not additived.

The procedure is the following: by means of a suitable absorbent medium, an attempt is made to eliminate the potential generators of thermal instability, thus obtaining what could be termed "ideal kerosene". This is submitted to severe test conditions in order to evaluate its thermal resistance, and also to evaluate the action of 4 additives.

2.1 Elimination of the generators of thermal instability

The kerosene A was percolated through neutral alumina which had been previously activated during 4 h. at 400ºC. For this we used a OMNIFIT column of 500 mm length and with an interior diameter of 25 mm, and a pressure regulation mechanism with a manometer. A complete specification test was carried out on the percolated sample, giving low values of gums (0.4 mg/100 mL), total sulphur (0.10% mass), olephins (0.2% vol.), mercaptans (0 ppm), total acidity (0.002 mg KOH/g) and nitrogen (0 ppm).

2.2 Ageing at increasing temperatures

The specimen obtained was subjected to an ageing series of 6 weeks duration with increasing temperature. The results obtained were:

* six weeks at 60°C.

SAMPLE	ACIDITY (mg KOH/g)	THERMAL STABILITY Press. drop (mmHg)	Tube aspect
KAP	0.002	0	1 No irid.
KAP + 24 mg/L Ad. 1	0.002	2	1 No irid.
KAP + 24 mg/L A. 2	0.002	0	1 No irid.
KAP + 24 mg/L Ad. 3	0.002	0	1 No irid

* Six weeks at 90°C

SAMPLEA	ACIDITY (mg KOH/g)	THERMAL STABILITY Press. drop(mmHg)	Tube aspect
KAP	0,008	0	1 No irid.
KAP + 24 mg/L Ad.1	0,006	0	1 No irid.
KAP + 24 mg/L Ad.2	0,006	0	1 No irid.
KAP + 24 mg/L Ad.3	0,006	0	1 No irid.
KAP + 5,7 mg/L ADM	0,01	0	1 No irid.
KAP + 24 mg/L Ad.1 + 5,7 mg/L MDA	0,006	5	1 No irid.

* Six weeks at 120°C

SAMPLE	ACIDITY (mg KOH/g)	THERMAL STABILITY Press. drop(mmHg)	Tube aspect
KAP	0,049	6	1 No irid.
KAP + 24 mg/L Ad.1	0,029	3	1 No irid.
KAP + 24 mg/L Ad.2	0,028	4	1 No irid.
KAP + 24 mg/L Ad.3	0,020	2	1 No irid.
KAP + 5,7 mg/L ADM	0,049	2	1 No irid.
KAP + 24 mg/L Ad.1 + 5,7 mg/L MDA	0,030	3	1 No irid.

* Six weeks at 150°C

SAMPLE	ACIDITY (mg KOH/g)	THERMAL STABILITY Press. drop(mmHg)	Tube aspect
KAP	———	16	1 No irid.
KAP + 24 mg/L Ad.1	———	13	1 No irid.
KAP + 24 mg/L Ad.2	———	13	1 No irid.
KAP + 24 mg/L Ad.3	———	13	1 No irid.
KAP + 5,7 mg/L ADM	———	12	1 No irid.
KAP + 24 mg/L Ad.1 + 5,7 mg/L MDA	———	12	1 No irid.

In this ageing, it was impossible to determine the degree of acidity because of shortcomings in the specimen due to evaporation losses.

The abreviations employed correspond to the following terms:

KAP = "ideal kerosene"
Ad. 1 = 2,6-di-tert-butyl-4-methylphenol
Ad. 2 = 2,6-di-tert-butylphenol
Ad. 3 = 2,4-di-methyl-6-tert-butylphenol
MDA = Metal deactivator additive: N,N'-disalicylidene-1,2-propanediamine

As can be seen from the results, the percolated kerosene A ("ideal"), singly or with any one of the additives incorporated, fulfills the thermal stability test's requirements, even after ageing at 150°C during 6 weeks. It is possible to affirm that the strong stability of the kerosene tested is due to the absence of nitrogen derivatives and mercaptan sulphur. Finally, we wish to underline the fact that we have not found any bibliographic reference mentioning a kerosene that overcomes such severe ageing.

2.2.1 Determination of the break point

The break point concept is considered as a highly useful tool having two possible applications:

1.- To overcome the qualitative criterion of go/not go in the thermal stability test.

2.- To quantify the degree of treatment effectiveness with a selective absorbent medium, with a view to increasing the thermal resistance of a given fuel.

Several of the authors consulted consider as break point that temperature in which the value TDR = 13 at Mark 8 is reached. We shall apply this criterion to the "ideal kerosene" obtained in 2.1. The results obtained were the following:

* Kerosene A, before percolating

TEMPERATURE (°C)	TDR	BREAK POINT (°C)
260	1,5	286
280	8	
290	15	
300	29	

* Kerosene A, after percolation through a neutral alumina ("ideal kerosene")

TEMPERATURE (ºC)	TDR	BREAK POINT (ºC)
290	5	
320	8	370 (extrapolated)

As can be seen, the qualitative jump obtained in the thermal stability of the kerosene is high. We consider that this is the appropriate method to achieve a fuel with a high thermal resistance.

3. ISOLATION AND IDENTIFICATION OF THE GENERATORS OF THERMAL INSTABILITY

From the bibliographic study, knowledge can be derived concerning the action that these compounds exercise upon the thermal stability of fuels, as well as their composition,which principally consists of the following:

a) Nitrogened compounds (aminics and heteroatomics)
b) Sulphur compounds (sulphurs, disulphurs and mercaptans)
c) Oxygened compounds (carboxilic acids and phenolics)

In a word, basic or acidic polar compounds. The operative procedures for achieving the two objectives of this point are described as follows:

3.1 Isolation

Chromatography in column has been selected as the technique to be used. The starting point was an thermically unstable unhydrogened kerosene, which from this point on will be known as B, with high values of total sulphur, mercaptans, nitrogen, acidity and gums.

The operative procedure was the following: 5 L. of kerosene B were percolated through an OMNIFIT column packed with 230g of previously activated neutral aluminum which acted as the absorbent medium. Once the fuel was percolated, the remaining kerosene was extracted from the column by n-hexane (1 L.), then a disabsorption of the stationary layer of the polar compounds was carried out by means of an inversion flow and using a mixture of 50:50 methanol/methylenechloride, isolating the said polar compounds by rotavapor. The efficiency was of 1.18g/L of kerosene.

In the percolated kerosene the instability disappeared, in both pressure drop and tube aspect. Regarding the other parameters, the total acidity diminished by 91%, the mercaptan sulphur by 86% and the nitrogened compounds by 100%.

3.2 Identification

This was undertaken using a combination of various instrumental techniques: classic column chromatography at low pressure, infra-red spectroscopy, gas chromatography and mass spectroscopy. The method was the following:

300 mg of polar extract, isolated as described in 3.1 were put at the head of a chromatographic column of 250 mm long and 6.2 mm interior diameter. A 50:50 mixture of previously activated silica gel and neutral alumina were used as an absorbent medium. As eluotropic serie, one with a growing polarity formed by the following dissolvents was used:

Pentane
Pentane/carbon tetrachloride 1:1
Benzene/methylene chloride 1:1
Methylene chloride/ether ethylic 1:3
Ether ethylic/acetone 1:1
Methanol

Seven fractions were collected in total, and their respective masses quantified after the dissolvents were dried in an oven during 48 hours at 60ºC. The IR spectrum of each of the 7 fractions was obtained, and the presence of several functional groups was detected in them according to expectation. Logically, this technique is approximative.

Gas chromatography was used to make an exhaustive identification of the compounds included in each fraction. The model employed was a Perkin-Elmer Auto System connected to a Perkin-Elmer mass detector, model Q-Mass 910. A capillary column of methyl-phenyl silicon was selected.

For each fraction, specific chromatographic conditions were selected, and once optimized the connection column-camera was made by means of the transference line. The mass detector is of the ion-trap type, with thermal bombardment of electrons at 80 eV and a vacuum of 10^{-5} Torr. A Digital DeCstation 316 Sxcomputer was used for identifying the chromatography peaks. The mass spectra obtained were compared to those stored in a NIST collection of over 60.000 spectrums. A total of 58 compounds were identified with an approximation of over 90%.

These figures show an example of the methodology followed.

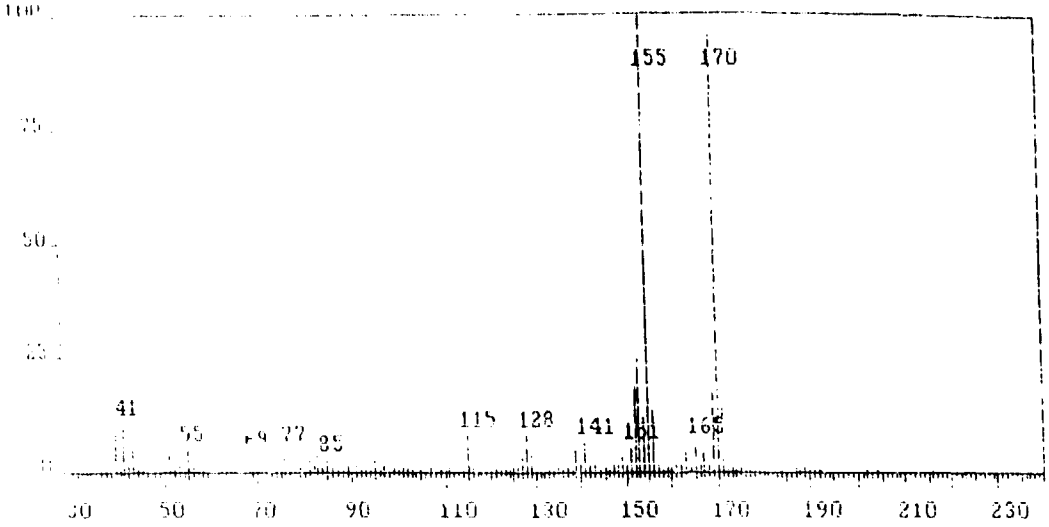

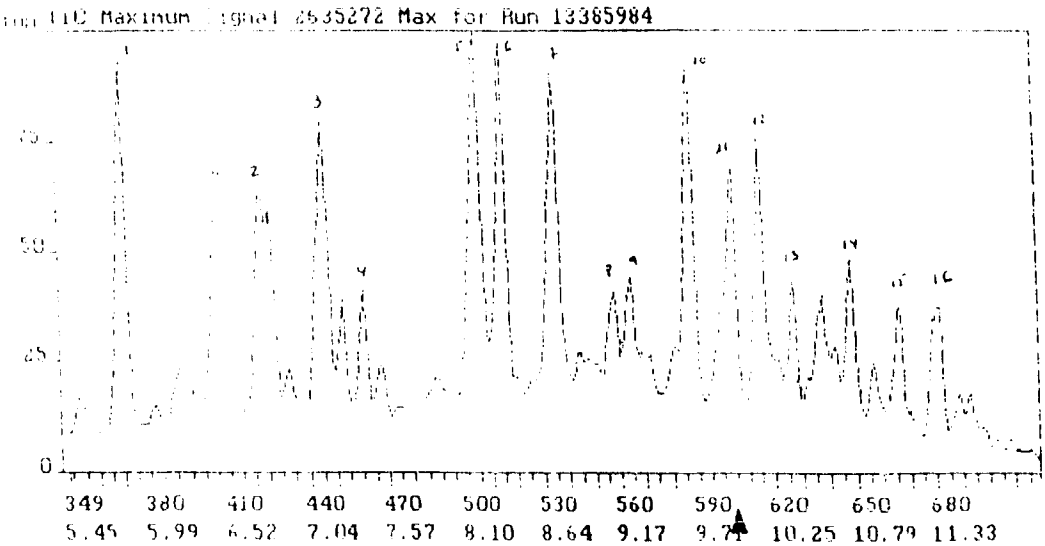

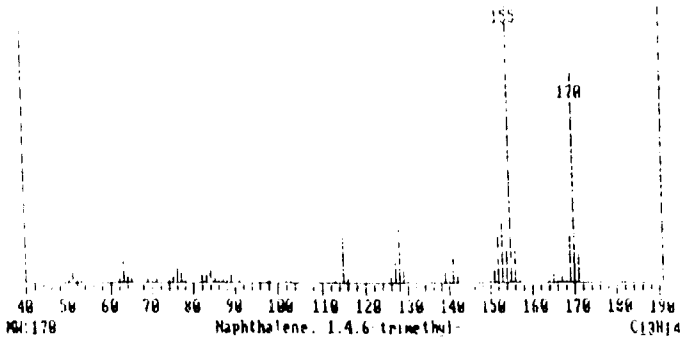

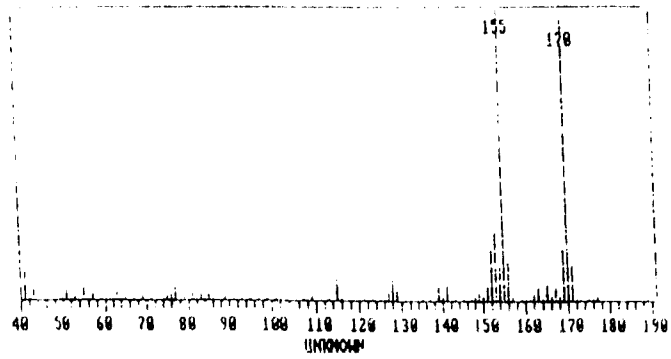

In this case the TIC corresponds to the fraction eluted with pentane of the numbered peaks, number 11 was the one selected, and its spectra is shown in the figures. The comparison of the unknown peak and the NIST collection, leads to the identification of peak 11 as 1,4,6 trymethyl naphtalene.

4. REGENERATION OF THERMALLY UNSTABLE KEROSENES

To achieve this, we started from a non-hydrogenated kerosene called B. We found no specific work on this topic in the literature, but in some instances the regeneration problem is treated using expensive absorbents at laboratory scale.

On our part, we approached the problem studying the behaviour of three different absorbent clays and selecting one of them as the most suitable through a process of elimination. Said process consisted of two stages of increasing exhaustiveness which we will now proceed to describe.

4.1 First stage. Yield assessment

The object of this is to carry out a yield study at laboratory scale of the clays, evaluating the following aspects:

- Elution velocity (operativity)
- Optimum granule
- Break point determination.

The method was the following:

Using liquid chromatography in column at low pressure 5 liters of kerosene B were percolated through a glass OMNIFIT column of 500 mm long, and 25 mm of interior diameter. This was completely packed with the clay under study. The clay had been dried previously for two hours at 115ºC to eliminate the humidity present which oscillated between values of 7% and 12%. A pressure of 1kg/cm^2 was applied. In the break point determination, to avoid extrapolations, we have used the reference value 10 (instead of 13) in the TDR.
The results obtained are shown in the following page.

The results for the 13 clays were:

	Elut.velocity L/h	Temp. ºC	TDR	Break point (TDR=10,ºC)
Kero B before percolating		245 260	8 12	252,5
Kero B after percolation through:				
Calcic bentonite>120	0.2	295 310	6 14	302,5
Attapulgite A 50/80	1.3	290 305	6 8	320
Sepiolite A 30/60	1.4	260 300	1 11	296
E. of diatom A>120	0.4	260 290	1 13	282,5
Attapulgite B 40/60	1.3	290 305	4 12	302
Sepiolite B 60/120	1.4	305 315	8 27	310
Sepiolite C>120	0.8	260 290	3.5 13	280
E. of diatom B>120	Leak	___	___	___
E. of diatom C>120	Leak	___	___	___
Attapulgite C>120	1	260 290	3 11	286,5
Bentonite>120	Leak	___	___	___
Saponite>120	Leak	___	___	___
E. of diatom D>120	0.4	280 300	5 18	284

Analyzing the results,the following can be taken into consideration.

a) Operativity: The best results were obtained for clays in the range 40-120 mesh ASTM.

b) Break point: Outstanding performance of three clays:

- Sepiolite B 60/120
- Attapulgite A 50/80
- Attapulgite B 40/60

4.2 Second stage. Efficiency assessment

This consists mainly in solving the following question with respect to the clays selected: what volume of thermically unstable kerosene can be regenerated per unit of mass of a given clay? Or, what is the same thing, when does the clay become inactive?

In order to answer this question we used an OMNIFIT column of 250 mm of length and 12 mm of internal diameter. Eluted kerosene was collected in numbered 1 litre vessels. Every 5 liters the thermal stability and total acidity was determined. We also evaluated the elution speed and the degree of compactness of the clay.

The results obtained are shown in the following figures:

* **With Sepiolite B 60/120**

	THERMAL STABILITY (260ºC) Press drop(mm Hg)	Tube aspect	ACIDITY (mg KOH/g)
5th L	0	1 No irid.	0,002
10th L	0	1 No irid.	0,006
15th L	9	1 No irid.	0,019
18th L	13	1 No irid.	0,019
20th L	14	1 No irid.	0,021
22th L	14	1 No irid.	0,022

At this point the test was interrupted by elution problems. Given that the mass of clay introduced into the columna was 25,39g, it can be deduced that a metric ton of this clay is capable of regenerating 866 m^3 of thermally unstable kerosene.

* **With Attapulgite A 50/80**

	THERMAL STABILITY (260ºC) Press.drop(mm Hg)	Tube aspect	ACIDITY (mg KOH/g)
5th L	0	1 No irid.	0,002
10th L	0	1 No irid.	0,007
15th L	0	1 No irid.	0,007
20th L	4	1 No irid.	0,014
25th L	7	1 No irid.	0,018
30th L	12	1 No irid.	0,025
35th L	16	1 No irid.	0,026

The behaviour observed was similar to that of Sepiolite B. Both presented problems with the elution of the final litres. Given that the mass of clay introduced into the column was 17,06g, it can be deduced that a metric ton of this attapulgite is capable of regenerating 2.051m^3 of thermally unstable kerosene.

* With Attapulgite B 40/60

	THERMAL STABILITY (260ºC) Press. drop(mm Hg)	Tube aspect	ACIDITY (mg KOH/g)
5ml/L	0	1 No irid.	0,002
10ml/L	0	1 No irid.	0,014
15ml/L	0	1 No irid.	0,018
20ml/L	0	1 No irid.	0,020
25ml/L	0	1 No irid.	0,020
30ml/L	1	2 No irid.	0,022
35ml/L	3	2 No irid.	0,022

At this point the test was interrupted by elution problems, but as 19,46g of attapulgite B was introduced into the column, it can be deduced that a metric ton of this clay is capable of regenerating 1.798 m³ of thermally unstable kerosene.

We conclude that, among the three tested clays, the most efficient was Attapulgite A 50/80 mesh ASTM because, though it presented larger press drop at JFTOT test, its tube aspect was better and specially its break point temperature (table "results for 13 clays") was higher (320ºC) than of Attapulgite B 40/60 mesh ASTM (302ºC).

5. CONCLUSIONS

The presence of determined compounds in the kerosene creates problems of thermal instability. Their elimination by means of a simple operative procedure such as the percolation of the fuel through an absorbent medium is the optimum means of increasing their thermal stability.

The best way to evaluate the efficiency of the treatment is to determine the temperature of the break point, as this permits the quantitative estimation of the criterion go/not go of the standardized test.

Bibliographic references

1.- S.M. Cohen. "Fuels research - fuels thermal stability overview". NASA Lewis Research Center (1989).

2.- R.N. Hazlett & G. Kelso. "Acid base phenomena in distillate fuel stability" 2nd International Conference on Fuel Stability . San Antonio (Texas) (1986).

3.- A.C. Antoine. "Effect of some nitrogen compounds on thermal stability of jet A" NASA technical memorandum 82-908 (1982).

4.- A. Uranus & P.S. Martney. "Experimental study of aircraft fuels at elevated temperature". NASA report CR-165165.

5.- Bernasconi et al. "Middle distillates stability: composition and additive utilization effects on their aging at different temperatures" 3rd International Conference on Fuel Stability. London (1988).

6.- L.M. Peloche & S. Asensio. "Study of color instability in gas oils" INTA (1992).

7.- M. Dorbon et al. "Storage stability of fuels. Efficiency of hydrotreatment" Fuels Science and Technology International (1992).

8.- J.S. Mills & F.R. Edwards. "The thermal stability of aviation fuel". ASME PAPER 84-GT-69 (1984).

9.- L.M. Peloche & S. Asensio. "Thermal stability of aviation kerosenes". INTA 1.990.

ACKNOWLEDGMENT: This work has been funded by BP OIL SPAIN within OCIPETROL programme.

Research and Development of High Thermal Stability Fuels

T. Edwards, W. M. Roquemore, W. E. Harrison, S. D. Anderson
USAF Wright Laboratory
WL/POSF Bldg 490
1790 Loop Rd N
Wright-Patterson AFB OH 45433-7103
USA

1. SUMMARY

Increases in aircraft performance are leading to increases in thermal stress on the primary aircraft coolant--the fuel. Fuel thermal stability limitations may offset future aircraft performance gains. The Air Force's Wright Laboratory is sponsoring several research programs to address this problem. The development of an additive package for JP-8 to improve its thermal stability is the primary focus of this paper. This program involves extensive testing of fuels and additives in a variety of test devices, culminating in tests in a fuel system simulator and engine tests. These tests involve Air Force personnel, on-site contractors (University of Dayton Research Institute, Systems Research Laboratories), Pratt and Whitney Aircraft Co., additive manufacturers, and Sandia National Laboratory. The test devices include several flowing and static tests, where the behavior of a fuel is investigated in a wide variety of environments. The study of several baseline fuels in these devices has led to some new insights into the mechanisms of fuel thermal (in)stability. It is becoming clear that a fuel's tendency to oxidize (to form peroxides, for example) is often inversely proportional to its tendency to form insoluble deposits.

2. INTRODUCTION

Emerging threats require the development of highly maneuverable aircraft with high-performance engines, enhanced avionics, and expanded flight envelopes. Aircraft subsystems (environmental control, power generation, hydraulics, engine, etc.) generate waste heat that must be removed to ensure adequate component reliability and life. Technology advances and requirements for increased aircraft performance are causing increases in aircraft subsystem and engine heat loads. Specifications for current Air Force aviation turbine fuels (JP-4 and JP-8) are designed to provide adequate energy content, combustibility, fluidity, thermal stability, storability, and safety while maximizing availability and minimizing cost. Until recently, JP-4 and JP-8 provided adequate heat sink to allow their effective use as coolants for critical on-board subsystems. However, these fuels are limited to a maximum operating temperature of 163°C (325°F) as measured at the inlet to the fuel nozzles on the engine because of thermal stability limitations.

Management of aircraft thermal requirements is becoming more complex and affects the design and maintenance requirements of the aircraft. Ram air and fuel are the primary heat sinks available for aircraft waste heat dissipation. Ram air is used extensively on current aircraft to provide the necessary cooling. Ram air, however, restricts the flight envelope, reduces component performance due to its relatively poor heat transfer characteristics and, thus, reduces component life and reliability. In addition, as aircraft speed increases above approximately Mach 1, the stagnation temperature of air precludes its use as a coolant. Increasingly, aircraft designers are utilizing the fuel to provide subsystem cooling. Many recently fielded aircraft utilize all the available heat sink capacity of JP-4 and/or JP-8 fuels. In addition, most of these aircraft recirculate fuel to match heat loads with available fuel heat sink. Studies indicate that future aircraft will be forced to carry large quantities of excess fuel for thermal management, thus reducing range or payload.

To reduce the penalties associated with carrying excess fuel for thermal management purposes, the Air Force has embarked on a program to develop high temperature thermally stable (HiTTS) fuels [References 1-4]. Two fuels are currently under development. The objective of the HiTTS 100 ("JP-8+100") program is to develop an additive package to increase the thermal stability of JP-8 from 163°C (325°F) to 218°C (425°F) and thereby increase the available heat sink by 50%. Furthermore, since the sole intent of the additive package is to improve thermal stability, the package which is developed should not significantly alter any fuel characteristics other than thermal stability. The objective of the HiTTS 900 ("JP-900") program is to develop a new fuel with a thermal stability of 482°C (900°F) thereby increasing the heat sink by 500% through the use of innovative experimental techniques in conjunction with phenomenological modeling. The HiTTS 900 program offers not only the opportunity to develop a new fuel with superior stability, it also offers the chance to make great strides in our fundamental understanding of the many processes that contribute to deposition in jet fuels.

A jet fuel is exposed to many different regimes of temperature and residence time, as shown in Figure 1. The temperatures a fuel experiences vary widely throughout a mission, with the numbers in Figure 1 representing a worst case. The thermal stability of a

Presented at an AGARD Meeting on 'Fuels and Combustion Technology for Advanced Aircraft Engines', May 1993.

fuel is a measure of its tendency to cause fuel system problems (deposits, filter plugging) under the conditions of Figure 1. The additive package for JP-8+100 is being designed to improve the fuel's performance in a variety of thermal environments consistent with those shown in Figure 1.

To assess the performance of the additives, a hierarchy of tests has been created. The tests are being performed by research teams consisting of industry, research laboratories, universities, a national laboratory and an Air Force laboratory. Pratt & Whitney has the responsibility of screening the additives received from numerous oil and chemical companies. They use a Hot Liquid Process Simulator (HLPS, a modular JFTOT) and an Isothermal Corrosion oxidation test (ICOT, a "flask" test), in the initial screening process. The best additives are sent to Wright Laboratory where more detailed experiments are performed with small scale test devices operated by on-site contractors and the Air Force. The University of Dayton Research Institute (UDRI) has developed a single-tube test device ("Phoenix Rig")[5-7] that simulates a heat exchanger tube or the feed arm of a fuel nozzle. Systems Research Laboratories (SRL) developed an isothermal single-tube heat exchanger [8] to study the decomposition and deposition processes under well defined flowing conditions. Additives are also evaluated by various researchers in several different flask tests [9-13]. A vaporization test [14] conducted by the Air Force is used to evaluate the additives as a means of reducing deposits in afterburner spray bars. UDRI and the Air Force are investigating the compatibility of the additives with fuel system materials. The best additive(s) will then be tested in several fuels with different processing histories before further testing in an Extended Duration Thermal Stability Test (EDTST) and a Reduced Scale Fuel System Simulator (RSFSS) [15], followed by engine tests. The various test devices have been run under a variety of conditions to gain an understanding of the performance of jet fuels in the devices.

Various thermal stability diagnostics are being developed as part of this program. UDRI developed several test devices based on cyclic voltammetry (the basis of the oil oxidation tester RULER) to measure the oxidation characteristics of additives in fuel [16], and to determine the concentration of peroxides and total acid number in thermally stressed fuel. Sandia National Laboratory developed a photon correlation spectroscopic technique to measure the size distributions of particle formed in thermally stressed fuel [17,18]. They also developed a quartz crystal microbalance that can detect nanograms of deposit [18,19]. Computational Fluid Dynamic modeling of fuel flow in aircraft components, including fuel degradation chemistry, is being developed by SRL and the Wright Laboratory [20,21].

This paper summarizes some of the research results obtained by the different research teams. Note that in this paper "thermal stability" refers to the tendency of a fuel to form fuel-insoluble products; a thermally stable fuel will create few insoluble products, but may create many products that remain dissolved in the fuel. The insoluble products are the solids that plug screens and filters and foul heat exchangers and nozzles. It is generally accepted that fuel thermal instability in most jet fuels is caused by reactions involving dissolved oxygen [22]. However, recently it has become clear that a fuel's propensity to consume oxygen and form soluble oxygenated products such as peroxides is not directly related to the formation of insoluble products. In fact, an inverse relationship exists for many fuels, as shown in Figure 2 [23]. Fuels that form peroxides readily tend to be relatively stable, while thermally unstable fuels tend not to form peroxides readily [24,25]. Note that oxygen consumption is still a key parameter--the question is whether the oxygenated products are soluble or insoluble.

3. BASELINE FUELS

Two baseline fuels have been chosen for this study, with properties shown in Table 1. One baseline fuel (Jet A 2827) is a straight-run jet fuel with a relatively low thermal stability as measured by the JFTOT (but still within specification limits). A quantitative measure of the JP-8+100 goal has been selected to be the thermal stability of the second reference fuel, JPTS 2799. JPTS is a highly processed thermally stable fuel that is significantly more expensive than JP-8 ($1.71/gal vs. $0.75/gal for JP-8 in FY 93). Another fuel that has been tested in many of the research devices discussed below (Jet A-1 2747) is a hydrotreated fuel with a relatively high thermal stability. The Jet A and Jet A-1 fuels are commercial fuels and do not contain the military specification additives (icing inhibitor, corrosion inhibitor, anti-static additive). The severest qualifying test for an additive in a given test is to improve the performance of Jet A 2827 to that of JPTS 2799. During the selection of the best additive(s), a number of other fuels are being tested to assure that the additives are universally effective across a broad range of fuels.

3.1 Flowing Tests

In flowing tests, the baseline fuels range from very stable (JPTS 2799) to marginally stable (Jet A 2827). In tests with a single tube heat exchanger (Phoenix Rig) [5,6] with a dissolved oxygen detection capability [7], it was found that the thermal stability of the fuel was inversely proportional to the temperature at which the fuel began to rapidly consume oxygen; i.e., the most stable fuel consumed oxygen at the lowest temperature and vice versa. The oxygen consumption for the baseline fuels is illustrated in Figure 3, with the

surface deposition shown in Figure 4. The JFTOT breakpoints for the baseline fuels (Table 1) show the same stability trend as Figure 4: JPTS 2799>Jet A-1 2747>Jet A 2827.

Other measures of fuel oxidation show the same trend. For example, cyclic voltammetry [16] has shown that the low stability fuel (Jet A 2827) has easily oxidizable species, as compared to the more stable fuels. This is shown in Figure 5, where the lower the voltage the greater the ease of oxidation. These results have been interpreted to mean that the easily oxidizable species are acting as "natural anti-oxidants" and interfering with the auto-oxidation free radical chain reaction. Thermally stable fuels lack these natural anti-oxidants, which include heteroatomic species such as sulfur and nitrogen. In fact, hydrotreating fuels to improve their thermal stability removes the natural anti-oxidants and thus anti-oxidants are usually added to hydrotreated fuels. A key point here is that the consumption of oxygen by these natural anti-oxidants tends to form insolubles, while the consumption of oxygen by the fuel matrix tends to form soluble products.

In isothermal flow tests, it has been found that most of the insolubles are formed after the oxygen is mostly consumed [8]. This is illustrated in Figure 6. The surface deposition peaks at 5-7 minutes, subsequent to the oxygen consumption at ~3 minutes. Oxygen-saturated fuels yield similar peak deposition rates, but the peak shifts to 7-8 minutes and is broader. This has been interpreted as the oxygen consumption reactions being zeroth order in dissolved oxygen [8]. Tests at various flow rates tend to fall on similar deposition vs residence time curves, for both the Phoenix Rig and the isothermal test [6,8]. Thus, when different tube sizes are used, as shown in Figure 7, the deposition peak shifts. The peak in the larger tube shifts toward the tube entrance. The two peaks do not coincide when the deposition is plotted as a function of residence time. The reason for this shift is not understood but it is evidently related to the different surface to volume ratios in the two tubes. In the isothermal test, surface deposition and bulk (filterable) insolubles are both measured. An interesting observation is that the solids formed during the early stages of oxygen consumption tend to remain suspended in the fuel. As the oxygen is completely consumed, the relative amounts of suspended deposits and surface deposits tend to remain constant. This is true even for large increases in residence time. This is illustrated in Figure 8. This has been interpreted as indicating that the surface and bulk insolubles are functionally different species [8].

The rate of oxygen consumption at various temperatures has been measured in the isothermal test, as shown in Figure 9. These data are complementary to the Phoenix Rig data in Figure 3. Both sets of data have been used to calculate Arrhenius parameters for oxygen consumption [5,6,8]. Below about 170°C, the oxygen consumption becomes very slow. One common aspect of these flowing tests is that the oxygen present is usually (and realistically) limited to the air-saturation value of 70 ppm (50 mg/L) at ambient conditions. Flask tests where oxygen is continuously added can lead to very different results as discussed below. Fuel recirculation systems (Figure 1) that allow recirculated fuel to be re-exposed to air could dramatically affect the deposition from the fuel. The Phoenix Rig has been used to examine the behavior of fuels with varying oxygen concentrations. The oxygen consumption and deposition profiles in the Phoenix Rig for varying levels of oxygen in the fuel are shown in Figures 10 and 11. The oxygen consumption curves have been interpreted as pseudo zeroth order in oxygen until low levels of oxygen are reached [8,6]. These oxygen consumption and deposition data are being used to develop computational fluid dynamics models of the fouling processes [21]. Matching both the deposition and oxygen consumption behavior of a given fuel over the wide variety of conditions discussed in this section is a difficult challenge.

3.2 Static Tests

Static tests (or "flask tests") are an interesting complement to the flowing tests [9-13]. In these tests, continuously-stirred fuel is heated at atmospheric pressure to a temperature from 160-200°C. Oxygen is continuously fed to the fuel via some type of sparging system. Samples are periodically withdrawn to measure the extent of oxidation. The oxidation products are usually measured by filtration of ambient temperature fuel, with the following nomenclature: soluble gums=filterable solids soluble in heptane; insoluble gums=filterable solids insoluble in heptane/soluble in acetone; insoluble solids=filterable solids insoluble in acetone or heptane. Presumably, the soluble gums are soluble in hot fuel. Metal disks can be suspended in the fuel to assess surface deposition onto metals. The static test used in additive evaluation is denoted as the Isothermal Corrosion Oxidation Test (ICOT).

With a cursory examination of the flask test, one would expect that this situation bears little resemblance to a flowing test where the amount of oxygen is limited to the saturation value. However, there are a number of complicating factors which can change this perception. At typical reaction temperatures of ~185°C, the reaction of the fuel with oxygen can be very rapid. Additionally, the solubility of oxygen at 185°C at atmospheric pressure is significantly less than at ambient temperature. Thus, for some fuels a "steady-state" situation prevails where the oxygen reacts as fast as it is added, with a dissolved O_2 concentration not far different from ambient air-saturated fuel. The product concentrations (soluble gums, etc.) will be much larger than would be encountered in an oxygen-limited flowing test.

However, if it is assumed that these products are inert and do not affect the oxygen consumption reactions, the kinetics observed in the flask test may be relevant to flowing tests at similar temperatures.

The results of flask experiments for two of the baseline fuels are illustrated in Figures 12 and 13 [11]. The "stable" fuel (2747) forms large quantities of oxidation products, especially soluble gums (Figure 12). Behavior of JPTS and hexadecane are similar to 2747. The "unstable" fuel forms smaller quantities of oxidation products (Figure 13). The linear production rates of the products suggest that they are formed by parallel, independent channels. If, for example, the formation was sequential (SG -> IG -> IS), then the IS and IG curves (especially in Figure 12) should be turning upwards as the soluble gum concentration builds up. The deposition onto stainless steel disks suspended in the fuel is also linear with time, as shown in Figure 14.

These results confirm the results of the flowing tests to some extent. The stable fuel is more reactive towards oxygen, forming soluble products. The unstable fuel is less reactive toward oxygen, forming mostly insoluble products. These results are emphasized when one examines the oxidation product formation as a function of oxygen flow rate. For the stable, reactive fuel, product formation is proportional to oxygen flow rate over a wide range. As shown in Figure 15, this indicates that the oxygen is reacting as fast as it can be fed to the fuel. Conversely, the unreactive fuel quickly plateaus with increases with oxygen flow rate, indicating much slower oxidation kinetics (Figure 16). Thus the "stable" fuel is in the steady-state regime where oxygen is actually limited because of limited solubility and fast reactions.

4. ADDITIVE RESULTS

As discussed in the Introduction, many additives are being tested in this program. Some initial results for additives in Jet A 2827 are reported here. The results are compared to results for Jet A 2827, Jet A 2827 + 12 mg/L JFA-5, and JPTS 2799. JPTS is a thermally stable (hydrotreated) base fuel with a thermal stability additive package, JFA-5, which contains a metal deactivator, an anti-oxidant, and a dispersant. JFA-5 is thus the de facto additive baseline in these tests. However, the JPTS base fuel has been tested without additives and is a very stable fuel without the JFA-5.

The additives are initially screened in the HLPS and ICOT. The HLPS is a modified JFTOT in which fuel flows for 5 hours at 3 ml/min around a heated stainless steel rod with a maximum rod temperature of 335°C and then through a 17 μm filter. Fuel thermal stability is assessed by the deposits on the tube surface (measured by carbon burnoff) and by pressure drop across the filter. The ICOT is a variant of the flask test, where 70 ml of fuel is heated to 180°C in a flask with oxygen introduced through a blower tube at 10 l/hr for five hours. Deposits are measured by filtering the fuel after the test through a 1 μm filter and by measuring the deposits on the blower tube surface. Both deposits are measured by carbon burnoff. The study of additives in most of the other test devices aside from the HLPS and ICOT is still in its early stages. However, generalizations can be made. Additives which give significant increases in pressure drop in the HLPS generally cause significant fouling of filters in the single-tube heat exchanger devices and large deposits in the vaporization test. However, these same additives may cause a significant reduction in surface deposits on hot metal walls. JFA-5 reduces surface deposition significantly in most experiments with Jet A 2827, although the deposition is still significantly above JPTS levels. For example, single-tube heat exchanger results with JFA-5 are shown in Figure 17. Both of the single-tube heat exchangers (the Phoenix Rig and the isothermal test) are now set up to measure deposition in a hot section and a downstream cooling section. This allows some measure of fouling that could be expected in a system with significant fuel recirculation. Filters are used between the hot and cold section as well as downstream of the cold section.

Several additives have shown significant improvements in the thermal stability of Jet A 2827 in rig tests. These results are summarized in Table 2. In the augmentor fouling simulator, fuel is vaporized at 1.5 ml/min in a stainless steel tube for 7 hours [14]. At 30 minute intervals, 1500 ml of fuel is surged through the tube at 3000 ml/min. Deposition is measured at the point in the tube where the fuel vaporizes. The isothermal heat exchanger results in Table 2 were obtained at 0.25 ml/min for 6 hours at 185°C [33]. The additives are "A2894", a detergent/dispersant, and "A2727", a detergent. As can be seen, the A2894/A2727 additive combination shows significant promise in reaching the thermal stability of JPTS in several of the tests. A2894 was selected because of its performance in the HLPS and A2727 because of its performance in the ICOT. Additive testing in a wider range of fuels is underway.

5. JP-900 TEST RESULTS

The baseline fuels have also been run in a single tube heat exchanger where the fuel is heated to 900°F. These types of tests are part of the development of JP-900. The results of one such test are shown in Figure 18 for the three fuels discussed in this paper [26,27]. The deposit under these conditions is much narrower than that seen in lower temperature tests (e.g., Figures 11,17). In these high temperature tests, it is typical to see this sharp deposition peak; this type of behavior has been seen in heated tube tests at the United Technologies Research Center [28], Esso (Exxon) [29],

and the Naval Research Laboratory [30], and in an earlier version of the Air Force Fuel System Simulator [31]. It has been proposed that this deposition peak may be due to supercritical solvent effects of the fuel [29] or high temperature breakdown of deposit precursors [30]. Recent work at WL has shown that this deposit peak is independent of fuel critical temperature over the range from n--octane to n-hexadecane [26]. Rather than a supercritical effect, it appears that the deposition peak is a chemical kinetic effect related to the heating rate of the fuel. The amount and location of the deposition can be varied over a wide range of fuel and wall temperatures by varying the rate at which the fuel is heated [26]. The exact mechanism of how heating rate affects deposition is not yet clear. It may be that heating rate affects the relative reaction rates of fuel to soluble and insoluble products. This offers the opportunity of controlling deposition by controlling the rate at which heat is added to the fuel. This relationship between peak deposition and heating rate has been recently reported by others [32]. The surface deposition in this test is well correlated by the JFTOT breakpoint of the fuel, as shown in Figure 19. The filterable deposits are not well correlated by JFTOT breakpoint, however, with JP-7 standing out as a high bulk deposit generator.

6. DISCUSSION

It is interesting to compare the deposition levels for Jet A 2827 and Jet A-1 2747 in the various tests described in this paper: the gravimetric JFTOT (Figure 2), the Phoenix Rig (Figure 4), the isothermal test (Figures 6 & 8), and the JP-900 test (Figure 18). Comparative operational data for the tests are presented in Table 3. All the tests consist of fuel flowing through a heated stainless steel test section, with subsequent filtering. In the gravimetric JFTOT and the JP-900 test, the fuel is cooled before filtering; in the other tests the fuel is filtered before and after cooling.

The results for Jet A 2827 are presented in Table 4. The results are presented as ppm, i.e., total µg deposit (carbon)/total g fuel flowed. The gravimetric JFTOT results are based on deposit mass, the others are based on deposit carbon mass. In the gravimetric JFTOT it was found that 2827 generated about 1 ppm of total insolubles, almost entirely bulk (filterable) deposits. Bulk (filterable) insolubles generally were about 10X larger than surface insolubles for a group of JP-5 fuels studied [23]. In contrast, the surface and bulk values in the JP-900 and Phoenix Rig tests are fairly close. From Figure 8, the isothermal flow test generated about 6 ppm of total insolubles (5 µg deposit carbon/cc fuel / 0.8 g/cc) with the bulk/surface ratio roughly equal to 0.7 for complete oxygen consumption. These values are significantly larger than the Phoenix Rig and JP-900 tests, although the surface and bulk deposits are again similar in magnitude. For Jet A-1 2747 (Table 5), the deposits are much smaller. Again, the gravimetric JFTOT yields a much higher ratio of bulk to surface deposits than the JP-900 test.

One possible reason for the discrepancy can be seen by comparing two sets of results for Jet A 2827 in the Phoenix Rig. The two sets of data are shown in Figure 20. In the test with the lower outlet temperature, the surface deposition was still increasing at the outlet of the tube, in contrast to the behavior shown in Figure 6. This condition created tremendous deposits on the cold filter. The ratio of the filterable insolubles to the hot tube deposits for this condition is 23, a similar ratio as that seen in the gravimetric JFTOT. Thus, small variations in heating conditions can create dramatic differences in filterable deposits. This phenomenon is not well understood at present, but may explain the differences between the gravimetric JFTOT results and the other test results.

7. CONCLUSIONS

It seems clear that an understanding of the oxidation reactions of the fuel's "natural anti-oxidants" will be required to control the formation of insolubles from typical jet fuels. It is not clear if the detergent/dispersant additives that are effective in reducing insolubles formation in the tests are acting to keep the insolubles small enough to pass filters, or if the additives are actually reducing the formation of insolubles. More research is also needed to determine the mechanism behind the large increases in bulk deposits seen under some test conditions. In future aircraft that will employ recirculation of hot fuel, this phenomena may be a key determinant of fuel system reliability and maintainability.

8. ACKNOWLEDGMENTS

The authors would like to acknowledge the researchers involved in the various tests. The isothermal heat exchanger tests and flask tests were performed by Grant Jones and Walt Balster of Systems Research Laboratories. The Phoenix Rig tests were performed by Ted Williams and Chuck Martel of the University of Dayton Research Institute (UDRI). Cyclic voltammetry measurements of fuel oxidation were performed by Bob Kauffman of UDRI. The HLPS and ICOT tests on fuels and additives were performed at Pratt and Whitney Aircraft Corp., West Palm Beach, FL, under the direction of Tedd Biddle.

9. REFERENCES

(1) Harrison, W. E., Edwards, T., Anderson, S. D., "U. S. Air Force Improved JP-8 Development Program -- An Overview," paper to be presented at 2nd International Symposium on Jet Fuel Specifications, Brighton, England, 11-14 May, 1993.

(2) Edwards, T., Anderson, S. D., Pearce, J. A., and Harrison, W. E., "High Temperature, Thermally Stable JP Fuels -- An Overview," AIAA Paper 92-0683.

(3) Edwards, T., "USAF Supercritical Hydrocarbon Fuels Interests," AIAA Paper 93-0807, presented at AIAA Aerospace Sciences Meeting, Reno NV, January 14, 1993.

(4). Edwards, T., "Jet Fuel Thermal Stability Research at USAF Wright Laboratory," Proceedings of the 4th International Conference on the Stability and Handling of Liquid Fuels, Orlando FL, USA, November 19-22, 1991, Vol. 1, pp. 768-781.

(5) Heneghan, S. P., Martel, C. R., Williams, T. F., and Ballal, D. R., "Studies of Jet Fuel Thermal Stability in a Flowing System," ASME Paper 92-GT-106, June 1992.

(6) Heneghan, S. P., Martel, C. R., Williams, T. F., and Ballal, D. R., "Effects of Oxygen and Additives on the Thermal Stability of Jet Fuels," paper to be presented at the 38th ASME International Gas Turbine and Aeroengine Congress, May 24-27, 1993, Cincinnati OH.

(7) Rubey, W. A., Tissandier, M. D., Striebich, R. C., and Tirey, P. A., "In-Line Gas Chromatographic Measurement of Trace Oxygen and Other Dissolved Gases in Flowing High Pressure Thermally Stressed Jet Fuel," ACS Petroleum Chemistry Division Preprints, Vol. 37, No. 2, pp. 371-376, 1992.

(8) Jones, E. G., Balster, W. J., and Post, M. E., "Degradation of a Jet A Fuel in a Single-Pass Heat Exchanger, " paper to be presented at the 38th ASME International Gas Turbine and Aeroengine Congress, May 24-27, 1993, Cincinnati, Ohio.

(9) Heneghan, S., Byrd, R., Schulz, W. D., Locklear, S., and Anderson, S., "Evaluation of Jet Fuel Additives in Static Systems," Journal of Propulsion and Power, Vol. 9, No. 1, pp. 5-9, 1993 (AIAA Paper 92-0686).

(10) Jones, E. G., and Balster, W. J., "Application of a Sulphur-Doped Alkane System to the Study of Thermal Oxidation of Jet Fuels," ASME Paper 92-GT-122, presented at the 37th ASME International Gas Turbine and Aeroengine Congress, June 1-4, 1992, Cologne, Germany.

(11) Jones, E. G., Balster, W. J., and Anderson, S. D., "Formation of Insolubles in Jet Fuels: Effects of Oxygen," ACS Petroleum Chemistry Division Preprints, Vol. 37, No. 2, pp. 393-402, 1992.

(12) Schulz, W. D., "Oxidation Products of a Surrogate JP-8 Fuel," ACS Petroleum Chemistry Division Preprints, Vol. 37, No. 2, pp. 383-392, 1992.

(13) Schulz, W. D., "Analysis of Jet Fuel Additives," ACS Petroleum Chemistry Division Preprints, Vol. 37, No. 2, pp. 477-483, 1992.

(14) Edwards, T., "Deposition During Vaporization of Jet Fuels in a Heated Tube," AIAA Paper 92-0687, presented at AIAA Aerospace Sciences Meeting January 8, 1992, Reno NV.

(15) Morris, R. W., and Binns, K. E., "Evaluation of the Effects of a Pipeline Flow Improver on Aircraft Fuel Systems." Wright Laboratory TR in preparation.

(16) Kauffman, R. E., and Tirey, D. A., "New Techniques to Predict and Evaluate the Effectiveness of Antioxidants in Jet Fuels," ACS Petroleum Chemistry Division Preprints, Vol. 37, No. 2, pp. 412-419, 1992.

(17) Trott, W. M., O'Hern, T. J., and Klavetter, E. A., "In-Situ Measurement of Particle Formation in Heated Jet Fuels--A New Application of Photon Correlation Spectroscopy," ACS Petroleum Chemistry Division Preprints Vol. 37, No. 2, pp. 442-450, 1992.

(18) O'Hern, T., Trott, W., Martin, S., and Klavetter, E., "Advanced Diagnostics for In-Situ Measurement of Particle Formation and Deposition in Thermally Stressed Jet Fuels," AIAA Paper 93-0363, presented at AIAA Aerospace Sciences Meeting January 12, 1993, Reno NV.

(19) Martin, S. J., Frye, G. C., Klavetter, E. A., and Ricco, A. J., "Monitoring Jet Fuel Degradation Using Quartz Crystal Microbalances," ACS Petroleum Chemistry Division Preprints, Vol. 37, No. 2, pp. 456-462, 1992.

(20) Katta, V. R., and Roquemore, W. M., "A Numerical Method for Simulating the Fluid-Dynamic and Heat Transfer Changes in a Jet Engine Injector Feed Arm Due to Fouling," AIAA Paper 92-0768, presented at AIAA Aerospace Sciences Meeting January 8, 1992, Reno NV.

(21) Katta, V. R., Jones, E. G., and Roquemore, W. M., "Development of a Mathematical Model for Jet Fuel Thermal Stability Based on the Observations Made from Static and Flowing Experiments," paper to be presented at May 93 AGARD Meeting on "Fuels and Combustion Technology for Advanced Aircraft Engines."

(22). Hazlett, R. N., "Thermal Oxidation Stability of Aviation Turbine Fuels," ASTM Monograph 1, American Society for Testing and Materials, Philadelphia PA, 1991.

(23) Hardy, D. R., Beal, E. J., and Burnett, J. C., Proceedings of the 4th International Conference on Stability and Handling of Liquid Fuels, US DOE, Washington DC, 1991, p. 245-271 (two papers).

(24) Heneghan, S. P., and Harrison III, W. E., "Anti-Oxidants in Jet Fuels: A New Look," ACS Petroleum Chemistry Division Preprints, Vol. 37, No. 2, pp. 404-411, 1992.

(25) Heneghan, S. P., and Zabarnick, S., "Oxidation of Jet Fuels and the Formation of Deposits," accepted for publication in Fuel.
(26) Edwards, T., and Zabarnick, S., "Supercritical Fuel Deposition Mechanisms," Paper 58d presented at AIChE Nat'l Meeting, Miami Beach, November 1992.
(27) Edwards, T., Liberio, P., "The Thermal Oxidative Stability of Fuels at 900°F (480°C)," paper in preparation for 3/94 ACS meeting, San Diego CA.
(28) Marteney, P.J. and L.J. Spadaccini, "Thermal Decomposition of Aircraft Fuel," Journal of Engineering for Gas Turbines and Power (ASME Transactions), Volume 108, pp. 648-653, 1986.
(29) Taylor, W.F., "Deposit Formation from Deoxygenated Hydrocarbons. 1. General Features," Ind. Eng. Chem. Prod. Res. Dev., Vol. 13(2), pp. 133-138, 1974, and "4. Studies in Pure Compound Systems," Ind. Eng. Chem. Prod. Res. Dev., Volume 19, pp. 65-70, 1980.
(30) Hazlett, R.N., J.M. Hall, and M. Matson, "Reactions of Aerated n-Dodecane Liquid Flowing Over Heated Metal Tubes," Ind. Eng. Chem. Prod. Res. Dev., Volume 16(2): p. 171-177, 1977.
(31) Bradley, R., R. Bankhead, and W. Bucher, "High Temperature Hydrocarbon Fuels Research in an Advanced Aircraft Fuel System Simulator on Fuel AFFB-14-70," Air Force Aero Propulsion Laboratory Report AFAPL-TR-73-95, April 1974.
(32) Cliff Moses, Southwest Research Institute, work on NASA Grant NAG 3-1342, 1992.
(33) Jones, G. J., and Balster, W., unpublished results, 1993.

Table 1. Baseline Fuel Information

POSF designation	91-2799	91-2827	90-2747
Fuel sold as	JP-TS	Jet A	Jet A-1
Hydrotreated?	Yes	No	Yes
ASTM D1319 Aromatics, Vol %	9.6	19	19
ASTM D4294 Sulfur, Total Wt %	0.0	0.1	0.0
ASTM D5340 Fuel System Icing Inhibitor, Vol %	0.11	--	--
JFTOT Breakpoint. C	399	266	332
Dissolved oxygen in air-saturated fuel, ppm (measured by R. Striebich, Univ. of Dayton Research Inst. by GC/MS)	77	65	73

Table 2. Additive test results. JFA-5 added at 12 mg/L, "A2894" at 100 mg/L, "A2727" at 300 mg/L.

Test	Jet A 2827	Jet A 2827+ JFA-5	JPTS 2799	Jet A 2827+ A2894	Jet A 2827+ A2727	Jet A 2827+ A2894+ A2727
HLPS surface carbon, µg/cm^2	47	30	7	16	342	69
HLPS filter DP/time (psi/min)	300/180	0/300	1/300	0/300	300/270	4/300
ICOT blower, µg C	3196	497	74	590	113	68
ICOT bulk, µg C	2971	900	584	397	2944	468
augmentor fouling simulator, µg C	1378	1590	237	n/a	n/a	323
Isothermal surface deposit, µg C/cc [8,33]	3.0	3.4	n/a	1.3	4.1	2.0
Isothermal bulk deposit, µg C/cc [8,33]	2.0	3.0	n/a	0.8	1.3	0.6

Table 3. Experimental variables for various tests. Residence time calculated for cold fuel.

Test	nominal res time, sec (typical flow rate, cc/min)	surf/vol, 1/cm	bulk fuel outlet T, C	max wall T, C	filters (fuel T during filtration)
gravimetric JFTOT [23]	6.2 (3)	17	260	260	0.8 μ (cold)
JP-900 test [26,27]	9.4 (12)	28.6	480	570	2 μ (cold)
Phoenix Rig [5,6]	7.6 (16)	18.5	260	300	2 μ (hot+ cold)
isothermal test [8]	715 (0.25)	18.5	185	185	0.45 μ (hot)

Table 4. Comparison of deposition results for various test devices with Jet A 2827. All test results aside from gravimetric JFTOT are μg deposit carbon/ g fuel; gravimetric JFTOT results expressed as μg deposit/g fuel.

Test	surf dep, ppm	filter dep, ppm	filter/surf	total, surf + filter, ppm
gravimetric JFTOT [23]	0.036	0.93	26	0.97
JP-900 test [27]	0.74	0.69	1	1.44
Phoenix Rig [5,6]	0.63	0.84	1.33	1.47
isothermal test [8]	3.75	2.5	0.67	6.25

Table 5. Comparison of deposition results for various test devices with Jet A-1 2747.

Test	surf dep, ppm	filter dep, ppm	filter/surf	total, surf + filter, ppm
gravimetric JFTOT [23]	0.036	0.20	5.6	0.24
JP-900 test [27]	0.38	0.15	0.35	0.51
Phoenix Rig [5,6]	0.10	n/a	n/a	n/a

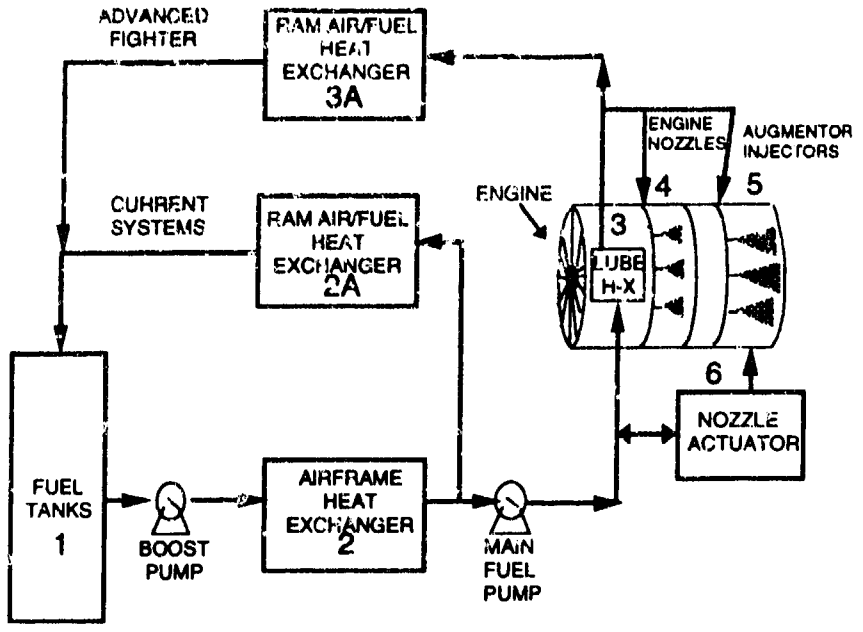

	1	2	2A	3	3A	4	5	6
TEMP, C	< 70	< 120	< 120	135 - 163	< 163	163 +	260 +	< 175
PRESS, PSI	< 25	< 80	< 80	1200-2000	< 80	< 40 ‡	< 40 ‡	1500-4000
TIME	MIN TO HRS	< 15 SEC	< 2 SEC	< 3 SEC	< 2 SEC	2 SEC +	MIN ¤	< 20 MIN

¤ TIME <.1 SEC

‡FLOW PRESS 1200 - 2000

Figure 1. Temperatures (worst case) and pressures experienced by fuel in various engines parts [2]. For the combustor and augmentor injectors (4 and 5), problems appear to be most severe after flow is shut off or cycled, hence the low pressures and long times indicated in the table. During normal (flowing)operation, the residence times are fractions of a second at 1200-2000 psi.

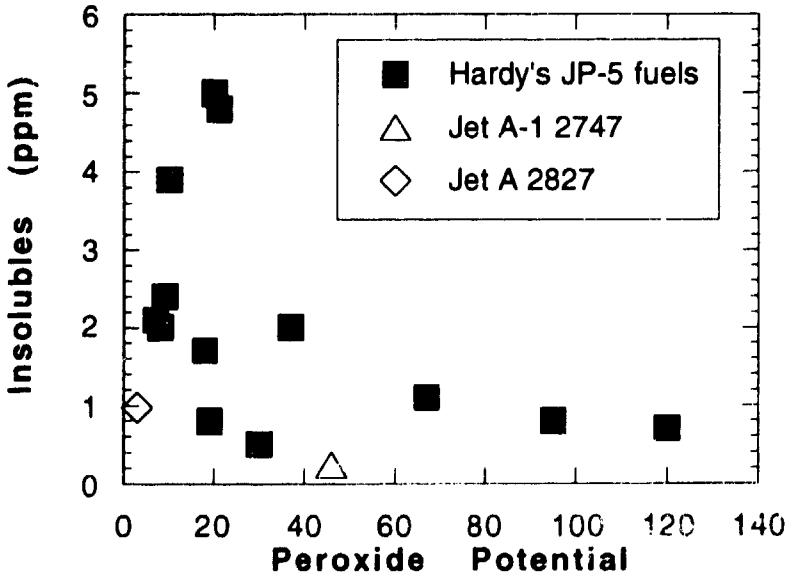

Figure 2. Peroxide potential versus gravimetric JFTOT of 15 fuels [23].

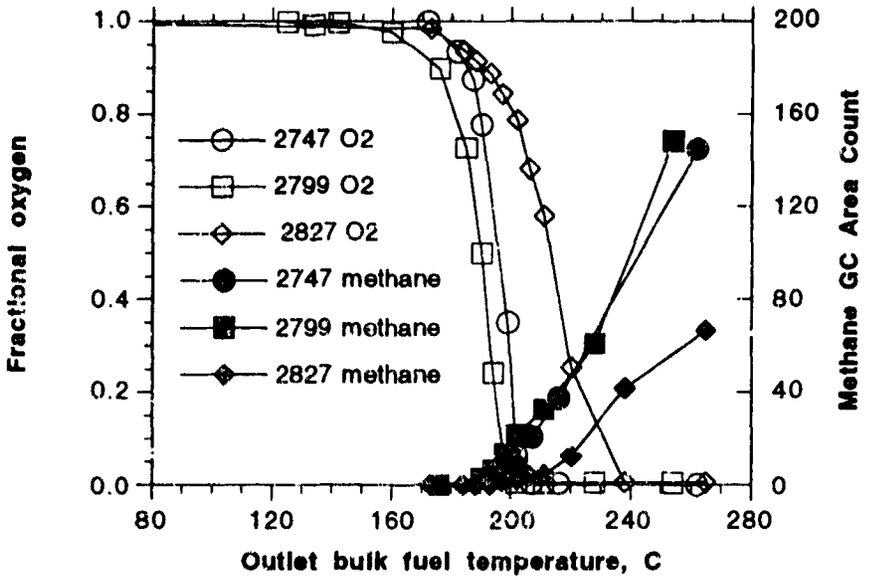

Figure 3. Dissolved oxygen and methane concentrations versus output bulk temperature from a single tube heat exchanger [5]. Input temperature = 30°C, Input concentration of Oxygen = 70 ppm. Residence time in heat exchanger ~ 7 seconds.

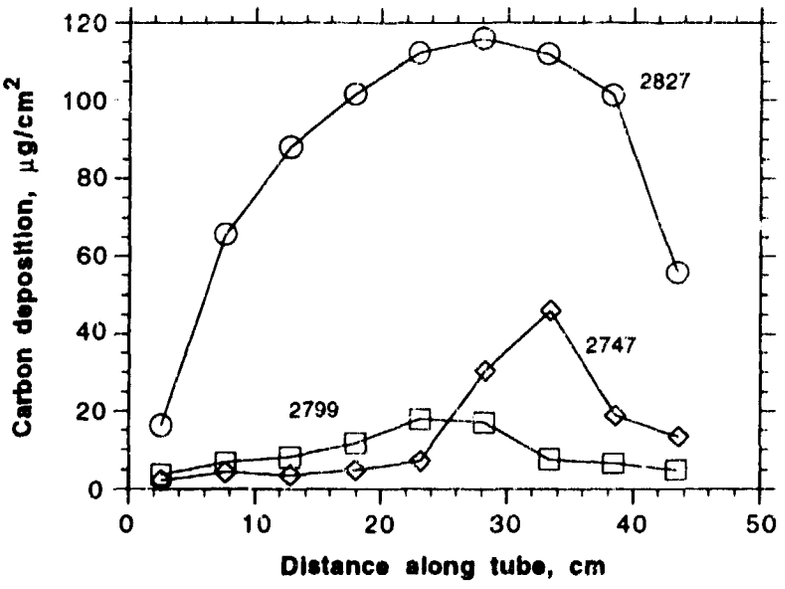

Figure 4. Surface concentration of carbon deposits along the test section for three baseline fuels during a six-hour test [5]. 300°C block temperature, 16 ml/min, 260°C fuel outlet temperature, 2.48 MPa (24 atm).

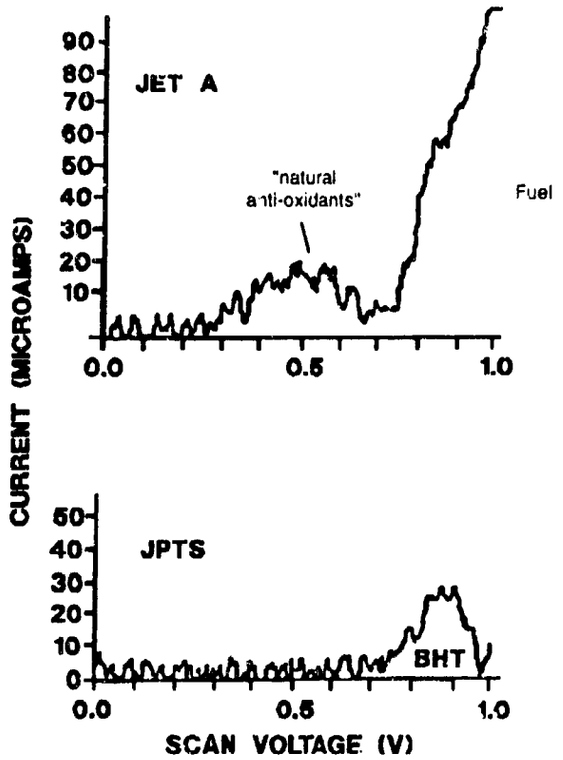

Figure 5. Voltammograms (derivative current versus scan voltage plots) produced by cyclic voltammetric antioxidant test for fresh Jet A 2827 and JPTS 2799 fuels [16]. Lower voltages indicate greater ease of oxidation.

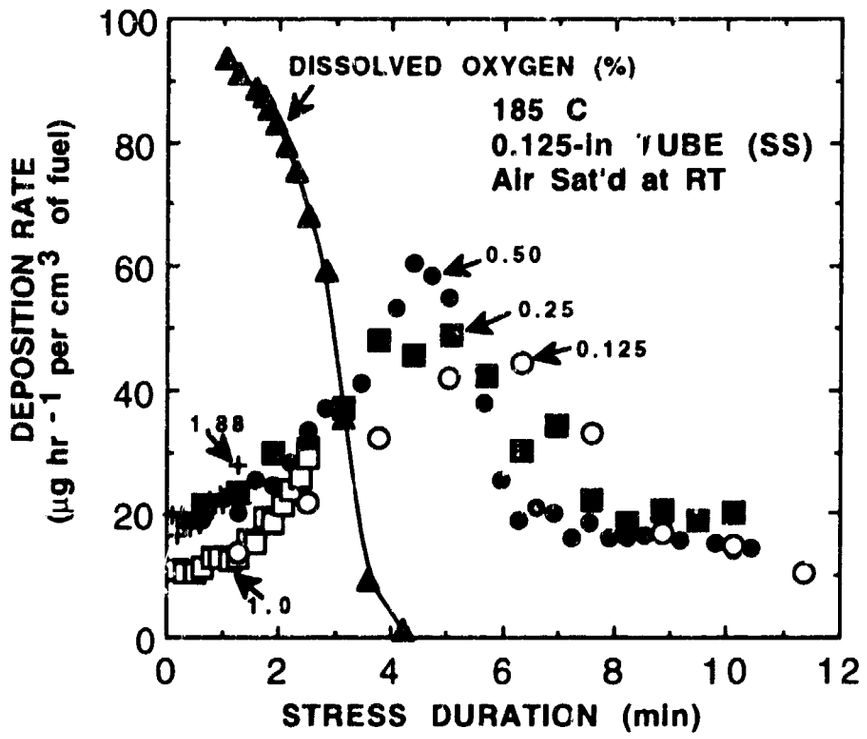

Figure 6 Deposition from Jet A 2827 at 185 C, 2.48 MPa in isothermal heat exchanger as a function of stress duration (residence time) [8]. Superimposed is dissolved oxygen as a function of stress duration. Flow rates in cc/min indicated on plot.

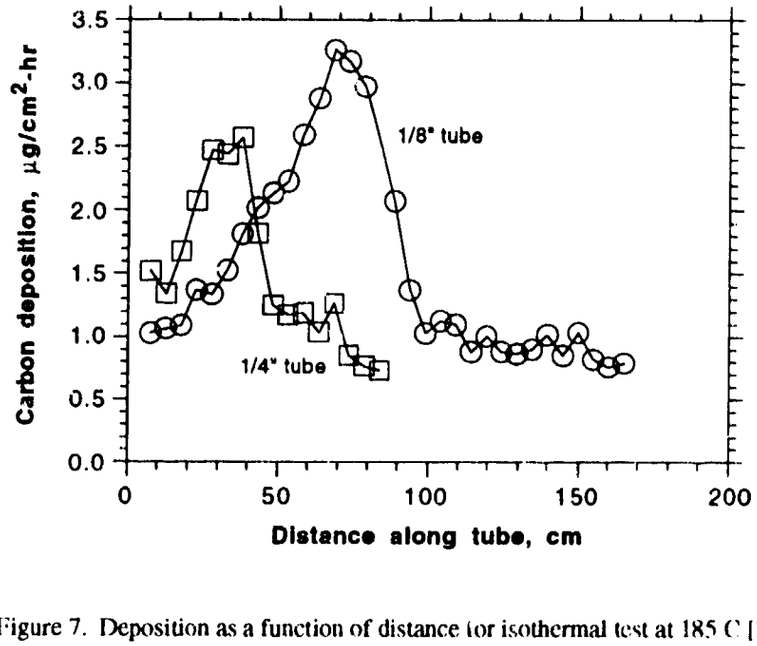

Figure 7. Deposition as a function of distance for isothermal test at 185 C [21].

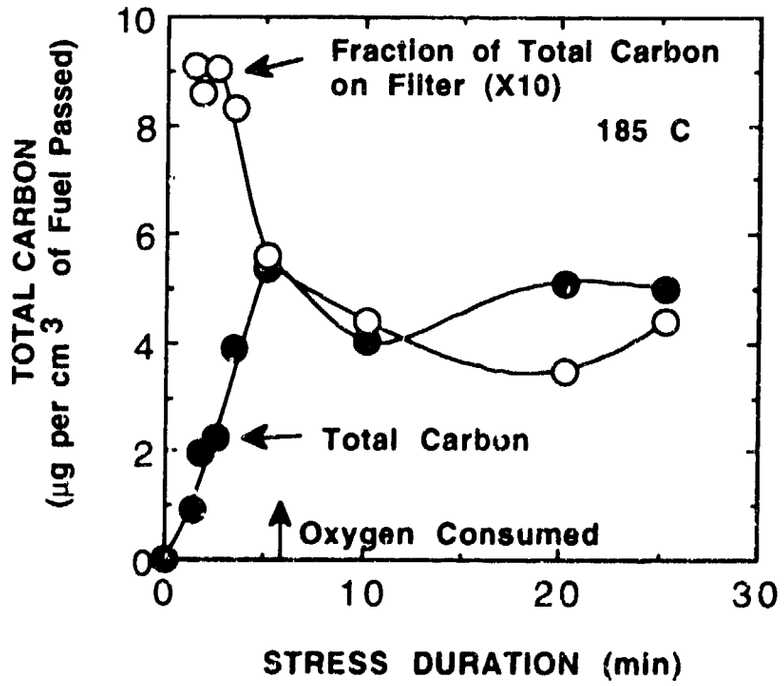

Figure 8. Total carbon in surface deposits and bulk insolubles formed as a function of stress duration in isothermal test [8]. Superimposed is that fraction of total carbon measured on filter.

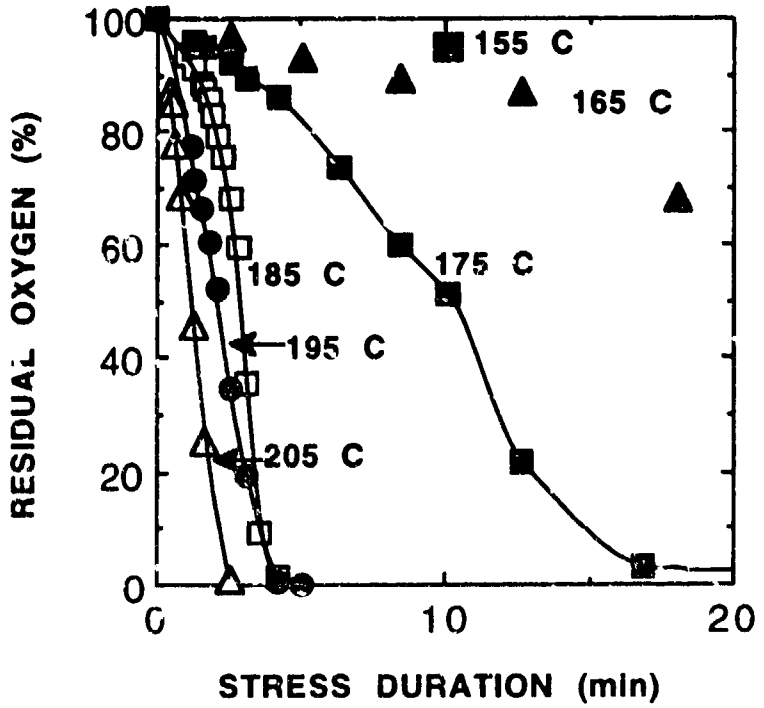

Figure 9. Dissolved oxygen content of outlet fuel in isothermal test [8].

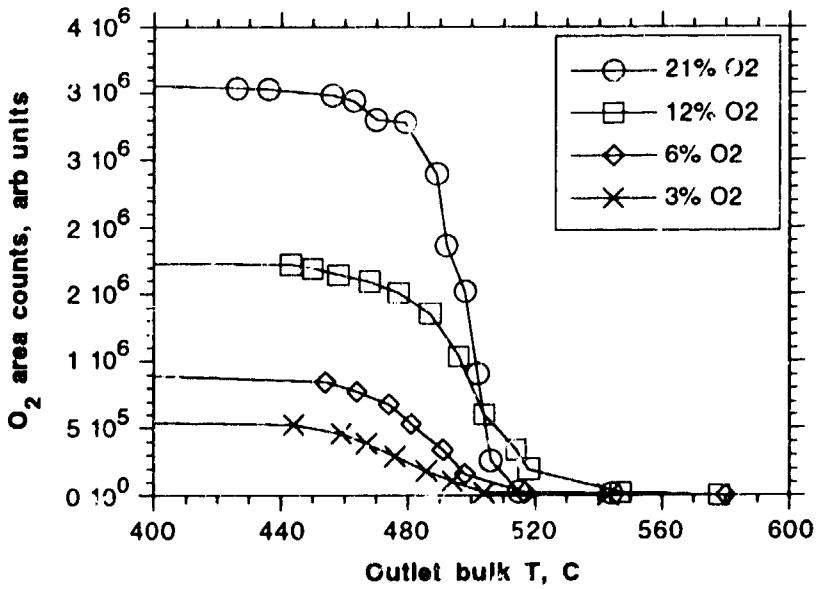

Figure 10. Oxygen consumption as a function of fuel sparge O_2 concentration [6].

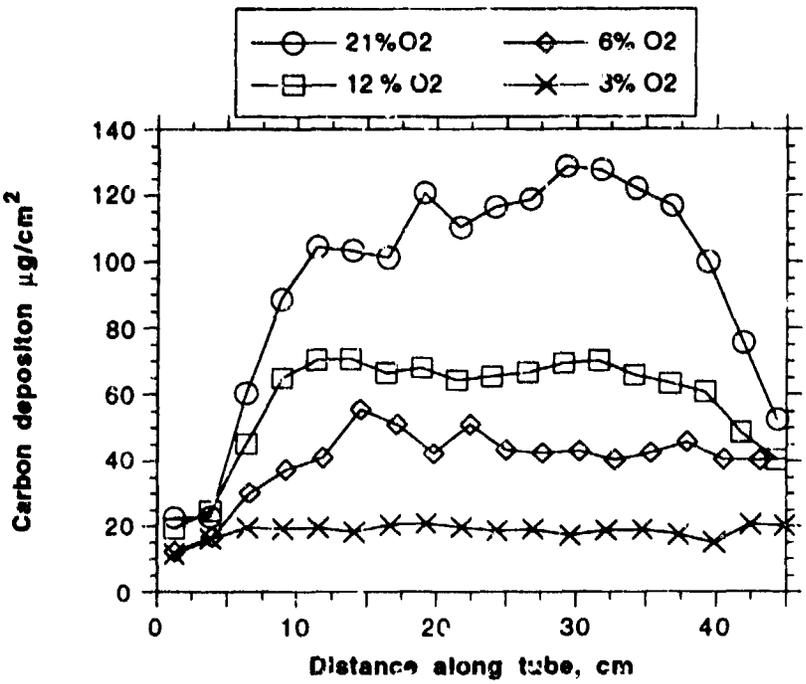

Figure 11. Carbon deposition for varying levels of oxygen in fuel in Phoenix Rig [6].

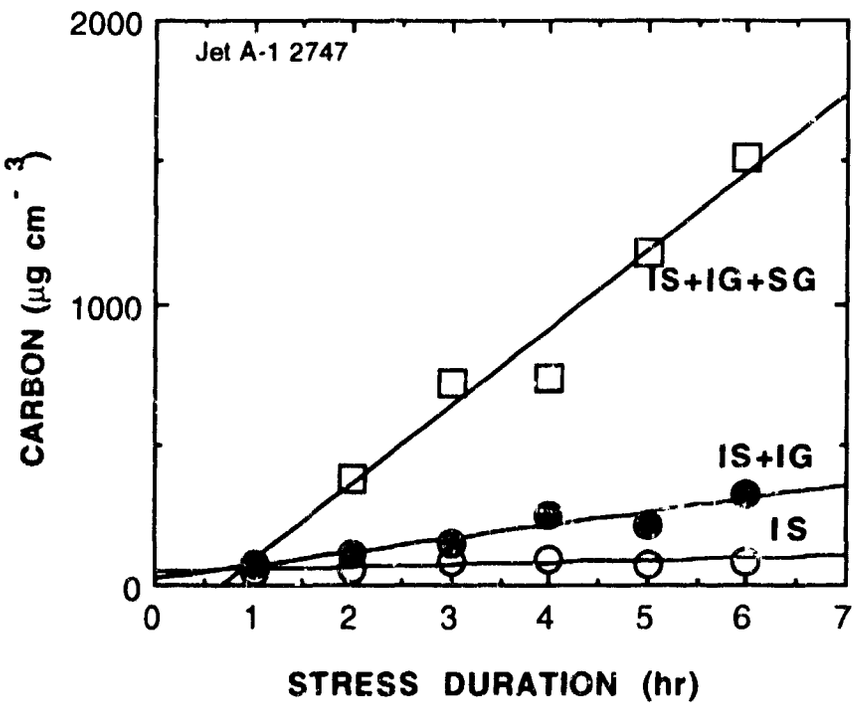

Figure 12. Weight of carbon in samples removed by bulk filtration of liquid samples as a function of stress duration. Jet A-1 2747, 185°C, O_2 flow 0 20 $cm^3 min^{-1}$ per cm^3 of solution [11].

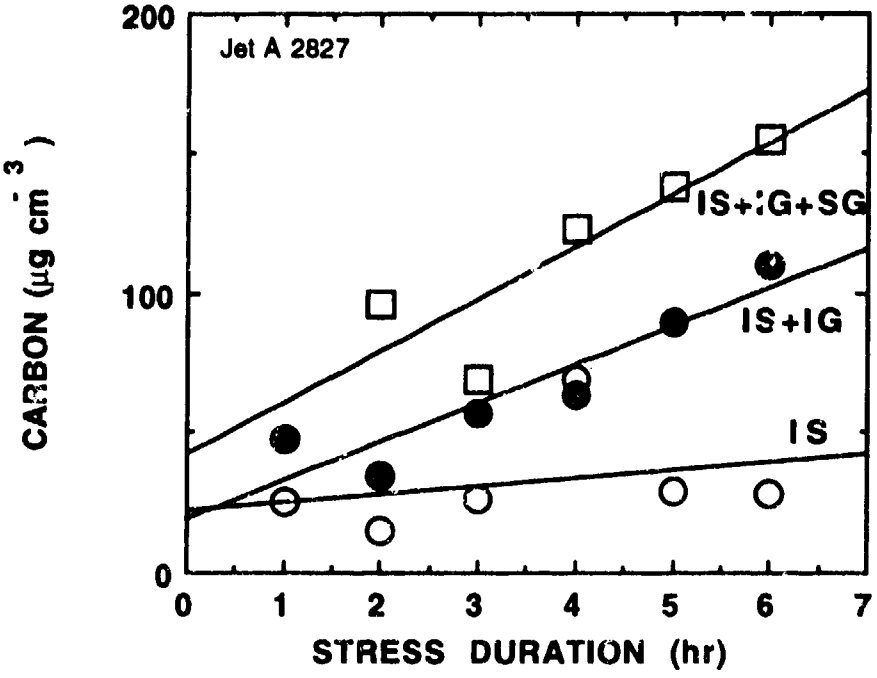

Figure 13. Weight of carbon in samples removed by bulk filtration of liquid samples as a function of stress duration. Jet A 2827, 185°C, O_2 flow 0.20 $cm^3 min^{-1}$ per cm^3 of solution [11].

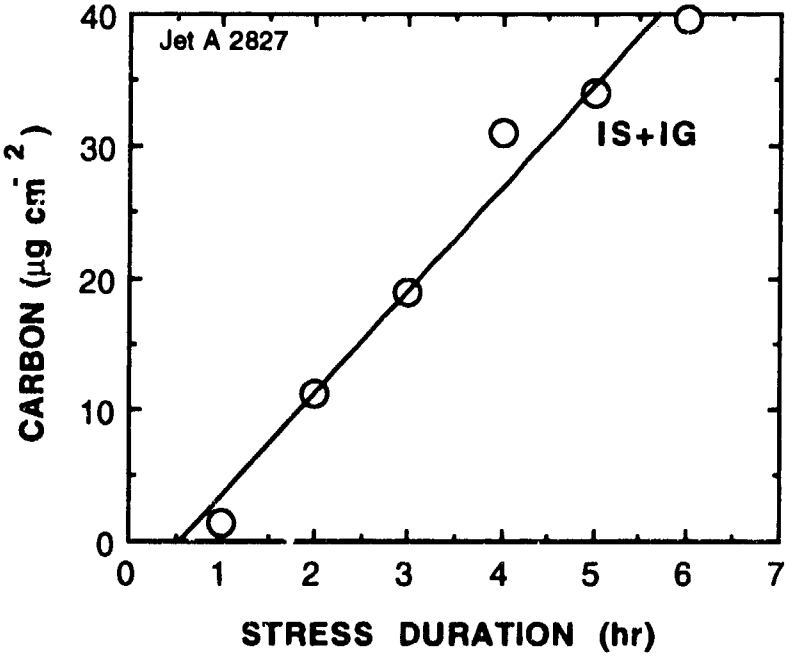

Figure 14. Surface deposition (SS disks) for 2827 [11].

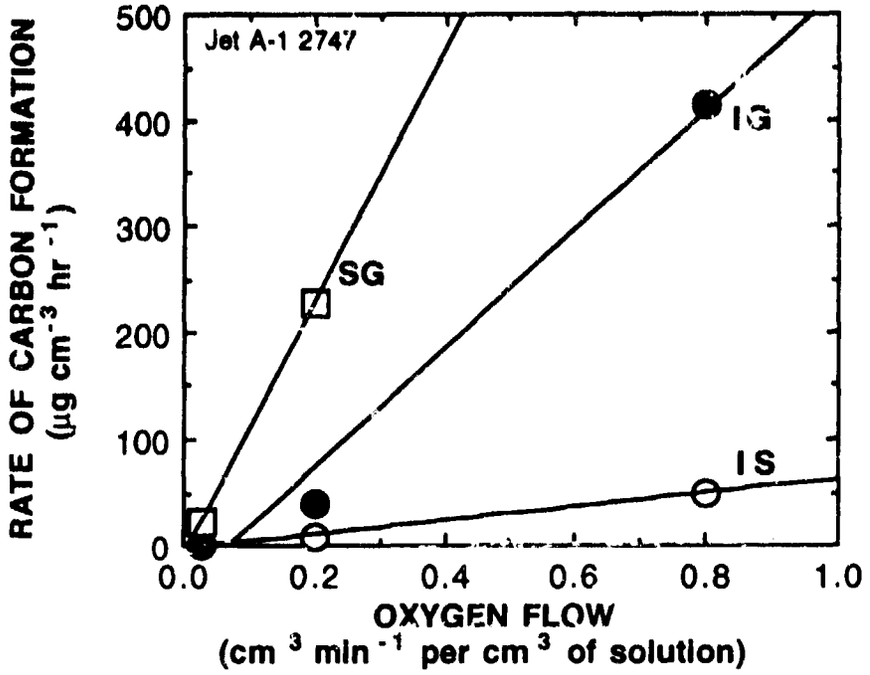

Figure 15. Dependence of rate of formation of IS, IG, and SG upon oxygen flow for Jet A-1 2747, 185°C [11].

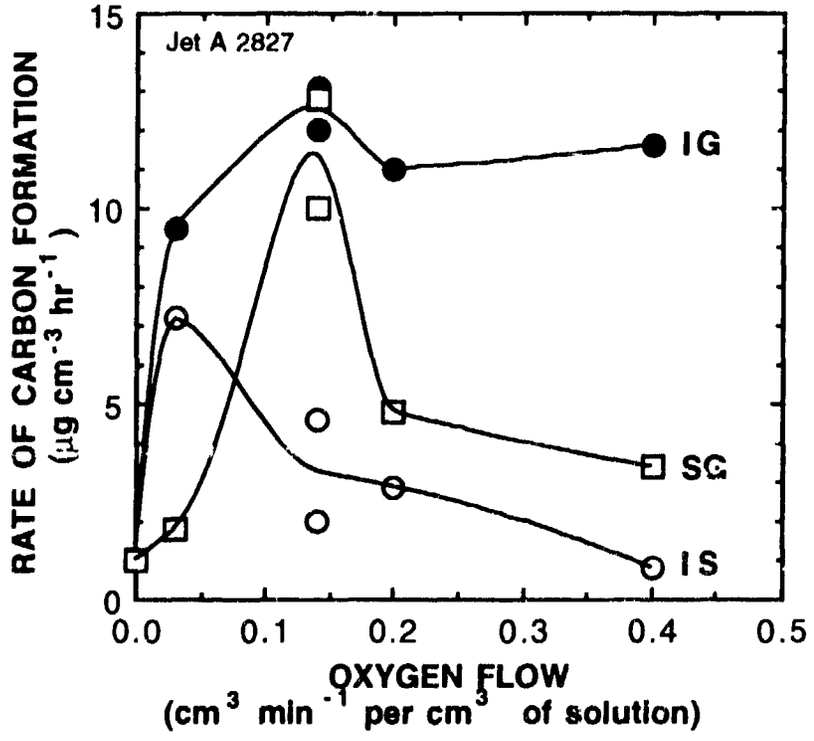

Figure 16. Dependence of rate of formation of IS, IG, and SG upon oxygen flow for Jet A 2827, 185°C [11].

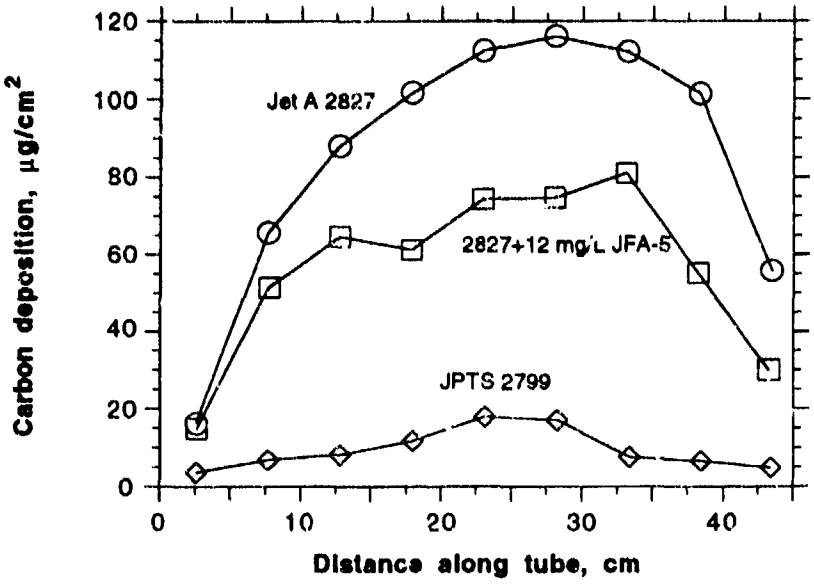

Figure 17. Phoenix Rig deposition data for JFA-5 in Jet A 2827 [5,6].

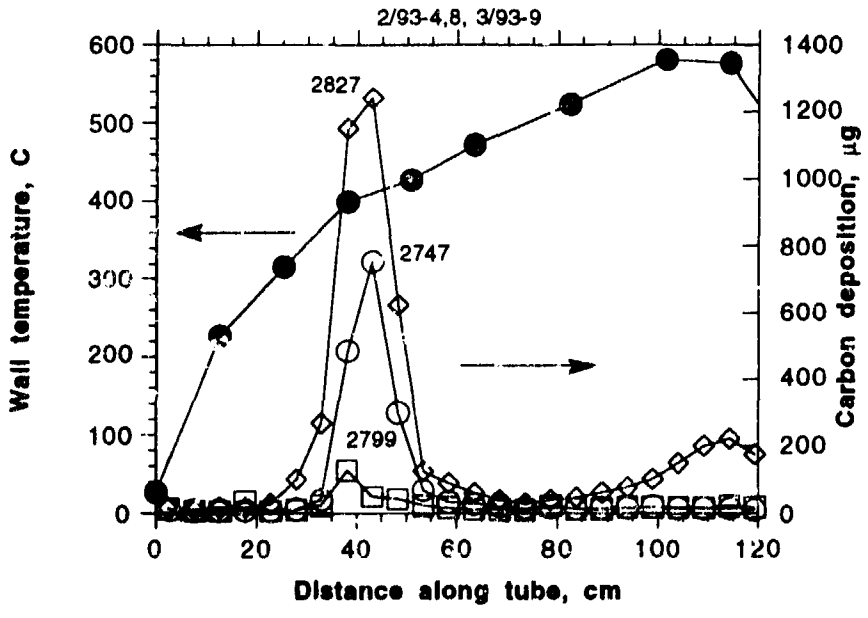

Figure 18. Deposition rates in a heated tube test for baseline fuels [27]. Fuel outlet temperature ~480°C (900°F), pressure 70 atm (1000 psig), residence time ~ 6 seconds, 7 hr tests.

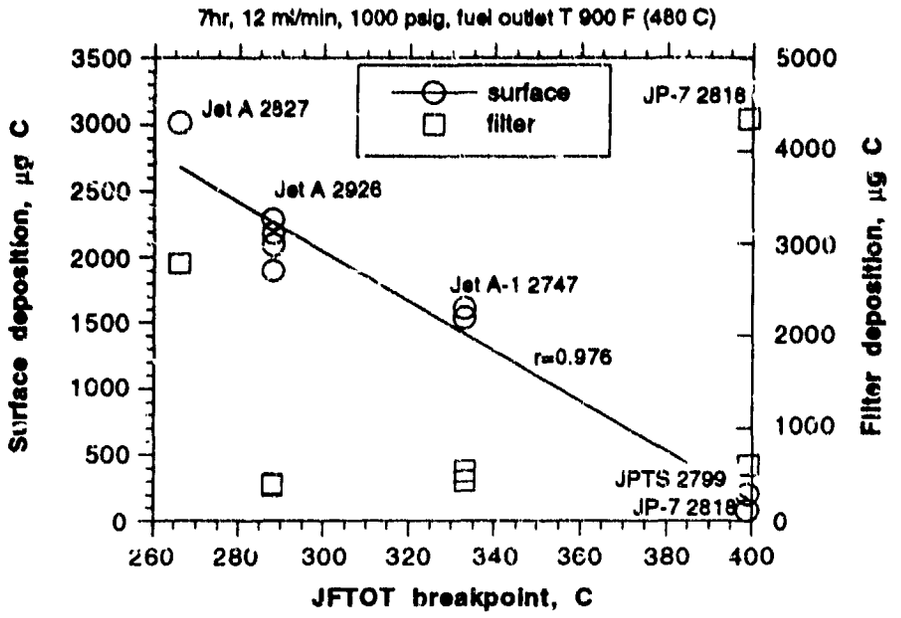

Figure 19. Relationship between JFTOT breakpoint and surface/filter deposition [27]. 7 hr tests, 1000 psig, 12 ml/min.

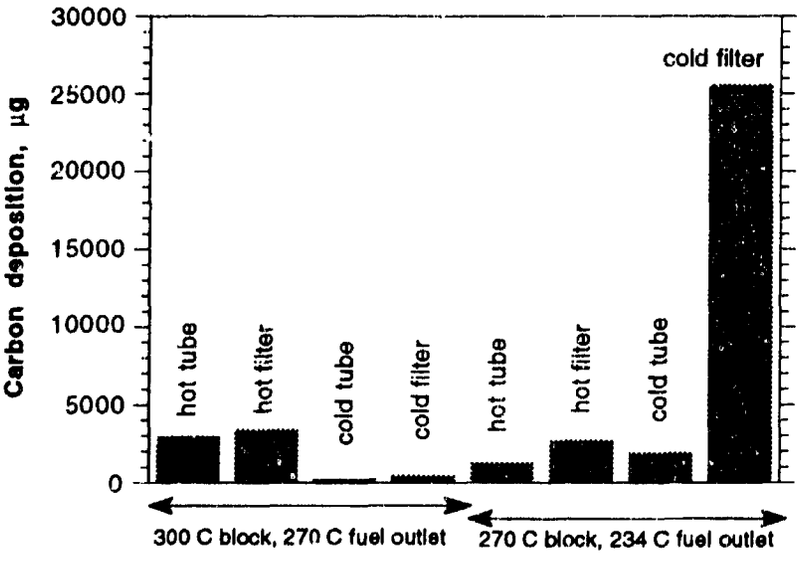

Figure 20. Phoenix Rig results for two conditions [6]. 16 ml/min, Jet A 2827.

Discussion

Question 1. W. Dodds
What effect will high thermal stability fuel have on management of fuels in a battlefield situation? For example, storage, testing, deterioration?

Author's Reply
We do not anticipate any effects. The thermal stability additive package will probably be put into the fuel when the fuel is produced, just as is done with current additives. The fuel will then be handled just like JP-8. The performance characteristics of JP-8+100 fuel will be just like JP-8 except for the improved thermal stability.

Question 2. K. McCaldon
Did you measure a particle size distribution for the insolubles which you filtered out of the fuel?

Author's Reply
The particle size distribution was measured with a photon correlation technique. The size distribution varied between 0.3 and 0.8 microns.

Question 3. D. Santavicca
Are there concerns that the fuel additives may affect the combustion process, e.g., ignition delay?

Author's Reply
The additives will be present in such small concentrations (ppm level) that we do not anticipate combustion problems. The experience with the thermal stability additive JFA-5 supports this. However, as part of the qualification tests for the new additives, combustion experiments in both research combustors and actual engines will be performed.

DEVELOPMENT OF GLOBAL-CHEMISTRY MODEL FOR JET-FUEL THERMAL STABILITY BASED ON OBSERVATIONS FROM STATIC AND FLOWING EXPERIMENTS

V. R. Katta and E. G. Jones
Systems Research Laboratories, Inc.
A Division of Arvin/Calspar
2800 Indian Ripple Road
Dayton, OH 45440-3696
USA

and

W. M. Roquemore
Wright Laboratory, Aero Propulsion and Power Directorate
Wright-Patterson Air Force Base, OH 45433-7103
USA

ABSTRACT

Two global-chemistry models for oxidative deposition of jet fuels are evaluated by integrating them into a Computational Fluid Dynamics with Chemistry (CFDC) code. A previously developed two-step global-chemistry model was found to be insufficient to describe the thermal-oxidation and -deposition rates associated with a Jet-A fuel. A new global-chemistry model has been developed systematically based on observations from flowing and static experiments. The global-autoxidation reaction is modified such that the reaction rate becomes zeroth-order with respect to the dissolved oxygen concentration. The generation of deposit-forming precursor is coupled with the autoxidation reaction by introducing a radical species ROO·. A formulation for the sticking probability has also been developed. Deposition profiles are well represented by this new model under a variety of temperature and flow conditions. The model correctly predicts the changes in magnitude and spatial location of the deposition peak due to changes in flow. The CFDC model, which is designed for flowing systems, has been extended to static experiments. The model incorporates a non-depleting species F_s representing all non-oxygen compounds responsible for deposition. Static experiments were found to provide a useful and inexpensive method for estimating the concentration of F_s in the fuel.

1 INTRODUCTION

An increase in the operating temperatures of fuel-system components in future high-performance aircraft requires improvement of the thermal-stability of jet fuels.[1] Several laboratory methods[2,3] have been developed for evaluating the thermal stability of current and future fuels. High temperatures are normally used to accelerate these experiments. Often there is neither clear correlation between the results of the different laboratory experiments nor knowledge of how the results are related to the thermal decomposition of the fuel in aircraft fuel-system components. Recently a general theoretical framework has been established by integrating the Computational Fluid Dynamics conservation equations with global-chemistry models for thermal-decomposition processes.[4] The resulting CFDC-type models offer potential for predicting fuel behavior in an engine component based on knowledge gained from laboratory experiments. The success of this approach depends on the development of a universal global-chemistry model that can be calibrated for each fuel by laboratory experiments and the ability of the model to predict deposition over a wide range of flow and temperature conditions for any fuel-system component.

Although CFD part of the model is well developed, the global chemistry for thermal oxidation and deposition part is not. Significant progress has been made in using CFD models to predict fluid and thermal characteristics in the complex geometries of practical systems. On the other hand, development in the chemistry modeling of thermal deposition has been hindered by the lack of fundamental understanding of the complex fuel-degradation processes. Krazinski et al.[4] and Katta and Roquemore[5] have achieved some success in the use of the CFDC approach with simple global-chemistry models to predict fuel fouling under different conditions in heated-tube experiments. These successes offer hope that CFDC models will become useful tools for research as well as fuel-system component design.

This paper demonstrates that the previously developed global-chemistry models[5,6] were insufficient for predicting both oxidation and deposition rates in recent experiments. A new global-chemistry model is presented which uses knowledge gained from a variety of flowing and static experiments conducted with the same fuel. The ability of the new model to predict both oxidation and deposition rates in the test sections of the heated tube and near-isothermal rigs is evaluated. Finally, a calibration procedure is discussed for extending this model to a different fuel.

2 FLUID-DYNAMIC AND HEAT-TRANSFER MODELING

Fluid motion inside the tubular test section is assumed to be axisymmetric and bounded by the fuel-deposit interface. The time-dependent Navier-Stokes

Presented at an AGARD Meeting on 'Fuels and Combustion Technology for Advanced Aircraft Engines', May 1993.

equations along with the turbulent-energy, species-conservation, and enthalpy equations are solved in the z-r cylindrical coordinate system. The transport properties along with the enthalpy and density at a given temperature are obtained from the curve fits developed for Jet-A fuel. The governing equations are discretized utilizing a hybrid scheme[6] which is a second-order central-differencing scheme everywhere but changes to a first-order upwind scheme when the local Peclet number becomes greater than two. An implicit approach is employed to advance the calculations using a time-step. This allows the calculations to be performed for real times ranging from minutes to thousands of hours. For the turbulent-flow calculations, wall functions have been used to determine the variations of the flow variables near the fuel-deposit interface.

The mathematical formulation of the problem[5] takes into account the changes in fluid and thermal characteristics of the system as the deposit builds up on wall surfaces. After each time-step the geometry of the fuel-deposit interface is allowed to change as part of the solution procedure. The computational domain is bounded by the axis of symmetry and the fuel-deposit interface, and the grid system is reconstructed after each time-step to take into account the changes in the boundary shape. Fluid flow, heat transfer, and deposit formation are treated using an integrated approach to simulate the time evolution of deposition inside heated tubes. Conjugate heat-transfer calculations are performed to obtain the heat distribution in the deposits, tube walls, and bulk fuel simultaneously.

3 AUTOXIDATION MODELING

Jet fuels are composed of hundreds of compounds. Dissolved oxygen is one of the most important species in the fuel contributing to deposition on metal walls. Several experiments[7,8] have shown strong coupling between oxygen depletion rate and deposit growth. Several reaction mechanisms[8,9] have been proposed to describe autoxidation in fuels. Variations in the reaction kinetics itself indicate that the autoxidation process is also dependent on the fuel under study. The previous and new CFDC models attempt to represent this complex autoxidation process by the following single-step global-reaction equation

$$F + O_2 \xrightarrow{k_1} P, \qquad \text{(R1)}$$

which requires calibration for the reaction rate for a given fuel. Here, F and P represent the fuel and precursor to deposit, respectively. As the mass fraction of the base fuel is far greater than those of the species that involve in thermal-decomposition process, the value of the fuel concentration in the rate expression is treated as a part of the pre-exponential. To date calibration for different fuels has been limited to determining the pre-exponential factor and the activation energy of the global-autoxidation reaction. Recent experiments where an abundance of oxygen-depletion-rate data has been collected using gas chromatography (GC)[7,10] suggest that the rate of oxygen depletion in some fuels is not a function of dissolved-oxygen concentration. This means that calibration of global-chemistry model for such fuels should also include estimates of the order of the reaction with respect to the oxygen.

Dissolved oxygen measured in a Jet-A fuel identified as 2827 by the U. S. Air Force at different temperatures is shown in Fig. 1. These experiments were conducted in a constant-temperature heated-tube test apparatus referred to as the Phoenix rig.[7] The heated tube consists of a 0.3175-cm-o.d. and 50.8-cm-long stainless-steel fuel tube and a 40.64-cm-long heated copper block. The fuel tube was clamped inside the copper block in such a way that only the central 40.64-cm section was heated. Temperature of the copper block was maintained at 573 K. Fuel was passed through the fuel tube at a steady flow rate, and measurements for bulk-fuel temperature and oxygen were made at the exit of the tube. Oxygen content in the fuel at different temperatures was obtained by changing the fuel-flow rate (i.e., indirectly, the heat flux). Oxygen depletion with temperature for different initial levels of dissolved oxygen was then obtained by repeating the experiments. Calculations for the same experimental conditions (initial dissolved oxygen of 65 ppm) were made using the global-chemistry model that was calibrated for a JP-5 fuel used in experiments at United Technologies Research Center (UTRC).[4] The results are shown in Fig. 1 (short-dashed line). Model predictions indicate that the consumption of oxygen in

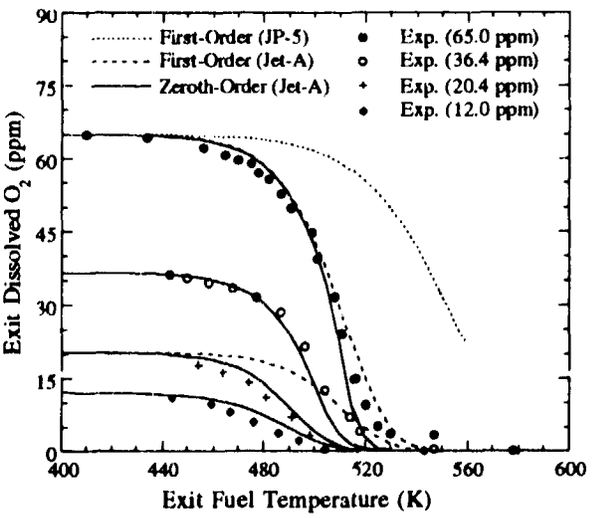

Fig. 1. Oxygen depletion as function of fuel temperature in Jet-A fuel for different levels of initial dissolved oxygen. Data were obtained at end of 50.4-cm-long tube heated with a 573-K copper block and by varying the flow rate. Calculations were made using different global-oxygen-consumption models.

the Jet-A (USAF-2827) fuel is much more rapid than in the JP-5 fuel used by UTRC.[11] Interestingly, the latter fuel yielded peak deposit of ~1000 μg/cm^2/h--an order of magnitude greater than that of the Jet-A fuel. The very large deposition rate with JP-5 could be partly due to the high flow rates used in the UTRC experiments. However, Heneghan and Zabarnick[9] have also observed this inverse behavior--fuels that oxidize easily tend to produce less solids--and attributed it to the natural antioxidant molecules inherently present in nonhydrotreated fuels.

The global-autoxidation rate

$$k_1 = [O_2]^{\alpha} A_1 e^{(-Ea/RT)}, \qquad (1)$$

was recalibrated for the Jet-A (USAF-2827) fuel, and the best fit to the oxygen-depletion data with initial oxygen concentration of 65 ppm is shown by the long-dashed line in Fig. 1. In the above equation, α represents the order of the reaction with respect to the oxygen concentration. In this model, α was assumed to be equal to one, which is consistent with the model developed by Krazinski et al.[4] The new Arrhenius parameters (A = 1.65 x 10^{14} s^{-1}, Ea = 35.5 kcal/mole) resulted a good fit to the experimental data with an initial oxygen concentration of 65 ppm. However, the predictions of oxygen depletion for the 19.5-ppm oxygen level are not so good as noted in Fig. 1. Since the global autoxidation reaction is first-order with respect to oxygen concentration, the depletion rate is much lower than that observed when the initial oxygen concentration was 65 ppm. However, the experimental data show a higher depletion rate, even when the initial dissolved oxygen was 19.5 ppm, suggesting that the autoxidation reaction depends only weakly on oxygen concentration. The global-autoxidation reaction was recalibrated for the Jet-A fuel using different values for α in the rate expression (1). The best representation of the experimental data was achieved when α was set equal to zero. Also the autoxidation reaction with respect to oxygen was assumed to change from zeroth order to first order when the amount of dissolved oxygen fell below the 10-ppm level. The lower depletion rates observed in the experiments at lower oxygen levels support this assumption. The recalibrated oxygen depletion from the 65-ppm level and the predicted depletion curves from different lower initial oxygen concentrations are plotted in Fig. 1 with solid lines. The Arrhenius parameters for this model are A = 2.53 X 10^{13} mole/m^3/s and Ea = 32 kcal/mole. Agreement between the zeroth-order model predictions and the experiments is favorable for all initial oxygen concentrations. Choice of α = 0 in Eq. (1) is also in agreement with the recent findings of Jones et al.[8]

4 DEPOSITION MODELING

Hydroperoxides are felt to have direct bearing on wall deposition. Although, the formation of hydroperoxides in the fuel through the peroxy radicals is reasonably well understood, the transformation mechanism of hydroperoxides into deposits is not. However, hydroperoxides are assumed to produce a precursor to deposits which can be transported by convective and diffusive motions to the wall surface and adhere to it. The precursor is then transformed to deposit. It should be noted that this assumed wall-deposition process is dependent on a sticking phenomenon which must also be modeled.

Carbon-deposition experiments were conducted using the Phoenix rig[7] for the oxygen concentrations shown in Fig. 1. Jet-A (USAF-2827) fuel was continuously passed through the test section at a constant flow rate and copper-block temperature. The fuel was sparged with ambient air to yield a 65-ppm initial concentration of dissolved oxygen before being passed through the test section. After 6 h, the tube was removed from the copper block and cut into 2.54- or 5.08-cm-long sections. The total deposit inside each of these small sections was measured using the carbon-burn-off technique. The deposition rate along the length of the tube in units of μg/cm^2/h is shown in Fig. 2 for two different block temperatures and a flow rate of 16 cc/min. In the present paper, these data are used to calibrate the deposition part of the Krazinski et al.[4] model and the new model. The calibrated models are then used to predict the deposition for the 4-cc/min flow-rate data shown in Fig. 3.

Two-Step Chemistry Model

In the two-step global-chemistry model proposed by Krazinski et al.,[4] a precursor to the wall deposits was assumed to be formed directly from the autoxidation reaction. A unity sticking probability for the precursor was also assumed. A precursor removal reaction was

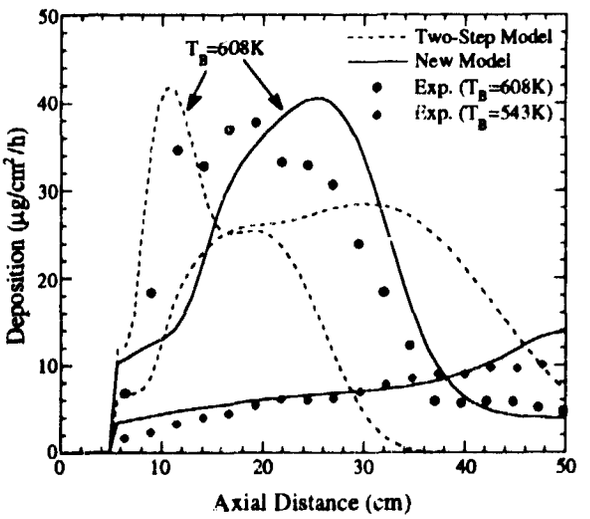

Fig. 2. Deposition as function of tube length or axial distance. Measurements made using carbon burn-off technique. Fuel flow rate was 16 cc/min. Global-chemistry models were calibrated for these data.

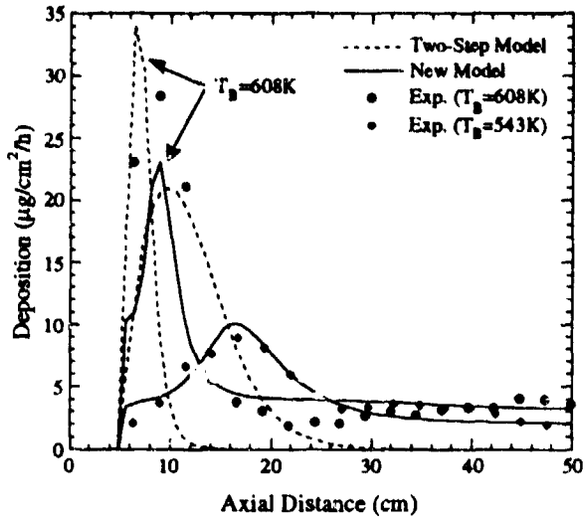

Fig. 3. Predicted and measured deposition in heated tube for different wall temperatures at fuel-flow rate of 4 cc/min.

introduced to limit the deposition at higher temperatures (> 500 K). The deposition model is as follows:

$$F + P \xrightarrow{k_2} \text{Solubles}, \qquad \text{(R2)}$$

$$P \xrightarrow{k_3 = \infty} D_{Bulk}. \qquad \text{(R3)}$$

The strategy for calibrating this model for a given fuel is to determine the Arrhenius parameters for the autoxidation reaction using the oxygen-depletion data and then for the precursor-removal reaction using wall-deposition data. As discussed in the previous section, the autoxidation reaction for the Jet-A fuel was calibrated using the 55-ppm initial dissolved-oxygen-concentration data (short-dashed line in Fig. 1). Calculations for the 16-cc/min flow rate and T_B = 608 K were repeated by adjusting the Arrhenius parameters of the precursor-controlling reaction (R2) to obtain a wall-deposition profile close to that of the experiment. The best-fit profile was obtained with A = 2.1 x10^{14} s^{-1}, Ea = 30 kcal/mole and is shown by the broken line in Fig. 2. Also shown are predictions in Fig. 2 for a lower block temperature of 543 K using this model. Since the initial 5-cm section of the tube was not heated, deposition did not occur there.

A comparison of calculations and experimental data (cf Fig. 2) elucidate the limitations of the two-step chemistry model. The first important difference is that calculations at T_B = 608K yielded a deposition peak which is narrower than that observed in the experiments. This is due to the direct transformation of oxygen to the precursor [cf reaction (R1)] in the model. The high rate of oxygen depletion gives rise to a rapid increase in the deposition rate (from 10 to 40 μg/cm²/h) when the fuel enters the heated section. A high precursor-removal reaction rate is used to limit the peak deposition at ~ 40 μg/cm²/h which, in turn, yielded a narrow peak. A change in the calculated deposition rate seen at x = 16 cm is due to the flow transition to turbulence. The increased mixing due to turbulence transported more precursors to the wall; hence, more deposition occurred. The dip in the experimental data at x = 14 cm is believed to be due to the same flow transition. The second important difference is that at downstream locations (x > 35 cm), the model tends to decrease the deposition rate to zero, whereas the experiments show a deposition of the order of 5 μg/cm²/h. Once the oxygen in the fuel is completely depleted, the precursor concentration decreases exponentially due to the precursor removal reaction. After a certain residence time, the precursors have either been transported to the walls or become solubles leaving fuel downstream precursor-free. This poses a serious problem in the prediction of fouling associated with pre-heated fuel systems. For example, in the experiments of Chin et al.,[12] fuel pre-heated to about 550 K was used. They observed significant deposition in the test section under a variety of flow and block-temperature conditions. Two-step chemistry-model calculations of this experiment predict no deposition in the test section because the chemistry described by the two-step model is completed within the pre-heater, leaving the fuel throughout the test-section precursor-free. The third important difference is that when the block temperature is reduced from 608 to 543 K, the peak measured deposition rate decreases from 40 to 10 μg/cm²/h, while the location of the peak shifts axially from 20 cm to the end of the tube. These changes in the deposition rate are poorly predicted by the two-step chemistry model, as noted in Fig. 2. At T_B = 543 K the calculations show a significant amount of deposition along the length of the tube, with a peak at ~ 18 cm. In fact, the total amount of deposit predicted inside the tube at T_B = 543 K is more than that obtained at 608 K. This result is not in agreement with the experimental results. The inability to predict the correct wall temperature dependence of the deposition rate is felt to be due in part to the unity-precursor-sticking-probability assumption.

Predictions made with the two-step global-chemistry model for a fuel-flow rate of 4 cc/min (broken lines) are compared with the experimental data in Fig. 3. The peaks in the deposition have moved closer to the tube entrance; however, again their location and magnitude are not in agreement with the experiments. Because of the longer residence time (~ 30 s), no deposition is predicted beyond x = 30 cm.

The above comparisons of model predictions and experimental data indicate that the simple two-step global-chemistry model can not adequately describe the deposition process for a fuel such as the Jet-A (USAF-2827). In general, the model provides reasonable predictions when the flow and heating conditions are only slightly different from those used for calibration, as noted in Fig. 2. However, a more robust global-chemistry model must be developed if CFDC codes are expected to predict fouling in experiments where flow conditions differ greatly.

New Chemistry Model

Experiments of Kauffman et al.[13] suggest that deposit-forming precursors are generated through chemical reactions involving hydroperoxides but not directly formed from the autoxidation process. Therefore, with this in mind, the peroxy-radical was introduced in the new model as a separate species. Jones et al.[14] conducted non-flowing, static experiments by heating a flask containing fuel and metal coupons. Deposition on the metal-coupon surfaces and growth of insoluble particles in the bulk fuel were studied as functions of time for a fixed temperature. They observed that the deposition rate on the metal coupons remained constant, even though the concentration of the bulk-insoluble materials increased linearly with time which implies that the deposition rate is independent of bulk-insoluble concentration in the bulk fuel. This led to the interesting conclusion that the bulk-insoluble materials and the deposit-forming precursors are generated through separate pathways but probably involve the same hydroperoxides. In time, the bulk insolubles probably agglomerate; and, in a flowing system, the large bulk-insoluble particles may stick to the walls upon collision and become deposits. The new global-chemistry model developed using these ideas, consists of four species; namely, O_2, ROO°, P, and D_{Bulk}. The global-chemical kinetics involving the above species is given in Tables 1 and 2.

Table 1: Bulk-fuel reactions used in new global-chemistry model

Reaction					Activation Energy (kcal/mole/K)	Pre-Exponential	Reaction No
F	+	O_2	$\xrightarrow{k_4}$	ROO°	32.0	2.5×10^{13} $(\frac{mole}{m^3 s})$	(R4)
ROO°	+	F	$\xrightarrow{k_5}$	Solubles	10.0	1.0×10^{4} (s^{-1})	(R5)
ROO°	+	F_s	$\xrightarrow{k_6}$	P	15.0	8.0×10^{9} (s^{-1})	(R6)
ROO°	+	F	$\xrightarrow{k_7}$	D_{Bulk}	10.0	2.0×10^{2} (s^{-1})	(R7)
P	+	F	$\xrightarrow{k_8}$	Solubles	30.0	3.2×10^{12} (s^{-1})	(R8)
D_{Bulk}	+	F	$\xrightarrow{k_9}$	$2\,D_{Bulk}$	0	1.0×10^{-3} (s^{-1})	(R9)

Table 2: Wall reactions used in new global-chemistry model

Reaction					Activation Energy (kcal/mole/K)	Pre-Exponential	Rection No.
O_2	+	F	$\xrightarrow{k_{10}}$	P	12.0	5.2×10^{-3} (m/s)	(R10)
		P	$\xrightarrow{k_{12}}$	D_{Wall}	17.0	260 (m/s)	(R11)
		D_{Bulk}	$\xrightarrow{k_{12}}$	D_{Wall}	10.0	0.80 (m/s)	(R12)

Reactions (R4) - (R9) occur in the fuel, whereas (R10) - (R12) are the termination reactions that occur on the walls. With this chemical mechanism, the peroxy radicals that are generated through the autoxidation reaction (R4) are assumed to have zeroth-order with respect to dissolved-oxygen concentration. However, as the oxygen concentration falls below the 10-ppm level, the mechanism switches to first-order reaction with oxygen. Some of the peroxy radicals are assumed to decompose to solubles through the reaction (R5). The remaining peroxide radicals are assumed to be involved in the generation of deposit-forming precursors (P) and bulk insolubles (D_{Bulk}) through separate pathways (R6) and (R7). Here, F_s is the component of the fuel that is assumed to be responsible for characterizing the thermal stability of the overall fuel. It could represent species such as copper, sulfur, and nitrogen. Note that F_s is a non-depleting species in the model and therefore, can also be viewed as a part of the pre-exponential of the Arrhenius rate expression for (R6). The precursor-removal reaction is retained in this model as (R8). Finally, the agglomeration of the bulk insolubles is chemically expressed as (R9). A zero activation energy for this reaction allows the growth of large-size particles in time. Note that the units for pre-exponentials in Tables 1 and 2 do not correspond to the bimolecular reactions as the concentrations of species F and F_s are assumed to be constant and are treated as portions of the respective pre-exponentials.

The above reaction mechanism yields precursors and bulk insolubles in the fuel which are then transported to the walls by diffusion and convection. All species except D_{Bulk} are assumed to have the same diffusion coefficient as oxygen. A measured value of 8.0×10^{-8} cm^2/s is used for the diffusion coefficient for the large D_{Bulk} particles;[15] this is ~ 10,000 times smaller than the diffusion coefficient of the oxygen molecules and corresponds to a particle having a diameter of 0.3 μm. The number of P and D_{Bulk} particles that attach to the wall and transform into wall deposit, D_{wall}, is dependent on the sticking probability and the concentration gradient of the respective species. The sticking probability is defined as the probability that a particle reaching the wall will remain at the wall and is usually characterized by an Arrhenius-type dependence on surface temperature.[16] It is also known that the sticking probability decreases with increasing fuel velocity or flow rate due to shear force. Watkinson and Epstein[17] argued that the sticking probability might display a stronger-than-linear dependence on the reciprocal of friction velocity (or square root of shear stress). Table 2 shows the wall reaction mechanism that is developed by considering the effect of temperature and velocity on the sticking probability.

The high viscosity of the fuel causes a laminar sublayer of very slowly moving fluid to form adjacent to the walls. The longer residence time associated with this fluid and other unknown factors appear to cause the autoxidation reaction (R4) to under predict the chemical-reaction rate within this layer. Therefore, another autoxidation reaction which yields precursors directly is included as a wall reaction (R10) in the model. The reactions (R11) and (R12) represent the attachment of particles P and D_{Bulk} to the wall. Finally, the rate of deposition on the wall is expressed as

$$\frac{d[D_{wall}]}{dt} = \frac{c}{(\tau_{wall})^{0.7}} \left\{ [P]_{wall} A_{11} e^{\left(-\frac{E_{11}}{RT}\right)} + [D_{Bulk}]_{wall} A_{12} e^{\left(-\frac{E_{12}}{RT}\right)} \right\} \quad (2)$$

where τ_{wall} is the shear stress at the wall and c is a constant that takes the units of $\tau^{0.7}$.

The new global-chemistry model described above is calibrated for Jet-A (USAF-2827) fuel using the experimental data in Figs. 1 and 2. It is assumed that the concentration of sulfur and other deposit-generating species (F_s) in this fuel is ~ 100 ppm. Values obtained for the pre-exponential and activation energy of each of the reactions (R4) - (R12) are given in Tables 1 and 2.

The calibrated deposition profiles at T_B = 608 and 543 K are shown in Fig. 2 with solid lines. The new model is able to correctly represent the changes in the magnitude and location of the deposition peaks for the two block temperatures. The broad-peak characteristic at higher block temperatures is well reproduced. At downstream locations (x > 40 cm), the attachment of bulk-insoluble particles to the walls yields a fairly constant deposition which matches the experimental data. Overall, the new model yields a fairly accurate calibration for the experimental data.

With all values in Tables 1 and 2 being maintained constant, predictions are made for the 4-cc/min flow-rate case. Results in the form of deposition rate are shown with solid lines for the two block temperatures in Fig. 3. The deposition peak at this flow rate has moved from 9 to 16 cm when the block temperature was decreased from 608 to 543 K. This agrees favorably with the experimental results. The predicted shift in peak-deposition location with block temperature is due in part to the low activation energy (15 kcal/mole) used for the precursor-generation reaction (R6) and in part to the change in heat transfer. On the other hand, the shift in the peaks obtained by the simple two-step global-chemistry model (cf dashed lines in Fig. 3) was mainly due to the change in heat transfer as a result of the high activation energy (32.5 kcal/mole) of the autoxidation/precursor formation reaction. Choice of such a low activation energy for reactions similar to (R6) can also be found in the literature. In a study of autoxidation chemistry, Zabarnick[18] proposed an activation energy of 10 kcal/mole for hydroperoxides formation based on H-atom abstraction reactions.[19]

The new model predictions for deposition profiles, including the tail regions at both block temperatures (solid lines in Fig. 3), are in good agreement with the experimental data. It is apparent from the shapes of the deposition profiles at T_B = 608 K in Figs. 2 and 3 that 1) the chemistry shown in Tables 1 and 2, except for reactions (R9) and (R12), is completed within the test-section and 2) the total deposition (i.e., area under the

curve) of 620 μg/h at 16 cc/min is nearly four times that of 182 μg/h at 4 cc/min. Reaction (R9) progresses very slowly and yields only small amounts of deposit at these flow rates. Since oxygen is the only consumable reactant in the model, the observation that the chemistry is completed in the test section suggests that the incoming oxygen is being totally consumed within the test section at both the 4- and 16-cc/min flow rates. Also, the total deposition for 16 cc/min is about 4 times that at 4 cc/min which, suggests that the total deposition is nearly proportional to the total amount of oxygen flowing through the tube.

The strong dependence of deposition on oxygen was studied experimentally by changing the amount of initial dissolved oxygen in the Jet-A fuel. The block temperature and fuel-flow rate were fixed at 573 K and 16 cc/min, respectively. The desired concentration of dissolved oxygen was achieved by initially sparging the fuel with nitrogen and then with a mixture of oxygen and nitrogen with a specified volumetric ratio. A GC system was used to measure the relative dissolved-oxygen concentration.[10] This system was calibrated by assuming that the oxygen level obtained when the fuel was sparged with pure oxygen was the saturation value of 298 ppm. The total deposit inside the test section after 6 h of stressing was measured and the data are plotted in Fig. 4 for different initial dissolved-oxygen concentrations. The data show that the total deposition increases linearly with the amount of dissolved oxygen. Extrapolation of these data to very low oxygen concentrations indicates a threshold concentration below which no deposition occurs. This could be due to the well-known induction phenomenon[20] associated with fouling.

Calculations have been made for the same conditions using the two chemistry models discussed earlier. The results are shown in Fig. 4 along with the experimental data. It is important to note that the two-step and new global-chemistry models have been calibrated for the experimental data obtained with T_B = 608 K. Both the two-step (dashed line) and new (solid line) models predict zero deposition only when no dissolved oxygen is present initially. This is expected since neither model takes into account induction behavior. In general, the two-step model over predicts deposition; however, it predicts the linear dependence between deposition and initial oxygen concentration. Predictions of the new model are in good agreement with the experimental results. The change in slope for the new-model calculations at about 7% initial oxygen concentration is due to the constraint that autoxidation switches from zeroth to first-order when the local oxygen level falls below the 10-ppm level used in the model.

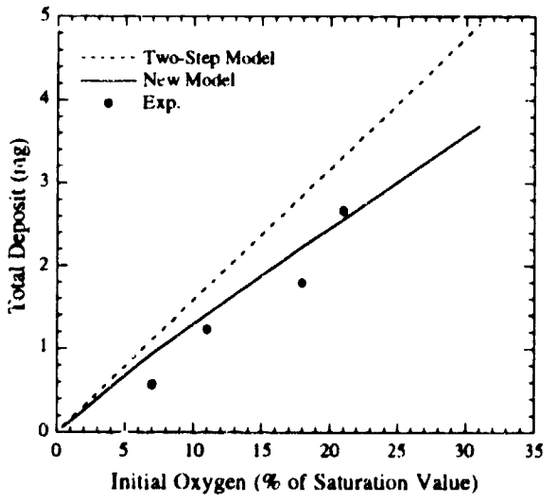

Fig. 4. Total deposit in tube for different levels of initial dissolved oxygen. Fuel flow rate 16 cc/min and T_B = 573 K.

Near-Isothermal Experiment

The ability of the models was further tested through prediction of deposition under different flow and temperature conditions. Using very low flow rates and longer test sections, Jones et al.[8] were able to develop a near-isothermal heated-tube test section. They used the same Jet-A (USAF-2827) fuel as that employed in the Phoenix rig. The outside diameter and the length of the standard fuel tube were 0.3175 and 91.44 cm, respectively. Experiments were also conducted with tubes having a bore size about twice that of the standard ones. The central 81.28-mm section of the fuel tube was heated with a copper block which was maintained at a constant temperature. In some experiments a second heated test section was connected in series with the first one to capture the entire deposition profile. The experiments reported here were made at a copper block temperature of 458 K. Because of the low flow rates (usually less than 1 cc/min), fuel attains the block temperature within the initial 10 cm of the test section and remains isothermal in the remainder of the test section.

For a flow rate of 0.5 cc/min, the predicted and measured deposition inside the standard-size and larger-bore tubes is plotted in Fig. 5. In both tubes the deposition peaks predicted by the simple two-step model (dashed lines) are very close to the entrance to the heated section (note that the initial 5.08 cm of the tube was not heated). Whereas, in experiments, deposition peaks in the standard-size and larger-bore tubes occurred at about x=70 and 35 cm, respectively.

Results obtained with the new model are shown in Fig. 5 with the solid lines. The new model estimated the maximum deposition fairly well, but the locations of the predicted peaks do not match with those obtained in the experiments. However, the model predicted a shift in the locations of the peak deposition from x = 27 to 11 cm when the tube size was changed from standard to larger bore, which qualitatively agrees with experiments. The shift in deposition profiles in the calculations is occurring due to the difference in fuel residence times (fuel velocities) in the two tubes. Since the fuel in the two tubes is at a nearly constant temperature, the chemical reactions should progress

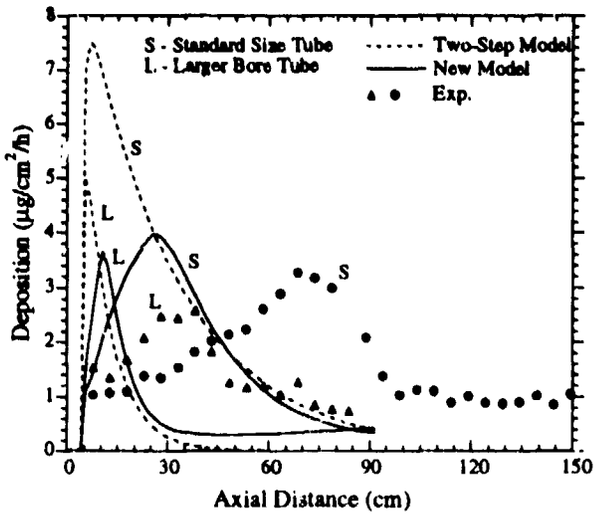

Fig. 5. Predicted and measured deposition in near-isothermal (458 K) heated-tube experiment using two different bore sizes.

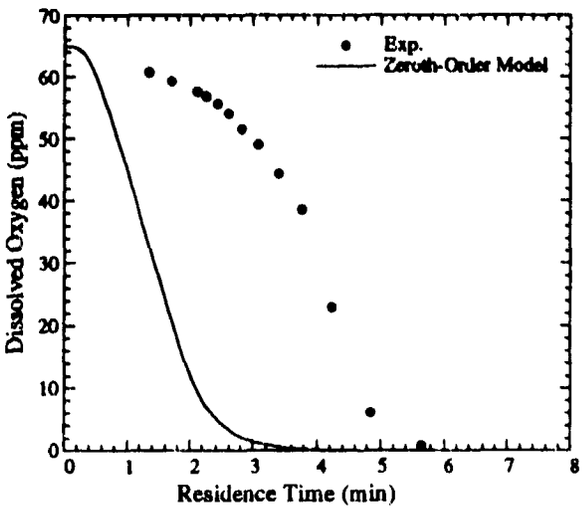

Fig. 6. Measured and computed dissolved oxygen for different residence times in near-isothermal (458 K) heated-tube experiment.

identically with respect to residence time. As the same flow rate is employed, fuel in the larger-bore tube flows at a velocity equal to one-fourth that in the standard-size tube. If the initial 5.08 cm of tube section which is not heated is neglected, the two predicted spatial locations of the deposition peaks correspond to the same point on the residence time scale. However, the experimental data do not support this prediction. Peak deposition in the larger-bore tube occurs much later in time than that in the smaller, standard-size tube. In order to understand this difference between the calculations and the experimental data, oxygen consumption in the near-isothermal system is examined.

The expected amount of dissolved oxygen remaining in the fuel along the length of the standard-size tube is plotted in Fig. 6. Note that axial distance is replaced by residence time in this plot. Both the experimental and computed data were obtained by measuring oxygen content in the fuel at the exit of the tube at different flow rates (or residence times). It is evident that oxygen is depleting in the model much earlier than in the experiment (Fig. 6). This is felt to be the reason for the difference in the predicted and experimental deposition profiles in Fig. 5. The zeroth-order autoxidation reaction in the new model was actually calibrated using the data obtained at higher temperatures on a different rig. The data of Fig. 6 suggest that a single set of Arrhenius parameters is not sufficient to describe the autoxidation process in Jet-A fuel over a wide range of temperatures. These experimental data also indicate that initially oxygen consumption progresses very slowly and then at a rapid rate--a feature not observed at elevated temperatures. Jones et al.[8] felt that some sort of autocatalysis mechanism triggers the higher oxygen consumption rate, while Heneghan and Zabarnick[9] argued that radical chain reactions are responsible for this behavior. In either case, a single-step autoxidation reaction cannot explain the change in oxygen consumption rate. Future efforts should be focused on improving the autoxidation reaction for a global-chemistry model which will be valid over a wide range of temperatures.

Overall, the new model has provided significant improvement in the prediction of fouling in heated tubes (cf Figs. 2 - 5). Although the chemistry model (cf Tables 1 and 2) contains several constants, most of them are felt to be fuel independent. To extend this model to a different fuel, one must calibrate the autoxidation reaction (R4) and determine the concentration of F_s in the fuel. Since F_s represents unknown species in the fuel, it will not be possible to measure its concentration in the near future. However, it may be possible to estimate F_s by conducting some simple static experiments.

Calibration of New Model with Static Experiments

Jones et al.[15] have conducted static experiments in which a small amount of Jet-A fuel (330 cc) was placed in a flask and heated it to 485 K. Oxygen was continuously bubbled into the fuel at ~ 0.2 cc/min/cc of fuel. This agitation helped maintain equilibrium conditions for the fuel in the flask and replenished the fuel with oxygen as it was consumed. Off-line GC measurements showed a constant 49.5-ppm concentration of dissolved oxygen in the fuel. Small metal coupons, suspended in the flask, were submerged completely in the fuel. Typically, the experiments were conducted over a period of 6 h. Periodically, some of the metal coupons and small quantities of the fuel were extracted from the flask to determine the amount of insoluble solids present. The static flask experiments

are examined below to determine their usefulness in estimating values of F_s in the new model.

The static experiment may be treated mathematically as a flowing system under the following conditions. First, the fuel is made to flow at a sufficiently low velocity through a tube such that it is basically static in the tube for the duration of the experiment. The tube is assumed to be heated with a copper block. The tube surface represents the metal coupons in the flask, and the bulk fuel in the tube represents the bulk fuel in the flask. Second, the isothermal conditions in the flask are simulated by instantaneously preheating the fuel to 485 K, the flask temperature, at time t = 0. This temperature is maintained for the duration of the experiment. Third, the dissolved oxygen in the fuel is replenished continuously as it is consumed (i.e., mathematically, the net rate of consumption of oxygen = 0). Because of the very low flow rate, fuel inside the tube attains chemical equilibrium very quickly which results in a uniform deposition rate along the tube. Assuming that all the constants in Tables 1 and 2 are fixed for the given fuel (for example Jet-A) then this deposition rate becomes a function of the concentration of F_s only.

Predicted depositions on the tube wall for different concentrations of F_s are shown in Fig. 7 as functions of stress duration (not residence time, since the fuel velocity is extremely low and only a small amount of fuel exits the tube). The computed deposition rates for F_s concentrations of 150, 100 and 50 ppm are 6.25, 4.84, and 3.04 $\mu g/cm^2/h$, respectively. Experimental data obtained from the metal coupons are also plotted in Fig. 7. The slope of the bestfit line representing the experimental data is 3.58 $\mu g/cm^2/h$. This rate could be slightly higher since the deposit on the metal coupons in a static experiment is loosely bonded, and a fraction of

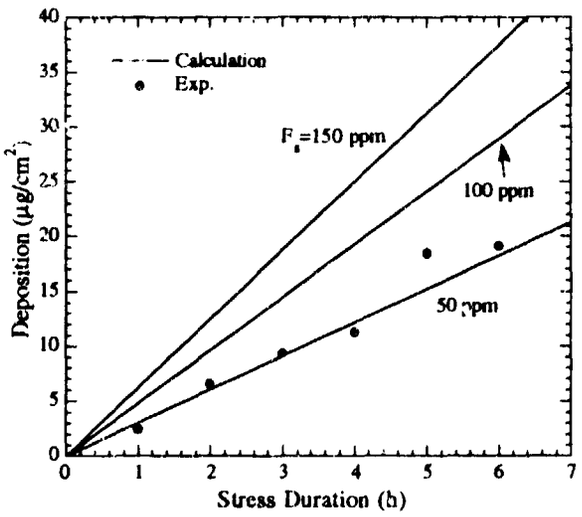

Fig. 7. Calculated and measured deposition on discs in static experiment. Small metal coupons (discs) were immersed in fuel at 458 K contained in a flask. Calculations were used to estimate concentration of F_s in Jet-A fuel.

the total deposit might be lost during the washing and rinsing processes. With this in mind, a comparison between the calculated and experimental data yields a concentration between 50 and 100 ppm for F_s in Jet-A. As seen from Figs. 2 - 5, a value of 100 ppm for F_s yielded reasonable predictions for deposition for different temperatures and flow rates. A possible strategy for calibrating the new global-chemistry model given in Tables 1 and 2 for a new fuel is as follows: 1) determine the Arrhenius parameters for the autoxidation reaction (R4) by conducting relatively simple oxidation experiments using flowing systems such as the Phoenix rig, and 2) with all other constants unaltered, estimate the amount of F_s present in the fuel by performing the inexpensive static experiments discussed above.

5 SUMMARY AND CONCLUSIONS

The simplified two-step global-chemistry models developed previously are not sufficient for simultaneous prediction of the deposition and oxidation rates associated with different fuels and operating conditions. Recent experiments with a Jet-A fuel have suggested that: 1) the rate of oxygen consumption is independent of the amount of dissolved oxygen, 2) wall deposition is not closely following the oxygen depletion even though the former strongly depends on the latter, and 3) wall temperature has a pronounced effect on deposition. Static experiments with this fuel also indicate that bulk insolubles and wall deposits are generated through separate chemical pathways. Based on these observations a new global-chemistry model was developed for fouling in heated tubes. A zeroth-order autoxidation reaction is incorporated into the model and is found to predict correctly oxygen depletion starting from different initial concentrations. More realistic wall-deposition profiles are obtained by introducing an intermediate species ROO,* which is felt to be a product of fuel autoxidation, for the generation of deposit-forming precursors. Bulk insolubles are generated through the reaction (R7) and are allowed to agglomerate. The sticking probability which is a function of both wall temperature and friction velocity is incorporated into the new model for the attachment of precursors and bulk particles to the wall. The model has been successfully used to predict the changes in magnitude and location of the deposition peaks for the high temperatures and flow velocities of the Phoenix-rig experiments.

For near-isothermal, lower temperature, long-residence-time experiments, the new model did not correctly predict the location of peak deposition for two different tube diameters. The model predicted consumption of oxygen much earlier in these tubes than what was observed in the experiments. The disagreement between experimental results and predictions of the new model is possibly due to the lack of an autocatalysis-type mechanism in the global-chemistry model. Since the predicted deposition profiles for low-temperature conditions seem to be shifted only spatially from the experimental profiles (cf

Fig. 5), introduction of autocatalysis into the model might alleviate this problem.

The bulk insolubles D_{Bulk} in this study were used only to provide small amounts of deposit toward the end of the test section. In flowing experiments which employ pre-heated fuel, part or all of the precursor related-reactions could be completed within the pre-heater. Therefore, D_{Bulk} is expected to be the major contributor to wall deposition in preheated experiments. The new model has the potential for predicting deposition in such pre-heated-type flow systems. In order to explore this capability, the reactions (R7) and (R8) must be calibrated more accurately. Bulk insolubles that remain in the fuel also represent the filterable bulk deposits. Since the deposits that are collected by filters in the experiments represent only a fraction of the total bulk deposits (due to the practical size of the filter), no attempt is made to calibrate the model for bulk insolubles. However, future experiments with filters of different sizes might facilitate the determination of Arrhenius parameters for the reactions (R7) and (R8).

The CFDC model designed for flowing experiments has been successfully extended to simulation of static flask experiments in which metal coupons are used. Results suggest that the concentration of F_s in a given fuel can be estimated using the quick and inexpensive static experiments. The flask experiments of Jones et al.[15] also provide information on the growth of insolubles' in the bulk fuel, in addition to the deposits on the metal coupons. If the reactions (R7) and (R8) could be calibrated using this information, then the static experiments would become an important tool in model calibration and development. However, this procedure must be examined in the future.

6 ACKNOWLEDGMENT

This work is supported, in part, by U. S. Air Force Contract F33615-90-C-2033 and, in part, by the Aerospace Sciences Directorate of the Air Force Office of Scientific Research under Work Unit 2308P700. The authors would like to thank Messrs. Chuck Martel and Ted Williams for providing with Phoenix-rig data and Steve Zabarnick and Shawn Heneghan for their helpful comments. Special thanks is given to Mrs. Marian Whitaker for editing this paper.

7 REFERENCES

1. Edwards, T., Anderson S. D., Pearce, J. A., and Harrison, W. E., "High Temperature Thermally Stable JP Fuels--An Overview," AIAA 92-0683, Presented at 30th Aerospace Sciences Meeting and Exhibit, Jan. 6-9, 1992, Reno, NV.

2. Marteney, P. J., and Spadaccini, L. J., "Thermal Decomposition of Aircraft Fuels," ASME Journal of Engineering for Gas Turbines and Power, Vol. 108, October 1986, pp. 648-653.

3. Edwards, T., Roquemore, W. M., Harrison, W. E., and Anderson S. D., "Research and Development of High Thermal Stability Fuels," Paper to be presented at AGARD Meeting on Fuels and Combustion Technology for Advance Aircraft Engines, Paper No. PEP-18, May 10-14, 1993, Colliferro, Italy.

4. Krazinski, J. L., Vanka, S. P., Pearce, J. A., and Roquemore W. M., "A Computational Fluid Dynamics and Chemistry Model for Jet Fuel Thermal Stability," Journal of Engineering for Gas Turbines and Power, Vol. 114, January 1992, pp. 104-110.

5. Katta, V. R., and Roquemore, W. M., "Numerical Method for Simulating Fluid-Dynamic and Heat-Transfer Changes in Jet-Engine Injector Feed-Arm due to Fouling," Journal of Thermophysics and Heat Transfer, Vol. 7, No. 3, July-Sept. 1993.

6. Patankar, S. V., and Spalding, D. B., "A Calculation Procedure for Three-Dimensional Parabolic Flows," International Journal of Heat and Mass Transfer, Vol. 15, October 1972, pp. 1787-1805.

7. Ballal, D. R., Byrd, R. J., Heneghan, S. P., Martel, C. R., Williams, T. F., and Zabarnick, S., "Combustion and Heat Transfer Studies Utilizing Advanced Diagnostics: Fuels Research," Wright Laboratory Technical Report WL-TR-92-2112, Nov. 1992, Wright-Patterson AFB, OH.

8. Jones, G., Balster, W. J., and Post, M. E., "Degradation of a Jet-A Fuel in a Single-Pass Heat Exchanger," to be presented at the International Gas Turbine and Aeroengine Congress and Exposition, May 24-27, 1993, Cincinnati, Ohio.

9. Heneghan, S. P., and Zabarnick, S., "Oxidation of Jet Fuels and the Formation of Deposits," To appear in Fuels, 1993.

10. Rubey, W. A., Tissandier, M. D., Striebich, R. C., and Tirey, D. A., "In Line Gas Chromatographic Measure of Trace Oxygen and other Dissolved Gases in Flowing, High Pressure, Thermally Stressed Fuel," Preprints Symposia - Structure of Jet Fuels III, Division of Petroleum Chemistry, American Chemical Society, Washington, D. C., Vol. 37, No. 2, pp. 371-376.

11. Marteney, P. J., "Thermal Decomposition of JF-5 in Long Duration Tests," Technical Report NAPC-PE-201C (Naval Propulsion Center, Trenton, NJ, 1988).

12. Chin, J. S., and Lefebvre, A. H., "Influence of Flow Conditions on Deposits from Heated Hydrocarbon Fuels," ASME Paper 92-GT-114.

13. Kauffman, R. E., University of Dayton Research Institute, Ohio, Private communications, 1993.

14. Jones, E. G., Balster, W. J., and Anderson, S. D., "Formation of Insolubles in Jet Fuels: Effects of Oxygen," Preprints Symposia-Structure of Jet Fuels III,

Division of Petroleum Chemistry, American Chemical Society, Washington, D. C., Vol. 37, No. 2, pp. 393-402

15. O'Hern, T., Sandia National Laboratories, Albuquerque, New Mexico, Private communication, Feb. 1993.

16. Epstein, N., "Fouling of Heat Exchangers," in Heat Exchangers Sourcebook, Ed., Pale, J. W., Hemisphere Publishing Co., Washington, D.C.

17. Watkinson, A. P., and Epstein, N., "Particulate Fouling of Sensible Heat Exchangers," in Proceedings of the 4th International Heat Transfer Conference, Vol. 1, Paper HE 1.6, pp. 12.

18. Zabarnick, S., "Chemical Kinetics Modeling of Jet Fuel Autoxidation and Antioxidant Chemistry," To be published in Fuels, 1993.

19. Benson, S. W., Thermochemical Kinetics, Wiley, New York, 1976.

20. Kendall, D. R., Houlbrook, G., Clark. R. H., Bullock, S. P., and Lewis, C., "The Thermal Degradation of Aviation Fuels in Jet Engine Injector Feed-Arms: Part 1 - Results from a Full-Scale Rig," Presented at the 30th International Gas Turbine Congress, Tokyo, October 1987.

Discussion

Question 1. M.F. Bardon
Are the various high temperature targets technically possible but too expensive at present, or are the higher ones, such as 900 degrees F, impossible at any price right now?

Author's Reply
The aircraft fuel with the highest thermal stability is JP-7. If one removes the dissolved oxygen from this fuel, it will come close to being JP-900 fuel. Our research is not far enough along to know if a JP-900 fuel can be developed when dissolved oxygen remains in the fuel.

Question 2. Dr L. Ianovski
Your new global chemical model is approximate. How have you determined the values of the kinetic parameters? Metal is deactivated by coke deposits. What methods are used to take this into account in your model?

Author's Reply
The values of the parameters given in Tables 1 and 2 were determined by experience and the trial and error fitting with experimental data. A more systematic approach is needed but we have not yet looked into how to do this.

The model has a surface activation term that is important at low temperatures. In Reference 5, we used an empirically determined surface thickness term to change the rate of surface reaction. This term has not been put into the present model because there is concern about it being physically correct.

FUEL INJECTOR DESIGN FOR HIGH TEMPERATURE AIRCRAFT ENGINE

R.W. Stickles and W.J. Dodds
Advanced Engine Combustor Aero Design
GE Aircraft Engines
Mail Drop A309; P.O. Box 156301
One Neumann Way, Cincinnati, Ohio, USA 45215–6301

T.R. Koblish and J. Sager
New Products Development
Fuel Systems Textron, Zeeland, Michigan

S. Clouser
Naval Air Warfare Center, Trenton, New Jersey

1. SUMMARY

The objective of the Innovative High Temperature Aircraft Engine Fuel Nozzle Program was to design and evaluate a nozzle capable of operating at a combustor inlet air temperature of 1600°F (1144 K) and a fuel temperature of 350°F (450 K). The nozzle was designed to meet the same performance requirements and fit within the size envelope of a current production dual orifice fuel nozzle. The design approach was to use improved thermal protection and fuel passage geometry in combination with fuel passage surface treatment to minimize coking at these extreme fuel and air temperatures. Heat transfer models of several fuel injector concepts were used to optimize the thermal protection, while sample tube coking tests were run to evaluate the effect of surface finish, coatings and tube material on the coking rate. Based on heat transfer analysis, additional air gaps, reduced fuel passage flow area and use of ceramic tip components reduced local fuel wetted wall temperatures by more than 200°F (110 K) when compared to a current production fuel nozzle. Sample tube coking test results showed the importance of surface finish on the fuel coking rate. Therefore, a one micro–inch (0.025 micron) roughness was specified for all fuel passage surfaces. A novel flow divider valve in the tip was also employed to reduce weight, allow room for additional thermal protection, and provide back pressure to reduce the risk of fuel vaporization. The fuel nozzle was fabricated and evaluated in a series of high temperature coking tests. Initial results of these tests indicate that thermal protection and surface treatments were partially successful in preventing nozzle fouling, but additional refinement of the internal flowpath is needed to prevent buildup of coke particles that partially blocked the spin slots which meter the nozzle fuel flow.

2. INTRODUCTION

Advanced military high performance gas turbines will require both increased pressure ratio for improved cycle efficiency and increased use of fuel as a heat sink for both airframe and engine cooling. These two trends will increase both combustor inlet air and fuel temperatures. Therefore, innovative fuel injector designs will be required to successfully operate in this thermally hostile environment.

The primary concern in the design of high temperature fuel injectors is the phenomenon of fuel coking. Coking is the formation of insoluble hydrocarbon compounds in the fuel by autoxidation. This results in deposits of gum, tars, varnish and solid carbon on fuel passage surfaces. The deposits restrict flow and can, in turn lead to a significant reduction in combustor performance and life. Coking rates depend on many factors such as wetted wall temperatures, fuel residence time at temperature, total volume of fuel passed through the system, and fuel thermal stability (Lyon, 1992). Therefore, a simple bulk fuel or wetted wall temperature design limit does not exist. However, GEAE experience has shown that fuel nozzle coking becomes a significant problem in current production fuel injectors when wetted wall temperatures approach 400°F (477 K). Maintaining the 400°F maximum wetted wall temperature guideline at the design goals of this program (Table 1) is an extreme challenge.

Table 1. Innovative Fuel Nozzle Design Goals.

Air Temperature	1600°F (1144 K)
Fuel Temperature	350°F (450 K)
Operability	Full Envelope
Smoke	Invisible with JP-5 and 12.5% H2 fuel
Life	Full Aircraft Life
Fuel Capability	JP–5, DFM (JFTOT $\geq$ 477 K)

There are four basic approaches to minimize fuel injector coking: 1) Change to a more thermally stable fuel 2) Actively cool the fuel injector with air or fuel in a separate cooling circuit. 3) Improve fuel

passage geometry and thermal protection to reduce wetted wall temperatures. 4) Treat fuel passage surfaces to inhibit coking.

Changing fuels was not an option in this program. In fact, future fuel thermal stability will probably decrease (Lyon, 1992). Actively cooling the injector would reduce coking, but it is in conflict with the continuous effort to reduce weight and simplify the fuel system. Thermal protection alone will not meet the goals of this program. However, fuel passage surface treatment offers the potential to reduce the coking rate to acceptable levels at elevated wetted wall temperatures. Therefore, the GEAE/Fuel Systems Textron approach was a combination of improved thermal protection and surface treatment.

The innovative fuel nozzle designed for this program meets the flow and spray requirements and fits within the size envelope of the Textron F404 dual orifice fuel nozzle shown in Figure 1. All temperature predictions and design features will be compared to the F404 baseline.

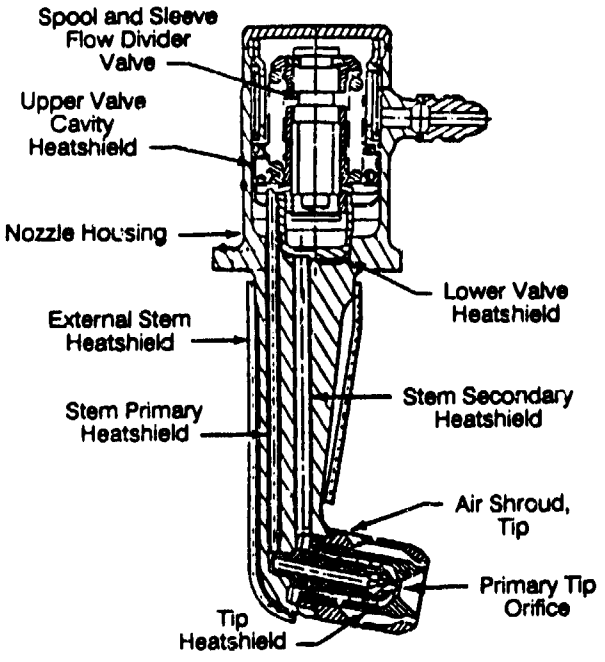

Figure 1. Production F404 Fuel Nozzle used as Baseline for Innovative Design

3. THERMAL PROTECTION FEATURES

Heat transfer analyses were conducted to develop insulating and hydraulic tip designs that would minimize wetted wall temperatures. Past experience has shown that maximum wetted wall temperatures along with the associated coking problems occur in the nozzle tip. This is due to a lack of adequate space for proper heat shielding, combined with the smaller fuel flow passages that are easily plugged by coke particles. More specifically, because it is the outer fuel annulus, the secondary fuel passage in a dual orifice nozzle is where the most severe wetted wall temperatures occur.

An axisymmetric heat transfer model of the F404 tip was used to evaluate thermal design features to reduce nozzle wall temperatures. The model has been described by Stickles et al. (1992). Maximum steady state wetted wall temperatures in the fuel nozzle occur at a cruise condition rather than at maximum thrust condition. This is due to the cooling effect of the high fuel flow rate at the maximum thrust condition. At cruise, combustor inlet temperature is still high, but fuel flow is much lower. Thus, wetted wall temperatures are at a maximum. A cruise condition with a combustor inlet temperature of 1166°F (903 K) was used to compare tip designs. The fuel inlet temperature was 350°F (450 K).

Twenty-seven tip designs were evaluated. Design features included reduced fuel flow area, additional air gaps, modifications to the tip inlet (elbow), ceramic nozzle body, ceramic inserts, thermal barrier coatings, reduced emissivity coatings, and vacuum sealed insulating gaps. All designs maintained the basic F404 dual orifice fuel passages and fit within the baseline envelope.

Fuel Flow Area

The highest temperature region in the baseline F404 nozzle was the tip entrance or elbow. In this region fuel dumps from the secondary fuel delivery tube in the support, to a collecting area at the elbow. Low fuel flow velocity leads to very high wetted wall temperatures. Figure 2 shows the dramatic reduction in wetted wall temperatures when the flow area in the elbow region is reduced.

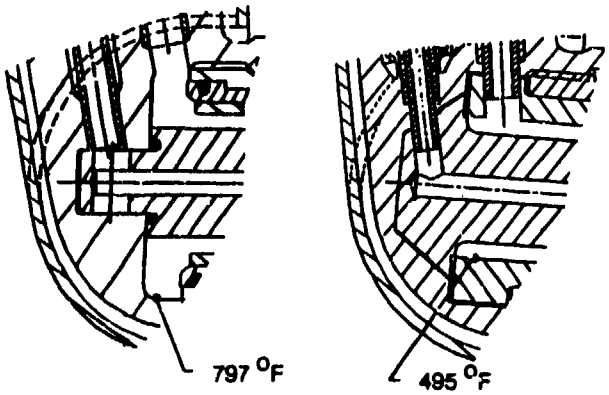

Figure 2. Redesign of Elbow Significantly Reduces Wetted Wall Temperatures.

Figure 3 shows the relationship between secondary fuel flow area, heat transfer coefficients and wetted wall temperatures. This also confirms the need for maintaining high fuel velocity throughout the nozzle. In addition to heat transfer considerations, increased fuel velocity also reduces residence time in the fuel nozzle, which reduces the time available for the coking process.

Use of Solid Ceramics for Insulation

Current fuel nozzle thermal protection in the tip is generally an insulating air gap that separates the fuel wall from high temperature combustor inlet air. An alternative would be to use insulating materials such as ceramics. However, replacing the baseline secondary stainless steel/air gap construction with a solid piece of partially stabilized zirconia actually increased wetted wall temperatures by

nearly 100°F (56 K). The wetted wall temperature was reduced 20°F(11 K) from the baseline when the stainless steel/air gap design was replaced with an identical zirconia/air gap design. However, this part is not practical to manufacture because of the thin ceramic walls.

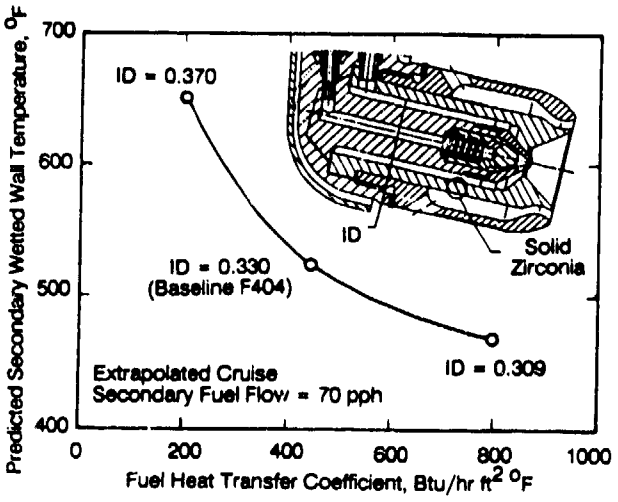

Figure 3. Reducing Fuel Flow Area Lowers Wetted Wall Temperature.

Super Insulated Fuel Delivery Tube

In addition to heat transfer analysis on the injector tip, a super-insulated delivery tube was designed to minimize fuel temperature rise in the injector support. Under steady state cruise conditions fuel flow is high enough to minimize bulk fuel temperature rise, but improved insulation becomes crucial to prevent heat soak-back at the low flow rates associated with idle descent. State-of-the-art tube insulation designs utilize annular air gaps surrounding the fuel delivery tube. This appears to be effective for current engine cycles at high fuel flow rates. In this program the high temperature level will add a substantial radiative heat load along with the existing convective heat flux on the injector support. In order to compensate for the increased radiation load, a double wall fuel transfer delivery tube (as shown in Figure 4), has been developed. A normal air gap is still utilized between the strut (structure) and the outer shell of the transfer tube. However, the double wall construction of the tube is filled with Perlite powder. Perlite is an insulative material used extensively for applications where radiation is a significant heat transfer mode. As shown in Figure 4, a slip joint was incorporated to compensate for substantial thermal gradients during full power, cruise and soak-back conditions. As the outer structure grows with the surrounding air temperature, the innermost tube length is relatively constant at the 350°F (450K) fuel temperature. The slip seal is designed to retain the Perlite bulk packing density while allowing the outer tube wall to grow with radiation load. Calculated inner wetted wall temperatures at the conditions investigated for the Perlite tube were:

Compressor Discharge Temperature, °F(K):	1200(922)	1600(1144)
Fuel Velocity, fps(m/s):	20(6)	40(12)
Wetted Wall Temperature °F(K):	365(458)	360(455)

At these conditions bulk fuel temperature rise through the support will be minimal.

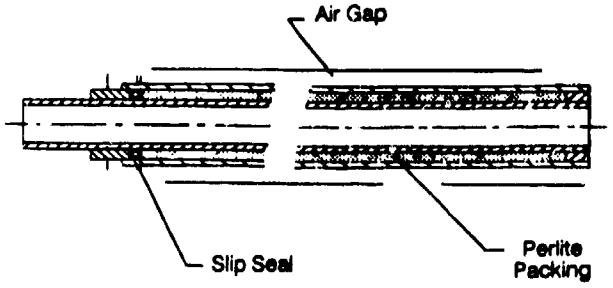

Figure 4. Slip Seal Allows for Thermal Differences

Key Thermal Design Features

Heat transfer analysis confirmed that heat shields and insulation alone would not meet the goals of this program. In all tip designs evaluated wetted wall temperatures were well above the 400°F (477K) limit. However, the analysis did point to important design features for reducing wetted wall temperatures:

- Reduce fuel flow passage area.
  - Increases fuel velocity
  - Increases heat transfer coefficients
  - Reduces wetted wall temperatures
  - Reduces fuel residence time
- Add air gaps.
  - Metal with air gaps more effective than solid ceramics
- Substitute ceramic for metal parts
  - Ceramics in combination with air gaps
- Avoid bends and steps in the fuel flow path.
  - Causes stagnant fuel regions which have low heat transfer coefficients and thus high wetted wall temperatures
  - Provides coking initiation sites
- Add the Perlite filled super-insulated fuel delivery tube in the injector support.
  - Minimizes bulk fuel temperature rise in support.

Reduced emissivity coatings, vacuum gaps and thermal barrier coatings did not demonstrate a significant reduction in wetted wall temperatures.

4. FUEL PASSAGE SURFACE TREATMENT

Heat transfer analysis showned that thermal protection alone will not meet the goals of this program. Therefore, an attempt was made to reduce the fuel coking rate with surface treatment, including surface finish and composition. Previous data have clearly shown that certain elements in the fuel system dramatically increase fuel coking. Table 2 from Taylor and Frankenfeld (1975) shows the effect of some metals on the coking rate of JP-5. Thus, various inert surface coatings were evaluated under this program to investigate the potential for coking reduction.

Table 2. Effect of Metal Surface on Carbon Deposition (Taylor, 1975).

Metal Surface	Deposit Formation Rate at 400°F (mg/sq cm hr)
Copper	0.00525
Ti–6Al–4V	0.00375
Ti–8Al–1V–1Mo	0.00240
Pure Titanium	0.00093
Stainless Steel 304.	0.00093
Aluminum	0.00093

Marteney and Spadaccini (1986) suggested two basic coking processes: 1) A homogeneous oxidation reaction occurring in the fuel freestream forming coke particles which adhere to the fuel passage surface. 2) A heterogeneous catalytic reaction occurring at the fuel passage surface. If mechanism #2 dominates, an inert surface should reduce the coking rate. If mechanism #1 dominates, a polished surface may prevent carbon from adhering. This work indicates that both processes occur, but the dominant one depends on wetted wall temperature. Below wetted wall temperatures of 530°F (550 K), a line representing an activation energy of 10 kcal/mole fits the data. This is typical of a heterogeneous reaction system at the wall. Above 530°F, the 40 kcal/mole activation energy line is typical of a homogeneous oxidation reaction (liquid phase). At very high fuel temperatures (> 800°F (700 K)) the coking mechanism is pyrolysis controlled (Chin and Lefebvre, 1991).

Surface Coking Tests

Evaluation of the various approaches to eliminate or reduce fuel coking was conducted in a heat transfer/coking rig described by Stickles et al.(1992) and illustrated in Figure 5. Two heat exchanger units were utilized in the rig to obtain fuel temperature as high as 400°F (477 K). A constant flow pump provided continued recirculation of the fuel within the two heater units to prevent stagnant thermal stress zones. In order to promote fuel thermal decomposition, the supply fuel was bubbled with air to ensure oxygen saturation.

In addition to the fuel heater, the test stand also provided electrically heated air to supply the heat source for conducting either coking or heat transfer tests of the various specimens. Air temperatures of

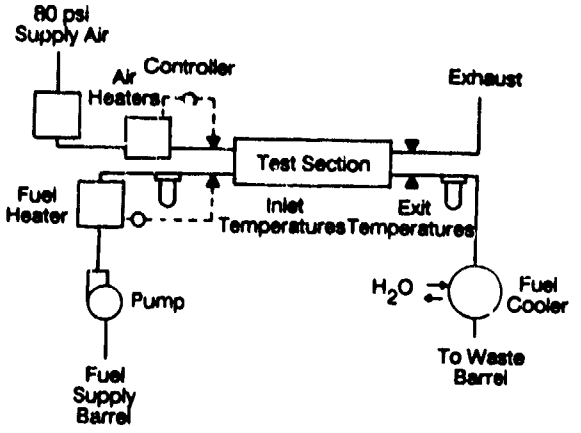

Figure 5. Heat Transfer/Coking Test Rig.

1600°F (1144K) to simulate the engine compressor discharge temperature levels and heat transfer coefficients were also obtained.

The test fixture is shown in Figure 6. All sample coking specimens tested were 3.35 inches (8.5 cm) long by 0.43 inch (1.1 cm) diameter tubes. As shown, the test fixture was designed to accommodate two specimens in series. All test specimen candidates were evaluated relative to a reference specimen (Stainless 347, standard surface finish) typical of the F404 nozzle passage design. Heated air flowed through the I.D. passage of the specimen tube while heated fuel flowed over the O.D. surface through an annulus which simulated typical nozzle design flow passages (i.e., flow velocities and fluid residence times). During a coking evaluation the outer surface of the specimen tube was set at a specific temperature (wetted wall temperature). A constant surface temperature was maintained by adjusting the heated air temperature and/or mass flow.

A fluoroptic thermometry system was utilized to measure the wetted wall temperature without obstructing the fuel flow or surface geometry. Testing at Fuel Systems Textron confirmed claims by the manufacturer (Luxtron) that distillate fuels would not affect the transmission of fluorescent signals and that system accuracy is within the quoted ± 1°C (Wickesheim and Sun, 1985).

The test procedure was first to screen specimens using an 8–hour test cycle. The objective of these tests was to determined coke deposition rate by measurement of weight gained by the candidate specimen. A tandem baseline specimen was used as a reference. The more promising candidates were then subjected to 30–hour evaluation tests to confirm their potential effectiveness. In all evaluations and baseline testing of specimens, JP–5 fuel was oxygenated, heated and passed over the surface on a one pass basis in order to simulate actual operational conditions.

Ten specimen tubes were screened in eight hour tests, as described in Table 3.

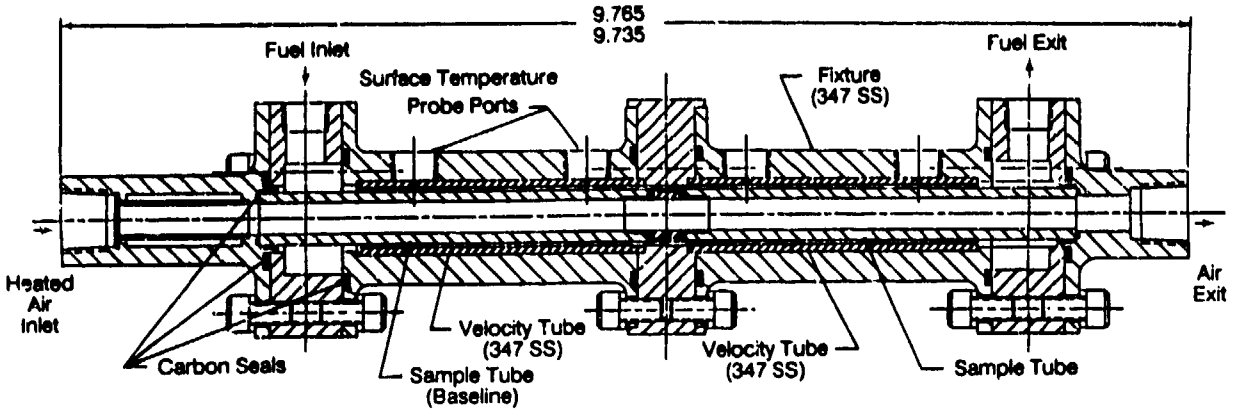

Figure 6. Tandem Tube Test Fixture.

Table 3. Coking Specimen Tubes.

Material	Surface Finish (Micro in.)	Surface Finish (Microns)
347 Stainless Steel	125	3.18
347 Stainless Steel	65	1.65
347 Stainless Steel	10	0.25
Aluminum Oxide Coated 347	Rough	
Pyrolytic Glass Coated 347	10	0.25
Chromium Carbide Coated 347	10	0.25
Titanium Nitride Coated 347	10	0.25
Catalytic Glass Coated 347	10	0.25
Zirconia	10	0.25
High Temp Glass Coated 347	10	0.25

The tests were run at the following conditions:

Inlet Fuel Temperature = 350°F (450K)
Inlet Wetted Wall Temperature = 575°F (575K)
Fuel Velocity = 10 fps (3mps)
Test Time = 8 hours

Visual observation suggested that the zirconia and the chromium carbide coated tubes were more resistant to carbon deposits. Attempts to quantify the deposition were unsuccessful because the phosphor patch on all the sample tubes used for optical surface temperature measurement eroded during the tests. This skewed the before and after weight difference.

A series of 30 hour coking tests was then run at the following conditions:

Inlet Fuel Temperature = 350°F (450 K)
Inlet Wetted Wall Temperature = 475°F (519 K)
Fuel Velocity = 10 fps (3 mps)
Test Time = 30 hours

In these tests, both tubes were identical and the phosphor patch was only used on the forward tube to set the conditions. This allowed accurate before and after weights of the aft tube to be obtained. Table 4 summarizes the carbon deposition rates. Wetted wall temperature increased along the length of the tubes. The average wetted wall temperature on the aft tube was 50°F (28K) above the inlet wetted wall temperature, so the deposition rates quoted are for an average wetted wall temperature of 525°F (547K).

Table 4. Total Carbon Deposition Results -475°F Tests.

Material	Finish (Micro-in.)	Carbon Deposition (mg)	Rate (mg/sq cm hr)
347 SS	10	2.0	0 00228
Zirconia	10	2.2	0.00251
Chromium Carbide	10	2.6	0.00297
347 SS	125	2.7	0.00308

Deposition rates for all tubes were similar. Polished 347 stainless steel was the most coke resistant material tested. Both Taylor and Frankenfeld (1975) and Meyer et al. (1991) also found stainless steels superior to other candidate fuel passage materials. However,

the difference between the coking rates of the two 347 SS sample tubes does indicate a surface finish effect.

Figure 7 shows the deposition rate as compared to other available JP-5 data. There is a great deal of scatter, but the deposition rates measured in this program are significantly lower. A possible explanation for this is that in both Taylor and Frankenfeld (1975) and Marteney and Spadaccini (1986) fuel was not preheated before introduction to the hot stainless steel surface. In this study the fuel was preheated to a 350°F (450K) bulk temperature and carbon particles were filtered out before entering the test section. Therefore, it may be possible that the fuel was prestressed to a point where fewer radicals were available to participate in the coking process inside the test section. Marteney et al. (1982) also observed a reduction in diesel fuel coking rate when it was preheated to 300°F (422K).

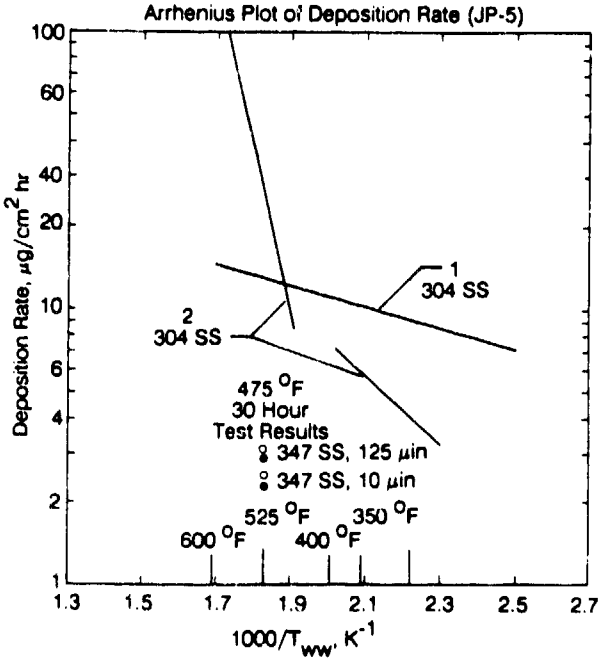

Figure 7. Coking Rake much Lower than Other Reported Data (1) Taylor and Frankenfeld (1975) (2) Marteney and Spadaccini (1986).

Examination of the carbon depositions with a scanning electron microscope (SEM) provided some interesting details. SEM photographs clearly showed two distinct types of deposition – a soft carbon and a hard varnish. All of the 575°F wall temperature test specimen tubes had a soft carbon deposit. On the other hand, most of the same specimen tubes had a varnish deposit when run at the 475°F wall temperature condition. Figure 8 compares the two types of deposition on 347 stainless steel tubes. Possibly, depositions start out as a varnish on the surface, but the exposure to the higher 575°F wall temperature continues the hydrocarbon breakdown until only soft carbon is left.

With one surface, the type of deposition was not a function of temperature. Partially stabilized zirconia tubes had soft carbon as shown in Figure 9 at both the 475°F and 575°F test conditions. Although the exact cause is not clear, this result does suggest that the fuel tube composition does affect the coking mechanism.

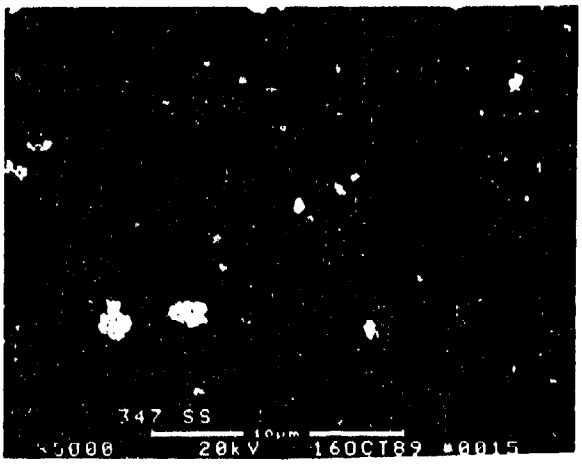

Note: Bright flakes in photo are from gold sputter, not carbon.

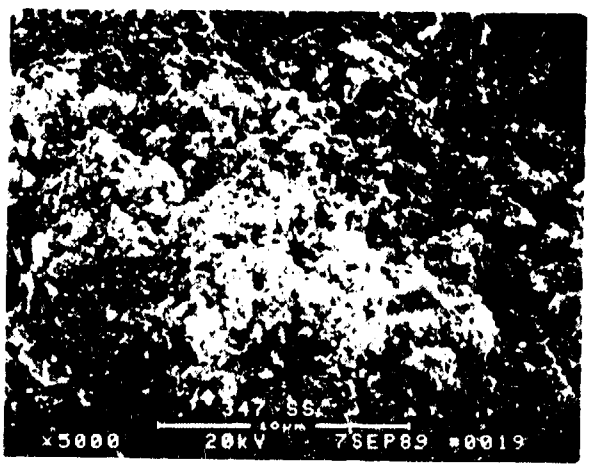

T_{ww} + 575°F

Figure 8. Varnish Forms on 10μrn-inch 347 SS at T_{ww} – 475°F while Soft Carbon Deposits at 575°F.

Based on this result, partially stabilized zirconia may be an excellent material for the tip fuel passages since it only forms soft carbon which could be washed out of the tip at high fuel flow conditions. Varnish, on the other hand, tends to build up and then spall off in larger chunks that could plug the nozzle secondary spin slots. In addition, zirconia has lower thermal conductivity than stainless steel; therefore it acts as an insulator to minimize wetted wall temperatures.

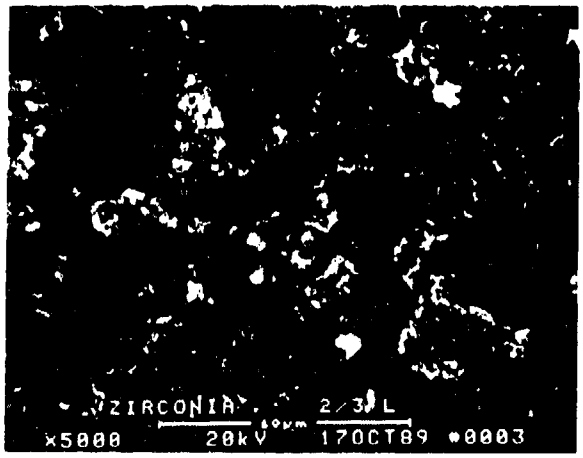

T_{ww} = 475°F

Figure 9. 10μ-inch Zirconia Tube had Soft Carbon Rather than Varnish Deposits at 475°F (5000x).

In addition to the two types of deposition observed from SEM inspections, the effect of surface finish was also evident. Figure 10 shows SEM back-scatter photographs of 347 stainless steel tubes of 125 and 10 micro-inch surface roughness after the 575°F coking tests. Machine lines are clearly visible on the 125 micro-inch surface at 100x. Carbon deposits concentrated on those machine lines (carbon is dark on back scatter). On the 10 micro-inch finish the machine lines have been polished out, but some other surface defects are visible. Once again carbon deposition is evident on the surface defects.

Quantitative measurements (Table 4) indicated a 26% reduction in carbon deposition when the surface roughness was reduced from 125 to 10 micro-inches. To help verify this trend and to take it one step further, two stainless steel tubes were polished to a one micro-inch finish with a grit polishing process. One tube was left uncoated and the other was coated with chromium carbide vapor deposition. Both tubes were run at the 475°F, 30 hour test. Although there was some discoloration of the tubes, there was no measurable (<0.1 mg) deposition on either tube. These results strongly suggest that surface finish plays an important role in coke initiation.

5. FUEL NOZZLE DESIGN AND FABRICATION

The need to provide additional room for thermal protection resulted in the incorporation of a simple reed valve concept shown in Figure 11. The standard sliding spool and sleeve valve configuration of the baseline F404 integral valve body/support design was replaced by a single curvilinear-cantilever leaf-spring valve located in the tip of the fuel injector. This concept combines the functions of the sliding spool which meters and divides fuel flow to both primary and secondary passages of the nozzle tip. In addition, the tip location of the

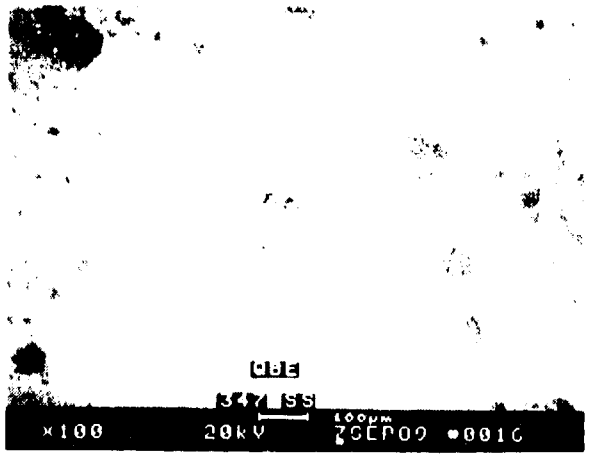

10μ in
T_{ww} = 600°F

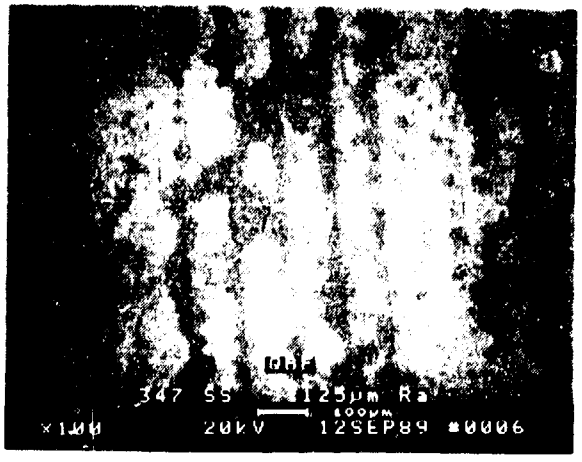

125μ in
T_{ww} = 600°F

Figure 10. Dark Spots are Carbon on 100x Back Scatter Analysis. Machine Lines and Surface Defects are Initiation Sites.

reed valve eliminates one of the two (primary and secondary) fuel delivery tubes down the support structure of the fuel injector. A single fuel feed simplifies construction and affords improved thermal protection along the support path. The reed valve also reduces the risk of fuel vaporization by maintaining back pressure during heat soak-back conditions. Reed valve design considerations include geometric relations between leaf movement and the discharge orifice, material selection, cantilever geometry and flow chamber shape. Development tests of the reed valve included one million on/off cycles, hot and cold fuel flow checks and limited contamination testing. The baseline F404 flow curve was matched with the excep

tion of a delayed reed valve closing hysteresis as shown in Figure 12. The hysteresis was repeatable so it was considered acceptable for this program. Moving the flow divider valve into the high temperature flowpath does increase the risk of leakage and valve hysteresis due to coke or varnish formation. However, the simple reed valve design and potential payoffs warrant the risk.

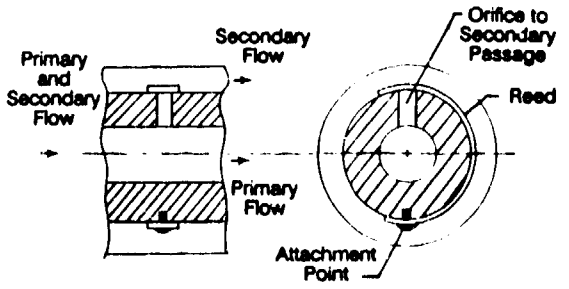

Figure 11. Read Valve Divides Primary/ Secondary Flow in Tip.

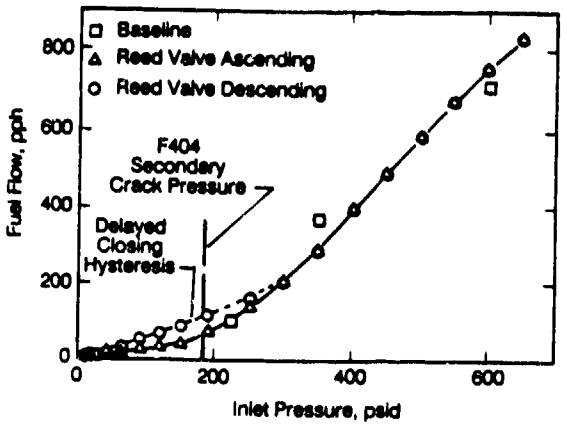

Figure 12. Delayed Closing Hysteresis is Very Repeatable.

Fuel Nozzle Tip Design

The innovative nozzle tip design is compared to the baseline in Figure 13. The reed valve in the tip provides the primary/secondary fuel flow dividing function. The valve saves weight (over 5 pounds on a set of 18 nozzles), allows extra room for insulating air gaps and back pressures the fuel flow to reduce the risk of vaporization. The partially stabilized zirconia in the tip provides additional insulation and inhibits the formation of hard varnish. Several additional insulative air gaps have been added to the tip. A Perlite filled super-insulating fuel delivery tube is included in the support. All fuel passages have been polished to a mirror-like 1 micro-inch roughness. Figure 13 shows that local wetted wall temperatures have been reduced more than 200°F when the final nozzle tip design is compared to the baseline F404.

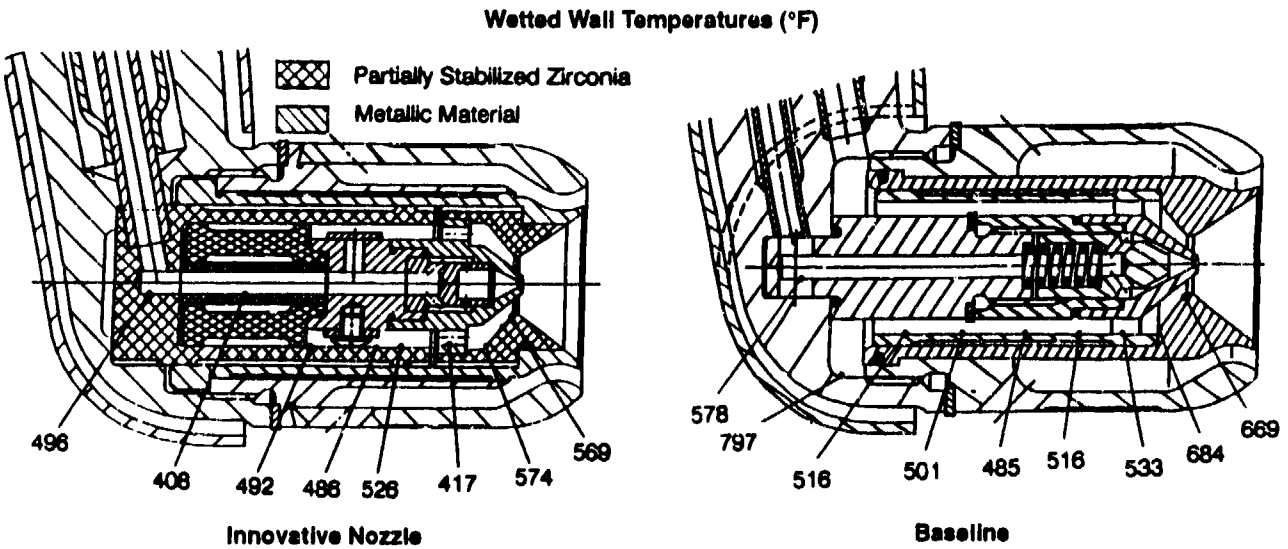

Figure 13. Wetted Wall Temperature are Significantly Lower than the Baseline F404. Hot Spots are Downstream of Secondary Spin Slots.

Nozzle Fabrication

An exploded view of the final fuel nozzle hardware is shown in Figure 14. The primary and secondary metering sets are identical to the baseline nozzle, but are encased in ceramic components. Each metering set consists of an array of fuel swirl slots, a spin chamber and an orifice. The size and angle of the swirl slots and the orifice diameter determine the spray drop size and spray angle. Use of the baseline metering sets ensures that the spray characteristics of the innovative nozzle will be equivalent to the baseline injector, so that combustor performance will not be affected.

During assembly, the reed valve body was first brazed to the secondary metering set. The ceramic (zirconia) spool component was then brazed to the reed valve body using a brazing alloy and process designed especially for ceramic–to–metal joints. Extensive trials were conducted by Fuel Systems Textron to develop a successful combination of braze alloy, braze heating cycle, clearance between parts to be brazed and ceramic surface treatment prior to braze.

Final assembly was completed by attaching the reed valve to the valve body with a precision ground alignment pin and hardened hold–down screw. Next, the superinsulating fuel tube was installed into the stem. The ceramic tip components and metallic heat shield were then positioned within the tip body, and the tip body was welded to the fuel nozzle stem.

6. NOZZLE THERMAL CYCLIC TESTS

The baseline and innovative nozzles were evaluated in a series of thermal cyclic tests to demonstrate durability with high temperature fuel and airflow.

Test Rig

The baseline and innovative nozzles were tested simultaneously in the cyclic fuel nozzle coking test rig illustrated in Figure 15. The rig was designed to closely simulate the actual engine fuel nozzle environment. Two nozzles were tested at one time to allow a direct comparison of durability under identical test conditions. The nozzles were installed into actual engine air swirlers mounted on a combustor dome structure to accurately simulate the airflow velocities which affect the heat transfer boundary conditions around the fuel nozzle tip. Fuel exiting the nozzle was burned just downstream of the nozzles to provide a realistic level of flame radiation to the nozzle tips. Upstream of the nozzles is a simulated diffuser with exit slots that are sized and located to duplicate the air jet that exits the prediffuser in the actual engine. A natural gas fired preheater is used to provide vitiated air to the rig at the desired inlet temperatures.

The test fuel was pumped from the fuel storage tank, through a 90 micron fuel filter and a turbine flow meter, then split into a high flow leg and a low flow leg. The high flow leg had valves designed to meter the fuel flow at the simulated cruise operating condition, while the low flow leg was sized for a flight idle condition. Use of the two legs provided capability to cycle fuel flow from high flow to low flow conditions rapidly and without without large swings in fuel temperature.

Downstream of the flow control valves was a co–flow tube and shell heat exchanger. Thermanol 55 oil heated using a Chromalox Electric Fluid Heat Transfer System was used to heat the fuel. A very large heat exchanger was used to minimize prestressing of the fuel due to high temperature surfaces in the heat exchanger. For example, the Thermanol 55 temperature was only required to be 375°F (464 K) to heat the fuel to 350°F (450 K).

All of the test fuel was burned within the test rig. None of the fuel was recycled because of the concern that recycled fuel would affect the thermal stability characteristics of the test fuel.

The test fuel, provided by the US Navy, was JP–5 from a batch designated as NAPC–33. This was a fuel with poor thermal stability that was selected intentionally to increase the severity of the cyclic durability tests. Fuel properties from a pretest laboratory analysis are summarized in Table 5.

The test fuel thermal stability does not meet the JP–5 Specification, probably due to high copper levels. The fuel failed at 260°C because it plugged the upstream filter. The fuel was rated as marginally acceptable at 260°C when the sample was filtered before conducting the JFTOT test. Specific gravity, hydrogen content and sulfur content are typical of available JP–5 fuels.

Table 5. Test Fuel Properties.

Property	Test Fuel	Specification
JFTOT Breakpoint, °C	240	>260
Specific Gravity	0.8169	0.788–0.845
Hydrogen Content, Wt %	13.61	>13.40
Sulfur Content, %	0.071	<0.4
Copper Content, ppb	50.6	N/A

Test Procedures

The most severe flight condition for a fuel injector is typically the transient throttle chop from cruise to flight idle. The test conditions used in the cyclic durability evaluation simulated an extreme example of the transient with the following two–minute cycle:

Condition	Cruise	Flight Idle
Time, min	1.0	1.0
Inlet Air Temperature, °F(K)	1200(922)	500(533)
Pressure, psia(Atm)	17.3(1.18)	16.5(1.12)
Airflow, pps(kg/s)	0.86(0.39)	0.86(0.39)
Fuel/Air Ratio	0.0226	0.0065
Fuel Temperature, °F(K)	350(450)	310(428)

The airflow rate of 0.86 pps (0.39 kg/s) provides an average Reynolds number at the simulated diffuser exit that is very close to the engine condition during cruise operation. This provides heat transfer characteristics in the rig that are similar to those in the engine.

Fuel nozzle testing was completed in two test periods. The first test period consisted of 40 hours of testing (1200 cycles) at the above test conditions. An additional 36 hours of testing (1080 cycles) was

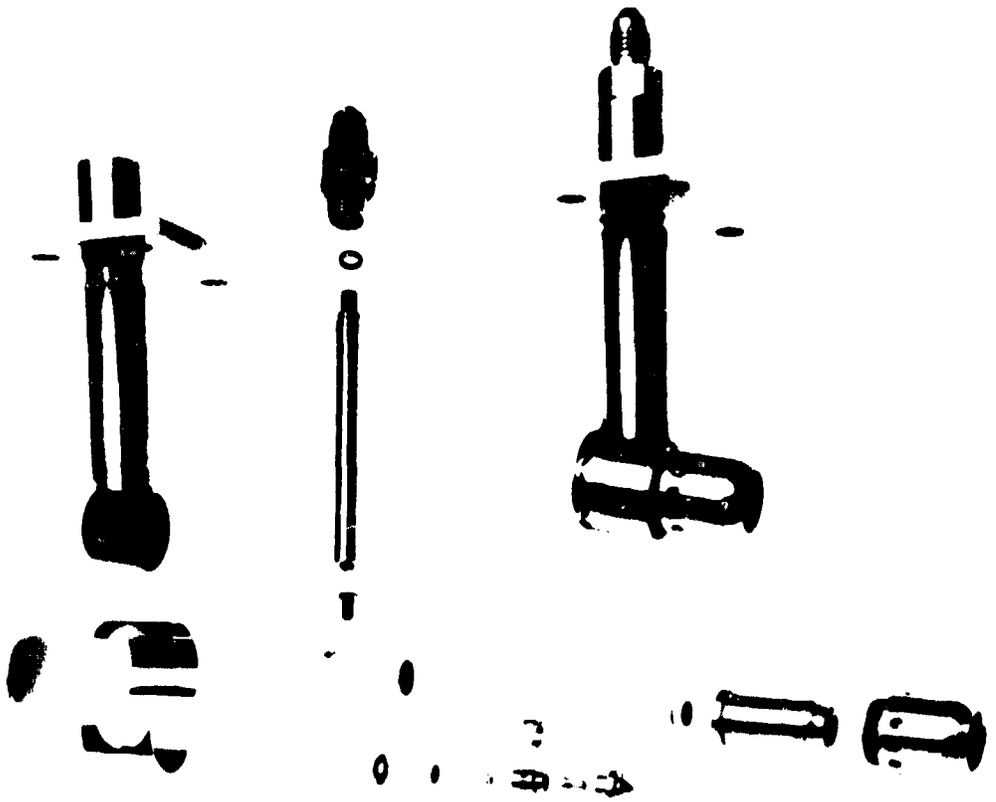

Figure 14. Exploded View of Innovative Fuel Nozzle Shows Internal Components.

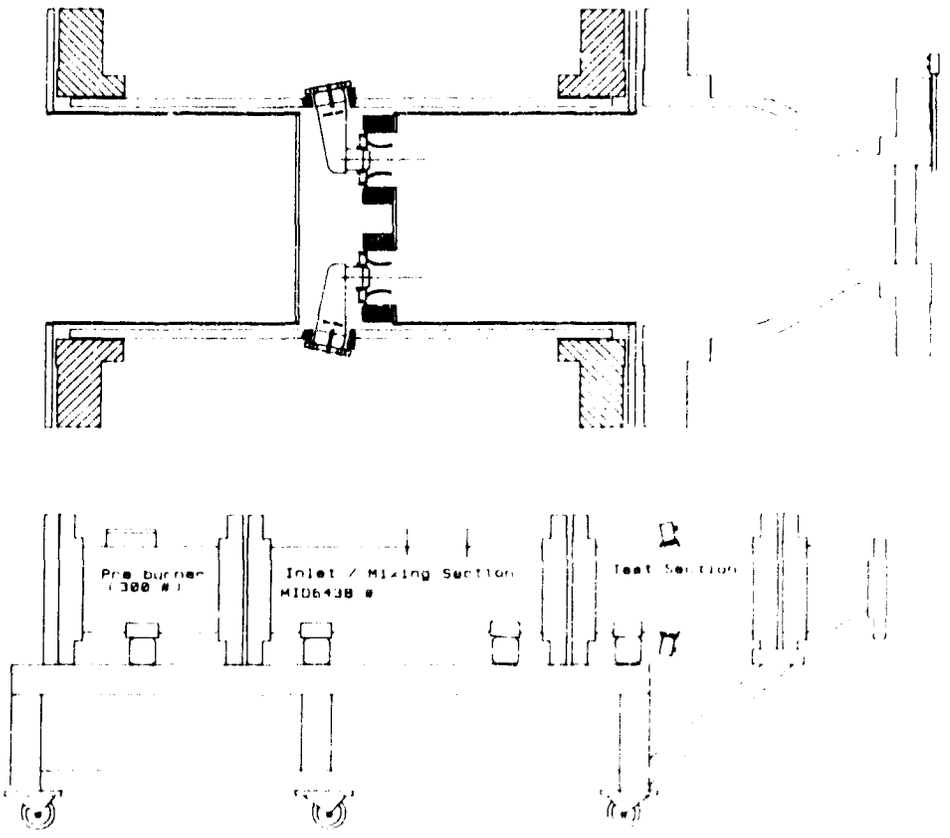

Figure 15. Thermal Cyclic Test Rig Evaluates Two Fuel Nozzle at Once.

completed with fuel temperature at the cruise condition increased to 375°F (464 K). During the tests, fuel pressure was monitored to determine if the fuel nozzles were becoming blocked.

Test Results

After the initial 40-hour test period was completed with no clear indication of flow reduction based on rig fuel pressures, the fuel nozzles were removed and precision flow caliorated to determine whether any blockage had occurred. These flow calibration tests indicated that the metering area in the secondary circuit of both the baseline and innovative nozzles had been reduced by five to seven percent.

The additional 36 hour test period was then completed with fuel at higher temperature to accelerate the rate of deposit formation within the nozzles. After this second test period was concluded, the nozzles were again removed and recalibrated. The innovative nozzle flow area was found to be reduced by 20 percent. while the baseline nozzle flow area was reduced by 13 percent.

At the conclusion of the second test period, the fuel injectors were examined using a GE X-Ray Inspection Module using a 420KeV x-ray source to determine where the flow blockages were occurring.

Computed Tomography (CT) images of the innovative fuel nozzle tip are shown in Figure 16. Carbon accumulation is indicated by an uneven intensity in the image, as described in the lower right-hand view of the innovative nozzle tip. The flow reduction in the innovative injector appears to be due to buildup of small carbon particles at the inlet to the secondary injector swirl slot.

The buildup of carbon shown in the CT scan images of the innovative nozzle is probably due to accumulation of small particles which form upstream in the nozzle and adhere to the secondary metering set in the low velocity region upstream of the secondary orifice swirl slots. Recall that the metering set used in the innovative nozzle is the same geometry and material used in the baseline nozzle. This could be an indication that the smooth, inert surfaces upstream of the metering set are working properly in preventing particles from adhering to the surface. However, the particles appear to move downstream with the fuel and stick to the metering set, which does not have any special surface treatment. Accumulation of particles could potentially be avoided by streamlining the flowpath at the inlet to the metering slots and polishing the surface of the swirl slots to minimize sticking of the particles.

Additional thermal cyclic durability tests will be conducted to build up additional deposits in the baseline and innovative fuel nozzles. The additional tests will be conducted using a US Navy supplied marine diesel fuel to accelerate deposition. The nozzles will then be cut open to identify the exact location of blockages.

7. CONCLUSIONS

An innovative single-inlet/dual-orifice fuel nozzle was designed to operate at maximum combustor air and fuel temperatures of 1600°F (1144 K) and 350°F (450 K), respectively. The design approach was to minimize fuel passage wetted wall temperatures with improved heat shielding and reduce the fuel coking rate by treating the fuel passage surfaces. A novel flow divider valve in the tip was also included in the design.

Heat transfer analysis showed that reduced fuel passage flow area, additional insulating air gaps and replacement of metallic tip components with ceramics minimized the wetted wall temperatures. Vacuum gaps, reduced emissivity coatings, and thermal barrier coatings did not offer significant wetted wall temperature reductions.

Sample tube coking tests showed that polishing the fuel passage surface reduced the coking rate. The coking tests also demonstrated that the type of deposition depended on the wetted wall temperature. Hard varnish formed at wetted wall temperatures of 475°F (519K) and soft carbon deposits occurred at wetted wall temperatures of 575°F (575K). However, the partially stabilized zirconia surface formed soft carbon at both 475 and 575°F.

Cyclic coking tests showed that additional smoothing of the aerodynamic flowpath and improved surface treatments will be required in the fuel nozzle tip to meet the high temperature durability goals of this program.

8. ACKNOWLEDGMENTS

This work was funded by the Naval Air Warfare Center (NAWC) under contract N00140-87-C-6321. Portions of this paper were modified from ASME Paper 92-GT-132.

9. REFERENCES

Chin, J.S. and Lefebvre, A.H., "Temperature Effects on Fuel Thermal Stability," ASME Paper 91-GT-97, June 1991.

Lyon, T.F., "Fuel Thermal Stability Outlook for GE Aircraft Engines in 1991," Aviation Fuel: Thermal Stability Requirements, ASTM STP 1138, Perry W. Kirklin and Peter David Eds., ASTM, Philadelphia, 1992.

Marteney, P.J., Colket, M.B., and Vranos A., "Experimental Study of the Thermal Stability of Hydrocarbon Fuels," NASA CR-168027, December 1982.

Marteney, P.J. and Spadaccini, L.J., "Thermal Decomposition of Aircraft Fuel," ASME Paper 86-GT-35, June 1986.

Myers, G.D., Armstrong, J.P., White, C.D., Clouser, S., Harvey, R.J., "Development of an Innovative High Temperature Gas Turbine Fuel Nozzle," ASME Paper 91-GT-36, June 1991.

Stickles, R.W., Dodds, W.J., Koblish, T.R., Sager, J. and Clouser, S., "Innovative High Temperature Aircraft Engine Fuel Nozzle Design," ASME Paper 92-GT-132, June 1992.

Taylor, W.F. and Frankenfeld, J.W., "Development of High Stability Fuel," Final Report for Phase II Naval Air Propulsion Center Contract N00140-74-C-0618, December 1975.

Wickesheim, K. and Sun, M., "Phosphors and Fiber Optics Remove Doubt from Difficult Temperature Measurements," Research and Development, November 1985.

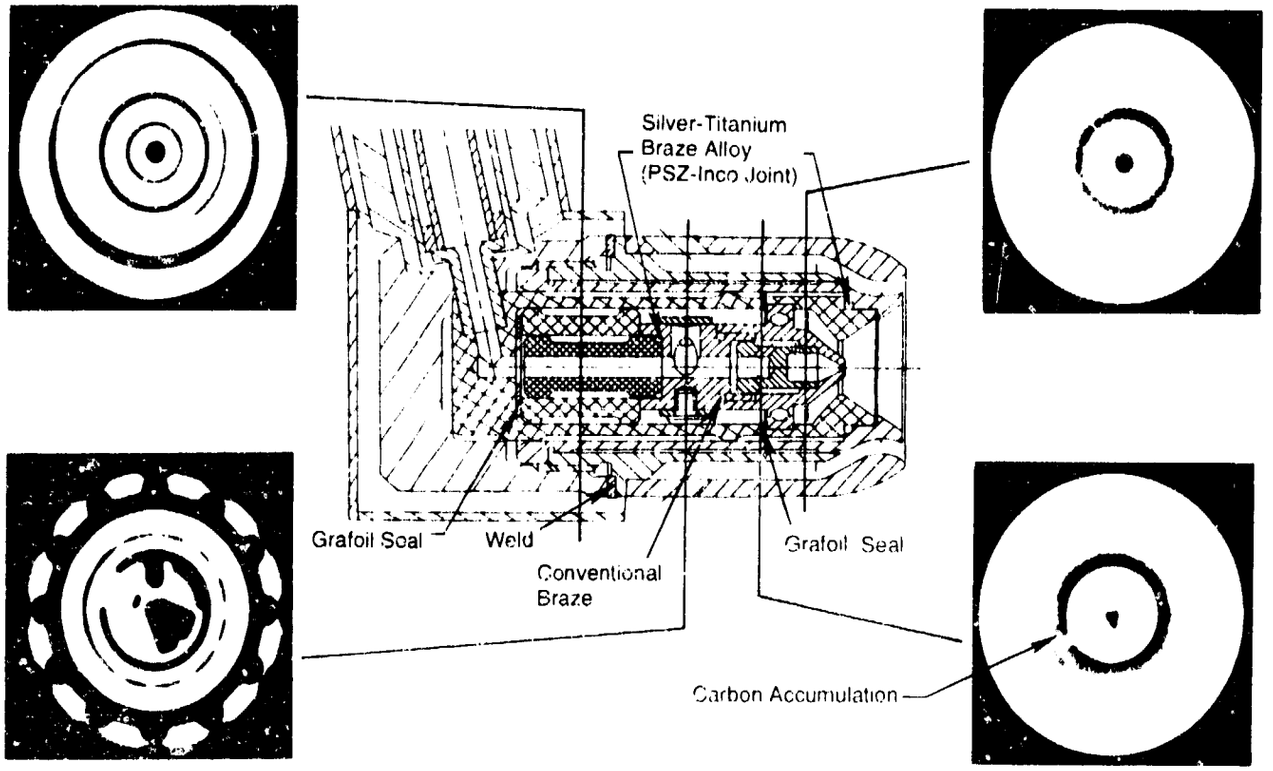

Figure 16. Computed Tomography Images of Innovative Fuel Nozzle Tip.

Discussion

Question 1. R. Jeckel
The 76 hour test demonstrated that the coke deposition has been decreased dramatically by using polished surfaces. However, is this of significance with respect to the typical times that aircraft are in the air between maintenance checks?

Author's Reply
Even though the test was conducted over a period of only 76 hours, the cyclic nature of the test (2,280 cycles) and the use of poor fuel made each test hour equivalent to many flight cycles.

Design Aspects in Small Aircraft Gas Turbine Fuel Injectors

K. McCaldon, L.A. Prociw, P. Sampath
Pratt & Whitney Canada Inc.
A Division of the United Technologies Corporation
6375 Dixie Road, Mississauga, Ontario, Canada L5T 2E7

1.0 Summary

The causes of fuel injector spray deterioration and the effects of this deterioration on engine durability and performance are discussed. Small aircraft gas turbine fuel injectors present special design challenges due to low fuel flow rates involved and the physical size limitations. The principal fuel injector performance requirements are discussed in relation to their effect on the hydraulic, aerodynamic, and thermal design of aerating fuel injectors.

2.0 Introduction

Fuel injectors play a crucial role in the durability and performance of gas turbine engines[1]. Fuel injector deterioration can influence starting, carbon deposition, smoke, exhaust emissions, hot end durability, and combustion noise. The ability of an injector design to maintain consistent performance over the period of operation between engine overhauls is critical to hot end durability and low operating cost. It is widely accepted that fuel injector designs, particularly aerating injectors, must be closely integrated with the design of the combustor.

The requirements of small gas turbine engines bring some special challenges to the design of a fuel injector. Small physical size, complex geometry, and requirements for precise control of small flows, both fuel and air, can all lead to undesirable fuel system performance deteriorations caused by minute flow perturbations. The need for improved understanding of the operation of the combustion system underscores the requirement for better modelling of flow interactions between the combustor and the fuel injector. This paper takes a close look at some of the details of injector component design for small gas turbine engines.

3.0 Operational Problems

Many older designs of gas turbines have used pressure swirl atomizers to atomize and distribute the fuel within the combustor. In small gas turbines, particularly those with reverse flow annular combustors, the fuel flow rates per injector and therefore nozzle Flow Numbers, are low so as to ensure good fuel distribution and adequate fuel pressure drops for atomization under all conditions. As a result, the swirl inducing and fuel metering orifices can have linear dimensions as small as 200 microns (0.008 in.), Figure 1. The fuel passages are often convoluted, particularly in the regions near the fuel metering orifices. This geometry creates local regions immediately adjacent to the fuel metering orifices where the fuel velocity is low, and thermal degradation and coking can occur.

In addition, the heat load in this region is often magnified by minimal wall thicknesses, exterior air flows introduced to prevent soot accumulation, and radiative heat load from combustion gases (Figure 2). Even with the relatively modest compressor discharge air temperatures of small gas turbines, the heat load can easily create conditions conducive to coking. The small fuel metering hole sizes inevitably make the pressure swirl atomizer extremely sensitive to solid coke formation. Coke agglomerates can break off from the regions where they form by subsequent engine operations and be carried into the metering passages. Engine operations may also contribute to internal coke formation; engine decelerations from high power or hot shutdowns may greatly reduce or completely shut off fuel flow in hot fuel passages, contributing to the coking described above. Such degradations can affect the durability of the combustor and the rest of the engine hot end.

The use of airblast injectors in small engines was initiated in an attempt to improve fuel/air mixing and obtain the advantages offered by larger injector passage. Utilising the combustor air pressure drop to atomise the fuel allows the Flow Number of the nozzle tip to be set by the fuel distribution requirements and much larger fuel passages can be used in the nozzle tip. Trim restrictors can be used in relatively cool regions to control the circumferential fuel distribution within the engine, keeping the smallest fuel passages upstream of the regions where coke is prone to occur (Figure 3).

Unlike the success found with large engines, the benefit of airblast injectors has not always been realized in small engine applications. Typical cold day starting, often requires ignition at combustor pressure drop levels of less than 25 mm (1 inch) of water with high viscosity (22cs) fuel. The inability of airblast systems to meet these requirements has prevented pure airblast systems from completely displacing pressure atomizers from small engine designs[2]. In such cases airblast must be supplemented with pressure atomizers in a hybrid configuration to maintain adequate performance over the entire operating envelope (Figure 4).

In addition to poor sub-idle performance, low pressure fuel systems can lead to fuel distribution problems at very low flow rates when effects of gravity become dominant. This can be a detriment to the performance of the fuel system, and to the durability of the injector. Various means of correcting this problem have been found but at additional cost and complexity to the system.

The effects of a partially or totally blocked fuel metering passage will vary with the fuel system design and engine operating conditions. Figure 5 is a comparison of spray patternation from an airblast nozzle before and after engine test, demonstrating the effect of partial blockage and coking on spray distribution. The global effects of progressive fuel system deterioration on combustor exit temperature profiles are shown in Figure 6. As more and

Presented at an AGARD Meeting on 'Fuels and Combustion Technology for Advanced Aircraft Engines', May 1993.

more fuel metering holes are obstructed with increasing operating time, more fuel is forced through the remaining nozzles. Consequently, engine damage may be caused by those injectors which, if tested individually, still flow within tolerances. Indeed, of the fuel injectors represented in Figure 6, only about 30% were outside of required flow tolerance limits.

These local flow deviations can also have other undesirable side effects, such as reduced stability, increased smoke, combustor carbon growths, and torching on start. Deteriorated fuel systems may also have disproportionate effects at off-design conditions, particularly during the acceleration to idle, as seen in Figure 7. During starting, fuel/air ratios can be so high that turbine temperatures can easily exceed those experienced during the rest of the cycle. Local increases in fuel flow rate caused by fuel system deterioration can magnify this effect, and may cause dramatic hot end damage.

In summary, the following overall design strategies can be employed to improve the resistance of a fuel system design to deterioration:

- Minimize the temperature of metal exposed to the fuel (wetted wall temperature), and the temperature of the incoming fuel, to prevent thermal degradation of the fuel.
- Maintain both a minimum fuel velocity and a minimum fuel passage size through all the fuel injector regions exposed to compressor discharge air, throughout the normal engine operating cycle.

4.0 Detailed Design Considerations for Airblast Injectors

Although the external airflow around typical pressure atomizer designs can be quite substantial, Figure 2, very little effort has traditionally been expended to utilize this air in a role other than attempting to wash the injector face. Often, the use of air as a means of controlling face carbon was not entirely successful. However, it is also recognized that air in a pressure atomizer plays a useful role in neutralizing effects of streaky sprays and drooling, and in emission control.

Airblast injectors depend on efficient use of air to assist in fuel atomization. Through careful engineering of aerodynamics, recognizing the forces involved in atomization, the use of air improves spray development at much lower fuel pressure than with a pressure atomizing nozzle. The addition of air with the fuel through the injector has also been found to be an effective method of reducing smoke and emissions. To meet new emission requirements, particularly oxides of Nitrogen, even more air may be used in future injector designs.

In current configurations, it is not uncommon for airblast injectors to be operating with air to fuel ratio in the range 2 or 3 to 1[1]. The total flow through the injectors may represent 20 - 30% of the primary zone flow. Because it is introduced through relatively small number of locations, the injector flow represents a high mass and momentum concentration relative to the remainder of the air entering the combustor primary zone and can affect all aspects of combustor performance - starting, smoke, emissions, pattern factor, stability and wall temperatures. The fuel injector design cannot therefore be treated in isolation of the combustor design.

4.1 Injector Component Details

The typical small engine airblast injector is comprised of three basic components. These are the outer air swirler, the fuel swirler and the core air swirler Figure 8.

4.2 Outer Swirler Design Considerations

The outer swirler plays an important role in atomization, fuel distribution (patternation) and development of flame stability. Because of its large diameter, this swirler carries the greatest proportion of the injector flow. The angular momentum injected by the outer swirler results in a central recirculation zone along the axis of the injector flow field, Figure 9. This recirculation is important to stability and ignition, creating a zone where low speed flame fronts can exist to anchor the flame.

Conventional outer swirler designs have utilized bladed axial swirlers or stators to impart angular momentum to the air stream. Feed air is usually swirled at a large diameter and subsequently accelerated through an annular nozzle to interact with the fuel film at a pre-defined air fuel interface. Although there is scope in larger injectors to design the swirler blades according to aerodynamic rules with respect to incidence angles, blade thickness to chord ratios and curvature effects, size and low cost requirements often make this practice prohibitive for practical small injectors. Small scale designs tend to use a minimum number of straight blades of relatively thick construction. The discharge coefficients (Cd) of the resultant air passages are adversely affected by these characteristics and this generally results in either a lower through flow than desired for a given diameter of injector, or a larger injector diameter requirement. Unlike conventional large engine designs, the approach flow in small combustors may not be along the axis of the nozzle. This further aggravates the incidence on the air passage entrances and can lead to large scale separations in the swirler passages as shown in Figure 10. The wakes and separations from the thick blades give rise to a downstream flow field resembling discrete jet flows which coalesce before approaching the nozzle tip. The appearance of these jet like flows can be seen in the Computational Fluid Dynamic (CFD) results and similar patterns are also visible in experimental nozzles, Figure 11. These jet structures are considered useful by some in that they add both mixing and stability to the eventual combustor flow field. However since their design is seldom deliberate, the pressure drop penalty and the possibility of vortex shedding and other oscillatory behaviour leading to instability are usually considered to be negative features of this flow behaviour.

Since angular momentum is added to the flow before the contracting section, an unfavourable pressure gradient due to swirl develops in the nozzle, opposing the air flow. This gradient is inversely proportional to the radius of the injector and hence is more severe in small injectors. The gradient not only results in an additional penalty to the overall Cd of the swirler, but can also lead to premature separation of the flow from the inner face of the injector near the end of the outer shroud. This flow separation can promote carbon deposition and excessive heating of the critical interface area and contribute to coking inside

the injector on the fuel swirler face. The dark area seen around the fuel lip in Figure 12 is a result of flow separation. In addition, the penetration of the shroud into the combustor must be minimized so as not to interfere with the fuel spray trajectory during low air flow conditions such as slam accelerations.

A lost cost alternative is the use of radially oriented, off axis jets to serve as swirlers, Figure 12, eliminating the need for axial blades. The flow in this swirler eliminates the adverse pressure gradient due to centrifugal effect. Detailed laser measurements have indicated that an adequate swirling field can be generated within the combustor from this arrangement. Atomization achieved is also satisfactory. The absence of the adverse radial pressure gradient allows greater impact of the air at the fuel interface and the separation tendencies in the critical fuel interface areas are eliminated. The simplicity of the arrangement as well as its relatively compact size is evident from the geometry.

4.3 Core Air Swirler Design Considerations

While an outer swirler can be added to any fuel injection device, the presence of the core swirler separates the airblast injector from the pressure atomizer. This swirler does not usually carry as much air as the outer swirler due to its location along the axis of the injector. However, its role is crucial in keeping the face of the injector clean and in achieving good atomization quality fuel film. The core swirler also plays a role in developing the stability generated by the injector. Unswirled core flows have resulted in unacceptably high concentrations of fuel from the injector, Figure 13, and lead to excessive smoke and high wall temperature gradients, which can be difficult to control.

A simple design of core air swirler employees an air tube with multiple tangential jet feeds around its periphery, Figure 8. This design is effective in generating core swirl; however contamination from rich combustion products can occasionally occur under back flow conditions generated in some designs, Figure 14. A simple bullet placed within the core alleviates the back flow for the most part although contamination of the bullet surface is still possible. Recent designs have also included a small core jet air flow in the bullet, Figure 15, to remove the possibility of contamination of any injector surface. The LDV data, Figure 16, indicates that although a negative flow exists along the core of the flow field, the velocity falls to zero before entering the injector.

4.4 Fuel Swirler Design

The fuel swirler is a major controlling influence on the spray patternation quality. Its main function is to produce a uniform, annular fuel film from discrete jets metering fuel into the injector. The configuration of the swirler determines the ability of the injector to produce adequate sprays at low pressure for ignition and the ability to produce a useful spray with little or no air, which is required during transients such as slam acceleration manoeuvres. The fuel swirler plays a role in determining spray parameters such as cone angle and drop size distribution. Its ability to remain uncontaminated determines the durability of both the injector and ultimately the entire hot end of the engine.

5.0 CFD as a Design Tool

The components of injectors are so small that gaining flow information about the processes occurring within a component is extremely difficult. The capabilities of Computational Fluid Dynamics (CFD) are often used to gain insight into the flow field generated within the components and how these fields may interact with the combustor. This is particularly true for details involving the flow within the fuel filmer. Figure 17 is an example of a study which was conducted to determine the minimum fuel distributor jet injection angle required to generate a continuous film within the geometry of the fuel filmer chamber. The minimum angle was sought in an attempt to minimize the resulting fuel spray cone angle without the use of air. This is important to the design of the injector since under some transient conditions, such as slam acceleration, when the fuel flow increase leads the air flow rise during the acceleration process. Under these conditions excessive fuel swirl can result in spray cone angles exceeding 180 deg. When combined with surface tension forces, the fuel may cling to the surface of the injector face and exit through the outer swirler out of the combustor.

Fuel jets varying in orientation from 10 to 40 degrees from the axial were modeled. The velocity distribution at the end of the fuel filmer was monitored to determine the first indication of a uniform, continuously distributed film. At ten degrees injection angle, the flow at the end of the swirler section was predicted to be discontinuous and unable to form a uniform film for the atomization process. At twenty degrees injection angle the flow was predicted to be continuous and adequate for design of the injector. Modelling results were also verified by experiment, Figure 18. The 20 degree injector angle resulted in continuous & well shaped filmer flows.

A second example of the use of the CFD in the injector design process is in the prediction of flow distortions to the feed of an injector swirler. As mentioned previously, the flow feeding the swirler in small engines is seldom oriented with the axis of the injector. In many situations, injectors that are mounted radially with respect to the combustor are encapsulated within a sheath as shown in Figure 3. The sheath size can impose unfavourable effects on the flow field into the swirler. To assess this impact a CFD model of the injector and the surrounding sheath was utilized. Diminishing flow distortions resulting from increasing sheath diameters are shown in Figure 19.

6.0 Conclusions

Although constrained by size, weight, and cost limitations, proper hydraulic and aerodynamic design practices can help ensure durable fuel injectors for small gas turbine engines. As general rules, minimising the temperature of the incoming fuel and the metal in contact with it, maintaining a minimum fuel velocity within the region of the fuel injector exposed to compressor discharge air and maintaining a minimum fuel passage size will help desensitize the fuel system to thermal degradation of the fuel. Proper fuel system design to prevent fuel shut off of some fuel injectors during engine deceleration, and adequate cool down time prior to engine shut down also help prevent fuel breakdown. Ultimately, the ability of a design to maintain consistent performance

over the period of operation between engine overhauls is critical to hot end durability and minimum repair cost.

Computational Fluid Dynamics can be useful to gain insight into the complicated flow fields generated by the various components of an aerating fuel injector. CFD has been used to accurately represent the flow in and around small gas turbine fuel injectors, and has been instrumental in identifying design problems and solutions.

The importance of careful design of the core and outer air flows, and the fuel filming devices have been reiterated. Alternative designs to ensure good injector performance have been suggested.

References:

1. "Gas Turbine Combustion" - A.W. Lefebvre, McGraw Hill Series, 1983.

2. I. Critchley, P. Sampath, F. Shum, Cold Weather Ignition Characteristics of Advanced Small Gas Turbine Combustion Systems, AGARD Propulsion & Energetics Panel, 76th Symposium, October 1990.

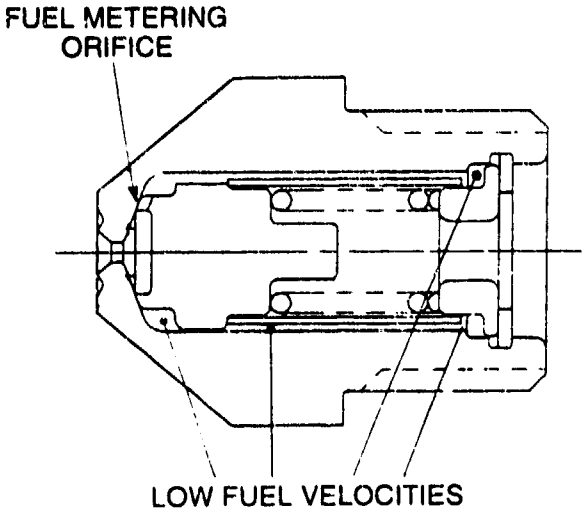

Fig. 1: Typical pressure atomizing fuel injector

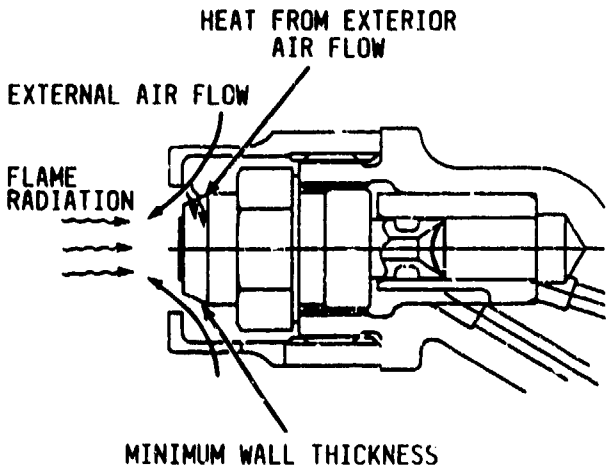

Fig. 2: Flow fields around typical pressure atomizing fuel injector

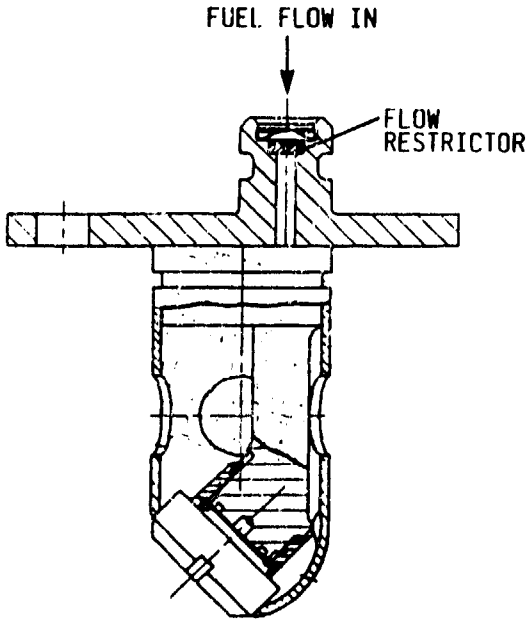

Fig. 3: Typical aerating fuel injector

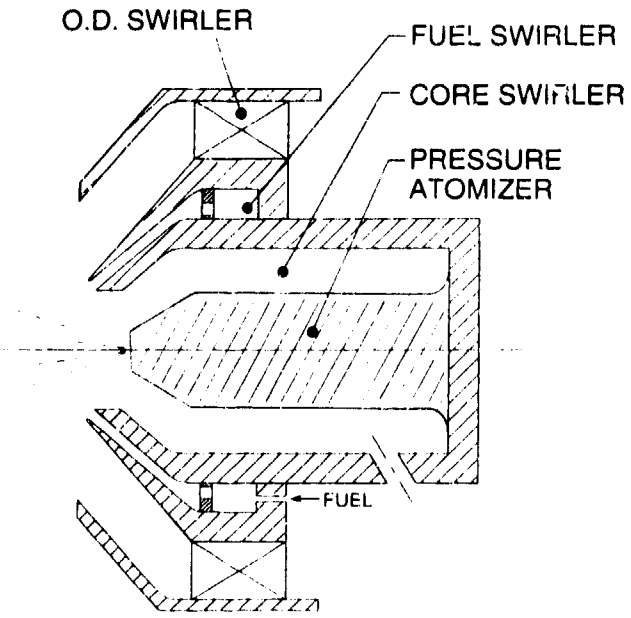

Fig. 4: Schematic of a hybrid injector

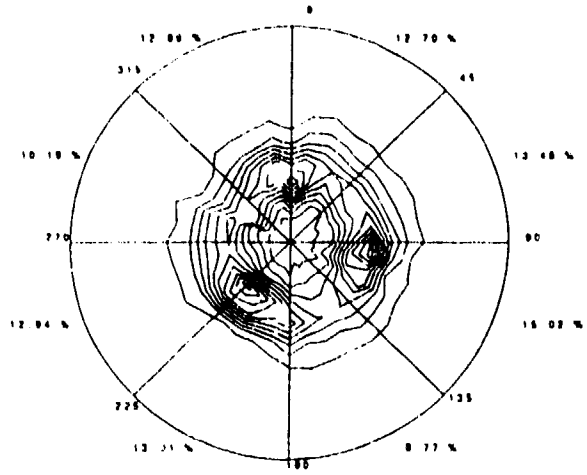

CLEAN NOZZLE

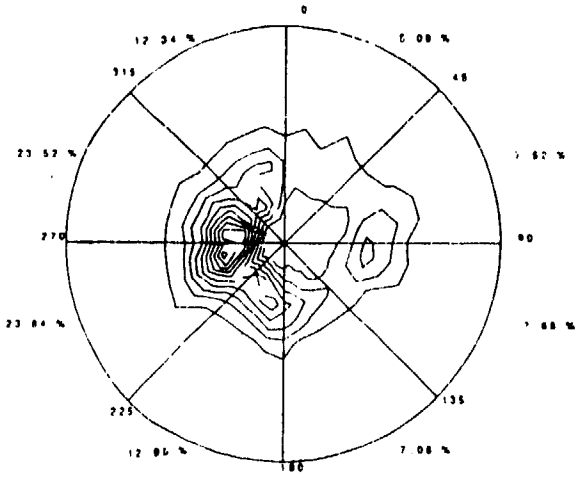

COKED NOZZLE

Fig. 5: Effect of coking on aerating fuel nozzle flow distribution

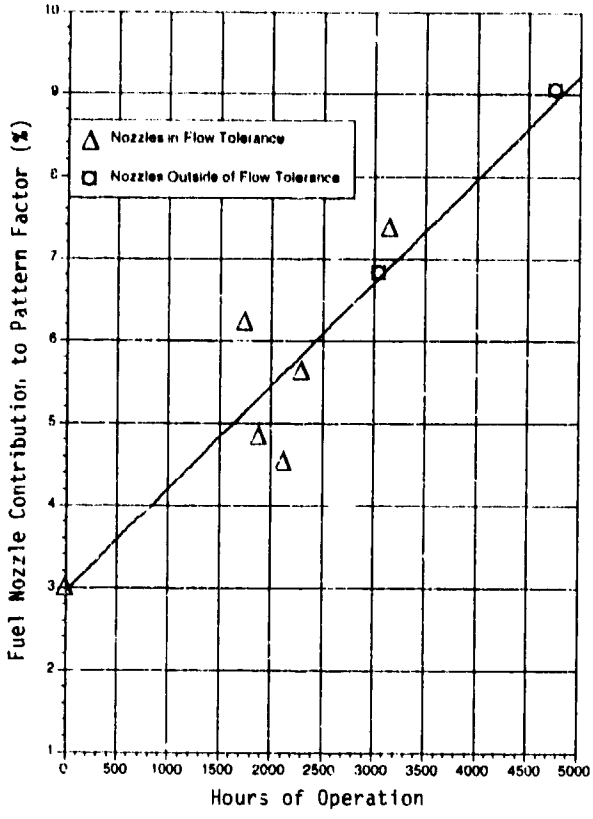

Fig. 6: Effect of fuel injector blockage on combustor exit temperature profile

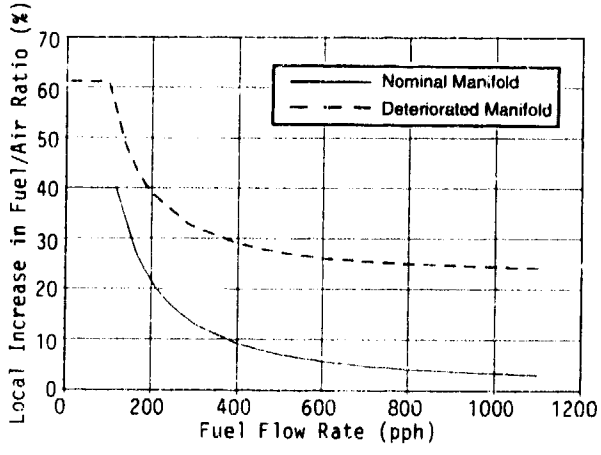

Fig. 7: Effect of injector deterioration on local fuel/air ratio

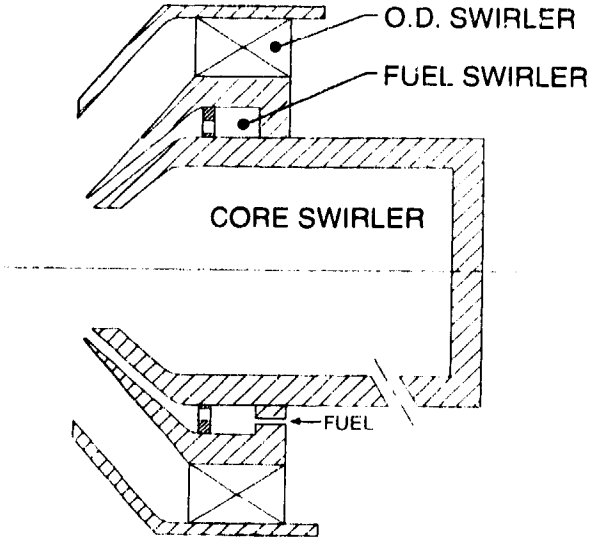

Fig. 8: Basic components of a typical airblast injector

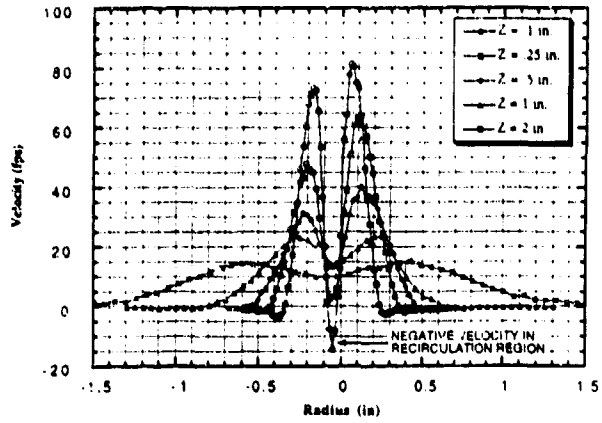

Fig. 9: Axial velocity distribution downstream of a typical airblast injector

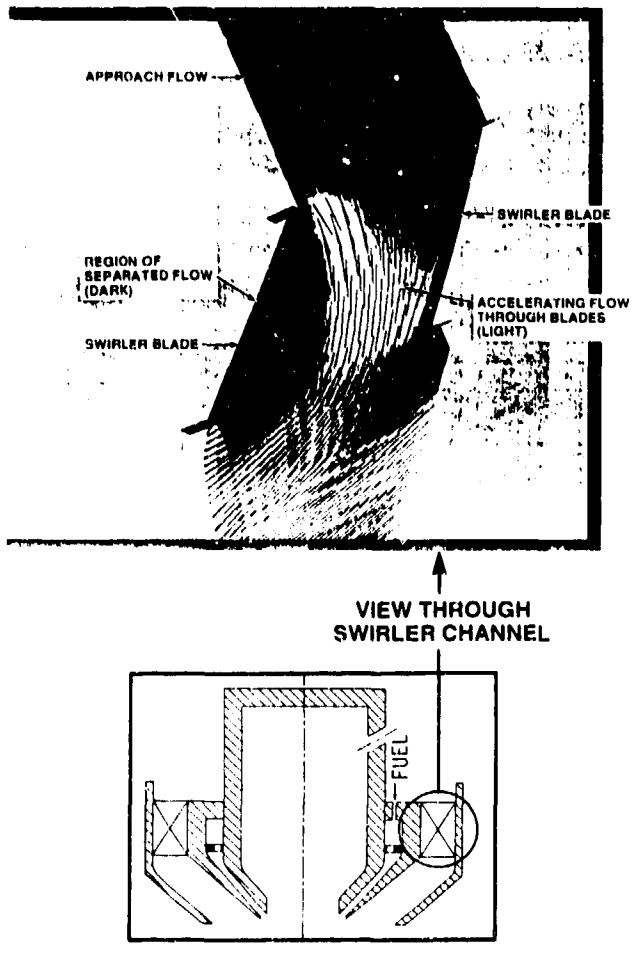

Fig. 10: CFD result of flow through O.D. swirler

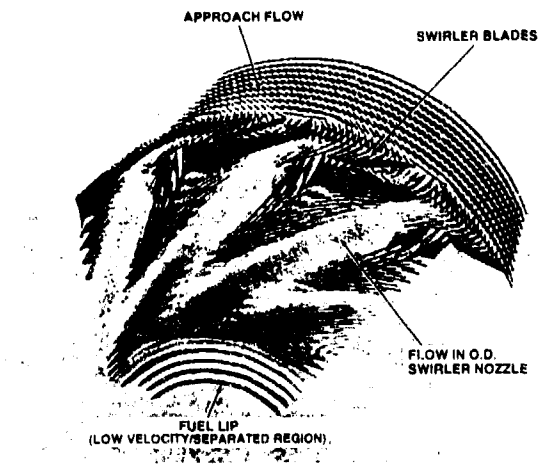

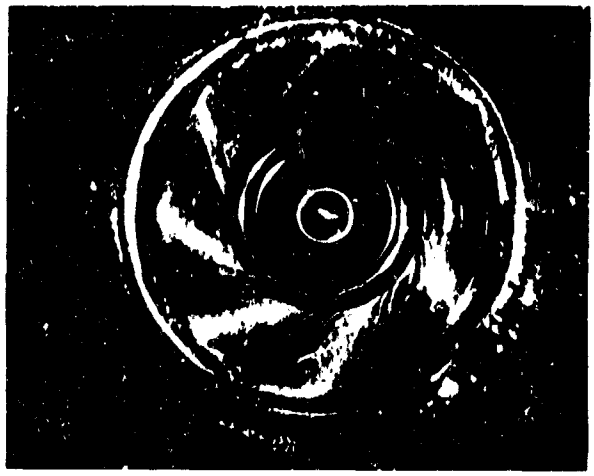

Fig. 11: Jet like flows arising in wake of swirler blades

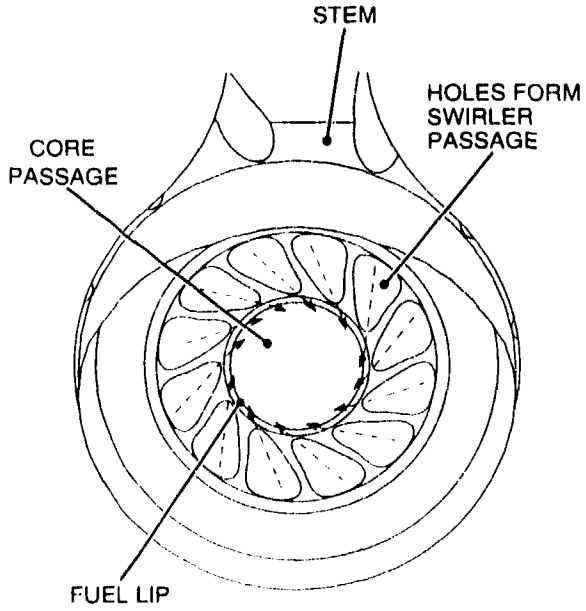

Fig. 12: Front view of a generic swirler formed from round jets

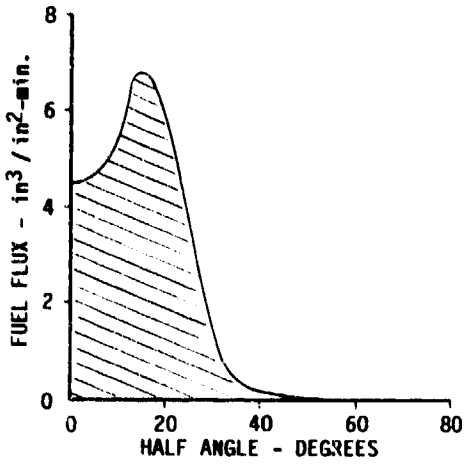

WITH NO CORE AIR SWIRL

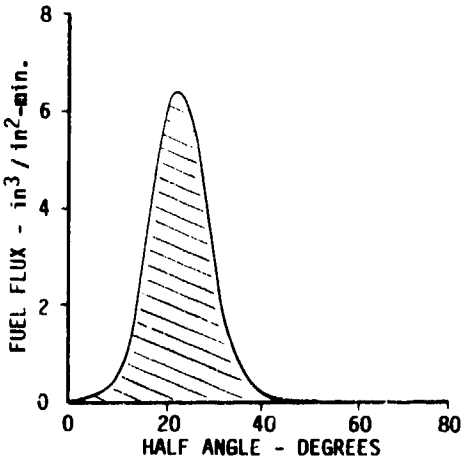

WITH CORE AIR SWIRL

Fig. 13: Effect of core air swirl on airblast atomizer performance

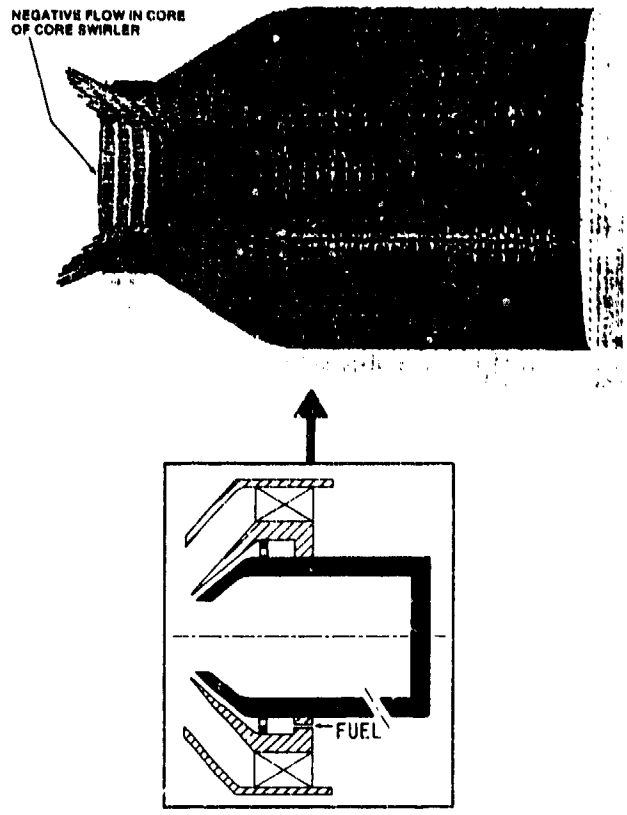

Fig. 14: CFD result showing negative or backflow into core swirler

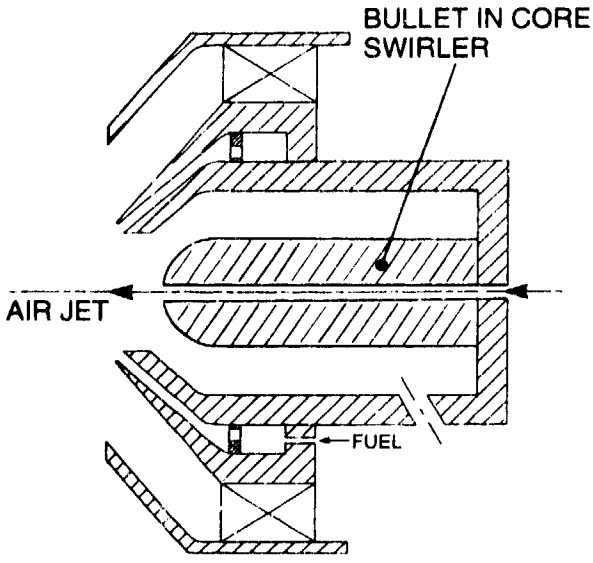

Fig. 15: Addition of a bullet in core with a simple jet through bullet

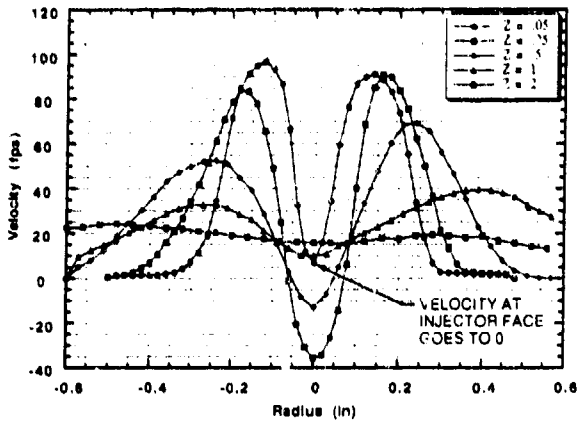

Fig. 16: Effect of bullet flow jet on axial velocity distribution

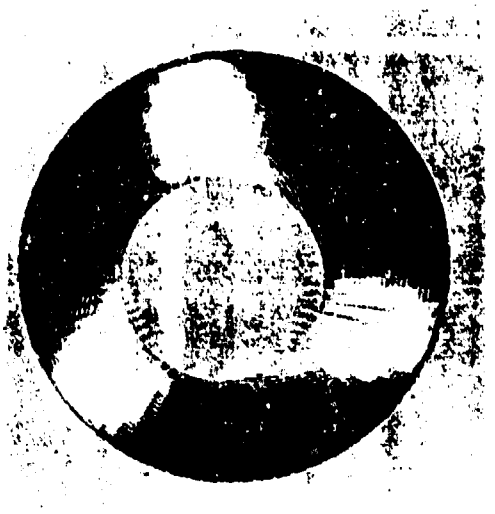

10° INJECTION ANGLE

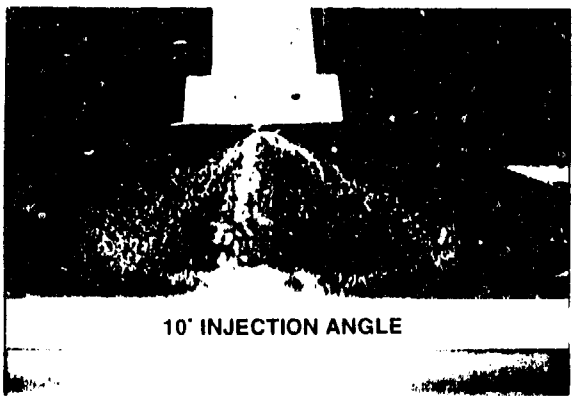

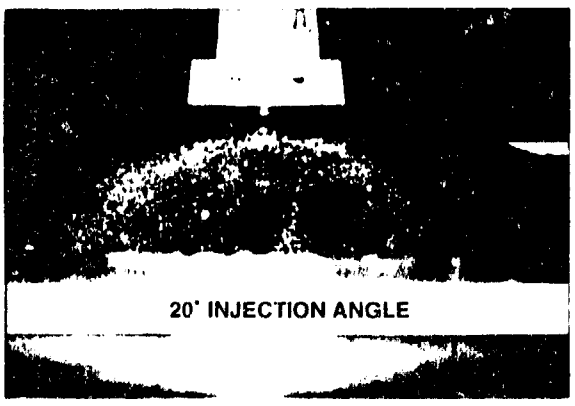

Fig. 18: Fuel spray distribution with 10 & 20 degree injection angles

20° INJECTION ANGLE

Fig. 17: Effect of distributor jet angle on fuel film continuity

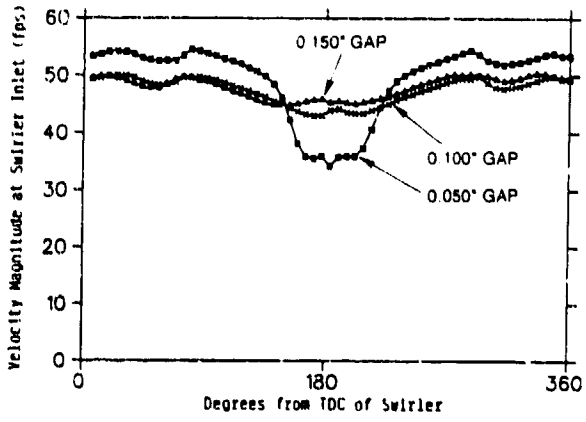

Fig. 19: Velocity distribution at swirler inlet as a function of minimum gap between sheath and injector

THE EFFECT OF INCOMPLETE FUEL-AIR MIXING ON THE LEAN LIMIT AND EMISSIONS CHARACTERISTICS OF A LEAN PREVAPORIZED PREMIXED (LPP) COMBUSTOR

D. A. Santavicca
R. L. Steinberger
K. A. Gibbons
J. V. Citeno
S. Mills
Department of Mechanical Engineering
Propulsion Engineering Research Center
Penn State University
University Park, PA 16802
USA

SUMMARY

Results are presented from an experimental study of the effect of incomplete fuel-air mixing on the lean limit and emissions characteristics of a lean, prevaporized, premixed (LPP), coaxial mixing tube combustor. Two-dimensional exciplex fluorescence was used to characterize the degree of fuel vaporization and mixing at the combustor inlet under non-combusting conditions. These tests were conducted at a pressure of 4 atm., a temperature of 400°C, a mixer tube velocity of 100 m/sec and an equivalence ratio of .8, using a mixture of tetradecane, 1 methyl naphthalene and TMPD as a fuel simulant. Fuel-air mixtures with two distinct spatial distributions were studied. The exciplex measurements showed that there was a significant amount of unvaporized fuel at the combustor entrance in both cases. One case, however, exhibited a very non-uniform distribution of fuel liquid and vapor at the combustor entrance, i.e., with most of the fuel in the upper half of the combustor tube, while in the other case, both the fuel liquid and vapor were much more uniformly distributed across the width of the combustor entrance. The lean limit and emissions measurements were all made at a pressure of 4 atm. and a mixer tube velocity of 100 m/sec, using Jet A fuel and both fuel-air mixture distributions. Contrary to what was expected, the better mixed case was found to have a substantially leaner operating limit. The two mixture distributions also unexpectedly resulted in comparable NO_x emissions, for a given equivalence ratio and inlet temperature, however, lower NO_x emissions were possible in the better mixed case due to its leaner operating limit.

INTRODUCTION

A major consideration in the development of advanced high performance gas turbine engines for aircraft applications is reduced NO_x emissions. This is especially true as combustion chamber temperatures and pressures are increased in order to improve engine performance, since both of these factors result in greater NO production. The need for reduced NO_x emissions is motivated by concerns regarding the impact of NO_x emissions on the upper atmosphere, particularly in terms of the destruction of ozone [1-3]. These concerns have led to the establishment of strict aircraft emissions regulations [4,5].

Over the years, a number of strategies have been considered for reducing NO_x emissions from gas turbine combustion systems, including variable geometry combustors [6-10], staged combustors [11-13], catalytic combustors [14,15], lean prevaporized premixed combustors [8-10,16], direct injection combustors [17-19] and rich burn-quick quench-lean burn combustors [20-22]. All of these low NO_x combustor concepts are based on the fact that thermal NO production is reduced when operating away from stoichiometric conditions. Another important feature of all the low NO_x combustor concepts is that proper control of fuel-air mixing is essential for their successful implementation. This pertains not only to achieving low NO_x emissions but also to achieving acceptable lean stability limits.

Of particular interest in this paper is the lean prevaporized premixed (LPP) concept. The LPP combustion process can be separated into three different regions. The first region is for fuel injection, vaporization and mixing, and ideally results in a totally vaporized, uniform, lean fuel-air mixture. In the second region, the flame is stabilized by the creation of a recirculation zone, while the third region is for the post-flame combustion process which is required to completely oxidize the intermediate hydrocarbons and CO. If the fuel is completely vaporized and mixed before the flame, the overall fuel lean conditions result in very low NO production. In practice, however, it is difficult to achieve complete fuel-air mixing. As a consequence, temporal fluctuations and/or spatial non-uniformity in the equivalence ratio can result in locally near-stoichiometric conditions which produce NO in excess of what is produced under perfectly mixed conditions. This suggests that the optimum LPP combustor would be one with complete fuel vaporization and mixing. Unfortunately, premixed combustors also have disadvantages in that they are prone to flashback and they have poor lean limit characteristics, both in terms of combustion stability and CO emissions. As a

Presented at an AGARD Meeting on 'Fuels and Combustion Technology for Advanced Aircraft Engines', May 1993.

result, LPP combustors exhibit a characteristic trade-off between NO_x emissions and the lean stability and lean CO emissions limits as the degree of fuel-air mixing is varied [16,18,23].

The generally accepted notion that incomplete fuel-air mixing affects both the NO_x emissions and the lean limit characteristics of premixed gas turbine combustors is based on substantial evidence from actual combustor tests [8,16,23-30]. In most of these tests, the degree of fuel-air mixing has only been varied qualitatively, e.g., by varying the fuel injection pressure. There have also been, however, a few well-controlled studies of this phenomenon, i.e., where the degree of fuel-air mixing was quantified and systematically varied, which support this view.

In 1973, Appleton and Heywood [31] reported on an experimental study of the effect of incomplete fuel-air mixing on NO and CO formation in a liquid fueled combustor. Kerosene fuel was injected on the centerline of the burner inlet using an air assisted atomizer, allowing the degree of fuel-air mixing to be varied by varying the atomizing air pressure. The degree of fuel-air mixing, which was defined as the rms fluctuation in the fuel-to-air ratio divided by the mean fuel-to-air ratio, was measured using a technique which relates the rms fluctuation in the fuel-to-air ratio to the oxygen concentration in the burned gases. They found that for near stoichiometric conditions, the NO_x emissions increased by a factor of two with increasing atomizing air pressure, i.e., better mixing, while for fuel-lean conditions, the NO_x emissions decreased with better mixing by a factor of ten over the same range of atomizing air pressure.

In 1979, Semerjian, Ball and Vranos [32] reported on the results from an experimental study very similar to the one conducted by Appleton and Heywood [31]. Jet A liquid fuel was injected on the centerline of the combustor inlet using a pressure atomizing nozzle. Unlike the Appleton and Heywood experiment where the flow was relatively uniform radially, they found the flow to vary significantly over the combustor cross-section. Therefore, not only were there temporal fluctuations in the fuel-to-air ratio, but the mean fuel-to-air ratio was spatially non-uniform. They used a technique similar to that used by Appleton and Heywood to determine the rms fluctuation in the fuel-to-air ratio, which they found varied with the fuel pressure, i.e., the fuel-to-air ratio. Their results also showed that poorer fuel-air mixing resulted in increased NO_x emissions for overall fuel lean flames and in decreased NO_x for near-stoichiometric flames, where the cross-over point occurred at an overall equivalence ratio near 0.6, as compared to a value of approximately 0.8 in Appleton and Heywood's study.

In 1981, Lyons [33] reported on an experimental study of the effect of inlet fuel-to-air ratio profile non-uniformity on NO_x emissions. The experiments were conducted at 3 atmospheres using Jet A liquid fuel. A multi-point fuel injector consisting of 17 individual injectors was used to achieve different mean fuel-to-air ratio profiles across the diameter of the flame tube. The mean fuel-to-air ratio profiles were measured using a gas sampling probe; however, the temporal rms fluctuations were not characterized. The results showed that spatial non-uniformity in the fuel-to-air ratio resulted in increased NO_x emissions for overall equivalence ratios below 0.7 and decreased NO_x emissions for overall near stoichiometric equivalence ratios.

In 1992, Flanagan *et al.* [34] reported on an experimental study using a simple mixing tube with a bluff body flame stabilizer at its exit. By changing the location of fuel (natural gas) injection along the length of the mixing tube, the degree of fuel-air mixing at the flame stabilizer was systematically varied. This method of fuel-air mixing can be expected to result in both temporal fluctuations and spatial non-uniformity in the fuel-to-air ratio. Unfortunately, the degree of fuel-air mixing was not characterized in this study. Nonetheless, the results are very interesting, given the simple experimental configuration and the systematic manner in which the degree of fuel-air mixing was varied. In the leanest case (ϕ = .66), a nearly five-fold increase in NO_x emissions was observed in going from well-mixed to incompletely-mixed conditions. It was also shown that incomplete fuel-air mixing results in greater NO_x emissions at overall equivalence ratios up to approximately 0.9.

In 1992, Fric [35] reported on an experimental study using an experimental configuration very similar to that of Flanagan et al. Fric, however, did quantify the degree of fuel-air mixing at the flame stabilizer location using an NO_2 fluorescence technique [36]. His tests were conducted at 1 atm using natural gas fuel with temporal fluctuations in the fuel-to-air ratio as large as 20 percent and spatial non-uniformities in the fuel-to-air ratio as large as 50 percent. He found that both spatial non-uniformities and temporal fluctuations in the fuel-to-air ratio can result in significantly increased NO_x emissions compared to the perfectly mixed case. For example, 10 percent temporal fluctuations resulted in a doubling of the NO_x emissions.

In order to understand the effect of incomplete fuel-air mixing on the emissions and lean limit characteristics of premixed gas turbine combustors, a number of fundamental issues need to be better understood. These issues can best be explained with reference to the simplified illustration in Figure 1. As shown, the fuel-air mixture enters the flame as pockets of reactants with different equivalence ratios. The range of equivalence ratio variation represents the rms fluctuation in the fuel-to-air ratio, and the size of the pockets represents the length scale of the fuel-to-air ratio fluctuations. It is

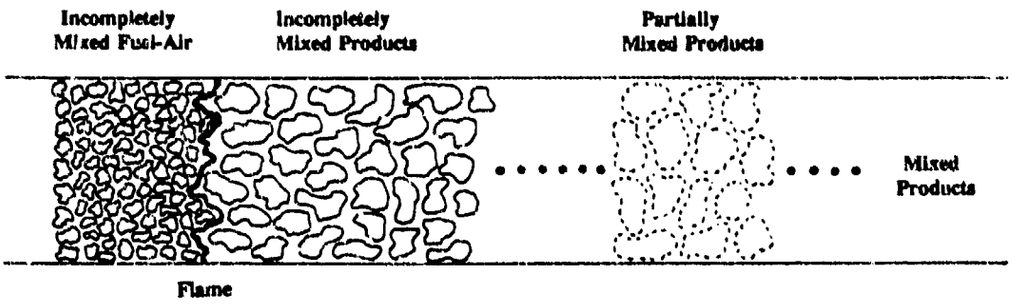

Figure 1. A phenomenological description of the effect of incomplete fuel-air mixing.

assumed in this simplified phenomenological description that within each pocket, the fuel and air are well mixed and, therefore, the local flame properties, e.g., flame speed and flame temperature, are determined by the local equivalence ratio. As a result, the spatial and temporal fluctuations in the fuel-to-air ratio will have a significant effect on the structure of the flame, and more importantly, on the overall mass burning rate and thereby the lean blowout limit of a combustor.

Referring back to Figure 1, it is shown that as the pockets of reactants pass through the flame front, they increase in size as a result of the volumetric expansion which accompanies the constant pressure heat release. The temperature and composition of the pockets of combustion products reflect the variations in the equivalence ratio among the pockets of reactants. Therefore, there are significant temporal and spatial fluctuations in the temperature and composition of the burned gases when the fuel and air entering the flame are not well mixed. Due to turbulent mixing, however, the spatial and temporal non-uniformities in the combustion products mix and become uniform at some distance downstream of the flame. The rate of mixing of the combustion products can have a significant effect on both the CO and NO_x emissions due to the relatively slow CO oxidation and NO formation chemistry. For example, if the rate of post-flame mixing is much slower than the rate of NO formation, then the amount of NO produced in each product pocket will depend on the equivalence ratio of the reactant pocket from which it originated. Due to the non-linear relationship between NO formation and equivalence ratio, the total NO_x emissions will be different from that which would be obtained if the reactants were well mixed. The effect of incomplete fuel-air mixing on the total amount of NO produced, assuming the rate of post-flame mixing is much slower than the NO chemistry, is shown in Figure 2 for rms fluctuations in the fuel-to-air ratio of 10%, 20% and 28% [3.3]. These results were calculated assuming a Gaussian pdf for the distribution of equivalence ratios and using the NO versus equivalence ratio result for the completely mixed case, which is also shown for comparison. As shown in Figure 2, at fuel-lean conditions, incomplete fuel-air mixing results in increased NO production, however, at near stoichiometric conditions, the total amount of NO is actually reduced. Recall, however, that these results are for the case when the rate of post-flame mixing is much less than the rate of NO formation. As the rate of post-flame mixing is increased, one would expect the total amount of NO produced to approach the completely mixed result.

DESCRIPTION OF EXPERIMENT

The experiments were conducted in a combustor test facility which is capable of operating at pressures up to 10 atmospheres, at inlet temperatures up to 800 K (~1000°F) and with flow rates of air or nitrogen up to 0.3 kg/sec (0.67 lb/sec). A schematic drawing of this facility is shown in Figure 3. The test section, which houses both the fuel-air mixer and the combustor, has provisions for optical access through four quartz windows (5 cm by 25 cm), as illustrated in Figure 3. The facility also provides access for a traversing, water-cooled, stainless steel gas sampling probe, which can be used to sample combustion products along the entire length of the combustor.

The fuel-air mixer is a cylindrical tube which is followed by a larger diameter coaxial combustor tube. Liquid fuel is injected near the entrance of the mixing tube and the flame is stabilized at the rearward facing step separating the mixer and the combustor tubes. Fuel-air mixtures with different spatial distributions at the combustor inlet

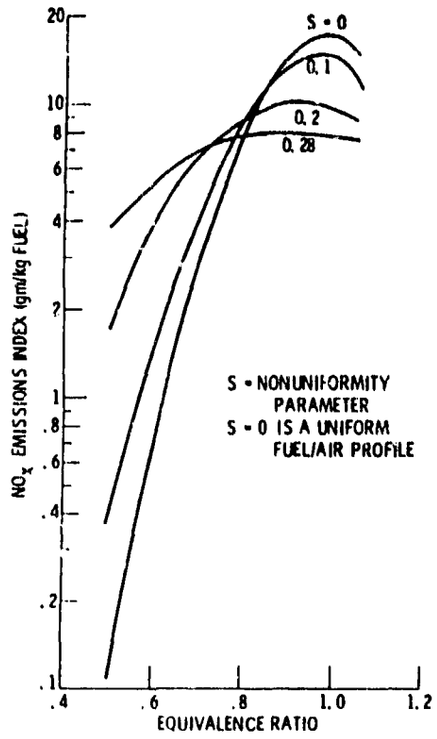

Figure 2. The effect of incomplete fuel-air mixing on NO production [33].

are achieved by changing the fuel injection configuration. In the work presented in this paper, two different fuel-air mixture distributions were studied.

Separate tests were conducted to characterize the fuel-air mixing and to characterize the emissions and lean stability limits. The fuel-air mixing tests were conducted at one operating condition, i.e., at 4 atmospheres, at an inlet temperature of 400°C (750°F), at a mean velocity of 100 m/sec in the mixer tube and at an overall equivalence ratio of .8. The emissions and lean stability limit tests were also conducted at 4 atm and at a mean mixer tube velocity of 100 m/sec; however, the inlet air temperature was varied (360°C, 400°C, 450°C) and the equivalence ratio was varied from the lean limit to near stoichiometric conditions.

The technique which was used to characterize the fuel-air mixing was exciplex fluorescence [37]. The main advantage of this technique is that the liquid phase fluorescence is at a different wavelength than the vapor phase fluorescence. Therefore, by simple optical filtering, it is possible to distinguish between fuel liquid and fuel vapor. The disadvantages of the technique are that oxygen very effectively quenches the fluorescence signal, and therefore, the measurements must be carried out in a nitrogen rather than air environment, that it only provides a qualitative measure of the relative fuel vapor or fuel liquid concentration, and that the actual fuel must be replaced by an appropriately chosen simulant which exhibits the exciplex behavior. Nonetheless, it is an extremely useful and valuable technique for making qualitative assessments of the degree of fuel vaporization and mixing. The fuel simulant which was chosen for these tests was a mixture of tetradecane, 1 methyl naphthalene and TMPD. This particular mixture was chosen, in part, because the boiling points fall near the middle of the boiling point range of the Jet A fuel used in the combusting tests. The frequency tripled output of a pulsed Nd:YAG laser at 355 nm was used to excite the exciplex fluorescence. Optical access was obtained to

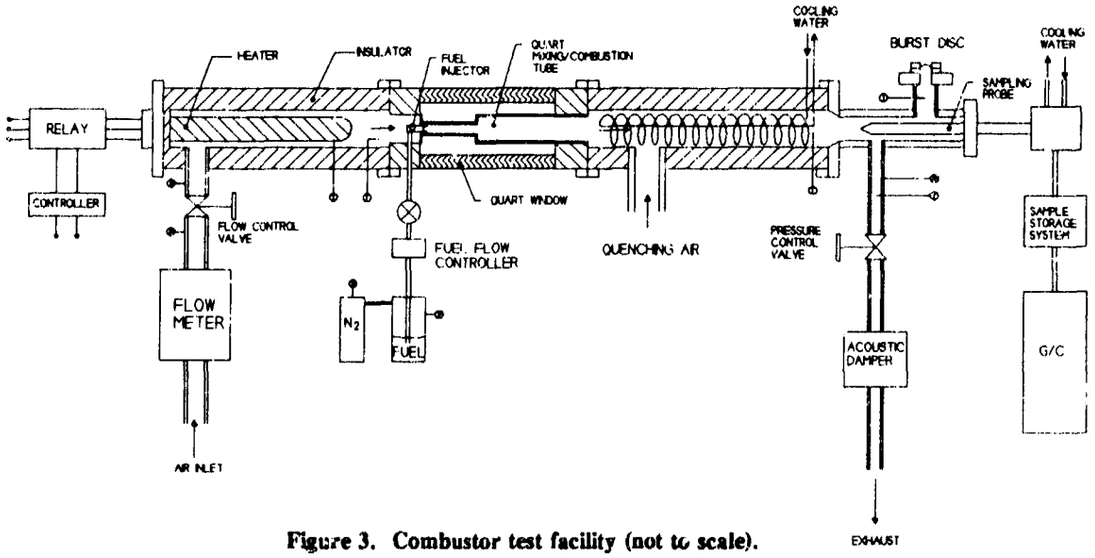

Figure 3. Combustor test facility (not to scale).

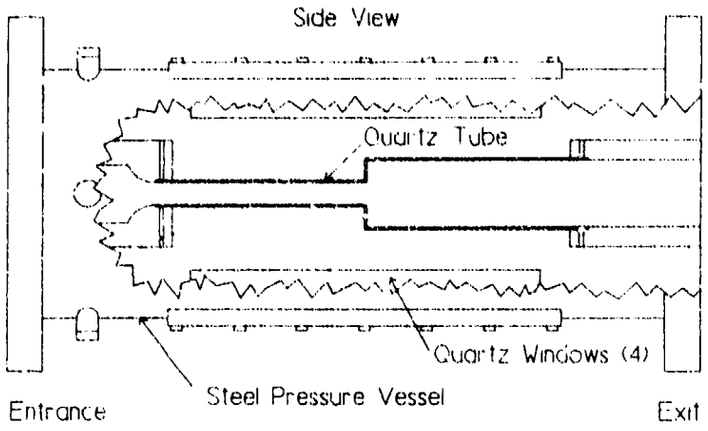

Figure 4. Optically accessible mixer-combustor assembly for fuel-air mixing tests (not to scale).

both the mixer tube and the combustor tube through the previously mentioned quartz windows. In addition, a quartz version of the mixer-combustor tube assembly was used, as illustrated in Figure 4. The laser beam was formed into a laser sheet which was approximately 0.5 mm thick and 50 mm wide, where it passed through the mixer-combustor tube. The exciplex fluorescence signal from the laser sheet was imaged at 90 degrees onto an intensified CCD camera with a maximum gain of approximately 10^5. Optical filters were used to isolate the fuel vapor fluorescence and the fuel liquid fluorescence.

For the combusting tests, the mixer tube was fabricated from stainless steel and the combustor tube was made from Hastelloy and was air-cooled to keep the combustor wall temperature below 900°C. A schematic drawing of this assembly is given in Figure 5. The lean limit was defined by the occurrence of flame blowout which was detected by a marked decrease in the combustor wall temperature. The emissions measurements were made using the water-cooled, stainless steel gas sampling probe located near the combustor tube exit. The combustor residence time was nominally 6 milliseconds in all of the tests. The gas samples were analyzed using conventional gas analysis. Although the gas sampling probe was located on the center line of the combustor, it is reasonable to assume that the combustion products were well mixed at the combustor exit due to the relatively long length of the combustor tube, i.e., L/D = 20.

RESULTS AND DISCUSSION

The results from the fuel-air mixing tests are shown in Figures 6-13. As noted previously, the exciplex measurements were made at one operating condition for two fuel-air mixture distributions, subsequently referred to as A and B. In addition, measurements were made both from the side view, and from the top view. The objective of these measurements was to determine qualitative differences between the two fuel-air mixture distributions with respect to both the degree of fuel vaporization and the degree of fuel-air mixing. The results are presented as normalized iso-intensity plots, where a value of one corresponds to the maximum fuel vapor or liquid concentration and, where for qualitative comparisons, the fuel vapor and liquid concentration can be assumed to scale linearly with the normalized intensity. The results shown in Figures 6-13 are averages of five exciplex images obtained at the same conditions; however, it should be noted that there were no significant variations from image to image for the same condition. The field of view in these images is centered on the transition between the mixer and combustor tubes. Figures 6 and 7 show the side and top view, respectively, fuel liquid results for fuel-air mixture distribution A. Note that the band which occurs at the mixer-to-combustor transition, where it appears that there is little or no fuel, is actually due to the poor optical quality of the quartz mixer-combustor assembly at this location. The first observation is that there appears to be significant liquid fuel which has not yet been vaporized at the entrance to the combustor tube. From the top view it appears that the liquid is relatively uniformly distributed across the width of the mixer tube, however, from the side view it is apparent that the liquid is wetting the upper wall of the mixer tube. It is also interesting to note that the liquid remains near the centerline of the combustor tube without being dispersed outward to the combustor walls.

Figures 8 and 9 show the side and top view, respectively, fuel vapor results for fuel-air mixture distribution A. The spatial distribution of the fuel vapor is similar to that of the fuel liquid, showing clear

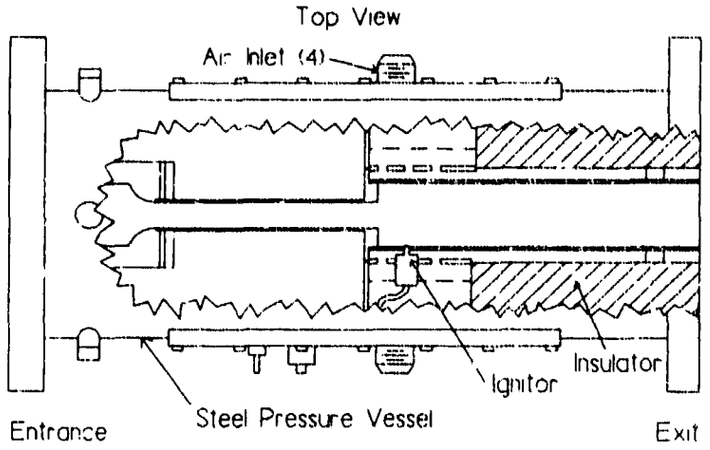

Figure 5. Mixer-combustor assembly for lean limit and emissions tests (not to scale).

evidence of an asymmetric distribution in the side view; however, there is an important difference in that the fuel vapor has been dispersed out to the combustor walls, particularly as shown in the top view.

Figures 10 and 11 show the side and top view, respectively, fuel liquid results for fuel-air mixture distribution B. Again, it is evident that a significant amount of liquid fuel is not vaporized at the combustor entrance. In this case, the fuel distribution is noticeably more uniform, as viewed both from the top and the side. It is still apparent, however, that the liquid tends to stay on the centerline of the combustor tube without dispersing out to the combustor walls.

Figures 12 and 13 show the side and top view, respectively, fuel vapor results for fuel-air mixture distribution B. Again, the spatial distribution of the fuel vapor is similar to that of the fuel liquid, i.e., it is relatively uniform in both the top and side views. The fuel vapor, however, has again been more effectively dispersed across the entire diameter of the combustion tube.

In summary, both fuel-air mixture distributions show that there is incomplete fuel vaporization at the entrance to the combustor tube. Fuel-air mixture distribution B, however, exhibits a significantly more uniform distribution of fuel liquid and vapor at the combustor entrance.

The lean limits were determined for both fuel-air mixture distributions, and it was found that distribution B, which was significantly more uniform, resulted in a significantly lower lean limit. This result was not expected, since, as previously discussed, it is generally accepted that better mixing has an adverse effect on the lean limit. From an analysis of lean limit data from a variety of different studies, it has been observed [36] that the lean limit corresponds to the case of constant adiabatic flame temperature, for a given experimental configuration. Over the range of conditions tested in this study, it was found for both fuel-air mixture distributions that the adiabatic flame temperature at the lean limit was constant within 150°C, although there was a difference of approximately 400°C between the lean limit flame temperature for the two fuel-air mixture distributions.

The CO, CO_2 and O_2 emissions measurements were used to calculate the combustion efficiency over the range of test conditions, and it was found that the combustion efficiency was greater that 99.5% at equivalence ratios below 0.9 for both fuel-air mixture distributions. The two fuel-air distributions, however, did show different lean limit behavior in that a significant increase in CO emissions was observed at the lean limit of the better mixed case, i.e., fuel-air mixture distribution B; whereas no appreciable increase in CO emissions was observed at the lean limit with fuel-air mixture distribution A.

And lastly, the two fuel-air mixture distributions were unexpectedly found to result in comparable NO_x emissions for a given equivalence ratio and inlet temperature. Fuel-air mixture distribution B, however, had the advantage of being able to operate leaner and thereby achieve lower NO_x emissions.

CONCLUSIONS

The degree of fuel vaporization and fuel-air mixing in a coaxial, mixing-tube combustor was qualitatively characterized using exciplex fluorescence. Two fuel-air mixture distributions were studied. Both had appreciable unvaporized fuel at the combustor inlet, while one had a very non-uniform fuel distribution and the other had a

relatively uniform fuel distribution. Unexpectedly, the better mixed case had a significantly leaner lean limit, while the NO_x emissions were comparable for the two fuel distributions. The more uniform case, however, was capable of lower NO_x emissions due to its ability to operate leaner.

ACKNOWLEDGEMENT

This research was supported by General Electric Aircraft Engines with funds provided by NASA-Lewis. The authors would like to acknowledge John Matulaitis and Paul Heberling of GE Aircraft Engines for numerous helpful discussions and suggestions.

REFERENCES

1. Crutzen, P. J., "The Influence of Nitrogen Oxides on the Atmospheric Ozone Content," *Quant. J. Roy. Met. Soc.*, Vol. 96, pp. 320-325, 1970.
2. Johnston, H. S., Kinnison, D. E. and Wuebbles, D. J., "Nitrogen Oxides from High Altitude Aircraft: An Update of Potential Effects of Ozone," *J. Geophys. Res.*, Vol. 94, pp. 16351-16363, 1989.
3. Wuebbles, D. J. and Kinnison, D. E., "Sensitivity of Stratospheric Ozone to Present and Possible Future Aircraft Emissions," *Proceedings of a DLR International Colloquium on Air Traffic and the Environment - Background, Tendencies and Potential Global Atmospheric Effects*, Springer-Verlag, 1990.
4. Environmental Protection Agency, "Control of Air Pollution from Aircraft and Aircraft Engines," *Fed. Reg.*, Vol. 38, No. 136, Pt. II, 1973.
5. Environmental Protection Agency, "Control of Air Pollution from Aircraft and Aircraft Engines," *Fed. Reg.*, Vol. 43, No. 58, 1978.
6. Odgers, J. and Kretschmer, D., "Design Features for a Pre-Mixed Variable Area Combustor," *AGARD Conference Proceedings*, No. 205, Paper No. 26, 45th PEP Symposium, Paris, Sept. 6-9, 1976.
7. Adkins, R. C. and Eisaftawy, A. S., "A Double Acting Variable Geometry Combustor," ASME 79-GT-197, March, 1979.
8. Fiorentino, A. J., Green, W., Kim, J. C. and Mularz, E. J., "Variable Geometry, Lean, Premixed Prevaporized Fuel Combustor Conceptual Design Study," ASME Paper 80-GT-16, 1980.
9. Fear, J. S., "Advanced Low Emissions Combustor Program," AIAA-87-2035, 23rd Joint Propulsion Conference, June 29-July 2, 1987.
10. Rizk, N. K. and Mongia, H. C., "Lean Low NO_x Combustion Concept Evaluation," *Twenty-Third Symposium (International) on Combustion*, pp. 1063-1070, 1990.
11. Lefebvre, A. H. and Fletcher, R. S., "A Preliminary Study of Fuel Staging on Nitric Oxide Emissions from Gas Turbine Combustors," *AGARD Conference Proceedings*, 125 on Atmospheric Pollution by Aircraft Engines, Sec. 30, 1973.
12. Gleason, C. C., Rogers, D. W. and Bahr, D. W., "Experimental Clean Combustor Program, Phase II, R76AEG422, General Electric Co., NASA CR-134971, August 1976.
13. Sjoblom, B. G. A., "Premixing and Flash Vaporization in a Two-Stage Combustor," ASME 81-GT-41, March 1981.
14. Blazowski, W. S. and Bresowar, G. E., "Preliminary Study of the Catalytic Combustor Concept as Applied to Aircraft Gas Turbines," AFAPL-TR-74-32, Air Force Aero Propulsion Lab, Wright-Patterson AFB, May 1974.
15. Rosford, T. J., "Catalytic Combustors for Gas Turbine Engines," AIAA Paper No. 76-46, January 1976.
16. Smith, K. L. and Cowell, L. H., "Experimental Evaluation of a Liquid-Fueled, Lean-Premixed Gas Turbine Combustor," ASME 89-GT-264, 1989.
17. Anderson, D. N., "Ultra Lean Combustion at High Inlet Temperatures," ASME 81-GT-44, March 1981.
18. Al Dabbagh, N. A. and Andrews, G. E., "The Influence of Premixed Combustion Flame Stabilizer Geometry on Flame Stability and Emissions," *J. of Engrg. for Power*, Vol. 103, pp. 749-758, October 1981.
19. Al Dabbagh, N. A., Andrews, G. E. and Shahabadi, A. R., "Combustion and Emissions Performance of a Rapid Fuel and Air Mixing Combustor," *Seventh Int'l. Symp. on Air Breathing Engines*, pp. 804-812, ISABE 85-7096, 1985.
20. Novick, A. S. and Troth, D. L., "Low NO_x Heavy Fuel Combustor Concept Program," NASA CR-165367, DoE-NASA-0158-1, 1981.
21. Nguyen, H., Bittker, D. and Niedzwiecki, R., "Investigation of Low NO_x Staged Combustor Concept in High Speed Civil Transport Engines," AIAA 89-2942, 25th Joint Propulsion Conference, July 10-12, 1989.
22. Rizk, N. K. and Mongia, H. C., "Three Dimensional NO_x Model for Rich/Lean Combustor," AIAA 93-0251, 31st Aerospace Sciences Meeting, Jan. 11-14, 1993.
23. Marek, C. J. and Papathakos, L. C., "Exhaust Emissions from a Premixing, Prevaporizing Flame Tube Using Liquid Jet A Fuel," NASATMS-3383, April, 1976.
24. Roberts, P. B., Kubasco, A. J. and Sekas, N. J., "Development of a Low NO_x Lean Premixed Annular Combustor," ASME 81-GT-40, 1981.

25. Becker, B., Berenbrink, P. and Brandner, H., "Premixing Gas and Air to Reduce NO_x Emissions with Existing Proven Gas Turbine Combustion Chambers," ASME 86-GT-157, 1986.
26. Sattelmayer, Th., Felchlin, M. P., Hanman, J., Hellat, J., and Styner, D., "Second Generation Low-Emission Combustors for ABB Gas Turbines: Burner Development and Tests at Atmospheric Pressure," ASME 90-GT-162.
27. Washam, R. M., "Dry Low NO_x Combustion System for Utility Gas Turbines," ASME 83-JPGC-GT-13, 1983.
28. Nagey, T. F., Mykolenko, P., Naylor, M. E. and Verkemp, F. J., "The Low Emission Gas Turbine Passenger Car - What Does the Future Hold?" ASME 73-GT-49, 1973.
29. Wade, W. R., Shen, P. I., Owens, C. W., McLean, A. F., "Low Emissions Combustion for the Regenerative Gas Turbine," ASME 73-GT-12, 1973.
30. Krockow, W. and Fiorentino, A. J., "Low Emissions Silo Combustor," ASME 81-GT-46, 1981.
31. Appleton, J. P. and Heywood, J. B., "The Effects of Incomplete Fuel-Air Mixing in a Burner on NO Formation from Nitrogen in the Air and the Fuel," *Fourteenth Symposium (International) on Combustion*, pp. 777-786, 1973.
32. Sermejian, H. G., Ball, I. C. and Vranos, A., "Pollutant Emissions from "Partially" Mixed Turbulent Flames," *Seventeenth Symposium (International) on Combustion*, pp. 679-687, 1979.
33. Lyons, V. J., "Fuel-Air Nonuniformity–Effect on Nitric Oxide Emissions," AIAA 81-0327, 19th Aerospace Sciences Meeting, Jan. 12-15, 1981.
34. Flanagan, P., Gretsinger, K., Abbasi, H. A. and Cygan, D., "Factors Influencing Low Emissions Combustion," ASME PD-Vol. 39, *Fossil Fuels Combustion*, 1992.
35. Fric, T. F., "Effects of Fuel-Air Unmixedness on NO_x Emissions," AIAA 92-3345, 28th Joint Propulsion Conference, July 6-8, 1992.
36. Gulati, A. and Warren, R. E., "NO_2-Based Laser-Induced Fluorescence (LIF) Technique to Measure Cold Flow Mixing," AIAA 92-0511, 30th Aerospace Sciences Meeting, January 6-9, 1992.
37. Melton, L. A. and Verdieck, J. F., "Vapor-Liquid Visualization for Fuel Sprays," *Combustion Science and Technology*, Vol. 42, p. 217, 1984.
38. Tacina, R., personal communication.

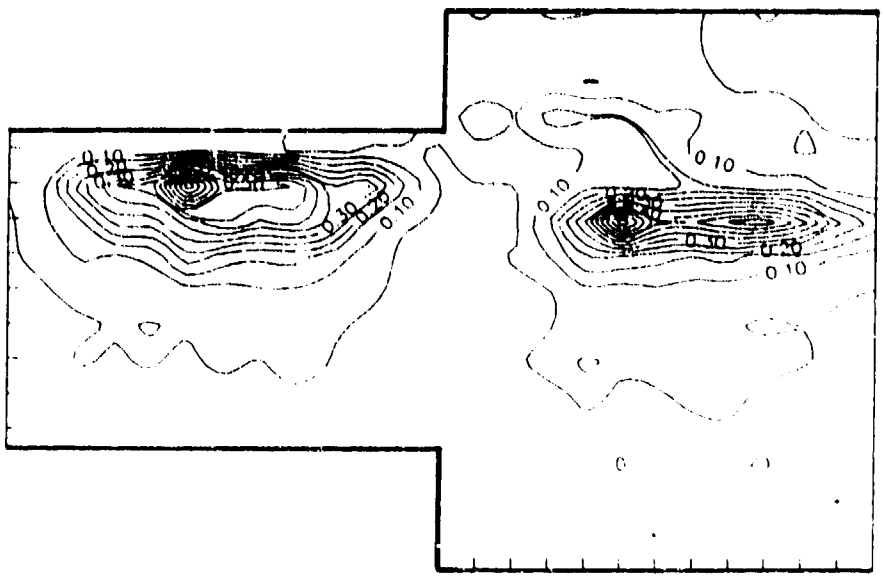

Figure 6. Exciplex fluorescence measurements: fuel liquid, side view, fuel-air mixture distribution A.

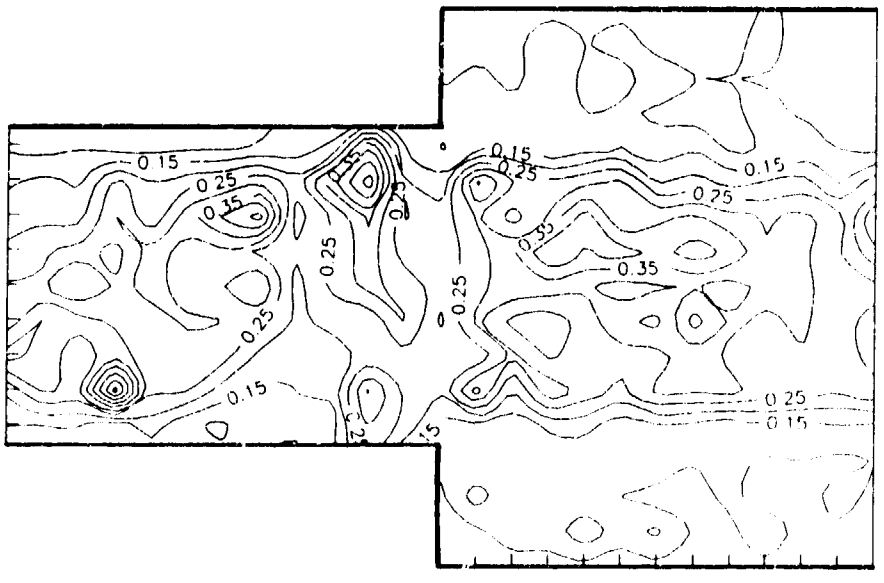

Figure 7. Exciplex fluorescence measurement: fuel liquid, top view, fuel-air mixture distribution A.

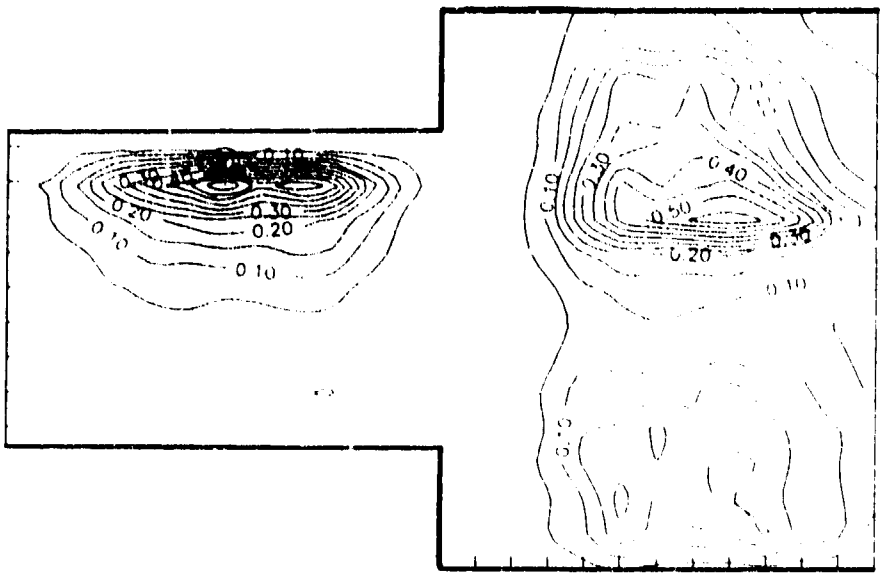

Figure 8. Exciplex fluorescence measurements: fuel vapor, side view, fuel-air mixture distribution A.

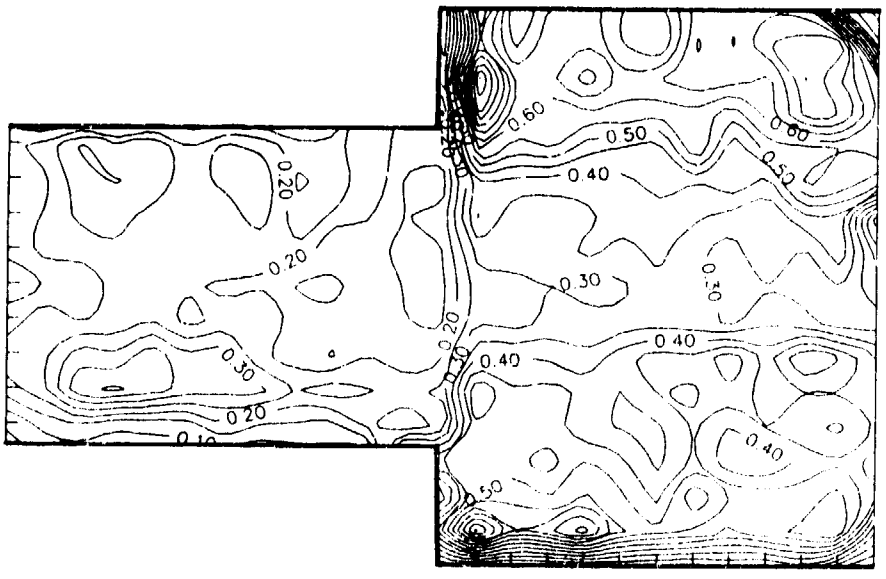

Figure 9. Exciplex fluorescence measurement: fuel vapor, top view, fuel-air mixture distribution A.

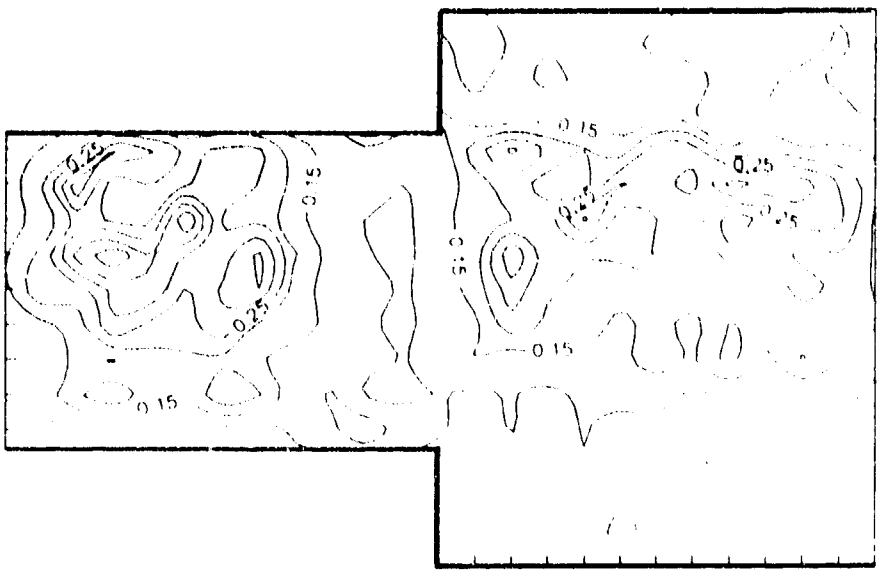

Figure 10. Exciplex fluorescence measurement: fuel liquid, side view, fuel-air mixture distribution B.

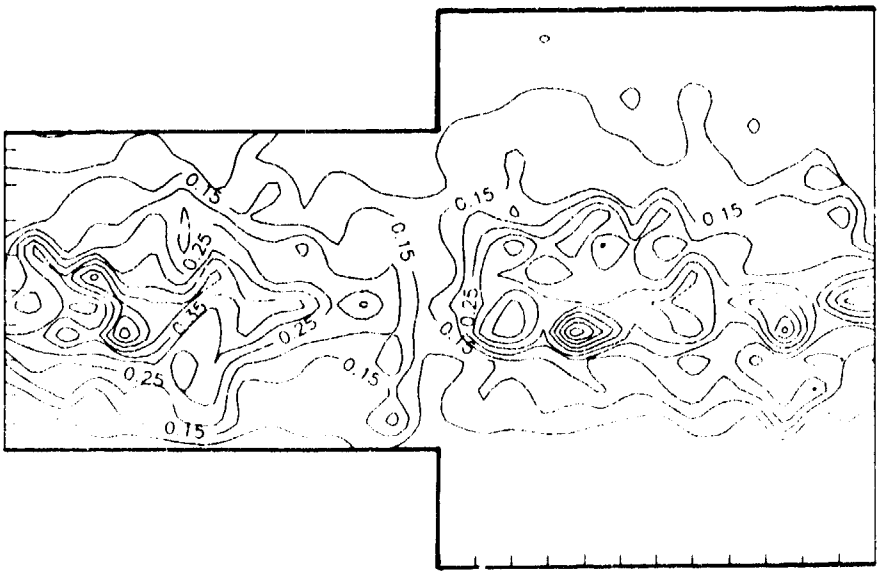

Figure 11. Exciplex fluorescence measurement: fuel liquid, top view, fuel-air mixture distribution B.

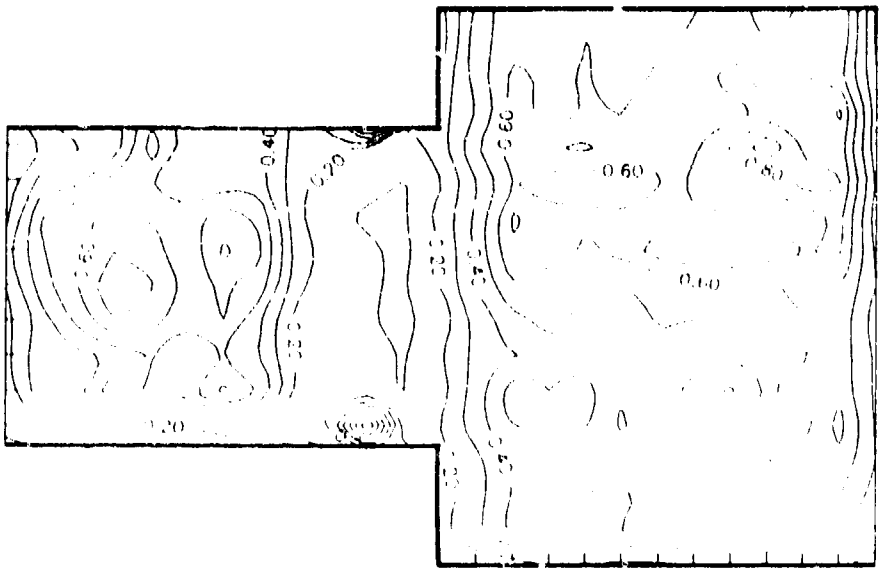

Figure 12. Excipiex fluorescence measurement: fuel vapor, side view, fuel-air mixture distribution B.

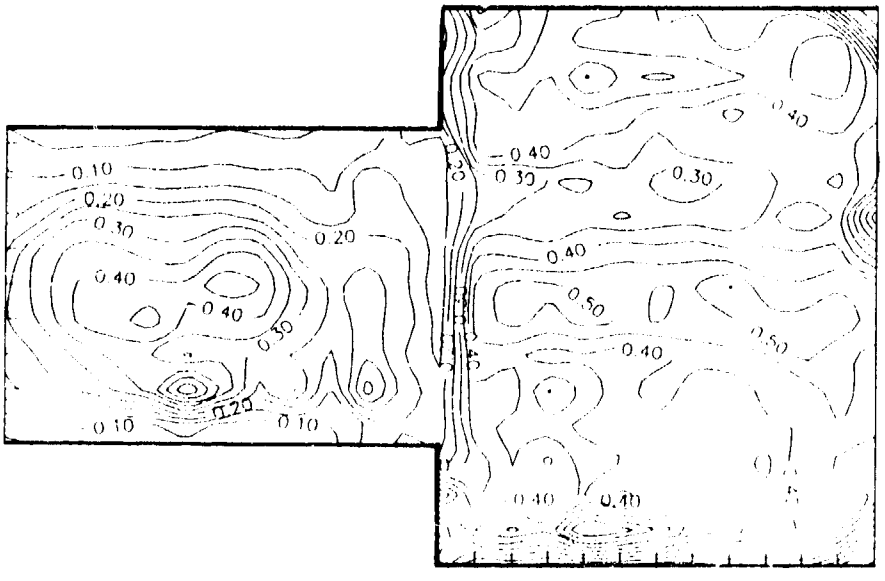

Figure 13. Exciplex fluorescence measurement: fuel vapor, top view, fuel-air mixture distribution B.

STUDIES OF LEAN BLOWOUT IN A RESEARCH COMBUSTOR

by

D.R. Ballal, M.D. Vanganess and S.P. Heneghan
University of Dayton
300 College Park
Dayton, Ohio 45469
United States

G.J. Sturgess
Pratt and Whitney Engineering
East Hartford, CT 06108
United States

1. SUMMARY

A prime requirement in the design of a modern gas turbine combustor is good lean blowout (LBO) stability to ensure an adequate stability margin. Therefore, a geometrically simple, optically accessible, and acoustically decoupled research combustor was designed to reproduce the gross features of the flow field in a modern annular gas turbine combustor. Its LBO was measured using methane and propane fuels. We successfully observed and documented a systematic and detailed sequence of events comprising an attached flame, a lifted shear flame, an intermittent shear flame, the large-scale instability of the flame front, and LBO. Also, for the sake of comparison, a generic gas turbine combustor was tested and its LBO limits were measured.

We found that LBO in the research combustor behaved like a perfectly stirred reactor (PSR) for values of combustor-loading spanning three orders of magnitude. Also, LBO was successfully correlated using a simple PSR theory. Finally, Swithenbank's dissipation gradient approach and an eddy dissipation model with a built-in characteristic extinction time criterion, when coupled with CFD, offer the possibility of an *a priori* calculation of LBO. The lean stability of a generic gas turbine combustor at peak heat release rates was less than that in a research combustor. Also, in the generic combustor, the flame changes from a lifted to an attached position depending upon how combustor loading is achieved. Due to such complications, modeling of the LBO process that works reasonably well with the research combustor will be seriously challenged by the blowout behavior evidenced in the generic gas turbine combustor.

LIST OF SYMBOLS

C_μ	constant
D	laminar diffusion coefficient
E	activation energy
K	turbulent kinetic energy
LBO	lean blowout
LP	loading parameter
L/D	length/diameter ratio
m	mass flow rate
n	reaction order
P	pressure
PSR	perfectly stirred reactor
R	gas constant
Re	Reynolds number
S	species source term
T	temperature
V	combustion volume
x,y,z	radial, transverse, and axial distance resp.
ε	turbulent dissipation rate
ϕ	equivalence ratio
ν	kinematic viscosity
ρ	density
σ	Schmidt number
τ	residence time

Subscripts

a	air
ext	extinction
f	fuel
o	oxygen
nit,N_2	nitrogen
tot	total

2. INTRODUCTION

A prime requirement in the design of a modern gas turbine combustor is good combustion stability, especially near lean blowout (LBO), to ensure an adequate stability margin. For the aircraft engine, combustor blow-off limits are encountered during low engine speeds at high altitudes over a range of combustor air loading parameters. This is illustrated in Fig. 1 as a loss in the operating envelope. It is the task of the combustion engineer to design a combustor such that all its steady-state operating points lie inside the envelope. This envelope should be extensive enough to encompass the under- and over-shoots associated with the different response rates to the throttle movements of the fuel system and the rotating machinery. Further, the current and likely future design trends towards airblast atomization, high temperature rise, and low emissions are eroding the safety margins. For these reasons, the U.S. Air Force Wright Laboratory, Aero Propulsion and Power Directorate (WL/PO), Wright-Patterson Air Force Base, Ohio initiated a joint Government, Industry, and University research program to understand and model LBO in aircraft combustors. This paper describes the major results and discusses various factors that influence LBO in research and practical combustors.

In a modern annular gas turbine combustor (Fig. 2), flame is stabilized by producing a recirculation zone in the flow field. This zone is generated by a combination of three mechanisms: an axial swirling air jet associated with each

Presented at an AGARD Meeting on 'Fuels and Combustion Technology for Advanced Aircraft Engines', May 1993.

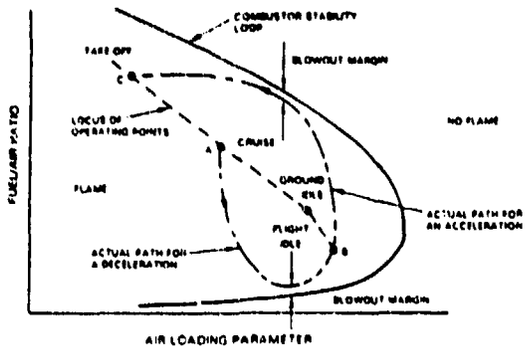

Fig. 1: Engine operating envelope superimposed on the combustor stability loop, illustrating the stability margins at blowout.

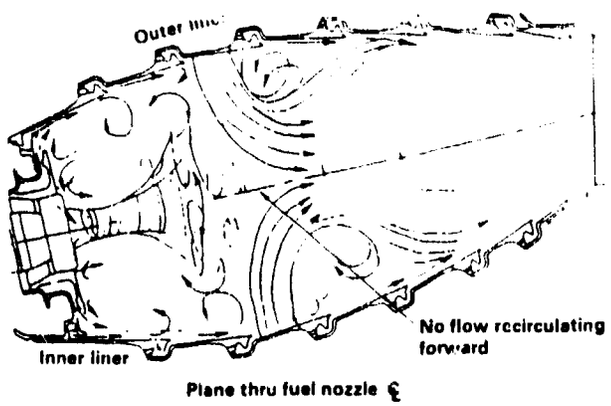

Fig. 2: Flow pattern in a modern annular combustor.

fuel introduction, sudden expansion of the axial swirling jets as they enter the primary zone, and back pressure provided by an array of radial air jets at the end of the primary zone. To obtain low exhaust emissions, Pratt & Whitney currently tailors the combustor flow control mechanisms to produce an "inside-out" recirculation pattern (Fig. 2). Therefore, the research combustor was required to reproduce this type of recirculation pattern. At the same time, it had to provide stable combustion over a reasonably wide variation in its loading, be geometrically simple for ease of experimentation and computation, and provide adequate optical access for measurements.

This paper discusses fundamental processes in the near-field region of the combustor that elucidate how LBO occurs in practical combustors, factors relating to combustor geometry (e.g., back pressure) and operating conditions (e.g., equivalence ratio, fuel and air velocity) that influence LBO, a map of flame behavior vs. combustor loading, and the application of reaction rate theory to the correlation of LBO results.

3. EXPERIMENTAL WORK

Research Combustor: We designed a research combustor to simulate three main features of the flow field in a modern annular gas turbine combustor; (i) a reactive shear layer formed between fuel and air jets, (ii) the inside-out type of recirculation zone, and (iii) the interaction between and back-pressure exerted by transverse combustion air jets and axially directed jets of fuel-air mixture. A complete description of the combustor design and development is provided by Sturgess et al. [1].

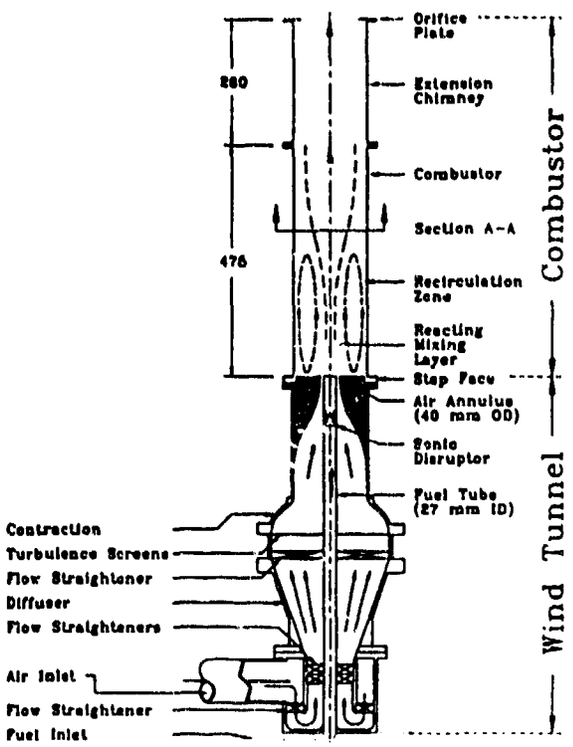

Fig. 3: Schematic diagram of a research combustor for LBO studies.

Fig. 3 shows a schematic diagram of the research combustor. It consists of a 27-mm (i.d.) central fuel tube of low-speed gaseous propane or methane surrounded by a 40-mm (i.d.) high-speed coaxial air jet exhausting into a dump combustor. This arrangement produces an intense reactive shear layer between fuel and airstreams. The duct is closed at its forward end to yield a 55-mm-high, backward-facing step. This step provides an inside-out recirculation zone which feeds high-temperature combustion products into the shear layer and thus provides a source of continuous ignition to

stabilize the flame. A perforated conical baffle inserted five diameters upstream of the fuel tube serves to acoustically isolate the fuel supply from the combustion process. As shown in Fig. 3, the step combustor is mounted vertically on a small wind tunnel. The combustor duct is comprised of two separate sections. The first section holds optical quartz windows (or metal panels with thermocouples and static pressure tappings for wall temperature and pressure measurements, respectively) on all four sides; the second one is a 250-mm extension inconel chimney. The chimney exit is blocked with an orifice plate which simulates the back-pressure effect of a practical combustor. The combustor has a hydraulic mean diameter of 150 mm, is 475 mm long, and has an exit orifice blockage of 21%, 45%, or 62%. The combination of combustor and its extension chimney yields (L/D) ratios of 3.17, 4.9, and 6.5, respectively.

Test Conditions: The combustion laboratory provides gaseous propane anane fuels up to 20 Kg/hr. Both fuelstream (Re = 1,733 to 17,333) and airstream (Re = 7,233 to 72,322) were monitored to within 1.5%. Ignition of the combustor was satisfactorily accomplished using a retractable torch igniter. As the LBO condition was approached, the attached diffusion flame lifted from the fuel tube and was stabilized slightly downstream. This was the region of most interest and relevance to the present study.

Instrumentation: A three-component LDA system for velocity measurements and a CARS system for flame-temperature measurements were used. The optical window size permitted data acquisition in the range x = -70 to + 70 mm, y = -33 to +33 mm, and z = 2 to 360 mm.

The LDA uses the green (514.5 nm) and blue (488 nm) lines of a 15 W Argon-ion laser as a source; two measurement channels were separated by polarization while a third uses the blue beam. The scattered signals were collected in a forward direction at 10 degrees off axis. The effective probe volume was 50 x 300 x 750 μm, the Bragg cell frequency shift was 5 MHz, and Al_2O_3 seed particles were used. After allowing for seed biasing, the measurement uncertainty in mean velocity was 1%, in rms velocity it was 5%, and in skewness and kurtosis it was 7%.

The CARS system employed a BOXCARS configuration. Here, the frequency-doubled source green beam (532 nm) was split into four beams. A 25-x-250-μm measuring spot size was achieved. The CARS temperatures were determined, see Heneghan et al., [2], by applying the principle of local thermodynamic equilibrium. Usually, 500 samples were taken for each CARS measurement. It was estimated that the overall CARS mean temperature measurement accuracy is within 50K, while the precision is well within 20K. Unlike the LDA, the CARS measurements are time-averaged without density-biasing effects.

4. RESULTS

Acoustic Decoupling: Combustion-induced acoustic oscillations can severely limit the operating range of some practical combustors--especially parallel-wall duct combustors. The acoustic characteristics of this research combustor were investigated because it was feared that eddy-shedding off the step might satisfy the Rayleigh criterion, which, in turn, could set up resonance in the combustor and fuel supply tube. Heneghan et al. [3] have described the results of this investigation in detail. It was found that an acoustic isolator in the fuel tube and an air inlet convergence that eliminated vortex generation at the inlet significantly decrease acoustic coupling. Finally, a research step combustor with an L/D = 4.9 and fitted with an orifice plate with a blockage ratio = 0.45 provided the best combination of LBO and freedom from acoustic coupling.

Isothermal Flow Field: Next, we measured the isothermal flow field in the combustor corresponding to the fuel and air-jet velocity ratios at the combustor blowout conditions. This investigation is described by Sturgess et al. [4]. Fig. 4 shows a typical result. The LDA measurements revealed the presence of the primary zone flow features (i.e., a near-field region comprising the jet shear layer and a small, central recirculation zone generated by the large momentum ratio between the fuel and the air jets; an outer recirculation zone stabilized on the step; and the far-field region, in which the individual jets lose their identity and exhibit self-similarity).

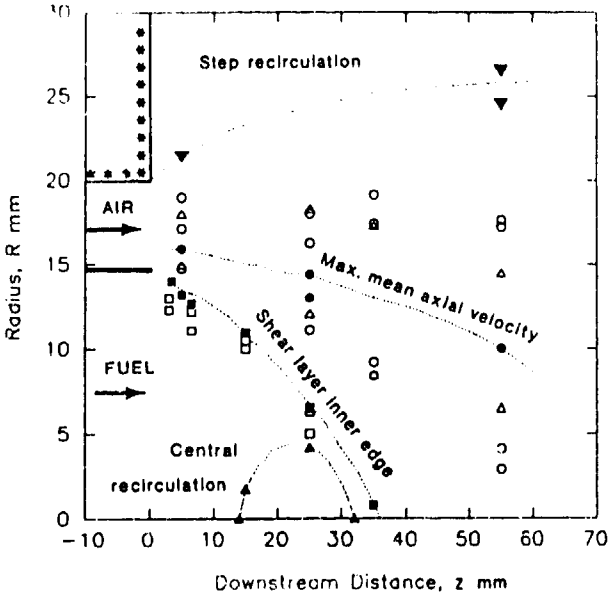

Fig. 4: Isothermal flow field results illustrating the near-field region, recirculation zones, and the far-field region; (■, ▲, ▼-mean axial velocity, □, ○-turbulence intensities, and Δ-max. velocity gradient).

Flame Visualization: Fig. 5 illustrates the sequence of events leading to LBO. As the overall equivalence ratio was reduced below unity, the attached flame moved further downstream into the combustor in a characteristic lifted-flame position and form. Continuing reduction in the

equivalence ratio produces an onset of flow instability in the lifted flame, an increase in the amplitude of the instability, the onset of intermittency, severe intermittency, and, finally, the onset of strong axial flame instability. This sequence clearly highlights the complexity of the LBO mechanism in a modern annular gas turbine combustor.

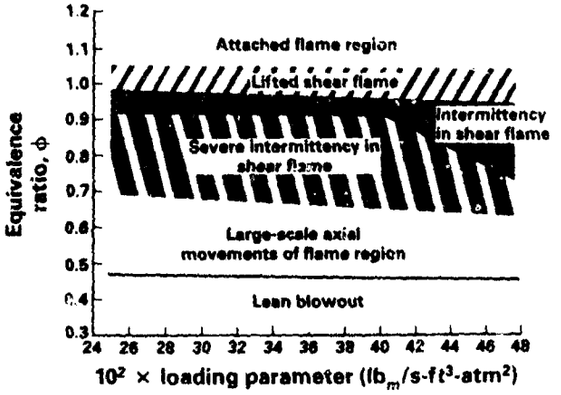

Fig. 5: Sequence of events leading to LBO as observed by flame visualization.

In our research combustor, the piloting action of the flame in the jet shear layers by the attached flame at the step appears to be crucial to combustor stability. Thus, successful modeling of the combustor stability requires the prediction of the attached flame and its lift. The OH images of the attached flame, see Sturgess et al., [5], show that its structure at any given time is associated with local vortices shed from the inner edge of the combustor step. Also, the instantaneous OH images reveal that combustion takes place in a more distributed form via relatively large "packets" of reaction.

Lean Blowout: We measured LBO as a function of air loading parameter (LP) over a range of propane fuel flows. However, this did not yield a complete combustor stability loop. To achieve a wide variation in LP with the simple atmospheric pressure research combustor, a subatmospheric pressure simulation was used. As explained in Ref. [6], excess gaseous nitrogen was introduced into the air supply upstream of the combustor as a diluent to lower the concentration of reactants and/or reaction temperature by virtue of its heat capacity. Fig. 6 illustrates a calibrated relationship between equivalent pressure and (nitrogen/fuel) mass ratio at blowout in the research combustor. This technique permitted (i) the simulation of subatmospheric pressure as low as 0.1 atm, (ii) the completion of the combustor stability loop (ranging from ϕ = 0.5 to 0.9), and (iii) increased LP by two orders of magnitude.

Fig. 7 shows the LBO performance of our research combustor and stability loops for several well-stirred reactors from the

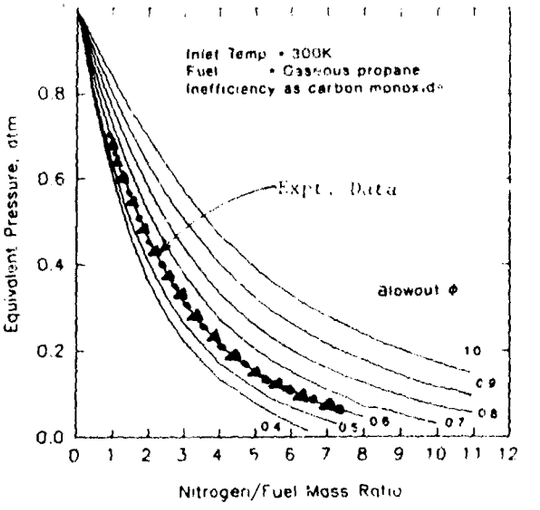

Fig. 6: Calibration curves for simulating subatmospheric pressure by using nitrogen dilution.

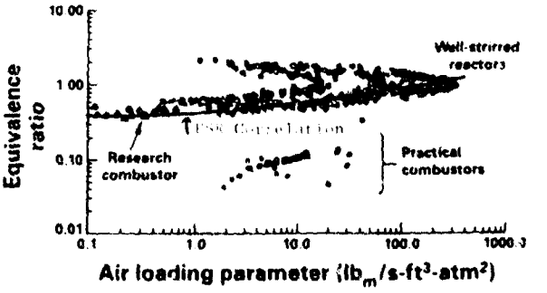

Fig. 7: LBO vs. LP data for the research combustor showing a comparison between the measured and the predicted results.

literature, as well as two partial loops for practical gas turbine combustors. For these results, the standard LP was derived from the global reaction rate theory, but modified to include the effects of inert excess nitrogen;

$$LP = \dot{m}_{tot}/(VP^n), \qquad (1)$$

$$\dot{m}_{tot} = \dot{m}_f + \dot{m}_a + \dot{m}_{nit}, \qquad (2)$$

and

$$n = 2\,\phi_{LBO}/(1 + \dot{m}_{nit}/\dot{m}_a). \qquad (3)$$

The trend of LBO vs. air loading shown in Fig. 7 is very similar to that found for a perfectly stirred reactor (PSR); the latter approaching the characteristics of a future generation of

ideal premixed, prevaporized, near-stoichiometric combustors. Thus, it is reasonable to conclude that our research combustor correctly reproduced the LBO processes of a real gas turbine combustor. Also plotted in this figure are results for a gas turbine combustor fitted with a vaporizer tube and another one fitted with a strongly swirling prefilming airblast atomizer. In addition to their different fuel injection patterns, these two combustors had completely different flow fields (as compared to the combustor of Fig. 1) due to their different shapes, method of fuel introduction, and liner hole patterns. These results clearly suggest that a simple and general correlation for LBO is not possible. However, as will be shown later, direct calculation for each combustor offers the only possibility of making reliable *a priori* estimates of stability in gas turbine combustors.

To simulate the presence of dilution air jets, we investigated the effects of back pressure on the LBO in our research combustor. These results are discussed in detail in Ref. [7]; a typical result is presented in Fig. 8. As seen in the figure, LBO was improved by increasing the exit blockage. However, we found that (see Ref. 7) above a blockage of 45%, (i) significant interference occurs between the outlet and the combustor flame holding, and (ii) LBO does not improve much. Thus, we concluded that an exit blockage of 45 percent provides the best combustion stability and optimal configuration (i.e., for a combustor of exit blockage = 45 percent and L/D = 4.9, the LBOs were virtually independent of blockage and acoustic coupling). For a lightly loaded combustor (near the flammability limits), exit blockage exerts a weak influence on LBO, primarily through its effect on the jet and the recirculation zone shear layers. For high combustor loadings (near the peak heat release rate), exit blockage had a strong effect on the LBO via the dynamic behavior of the flow in the near-field (especially the interaction of the central recirculation bubble with the jet shear layers) and of the jet shear layers with the step recirculation zone.

5. ANALYSIS

Complete calculation of stability by using the CFD techniques to define the combustor flow field locally is not a viable approach. LBO is dominated by the kinetics of chemical reaction; therefore, CFD calculations of a large number of chemical reactions would be required to yield the correct heat release. For example, for hydrocarbon fuels, a general transport equation of the form,

$$\partial/\partial x_j \langle \rho u_j m_i - \Gamma_{eff} (\partial m_i/\partial x_j) \rangle = S_m \qquad (4)$$

where i denotes chemical species, m_i is the mass fraction of i, and S_m is a species source term, would have to be solved for each species. The computational burden of doing so is presently unacceptable in the context of the complicated flow field and confining boundaries of the real gas turbine combustor. Therefore, the chemistry was uncoupled from the fluid dynamics and analysis of LBO was addressed at three levels of increasing difficulty:

1. characteristic time modeling based on a phenomenological approach, with CFD providing local flow properties,
2. stirred reactor network modeling established on the basis of CFD analysis of the flow field, and
3. subgrid-level stirred reactor modeling using reactor extinction criteria based on the characteristic time model (1) above.

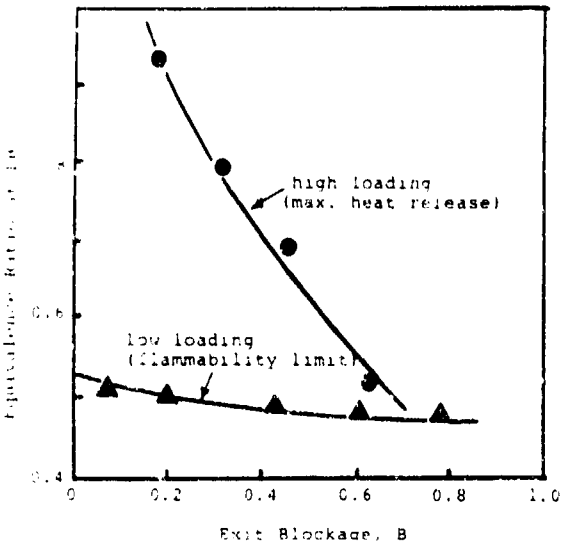

Fig. 8: Influence of exit blockage on LBO at low and high combustor-loadings.

Characteristic Time Approach: This approach is based on the reaction-quench model which assumes that, at LBO, flame propagation will cease when the rate of mixing between small turbulent eddies of cold reactants and hot products is greater than the local chemical reaction rate. This quenching criteria finds its origin in the work of Lockwood and Megahed [8] and yields:

$$1.5\{D + C\mu K^2/\sigma_t \varepsilon\}/\nu\{1 + S_L/(\varepsilon\nu)^{0.25}\} > 1.0 \qquad (5)$$

where D is the laminar diffusion coefficient, K is the kinetic energy of turbulence, ε is the dissipation rate, C_μ is a constant, σ_t is the turbulent Schmidt number, and S_L is the laminar flame speed.

Since the quenching criterion requires turbulence parameters for evaluation, isothermal flow CFD calculations were performed to provide this information at each grid node. Quenching was examined on a point-by-point basis to ascertain if any part of the flow field could support combustion. Further, two additional conditions were imposed; (i) local fuel/air ratio must be within the flammability limits, and (ii) local mean velocities should be

less than or equal to turbulent burning velocity. In a somewhat limited evaluation, Eq. (5) showed promise in the step combustor in delineating between operating conditions where combustion was possible and where it was not. Eventually, this approach provided the reactor extinction criteria for the subgrid-level stirred reactor modeling.

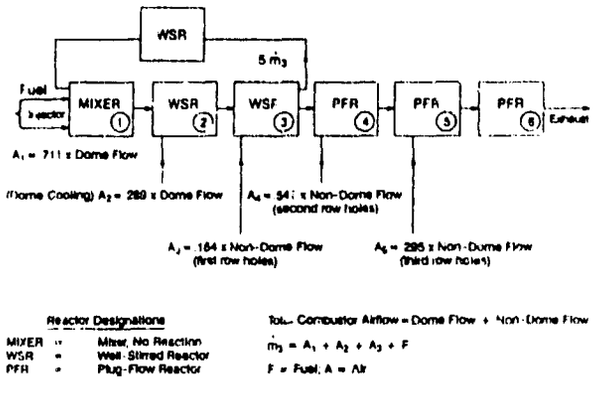

Fig. 9: A typical simulation of a combustor primary zone using the PSR network.

Local Stirred Reactor Modeling: In this approach, the combustor volume is represented by an equivalent global stirred reactor network. This enables the calculation of stability from thermo-chemistry considerations. We applied Swithenbank's [9] dissipation gradient approach for defining PSR regions in the combustor. Fig. 9 shows a typical reactor network that simulates the generic combustor primary zone. To establish such a global reactor network, considerable and careful post-processing of a CFD solution for the generic combustor was performed. Flow structures were identified by visualization, connectivity and local mass flow rates were assigned, and flow topology mapping techniques, e.g., Ref. [10], were used. Based on the Swithenbank approach [9], a rapid mixing region of the combustor was established from CFD calculations. This region was defined as the volume contained within a surface contour containing 96% of the turbulence kinetic energy and 99% of its dissipation rate, and over which the total dissipation gradient was not less than ten times the minimum value recommended by Swithenbank. From within this rapid-mixing region, a PSR volume was defined by super-imposing an additional space encompassing fuel/air mixtures falling inside the flammability limits for propane and air. For the research combustor, the resulting reactor was 44% of the combustor volume and corresponded reasonably well to the lifted flame observed in the real combustor. As shown in Ref. [6], good agreement was found between predictions and experiments for the research combustor.

Thus, networks of stirred reactors, particularly when established from CFD calculations, appear to offer possibilities for calculating limiting LBO performance. However, care may be needed in interpreting the results of such calculations since only the thermochemical limits to combustion can be determined.

Subgrid Scale Reactor Modeling: The eddy dissipation concept (EDC) of Byggstoyl and Magnussen [11] represents a general model for chemical reaction in turbulent flow. In the EDC model, the reactants are homogeneously mixed within the fine structure (Kolmogoroff eddies) of turbulence; therefore, these fine structures can be treated as PSRs. If the volume and the mass exchange rate between the reactors and the surrounding fluid are known, chemical reactions occurring within the PSRs can be calculated using a system of equations. Since the Kolmogoroff scale is always less than the CFD grid size, the modeling represents a subgrid scale approach. In contrast to the characteristic time analysis and local stirred reactor modeling, this approach tests the individual reactor stability within the CFD calculations.

Use of full or even reduced chemical kinetics imposes a high cost on the calculations. Therefore, an alternative approach was to assume a one-step, irreversible reaction step and/or fast chemistry, then use a local quenching criterion. The validity of the calibrated, global, single-step reaction mechanism approach was tested by comparing it to the data of Kretschmer and Odgers [12] and Clarke et al. [13]. Also, an extinction residence time was defined as $\tau_{ext} = (\rho/\dot{m})_{ext}$, where $\dot{m}$ is the total inlet mass flow rate per unit volume of the reactor. Thus, when $\tau_{hydro} \leq \tau_{ext}$ reactions occur, the hydrodynamic residence time in the fine scales can be related to the bulk fluid through the mass fraction of fine structures present in the flow. This characteristic time approach to LBO within the EDC model was implemented with fast chemistry for propane-air combustion and tested for an attached flame at fuel-rich conditions.

The axisymmetric CFD calculations were made using the Pratt and Whitney two-dimensional PREACH code. Three constraints were applied on the chemical reaction; (i) the EDC model with characteristic time-based extinction criterion was implemented, (ii) the local mixture should be within flammability limits (lean ϕ = 0.2 or 0.5 depending upon reactant temperature and upper ϕ to 2.0), and (iii) turbulence effects on the flame burning velocity. Fig. 10 shows typical calculated isotherms for what should be the attached-flame condition. These results show that the stoichiometric contour crosses the step recirculation zone from the confluence of the jets and reaches the combustor wall about halfway between the step and the recirculation reattachment plane. We can infer from these temperature contours that the main flame exists in the jet shear layers and originates about 10 cm from the step-plane (i.e., it is lifted and not attached). It is thick and follows the stoichiometric contour across the recirculation zone. There is some agreement between the characteristics of the inferred flame and the actual flame observed in the time-mean photographs and in the near-instantaneous pictures of laser-induced OH fluorescence where concentrated islands of reaction in the jet shear layer thicken the flame region. However, it was found that this model calculated the lifted-flame condition but was

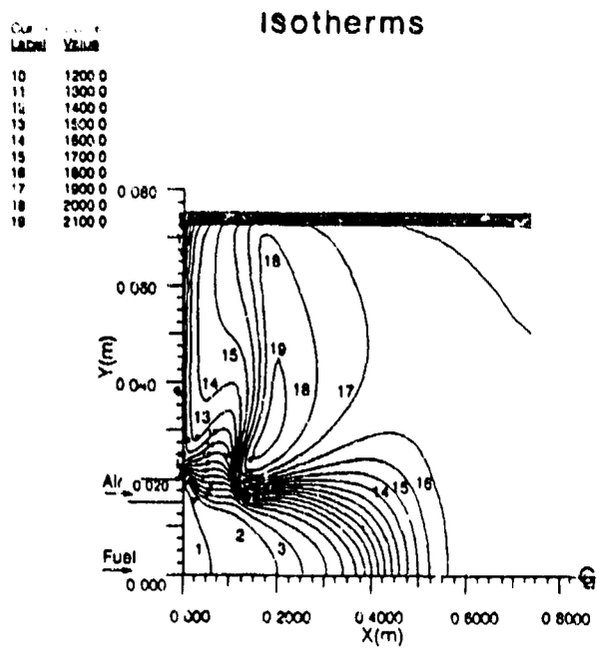

Fig. 10: Isotherms (curve values in degrees K) calculated using the EDC model for the attached-flame conditions in a research combustor

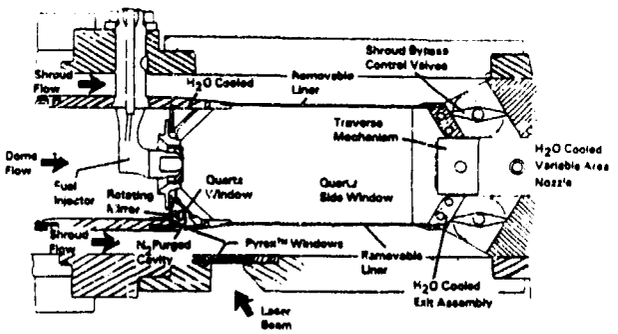

Fig. 11: Schematic diagram illustrating the design features of the generic gas turbine combustor.

unsuccessful in predicting the all-important attached-flame condition. Summarizing:

(a) A research step combustor was successfully developed. It produced three important features of the flow field that affect LBO in a practical combustor; (i) a reactive shear layer at the exit to the fuel nozzle, (ii) inside-out recirculation zones, and (iii) back pressure provided by dilution air jets.

(b) The step combustor acoustic characteristics were optimized; this permitted its operation in a stable and predictable manner. A detailed sequence of events leading to LBO and comprising the attached-flame region, lifted shear flame, intermittent shear flame, and the large-scale instability of the flame front was observed.

(c) The combustor flow-field measurements revealed three regions: near-field step-recirculation, and far-field regions. In these regions, the turbulent fuel-air mixing and entrainment were governed by a potential core, a central recirculation bubble, and a self-similar jet development, respectively.

(d) The LBO process (ϕ = 0.4 to 1.2) in the step combustor behaved like a PSR for LP values in the range of 0.1 to 100 lb/s-ft^3-atm^2. Also, the LBO was successfully correlated with a standard LP derived from the PSR theory. Finally, Swithenbank's [9] dissipation gradient approach and an EDC model (Ref. 11) with a built-in characteristic extinction time criterion offer the possibility of an *a priori* calculation of LBO.

6. GENERIC GAS TURBINE COMBUSTOR

A final test of this research and modeling effort is to be able to predict LBO in an actual gas turbine combustor. To perform such a test, a generic gas turbine combustor was designed with three special requirements; (i) its LBO performance should be consistent with that of an actual gas turbine combustor, (ii) its geometric configuration and flow distribution should be variable so that the effects of residence time and mixture ratio on the LBO can be studied, and (iii) good optical access should be available for descerning the flow field and combustion zone.

Fig. 11 shows a schematic of a Pratt and Whitney designed generic combustor which is a four-injector, planar-section, simplified geometry version of a modern Pratt and Whitney annular combustor sector. This sector employs airblast-atomizing fuel injectors, an engine-type injector/dome interface, and the "inside-out" recirculation zones. The liners, upper and lower, are removable and may contain any desired pattern of air ports. The metal liners do not have any specific internal film cooling but are provided with a thermal-barrier coating and are convectively cooled by the shroud flows. Ignition is accomplished by means of a hydrogen torch ignitor. Individually metered air is supplied to the dome and upper and lower shrouds, provisions are made to supply gaseous nitrogen for subatmosheric pressure simulation, and, finally, fuel can be either propane or methane. This combustor is designed to operate at 65 psia with a variation in dome air from 10% to 40% of the total combustor air flow. The facility in which the combustor is installed is capable of supplying air up to 30 lbs/sec at ambient temperature and fuels up to 30 lbs/hr. Finally, side walls made of fused quartz and contained in water-cooled housings are provided for flow visualization. Sturgess and Shouse [14] have provided a detailed description of the construction, operation, and LBO tests on this combustor.

Fig. 12 illustrates the primary zone stability (LBO) of the generic combustor with lifted and attached flames against the LBO data obtained from the research combustor as well as

the predictions for the research combustor. The generic combustor data were obtained for the 10%, 15%, and 20% dome flow. Since the flames near blowout in the research combustor were all lifted, the partial premixing characteristic of the lifted flames in both combustors should be similar. The LBO stability of the generic combustor at peak heat release rates appears to be less than that of the research combustor. One likely reason may be the different fuel-air mixing rates in the generic combustor.

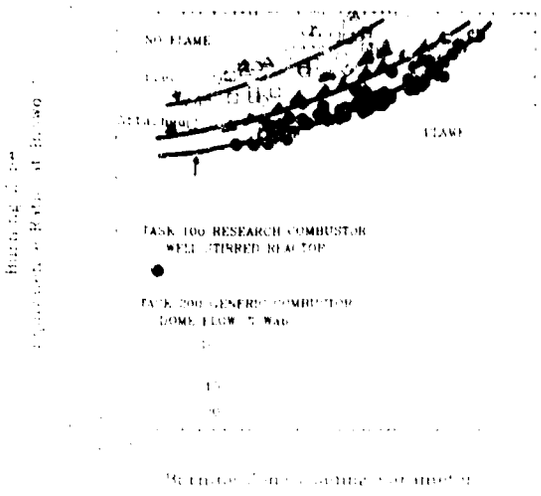

Fig. 12: LBO vs. LP data for the generic gas turbine combustor operating in the lifted- and attached-flame modes compared with data for the research combustor.

It appears that the gross features of the LBO can be successfully correlated by the combustor-loading parameter based on the PSR approach for a specific combustor. However, a simple phenomenological correlation is unlikely to explain the details of the LBO process. For example, the LBO process at simulated low pressures is rather complicated in a generic combustor. It contains quasi-staging of fuel as the loading increases with subsequent flame stabilization by the combustion air jets as well as the primary zone. When jet stabilization exists, LBO is insensitive to dome airflow and vice versa. Finally, the flame changes from a lifted to an attached position and, at a given loading, either flame can exist depending on how combustor-loading is achieved. Due to such complications, correlations of experimental data cannot be general enough to form a unique design curve which can determine the LBO stability margin of a practical gas turbine combustor. Thus, modeling of the LBO process, which works reasonably well with the research combustor, will be seriously challenged by the blowout behavior evidenced in the generic gas turbine combustor.

7. CONCLUSIONS

Following is the summary and conclusions of our research.

1. A geometrically simple, optically accessible, and acoustically decoupled research combustor to reproduce the gross features of the flow field in a modern annular gas turbine combustor was designed and its LBO was measured.

2. We successfully observed and documented a systematic and detailed sequence of events comprising an attached-flame, lifted shear flame, intermittent shear flame, large-scale instability of the flame front, and the LBO. These individual events clearly highlight the complexity of the LBO mechanism.

3. Simple phenomenological correlation based on PSR theory was successful. The LBO process (ϕ = 0.4 to 1.2) in the research combustor behaved like a PSR for LP values in the range of 0.1 to 100 lb/s-ft^3-atm^2. Also, the LBO was successfully correlated with a standard LP derived from the PSR theory. Finally, Swithenbank's [9] dissipation gradient approach and an EDC model (Ref. 11) with a built-in characteristic extinction time criterion offer the possibility of an *a priori* LBO calculation.

4. LBO stability at peak heat release rates in a generic gas turbine combustor was less than in the research combustor. Also, the flame changes from a lifted to an attached position and, at a given loading either flame can exist depending on how combustor-loading is achieved. Due to such complications, it was not possible to uniquely determine the LBO stability margin of a practical gas turbine combustor. Thus, modeling of the LBO process, which works reasonably well with the research combustor, will be seriously challenged by the blowout behavior evidenced in the generic gas turbine combustor.

8. ACKNOWLEDGEMENTS

This research was supported by the U.S. Air Force Wright Laboratory, Aero Propulsion and Power Directorate, Wright-Patterson Air Force Base, OH, under Contract No. F33615-92-C-2207. Mr. C. M. Frayne served as the Technical Monitor.

9. REFERENCES

1. Sturgess, G. J., Sloan, D. G., Lesmerises, A. L., Heneghan, S. P., and Ballal, D. R., "Design and Development of a Research Combustor for Lean Blowout Studies," ASME Journal of Engineering for Gas Turbines and Power, *114*, 1990, pp 13-19.

2. Heneghan, S. P., Vangsness, M. D., and Pan, J. C., "A Simple Determination of the Slit Function in Single Shot CARS Thermometry," Journal of Applied Physics, *69*, 1991, pp 2692-2695.

3. Heneghan, S. P., Vangsness, M. D., Ballal, D. R., Lesmerises, A. L., and Sturgess, G. J., "Acoustic Characteristics of a Research Step Combustor," AIAA Paper No. AIAA-90-1851, to appear in AIAA Journal of Propulsion.

4. Sturgess, G. J., Heneghan, S. P., Vangsness, M. D., Ballal, D. R., and Lesmerises, A. L., "Isothermal Flow Fields in a Research Combustor for Lean Blowout Studies," ASME Journal of Engineering for Gas Turbines and Power, *114*, 1992, pp 435-444.

5. Sturgess, G. J., Sloan, D. G., Roquemore, W. M., Shouse, D., Lesmerises, A. L., Ballal, D. R., Heneghan, S. P., Vangsness, M. D., and Hedman, P. O., "Flame Stability and Lean Blowout-A Research Program Progress Report," in Proceedings of Tenth ISABE, Nottingham, England, 1991, pp 372-384, Paper No. 91-7037.

6. Sturgess, G. J., Heneghan, S. P., Vangsness, M. D., Ballal, D. R., and Lesmerises, A. L., "Lean Blowout in a Research Combustor at Simulated Low Pressures," ASME Paper No. 91-GT-359, to appear in ASME, Journal of Engineering for Gas Turbines and Power, 1992.

7. Sturgess, G. J., Heneghan, S. P., Vangsness, M. D., Ballal, D. R., Lesmerises, A. L., and Shouse, D., "Effects of Back Pressure in a Lean Blowout Research Combustor," ASME Paper No. 92-GT-81, to appear in ASME, Journal of Engineering for Gas Turbines and Power, 1992.

8. Lockwood, F., and Megahead, I. E. A., "Extinction of Turbulent Reacting Flows," Combustion Science and Technology, *19*, 1978, pp 77 80.

9. Swithenbank, J., "Flame Stabilization in High Velocity Flows," Combustion Technology-Some Modern Developments, ed. H. B. Palmer and J. M. Beer, Academic Press, New York, NY, 1974, pp 91-125.

10. Perry, A. E., and Chong, M. S., "A Description of Eddying Motions and Flow Patterns Using Critical-Point Concepts," Annual Reviews of Fluid Mechanics, *19*, 1987, pp. 125-155.

11. Byggstoyl, S. and Magnussen, B. F., "A Model for Flame Extinction in Turbulent Flow," Turbulent Shear Flows-4, edts. L. J. S. Bradbury, F. Durst, B. E. Launder, F. W. Schmidt, and J. H. Whitelaw, Springer-Verlag, Berlin, 1985.

12. Kretschmer, D., and Odgers, J., "Modeling of Gas Turbine Combustors-A Convenient Reaction Rate Expression," ASME, Journal of Engineering for Power, *94*, 1972, pp 173-180.

13. Clarke, A. E., Harrison, A. J., and Odgers, J., "Combustion Stability in a Spherical Combustor," Seventh Symposium (Int.) on Combustion, The Combustion Institute, Pittsburgh, PA, 1958, pp 664-673.

14. Sturgess, G. J., and Shouse, D., "Lean Blowout Research in a Generic Gas Turbine Combustor with High Optical Access," A Paper Submitted to the 38th ASME Gas Turbine and Aeroengine Congress and Exposition, Cincinnati, OH, May 24-27, 1993.

Discussion

Question 1. D.K. Hennecke
In the experiments, you did not simulate the cooling films. Don't you think that they would influence the size and shape of the "inside out" vortex as the films flow against the vortex flow?

Author's Reply
The influence of the cooling film on the size and shape of the "inside out" recirculation zone is negligibly small. This is because in modern annular combustors the cooling air film is pretty much confined to the wall boundary layer. Also, the mass and momentum of the "inside out" recirculation zone is perhaps two orders of magnitude (or more) greater than that of the cooling film. Therefore, the cooling film, at best, causes only a minor perturbation of the "inside out" vortex flow. For this reason, it was not considered worthwhile to add complexity of simulating the cooling film in the research combustor hardware.

ULTRA LOW NOx ULTRA LEAN GAS TURBINE PRIMARY ZONES WITH LIQUID FUELS

G.E. Andrews, H.S. Alkabie, U.S. Abdul Hussain and M. Abdul Aziz

The Department of Fuel and Energy
The University of Leeds
LEEDS, LS2 9JT, UK.

SUMMARY

Three low NOx gas turbine combustor design concepts, Jet Mix, Grid Mix and radial swirlers, which have been demonstrated to give very low NOx emissions using gaseous fuels have been successfully tested on liquid fuels and low NOx emissions demonstrated. The Jet Mix design was shown to have low NOx emissions at atmospheric pressure and has been tested at pressure, with similar low NOx results. Kerosene performance and emissions was very similar to that for propane as the fuel. The scale up of the Jet Mix was found to be possible without increasing the NOx emissions greatly and is a preferable design option to the use of large numbers of smaller Jet Mix modules. Sector tests at pressure showed the Jet Mix design produced emission reductions close to the best of the NASA clean combustor results. The Grid Mix low NOx design was shown to be capable of low NOx performance using kerosene. There was a much wider flame stability than for the Jet Mix design and lower NOx emissions were demonstrated. The radial swirler with vane passage or 76mm wall fuel injection was shown to have ultra low NOx emissions with liquid fuels, only slightly higher than for gaseous fuels. For a high air flow radial swirler it was found that central kerosene injection gave lower NOx emissions than for gaseous fuels and had the potential to yield a NOx EI of below 10 at simulated take off conditions.

1. INTRODUCTION

Aircraft engines are relatively small contributors to the overall and local NOx emissions burdens (1,2). However, NOx emissions from any source are contributing factors in the formation of photochemical smog and of acid rain. Thus, the reduction of NOx emissions from all combustion sources is of vital importance and is the most important combustion problem at present. This has led to a renewed interest in the reduction of NOx emissions from aero-gas turbine engines. Severe legislation already exist for reduced NOx emissions from industrial gas turbines for power generation use and combustor design techniques to meet these regulations have been developed (3-6). This work considers the problems of the applications of some of the industrial gas turbine low NOx combustor designs to aero-engine gas turbine combustors using liquid fuels rather than natural gas.

Environmental impact studies indicate that NOx emissions introduced into the upper troposphere and lower stratosphere can contribute to the formation of ozone at these altitudes and that the resulting ozone can be a contributing factor in causing global warming (2,7). Subsonic aircraft typically cruise at these altitudes and hence a reduction in NOx at cruise conditions is desirable, although at present not a legislated requirement. Existing NOx regulations for aero-gas turbines are concerned with emissions in the vicinity of airports using the landing and take off cycle with the four engine operating conditions of take-off, climb, approach and idle (8,9).

Industrial gas turbines have been developed to meet severe NOx emissions legislation in many countries of the world. The renewed interest in aero gas turbine NOx emissions (8) with the pressures for more stringent aero-engine NOx standards will require extensive development of radically different complex aero-engine combustors (9). The current industrial gas turbine NOx regulations are usually met by using water or steam injection. However, there is a performance and capital cost penalty associated with these reduction techniques and the development of dry low NOx combustor designs to meet NOx regulations is the current preferred option. For aero-gas turbines the use of water or steam injection is not a design option and the reduced NOx requirements must be met by combustor redesign. The present work discusses the fundamental principles of ultra low NOx combustor designs and presents some experimental results of low NOx simulated primary zone designs for liquid fuels, with comparison with propane to represent a fully vaporised aviation liquid fuel. Both swirling and non-swirling systems of direct fuel injection into jet shear layers were investigated.

Many reduced NOx design variants of conventional gas turbine combustors have been attempted by research groups in the USA, UK, Japan and Europe (3,4,8, 10-13) without success. In the seventies the bulk of this effort was directed at the aero gas turbine (10-13), where the operational requirements are quite different from industrial gas turbines. However, in recent years there has been much more attention placed on the development of low NOx industrial gas turbines (3-6,12,13). The only successful applications of industrial low NOx combustor designs have been in very large industrial gas turbines using air staging (12) or fuel staging (13) for enhanced stability, with premixed combustion at high power conditions. However, these concepts are difficult to apply to the type of gas turbine combustors typical of aero gas turbines or their industrial derivatives. An example of this is the complete redesign of the RR RB211 industrial gas turbine combustor, including a new outer pressure casing to accommodate reverse flow combustor cans. This type of design change is not an option for aero gas turbines.

With industrial gas turbines there is a requirement for natural gas and liquid fuel dual firing. At present, and for many years hence, natural gas is and will be the prime specified fuel for industrial gas turbines. This considerably eases the problems of NOx reduction as natural gas has lower NOx emissions than higher hydrocarbon fuels at the same flame operating conditions (14). However, any proposed design also has to be capable of

Presented at an AGARD Meeting on 'Fuels and Combustion Technology for Advanced Aircraft Engines', May 1993.

operating on liquid fuels as well, and with the lowest possible NOx emissions. Thus there is no reason why the concepts used for low NOx in industrial gas turbines cannot be applied to liquid fuelled aero-designs.

Although the general design principles for ultra low NOx are known, very lean primary zones and good fuel and air mixing, methods for successfully achieving these aims have yet to be established for liquid fuels, that do not compromise the stability requirements of gas turbine combustors. All available evidence, including that for premixed systems (15), indicates that measured NOx emissions are higher than expected from the conventional thermal Zeldovich NOx generation mechanism. Thermal NOx generation is negligible below 1800K and yet premixed combustion systems have significant NOx emissions below this temperature (6). The origins of NOx emissions at mean flame temperatures below 1800K are not fully understood, but may possibly be generated by a prompt NOx mechanism.

Lean premixed combustion systems do not generate ultra low NOx emissions as their region of low NOx operation is too close to the weak extinction or inefficient combustion limit. With an adequate stability margin the NOx emissions for premixed combustion are not ultra low, as shown below. In the present work shear layer stabilised flames are investigated with direct fuel injection into the jet shear layers. These shear layers can be generated either from swirling jets or from plain jets. The crucial design feature is the individual fuel supply to each shear layer. The jet shear layers with liquid fuels provide good air blast atomisation and simultaneous fuel and air mixing. However, at the base of each shear layer there is a local rich zone that stabilises the flames outside the stability limits of premixed combustion. The additional stability of directly fuelled jet shear layer combustion systems allow leaner mixtures to be burned and ultra-low NOx emissions to be generated.

A major problem with lean well mixed primary zones is the wall film cooling air. This, when mixed with the lean combustion, can lead to local gas phase quenching and resultant increases in CO and UHC emissions. NO2 formation in the low temperature mixing region may also be a problem. Low NOx emissions have to be met with very low CO and UHC emissions and the increase in CO and UHC due to the film cooling air is a current problem with lean low NOx combustors. A technique that the authors have developed to overcome this problem with lean low NOx combustors is to eliminate the film cooling air and use external cooling of the flame tube using low pressure loss full coverage impingement cooling (16,17), as shown schematically in Fig. 1.

2. PRINCIPLES OF JET SHEAR LAYERS FOR FLAME STABILISATION AND RAPID FUEL AND AIR MIXING.

The authors have developed an approach to the design of low NOx gas turbine combustors based on the injection of fuel at the base of swirling or non-swirling jet shear layers. The primary zone designs have also been shown to have applications to low NOx process burners (18). In this paper three quite different shear layer combustion systems, that have demonstrated low NOx emissions with gaseous fuels are used with liquid fuels. The three systems are Jet Mix, Grid Mix and radial swirlers with swirler outlet plane peripheral fuel injection.

2.1 Jet Mix

The Jet Mix design is shown in Fig 2, it uses a ring of radial fuel and air jets impinging into a similar number of larger air jets. This configuration has been shown to give extremely rapid mixing. Fuel and air were shown to be well mixed, to within 20% of the mean mixture, with less than 20% turbulent fluctuations of the local mixture ratio, within six axial hole diameters (20). This is very rapid mixing, within the potential core length of an axial free jet. It has been shown to give very low NOx emissions for gaseous fuels (14). The high velocity air jets in the radial and axial jets give very good air assist atomisation (21), which has been shown to be better than most other published drop size data for the same pressure loss. Thus the use of this design with liquid fuels should result in rapid fuel atomisation and vaporisation, with a resultant performance close to that of a gaseous fuel. It was the objective of the present work to demonstrate this by comparison of the emissions results for kerosene and propane.

This Jet Mix design was originally developed whilst one of the authors (GEA) worked at the AJT combustion laboratories (formerly Lucas Aerospace). A multi-fuel injector system was developed that demonstrated lower NOx emissions at pressure for kerosene than any other low NOx system under investigation at the time. A version of this design is currently commercially available and is being developed for Westinghouse (22), EGT (23) and others. At Leeds this system (14-16) has been investigated in terms of its potential to be scaled in size and hence to use fewer fuel injection points. However, the results (14) indicated an increase in NOx emissions as the recirculation zone size downstream of the central blockage is increased. For the lowest NOx emissions a large number of small Jet Mix fuel and air mixing modules is required (22,23). This has problems of fuel supply to the large number of injectors, which is worse for liquid fuels.

This Jet Mix design will be investigated at atmospheric pressure in a single Jet Mix system in 76 and 140mm combustor sizes, so that the influence of scale up of a single Jet Mix injector on NOx emissions for kerosene can be determined. These results will be compared with results at 7 bar pressure for seven smaller Jet Mix in a Spey size combustor using kerosene. Applications of the systems to an annular combustor are also discussed and the results compared with the best systems in the NASA Clean Combustor programme.

2.2 Grid Mix

The aim of direct fuel injection into the base of jet shear layers is to mix the fuel and air as the jet develops. Ideally the only fuel rich zones would be at the base of the shear layer and by the end of the potential core region, where turbulence is at a maximum, mixing should be nearly complete. For a single jet shear layer in a 76mm combustor size a 2-4% design pressure loss results in a relatively large hole size at the gas turbine combustor reference primary zone Mach number in the 0.03 - 0.05 range. The potential core would be 2/3 the minimum combustor length of 330mm. To achieve a shorter jet shear layer region multi-hole flame stabilisers may be used (23,24) with individual fuel feeds to each jet.

The NOx emissions and combustion efficiency have been shown to be linked to the pressure loss which controls the turbulent mixing of fuel and air and the velocity gradients in the shear layer (25,26). This system has been shown by the applicant to be capable of ultra low NOx emissions (23-25) for gaseous

fuels and the potential of this system to achieve low NOx with liquid fuels is investigated in the present work. The lowest NOx configuration found in the work on gaseous fuel, shown in Fig. 3, was investigated. The gaseous design was simply made again with smaller radial fuel holes of 0.5mm, using four fuel injection holes for each air jet shear layer. The high velocity air jet would atomise the liquid fuel, by the same process as for the Jet Mix design (21).

2.3 Radial Swirlers

Previous work of the authors with radial swirlers has demonstrated for gaseous fuels some of the lowest NOx emissions ever published for gas turbine applications (5,6,27,28). The NOx emissions were strongly dependent on the method of fuel injection into the radial swirler (5,27,28) and central radially outward, injection into the radial vane passages and swirler periphery radially inward fuel injection are investigated in the present work. The different methods of fuel injection are shown in Fig. 4. Swirling jets have the advantage over simple non-swirling jets in that the swirl induces a much more rapid jet spread and hence a shorter outer shear layer. Thus a single swirler can be used within a 330mm length without the need for multifuel injection points.

A disadvantage of single swirlers is that if a large proportion of the combustion air is passed through the swirler then a strong swirling flow may still be present at the turbine inlet, which may not be desirable. For annular combustors this can be overcome using alternate clockwise and anti-clockwise swirl (29).

3. EXPERIMENTAL TECHNIQUES

An atmospheric pressure combustion facility was used with electrical preheat of the combustion air to compressor outlet temperatures. This permits full airflow simulation of a practical can size combustors. The correct Mach numbers of gas turbine combustors were simulated together with combustor pressure losses in the practical 2-4% range and air inlet temperatures in the range 400-740K. The proportion of air simulated in the combustor primary zone was set by the operating reference Mach number, based on the combustor diameter. For all the combustion air a reference Mach number of 0.05 was used, which is typical of current gas turbines. A Mach number of 0.03 represents a 60% simulated proportion of air into the primary zone, this will be used as the main comparison condition for the various geometries.

Two main combustor sizes were used, 70 and 140mm diameter combustors. The former is a representative size for testing single burners for annular combustors or for testing single burners from a larger array of burners, of the type used in large industrial low NOx combustors (4). The 140mm combustor is similar to the Rolls-Royce Spey, Tay combustors as well as a number of other gas turbine combustors in this power range.

For comparison with the atmospheric pressure testing the Jet Mix design was also tested at pressure at the AIT Laboratories in Burnley. This had a clean air preheat system and both can and annular combustor sector configurations were used. A mean exhaust plane traverse was carried out to determine the exhaust emissions distribution, but this was shown to agree quite well with the mean gas analysis from an EPA multi-hole gas sampling probe well downstream of the exhaust were the gases were well mixed. This mean sample was used in some of the work were the air/fuel was varied over a wide range.

4. ATMOSPHERIC PRESSURE TESTING

Atmospheric pressure testing is much cheaper and quicker than full pressure testing. Atmospheric pressure testing of gas turbine combustors is often criticised as unrealistic due to the high pressure operation of gas turbines (10-16 bar typically for industrial gas turbine and up to 40 bar for aero gas turbines at take off). However, most essential features of the combustion are not pressure dependent. In particular the combustor percentage pressure loss, turbulence intensity, gaseous fuel and air mixing intensity, mean residence time, mean reference velocity, jet mixing shear layer aerodynamics and the global combustor aerodynamics are all not dependent on the pressure.

Provided that the value of these parameters that apply for high pressure operation are simulated at atmospheric pressure, as is the case in the present work, then the atmospheric combustion tests will correctly simulate the combustion aerodynamics at pressure. Atmospheric pressure investigations of gas turbine combustor aerodynamics and pressure loss have been in use in the gas turbine industry for 50 years.

The most important effect of pressure on combustion is the associated increase in inlet temperature that occurs as the compressor pressure ratio is increased. It is essential that the correct inlet temperature is simulated at atmospheric pressure using a clean air preheat system, as in the present work. Inlet temperature has a very strong influence on flame stability, flame length, combustion efficiency and all pollution parameters and this is much greater than any influence of pressure on combustion.

Pressure may influence combustion performance in several ways. It may change the overall flame stability limits due to the well known widening of flammability limits with pressure. However, tests at atmospheric will be conservative in terms of a low NOx design. If pressure did improve the stability then it would be possible either to reduce the NOx emissions at pressure by operating with a leaner primary zone or to increase the stability margin by operating at the same lean equivalence ratio at pressure as at atmospheric pressure. It is this latter approach that is adopted in the present work and no change in the primary zone equivalence ratio is envisaged at pressure.

Pressure may also change the position of flame stabilisation within a combustor. However, if the flame is stabilised close to the head of the combustor at atmospheric pressure then pressure cannot change the flame position. This was determined in the present work using measurements of the wall temperature profile and by visual observation through an air cooled observation window on the combustor centreline. For all flame stabilisers under investigation it was ensured
that all the designs investigated operated with an attached flame in the head region

Liquid fuels are more sensitive to pressure effects as atomisation and vaporisation processes are pressure dependent. However, the authors have shown that air blast atomisation in large air flow jet shear layers is extremely good and better than most conventional air blast atomisers using small proportions of the airflow (21). The authors have shown that at atmospheric pressure very high combustion efficiencies (99.9%) can be achieved with various swirling and non-swirling jet shear layer fuelled designs (5,6,25,26,28). In these circumstances pressure can have no significant influence on the combustion efficiency. It is these types of high combustion efficiency designs that are the subject of the present work and pressure is unlikely to have any significant influence on the combustor performance.

Pressure does have a significant influence on CO and NOx emissions. CO emissions are decreased with pressure and existing equations for global CO oxidation may be used to predict this effect. However, current emission regulations for industrial gas turbines specify that 10ppm CO at 15% oxygen is achieved at pressure. The present type of shear layer designs have demonstrated with gaseous fuels 10-20ppm CO at atmospheric pressure and hence it can be assumed that at pressure there should be no problem in meeting a 10ppm CO target. This work will investigate any deterioration in the CO emissions with liquid fuels.

NOx emissions increase with pressure. This is mainly due to the action of pressure on the thermal NOx kinetics and can be shown from thermal NOx kinetics to be a square root pressure effect. Many experimental investigations of the pressure effect on NOx have confirmed that a square root pressure dependence of NOx is reasonable, although there is some combustor to combustor variation. The increase in NOx with pressure can be used to scale down NOx regulations to 1 bar. The EPA 75ppm NOx emission regulation at 15% oxygen scales to 20-24ppm for engine pressures from 10-15 bar. A more stringent Dutch NOx regulation is 40ppm at 16 bar which scales to 10ppm at 1 bar. Some California regulations are requiring 10ppm NOx at pressure, requiring 2.5ppm at atmospheric pressure. It is the aim of the present work to investigated the process of NOx formation in jet shear layer designs that can achieve inside the 10ppm target (2.5ppm at 1 bar for natural gas at atmospheric pressure).

For aero engine applications NOx emissions are usually given as an emission index (EI, g NOx/kg fuel). A typical take off NOx EI for a modern civil jet engine (30,31) is 35 at 33 bar. This would result in a NOx EI of 6 at 1 bar and if a 50% reduction was required than NOx EI below 3 at 1 bar needs to be demonstrated. A NOx EI below 1 at 1 bar is the design aim of the present work. However, results at one bar in the range 1-3 EI will represent low NOx emissions for liquid fuels. It may be shown that this is equivalent to a NOx corrected to 15% oxygen of 10-30 ppm at 1 bar. Some of the results will be reported as NOx corrected to 15% oxygen and the above conversion factor between the two units will be used.

5. JET MIX RESULTS FOR IN LINE RADIAL AND AXIAL JETS

5.1 76mm Combustor Results for 20% Radial Air and 2% Pressure loss.

The initial Jet Mix results were obtained using a single injector with eight holes and radial and axial holes in line. For 20% of the total air through the radial holes and for the radial and axial jets in line, which was the lowest NOx configuration, the NOx results are shown in Fig. 5 for the 76mm diameter combustor. This compares the premixed results for the same Jet Mix stabiliser with those for propane and kerosene injection. All the results were for an inlet temperature of 600K, a pressure loss of 2% and a Mach number of 0.047, based on the combustor diameter and the inlet temperature, this simulates all of the combustion air passing through the Jet Mix stabiliser with no dilution or film cooling air. NOx emissions of the order of 20ppm corrected to 15% oxygen or 2EI were achieved for kerosene, which is within the desired NOx reduction range. The kerosene results were lower than for propane but higher than for premixed fuel and air. The atomisation and vaporisation delay for kerosene was considered to permit more fuel and air mixing to take place prior to combustion and hence to reduce the NOx emissions due to local near stoichiometric burning. An equivalence ratio of 0.6 was required for kerosene to achieve the lowest NOx emissions, compared with 0.5 or lower for propane. There was no evidence of single droplet local stoichiometric zone burning, which would have increased the NOx emissions.

An interesting feature of these results, which has been found in the other low NOx emissions designs discussed below, is that the NO2 emissions increased as the NOx emissions were reduced, as shown in Fig. 6. This shows that kerosene combustion produced more NO2 than propane combustion. The main route for the generation of NO2 is the reaction between the HO2 radical flame the reaction zone with NO to form NO2, which is a fast reaction at low temperatures. It is the reduction in temperature as the mixture is made leaner that promotes the conversion of NO to NO2.

5.2 76mm Combustor with 11% Radial Air and 4% Pressure Loss

The results also showed that the combustion efficiency at 600K inlet temperature was only 98%. To overcome this problem the proportion of radial jet air was reduced to 11%, for the same total air flow area and the pressure loss was increased from 2% to 4%, to improve the kerosene atomisation and to increase the fuel and air mixing rates. The radial and axial jets were kept in the lowest NOx configuration with in line jets. The reduced radial jet air was investigated as the stability of the 20% of total airflow radial jet system was poor with kerosene at an equivalence ratio of 0.54. The results of the new Jet Mix design at the same 0.047 Mach number are shown in Figs. 7 and 8. The desired improvement in the combustion efficiency was achieved, with a 99.7% efficiency as shown in Fig. 7.

The NOx and the combustion efficiency results were similar to those for propane, indicating that the kerosene was vaporised and mixed with combustion air in a similar way to propane. However, the higher pressure loss resulted in better atomisation due to the higher air jet velocities (21) this reduced the vaporisation period and brought the performance with kerosene closer to that with propane, compared with the results for a 2% pressure loss. However, the NOx emissions were still lower than for propane, indicating some mixing prior to combustion during the vaporisation delay period. The stability of the new Jet Mix design was much better than the 0.54 weak extinction of the 2% pressure loss 20% radial air flow design, as shown in Figs. 7 and 8, where efficient combustion was achieved at equivalence ratios as lean as 0.35 with kerosene. The leaner combustion allowed lower NOx emissions to be demonstrated, with stable efficient combustion with kerosene with NOx emissions corrected to 15% oxygen as low as 12 ppm. These results indicate that NOx emissions of 1-2EI at 1 bar may be achieved with kerosene.

The main difference between the results in Figs. 5 and 8 was the equivalence ratio at which the minimum NOx emissions was achieved. For the same 20ppm NOx emissions corrected to 15% oxygen the 2% pressure loss 20% radial flow design requires an equivalence ratio of 0.6 compared with 0.45 for the 4% pressure loss 11% radial air jet design. This would require quite a different air flow arrangement in a practical combustor. Both designs have minimum NOx at an equivalence ratio richer than the overall equivalence ratio at maximum power. Hence, the use of a 0.047 Mach number as the test condition is inappropriate as a reduced air flow would be required to achieve the desired Jet Mix primary zone equivalence ratio at a

leaner overall mixture. This would result in a lower Mach number as the primary zone condition.

A typical high power overall equivalence ratio is 0.3 and this would require 50% of the air flow to a Jet Mix primary zone to achieve 0.6 equivalence ratio and 67% to achieve 0.45, corresponding to primary zone Mach number of 0.023 and 0.031 respectively. Reducing the primary zone Mach number for the same pressure loss will improve the combustion efficiency and has been shown to have no adverse effect on NOx emissions (6,14,16). These lower Mach number were also used in the scale up to 140mm combustor diameter size of the single Jet Mix design, discussed below.

5.3 Influence of the Proportion of Radial Jet Airflow

A significant influence on the difference in the above two Jet Mix designs was the proportion of the radial jet air flow. The proportion of the radial jet airflow influences the extent of initial fuel and air mixing and limits the extent of local rich zones. The variation of the minimum NOx emissions with the proportion of the radial flow air for the 76mm combustor is shown in Fig. 9 for the minimum NOx equivalence ratio of 0.4 and an inlet temperature of 600K and 0.047 Mach number. The kerosene and propane results were similar, but the kerosene combustion was not stable for radial jet proportions of 20% or higher. However, by delaying the fuel and air mixing, using offset radial and axial air jets, the stability could be increased and higher radial jet proportions used (16). The disadvantage of this was the large increase in NOx emissions caused by the rich radial jet burning (14,16) and this offset jet design was not used in the present work. Fig. 9 shows that the Jet Mix design with a mean equivalence ratio of 0.4 could achieve a NOx EI of 1 g/kg at one bar, equivalent to an EI of 6 at 36 bar using a square root pressure dependence.

Figure 9 also compares the present results with those carried out on a 7 Jet Mix configuration in a RR Spey sized combustor (32). These results were obtained by one of the authors (GEA) at the AIT laboratories. The results at 6.9 bar have been reduced to atmospheric pressure conditions using both a square root and a 0.65 pressure exponent correction. The 0.65 pressure exponent was determined experimentally on the 7 Jet Mix array in a Spey can pressure casing. The agreement with the propane results identifying 20-30% radial flow proportion as the optimum was good. However, the NOx emissions based on the measured 0.65 pressure exponent were much higher than for the present propane or kerosene results, for radial jet proportions from 7% to 30%. This may have been due to the large number, 42, of fuel injection holes and the difficulty of manufacturing them of precisely equal size. Also there was a practical lower fuel jet size of approximately 0.5mm below which fuel hole blockage could become a problem. Ideally it was considered that for adequate fuel distribution between 42 holes a hole jet size of 0.25mm would be required, these are now routinely used in diesel engine fuel injectors and should be feasible in any engine applications of these designs. This problem of oversized and unequal fuel holes may have resulted in a worse fuel distribution than in the present work and hence to higher NOx emissions.

5.4 Large Scale Single Jet Mix Designs

The problem of the large number of fuel injection holes in multi-arrays of smaller Jet Mix stabilisers could be overcome if a single Jet Mix stabiliser could be increased in size to be equivalent to that of the 7 stabilisers in the Spey sized combustor. This was investigated in a 140mm diameter pipe combustor, of similar size to the Spey combustor. The Jet Mix design used in line radial and axial jets, but placed the axial jets midway between the radial jets outer and the outer diameter of the combustor. This produced a relatively larger distance between the radial jet outlet and the axial jet, in an attempt to increase the radial jet burning and to give an improved flame stability, by delaying the radial and axial jet mixing. A Mach number of 0.028 was used, to be closer to the actual primary zone air flow residence times at the low NOx primary zone conditions, as discussed above. The design pressure loss was 4%.

A comparison between the propane, kerosene and gas oil results is made in Figs. 10 and 11. This shows again that there was good agreement between the propane and kerosene results, albeit at a slightly inferior combustion efficiency. The kerosene results showed a minimum NOx emissions of 20ppm corrected to 15 % oxygen (EI approximately 2) at an inefficiency of 0.2%. The higher combustion efficiency results for propane at leaner mixtures allowed the propane Jet Mix combustor to achieve 10ppm NOx at 0.1% combustion inefficiency. The gas oil results had much higher NOx emissions, possibly due to low level fuel nitrogen in this fuel (typically levels are 60ppm). The gas oil results will also be influenced by the lower volatility of gas oil compared with kerosene and the increased viscosity. These physical property changes will lead to an increase in the spray drop size and a decrease in the vaporisation rate. This will lead to a decrease in the fuel and air mixing rate and an increase in the NOx emissions.

The NOx results are shown as a function of flame temperature in Fig. 10. This shows that the kerosene results were slightly higher than those for propane for the same flame temperature, indicating inferior fuel and air mixing with kerosene. The results for natural gas are also shown in Fig. 10 and are much lower than for propane, indicating the importance of the fuel composition in gas turbine NOx emissions. The ratio a half for natural gas NOx emissions relative to those of propane has been found in other gas turbine low NOx combustor designs (27). Although part of the difference is due to small differences in the peak flame temperature it is considered that a significant contribution is from a form of prompt NOx, based on the very short duration rich mixtures in the radial jet combustion. Prompt NOx requires the presence of higher hydrocarbon fractions than methane and this could a more significant source of NOx for kerosene than for propane.

5.5. Seven Jet Mix Spey Size Combustor at Pressure

The above large scale single Jet Mix results were compared with those for the 7 Jet Mix Spey design in Fig. 12. This shows the 6.9 bar gauge pressure NOx results as a function of the flame temperature. This is the turbine entry temperature in a combustor with dilution zones and/or wall cooling, but was the primary zone mean exit temperature when compared with the atmospheric pressure results. The use of the flame temperature enables differences in inlet temperature to be accounted for in the comparison. The data in Fig. 12 at pressure was obtained from tests over inlet temperatures from 600 to 788K, covering simulated approach, cruise, climb and take off conditions. Two radial air flow proportions, 10 and 30%, were investigated in the 7 Jet Mix Spey designs and Fig. 12 clearly shows the lower NOx emissions of the larger radial air flow proportion. Comparison is also made in Fig. 12 with the NOx emissions from conventional gas turbine combustor designs at the same test conditions. At 1500K a NOx reduction of 68% was

demonstrated at pressure for the 30% radial flow design, compared with an approximately 72% reduction based on the present results for a scaled single Jet Mix design using a 0.65 pressure exponent.

The 140mm single 8 hole Jet Mix results were scaled to the 6.9 bar pressure of the high pressure results using 0.5 and 0.65 pressure exponents. For the 7 Jet Mix design an experimental pressure exponent was determined at 0.65 and this has been used for comparison with the more usual 0.5 NOx pressure exponent. The same 30% radial air flow proportion was used as in the 7 Jet Mix work. Fig. 12 shows that the single large Jet Mix results had lower NOx emissions than for the seven Jet Mix combustor, whichever pressure exponent was used. However, the difference was relatively small for the 0.65 pressure exponent. Part of this improvement could have been due to the improved fuel distribution from the use of 8 fuel injector holes instead of 42, but similar hole diameters.

This difference in NOx emissions may also have been contributed to by the use of wall film cooling in the 7 Jet Mix high pressure tests. Rolls Royce transply wall cooling was used to minimise the amount of film cooling air to approximately 15% of the total air flow. Nevertheless, the use of part of the air for film cooling would effectively make the main combustion richer for the same overall equivalence ratio. This would increase the NOx emissions. This was one of the main reasons for using no film cooling in the present work and the development of impingement regenerative cooling, as shown in Fig. 1. These results indicate that for the same Jet Mix configuration scaling up the size of the Jet Mix system may be preferable for lower NOx than the use of a large number of smaller Jet Mix. The problem of the large number of fuel supply pipes is drastically reduced using this procedure.

5.6 Sector Results at Pressure

A one sixth sector of an annular combustor was investigated using an array of small Jet Mix devices. There were two rows of Jet Mix with an outer recessed pilot row of Jet Mix, which had a 70mm axial length prior to dump mixing with the main Jet Mix burner flow. The pilot Jet Mix had 10% radial air flow and the main Jet Mix had 30% radial air flow. Transply wall film cooling was used for the main and pilot combustors. The recessed pilot was used with fuel staging to the pilot to improve the turn down ratio of this system. Fuel was staged to the pilot at idle and the recess was to prevent the fuel mixing with the unfuelled Jet Mix when the main fuel was shut off. Without this recess there was too much cross mixing between the fuelled and unfuelled Jet Mix modules to achieve efficient combustion at idle.

A low NOx pilot was considered to be an essential feature of a low NOx combustor that meets the EPA and ICAO LTO cycle, because of the long period spent at idle. If a conventional pilot is used with high NOx emissions, this can prevent the achievement of low NOx emissions. This has occurred in industrial gas turbine applications of the Jet Mix concept where conventional pilots have been used for low power operation and the achievable NOx reductions were well below the capabilities of the Jet Mix design, due to the NOx produced in the pilot at high power conditions (22,23). In aero applications it is unlikely to be acceptable to switch off the pilot combustor at high power conditions and hence the pilot will give a contribution to high power NOx emissions.

This design was used to produce emissions data at the simulated take-off, climb, approach and idle conditions of the EPA landing and take off cycle. Results were obtained at 6.9 bar gauge pressure over a range of flame temperatures and the NOx emissions for any engine where the flame temperature or turbine entry temperature are known can be predicted. A 0.65 pressure exponent for NOx was used in the prediction of NOx at take off and climb conditions. No change in the CO and UHC results with pressure were assumed, which is a pessimistic assumption and will result in the overprediction of CO and UHC. However, no reliable pressure correction procedure for CO and UHC is available.

The results are summarised for the EPA landing take-off cycle (also adopted by ICAO) in Table 1. Applications of the data have been made to the RB211-22B, the JT9D-7 and the CF6-50 using engine conditions that applied in 1977. Comparison is made in Table 2 with the lowest NOx emissions configurations from Phase II of the NASA Clean Combustor programme (10,11). The predictions for the Jet Mix system are close to the best of the NASA Clean Combustor Programme. Subsequent work has shown that the two rows of main Jet Mix burners can be replaced with one row of large burners with little deterioration in NOx emissions, as shown above for the Spey combustor sized results where 7 Jet Mix modules were replaced with a single injector.

Table 1 Jet Mix Sector Predictions for the EPA LTO Cycle RB 211-22B (1977 conditions).

Condition	Time	NOx	CO	UHC	Cycle Pollutants, pounds		
	mins	EI	EI	EI	NOx	CO	UHC
Take Off	0.7	14.9	1.7	0.0	2.6	0.3	0.0
Climb	2.2	10.9	3.4	0.1	4.8	1.5	0.04
Approach	4.0	11.4	8.9	0.7	3.4	2.7	0.2
Idle	26.0	2.8	15.6	7.6	1.8	10.3	5.0

NOx pounds/1000 pounds thrust hour/cycle 3.4
CO pounds/1000 pounds thrust hour/cycle 4.0
UHC pounds/1000 pounds thrust hour/cycle 1.4

The CO and UHC emissions parameters were reduced to 2.7 and 0.2 respectively if the main stage Jet Mix radial airflow was reduced from 30% to 20%, there was little change in NOx, at 3.5, for this configuration.

Table 2 Jet Mix Sector Combustor EPA LTO Cycle Predictions and Comparison with NASA Clean Combustor Results for the GE CF6 and PW JTD-7(10,11).

	EPA Emissions Parameter		
	NOx	CO	UHC
	pounds/1000 pounds thrust hour/cycle		
Jet Mix Sector (Radial Jet Pilot/Main 10%/20%)			
RB211 22B (1977)	3.5	2.7	0.2
JT9D-7 (1977)	2.5	2.2	0.2
CF6-50 (1977)	4.6	1.8	0.2
NASA Clean Combustor Best Phase II Results (10,11)			
JT9D-7 (1977)	2.3	10.2	0.3
Lowest NOx, Configuration VORBIX S-17			
Lowest CO, S-20	3.5	6.3	0.6
CF6-50 (1977)	3.6	5.5	0.2
Lowest NOx, Configuration DOUBLE ANNULAR D/A-7			
Lowest CO, D/A-8	4.5	2.8	0.2

6. GRID MIX RESULTS

The radial Grid Mix design shown in Fig. 3 injects fuel radially into the air jets and has been shown to have ultra low NOx emissions using gaseous fuels. The fuel is injected into the high air jet velocity upstream of the shear layer and has some partial premixing prior to encountering the shear layer where the flame develops. The turbulent energy for mixing and flame propagation is generated in the shear layer. Fuel cannot pass through the shear layer without encountering the turbulence for mixing and hence the combustion occurs in a well mixed mixture. The ultra low NOx emissions achieved with propane as the fuel are shown in Fig. 13 (19) for a 4 hole 76mm combustor at 600K. The results for three Mach numbers and pressure loss were very similar and close to those for a fully premixed four hole grid plate at the same pressure loss, as shown in Fig. 13. However, the mixing in the shear layers results in some local rich zones in the shear layer which stabilises the flame outside the weak extinction of the premixed system. Thus, as shown in Fig. 13, lower NOx emissions can be achieved with direct fuel injection into the radial Grid Mix stabiliser than can be achieved with fully premixed fuel and air, as leaner mixtures can be burnt efficiently with an adequate stability margin.

The direct fuelling of each shear layer is crucial to the low NOx performance of this design. This is shown in Fig. 14 where a central four hole radial outward fuel injector surrounded by four axial air jets is compared with the radial Grid Mix design. The jet aerodynamics are identical and only the fuel placement is different. Fig. 14 shows that the NOx emissions were dramatically higher, for two inlet temperatures, with the central four hole injector. In adapting this design for liquid fuel applications its was therefore essential to maintain the radial inward fuel injection into each air jet shear layer. The main design change was the use of only 4 holes per air jet, compared with 8 for gaseous fuels. These holes were 0.5mm diameter.

The high velocity crossflow by the peak jet velocity would give good atomisation of the fuel (21). Although the addition of a vaporisation tube to this design appears to be attractive, as advocated by McVey et al (33) in a similar low NOx design, it was found to be detrimental to the performance of the system. Atomisation was inferior with considerable vaporisation tube wall wetting. Flame stability was much worse, as were the NOx emissions and combustion efficiency. The main problem of the basis radial Grid Mix design with liquid fuels was the heating of the fuel contained within the grid plate, which caused local vapour bubbles at some test conditions which could stop the fuel flow to one or more air jets. It is recommended that individual fuel feed tubes are used to each injection hole in future work.

The radial Grid Mix results with kerosene injection into a four hole 76mm combustor configuration are shown in Figs. 15 and 16. The results at the three different Mach numbers were obtained at the same pressure loss by changing the Grid Mix stabiliser to have a smaller hole size as the Mach number was reduced. This kept the pressure loss, the shear layer jet velocity and the atomisation the same as the Mach number was reduced. Fig. 15 shows that the NOx emissions were then relatively insensitive to the Mach number. If the Mach number was varied at constant jet diameter then the pressure loss decreased with Mach number and there was a serious deterioration in the combustion efficiency with decrease in Mach number.

Comparison of the Jet Mix results in Fig. 10 with the Grid Mix results in Fig. 15 shows that both systems had similar low NOx emissions at the same flame temperature. However, the Grid Mix results in Fig. 15 show a much wider flame stability with mixtures burning efficiently at mean flame temperatures of 1300K, whereas the Jet Mix design could not operate efficiently below 1550K. The weak extinction was below an equivalence ratio of 0.3, with the minimum NOx and combustion inefficiency condition being at 0.4 equivalence ratio giving a very wide stability margin compared to that for the Jet Mix design. The reason for this flame stability difference is the use of the radial air jet mixing with part of the fuel prior to the main combustion zone. This effectively limits the richest local zones at the base of the shear layer and these control the flame stability. This was shown with the Jet Mix system in test where the radial flow was reduced to 6% and there was a wide extension of the lean stability, but a large increase in the NOx emissions.

The combustion inefficiency is shown as a function of the NOx emissions corrected to 15% oxygen in Fig. 16. The wider stability enables NOx emissions of 16 ppm to be achieved (approximately 1.6 EI), which is lower than for the Jet Mix system in Fig. 11. However, the combustion inefficiency of the Grid Mix design was much worse than for the Jet Mix design. The reason for this was uncertain as at 400K almost the same Grid Mix combustion inefficiency had been found as at 600K, whereas there is usually a large decrease in the combustion inefficiency. It is considered that this problem may be associated with the problems associated with the heating of the fuel inside the Grid Mix stabiliser. This should be overcome in future better designs of the Grid Mix stabiliser.

7. RADIAL SWIRLER RESULTS

The radial swirler used with the various methods of fuel placement are shown in Fig.4 . Previous work (5,6,19,27) has shown very low NOx emissions using this swirler design with gaseous fuels. The NOx emissions were also very sensitive to the fuel injection location and ultra low NOx emissions were achieved with swirler vane passage and swirler outlet plane wall injection. The strong influence of the fuel injection location on the NOx emissions is shown in Figs. 17 and 18 for propane at 600K. Fuel injection into the dump expansion zone downstream of the swirler (140mm wall injection) produced high NOx emissions, due to the creation of rich long residence time zones in this region. These results also indicated that if any of the fuel injected elsewhere is transported into these recirculation zones then high NOx emissions will result. McVey et al (33) investigated this design at pressure and reported high NOx emissions and it is considered that the radial swirler design that he used would allow the fuel to be transported into the dump recirculation zone.

Fig. 18 shows that central radially outward fuel injection achieved low NOx emissions of 10 ppm NOx at 15% oxygen (approximately 1 EI). However, with either vane passage or 76mm wall radially inward fuel injection the NOx emissions were 3 and 1 ppm respectively (0.3 and 0.1 EI). These NOx emissions were as low as could be achieved using premixed combustion, and the 76mm wall injection results were lower than for premixed combustion. These radial swirler designs were ideally suited to applications with liquid fuels as the high vane swirler air velocities would provide good air blast atomisation.

For vane passage injection the liquid fuel atomisation should be at an optimum and there is the presence of the vane passage length as a vaporisation period. Fig. 19 shows the internal

traverse of the resultant flames for propane and kerosene for a 0.43 equivalence ratio and a 600K inlet temperature. The traverses were carried out close to the swirler exit at 10 and 30mm from the swirler outlet plane. Further downstream kerosene and propane had very similar composition profiles, except for the magnitude of the NOx which maintained the differences shown in Fig. 19 at the 30mm position. The fuel placement with kerosene was different in the near burner region with more fuel reaching the central region. This resulted in a higher central zone temperature and NOx formation and a slower flame development with kerosene into the leaner outer region of the flow. The higher NOx emissions at the combustor exit were thus entirely due to these small differences in fuel placement in the near burner region.

The mean NOx emissions as a function of the equivalence ratio are shown in Fig. 20 for gaseous and liquid fuels. The kerosene NOx emissions were very close to those for propane and the differences were due to the initial fuel placement differences, as shown by the internal gas composition traverses. Thus the atomisation and vaporisation influences with kerosene were small. Fig. 21 shows that the minimum NOx corrected to 15% oxygen, compatible with better than a 0.1% combustion inefficiency, was 5ppm (0.5 EI) for kerosene and 2.5ppm for propane at an equivalence ratio of 0.4 for both fuels. Even for gas oil the minimum NOx was a low as 10ppm as shown in Fig. 21. These are extremely low NOx emissions for liquid fuels and indicate that very low NOx emissions could be achieved at pressure conditions. Comparison of Fig. 20 with Fig. 8 shows that for the same equivalence ratio the NOx emission for kerosene were substantially lower for the radial swirler with passage fuel injection.

Figures 17 and 18 show that even lower NOx emissions were achieved for propane with 76mm wall injection at the swirler outlet plane. Passage injection of liquid fuel in high pressure high inlet temperature gas turbines may lead to spontaneous ignition in the vane passages. The wall fuel injection technique does not have this problem as the fuel is injected downstream of the swirler directly into the combustion zone. The radially inward fuel injector was designed for dual fuel firing with two separate fuel supply rings to separate gaseous and liquid injection points, one per vane passage outlet. There were no combustion performance problems with this design for liquid fuels and there was an adequate flame stability.

The results are compared with those for gaseous fuels in Figs. 22 and 23. The kerosene and gas oil minimum NOx emission results were slightly higher than for vane passage injection, even though the propane results were lower. However, the results still indicate that very low NOx emissions could be achieved at pressure conditions using liquid fuel.

All the above radial swirler work was carried out in the 140mm combustor size but was at a relatively low Mach number of either 0.014 or 0.022. For the optimum equivalence ratio of 0.4 for minimum NOx emissions, at least 60% of the combustor air flow is required to pass through the radial swirler at maximum power conditions and this requires a Mach number of approximately 0.03. To achieve this Mach number at an acceptable pressure loss the radial swirler air flow was increased by placing together two existing radial swirlers with the central 76mm backplate removed from the downstream swirler. This produced a split radial swirler of total passage depth of 26mm

Test of this design with radial passage and 76mm wall gaseous injection, all showed that the ultra low NOx emissions of the earlier lower Mach number work could be repeated. However, for liquid fuels the wall fuel injection appeared to transport the fuel into the outer recirculation zone and high NOx emissions were produced. Techniques to overcome this problem have been developed. However, it was found that with this higher air flow capacity central liquid fuel injection performed with lower NOx emissions than for gaseous fuels. These results are shown in Fig. 21 and 22 and the very low NOx emissions for kerosene are demonstrated. NOx emissions for kerosene as low as 3ppm at 15% oxygen are shown in Fig. 22, compared with 12ppm for propane and 10ppm for natural gas. This lower value for kerosene is likely to have been due to slightly different fuel placement in the near burner region.

Comparison of Fig. 21 with Figs. 10 and 15 shows that these large air flow capacity radial swirlers have an order of magnitude lower NOx emissions than for the Jet Mix or Grid Mix designs. These results offer the possibility of achieving an EI of well under 10 at take off conditions and possibly near unity EI. Development of the design to meet full gas turbine combustor operating conditions is warranted.

CONCLUSIONS

1. Three low NOx gas turbine combustor design concepts, which have been demonstrated to give very low NOx emissions using gaseous fuels have been successfully tested on liquid fuels and low NOx emissions demonstrated.

2. The Jet Mix design was shown to have low NOx emissions at atmospheric pressure and has been tested at pressure, with similar low NOx results. Kerosene performance and emissions was very similar to that for propane as the fuel.

3. The 6.9 bar pressure tests for a seven Jet Mix design for the Spey size combustor gave NOx emissions results close to those obtained with a single large Jet Mix in a 140mm combustor, scaled to pressure conditions using an experimentally determined 0.65 pressure exponent.

4. Tests on a sector rig of a two stage low NOx combustor using Jet Mix low NOx systems was shown at pressure to yield NOx emissions close to the best demonstrated in the NASA clean combustor programme.

5. The Grid Mix low NOx design was shown to be capable of low NOx performance using kerosene. There was a much wider flame stability than for the Jet Mix design and lower NOx emissions were demonstrated.

6. The radial swirler with vane passage or 76mm wall fuel injection was shown to have ultra low NOx emissions with liquid fuels. For a high air flow radial swirler it was found that central kerosene injection gave lower NOx emissions than for gaseous fuels.

ACKNOWLEDGEMENTS

We would like to thank the UK SERC for a series of grants in support of part of this work.

REFERENCES

1. National Air Pollution Emissions Estimates, 1940-1989, US EPA, EPA-450/4-91-004, 1991.
2. Johnson, C., Henshaw, J. and McInnes, G., Impact of Aircraft and Surface Emissions of Nitrogen Oxides on Troposhperic Ozone and Global Warming, Nature, Vol. 355, 1992.
3. Kuroda, M. et al, Development of a dry two stage low NOx combustor for a gas turbine, ASME Paper 87-GT-64, 1987.
4. Becker, B., Berenbrink, P. and Brandner, H., Premixing gas and air to reduce NOx emissions with existing proven gas turbine combustion chambers, ASME Paper 86-GT-157, 1986.
5. Al Kabie, H.S. and Andrews, G.E., Radial swirlers with peripheral fuel injection for ultra-low NOx emissions, ASME Paper 90-GT-102, 1990.
6. Andrews, G.E., Abdul Aziz, M.M., Al Dabbagh, N.A., Ahmad, N.A., Al Shaikhly, A.F., Al Kabie, H.S. and Kowkabi, M., Low NOx combustor designs without premixing for aero-engine applications, Proc. European Propulsion Forum: Futures civil Engines and the Protection of the Atmosphere, DGLR, AAAF, RAeS, DLR Research Center, Cologne, Paper 90-020, pp. 161-174, April, 1990.
7. Haughton, J.T., Jenkins, G.J. and Exphraums, J.J., 'Climate change - The IPCC scientific assessment', Intergovernmental panel on climate change, Cambridge University Press, 1990.
8. Proceedings of the European Propulsion Forum: Future Civil Engines and Protection of the Atmosphere, DGLR, AAAF, RAeS, April 3-5, DLR Research Center, Cologne, 1990.
9. Lister, D.H., International Regulation of Aero-Engine Emissions, Paper 90-003, pp.27-31, Proc. European Propulsion Forum: Future Civil Engines and Protection of the Atmosphere, DGLR, AAAF, RAeS, Cologne, April 1990.
10. Gleason, C.C., Rogers, D.W. and Bahr, D.W, Experimental clean combustor program - Phase 11, NASA CR-134969, 1976.
11. Roberts, R., Peduzzi, A. and Vitti, G.E., Experimental Clean Combustor Program - Phase 11, NASA CR-134969, 1976.
12. Sotheran, A., Pearce, D.E. and Overton, D.L., Some practical aspects of staged premixed low emission combustion, ASME Paper 84-GT-88, 1984.
13. McVey, J.B. and Kennedy, J.B., Lean stability augmentation study, NASA CR 159536.
14. Abdul-Hussain, U.S., Andrews, G.E., Cheung, W.G. and Shahabadi, A.R., Low NOx primary zones using jet mixing shear layer combustion, ASME 88-GT-308, 1988.
15. Al-Dabbagh , N.A. and Andrews, G.E., Influence of flame stabiliser geometry on premixed combustion flame stability and emissions, Trans. ASME, J.Eng.Power, Vol.103, pp.749-758, 1981.
16. Abdul Aziz, M.M., Abdul-Hussain, U.S., Al-Dabbagh, N.A., Andrews, G.E. and Shahabadi, A.R., Lean Primary Zones: pressure loss and residence time influences on combustion performance and NOx emissions. The 1987 Tokyo International Gas Turbine Conference, Vol.111, p.89-96, 1987.
17. Abdul Husain, R.A.A. and Andrews, G.E., Full coverage impingement heat transfer at high temperatures, ASME Paper 90-GT-285, 1990.
18. Abdul Husain, R.A.A. and Andrews, G.E., Enhanced full coverage impingement heat transfer with obstacles in the gap, ASME Paper 91-GT-346, 1991.
19. Andrews, G.E. et al, High intensity burners with low NOx emissions, Proc. I.Mech.E. Vol.206, pp.3-17, 1992.
20. Andrews, G.E. and Abdul Hussain, U.S., Concentration fluctuations in turbulent cross mixing, ASME paper 92-GT-346, 1992.
21. Abdul Hussain, U.S. and Andrews, G.E., Air blast atomisation as a function of pressure loss for large air flow rates, ASME Paper 90-GT-277, 1990.
22. Antos, R.J., Mumford, S.E. and Winter, J.A., A dual fuel dry low NOx combustion system for industrial combustion turbines, American Power Conference 53rd Annual Meeting, April 29, 1991.
23. Cannon, M.F., Ecob, D.J., Stringer, F.W. and DePietro, S.M., The development of a dry low NOx combustor for the 6.2 MW Tornado industrial gas turbine engine, IMechE Conference, Combustion in Engines, MEP, 1992.
24. Tacina, R.R., Low NOx Potential of Gas Turbine Engines, AIAA Paper 90-0550, NASA TM 102452, 1990.
25. Al-Dabbah, N.A. and Andrews, G.E., The influence of flame stabiliser pressure loss on mixing, combustion efficiency and flame stability. Sixth International Symposium on Air Breathing Engines, 1983, pp.172-181, AIAA.
26. Al-Dabbagh, N.A., Andrews, G.E. and Monaharan, R., Shear layer mixing for low emission gas turbine primary zones, ASME Paper 84-GT-13, 1984.
27. Al Kabie, H.S. and Andrews, G.E., Ultra low NOx emissions for gas and liquid fuels using radial swirlers, ASME Paper 89-GT-322, 1989.
28. Al Kabie, H.S., Andrews, G.E. and Ahmad, N.T., Lean low NOx primary zones using radial swirlers, ASME Paper 88-GT-245 at the 1988 ASME International Gas Turbine and Aeroengine Congress in Amsterdam, June 1988.
29. Ahmad, N.T. and Andrews, G.E., Enclosed swirl flames: interaction between swirlers in lean primary zones, Int. J. Turbo and Jet Engines, Vol.3, p.269-279, 1986.
30. Bahr, D.W., Aircraft engine NOx emissions - abatement progress and prospects, ISABE 91-7022, 1991.
31. Bahr, D.W., Aircraft turbine engine NOx emissions imits - status and trends, ASME Paper 92-GT-415, 1992.
32. Bunn, G.E. and Winter, J , The evolution of a low emission combustion system for aircraft engine application, Oral presentation, 24th ASME Gas Turbine Conference, San Diego, March 1979.
33. McVey, J.B. et al., Evaluation of low NOx combustor concepts for aeroderivative gas turbine engines, ASME Paper 92-GT-133, 1992.

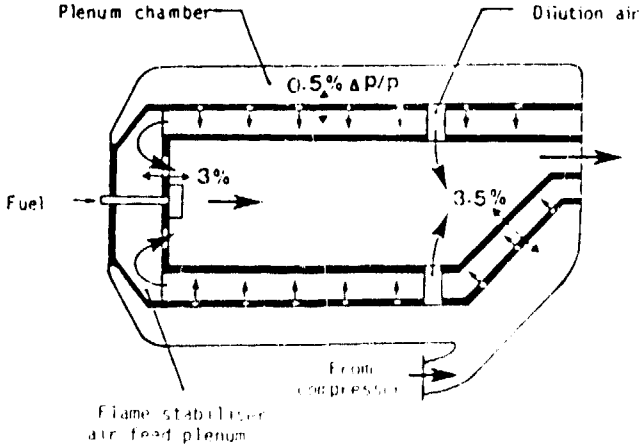

Fig.1 Schematic of a completely impingement cooled reverse flow combustor, with a typical improvement with the combustor pressure loss of 0.5 and 3% respectively.

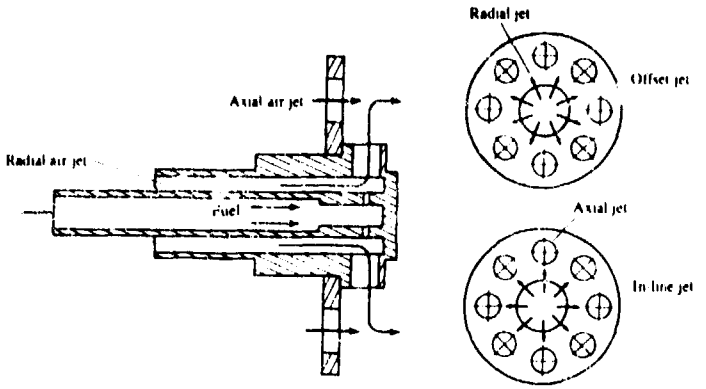

Fig. 2 Jet mix flame stabilizer and the two ways of injecting the fuel

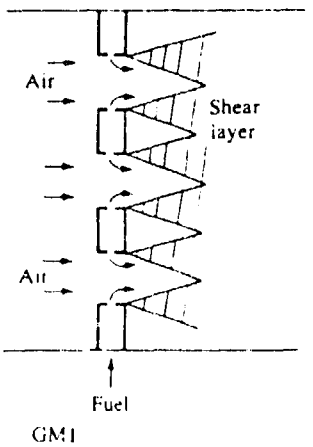

GM1

Fig.3 Radial fuel injection Grid Mix flame stabiliser.

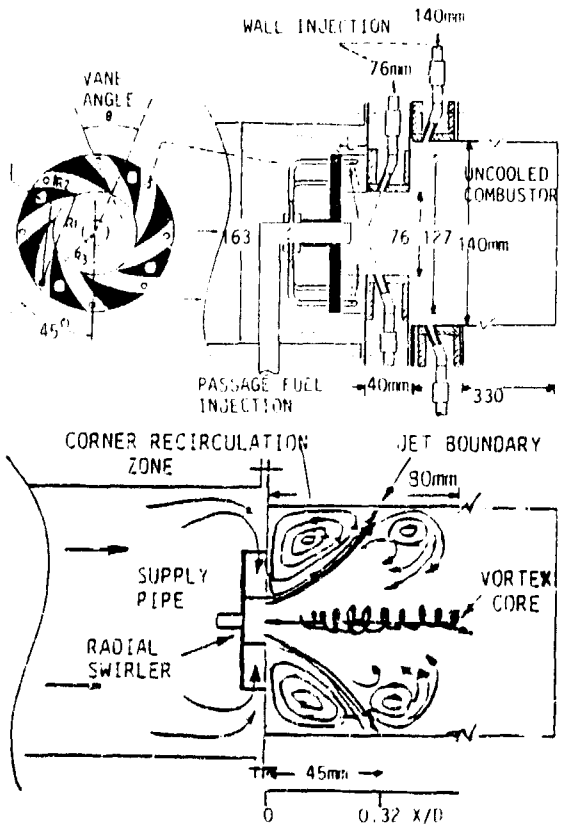

Fig. 4 Radial swirler and fuel injection configurations and the flow patterns observed using a water flow visualization tunnel

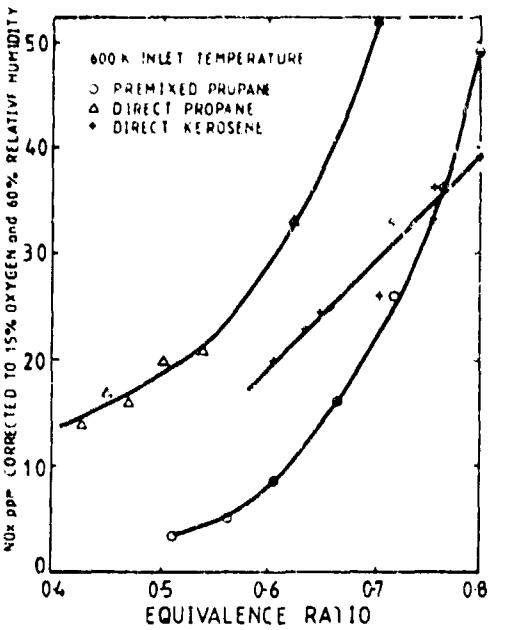

FIG. 5 NO_X CORRECTED TO 15% O_2 AS A FUNCTION OF EQUIVALENCE RATIO

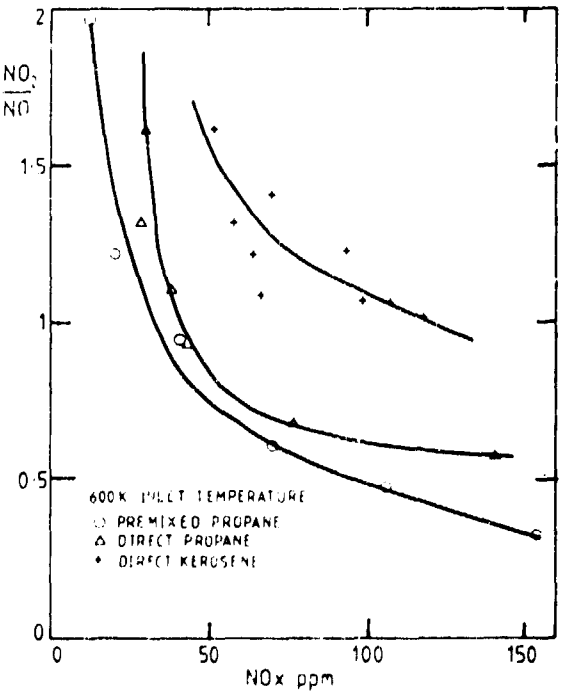

FIG. 6 NO_2/NO AS A FUNCTION OF NO_X

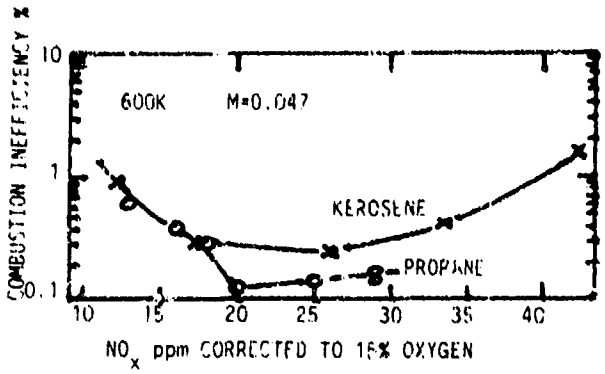

Fig.7 Comparison of the combustion inefficiency as a function of NOx for propane and kerosene fuelling of an inline Jet Mix 76mm combustor with 11% radial air flow.

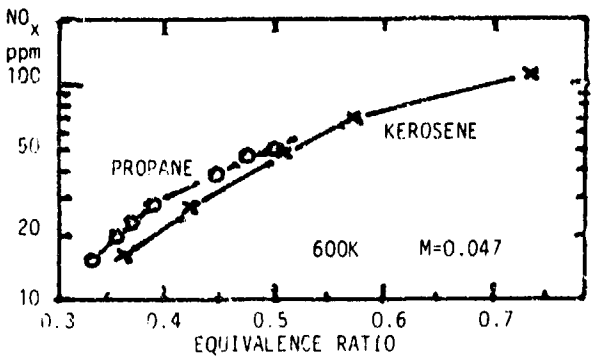

Fig.8 NO_x emissions as a function of equivalence ratio for the inline Jet Mix with 11% radial air flow, comparison of propane with kerosene.

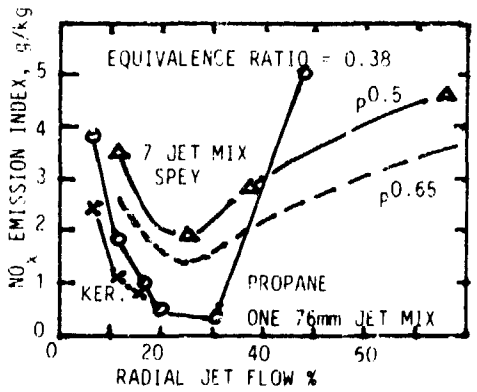

Fig.9 Influence of the Jet Mix radial jet flow on the NOx emissions. Comparison of the present propane and kerosene results for a single 76mm Jet Mix with a 7 Jet Mix design on a Spey size flame tube, tested at 6.9 bar with the NOx reduced to one bar conditions using a 0.65 and 0.5 pressure exponents (32).

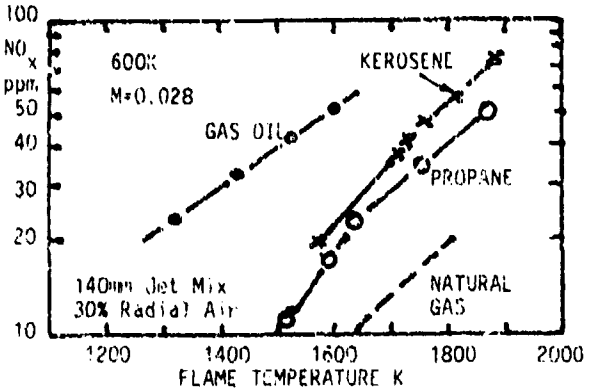

Fig.10 140mm single Jet Mix combustor with inline jets, comparison of the influence of fuel type on NO_x emissions as a function of flame temperature. 30% radial air flow.

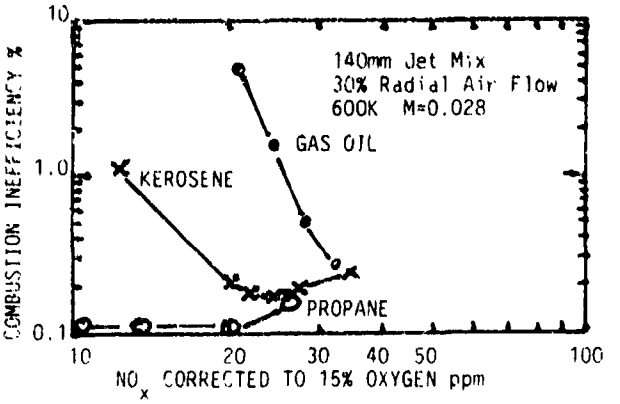

Fig.11 NO_x corrected to 15% oxygen as a function of combustion inefficiency for a single Jet Mix with 30% radial jet air flow in a 140mm combustor, comparison of propane with kerosene and gas oil.

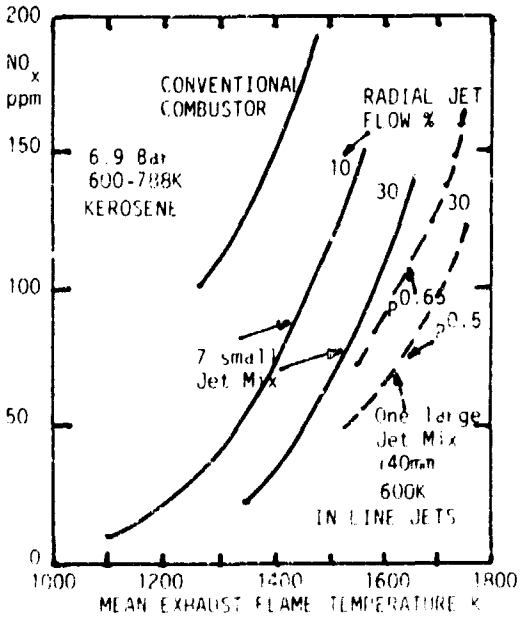

Fig. 12 NOx emissions as a function of flame temperature, comparison between the 7 Jet Mix Spey size combustor results at 6.9 bar (AFT Ltd) with the present 140mm single Jet Mix combustor results scaled to 6.9 bar using 0.5 and 0.65 pressure exponents for the NOx pressure dependence.

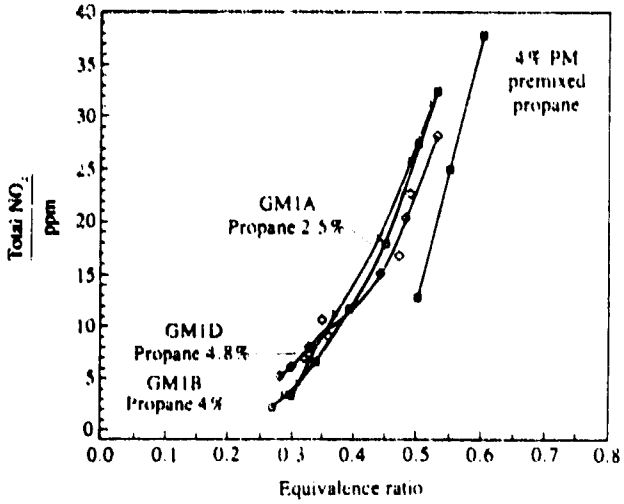

Fig. 13 The NO_x as a function of equivalence ratio using grid mix configurations (GM1B, GM1A, GM1D), propane injection and air inlet temperature at 600 K

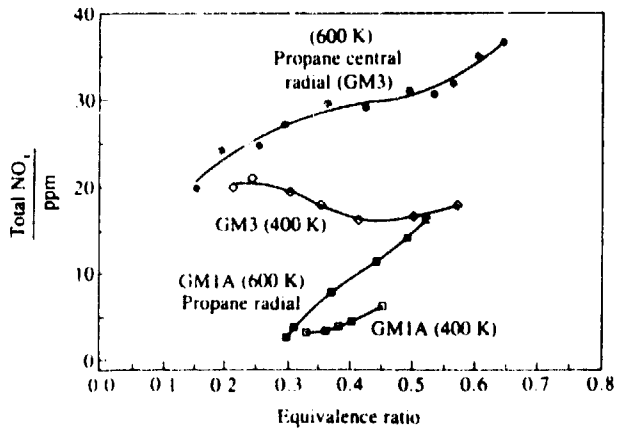

Fig. 14 NO_x corrected to 15 per cent oxygen as a function of equivalence ratio using grid mix fuelled with propane, for two inlet temperatures at 400 and 600 K

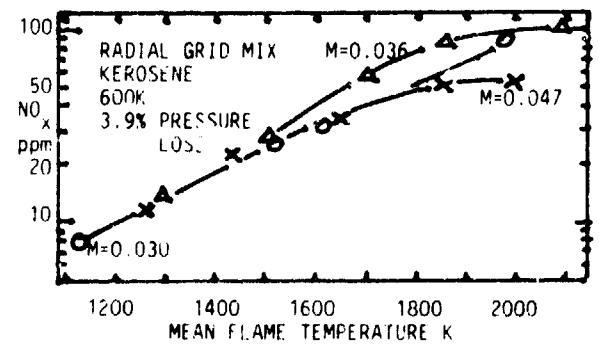

Fig. 15 NOx emissions as a function of the flame temperature for the radial grid mix 4 hole 76mm combustor.

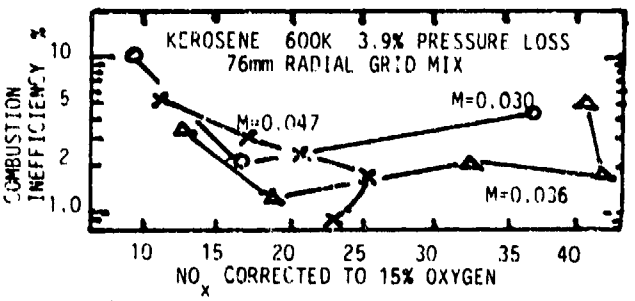

Fig. 16 Combustion inefficiency as a function of the NO_x emissions corrected to 15% oxygen for the radial Grid Mix 76mm combustor with four jet shear layers and 16 0.5mm radial kerosene injection points.

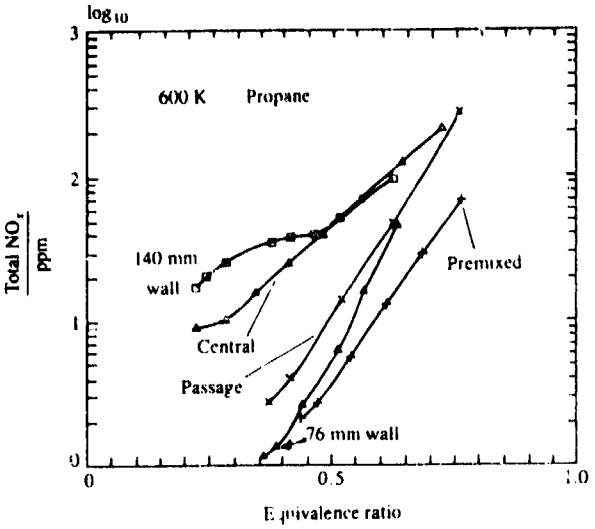

Fig. 17 Influence of the method of fuel injection on mean exit plane NO_x emissions as a function of the mean equivalence ratio, using radial swirler with various modes of fuel injection fuelled with propane at 600 K inlet air temperature

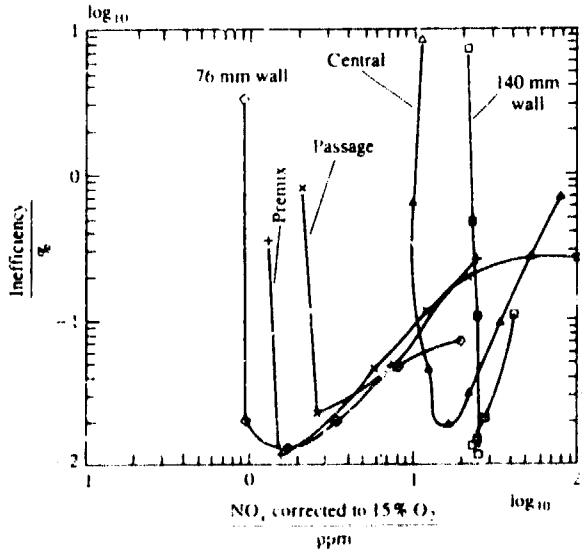

Fig. 18 Influence of the method of fuel injection on the combustion inefficiency as a function of NO_x corrected to 15 per cent oxygen, using radial swirler with various modes of fuel injection fuelled with propane at 600 K inlet air temperature

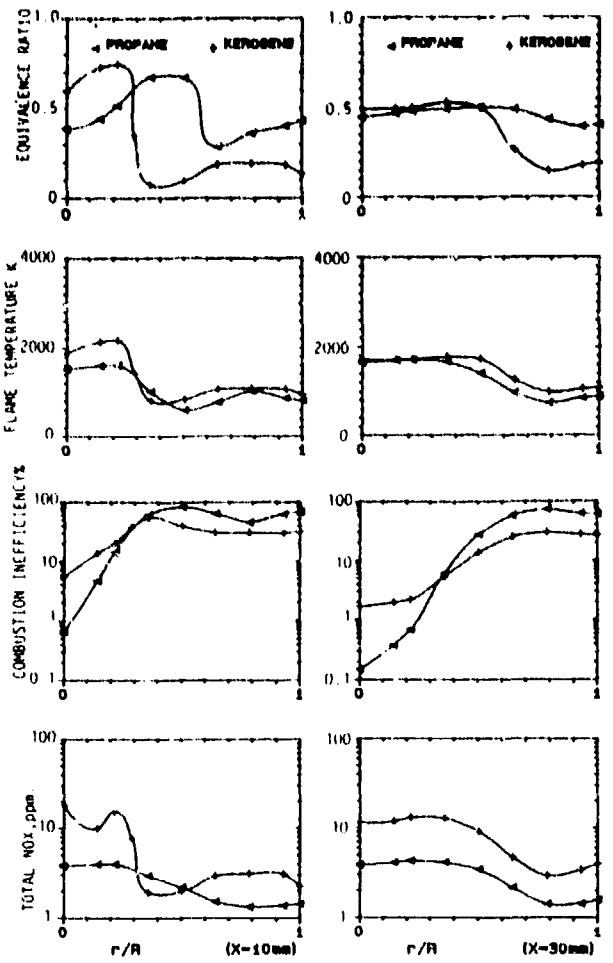

Fig.19 VARIATION OF LOCAL TEMPERATURE AND SPECIES CONCENTRATION AT PLANE 10 & 30mm AWAY FROM THE SWIRLER WITH PASSAGE INJECTION AND AIR INLET TEMPERATURE 600 K.

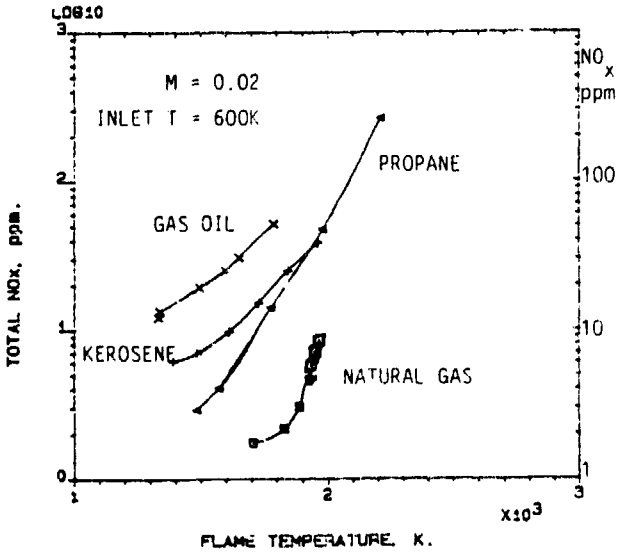

Fig.20 NO_x emissions as a function of the mean exhaust plane flame temperature for radial vane passage injection of four fuels using swirler B in the 140mm diameter combustor.

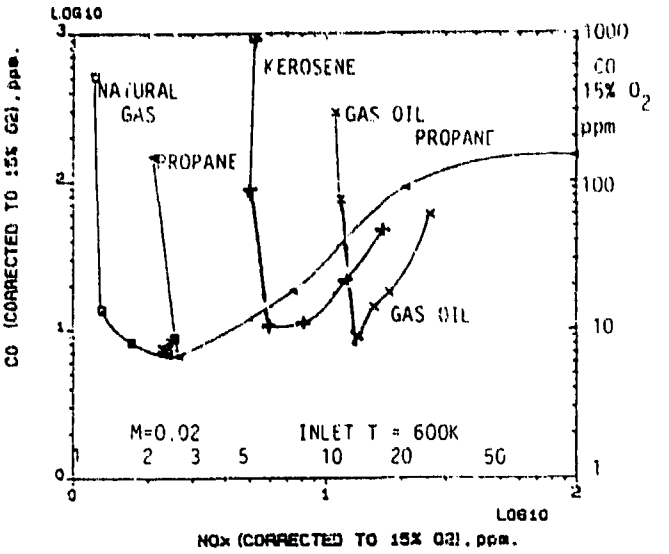

Fig.21 CO emissions as a function of NOx emissions with both corrected to 15% oxygen. Radial swirler B passage injection for 4 fuels.

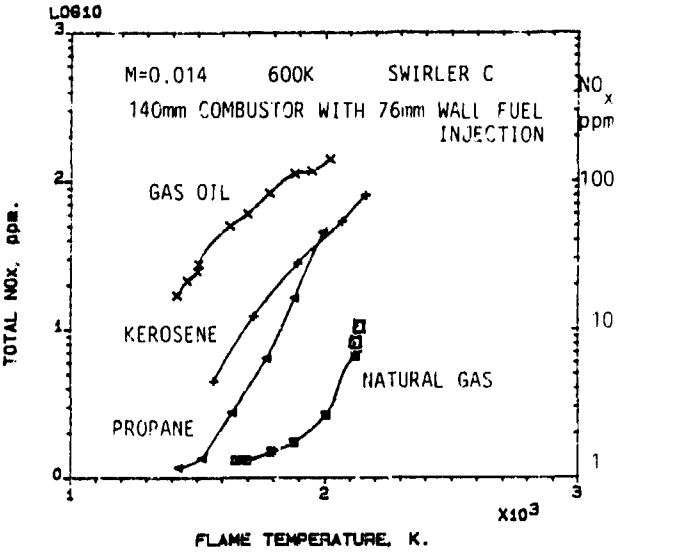

Fig.22 Influence of the fuel type on the NO_x emissions as a function of the adiabatic mean temperature based on the rig metered air/fuel and the combustion inefficiency, swirler C at M=0.014 and 600K inlet temperature, fuel injection at the 76mm wall swirler outlet plane.

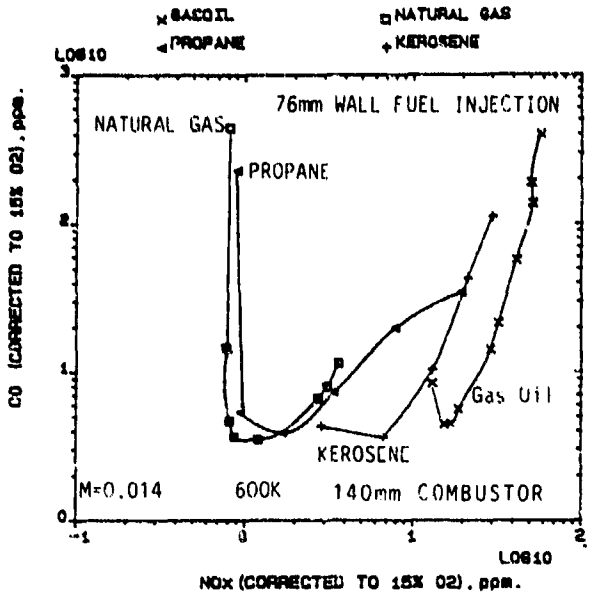

Fig.23 The interdependence of CO and NO_x emissions corrected to 15% oxygen for a range of fuels with 76mm peripheral wall injection into swirler C at M=0.014 and 600K.

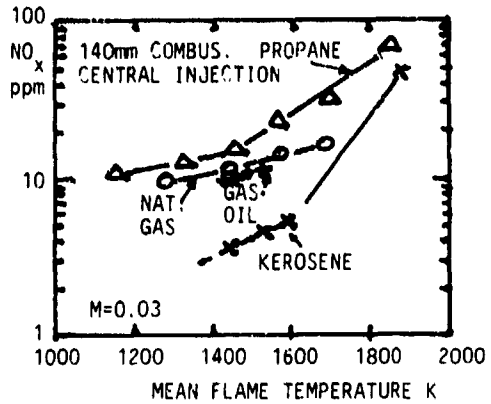

Fig.24 Large airflow capcity radial swirler NOx emissions as a function of the mean flame temperature for four fuels, central radially outward 8 hole fuel injector.

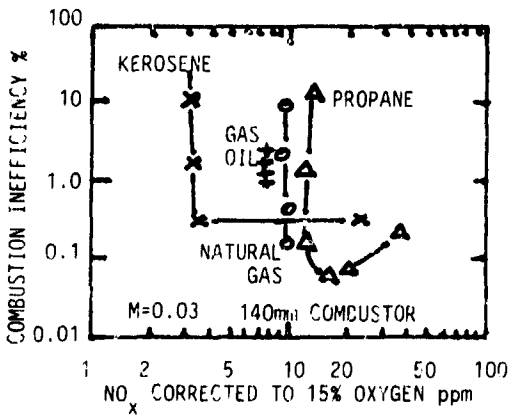

Fig.25 Combustion inefficiency as a function of NOx corrected to 15% oxygen for a large airflow radial swirler (45° vane angle) with central radially outward 8 hole fuel injection, comparison of four fuels.

Discussion

Question 1. T. Rosfjord

I agree that placement of fuel in the correct location in the airflow is crucial to low NOx. The challenge is to inject gaseous or liquid fuel into a swirling airflow. How do you predict such a penetration?

Author's Reply

We have been trying to model the swirler results using CFD and the low NOx post-processing package (Paper 3). The NOx was overpredicted because the temperature was overpredicted because the fuel/air mixing in the shear layer was not predicted correctly. The prediction of fuel placement from fuel injector holes is a problem we have not yet solved using CFD and we may need to use simpler momentum scaling rules. The problem of rapid fuel/air mixing in shear layers is also very difficult to predict using current CFD codes.

COMPUTATIONAL AND EXPERIMENTAL RESULTS IN HIGH PRESSURE COMBUSTIONS OF H_2/AIR AND $H_2/O_2/H_2O$

by

Dino Dini
C.R.E.S.A.M. (Centro Ricerche Esperienze Studi Applicazioni Militari)
San Piero a Grado, 56100 Pisa, Italy

SUMMARY

The first results of a research and development program on combustion characteristics of gaseous hydrogen fuel in a "can" type gas turbine combustor,both in combination with air or with oxygen and water, are here presented. Application of a $H_2/O_2/H_2O$ combustion chamber is suggested for the launch-boost phase of an advanced turboramjet.
Experiments have been conducted to determine the configuration and the operation of the hydrogen-air combustion chamber test facility, to be transferred to two different kinds of small power turboshafts. Computations,project details and tests,are presented regarding high pressure and temperature stoichiometric H_2/O_2 combustion in which water is gradually injected.
Referring to an already realized and operated (on behalf of the author) $H_2/O_2/H_2O$ combustor for a water steam closed cycle in a turbine/alternator electrically propelled automobile, a detailed design is developped for a quite higher steam temperature, as required in high performance boost phase of a low noxious emission advanced turboramjet, in which H_2 and O_2 are stored in liquid form.

1 INTRODUCTION

Combustion characteristics of gaseous hydrogen fuel in a "can" type gas turbine combustor, both in combination with air and with oxygen and water are presented. These are the first results of a research program in cooperation with the Department of Energetics of the University of Pisa and the Italian National Research Center (C.N.R.).
There has been much renewed interest in hydrogen, both as a source of new energy for car and aircraft propulsion, and as alternate fuel. Along with research into production, safety and storage, techniques, investigations have focused on several areas of utilization.
The recent energy crisis and the serious atmospheric pollution arising from use of fossil fuels made our interest turned to hydrogen. In the field of the gas turbine engine, hydrogen is considered to be the easiest energy source for utilization.
Among others hydrogen has the advantage of zero pollutant emission if in combustion in oxygen and water. On the other hand, hydrogen-air combustion is not producing at all CO, CO_2 and HC, with the exception of the oxides of nitrogen at the exhaust of air-breathing engines.
The objective of our research program is to study experimentally the unknown technological problems associated with hydrogen use for the small gas turbine engine, in order to investigate the degree of difficulty for the hydrogen conversion.
Regarding the H_2/Air combustion, tests on a combustor of a small gas turbine engine are in progress over a range of fuel-air ratios, inlet air pressures and temperatures, fuel injectors, and combustor loadings. Several parameters are already investigated, including metal temperatures, flame characteristics, combustion efficiency, operating stability and NO_x emissions.
Regarding the $H_2/O_2/H_2O$ combustion a detailed design of a small combustor has been made from which the real combustion tube has been derived for testing.Hydrogen and oxygen are injected. By adding water used before for the cooling of the combustion chamber wall, the combustion-gas temperature of over 3300 K is gradually decreased to the desired water steam temperature, ranging between 830 K and 1300 K. The water is injected radially into the combustion chamber by means of several injection rings. The steam is supplied subsequently to the steam turbine.
The experimental version has been tested so far at steam pressure between 40 and 70 bar as well as temperature between 830 and 1273 K. The energy conversion efficiency amounts to 99% at a range from 50% partial load to full load. The concept allows fast variation of capacity and steam conditions according to selectable desired values. The development method of stoichiometric H_2/O_2 mixture supply allows to maintain very narrow tolerance, Ref. [1].
Both the new combustion technologies,either with H_2/Air gas, for low-NO_x combustor, or with $H_2/O_2/H_2O$ gas, for zero NO_x combustor, and advanced high-pressure/high-temperature cycle engines result in unique problems in design and performance.

2 H_2/AIR CAN COMBUSTOR SYSTEM

The can combustor system provided a relatively rapid means of investigating performance over a wide range of operating parameters. Comparison of combustion performance between hydrogen and kerosene fuels was made using this system, to get an hydrogen fuelled engine with a very similar behaviour.Due to the fact that the hydromechanical kerosene controller is not able to control gaseous hydrogen, it was decided to use a digital one, consisting of an electronic control

Presented at an AGARD Meeting on 'Fuels and Combustion Technology for Advanced Aircraft Engines', May 1993.

box and an electrical/pneumatical valve for the hydrogen.
For a safe ignition of the gas mixture and for the design of control laws of the digital hydrogen controller, the steady state and the dynamic performance of the engine has to be known, expecially the relation between speed and fuel flow as a function of the time during engine acceleration from zero to idle speed and for the uncontrolled engine. Making the assumption that the differences in the engine behaviour are not too big using Jet A1 fuel respectively hydrogen, the design of the controller can be made with data of the Jet A1 fuel driven engine. To achieve these data, the engine has to be started and stabilized at idle speed with open loop control and then idle-fuel-flow has to be changed by a certain amount.

The adopted can combustor, figure 1, has primary, intermediate and dilution, zones and cooling louvres. A single fuel injector is mounted axially at the combustor head where tangential entry holes provide swirling air to the primary zone. A standard simple nozzle is used with Jet A1 fuel while a multihole nozzle, figure 2, is tested with hydrogen. The fuel is injected along an annulus with air flowing through the centre of the nozzle. The hydrogen supply is taken from a 200 bar commercial bottle. Hydrogen flow is measured using a standard Venturi, and flow control is provided by a precision valve and pressure regulators. As part of the safety precautions, a flash-back arrestor is installed upstream of the test section to isolate any flash-back of the flame and a nitrogen purge system provided for flushing the fuel line before and after each test.

This single can-type combustor is simulating the combustion performance of conventional 40÷200 kW small turbines, which will be mentioned here later. A low tension igniter is mounted at the outside of the recirculation zone in the combustion liner.

Pressure sensors and Pt-Ph thermocouples are fixed in the combustor to measure pressure and temperature distributions. To reduce errors due to radiation from/to the wall, the hot junctions are shielded.
Combustion efficiency and gaseous emissions are monitored with a multi-point sampling probe in the exit plane of the combustor. Hydrogen content in the exhaust is measured using a thermal conductivity analyser, and NO_x concentration using a chemiluminescent analyser. The quartz window at the back of the rig allows direct observation of flame behaviour.

A comparison of physical and chemical properties of hydrogen and Jet A1 fuels is shown in Table I.

Reference has been made, in our conversion to hydrogen fuel, to two small turboshaft engines, which were designed more than 20 years ago, originally for Jet A1 fuel and the following specifications:

Turboshaft	A	B
- shaft horse power	42 kW	202 kW
- air mass flow	0.9 kg/s	1.5 kg/s
- fuel mass flow	0.0175 kg/s	463 g/kWh
- compressor pressure ratio	2.5	8.4
- turbine inlet temperature	1173 K	1233 K

TABLE I - Hydrogen and Jet A1 Properties

	Hydrogen	Jet A1
Molecular weight	2.016	170
Liquid Density, kg/m³	70.8	827
Heat of Combustion		
Volumetric, MJ/m³	10.2	35,3
Gravimetric, MJ/kg	122.8	42.8
Heat of Vaporization, kJ/kg	446	295
Normal Boiling Point, K	+20	444 to 540
Freezing Point, K	+14	423
Limits of Flammability, % fuel vol.	4 to 74	1 to 5
Flammability Range, equivalence ratio	.1 to 6.8	.5to 4
Minimum Spark Ignition Energy, MJ	.019	.25
Maximum Flame Temperature, K	2400	2300
Quencing Distance, cm	.057	.3
Detonation Velocity, m/s	1900	1800
Specific Heat, kJ/kg/K	9.663	1.966
Specific Gravity of Gas at 273 K and 1 atm, (Air = 1)	.0695	

Steady state performance tests are performed simulating conditions from ground idle to the maximum rating on the turboshaft A and B cycles.
At each condition gaseous emissions and liner skin temperatures are measured.
Combustion efficiency is determined from measured concentrations of unburnt hydrogen.
Additional parametric tests are performed to evaluate the effects of inlet pressure, temperature and fuel-air ratio on NO_x emissions and liner skin temperatures.

3 EXPERIMENTS ON CAN COMBUSTOR

Firstly, experiments are conducted to determine the behaviour of the chosen nozzle on such a can combustor. To establish the supply pressure of hydrogen to the combustor, pressure losses across the fuel nozzle are needed. Figure 3 shows the pressure loss coefficient $\zeta = \Delta p \cdot 2g/\gamma_H \cdot V_H^2$, where V_H is the hydrogen velocity at the nozzle orifice given by using the hydrogen mass flow rate, specific weight γ_H and the whole area of the orifice. Nozzle Reynolds number R_e is calculated from V_H and the hydraulic diameter obtained from the whole area of the nozzle orifice. As it can be seen on figure 3, the pressure loss coefficient of such multihole type is approximately constant in the

covered range of the R_θ number.
When the hydrogen operation starts it is necessary to light immediately at the lower concentration of the hydrogen-air mixtures.
Ignition limits are established by recording the minimum fuel flow required to obtain stable combustion. The flow factors that can be aspected to affect ignition limits include air pressure, temperature and velocity. Figure 4 shows the ignition fuel-air ratio versus air flow rate at ambient condition. The minimum fuel-air ratio for ignition with hydrogen is much lower (<40%) than that with Jet A1 fuel even after correcting for the difference in heating values between the two fuels. The multi-hole nozzle, with locally strong concentrations of hydrogen in the primary zone, provides better conditions for diffusion. Increasing air pressure improves ignition characteristics, figure 4. Then the ignition test is made to obtain the ignition limits of the combustor.

The hydrogen mass flow rate is then increased slowly until the ignition occurs. When hydrogen is ignited, a "pop" sound similar to explosion is accompanied with initiation of the combustion. This becomes stronger at excess hydrogen flow even at lower air flow rate, or at large amount of fuel-air mixtures.
Once the ignition is attained, the combustion can be hold even at considerably small amount of hydrogen flow.

The combustion efficiencies of hydrogen is around 100%, calculating from the entalpy differences. The hydrogen concentration in the combustion gases at the outlet of the combustor is checked by a chromatograph.
The ignition performance and operating efficiency of the can combustor points to excellent mixing and combustion characteristics of hydrogen. The results once again indicate possibility of using much smaller combustors for hydrogen fuel while achieving adequate performance.

4 PERFORMANCE OF H_2/AIR TURBINE

Two conventional small gas turbines are used for the operation test with hydrogen fuel. The can-type combustor is a simulation of these kinds of engines. In order to accommodate the geometrical differences, the can combustor and the real flow in the turbine combustion chamber, modelling parameters are used to define the can combustor rig air flows which simulate actual conditions on the full engine. An air loading parameter simulates reaction rate and residence time at low power and an air velocity parameter simulates flow characteristics at high power. Thus the air mass flows for the can combustor rig tests are determined from such modelling parameters, while inlet pressures, temperatures, and overall fuel-air ratios are kept the same as in the engines. Fuel flows are adjusted according to the net heating value of the test fuel relative to that of Jet A1.
The hydro-mechanical controller is not able to control gaseous hydrogen. Therefore a digital electronic controller is used which is modulating an electrical valve as a function of engine speed. Driving the turboshaft (figure 5) with hydrogen, there are different metering and shut off valves, which are important for the safety point of view; it is necessary to rinse the fuel pipes before and after each engine run.

The control of the turboshaft using hydrogen as fuel consists of two parts: acceleration from zero to idle speed (open loop); normal engine control (closed cycle).
In fact here, the digital controller measures the hydrogen into the combustion chamber as a function of speed, whereas, specially at the first moment, the mass flow is only a few percent of that of the corresponding Jet A1 mass flow to keep the gas volume at the ignition point as small as possible. This acceleration from zero to idle speed is done as a open loop control.
At about the idle speed, the normal engine control as closed loop is activated. The increase of the fuel as a function of speed (or time) is slightly smoother.

Experimental tests are in progress and it is too early to present reliable operating data and transient characteristics.

The NO_x emission rates in hydrogen use are relatively greater than those in Jet A1 combustion, in the entire range of the loading operation of the power spectrum; this is problably associated with higher flame temperature, evidenced as well by higher liner temperatures.
Combustion with the multiple nozzle may be influenced more by diffusion of individual jets of hydrogen, which can result in higher local temperatures and hence higher rates of NO_x formation.
While the can combustor data with kerosene fuel shows NO_x emissions lower than in current production engines, corresponding data for hydrogen shows considerably higher NO_x emissions. Reducing these emissions can likely be achieved by leaning out the front end of the liner, or reducing primary zone residence time by moving up the location of dilution orifices. In this combustion system, such changes are not likely to result in much penalty in other performance parameters such as ignition, stability or combustion efficiency.

The temperature distributions on the liner wall of the combustor were observed by using thermocouples. The wall temperatures with hydrogen were much higher than with Jet A1, especially in the primary zone where temperatures in excess of 1100 K were indicated for hydrogen compared to 800-1000 K

for Jet A1.

Based on the work here presented, the following conclusions are obtained:
- conventional gas turbine operated with Jet A1 fuel can be converted, with a minimum effort, to use hydrogen as an alternative fuel;
- perfect combustion of hydrogen is obtained in the operation tests of the gas turbines. Thermal efficiency in hydrogen operation agreed with the value in Jet A1 operation;
- NO_x emission level in hydrogen combustion is greater than that with Jet A1.

5 LESS EMISSIONS WITH HYTHANE

Conversion to Hythane combustion is next experiment to be made with the turboshafts. Mixing a bit of hydrogen with compressed natural gas (CNG) could yield the cleanest-burning alternative fuel yet.
A feasibility test of Hythane - 5 percent hydrogen by energy content, 15 percent by volume - has produced hydrocarbon emissions less than half of those from CNG, and nitrogen oxide levels 24 percent of those from CNG.
Taking suggestion from automobile application, pure hydrogen in gaseous form asks up 12.9 times as much space as gasoline required to travel an equivalent distance and 3.8 times as much space as natural gas. Enough Hythane to make a trip of about 200 miles can be packed into a tank 3.4 times the size of an equivalent gas tank - if it is compressed to about 3,000 pounds per square inch.
It is theorized that natural gas and hydrogen can act symbiotically - one complimenting the other - to produce a more efficient burning fuel. Natural gas plays a positive role in the fuel partnership by contributing cost advantage, domestic availability, and existing infrastructure to the scenario.
Another potential benefit of Hythane use - extending the supply of natural gas - can be accomplished if hydrogen is formed from renewable energy sources rather than natural gas reformation. Although natural gas is clean-burning, there is still a need to lower the carbon monoxide (CO), hydrocarbon (HC) and nitrogen oxide (NO_x) levels to accommodate the projected emission standards.
Current emission standards in USA, for automobiles, impose less than grams per mile: 0.97 (THC); 0.8 (NMHC); 10.0 (CO); 1.2 (NO_x).
Proposed California "ULEV" (Ultra Low Emission Vehicle) are: 0.05 (THC); 0.04 (NMHC); 1.7 (CO); 0.2 (NO_x).
At present, Hythane used in automobiles has reached: 0.01 (NMHC); 0.7 (CO); 0.2 (NO_x).

In advanced aircraft turbo-engines, Hythane combustion with air has to be considered an up to date procedure, even though storaging aboard of hydrogen and natural gas must be separately and in cryogenic liquid form.

6 $H_2/O_2/H_2O$ COMBUSTION CHAMBER

This kind of combustion chamber is based up on the possibility of applying the $H_2/O_2/H_2O$ burner as shown on Figures 6 and 7, in which hydrogen and oxygen are injected continuosly. They are ignited by means of a centrally mounted spark/torch igniter. By adding water, the combustion gas temperature is decreased to the desired steam value. The water is injected pulverized radially by means of injection rings. In order to minimize the quantity of not-condensable components in the produced steam, O_2 and H_2 must be supplied very closely to their stoichiometric mixture ratio (7.95 as weight). The burner is composed of some segments to provide an adequate water mixing.
In a previous study, Ref. [2], three different configurations, Figure 8, of the burner were considered:
- A, with an axial flow of the reactants and the wall cooling water, with holes in the internal tube;
- B, with a flame tube to reduce the maximum wall temperature;
- C, with all axial fluid flows.

Hydrogen, oxygen and water, to be used to reach a given steam temperature value are so deduced. Approximately, it is, calling α, β and γ, respectively, the weight fractions of the combustion products GH_2-GO_2, of the water injected gradually, and of the hydrogen

$$\alpha = (H_s - \beta \cdot H_w)/H_1 \cdot \eta_c \qquad (1)$$

$$\alpha + \beta = 1 \qquad (2)$$

where: H_1 is the entalpy of the gas produced by the GH_2-GO_2 combustion; $\eta_c = 0.98$ is the energy conversion efficiency including heat losses.; s and w mean superheated and water.
Combining (1) and (2), it is

$$\beta = (H_1 \cdot \eta_c - H_s)/(H_1 \cdot \eta_c - H_w) \qquad (3)$$

being $$\gamma = \alpha/8.95 \qquad (4)$$

Considering the expander efficiency η_e and the reduction coefficient η_r (for taking into account the energy for accessories), the hydrogen fuel is used at the overall thermal efficiency

$$\eta = \eta_e \cdot \eta_r (H_s - H_e)/\gamma \cdot k_i \qquad (5)$$

where H_e is the entalpy of the steam at the end of the expansion, and k_i is the low heat of combustion.

The $H_2/O_2/H_2O$ combustion chamber has been designed and tested for application to a closed cycle small steam turbine, to be used in a non-polluting automobile propulsion system, as in the sketch on Figure 9, Ref.s [3], [4] [5].
In such application, admission and exhaust

pressures and temperatures have chosen, for a turbine working fluid power of 100 kW:

- p_1 = 70 bar and T_s = 1073 K;
- p_2 = 0.06 bar and T_{2o} = 428 K

The results are collected in the Table II. (steam expansion on Figure 10)

TABLE II - Turbine expander (100 kW)

p_1	1)	(bar)	70
p_2	2)	"	0.06
T_s	3)	(K)	1073
H_s	4)	(kJ/kg)	4130
H_2	5)	"	2340
η	6)		
$\eta \cdot (H_s - H_2)$	7)	(kJ/kg)	1342
H_{2o}	8)	"	2787
T_{2o}	9)	(K)	428
r_{2o}	11)	(kJ/kg)	2412
$(H_{2o} - H_2) + r_{2o}$	12)	"	2859
v_{2o}	14)	(m^3/kg)	32.5
$\bar{\eta}_C$	18)		0.446
$\eta_t = \bar{\eta}_C \cdot \eta$	19)		0.334
$100 \cdot \eta \cdot (H_s - H_2)$	21)	(kJ/kg)	213
c_p	22)	(kJ/kg·K)	1.005
ΔT	23)	(K)	20
$Q_{air} = 213/c_p \cdot \Delta T$	24)	(kg/s)	10.6
Δp	25)	mm H_2O	20
Δ_p/δ	26)	(m)	16
$Q_{air} \cdot \Delta p/\delta \cdot 0.4 \cdot 102$	27)	(kW)	4.15
H_w (at 70 bar)	28)	(kJ/kg)	165
H_1	29)	"	20626
η_c	30)		0.98
β	31)		0.802
α	32)		0.1978
γ	33)		0.0221
$\alpha - \gamma$	34)		0.198
$100 \cdot 3600/\eta \cdot (H_s - H_2)$	35)	(kg/h)	268
$\beta \cdot 268$	36)	"	215
$\alpha \cdot 268$	37)	"	53
$\gamma \cdot 268$	38)	"	5.9
53-5,9	39)	"	47.1
$\Delta p/\delta$ (LH_2)	40)	(m)	9862
$\Delta p/\delta$ (LO_2)	41)	"	613.5
$\Delta p/\delta$ (H_2O)	42)	"	700
η_{pump}	43)		0.5
LH_2 (pump power)	44)	(kW)	0.318
LO_2 " "	45)	"	0.157
H_2O " "	46)	"	0.82

The numbers in the Table II mean:

- 18: equivalent Carnot efficiency;
- 19: real thermal efficiency;
- 21: condensation heat to be extracted from the steam flow in the air radiator;
- 24: air flow of the radiator fan;
- 25: air pressure loss across the radiator;
- 26: fan total head;
- 27: required radiator fan power.

The $H_2/O_2/H_2O$ combustion chamber has been realized for developping the steam weight flow required for the 100 kW full power, as shown on Figure 11 for the real injection head.
During the first tests carried out, the foreseen steam temperature of 1273 K has been obtained, but with some problems in the flame zone. Through reception of the heat of reaction, the water went instantaneously into the steam phase. The remaining energy led to increased temperature of the steam to the desired value. Through the regulation of the mass flow of gaseous hydrogen and oxygen and of the water, the steam condition parameters (temperature and water content) and steam quantity were reproducibly adjusted. They could also be temporarily changed.

The steam generator apparatus consists of three functional structural groups: steam generator, media contro unit, and electronic control system and regulator.
The steam generator, Figure 11 (according Figures 6 and 7), is the core of the arrangement. It consists of the ignition-,the combustion-, and the evaporation chamber. In the ignition chamber a combustable gas mixture at low oxider/fuel-mixture ratio is electrically ignited by means of a sparkplug. After conclusion of the ignition process, the flame shifts to the combustion chamber. The residual oxidizer is supplied to the combustion process, to adjust the total mixture ratio exactly to the stoichiometric one. The water to be evaporated is injected radially through holes in the rings. Before hand the water passes through the double mantle of the combustion chamber and cools the wall. In the adjoining evaporation chamber, which also serves to homogenize the steam, two temperature gages are integrated to control the steam temperature and to monitor the apparatus.
The media control unit regulates the gas supply and the water supply of the system. A pressure equalizer keeps the supply pressure of the gases, hydrogen and oxygen, equal. With the help of sonic nozzle that are installed in the gas pipes, the stoichiometric mixture ratio is achieved. By changing the gas supply pressure, the gas mass flow rate change synchronically and linearly, so that the mixture ratio remains stoichiometric. The gas supply is adjustable by a pressure regulator valve with motor drive. The water mass flow rate is provided by a gear pump with regulated rotational speed.
The electronic regulator and control are realized on a microprocessor basis, with the following functions: valve control; regulation of gas supply pressure, e.g. the steam generator performance; regulation of water supply; ignition of the gas mixture; monitoring of the ignition process; regulation of the steam temperature; safety control.

Hydrogen and oxygen gases (in liquid form in the actual application on board of vehicles) are supplied from gas storage cylinders to the burner through a float type flow meter and a back fire preventer respectively. Flow rates are manually controlled with a needle valve of the flow meter. In the case

of gas sampling, a conical gas collecting hood is put above the burner and a sampling probe is fixed at the exit of the collecting hood. The sampled gas is pumped to gas analyzers after the steam in the sampled gas is removed with an electric gas cooler. Since much of the sampled gas is steam and is condensable, nitrogen at a specified flow rate is introduced inside of the collecting hood as a reference gas. Concentrations of the unburned hydrogen and the unused oxygen are measured with a chromatograph. Purity of the supplied gas is 99.99% for hydrogen and 99.93 for oxygen and nitrogen.

The operation of the steam generator is very simple, since, after the selection of the desired capacity and the steam temperature, the required mass flow rates of the media are automatically regulated.The same applies also for the changing of the operating parameters. The process steps are programmable and can be restored, so that, for example, steam temperature/time are realized without problem.

According to Ref. |6|, an experimental version of an H_2/O_2-steam generator has been tested so far successfully at steam pressures between 40 and 90 bar as well as temperatures between 835 and 1225 K and thermal capacities between 15 and 40 MW, and a properly functioning of a non-linear state-space feedback control concept for simultaneous control of steam pressure,temperature and mixture ratio, has been demonstrated.

7 $H_2/O_2/H_2O$ COMBUSTION IN TURBORAMJETS

A satisfactory launch speed might rapidly be reached at relatively low altitude by a turbo-ramjet-rocket multicycle missile, operating with the $H_2/O_2/H_2O$ combustion chamber as on Figures 6 and 7, Ref. |7|.
Such kind of hybrid engine is enough flexible to meet a large variety of flight conditions, with speed as high as Mach 4. Like turbo-ramjet, this propulsion system, Figure 12, using $H_2/O_2/H_2O$ combustion only in the boost phase, is arranged of course with a lot of inlet and exhaust variable geometries.
A $H_2/O_2/H_2O$ combustion chamber is used to produce high pressure and temperature superheated water steam during the count down and take-off phases, at variable injected water.

The steam from the combustion chamber flows to drive a turbine in a first stage of expansion, while useful propulsion energy is obtained through a variable geometry plug nozzle. The turbine is giving power to air compressors in two ramjet ducts during their take-off and acceleration phases.
Hydrogen-air ramjet propulsion is following the boost phase.

Gaseous hydrogen GH_2 and oxygen GO_2 might be directly obtained through water electrolysis at the launch site.
The most electrolytic cells are producing 0.2 Nm^3 of GH_2/kWh (0.0555 Nm^3/MJ) and 0.1 Nm^3 of GO_2/kWh (0.0277 Nm^3/MJ), i.e.,respectively, with specific gravities 0.881 N/Nm^3 and 14.013 N/Nm^3 (0.04896 N/MJ and 0.38925 N/MJ). The weight mixture ratio for the combustion is becoming 0.38925/0.04896 = 7.95, corresponding about to stoichiometric ratio if all the electrolysis products are used. Costs for producing gaseous and liquid hydrogen and oxygen are carried out in Ref.s |1|, |4| and |5|.
Energy need for a modern electrolyzer may be at present 14.45 MJ for producing 1 N of GH_2 and 7.95 N of GO_2. Liquefaction (L) may require 3.65 MJ per 1 N of LH_2 and 0.19 MJ per 7.95 N of LO_2. Therefore, the total energy need for gasification and liquefaction (liquid form on board), at atmospheric pressure, of 1 N of LH_2 and 7.95 N of LO_2 is about 18.49 MJ, corresponding to 18.49/8.95= 2.066 MJ per N of stoichiometric (LH_2-LO_2) mixture.

On the basis of equations from (1) to (5), and with the computational procedure in Table II, a $H_2/O_2/H_2O$ combustion chamber,for a turbo-ramjet as in Figure 12 of given performances, may be designed.

REFERENCES

|1| Sampath P. and Shum F., "Combustion Performance of H_2 in a Small Gas Turbine Combustor", Proceedings of the 5th World Hydrogen Energy Conference, Toronto, 15 20 July 1984, Vol. 4, pp 1467 - 1479.

|2| Montagnani G. and Psaroudakis P., "Prospettive di Impiego di Generatori di Vapore non Convenzionali per l'Utilizzazione del Combustibile Idrogeno", Proceedings del 40° Congresso Nazionale ATI, Trieste, Italy, 14-17 September 1985.

|3| Dini D., "Liquefattori di H_2 e N_2 di Alimentazione al Banco di Motori Automobilistici Ecologici", Proceedings del 45° Congresso Nazionale ATI, Cagliari, Italy, 18-21 September 1990.

|4| Dini D., "Feasible Non-Polluting Car Engines Using Air-Water Components", Proceedings of the SAE-AIEC Conference,Buenos Aires, 3-6 September 1991,pp 53-67.

|5| Dini D., "Closed Cycle Water Steam (from $H_2/O_2/H_2O$ Combustion) Car Engine", Proceedings of the 9th World Hydrogen Energy Conference, Paris, France, 22-25 June 1992, Vol. 3, pp 1351-1361.

|6| Sternfeld H.J., "A Hydrogen/Oxygen Steam Generator for the Peak-Load Management of Steam Power Plant", Proc. of the 5th World Hyd.En.Conf.,Toronto,Vol.4,pp1595-1606

|7| Dini D., "Design of Hydrogen Fueled Ramjets and Ramrockets", Proceedings No307 of the AGARD-PEP 58th Symposium, London UK, 26-29 October 1981, pp 26-1 - 26-8.

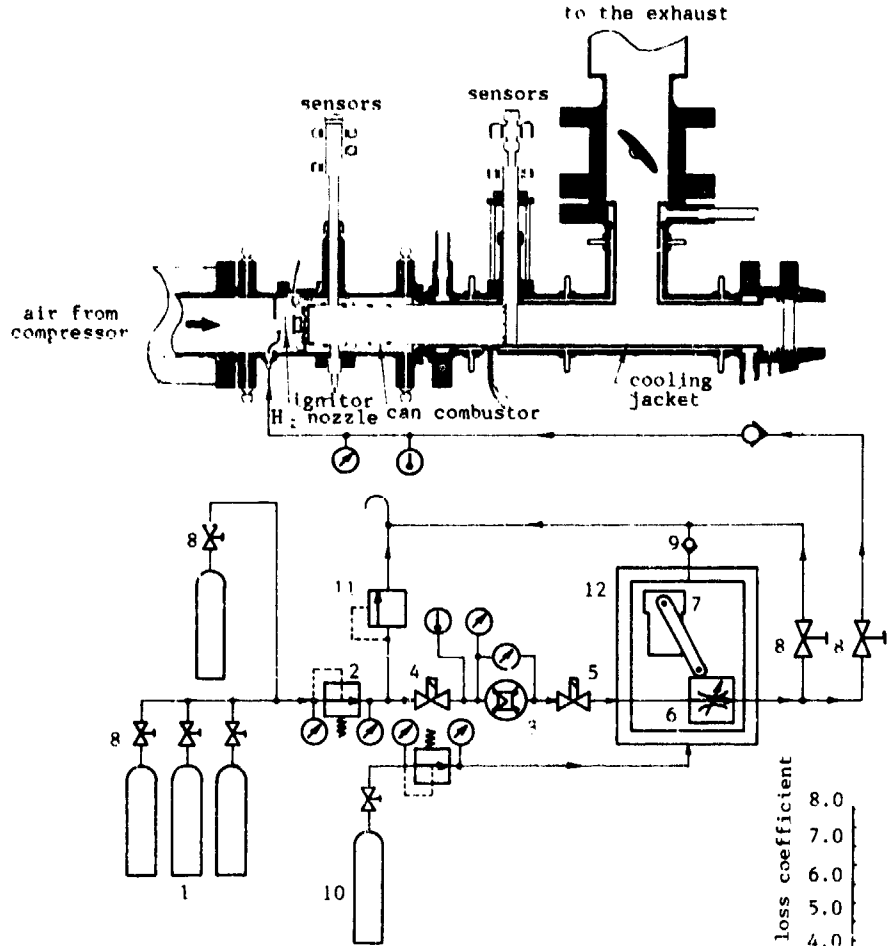

1. H_2 storage cylinders
2. pressure regulators
3. flow meters
4. emergency shut off valve
5. fuel supply valve
6. fuel metering valve
7. actuator
8. manual shut off valve
9. check valves
10. N_2 cylinder for purging
11. relief valve
12. H_2 leakage-proof box
13. remote discharge line for purging

Fig. 1 - Combustor test rig and H_2 supply system

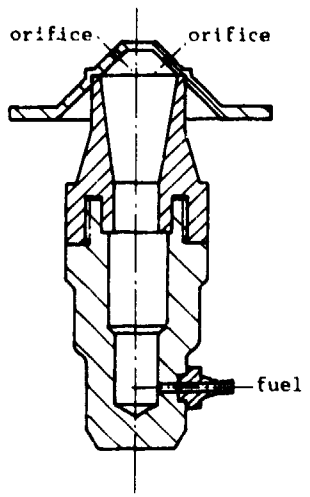

Fig. 2
H_2 multi-hole nozzle

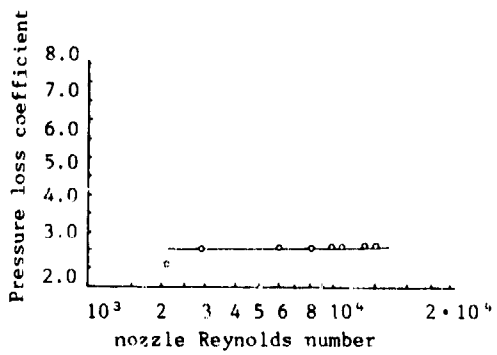

Fig. 3 - Pressure loss coefficient of the H_2 fuel nozzle

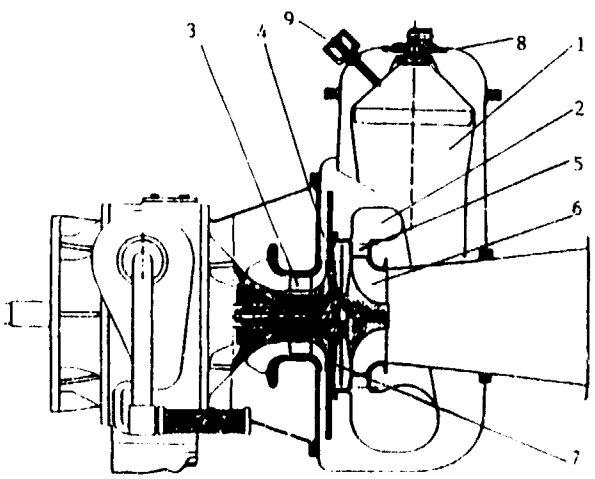

1. combustion chamber
2. housing
3. radial compressor
4. stator, compressor
5. stator, turbine
6. radial turbine
7. housing
8. injection nozzle
9. sparkling plug

Fig. 5 - 42 kW turboshaft

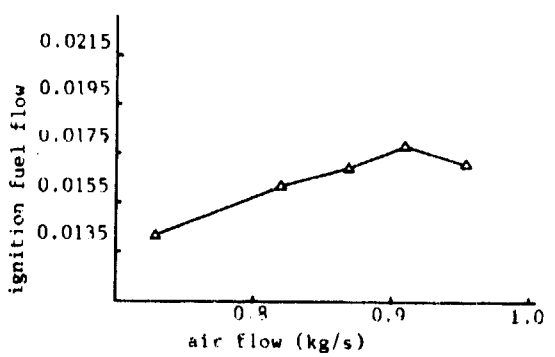

Fig. 4 - Ignition H_2 flow versus air flow

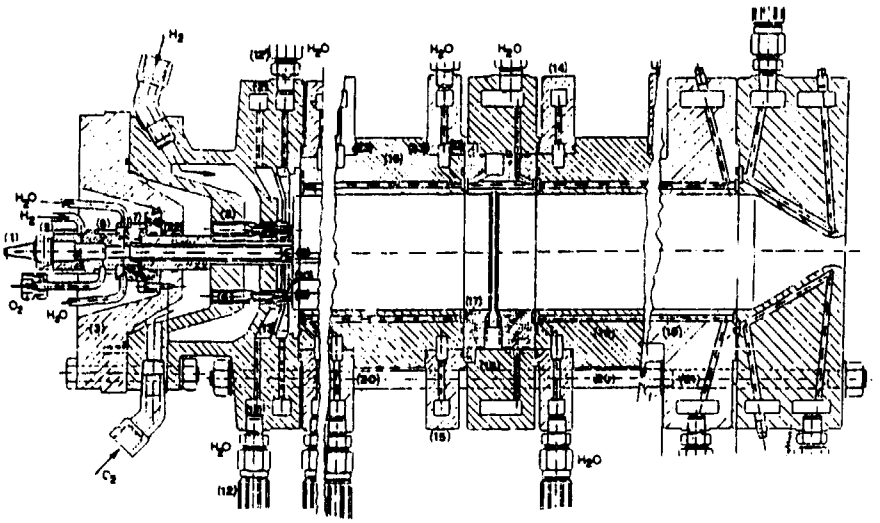

1. spark plug - 2. injector flange - 3. back flange - 4. injector body - 5. H_2 jacket - 6. O_2 jacket 7. water jacket - 8. injector - 9. flame-holder - 10. diaphragm - 11. external circumferential chamber 12. and 12' inflow and outflow flexible ducts - 13. water internal chamber - 14. water inlet flange 15. water outlet flange - 16. internal body - 17. closing rings - 18. collector flange - 19. atomizer body - 20. longitudinal collecting rods - 21. end collecting rods - 22. O - rings seal - 23 steam sealing rings - 24. cooling water inflow/outflow ducts.

Fig. 6 - $H_2/O_2/H_2O$ combustion chamber fo a thermal power 20 MW

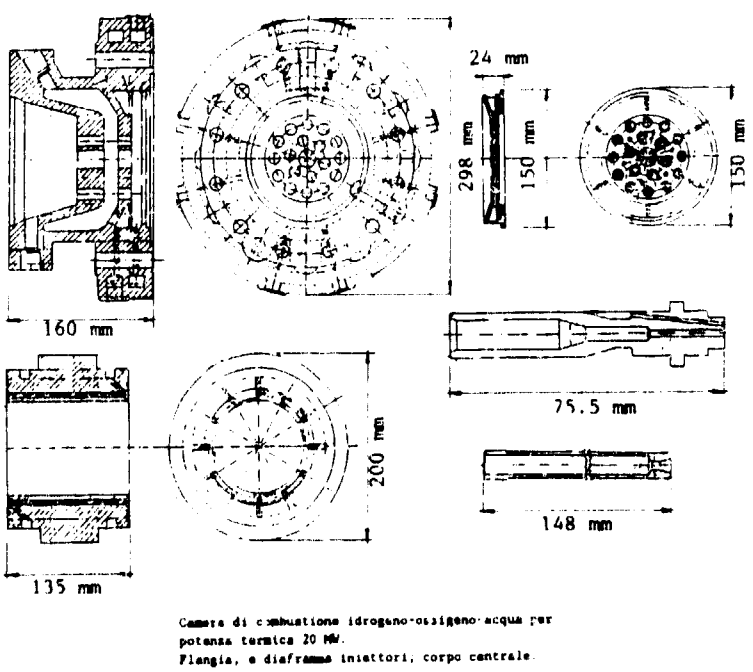

Camera di combustione idrogeno-ossigeno-acqua per potenza termica 20 MW.
Flangia, e diaframma iniettori, corpo centrale.

Fig. 7 - $H_2/O_2/H_2O$ combustion chamber for 20 MW Thermal power: fiang, and injector diaphragm; central body segment

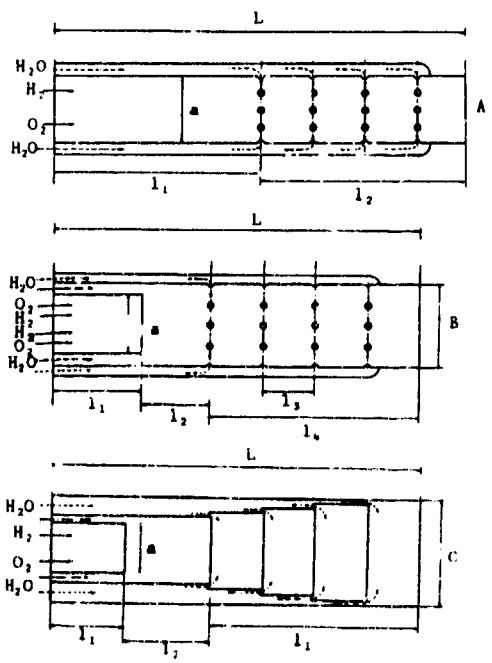

Fig. 8 - $H_2/O_2/H_2O$ burner possibl configurations

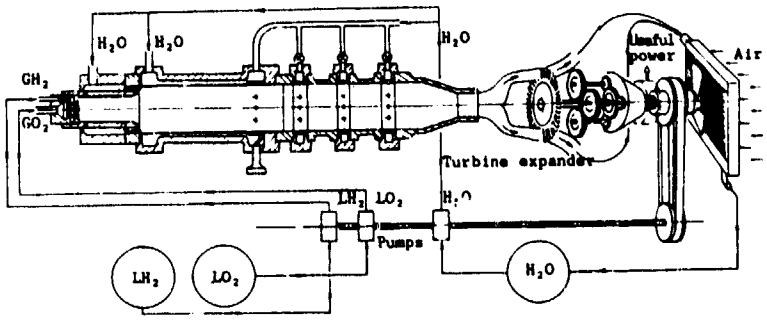

Fig. 9 - $H_2/O_2/H_2O$ combustion chamber applied to a closed cycle turbine engine for car propulsion: working fluid power 100 kW

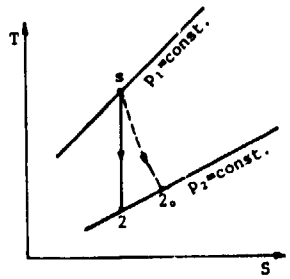

Fig. 10 - Steam expansion (Table II)

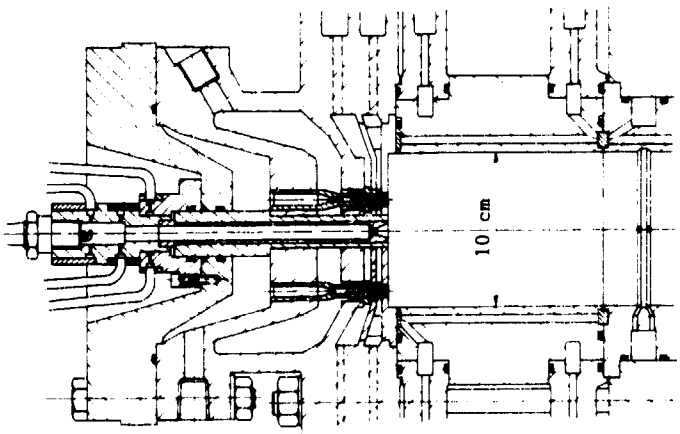

Fig. 11 - Head of the $H_2/O_2/H_2O$ combustion chamber for the 100 kW turbine of figure 9

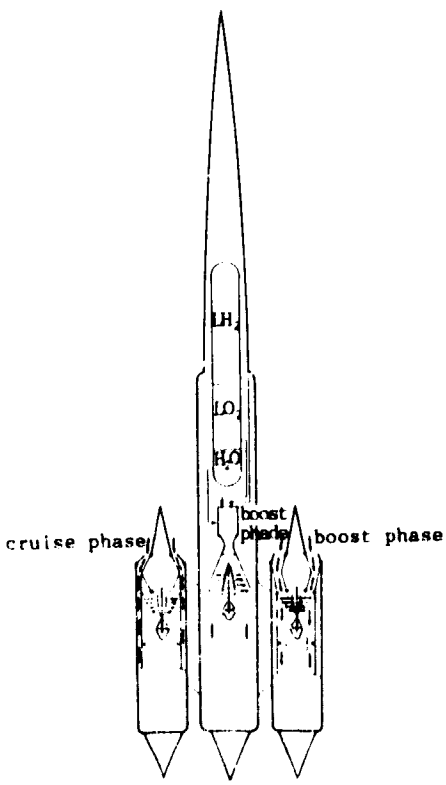

Fig.12 - $H_2/O_2/H_2O$ combustion chamber launch-boost phase of a turboramjet

Discussion

Question 1. John Tilston
Is it possible to condense the steam using liquid hydrogen as it evaporates rather than using a radiator?

Author's Reply
Liquid hydrogen or liquid oxygen could be used for condensing the steam coming from the expansion turbine, although it is not sufficient for conversion of the complete working fluid from steam to water. However, the head of the combustion chamber must also be well cooled. However, I have encountered no problem in burning hydrogen and oxygen injected as liquid in the combustor, although hydrogen normally arrives at the head of the combustor as a gas. I will consider your suggestion during my later tests.

Question 2. Dr L. Ianovski
It is difficult to store liquid hydrogen in an aircraft. Have you compared different technologies for producing hydrogen, for example, the catalytic water-steam conversion of liquid hydrocarbons?

Author's Reply
Your suggestion could be considered for hydrogen production directly on board, considering that large quantities of hydrocarbon do not need much volume to transport. However, too much energy is required to compress gaseous hydrogen. Moreover, oxygen must also be stored on board. With electrolysis, we get gaseous hydrogen and oxygen in stoichiometric ratio, just as needed for combustion. Their liquefaction is well known technology.

Evaluation of the Transient Operation of Advanced Gas Turbine Combustors

T. J. Rosfjord and J. M. Cohen
United Technologies Research Center
Aerothermal Technology/Chemical Sciences
Silver Lane
East Hartford, CT, USA 06108

1. SUMMARY

A unique test capability has been defined and used at the United Technologies Research Center to evaluate the transient response of advanced gas turbine combustors. This UTC Transient Combustion Facility offers the opportunity to achieve pre-defined time variations of the air and fuel flow rates and air temperature delivered to a combustor model. This capability can be used for model scales ranging from multi-nozzle combustor sectors to smaller setups focusing on one component or process. A dedicated control computer aids in establishing time profiles for the input parameters and automatically executing the transient test. Among its applications, the facility has been used to study the occurrence of in-nozzle fuel vaporization during Bodie cycles and to assess the tolerance of a fuel-staged combustor to rapid fuel redistribution.

2. INTRODUCTION

The aircraft gas turbine engine continuously undergoes operational transients. From the moment the engine is ignited, and through taxi, take-off, climb, cruise, descent, and landing of the aircraft, the engine is requested to vary its thrust level. Often these variations are accomplished over a long time period so that the rate-of-change is small and the engine is essentially operating in a "quasi-steady-process." In such instances, both the engine response and the aircraft maneuvers are smooth: this is a goal of commercial aircraft operation.

In other instances, the requested variations are rapid rates-of-change of power, altitude, and attitude. These conditions alone may result in transient inputs to the combustor, or they may cause other engine components to enter unsteady operation such as compressor stall. Correspondingly, the conditions approaching and within the combustor are truly transient. While such maneuvers can be easily imagined for high-performance military aircraft, they can also be encountered by commercial aircraft during emergency avoidance procedures. These engine transients are not a series of steady-states, but a combination of coupled, unsteady processes. In the combustor, processes including fuel delivery and atomization, air flowfield structuring, fuel-air mixing, and combustion interact to determine the instantaneous performance and emissions of the burner.

Traditionally, the performance of gas turbine combustor systems and components is evaluated only at steady-state conditions. That is, design point combinations of the burner air and fuel flowrate, air temperature and pressure are set, and combustor exit temperature and emissions profiles are measured. Even the stability evaluation of lean blowout is determined under quasi-steady conditions, with slow variations of the fuel flow rate for fixed levels of air flow rate and temperature. The operability of the combustor -- that is, the tolerance of the combustor performance and stability to rapid transients in burner conditions -- is evaluated only after completing the development of the total engine. At this point in the development cycle, it is difficult and costly to accomplish major changes that overcome deficiencies. Sometimes the only practical strategy is to contract the operating envelope of the system with an obvious loss in capability.

This situation is worse for advanced gas turbine combustors in which processes are highly coupled. For example, acceptable performance of aerating fuel nozzles relies upon maintaining a balance of air and fuel momenta to achieve desirable atomization and distribution characteristics. Transient flows may disrupt this balance and dramatically alter the resulting fuel-air ratio distribution within the burner. Further, combustor systems being considered to achieve low emissions of NO_x may employ fuel or air staging. The transition through the staging points during engine acceleration or deceleration must be studied to assure that burner operability is preserved.

The United Technologies Research Center (UTRC), working with Pratt and Whitney of the United Technologies Corporation (UTC), has developed and is using a unique test capability to evaluate the operability of gas turbine combustors during transient events. The UTC Transient Combustor Facility offers the opportunity to achieve controlled time variations of combustor air and fuel flow rates, and air temperature delivered to a combustor model. This paper will describe the facility operation and illustrate its use in evaluating operability issues encountered with advanced gas turbine combustors.

3. TRANSIENT COMBUSTOR FACILITY

3.1 Transient Operation Goals and Flowrates

The UTC Transient Combustor Facility was conceived to evaluate the non-steady-state response of combusting or non-combusting systems when subjected to prescribed, controlled variations of the input parameters. In particular, it was sought to control the total air and fuel flow rates and the air temperature delivered to an experimental model. This capability was desired for model scales ranging from a multi-nozzle sector

Presented at an AGARD Meeting on 'Fuels and Combustion Technology for Advanced Aircraft Engines', May 1993.

of a gas turbine combustor to an experimental setup focusing on one component or process. In the latter category, the model might contain a single aerating fuel nozzle or a rearward-facing step to study the influences of transient flows on atomization or stabilization, respectively.

The facility and its control system were specified to achieve flow transients as depicted in Fig. 1. Two types of time variation were sought: monotonic and oscillatory.

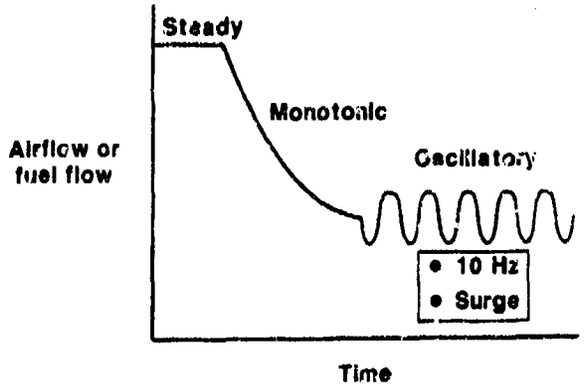

Fig. 1 Target Transient Profile

The monotonic variations, represented as combinations of 10-msec duration linear segments, characterize events occurring over a nominal 0.5-sec period or longer. While the variation during each segment is monotonic (e.g. an increase or decrease in a flow rate), the combination of them need not be monotonic but could trace increasing and decreasing flows. As indicated below, the control system updates its setpoint every 10 msec. Hence, variations on this time scale are possible for this "slow" mode. However, most large-scale engine transients follow specific time profiles over their duration. The 10 msec period permits 50 updates of the flow setpoint during a 0.5 sec event, enabling a controlled transition during it. Typically, setpoint changes by a factor of two are accomplished during a 1-sec period which precisely track a desired time profile. The air and fuel flowrates and air temperature can be controlled to follow such variations.

Oscillatory variations can be achieved for air and fuel flowrates but not for air temperature. The variation is prescribed by defining the amplitude, frequency and phase-lag associated with a cosine wave form, and a single start and stop time combination of the oscillation. If it is desired to synchronize air and fuel flow rate variations, then the maximum air or fuel flow oscillation is 10 Hz. If synchronization is not required (e.g. airflow oscillation with constant fuel flowrate), airflow oscillation frequencies up to 60 Hz can be accomplished although at the expense of an approximately 50 percent attenuation of the amplitude. Typically, the amplitude of the oscillations can range up to 75 percent of the mean. For operation up to a frequency of 10 Hz, no significant phase-lag or amplitude attenuation is experienced.

The two types of flow variations can be accomplished either alone or in combination. Figure 1 is an example of a combined variation which might simulate an engine deceleration leading to a stalled (i.e. oscillatory) airflow entering the burner. The monotonic variation mode can be used to produce ramps, steps or non-sinusoidal variations. Alternatively, oscillatory variations of air and/or fuel flowrates can be requested for steady mean values.

The model scale and transient profile goals led to defining a test facility with the following flow capabilities:

1. Controlled air flowrates to a test model of up to 15 lb/sec for a 225 psia model pressure and down to 1 lb/sec for 20 psia.

2. Airflow heating to produce controlled temperatures ranging from 300 F to 850 F at the test model.

3. Three independently controlled liquid fuel delivery systems with flowrate capability ranging from 30 PPH to 300 PPH for two systems, and a range of 60 PPH to 2000 PPH for the third system.

4. Steam heating of the fuel to produce a steady fuel temperature up to 300 F.

3.2 Transient Test Control System

A key element of the Transient Combustion Facility is the control system which guides the setup and execution of the transient test. The control strategy is based upon, firstly, establishing a profile set of the desired time variations of test model inputs, and secondly, stepping through this profile set in 10 msec increments to send new target signals to the hardware responsible for achieving the flows (depicted in Fig. 2). The control computer storage permits executing transient tests with a total duration of 30 sec.

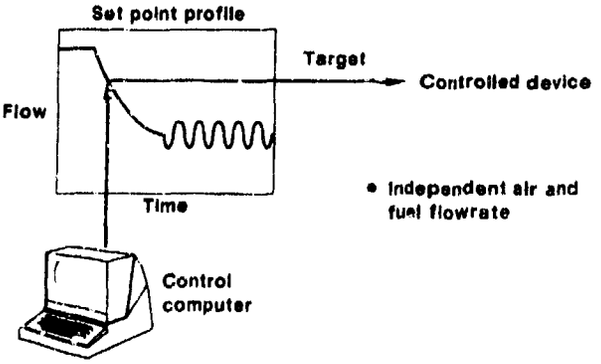

Fig. 2 Transient Control Logic

Five profiles constitute the set for a desired transient test, one each for air flowrate and temperature, and three for the fuel flowrates. As described above, the profiles for air or fuel flowrate can consist of combined monotonic and oscillatory transients. The monotonic portion of each profile is defined by up to 45 coordinate pairs of time and flowrate. The pairs do not have to be incremented by the 10 msec setpoint update period; setpoints are determined every 10 msec by linear interpolation between sequential coordinate pairs. The oscillatory portion of a profile is described by its amplitude and frequency. The monotonic and oscillatory portions are added to form the total profile for air or fuel flowrate. The air temperature profile can consist only of a monotonic profile.

A typical transient test consists of establishing a steady-state condition matching the initial conditions of the transient, followed by a computer-controlled stepping through the set-point profile set. Every 10 msec, new targets for air flowrate, fuel flowrate and air temperature are established and sent to the control hardware for closed-loop control. As described below, the air flowrate control is achieved by using measured air pressure and temperature conditions to determine the an appropriate flow area, and positioning a pintle in a venturi to achieve the area. Fuel flowrate control is achieved by actuating a valve until the metered flowrate equals the target. The air temperature control is achieved indirectly. The temperature profile is translated into a heater fuel flowrate profile using thermochemistry and heat loss considerations. The profile is shifted in time to account for the convection time delay from the heater to the test model. This two-step translation of the air temperature profile occurs automatically during a brief period once the transient test has been initiated.

3.3 Airflow Control System

An airflow system capable of delivering controlled ramp, oscillatory or combined ramp-oscillatory transient airflow to a test model has been acquired. Consideration of the above system goals led to specifying a system with the following features as depicted in Fig. 3 and 4:

1. A propane-fired, vitiating air heater is used to achieve the desired test section inlet air temperature. Replenishment oxygen is added upstream of the heater to achieve an oxygen mole fraction of 21 percent in the gas delivered to the combustor model. During a test, the pressure in the heater remains constant. The heater fuel flowrate can be ramped to achieve a changing air temperature using a closed-loop control valve-flow meter system.

2. The heated air is delivered to a plenum which, in turn, supplies the test model airflow. An axisymmetric venturi, sized to operate choked, is located between the heater and the plenum to both isolate the heater from plenum pressure variations and to acoustically define the plenum volume. Since this venturi is choked and the heater pressure is held constant, the heater air flowrate varies inversely with the heater exit temperature.

3. The airflow to the combustor model is metered by a two-dimensional venturi containing a variable-position pintle centerbody. The pintle is always positioned to assure choked flow to the model. This condition establishes a clear upstream boundary condition to the test model. Ramp and oscillatory combustor airflow rates are achieved by re-positioning the pintle in the venturi.

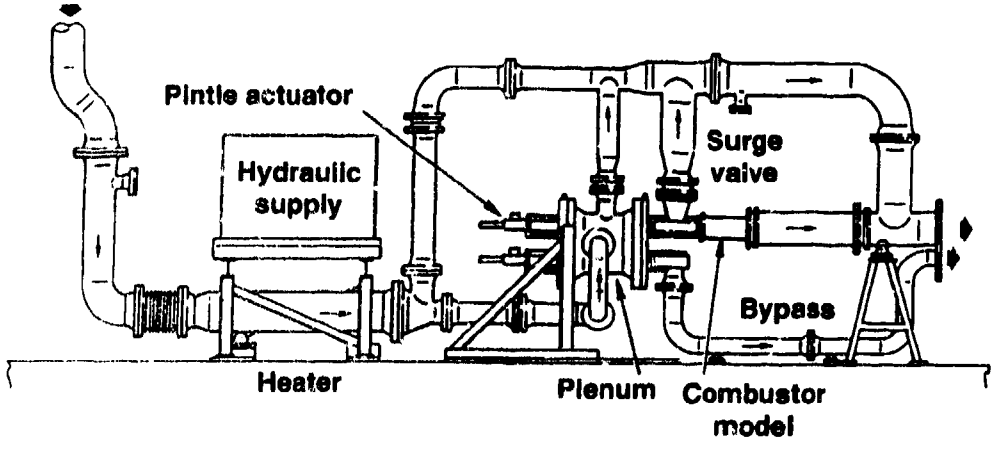

Fig. 3 Transient Airflow System

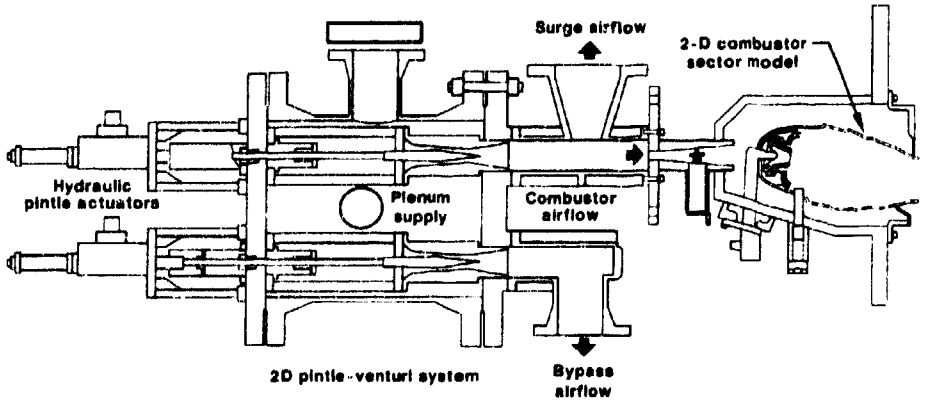

Fig. 4 Transient Combustor Airflow Paths

In an attempt to minimize pressure oscillations in the plenum, an identical two-dimensional venturi-pintle system exhausts a bypass flow from the plenum. The combustor pintle and bypass pintle are always actuated out-of-phase and with equal displacement to provide a constant total flow area through the venturi pair. Note that the equal displacement guideline is not as stringent as specifying that the two areas vary over the same absolute range (i.e. both having the same mean area); only the change in area must be compensated. This feature is useful to tailor the total airflow to the desired transient test. For example, the air heater may not operate stably at a very low air flowrate. Hence for a low test model air flowrate, the bypass airflow can be set sufficiently high to raise the total flowrate and assure stable heater operation.

Each pintle-venturi system consists of a two-dimensional venturi with a wedged-shaped pintle (Fig. 5). Airflow approaches along the constant height portion of the pintle and passes through the minimum flow area (i.e. throat) at the pintle shoulder. The dimensions and angles of the pieces were specified to achieve a desired range of flowrates while retaining adequate positioning sensitivity when driving the pintle for low flowrate variations. The throat will always occur upstream of the minimum venturi body height. The divergence angle of the venturi body and the apex angle of the pintle were specified to assure a diverging flow area downstream of the shoulder. Assuming a plenum-to combustor pressure ratio of 1.3, the minimum flow goal implied a nominal flow area of 1.5 in^2. To assure adequate positioning sensitivity, it was desired to require a 0.1 in. pintle movement to achieve a 10 percent change in this area. This requirement was equivalent to achieving a linear area change of 1.5 in^2 per inch of pintle travel. As fabricated, the venturi width is 9.010 in. with a half angle convergence of 4.8 degrees. Together these dimensions yield an area change of 1.51 in^2 per inch of travel. The minimum venturi height is 1.360 in. and the maximum pintle thickness is 1.340 in.; the minimum pintle area is 0.180 in^2. Each pintle is driven by a hydraulic actuator with a 6-in. stroke. The maximum pintle area is nominally 9.0 in^2, which is consistent with the airflow goal at a high inlet air temperature and low rig pressure. Each pintle is guided with impregnated bronze bars along the venturi centerline. Holes were bored into each pintle to reduce its mass.

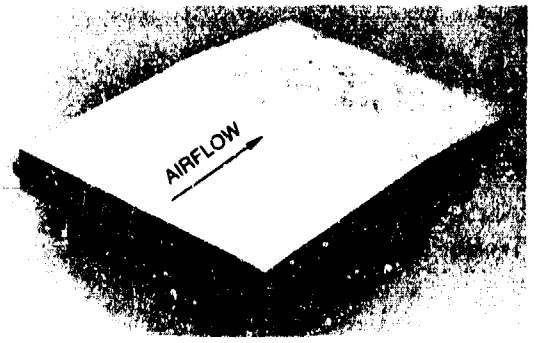

a) PINTLE

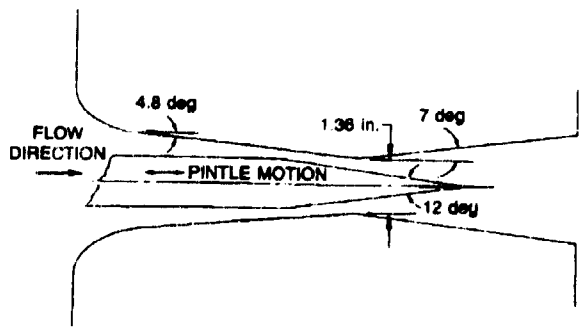

b) PINTLE – VENTURI ENGAGEMENT

Fig. 5 Pintle-Venturi System

The two venturi-pintle systems are contained within the plenum on a fixture designed to minimize the effects of assembly and thermal growth. As depicted in Fig. 4, the two venturi bodies are mounted to a cage structure which is bolted to the head end flange of the plenum; each pintle is driven on a shaft through this flange. This fixture was designed and toleranced to assure a quality alignment of each pintle in its venturi. The venturi does not attach to the downstream plenum flange; a sliding seal is accomplished by use of packing. By using a common fixture, the extent of pintle engagement in the venturi is not dependent on assembly factors such as bolt torque or gasket crush. Additionally, the cage bars produce a thermal growth in the venturi location similar to that expected for the pintle drive shaft.

The dynamics of the pintles were evaluated in specifying the actuation mechanism. The required pintle acceleration and force for candidate oscillations, and aerodynamic load (i.e. pintle drag) for particular operating conditions were computed. These analyses, and the consideration of the desired linear velocity and stroke for a pintle, led to obtaining a hydraulic actuation system rated at 60 GPM at 3000 psi. This system, with a 60 gal tank, was sufficient to satisfy the flow and force requirements of the two pintle systems and the surge valve. A later evaluation of a particular surge transient indicated that greater aerodynamic pintle forces might be encountered. A pneumatic booster consisting of a 3.5-in. dia piston contained in a cylinder was added to each pintle shaft outside the plenum. The cylinder is pressurized by the plenum. Then while aerodynamic force acts to engage the pintle into the venturi, the booster applies an opposing force to the shaft to offset the pintle drag.

Each pintle is driven by a Moog A085 servoactuator (1.1 in^2 area, 6 in. stroke) with the hydraulic flow regulated by a Moog 760-104A servovalve. The system employs closed-loop control for actuator position by use of a linear variable differential transformer (LVDT) for position sensing. The LVDT is excited and its signal conditioned by a Moog oscillator/demodulator (F123-204) which is fed to a Moog servoamplifier (F122-202). In operation, an instantaneously desired venturi area is computed from the setpoint air flowrate and measured plenum conditions. This area is translated (by use of an area-voltage calibration) to a pintle position target signal which ranges between -10 VDC to +10 VDC. The target is sent from the control computer to the servoamplifier which commands the servovalve to alter the hydraulic flow until the LVDT feedback matches the target position. A Hewlett Pack-

ard dynamic analyzer was used to characterize the response of the pintle system. In these tests, the analyzer delivered a fixed amplitude, sinusoidal voltage to the servoamplifier which began at 0.1 Hz and slowly increased until the test was completed. The LVDT feedback was received by the analyzer to determine the amplitude attenuation and phase-lag as compared to the target signal. Figure 6, taken from Ref. 1, depicts attenuation and phase-lag traces for a test with the combustor pintle system. The -3 dB bandwidth was 55 Hz; the system response up to the 10 Hz range of interest is sufficient to reliably produce controlled, oscillatory airflow transients.

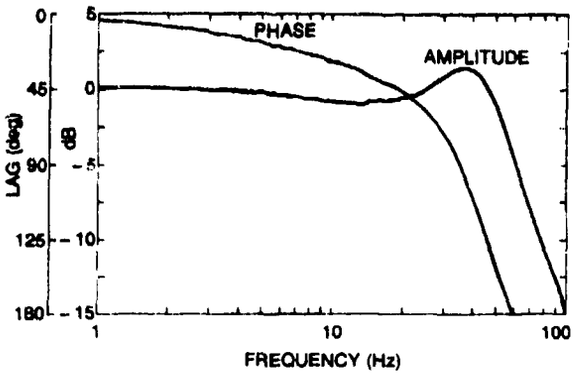

Fig. 6 Airflow Pintle Dynamics

ity were specified for delivery of a liquid propane volume flowrate of up to 4.2 GPM at a pressure drop of 100 psid. The electronic module provides closed-loop control for flowrate at the valve. That is, a target voltage corresponding to the desired flow is delivered to the module. The feedback signal from the flowmeter is compared with the target, with the difference causing the solenoid to alter the valve capacity until the difference (or "error") is nulled.

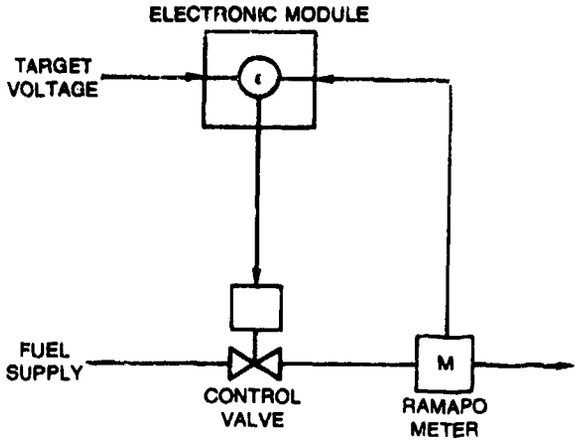

Fig. 7 Fuel Control System

4. An exhaust flow can be used to promote a periodic, reverse flow in the test model. This flow stream originates downstream of the combustor venturi but upstream of the model. The valve (identified as the Surge valve) can be actuated at the same frequency but out-of-phase with the combustor pintle. Hence when the delivery of combustor airflow is minimized, the exhausting flow is maximized.

The surge valve is a hydraulically-actuated, 8-in. butterfly valve with a maximum flow coefficient (Cv) of 2245. The valve is driven by an ExCello rotary actuator fed by a Moog 78 series servovalve. A potentiometer on the valve shaft, supported by UTRC-designed electronics, provides a feedback signal to another Moog servoamplifier to achieve closed-loop control of the surge valve angular position. The dynamic response of this valve was also investigated using the Hewlett-Packard Dynamic . . alyzer and found to have acceptable amplitude and phase characteristics.

3.4 Air Heater Control System

The air heater fuel control system was obtained from Marotta Scientific Controls, Inc. and consisted of a LV53A valve, a Ramapo Mark V-1/2 flowmeter, and an electronics control module (Fig. 7). The valve, an adaptation of a standard Marotta product, is an electrically-operated, 4-way proportional flow control device. It uses a integrally-mounted solenoid valve to vary the instantaneous flow capacity of the valve. The flowmeter employs a target mounted on a cantilever beam in the flow stream. The measured strain in the beam provides an indication of the drag on the target and, for known liquid density, an imposed flow velocity. This meter has the shortest response time of devices considered, with a quoted full response to a step change in 2 msec. The valve and meter capac-

A simple two-tier oxygen flow control was defined and used with the Transient Combustion Facility to supply the heater replenishment oxygen. In this approach, a fixed, gaseous oxygen supply pressure is available to two parallel paths. Each path contains a orifice sized to operate choked; one path also contains a shut-off valve. The line without the valve is termed the low flow path, and the valved line is termed the high flow path. If the temperature increases with time, the propane flowrate is initially low and only the low oxygen flow path is active; the valve is closed. When the control computer determines that the propane flow has exceeded a threshold, the valve is opened to also deliver through the high flow oxygen line. Appropriate combinations of supply pressure and orifice sets adequately match the replenishment oxygen flowrate to the propane flowrate for a transient test.

3.5 Test Model Fuel Control System

The test model fuel control system consists of three, independently-controlled liquid fuel systems containing hardware similar to that contained in the heater fuel control system. Each contains a Marotta LV53a control valve, a strain-gauge based flowmeter, and an electronics module. Two of the systems contain flowmeters with a range of 30-300 PPH with the third system flowmeter sized for 60-2000 PPH. Again, the electronic module provides closed-loop control of each flow at the valve as depicted in Fig. 7. The module receives the control system target voltage, compares it with the flowmeter feedback, and sends an error signal to the control valve to cause it to achieve the desired flowrate. The system response is capable of tracking a 10 Hz sinusoidal oscillation without significant phase-lag or amplitude attenuation. A steam-fed heat exchanger is located in the fuel systems downstream of the control devices. Constant fuel temperatures up

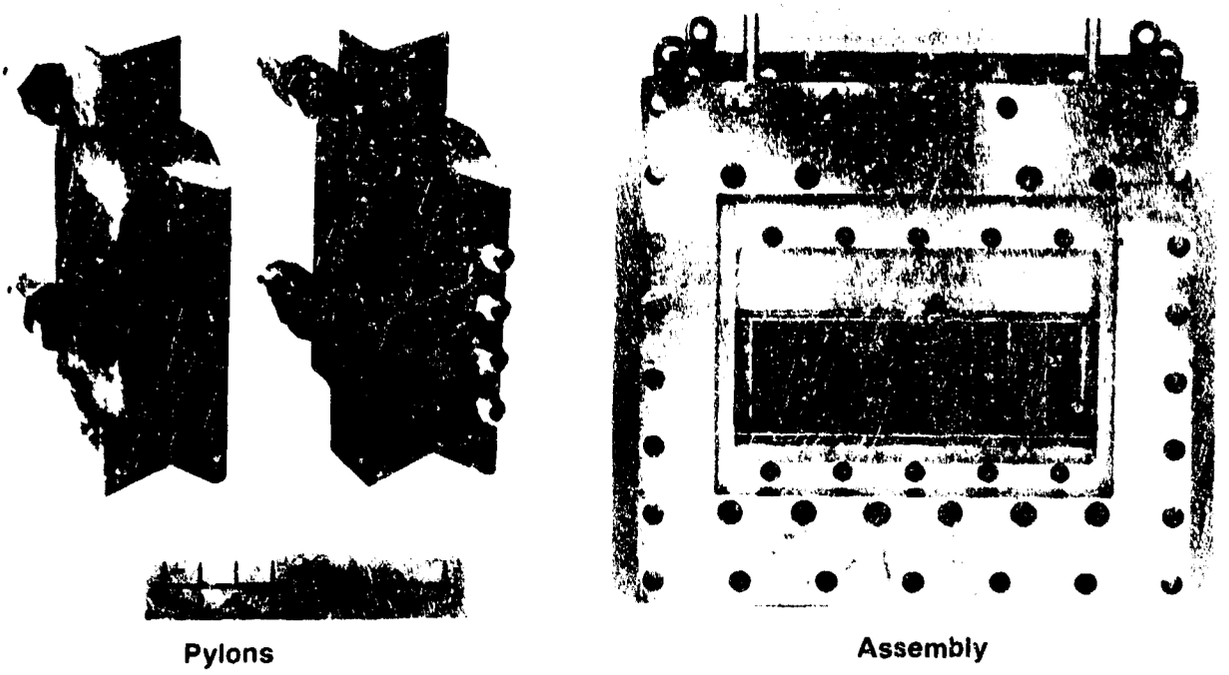

Fig. 8 Water-Cooled Exhaust Valve

to approximately 300 F can be maintained even for large variations in the delivered flowrate.

3.6 Test Model Requirements

It is important to realize that in order to study the transient response of a particular system, the system dynamics must be preserved. For example, to study the transient response of a combustor, the burner must be contained in a volume representative of the actual application. This consideration requires that the test model case matches the combustor case, and that inlet and exit flows are acoustically-isolated from the environment. Tests of a can combustor in a cylindrical case can satisfy the volume requirement while offering a structure easily suitable for high pressure. Sector combustors must be contained in a high-pressure sector case. The common practice used for steady-state testing of providing false walls around a combustor sector to define the flow path, and then mounting the assembly in a cylindrical pressure vessel, is unacceptable for transient testing; the response will likely follow the transient behavior of the pressure vessel.

Achieving acoustic isolation at the test model boundaries is also important to obtain the transient response of the model. The Transient Combustion Facility provides upstream isolation through the use of choked pintle-venturi systems. The test conditions and model hardware should provide the means to achieve a choked flow condition at the exit also. A water-cooled, two-dimensional exhaust valve is available with the Transient Combustion Facility to achieve the choked-flow boundary condition for combustor sector models (Fig. 8). The valve consists of a housing with a 3.7-in. by 12.0-in. rectangular opening for the exhaust flow, and up to 10 vane-shaped, cooled pylons. The pylons mount to rails in the housing and can be arbitrarily spaced across the opening; fewer pylons can be used. Each pylon has a wedge cross-section which establishes a series of minimum area slots for the flow. One version of the pylon contains four ports to accept total pressure or temperature instrumentation. The ports have a 0.16-in. ID and are equally-spaced over the central 2.0-in. of the pylon.

4. TRANSIENT COMBUSTOR STUDIES

The UTC Transient Combustion Facility has been evaluated to verify its capability to deliver controlled time-variations of air and fuel flowrate and air temperature to a combustor model (Ref. 1), and has been used to study the transient response of gas turbine combustor sector models. Two applications will be described: the effect of transient fuel heating in the stem of an aerating fuel nozzle; and the evaluation of a fuel-staged combustor during a cycle passing through its staging point. The former was part of part of a US Navy sponsored effort with Pratt & Whitney, GESP (Refs. 2 and 3), while the latter is part of combustor research and development activity within UTC.

4.1 Verification of Capability

The capabilities of the Transient Combustion Facility have been verified in testing performed at UTRC. These capabilities are well illustrated by the results from an ambitious, isothermal air flowrate transient. During this test, the airflow delivered to a representative model combustor began at a steady flowrate of 10 lb/sec, and, in sequence, was linearly reduced to 5 lb/sec in 1 sec, held constant for 0.5 sec, oscillated with 25 percent amplitude at 5 Hz for 1 sec, held constant for 0.5 sec,

and stepped back to the original 10 lb/sec. Figure 9 presents the pressure history, acquired at approximately a 1 kHz rate by a transient digital recorder (TDR), during the transient airflow profile. Every temporal flow feature of the airflow was achieved. The deceleration ramp was specified only by its endpoints, but during execution it consisted of 100 segments (10 msec duration) to assure a linear reduction. The dwell and oscillation periods, and oscillation frequency, matched the profile. The step change began abruptly and tracked the characteristic-time response of the model combustor. Results such as these established that the UTC Transient Combustion Facility had the capability to uniquely study non-steady-state flow phenomena.

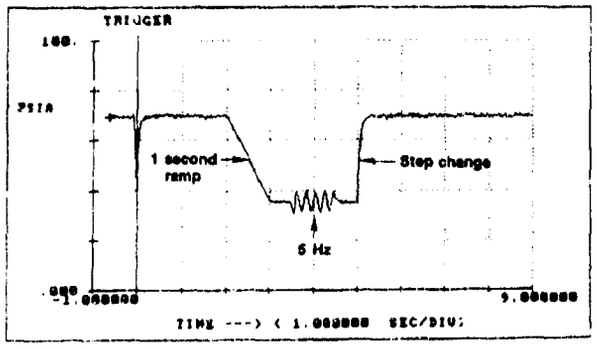

Fig. 9 TDR Record of Ambitious Airflow Variation

4.2 Transient Fuel Heating in an Aerating Fuel Nozzle

Gas turbine fuel nozzles are required to inject fuel over the wide flow range that satisfies idle to sea-level takeoff power requirements. Throughout this range, finely-atomized and spatially-distributed sprays must be produced. The aerating fuel nozzle satisfies these demands by using airflow momentum to control the spray quality. The fuel flow pressure loss is low and, hence, the fuel pressure in the nozzle is essentially equal to the burner pressure. This situation is in contrast to that existing in a pressure-atomizing fuel nozzle. This design uses the high momentum produced by high fuel flow pressure loss across the nozzle tip to atomize and distribute the flow; the fuel pressure in the nozzle greatly exceeds the burner pressure.

An important aspect of the fuel nozzle design is its ability to limit the temperature rise of the fuel flowing within it. The temperature of the fuel delivered to a nozzle is often greater than 250 F because of its use as a heat-sink for other engine systems. Any additional fuel heating is undesirable in order to avoid temperatures which promote fuel coking. The nozzle support stem is immersed in high temperature combustor inlet airflow. Heat shielding and insulation in the stem limit the heat transfer to the fuel; while flowing, the fuel temperature rise is minimal. Similarly, heat shielding is used in the head of an aerating fuel nozzle to limit fuel heating from the atomizer airflow.

Operability concerns may exist for rapid fuel heating such as encountered when the fuel flowrate rapidly decreases to a low value in a snap-decel maneuver. In this instance, the heat transfer through the nozzle body to the fuel would be high while the flowrate would be low; high fuel heating rates might be encountered. For sufficient heating and low fuel pressure, the fuel would vaporize and displace the liquid from the nozzle. If this event is followed by a rapid accel, the vapor might collapse and interrupt the fuel delivery into the combustor, promoting a blow-out. Fuel vaporization would be more likely to occur in an aerating nozzle than in a pressure atomizer because of the lower fuel pressure encountered in the nozzle stem.

Transient combustor tests were performed as part of a US Navy sponsored study to determine burner conditions and nozzle configurations which result in a blow-out during a decel-accel sequence (also known as a "Bodie"). A four nozzle, advanced combustor sector was used; the sector was modified to admit excess airflow into its corners to eliminate preferential flameholding. Inlet air flowrate and temperature, fuel flowrate and temperature, and burner pressure and exit temperature were measured at a 30 Hz data rate. Tests were performed using either single-flow (one low pressure drop fuel passage) or dual-flow (one low pressure drop passage, one high pressure drop passage) nozzles. The test fuels were JP4 and JP5 heated to 300 F.

Each test consisted of a sequence of three Bodie cycles (Fig. 10). For each, the burner air and fuel flowrates, and air temperature, began at a steady high-power level. In the first cycle, each of these parameters was synchronously ramped to a low-power level in 1 second, held at this level for 2 seconds, and ramped back to the high power level in again 1 second. At low power, the air and fuel flowrates were 40 percent and 60 percent respectively, of the high-power condition. The second cycle began after a 2 second hold at the high-power level. This cycle was similar to the first except that the air and fuel flowrates at the low-power condition were only 30 percent and 40 percent, respectively, of the high-power levels. The third cycle achieved the same parameter values as the second cycle, except the air temperature remained at the high-power level into the low-power plateau. These three cycles progressively offered more favorable conditions for the occurrence of fuel vaporization in the nozzle. Cycle 2, with its lower flowrates, produced a lower burner pressure than Cycle 1, and Cycle 3 promoted fuel heating at this condition by extending the time period of nozzle exposure to high temperature inlet air. Figure 10 is a data trace of these transient input parameters and illustrates that these three synchronized cycles were faithfully produced by the Transient Combustion Facility.

Data from tests using JP4 fuel for combustors configured with either the dual-flow nozzles (Fig. 11) or single-flow nozzles (Fig. 12) illustrated the consequences of in-nozzle fuel vaporization (Ref. 2 and 3). Both figures trace the measured burner pressure; the transient air flowrate is included as a reference to the cycles. For test using the dual-flow nozzles (Fig. 11), the burner pressure recovered to the high-power level (following the low-power excursion) for each cycle. In contrast, the burner pressure did not recover following the low-power dwell of Cycle 2 in tests using the single-flow nozzles (Fig. 12) indicating a combustor blowout.

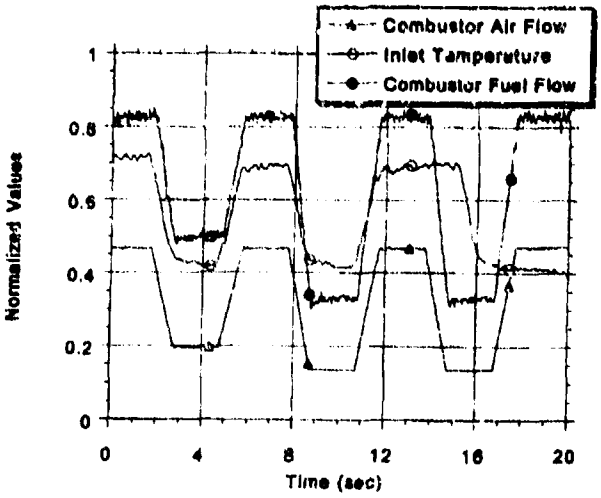

Fig. 10 Three Cycle Bodie Transient

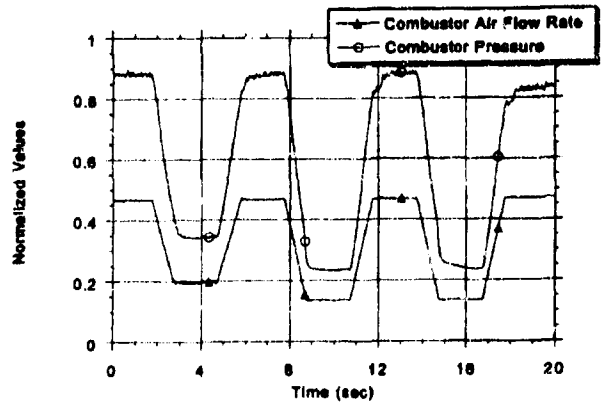

Fig. 11 Combustor Response to Bodie Cycles with Dual Passage Fuel Nozzles

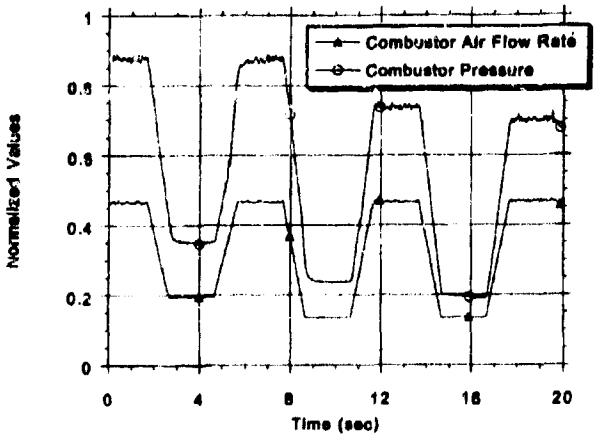

Fig. 12 Combustor Response to Bodie Cycles with Single Passage Fuel Nozzles

The blowout during the test with the single-flow nozzles resulted from a momentary interruption of the fuel flow injected into the combustor. During the low-power dwell, in-nozzle fuel vaporization of the volatile JP4 occurred in the low fuel pressure circuit of this aerating nozzle and displaced the liquid fuel; vaporized fuel was being injected into the burner. At the beginning of the accel, the liquid fuel delivered to the nozzles re-pressurized the vapor and collapsed it. The time period required to restore the injection of liquid fuel into the burner represented an interruption in fuel flow. In contrast, the primary (high pressure drop) circuit of the dual-flow nozzle sustained high fuel pressure and prevented vaporization. This sequence was as predicted by TRANSI, a time dependent, lumped parameter model of a combustor (Ref. 2) developed at Pratt and Whitney/GESP. In other tests, combustors fueled with JP5 did not blowout with either nozzle (Ref. 3). In this case, neither low fuel pressure nor longer exposure to high temperature inlet airflow was sufficient to promote the vaporization of this less volatile fuel.

4.3 Staged Combustor Transients

Modern combustor concepts seek to minimize emissions such as NO_x over a wide range of operating conditions. One strategy for reducing NO_x emissions involves fuel staging. In a fuel-staged combustor, there are multiple stages (two in this case) of fuel injectors. If only one stage of fuel injection were used at high engine power levels, the fuel/ air ratio in the primary combustion zone could lead to temperatures high enough to form significant amounts of thermal NO_x. The fuel staging strategy seeks to solve this problem by distributing the fuel more evenly throughout the combustor at high power, so that the local peaks of fuel / air ratio (and therefore temperature) are greater in number but significantly lesser in magnitude. At low power levels, the combustor would operate on one stage only, so that the lean stability characteristics of a non-staged combustor would be maintained (primary zone temperatures at low power are low enough so that only minimal NO_x is formed).

If the combustor operates on one zone at low power, but two zones at high power, this implies that, as the engine accelerates, the combustor must make a smooth transition from one-stage to two-stage operation. During this transition, the secondary stage must be lit off without affecting the engine performance in any way. Conversely, there must be a point during deceleration at which the secondary zone is turned off. Not only is a fueled zone of the combustor being turned on and off, but fuel is being shuttled back and forth between injection zones, depending upon the rate of increase of engine power level. The operability and performance of the combustor as it proceeds through these staging points are of crucial importance. For example, if one zone is too lean because it only receives 5% of the total fuel flow, it may blow out, leading to a 5% decrement in combustion efficiency, and a decrease in engine thrust. Staging schedules must account for the transient flight profiles of air flow and total fuel flow and also for the split of the fuel flow between the two zones at all points in the operating envelope.

For each transient flight event, the air flow, total fuel flow and air temperature profiles follow a fixed path, dependent upon

the nature of the flight maneuver. The staging strategy determines how the fuel flow is split between the two zones at any power level. It determines the point at which staging starts, and the rate at which fuel is shuttled between zones as the power level changes within the two-zone regime. Staging schedules must be evaluated based on their impact on the operability, emissions and performance of the combustor relative to a single-stage combustor.

It is necessary, then, to characterize the transient operation of a staged combustor as it proceeds through these staging points and encounters the rapid shuttling of fuel between injection zones. Prospective staging strategies may be evaluated at a sector level in the Transient Combustion Facility. The ability to simultaneously control air flow, air temperature and two separate fuel flows is used. Each fuel injection zone has its own dedicated fuel control system. The transient flow profiles of each fuel system can be varied to simulate different staging strategies for a given transient event.

One transient event of interest occurs when the airplane lands. Initially, the airplane is in its final approach condition. It then decelerates and loses altitude until it lands. Then, after a short delay, the pilot re-accelerates the engines to provide thrust reverse for braking. This entire process, known as and Approach-Touchdown-Reverse transient, typically takes less than 20 seconds. During this event, it is crucial that the combustor respond smoothly and as expected. For the combustor, it results in "bucket" profiles for air flow, air temperature and total fuel flow vs. time (Fig. 13). That is, each parameter initially decreases over a few seconds, followed by a short hold and an increase. In a staged combustor, the fuel flow split between injection zones changes even more rapidly during both the deceleration and acceleration portions of the transient (Fig. 14). Initially, the fuel flow is split almost evenly between the primary and secondary zones. As the engine decelerates, the percentage of fuel flow to the secondary zone is decreased, and the percentage of flow to the primary zone is increased. The inverse of this happens again during acceleration. The application of the fuel staging schedule results in the zonal fuel flow rate profiles shown in Figure 15. The two fuel flow rate profiles are controlled independently of each other, so that the total fuel flow rate at any instant is merely the sum of the two individually controlled zonal flows, and is not controlled explicitly. The "peaks" in total fuel flow rate profile (Fig. 13) result from a slight mis-coordination of the two zonal profiles.

Figure 16 shows the average combustor exit temperature and combustor pressure response during an Approach-Touchdown-Reverse transient cycle. Neither of these is explicitly controlled (only air flow, fuel flow and inlet temperature are controlled), so they act as good indicators of the tolerance of the combustor to rapid fuel redistribution. Both the pressure and temperature react smoothly, in concert with changes in the total flows. Neither shows evidence of any staging effects during the deceleration or acceleration staging. It should be noted that the exit temperature profile reflects only the resultant total fuel flow profile; the peaks in temperature at the beginning and end of the transient are in response to the "peaks" in the total fuel flow profile. As expected, the pressure does not respond to these small spikes in fuel flow, and the combustor passes through them without any compromise of operability.

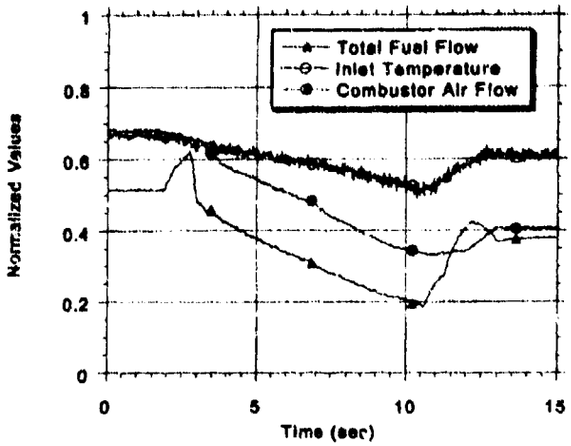

Fig. 13 Total Flow Profiles for Approach – Touchdown – Reverse Cycle

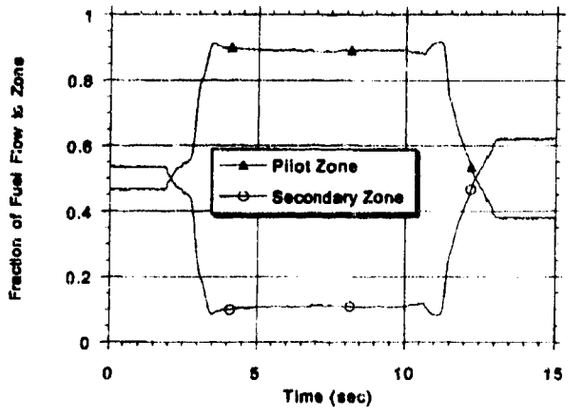

Fig. 14 Fuel Staging Schedule for Approach – Touchdown – Reverse Cycle

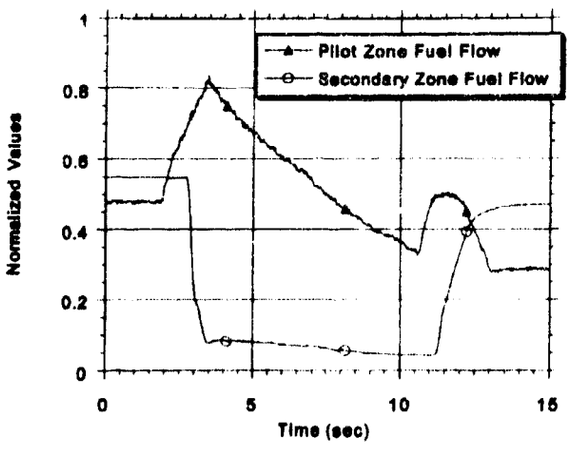

Fig. 15 Zonal Fuel Flows for Approach – Touchdown – Reverse Cycle

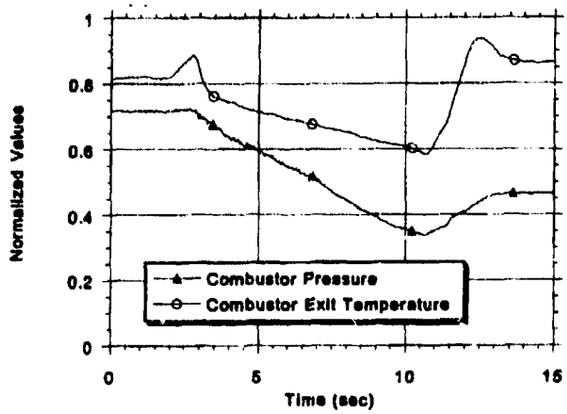

Fig. 16 Combustor for Response to Approach – Touchdown – Reverse Cycle

5. CLOSURE

Successful development of advanced gas turbine combustors will likely require the evaluation of components and systems at both steady-state and transient conditions. The unique UTC Transient Combustion Facility provides the opportunity to study the tolerance of a new design to transient operation during its evolution. Rapid, controlled time variations of air and fuel flow rates and air temperature can be delivered to a test model. This capability has been used to study combustor systems, particular components and isolated combustor processes. A growing transient-response experience base will permit the design and development of more robust advanced gas turbine combustors.

6. ACKNOWLEDGEMENTS

The UTC Transient Combustor Facility has been designed, fabricated and installed at the United Technologies Research Center under the sponsorship of the Pratt & Whitney. The study of fuel heating in the stem of an aerating fuel nozzle was performed as part of U.S. Navy contract N00140-87-C-9902 monitored by Mr. Stephen Clouser.

7. REFERENCES

1. Rosfjord, T. J., J. Haley, Jr., and J. M. Bonnell, "Unique Transient Combustor Test Capability," AIAA Paper 88-3197, July 1988.

2. Clark, J. A. and J. W. Green, "Modeling Gas Turbine Combustor Performance Under Transient Conditions," AIAA Paper 90-2161, July 1990.

3. Caron, T. J., "Fuel Effects on Gas Turbine Combustor Dynamics," Final Report for U.S. Navy contract N00140-87-C-9902; P&W Report FR-21669, October 1991.

Discussion

Question 1. G.D. Xistris
How was the air inlet temperature controlled to match the variations in pressure profiles for the air and fuel flows?

Author's Reply
We use a propane fired vitiating heater to achieve the desired inlet air temperature. Replenishment oxygen is added to achieve 21% at the heater exit. Both propane and oxygen flows are controlled by temperature setpoint profile. A 1-D analysis is used to compensate for the time lag as the heated air is convected to the test model.

Question 2. S. Samuelsen
What diagnostics are you presently employing, and what diagnostics are you considering for the future?

Author's Reply
Any diagnostic must offer time-resolved capability. Pressure and fine wire thermocouples have been used for quantitative measurements. A fibre optic probe has been used to obtain qualitative images during a transient. Currently, J. Cohen, a co-author, is using a PDPA in an LV mode to obtain phase-averaged velocity measurements in his study of rearward-facing step stabilization exposed to unsteady boundary conditions.

TECHNOLOGY RIGS - A TOOL FOR AFTERBURNER DEVELOPMENT

G. RICCARDI
A. TASSSELLI
A. TROVATI
Fiat Avio S.p.A.,Direzione Progettazione,C.so Ferrucci 112, 10138 Torino, Italy

ABSTRACT

To develop a component of an advanced aircraft engine. heavy experimental activities are necessary. To avoid very long and very expensive test campaigns on development engines, tests on the so-called technology rigs are fundamental.
Particularly in the case of combustion components, whose analytical simulations by means of computer code are still not completely satisfactory and where very high gas temperatures may cause important problems of mechanical integrity, it is essential to check the behaviour of the component on the rig before testing on the engine.
This paper gives an overview of the test rigs which are used by FiatAvio in the development of the afterburner system for an advanced fighter aircraft engine.
The tests which are carried out on these rigs are described and some of the most important results are reported, discussing the benefit they have given to the engine development.
Even if this paper obviously does not cover all the results obtained from rig tests over years of engine development, the few examples reported clearly show the importance of these rigs and confirm that the financial outlay to build and update the rigs, test plants and models is worthwhile.

SUMMARY

In developing the afterburner of an advanced fighter aircraft engine, the experimental activities play a big role. This empirical approach is due to the present state of art of combustion theoretical modelling, which is still very approximate.

Technology rigs are very useful to investigate innovative concepts, above all in early phase of the programme, to trade off different solutions on a back-to-back basis, offering a high level of flexibility (builds, dedicated instrumentation, ...) helping to reduce development costs, both in terms of investments (large facilities setting up, engine tests, ... are very expensive) and in time saving.

The paper outlines the experience gained by FiatAvio in using them to develop an advanced afterburner.

1. INTRODUCTION

The development of an advanced aeroengine component is undoubtedly a complex activity, involving a mixture of experience, theory and experimental tests. This process necessarily starts from the best of design experience gained from previous projects, in terms of design criteria, but also from the "lessons learned" from the experience in service monitoring performance, recording failure modes and failure rates, and so on.

Although experience of existing products is invaluable, nevertheless a continuous progress is necessary to satisfy a competitive market which always demands better engines, in terms of performance, reliability, durability, maintainability, weight and cost.
This means that the design technology has to be continually updated in a non-stop effort to exploit the best available solutions. It is clear that it is not possible to only rely on past experience.
Research and technological advance are necessary. each new component requires the best available knowledge, with regard to materials and manufacturing processes as well as to theoretical design calculations.
All design improvements require some experimental confirmation, either on the single components or on the whole engines: this is particularly true when the state of the art of theoretical and computational analyses is not sufficiently advanced to model satisfactorily the physical phenomena.
This is particularly true of combustion components. In fact, in spite of heavy efforts to improve computational codes and therefore to limit the amount of expensive and time consuming experimental development, the modelling of combustion phenomena (involving multiphase flows with a high degree of turbulence and complex chemical reactions) is still quite approximate and does not allow to properly investigate very sensitive design aspects like, for example, combustion instabilities or production of pollutant emissions.
Moreover, even when computational codes are available, as it is the case of flow field patternation and heat transfer calculations, their application to combustion flows is not always a straightforward exercise: experimental checks and validations are often still necessary.

Having recognised the requirement for an experimental development phase, different options are possible: rig tests on small size models, rig tests on full size components and engine tests. It is obvious that only engine tests can give the final confirmation of the design, allowing to exactly reproduce not only the behaviour of the single component, but also the interactions with other engine modules.
Engine tests have in any case considerable drawbacks related to the complexity of test set up.

Presented at an AGARD Meeting on 'Fuels and Combustion Technology for Advanced Aircraft Engines', May 1993.

Firstly, the assembly of the engine is a costly and time consuming activity, precluding test flexibility, because it is not possible to repeat the tests with different configurations in a short time. As each test needs, of course, the availability of all engine components, programme delays are inevitable. Also, the cost of engine altitude test facilities is considerable, and far exceeds that for individual component testing
Last but not least, the overall amount of instrumentation available in the engine test cell is often limited and this may prevent single components to be fully analysed in detail.

Clearly, during the development of a component it is essential to be able to test various design configurations in a quick, flexible and cheap manner, in order to investigate as many as possible different concepts, and it is also essential to have all the instrumentation required for each particular test. Also if the experimental investigations are devoted to check and confirm computational results, this is only possible when detailed instrumentation is fitted.
The above mentioned reasons confirm the validity of an experimental approach by using the so-called "technology rigs" as development tools before the final verification on prototype engines.

This paper deals in particular with FiatAvio experience in developing an afterburner system for a turbofan engine to be installed on an advanced fighter aircraft. The importance of technology rigs is described and some of the most important results obtained from those rigs are presented.

2. FIAT AVIO TECHNOLOGY RIGS

Different kinds of technology rigs are being currently utilised for the development of an advanced afterburner system. Some of them, namely, a water rig for flow visualisation tests, an isothermal airflow rig for pressure measurements and flow field surveys and a combustion rig, work on full size sector models. In addition, a full scale rig has been designed and used to test the complete engine exhaust system (afterburner and con-di nozzle).

This chapter gives a description of the above mentioned rigs and of relevant test plant capabilities. Typical tests which are carried out are also described.

Water Analogy Rig

The aim of this kind of rig, widely utilised in the design and development of combustors, is to obtain a description, at least "qualitative", of the aerodynamic flow patterns within the components [1].

To obtain significant results, similarity to engine operating conditions must be respected, in particular the engine component and the test article must be geometrically similar and the Reynolds numbers must be similar.

Even if the flow pattern is, of course, dependent on the temperature gradients due to the combustion, it is well known that an isothermal visualisation gives lower velocities, because of the higher density, but with little alteration of the basic flow pattern [2].

In the development of this afterburner module, the first condition of similarity has been satisfied by designing a full size model. To limit the model dimensions and the water plant requirements, only a 1/5 (72°) sector model was built, which is large enough to give a representative flow pattern of the complete component. The internal features of the afterburner (fuel injectors, flame stabilisers, etc.) are 15 equispaced: then, the 1 : 5 scale of the sector was selected. Since the circumferential variation of the afterburner inlet conditions is relatively small, the inlet flow has been considered to be axisymmetric and therefore 2-dimensional.
The Reynolds number similarity is obtained by the appropriate flow-rate of water through the model: water was selected as a working fluid because it is very easy to handle and readily available.
Nevertheless, it is important to avoid contaminants in the water, which could disturb the flow visualisation, and so de-mineralised water is used. The water, stored in a tank, is pumped to the test section and then recirculated to the tank, which is large enough to damp flow disturbances through the pipelines (fig. 1).

The water pump has the following capacity:

- water flow-rate: 150 l/s max.,
- water pressure: 150 kPa (abs.).

The test article is put in a vertical position to avoid any alterations of the visualisation results due to buoyancy effects. The test articles are manufactured in perspex: this material has the necessary transparency and is very easy to work, allowing to accurately model the internal details of the afterburner. Moreover, it is cheap and can be easily re-worked to test different configurations.
In the design of the test articles, the internal details have the actual dimensions of engine components. The external walls must be thin enough to guarantee the required transparency level; nevertheless, even if perspex is a relatively strong material, care has to be taken not to overload it. To relieve the differential pressure between the inside operating pressure and the ambient, the entire model is put into a larger tank filled with water. This is an important precaution to avoid explosion of the model under the pressure provided by the water head in the duct above the model itself.

To visualise the flow, different type of tracers are used the most common of which are dyes, beads of polystyrene (or similar material with density similar to water) or air bubbles. Dyes have the drawback of "contaminating" both the model walls and the water flow, requiring frequent stops to clean the model and to replace the de-mineralised water in the tank. Polystyrene beads have been reported to sometimes cause trouble to the pump system.
Because of this, it was preferred to use air bubbles as flow tracers. An injection system was initially studied to introduce small air bubbles upstream of the model inlet, but the first runs of the rig demonstrated that the air bubbles generated by turbulence in the pump can be used with equal effect as tracers and the external air injection system was never needed.
The water flow velocity was found to be a key parameter to obtain a regular air bubble seeding. If this velocity is too high, very large bubbles, useless for visualisation purposes,

are formed. If the velocity is too low, the number of air bubbles is insufficient.
A by-pass valve allows the water flow velocity to be regulated in order to get the best visualisation effects: this optimum velocity was experimentally determined to be 1 - 1.5 m/s.

This water analogy rig is used only for flow visualisation purposes, therefore no instrumentation is fitted on the model. The observation of the flow is made possible using a slit of light which illuminates the model in a vertical plane. It is possible to rotate the support of the light around the test section, to give any desired viewing vertical plane. The recording of the flow is obtained by photograph or video.

Airflow Rig

The same perspex models used for the water tests may be also tested on an isothermal airflow rig. The aim of this rig is to flow check the models, verifying the internal pressure distribution, checking pressure loss coefficients and effective flow areas. The tests are carried out over a range of air mass flow-rates in order to check possible dependence of the results on Reynolds number.
Also visualisation tests by means of wool tufts or fluorescent paints can be performed.

The air is supplied by a compressor, with a capacity of:

- air mass flow-rate: 6.5 kg/s max.

A transition duct is placed between the compressor outlet line and the model inlet, in order to obtain a smooth transition from the pipe circular section to the sector model.
The rig discharges to the atmosphere: air pressure is related to the required mass flow-rate. Again, as for the water tests, care has to be taken to avoid high internal pressures which could damage the perspex model. Usually the differential pressure, relative to ambient, is maintained below 30 kPa.
Air temperature is that due to compression only and at the low required pressure ratios there is therefore no risk of perspex overheating (maximum allowable temperature is, in fact, about 70 - 80 °C).

The typical instrumentation for the airflow tests are wall static pressure tappings and total-static Pitot tubes. To obtain pressure patterns across the model, adjustable traversing Pitot tubes and Pitot rakes are used (fig. 2).
When the visualisation tests are performed, the photographic and video recording systems, as for the water flow tests, are utilised.

The same compressor output is also used for flow checks of small engine components, i.e. to establish the air mass flow-rate versus pressure characteristics. In afterburner development this facility is typically used to flow check the single air-cooled flameholders (flame stabilisers).
During these tests, the compressor is connected to a plenum chamber, to which the flameholder air inlet is also connected, and the flameholder cooling air is discharged to ambient (fig. 3).

2D Hot Combustion Rig

This rig is used to carry out combustion tests, to verify metal temperature distributions, cooling effectiveness and combustion efficiency.
In order to simulate the afterburner of a turbofan engine, two separate air supplies, one hot "core" air and the other cold "by-pass" air supplies are available (fig. 4).
Maximum capacity of the rig air supply lines are shown in the following table:

	By-pass	Core
Air flow-rate	2 kg/s max	4.5 kg/s max
Air pressure	150 kPa abs. max	150 kPa abs. max
Air temper.	500 K max	1250 K max

The two lines can be independently regulated, allowing the by-pass ratio to be changed.

The rig is also equipped with a moveable gas sampling rake to investigate the completeness of the combustion at different longitudinal planes downstream of the flameholders.
By removing the model liner and jet-pipe, combustion video recording is also possible.
While the general objective is to simulate afterburner inlet conditions at the rig inlet and to reproduce reheat conditions, some simplifications were accepted, namely:

- to limit the required air mass flow-rates, only a 2/15 sector (48°) of afterburner geometry is modelled,

- rig inlet pressures are also limited, by the compressor,

- while on the engine the afterburner core inlet temperature is the gas temperature downstream of turbine expansion, on the rig this temperature is obtained using a kerosene combustion chamber as a preheater and there isn't any work extraction between the preheater and the test article: this means that, for a given afterburner inlet temperature, the air vitiation ratio cannot be the same. For simplicity, no compensation for this vitiation ratio, like make-up oxygen or water injection, is provided,

- by-pass air is heated by an electric preheater,

- only a convergent nozzle with fixed throat section was designed, instead of the actual con-di nozzle on the engine.

- only the internal ("hot") components, like fuel injectors, flame stabilisers and the liner, are engine components while the external jet-pipe is manufactured in a cheaper material (stainless steel) and is water cooled.
The most relevant consequences of the above mentioned "simplifications" of rig design, are the following:

- it is possible to exactly simulate only one peculiar point of the flight envelope, about z = 11 km / M = 0.7,

- combustion efficiency is affected by the inlet air vitiation ratio and by heat transfer to the water-cooled walls, so the computed values cannot be directly transferred to the engine.

Nevertheless, this rig is a powerful investigation tool, since metal temperatures of internal components proved to be in good correlation to theoretical calculations and to engine measurements.

Although absolute values of combustion efficiency cannot be directly correlated to engine measurements, the trend, as a function of fuel-air-ratio or geometric configurations, compares well to engine behaviour and back-to-back tests are then possible.
The test article is instrumented with total and static pressure tappings to exactly calculate the air flow distribution (e. g. cooling flows).
Pressure measurements are also used to derive combustion efficiency: the analysis of relevant scan data is carried out with a FiatAvio computer programme.
Wall thermocouples are fitted on the model to monitor metal temperatures during the tests, however thermal investigations are usually best carried out by means of thermal paints which give a more complete picture.

The "Reheat Full Scale Rig"

The "sector" rigs are very useful for technology or development parametric studies, because their utilisation is relatively cheap and geometric modifications can be made quickly.
Nevertheless, these tests are limited because of the relatively narrow range of operating conditions which can be simulated and by the fact that they cannot simulate the full 3-D afterburner flow field.

To overcome these limitations engine tests are necessarily carried out, but it is preferable to engine-test only when good confidence on the component behaviour has been obtained. This can be achieved on the so-called "Full Scale Rig", where the complete exhaust system (afterburner and nozzle) is tested.
On this rig inlet conditions are simulated by using compressors and preheaters to reproduce thermodynamic parameters at engine turbine exit. To have a complete survey of the operating envelope, the capability to simulate altitude conditions by reducing the pressure at nozzle exit is also required.
In order to say time and money, it was preferred to exploit one of the existing European test facilities, rather than building a new one.
Therefore it was decided to perform the full scale tests in Cell 2 at DRA (Pyestock, England), which allows a large portion of the engine flight envelope to be investigated (fig. 5).

To have the correct interface between the test cell piping and the test article, which is an engine module, a "simulator" was designed and manufactured (fig. 6)

Main features of this simulator are:

- by-pass air is heated by an electric preheater,

- core air is heated by a kerosene vitiator,
- hydrogen injection in the core flow is possible, to modify the gas temperature profile,

- water injection in the core flow is also possible, to have the correct oxygen content in the vitiated air when combustion stability tests are performed,

- two sets of vanes are available, to be installed at the exit of simulator core duct to simulate the engine guide vanes: one set has straight vanes whereas the vanes of the second one have a curved profile to modify swirl angle,

- to simplify the installation, the exhaust diffuser is an integral part of the simulator and is water cooled.

To actuate the movable convergent-divergent nozzle, the engine actuation system and the relevant control box are used. The fuel system is test cell equipment and it is not possible to control the nozzle area as a function of afterburner fuel demand, as it is on the engine. Nozzle area must be set before changing afterburner fuel flow.
This means that only steady-state conditions can be investigated, but as in any case transient reheat performance depends on entire engine and engine control characteristics, this is not a limitation.

The tests which are carried out on the Full Scale Rig include:

- steady-state afterburner performance survey (for calculation of combustion efficiency, a performance analysis programme was provided which is analogous with the engine performance analysis programme);

- buzz and screech margin assessment;

- altitude margin (combustion stability) assessment (a water cooled periscope system, with video recording, is available to look into the afterburner system from the rear and detect flame extinction);

- afterburner and nozzle components thermal survey, with extensive use of thermal paints, and verification of mechanical integrity;

- assessment of cooling flows of flameholders, liners and nozzle.

To carry out the buzz, screech and combustion stability tests, a rapid scanning system with recording on magnetic tape of selected parameters, e.g. flame duct pressure oscillations, is available.
All the aforementioned tests can be performed either at Sea Level or at simulated altitude conditions.

Pressure traversing and gas sampling tests at different longitudinal planes are also carried out using water cooled rotating rakes (figs. 6 and 7), but in these cases the divergent portion of the nozzle has to be removed to install the rakes and
this together with other installation requirements means that tests at altitude cannot be carried out.

3. EXPERIMENTAL RESULTS

The test results obtained from the above mentioned rigs have been, and currently are, widely used in the afterburner development process, to verify the design, identify the outstanding problems and to test and validate solutions or improvements of the design.
This chapter outlines the most interesting of those results and the impact they have had on the development. Some examples are given for each rig.

Water Analogy Rig

This rig was mainly used in the very first phase of the project, to check the flow field and verify the position and the extension of flow recirculation regions within the afterburner system.
Those first tests generally confirmed design assumptions and preliminary CFD simulations, giving the necessary confidence to proceed with development. Particular care was dedicated to check the flow along the afterburner inlet diffuser cone, whose diffusion angle was chosen as the best compromise to make the duct as short as possible while avoiding boundary layer break-away: the water flow tests verified that no flow separation occurs.

Airflow Rig

The first aim of the airflow tests had been to verify "dry" (not related to the combustion, i. e. friction, diffusion, turbulence, etc.) pressure loss of the "core" and "by-pass" ducts.
These losses are a requirement of the engine specification, but they are very difficult to measure in any detail during engine operation, where only the overall pressure loss can be defined. On the airflow rig it is possible to perform tests to evaluate the single-component pressure loss contribution to the overall loss .
Pressure loss of the whole perspex model and of the core and by-pass streams were therefore measured and the pressure loss coefficients were derived. A comparison with the required values is presented in the following table, where it is apparent that the specified losses were not exceeded. The revised pressure loss coefficients were therefore introduced in the updated version of engine performance synthesis.

Pressure loss coefficients

	Specified	Measured
Core duct	0.438	0.362
By-pass duct	0.688	0.578

The further tests were dedicated to measure flow effective areas, which were in line with the design, and to make more detailed investigations on discharge coefficients.
Among others, the effective areas of heat shield cooling holes and of the by-pass duct at the fuel injection section were measured.
Also these values were used to revise design assumptions and to more accurately estimate the flow distribution, which is important not only for the verification of the afterburner system but also to control the mixing process of core and by-pass flows and engine matching.
For example, the discharge coefficient of the bypass fuel injection throat section (Cd ≅ 0.9) was about 20% higher than the value assumed in the preliminary design, necessitating, in the short term, metal trimming segments to bring the effective area back to the design value.

A third example of the utilisation of an airflow rig is the flow check of the flameholder cooling air ducts. In this case the test article is a single flameholder, not a perspex model, and very simple tests were performed to establish the "air mass flow-rate vs. pressure ratio" characteristic curves for different configurations of the cooling system. Those results have been used to improve the input data of the computer programme which is used to predict flameholder metal temperatures.

2D Hot Combustion Rig

The first test campaigns performed on this rig were scheduled to map the metal temperature distributions with thermal paints and to evaluate combustion efficiency as a function of the fuel split between vaporisers, core and by-pass sprayers.
The temperature profile cannot be directly applied to the full engine geometry, nevertheless the rig demonstrated to be a very good comparative tool to test different configurations and to compare the metal temperatures on a back-to-back basis.

A significant example of the benefit of this rig is the improvement of the radial flameholder cooling. When the first runs of the Full Scale Rig and of engines showed that these components were hotter than acceptable, rapid remedial action was necessary.
In order to enhance the heat transfer coefficients, turbulence promoters (ribs) were introduced in the coolant duct (fig. 8) and a different configuration of the cooling air exhaust was identified.
These modifications were tested and a significant reduction of peak temperature was obtained (fig. 9), later also confirmed by engine tests.

In order to optimise the geometry and obtain a further reduction, different configurations of the ribs (rib orientation and the pitch-to-height ratio) were studied [3] and a "theoretical" optimum design was identified (figs. 10 and 11). Since the literature refer principally to turbine blade cooling cavities, whose geometry is dissimilar, an experimental

confirmation of the analytical studies was sought and various test articles were manufactured.
The testing phase of this advanced design is still in progress, but the preliminary first evidence shows that some improvements are possible, and also confirms the analytical predictions (fig. 12).

For combustion efficiency investigation, tests were conducted reproducing the engine fuel-air-ratios and simulating many different fuel splits, to evaluate efficiency trends in advance of either Full Scale Rig or engine test. The typical efficiency trends and the effects of the fuel splits were later also confirmed by engine tests.

The 2D Hot Combustion Rig also played an important role in the studies of advanced flameholders in composite (Carbon-Carbon) material.
As well as tests to characterise the material and its ceramic coating (oven tests, thermal fatigue tests and vibration tests), one of these composite material flameholders was tested on the rig, to verify combustion performance and to carry out short endurance testing.
In this case, the combustion rig allowed the component to be tested in conditions similar to the operating environment. The endurance test indicated a critical region near the bolted interface between the composite flameholder and the metal structure, where the ceramic coating cracked. Finite element analysis, applied to the multi-layered material, suggested by additional vibration testing, showed that the region where the failure occurred is a stress concentration zone. This indication led to an improved design, which is planned to be manufactured and tested.
The composite flameholder differs from the metal one because it is not cooled and has a "Vee" section (while the metal one is a "Delta" to create a cooling duct). Although the advantage of being uncooled is evident, a combustion performance test indicated some potential benefits of combustion efficiency coming from the composite configurations (fig. 13).

The "Reheat Full Scale Rig"

This rig is the vehicle for the final confirmation of the afterburner design and of relevant modifications before engine application.
Compared with engine tests, t is important to note that the Full Scale Rig not only has the already mentioned advantages in terms of flexibility , but it allows testing in controlled conditions which corresponds to the design thermodynamic cycle of the engine. Particularly during the first stages of the engine development, often some components, like the compressor or turbine, may not give the final expected performance and the actual afterburner working point during development will be different from the ultimate design point (e. g. by-pass ratio will be different due to engine matching variations). As on the rig the afterburner inlet conditions can be set as required, it is possible either to check the afterburner design operating points or, if preferred, to reproduce engine operating conditions

The first test campaigns were dedicated to perform a complete investigation of the behaviour of the original design configuration, measuring combustion efficiency within the flight envelope, altitude stability margins, buzz and screech margins and checking wall temperatures with thermal paints.
Performance tests confirmed very strong effects of fuel split on efficiency, already noted on the 2D Combustion Rig, and showed also the effect of by-pass ratio (fig. 14).
These efficiency values are derived from pressure measurements at the nozzle throat section and are a "propulsive" efficiency rather than a "combustion" efficiency, because they depend not only on the completeness of the combustion processes but also on the afterburner exhaust temperature profile, which is affected by the by-pass ratio as well as by the nozzle cooling film. To have a better understanding of these phenomena, gas sampling tests were performed at different by-pass ratios, confirming that "combustion" efficiency (i.e. the degree of completion of chemical reactions) is almost unity (fig. 15). This information was of course very important to direct following design efforts to furtherly improve afterburner performance.

For mechanical integrity, rig investigations have been very helpful to understand the reasons for overheating of the first liner (screech damper and heat shield) configuration and to test relevant modifications. As an example, on the screech damper the problems were related to possible local ingestion of hot combustion gases into the liner nozzle cooling duct, because of a very low static-to-static pressure ratio: a modification of the geometry of the damping holes (fig. 16), avoiding reverse flow from mainstream to by-pass, allowed the problem to be recovered.

4. CONCLUSIONS

Although the daily-increasing capabilities of computers and CFD are bringing to the combustion engineer powerful tools for component modelling, the "design-right-first-time" philosophy is not yet a reality, nor likely to be for some time to come owing to the complexity of the 3D-flows involved. Components and module rig testing, as outlined in this paper, is therefore today, and likely to remain in the foreseeable future, a necessary step in the development process of afterburner systems, often providing the cheapest and quickest means of achieving results.

5. ACKNOWLEDGEMENTS

The authors would like to thank the FiatAvio Testing Department people, who supplied information about rigs and test plants and who gave their valuable contribution to the test activities. We would like also to acknowledge the activity of DRA (Pyestock) test cell operators and the continuous support of Rolls Royce specialists.

6. REFERENCES

[1] Odgers, J. and Kretschmer, D., "Experimental Techniques", *in* " The Design and Development of Gas Turbine Combustors", NREC Report No. 1344-2, 1980, Chapter 7.

[2] Priddin, C. H., "Practical Application of Gas Turbine Combustor Calculation", Cranfield Lecture *in* "Gas Turbine Combustion Short Course", July 1988.

[3] Han, J. C., Park, J. S. and Lei C. K. , "Heat Transfer and Pressure Drop in Blade Cooling Channels with Turbulence Promoters", NASA Contractor Report 3837, 1984.

Fig. 1 - WATER ANALOGY RIG

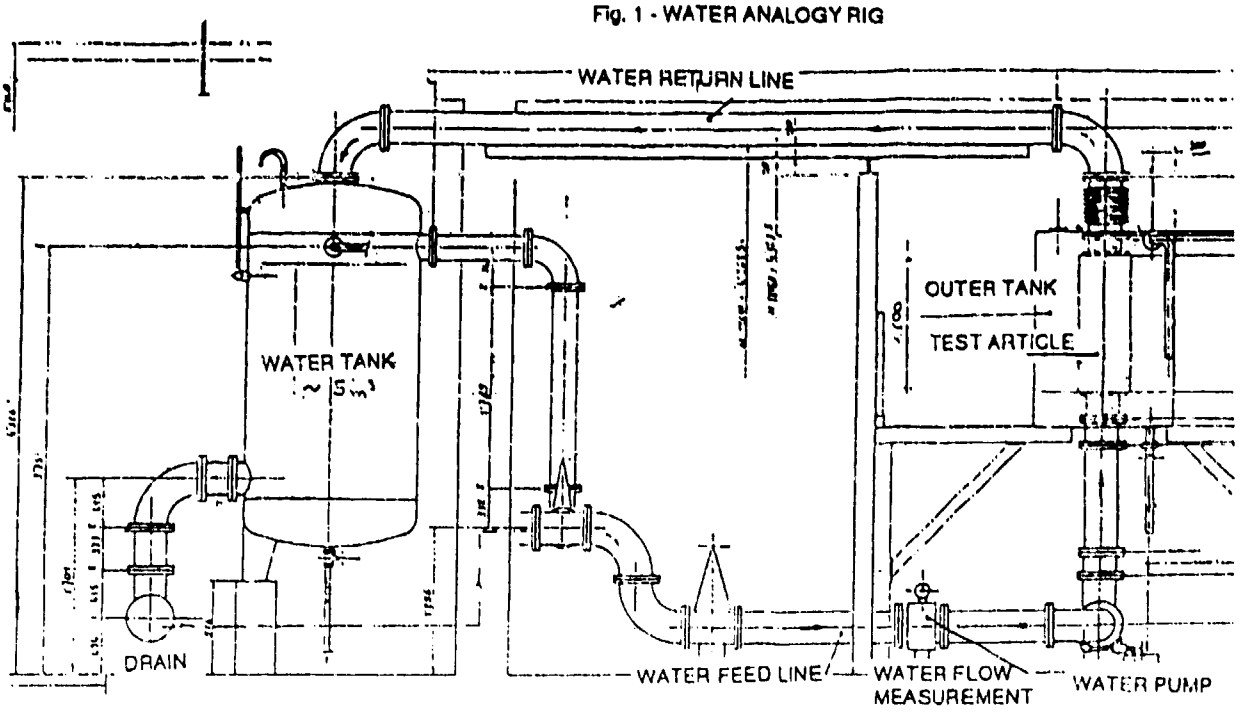

Fig. 2 - AIRFLOW RIG - TYPICAL MODEL INSTRUMENTATION

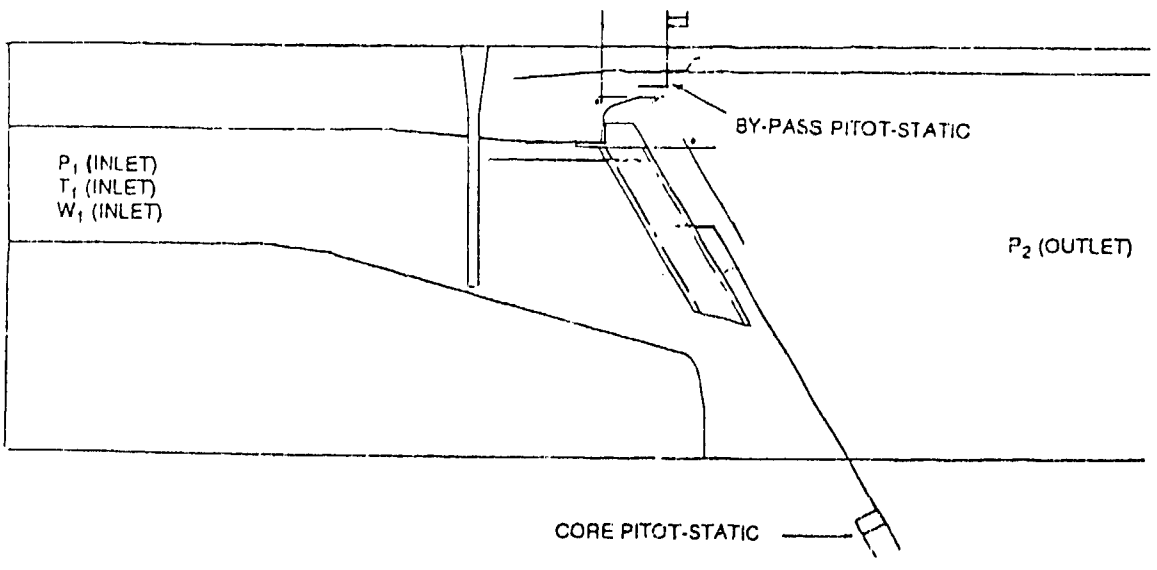

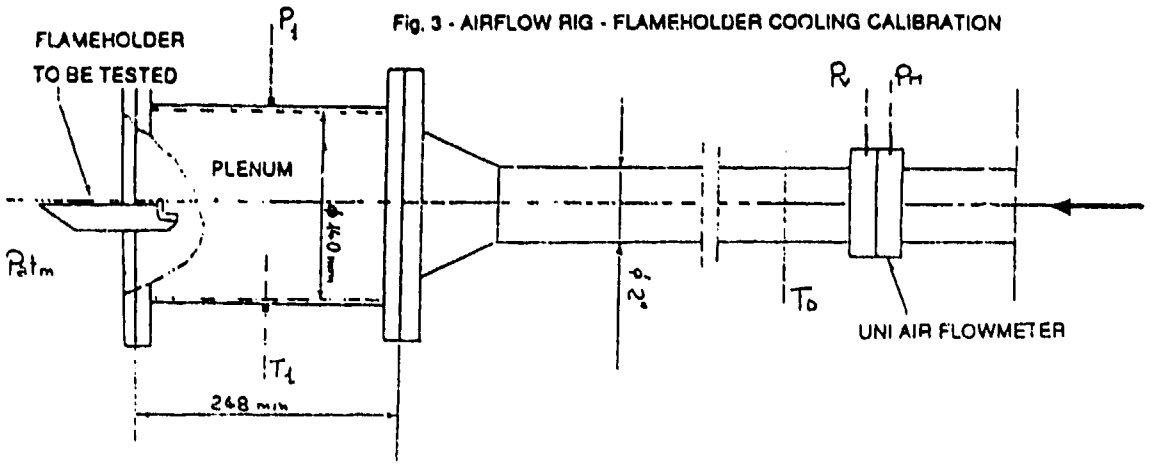

Fig. 3 - AIRFLOW RIG - FLAMEHOLDER COOLING CALIBRATION

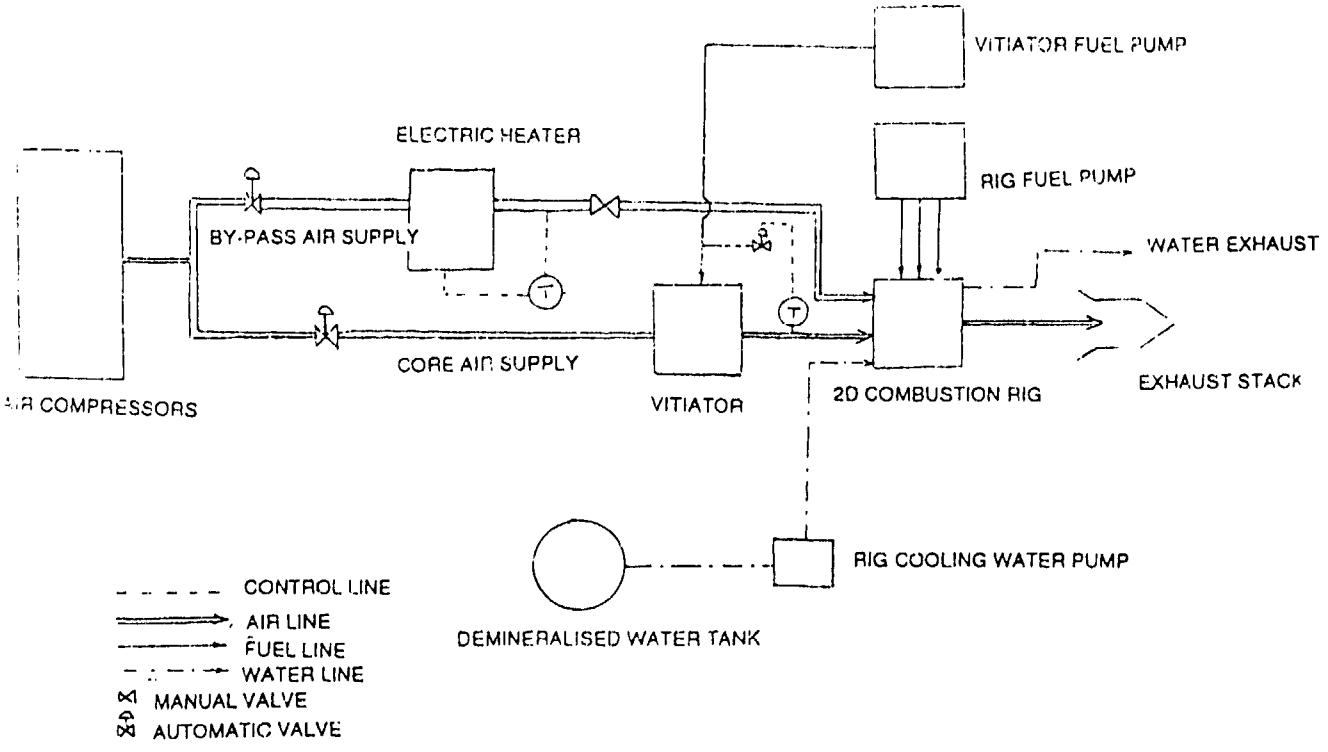

Fig. 4 - 2D HOT COMBUSTION RIG

Fig. 5 - GENERAL ARRANGEMENT OF AFTERBURNER RIG IN DRA CELL 2 (PYESTOCK)

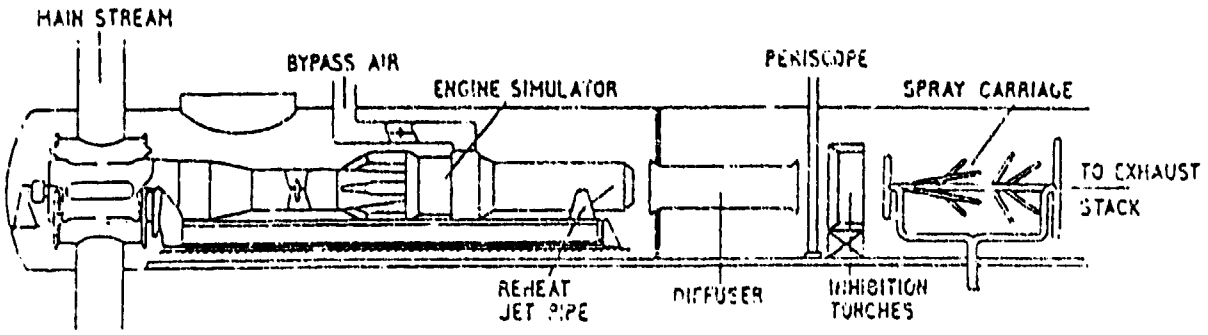

Fig. 6 - REHEAT FULL SCALE RIG - ENGINE SIMULATOR

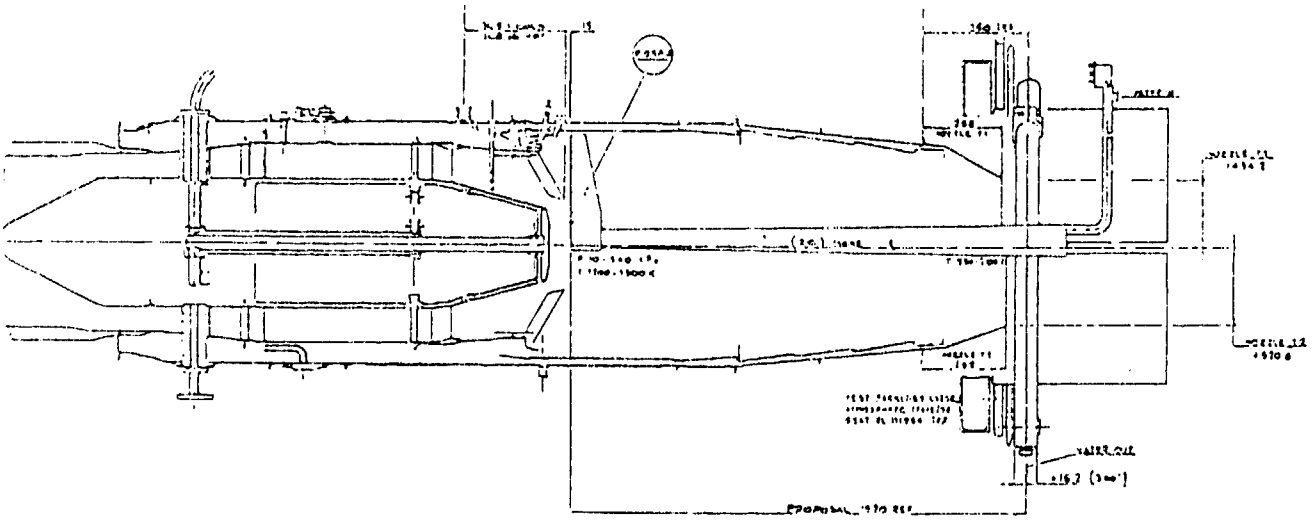

Fig. 7 - REHEAT FULL SCALE RIG - ROTATING RAKE FOR GAS SAMPLING AT NOZZLE THROAT SECTION

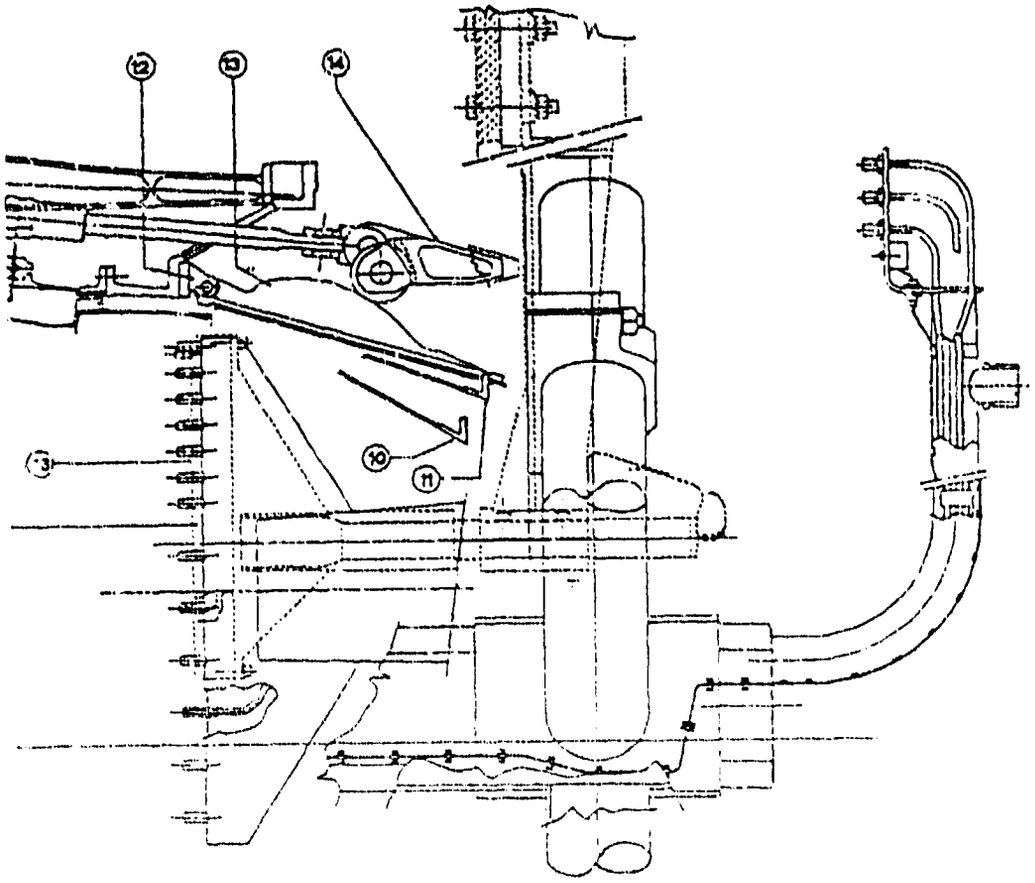

Fig. 8 - FLAMEHOLDER COOLING DUCT - TURBULENCE PROMOTERS: ORIGINAL CONFIGURATION

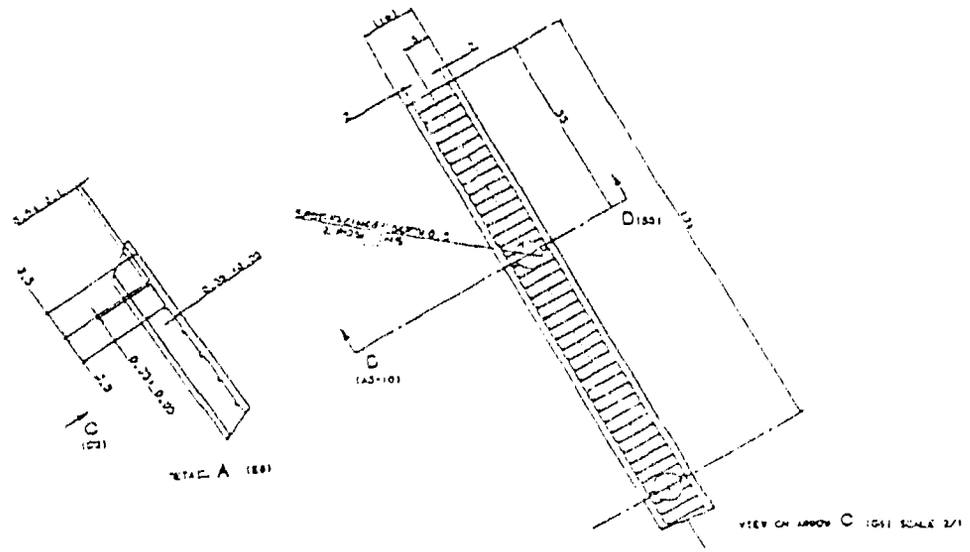

FIG. 9 – FLAMEHOLDER TEMPERATURE

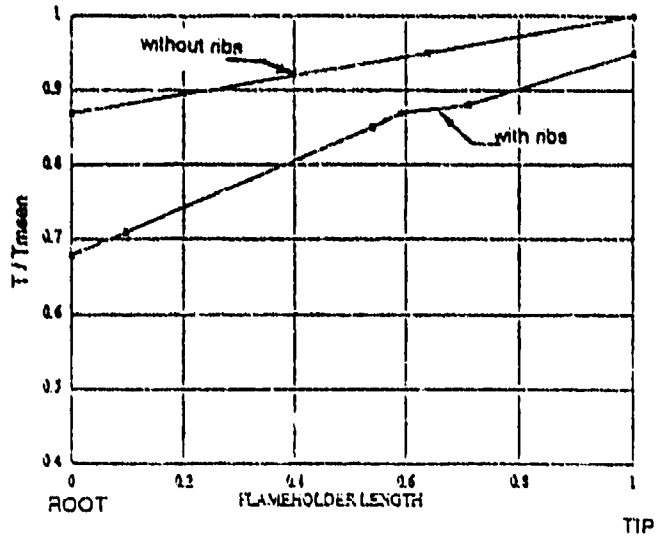

Fig. 10 - Stanton Number (e/D = 0.125, Re = 40000)

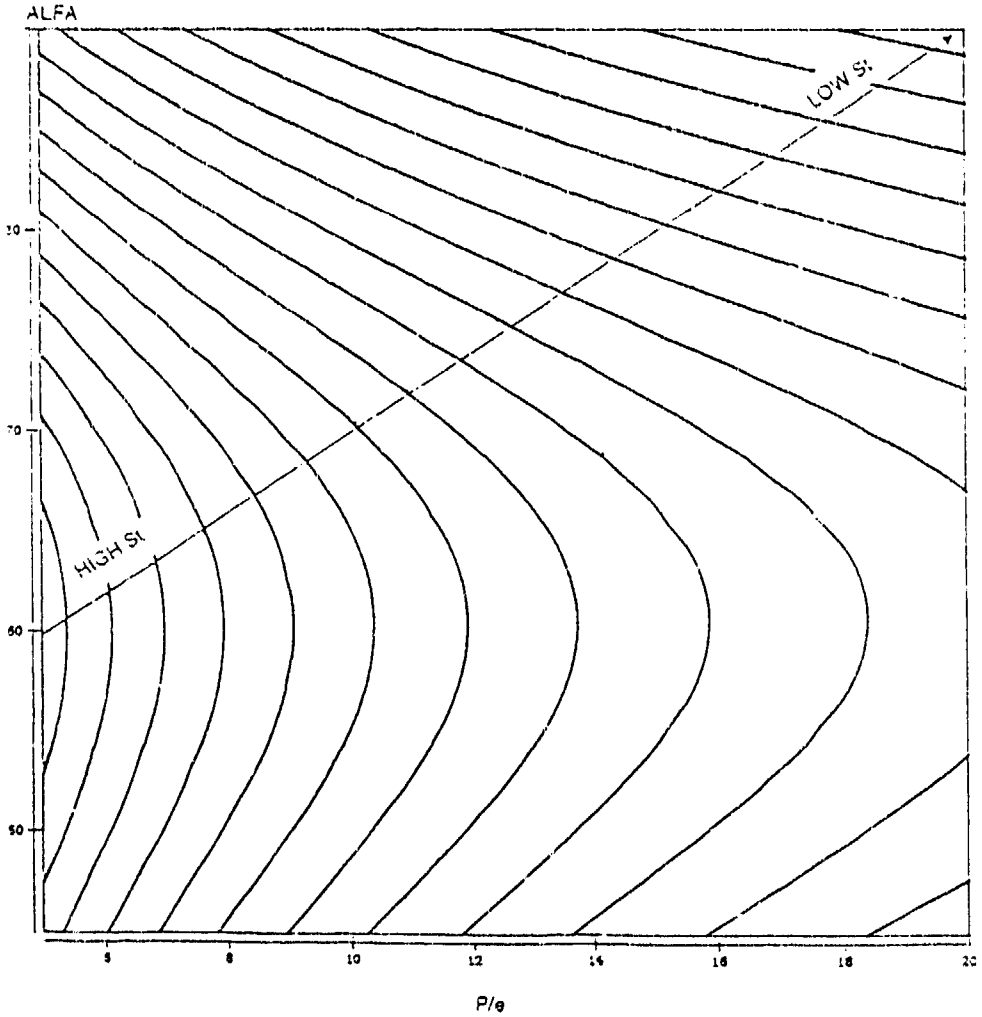

P/e = Rib pitch / height ratio

e/D = Rib height / cooling duct hydraulic diameter

ALFA = Angle between coolant flow and rib (90° = rib original configuration)

Fig.11 - FLAMEHOLDER COOLING DUCTS WITH MODIFIED ORIENTATION OF TURBULENCE PROMOTERS

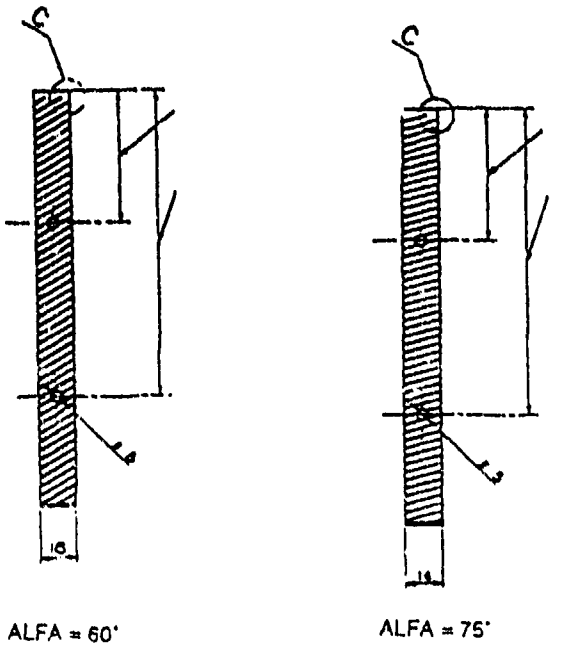

ALFA = 60°

ALFA = 75°

FIG. 12 - FLAMEHOLDER TEMPERATURE - Improved geometry of turbulence promoters

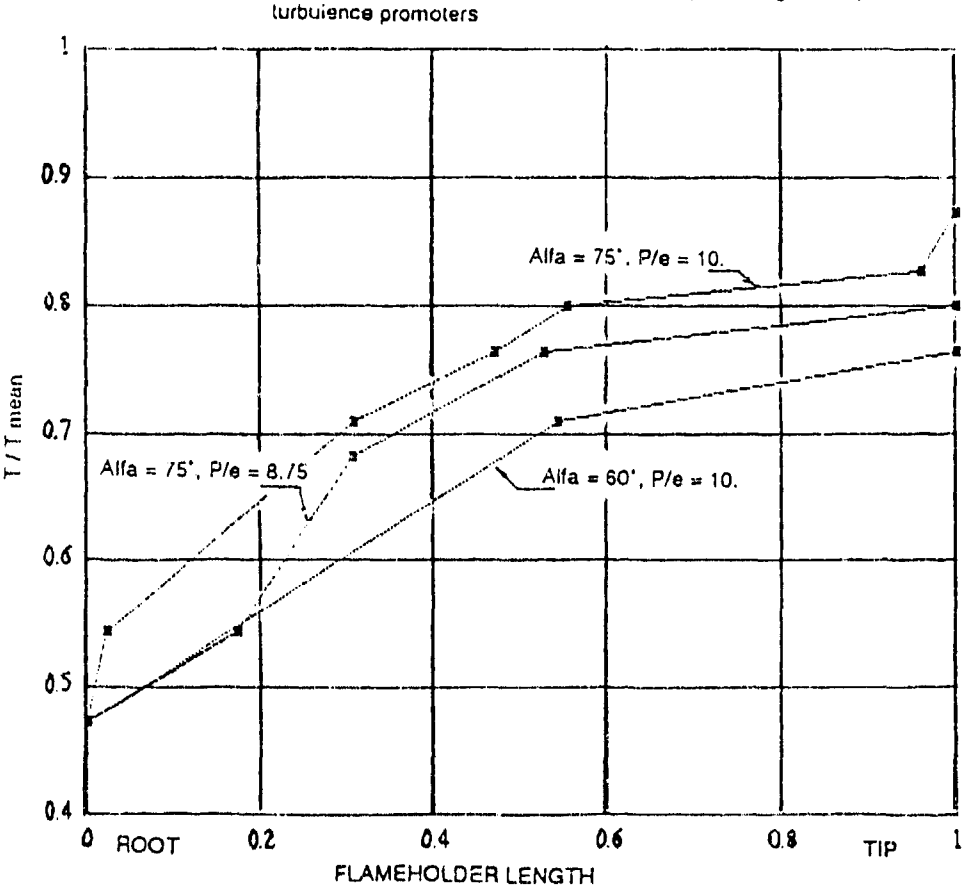

(Reference T mean is the same of Fig. 9)

Fig. 13 - CARBON/CARBON FLAMEHOLDER

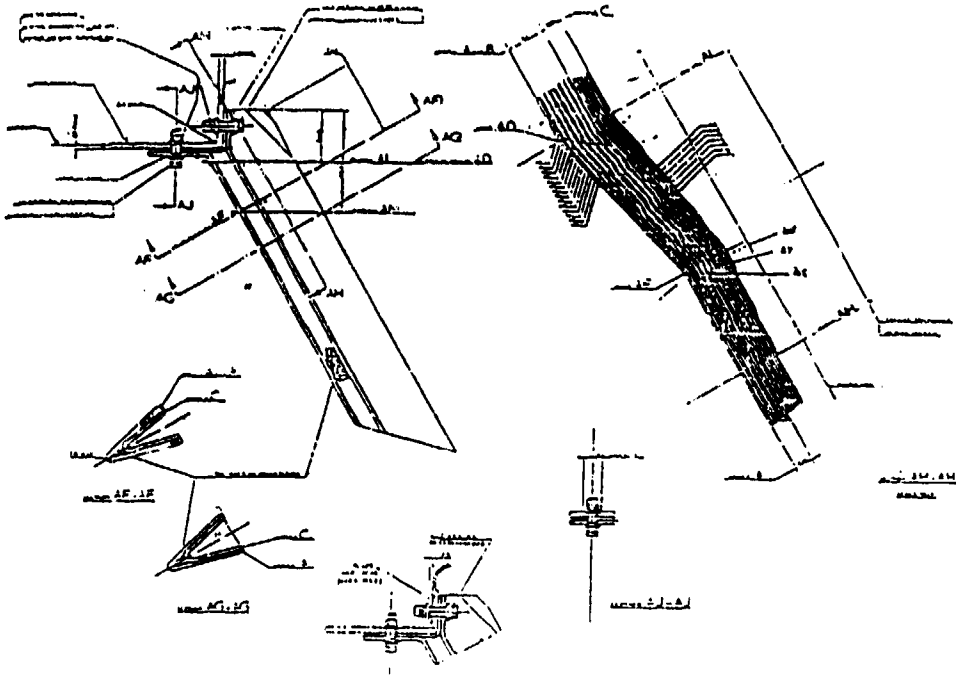

Fig. 14A - REHEAT FULL SCALE RIG
EFFECT OF ENGINE BY-PASS RATIO ON AFTERBURNER EFFICIENCY - BPR = 0.39

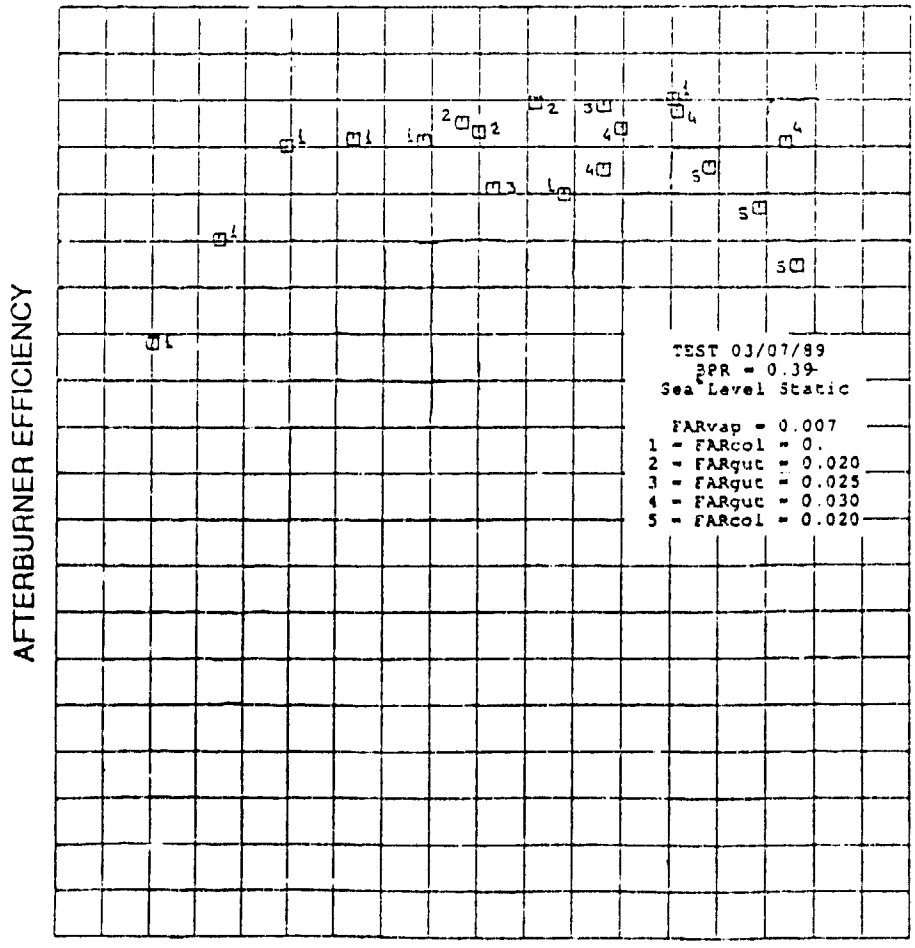

Fig. 14B - REHEAT FULL SCALE RIG
EFFECT OF ENGINE BY-PASS RATIO ON AFTERBURNER EFFICIENCY - BPR = 0.54

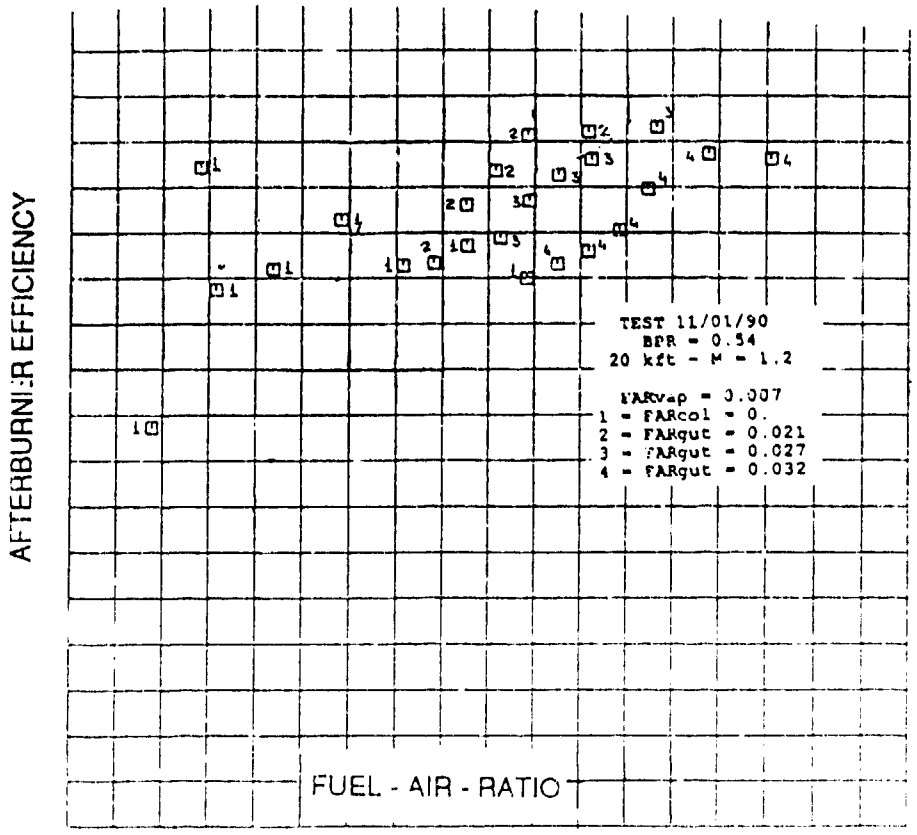

Fig. 14C - REHEAT FULL SCALE RIG
EFFECT OF ENGINE BY-PASS RATIO ON AFTERBURNER EFFICIENCY - BPR = 0.65

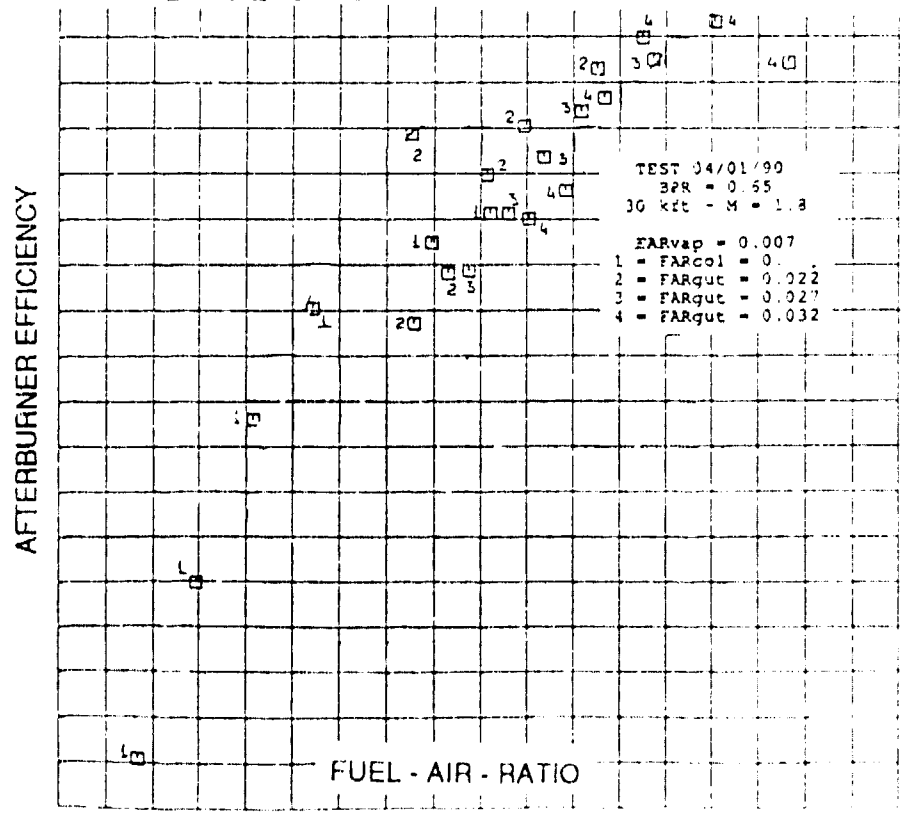

Fig. 15 - REHEAT FULL SCALE RIG - GAS SAMPLING TESTS - MAX A/B
COMBUSTION EFFICIENCY AT NOZZLE ENTRY

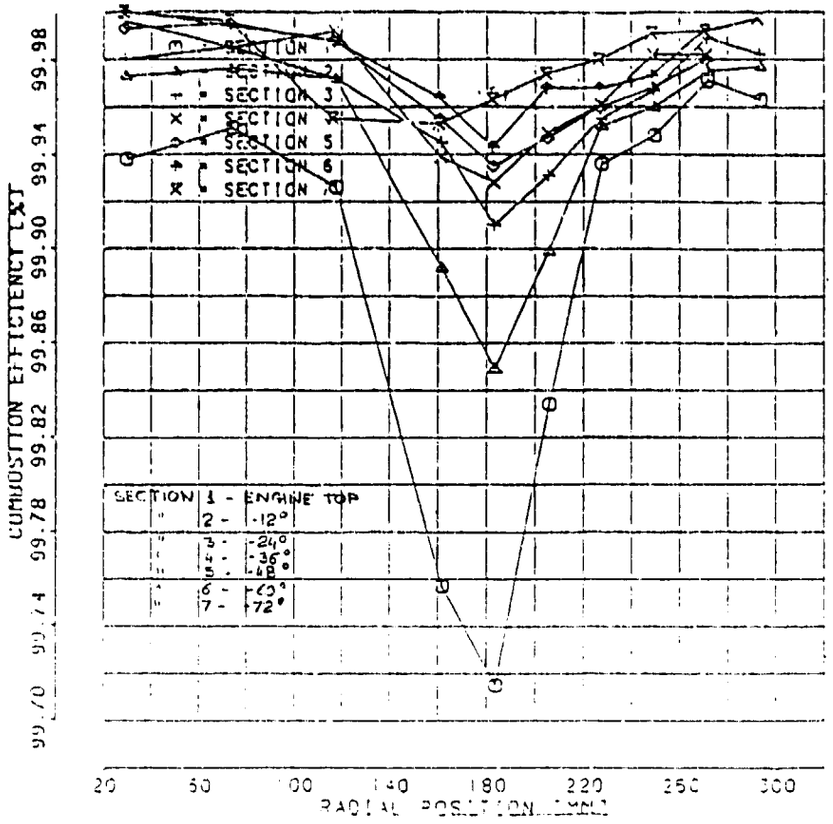

Fig. 16 - SCREECH DAMPING HOLES

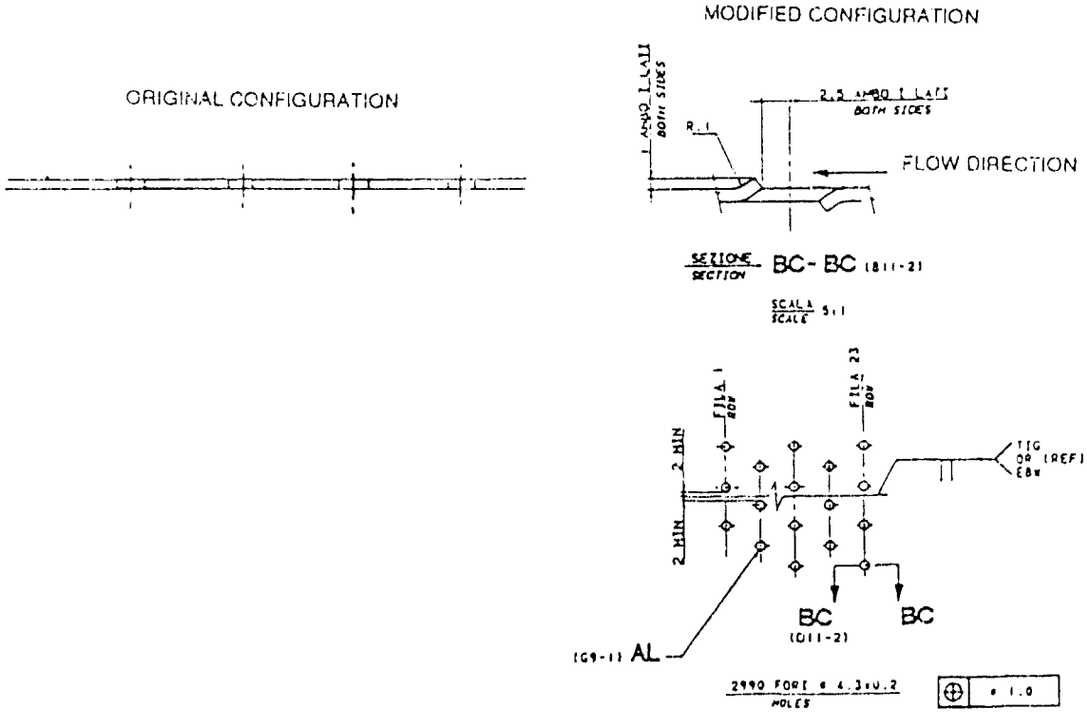

Discussion

Question 1. D.K. Hennecke
You did not mention flying test beds and flight testing. Please comment.

Author's Reply
The aim of rig and engine ground tests is to obtain good confidence in the design in order to ensure the capability of the engine to fly satisfactorily. This, of course, will be finally proven by flight tests. Rig tests are the first steps to achieve confidence before engine ground tests, and the latter can be seen as preparation for flight tests. Nevertheless, at the time of the first flight the engine must already be close to the desired performance.

POLLUTANT EMISSIONS FROM AND WITHIN A MODEL GAS TURBINE COMBUSTOR AT ELEVATED PRESSURES AND TEMPERATURES

S.A. Drennan
C.O. Peterson
F.M. Khatib
W.A. Sowa
C.S. Samuelsen*

UCI Combustion Laboratory
Institute of Combustion and Propulsion Science and Technology
University of California
Irvine, California 92717-3550

ABSTRACT

Conventional and advanced gas turbine engines are coming under increased scrutiny regarding pollutant emissions. This, in turn, has created a need to obtain in-situ experimental data at practical conditions, as well as exhaust data, and to obtain the data in combustors that reflect modern designs. The in-situ data are needed to (1) assess the effects of design modifications on pollutant formation, and (2) develop a detailed data base on combustor performance for the development and verification of computer modeling. This paper reports on a novel high pressure, high temperature facility designed to acquire such data under controlled conditions and with access (optical and extractive) for in-situ measurements. To evaluate the utility of the facility, a model gas turbine combustor was selected which features practical hardware design, two rows of jets (primary and dilution) with four jets in each row, and advanced wall cooling techniques with laser drilled effusive holes. The dome is equipped with a flat-vaned swirler with vane angles of 60°. Data are obtained at combustor pressures ranging from 2 to 10 atmospheres of pressure, levels of air preheat to 427°C, combustor reference velocities from 10.0 to 20.0 m/s, and an overall equivalence ratio of 0.3. Exit plane and in-situ measurements are presented for HC, O_2, CO_2, CO, and NO_x. The exit plane emissions of NO_x correspond to levels reported from practical combustors and the in-situ data demonstrate the utility and potential for detailed flow field measurements.

Nomenclature

A_c	combustor cross-sectional area
ALR	nozzle air to liquid ratio
D_{10}	number mean diameter
D_{32}	Sauter mean diameter
FN	flow number
H	combustor dome height
L	length
P_3	combustor inlet pressure
T_3	combustor inlet temperature
V_r	velocity
ρ	density

1. INTRODUCTION

The emission of nitric oxide from military and commercial aircraft gas turbine combustors has become a topic of intense scrutiny in recent years. There is concern, for example, on the impact of nitric oxide (NO) emissions on stratospheric ozone from the flight of conventional and future generation aircraft powered by gas turbine engines at high altitudes (References 1 and 2).

The principal source of nitric oxide is "thermal NO" where nitric oxide is formed from the dissociation of air bound nitrogen (Ref. 3). The formation of thermal NO is (1) strongly dependent upon temperature, and (2) exhibits elevated formation rates at temperatures exceeding 1900K (Ref. 4). As a result, any modification to the combustor operating conditions or geometry which will induce lower peak reaction temperatures and/or lower residence times should reduce the emission of thermal NO. As flame temperatures are lowered, however, a tradeoff can arise between NO_x reduction and an increased formation of carbon monoxide (CO) and unburned hydrocarbons (HC). The challenge is to reduce CO, HC, and NO_x emissions simultaneously. Exacerbating this challenge is the trend toward higher combustor inlet pressures and temperatures.

To date, the combustor designer has relied on "in-and-out" combustor rig measurements for guidance on the effect of geometrical and operating changes on pollutant emission and overall performance. This is no longer sufficient to address the challenge of higher combustor inlet pressures and temperatures and to provide needed data to substantiate models for design (e.g., Ref. 5 and 6). An improved understanding of the processes occurring within the combustor is required. While substantial progress has been made at the UCI Combustion Laboratory in the acquisition of in-situ data in model combustors (e.g., Ref. 7), model sprays (e.g., Ref. 8), and practical hardware (e.g., Ref. 9), these data have been acquired under atmospheric conditions. Such data have been invaluable, providing

*Corresponding Author

Presented at an AGARD Meeting on 'Fuels and Combustion Technology for Advanced Aircraft Engines', May 1993.

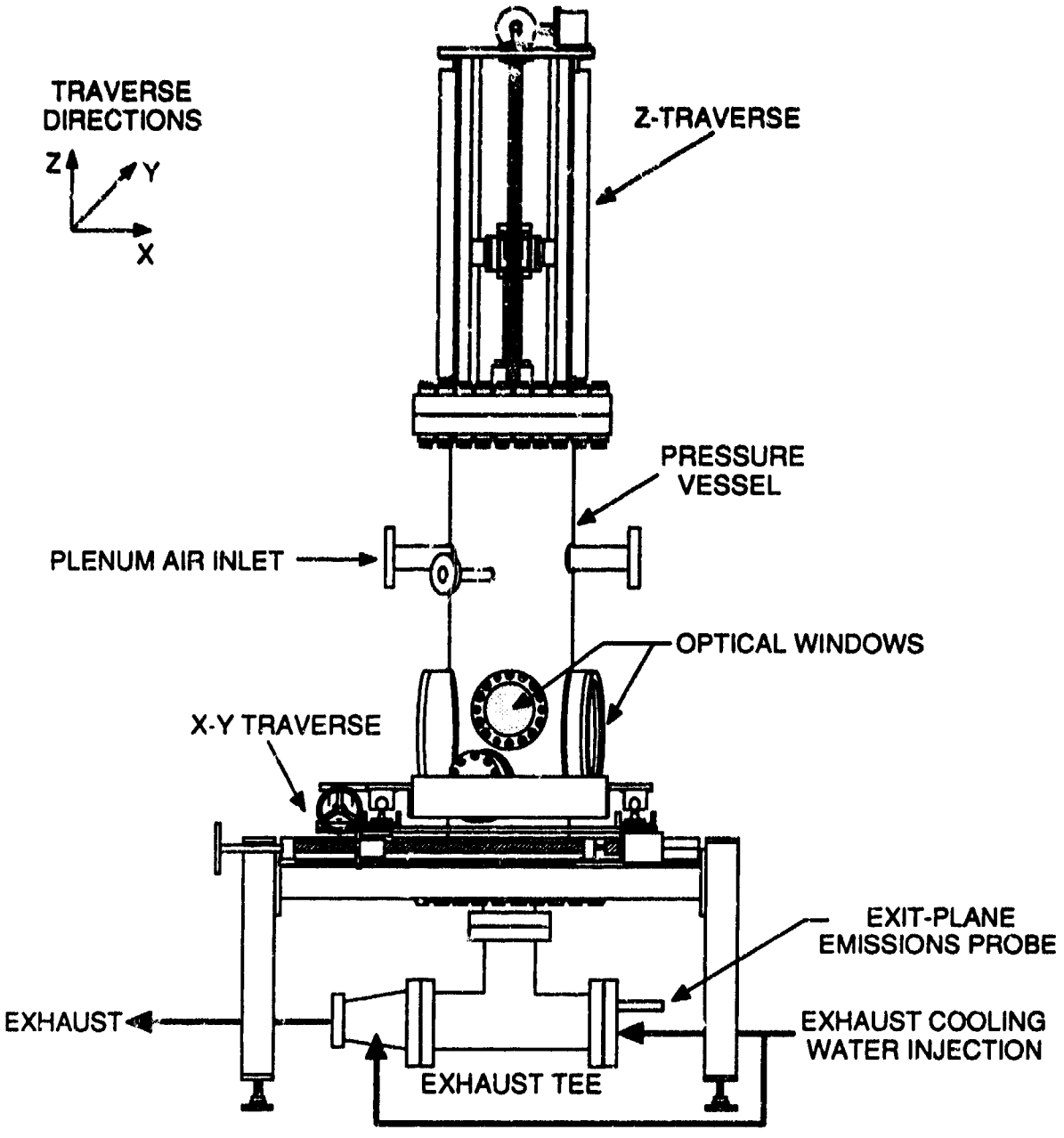

Figure 1: Pressure Vessel and Traverse System

data bases for the development of numerical codes (e.g., Ref. 10) and needed insight into the physics of fuel preparation and dispersion (e.g., Ref. 11). Even more desirable are in-situ data acquired under the practical pressures and temperatures encountered in practical combustors.

The present study reports on an experimental facility designed for the acquisition of in-situ data under the practical operating conditions of gas turbine stationary and aeroengine combustors. The challenges of such a facility are the provision of high pressure and high temperature air, the containment of the high temperature and high pressure air, the presentation of the air to the combustor hardware, the provision of optical access to the combustor hardware, the traversing of the hardware to facilitate the acquisition of three-dimensional maps, and the treatment of the exhaust to protect the back pressure value.

2. TEST FACILITY

The high pressure combustion facility was designed to provide elevated ambient pressures and temperatures that are representative of both current and future gas turbine combustor designs, and to accommodate combustors of practical design.

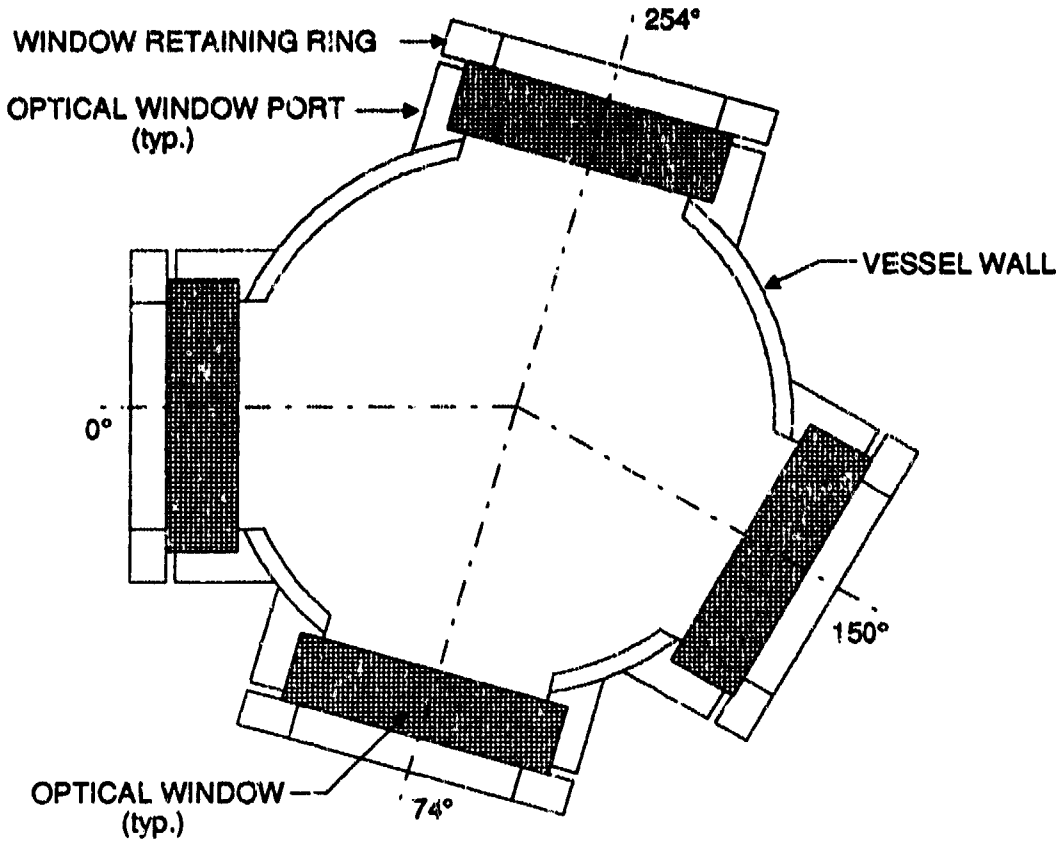

Figure 2: Optical Port Arrangement

2.1 Pressure Vessel

The pressure vessel, as shown in Figure 1, is constructed of a 40.6 cm diameter, 12.7 mm thick, 1-1/4% Chrome-Moly steel for increased strength at temperatures exceeding 427°C. The vessel body is cylindrical with a top blind flange on which the nozzle tube traverse is mounted and through which the nozzle tube passes. A blind flange is attached to the bottom of the pressure vessel and a stainless steel tee is affixed to the bottom flange The pressure vessel has an internal diameter of 38.1 cm and is 142.2 cm long from the top flange to the bottom flange. The steel shell is rated for a maximum operating pressure of 18 atm at a temperature of 482°C. To prevent the possibility of system over-pressurization, a burst disc is connected to the vessel. The internal walls of the vessel are insulated to accommodate temperatures exceeding 650°C at pressures to 18 atm. A detailed description of the high pressure vessel design is provided in Drennan (1990, Ref. 13).

For spatially-resolved optical measurements, such as advanced laser diagnostics, the pressure vessel is equipped with a three-dimensional traverse system (also in Figure 1). The approach adopted is to translate the vessel in the horizontal plane, and to translate the test article within the vessel in the vertical plane. The latter requires a translatable test fixture support that penetrates the top of the vessel through a high-temperature pressure seal. Optical access into the pressure vessel is obtained with a set of four windows. Figure 2 is a cross section of the pressure vessel at the optical height. Two of the windows are 180° apart to be used with sheet laser diagnostics or photography. The other two windows are 150° apart for use with laser anemometry and phase Doppler interferometry.

2.2 Fluid Circuits

Two air circuits, nozzle air and plenum air, are fed by two house air pressure sources (Figure 3). The low pressure air is supplied by three, 300 HP rotary compressors at a maximum air pressure of 1.14 MPa (150 psig) and a total mass flow rate of 2.05 kg/s. The high pressure air is delivered by a positive displacement booster compressor at pressures up to 3.55 MPa (500 psig) at a maximum mass flow rate of 0.68 kg/s. Electro-pneumatic control valves regulate the air pressure upstream of sonic venturi nozzles to enable air flow rate control.

The fuel system consists of a high pressure fuel pump capable of producing fuel pressures up to 10.4 MPa (1500 psig). The fuel passes through a pulsation

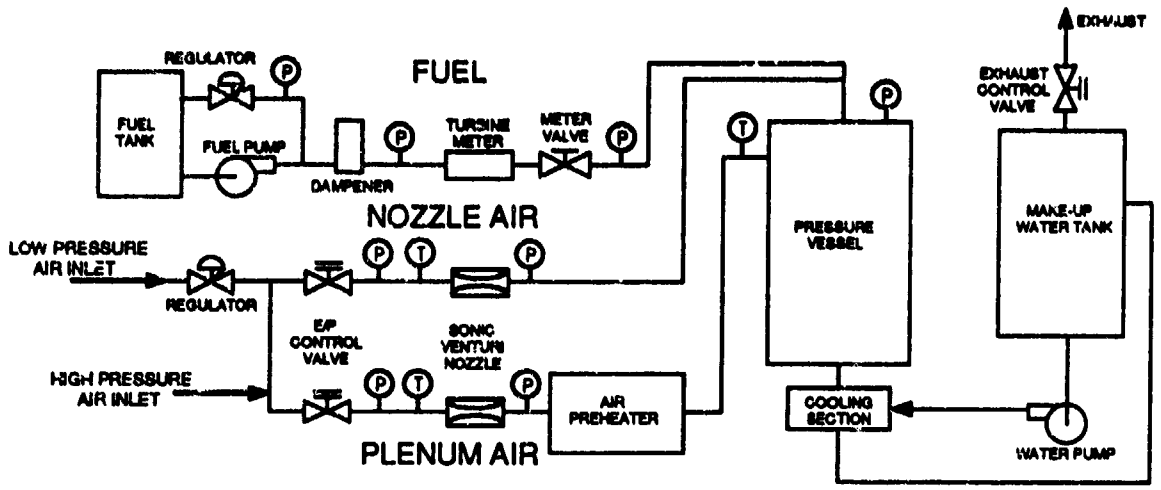

Figure 3: High Pressure Flow Schematic

dampener, a fine filter, a turbine meter to measure the flow rate, and finally a metering valve prior to injection into the pressure vessel. The fuel line also has a solenoid valve to provide remote fuel shut off capability.

The facility utilizes a bank of three electric air circulation heaters to provide up to 650°C air preheat. These three heaters have electrical power ratings of 250 kW, 167 kW, and 67 kW. They are equipped with closed loop temperature controllers that provide stable outlet temperatures over a wide range of operating pressures and desired outlet temperatures. The piping leading from the exit of the air preheaters to the pressure vessel is insulated to minimize thermal losses.

The exhaust system is designed to condition the hot combustion products exiting the combustor at high pressure in order to protect the exhaust valve that throttles the combustor pressure. This cooling is provided by injecting water at high pressure from a water pump directly into the exhaust by means of specially located nozzles. This water evaporates, cooling the exhaust gases, and then the unevaporated water is separated in a make-up water tank and re-supplied to the water pump.

3. EVALUATION

3.1 Combustor

The combustor used for evaluation is itself novel in construction although patterned after a model atmospheric laboratory combustor introduced by Cameron, Brouwer, and Samuelsen (1988, Ref. 14). While the original combustor was designed with separately metered wall jets and a water cooled wall for atmospheric pressure studies, the combustor designed for the present application is distinctly different in order to (1) accommodate the pressures and temperatures experienced in practical systems, and (2) represent combustor features of practical design and construction. The first distinction is that the combustor is plenum fed. Second, the combustor is fabricated with design features and materials that are representative of practical state-of-the-art systems. In particular, the combustor (Figure 4) is manufactured from a high temperature alloy, Hastelloy-X, which is commonly used for industrial gas turbine combustor construction. Third, wall cooling is provided by a matrix of laser drilled effusive cooling holes in the combustor wall. These holes, 0.5 mm in diameter, are drilled at an angle of 20°. There are three effusive cooling hole pattern densities along the length of the combustor. The most dense pattern exists from the inlet plane of the combustor to the beginning of the dilution holes, the medium density pattern then extends through half of the remainder of the combustor length with the least dense pattern extending the remainder of the combustor length. The combustor has an internal diameter of 80 mm, a length of 45.7 cm, and features two rows of wall jets ("primary" and "dilution" holes) with four jets per row. The two rows are located one and two combustor diameters downstream of the atomizer plane, respectively.

The inlet of the combustor is attached via a flange to a headstock mounted onto the translatable vertical test fixture support. The exit is connected to an exhaust seal tube which forces all of the plenum air through the combustor. The aerodynamic swirler is mounted to the face of the headstock and is also plenum fed. The exhaust seal tube is 35.6 cm long with an axial sliding

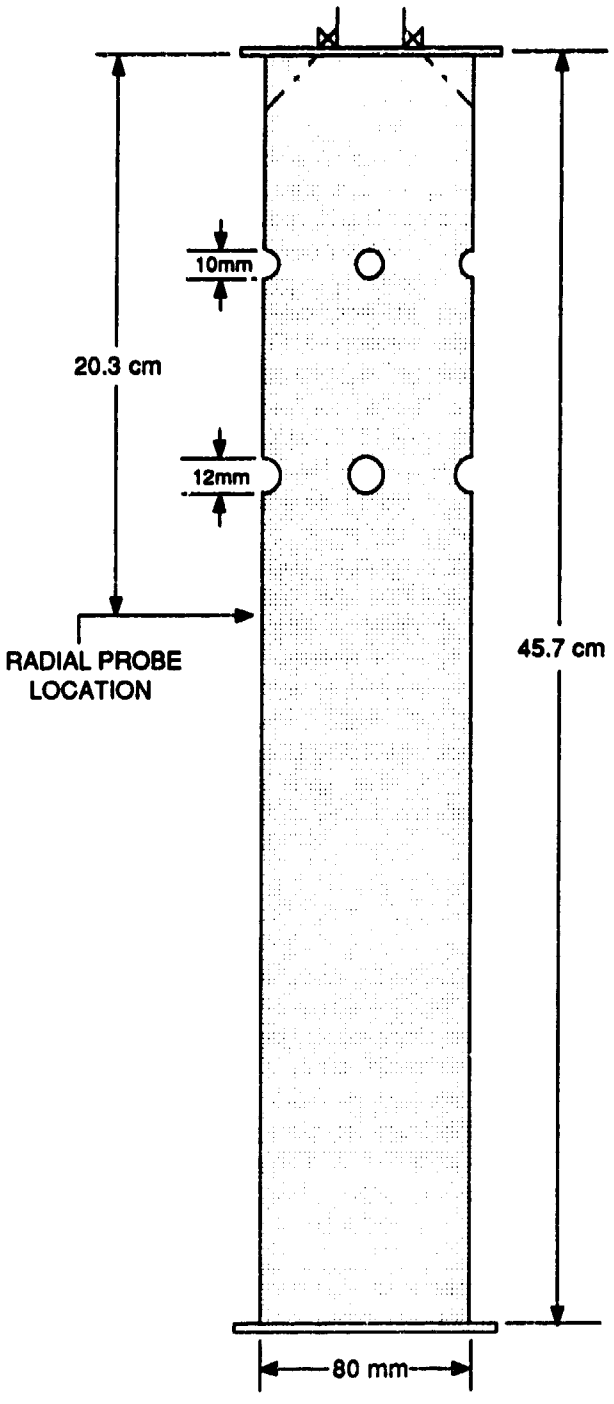

Figure 4: Model Combustor

seal mounted on its outside. The exit of the seal tube is 81.3 cm from the injector plane.

The combustor is ignited using a permanently-mounted hydrogen torch ignitor located just upstream of the aerodynamic swirler. The torch flame is ignited by an electric spark, passes through the swirler with the plenum air, and contacts the outer edge of the liquid fuel spray.

The dome assembly is flexible and is varied to meet the needs of the experiment. The aerodynamic swirler in the present application has 60° flat swirl vanes with an inner diameter of 27.5 mm and an outer diameter of 36.6 mm. The theoretical swirl number for the swirler is 1.57. The expansion from the outside diameter of the swirler to the combustor duct diameter is achieved with a stainless steel quarl at an angle of 45°. The air flow partitioning within this combustor geometry is determined from pressure drop measurements at atmospheric pressure. The flow splits for the swirler, primary jets and dilution jets are 1:1:2 excluding wall cooling air. This partitioning of air within the combustor results in a near stoichiometric overall primary zone equivalence ratio.

3.2 Atomizers

The facility is designed to incorporate several different atomizers ranging from practical air blast to research air assist. To provide the wide fuel flow range and controlled atomizer characteristics required for the present study, a twin-fluid, air-assist atomizer was employed with two different inserts. This atomizer, shown in Figure 5, was developed by Parker Hannifin and produces a high degree of symmetry and reproducibility for inter-laboratory comparison.

The core of the atomizer is an externally mixing, air-assist nozzle, called the Research Simplex Atomizer (RSA). The fuel exits from a centrally located simplex atomizer tip and is contacted by swirling atomizing air. The swirl of the atomizing air and the combustor aerodynamic swirler are co-swirling. The simplex tip of the RSA is interchangeable to vary liquid flow rate range, droplet diameter, and spray cone angle. The difference between the low and high flow rate configurations lies only in the simplex tip (i.e., the atomizer geometry and nozzle air swirler remain constant). The two simplex tips have Flow Numbers (FN) of 1.35 and 4.57 $[(lb/hr)/(psi)^{0.5}]$ and produce nominally 30 micron droplets as measured by the laser diffraction technique at a fuel pressure drop of 687 kPa (100 psid). While the RSA is not a production industrial gas turbine atomizer, the atomizer displays many of the features of practical gas turbine atomizers such as (1) a pressure atomizing simplex tip and (2) air injection to aid in the formation of a fine fuel spray.

3.3 In-Situ Species Measurement

The combustor is fitted with emissions probes in two locations, a traversable radial probe at an L/H of 2.66 and an exit plane probe at an L/H of 10.16. The traversable probe can be fitted into ports on the combustor that are between the dilution jets or directly in line with the dilution jets. The traversable probe is constructed of 9.5 mm stainless steel outer tube and features closed circuit water cooling. Axial seals are used at both the junction of the probe into the

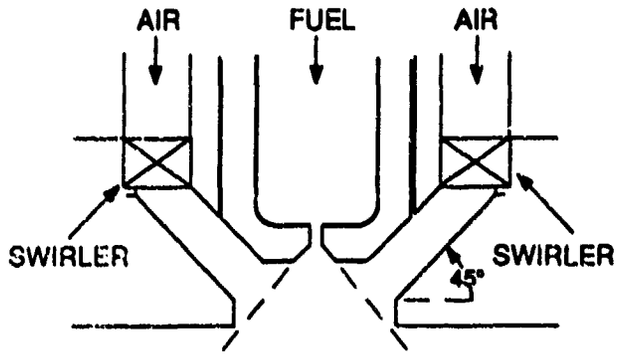

Figure 5: Research Simplex Atomizer

combustor and where the probe passes through the pressure vessel wall. A stepper motor is used to drive the probe along its traverse. The exit plane emissions probe is constructed from a 12.7 mm stainless steel tube that is mounted perpendicular to the exhaust flow of the vertically down-fired combustor. Three small holes are located along the length of the exit plane emissions probe. This arrangement provides an area-weighted average of the total combustor emissions. Liquid cooling for the exit plane emissions probe is supplied through the base of the probe and exits into the exhaust system from a small orifice at its end. While the use of intrusive emissions probes can pose a flow perturbation problem, the probe diameters were reduced to an extent which minimizes flow perturbations while maximizing probe lifetime.

The emissions sample is retained in a heated state to prevent hydrocarbon and water condensation. Particulate is removed using in-line filters and a meter valve controls sample the flow rate at high test pressures. The sample then passes through a heated sample line to either an emissions console or a hot Flame Ionization Detector (FID). The emissions console consists of a chemiluminescent NO_x analyzer and separate instruments to measure the concentrations of CO, CO_2, and O_2. The hot FID is used to determine the number of carbon atoms in CH bonds that are present in the emissions sample.

Note that optical diagnostics are not included in this study. While optical measurements have been made and reported under non-reacting conditions (Ref. 13), attention is directed here to exhaust measurements (to assess overall performance and utility of the facility), and in-situ extractive probe measurements (to assess the utility and value of in-situ measurements). Optical measurements, while valuable, need to be applied under select conditions of particular interest. One objective of this study is to establish conditions for conducting the relatively complex and time-intensive optical measurements.

3.4 Test Conditions

The operating conditions investigated in this study were conducted at a constant equivalence ratio of 0.3 and a nozzle air-to-liquid ratio (ALR) of one. The combustor was fired with liquid Jet-A fuel. Variations in reference velocity, air preheat temperature, and combustor pressure were explored. Three reference velocities were considered (10, 15 and 20 m/s) to provide a variation in combustor residence time and pressure drop across orifices in the combustor. (Residence velocity is defined here at the combustor inlet density, ρ_3, and the combustor cross-section area, A_c). Air preheat temperatures of 204°C, 315°C, and 427°C were evaluated to provide data from the absence of air preheat to conditions approaching the regime of practical gas turbine combustor inlet temperatures at cruise. Combustor pressures tested were 2, 4, 5, 6, 8 and 10 atm. The test matrix for this first demonstration did not include all possible combinations of these operating conditions to (1) preclude the possibility of combustor damage from exceedingly high combustor wall temperatures, and (2) ensure minimum heater air flow rates.

4. RESULTS

4.1 Facility

The facility operated as designed. While many minor hurdles had to be surmounted during the initial operation and shake-down, no major or unexpected challenges were encountered. Operation over hours of testing time became routine. The following section presents results from the evaluation study to illustrate the type and utility of data that can be acquired from in-situ measurements under practical operating conditions.

4.2 Combustor

The combustor exhibited stable operation over the range of operating conditions adopted for the evaluation study. Emissions data were acquired with both the traversable radial emissions probe and the exit plane probe.

4.2.1 Exhaust Measurements

The combustion efficiency was high at air preheat levels representative of most practical gas turbines (e.g., 260°C). For all cases at and above this temperature, the combustion efficiency exceeded 99.9%.

The effect of operating conditions on NO_x exit plane emissions is shown in Figure 6. NO_x emissions increase with increasing inlet air temperature and air

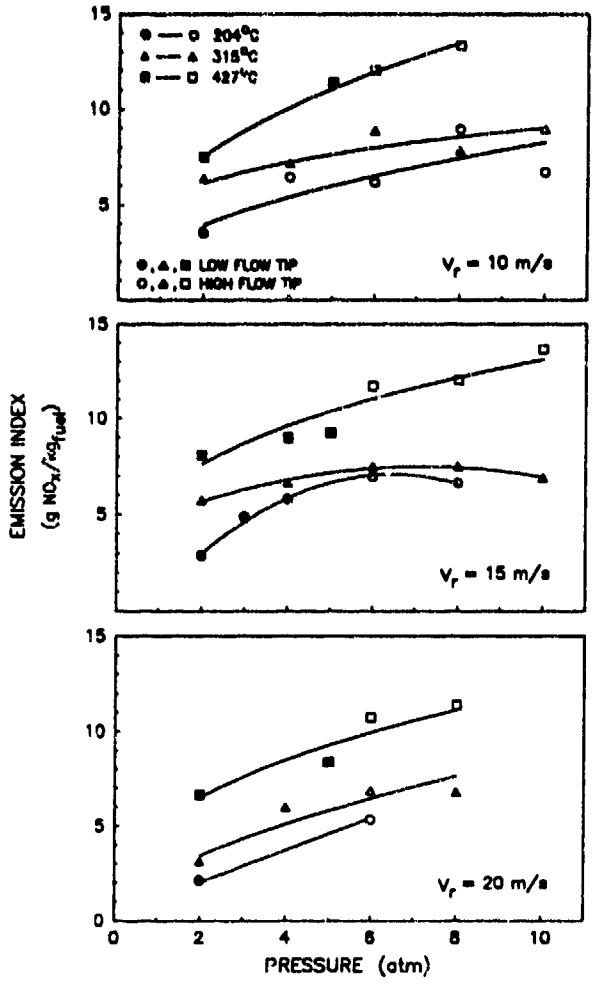

Figure 6: Exit Plane NO_x Emissions

pressure, and with decreasing combustor relative velocity. While the inlet air temperature has a strong effect on NO_x emission, the effect of increased combustor pressure is less pronounced. The NO_x concentration (210 ppm; EI of 13.5 gNO_x/kg_{fuel}) at the highest inlet temperature and pressure considered (800°F, 10 atm and 15 m/s) is approximately the same as reported by Lefebvre (1983, Ref. 15) in practical hardware at similar operating conditions.

The effect of residence time is clarified in the plot of Figure 7 where the data are presented for one inlet temperature. An increase in relative velocity has two effects: (1) A reduction in residence time and an associated decrease in the production of NO_x, and (2) an increase in the pressure drop across the combustor liner and corresponding increase in mixing effectiveness within the combustor.

4.2.2 In-Situ Measurements

Figure 8 illustrates in-situ data for O_2, CO, HC and NO_x for representative traverses from the radial emissions probe. The data, collected in this case

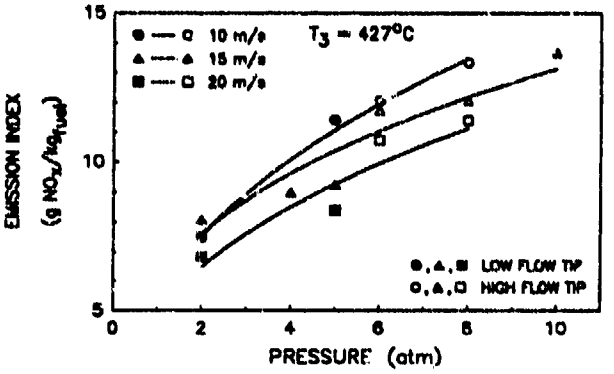

Figure 7: Effect of Relative Velocity.

along a radius bisecting the dilution jets, reveal that the jets penetrate to the centerline. Oxygen concentrations, for example, are high along the centerline, and concentrations of NO_x, CO and HC are relatively low due, in part, to the dilution of the jets. The effluent from the dome is forced between the jets as reflected by the elevated concentrations of HC and CO (at the low air preheat temperature) and NO_x (at both air preheat temperatures). At the higher air preheat temperature, CO and HC are effectively oxidized and NO_x, as expected, increases. Note that this region of the combustor represents the largest mass emission and, as a result, is the least desirable region in which to experience a peak in NO concentration.

5. SUMMARY

The current study describes a novel high pressure facility for the conduct of controlled gas turbine combustion experiments with the capability to obtain in-situ measurements under practical operating conditions using both extractive probes and optical diagnostics. A demonstration study has been conducted to both evaluate the operation of the facility and to illustrate the utility of acquiring in-situ data under controlled conditions. In addition, an example of a model laboratory combustor that is plenum fed, fabricated from state-of-the-art combustor liner materials, and constructed with state-of-the-art liner cooling design has been introduced. The data acquired reveal that:

- The NO_x production from the combustor corresponds to that obtained from practical gas turbine combustors at similar operating conditions. Thus, data can be produced that serve as a baseline comparison to other conventional and advanced gas turbine combustor designs.

- The emissions of NO_x increase with increasing ambient temperature, increasing combustor pressure, and decreased relative velocity.

a) HC, CO, O_2

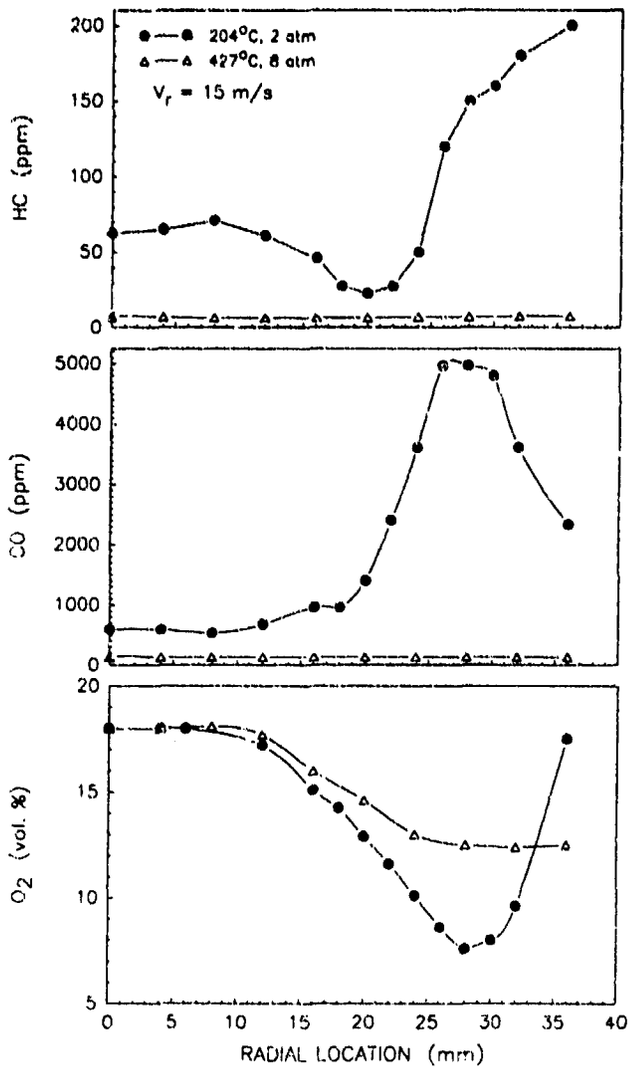

b) NO_x

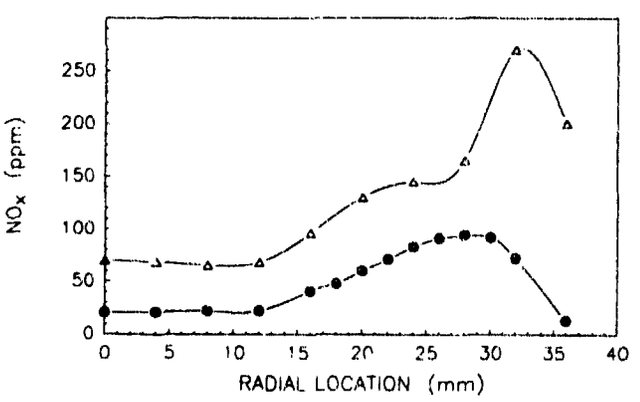

Figure 8: In-Situ Concentrations

- The in-situ measurements provide insights into the aerothermochemistry processes occurring within the combustor. As NOx emissions are lowered by regulatory mandate, an understanding of these processes will be needed. At a minimum, additional in-situ data will be desirable using extractive probes. In addition, optical measurements (and the time resolution, spatial resolution, and absence of perturbation that they offer) appear attractive if not, in fact, necessary under select conditions.

6. ACKNOWLEDGMENTS

This research was supported by the Air Force Services Center, Environics Division, Contract #FO8635-90-C-0100. The facilities described here also received significant support from NASA (Contract #NAG3-1124) and the Northrop Corporation (Contract #HHH451427). The authors would like to express their appreciation as well to Howard Crum, Robert Brady, Massie Hatch and John Kroll for their major contributions to both the design and fabrication of the facility. The efforts of Tom Fang and Matt Miyasato in the design and construction of the emissions system are appreciated. The provision of an atomizer by Parker Hannifin is gratefully acknowledged.

REFERENCES

1. Strack, W.C., and Morris, S.J., "The Challenges and Opportunities of Supersonic Transport Propulsion Technology", 1988, AIAA Paper No. 88-2985.

2. Shaw, R.J., "Engine Technology Challenges for a 21st Century High Speed Civil Transport", NASA TM 104363, presented at the AIAA Tenth International Symposium on Air Breathing Engines, 1991.

3. Zeldovich, J., *Acta Physiochim.* U.R.S.S. *21*, 577, (1946).

4. Samuelsen, G.S., "The Combustion Aspects of Air Pollution", *Advances in Environmental Science and Technology*, Wiley, 1975, pp. 219-322.

5. Rizk, N.K., and Mongia, H.C., "Gas Turbine Combustor Design Methodology", 1986, AIAA Paper No. 86-1531.

6. Burrus, D.L., "Application of Numerical Models for Predictions of Gas Turbine Combustor Performance", Paper presented at the 33rd ASME/IGTI Turbo Expo, Toronto, Canada, ASME Paper 89-GT-251.

7. Charles, R.E., and Samuelsen, G.S., "An Experimental Data Base for Computational Fluid Dynamics of Combustors", *Journal of Engineering for Gas Turbines and Power*, *11*, 1, 1989, pp. 11-14.

8. McDonell, V.G., and Samuelsen, G.S., "Effect of Fuel Injection Mode on Fuel Vapor in Reacting and Non-Reacting Methanol Spays", *Twenty-Fourth Symposium (International) on Combustion*, The Combustion Institute, 1992, pp. 1557-1564.

9. Wang, H.Y, McDonell, V.G., Sowa, W.A., and Samuelsen, G.S., "The Effect of Scale on Droplet Dispersion in the Dome Region of a Gas Turbine Counter-Swirling Combustor Swirl Cup", *Journal of Engineering for Gas Turbines and Power*, in press, 1992.

10. Tolpadi, A.K., Burrus, D.L., and Lawson, R., "Study of Two Phase Flow Downstream of a Gas Turbine Combustor Dome Swirl Cup", submitted for presentation at the 38th International Gas Turbine and Aeroengine Congress and Exposition, 1993.

11. Wang, H.W., McDonell, V.G., and Samuelsen, G.S., "Influence of Hardware Design on the Flow Field Structure and the Patterns of Droplet Dispersion, Part I. Mean Quantities", to be presented at the 38th ASME International Gas Turbine and Aeroengine Congress and Exposition, Cincinnati, 1993.

12. Drennan, S.A., "The Development of a High Pressure Nozzle Characterization Facility with Optical Access", Master's Thesis, UCI Combustion Laboratory Report ARTR-90-7, University of California, Irvine, 1990.

13. Drennan, S.A., Sowa, W.A., and Samuelsen, G.S., "The Effect of Ambient Pressure on the Spray Characteristics of a Twin-Fluid Atomizer", 1990, Paper presented at the 34th ASME/IGTI Turbo Expo, Brussels, Belgium, ASME Paper 90-GT-393.

14. Cameron, C.D., Brouwer, J., and Samuelsen, G.S., "A Model Gas Turbine Combustor with Wall Jets and Optical Access for Turbulent Mixing, Fuel Effects, and Spray Studies", *Twenty-Second Symposium (International) on Combustion*, The Combustion Institute, 1988, pp. 465-474.

15. Lefebvre, A.H., *Gas Turbine Combustion*, McGraw Hill, 1983.

Discussion

Question 1. C. Bruno

1. What was the carbon number of your HC measurements?
2. a) Did you extract a pressure-dependence from the NO_x vs. P, U_{air} data?
   b) Did you see a clear pressure exponent dependence on U_{air}?

Author's Reply

1. The carbon number of the HC measurements is one. The hot flame ionization detector used for the HC measurements was calibrated using propane in nitrogen at a concentration of 152 ppm. The instrument was then set to read three times the propane calibration concentration to account for the number of carbon atoms per propane molecule.

2a The data acquired to date are too sparse to statistically address the pressure exponent. For this reason, pressure exponent data are not presented in the paper. This notwithstanding, we have conducted a cursory analysis to establish a general trend, if any. The data were fitted to the expression:

$$NOx\ [EI] \propto aP^n$$

where a = constant
P = pressure in atm
n = pressure exponent

The majority of the data reveal a pressure power relationship with exponents that range between 0.2 and 0.5. However, some cases reveal pressure exponents as high as 0.86 and as low as 0.13. In addition to affecting the chemistry, the ambient pressure will affect atomization quality and fuel distribution in the dome, and the mixing process within the combustor. This facility offers the opportunity to explore, in the future, these factors in a controlled environment.

2b The data are not yet sufficient to explore for a consistent pressure exponent dependence on U_{air}.

Question 2. Dr Gordon Andrews

Congratulations on the development of a fine high pressure combustion test facility. Your results appear to indicate a NO_x pressure exponent on 0.5 at the highest and well below this for other configurations. Was the NO_x exponent influenced by the change in fuel injector with pressure?

Author's Reply

The NOx pressure exponent was affected by a change in the simplex fuel injector tip. Figure 7 shows this variation quite well at a temperature of 427°C. The cases corresponding to a 15 and 20 m/s reference velocity illustrate an increase in the emission of NO_x when the low flow tip is exchanged with the high flow tip. For the 15 m/s case, the data reveal a NO_x pressure exponent of 0.15 for the low flow tip, 0.29 for the high flow tip, and 0.34 for the overall low and high flow tip data combined. The 20 m/s case has a 0.26 pressure exponent for the low flow tip, 0.20 for the high flow tip and a 0.39 pressure exponent for the combined low and high flow tip data. The change in NO_x emission that results from a change in the simplex tip illustrates that fuel/air mixing in the primary zone can affect the production of NO_x. In addition, the range of pressure dependency for each tip suggests that atomization quality may be a factor (in addition to chemistry, and turbulent mixing) in establishing the dependency of NO_x on combustor pressure.

Question 3. Cliff Moses

What do you consider to be the reason for the effect of reference velocity? Shorter residence time or increased turbulent mixing associated with the higher liner pressure drop?

Author's Reply

While an increase in reference velocity results in a decrease in the residence time that gases are in the thermal NO production regime, the complete mechanism for the effect of reference velocity on NO emission is not clear from the sparse data that have been acquired to date. An increase in the reference velocity increases the liner pressure drop and, as a result, the turbulent mixing which may change the number and lifetime of high temperature pockets of gas which produce excessive quantities of NO. Additional data are required to delineate, in this particular combustor, the relative roles of mixing and residence time on the production of NO_x as reference velocity is increased.

REDUCTION OF NOx BY FUEL-STAGING IN GAS TURBINE ENGINES - A COMMITMENT TO THE FUTURE

I. Segaiman, R. G. McKinney, G. J. Sturgess and L-M. Huang
Pratt & Whitney, M.S. 163-16
400 Main Street
East Hartford, Connecticut 06108 USA

ABSTRACT

As part of an ongoing program of continuous improvement by control of gaseous emissions from the combustors of gas turbines, a unique fuel-staged annular combustor is being developed for application to current and future Pratt & Whitney aircraft engines. The configuration advantages of this combustor are outlined, and discussions are presented on staging considerations and fuel system impacts. Development of the fuel-staged combustor is described by reference to supporting mixing experiments and computational fluid dynamic studies, and rig tests at high pressures. Measured results are given appropriate for the International Aero Engines (IAE) V2500 engine that show progressive reductions in achieved emissions compared to the goals established for this program.

NOMENCLATURE

ADP	Advanced ducted propfan
ASC	Axially-staged combustor
CAS	Coke avoidance system
EI	Emissions index, gm pollutant/kg fuel burned
EPAP	Environmental Protection Agency parameter, the integrated emissions around a defined landing and takeoff cycle, gm pollutant/kN rated thrust
F	Rated thrust, kN
H	Combustor (effective) dome height
K	Kinetic energy of turbulence
L	Combustor (burning) length
OFAR	Combustor overall fuel to air ratio by mass
P, (P3)	Air pressure at combustion section inlet
PHI	Equivalence ratio, FAR divided by that for stoichiometric burning
RBQQLB	Rich burn, quick quench, lean burn combustor configuration
SFC	Specific fuel consumption
SN	SAE smoke number
T, (T3)	Air temperature at combustion section inlet
W, (WAB)	Combustor total airflow
$\dot{m}_f$	Fuel mass flow rate
t	Time in operating mode for EPAP calculation
ε	Dissipation rate of kinetic energy of turbulence
ΔT	Temperature rise across combustor

1. INTRODUCTION

Public and Governmental concerns over the environment have again become matters of often-vigorous discussion throughout the world, and especially so in Europe. Of particular interest is the direction and magnitude of possible climatic changes (Ref. 1) through acceleration of global warming, and ozone depletion, due to man-made pollutants being introduced into the upper atmosphere. Although aircraft operations are currently only small contributors to the overall annual emission of pollutants, aircraft are a direct source of these pollutants in the upper atmosphere. There is speculation that persistent local concentrations of pollutants introduced by aircraft can exist along heavily-travelled air corridors such as the Western Approaches to Europe, North-South routes along the Eastern seaboard of the United States, and U.S. East-West transcontinental routes. If these concerns are justified, the growth of air operations can only exacerbate the problem (Ref. 2).

The gaseous pollutants from aircraft operations that are of concern are unburned hydrocarbons (UHC), carbon monoxide (CO), carbon dioxide (CO_2), water vapor, and oxides of nitrogen (NOx); particulate matter in the form of soot is also important. Carbon dioxide and water vapor are the products of complete combustion of hydrocarbon fuels in air. Combustion inefficiencies produce UHC (mostly methane but with traces of many hydrocarbons including odorants), CO, and soot particles; the ratio of UHC to CO is usually much less than unity. The oxides of nitrogen (mostly nitric oxide {NO} with a few percent of nitrogen peroxide {NO_2} together with a little nitrous oxide {N_2O} and nitrogen tetroxide {N_2O_4}) appear from two causes: from so-called "prompt NOx" where in fuel-rich regions of the combustor fuel fragments react preferentially with atmospheric nitrogen to form cyanogen, which is subsequently reacted via the radical pool to NO via NH_2, and, from direct thermal fixation of atmospheric nitrogen due to the high temperatures present in the combustor. For total levels typical of current engines, the majority of the NOx is NO produced by thermal fixation. Nitric oxide produced in the combustion process is oxidized in the presence of excess oxygen relatively slowly to NO_2 in the lower temperature exhaust plume. Nitrogen tetroxide appears to exist in equilibrium with NO_2.

Since temperature is a major driving force in the production of all of these pollutants, the proportions of the constituents in the exhaust vary in general, according to the power setting of the engine. Thus, most of the UHC and CO are produced at low temperature, low power operation; and most of the NOx and soot are produced at high temperature, high power operation.

The effect on the atmosphere of the pollutants depends strongly on altitude, and three atmospheric bands have to be considered: sea level, the troposphere, and the stratosphere.

At sea level and in the lower atmosphere, the CO, UHC and NOx can contribute to photochemical smog. NOx can result in damage to plant life, as well as add to the acid rain problem to a limited extent. N_2O_4 is very poisonous. It and N_2O are brown-colored gases that can give the engine exhaust plume a characteristic brownish tinge when their concentrations are sufficiently high and the level of soot is low. The soot particles are not pure carbon but are actually fibrous conglomerates of carbon and partially-reacted fuel fragments. They are extremely small and, therefore, do not settle out from the air very readily. The number density of these particles is very large, although the mass involved is not high. These are all mostly local effects that are confined to airport environs.

At altitude, the particulate matter and water vapor can result in local modifications to cloud cover (Ref. 3), with possible long-term effect on the Earth's albedo. The soot particles may also serve as condensation nuclei and active sites for other atmospheric chemistry - both good and bad. Carbon dioxide,

Presented at an AGARD Meeting on 'Fuels and Combustion Technology for Advanced Aircraft Engines', May 1993.

methane, water vapor and nitrous oxide are all greenhouse gases that can contribute to atmospheric warming trends by trapping infrared radiation from the Earth. Carbon monoxide is not a greenhouse gas, but reduces presence of the hydroxl radial (OH), which in turn tends to harm the self-cleansing capability in the troposphere through minimizing the action of OH in removing ozone, which is a greenhouse gas. In the troposphere, NO can create ozone, thus adding to the greenhouse effect (Ref. 4).

In the stratosphere under the influence of ultraviolet radiation from the sun, photo-dissociation and photolysis of ozone and water vapor can produce OH. NO and OH can destroy atmospheric ozone by catalytic scavenging, which is an extremely efficient process.

European airlines appear to be especially aware of environmental pressures (Ref. 5) from their communities. In their desire to be "good neighbors," these airlines wish to do something, and are requesting the assistance of the engine manufacturers for both near-term but worthwhile emissions reductions, and more substantial reductions for the longer term. The regulatory agencies, such as the U.S. Environmental Protection Agency (EPA), are reviewing existing legislation in light of the long-term effects of atmospheric pollution. For the first time, consideration is being given to requirements for reduction of emissions generated at aircraft cruising altitudes, in addition to tightening up the permissible levels around the landing and takeoff cycle presently covered by existing International Civil Aviation Organization (ICAO) regulations for aircraft (Ref. 6). Government research agencies like the U.S. National Aeronautics and Space Administration (NASA) are beginning to undertake studies and active programs on all aspects of atmospheric pollution by aircraft (Refs. 7,8).

There are many unresolved questions concerned with the detailed effects of atmospheric pollutants on the atmosphere, how to make emissions measurements at altitude and how to scale those measurements to other conditions, and mechanisms whereby engines actually produce emissions at altitude. Despite these unknowns and although the direct correspondences of aircraft emissions with climate and health are not precise, the engine manufacturers are responding positively to the concerns and needs of their customers, and are also cooperating actively with the various government agencies.

The engine manufacturers recognize the social responsibility incumbent upon the airline industry, and in consequence have committed to programs of long-term research and development effort to achieve continuous improvement in emissions reduction. They also understand that emissions reductions cannot be achieved at the expense of deteriorations in engine reliability, safety, repairability, overhaul lives or direct operating costs.

2. BACKGROUND

Past efforts at emissions control have resulted in the modern, large, turbofan engine having combustion efficiencies that are in excess of 99 percent at and above idle power levels, and exhaust plumes at takeoff power that are essentially free from visible soot traces.

The improvements in idle power combustion efficiency were achieved in two ways: first, by raising the combustor burning zone equivalence ratio to increase gas temperatures and so enhance chemical reaction rates; and second, by changing the fuel injector liquid spray characteristics to keep unreacted and partially-reacted fuel out of the relatively low temperature film cooling air introduced for combustor liner durability. Incompletely reacted fuel entering the film cooling can be chilled and the composition frozen through to the combustor exit. The smoke problems at high engine power settings were addressed by replacing pressure-atomizing fuel injectors with airblast-atomizing types to take advantage of the superior atomization, better fuel/air mixing and constant spray trajectories offered by these designs. These techniques have proved to be highly successful.

Without a change in fuel type, the only way to produce less CO_2 and water vapor in the engine exhaust is to burn less hydrocarbon fuel. The continuing improvements with time in engine specific fuel consumption that high pressure ratios, high bypass ratios and high turbine inlet temperatures have brought, together with improvements in aircraft efficiency, have resulted in modern transport aircraft on a seat-kilometer basis, only burning about 40 percent of the fuel used by the first Boeing 707 transport that entered transatlantic service in 1958 (Ref. 9). This progress in reduction of fuel burn will continue with the advent of the Advanced Ducted Propfan (ADP) engine which has an ultra-high bypass ratio, gear-driven fan, and similar machines, that can offer another 10 percent or more reduction in specific fuel consumption.

Not only does reduced fuel burn lower direct operating costs to the airlines, it also reduces pollution, i.e., a reduction in ***all*** pollutants - CO_2 and water vapor directly, and CO, UHC and NOx indirectly through the takeoff-landing cycle-integrated parameter,

$$D_p/F_\infty(EPAP) = \frac{\sum_{cycle}(EI \times t \times \dot{m}_f)}{F} \quad gm.\ pollutant/kN\ thrust$$

Unfortunately, those very combustor design features and engine cycles that produce these performance gains and reductions in selected exhaust emissions result in increased operating temperatures in the burning zones of the combustor at all engine power levels. These higher reaction temperatures have tended to elevate the formation rates of NOx. Thus, although the NOx EPAP of the ADP engine can fall due to the favorable influence of SFC, the absolute level of NOx, expressed as an emission index (EI), where,

$$EI = gm\ pollutant/kg\ fuel\ burned$$

can rise due to the increased formation rate. It is apparent, therefore, that the major pollutant of immediate concern to the combustion engineer is NOx.

3. PROGRAM STRATEGY AND GOALS

Pratt & Whitney selected the IAE V2500-A5/D5 engine as the lead vehicle for its emission reduction efforts. The reason for this choice was the relatively small size of the engine (133.4 kN thrust). As the smallest modern turbofan engine with which Pratt & Whitney is associated, the V2500 presented the most severe challenge in terms of available spatial envelope within which modified or redesigned combustors would have to be accommodated. The technology resulting from the program could then be readily applied to other, larger engines, as appropriate.

Pratt & Whitney decided upon a three-phase program plan with continuing reductions in NOx. By these means, the airline customers could select a suitable level of NOx reduction for compliance with regulations, and demonstrate progressive improvements to the environmental groups.

The different phases of the program were delineated by the technology level and degree of engine modification required. Phase I was defined as representing a conventional combustor with modest modifications for which the technology was in hand. Phase II was defined as a significantly modified combustor design for which technology development would be necessary. Phase III was defined as a combustor having significant

departures from conventional design for which both research and technology development would be required.

The goals and schedule for the program were established as shown below:

Table 1
Program Goals and Schedule

Phase	Delta NOx EPAP (%)	Thrust (kN)	Date (Month/Year)
I	-15	133.4 (A5)	12/92
	-30	111.2 (A5)	12/92
II	-40	133.4 (A5)	12/95
III	-70	133.4 (A5)	+2000

The delta NOx EPAPs in the table are relative to the conventional V2500 combustor in the -A1 model of the engine. The Phase I goals quoted at two levels represent the -A5 model cycle operated at its rated thrust and at the -A1 model lower thrust level.

4. NOx REDUCTION STRATEGIES

Starting in November 1989 and using technology that was already in hand, a Phase I combustor was quickly produced, developed and certified. Figure 1 illustrates the emissions reductions achieved by the Phase I modifications to the combustor. It shows that the predetermined goals were, in fact, met.

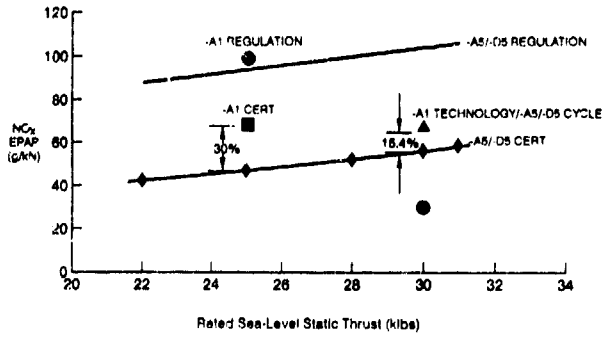

Fig. 1 Nox Status in V2500-A5/-D5 Engine, Showing Phase I Improvements

The Phase I success did not come at the expense of CO, UHC or smoke emissions, all of which remain at extremely low levels. The combustor durability and stability were not adversely affected, and pattern factors and radial temperature profiles are acceptable to the turbine. The Phase I technology is described in Reference 10; it relies on an axial adjustment of the stoichiometry distribution along the combustor to simulate some aspects of fuel staging. The -A5 Phase I combustor is also a candidate for retrofit into the existing fleet of -A1 engines.

Emission control strategies have been reviewed by Lefebvre (Ref. 11), and a summary of an earlier generation of low emissions hardware is provided in Reference 12. Given the success of quasi-fuel staging (Ref. 10) in Phase I and Pratt & Whitney's previous true fuel staging experience, it was natural to continue to exploit the advantages of fuel staging (Ref. 11) for the Phase II approach. The actual selection process used at Pratt & Whitney involved a rigorous screening effort that investigated candidate concepts and configurations using an analytic method and numerical scoring system.

The intent of the Phase II effort was decided as implementation of true fuel staging by means of separately-controlled fuel supplies to distinct initial and secondary burning zones. Geometric modifications to the combustor would be only those necessary to accommodate the two stages. Other than staging, no additional technology change was planned for the initial Phase II combustor.

In anticipation of Phase III, research is being pursued into the logical extension of the Phase I approach. As implemented in Phase I, the quasi-fuel staging approach, which is really a rich burn, quick quench, lean burn (RBQQLB) system, is constrained by the limitations of introducing it in a conventional combustor format. For example, in Phase I the rich initial burning zone has near-stoichiometric interfaces with conventional liner film cooling air that result in high local NOx formation rates, and the conventional dilution zone does not provide either an effective quick-quench or a well-mixed lean secondary burning zone, both shortcomings again resulting in higher than possible NOx. For Phase III in the year 2000+ time-frame, the rich initial burning zone can be designed with allowance for anticipated developments in materials science and fuel injector design. The anticipated advancements in these areas will result in avoidance of stoichiometric interfaces in the initial burning zone, and will allow it to operate much richer without the production of excess smoke. Similarly, the shape of the combustor can be altered to produce a much-improved quick-quench section. Finally, advances in fuel/air mixing capability should result in a well-mixed lean secondary burning zone. Together, these changes result in a level of technology that should allow the RBQQLB concept to reach its full potential of NOx reduction.

5. HISTORICAL PERSPECTIVE ON FUEL-STAGING

As an emissions reduction approach, fuel-staging has much to commend it (Ref. 11). Fuel-staged combustors had their origin in the NASA Experimental Clean Combustor Program (ECCP) (Ref. 13) that was initiated in the early 1970s to address initial concerns with atmospheric pollution and the anticipated EPA regulations for aircraft engines.

As part of the ECCP effort, Pratt & Whitney designed and rig-evaluated staged combustors in can form for the JT8D engine and in annular form for the JT9D engine. Two annular configurations were considered for the JT9D engine. These were a diffusion flame, swirl-stabilized design called the Vorbix (Ref. 14), and a partially-premixed, perforated plate flameholder design. In all of these designs except for the latter, the two combustion zones were arranged in series. The stages in the partially-premixed, perforated plate flameholder combustor were in a staggered in-line arrangement, necessary to accommodate the flameholder for the main stage (secondary burning zone). Figure 2 shows the arrangement of this combustor. The annular configurations were actually engine-tested, the Vorbix in an experimental JT9D-7 and the perforated plate configuration in an experimental "10-tonne" engine, as well as the experimental JT9D.

An additional axially fuel-staged annular combustor, with a single-sided, carburetor tube main stage, was designed and rig-tested for the NASA Energy Efficient Engine (E^3) program (Ref. 15).

Table 2 lists the emissions reductions achieved by the fuel-staged, partially-premixed, perforated plate flameholder and the Vorbix combustors in the experimental JT9D-7A engine. The results are expressed as a percentage of the unmodified engine emissions for the EPA (earlier definition) EPAPs (Ref. 16).

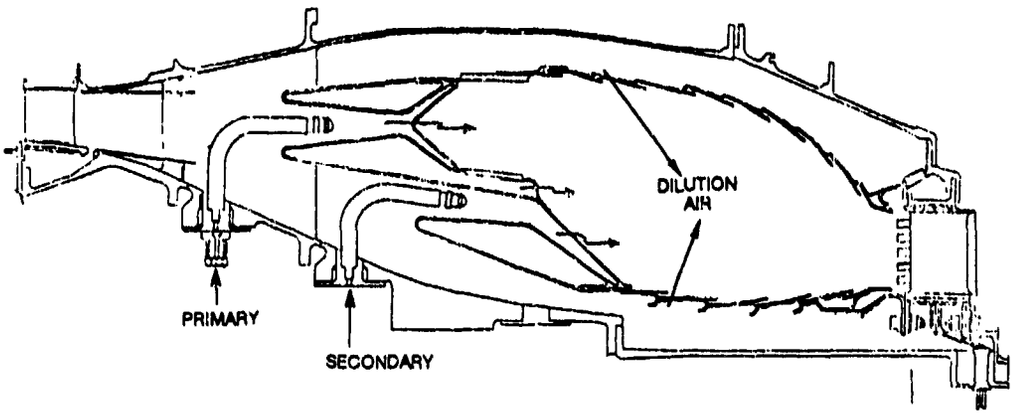

Fig. 2 Partially-Premixed, Perforated Plate Flameholder, Fuel-Staged Combustor for Experimental JT9D Engine, Showing Staggered Inline Stages

Table 2
Emissions Reduction Demonstrated in Early Fuel-Staging Tests

	Delta NOx EPAP (%)	Delta CO EPAP (%)	Delta UHC EPAP (%)	Delta Smoke SAE 1179 (%)
Partially-premixed (Ref. 17)	-53.8	-65.7	-84.2	-75.0
Vorbix (Ref. 18)	-58.5	-76.6	-95.8	+high

Comparison of this table with the present program goals (Table 1) indicates the potential of fuel-staging for satisfying the Phase II aims.

The original fuel-staged combustors, although showing great promise in reducing emissions, had a large number of operational difficulties that would have required a tremendous development effort to eliminate. However, the major drawback that precluded further exploitation at that time was the need to control the staging not just along an engine sea level power curve, but over the complete array of all power settings, all flight altitudes and all aircraft flight speeds, i.e., continuous control over the complete engine operating spectrum. The hydromechanical fuel controllers of that time were just not adequate for this complex additional task. For this and other reasons, less stringent emissions regulations were adopted by the EPA and ICAO.

Staging did not really become viable until the advent of the Full Authority Digital Electronic Control (FADEC) with its on-board computer capability and capacity. Once a solution to the control difficulties was available, fuel-staging made its reappearance in high temperature rise combustors for military application (Refs. 19,20). The purpose in this instance was to control exhaust smoke through limiting primary burning zone equivalence ratio, as Figure 3 illustrates.

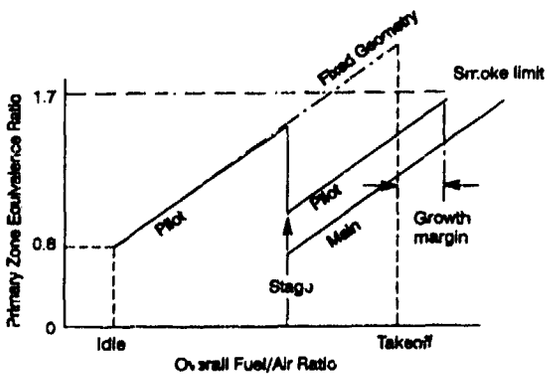

Fig. 3 Comparison of Operation of Conventional and Fuel-Staged Combustor Primary/Pilot Zones

6. STAGING AND STAGE ARRANGEMENT

The concept of fuel staging divides the total engine fuel flow into two parts and supplies the divided flows separately to two distinct combustion zones. One combustion zone is fueled continuously, and provides engine starting and idling, and basic combustion stability. In this capacity, it serves as a pilot stage combustor. To provide these functions, the design of the pilot stage is entirely conventional. In order to achieve acceptable CO and UHC emissions at idle power, the combustion efficiency has to be in excess of 99 percent. It has been demonstrated (Ref. 21) for typical primary zones at engine idle conditions that an equivalence ratio of about 0.8 is necessary to satisfy this efficiency level. The pilot stage fuel flow is a small portion of the total. Therefore, although the conventional pilot can then result in high NOx formation rates, its contribution to overall NOx is small. The bulk of the engine total fuel flow is burned in the second combustion zone. This being so, this zone serves as a main stage combustor. The main stage is only fueled at higher power points, and is generally designed to operate lean at full power, as indicated in Figure 3.

The low NOx characteristics of a fuel-staged combustor are derived from two features of the approach. First, the bulk of the fuel is burned fuel-lean, and even allowing for unmixedness effects (Ref. 22) this reduces the NOx formation rates. Second, the total fuel flow is divided (albeit unequally) between an increased number (usually twice the number) of fuel injectors. Thus, even though the main stage fuel injectors might be of conventional design, the presentation of the fuel to atomizing/combustion air is improved, thereby increasing both atomization and mixing, and reducing unmixedness. As a result, more of the main stage fuel is burned at the (lean) bulk equivalence ratio and within a narrower band of equivalence ratios about the bulk value (Ref. 23). This tends to minimize exposure to the high temperatures associated with the generation of thermal NOx.

Implementation of fuel-staging in an annular combustor can be made in a number of ways:

a. Circumferentially
b. Radially
c. Axially
d. Combinations of (a) through (c).

Circumferential staging (Ref. 24) can be applied in a conventional looking combustor, to alternate fuel injectors or to circumferential blocks of injectors, for local enrichment. It has two serious problems associated with it. First, severe chilling of chemical reactions can occur at the edges of zones due to interfacing of fueled and unfueled (and hence relatively cool) zones. This chilling can result in production of excess CO and UHC emissions, and possibly serious loss in combustion efficiency at part-power. Second, depending on the circumferential fueling pattern used, the resulting circumferentially nonuniform exit temperature distribution can distort turbine cases, result in loss of turbine efficiency, and cause possible rubbing damage to the turbine outer air seals.

Radial staging consists of two combustor domes displaced radially from each other with a short interface splitter between them, and having a common entry plane so that the combustion zones are radially inline. The arrangement allows the fuel injector tips for both stages to be mounted on a common support, which includes active fuel cooling of the mains stage injectors by the continuously-flowing pilot stage supply. The fuel cooling is necessary to avoid coking of the main stage fuel injectors when they are unfueled but exposed to the hot environment of the operating engine. The common support for the injectors allows just a single penetration plane of the diffuser pressure casing. However, the outer wall of the diffuser case tends to be increased in diameter in order to accommodate the double domes. The radially-staged combustor before staging also suffers from potential sharp peaks in the average radial temperature profile at the combustor exit. These peaks may be severely displaced radially, and further, can shift in radial position after staging. The turbine performance can be adversely affected by such profiles and their shifts, and the potential exists for either outer air seal or first vane platform damage. Although the combustor length/overall annular height ratio (L/H) is small, it is because L is usually close to normal (as it would have to be for retrofit of the combustor to existing engines) while H is larger than normal. For this reason, together with the addition of the splitter between stages, the cooling air requirement for the radially-staged arrangement can be high.

Axial staging has several distinct advantages. Since the main stage is axially inline with, and downstream from, the pilot stage, ignition of the main stage directly from the pilot is both reliable and rapid. The gas flow into the main stage from the pilot stage is always hot and contains active radicals, so that achieving high combustion efficiency from the main stage, even at initially quite low equivalence ratios, is not difficult. Consideration of Figure 3 indicates that this can lead to very low NOx generation from the main stage. This is because the ease of achieving high combustion efficiency allows the equivalence ratio of the main stage at staging to be set well below the minimum desirable 0.8 value required in the pilot. Thus, at takeoff power levels the maximum equivalence ratios in the main stage will be proportionately lower also. The NOx generation is then reduced due to the lower bulk-average flame temperatures, and also because the standard deviations from the bulk equivalence ratio have been shown to be reduced with lower bulk equivalence ratios (Ref. 11). Finally, the average radial temperature profile at exit from the combustor is fairly conventional at all conditions, and does not undergo any significant shifts at staging. Development of exit temperature traverse quality by means of conventional dilution air does not have any special difficulties.

There are three disadvantages to axial staging. First, the inline arrangement of stages tends to result in a somewhat lengthy combustor that might be difficult to accommodate for retrofit of some engines. There is also increased liner surface area, relative to conventional combustors, that needs to be film cooled. Second, the fuel injectors for the stages have to be carried on separate supports. Therefore, two penetration planes of the diffuser case are necessary. A weight penalty is associated with these needs. Third, being as the pilot and main stage fuel flows are introduced into the combustor via separate supports, pilot fuel cannot be conveniently used for cooling the main stage fuel injectors.

The easiest staging concept to implement is circumferential staging, but unfortunately, circumferential staging has the least emissions reduction potential. The best choice between radial and axial staging is not immediately clear since each configuration has both good and bad features that must be traded against one another. In order to achieve a suitable compromise, a configuration might be devised that combines the best features from both radial and axial staging, while minimizing the worst ones.

Pratt & Whitney examined all configurations and decided that the high emissions reduction potential of axial staging was worth preserving, and that the excessive length drawback of axial staging could be avoided. A combined configuration offering these characteristics could be used, and the staggered inline arrangement used for the earlier, staged partially-premixed, perforated-plate flameholder combustor (Figure 2) formed the basis for this.

7. AXIALLY STAGED COMBUSTOR CONFIGURATION

Figure 4 shows a final cross-section of the resulting Axially Staged Combustor (ASC) (Ref. 25); flow is from left to right, with the engine centerline to the bottom of the figure. For clarity, the main stage fuel injectors have been shown rotated half an injector pitch, to be in plane with the pilot stage injectors. Wherever possible, existing hardware and designs were used in order to expedite the path to certification, and to minimize risk. The design complies with the ground rules established for Phase II of the emissions reduction program.

The ASC fits into the existing V2500-A5 engine using a conventional front-pin mounting system, with a new outer diffuser case having appropriate pads to accommodate mounting of the two sets of fuel injectors. The combustor has the benefits of the axially inline stage arrangement without any length penalty. As a result of the stage-staggering, the shroud airflows are a little more complex than for the conventional V2500 combustor (Ref. 10), and there is a small increase in liner surface area to be cooled. The supports for the main stage fuel injectors are short. The fuel injector tip design is similar for both stages, and follows that of the regular airblast-atomizing fuel injector used in the conventional combustor. The short lengths of the main stage combustion and dilution zones are noteworthy, being together about one-half the overall length of the conventional combustor that the ASC replaces.

7.1. Fuel System

Fuel staging results in two fuel delivery schedules that the fuel system must provide. The resulting two fuel streams to be delivered to the combustor cause an increase in the complexity of the fuel system. The Pratt & Whitney approach to insure fuel system reliability and maintainability is to employ proven concepts and components from existing fuel systems wherever possible (Ref. 26).

A schematic diagram of the fuel system (Ref. 27) is displayed in Figure 5. The actual system is a little more complex than that shown, due to various operational considerations, but the salient features are illustrated.

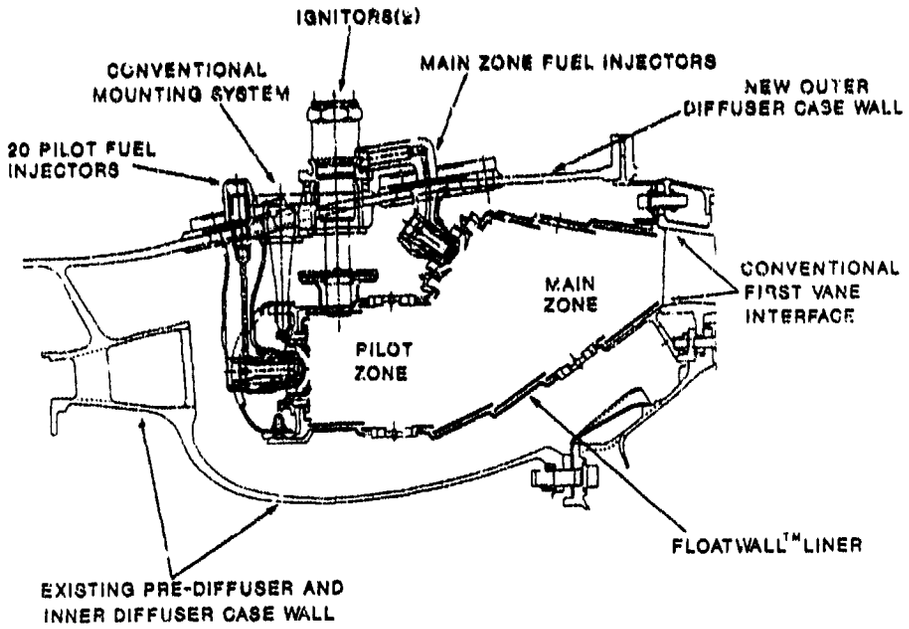

Fig. 4 Longitudinal Cross-Section of ASC in V2500-A5/-D5 Combustion Chamber Envelope

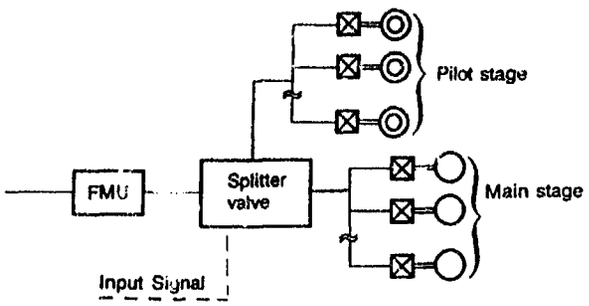

Fig. 5 Flow Diagram of Simplified ASC Fuel System

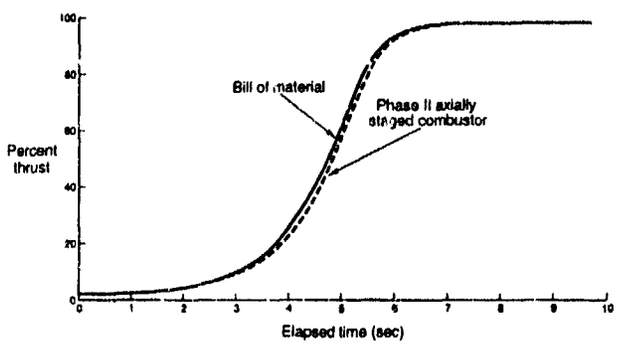

Fig. 6 Dynamic Simulation of Snap Acceleration from Idle to Takeoff for ASC Compared to Conventional Combustor

The fuel metering unit (FMU) delivers the engine total fuel flow demanded by the FADEC. This fuel stream enters a flow splitter valve (FSV) that divides the total flow into pilot and main stage fuel streams according to a signal from the FADEC. Each stream is then delivered to a flow distribution valve (FDV). Before reaching its own FDV, the pilot fuel flow is used to cool the main fuel FDV. This cooling is required by Federal Aviation Administration fire regulations, and also takes care of heat soak-back from the engine. This is necessary because the main FDV will contain stagnant main fuel prior to staging. The FDVs distribute fuel to the fuel injectors via individual manifolds, each one of which feeds a pair of fuel injectors. The main stage fuel injectors and supports are provided with a coke avoidance system (CAS).

Figure 6 presents the predicted transient engine thrust response as the main stage is fueled and the engine is accelerated from idle power to 100 percent sea level thrust. By fueling the main stage at a slightly accelerated rate in order to minimize the time necessary to fill the short individual manifolds feeding the main stage fuel injectors, the time to full thrust is maintained. Only a minor lag of less than 0.1 second is expected in the middle of the transient, but no overall lag.

8. COMBUSTOR DEVELOPMENT APPROACH

For the initial version of the Phase II reduced emissions ASC, a combustor development plan was established. The approach relies on the following major elements prior to the first engine to test (FETT): design studies, a high-pressure sector rig, computational fluid dynamics (CFD) refinement of the preliminary design and sector rig-derived modifications to it, and a high-pressure, full annular rig. Eight experimental engines will be used in the engine certification program, which is scheduled to being in late Spring of 1993 for a December 1995 certification. Figure 7 illustrates the approach in diagrammatic form.

The design portion involved design studies and simple bench-scale experimental testing of projected combustor components, such as fuel injectors and air swirlers. The design portion defined a preliminary combustor design for the sector rig, and suggested a series of parametric optimization tests to be made. The sector rig program was to investigate emissions,

stability and efficiency trade factors. CFD modeling was used in conjunction with the sector rig to explore the optimization processes and to predict the behavior of the full-scale configuration, e.g., circumferential curvature effects, etc. In addition to normal operation, the sector rig was also used in a transient combustion test facility in order to examine the response of the ASC to simulated engine accelerations, including main combustion zone staging operation. The purpose of the annular rig program is to verify performance and emissions levels, assess potential durability, and to develop exit temperature traverse quality.

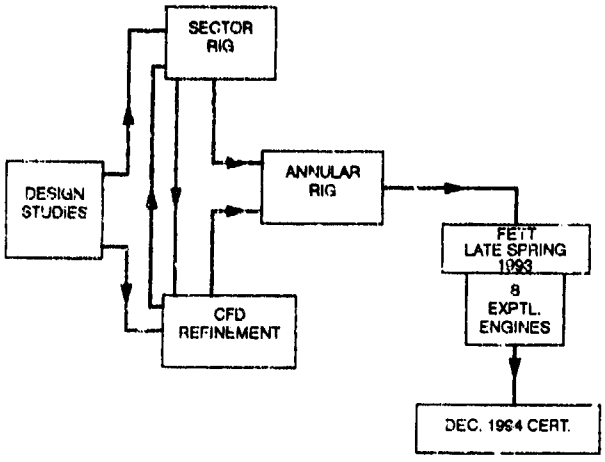

Fig. 7 Diagrammatic Representation of Phase II Effort

The overall objective of the rig program is to provide a combustion system that is optimized and thoroughly evaluated prior to incorporation into an experimental engine (FETT). The experimental engines themselves serve as final demonstrators of intended performance and emissions, and then permit concentration on developing the reliability, durability and operability of the combustion subsystem as part of the overall engine system.

8.1. Test Rigs and Facilities

The majority of the experimental results to be presented below are taken from the sector rig portion of the overall development program. The sector rig was modified from an existing V2500-A1 conventional combustor sector rig. It now contains a combustor that is actually a planar representation of the ASC, encompassing three or four pilot stage fuel injectors and main stage fuel injectors (depending on the arrangement of stages, i.e., inline or staggered), together with their associated aerodynamic packages, i.e., it is one-fifth of the full annular combustor. The main stage injectors are generally transversely displaced one-half a pilot injector spacing, relative to the pilot injectors. The resulting flow path very closely matches the true annular configuration with respect to both pilot and main stage lengths and volumes. The combustor itself was designed to permit rapid configuration changes. The side-walls are cooled by air introduced through seven vertical rows of small, angled holes. The combustor is effusion cooled in a similar manner. The two fuel injection bulkheads are provided with impingement-cooled heat shields. A number of axial stiffening ribs are welded to the combustor liner outer surfaces.

The rig inlet contains flow conditioners and a simulated prediffuser and dump, similar to those shown in Figure 4, to provide a representative inlet boundary condition. It was expedient to use existing fuel injectors and supports, without modification, for both stages. In order to accommodate these fuel injector supports, it was necessary to introduce the pilot stage and main stage fuel supplies from opposite sides of the rig. Therefore, accurate simulation of the shrouds and shroud flows feeding the combustor could not be made. The combustor exit boundary condition is provided by 12 exit guide vanes.

To provide information at the combustor exit, each of the exit guide vanes is instrumented with seven, equally-spaced, sampling probes for gas temperature and emissions measurements (there are two separate vane packs), although readings from only the center eight vanes are used to provide data. The sampling probe inlets are inline with the combustor exit. For emissions measurements, samples from these eight center vanes are manifolded together prior to passing the collected sample to the emissions analyzers (according to SAE Aerospace Recommended Practices 1179 and 1256). To measure inlet conditions at the prediffuser inlet, two 5-headed total pressure rakes and two thermocouples are provided, together with four static pressure taps (two per wall). Twenty-two static pressure taps are distributed in the shrouds, together with four static pressure taps in the dome, to provide pressure drops across the combustor. Two thermocouples are mounted on each of the inner and outer combustor liners to monitor wall temperatures.

The sector rig was tested for steady-state operation in the Pratt & Whitney High Pressure Combustion Laboratory (HPCL). The HPCL uses an FT-4 drive-engine for compressors, and a gas-fired indirect heater to deliver nonvitiated high-pressure air to several test cells. Typical high power test conditions for this program are as follows: inlet pressure 32.2 bar, inlet temperature 854K, and total airflow 11.9 kg/sec; however, the sector rig was normally operated at pressures between 5 and 18 bar, with emissions optimization being done in this range for operational convenience.

It is particularly important that the fuel-staging system operate without introducing any significant lags in the engine thrust response. Transient operation of the ASC was therefore investigated by installing the sector rig in the United Technologies Research Center Transient Combustion Facility (TCF) (Ref. 28). In the TCF the flow delivery system can simulated by means of hydraulically actuated pintle valves, varying pressure, temperature and airflow rates encountered during engine accelerations. The correct parameter time constants can be reproduced (Ref. 28).

The annular rig contains a full-scale annular ASC with a flow path that is similar in cross-section to the view shown in Figure 4. The liner construction is that to be used in the engine tests. The inlet to the rig includes transitional spool-pieces to allow boundary layer flow development to simulate the velocity profile present at the engine compressor exit. The exit transition and measurement section permits measurements to be made of temperature and emissions at the combustor exit plane by means of a rotating, multi-headed, gas-sampling or thermocouple probe-head; both heads may be installed (off-set) simultaneously if desired. Internal instrumentation is similar in character to that of the sector rig Testing in the HPCL is conducted up to correct V2500-A5 engine takeoff power conditions.

Figure 8 shows a pilot dome and outer liner of a full annular, experimental ASC. The liner is of Floatwall™ construction, where individual cast panels are bolted to a support shell to make up the hot-side surface. Figure 9 shows the fully-assembled annular rig itself, ready for installation in the test facility.

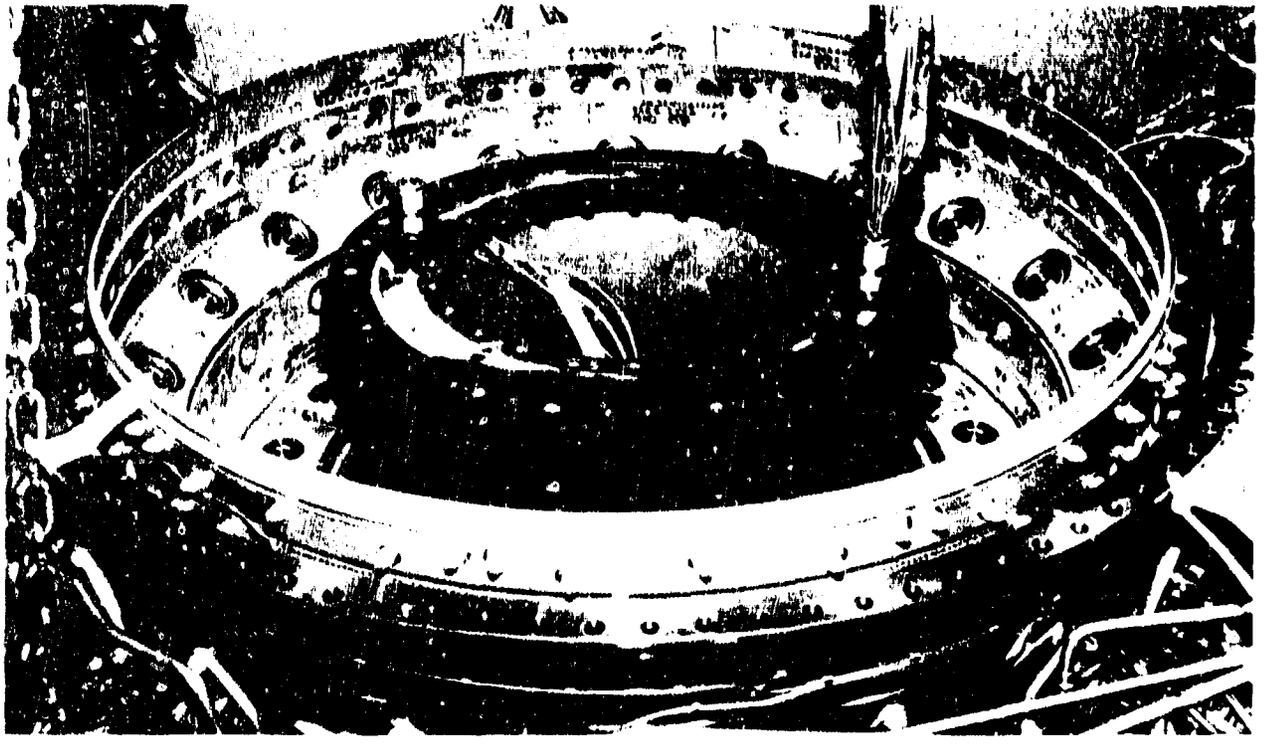

Fig. 8 Outer Liner, Dome and Hood of ASC for the Annular Rig

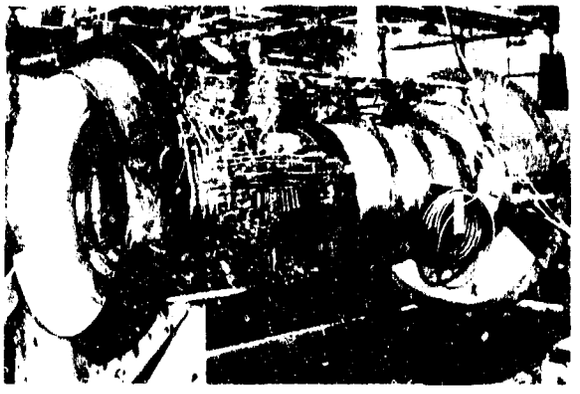

Fig. 9 Annular Rig Ready for Mounting in Test Facility

9. COMBUSTOR REFINEMENT BY CFD

CFD analysis of the ASC was conducted in support of the rig program using the NASTAR (Navier-Stokes Analysis for Arbitrary Regimes) computer code described by Rhie & Stowers (Ref. 29). The code solves the steady-state Favre-averaged Navier-Stokes equations, written in general curvilinear coordinates, on a body-fitted, three-dimensional grid. Eddy viscosity is provided by the familiar K-ε turbulence model (Ref. 30). The version of the code used in these studies incorporated the infinitely-fast chemistry assumption of the eddy breakup combustion model (Ref. 31).

With the limitations of the eddy breakup combustion model, the NASTAR code cannot be used directly to estimate emissions. The major tasks of the CFD analyses were to study the effects on combustor gas temperature distributions of the alignment of the pilot and main stage fuel injectors, examine the interaction of the pilot stage air jets with the pilot flow, assess the best circumferential location for air addition in the main stage, and determine the effects of lack of lateral curvature in the planar sector rig. The prime objectives of these refinements were to provide configurations for rig test that minimized NOx production while preserving low CO, maintained the quality of the exit temperature distribution, and avoided hot-spots on the combustor liners.

To achieve the first of these prime objectives, it was assumed that the majority of NOx production in the ASC would be due to thermally-generated NO. It then follows that minimizing exposure of the working fluid to excessive flame temperatures will result in reduced thermal NO. Post-processing of a conventional CFD solution for a combustor, for the number and volumes of gas pockets above and below the respective critical temperatures (>2033K and <1810K), for excess NO and CO formation (Ref. 23), enables the emissions characteristics to be determined.

The secondary objective of the CFD effort was to provide guidance in interpreting the sector rig test results.

Calculations were performed for sections of the respective sector and annular rig combustors, centered on and encompassing a single pilot stage fuel injector and a single main stage injector or two main stage half-injectors, depending on the stage alignment being investigated. Periodic conditions were applied to the lateral boundaries of the calculation domain. Typical grids employed 328,653 grid nodes (117 x 53 x 53) for the sector model and 370,788 grid nodes (132 x 53 x 53) for the annular model. Figure 10 shows an isometric projection of the grid onto the physical surfaces of the combustor for the annular combustor section, in this case with the pilot and main fuel injectors inline with each other (contrast with Figure 8). The representation allows for the periodic injection of film cooling air along the inner and outer liner surfaces. The liquid fuel streams were introduced as pseudo-gases with correct mass, momentum and heating value.

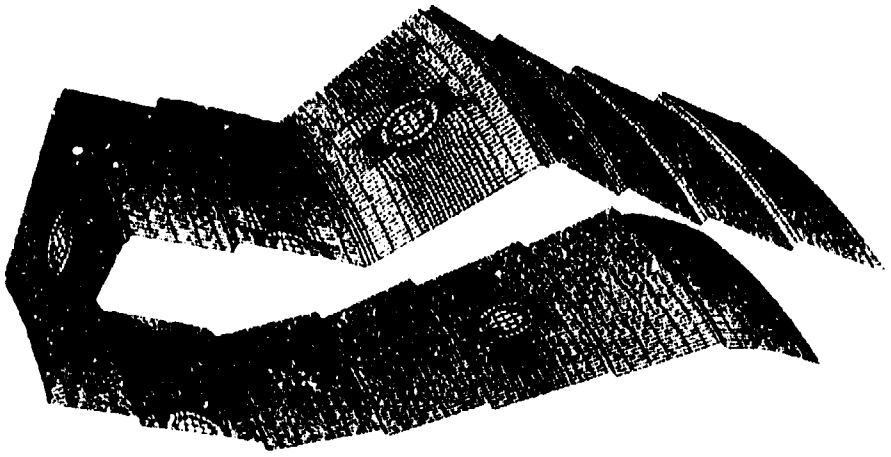

Fig 10 An Example of the Calculation Domain and Computational Grid for CFD Studies of the ASC

Solution convergence was judged on the basis of the overall residuals, achieved temperature rise and the stability of major flow features. Grid-independent solutions are not claimed, but the boundaries of the calculation domain are well-represented, as are the shapes of the major entering fluid streams. The solutions obtained can be considered as being ones of engineering pragmatism rather than of scientific exactitude, and as such are entirely satisfactory for their intended purpose.

The results of the CFD calculations were post-processed on a Silicon Graphics IRIS workstation using PLOT3D and FAST (Ref. 32) visualization software packages developed by NASA-Ames Research Center. It is only possible to display here a small selection of the data generated. Figure 11 shows isotherms (in degrees Rankine) calculated for takeoff power (both stages fueled) in the annular combustor, where the pilot and main stages are staggered relative to each other.

The gas temperature characteristics shown in Figure 11, inline with the injectors in each stage, are largely as might be expected, although circumferential spreading of the flame from the pilot injectors to interact toward the inner liner in the main stage with flame developed by the main stage injectors, can be seen. The particular air addition arrangement used in the main stage for this calculation is such that the circumferentially-averaged radial temperature profile at the combustor exit is peaked toward the combustor inner liner. This is more clearly evident in Figure 12 where the isotherms in the exit plane are compared for this configuration and for the identical configuration except for the stage fuel injectors being placed inline with each other. Areas in both cross-sections, where the local temperatures equal and exceed the critical value for high NOx formation rates (2033K), have been shaded. It can be seen that for the inline stage-arrangement the total of these areas is greater than for the staggered stage-arrangement. This is indicative that the inline stage-arrangement might produce more NOx than the staggered stage-arrangement. Similar consideration of Figure 11 suggests that the major source of NOx for the complete combustor is the main stage.

Although not identifiable in Figure 10, the model does contain air-addition ports in the main stage for both stage alignments. They are not visible because the main stage ports were defined by designating appropriate blocks of surface grid elements as "open" to admit air into the combustor. Despite the jet shapes then being incorrect and small compromises being necessary in representing jet mass flow and/or jet momentum (due to the port area being determined by the grid), this approach represents the most convenient way to change the mass quantities and positions of these air jets, without having to develop a new grid for each port change.

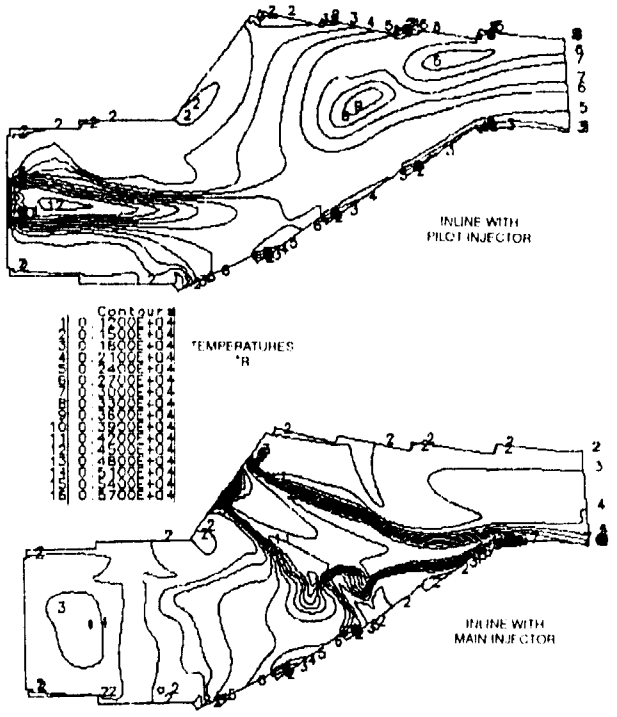

Fig. 11 Longitudinal Cross-Sections Inline with Fuel Injectors, Showing Calculated Isotherms in a Staggered-Stage ASC at Takeoff Power

Figure 12 indicates that change of the main stage air jets in the staggered-stage combustor is necessary to achieve a more desirable mean outlet temperature profile (either a center or slightly outer peaked profile).

The CFD calculations were used in the fashion described above to derive a combustor configuration that produced desirable combustion characteristics and low emissions potential. As a result of these efforts, a considerable amount of time-consuming and expensive experimental testing was saved from the program, and interpretation of some of the rig experimental behavior was facilitated.

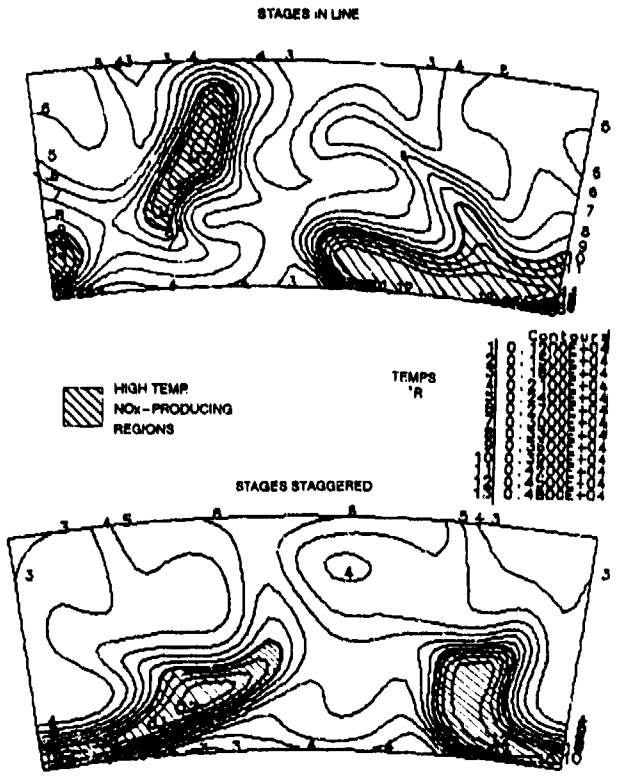

Fig. 12 Comparison of Outlet-Plane Isotherms in Transverse Cross-Sections of Inline and Staggered-Stage Alignments, Showing Regions of High Thermal NO Formation Rates

10. SECTOR RIG RESULTS

The sector rig was assigned a total of six important tasks in the overall development of the ASC:

1. Optimization of the pilot stage for good idle-power combustion efficiency, and flame stability at off-design conditions
2. Establishment of an appropriate pressure scaling law for NOx to allow extrapolation of rig results up to full power conditions
3. Determination of the dependency of NOx on stage fuel flow split
4. Examination of the effect of staging on combustion efficiency via steady-state simulation of staging
5. Limited evaluation of different main stage fuel injector design on NOx
6. Assessment of the optimized ASC configuration prior to the annular rig test program.

To complete these assigned tasks, the sector rig testing was carried out in the HPCL over a range of operating conditions involving limited parametric exploration where appropriate. The inlet pressure, temperature and air mass flow rate were selected to cover where possible representative low and intermediate engine power levels.

The pilot stage of the ASC is a fairly conventional primary zone, and utilizes standard airblast-atomizing fuel injectors from the V2500-A5 engine combustor. Acceptable combustion efficiency was achieved in usual fashion by adjusting the pilot equivalence ratio (Refs. 10,21) at the idle power value of overall fuel to air mas ratio (OFAR) (main stage unfueled). This is shown in Figure 13 at constant inlet pressure and temperature. The efficiencies are based on an emissions-measured carbon balance. Richening the pilot zone to an equivalence ratio of 0.90 raised the idle power combustion efficiency to 99.8 percent, more than acceptable to satisfy emissions requirements. This can be appreciated from Figure 14, that shows the emission index (EI) of CO characteristic with pilot stage equivalence ratio. The EI reaches a minimum around unity equivalence ratio. Figure 14 also displays the pilot stage NOx characteristic, which reaches a maximum at just under 1.1 equivalence ratio.

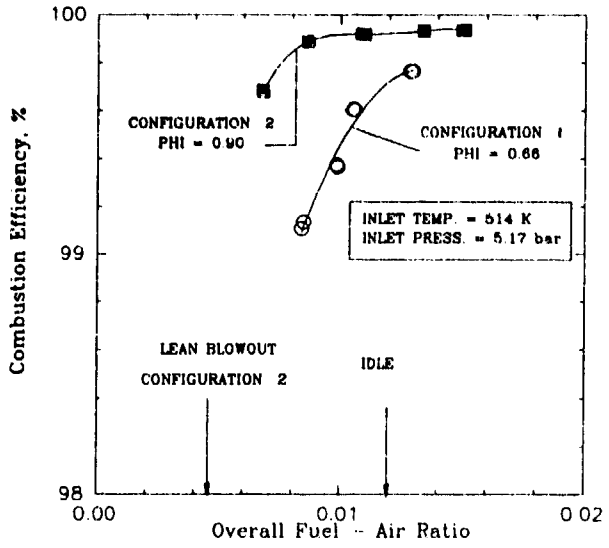

Fig. 13 Pilot Stage Combustion Efficiencies in the Sector Rig, Showing Influence of Equivalence Ratio

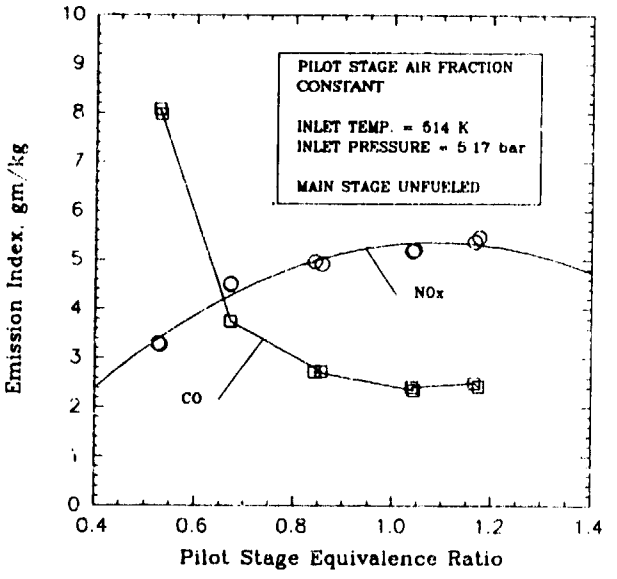

Fig. 14 Emissions of NOx and CO from Efficiency-Optimized Pilot Stage, Showing Response to Equivalence Ratio with Optima

Flame stability is controlled by the injector package (consisting of the injector inner and outer air swirlers, and the insert swirler) swirl number and dome height (together governing recirculation), and by primary zone equivalence ratio (determining recirculated gas temperature and active chemical species). With the adjusted equivalence ratio, existing injector packages and a carefully-chosen dome height, a lean blowout limit was obtained at an OFAR of 0.0045. This value is 40 percent below the minimum OFAR operationally encountered anywhere in engine transient operation, and satisfies the Pratt & Whitney design criterion for stability.

The optimized pilot zone obtained from the above work was maintained for all subsequent sector rig testing.

To protect the relight capability of the engine, the ASC was evaluated at low pressures (in a separate facility) simulating windmilling and starter-assisted high altitude flight. Figure 15 demonstrates that the ASC system is more than capable of meeting the 9000 meter plus, commercial altitude relight requirement.

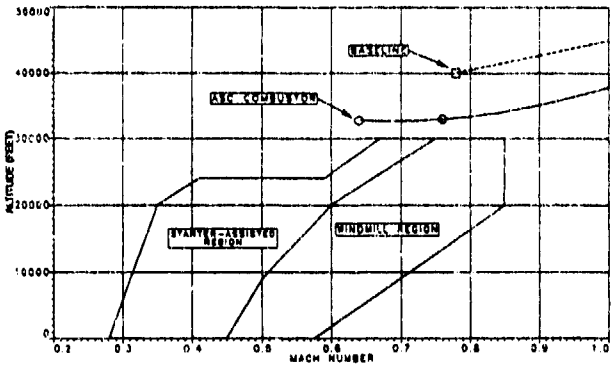

Fig. 15 Comparison of Altitude Relight Capability for ASC with Conventional Combustor (High Altitude Test Facility)

To establish an appropriate pressure-scaling law for NOx, the initial ASC configuration (with staggered stages) and the optimized pilot stage was operated over a range of OFARs at three pressure levels from 8.6 to 17.2 bar. Both stages were operative, and the pilot stage equivalence ratio was maintained constant at 0.39 (pilot stage fuel flow is reduced when the main stage is fueled, although the pilot air fraction remains constant). The inlet air temperature was also constant at 818.3K.

At a given pressure level in the range covered, the emissions index of NOx increases slightly with OFAR in linear fashion; this gradient, however, reduces, again slightly, with increasing pressure level, also within the range covered. The pressure dependencies of NOx at two OFARs are given in Figure 16, and they decrease slightly with increasing OFAR. The values for this range of OFAR are less than the familiar 0.5 exponent obtained from a simple kinetic analysis for NOx, based on assumptions of oxygen atom equilibrium with oxygen molecules (Ref. 33). While the behavior with OFAR might be attributed to experimental data scatter, the values are consistent with levels and trends obtained in other Pratt & Whitney studies for single-stage combustors where the pressure-dependency of NOx is shown to be a complex function of equivalence ratio and adiabatic flame temperature. (The approach is similar to that of Reference 34.)

Note that the pressure-dependency of NOx obtained above should not be considered as a general pressure scaling law since the range of parameter variation covered is very limited. However, this dependency was used, with some caution, for scaling the sector rig results to higher engine power conditions where necessary.

Given the pollutant generation mechanisms and their temperature dependencies described earlier, a trade-relationship between the emissions of NOx and CO is to be anticipated. Such a relationship exists in the ASC, as Figure 17 illustrates for the test points of Figures 14 and 16 (with the optimized pilot stage), and for some additional data. These latter data are for a range of OFAR at 643K air inlet temperature and 8.62 bar inlet pressure, with a constant pilot stage equivalence ratio of 0.39 (pilot fuel modulated). The figure shows that the EI of NOx decreases as that of CO increases, in exponential fashion for this range of conditions. Note that the residence times are the same for both processes at each operating condition.

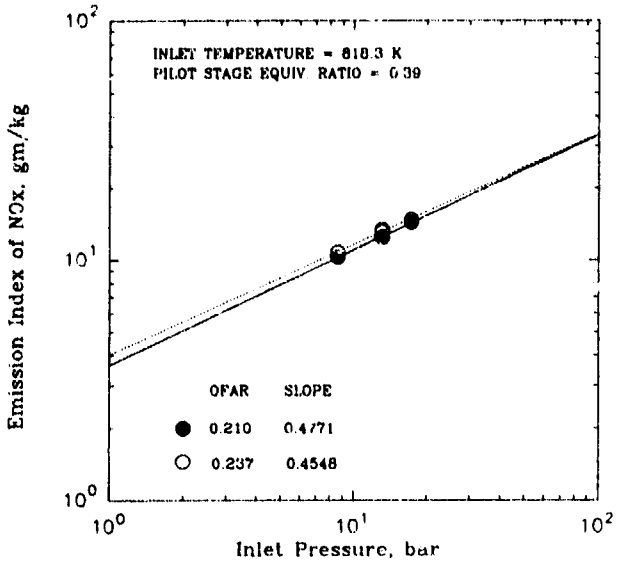

Fig. 16 NOx-Pressure Sensitivity of Pilot and Main Stages Operating Together at Fixed Inlet Temperature and Pilot Stage Equivalence Ratio

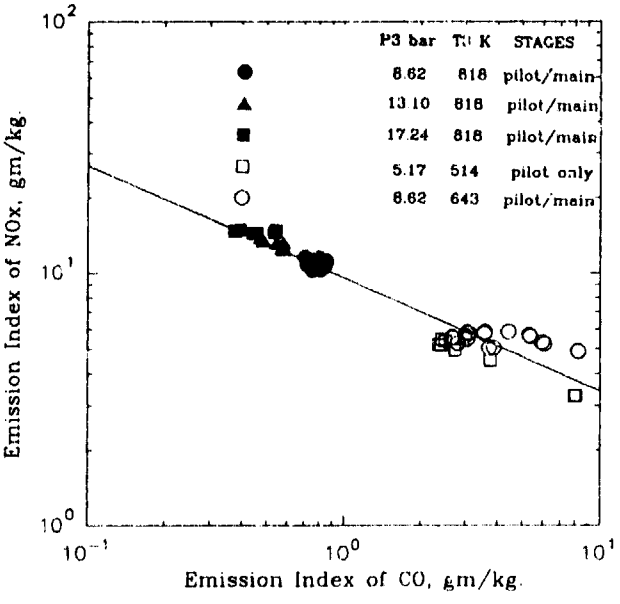

Fig. 17 Demonstration of the Trade Between Total NOx and CO Over a Range of Conditions

The importance of stage residence time to low CO emissions is displayed in Figure 18 for the 0.390 equivalence ratio pilot stage over a range of OFAR where air inlet temperature and pressure are respectively 643.3K and 8.62 bar, and over a range of OFAR where these conditions are 818K and 8.62, 13.1 and 17.24 bar. The flow function $(W\sqrt{T})/P$ is 9.74 $kg.K^{1/2}$/sec. bar for the first data set, and 8.88 $kg.K^{1/2}$/sec.bar for the second, i.e., the residence time is less for the first condition than for the second condition. The CO emissions are presented as an excess emission, that is, in terms of the difference between the measured EI and the equilibrium value calculated at appropriate stage conditions, through the EQLBRM computer program (Ref. 35).

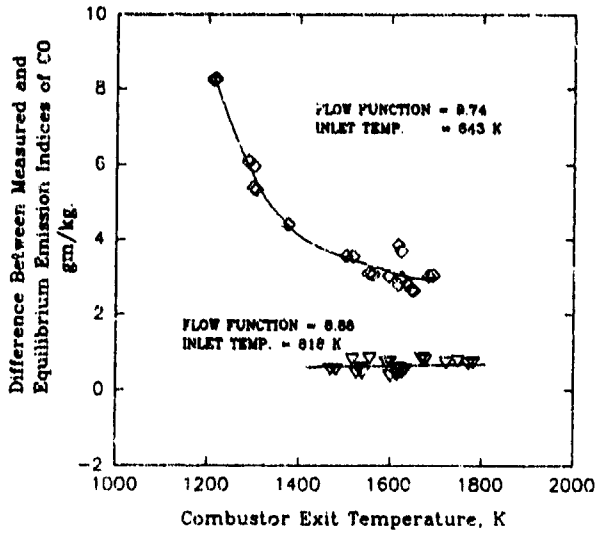

Fig. 18 Effect of Combustor Exit Temperature on Emissions of CO at Two Residence Times

The ASC operated at the lower residence time has the higher excess CO emission over the range of exit temperatures. Note that, for this lower residence time, the excess CO exhibits a sharp increase when the combustor exit temperature is below the critical value (1810K) for significant CO-consumption rates (Refs. 10,23). Also, even at the critical temperature level, the CO excess emissions curve is becoming asymptotic to a value significantly above zero, indicating a residence time limit for this combustor length under these operating conditions.

Curves for the difference in equilibrium and measured EI of NOx at these conditions are the inverse of the excess CO plot, with longer residence time producing greater NOx than the shorter residence time.

The collected NOx data from the foregoing plots were found to correlate only on a basis of the maximum adiabatic flame temperature existing for the appropriate test conditions. This implies that most of the NOx is thermal NO, generated at stoichiometric temperatures in diffusion flames, just as it is in single stage combustors. Figure 19 compares this correlated data with the NOx-correlation by Kretschmer & Odgers (Ref. 36) of collected engine data for single stage combustors. The present correlated ASC data parallel the single stage combustor NOx-data at a lower NOx-level. It is not immediately clear if the reduced NOx levels of the ASC are due to a favorable change in the equivalence ratio probability distribution functions (p.d.f.'s), i.e., a *small* improvement in fuel/air mixing due to doubling the number of fuel injectors so that *less* fuel is reacted stoichiometrically, or, due to reductions in the available time for the NO-reaction because of the short length of the main stage.

Figure 20 presents NOx data as a function of OFAR for three values of pilot stage equivalence ratio at constant inlet conditions of 818K temperature and 8.6 bar pressure; the configuration of the main stage is slightly different from that for all preceding plots, although the pilot stage is identical. It can be seen that at given OFAR the EI of NOx increases as pilot stage equivalence ratio increases, and that the sensitivity to OFAR, while not great, depends also on the pilot stage equivalence ratio. These characteristics imply that NOx production may be minimized by reducing pilot stage equivalence ratio at any operating condition, commensurate with maintaining overall combustion efficiency and flame stability. Figure 21 illustrates this benefit at an overall equivalence ratio of 0.36, showing that NOx increases and CO decreases (slightly) with increase in pilot stage equivalence ratio.

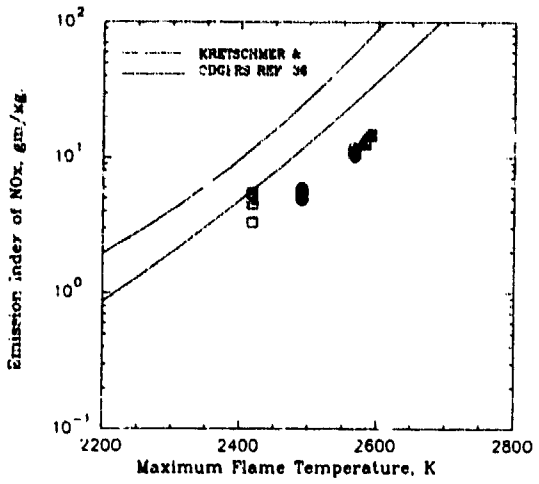

Fig. 19 Correlation of ASC NOx Data with Adiabatic Flame Temperature, and Comparison with Kretschmer & Odgers Collected Data from Conventional Combustors

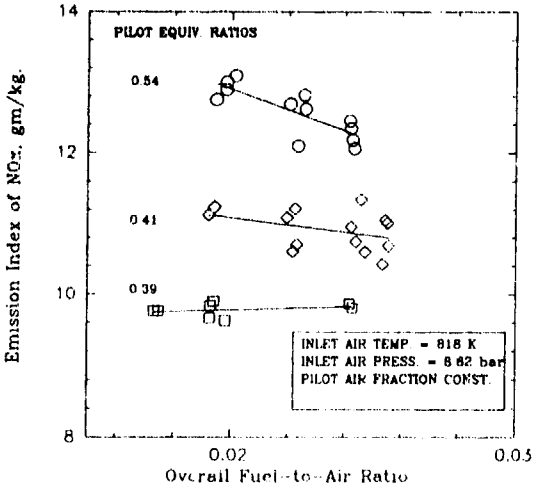

Fig. 20 Variation of Total NOx with Overall Fuel to Air Ratio, Showing Influence of Pilot-Stage Equivalence Ratio

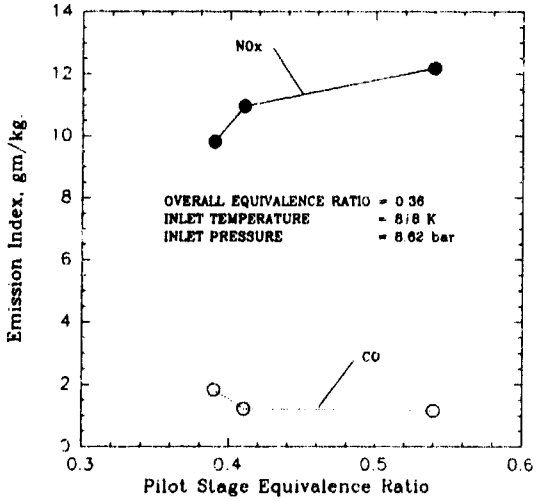

Fig. 21 Direct Influence on NOx of Pilot-Stage Equivalence Ratio at Fixed OFAR (Moderate Temperature Rise), Showing Benefits of Minimizing Pilot-Stage Equivalence Ratio

It is interesting to note that extrapolation of lines fitted by linear regression analysis through the data of Figure 20 for each pilot stage equivalence ratio, intersect at an OFAR of 0.04. With the variation in pilot stage equivalence ratio, this OFAR corresponds to an approximately constant bulk temperature for the main stage, and about equal pilot stage contributions to overall NOx. The common value of NOx is about 10 gm/kg of total fuel burned. To assist in understanding this better, Figure 22 shows the variation in pilot to main stage fuel mass flow rate ratio with OFAR, while Figure 23 gives the variation of main zone equivalence ratio.

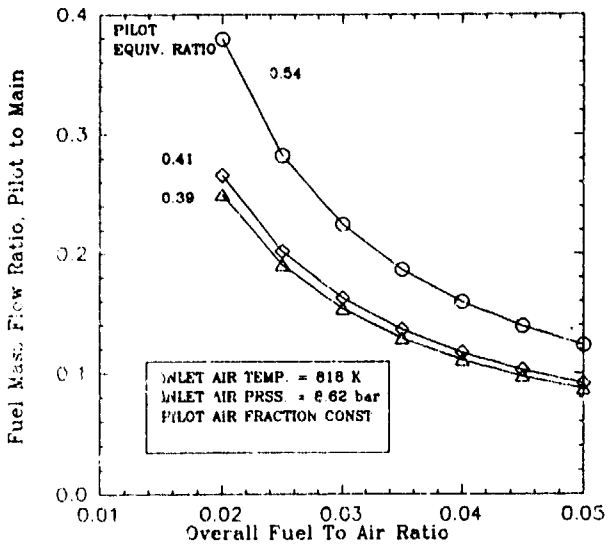

Fig. 22 Variation of Ratio of Pilot to Main Fuel Flow Rates with OFAR and Pilot-Stage Equivalence Ratio

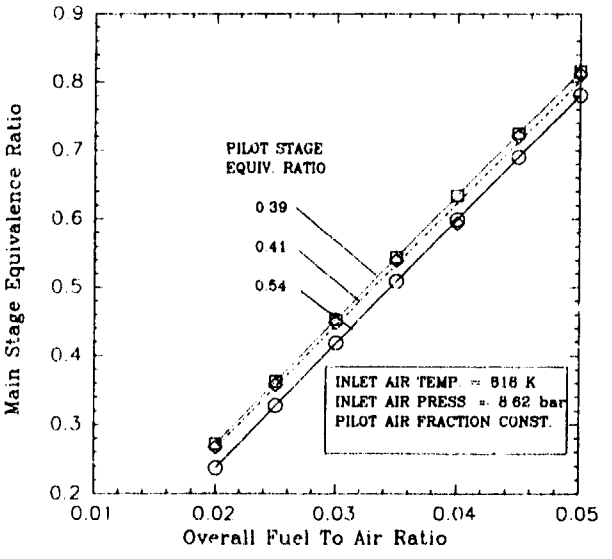

Fig. 23 Variation of Main-Stage Equivalence Ratio with OFAR and Pilot-Stage Equivalence Ratio

The emission indices of main stage NOx (gm NOx/kg main stage fuel) were found as a function of main stage equivalence ratio by scaling NOx measured for this pilot operating alone (Figure 14), up to present operating conditions using the scaling laws given in Reference 34, and then subtracting them from the measured total NOx using the expression,

$$(EI_{NOx})_{overall} = \left[\frac{\dot{m}_{f,pilot}}{\dot{m}_{f,total}} (EI_{NOx})_{pilot} + \frac{\dot{m}_{f,main}}{\dot{m}_{f,total}} (EI_{NOx})_{main} \right]$$

where,

$(EI_{NOx})_{pilot}$ = gm NOx generated in pilot stage per kg. pilot stage fuel burned

$(EI_{NOx})_{main}$ = gm NOx generated in main stage per kg. main stage fuel burned

$(EI_{NOx})_{overall}$ = gm NOx measured at exit from ASC per kg of total fuel burned.

Figure 24 shows that main stage NOx is approximately constant, within the accuracy of determination, over a wide range of main stage equivalence ratio. Comparison of Figure 24 with Figure 20 shows that at these conditions more of the NOx is generated in the main stage, and that differences in NOx level and variation with OFAR are due to the pilot behavior. The constant main stage NOx characteristic is consistent with Figure 19, where overall NOx is shown to depend on local adiabatic flame temperature for the 0.39 equivalence ratio pilot.

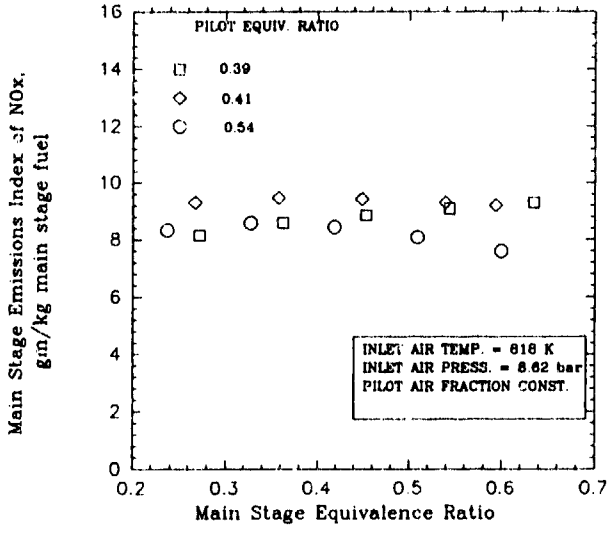

Fig. 24 Demonstration of Constancy of Main-Stage NOx with Main-Stage Equivalence Ratio, Regardless of Pilot-Stage Equivalence Ratio

It should be noted that the apparent cross-over of the extrapolations of the data in Figure 20 implies that reducing the pilot stage equivalence ratio is only of benefit for moderate temperature rise (OFAR < 0.04) combustors. For high temperature rise staged combustors, it might be beneficial to NOx to increase pilot stage equivalence ratio at high power.

Smoke increases with increasing OFAR at fixed inlet temperature and pressure of 818K and 8.62 bar respectively, for the original main stage configuration with a fixed pilot stage equivalence ratio of 0.390. This is given in Figure 25. Since the pilot is fixed, the observed smoke increases must originate in the main stage.

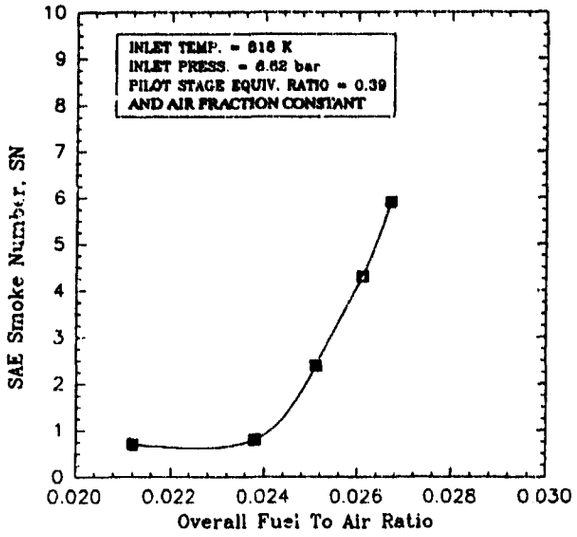

Fig. 25 Relation of Exhaust Smoke to OFAR for Fixed Inlet Conditions

The smoke emitted is the result of two competing processes that operate in series in conventional combustors: smoke production in over-rich regions, followed by smoke burnout in higher temperature regions as the stoichiometric contour is passed through by the reacting mixture. Increasing OFAR with fixed pilot stage equivalence ratio results in an increasing main stage equivalence ratio. The higher fuel flow rate to the main stage produces a pronounced richening of the conventional main stage airblast fuel injector packages. In turn, this results in local equivalence ratios in excess of unity immediately downstream from the injectors. These locally over-rich regions are the source of smoke generation. Increasing the main stage bulk equivalence ratio will also expand the spatial extent of the stoichiometric contour in the main stage. This will tend to increase NOx production, eventually. Figures 20 and 24 indicate that this has not yet happened to any great extent. The expanding stoichiometric contour will also eventually enhance smoke burnout in the main stage, provided that the residence time is adequate for this. Figure 25 suggests this is not yet taking place either for these conditions. Taken together, these processes imply that a trade might also exist between NOx and smoke, regardless of any possible chemical reduction interaction between smoke and NOx that might take place.

Figure 26 is a plot of the EI of NOx against smoke number (SN) for the conditions of Figure 25. The precision is not great, and the data range is very limited. It is also apparent from Figures 20 and 25 that some of the interesting smoke ~ NOx interactions have not yet taken place to any great extent at these operating conditions. Therefore, it is difficult to draw definite conclusions. However, smoke and NOx do appear to initially increase together as OFAR increases. The implication of this is that they are responding to a common influence. Should the following turndown indicated by the 3rd order regression fit to the data be real, it would imply a definite direct interaction between smoke and NOx, since OFAR is still increasing.

As discussed above, it is unacceptable for any combustion system to introduce a lag in engine thrust response. In the case of the ASC, fuel-staging must take place smoothly without delays due to valve operation, line fill-time, or loss in combustion efficiency. Actual dynamic responses of the system were to be investigated in the UTRC transient combustion facility. The combustion efficiency aspect was investigated with the sector rig at discrete, steady-state simulations of the transition progress from low power operation on the pilot stage, through main stage light-off, and high-power staging operation. Provided that combustion efficiency remains relatively high through these progresses, the probability will be low that the ASC will induce an engine thrust lapse during staging.

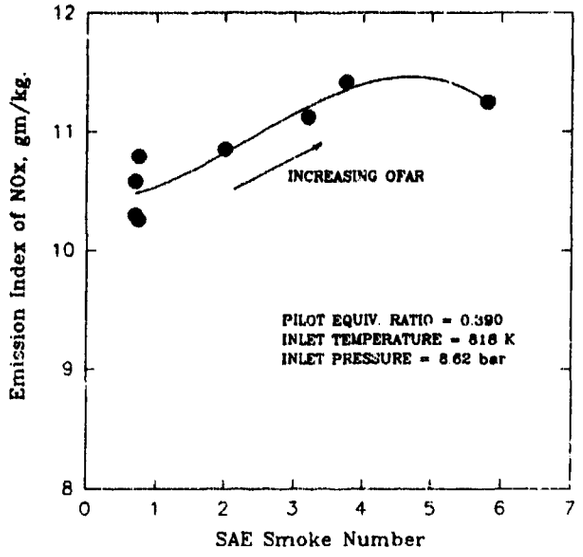

Fig. 26 Possible Trade of Overall NOx with Exhaust Smoke

Figure 27 is a plot of combustion efficiency variations with simulated engine power level for the optimized pilot and the main stage with two different injector configurations. Engine power is represented by OFAR, and the combustor inlet temperatures and pressures were appropriate to a simulated approach condition. Combustion efficiencies for the pilot alone, and the pilot and main together after staging, are high over wide ranges of OFAR for the airblast conventional fuel injector used in both stages. Combustion efficiencies are more than sufficiently high that thrust lapses in the engine due to this cause are not expected based upon pseudo-transient and true transient testing.

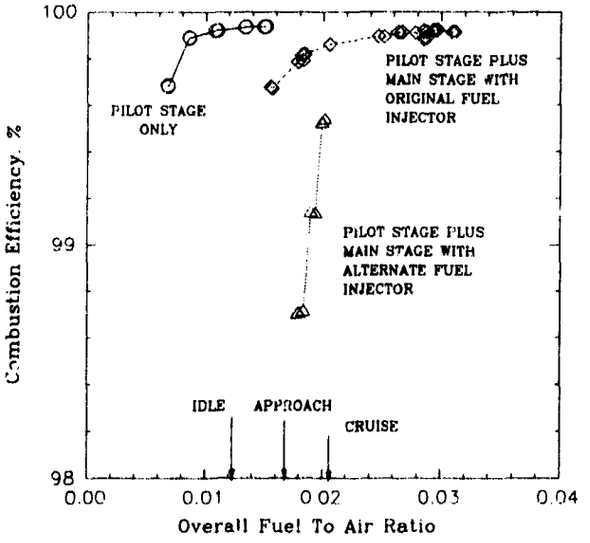

Fig. 27 Steady-State Demonstration that Pilot and Main-Stage Efficiencies Can Remain High During Staging, and an Indication of the Importance of Main-Stage Fuel Injector Design

The combustion efficiency for the non-airblast fuel injector design used in the main stage only, falls off rapidly with OFAR at approach conditions. This fuel injector also resulted in NOx levels that were 18 percent higher than those of the airblast injector. It is clear that main stage fuel injector design is critical in the pursuit of low NOx and low smoke.

The NOx characteristic with engine power of the final configuration for the sector rig version of the ASC is shown in Figure 28 compared to that of the conventional combustor. The effect of staging on NOx is clear, and it is interesting to compare Figure 28 with the quasi-staging characteristic given in Reference 10. Fuel staging reduces the high power NOx levels by very worthwhile amounts.

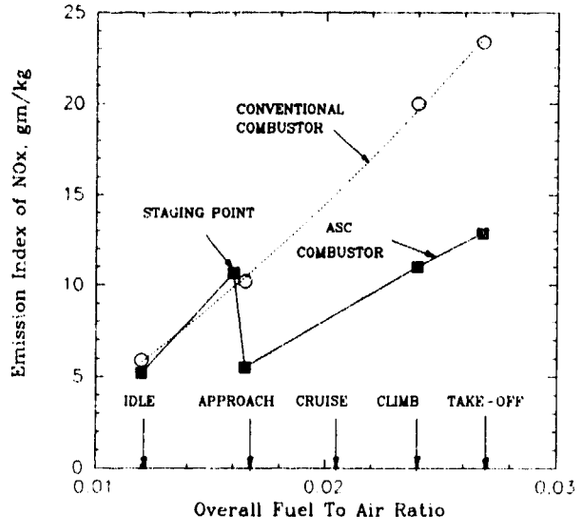

Fig. 28 Comparison of NOx Characteristics for Conventional and Fuel-Staged Combustors

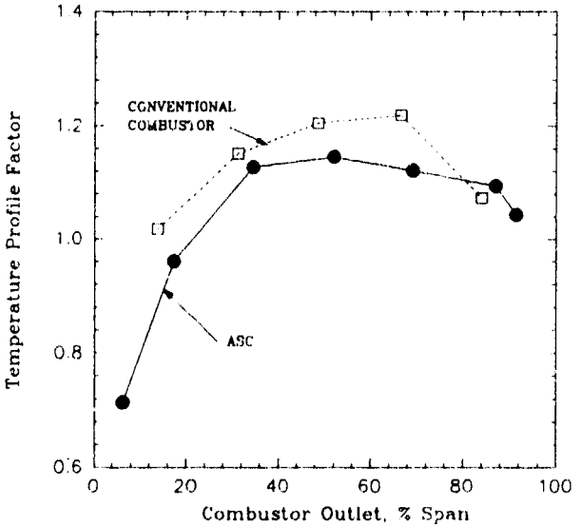

Fig. 29 Comparison of Mean Radial Temperature Profiles for V2500 Conventional Combustor and the ASC in the Annular Rig

11. ANNULAR RIG RESULTS

Annular rig testing at representative engine conditions was initiated during the fourth quarter of 1992, and for completeness an early set of data from the annular rig is presented; suffice it to observe that the low emissions characteristics of the sector-version of the ASC were confirmed in the annular rig.

The data from the annular rig that is to be presented concerns the extremely important mean radial temperature profile with both stages operating. Compared to the conventional combustor in Figure 29, the initial profile of the ASC is not too dissimilar. It does not change with simulated power level, and is amenable to development by the usual dilution air manipulation. The pattern factors are also encouraging, and initially were only about 5 percent (by ΔT) higher than those of the conventional combustor.

12. DISCUSSION AND CONCLUSIONS

A continuing and multiphase research and development effort to reduce the exhaust emissions of recognized pollutants in aircraft gas turbine engines has been presented. The second phase of this effort has been highlighted by descriptions of part of the rig test program and the supporting CFD studies. The emissions reduction technique addressed is that of fuel-staging.

It had been questioned in some quarters whether fuel-staging alone, without simultaneous and directed improvements in fuel/air mixing, could really reduce NOx emissions. The reason for this doubt was expressed as, "unless premixing is used, stoichiometric burning is stoichiometric burning, regardless of the design values of stage bulk equivalence ratios always being fuel-lean." The rig test program has reconfirmed the emissions reduction potential offered by fuel-staging. An emissions reduction in NOx in excess of 35 percent beyond the Phase I goals has been achieved with just fuel-staging, while holding low smoke, CO and UHC levels. The Phase II goals established in the Pratt & Whitney emissions reduction program have been met in the rig test program. Figure 30 shows the progress achieved in emissions reductions in the IAE V2500 engine as a result of Phases I and II of the Pratt & Whitney program. EPAP emissions levels of NOx, CO and UHC are expressed as a percent of the current ICAO regulation; although not shown, smoke levels are invisible in all cases. The Phase I data are from an engine and the Phase II data are projected from the rig results. The ASC configuration has achieved this milestone within the overall length of the V2500-A5/D5 engine conventional combustor. It has also achieved it without compromising satisfactory operational characteristics, such as pilot stage stability and idle and sub-idle power combustion efficiencies, combustion efficiency during staging, and pattern factor and mean radial temperature profile at exit; engine thrust-response should also be unaffected.

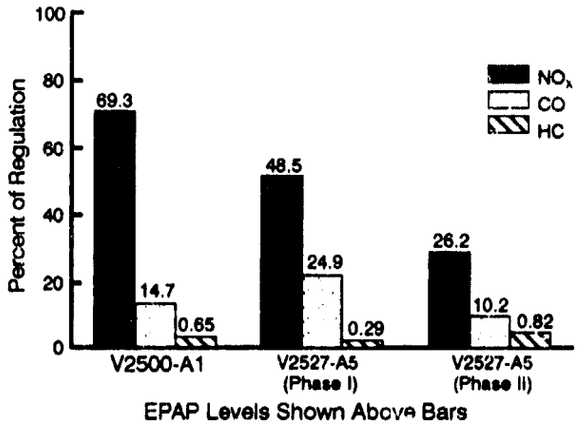

Fig. 30 Summary of Phases I and II Emissions Reduction Progress in V2500

The emissions behavior in the ASC is much more complex than it is in a conventional combustor. There are many emissions trades to be understood and defined. Great care, therefore, has to be taken in the planning of rig test programs to ensure that the investigation really does relate to engine operations. At the same time, parametric studies to ascertain the reasons behind the emissions behavior, and to establish design rules, are clearly necessary.

The benefits to low NOx of reducing the pilot stage equivalence ratio at higher engine power levels in moderate temperature rise combustors (Figure 21) are most important. The axially-staggered configuration of the ASC enables benefit to be taken of this trade without any adverse effects on the mean radial temperature profile at the combustor exit.

The behavior of the NOx data, e.g., Figures 17 and 19, strongly suggests that most of the NOx measured at the combustor exit plane is nitric oxide produced by thermal fixation of atmospheric nitrogen. This is the reason that the CFD thermal fields are such good indicators of the NOx reduction potential of various combustor configurations.

The rig program has again confirmed the usefulness of CFD as a design synthesis and diagnostic tool in developing a complex combustor. It is apparent that, if used with care, consideration and knowledge, a CFD solution does not have to possess scientific exactitude to be useful for many (but not all) purposes. This is fortunate because of the large resource needed to achieve scientific exactitude for complex reacting flows. However, vigorous efforts are still needed in improving the case setup, i.e., grid generation and application of boundary conditions, for this tool to achieve its full potential.

Although there were no directed efforts to improve fuel/air mixing in the ASC, there are suggestions that mixing in the main stage is different from that in conventional single-stage combustors. Figure 24 indicates that over a wide range of main stage equivalence ratio, the NOx generated in the main stage is independent of this ratio, with the EI being roughly 8.8 gm NOx per kg of main stage fuel. For the operating conditions of Figure 24, the adiabatic flame temperature is 2566K (from EQLBRM, Ref. 35). This data point then plots on Figure 19 in good agreement with the other ASC data, i.e., the main stage NOx in Figure 24 depends only on the adiabatic flame temperature (indicative of stoichiometric burning), but at a lower level than the collected data (Ref. 36) for conventional combustors. This implies a change in the mixture p.d.f. in the main stage.

The insensitivity of main stage NOx to OFAR, as shown in Figure 24, indicates a certain "robustness" of the emissions reduction. This is important since operating OFARs have a tendency to creep upward from original design values during the normal engine development process or during the engine service life.

At the present stage of development, the ASC has achieved its design goals; the efforts are now concentrated on integrating it into the V2500 engine system and carrying it across to other Pratt & Whitney engines. Research work for Phase III of the emissions reduction program is in progress for the 2000+ AD time-frame. However, it is by no means clear that the ASC cannot achieve still further reductions in NOx. Figure 19 offers the possibility that, although a large portion of the main stage fuel is still reacted stoichiometrically in the ASC, some changes in burning have occurred. In addition, small changes in main stage injector design have resulted in significant changes in NOx emissions. Therefore, it appears worthwhile to investigate the benefits of improvements in fuel/air mixing in the ASC main stage. A separate program of research is just beginning in this area.

ACKNOWLEDGEMENTS

The authors wish to thank United Technologies Corporation, Pratt & Whitney, for permission to publish this paper. Thanks also to members of the International Aero-Engines team and the Pratt & Whitney V2500 Project Group for their encouragement and support. Appreciation is expressed to our customers for their useful input. Finally, the authors wish to acknowledge the support and assistance of their colleagues, especially James B. Hoke who conducted most of the rig testing.

REFERENCES

1. Mintzer, I. M., "Energy, Greenhouse Gases and Climate Change," Ann. Rev. Energy, *15*, 1990, pp. 513-550.

2. Air Pollution - Global Pollution from Jet Aircraft Could Increase in the Future, United States General Accounting Office, Rept. GAO/RCED-92-72, January 1992.

3. Schumann, U., et al., "Analysis of Air Traffic Contrails from Satellite Data - A Case Study," Proc. European Propulsion Forum: *Future Civil Engines and the Protection of the Atmosphere*, DLR Research Center, Cologne-Porz, Germany, April 3-5, 1990, pp. 49-57.

4. Johnson, C. E., and Henshaw, J., "The Impact of Aircraft NOx Emissions in the Troposphere," Final Report of Study Contract EV4V-0205-UK(A) prepared for Commission of the European Communities, by Modelling & Assessments Group, AEA Environment and Energy, Harwell Lab., U.K., January 1991.

5. "The Global Warming Panic," Forbes, December 25, 1989, pp. 96-102.

6. International Civil Aviation Organization (ICAO), Annex 16, Volume II, 1981.

7. Prather, M. J., et al., "The Atmospheric Effects of Stratosphere Aircraft: A First Program Report," NASA RP 1272, January 1992.

8. Oliver, R. C., "Atmospheric Effects of En Route Subsonic Aircraft," prepared for NASA by Institute for Defense Analyses, IDA Document D-1167, August 1992.

9. Koff, B., "Spanning the Globe with Jet Propulsion," AIAA/SAE William Littlewood Memorial Lecture, AIAA Paper 2987, presented at AIAA 1991 Annual Meeting and Exhibit, Arlington, Virginia, 1991.

10. Sturgess, G. J., McKinney, R., and Morford, S., "Modification of Combustor Stoichiometry Distribution for Reduced NOx Emission from Aircraft Engines," ASME Paper 92-GT-108, presented at International Gas Turbine and Aeroengine Congress and Exposition, Cologne, Germany, June 1-4, 1992, (to be published in ASME Transactions).

11. Lefebvre, A. H., "Pollution Control in Continuous Combustion Engines," *Fifteenth Symposium (International) on Combustion*, The Combustion Institute, 1974, pp. 1169-1180.

12. Lefebvre, A. H., *Gas Turbine Combustion*, Hemisphere Publishing Corp., McGraw-Hill Book Company, 1983, Chapter 11.

13. Jones, R. E., "Advanced Technology for Reducing Aircraft Engine Pollution," NASA TM X-68256, November 1973, (see also, Trans. ASME, *J. Engineering for Industry*, November 1974, pp. 1354-1360).

14. Markowski, S. J., Lohmann, R. P., and Reilly, R. S., "The VORBIX Burner - A New Approach to Gas Turbine Combustors," Trans. ASME, *J. Engineering for Power*, January 1976, pp. 123-129.

15. Greene, W., Tankut, S., and Sokolowski, D. E., "Development and Operating Characteristics of an Advanced Two-Stage Combustor," Trans. ASME, *J. Energy*, Vol. 7, No. 4, July-August 1983, pp. 354-360.

16. Environmental Protection Agency: "Control of Air Pollution from Aircraft and Aircraft Engines; Emissions Standards and Test Procedures for Aircraft," U.S. Federal Register, 38, (Vol. 136), Part II: 19076, July 1973.

17. Pratt & Whitney internal report, 1975.

18. Roberts, R., Fiorentino, A, and Greene, W., "Experimental Clean Combustor Program Phase III - Final Report," NASA CR-135253, October 1977.

19. Bahr, D. W., "Technology for the Design of High Temperature Rise Combustors," *J. Propulsion*, Vol. 3, No. 2, March-April 1987, pp. 179-186.

20. Kress, E. J., Taylor, J. R., and Dodds, W. J., "Multiple Swirler Dome Combustor for High Temperature Rise Applications," Paper No. AIAA-90-2159, presented at AIAA/SAE/ASME/ASEE 26th Joint Propulsion Conference, Orlando, Florida, July 16-18, 1990.

21. Sturgess, G. J., "Advanced Low-Emissions Catalytic Combustor Program - Phase I Final Report," NASA CR-159656, June 1981.

22. Heywood, J. B., and Mikus, T., "Parameters Controlling Nitric Oxide Emissions from Gas Turbine Combustors," presented at AGARD Propulsion & Energetics Panels 41st Meeting, on *Atmospheric Pollution by Aircraft Engines*, London, England, 1973.

23. Morton, H. L., and Marshall, R. L., "Impact of Emissions Regulations on Gas Turbine Combustor Design," Canadian Aeronautics and Space Journal, Vol. 20, No. 3, March 1974, pp. 101-109.

24. Bahr, D. W., "HC and CO Emission Abatement Via Selective Fuel Injection," ASME Paper No. 82-GT-178, 1982.

25. Koff, B., "Aircraft Gas Turbine Emission Challenge," presented at the Aero Engine and Environment Symposium, Berlin, Germany, June 17, 1992.

26. Segalman, I., "Approaches to Reduced Aircraft Emissions," presented to 3rd Intl. Congress of Space & Aeronautics of Mexico, Mexico City, Mexico, October 29, 1992.

27. Marshall, R. L., "An Approach to Aircraft Pollution Abatement," presented to Intl. Air Quality Seminar, Birmingham Intl. Airport, Birmingham, England, November 5, 1991.

28. Rosfjord, T. J., Haley Jr., J., and Bonnell, J. M., "Unique Transient Combustor Capability," Paper No. AIAA-88-3197, presented at AIAA/SAE/ASME/ASEE 24th Joint Propulsion Conference, Boston, Massachusetts, July 11-13, 1988.

29. Rhie, C. M., and Stowers, S. T., "Numerical Analysis of Reacting Flows Using Finite Rate Chemistry Models," Paper No. AIAA-89-0459, presented at AIAA 27th Aerospace Sciences Meeting, Reno, Nevada, January 1989.

30. Launder, B. E., "Turbulence Transport Models for Numerical Computation of Complex Turbulent Flows," Lecture notes for a course entitled: *Prediction and Measurement of Complex Turbulent Flows*, organized by Flow Research Corp., Seattle, Washington, August 18-22, 1980.

31. Magnussen, B. F., and Hjertager, B. H., "On Mathematical Modelling of Turbulent Combustion with Special Emphasis on Soot Formation," Proc. *16th Symposium (International) on Combustion*, The Combustion Institute, 1973, pp. 601-606.

32. Walatka, P. P., et al., *FAST User Guide*, (Beta 2.1), RND-92-013, NASA Ames Research Center, June 1992.

33. Sarli, V. J., Eiler, D. C., and Marshall, R. L., "Effects of Operating Variables on Gaseous Emissions," presented to Air Pollution Control Association (APCA) Specialty Conference on *Air Pollution Measurement Accuracy as it Relates to Regulation Compliance*, New Orleans, Louisiana, 1975.

34. Nicol, D., et al., "NOx Sensitivities for Gas Turbine Engines Operated on Lean-Premixed Combustion and Conventional Diffusion Flames," ASME Paper 92-GT-115, presented at 37th ASME International Gas Turbine & Aeroengine Congress and Exposition, Cologne, Germany, June 1-4, 1992.

35. Pratt, B. S., and Pratt, D. T., "An Interactive Code for Calculation of Gas-Phase Chemical Equilibrium," NASA CR-168337, 1984.

36. Kretschmer, D., and Odgers, J., "Modeling of Combustors: The Effects of Ambient Conditions on Performance," ASME Paper No. 73-WA/GT-6, 1973.

Discussion

Question 1. J. Tilston
Do you optimize pilot zone air/fuel ratio for altitude relight?

Author's Reply
The pilot air/fuel ratio has normally been optimized for lean blowout during sea level testing because it is logistically easier to accommodate. However, there is a relationship between sea level blowout and altitude relight, i.e. if it is good at sea level, it is good at altitude.

LES FOYERS DE TURBOREACTEURS A GEOMETRIE VARIABLE : UNE REPONSE A LA MAITRISE DE LA POLLUTION DANS DES CYCLES A HAUTE TEMPERATURE, HAUTE PRESSION

S. MEUNIER
D. ANSART
P. CICCIA
Snecma
Département YKC
Centre d'Essais
de MELUN-VILLAROCHE
77550 MOISSY CRAMAYEL

SUMMARY

The pollutants emissions decrease doesn't seem easily achievable, particularly with advanced engines cycles conditions with high pressure, temperature and fuel to air ratio.
For a given fuel and air split, the combustor size can't be reduced without leading to relight altitude, combustion stability and emissions concerns.
In addition, the liners areas to be cooled remain considerable, the cooling airflow increase leads to higher fuel to air ratio in the primary zone and finally to unacceptable Nox emissions levels due to higher flame temperatures.
In order to satisfy the trade off in between the combustor performance at low and high engine ratings, several combustor concepts are in development.
Among them, the use of variable geometries to modulate the primary zone airflow seems promotive.
Indeed, this concept allows to satisfy the compromise between the different ratings taking into account the decrease of the combustor panels areas to be cooled.
That is the reason why this variable geometry concept is particularly suitable to high pressure and temperature engines cycles.
In this paper, tests results recorded on a five-cups sector fitted with a variable geometry injection system, and some measured performance on a full annular combustor are commented.
It appeared that acceptable performance in term of combustion stability can be met with a low volume combustor. The cooling airflow reduction and the primary zone fuel to air ratio control allow to meet quite good and homogeneous combustor exit temperature profiles whatever the engine rating.

RESUME

La réduction des émissions de polluants, semble difficilement conciliable avec une élévation des pressions et températures de fonctionnement des chambres de combustion de turboréacteurs.
A répartition d'air et de carburant fixée, la taille du foyer ne peut pas être réduite sans se heurter aux limites de rallumage en altitude et sans conduire à l'émission d'imbrûlés. De plus, les surfaces à refroidir restant importantes, une partie de l'air disponible ne peut pas participer à la combustion dans la zone primaire, conduisant ainsi à des richesses locales, donc à des températures élevées et en conséquence à des niveaux d'oxydes d'azote inacceptables.

Afin de lever les contraintes que fait peser le compromis entre performances de rallumage et plein-gaz, plusieurs concepts technologiques sont en cours de développement. Parmi eux l'utilisation de géométries variables permettant de moduler l'air participant à la combustion dans la zone primaire du foyer semble particulièrement prometteuse. En effet, avec ce concept technologique, le compromis entre les différents régimes peut être atteint avec une réduction des surfaces à refroidir. Ainsi ce concept est-il particulièrement bien adapté aux cycles hautes pressions, hautes températures.
Dans cet article, des résultats obtenus sur un secteur de chambre bidimensionnel muni de cinq injecteurs ainsi que quelques résultats sur foyer annulaire équipé d'un système d'injection à géométrie variable sont rapportés.
Il apparaît que de bonnes performances de stabilité peuvent être obtenues avec un foyer de volume réduit. Les débits d'air de refroidissement modérés, l'optimisation de la répartition de richesse en zone primaire conduisent à des profils de température sortie chambre de combustion homogènes à tous les régimes.

INTRODUCTION

Le dimensionnement d'un foyer de turboréacteur résulte d'un compromis entre les différentes performances à des conditions de fonctionnement extrêmes : ralenti et plein gaz. Par exemple si le volume du foyer est accru, l'augmentation du temps de résidence des gaz va entraîner une meilleure combustion, donc une diminution des niveaux d'imbrûlés au ralenti /1/. De même le rallumage en altitude sera facilité et la stabilité meilleure.
En contrepartie avec la même géométrie de zone primaire, les temps de résidence élevés vont permettre à la cinétique chimique de production des oxydes d'azote, certes lente, de se dérouler de façon plus complète (cf figure 1).

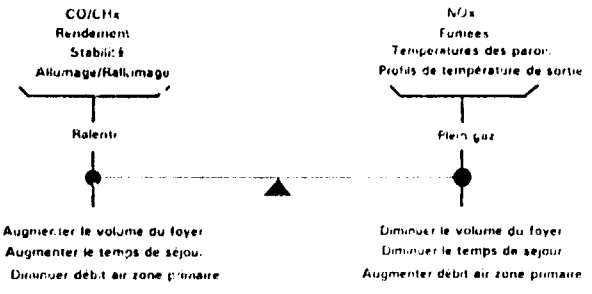

Figure 1 : Compromis de dimensionnement d'un foyer de turboréacteur

Presented at an AGARD Meeting on 'Fuels and Combustion Technology for Advanced Aircraft Engines', May 1993.

L'accroissement du rapport poussée sur masse des systèmes propulsifs nécessite le développement de chambres de combustion conduisant à des élévations de températures, donc de richesse foyer de plus en plus importantes /2/. En parallèle les taux de compression augmentant également, la température d'entrée foyer, donc la température de l'air utilisée pour refroidir les parois est de plus en plus élevée. En conséquence à efficacité de refroidissement constante, il reste de moins en moins d'air pour participer à la combustion en zone primaire.
D'autre part, la température sortie foyer devenant de plus en plus élevée le distributeur de turbine et la turbine haute pression deviennent de plus en plus sensibles aux hétérogénéités de température.
Il apparaît que la réalisation d'un compromis conduisant à des performances satisfaisantes à tous les régimes ne peut, pour les cycles les plus avancés, être obtenue sans libérer certaines des contraintes liées aux architectures conventionnelles de foyer.
En particulier les distributions de richesse zone primaire doivent pouvoir être modulées en fonction du régime. Ce point conduit à deux concepts différents /3/ :

- L'étagement du fuel (chambres à plusieurs points d'injection. Deux têtes en particulier).
- La modulation de l'air : il s'agit du concept dit "à géométrie variable".

Snecma travaille depuis de nombreuses années sur ces deux voies /4/, /5/.
En particulier un foyer avec modulation du débit d'air au moyen de diaphragmes des vrilles d'injection d'air a été développé.
Un programme de recherche incluant, entre autres, une optimisation de l'aérodynamique et de la distribution de richesse zone primaire, et du système d'injection sur secteur bidimensionnel à cinq injecteurs a été réalisé.
Les solutions retenues ont ensuite été implantées sur un foyer annulaire, afin de vérifier le comportement global du foyer, en particulier en ce qui concerne la stabilité en dépression et les facteurs statistiques dans un premier temps.

1. CONCEPTS A ETAGEMENT DU DEBIT D'AIR

Le principe d'étagement du débit d'air dans la chambre de combustion peut être assuré de plusieurs manières pour adapter le débit d'air dans la zone primaire à chaque condition de fonctionnement. En effet, différents concepts à géométrie variable peuvent être implantés au niveau des casquettes, des systèmes d'injection, des trous de dilution et des combinaisons des trois peuvent être envisagés pour limiter l'évolution de la perte de charge globale du module de chambre de combustion entre les conditions ralenti et plein gaz.
Pour maintenir la richesse en zone primaire à un niveau optimal du ralenti jusqu'au plein gaz et satisfaire les performances respectives, l'utilisation d'un système d'injection à géométrie variable est particulièrement attractive. Ce système permet de moduler le débit d'air intervenant directement dans la zone primaire.
Snecma dispose à ce jour d'une forte expérience sur un type de chambre à système d'injection équipé de vrilles à géométrie ou section de passage variable (figure 2).

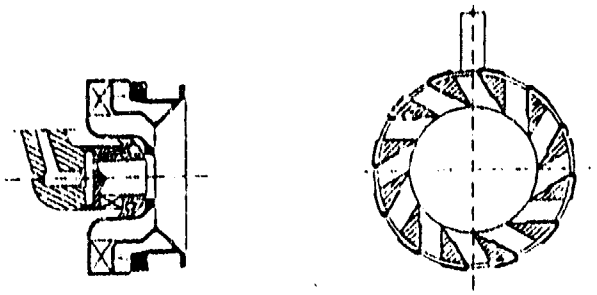

Figure 2 : Système d'injection à géométrie variable

Ce concept permet de moduler la richesse zone primaire en fonction de la richesse globale de fonctionnement du foyer (cf figure 3) permettant ainsi d'élargir le domaine de fonctionnement de ce dernier.

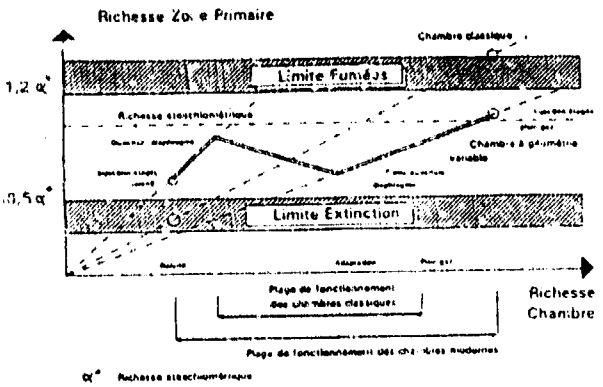

Figure 3 : Chambre à géométrie variable

En effet, au régime ralenti, les vrilles sont fermées de telle sorte que la richesse zone primaire soit ainsi supérieure à celle que l'on aurait dans un foyer classique, permettant ainsi de conserver une stabilité satisfaisante.
Au régime plein gaz les vrilles, totalement ouvertes, admettent un débit d'air zone primaire supérieur à celui rencontré dans un foyer conventionnel, permettant d'obtenir des richesses et des températures plus faibles, donc des niveaux de fumées et d'oxydes d'azote beaucoup plus bas.

2. OPTIMISATION DE LA DISTRIBUTION DE RICHESSE ZONE PRIMAIRE

Le fait de moduler le débit d'air fond de chambre, permet de conserver dans tout le domaine de fonctionnement du moteur des richesses zone primaires optimales.
En conséquence les cartes de température issues de la zone primaire s'avèrent plus régulières que sur un foyer conventionnel. La présence d'une zone de dilution n'est plus aussi strictement indispensable.
La position des trous primaires par rapport au fond de chambre, ainsi que la distribution de richesse dans la zone primaire deviennent des paramètres à optimiser. Des études ont été réalisées en ce sens à Snecma sur un secteur bidimensionnel à cinq injecteurs (figure 4) testé à pression modérée.

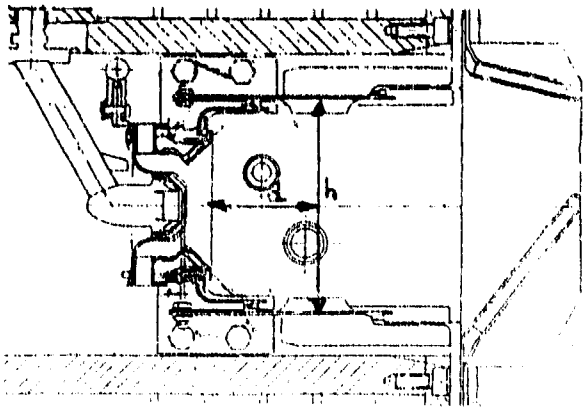

Figure 4 : Chambre à géométrie variable secteur 2D

L'influence de plusieurs paramètres a été testée.
En particulier la position des trous primaires par rapport au fond de chambre a été modifiée. La variation du domaine de stabilité qui en résulte est rapportée (figure 5).

d/h	0.5		0.6	
Pression en kPa	60	30	60	30
Richesse extinction /Richesse mini	1.6	5.4	1	2.8

Figure 5 : Evolution de la richesse d'extinction en fonction de la distance des trous primaires au fond de chambre. Résultats sur secteur à cinq injecteurs.

Il apparaît très logiquement une amélioration sensible de la stabilité lorsque les trous primaires sont éloignés du fond de chambre. Les niveaux d'oxydes d'azote obtenus, bien que très inférieurs aux valeurs qui seraient atteintes sur un foyer conventionnel, se dégradent cependant de 15 % environ.

En parallèle le rendement ralenti s'améliore de 96 à 93 %.
Dans le concept à géométrie variable étudié, le débit d'air fond de chambre traversant les swirlers varie suivant les régimes. En conséquence l'aérodynamique de la zone primaire est modifiée, en particulier dans les configurations où les jets primaires sont très proches du fond de chambre.
Afin de quantifier ces phénomènes, des études d'analogie hydraulique ont été effectuées sur une maquette en plexiglas par le CERT-ONERA.
Le débit des orifices primaires recirculant diminue lorsque le débit au travers des swirlers augmente (figure 6).

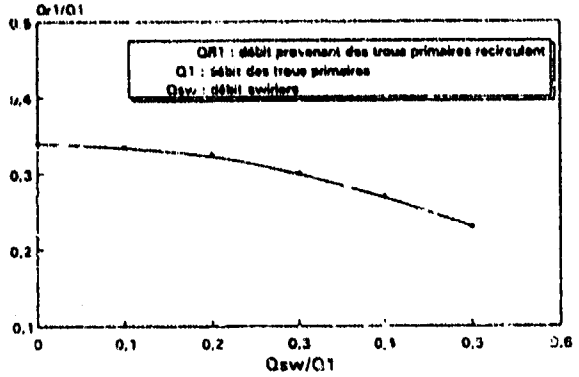

Figure 6 : Détermination expérimentale du débit recirculé Q_{R1} en fonction du débit swirlers

En plus de ces études plusieurs concepts différents de volles ont été caractérisés afin de sélectionner ceux conduisant aux résultats les plus satisfaisants.

3. CARACTERISATION GLOBALE DU CONCEPT

Les études d'optimisation de zone primaire et d'injection, dont certaines sont décrites précédemment, ont servi de base à la définition d'un foyer annulaire à géométrie variable (cf figure 7)

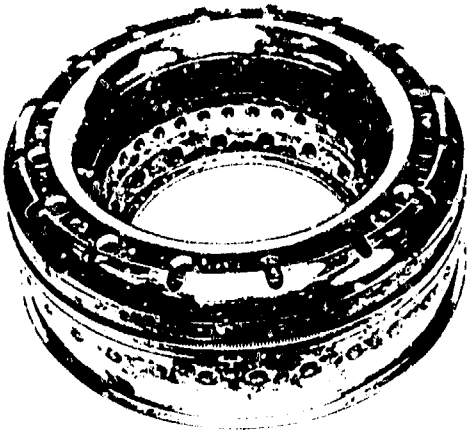

Figure 7 : Chambre à geométrie variable

Cette chambre présente la particularité d'être très courte par rapport à une chambre conventionnelle (d'environ 20 %), ce qui permet de réduire de façon sensible le débit de refroidissement.
Les performances en stabilité sont très satisfaisantes.
Bien que la quantité d'air admise en zone primaire soit plus importante que sur un foyer conventionnel (+ 40 %) la stabilité à pression atmosphérique est comparable. Les pressions de rallumage en altitude sont améliorées d'environ 10 kPa.
Les profils de température sortie foyer sont, malgré la faible longueur, et l'absence de zone de dilution très bons (figure 8)

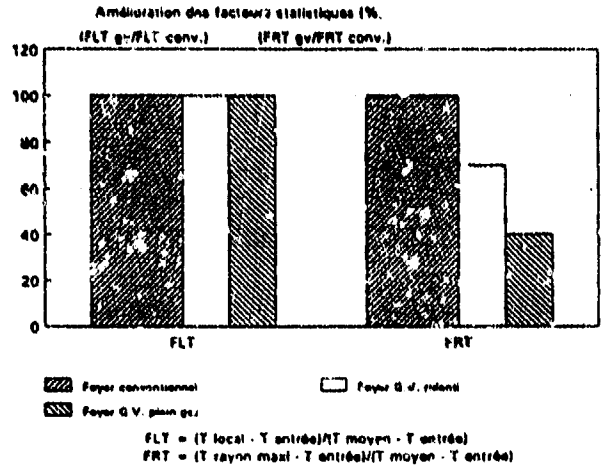

Figure 8 : Profils de température en sortie foyer

Cette performance, due à l'optimisation de la zone primaire, s'avère particulièrement précieuse dans le cas de cycles thermodynamiques très chauds. Il faut noter d'autre part que la variation de ces paramètres suivant les régimes de fonctionnement est faible.

CONCLUSION

Les bons résultats obtenus à Snecma à la fois sur secteur bidimensionnel et sur chambre annulaire démontrant l'aptitude du concept à géométrie variable à répondre aux spécifications de performances des chambres de combustion des moteurs caractérisés par de fortes températures de sortie foyer.
En effet, un bon compromis peut être obtenu entre les performances plein gaz et les performances ralenti, tout en conservant en parallèle des profils de température très homogènes.
Les travaux de recherches continuent sur ce thème à la fois sur le plan expérimental et en utilisant des méthodes de prédiction 3D afin d'adapter ce concept à des cycles encore plus chauds, c'est à dire à richesse de fonctionnement foyer encore plus importante. Pour ce faire le débit de refroidissement doit être aussi bas que possible. En parallèle le système d'injection doit permettre le passage d'une masse d'air de plus en plus importante.

La réalisation de foyer fonctionnant à des richesses très élevées n'est plus concevable sans lever certaines contraintes induites par une géométrie fixe de foyer à une seule tête. Malgré la relative complexité technologique induite, les systèmes à géométrie variable permettent de résoudre ces difficultés.

Les auteurs remercient la DRET/GT et le STPa/Mo pour le soutien financier qu'ils ont apporté à la réalisation de ces travaux.

REFERENCE

/1/ G. BAYLE-LABOURE
Pollutant emissions from aircraft engines
Forum Européen sur la Propulsion
DGLR - AAAF - Avril 1990, Cologne

/2/ A.J. CIFONE and L. KRUEGER, Combustion Technology : a Navy Perspective, AIAA/SAE/ASME/ASEE 21st joint Propulsion Conference, AIAA paper 85 - 1400, July 1985

/3/ D.W BAHR
Technology for the design of high temperature rise combustors
AIAA - 85 - 1292

/4/ G. BAYLE-LABOURE
Developpement of new combustor technologies at Snecma, 7th ISABE, September 1986

/5/ M. DESAULTY
Turbine engine combustor design at Snecma
ISABE 91/09
Nottingham E-B

The Influence of Air Distribution on Homogeneity and Pollutant Formation in the Primary Zone of a Tubular Combustor

J R Tilston, M I Wedlock and A D Marchment

Defence Research Agency (Pyestock)
Farnborough
Hampshire
GU14 OLS
England

SUMMARY

This Paper summarises the work undertaken by the Defence Research Agency (DRA Pyestock) for the BRITE/EURAM Low Emissions Combustor Technology Project No 1019. The work was jointly funded by the CEC (DGXIIH), the UK DTI (CARAD - ATF4) and the UK MOD (DCSA).

The gas turbine emissions problem is summarised and the design philosophy of the experimental programme is described. The principal objective was to demonstrate a simultaneous reduction of NO_x and smoke emissions together with acceptable idling emissions and stability in an unstaged combustor. A secondary objective was to demonstrate the extent to which NO_x and smoke could be reduced if the combustor was to be used as the main stage of a staged combustor where a poorer idling performance could be accepted. The work consisted of a parametric investigation of the principal factors controlling the emissions produced in the combustor primary zone. Particular emphasis was placed on the influence of the distribution, number and size of air entry holes and of residence time on pollutant formation.

The results from the complete experimental programme are summarised. These suggest that NO_x reductions of about 30-40% should be possible together with excellent smoke and idling performance. The results suggest that NO_x was formed very close to stoichiometric flame temperatures even at very weak combustor mixture strengths and under well mixed conditions. The reductions that were achieved were largely as a result of reductions of residence time.

1 INTRODUCTION

The significant emissions that are generated by gas turbines are unburned fuel, carbon monoxide, smoke and oxides of nitrogen (NO_x). For stationary gas turbine sources, limits have been placed on most of these emissions by National regulatory authorities whilst for aviation recommended levels have been set by ICAO.

In the past, the emission of oxides of nitrogen has been seen as such an intractable problem that the "control" of these emissions has been no more than a capping level set at a value that represents the status quo. Part of the argument in favour of this approach has been that higher efficiency cycles inherently produce more NO_x and that fuel efficiency is more important than the relatively small NO_x emissions from gas turbine sources. In more recent times the problems of acid rain, photochemical smog, high ozone concentrations at sea level and ozone depletion in the stratosphere have become much more evident. All these problems are, to some extent, a result of NO_x emissions. It is clear that the tolerant view of gas turbine NO_x emissions is no longer acceptable and that much more than a token reduction will be required to improve the situation.

Reductions in NO_x of the order of 30% relative to the traditional levels such as those described by Lipfert[1] can be achieved by optimisation of "traditional" combustion geometries. However, at the time when this research programme was planned no engineworthy technology existed to reduce NO_x by more substantial amounts on a predictable basis without severe smoke, stability or efficiency penalties. At the same time as the reductions in emissions are being required, combustors are being run increasingly rich as a result of increases in cycle efficiency. As a result it is becoming increasingly difficult to achieve a satisfactory allocation of the limited air supply to the various uses such as wall cooling, the control of pattern factor and emissions control.

2 THE DESIGN OF THE EXPERIMENT

Because emissions measurements are made at the combustor exit plane, the emissions production/consumption performance of a given design of primary zone can be masked to a large extent by any chemistry that takes place further down the combustor. It is easy to see, for instance, that the performance of a low NO_x primary zone would be masked if high levels of NO_x were produced further down the combustor. For this reason, the work described here was based on a series of experiments performed on isolated primary/intermediate zones.

Presented at an AGARD Meeting on 'Fuels and Combustion Technology for Advanced Aircraft Engines', May 1993.

These were run at air loadings typical of advanced aero combustors appropriate to both military and civil applications.

3 TEST PROGRAMME

A generalised view of a combustor within the test rig environment is shown in Figure 1. Three basic types of combustor configuration were studied. These ranged from the "conventional", with an overall recirculation zone, to "plug flow" combustors with direct air injection through the combustor head from a very large number of air entry holes (see Figures 2a to 2c). Jet mixed combustor designs were used in this programme because of their simplicity[2,3] and the ease with which air mass flow (and therefore air/fuel ratio and residence time) could be calculated.[4]

The programme used a relatively small number of items of hardware. These were permutated to produce a range of geometries and conditions so that the separate effects of parameters such as atomiser air/fuel ratio, combustor pressure loss, overall residence time and air placement could be identified. All the combustors used in the programme were identical in shape and volume. They were constructed from Rolls-Royce "transply" sheet material[5] so that, before the primary combustion entry air holes were drilled, they were all of equal porosity.

At the design stage the flow distribution and pressure loss were calculated for each type of combustor configuration. The air entry holes were sized such that all the combustors would have the same pressure loss (about 4%) at standard operating conditions. Two additional versions of each datum combustor type were then designed with exactly the same hole configuration but with primary holes 20% greater and 20% smaller in area. These variations in primary hole area affected the overall combustor porosities by about 9% and combustor pressure loss by about 18% (depending on the exact combustor configuration). It was assumed that the relatively small change in primary hole diameter itself would have negligible effect on the combustion process.

Aviation kerosine fuel (AVTUR) was used throughout the programme. The effects of varying operating conditions, such as pressure loss, would have changed the atomisation quality produced by an airspray atomiser and this would have masked the effect of other experimental variables on emissions. To avoid this problem an air assist atomiser, using an external compressed air supply, was used throughout the programme. This ensured that the atomisation quality and fuel placement was the same for all combustors and that valid comparisons could be made between different combustors and tests.

The spray from this atomiser was injected into a stream of combustor air flowing into the combustor through an annular passage around the atomiser head. Three simple, replaceable air control sleeves were used to alter the flow area of this annular passage and thereby to change the atomiser air/fuel ratio.

3.1 Combustor Design

Because of the very wide variations of geometry that are possible even within the three basic combustor types, two versions of each were built. In order to limit the size of the test programme these were subjected to a limited, preliminary test programme[6] in order to select the best combustor of each pair to go into a more comprehensive test programme. The full range of combustor builds employed in the programme is shown in Figure 3.

3.2 Test Conditions

The combustors were run at an idle condition typical of that of a modern, high pressure ratio engine: Combustor pressure 5.1 Bars, inlet air temperature 500K, residence time was approximately 3.24 ms (based on the mean exit temperature). Measurements were made at three different air/fuel ratios in order to determine the efficiency characteristic and to obtain some idea of the weak stability of each design. The combustors were then run at a simulated maximum power condition with a datum air mass flow, a reduced mass flow (-10 or 20 %) and an increased mass flow (+10 or 20%). Test points nominally at 24, 28 and 32 overall air/fuel ratio were set up for each air mass flow. These overall air/fuel ratios correspond to effective combustion process air/fuel ratios of 16,18 and 21 because of a relatively high percentage of wall cooling air. Simulated high power conditions were as follows: combustor pressure 5.1 Bars and air inlet temperature 850K. Residence times (based on a mean gas temperature of 2100K) varied between 2.4 and 4.1 ms depending on the air mass flow.

3.3 Test Conditions and Combustor Build Matrix

An example of the matrix of combustor builds and test conditions that were explored for each of the generic combustor types is shown in Figure 4. Point "A" indicates the atomiser air-fuel ratio/pressure loss characteristic of a combustor build having a fixed primary air entry hole area and a fixed porosity barrel. The combustor is being operated at a fixed (datum) air mass

flow. The atomiser air/fuel ratio of this combustor can be altered, for further tests, by changing simple mechanical sleeves that control the atomiser main airflow. When the control sleeve size is increased in stages (increasing main atomiser airflow) and the combustor is run again at the datum air mass flow the combustor characteristics move from A to B to C. At the same time there is a modest reduction in combustor pressure loss due to the small increase in atomiser air flow area. If a new combustor head is manufactured with the same hole geometry and the same number of holes but with slightly larger diameters this will produce combustor builds that have a new set of characteristics D, E and F. These combustor builds are being run at the same mass flow as A, B and C and therefore have the same residence time but have a lower pressure loss. As part of the analysis process the results of tests between builds A and D, B and E, and C and F, can be compared to see the effects of pressure loss on emissions. (Adjustments first need to be made to any data to correct for the effects of the small changes in atomiser air/fuel ratio).

If combustor builds on the A, B, C characteristic are run with 20% less airflow they will have the same pressure losses as combustors on the D, E, F characteristic but will have a 20% greater residence time. Conversely the builds on the D, E, F characteristic can be run at a 20% higher mass flow to give the same pressure losses as builds on the A, B, C characteristic but have a 20% lower residence time.

In a similar way, decreasing the combustor hole areas produces combustors G, H and I. These can either be run to give either a higher pressure loss than A, B and C or a higher residence time.

During the analysis of results the separate effects of varying residence times, atomiser air/fuel ratios and combustor pressure losses can be extracted from the results from this matrix of builds and tests by cross plotting and interpolation techniques.

4.0 MEASUREMENTS

Samples for gas analysis were taken from the combustor exit plane by means of a gas sampling probe that was cooled and conditioned to 150°C by means of a pressurised hot water system. At the start of the programme, for a limited number of tests, individual gas samples were taken, using a single point probe, to produce 55 point maps of the combustor exit. The gas samples were analysed for unburned fuel, carbon monoxide, carbon dioxide, oxygen, nitric oxide, nitrogen dioxide and smoke. Combustion efficiencies, emissions indices and gas temperatures were calculated from these measurements. Because of the wide range of gas temperatures in the gases leaving the combustor it was necessary to apply density weighting corrections to the gas analysis data in order to calculate true overall values[7]. After completion of this data processing the agreement between the air/fuel ratios measured by the rig meters and the averaged gas analysis air/fuel ratio was generally better than ±2%. The data generated from the 55 point survey was subsequently used to justify the use of a five hole averaging rake that allowed a much faster rate of data gathering. This probe was traversed across the combustor exit duct in eleven steps with full gas analysis and SAE smoke measurement at each step. The average species concentrations, gas temperatures etc were then calculated as before on a mass weighted basis from the eleven separate analyses.

Where comparisons have been made between experimental NO_x emissions and the Lipfert correlation the Lipfert Emissions Indices have been corrected down to experimental pressure levels using the familiar $P^{0.5}$ relationship. This allows the absolute experimental NO_x EI's to be used throughout the Paper.

Combustor wall temperatures were monitored using temperature sensitive paints. Because of the long duration (≈4 hours) of each test and the wide range of test conditions, the paints only gave an approximate indication of the highest temperature reached during the test.

Flow visualisation tests of the three combustor types were also undertaken.[8] In these the flow fields within the combustors were mapped together with surveys of residence time and mixedness throughout the combustor volume. These results are not presented here due to lack of space.

5.0 RESULTS

Many simple relationships between parameters (the dependency of NO_x on pressure loss, for example) are presented in this section. These have been generated at DRA by traditional interpolation and cross plotting methods to eliminate the effects of the other variables. One consequence of this process is that the data have been smoothed. These relationships should therefore be seen as trends rather than indicating absolute values.

In addition to the analysis undertaken at DRA a separate analysis was also made at Rolls-Royce[9] (with considerably less manual effort) using a statistical

method. The trends indicated by the DRA and Rolls-Royce analyses were in excellent agreement.

Due to the immense quantity of results that were generated in this programme, there is only space in this paper to publish quantitative data for one combustor. Detailed results from the entire programme have been published in references 6, 10 and 11.

Some builds of both Type 1 and Type 2 combustors produced excellent and comparable performances. In practical terms, the performances of the Type 3 combustors were inferior to those of the other two - largely because the fast, intimate mixing of fuel and air was not fully achieved. The results presented here concentrate largely on the quantitative data from the Type 2 combustors.

5.1 Performance of the type 1A combustor

A full set of data for these combustors has been published in Reference 10. The combustor that was judged to have returned the best performance was a low porosity build with a high atomiser air/fuel ratio. The combustor pressure loss (≈4.5%) was rather high as a result of the low porosity. Idling efficiency was ~98.8% at 60 AFR. High power smoke was about 8 SAE at 20 AFR falling to 1 SAE at 30 AFR. High power efficiency was close to that which could be achieved under chemical equilibrium conditions, (~98.5% at an overall AFR of 20). NO_x reductions of ≈ 18% were achieved at 20 AFR and reductions of ≈37% were achieved at 28 AFR.

The results of the analysis of the effects of individual parameters can be summarised as follows: The effect of increasing combustor pressure loss was to cause an increase in NOx. On the other hand increasing pressure loss also tended to produce a reduction in smoke emissions. This would seem logical since, in a relatively poorly mixed primary zone, improvements in mixing (as a result of increased mixing energy) would cause earlier, more complete combustion. This in turn would lead both to lower smoke and to higher NO_x.

NO_x emissions were strongly reduced by shortening combustor residence time. This reduction in NO_x appeared to be independent both of overall air/fuel ratio and atomiser air/fuel ratio. In contrast residence time variations had only a minimal effect on smoke and full power efficiency.

NO_x emissions were reduced quite strongly as a result of weakening overall air/fuel ratio. The rate of reduction of NO_x with air/fuel ratio was independent of the other variables such as pressure loss and residence time. Smoke emissions too decreased very strongly as the overall air/fuel ratio was weakened. As with the NO_x emissions there was a characteristic rate of smoke decrease with air/fuel ratio that was independent of other factors such as residence time and pressure loss.

The effect of atomiser air/fuel ratio on NO_x was more complex. For the lower pressure loss, high residence time conditions NO_x tended to rise as atomiser air/fuel ratio was weakened. At the same time the data suggested that the increase peaked or at least levelled out at atomiser air/fuel ratios in the range 1 to 2. For the high pressure loss, low residence time conditions the NO_x tended to fall initially and then rise as the air/fuel ratio was weakened further. Smoke levels were very markedly reduced as atomiser air/fuel ratio was weakened.

5.2 Performance of the 2B type combustor

A full description of the details of combustor design and performance for the full set of combustors has been reported in References 10 and 11. The emissions characteristics are shown in Figures 5a to 5d. This was a high porosity, medium atomizer air/fuel ratio combustor build. For this type 3 set of combustors there were several builds that were very close in performance to the one that was finally selected. Indeed some of these alternative builds produced distinctly better performance in some respects than the one that has been selected.

When test data for several tests of this type of combustor were analysed it was found that the combustion efficiencies of many gas samples were higher than would be predicted by chemical equilibrium calculations. In consequence calculated gas temperatures for these points were up to 100C higher than equilibrium values. For the richest mixtures and lowest efficiencies the equilibrium composition becomes difficult to define absolutely and efficiencies higher than "equilibrium" can readily be accepted. However close to stoichiometric conditions, equilibrium properties can be defined accurately and samples that appear to be more efficient are less easy to accept without investigation.

There was therefore some concern that these high efficiencies had been caused by recombination reactions as a result of a failure of the gas sampling probe to quench samples adequately. In order to investigate this possibility, the efficiencies of individual gas samples from this combustor were compared, Figure 6a, with those from combustor 1A at comparable conditions, Figure 6b.

This comparison showed that, at the most efficient conditions, a very large number of near stoichiometric samples from combustor 1A lay at the equilibrium concentration boundary or very close within it. This showed that the samples had been properly quenched and that the performance of the probe was satisfactory. Additional evidence was available in the form of abnormally high NO_x concentrations that were associated with the high efficiency/ high temperature samples. It was concluded that the high efficiencies in combustor 2B were a result of genuine super-equilibrium CO_2 concentrations in the near stoichiometric mixtures and were a feature of the combustor design.

As with combustor 1A, increases in combustor pressure loss caused an increase in NO_x emissions, Figure 7a. The rate of increase was higher for short residence times and for weak atomiser air/fuel ratios. In other words the combination of long residence time and good mixing produced most NO_x. Smoke emissions, Figure 7b, were reduced by increasing pressure loss however the effects were practically independent of residence time.

Reductions in residence time (increasing air mass flow), Figure 7c, produced reductions in NO_x emissions. These reductions were most pronounced for weak atomiser air/fuel ratios but only slight for rich air/fuel ratios. The rate of reduction appeared to be almost independent of pressure loss. Unlike the behaviour of combustor 1A, reductions of residence times in combustor 2B produced strong reductions in smoke levels, Figure 7d. It can be seen that there were associated effects of pressure loss and atomiser air/fuel ratio.

Weakening overall air/fuel ratio resulted in quite substantial reductions in NO_x emissions, Figure 7e. A combination of weak overall air/fuel ratio, weak atomiser air/fuel ratio and short residence time produced the overall best result. Idling efficiency was satisfactory for this combination of conditions but when it was weakened even further the combustor suffered from sudden weak extinctions at about 70 AFR. Smoke levels were very strongly reduced by weakening the overall combustor air/fuel ratio, Figure 7f.

Weakening the atomiser air/fuel ratio produced a NO_x characteristic having a maximum at an air/fuel ratio of about 2, Figure 7g. In contrast smoke emissions can be seen to pass through a minimum at about the same time, Figure 7h. The very low NO_x emissions at the rich atomiser AFR and the high smoke numbers at weak atomiser AFR are features of this method of data analysis and could not be achieved in practice.

5.3 Performance of type 3B combustors

A full set of constructional data and test results are given in References 10 and 11. The combustor build that is judged to have produced the best performance was a high porosity, high atomiser AFR version of the combustor type. None of the type 3B combustors produced both high idling efficiency and high full power efficiency. Full power efficiencies were much poorer than the efficiencies of the type 1 and type 2 combustors and always well below equilibrium levels.

Analysis of the distributions of individual gas samples showed that the data tended to fall into separate rich and weak distributions. At the richer conditions - around 22 AFR - NO_x emissions were the lowest recorded for any of the combustors tested in this programme. This, however, was the direct result of the low combustion efficiencies. For example NO_x emissions actually increased when the air/fuel ratio was weakened and the combustion efficiency improved. At the weakest conditions NO_x emissions were practically the same as those from combustors 1A and 2B although combustor 3B was still less efficient than the other two. The build of combustor that produced the best results suggests that it might be possible to achieve a very substantial NO_x reduction together with satisfactory smoke by running at 24 AFR. However, to achieve this it would be necessary to recover the missing combustion efficiency without producing any additional NO_x.

In contrast with combustor types 1 and 2 increasing pressure loss had the effect of producing modest reductions of NO_x and increases in NO_x. The reason for this anomalous behaviour is unclear. One argument would suggest that increased inlet air kinetic energy should have produced improvements in turbulent mixing and that this should have produced improvements in combustion and increases in NO_x. On the other hand it is probable that the combustors were poorly mixed, with the bulk of the combustion taking place in a low residence time, rich, core flow. Under these circumstances increases in inlet air velocity would further reduce residence time, with only a minimal improvement in mixing. This mechanism would be consistent with the known fluid dynamics of the combustors and with the observed effects of residence time and would explain the observed NO_x results.

Weakening the overall air/fuel ratio resulted in modest increases in NO_x. At the same time the very high smoke levels

(in the region of 50 SAE at 20 AFR) reduced to about 10 SAE at 29 AFR.

Increasing atomiser air/fuel ratio resulted in modest increases in NO_x throughout the range of air/fuel ratios tested. At the same time smoke emissions passed through aminimum at an atomiser air/fuel ratio of about 1.8 and then rose again.

6.0 DISCUSSION

Work was undertaken early in the programme[2], to construct models of NO_x production that would describe the results that had been obtained up to that time. It quickly became clear that it was only possible to predict sufficiently high NO_x emissions indices if production was assumed to occur at conditions very close to stoichiometric flame temperature. As the test programme continued, additional evidence was accumulated that supported this assumption. The evidence and arguments in support of the theory are described below.

The approach that was adopted, was to calculate the levels of NO_x that would have been produced if premixed combustion had taken place in mixtures weaker than stoichiometric. The calculations were validated using practical data from premixed combustion experiments. These predictions were then compared with measured data from the experimental tests.

Data from Coats experimental premixed combustion studies[12] is shown in Figure 8a. These data were obtained at similar temperatures and pressures to those employed in the present programme although the residence times were much longer (12 to 20 ms). A semi-empirical NO_x production equation from Reference 13 was selected to correct the Coats NO_x data to the temperature, pressures and residence times of the present experiment. First, in order to validate the equation, it was used to predict NO_x levels for one of Coats experimental conditions. The prediction, in Figure 8a, can be seen to compare well with the measured data. This validated equation was then used to calculate NO_x emissions indices over a range of premixed mixtures strengths, at the higher inlet temperature and the much shorter residence time of the present experiment. These predictions are also shown in Figure 8a. It can be seen, for example, that a NO_x emission index of about 11 would have been produced if combustion had taken place in a weak fuel/air mixture ($\Theta = 0.75$) in the experimental combustor. In contrast, Figure 8b shows data from individual gas samples taken at the exit plane of combustor 2B during the present work. This shows no examples of NO_x emissions indices lower than about 18[1]. Figure 8a therefore indicates that a NO_x emissions index of 18 must have been produced by combustion in an environment at 0.90 of stoichiometric or richer even if a longer than average residence time is assumed. It is not even possible to conclude that any combustion *did* actually take place as weak as $\Theta = 0.90$. This is because the lowest NO_x emissions indices that were measured could have been the result of low combustion efficiencies or shorter than average residence times.

The high emissions indices that can be seen in Figure 8b are almost certain to be simply the result of combustion products having long residence times at peak flame temperatures. However, the mean emissions indices for all three air/fuel ratio conditions lay between 22 and 25 and it must be concluded therefore, that the bulk of the NO_x was generated in environments very close to stoichiometric flame temperatures.

Although no evidence was found of combustion in weak mixtures, in practice, weakening the combustor air/fuel ratio was shown to reduce NO_x emissions. The principal reason for this would seem to be that weaker operation reduces the residence time at the high flame temperatures where NO_x is generated. This is either because of the reduction of flame volume if the fuel flow is reduced, or as a direct reduction of residence time if airflow is increased. If it is assumed, for example, that flame volume (residence time) is reduced by ≈ 20% when the combustor is weakened from 24 to 30 AFR then Figure 8a suggests that the NO_x emissions index would be reduced by the 2-3 units that were observed in practice.

In summary the evidence strongly suggests that, although attempts were made in some combustor designs to produce very fast mixing and weak combustion, the fluid dynamic mixing rates were always slower than chemical reaction rates. The result was that the combustion process always occurred very close to stoichiometric conditions before the fuel/air mixture could be diluted to weaker air/fuel ratios. What was actually achieved was a reduction in thermal NO_x as a result of reducing the residence time. Indeed in some of the Type 3 combustor builds the residence time was reduced so much that not only was NO_x reduced but the hydrocarbon combustion chemistry itself was not completed.

7.0 CONCLUSIONS

7.1 The effects of the air admittance geometry, combustor pressure loss, atomiser air/fuel ratio, residence time

and overall air fuel ratio on emissions have been systematically explored. Combustors having a wide range of air energy geometries have been constructed and thirty different combustor builds have been studied in detail.

7.2 The combustors and the test programme were designed so that the effects of individual variables, such as residence time, could be isolated by data reduction methods.

7.3 Some builds of well mixed combustor have been found to produce combustion efficiencies higher than equilibrium levels at air/fuel ratios in the region of stoichiometric. Low smoke emissions are produced under these conditions but high NO_x emissions are produced as a result of the higher than equilibrium temperatures.

7.4 For some of the more successful combustor builds, full power operation with short residence times and effective mixtures strengths of about 20 AFR (about 30 AFR overall) produced NO_x reductions of about 30 - 40%. At the same time full power efficiencies close to the theoretical equilibrium values were obtained together with low smoke emissions. Combustion efficiencies in excess of 99% were achieved at the equivalent idling condition.

7.5 The results suggest that the NO_x was generated in environments very close to peak flame temperatures. There is no evidence that any combustion took place in mixtures weaker than about 0.90 stoichiometric. As a result it is concluded that reaction rates were always much faster than fluid dynamic mixing rates and that the observed NO_x reductions were achieved by reducing residence times thereby limiting thermal NO_x production .

7.6 The parametric analysis of the results indicated a complex variety of trends amongst the various combustors depending on the combustor geometry. The results of these analyses have been described.

[1]*The sample stoichiometries shown in Figure 21b only indicate the sample mixture strengths as measured at the combustor exit plane and do not describe the history of the samples within the combustor*

Acknowledgements

The authors would like to record their appreciation of the work of colleagues at Rolls-Royce, AIT and the BRITE-EURAM Partners in support of this programme.

References

1 Lipfert — Correlation of gas turbine emissions data. ASME Paper No 72-GT-60 March, 1972

2 J R Tilston, J P D Hakluytt — The Design and Performance of a Combustor with a Multiple Jet Primary Zone AGARD, CP No 353 Cesme, Turkey, 1984

3 R V Cottington, J P D Hakluytt, J R Tilston — The Development of a Diesel Burning Combustion Chamber with a Multiple Jet Primary Zone ASME 87-GT-140 Anaheim, USA, 1987

4 M Ludascher — NO_x Prediction Model for an Aero Engine Combustor RAE Tech Memo P1211 Defence Research Agency, July 1991

5	A B Wassell J K Bhangu	The Development and Application of Improved Combustor Wall Cooling Techniques ASME 80-GT-66 March, 1980
6	J R Tilston M I Wedlock A D Marchment	Low Emissions Combustor Technology - The Influence of Air Distribution on Homogeneity and Pollutant Formation in the Primary Zone of a Tubular Combustor DRA Contract Report RAE/CR/PROP/0002 Defence Research Agency, February 1992
7	J R Tilston	The Averaging of Gas Analysis Data Allowing for Density and Velocity Weighting RAE Tech Memo P1213 August, 1991
8	J W Bateson	Flow Studies on a Perspex Primary Zone Research Model Aero & Industrial Technology Ltd Combustion Technology Centre Report No B49 907 October, 1991
9	R Britton	Application of Taguchi Statistical Experimental Design to DRA Combustor Experimental Data Rolls-Royce CRR 89731 February, 1992
10	M I Wedlock J R Tilston A D Marchment	Low Emissions Combustor Technology - The Influence of Air Distribution on Homogeneity and Pollutant Formation in the Primary Zone of a Tubular Combustor. Part II Combustor Builds and Test Builds Data Bank DRA Contract Report DRA/CR/AP5/92/01 Defence Research Agency, July 1992
11	J R Tilston M I Wedlock A D Marchment	The Influence of Air Distribution on Homogeneity and Pollutant Formation in the Primary Zone of a Tubular Combustor Part III - Design of the Experiment and Summary Report DRA Contract Report DRA/CR/AP5/92/02 June 1992.
12	C M Coats	Experiments on a High Pressure Premixing/Prevaporising Combustor RAE Tech Memo P1099 January, 1987
13	J Odgers D Kretschmer	The Predictions of Thermal NO_x in Gas Turbines Int. Journal of Turbo and Jet Engines 5, pp 225-232, Quebec, 1988

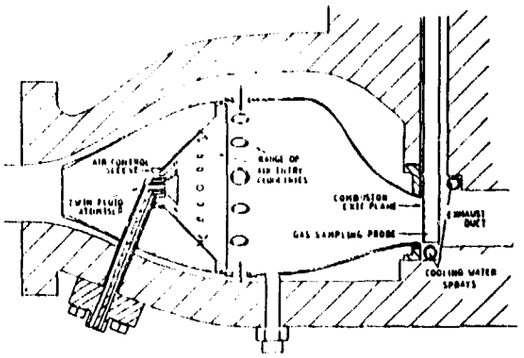

figure 1: General view of an experimental combustor in test rig.

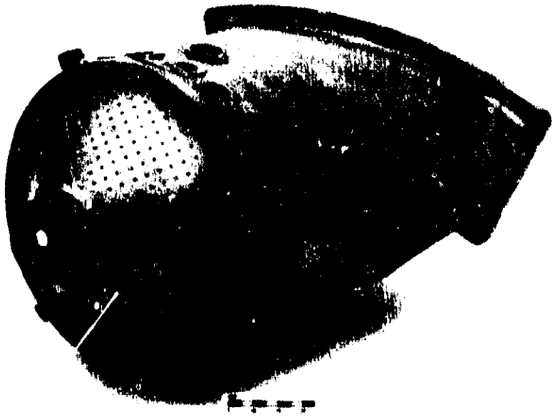

figure 2a: Combustor type 1A.

figure 2b: combustor type 2B.

figure 2c: Combustor type 3B.

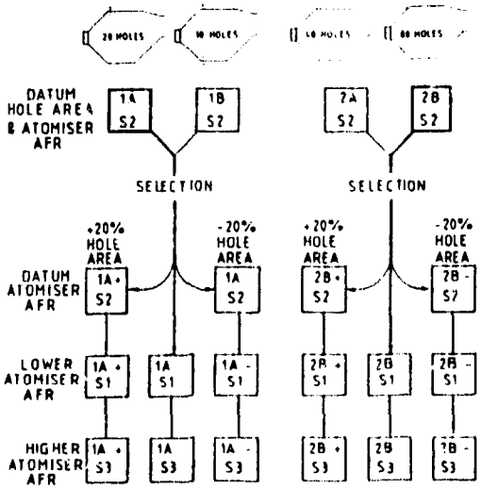

figure 3: Range of combustor builds used in test programme.

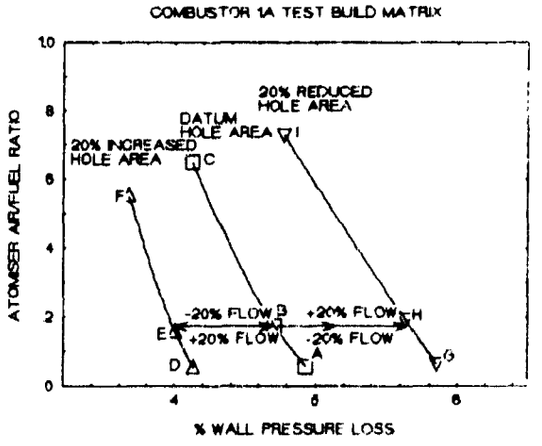

figure 4: Combustor build test matrix

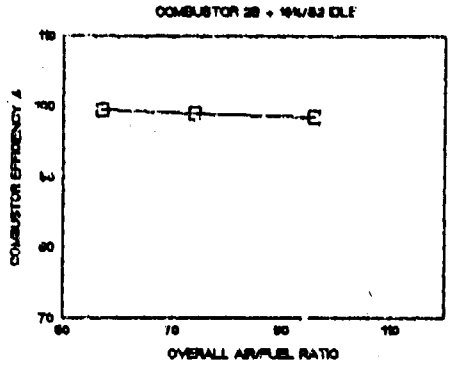

figure 5a: 2B Combustor-Effects of overall AFR on idle combustion efficiency.

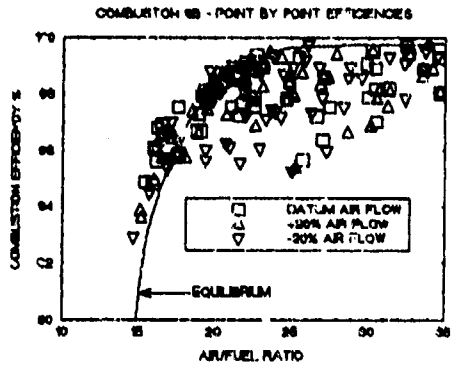

figure 6a: 2B combustor-Individual sample combustion efficiencies.

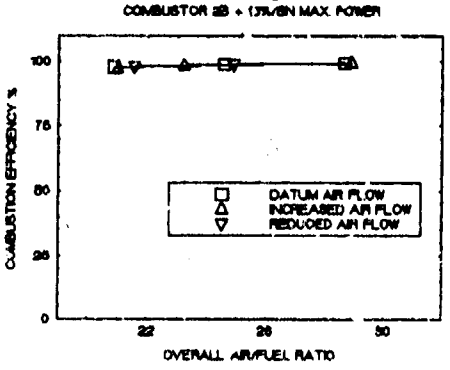

figure 5b: 2B combustor-Effects of overall AFR on max. power combustion efficiency.

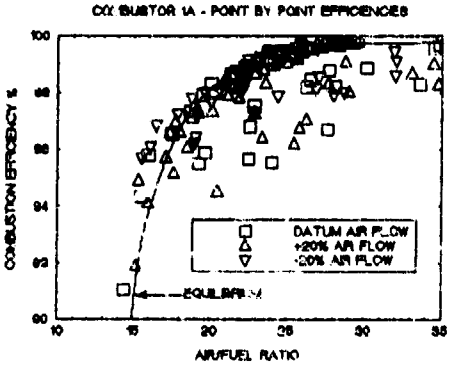

figure 6b: 1A combustor-Individual sample combustion efficiencies.

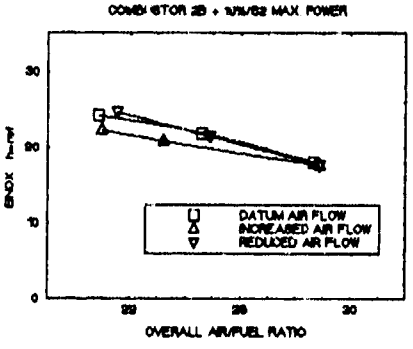

figure 5c: 2B combustor-Effects of overall AFR on NO_x.

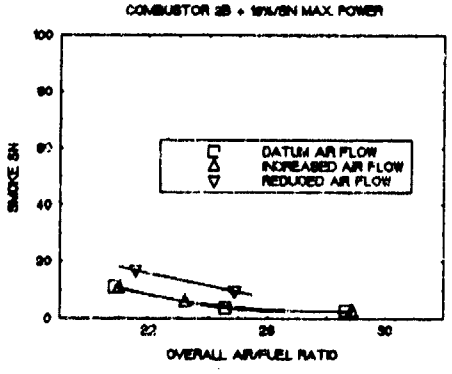

figure 5d: 2B combustor-Effects of overall AFR on smoke.

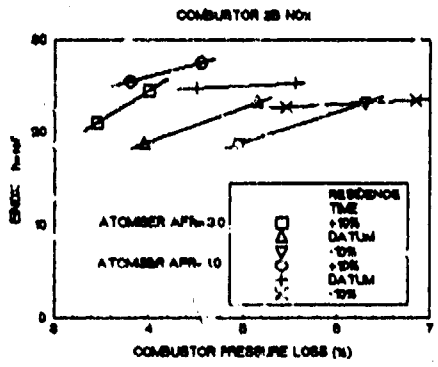

figure 7a: 2B combustor-Effects of pressure loss on NO_x.

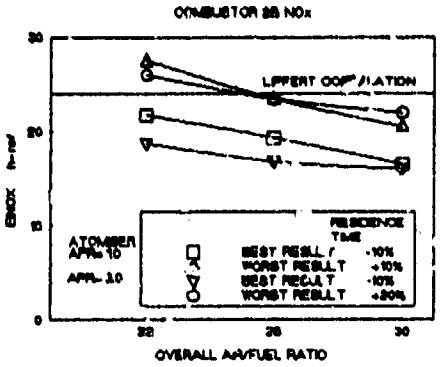

figure 8a: 2B combustor-Effects of overall AFR on NO_x.

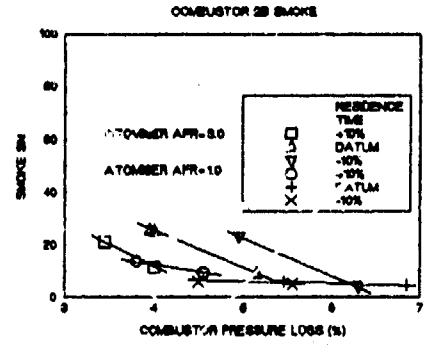

figure 7b: 2B combustor-Effects of pressure loss on smoke.

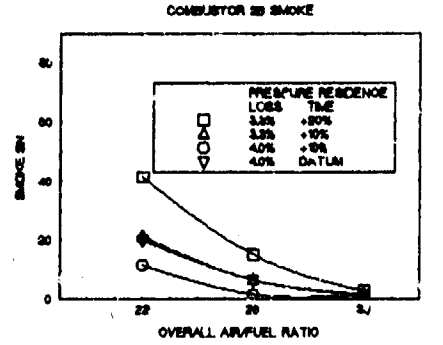

figure 8b: 2B combustor-Effects of overall AFR on smoke.

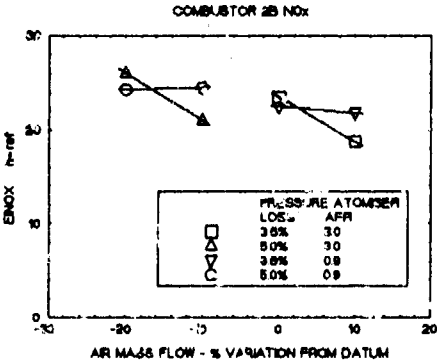

figure 7c. 2B combustor-Effects of residence time on NO_x.

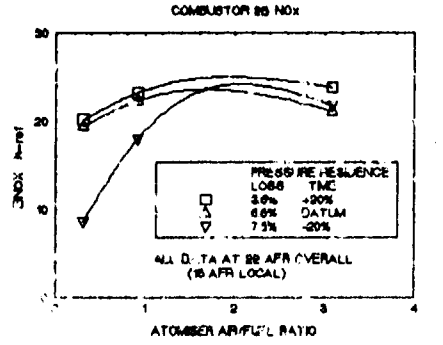

figure 8c: 2B combustor-Effects of atomiser AFR on NO_x.

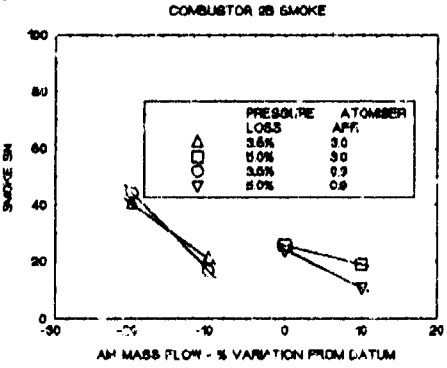

figure 7d: 2B combustor-Effects of residence time on smoke.

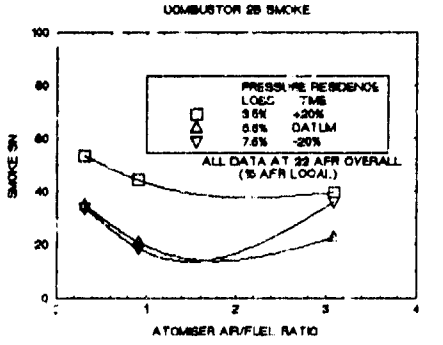

figure 8d: 2B combustor-Effects of atomiser AFR on smoke.

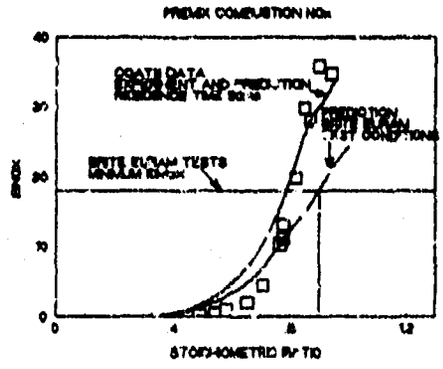

figure 9a: Predictions of lean combustion NO_x.

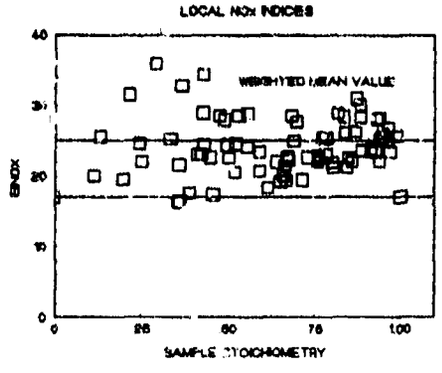

figure 9b: 2B combustor-Individual exit plane $EINO_x$ measurements.

Discussion

Question 1. P. Kotsiopoulos
What were the combustor wall temperatures observed, and how much were they affected by the differences in number, size and distribution of the holes?

Author's Reply
The measured temperatures were achieved at some unknown test condition or even during a rig operating transient, so it is difficult to be accurate. The "conventional combustor" had the highest wall temperatures and these were in the regions between the secondary air holes. This would agree well with the high NOx concentrations near these walls that were described by Professor Samuelson in Paper 28. This combustor suffered some damage during the test programme. The jet stirred combustor was significantly cooler. The plug flow combustor had very cool walls, but this was the result of a failure to distribute fuel adequately and does not indicate any improvement in integrity as a result of this design.

EFFECTS OF HYDROGEN ADDITION ON POLLUTANT EMISSIONS IN A GAS TURBINE COMBUSTOR

J. Salvá
G. López
Departamento de Motopropulsión y Termofluidodinámica
E.T.S.I. Aeronáuticos. Universidad Politécnica de Madrid
Plza. Cardenal Cisneros, 3
28040 Madrid, SPAIN

SUMMARY

This paper presents an experimental work on the control of pollutants produced in a tubular hydrocarbon fueled combustor, by the injection of hydrogen in small quantities (less than 4% of total fuel). Hydrogen is introduced in the primary zone premixed with the air. Using this technique, with lean primary zone, it is possible to reduce the NO_x emission level while maintaining CO and HC emission index at normal levels (CO and HC levels are greater without hydrogen injection).

Injecting butane, instead of hydrogen, shows that there is no beneficial effect, so the influence of hydrogen in CO and HC reduction is due mainly to factors such as hydrocarbon substitution and chemical kinetics. An analysis to estimate the contribution of these factors is also included.

LIST OF SYMBOLS

- α mass fraction of hydrogen within total fuel.
- EI emission index; mass of pollutant produced per unit mass of consumed fuel (gr/kg).
- η_q combustion efficiency
- f fuel to air mass ratio
- Φ overall equivalence ratio, $f/f_{estoichiometric}$
- Φ_{pz} primary zone equivalence ratio
- L heat of combustion per unit of fuel mass
- M molecular weight
- m total air mass flow rate
- $\dot{m}_p$ primary air mass flow rate
- $\dot{m}_s$ secondary air mass flow rate
- $\dot{m}_{pz}$ primary zone air mass flow rate
- $\dot{m}_h$ hydrogen mass flow rate
- $\dot{m}_k$ kerosene mass flow rate
- $\dot{m}_{ek}$ mass flow rate equivalent of kerosene
- P pressure
- T temperature
- V_r reference velocity
- X concentration (p.p.m.v.)

Subscripts

- h hydrogen
- i specie
- k kerosene
- z combustor inlet section

1. INTRODUCTION

A large fraction of the atmospheric pollution comes from the operation of combustion engines; about 70% of them use oil derived fuels. For aviation Gas Turbine the combustible average consumption represents a 2% out of the total, its repercussion on the atmospheric pollution can be relevant at the local levels. In fact approximately 50% of the measured pollution in airports and surroundings can be attributed to aircraft operation. On the other hand, the development of Gas Turbines with regenerative cycles and the use of ceramic materials allow a considerable increase in the turbine inlet temperature and fuel savings, what makes them competitive with reciprocating engines. So that Gas Turbines are now being considered as an alternative source of power for industrial, maritime and even for terrestrial vehicular use.

The problem of pollutants formation, as well as the influence of the operational and design variables, are basically independent of the Gas Turbine application. The reason is that the pollutants have their origin in the combustion process,and their later evolution in the turbine or the rest of elements is insignificant. It is known that, the pollutants produced by Gas Turbines are basically nitrogen oxides, unburned hydrocarbons and carbon monoxide. The smoke emissions, are almost non existent in todays engines. The production of nitrogen oxides increases with power. On the contrary, the production of unburned hydrocarbons unburnts and carbon monoxide reaches its maximum at idle.

Since the implementation of regulations on pollutants emissions, the studies and investigations of the problems of formation and pollutants reduction techniques have considerably increased [1-7]. The different techniques for the reduction of pollutants are essentially based on injector modifications [8], the state of fuel introduced into the chamber (cases of prevaporization and premixing), and the modification of the combustor geometry.

The simple modification of the combustor geometry, to achieve a lean primary zone and to reduce the residence time, is the usual technique to control the nitrogen oxides production. In conventional combustors, this technique leads to the excesive production of unburned and carbon monoxide at low power requirements, such as idle, as a consequence of an excessively lean primary zone and of the reduced residence time [9,10]. The development of non-conventional staged combustors with fixed geometry [3,11,12,13] and more recently the conventional combustors

Presented at an AGARD Meeting on 'Fuels and Combustion Technology for Advanced Aircraft Engines', May 1993.

with variable geometry, makes it possible to properly control the equivalence ratio of the primary zone at different power settings.

By other way, the injection of hydrogen in small quantities to lean primary zones reduces greatly the unburned hydrocarbons and CO emissions improving thus the efficiency. The application of this technique to continuous combustion chambers is only known through two experimental works carried out by NASA [9,16]. In the first one hydrogen was injected directly into the primary zone of a hydrocarbon fueled combustor; while in the second, it was premixed with propane and air in a experimental propane burner.

In order to asses the benefits and posibilities of the addition of hydrogen for pollutants reduction in combination with controled lean primary zones, at different power settings, an experimental work has been performed at E.T.S.I. Aeronauticos and its results are presented in this paper. A conventional tubular conbustor was used with the primary zone fuel ratio was controled by throttling devices that acted upon the primary and secondary flow. In addition the results of injecting gaseous butane instead of hydrogen are also presented for comparison purpose. Finally, the evaluation of the different factors by means of which hydrogen affects pollutant reduction is included.

2. TEST FACILITY

The experimental facility, whose detailed scheme is shown in figure 1, is basically composed of the following systems: Combustion chamber, air supply, fuel system and gas sampling and analysis system. The most relevant fuctions and characteristics of each system, are briefly described below.

2.1.Combustor

The combustor (see figure 2 for details) is of conventional tubular type. The air flow that penetrates into the primary zone, comes in part from the dome (primary air-flow), and in part from the intermediate zone, due to the back flow that recirculates to the primary zone. From the combustor geometries, working conditions, and data reported in the literature [17,18,19], it is deduced that a maximum of 11.6% of the secondary air flow enters through the orifices of the intermediate zone, and a maximum of 50% of it circulates back to the primary zone. Accordingly the air mass flow entering the primary zone is given by

$$\dot{m}_{pz} \simeq \dot{m}_p + 0.058\dot{m}_s \qquad (1)$$

and taking into account that

$$\dot{m} = \dot{m}_p + \dot{m}_s \qquad (2)$$

we can write

$$\dot{m}_{pz} \simeq \dot{m} - 0.942\dot{m}_s \qquad (3)$$

so that the primary zone equivalence ratio is related to the overall equivalence ratio through the expression:

$$\Phi_{pz} \simeq \frac{\Phi}{1 - 0.942\dot{m}_s/\dot{m}} \qquad (4)$$

Expressions (3) and (4) show that decreasing the secondary air flow rate, for a given $\dot{m}$, is an effective way to increase the primary zone air flow rate and to lean it. This was performed by a throttling device as will be described later.

2.2 Air supply system

The air flow is provided by a centrifugal fan (maximun pressure ratio of 1.08 at 1 m^3/s) and measured by means of a calibrated nozzle, located at the compressor inlet. The air enters to the combustion chamber, through two coaxial pipes, separating the primary from the secondary air flow. These pipes incorporate flow control devices together with temperature and pressure probes.

The inner pipe is supported by struts. It has a butterfly valve to reduce the primary air flow rate and a calibrated orifice plate to measure it. The secondary air flow passes through the annular area between the two pipes where it is throttled by a rubber membrane that close symmetrically the annulus when it is inflated with pressurized air, providing thus an effective and low perturbing method to decrease the secondary air flow rate.

An exhaust pipe is fitted to the combustor exit through two sealing segments, allowing relative rotation. It has a rack of four thermocouples, separated by 90 degrees, with their sensible extremes situated at different distances from the center. This configuration in conjuction with the rotation of the exhaust pipe provides the radial and circumferential combustor exit temperature distributions. Also, the exhausting duct incorporates a sampling probe and a total pressure probe. Further downstream there is a throttle valve to regulate the total air flow rate through the combustor.

2.3 Fuel system

The fuel supply system (fig.1) is composed of the kerosene and the hydrogen feeding systems. The kerosene supply system, consists of a tank, pumps, flowmeters, pressure transducers, closing and regulating valves, and filters. The kerosene flow rate is measured by means of calibrated flowmeters or through the pressure drop at the injector. The hydrogen supply system consists of a parallel battery of hydrogen bottles, pressure regulators, on-off and regulation valves, fire extinction valves and flowmeters. The hydrogen flow is measured by calibrated flowmeters

2.4 Gas sampling and analysis system

The sample probe, made of stainless steel, is placed diametrically as near as possible to the combustor exit. It has six orifices (3 mm in diameter) arranged to provide equal area of sampling.

The sampling line, conducts the sample to the analyzers of NO/NO_x and CO. All equipments are provided with a pump, filter and condensation filter as well as exhaust and bypass valves. The flow rate and the pressure of the sample are kept constant in each analyzer. The carbon monoxide analyzer is a Beckman 865, of the infrared absorption type. The NO/NO_x analyzer, a Beckman 951, is based on the method of chemiluminiscence. Unfortunately the unburned hydrocarbon is not measured, however, as it is known, its trends and dependence with operating variables are similar to that of carbon monoxide [3,24,25]. On the other hand, there are in the literature several excellent correlations $HC - CO$ [25], for similar conbustors, from which the emission levels of HC can be estimated. Consequently, for the determination of combustor efficiency, we will use the following correlation:

$$\ln EI_{co} = 2.77 + 0.485 \ln EI_{HC} \qquad (5)$$

3. OPERATING CONDITIONS

The pressure and temperature increments produced by the compressor are very low, and their effect over emissions is insignificant. Therefore, the combustor inlet conditions can be considered equal to the environment conditions. Nevertheless, using appropiate correlations [4,13,22,23] the obtained data can be used to estimate the combustor performance at other operating conditions.

The operating range of the overall equivalence fuel air ratio has been selected to be [0.14-0.3], which are representative values for idle and take-off conditions in aircraft engines respectively.

The air flow rate is selected indirectly through the parameter P_2T_2/V_r. This parameter controls the performance of combustors and particularly combustion efficiency. The results of test carried out for overall equivalence ratio of 0.27 are presented in fig.3; which shows the effect of the parameter $P_2T_2/V_r \left(\frac{kg}{cm^2} K \frac{s}{m}\right)$ on the efficiency(*) (four injectors have been used to take into account possible effects of the atomization degree). From this figure one can conclude that the most interesting operating range is $50 < P_2T_2/V_r < 100$. At values lower than 50, the efficiency drops steeply and the combustor works in unusual conditions. At values over 100, the primary zone residence time would increase, as well as NO_x emissions, without a significant increase in its perfomance.

The injectors used in tests are swirl chamber type, with a single orifice, producing atomization by pressure.
As the required injection pressure changes, due to demanded fuel mass flow, the jet angle and atomization degree change accordingly and this affects the emission level of pollutants. This effect is shown in figure 4, where it can be seen that the influence of injection pressure is meaningless for pressure values between 7-12kg/cm^2. So the injection pressure is mantained between 7-12 kg/m^2, for all tests, using a family of geometrically similar injectors.

The results with and without hydrogen are compared for the same energetic load. With the purpose to define the equivalent operating conditions of the combustor, for any case, an equivalent flow rate of kerosene, $\dot{m}_{ek}$, is used defined as:

$$\dot{m}_{ek} = \dot{m}_k + \dot{m}_h \frac{L_h}{L_k} \qquad (6)$$

so that for any case the fuel-air ratio, f, and the emission index, EI_i, are given by

$$f = \frac{\dot{m}_{ek}}{\dot{m}} \qquad (7)$$

$$EI_i = 10^{-3} \frac{M_i}{M} \frac{1+f}{f} x \qquad (8)$$

Expressing $\dot{m}_{ek}$ in terms of the weight fraction of hydrogen within total fuel, α, we have:

$$\dot{m}_{ek} = \dot{m}_k \left(1 + \frac{\alpha}{1-\alpha} \frac{L_h}{L_k}\right) \qquad (9)$$

4. RESULTS AND DISCUSSION

4.1 Effect of primary zone equivalence ratio

Figures 5 and 6 show the effect of the primary equivalence ratio on NO_x and CO emissions for a typical full power, overall equivalence ratio $\Phi = 0.3$, and three values of the parameter P_2T_2/V_r. One can see that the effect over NO_x emissions is very strong. A change in the primary equivalence ratio from $\Phi_{pz} = 0.94$ to 0.8 decreases NO_x by more than 50%. This is due mainly to the exponential growth of nitrogen oxides production with temperature and also to its dependance on the residence time, since it must be taken into account that an increase in the primary zone air flow rate not only produces a

(*)The efficiency is calculated by means of the expression:

$$\eta_q = 1 - \frac{EI_{CO} L_{CO} + EI_{HC} L_{HC}}{L}$$

leaner primary zone (less temperature), but simultaneously shortens the residence time. The effect over CO is contrary to the one mentionated above since lean primary zones and small residence times increase CO production. This detrimental effect can be evaluated also through its influence on combustion efficiency, since it has been estimated that an increment of 20 units on CO emission index means a 1% decrease in efficiency.

Fig. 7 depicts the function $EI_{CO} = f(EI_{NOX})$ obtained at two constant overall equivalence ratio $\Phi = 0.14$ and 0.3 by changing the primary equivalence ratio. The original or genuine combustor operating points for the two regimes are also shown, illustrating the known problem of fixed combustor geometry, that is, excesive production of CO at idle, due to very lean primary zone, and high NO_x emission levels at full power, due to reasons already explained. Figure 7 also illustrates the potential benefits that can be obtained by controlling the primary equivalence ratio. Effectively, it can be seen that at idle we can enrich the primary zone to decrease CO emissions with tolerable increase in NO_x; while, at fuel power, leaning the primary zone, the NO_x level can be greatly reduced but at expenses of an increase of CO and consequently at expenses of a loss in efficiency.

4.2 Effect of hydrogen addition

Hydrogen addition is interesting because it improves combustor efficiency in those cases in which the primary zone is lean. To asses this effect a series of tests have been carried out for values of primary equivalence ratio between 0.65 and 0.85. A variable fraction of hydrogen, between 0 and 4% in weight, was injected for several values of the overall equivalence ratio and of the paramenter P_2T_2/V_r.

Figures 8 and 9 show the typical influence of the addition of hydrogen over the emission levels of NO_x and CO, for the case of $\Phi = 0.3$ and $P_2 \cdot T_2/V_r = 70$. As it is shown in figure 8, the addition of hydrogen does not produce any significant effect over the emission level of NO_x. However, according to figure 9, CO emissions are decreased by about 40% for 4% hydrogen addition. This reduction is more remarkable at low hydrogen fractions where it is possible to achieve reductions of 30%, with hydrogen injections of about 1 to 1.5%.

The decrease in the CO emission index is obviously due in part to the fractional use of a carbon free fuel (hydrocarbon substitution) and also to other potential causes such as prevaporization and premixing and chemical kinetics. In the following we will attempt to estimate the contribution of each factor separately.

The relative emission index reduction due to substitution is given by the expression:

$$\frac{(IE^a_{CO})_{sub} - IE^o_{CO}}{IE^o_{CO}} = \frac{\dot{m}_k}{\dot{m}_{ek}} - 1$$

and taking into account the expression (q), we finally obtaine:

$$\frac{(IE^a_{CO})_{sub} - IE^o_{CO}}{IE^o_{CO}} = \frac{1}{1 + \frac{\alpha}{1-\alpha}\frac{L_h}{L_k}} - 1$$

The results given by this expression are depicted in figure 12 which shows that the reduction due to substitution represents about 25% of total.

Since the injected hydrogen is in gaseous phase and premixed with the primary air, the primary combustor zone become more homogeneous and in this conditions CO emission can be somewhat different. In order to evaluate this effect, a comparative test is made consisting in the addition of hydrogen or vaporized butane alternatively for the same operating conditions. The results are shown in figures 10 and 11. As it can be seen, NO_x emissions are roughly the same in both cases. But on the contrary, the EI_{CO} reduction is well within the expected values for the case of hydrogen addition, while there is no significant effect for the case of butane addition. Consequently, it is considered that gaseous injection and premixing of hydrogen is not by itself a significative cause for carbon monoxide reduction.

Consequently, we can thought that the main factor causing a significant CO reduction, apart of hydrocarbon substitution, is chemical kinetics. Effectively, when hydrogen is added, the rate of production of radicals originated by the system of reactions O_2/H_2 increases, and also the rate of heat released by these reactions; this enhances the step reactions involving C atoms, such as the reaction of oxidation of $CO (CO + OH \rightarrow CO_2 + H)$. The significance of chemical kinetics increases, obviously, with the fraction of hydrogen/hydrocarbon. It is especially important when the mixture hydrocarbon-air is bellow lean flammability limit but becomes flammable with the addition of hydrogen. So the contribution of chemical kinetics to CO reduction increases as one takes into consideration the non-uniformities of the mixture hydrocarbon air in the primary zone, because due to non uniformities there will be regions with a hydrogen/hydrocarbon fraction much greater than the average.

5. CONCLUSIONS

At full power combustor operating conditions, leaning the primary zone, by encreasing the primary air, is an efficient mean to reduce NO_x formation. but at a cost of efficiency because CO and HC emissions increases. By injecting 4% hydrogen to lean primary zones, the EI_{CO} can be reduced a 30%, without a significant increases in NO_x, due partially to hydrocarbon substitution and mainly to chemical kinetics.

Al idle combustor operating conditions, encreasing the primary zone, by decreasing primary air is an efficient mean to reduce CO and HC emissions , while mantaining NO_x formation to low level.

REFERENCES

[1] Bahr, D.W.: "Gas turbine Engine Emission Abatement-Status and Needed Advancements", Gas Turbine Combustor Design Problems, Edited by Lebrevre, 1979.

[2] Jones, R.E.; "Gas Turbine Emissions-Problems Progress and Future", Combustion and Environment, 1983.

[3] Lefebvre, A.W., "Gas Turbine Combustion", McGraw-Hill series in Energy, Combustion and Environment, 1983.

[4] Rubins, D.M. and Marchiona, N.R.: "Evaluation of NO_x Prediction Correlation Equations for Small Gas Turbines", Journal Aircraft, Aug. 1978.

[5] J.E. Peters "Current Gas Turbine Combustion and Fuels Research and Development", J. Propulsion & Power, Vol. 4 No.3 May. 1988.

[6] A. Sotheran, D.E. Pearce and D.L. Overton, "Some Practical Aspects of Staged Premixed Low Emissions Combustions". Journal of Engineering for Gas Turbines and Power. Trans. ASME Vol. 107 No. 1, jan. 1985.

[7] Touchton, G.L. "Influence of Gas Turbine Combustion Design and Operating Parameters on Effectiveness of NO_x Suppression by Injected Steam of Water". Journal of Engineering for Gas Turbines and Power. Trans. ASME Vol. 107 No. 3, july 1985.

[8] Norster, E.R. annd Lefebvre, A.H. "Effects of Fuel Inyection Method on Gas Turbine Combustor Emissions". Emissions from Continuous Combustion System, Cornelius, Sept 1971.

[9] Norgren, C.T. and Ingebo, R.D., "Effect of Primary Zone Equivalence Ratio and Hydrogen Addition on Exahust Emission in a Hydrocarbon-fueled", NASA TM X-3117, Oct. 1974.

[10] Singh, P.P., Young, W.E. and Ambrose, M.J.; "Formation and Control of Oxides of Nitrogen Emissions from Gas Turbine Combustion Systems", Journal of Engineering for Power. Trans. ASME, Oct. 1972.

[11] Aoyama, K. & Mandai, S.; "Development of a Dry Low NO_x Combustor for a 120-Mw Gas Turbine", Journal of Engineering for Gas Turbines and Power. Trans. ASME, Oct. 1984.

[12] Ross, P.T.; Williams, J.R. & Anderson, D.N. " Combustor Development for Automotive Gas Turbine", Journal of Energy, Oct. 1983.

[13] Sullivan, D.A.; "Premixing and Flash Vaporization in a Two-Stage Combustor", Journal of Engineering for Gas Turbines and Power. Trans. ASME, jan. 1982.

[14] Hoehn, F.W. and Dowdy, M.W.; "Hydrogen-Enriched Gasoline for Autos", Automotive Engineering, Nov. 1974.

[15] Houseman, J. and Cerine, D.J.; "On-Board Generator Supplies Hydrogen for I-C Engine", Automotive Engineering, Aug. 1974.

[16] Anderson, D.N.; "Effect of Hydrogen Inyection on Stability and Emissions of an Experimental Premixed Prevaporized Propane Burner", NASA TM X-3301, Oct. 1976.

[17] Graves, C.C. and Grobman, J.S.; "Theoretical Analysis of Total-Pressure Loss and Airflow Distribution for Tubular Turbojet Combustor with Constant Annulus and Liner Cross Sectional Areas", NACA Report 1373, 1957.

[18] Rosenthal, J., "Exploring Methods for the Determination of Gas Flow and Temperature Pattern in Gas Turbine Combustors", ARL/
ME 235, Aeronautical Research Laboratories, Australia, 1959.

[19] Tacina, R.R. and Grobman, J.S.; "Analysis of Total Pressure Loss and Airflow Distribution for Annular Gas Turbine Combustor", NASA TN D-5385, 1969.

[20] Aerospace Recommended Practice; "Procedure for the Continuous Sampling and Measurements of Gaseous Emissions from Aircraft Turbine Engines", SAE-ARP 1256A, Jan. 1971, REv. 1980.

[21] O.A.C.I.; "International Standards and Recommended Practices", OACI Annexe 16, Volumen II, 1982.

[22] Lefebvre, A.W.; "Fuel Effects on Gas Turbine Combustor", Journal of Engineering for Gas Turbine and Power, TRANS. ASME, April 1982.

[23] Sullivan, D.A.; "A Simple Gas Turbine Combustor NO_x Correlation Including the Effect of Vitiated Air", Journal of engineering for Power, TRANS. ASME, April 1977.

[24] Buchheim, R.; "Influence on Exhaust Emissions from Automotive Gas Turbines", Journal of Engineering for Gas Turbines and Power, Trans. Asme, Jan. 1979.

[25] Hammond, D.C.; "Evaluating Characteristic Time Emissions Prediction for Three Vehicular Gas Turbine Combustors", Journal of Energy, Aug. 1977.

[26] Grobman, J.S. "Effect of Operating Variables on Pollutant Emissions from Aircraft Turbine Engine Combustors", Emissions from Continuous Combustion System, Cornelius, 1971.

[27] Rudey, R.A. and Reck, G.M.; "Advanced Combustion Techniques for controlling NO_x Emissions of High Altitude cruise Aircraft", 27th. International Astronautical Congress, California, Oct. 1976.

[28] López Juste, G., Salvá, J. "Reducción de contaminantes con siembra de Hidrógeno en Cámaras de Turbinas de Gas: Evaluación de Diversos factores". Anales de Ing. Mecánica, pp 147-15', Diciembre de 1.986.

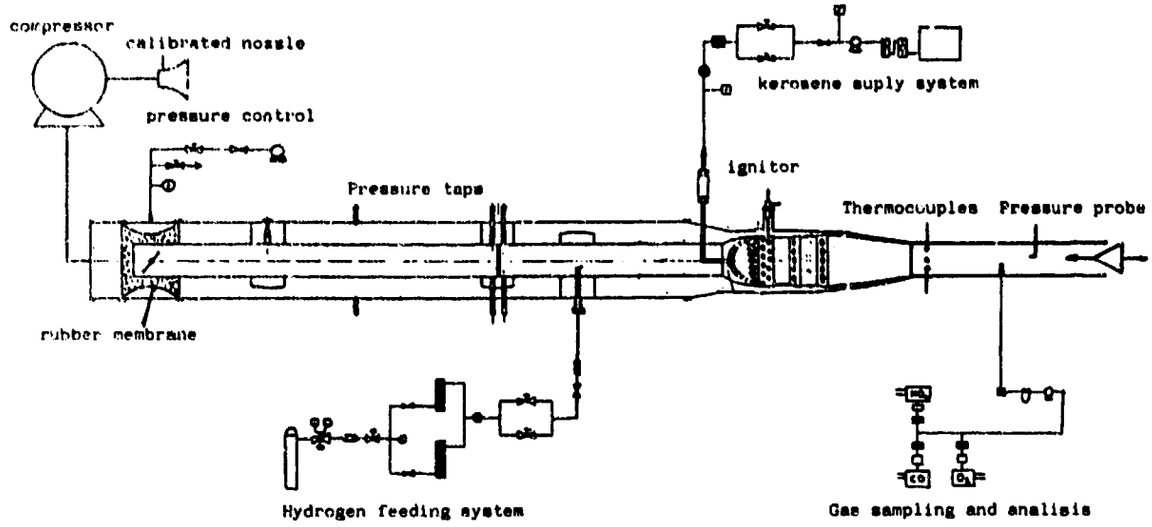

Fig.1 Test facility scheme

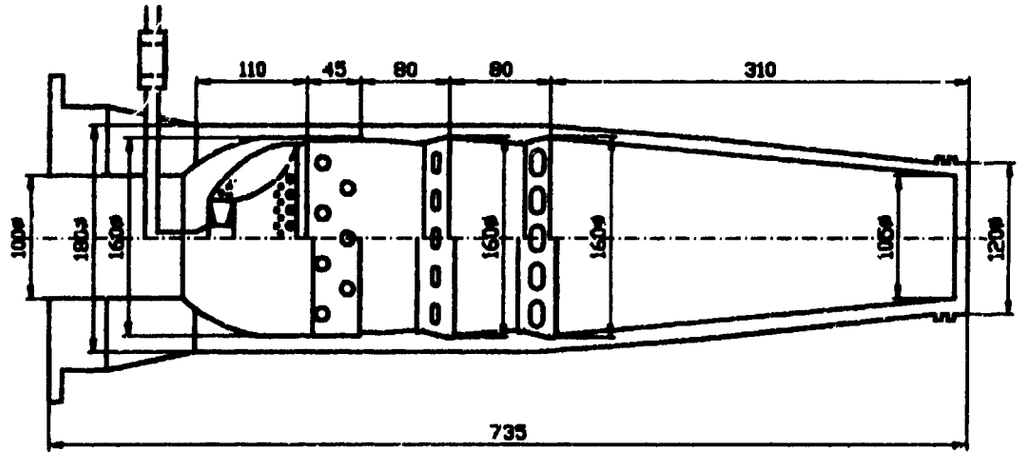

Fig.2 Combustor

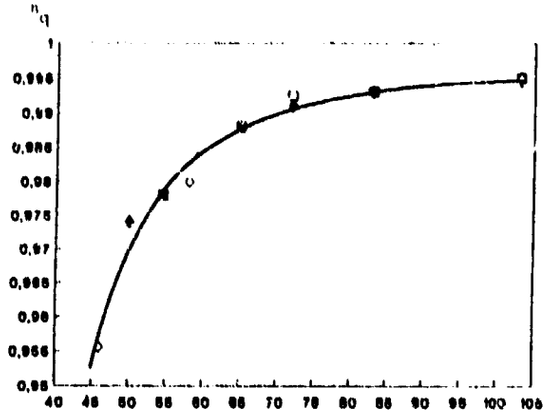

Fig.3 Influence of the reference velocity parameter on combustion efficiency (Φ=0.27, P_o= 702 mm Hg, T_o=16 °C, Ψ= 56%)

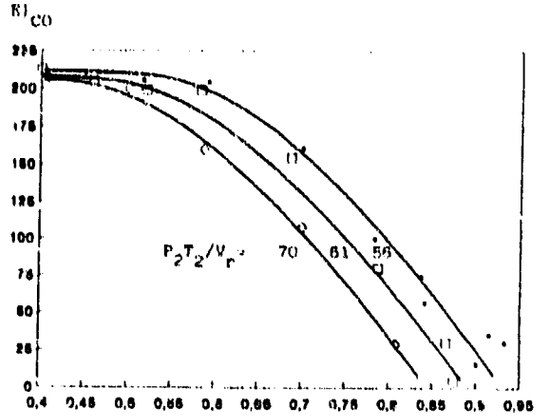

Fig.6 Effect of primary zone equivalence ratio on CO emissions (Φ=0.3; P_o= 706 mm Hg, T_o=10 °C, Ψ= 82%)

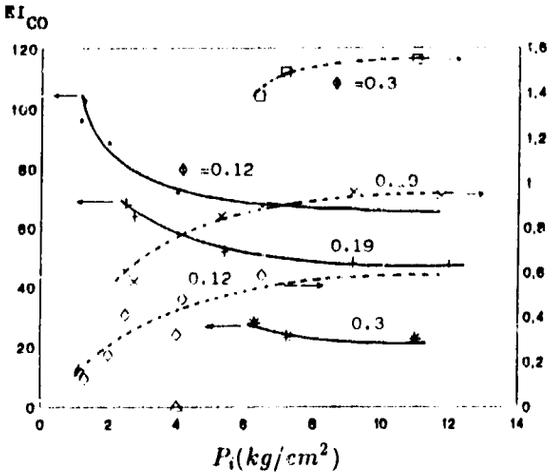

Fig.4 Effect of injection pressure on CO and NO_x emissions (P_2T_2/V_r=68; P_o= 70 mm Hg, T_o=15 °C, Ψ= 70%)

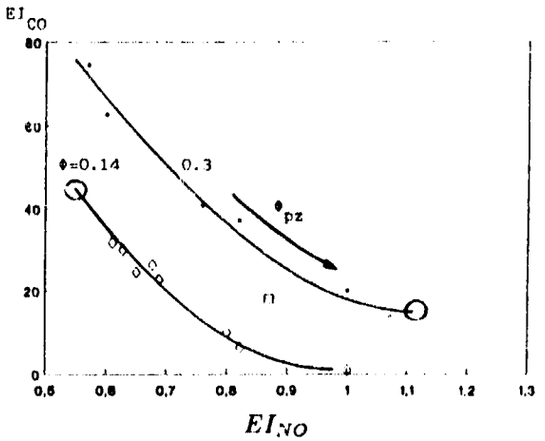

Fig.7 EI_{CO}-EI_{NO} map obtained changing the primary zone equivalence ratio (P_o= 690 mm Hg; T_o=14 °C, Ψ= 90%)

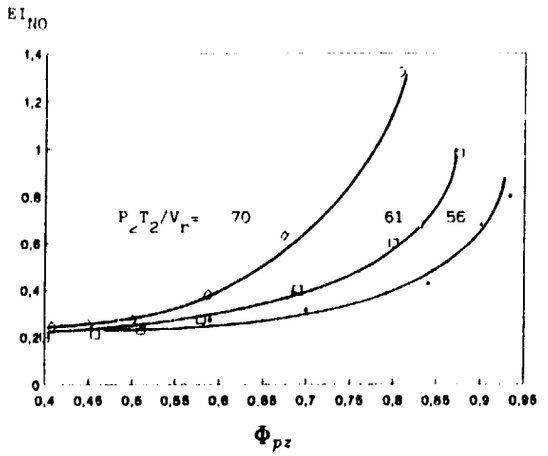

Fig.5 Effect of primary zone equivalence ratio on NO_x emissions (Φ=0.3; P_o= 706 mm Hg; T_o=10 °C, Ψ= 82%)

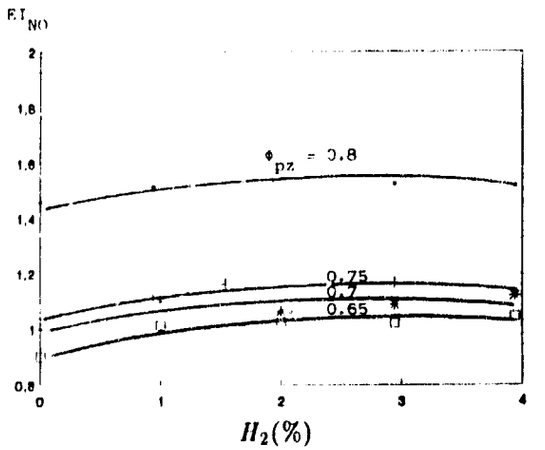

Fig.8 Effect of hydrogen addition on $EINO$(Φ= 0.3; P_2T_2/V_r=68)

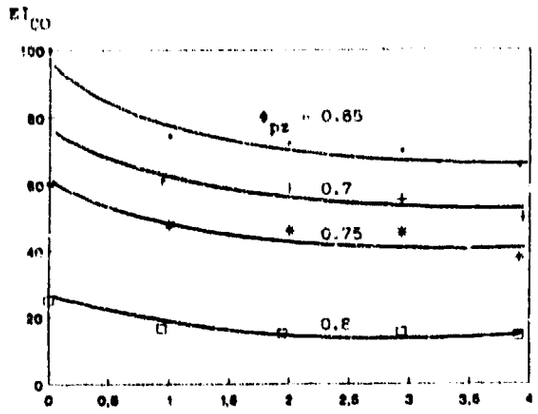

Fig.9 Effect of hydrogen addition on EI_{CO}(Φ= 0.3; P_2T_2/V_r=68)

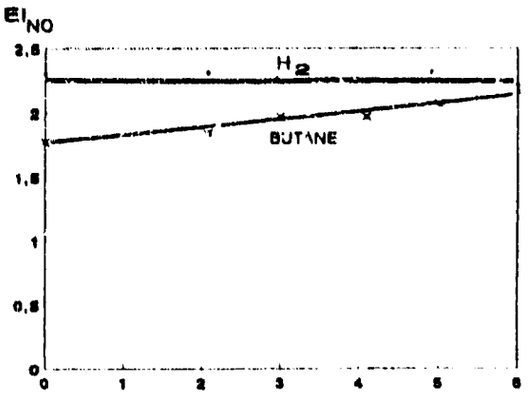

Fig.11 Effect of hydrogen or butane addition on NO emissions.

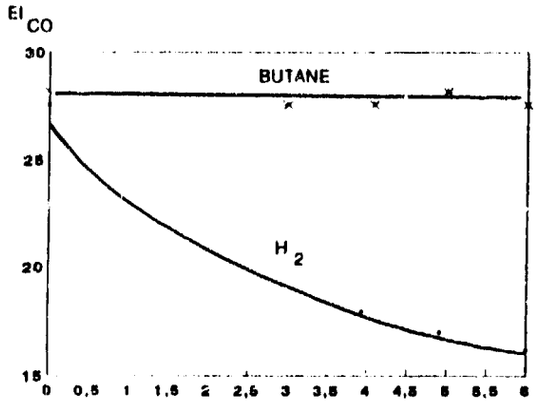

Fig.10 Effect of hydrogen or butane addition on CO emissions

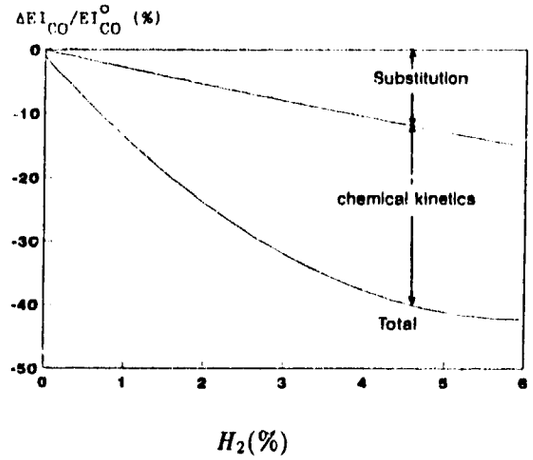

Fig.12 Estimated contribution of different factors on CO reduction.

Discussion

Question 1. P. Kotsiopoulos
Was there any other reason for limiting the amount of hydrogen fuel to 4%, apart from the observation that an excess beyond 2% hydrogen in the total fuel had no significant effect on emissions?

Author's Reply
This is effectively the main reason, plus the fact that, if this technique is implemented, it will be better to use the smallest quantity of hydrogen possible for safety reasons.

DUCTED KEROSENE SPRAY FLAMES

by

R.M. Perez-Ortiz, S. Sivasegaram and J.H. Whitelaw
Imperial College of Science, Technology & Medicine
Mechanical Engineering Department
Exhibition Road
London SW7 2BX
United Kingdom

ABSTRACT

Reaction progress in premixed methane-air flames in round ducts without and with kerosene sprays has been quantified on the basis of species concentration measurements for different fuelling arrangements of kerosene with equivalence ratio, proportion of liquid to gaseous fuel, duct length and air preheat temperature as variables in smooth and in rough combustion. The intensity of heat release close to the flame holder in rough combustion was greater than that in smooth combustion, and the duct length necessary to ensure complete combustion decreased with air preheat temperature and upstream turbulence intensity and was weakly dependent on the proportion of methane to kerosene in flow arrangements where the kerosene was sprayed upstream of the flame-holder. The injection of kerosene through the flame-holder at a velocity largor than that of the mean flow past the disk led to uneven mixing and incomplete combustion. Pulsed injection of kerosene through a pintle-type injector also resulted in incomplete combustion due to the larger droplet size than in arrangements with a steady flow of kerosene. Oscillations of large amplitude were induced at equivalence ratios usually associated with smooth combustion and oscillations in rough combustion ameliorated by pulsed injection of kerosene comprising around 10 % of the total fuel.

NOMENCLATURE

$c_{p,w}$	:	specific heat of thermocouple wire
d	:	flame-holder diameter (Fig. 1)
d_a	:	diameter of anvil (Fig. 1)
d_w	:	thermocouple wire diameter
f	:	frequency
k_g	:	thermal conductivity of gas
L	:	downstream duct length (Fig. 1)
$m_{a,1}$	:	mass flow rate of unswirled air (flow arrangement of Fig. 1b)
$m_{a,1}$	:	mass flow rate of swirl air (flow arrangement of Fig . 1b)
m_f	:	mass flow rate of fuel (flow arrangement of Fig. 1b)
m_k	:	mass flow rate of kerosene
$m_{k,s}$	:	stoichiometric mass flow rate of kerosene based on total air flow
p_{rms}	:	rms fluctuation of pressure
r	:	radial distance from duct axis
r_s	:	distance from duct axis to line if injection of swirl air and fuel (flow arrangement of Fig. 1b)
Re	:	Reynolds number = $\rho U/\nu$
Re_w	:	Reynolds number based on thermocouple wire diameter
Sw	:	swirl number
T	:	mean temperature
T_{rms}	:	rms fluctuation of temperature
U	:	bulk mean velocity of air in duct, based on unreacted flow
$U_{a,2}$	:	mean velocity of swirl air (flow arrangement of Fig. 1b)
U_f	:	mean velocity of fuel (flow arrangement of Fig. 1b)
x	:	axial distance of probe tip from flame-holder (Fig. 2)
X	:	upstream duct length (Fig. 1)
ν	:	kinematic viscosity
ρ	:	density of upstream air
ρ_w	:	density of thermocouple wire material
τ	:	time constant for thermocouple
ϕ	:	equivalence ratio = (air-to-fuel ratio at stoichiometry) / (air-to-fuel ratio)

Presented at an AGARD Meeting on 'Fuels and Combustion Technology for Advanced Aircraft Engines', May 1993.

1. INTRODUCTION

The efficiency and range of operation of gas turbine combustors depends on the combustor design, the geometric and flow parameters and the fuelling method, and detailed measurements of velocity, temperature and species concentration have been carried out in can and annular combustors burning gaseous and liquid fuel and involving a variety of fuelling arrangements [1-7]. Although these measurements were extensive in scope and have provided useful information about combustor performance, they have been limited by the complex geometry of the combustor and the cost in instrumentation, skills and time. Also the interpretation of results from laboratory models is subject to uncertainty arising from the dependence of combustion efficiency on variables including the distribution of the mean flow and temperature and the time and length scales of turbulence. An understanding of the combustion process in simple flow arrangements is, therefore, useful in planning experiments in model combustors and in interpreting the results.

Work has also been carried out to improve the design and performance of fuelling systems for gas turbines [8], especially where there is a need to supply liquid fuel as a fine spray to enhance combustion efficiency, and to characterise the atomising devices [9]. Testing of these fuelling devices in simple combustor geometries provides information about their performance and the combustion process and enhances understanding of results from more complex arrangements.

Oscillations of large amplitude associated with rough combustion and dominated by acoustic frequencies between 50 and 500 Hz occur in ducted combustors such as gas turbine augmentors and can limit the range of operation of the combustor. The importance of flame confinement and the distribution of heat release to these oscillations has been examined in premixed and partially premixed flows of relevance to augmentors [10, 11]. Recent research has also shown that such oscillations can be actively controlled by the oscillation of the flow rate of part of the fuel [12, 13]. The emphasis of the work on combustion oscillations and their control has, mainly, been on gaseous fuel, and there is a need to extend this work to liquid fuel systems, since practical combustors use liquid fuel and the large oscillatory inputs necessary to achieve control at large heat release rates may be provided by the periodic injection of liquid fuel. Control by the oscillation of liquid fuel involves time delay due to the evaporation of fuel besides that due to chemical reaction, which is small except for the conversion of CO to CO_2, and the droplet sizes generated by commercially available unsteady-flow injectors is larger than that in continuous injection and low frequency arrangements. Advance knowledge of the characteristics of the fuel spray and the effect of periodic injection of liquid fuel on the combustion process is therefore important to the design of control systems.

The present study concerns ducted kerosene spray flames stabilised behind a disk in a round duct and was carried out in five phases. The first comprised detailed measurements in premixed methane-air flames stabilised behind a round disk and behind a disk with radial spokes [14] and a three-dimensional bluff-body [15] and in swirl stabilised flows without a bluff-body so as to establish the minimum duct length necessary to ensure complete combustion in flows without and with oscillations. The next phase comprised measurements in methane-air flames to which an atomised spray of kerosene with known droplet characteristics [9] was added in the direction of the main flow and behind the flame-holder. The kerosene was injected against the main flow at an anvil located upstream of the flame holder in the third with upstream temperature as a variable, and, in the fourth, in the downstream direction through a hole at the centre of the flame-holding disk. In the final phase, kerosene was injected periodically using a commercially available pintle-type gasoline injector located at the duct wall and in the plane of the flame-holder with frequency of injection as variable and to control oscillations of large amplitude in rough combustion.

The measurements included free-field sound level and wall static pressure fluctuations, mean and rms values of temperatures at the duct exit and radial and longitudinal profiles of species concentration, with the downstream duct length, flow rate, overall equivalence ratio and the proportion of liquid to gaseous fuel as the main variables. The droplet characteristics of the pintle injector were also measured using a laser diffraction technique.

The next section contains a description of the flow and fuelling arrangements and the experimental method. The results are presented separately for each fuelling arrangement in the third, and the final section discusses the results and their implications.

2. FLOW AND FUELLING ARRANGEMENTS AND EXPERIMENTAL METHOD

The flow geometries and fuelling arrangements are shown in Fig. 1 and the important dimensions and ranges of flow conditions in Table 1. In the flow arrangement of Fig. 1a, natural gas (94 % methane) and air were premixed in a swirl register and flowed past a flow-straightening honeycomb and a flame arrestor screen before combustion in the stainless steel duct section downstream of the bluff-body flame-holder. In the arrangement of Fig. 1b, the flame was stabilised by adding swirl to the flow and without a bluff-body. The unswirled part of the air was added at the swirl register with its swirl removed before mixing with swirl air and natural gas injected tangentially further downstream. The geometric swirl number was defined by the formula

$$Sw = (m_f U_f r_s + m_{a,2} U_{a,2} r_s) / ((m_f + m_{a,2} + m_{a,1}) U D)$$

where m_f, $m_{a,2}$, and $m_{a,1}$ respectively, are the mass flow rates of the fuel, swirl air and unswirled air, U_f and $U_{a,2}$ are the mean injection velocities of fuel and swirl air at a distance of r_s from the axis of the duct of diameter D, and U is the bulk mean axial velocity of the downstream flow in the absence of combustion. The swirl number was varied by changing the proportion of the swirl to total air.

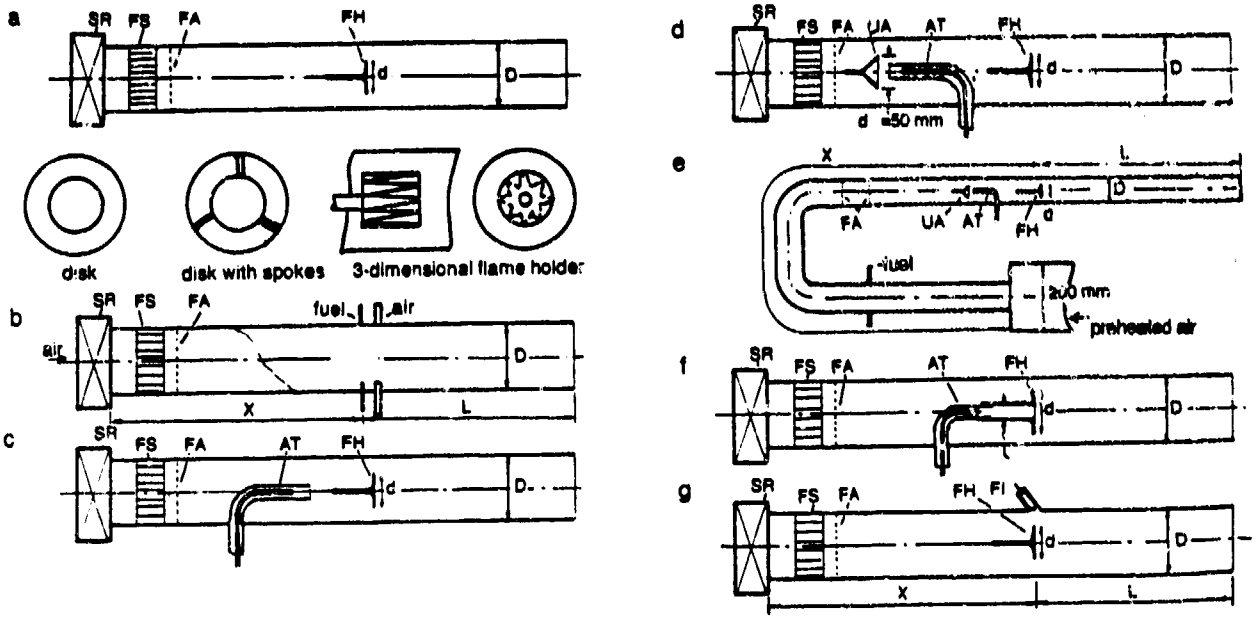

Figure 1: Flow arrangements
a) premixed methane-air flame; b) swirl stabilised flame; c) methane-air flame with forward injection of kerosene; d) methane-air flame with backward injection of kerosene; e) preheated methane-air flame with backward injection of kerosene; f) methane-air flame with injection of kerosene through disk; g) methane-air flame with pulsed injection of kerosene.
AT atomiser, FA flame arrestor screen, FH flame holder, FI fuel injector, FS flow straightener, SR swirl register, UA upstream anvil,

TABLE 1
Important Dimensions and Flow Conditions

flow arrangement	D/mm	d/mm	X/D	L/D	U/(m s^{-1})	Re	heat release/kW
Fig. 1a							
disk	50	25, 35	18	5 - 11	10 - 15	33 - 50 000	35 - 130
disk with spokes	50	25	18	8.5, 10.5	10	33 000	35 - 75
3-D bluff body	50	25	18	8.5, 10.5	10	33 000	35 - 75
Fig. 1b	50		18	8.5, 10.5	10	30 - 50 000	40 - 70
Fig. 1c	50	25	18	8.5, 10.5	8 - 15	25 - 50 000	35 - 75
Fig. 1d	50	25	18	8.5, 10.5	10	33 000	35 - 75
Fig. 1e	50	25	32	8.5, 10.5	8 - 15	33 000	35 - 75
Fig. 1f	50	25	18	8.5, 10.5	8 - 15	33 000	35 - 75
Fig. 1g	50	25	18	8.5, 10.5	8 - 15	33 000	35 - 75

The flow arrangements of Figs 1c, d, f and g are similar to that of Fig. 1a but with provision to add liquid kerosene fuel as a spray. The atomiser was similar to that of Ref [9] and comprised a stainless steel hypodermic tube of internal diameter 2 mm carrying kerosene which entered the preheated atomising air stream at around 250 °C in an outer duct of diameter 5 mm radially through six holes of diameter 0.5 mm located 40 mm from the exit of the outer duct. In the arrangement of Fig. 1g, kerosene was injected through a pintle-type injector (Keihin, 10450-PG7-0031) which could pulse the fuel injection with frequency between 0 and 200 Hz. The flow arrangement of Fig. 1d was modified as in Fig. 1e to enable preheating of the main air supply to the combustor duct, and natural gas was added radially through four equally spaced coplanar holes of diameter 3 mm on the duct wall. Uniformity of mixing of the gaseous fuel and air was ensured by locating a pair of wire-mesh screens downstream of the point of addition of fuel.

Since the flow conditions in the atomiser for the flow arrangements of Figs 1c, d and f were similar to those of Ref. [9], the droplet characteristics were assumed to be the same as those measured earlier. The characteristics of the spray from the pintle injector have been quantified for petrol by Hardalupas et al. [16] using phase-Doppler velocimetry and those for kerosene were measured with a laser diffraction instrument (Malvern Instruments, 2600c). All fluid flow rates were measured using calibrated float-type flow meters except in the arrangement of Fig. 1e where the flow rate of the unheated air was measured using a standard orifice plate. A water-cooled sampling probe with inner and outer diameters of 0.5 and 5 mm, respectively, was used to collect gas samples which were analysed in-line to give the concentration of unburnt

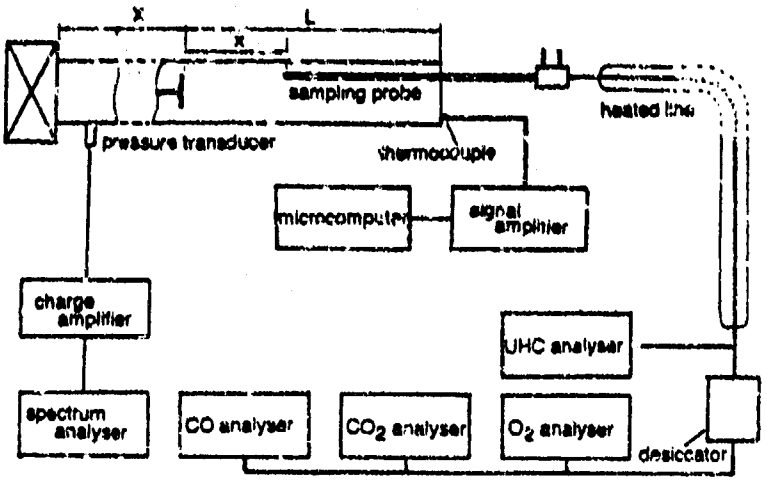

Figure 2: Instrumentation layout

hydrocarbon (Analysis Automation Series 520, FID Analyser) on a wet basis and those of carbon monoxide (Analysis Development Co., 336-4026), carbon dioxide (Analysis Development Co., 483-4027) and oxygen (Beckman, model E2) on a dry basis (see Fig. 2). Temperature measurements were obtained using platinum, 13% rhodium-platinum fine-wire thermocouples of wire diameter 50 μm and 80 μm supported on 500 μm wires of the same material with a separation 10 mm between them. The temperature signal was preamplified using a custom-built amplifier and digitiser (Data Translation, A/D board DT2824 PGL) before the evaluation of the mean and the rms values of the temperature and the power spectra by a microcomputer (Tandon, TM7104) using a mean value for the time constant τ for the thermocouple given by

$$\tau = (\rho_w c_{p,w} d_w^2 / 4 k_g) (0.24 + 0.56 Re^{0.45})^{1/2}$$

where ρ_w, $c_{p,w}$ and d_w, respectively, are the density, specific heat and diameter of the thermocouple wire, k_g is the thermal conductivity of the gas and Re_w the Reynolds number based on the wire diameter and the local mean gas velocity and kinematic viscosity. The time constant was assumed to be invariant with fluctuation in temperature in the flame and, following Ref. [17], taken to be 0.76 times that based on the properties of air at the same mean temperature and an estimated value of mean velocity

Transition to rough combustion was readily identified by an increase in free-field sound level (Bruel and Kjaer microphone 4134 with meter type 2215), measured 1 m away from the duct axis in the exit plane, by around 10 dB for an increase in equivalence ratio of as little as 0.02. Wall static pressure measurements (Kistler pressure transducer 6121 with charge amplifier 5007) were used to identify the dominant acoustic frequency mode. Oscillations of large amplitude in the arrangements of Figs 1a, c, d, f and g were associated with an acoustic quarter-wave in the duct length upstream of the flame-holder and the amplitude of oscillation was quantified on the basis of rms pressure at the antinode at the upstream end of the duct. Oscillations were dominated by either a half-wave or a full-wave in the upstream duct in the arrangement of Fig 1e and the pressure transducer was located at the antinode midway between the flame holder and at the upstream end for the half-wave frequency and a quarter of the duct length upstream of the disk for the full-wave. The output from the charge amplifier was processed using an FFT spectrum analyser (Spectral Dynamics 340) to give the power spectrum and the rms value of the fluctuation in pressure.

3. RESULTS

Preliminary measurements were carried out in the methane-air premixed flames behind a disk of area blockage ratio 0.25 with the downstream duct length (L) varied between 5 and 11 D. Inspection of the wall temperature distribution showed that the point at which the flame made contact with the wall decreased from around 7 D for an equivalence ratio of 0.6 and an upstream mean flow rate of 10 m/s to around 5 D at an equivalence ratio of 0.73. Larger equivalence ratios led to rough combustion dominated by a frequency of around 95 Hz associated with a standing acoustic quarter-wave in the upstream duct. Although rough combustion was observed in ducts longer than 5 D the amplitude of oscillations was small in ducts shorter than 7.5 D due to incomplete combustion. A duct length of 8.5 D led to an antinodal rms pressure of around 2.5 kPa and 10.5 D to 3.5 kPa at an equivalence ratio of 0.9 corresponding to a heat release rate of 60 kW. Ducts longer than 10.5 D did not give rise to larger amplitudes.

The amplitude did not change when the area blockage ratio of the disk was increased to 0.5, and an increase in the mean flow rate from 10 to 15 m/s with a duct length of 8.5 D led to amplitudes of around 3.5 kPa for a disk of area blockage ratio 0.25 due to the 50 % increase in heat release rate. The larger mean flow rate also resulted in a narrower stability range of 0.6 to 1.2 compared with 0.55 to 1.45 for the smaller flow rate. The larger disk of area blockage ratio 0.5 and an upstream flow rate of 15 m/s led to a narrower angle of flame spread, and rough combustion was observed only in ducts longer than 8.5 D. Extensive measurements in disk-stabilised flames were carried out with a disk of area blockage ratio 0.25 located centrally in the duct to a tolerance of within 0.25 mm and an upstream flow rate of 10 m/s in view of the wide range of equivalence

ratios at which flame stabilisation was possible in smooth and in rough combustion. The area blockage ratio was increased to 0.35 in the flow arrangement of Fig. 1f to accommodate a fuelling hole for atomised kerosene. Rough combustion in the flow arrangements of Figs 1a, c, d, f and g was dominated by a quarter-wave frequency of around 95 Hz in the upstream duct length and in the flow arrangement of Fig. 1e by a half-wave frequency of around 130 Hz which gave way to a full-wave frequency of around 240 Hz at equivalence ratios close to 0.9.

All flow arrangements except that of Fig. 1g led to axisymmetric flows and exit profiles of mean and rms temperature were symmetric to within 2 % and repeatable to within 1 % in the mean and 5 % in the rms, and radial profiles of unburnt hydrocarbon (UHC) measured between the exit and 4 duct diameters (D) upstream of the exit were symmetric to within 2 % of the overall mean hydrocarbon composition in the upstream duct and repeatable to within 2 %. The combustor duct was not insulated and this led to heat losses from the wall estimated at between 1.5 and 3.5 kW for heat release rates of around 60 kW. The effect of this heat loss on reaction progress was small since the flame spread from the centre of the duct towards the wall. The heat losses implied, however, that the temperature measurements close to the wall were not a measure of reaction progress. Carbon monoxide levels were low and less than 0.1 % at the duct exit at equivalence ratios less than unity and UHC values were used to quantify reaction progress. (The hydrocarbon content of the unreacted fuel-air mixture was around 6 % at an equivalence ratio of 0.6 and around 10 % at stoichiometry). Measurements of CO_2 and O_2 were carried out to validate the UHC measurements where necessary.

The results in the paragraphs that follow are for an upstream bulk-mean flow rate of 10 m/s, unless otherwise stated. Detailed measurements of UHC are presented for equivalence ratios mainly between 0.6 and 1.0 corresponding to heat release rates of around 40 and 65 kW.

Methane-air flames

Complete combustion of the fuel is not possible at fuel-to-air ratios greater than stoichiometric, and detailed measurements in the flow arrangement of Fig. 1a were for equivalence ratios less than unity and downstream duct lengths of 8.5 and 10.5 D, to examine the importance of duct length to complete combustion and to the amplitude of oscillations in rough combustion. The UHC values increased with distance from the duct axis and little UHC was detected at the centre of the duct in smooth combustion. Figs 3a and b show near-wall and centre-line values of UHC in the exit plane for the two duct lengths with equivalence ratio as variable. An increase in equivalence ratio from the lean limit to a value of around 0.7 resulted in a decrease in UHC at the exit to zero, and a further increase to 0.75 led to rough combustion. Although the agitation of the flow due to rough combustion led to a faster reaction rate close to the disk, the oscillation of the mean flow resulted in the presence of UHC at the exit in the shorter duct. An increase in the equivalence ratio to 0.9 or in the duct length to 10.5 D resulted in larger amplitudes of oscillation, more vigorous reaction and nearly complete combustion. The radial profiles of UHC at the exit of the shorter duct and at a distance of 8.5 D from the disk in the longer in Fig. 3b for two values of equivalence ratio in smooth combustion and two in rough combustion show that the increase in duct length is beneficial to reaction progress and that the reaction reaches completion over a smaller axial distance than in the shorter duct.

The mean and rms temperature profiles in the exit plane for the two duct lengths at an equivalence ratio of 0.7 associated with smooth combustion and a value of 0.8 and rough combustion, Fig. 4a, show that temperature fluctuations occurred only in rough combustion and close to the wall and did not increase with the antinodal rms pressure. The dominant frequency in the temperature power spectra in rough combustion (Fig. 4b) is the acoustic quarter-wave frequency and the large values of rms temperature close to the wall are due to the cyclic variation in reaction progress caused by the oscillation of the mean flow.

The amplitude of oscillations in rough combustion depends on the distribution of heat release close to the acoustic node at the flame-holder, and a reduction in the intensity of heat release could enable complete combustion without oscillations of large magnitude but will require an increase in duct length. Measurements were carried out with two bluff-body flame holders which are known to be less susceptible to rough combustion than a disk and in the flow arrangement of Fig. 1b where the flame was stabilised using swirl. The three-dimensional bluff-body [15] was less susceptible to combustion oscillations than the disk in ducts shorter than 7 D and the disk with radial spokes [14] averted transition to rough combustion at equivalence ratios less than unity in ducts shorter than 9 D. The antinodal rms pressures in Fig. 5 show that an increase in duct length to 10.5 D results in rough combustion in flames behind all three bluff bodies at equivalence ratios greater than 0.73 but not in flames stabilised by swirl.

The assumption of an exit velocity profile corresponding to fully developed turbulent flow and UHC and mean temperature distributions as in Figs 3 and 4 implies that a putative value of 1 % for the near-wall UHC (measured 2.5 mm from the wall) in smooth combustion with an equivalence ratio of 0.7 will correspond to 4 % of the total fuel being unburnt, and 8 % for rough combustion and an equivalence ratio of 0.8. Figure 6 shows the variation of near-wall and centre-line values of UHC with axial distance over a distance of 4 D from the exit of a duct of length 8.5 D for two values of equivalence ratio. The UHC distribution for the disk with radial spokes was asymmetric due to flame attachment to the spokes at equivalence ratios greater than 0.65, and near-wall values are shown in the plane of the spokes and between them. The UHC distributions point to a steady rate of reaction progress in smooth combustion and intense reaction close to the flame holder followed by slower reaction progress in rough combustion so that duct length of 8.5 D is sufficient to ensure complete combustion except at equivalence ratios close to the lean stability and flammability limits. Reaction progress in kerosene spray flames in the paragraphs that follow will, therefore, be compared mainly on the basis of near wall values of UHC in a duct of length 8.5 D

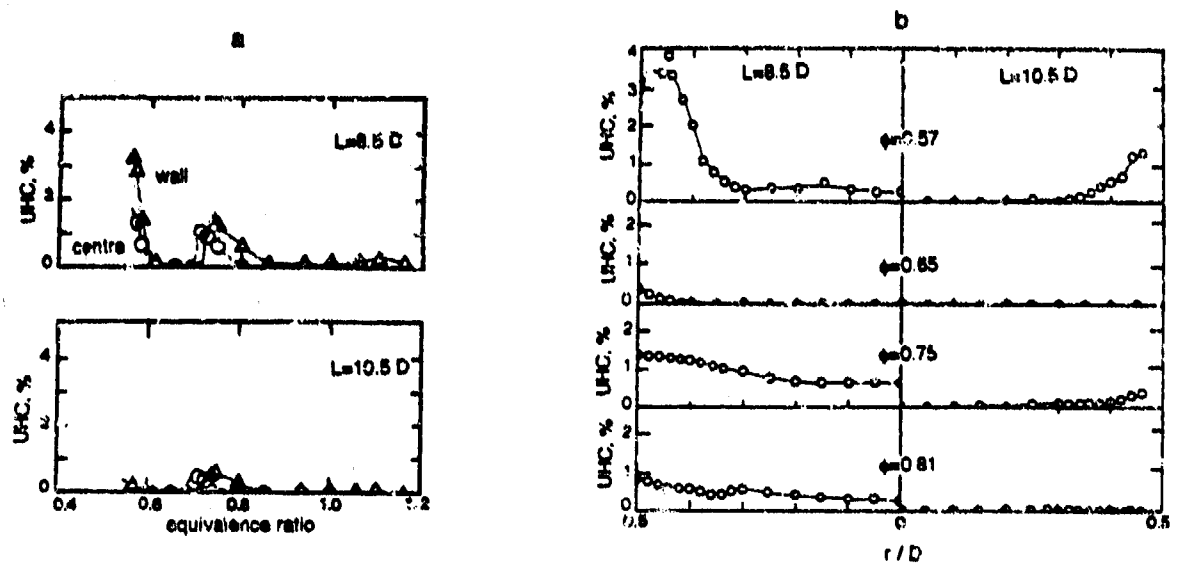

Figure 3. Unburnt hydrocarbon distribution in methane-air flame
Flow arrangement of Fig. 1a, disk, D = 50 mm, d = 0.5 D, X = 18 D, U = 10 m/s. a) near wall (r=0.45 D) and centre-line values at duct exit; b) exit profiles at x = 8.5 D for L=8.5 D and 10.5 D.

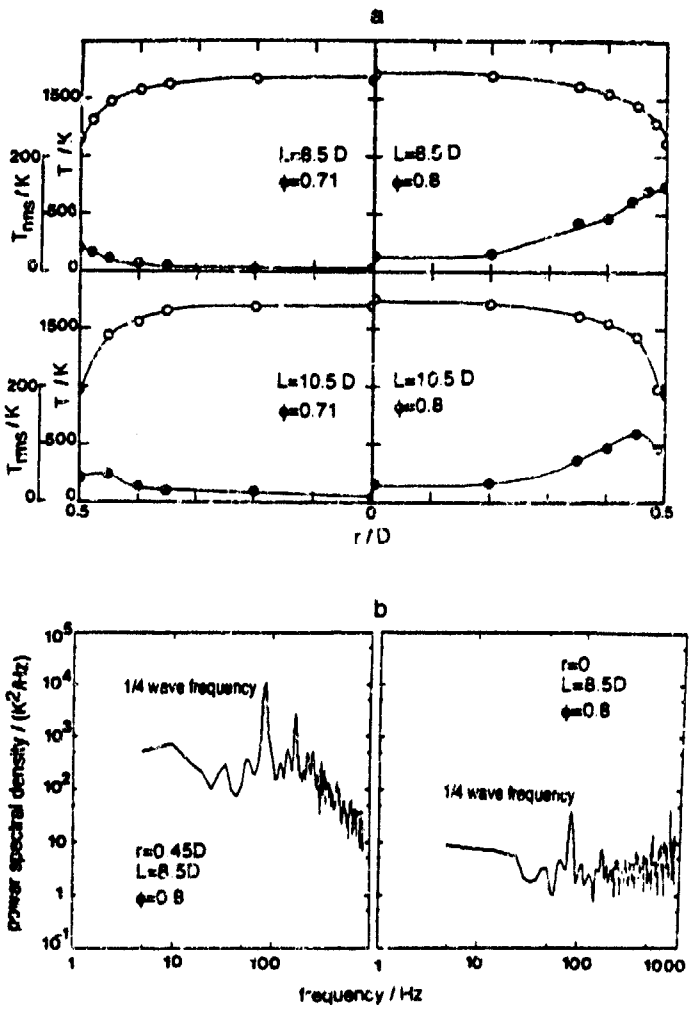

Figure 4: Temperature profiles at duct exit (uncorrected for probe heat losses)
Flow arrangement of Fig. 1a, disk, D = 50 mm, d = 0.5 D, X = 18 D, U = 10 m/s. a) mean and rms temperatures, o - T, e - T_{rms}; b) power spectra in rough combustion.

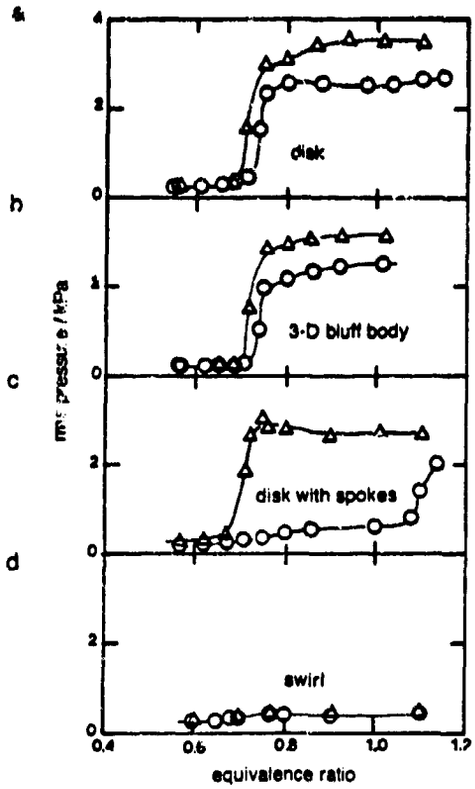

Figure 5: Antinodal rms pressures
a) flow arrangement of Fig. 1a, disk, D = 50 mm, d = 0.5 D, X = 18 D, U = 10 m/s; b) 3-dimensional flame-holder; c) disk with radial spokes; d) flow arrangement of Fig 1b, D = 50 mm, X = 18 D. o - L=8.5 D; Δ - L=10.5 D

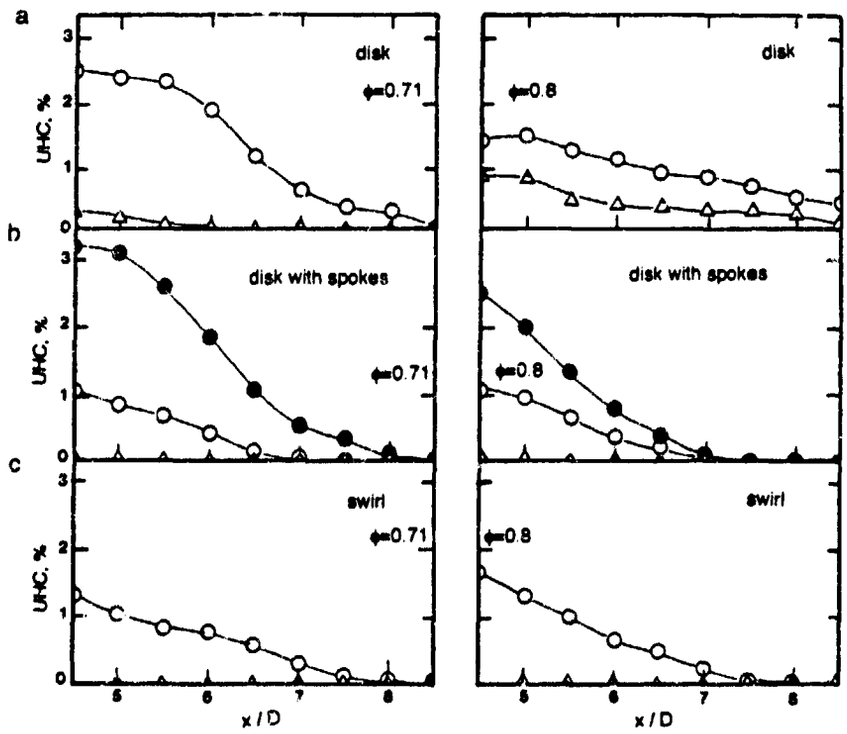

Figure 6. Longitudinal variation of UHC values
a) flow arrangement of Fig. 1a, disk, D = 50 mm, d = 0.5 D, X = 18 D, U = 10 m/s, o - near wall values; Δ - centre; b) disk with radial spokes, o - near wall values in the line of a spoke, e - between spokes; Δ - centre; c) flow arrangement of Fig 1b, D = 50 mm, X = 18 D, Sw= 2.4, o - near wall, Δ - centre

Forward injection of atomised kerosene behind disk

Liu et al. [9] reported detailed measurements of droplet size, flux and velocity using phase Doppler velocimetry for an atomiser similar to that used in the flow arrangements of Figs 1c, d, e and g, and it is sufficient for present purposes to note that the Sauter mean diameter of the droplets was around 60 μm for the atomising air flow rate of 1.05 g/s at 523 K corresponding to a mean velocity of around 110 m/s and flow rates of kerosene less than 0.5 g/s. Flame stabilisation required gaseous fuel since the upstream air was at around 20 °C, and experiments with flow rates of the liquid and gaseous fuels as variables showed that it was possible to stabilise flames with kerosene constituting around 65 % by mass of the total fuel at bulk mean flow rates around 10 m/s and close to the lean flammability limit. The proportion of liquid fuel decreased to less than 25 % at larger flow rates and equivalence ratios. The maximum flow rate of liquid fuel that could be used was also limited by the tendency of the fuel to drip following impingement on the flame holder at flow rates greater than 0.5 g/s corresponding to around 35 % of the stoichiometric mass of kerosene at an upstream bulk mean flow rate of 10 m/s, and the results presented in this paper are for kerosene flow rates which did not lead to dripping.

The stoichiometric fuel-to-air ratios are different for kerosene and methane and the results that follow are presented on the basis of the equivalence ratio expressed as the ratio of the stoichiometric air necessary to burn the fuel and the actual air supplied. With kerosene injection downstream of the flame-holder, the equivalence ratio of the methane-air mixture in the upstream duct was more useful in interpreting the results. The mass flow rate of kerosene is expressed in non-dimensional form as a fraction of the stoichiometric mass flow rate for the kerosene.

Inspection of the wall temperature distributions in the flow arrangement of Fig. 1c without and with liquid fuel suggested that the flame was making contact with the wall at a shorter distance from the disk than in the arrangement of Fig. 1a. Near-wall measurements of UHC were made in smooth combustion at a distance of 4 D from the exit of the duct of length 8.5 D, without and with unheated atomising air and in the absence of liquid fuel for an upstream flow rate of 10 m/s and an equivalence ratio of 0.7. The UHC value decreased from around 2.5 % without atomising air to around 1.2 % with unheated atomising air due to the impingement of the atomising air on the flame-holder. The resulting increase in upstream turbulence did not, however, lead to larger amplitudes of oscillation. Figure 7 shows the flammability limits for the flow arrangement of Fig. 1c and two values of upstream mean flow rate. The flow distribution past the flame-holder was altered by the injection of atomising air so that the flammability and stability limits were different from those for the premixed methane-air flame. In the absence of liquid fuel, the lean flammability limit for an upstream bulk mean velocity of 10 m/s was around 0.62 compared with 0.55 for the premixed flame without the atomising jet due to the dilution of the fuel-air mixture close to the disk. This also resulted in a reduction in heat release close to the disk and in smaller amplitudes of oscillation. The richer fuel-air mixture away from the disk and the larger turbulence intensity led, however, to faster reaction progress further downstream. An increase in the air flow rate to 15 m/s led to an increase in fuel composition closer to the disk and to larger amplitudes of oscillation comparable with those in premixed flows and a narrower flammability range due to the uneven distribution of fuel composition in the vicinity of the flame-holder.

The addition of a small amount of liquid fuel enabled flame stabilisation at a smaller equivalence ratio than without liquid fuel and an increase in the proportion of liquid fuel to values greater than 20 % of the total led to an increase in the lean stability limit based on the overall equivalence ratio due to most of the kerosene remaining in the liquid phase. The injection of liquid fuel resulted in a decrease in the amplitude of oscillations because of the decrease in intensity of heat release close to the disk caused by the combustion delay due to the evaporation of the droplets and, to a smaller extent, by some of the heat release being used in the evaporation of the droplets.

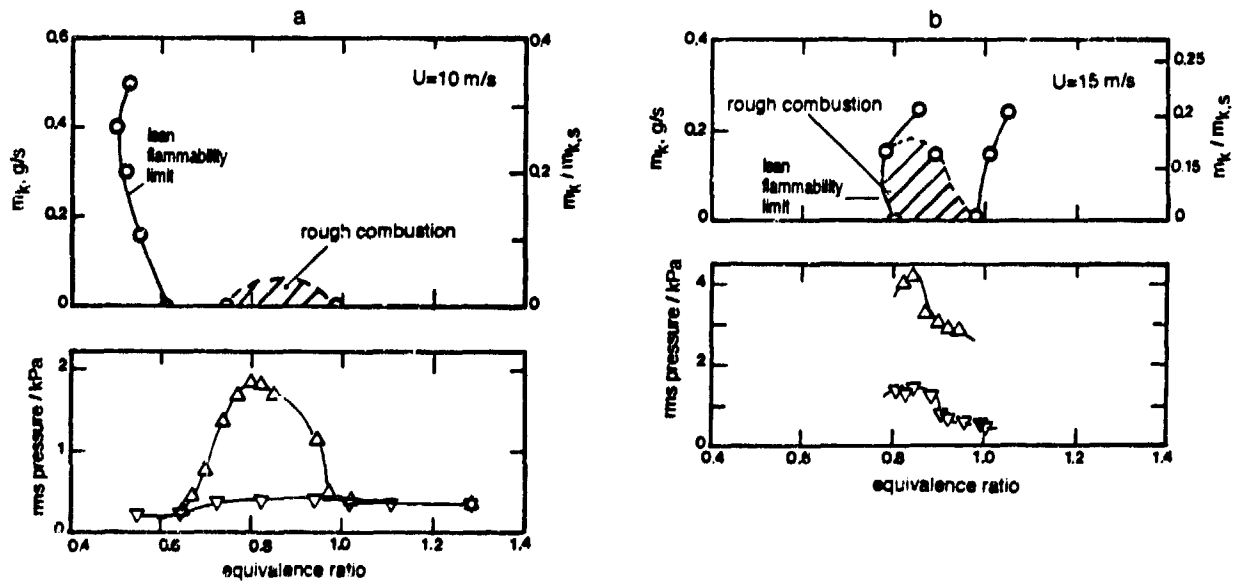

Figure 7 Lean flammability and stability limits and antinodal rms pressures
Flow arrangement of Fig. 1c, D = 50 mm, d = 0.5 D, X = 18 D. a) U = 10 m/s, Δ - m_k=0; ∇ - $m_k/m_{k,s}$=0.11; b) U=15 m/s, Δ - m_k=0; ∇ - $m_k/m_{k,s}$=0.08.

Measurements of UHC within the duct showed that a length of around 7.5 D was adequate to ensure complete combustion for equivalence ratios between 0.6 and 1.0 and in the absence of combustion oscillations. Rough combustion led to near-wall UHC values of order 0.7 % at the duct exit for the duct length of 8.5 D in Fig. 8, and an increase in duct length to 10.5 D resulted in complete combustion as in the flow arrangement of Fig. 1a. Figure 8 also shows that the UHC values measured 4.5 D from the disk decreased with equivalence ratio for the different values of kerosene flow rate.

The impingement of the jet of atomising air on the flame-holder led to an increase in upstream turbulence and to a faster rate of reaction. It also led to an uneven distribution of fuel close to the flame holder and flammability and stability limits different from those for the disk-stabilised flames in the flow arrangement of Fig. 1a. The differences in the reaction progress rates without and with liquid fuel, although small, were due to differences in the amplitude of oscillation, and UHC measurements in the flow arrangements of Figs. 1d and e with a more homogenous distribution of fuel and air are likely provide more conclusive evidence on the influence of atomised kerosene on reaction progress.

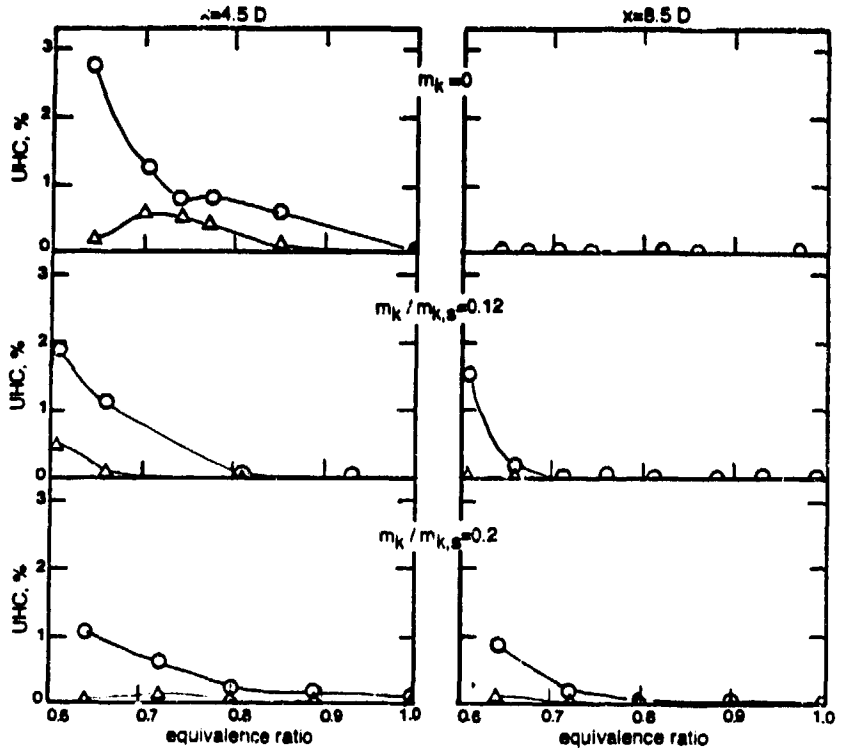

Figure 8: Longitudinal variation of UHC values
Flow arrangement of Fig. 1c, D = 50 mm, d = 0.5 D, X = 18 D, U = 10 m/s o - near wall; Δ - centre.

Backward injection of kerosene

The amount of kerosene that could be injected in the flow arrangement of Fig. 1d was, again, limited by the tendency of the liquid fuel to drip from the anvil, and detailed measurements were made with kerosene flow rates less than 0.3 g/s, corresponding to around 20 % of the stoichiometric mass of kerosene, for which all fuel was burned within the duct. Since the flammability and stability limits depend on the vapour phase of the fuel composition in the flow past the disk, the flammability and stability limits of Fig. 9 increased with the flow rate of kerosene due to kerosene remaining in the liquid phase and the amplitude of oscillations in rough combustion was similar to that in the flow arrangement of Fig. 1a. Inspection of the wall temperature indicated that the flame made contact with the wall at a shorter distance from the disk than in the methane-air flame in the flow arrangement of Fig. 1a and the values of UHC at the centre of the duct and near the wall at a distance of 4.5 D from disk (Fig. 10) were less than those for the methane air flame for an upstream flow rate of 10 m/s and a duct length of 8.5 D due to the higher turbulence intensity. Although the values of UHC at this location increased with the flow rate of kerosene due to the evaporation of the droplets, the exit values showed smaller differences.

The maximum flow rate of kerosene was increased to 0.5 g/s corresponding to 35 % of the stoichiometric mass of kerosene in the flow arrangement of Fig. 1e with the upstream air preheated to 150 °C. The higher mean temperature of the upstream flow implied a faster reaction rate than in the unheated flow arrangement of Fig. 1d, and the upstream mean flow rate was 15 m/s compared with 10 m/s in the other flow arrangements in order that the range of values of the mass flow and heat release rates were the same for all flow arrangements. The lean flammability and stability limits in Fig. 11 are nearly the same as those for the premixed flames in the flow arrangement of Fig. 1a and their variation with kerosene flow rate is small due to the evaporation of a larger part of the kerosene in the upstream duct. Rough combustion dominated by the half-wave frequency gave way to a full-wave frequency at an equivalence ratio of around 0.9 for all flow rates of kerosene due to the long upstream duct length and the larger mean velocity. The reaction progressed to completion over a shorter distance than in the flows with

unpreheated air due to the higher reaction rate at the higher temperature: the UHC values at a distance of 6.5 D from the disk (Fig. 12) are similar to those at a distance of 8.5 D in unheated flows without and with kerosene. The increase in UHC with the mass flow rate of kerosene further upstream at a distance of 4.5 D from the disk was, as in the unpreheated flow arrangement of Fig. 1d, due to some of the kerosene remaining in the liquid phase downstream of the flame-holder.

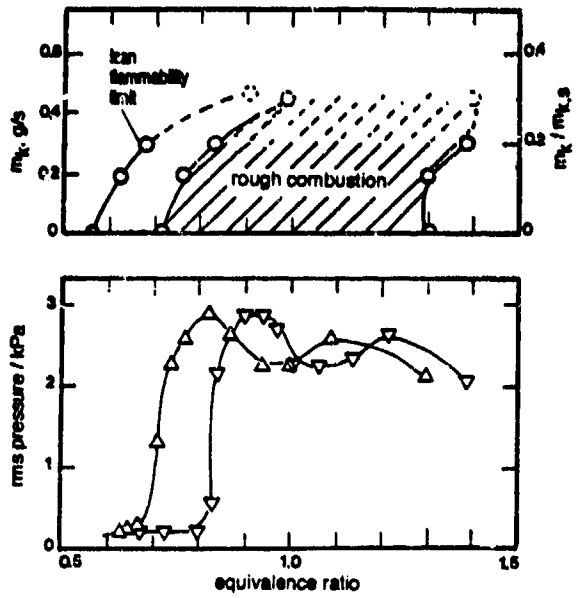

Figure 9: Lean flammability and stability limits and antinodal rms pressures
Flow arrangement of Fig. 1d, D = 50 mm, d = 0.5 D, X = 18 D, U = 10 m/s. △ - m_k=0; ▽ - $m_k/m_{k,s}$=0.2.

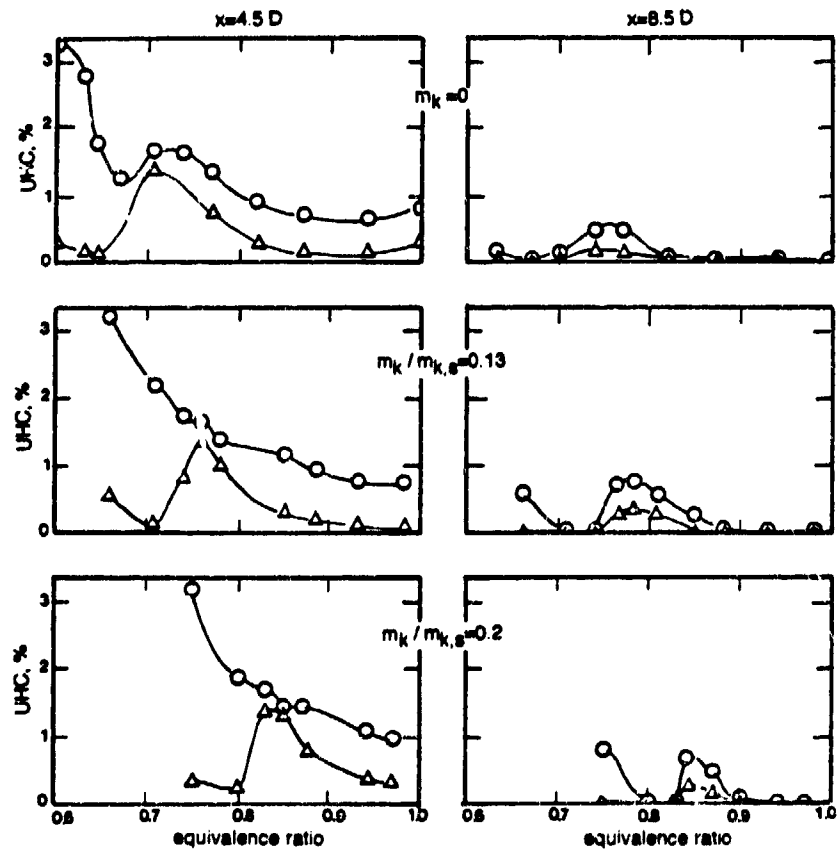

Figure 10: UHC values within the duct and at exit
Flow arrangement of Fig. 1d, D = 50 mm, d = 0.5 D, X = 18 D, U = 10 m/s. o - near wall; △ - centre.

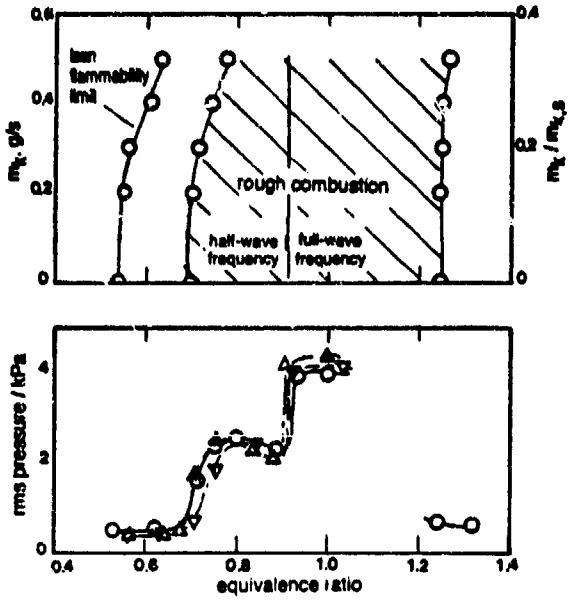

Figure 11: Lean flammability and stability limits and antinodal rms pressures
Flow arrangement of Fig. 1e, D = 50 mm, d = 0.5 D, X = 18 D, U = 15 m/s. o - m_k=0; Δ - $m_k/m_{k,s}$=0.13; ∇ - $m_k/m_{k,s}$=027.

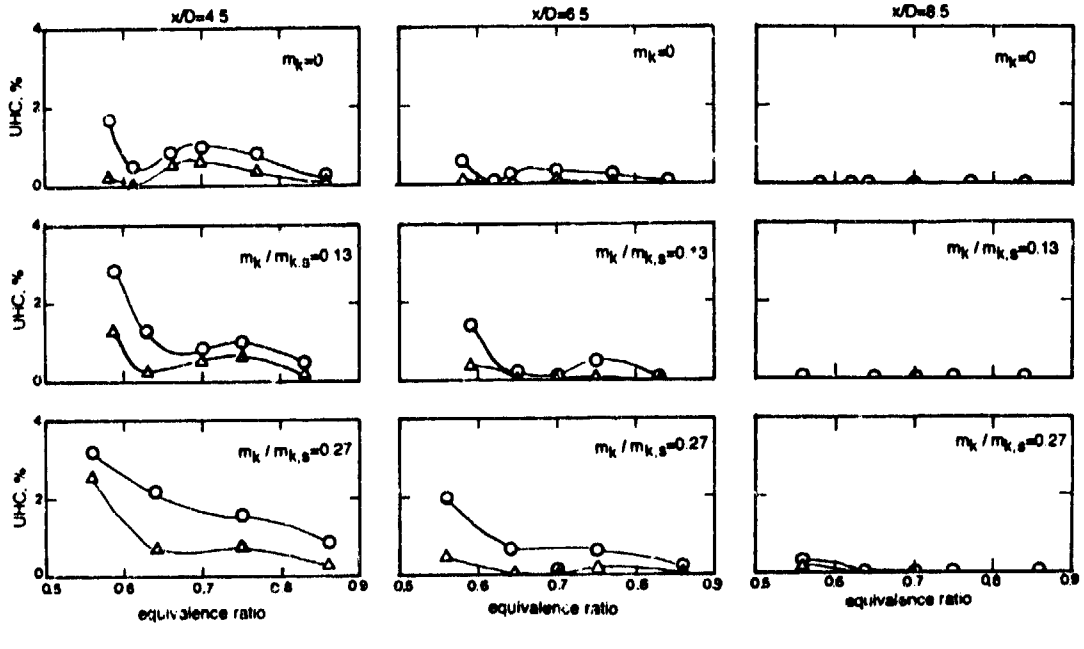

Figure 12: UHC values within the duct and at exit
Flow arrangement of Fig. 1e, D = 50 mm, d = 0.5 D, X = 18 D, U = 10 m/s. o - near wall; Δ - centre.

Forward injection of kerosene through the disk

In the flow arrangement of Fig. 1f, the fuel was injected through a 7 mm hole in a disk of diameter 30 mm with an area blockage of around 0.34 compared with 0.25 in the other fuelling arrangements. The increase in diameter was necessary to ensure flame stabilisation over a range of equivalence ratios similar to that for the disk of area blockage ratio 0.25. The diameter of the central hole in the disk was larger than that of the atomiser so as to reduce the bulk mean velocity of the atomising air to a value of around 50 m/s from around 110 m/s in the atomiser. The smaller axial velocity was more compatible with the mean flow rate in the combustor duct (13 m/s in the plane of the flame-holder and around 50 m/s at the exit) and prolonged the residence time of the liquid fuel within the combustor. The lean flammability limit for the flame with a central jet of air was higher than that for the disk without a central jet of air. Injection of kerosene resulted in a decrease in the flammability limit due to the fuel rich air flow on the inside of the annular recirculation zone behind the disk, and flame stabilisation was possible without gaseous fuel for kerosene flow rates greater than 0.4 g/s, corresponding to an equivalence ratio of 0.27, due to the establishment of a diffusion flame at the centre of the disk by the kerosene rich atomising jet. The lean stability limit based on the overall equivalence ratio increased with liquid fuel flow rate, and a

closer examination of the results showed that the stability limits based on the equivalence ratio of the premixed methane-air flow upstream of the disk in Fig. 13 for a downstream duct length of 8.5 D and a bulk mean flow rate of 10 m/s on a non-reacting basis were nearly invariant with the flow rate of kerosene. The figure also shows that the amplitude of oscillations depended mainly on the equivalence ratio of the gaseous fuel air mixture which determined the intensity of heat release close to the disk and was comparable with values in Figs. 4a and 8 for methane-air flames behind a disk of area blockage ratio 0.25.

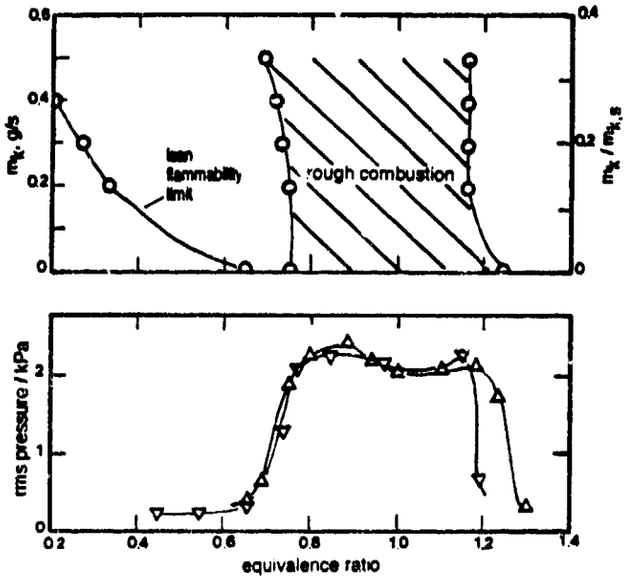

Figure 13: Lean flammability and stability limits based on upstream equivalence ratio, and antinodal rms pressures
Flow arrangement of Fig. 1f, D = 50 mm, d = 0.5 D, X = 18 D, U = 15 m/s. Δ · m_k=0; o · $m_k/m_{k,s}$=0.2.

Reaction progress in flows with a central jet of air was slower than in premixed flames behind a disk in the flow arrangement of Fig. 1a, and the addition of kerosene enabled complete combustion inside a duct of length 8.5 D for kerosene flow rates less than 0.3 g/s (corresponding to 0.2 of the stoichiometric mass) and smooth combustion. Unburnt hydrocarbon was evident at the duct exit on transition to rough combustion, and the exit profiles of Fig. 14 show that an increase in duct length to 10.5 D resulted in complete combustion. Larger flow rates of kerosene comprising more than 30 % of the total fuel led to soot formation and bright yellow flames because of the large fuel-to-air ratio in the central jet and the short residence time of the kerosene leading to incomplete combustion at the centre of the duct.

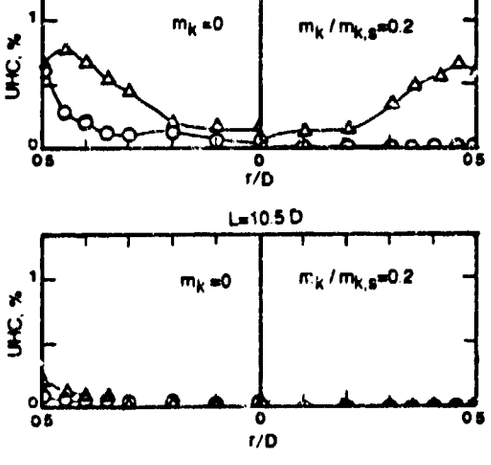

Figure 14: UHC profiles at exit
Flow arrangement of Fig. 1f. D = 50 mm, d = 0.5 D, X = 18 D, U = 10 m/s o · upstream equivalence ratio = 0.7; Δ · 0.8.

Oscillatory injection of kerosene

The Sauter mean diameter of the kerosene droplets from the pintle injector were measured by laser diffraction method to be around 140 μm and the mean velocity of the spray around 10 m/s in still air. The laser diffraction method, unlike phase Doppler velocimetry, underestimates the diameter by around 30 % [18] and the actual Sauter mean diameter of the droplets is likely to be around 200 μm compared with around 150 μm for petrol [16, 19]. The injector was located in the plane of the disk and the kerosene injected towards the centre of the duct at an angle of 45 ^{0} to the axis to direct the fuel into the burning zone close to the disk.

The influence of the frequency of injection and the equivalence ratio of the upstream fuel-air mixture were examined with downstream duct lengths of 8.5 and 10.5 D. The mean injection rate of kerosene, maintained at the possible minimum that will permit atomisation, varied linearly with frequency from 0.1 g/s at 50 Hz to 0.3 g/s at 150 Hz. An increase in the injection rate at a given frequency did not result in an increase in amplitude of combustion oscillations due to the slow evaporation of the fuel. The oscillation of fuel led to pressure fluctuations of large amplitude at equivalence ratios associated with smooth combustion only when the forcing frequency was close to the quarter-wave frequency the entire duct length. Amplitudes of up to 1.5 kPa at a frequency of 63 Hz were observed with a downstream duct length of 8.5 D and upstream equivalence ratios between 0.7 and 0.73. The amplitude of oscillations increased to around 1.8 kPa at a frequency of 61 Hz when the duct length was increased to 10.5 D. Oscillations dominated by the quarter-wave frequency of 95 Hz in the upstream duct with amplitudes greater than 2 kPa were observed in rough combustion at upstream equivalence ratios greater than 0.74. Figure 15 shows the variation of the rms pressure close to the upstream end of the combustor for a duct length of 8.5 D, an upstream flow rate of 10 m/s and two values of upstream equivalence ratio in the flow arrangement of Fig. 1g with frequency of oscillation of fuel as variable.

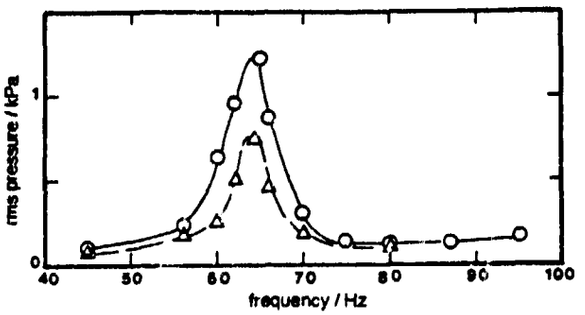

Figure 15: variation of rms pressure with frequency
Flow arrangement of Fig. 1g, D = 50 mm, d = 0.5 D, X = 18 D, U = 15 m/s. Δ - upstream equivalence ratio = 0.7; o - 0.71.

Combustion was incomplete because of the uneven distribution of fuel due to a large part of the fuel spray crossing the recirculation zone behind the disk. Part of the flame was yellow at the exit and there was evidence of soot formation. Figure 16 shows the exit profiles of UHC and CO for a duct length of 8.5 D and two values of equivalence ratio, one associated with a small amplitude of oscillation and the other with an antinodal rms pressure of around 1.3 kPa. The values of UHC and CO on the side of the wall opposite the point of injection of fuel are large due to the large concentration of kerosene in that part of the flow. Further away, the values of CO are smaller and the UHC values comparable with those for the premixed flow arrangement of Fig. 1a. An increase in duct length to 10.5 D did not result in a significant reduction in the large values of UHC resulting from an excess of fuel in one part of the flow.

Oscillations in rough combustion were ameliorated with a closed-loop control arrangement [13] by pulsing the fuel at the dominant quarter-wave frequency of 95 Hz in the upstream duct and out of phase with it. The characteristics of the injector determined that the mean injection rate of kerosene was around 13 % of the total fuel and the oscillatory input was, therefore, not varied. Control was applied to oscillations with antinodal rms pressure of up to 2 kPa in a duct of length 8.5 D to avert damage to the injector nozzle due to the heating of the wall by the oscillation of the flame front about the plane of the disk at larger amplitudes of oscillation, and the rms pressure was attenuated by around 10 dB (a factor of 3) as in active control by the oscillation of gaseous fuel at a constant amplitude [13]. Reaction progress was not affected by control since incomplete combustion was due the uneven distribution of fuel.

4. DISCUSSION

The most important result of the present study is that pulsed injection of liquid fuel can induce oscillations of large amplitude at equivalence ratios usually associated with smooth combustion and control oscillations of large amplitude in rough combustion. Pulsed injection of kerosene comprising around 10 % of the total fuel induced amplitudes similar to those induced by the oscillation of gaseous fuel comprising around 15 % of the total fuel behind the flame-holding disk in a duct of diameter 50 mm [20]. These amplitudes were possible despite the burning of a large fraction of the pulsed kerosene far downstream of the disk. The minimum value of the mean injection rate of kerosene at the dominant frequency determined that control was imposed with an oscillatory input of constant amplitude, and the attenuation of the antinodal rms pressure by 10 dB (a factor of 3) was the same as that reported by Hendricks et al. [13] for control by the oscillation of gaseous fuel at

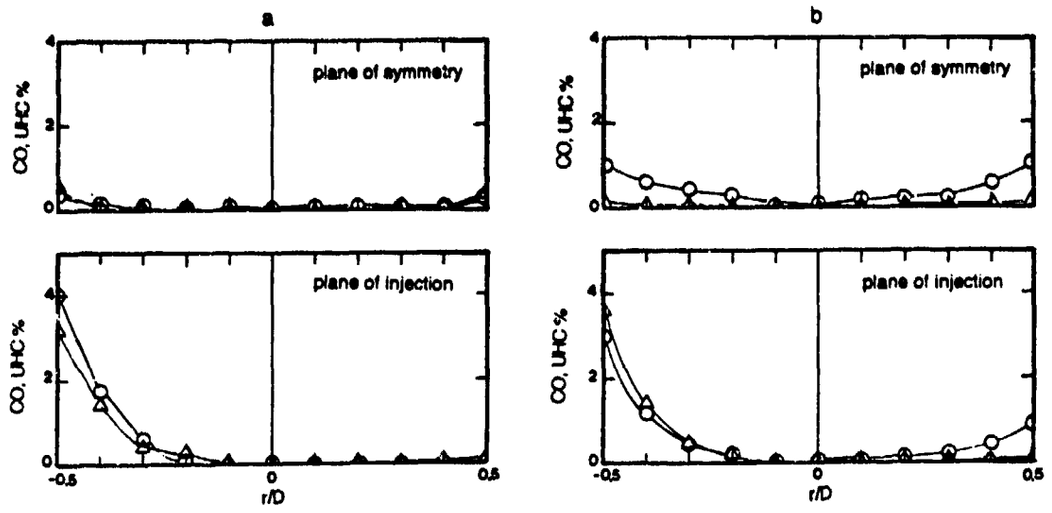

Figure 16: UHC and CO profiles at exit
Flow arrangement of Fig. 1g, D = 50 mm, d = 0.5 D, X = 18 D, U = 10 m/s, $m_k / m_{k,s} = 0.1$.
a) upstream equivalence ratio = 0.67; b) upstream equivalence ratio = 0.71; o - UHC; Δ - CO

constant amplitude but 5 dB (a factor of 1.7) less than that with a variable amplitude. The amplitude of the pulsed input can, however, be varied at larger heat release rates since the minimum value of the injection rate will be a smaller fraction of the total fuel. Preheating of the fuel, improved atomisation and optimisation of the direction and location of fuel injection will enable the burning of the oscillated fuel close to the flame-holder and increase the effectiveness of the oscillatory input so that the amount of fuel that needs to be pulsed will be a very small fraction of the total, and active control will still need to address the problem of modulating the oscillation of fuel, especially at heat release rates less than 1 MW.

The duct length necessary to ensure complete combustion decreases with the overall equivalence ratio of the fuel-air mixture and is nearly independent of the proportion of kerosene to methane in the vapour phase. An increase in the turbulence intensity upstream of the flame holder can lead to faster reaction rates: for example, complete combustion was possible over an axial distance of 7 D in smooth combustion for an equivalence ratio of 0.8 and a mean flow rate of 10 m/s in swirl stabilised flames and flames behind a disk with radial spokes and the higher turbulence intensity in the flow arrangement of Fig. 1c reduced this distance to around 4.5 D. The reaction rate also increases with upstream temperature in accordance with the expression for combustion efficiency in stirred reactors [21]:

$$\eta = f\,[p^{1.75}\, V_c \exp(T/b) / m]$$

where p and T are the pressure and temperature at the burner inlet, V_c is the burner volume, m is the mass flow rate and b is a parameter representing temperature dependence and taken as 300 for temperature expressed in Kelvin. This implies that, for a given mass flow rate, the duct length required for complete combustion with an upstream temperature of 150 ^{o}C as in the flow arrangement of Fig 1e will be 30 % less than that for a temperature of 20 ^{o}C in the flow arrangement of Fig. 1d. The axial distances necessary for the completion of combustion in the absence of liquid fuel were in good agreement with this estimate. Flows with liquid fuel showed similar trends although quantitative comparison is hampered by the presence of different proportions of the fuel in liquid phase.

Heat release distribution close to the flame holder can be altered, for instance by the addition of swirl [22], and an increase in the intensity of heat release leads to larger amplitudes and a decrease to smaller amplitudes and less susceptibility to rough combustion. The present measurements have confirmed the importance of the intensity of heat release close to the flame holder to rough combustion and that of flame confinement to the amplitude. The reason why certain flame holder designs are less susceptible to rough combustion than others cannot, however, be explained fully on the basis of the present results and detailed measurements of the mean and oscillating temperature and velocity in the near field of the flame holders are necessary.

The flammability and stability limits in kerosene-fuelled flames appears to depend on the vapour phase of the flow upstream of the flame holder, and measurements with preheated air have shown that the slower reaction progress in the section of the duct near the flame-holder in kerosene spray flames is due to part of the kerosene remaining in the liquid phase. The difference in the duct lengths necessary to ensure flame confinement in flames without and with kerosene was small except in fuelling arrangements which led to a large concentration of kerosene in a section of the flow. A variation in the proportion of kerosene by between 0 and 40 % did not result in a difference in amplitude of oscillations. This is in agreement with earlier comparisons between methane and propane fuelled premixed flames [23] and justifies the use of light hydrocarbons to model heavier hydrocarbon fuel combustion.

REFERENCES

[1] Tuttle, J.H., Altenkirch, R.A. and Mellor, A.M., Emissions from and within an Allison J-33 combustor - II: the effect of inlet temperature, Combustion Science and Technology, 1973, **7**, pp.229-241.

[2] Vranos, A. and Taback, E.F., Combustion product distributions in the primary zone of a gas turbine combustor, Combustion and Flame, 1976, **46**, pp. 129-131.

[3] Noyce, J.R., Sheppard, C.G.W. and Yamba, F.D., Measurements of mixing and species concentrations within a gas turbine type combustor, Combustion Science and Technology, 1981, **25**, pp.209-217

[4] Heitor, M.V. and Whitelaw, J.H., Velocity, temperature, and species characteristics of the flow in a gas-turbine combustor, Combustion and Flame, 1986, **64**, pp.1-32.

[5] Bicen, A.F., Tse, D.G.N. and Whitelaw, J.H., Flow characteristics of a model annular combustor, AGARD CP 422, paper 14, 1987.

[6] Chow, S.K. and Whitelaw, J.H., Scalar characteristics of a liquid-fuelled combustor with curved exit nozzle, **Aerothermodynamics in Combustors**, Springer Verlag, 1992, pp. 291-299.

[7] Jones, W.P. and Tober, A., **Measurement of gas temperature and concentration inside a can-type model combustor, Aerothermodynamics in Combustors**, Springer Verlag, 1992, pp. 327-338.

[8] Sotheren, A., The Rolls-Royce annular vaporizer combustor, Journal of Engineering for Gas Turbines and Power, 1984, **106**, pp.88-95.

[9] Liu, C.H., Perez-Ortiz, R.M. and Whitelaw, J.H., Vaporizer performance, Proceedings of the Institution of Mechanical Engineers, 1992, **206**, pp. 265-273.

[10] Sivasegaram, S. and Whitelaw J.H., Suppression of oscillations in disk-stabilised flames, Journal of Propulsion and Power, **3**, 1987, pp. 291-295.

[11] Sivasegaram, S., Thompson, B.E. and Whitelaw J.H., Acoustic characterisation relevant to gas turbines, Journal of Propulsion and Power, **5**, 1989, pp. 109-115.

[12] Langhorne, P.J., Dowling, A.P. and Hooper N., Practical active control system for combustion oscillations, Journal of Propulsion and Power, **6**, 1990, pp. 324-330.

[13] Hendricks, E.W., Sivasegaram, S. and Whitelaw, J.H., Control of oscillations in ducted premixed flames, **Aerothermodynamics in Combustors**, Springer Verlag, 1992, pp. 215-230.

[14] Perez-Ortiz, R.M., Sivasegaram, S. and Whitelaw, J.H., Comparison of oscillations in ducted premixed combustion, Department of Mechanical Engineering, Imperial College, London, Report TF/92/27, 1992

[15] Gutmark, E., Schadow, K.C., Nina, M.N.R. and Pita, G.P.A., Suppression of buzz instability by geometrical design of the flame holder, AIAA Paper 90-0270, 1990.

[16] Hardalupas, Y., Okomoto, S., Taylor, A.M.K.P. and Whitelaw, J.H., Application of a phase Doppler anemometer to a spray impinging on a disk, Sixth International Symposium on Application of Laser Techniques to Fluid Mechanics, Lisbon, Paper 25.2, 1992.

[17] Mastorakos, E., Thermocouple signal acquisition and processing system: an instruction manual, Department of Mechanical Engineering, Imperial College, London, Report TF/92/08, 1990.

[18] Coessali, E. and Hardalupas, Y., Comparison between laser diffraction and phase Doppler velocimeter techniques in high turbidity, small diameter sprays, Experiments in Fluids,1992, **13**, pp. 414-422.

[19] Hardalupas, Y., Taylor, A.M.K.P. and Whitelaw, J.H., Unsteady sprays by pintle injector, JSME International Journal, 1990, **33**, pp. 177-185.

[20] Papatheofrastou, M., **Oscillatory Jets in Parallel and Cross Flows in Ducts**, MSc Thesis, University of London, 1992

[21] LeFebvre, A.W., **Gas Turbine Combustion**, McGraw Hill, 1983.

[22] Sivasegaram, S. and Whitelaw. J.H., The influence of swirl on oscillationd in ducted premixed flames, Combustion and Flame, 1991, 85 195-205.

[23] Sivasegaram, S. and Whitelaw. J.H., Combustion oscillations in dump combustors with a constricted exit, Proceedings of the Institution of Mechanical Engineers, 1988, 202, pp. 205-210.

ACKNOWLEDGEMENTS

We are glad to acknowledge financial support from Rolls Royce Plc. and from the US Navy, Office of Naval Research, under grant N-00014-89-J-1721. Useful discussions with Dr. E. Hendricks are gratefully acknowledged and so is the assistance of Mr. R-F. Tsai with some of the measurements.

SPRAY COMBUSTION EXPERIMENTS AND NUMERICAL PREDICTIONS

by

Dr Edward J. Mularz
Vehicle Propulsion Directorate
U.S. Army Research Laboratory
Lewis Research Center
21000 Brookpark Road
Cleveland, Ohio 44135-3191
United States

Dr Daniel L. Bulzan
National Aeronautics and Space Administration
Lewis Research Center
Cleveland, Ohio 44135
United States

and

Dr Kuo-Huey Chen
University of Toledo
Toledo, Ohio 43606
United States

SUMMARY

The next generation of commercial aircraft will include turbofan engines with performance levels significantly better than those in the current fleet. Control of particulate and gaseous emissions will also be an integral part of the engine design criteria. These performance and emission requirements present a technical challenge for the combustor: control of the fuel and air mixing and control of the local stoichiometry will have to be maintained much more rigorously than with combustors in current production. A better understanding of the flow physics of liquid fuel spray combustion is necessary. This paper describes recent experiments on spray combustion where detailed measurements of the spray characteristics were made, including local drop-size distributions and velocities. Also, an advanced combustor CFD code has been under development and predictions from this code are compared with experimental results. Studies such as these will provide information to the advanced combustor designer on fuel spray quality and mixing effectiveness. Validation of new fast, robust, and efficient CFD codes will also enable the combustor designer to use them as valuable additional design tools for optimization of combustor concepts for the next generation of aircraft engines.

A. INTRODUCTION

Aircraft engines being envisioned now for the next-century aircraft will have requirements that present formidable technical challenges to the combustor designer. In the subsonic commercial transport arena, demand for low operating cost translates into reduced fuel consumption and improved durability and reliability. Higher operating pressures of the combustor are forecast, with higher resulting fuel system turndown ratios. Coupled with these performance requirements is the demand world wide for control of pollutant emissions from aircraft engines, especially oxides of nitrogen. In the arena of supersonic commercial transports, forecasts are predicting fleets of hundreds of transports operating at Mach 2.0 to 2.5, with airfares only slightly higher than today's long-range subsonic fares. Economical fuel consumption is a requirement. But the largest technical challenge here is low levels of oxides of nitrogen emissions during engine cruise such that there would be no adverse impact to the earth's environment, specifically the atmosphere's ozone layer.

These technical and environmental challenges represent design requirements for the combustor that are outside of engine companies' experience. Empirically based design methods are insufficient by themselves. To augment this design system, the companies are increasingly turning to computational fluid dynamics (CFD) computer codes. Severe limitations with currently available codes are excessive time requirements to run a CFD code to analyze a complex combustor design: a penalty both in turn-around time for design answers as well as cost for the calculations. We at NASA are attempting to improve this current situation in the industry by developing a fast, robust, efficient computer code for internal chemical reacting flows. The objective is to produce a CFD code that can be used as a more powerful design tool in the industry to analyze complex combustor designs in significantly shorter turn-around time than current computer codes can achieve.

An integral part of the development of a new CFD code is the validation of this code with experiments that represent the complex features of the flows which need to be analyzed. Therefore, at NASA we are also conducting experiments on liquid fuel spray combusting flows with increasingly complex features. This will provide some of the required data for validation of our CFD code and other's codes. Detailed measurements of both liquid sprays and gas characteristics are being obtained under both nonburning and burning conditions.

This paper will highlight recent results that NASA has obtained with its spray combustion experiment and describe

Presented at an AGARD Meeting on 'Fuels and Combustion Technology for Advanced Aircraft Engines', May 1993.

the formulation and physical modeling of its new spray combustion CFD code (ALLSPD). The application of this code to combustion problems will be illustrated by several examples.

B. SPRAY COMBUSTION EXPERIMENTS

Combusting sprays are very important for gas turbine engine applications. The investigation of combusting sprays should lead to a better understanding of the physics involved in this complicated process. Important processes involved in combusting sprays are the interactions between the droplets and the gas phase, the vaporization of the droplets, and chemical reactions with heat release. These physical processes are coupled and can only be completely described using numerical modeling. As part of an effort to improve the numerical modeling of gas turbine combustors, an experimental study has been undertaken to obtain a data set for a relatively simple liquid-fueled combustor that can be used for comparison with numerical models (Ref. 1).

Because of their practical applications, swirling flows with combustion have been studied by a large number of investigators. Earlier reviews of swirling flows both with and without combustion present some general trends (Refs. 2 to 4). These papers predate the development of nonintrusive, laser-based diagnostics; consequently all of the results described were obtained using intrusive instrumentation and detailed structure measurements for these types of flows were not possible. With the advent of newer instrumentation techniques, namely laser Doppler anemometry, additional details of the structure of these types of flows began to emerge. Laser Doppler anemometry velocity measurements in spray flames (Refs. 5 and 6) reveal some of the flowfield structure of swirling flames. The development of the phase/Doppler particle analyzer (Ref. 7), enabled the simultaneous measurement of droplet size and velocity. This instrument has been used by a number of investigators for measurements in spray flames in a variety of configurations (Refs. 8 to 12). This instrument has the capability to measure velocities of both the gas and droplet phases in a combusting spray.

B.1 EXPERIMENT

The combustor utilized in the present experiment is illustrated in Fig. 1. It consists of a center mounted air-assist fuel nozzle, Parker Hannifin research simplex air-assist atomizer, surrounded by a coflowing air stream. The nozzle orifice diameter was 4.8 mm. Both the air assist and the coflow air streams had swirl imparted to them using 45 degree swirlers. The swirlers were constructed by machining 45 degree slots into rings. Both streams were swirled in the same direction for the present study. The combustion air was not preheated and entered the combustor at 297 K. The top of the air-assist nozzle was water cooled to prevent overheating of an O-ring in the nozzle assembly. The temperatures of the fuel, atomizing air and coflow air streams were measured using Chromal Alumel thermocouples. Flow rates of the air streams were measured using calibrated orifices and the fuel flow rate was measured using a mass flowmeter. All results reported in the present study are reported for a coflow air flow rate of 13.88 g/s, an air-assist flow rate of 0.96 g/s, and a fuel flow rate of 0.38 g/s. The fuel used was heptane. The coflow stream entered the combustor in three radial locations, passed through a honeycomb flow straightener, and the swirlers before exiting the combustor. The swirler was located 140 mm upstream of the combustor exit. The flow from the combustor discharged into ambient, stagnant surroundings.

The combustor was mounted vertically within a large (1.8 m sq by 2.4 m high) enclosure. The entire enclosure was mounted on two sets of linear bearings and was traversed using stepper motors to provide motion in two directions. The combustor assembly itself could be traversed in the vertical direction using a third stepper motor to allow measurements at all locations in the flowfield. This arrangement allowed rigid mounting of all optical components.

The phase/Doppler particle analyzer was used for all measurements reported in this study. A schematic of the two-component instrument is shown in Fig. 2. The beam from a 6 W Argon-Ion laser is split into 488.0 and 514.5 nm wavelengths using a dichroic mirror. Each beam is then focused onto a rotating diffraction grating which splits each beam into several pairs. The two first-order beams for each wavelength are then recombined onto the optical axis using a dichroic mirror, collimated and focused at a point to form the two-component probe volume. In the present study, the transmitting optics utilized a 500 mm focal length lens. The receiving optics were located 30 degrees off axis in the forward-scatter direction. Light was collected using a 500 mm focal-length lens and then focused onto a 100 μm by 1 mm long slit. The collected light is then split and picked up by four photodetectors. Three are arranged to look at the signals from the 514.5 beams and one receives light from the 488 nm beams. Each of the three photodetectors for the green beams are imaged at a different area of the collection lens and the phase difference between the signals is used for the size determination. Details of the instrument can be found in Ref. 7.

In the present study, velocities of both the liquid and gaseous phases were measured. This was accomplished by seeding the gas phase with nominal 1 μm size aluminum-oxide particles. The coflow, air-assist flow, and the ambient surroundings were all seeded to minimize biasing. Phase discrimination is inherent in the instrumentation with the ability to size each measured particle. At each spatial location, two measurements were taken in order to accurately measure the velocity of each phase. A threshold voltage for the photodetectors at the specified laser power was determined experimentally, below which signals from the aluminum-oxide particles were not detected. For the droplet measurements, the photodetector voltage was kept below this threshold value in order to eliminate interference from the aluminum-oxide particles. Total laser power for all wavelengths was fixed at 1.5 W for all the measurements. Particles with diameters less than 2.4 μm were used to represent the gas phase velocity. Two complete traverses were taken in order to measure all three components of velocity and provide a check on flow symmetry. Each traverse measured axial velocity and either radial or angular velocity. Generally, 64 000 measurement attempts were made at each measurement location. The percentage of measurements actually validated depended on the number density and velocities of drops at each location and ranged from about 65 to 90 percent.

B.2 RESULTS AND DISCUSSION

In the present study, results are presented for a single axial location at 5 mm downstream of the nozzle. Gas phase results for mean velocities are presented in Figs. 3(a) to (c) for isothermal, single-phase flow without droplets and two-phase flow with combustion. Mean gas phase axial velocity, presented in Fig. 3(a), presents results from a complete traverse across the combustor and illustrates the symmetry of the flowfield. The combustor exit dimensions are illustrated on the x-axis of the figure for reference. A small recirculation zone is evident near the center of the nozzle. At this axial location relatively close to the nozzle, velocity gradients are extremely large in the flow from the air-assist stream containing the droplets. Effects of combustion on the flowfield are significant. Both the maximun and minimum mean axial velocities are increased for the combusting case compared to the isothermal case due to the gas expansion associated with the heat release. For the case with combustion, velocities increase from nearly 0 to 35 m/s and then decrease to -30 m/s within a radius of about 12 mm. Mean axial velocities in the coflow stream are not affected by the combustion at this axial location.

Figure 3b presents mean radial velocity for the gas phase. As shown in Fig. 3(b), effects of combustion are very dramatic for radial velocity. Maximum radial velocities increased from about 10 m/s for the isothermal case to about 40 m/s for the case with combustion due to the radial expansion of the gas. Again, the gas from the coflow stream is not affected by the combustion at this axial location.

Mean gas phase angular velocities are presented in Fig. 3(c). For this case, reaction and the presence of droplets decreases the maximum angular velocities in the flowfield. Some of the decrease in angular velocity for the gas phase can be attributed to the momentum transferred to the droplets since they do not initially have a swirl component.

Fluctuating gas phase velocities are presented in Figs. 4(a) to (c) for both the single-phase, isothermal and the two-phase, combusting cases. All fluctuating velocities presented are root-mean-squared (rms) values. Figure 4(a) presents radial profiles of gas phase fluctuating axial velocity. Maximum values of fluctuating axial velocity are similar for both the combusting and isothermal cases. The case with combustion does show larger values of axial rms velocity at radial locations between approximately 5 and 15 mm from the center of the nozzle. Axial velocities are also higher at these locations for the combusting case, see Fig. 3(a). Fluctuating radial velocities, illustrated in Fig. 4(b), show dramatic differences between the isothermal and combusting cases. The maximum velocity locations have shifted radially outward corresponding to the shift in mean radial velocity, see Fig. 3(b). The maximum fluctuating radial velocity has also increased from about 10 m/s to 15 m/s.

Fluctuating angular gas phase velocities are presented in Fig. 4(c). Similar to the results shown for mean angular gas phase velocities, fluctuating angular velocities generally decreased with combustion and the presence of the liquid phase compared to the single-phase, isothermal case. A small region from a radius of about 7 to 15 mm shows increased values of fluctuating angular velocity for the case with combustion.

Mean velocities for the drops are presented in Figs. 5(a) to (c) for the case with combustion. In the experimental study, velocities were measured for drop sizes ranging from 4 to 142 μm. Results are presented for drop sizes of 15, 32 and 52 μm. Measured gas phase velocities are also presented in the figure. Note that results are only illustrated from -15 to +15 mm for the radial direction because no drops were present at larger radial locations. Figure 5(a) presents mean drop axial velocity at 5 mm downstream. Similar to the results previously shown for the gas phase, the flowfield is very symmetric. Axial velocity is correlated with drop size in all regions. In the main region of the spray, at a radius of about 7 mm, the maximum velocity of the gas phase was about 38 m/s, and about 28 m/s for the 32 μm drops. Even the maximum velocity of the 15 μm drops lagged the gas phase by about 5 m/s. In the center of the flowfield is a small recirculation zone, see Fig. 3(a). There, only the 15 μm drops showed negative axial velocities while larger drops had positive velocities.

Mean drop radial velocities are presented in Fig. 5(b). Again, there is a correlation between drop size and velocity in the flowfield. Maximum mean radial velocities are slightly higher than maximum axial velocities for the drops due to the heat release and radial expansion of the gas. Mean angular velocities of the drops are presented in Fig. 5(c). Angular velocity is not as symmetric and is also much smaller than the other two components of velocity. The mean drop angular velocity is a strong function of the drop size with the smaller drops showing the least velocity difference with the gas phase.

Fluctuating droplet axial, radial, and angular velocity components for the three drop sizes and gas phase are presented in Figs. 6(a) to (c), respectively. The fluctuating drop velocities presented are root-mean-squared (rms) values. Generally, the smaller drops are affected more by the gas phase turbulence and have larger fluctuating velocities than the larger drops. Velocity fluctuations are clearly not isotropic since fluctuating axial and radial velocities are considerably larger than fluctuating angular velocities.

In addition to drop mean and fluctuating velocities, the liquid volume flux is important in two-phase flows. Drop number-flux measurements are presented in Fig. 7, where results are illustrated for four drop size groups. As shown in Fig. 7, number flux is nearly symmetric. The results show that smaller droplets have much larger number fluxes. The distribution of the larger droplets is still very important since much of the liquid mass is contained in the larger droplets. Relatively few drops are found in the center region of the flowfield due to the 45 degree swirler that is used in the air-assist stream.

C. COMBUSTION CFD CODE

The objective of the present work is to develop a numerical solution procedure which can efficiently handle the coupling between a spray model and a well-developed strongly implicit flow solution algorithm (Refs. 13 and 14). In the past, spray models have been coupled with different flow algorithms and shown some promising results (Refs. 15 to 17). However, most of the spray models were coupled with a flow solver employing a segregated approach, such as a TEACH-type code (Refs. 15 and 16), which has been used very extensively in the industries for the past two decades. Although simple

and easy to implement, the TEACH-type code usually suffers poor convergence due to the explicit (or semi-implicit) treatments of the chemical source terms and the sequential solution approach. Recent development of CFD techniques and the advent of computer technology have allowed us to explore more ambitious schemes to solve reacting flow problems. Strongly coupled and implicit numerical schemes, although requiring much more computer storage and complexity of the algorithm, have been very popular for nonreacting compressible (Refs. 18 and 19) and incompressible (Refs. 20 and 21) flow computations.

Shuen and Yoon (Ref. 22) developed a coupled scheme for high speed reacting flows, RPLUS, which has been used and studied quite extensively in recent years. However, like other compressible flow solution algorithms, RPLUS may not be suitable for low speed flow computations. There are two well-recognized reasons (Refs. 23 to 25) for the convergence difficulties related to compressible flow codes. First, the system's eigenvalues become stiff at low flow velocities. Second, the pressure term in the momentum equation becomes singular as the Mach number approaches zero, which yields a large roundoff error and smears the pressure variation field. This will not only result in slow convergence but often will produce inaccurate solutions. To circumvent the above difficulties, Shuen et al. (Ref. 13) developed a coupled numerical algorithm for chemical nonequilibrium viscous flows, ALLSPD, which utilizes the decomposition of the pressure variable into a constant reference pressure and a gauge pressure to reduce the roundoff errors and adds a preconditioning time derivative term to rescale the system eigenvalues. The results of these treatments show that the convergence properties are almost independent of the flow Mach number.

Numerous spray models have been proposed and investigated for different spray combustion problems (Refs. 26 and 27) in the past decade. Recent spray models differ in specific details, but generally may be divided into two categories: locally homogeneous flow (LHF) models and separated flow (SF) models. LHF models represent the simplest treatment of a multiphase flow and have been widely used to analyze sprays (Ref. 28). The key assumption of the LHF model is that interphase transport rates are fast in comparison to the rate of development of the flow. This implies that all phases have identical properties at each point in the flow. Clearly, LHF models are only formally correct for flows containing infinitely small droplets.

Numerous SF models have been proposed to consider interphase transport phenomena (Ref. 29). Among them, the discrete droplet approach (Refs. 26 and 30) has been adopted, since it reduces numerical diffusion while providing a convenient framework for dealing with multiple droplet size and complex interphase transport phenomena. Many discrete droplet models neglect the effects of turbulence on interphase transport (Refs. 26 and 30). This implies that droplets follow deterministic trajectories, yielding the deterministic separated flow (DSF) model. Neglecting the effects of turbulence on droplet transport is appropriate when characteristic droplet relaxation times are large in comparison to characteristic times of turbulent fluctuations. Few practical sprays, however, satisfy this condition. Dukowicz (Ref. 31) and Gosman and Ioannides (Ref. 32) have adopted stochastic methods to study droplet dispersion by turbulence. Faeth and coworkers (Ref. 33) extended the analysis of Gosman et al. to include the effects of turbulence on interphase heat and mass transport. Their stochastic separated flow (SSF) model (Ref. 33) has been evaluated in a wide variety of parabolic flows with very encouraging results.

In a recent paper (Ref. 34), the ALLSPD algorithm was extended to include a SSF spray model (Ref. 33), a recently developed low Reynolds number κ-ε turbulence model (Ref. 35) and a multiblock treatment to calculate the gas turbine combustion flows, where the liquid spray is an important ingredient of combustion. Although the turbulence model has been included in this study for turbulent combustion flow calculations, the mean flow quantities are still used in the chemistry calculations. The turbulence closure problem for chemistry is more complicated and computationally intensive. The consideration of a suitable turbulent combustion closure model is left for our next-phase study in the near future.

In this paper, in addition to the gas turbine spray combustion flow, a single-phase premixed turbulent combustion flow and a nonreacting turbulent flow are also included to demonstrate the current status of this research. In the following sections, a brief mathematical formulation of the governing equations for both gas and liquid-phases is described. The numerical method and discretization procedure are given next and finally some sample numerical results are presented.

C.I GOVERNING EQUATIONS

C.Ia Gas-Phase Equations

C.Ia(I) Navier-Stokes Formulation

The two-dimensional, unsteady, compressible, density-weighted time-averaged Navier-Stokes equations and species transport equations for a chemically reacting gas of N species written in generalized nonorthogonal coordinates can be expressed as

$$\frac{\partial \tilde{\mathbf{Q}}}{\partial \tau} + \frac{\partial\left(\tilde{\mathbf{E}} - \tilde{\mathbf{E}}_v\right)}{\partial \xi} + \frac{\partial\left(\tilde{\mathbf{F}} - \tilde{\mathbf{F}}_v\right)}{\partial \eta} = \tilde{\mathbf{H}}_c + \tilde{\mathbf{H}}_l \,. \qquad (1)$$

where the vectors $\tilde{\mathbf{Q}}, \tilde{\mathbf{E}}, \tilde{\mathbf{F}}, \tilde{\mathbf{E}}_v, \tilde{\mathbf{F}}_v, \tilde{\mathbf{H}}_c$, and $\tilde{\mathbf{H}}_l$ are defined as

$$\tilde{\mathbf{Q}} = \frac{\nu^{\delta}}{J}\mathbf{Q},$$

$$\tilde{\mathbf{E}} = \frac{\nu^{\delta}}{J}\left(\xi_t \mathbf{Q} + \xi_x \mathbf{E} + \xi_y \mathbf{F}\right),$$

$$\tilde{\mathbf{F}} = \frac{\nu^{\delta}}{J}\left(\eta_t \mathbf{Q} + \eta_x \mathbf{E} + \eta_y \mathbf{F}\right),$$

$$\tilde{\mathbf{E}}_v = \frac{\nu^{\delta}}{J}\left(\xi_x \mathbf{E}_v + \xi_y \mathbf{F}_v\right),$$

$$\tilde{\mathbf{F}}_v = \frac{\nu^{\delta}}{J}\left(\eta_x \mathbf{E}_v + \eta_y \mathbf{F}_v\right),$$

$$\tilde{\mathbf{H}}_c = \frac{1}{J}\mathbf{H}_c \,,$$

$$\tilde{\mathbf{H}}_l = \frac{1}{J}\mathbf{H}_l \,.$$

In the above expressions, τ, ξ, and η are the time and spatial coordinates in the generalized coordinates and ξ_t and η_t are the grid speed terms. The ξ_x, ξ_y, η_x, and η_y are the metric terms and the J is the transformation Jacobian. The power, δ,

is an index for two types of governing equations with $\delta = 0$ for two-dimensional and $\delta = 1$ for axisymmetric cases (with x being the axial and y the radial coordinates, respectively). The vectors Q, E, F, $\mathbf{F}_v$, $\mathbf{F}_v$, $\mathbf{H}_c$ and $\mathbf{H}_l$ in the above definitions are

$$\mathbf{Q} = \left(\rho,\ \rho u,\ \rho v,\ \rho E,\ \rho\kappa,\ \rho\varepsilon,\ \rho Y_1,\ \ldots,\ \rho Y_{N-1}\right)^T,$$

$$\mathbf{E} = \left(\rho u,\ \rho u^2 + p,\ \rho uv,\ (\rho E + p)u,\ \rho u\kappa,\ \rho u\varepsilon,\ \rho uY_1,\ \ldots,\ \rho uY_{N-1}\right)^T,$$

$$\mathbf{F} = \left(\rho v,\ \rho uv,\ \rho v^2 + p,\ (\rho E + p)v,\ \rho v\kappa,\ \rho v\varepsilon,\ \rho vY_1,\ \ldots,\ \rho vY_{N-1}\right)^T,$$

$$\mathbf{F}_v = \left(0, \tau_{xx},\ \tau_{xy},\ u\tau_{xx} + v\tau_{xy} + q_{xe},\ \tau_{x\kappa},\ \tau_{xe},\ q_{x1},\ \ldots,\ q_{x\,N-1}\right)^T,$$

$$\mathbf{F}_v = \left(0,\ \tau_{xy},\ \tau_{yy},\ u\tau_{xy} + v\tau_{yy} + q_{ye},\ \tau_{y\kappa},\ \tau_{ye},\ q_{y1},\ \ldots,\ q_{y\,N-1}\right)^T,$$

and the source term vectors $\mathbf{H}_c$ and $\mathbf{H}_l$ are

$$\mathbf{H}_c = \begin{pmatrix} 0 \\ -\frac{2}{3}\delta\frac{\partial(\mu_e v)}{\partial x} \\ \delta\left[p - \tau_{\theta\theta} - \frac{2}{3}\frac{\partial(\mu_e v)}{\partial y}\right] \\ -\frac{2}{3}\delta\left[\frac{\partial(\mu_e uv)}{\partial x} + \frac{\partial(\mu_e v^2)}{\partial y}\right] \\ y^\delta(\Psi - \rho\varepsilon) - \frac{2}{3}\delta\,\mu_t v\left(\frac{\partial u}{\partial x} + \frac{\partial v}{\partial y}\right) \\ y^\delta\left[\left(c_1 f_1 \Psi - c_2 f_2 \rho\kappa\right)\frac{\varepsilon}{\kappa} + \Lambda\right] - \frac{2}{3}\delta\mu_t v \\ \times\left(\frac{\partial u}{\partial x} + \frac{\partial v}{\partial y}\right)c_1 f_1\frac{\varepsilon}{\kappa} \\ y^\delta S_1 \\ \vdots \\ y^\delta S_{N-1} \end{pmatrix},$$

and

$$\mathbf{H}_l = \begin{pmatrix} \sum_p n_p\dot{m}_p \\ \sum_p n_p\dot{m}_p u_p - \frac{4\pi}{3}\rho_p r_p^3 n_p\frac{du_p}{dt} \\ \sum_p n_p\dot{m}_p v_p - \frac{4\pi}{3}\rho_p r_p^3 n_p\frac{dv_p}{dt} \\ \sum_p n_p\dot{m}_p h_{fs} - 4\pi r_p^2 n_p h\,\Delta T \\ 0 \\ 0 \\ \sum_p n_p\dot{m}_p \\ \vdots \\ 0 \end{pmatrix}.$$

where ρ, p, u, v, κ, ε, and Y_i represent the density, pressure, Cartesian velocity components, turbulent kinetic energy, dissipation rate of turbulent kinetic energy and species mass fraction, respectively; $E = e + \frac{1}{2}(u^2 + v^2)$ is the total internal energy with e being the thermodynamic internal energy; and S_i is the rate of change of species i due to chemical reactions. The normal and shear stresses, energy, species, and turbulent diffusion fluxes are given by

$$\tau_{xx} = 2\mu_e\frac{\partial u}{\partial x} - \frac{2}{3}\mu_e\left(\frac{\partial u}{\partial x} + \frac{\partial v}{\partial y}\right),$$

$$\tau_{xy} = \mu_e\left(\frac{\partial u}{\partial y} + \frac{\partial v}{\partial x}\right),$$

$$\tau_{yy} = 2\mu_e\frac{\partial v}{\partial y} - \frac{2}{3}\mu_e\left(\frac{\partial u}{\partial x} + \frac{\partial v}{\partial y}\right),$$

$$\tau_{\theta\theta} = \frac{4}{3}\mu_e\frac{v}{y} - \frac{2}{3}\mu_e\left(\frac{\partial u}{\partial x} - \frac{\partial v}{\partial y}\right),$$

$$q_{xe} = k_e\frac{\partial T}{\partial x} + \rho\sum_{i=1}^{N} h_i D_{im}\frac{\partial Y_i}{\partial x},$$

$$q_{ye} = k_e\frac{\partial T}{\partial y} + \rho\sum_{i=1}^{N} h_i D_{im}\frac{\partial Y_i}{\partial y},$$

$$\tau_{x\kappa} = \left(\mu_l + \frac{\mu_t}{\sigma_\kappa}\right)\frac{\partial\kappa}{\partial x},$$

$$\tau_{y\kappa} = \left(\mu_l + \frac{\mu_t}{\sigma_\kappa}\right)\frac{\partial\kappa}{\partial y},$$

$$\tau_{xe} = \left(\mu_l + \frac{\mu_t}{\sigma_e}\right)\frac{\partial\varepsilon}{\partial x},$$

$$\tau_{ve} = \left(\mu_l + \frac{\mu_t}{\sigma_e}\right)\frac{\partial e}{\partial y},$$

$$q_{xl} = \rho D_{lm}\frac{\partial Y_l}{\partial x},$$

$$q_{yl} = \rho D_{lm}\frac{\partial Y_l}{\partial y},$$

where T, μ_e, μ_t, μ_l, and k_e are the temperature, effective viscosity, turbulent viscosity, molecular viscosity and the effective thermal conductivity, respectively;

$$D_{lm} = (1 - X_l)/\sum_{j\neq l}^{N} X_j/D_{lj}$$

is the effective binary diffusivity of species l in the gas mixture, X_l the molar fraction of species l, and D_{lj} the binary mass diffusivity between species l and j. The quantities related to the source term in the turbulent equations are given as

$$\Psi = \mu_t\left\{\left[2\frac{\partial u}{\partial x} - \frac{2}{3}\left(\frac{\partial u}{\partial x} + \frac{\partial v}{\partial y}\right)\right]\frac{\partial u}{\partial x} + \left[2\frac{\partial v}{\partial y} - \frac{2}{3}\left(\frac{\partial u}{\partial x} + \frac{\partial v}{\partial y}\right)\right]\frac{\partial v}{\partial y} + \left(\frac{\partial u}{\partial y} + \frac{\partial v}{\partial x}\right)^2\right\} - \frac{2}{3}\rho\kappa\left(\frac{\partial u}{\partial x} + \frac{\partial v}{\partial y}\right),$$

$$\Lambda = \nu\mu_t\frac{\partial^2 u}{\partial y^2},$$

and

$$c_1 = 1.44, \quad c_2 = 1.92, \quad f_1 = 1.00, \quad f_2 = 1 - 0.22\ exp\left(-R_t^2/36\right), \quad \sigma_\kappa = 1,$$

$$\sigma_\varepsilon = 1.3, \quad R_t = \frac{\kappa^2}{\nu\varepsilon}, \quad \mu_e = \mu_l + \mu_t, \quad k_e = k_l + \frac{\mu_t C_{pm}}{Pr_t},$$

$$\mu_t = c_\mu f_\mu \rho\frac{\kappa^2}{\varepsilon}, \quad c_\mu = 0.09, \quad f_\mu = \left[1 - \exp\left(\alpha_1 R_\kappa + \alpha_3 R_\kappa^3 + \alpha_5 R_\kappa^5\right)\right]^2,$$

$$\alpha_1 = -1.5\times10^{-4}, \quad \alpha_3 = -1.0\times10^{-9}, \quad \alpha_5 = -5.0\times10^{-10}, \quad R_\kappa = \frac{\kappa^{1/2} y_n}{\nu},$$

where y_n in the expression of R_κ is the normal distance away from the wall, k_l is the molecular thermal conductivity, C_{pm} is the specific heat of the gas mixture and Pr_t is the turbulent Prandtl number.

The vector $\mathbf{H}_l$ in Eq. (1) represents the source term that accounts for the interactions between the gas and liquid phases. In vector $\mathbf{H}_l$, n_p is the number of droplets in the pth characteristic group of droplets; $\dot{m}_p$ is the evaporation rate of each particle group; ρ_p is the liquid density; r_p is the droplet radius; u_p and v_p are the particle velocities at the pth group; h_{fs} is the enthalpy of fuel vapor at the droplet surface and $h\Delta T$ is the convective heat transfer between two phases. Detailed discussions about the liquid phase equations will be described later. The temperature and pressure are calculated iteratively from the following equations

$$e = \sum_{l=1}^{N} Y_l h_l - \frac{p}{\rho}, \qquad h_l = h_{fl}^{\circ} + \int_{T_{ref}}^{T} C_{pl}\,dT,$$
$$p = \rho R_u T\sum_{l=1}^{N}\frac{Y_l}{W_l}, \tag{2}$$

where R_u and T_{ref} are the universal gas constant and reference temperature for thermodynamic properties, and W_l, C_{pl}, h_l, h_{fl}° are the molecular weight, constant pressure specific heat, thermodynamic enthalpy, and heat of formation of species l, respectively.

In reacting flow calculations, the evaluation of thermophysical properties is of vital importance. In this paper, the values of C_{pl}, k_{ll}, and μ_{ll} for each species are determined by fourth-order polynomials of temperature, as described in Shuen (Ref. 36). The specific heat of the gas mixture is obtained by mass concentration weighting of individual species. The thermal conductivity and viscosity of the mixture, however, are calculated using Wilke's mixing rule (Ref. 37). The binary mass diffusivity D_{lj} between species l and j is obtained using the Chapman-Enskog theory (Ref. 37).

C.1a(2) All-Mach-Number Formulation

As noted earlier in the introduction section, the two main difficulties that render the compressible flow algorithms ineffective at low Mach numbers are the roundoff error caused by the singular pressure gradient term in the momentum equations (the pressure term is of order $1/M^2$ while the convective term is of order unity in the nondimensional momentum equations) and the stiffness caused by the wide disparities in eigenvalues. To circumvent these two problems regarding the low Mach number calculations, following the approach by Merkle and Choi (Ref. 25), Shuen et al. (Ref. 13) added a time preconditioning term to rescale the system eigenvalues and decompose the pressure variable into a constant reference pressure part and a gauge pressure part. This all-Mach-number formulation has been extended to include the turbulent and spray equations. The resulting Navier-Stokes equations in a conservative form are

$$\Gamma\frac{\partial\hat{\mathbf{Q}}}{\partial\tau^*} + \frac{\partial\tilde{\mathbf{Q}}}{\partial\tau} + \frac{\partial\left(\tilde{\mathbf{E}} - \tilde{\mathbf{E}}_v\right)}{\partial\xi} + \frac{\partial\left(\tilde{\mathbf{F}} - \tilde{\mathbf{F}}_v\right)}{\partial\eta} = \tilde{\mathbf{H}}_c + \tilde{\mathbf{H}}_l, \tag{3}$$

where the primitive variable vector $\hat{\mathbf{Q}}$ and the preconditioned matrix Γ are given as

$$Q = \frac{p^*}{J}\begin{pmatrix} p_g \\ u \\ v \\ h \\ \kappa \\ \varepsilon \\ Y_1 \\ Y_2 \\ \cdot \\ \cdot \\ Y_{N-1} \end{pmatrix}, \quad \Gamma = \begin{bmatrix} 1/\beta & 0 & 0 & 0 & 0 & 0 & . & . & . & 0 \\ u/\beta & \rho & 0 & 0 & 0 & 0 & . & . & . & 0 \\ v/\beta & 0 & \rho & 0 & 0 & 0 & . & . & . & 0 \\ h/\beta - 1 & \rho u & \rho v & \rho & 0 & 0 & . & . & . & 0 \\ \kappa/\beta & 0 & 0 & . & \rho & . & . & . & 0 & 0 \\ \varepsilon/\beta & 0 & 0 & . & . & \rho & . & . & . & 0 \\ Y_1/\beta & 0 & 0 & 0 & . & . & \rho & . & . & 0 \\ Y_2/\beta & 0 & 0 & 0 & 0 & . & . & \rho & . & 0 \\ . & . & . & . & . & 0 & . & . & \rho & 0 \\ . & . & . & . & . & . & 0 & . & . & \rho \\ Y_{N-1}/\beta & 0 & 0 & . & . & . & . & 0 & . & \rho \end{bmatrix}$$

where τ^* is the pseudotime, β is a parameter for rescaling the eigenvalues of the new system of equations; and $h = e + p/\rho$ is the specific enthalpy of the gas mixture. The definition of vectors in Eq. (3) is identical to those in Eq. (1) except that the pressure terms in the momentum equations are replaced by gauge pressure, p_g. The derivation of the all-Mach-number formulation can be found in detail in Shuen et al (Refs. 13 and 14).

C.1b. Liquid-Phase Equations

C.1b(1) Droplet Motion Equations

The liquid phase is treated by solving Lagrangian equations of motion and transport for the life histories of a statistically significant sample of individual droplets. This involves dividing the droplets into n groups (defined by position, velocity, temperature and diameter) at the fuel nozzle exit and then computing their subsequent trajectories in the flow. The spray model used in this study is based on a dilute spray assumption which is valid in the regions of spray where the droplet loading is low (Refs. 17 and 33). The liquid fuel is assumed to enter the combustor as a fully atomized spray comprised of spherical droplets. The present model does not account for the effects due to droplet breakup and coalescence processes which might be significant in a dense spray situation. The Lagrangian equations governing the droplet motion are

$$\frac{dx_p}{dt} = u_p, \tag{4}$$

$$\frac{dy_p}{dt} = v_p, \tag{5}$$

$$\frac{du_p}{dt} = \frac{3}{16}\frac{C_D \mu_g Re_p}{\rho_p r_p^2}\left(u_g - u_p\right), \tag{6}$$

$$\frac{dv_p}{dt} = \frac{3}{16}\frac{C_D \mu_g Re_p}{\rho_p r_p^2}\left(v_g - v_p\right). \tag{7}$$

where the particle Reynolds number, Re_p, and the drag coefficient, C_D, are defined as

$$Re_p = 2\frac{r_p \rho_g}{\mu_g}\left[\left(u_g - u_p\right)^2 + \left(v_g - v_p\right)^2\right]^{1/2},$$

$$C_D = \begin{cases} \dfrac{24}{Re_p}\left(1 + \dfrac{Re_p^{2/3}}{6}\right) & \text{for} \quad Re_p < 1000, \\ 0.44 & \text{for} \quad Re_p > 1000. \end{cases}$$

The subscript g represents the gas-phase quantities and p represents the liquid-phase (or "particle") quantities. Equations (4) and (5) are used to calculate the new droplet positions and Eqs. (6) and (7) are used to update the new droplet velocities at the new droplet locations. A second-order Runge-Kutta scheme was used to integrate Eqs. (4) to (7).

C.1b(2) Droplet Mass and Heat Transfer Equations

As described by Faeth (Ref. 26), the following correlations were used to approximate the mass and heat transfer coefficients for a single isolated spherical droplet:

$$\frac{\dot{m}_p'' d_p}{\rho D_f} = 2N_s \ln(1 + B), \tag{8}$$

$$\frac{h d_p}{k} = \frac{2N_p \ln\left(1 + B\right)^{Le^{-1}}}{\left[\left(1 + B\right)^{Le^{-1}} - 1\right]}. \tag{9}$$

where h is the heat transfer coefficient, d_p is the droplet diameter, D_f is the fuel mass diffusivity, k is the thermal conductivity of fuel vapor and $\dot{m}_p''$ is the fuel mass evaporation rate per unit area. The N_s and N_p are defined as

$$N_s = 1 + \frac{0.276 Re_p^{1/2} Pr^{1/3}}{\left[1 + \dfrac{1.232}{Re_p Pr^{4/3}}\right]^{1/2}},$$

and

$$N_p = 1 + \frac{0.276 Re_p^{1/2} Sc^{1/3}}{\left[1 + \dfrac{1.232}{Re_p Sc^{4/3}}\right]^{1/2}},$$

where Sc and Le are the Schmidt and Lewis numbers, respectively. The Spalding number, B, in Eqs. (8) and (9) is defined as

$$B = \frac{Y_{fsp} - \bar{Y}_{fe}}{1 - Y_{fsp}} \tag{10}$$

where Y_{fsp} is the fuel vapor mass fraction at the surface of the droplet and $\bar{Y}_{fe}$ is the mean fuel mass fraction of the ambient gas. In the present study, Y_{fsp} is obtained from the following equation

$$Y_{fsp} = \frac{X_{fsp} W_f}{X_{fsp} W_f + \left(1 - X_{fsp}\right) W_a}. \tag{11}$$

where W_a is the molecular weight of gas excluding fuel vapor, W_f is the molecular weight of fuel and X_{fgp} is the mole fraction of fuel. The X_{fgp} is obtained from the assumption of Raoult's law. Based on this assumption, the mole fraction at the droplet surface is equal to the ratio of the partial pressure of fuel vapor to the total pressure. For the present spray calculation, the partial pressure of fuel vapor was computed based on the following empirical correlation (Ref. 37):

$$\ln\left(\frac{p_{vp}}{p_c}\right) = \frac{1}{1-x}\left[P_{v1}x + P_{v2}x^{1.5} + P_{v3}x^3 + P_{v4}x^6\right] \tag{12}$$

where $x = 1 - T/T_c$, $P_{v1} = -7.28936$, $P_{v2} = 1.53679$, $P_{v3} = -3.08367$, $P_{v4} = -1.02456$, T_c and p_c are the critical temperature and critical pressure of the fuel vapor, respectively.

C.1b(3) Droplet Internal Temperature Equations

As a single droplet enters a hot environment, the immediate small portion of the droplet near the surface will be heating up quickly while the center core of the droplet remains "cold". The heat will be conducted and convected to the entire interior as the droplet penetrates further into the hot ambient gas. Eventually, the temperature within the droplet will become nearly uniform before the end of its lifetime. To solve this transient phenomena within the droplet is not trivial. In the past, certain approximations (Ref. 38) are usually made to alleviate this computational burden while obtaining reasonably good results. Among them, the simplest one is the uniform temperature model. This model assumes that the thermal conductivity of the fuel is infinite. Of course, this is not valid at the beginning of the heating-up process of the droplet. Another model considers the heat diffusion inside the droplet. This yields a conduction model. The temperature distribution within the droplet is obtained by solving the one-dimensional heat conduction equation subject to the convective boundary conditions at the droplet surface. The conduction model completely neglects the convective phenomena within the droplet which might occur due to significant shear forces at the surface induced by high slip velocities. Tong and Sirignano (Ref. 39) developed a *vortex model* for the internal temperature of a single droplet which accounts for the convective effect of the Hill's vortex formation inside the droplet. In this study, Tong and Sirignano's vortex model is applied to obtain the internal temperature distribution of the droplet. The equation governing the internal temperature distribution based on this model is

$$\frac{\partial T_p}{\partial t} = 17\,\frac{k_l}{C_{pl}\rho_l r_p^2}\left[\alpha\,\frac{\partial^2 T_p}{\partial \alpha^2} + \left(1 + C(t)\,\alpha\right)\frac{\partial T_p}{\partial \alpha}\right] \tag{13}$$

and

$$C(t) = \frac{3}{17}\left(\frac{C_{pl}\rho_l}{k_l}\right) r_p\,\frac{dr_p}{dt}$$

where the value of α is between 0 and 1 with $\alpha = 0$ referring to the vortex center and $\alpha = 1$ referring to the droplet surface. The initial and boundary conditions for Eq. (13) are

$$t = t_{inj}, \quad T_p = T_{inj},$$

$$\alpha = 0, \quad \frac{\partial T_p}{\partial \alpha} = \frac{1}{17}\left(\frac{C_{pl}\rho_l}{\kappa_l}\right) r_p^2\,\frac{\partial T_p}{\partial t},$$

$$\alpha = 1, \quad \frac{\partial T_p}{\partial \alpha} = \frac{3}{16}\,r_p\left.\frac{\partial T_p}{\partial r}\right|_s$$

where $\left.\frac{\partial T_p}{\partial r}\right|_s$ is obtained from the energy balance at the droplet surface by the following equation

$$\left.\frac{\partial T_p}{\partial r}\right|_s = \frac{1}{k_l}\left[h\,\Delta T - \dot{m}_p'' h_{fg}\right] \tag{14}$$

where $\dot{m}_p''$ and h are calculated from Eqs. (8) and (9), respectively. h_{fg} is the latent heat of the fuel and $\Delta T = \bar{T}_g - T_{ps}$, where T_{ps} is droplet surface temperature and $\bar{T}_g$ is the mean gas temperature evaluated in the following way

$$\bar{T}_g = \frac{1}{3}\,T_g + \frac{2}{3}\,T_{ps}.$$

An implicit scheme was used to solve Eq. (13) subject to the initial and boundary conditions. Second-order central differences were used for the spatial differential terms and a first-order difference for the time term. These treatments rendered a scalar tridiagonal algebraic system and was solved by the Thomas algorithm (Ref. 40).

C.2 NUMERICAL METHODS

C.2a Discretized Equations

Equation (3) is the final gas-phase governing equation to be solved numerically. To obtain time-accurate solutions for time-evolving problems, a dual time-stepping integration method can be applied to Eq. (3). The solution converged in pseudotime corresponds to a time-accurate solution in physical time (Ref. 13). However, for the present study, since only the steady state solution is of our interest, the physical time term in Eq. (3) can be dropped and the solution can be marched completely in pseudotime to obtain the final steady state solution. One advantage of marching to the steady state solution in pseudotime is that the convergence of the marching (iterative) process is determined by the eigenvalue characteristics on the pseudotime space and not by the original stiff eigenvalues. The analysis of the eigensystem has been performed in our previous study (Refs. 13 and 14) and therefore will not be repeated here. It should be noted that the inclusion of the turbulent κ-ε equations in this study does not affect the system eigenvalues at all and, therefore, the properties of the all-Mach-number formulation analysis in previous papers (Refs. 13 and 14) are still valid.

After linearization and applying a first-order time differencing, Eq. (3) can be expressed in the following form:

$$\left[\Gamma - \Delta\tau^{*}\mathbf{D} + \Delta\tau^{*}\left(\frac{\partial \mathbf{A}}{\partial\xi} - \frac{\partial}{\partial\xi}\,\mathbf{R}_{\xi\xi}\,\frac{\partial}{\partial\xi}\right) + \Delta\tau^{*}\left(\frac{\partial \mathbf{B}}{\partial\eta} - \frac{\partial}{\partial\eta}\,\mathbf{R}_{\eta\eta}\,\frac{\partial}{\partial\eta}\right)\right]^{p} \times \Delta\hat{\mathbf{Q}} = -\Delta\tau^{*}(\mathbf{R})^{p}. \tag{15}$$

where

$$\mathbf{R}^{p} = \frac{\partial\left(\tilde{\mathbf{F}} - \tilde{\mathbf{F}}_{v}\right)^{p}}{\partial\xi} + \frac{\partial\left(\tilde{\mathbf{F}} - \tilde{\mathbf{F}}_{v}\right)^{p}}{\partial\eta} - \tilde{\mathbf{H}}_{c}^{p} - \tilde{\mathbf{H}}_{l}^{p}. \tag{16}$$

where p denotes the previous iteration level, $\mathbf{D}$ is the Jacobian for chemical and turbulent source terms, $\mathbf{A}$ and $\mathbf{B}$ are the inviscid term Jacobians and $\mathbf{R}_{\xi\xi}$ and $\mathbf{R}_{\eta\eta}$ are the viscous term Jacobians. The expressions for these Jacobians can be found in Shuen et al. (Refs. 13 and 14) except for the turbulent part. Central differences were used to discretize the spatial derivative terms in Eqs. (15) and (16) for both explicit and implicit operators. The resulting coupled algebraic equations are solved using a modified strongly implicit procedure (MSIP) proposed by Schneider and Zedan (Ref. 41), which is completely vectorizable along $i + 2j$ diagonal direction.

C.2b Boundary Conditions

The boundary conditions for gas phase equations are described as follows. Here, only the subsonic flow boundary conditions are considered in the present paper. At the inlet, all quantities are specified except pressure which is obtained through extrapolation from the pressure at interior points. At the exit, the governing equations are solved at the exit station by applying backward differences for the streamwise derivative terms (central differences are still used for cross-stream derivative terms). However, the streamwise pressure derivative terms are *centrally-differenced*. This treatment requires the pressure information at the station one step downstream (outside the computational domain) where a constant pressure condition is enforced. At the symmetry line, the governing equations are solved *via* the use of the symmetry conditions for two-dimensional flows. For the axisymmetric case, a singularity exists at this line and a simple one-sided difference is used to implement the symmetry conditions. At the solid wall, no slip conditions are used for the velocities and an adiabatic wall is assumed. Normal derivatives for species, Y_i, and $(p_g + 2/3\,\rho\kappa)$ are set to zero. For the turbulent quantities, the low Reynolds number turbulence model (Ref. 35) used in this study requires the specification of the κ and ε at the walls as follows:

$$\kappa = 0.250u_{\tau}^{2}$$

$$\varepsilon = 0.251\frac{u_{\tau}^{4}}{\nu}$$

where u_{τ} is the friction velocity at the wall.

Since a multiblock treatment is applied to the present numerical algorithm, the interfaces between blocks (or zones) become a special kind of boundary. At the interface, the governing equations are still solved without any distinction from the rest of the interior points. The flow variables have been carefully arranged in such a way that the information from the neighboring block(s) is automatically brought into the calculation at the interface of the current block. The multiblock treatment of the present study not only provides flexibility for complex geometry calculations but also reduces the size of the storage array for the MSIP coefficients due to the smaller sizes of the subdomains.

C.2c Spray Source Terms

In Eq. (3), the liquid-phase interaction with the Navier-Stokes equations is modeled as a source term which accounts for mass, momentum and energy exchanges between two phases. In order to compute this source term, the liquid-phase governing equations described in the previous section are integrated in time once initial conditions have been specified. As a liquid droplet begins its journey from the injection nozzle, its position, velocity, temperature and size, in general, will be changing according to the interaction between the gas-phase solution and the spray properties. In contrast to the Eulerian approach for the gas-phase equations, the Lagrangian treatment for the liquid-phase equations requires interpolation of the flow quantities from the Eulerian grid to the particle positions and redistribution of the spray source terms from the particle positions to the Eulerian grid for the gas-phase. Since the time step for the spray equations is usually much smaller than that for the flow equations (especially for the present MSIP scheme with which, in general, a large CFL number can be obtained) and a large number of particle groups are required to statistically represent the spray behavior, it is very important to keep the numerical efficiency of the present implicit scheme from being severely degraded down by the coupling (or inter-action) between the gas and liquid-phases. A strategy to overcome this problem, at least for steady state flows, has been successfully applied to the present study. It will be described in this section.

C.2c(1) Stochastic Process

As mentioned in the introduction section, there are two types of separated flow models for spray computations. One is the deterministic separated flow (DSF) model and the other the stochastic separated flow (SSF) model. For turbulent flow calculations, the DSF model completely neglects the dispersion effect due to the turbulent motion and, therefore, mean gas flow quantities are used to evaluate the right-hand-side of Eqs. (6) and (7). In the present study, the SSF model is applied to account for the dispersion effects on spray characteristics. In this model, the gas-phase velocity fluctuations, u_i and v_i, are generated by randomly sampling a Gaussian probability density distribution having a standard deviation of $(2\kappa/3)^{1/2}$. The instantaneous velocities are then used to evaluate Eqs. (6) and (7). A fixed number of samplings is conducted for each group of particles. The final spray quantities are obtained by averaging the results (source terms, trajectories, . . . , etc.) among the total samples. Details of the SSF model can be found in Refs. 26 and 33.

C.2c(2) Determination of Spray Time Step

For spray combustion calculations, there are several time scales involved in the flow field which can differ by several orders of magnitude. The chemical reaction time scale is usually very small compared with the rate of evolution of the gas flow. This is also true for an evaporating spray. To accurately calculate the particle trajectories, size and temperature, the integration time step has to be small. This is especially severe as the droplet becomes smaller and smaller toward the end of its lifetime. For an unsteady problem, the time step for the entire system will be controlled by the smallest time step. For a steady state calculation, however, the time step for chemical reaction is usually not a problem in the present formulation due to the implicit treatment of the chemical source term. Our experience indicates that, for single-phase combustion calculations, the same CFL number usually can be used for both nonreacting and reacting calculations with the present MSIP method. This ensures that the convergence properties for reacting flow calculations are not degraded using the present numerical algorithm. However, the time step for spray equations still remains small and has to be selected (computed) very carefully in order to obtain accurate spray results and to maintain stability. The determination of the spray time step will be discussed here and how the spray interacts with the gas flow is described in the next section.

The spray time step at any instant of time along its trajectory is determined based on the following time step constraints: (1) droplet velocity relaxation time (t_r), (2) droplet life time (t_l), (3) droplet surface temperature constraint time (t_s), (4) local grid time scale (t_g) and (5) turbulent eddy-droplet interaction time (t_i). The final spray time step (Δt_{spr}) is determined by taking the minimum of the above five time steps to ensure the accuracy and stability of the spray calculations. A factor between 0.1 and 0.5 is further used to multiply the selected time step in the current spray calculation. These time steps are described as follows.

Droplet velocity relaxation time (t_r): The local linearized droplet equations of motion, Eqs. (6) and (7), have exact solutions in terms of the local slip velocity with an exponential decay form. The time constant for the exact solution can be expressed as

$$t_r = \frac{16}{3}\left(\frac{\rho_l}{\rho_g}\right)\left(\frac{r_p^2}{\nu}\right)\left(C_D Re_p\right)^{-1}.$$

Droplet life time (t_l): To ensure that the drop size remains positive for the practical computational purpose, the droplet lifetime at any instant of time is estimated by the following equation

$$t_l = \frac{r_p}{3\dot{m}''_p/\rho_l}.$$

Droplet surface temperature constraint time (t_s): When the governing equation for the droplet internal temperature distribution, Eq. (13), is solved, the temperature solution can become completely incorrect due to the use of an inappropriately large time step. This is particularly important for fuel with a low boiling temperature (close to room temperature).

In order to ensure the success of the temperature calculation using Eq. (13), the exact solution of the infinite conductivity model (or uniform temperature model) is used to estimate the time step for the present vortex model. The temperature equation for the droplet based on this model is

$$\frac{dT_p}{dt} = \frac{6}{\rho_l C_{vl} d_p}\left[h\left(\bar{T} - T_p\right) - \dot{m}''_p h_{fg}\right] \tag{17}$$

Equation (17) has an exact solution (after local linearization) in the following form

$$\Delta T_p = A\left(1 - e^{-A't}\right),$$

where ΔT_p is the droplet temperature change within the integration time step, A, A', *and* B' are defined as

$$A = \left(\bar{T} - T_p - \frac{B'}{A'}\right),$$

$$A' = \frac{6}{\rho_l C_{vl} d_p} h,$$

$$B' = \frac{6}{\rho_l C_{vl} d_p} \dot{m}''_p h_{fg}.$$

Therefore, a time scale can be obtained based on the above solution if a desired ΔT_p is specified. This time scale is expressed as

$$t_s = \ln\left(\frac{1}{1 - \frac{\Delta T_p}{A}}\right)\Big/ A'$$

In our spray calculation, $\Delta T_p = 3$ K is specified for those particles just leaving the injector, where they experience a sudden temperature jump and $\Delta T_p = 0.5$ K for the rest of the calculation toward the end of their lifetime.

Local grid time scale (t_g): A particle can travel across several grids and may experience a sudden change of the local gas properties if the time step is too large. This not only causes inaccuracy in the integration but also increases the difficulties of locating the particle positions. Therefore, a time scale, t_g, is computed to ensure that the particle only moves less than one local cell size in one time step.

Turbulent Eddy-droplet interaction time (t_i): According to Shuen et al. (Ref. 42), a particle is assumed to interact with an eddy for a time which is the minimum of either the eddy lifetime or the transit time required for the particle to cross the eddy. These times are estimated by assuming that the characteristic size of an eddy is the dissipation length scale as

$$L_e = C_\mu^{3/4} \kappa^{3/2} / \varepsilon$$

and the eddy lifetime is estimated as

$$t_e = L_e/(2\kappa/3)^{1/2}.$$

The transit time of a particle was found using the linearized equation of motion for a particle in a uniform flow

$$t_t = -\tau \ln\left[1 - L_e\left(\tau\left|\vec{u}'' - \vec{u}''_p\right|\right)\right] \tag{18}$$

where

$$\tau = \frac{8\rho_p r_p}{3\rho_g C_D |\vec{u}'' - \vec{u}_p''|}$$

and $\vec{u}'' - \vec{u}_p''$, is the relative velocity at the start of the interaction. When $L_e > \tau|\vec{u}'' - \vec{u}_p''|$, the linearized stopping distance of the particle is smaller than the characteristic length scale of the eddy and Eq. (18) has no solution. In this case, the eddy has captured the particle and the interaction time is the eddy lifetime. Therefore

$$t_i = t_e, \quad if \quad L_e > \tau|\vec{u}'' - \vec{u}_p''|$$

$$t_i = \min(t_e, t_i), \quad if \quad L_e < \tau|\vec{u}'' - \vec{u}_p''|$$

C.2c(3) Interaction Between Two Phases

For the gas-phase equations, Eq. (3), the presence of the spray appears in the form of a source term, $\mathbf{H}_l$. This source term represents the interchange of the mass, momentum and energy between two phases. As the particles are injected into the flow domain, their subsequent behavior (positions, velocities, size, and temperature) is affected continuously by the neighboring gas properties and *vice versa*. Usually a large number of spray particles is desirable to accurately predict the spray behavior. However, this requires tremendous computational effort for the spray calculation alone. To minimize the computational time for the spray, the spray source term, $\mathbf{H}_l$, is not required to be updated at every gas-phase iteration (pseudotime time marching). Usually the spray source term is updated every 10 to 20 iterations in our spray calculations. When the spray source term is updated, each group of particles is integrated either to the end of its lifetime or until it leaves the computational domain. It should be noted that, for the present steady state spray combustion calculation, the spray time step determined previously is independent of the pseudotime used for the gas-phase equations, which is determined mainly from the obtainable maximum CFL number accord-ing to the local system eigenvalues. Therefore, this strategy maintains both the efficiency of the flow solver and the accuracy of the spray Lagrangian integration. This treatment of the gas-liquid interaction is different from those reported by Raju and Sirignano (Ref. 17) where time-accurate solutions were their primary concern. In the present computation, it is assumed that upon impingement with the walls, the droplets evaporate completely and assume the local gas flow velocities. The interpolation of the gas-phase properties from the Eulerian grid to the particle location and the redistribution of the spray source term from the particle location to the Eulerian grid is applied in a similar way as discussed in Raju and Sirignano (Ref. 17).

C.3 NUMERICAL TEST RESULTS

In this section, results obtained from the ALLSPD algorithm with and without spray are presented. These include (1) a nonreacting turbulent backward-facing step flow to demonstrate the validity of the current turbulence model, (2) a single-phase turbulent reverse jet combustion flow to assess the present combustion treatment and (3) a spray gas turbine combustion flow to qualitatively demonstrate the spray calculation for a complex geometry and the interaction between the two phases. The spray results shown here emphasize the numerical aspect rather than the spray physics. The accuracy validation for spray calculations will be considered in future calculations.

C.3a Backward-Facing Step Flow

The turbulent backward-facing step flow data of Kim et al. (Ref. 43) for a two-dimensional channel with an inlet to step height ratio of two is selected here to test the validity of the κ-ε turbulence model. A 136 × 100 grid, clustered near the step and the top and bottom walls, was used. No chemical reactions were included in the calculation.

The particle traces of the flow is shown in Fig. 8. The experimental reattachment length given by Kim et al. is 7.1 **H**, where **H** is the step height. The predicted value in our calculation is about 6.1 **H**, which represents a 14 percent underprediction. Figure 9 shows the mean velocity profiles at various axial locations. The agreement is quite good in all locations except near the reattachment point. The profiles for the turbulent kinetic energy and turbulent shear stress are given in Fig. 10. Good agreement is observed in these comparisons. Wall pressure coefficients along the step-side and opposite walls are shown in Fig. 11. The underprediction of reattachment length is also evident from this figure. The predicted pressure recovery downstream of the reattachment point is in excellent agreement with measured pressure levels. The convergence history for this calculation is illustrated in Fig. 12. The convergence property for the calculation is satisfactory.

C.3b Reverse Jet Combustion Flow

The flow configuration is a 51 mm I.D. (inner diam) times 457 mm cylindrical chamber containing a reverse jet flame holder which issues from a 1.32 mm I.D. (6.35 mm O.D.) tube. The jet is coincident with the chamber axis and located 80 mm upstream from the chamber exit. Both the main and jet flows are stoichiometrically premixed propane and air at a temperature of 300 K, with a mean velocity of 7.5 m/s for the main stream and 135 m/s for the jet. A complete description of the flow system is available in McDannel et al. (Ref. 44). A 117×61 grid (half domain) clustered near the jet tube was used. Five species (C_3H_8, O_2, N_2, CO_2, and H_2O) were considered in this calculation and the single-step global reaction chemistry model reported in Westbrook and Dryer (Ref. 45) was used for combustion. Figures 13, 14, and 15 show the particle traces, velocity vectors (colored by temperature) and temperature contours of the reacting flow, respectively. The experimentally measured temperature contours (directly taken from McDannel et al. (Ref. 44)) are also presented in Fig. 15 for comparison. The flow is clearly seen to consist of two distinct regions - the recirculation zone and the wake. The incoming flow is ignited by the hot combustion gas in the recirculation zone and further combustion takes place in the wake. For the test conditions considered here the reverse jet serves as a very effective flame holding device. The results in Fig. 15 indicate that the predicted temperatures are higher than the measured values. This is mainly attributed to the over-simplified chemistry model used in the present calculation. As reported by McDannel et al. (Ref. 44), there

was a significant amount of carbon monoxide (CO) observed in the combustion products, which lowered the combustion temperature. Also not included in the calculation is the radiation heat loss which will lower the flow temperature further. Ina addition, the thermocouple's used in the measurements were not corrected for radiation loss, indicating that the actual gas temperatures would be somewhat higher then measured.

C.3c Gas Turbine Spray Combustion Flow

A simplified model of General Electric's EEE (Energy Efficiency Engine) combustor is considered. Figure 16 shows the clustered 81×65 grid for this calculation and the general engine grid layout for the entire engine (Ref. 46). It is an annular combustor with a dual can combustor dome. The cooling air through the internal walls (two combustor domes) was omitted for simplicity. Also, the swirling effect was not included in the calculation. The present calculation does not completely simulate the typical gas turbine combustion characteristics, in which swirling and cooling are the two important ingredients. We would like to emphasize, in the present study, that the focus is to demonstrate the effectiveness of the interaction between the two phases based on the present spray solution procedure. Further studies with this algorithm will be conducted both on the spray accuracy evaluation and on the detailed swirling and cooling computation for gas turbine combustor configurations.

For the present spray combustion calculation, the spray injectors were located close to the inlet of the combustor domes. One hundred spray groups with 10 random samples for each groups were used, which can be seen in Fig. 17. The case studied here has a flow Reynolds number, $Re = 1.05 \times 10^5$, where the Reynolds number is based on the inlet maximum velocity and combustor inlet height. The inlet air temperature is 900 K and the pressure is 1 atm. The liquid n-pentane fuel was used and five species (C_5H_{12}, O_2, N_2, CO_2, and H_2O) were considered in this calculation. Again, the single-step global reaction chemistry model reported in Westbrook and Dryer (Ref. 45) was used for combustion. The fuel/air ratio is 0.02 (total fuel injected/total incoming air at the inlet, including bypass air). The injection velocity of the liquid fuel at the exit of the fuel nozzle is 20 m/s and the temperature is 290 K. The liquid fuel was assumed to be fully atomized with the initial diameters ranging from 20 to 100 μm. The liquid fuel was injected into the gas flow after the gas flow had been iterated to reach a nearly steady state solution. Upon the injection of the fuel, the cool fuel was suddenly exposed to a hot environment and the interaction between the two phases took place in terms of the interchange of mass, momentum and energy. An ignition source was placed downstream of the injector to ignite the "burning" of the fuel-air mixture. The ignitor was turned on right after the initiation of the spray and was turned off when the temperature in any of the ignition computational cells reached 1600 K. The spray source term, Π_i, in Eq. (3) was updated (computed) every 20 gas-phase iterations. The converged results are presented in the following figures.

Figure 10 shows the particle trajectories. The dots in the figure are not scaled to indicate the relative size of the actual liquid particles, although smaller particles evaporate much faster than bigger ones. The computed velocity vectors colored with temperature are presented in Fig. 18, where a converged solution of the cold flow (nonspray/noncombustion) with the same flow condition is also included for comparison. The combustion zones are confined near the inner walls. This is mainly due to the exclusion of the swirlers at the inlet of the combustor domes in the present calculation. Without swirl, the degree of the fuel-air mixing is relatively poor. As may be noted, there is no flame holding device for the present calculation. The recirculation zones near the inner walls are the only devices to hold the flame. Figure 19 shows the Sauter mean diameter, D_{32}, along the averaged trajectory for both the lower and upper domes. The increase of the D_{32} right after the injection indicates the rapid evaporation of the smaller particles. After reaching a peak, both mean diameters gradually decrease as more and more particles evaporate. To show the convergence properties for both nonreacting and spray combustion cases, the convergence histories for both cases are shown in Fig. 20. As can be seen in this figure, the spray was initiated after the gas-phase solution had been iterated 1000 times. A sudden disturbance from the spray injection causes the L2 norm residual to jump to a level higher than the initial gas-phase residual. As more and more spray particles evaporate and undergo combustion, the interaction between two phases can be clearly identified in this convergence pattern. Since in the present calculation, the spray source term was updated every 20 gas-phase iterations, a small residual spike along the convergence history can be seen very clearly. These small spikes persist toward the end of the present computation.

D. CONCLUDING REMARKS

Much work is required to develop a CFD code to the level necessary for a designer to be able to use it with confidence. We at NASA are proceeding with a commitment to do this. A three-dimensional version of our ALLSPD will be developed shortly and extensive validation against experimental data will be performed. At the same time we are exploring the use of advanced modeling to better represent the flow physics and chemistry of turbulent combustion. For example, modeling of dense sprays and sprays at super-critical conditions will be investigated. Modeling of the turbulence and chemistry interaction will be explored, using techniques such as PDF methods. The use of reduced hydrocarbon chemical kinetics models which represent the actual combustion processes are also necessary. And finally, an improved model to represent potentially high levels of radiation heat transfer is also needed.

The state of art for numerics also continues to advance at a rapid pace. Our code will be modified in the future as opportunities arise in areas such as unstructured grids and massively parallel computing. This ongoing effort to produce a modern chemical reacting flow CFD code holds promise to provide a powerful design tool for the industry's use in the analyses of the next generation of gas turbine engine combustor concepts.

E. REFERENCES

1. Bulzan, D.L., "Velocity and Drop Size Measurements in a Swirl-Stabilized, Combusting Spray," SPIE Paper No. 1862-12, 1993.
2. Chigier, N.A., "Gas Dynamics of Swirling Flow in Combustion Systems," Astronaut. Acta, Vol. 17, 1972, pp. 387-395.

3. Syred, N. and Beer, J., "Combustion in Swirling Flows: A Review," Combust. Flame, Vol. 23, 1974, pp. 143-201.
4. Lilley, D.G., "Swirl Flows in Combustion: A Review," AIAA J., Vol. 15, No. 8, 1977, pp. 1063-1078
5. Styles, A.C. and Chigier, N.A., "Combustion of Air Blast Atomized Spray Flames," Sixteenth Symposium (International) on Combustion, The Combustion Institute, Pittsburgh, PA, 1976, pp. 619-630.
6. Khalil, E.E. and Whitelaw, J.H., "Aerodynamic and Thermodynamic Characteristics of Kerosene-Spray Flames," Sixteenth Symposium (International) on Combustion, The Combustion Institute, Pittsburgh, PA, 1976, pp. 569-576.
7. Bachalo, W.D. and Houser, M.J., "Phase/Doppler Spray Analyzer for Simultaneous Measurements of Drop Size and Velocity Distributions," Opt. Eng., Vol. 23, No. 5, 1984, pp. 583-590.
8. McDonell, V.G. and Samuelsen, S., "Gas and Drop Behavior in Reacting and Non-Reacting Air-Blast Atomizer Sprays," J. Propuls. Power, Vol. 7, No. 5, 1991, pp. 684-691.
9. Zurlo, J.R., Presser, C., Gupta, A., and Semerjian, H.G., "Determination of Droplet Characteristics in Spray Flames Using Three Different Sizing Techniques," AIAA Paper 91-2200, 1991.
10. Edwards, C.F., Rudoff, R.C., and Bachalo, W.D., "Measurement of Correlated Drop Size and Velocity Statistics, Size Distribution, and Volume Flux in a Steady Spray Flame," Presented at the Fifth International Symposium on the Applications of Laser Techniques to Fluid Mechanics, Lisbon, Portugal, 1990.
11. McDonell, V.G. and Samuelsen, G.S.,"Application of Two-Component Phase Doppler Interferometry to the Measurement of Particle Size, Mass Flux, and Velocities in Two-Phase Flows," Twenty-Second Symposium (International) on Combustion, The Combustion Institute, Pittsburgh, PA, 1988, pp. 1961-1971.
12. Edwards, C.F. and Rudoff R.C., "Structure of a Swirl-Stabilized Spray Flame by Imaging, Laser Doppler Velocimetry, and Phase Doppler Anemometry," Twenty Third Symposium (International) on Combustion, The Combustion Institute, Pittsburgh, PA, 1990, pp. 1353-1359.
13. Shuen, J.-S., Chen, K.-H., and Choi, Y., "A Time-Accurate Algorithm for Chemical Non-Equilibrium Viscous Flows at All Speeds," AIAA Paper 92-3639, 1992.
14. Shuen, J.-S., Chen, K.-H., and Choi, Y., "A Coupled Implicit Method for Chemical Non-Equilibrium Flows at All Speeds," Accepted for Publication, J. Comput. Phys., 1993.
15. Solomon, A.S.P., Shuen, J.-S., Zhang, Q.-F., and Faeth, G.M., "Measurements and Predictions of the Structure of Evaporating Sprays," J. Heat Transfer, Vol. 107, 1985, pp. 679-686.
16. Shuen, J.-S., "Prediction of the Structure of Fuel Sprays in Cylindrical Combustion Chambers," J. Propuls. Power, Vol. 3, 1987, pp. 105-113.
17. Raju, M.S. and Sirignano, W.A., "Multicomponent Spray Computations in a Modified Centerbody Combustor," J. Propuls. Power, Vol. 6, 1990, pp. 97-105.
18. Liou, M.-S., "Newton/Upwind Method and Numerical Study of Shock Wave/Boundary Layer Interactions," Int. J. Numer. Methods Fluids, Vol. 9, 1989, pp. 747-761.
19. Meakin, R. and Suhs, N., "Unsteady Aerodynamic Simulation of Multiple Bodies in a Relative Motion," AIAA Paper 89-1996, 1989.
20. Pan, D. and Chakravarthy, S., "Unified Formulation for Incompressible Flows," AIAA Paper 89-0122, 1989.
21. Chen, K.-H., Kelecy, F.J., and Pletcher, R.H., "A Numerical and Experimental Study of Three-Dimensional Liquid Sloshing in a Rotating Spherical Container," AIAA Paper 92-0829, 1992.
22. Shuen, J.-S. and Yoon, S., "Numerical Study of Chemically Reacting Flows Using a Lower-Upper Symmetric Successive Overrelaxation Scheme," AIAA J., Vol. 27, No. 12, 1989, pp. 1752-1760.
23. Merkle, C.L. and Choi, D., "Application of Time-Iterative Schemes to Incompressible Flow," AIAA J., Vol. 23, No. 12, 1985, pp. 1518-1524.
24. Turkel, E., "Preconditioned Methods for Solving the Incompressible and Low Speed Compressible Equations," J. Comput. Phys., Vol. 72, 1987, pp. 277-298.
25. Merkle, C.L. and Choi, Y., "Computation of Low-Speed Flow with Heat Addition," AIAA J., Vol. 25, No. 8, 1987, pp. 831-838.
26. Faeth, G.M., "Evaporation and Combustion of Sprays," Prog. Energy Combust. Sci., Vol. 9, No. 1-2, 1983, pp. 1-76.
27. Sirignano, W.A., "Fuel Droplet Vaporization and Spray Combustion Theory," Prog. Energy Combust. Sci., Vol. 9, No. 4, 1983, pp. 291 322.
28. Shearer, A.J., Tamura, H., and Faeth, G.M., "Evaluation of a Locally Homogeneous Flow Model of Spray Evaporation," J. Energy, Vol. 3, No. 1, 1979, pp. 271-284.
29. Gosman, A.D. and Johns, R.J.R., "Computer Analysis of Fuel-Air Mixing in Direct-Injection Engines," Diesel Combustor and Emission, SEA P-86, SAE, Warrendale, PA, 1980.
30. Crowe, C.T., "Review-Numerical Models for Dilute Gas-Particle Flows," J. Fluids Eng., Vol. 104, No. 3, 1982, pp. 297-303.
31. Dukowicz, J.K., "A Particle-Fluid Numerical Model for Liquid Sprays," J. Comput. Phys., Vol. 35, No. 2, 1990, pp. 229-253.
32. Gosman, A.D. and Ioannides, E., "Aspects of Computer Simulation of Liquid-Fueled Combustors," J. Energy, Vol. 7, No. 6, 1983, pp. 482-490.
33. Shuen, J.-S., Solomon, A.S.P., and Faeth, G.M., "Drop-Turbulence Interactions in a Diffusion Flame," AIAA J., Vol. 24, No. 1, 1986, pp. 101-108.
34. Chen, K.-H. and Shuen, J.-S., "A Coupled Multi-Block Solution Procedure for Spray Combustion in Complex Geometries," AIAA Paper 93-0108, 1993.
35. Shih, T.H., "An Improved κ-ε Model for Near-Wall Turbulence and Comparison with Direct Numerical Simulation," NASA TM-103221, 1990.
36. Shuen, J.-S., "Upwind Differencing and LU Factorization for Chemical Non-equilibrium Navier-Stokes Equations," J. Comput. Phys., Vol. 99, No. 2, 1992, pp. 233-250.

37. Reid, R.C., Prausnitz, J.M., and Poling, B.E., "The Properties of Gases and Liquids, Fourth Ed., McGraw-Hill Publishing Co., New York, 1988.

38. Aggarwal, S.K., Tong, A.Y., and Sirignano, W.A., "A Comparison of Vaporization Models in Spray Calculations," AIAA J., Vol. 22, No. 10, 1984, pp. 1448-1457.

39. Tong, A.Y. and Sirignano, W.A., "Analytical Solution for Diffusion and Circulation in a Vaporizing Droplet," Nineteenth Symposium (International) on Combustion, The Combustion Institute, Pittsburgh, PA, 1982, pp. 1007-1020.

40. Anderson, D.A., Tannehill, J.C., and Pletcher, R.H., Computational Fluid Mechanics and Heat Transfer, Hemisphere Publishing Corp., New York, 1984.

41. Schneider, G.E. and Zedan, M., "A Modified Strongly Implicit Procedure for the Numerical Solution of Field Problems," Numer. Heat Transfer, Vol. 4, No. 1, 1981, pp. 1-19.

42. Shuen, J.-S., Chen, L.D., and Faeth, G.M., "Evaluation of a Stochastic Model of Particle Dispersion in a Turbulent Round Jet," AIChE J., Vol. 29, No. 1, 1983, pp. 167-170.

43. Kim, J., Kline, S.J., and Johnston, J.P., "Investigation of a Reattaching Turbulent Shear Layer: Flow Over a Backward-Facing Step," J. Fluids Eng., Vol. 102, No. 3, 1980, pp. 302-308.

44. McDannel, M.D., Peterson, P.R., and Samuelsen, G.S., "Species Concentration and Temperature Measurements in a Lean, Premixed Flow Stabilized by a Reverse Jet," Combust. Sci. Technol., Vol. 28, No. 5-6, 1982, pp. 211-224.

45. Westbrook, C.K. and Dryer, F.L., "Simplified Reaction Mechanisms for the Oxidation of Hydrocarbon Fuels in Flames," Combust. Sci. Technol., Vol. 27, No. 1-2, 1981, pp. 31-43.

46. Stewart, M.E.M., "Euler Solutions of an Unbladed Jet Engine Configuration," NASA TN-105332, 1991.

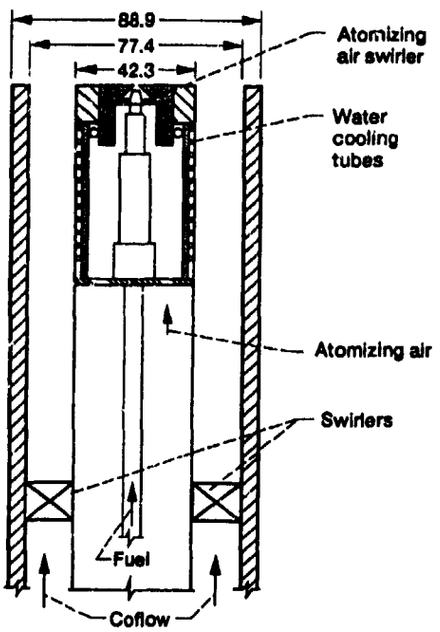

Figure 1.—Schematic drawing of the combustor. Dimensions in mm.

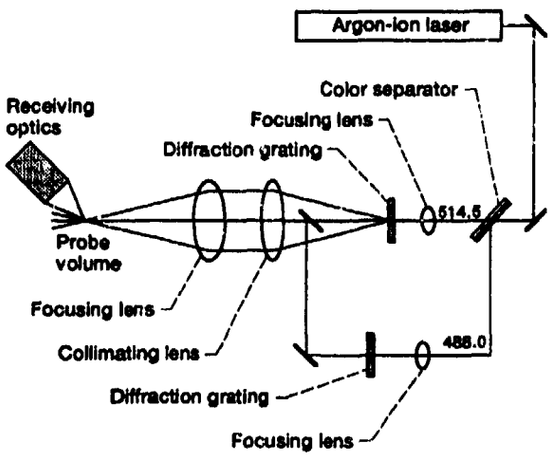

Figure 2.—Optical configuration of the phase/Doppler particle analyzer.

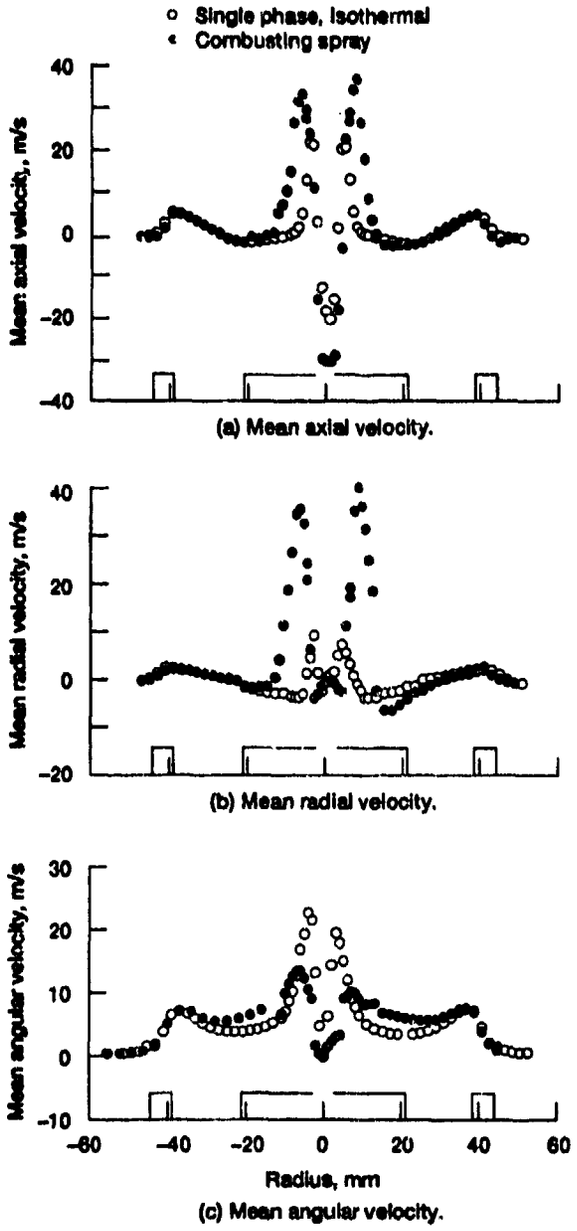

Figure 3.—Gas phase mean velocity at 5 mm downstream.

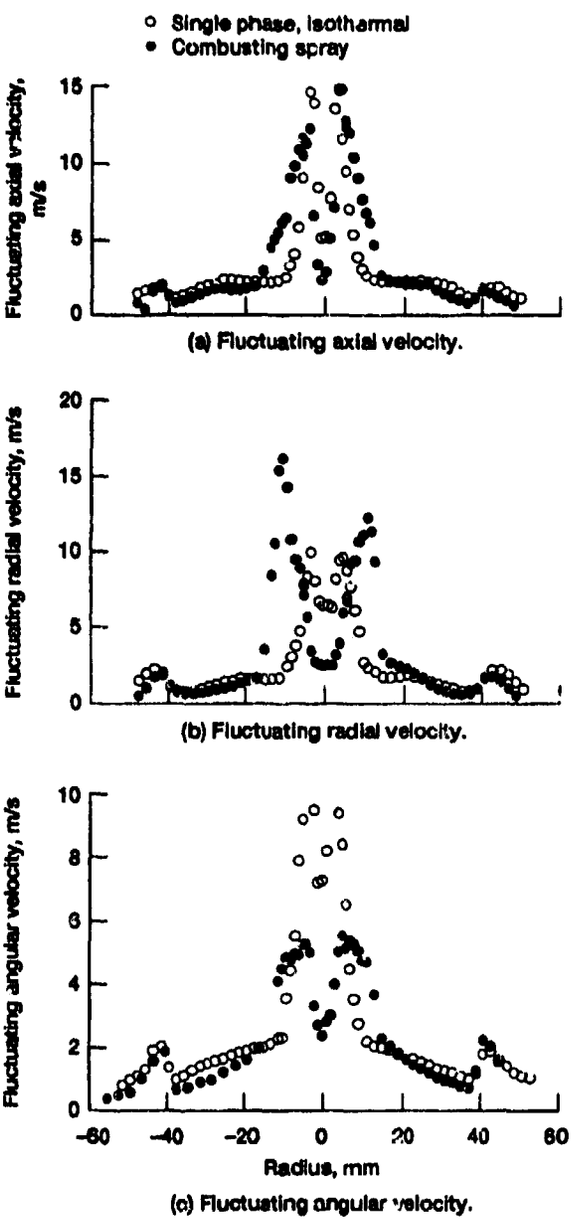

Figure 4.—Gas phase fluctuating velocity at 5 mm downstream.

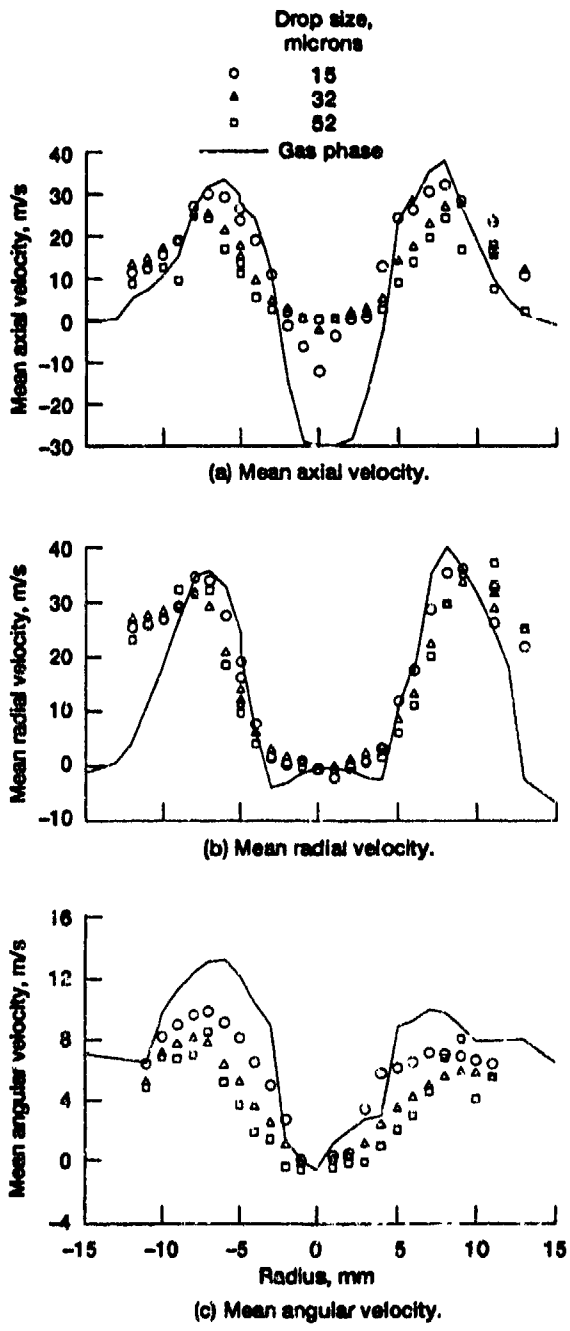

Figure 5.—Drop mean velocity at 5 mm downstream.

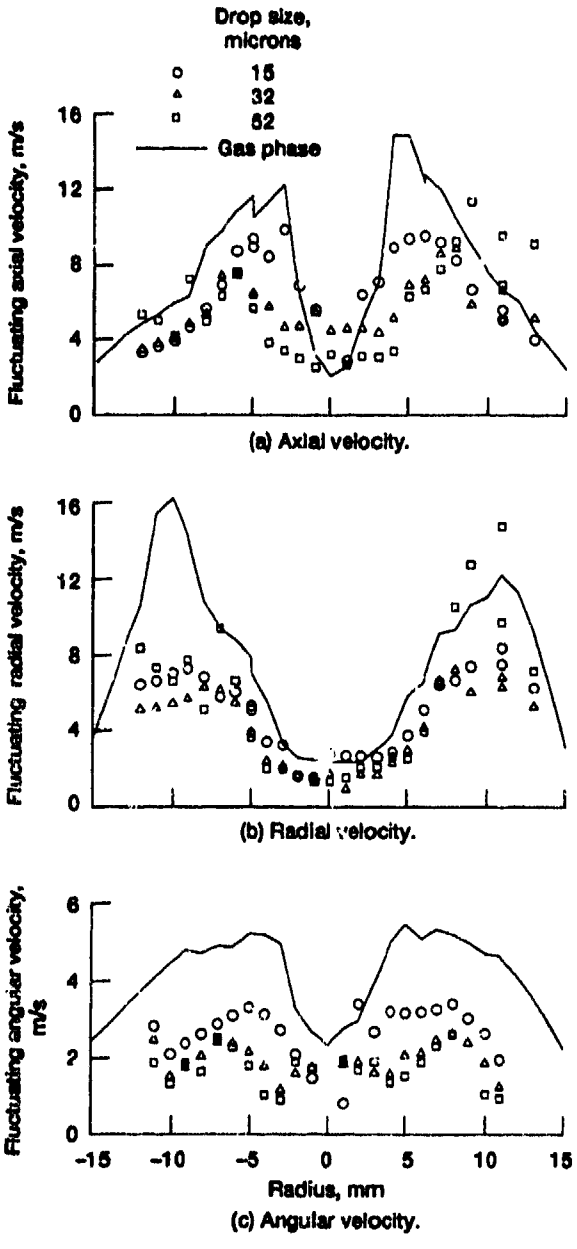

Figure 6.—Drop fluctuating velocity at 5 mm downstream.

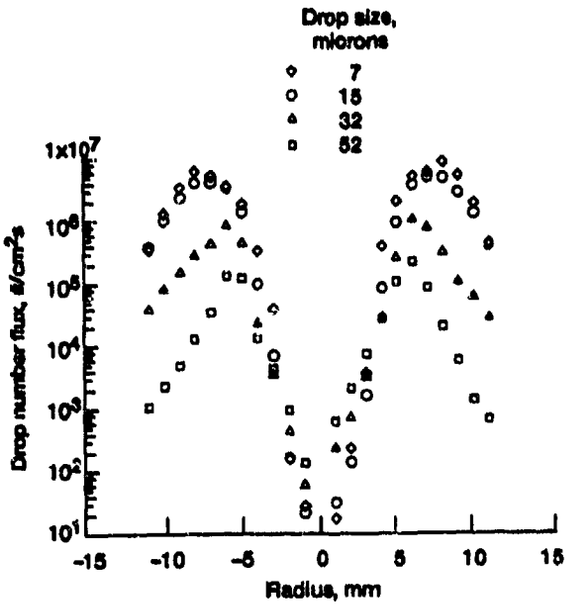

Figure 7.—Drop number flux at 5 mm downstream.

Figure 8.—Particle traces for turbulent backward-facing step flow.

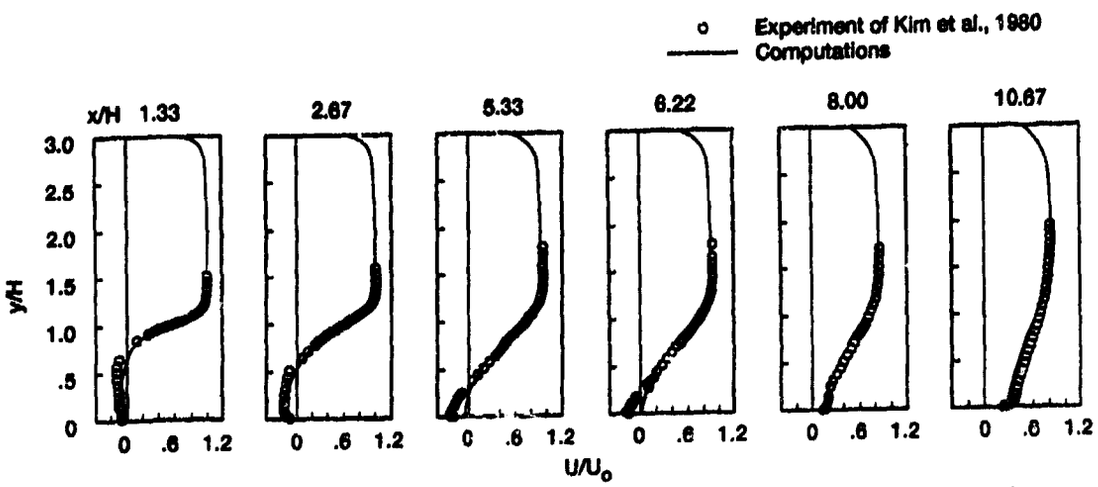

Figure 9.—Numerical predictions of the mean velocity profiles at selected axial locations for the turbulent backward-facing step flow.

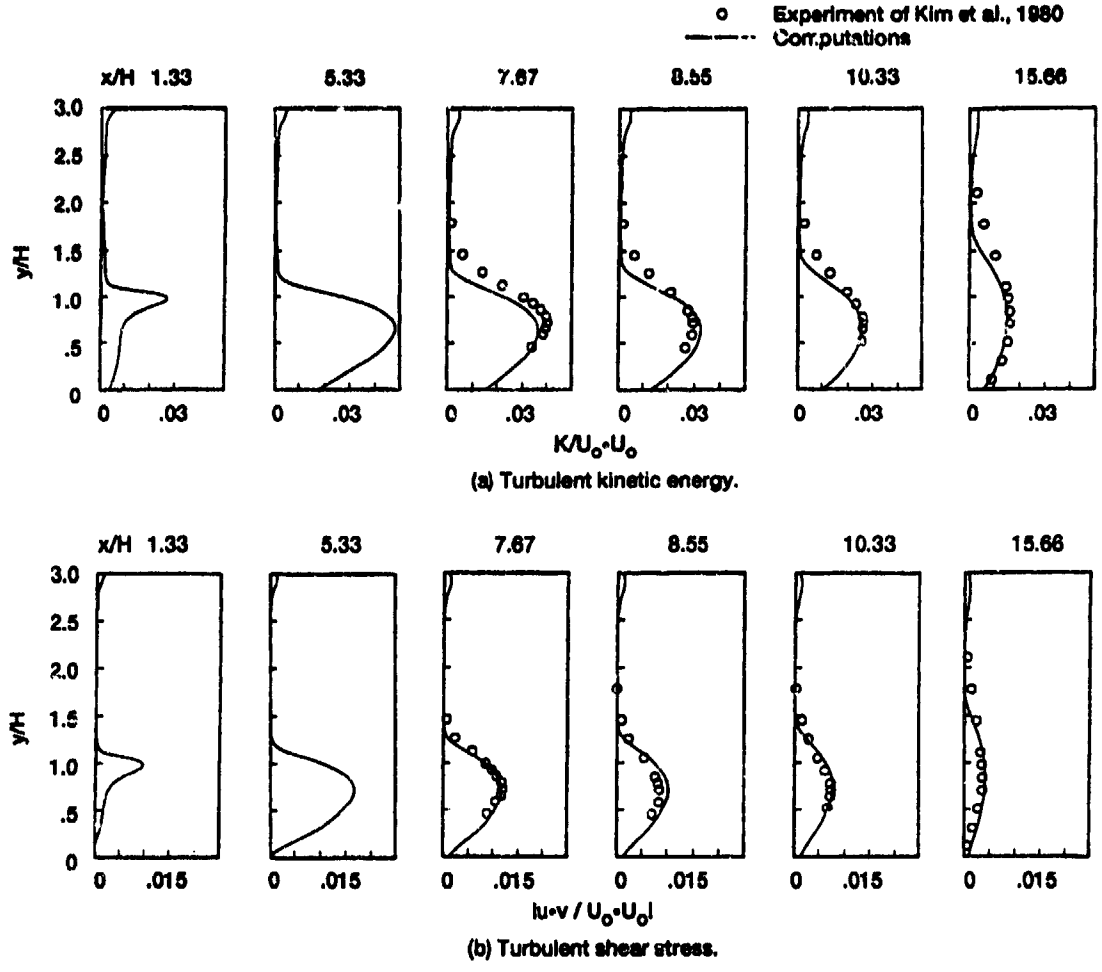

Figure 10.—Comparisons of (a) turbulent kinetic energy and (b) turbulent shear stress at some selected axial locations for the turbulent backward-facing step flow.

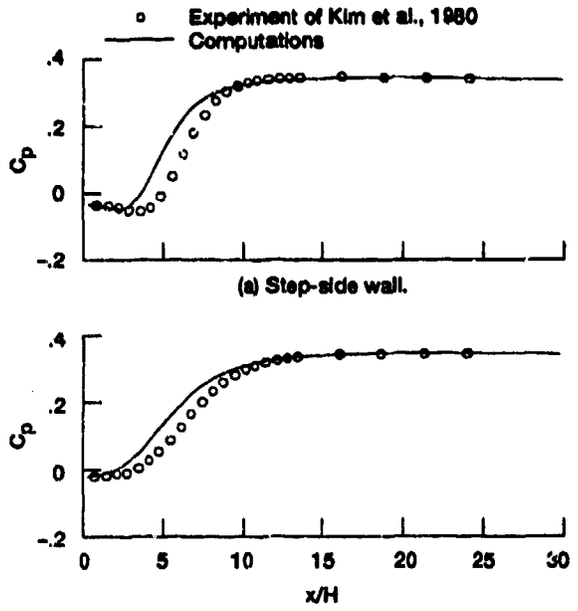

Figure 11.—Comparison of the wall pressure coefficients for the turbulent backward-facing step flow.

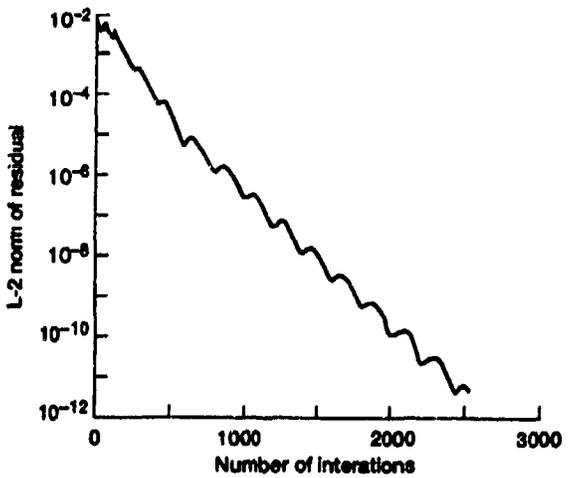

Figure 12.—Convergence history for the turbulent backward-facing step flow.

Figure 13.—Particle traces for the reverse jet combustion flow.

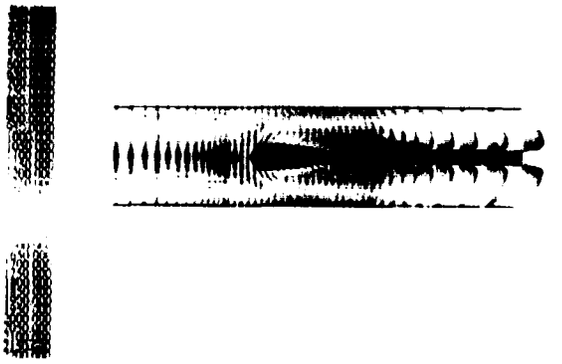

Figure 14.—Velocity vectors (colored by temperature) for the reverse jet combustion flow.

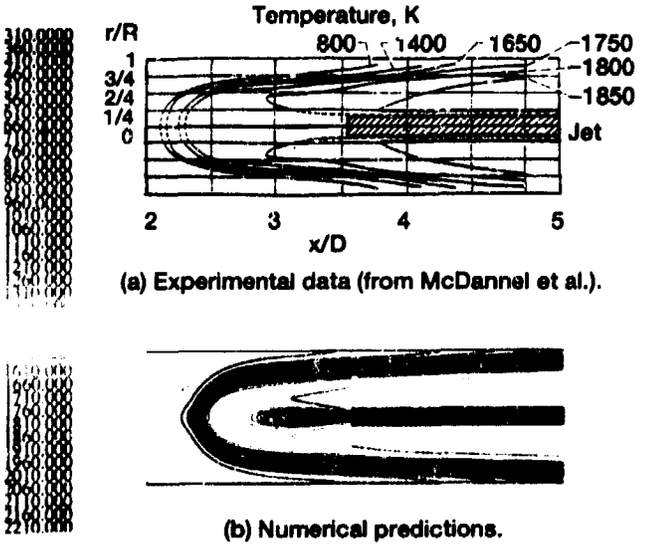

Figure 15.—Comparison of the temperature predictions with the experimental data for the reverse jet combustion flow.

THIS PAGE IS INTENTIONALLY BLANK

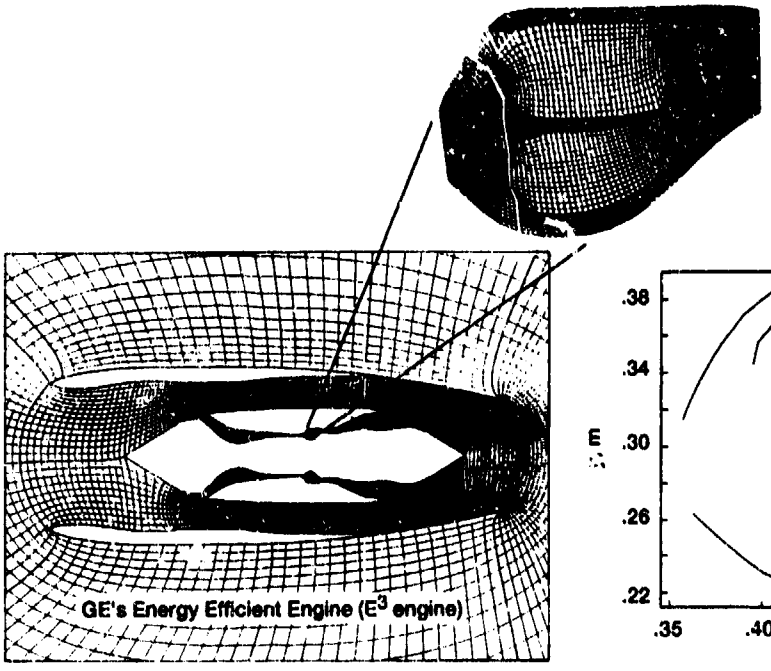

Figure 16.—Center-plane cut for GE's EEE gas turbine engine and the grid for the 2-D combustor.

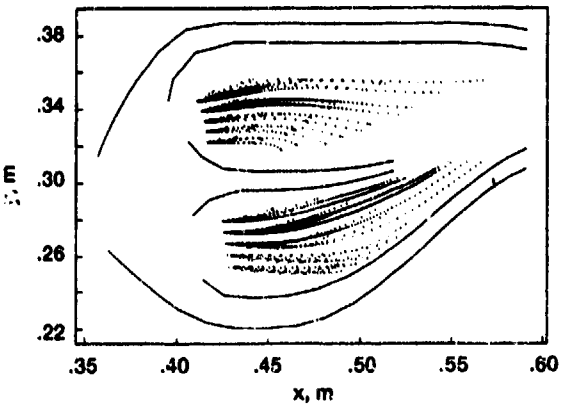

Figure 17.—Liquid fuel particle trajectories for the 2-D gas turbine spray combustion flow.

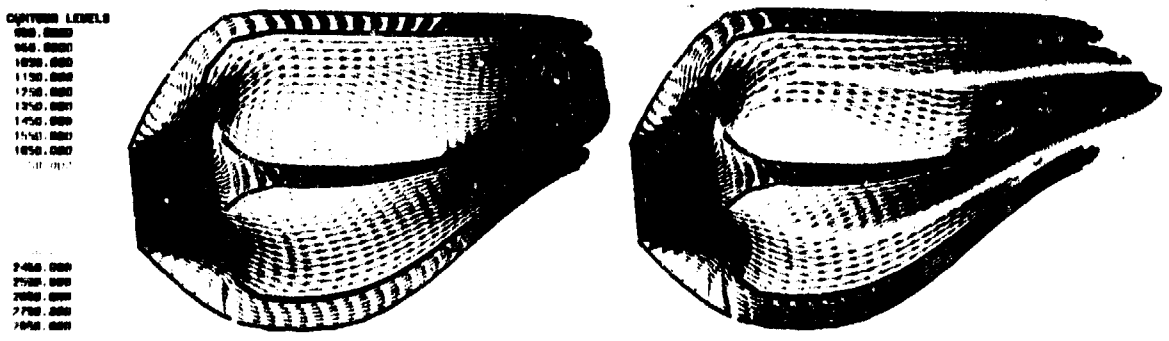

(a) Non-combustion flow (cold flow, no spray).

(b) Spray combustion flow.

Figure 18.—Velocity vectors (colored by temperature) for (a) non-combustion and (b) spray combustion cases for the 2-D gas turbine spray combustion flow.

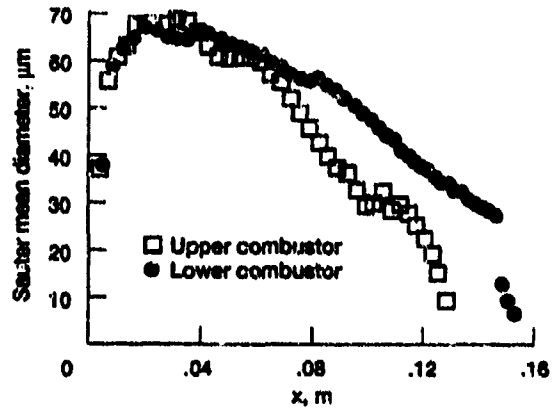

Figure 19.—Sauter mean diameter distribution for upper and lower combustor domes along the averaged trajectory for the 2-D gas turbine spray combustion flow.

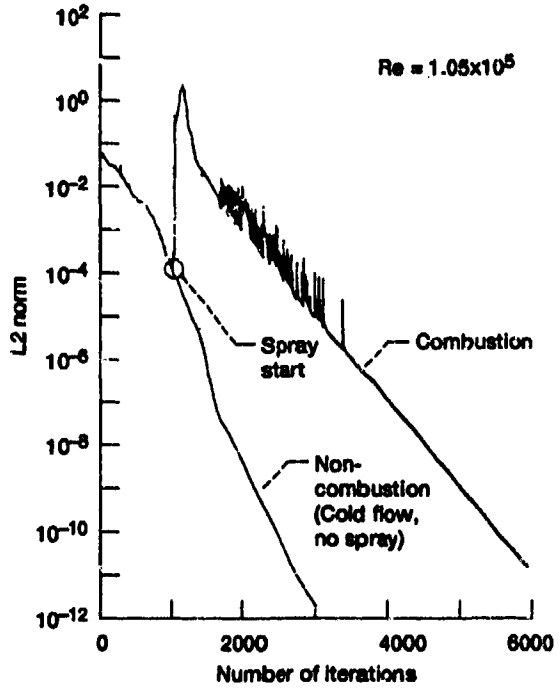

Figure 20.—Convergence history for both non-combustion and spray combustion cases for the 2-D gas turbine spray combustion flow.

Discussion

Question 1.
You mentioned that one of the objectives of the new CFD model is that it is more efficient than the TEACH or other codes. Can you give us some idea of these improvements?

Author's Reply
The code is designed to be more robust and efficient than the TEACH type codes. The TEACH type codes use explicit or semi implicit treatment of the chemical source terms and a sequential solution approach. The ALLSPD formulation utilizes a strongly coupled and implicit numerical scheme to solve the governing flow equations. A two-dimensional version of the code will be released in June, 1993. It is for domestic use only.

MODELISATION DE LA PHASE LIQUIDE DANS LES CHAMBRES DE COMBUSTION

P. HEBRARD, G. LAVERGNE, P. BEARD, P. DONNADILLE, P. TRICHET
CERT/ ONERA - BP 4025 - 31055 TOULOUSE CEDEX
FRANCE

RESUME

Ce papier présente des résultats expérimentaux, des modèles et des simulations numériques relatifs au comportement de la phase liquide dans les chambres de combustion. Ces études concernent les conditions initiales, les conditions aux limites et les validations des modèles des différents processus physiques qui doivent être intégrés aux codes de calculs d'écoulements réactifs. Plusieurs expériences sont présentées : caractérisation d'un jet de gouttes en sortie d'injecteur aérodynamique, dispersion des gouttes dans une turbulence de grille et dans un écoulement fortement instationnaire (zone de mélange, marche), trajectoires et évaporation des gouttes dans un écoulement turbulent, interaction des gouttes avec une paroi chaude. Les caractérisations des écoulements diphasiques sont réalisés par LDA et fil chaud pour la phase gazeuse et par anémogranulométrie Phase Doppler et techniques vidéo rapide associées au traitement d'image pour la phase liquide. Les techniques vidéo et le traitement d'image permettent de restituer les trajectoires des gouttes, leur vitesse ainsi que les principales statistiques de la dispersion (trajectoire moyenne, enveloppe, taux de présence). Les résultats expérimentaux, en particulier ceux provenant de la dispersion des gouttes, sont comparés avec des résultats de simulations numériques. La méthode lagrangienne est utilisée pour le transport des gouttes, leur dispersion peut être calculée à partir des deux approches suivantes [1,2] :

- la phase gazeuse est calculée par simulation directe, un modèle déterministe est retenu pour le transport des gouttes,
- la phase gazeuse est calculée à partir d'un modèle de turbulence du type K-ε, des modèles stochastiques sont utilisés pour le transport des gouttes.

En conclusion, seront déduits les modèles les plus appropriés aux écoulements diphasiques étudiés.

LISTE DES SYMBOLES

D_p diamètre de la particule

V_p vitesse de la particule

C_d coefficient de traînée

ρ masse volumique de l'air

ρ_p masse volumique de la particule

V vitesse de l'air

C_a coefficient de masse ajoutée

C_h coefficient d'histoire

μ viscosité dynamique de l'air

g accélération de la pesanteur

T_l échelle intégrale temporelle

L_d échelle intégrale spatiale

T_d temps d'interaction de la particule avec un tourbillon

X_r abscisse du point de recollement

σ_p tension superficielle de la particule

We nombre de Weber

$\frac{D}{Dt}$ dérivée matérielle fluide

$\frac{D^p}{Dt}$ dérivée matérielle particulaire

1. INTRODUCTION

Dans les écoulements réactifs tridimensionnels des chambres de combustion de turboréacteurs ou de statoréacteurs interviennent des processus physiques très complexes qui interagissent : aérodynamique 3D turbulente et fortement instationnaire, combustion turbulente, transfert de chaleur, cinétique chimique complexe. Dans le cas d'injection de carburant liquide la complexité de ces processus devient plus importante à cause de la présence des deux phases. Le système d'injection de carburant liquide a une influence prépondérante sur les performances des foyers (plages de stabilité, rendement de combustion...). Le développement rapide des calculateurs et des procédures de résolution numérique permet actuellement la modélisation d'écoulements réactifs tridimensionnels. Généralement, dans ces codes, le carburant est sous forme gazeuse dès son injection dans la chambre. Pour la prise en compte du carburant sous sa forme liquide dans ces simulations numériques, une bonne connaissance des conditions initiales (conditions d'injection), des conditions aux limites (conditions en paroi) et des phénomènes physiques élémentaires (dispersion, évaporation et combustion de gouttes...) est nécessaire pour rendre ces codes les plus prédictifs possible (figure 1). Un programme de recherche sur ces différents phénomènes a été initié au CERT/ONERA, dans lequel *la simulation numérique* et *l'approche expérimentale* sont menées en parallèle. Les conditions initiales (répartition des diamètres, des vitesses moyennes et des débits de gouttes) sont obtenues expérimentalement par anémogranulométrie et par techniques de visualisation et de traitement d'image. Les conditions aux limites concernent principalement les phénomènes d'interaction des gouttes avec les parois (rebond des gouttes, formation et évaporation d'un film liquide sur la paroi). Les phénomènes physiques élémentaires tels que la dispersion, l'évaporation et la combustion des gouttes font l'objet d'études plus approfondies. L'objet de cette contribution est donc de présenter les différentes approches expérimentales et de calcul numérique suivies au CERT/ONERA pour les études des différents processus physiques liés à l'injection de carburant liquide dans les chambres de combustion.

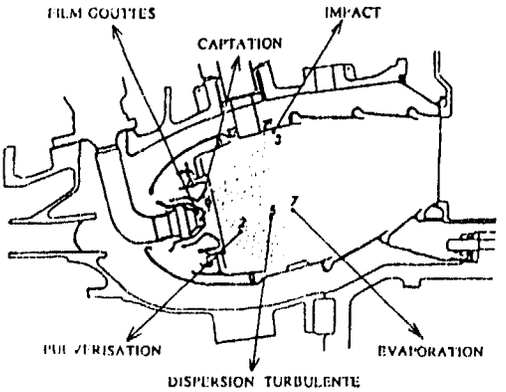

Figure 1 : Principaux phénomènes physiques élémentaires liés au carburant liquide

Presented at an AGARD Meeting on 'Fuels and Combustion Technology for Advanced Aircraft Engines', May 1993.

2. CARACTERISATION D'UN INJECTEUR AERODYNAMIQUE

Le comportement d'un jet de gouttes a une influence directe sur les performances d'une chambre de combustion. Des analyses détaillées sont nécessaires en tant que conditions initiales pour la modélisation et pour une bonne compréhension des processus physiques (mélange entre phases, transport de gouttes et combustion) qui se produisent dans les chambres de combustion.

Avec le développement récent des méthodes optiques non intrusives telle que PID (Phase Doppler Interferometry) [3,4], il est possible d'obtenir une mesure de la distribution des tailles de gouttes, de la vitesse des gouttes et du flux massique de la phase diluée.

2.1 Montage expérimental

L'injecteur retenu pour cette étude est représenté sur la figure 2. Il s'agit d'un injecteur aérodynamique (airblast) utilisé dans les chambres de combustion de turboréacteurs. Les conditions d'essais sont les suivantes :

- pression atmosphérique
- débit de liquide (eau) : 4,1 g/s
- perte de charge : $\Delta p/p = 4\ \%$

L'anémogranulomètre Phase Doppler, utilisé pour caractériser le spray, est un modèle à deux composantes (Aerometrics PDPA System 200). Les deux volumes de mesure sont produits en séparant la raie 488 nm (bleu) et la raie 514,5 (vert) d'un laser à Argon. Les mesures sont faites dans trois plans situés respectivement à 4,5 mm, 16,4 mm et 36,4 mm de la sortie de l'injecteur (figure 3). Dans chaque plan un maillage (maille 5 mm) a été adopté et en chaque point de ce maillage nous avons enregistré 4000 événements. Les résultats donnés par le PDPA sont les histogrammes de taille et de vitesse, la valeur de densité de gouttes et les corrélations taille-vitesse. Cependant nous ne présentons, pour cet injecteur, que les paramètres d'intérêt immédiat tels que le diamètre moyen de Sauter (DMS), et les composantes de la vitesse moyenne des gouttes.

La phase gazeuse a été caractérisée par technique LDA. L'écoulement, en l'absence de gouttes, étant ensemencé par des particules sub-microniques.

2.2 Résultats

a) Distribution de taille

Près de l'injecteur (z = 4,5 mm : figure 4), nous notons une répartition en "dôme" : les vrilles internes et externes produisent une distribution de taille presque uniforme, mais les jets à l'extrémité du bol provoquent une atomisation secondaire que l'on retrouve en périphérie. Des grosses gouttes sont observées au centre : elles doivent être produites par arrachement de la nappe liquide annulaire par le swirl interne.

Plus en aval (z= 16,4 mm : figure 5) la distribution de taille s'élargit. L'écoulement tournant fait recirculer des petites gouttes vers le centre [5,6]. Les jets de bols forment des indentations sur la périphérie du spray.

Dans la dernière section (z = 36,4 mm : figure 6), la distribution de gouttes est plus uniforme en périphérie et l'angle du spray augmente par effet de swirl. Nous retrouvons toujours les petites gouttes dans la partie centrale.

b) Champ de vitesse, comparaison entre phases:

Des profils suivant un diamètre montrent les variations locales de vitesse moyenne des gouttes (vitesse axiale : figure 7, vitesse radiale et vitesse tangentielle : figure 8).

Plan Z = 4,5 mm

Près de l'injecteur, la vitesse axiale présente deux maxima : ils sont dûs aux vrilles interne et externe. La vitesse au centre est nulle indiquant, sans doute, le début de la recirculation causée par le mouvement tournant. Les gouttes ont une vitesse assez uniforme, avec des petits pics sur l'extérieur, traduisant l'influence des jets issus des trous de bol. La phase gazeuse a une vitesse tangentielle plus importante que celle de la phase dispersée. Les effets radiaux sont assez similaires pour les deux phases, tout en restant faibles.

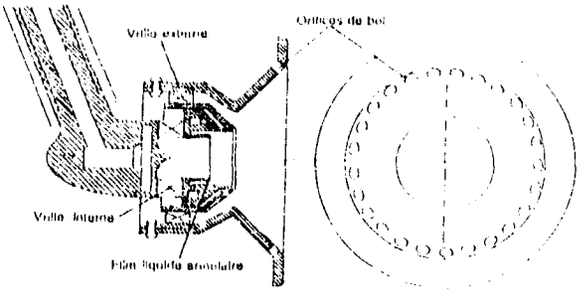

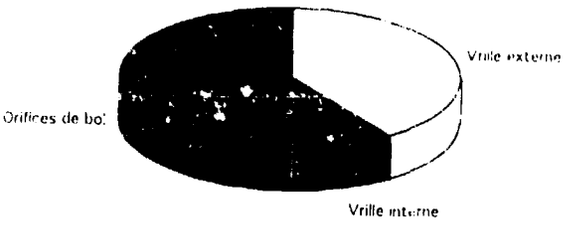

Figure 2 : Schéma de l'injecteur et débits aérodynamiques

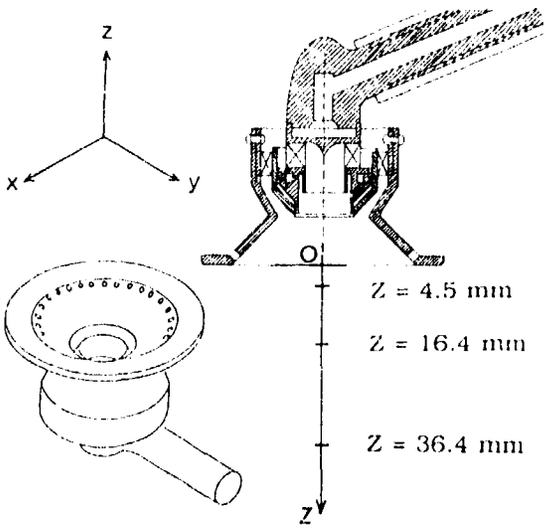

Figure 3 : Système d'axes et plans de mesure

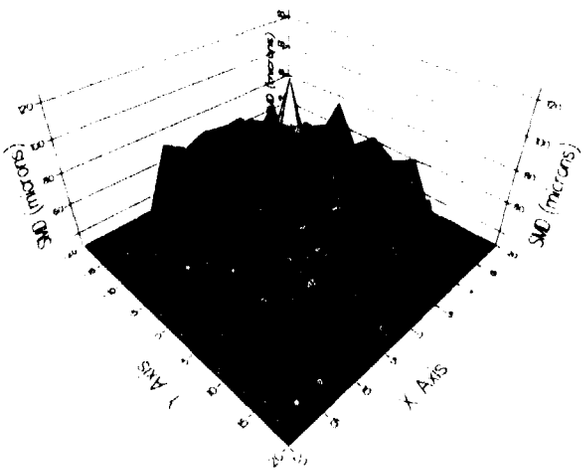

Figure 4 : Distribution du DMS (Z= 4,5 mm)

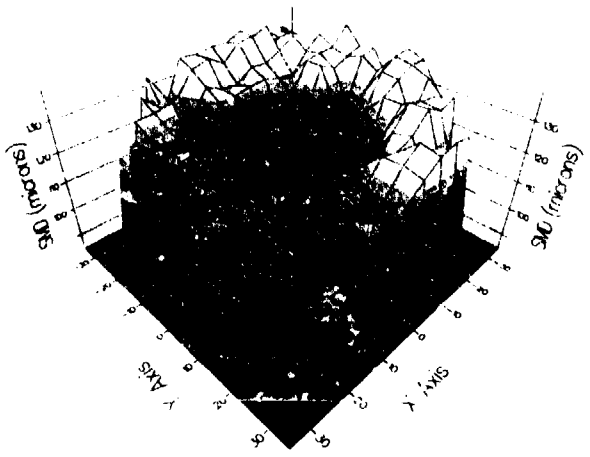

Figure 5 : Distribution du DMS (Z= 16,4 mm)

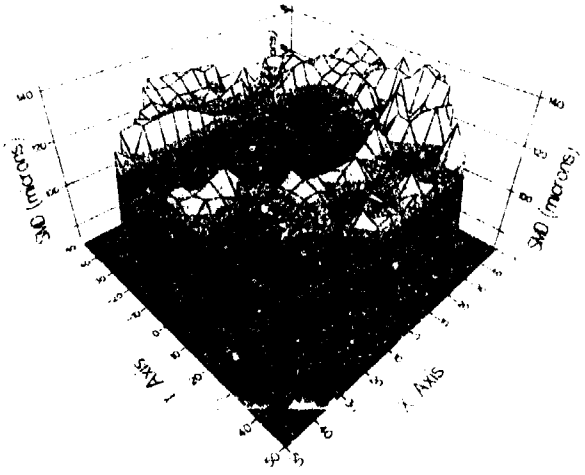

Figure 6 : Distribution du DMS (Z= 36,4 mm)

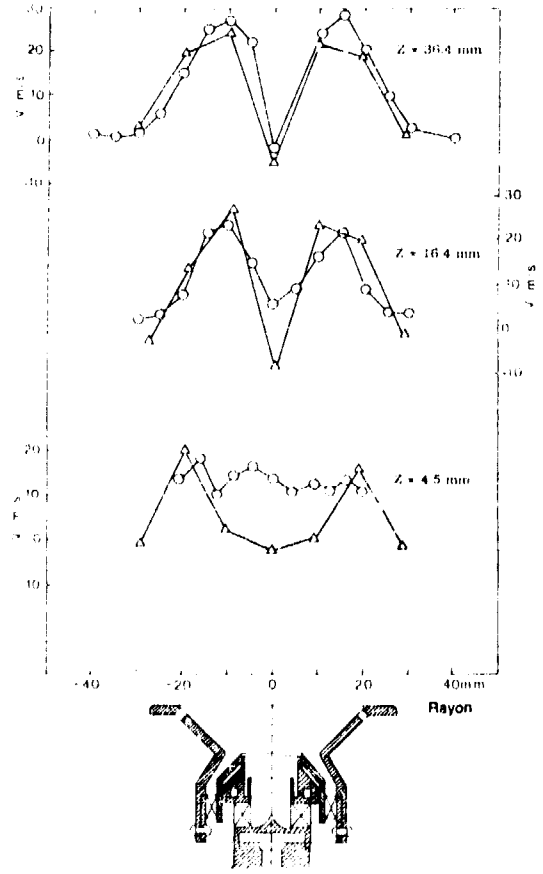

Figure 7 : Profils de vitesse axiale dans les trois plans
Phase gazeuse LDA : Δ
Phase dispersée PDPA O

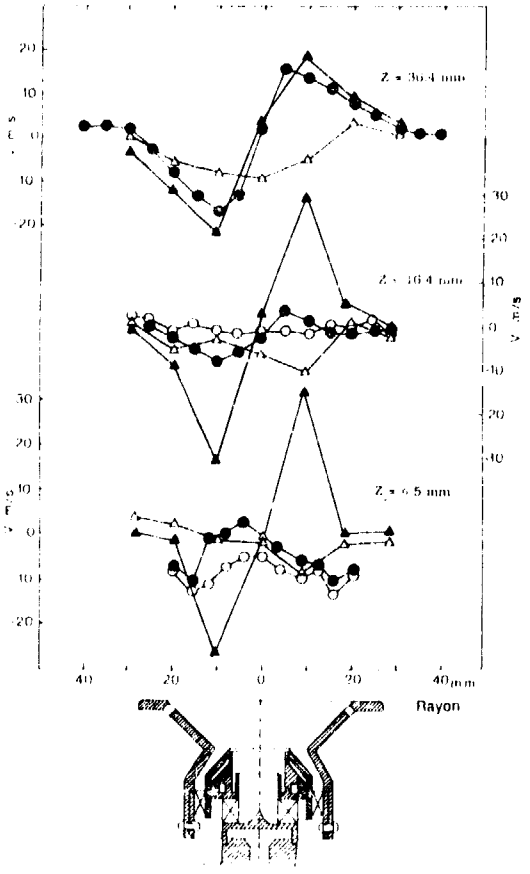

Figure 8 : Profils de vitesses radiale et tangentielle dans les trois plans
Phase gazeuse LDA V_t —▲— V_r —△—
Phase dispersée PDPA V_t —●— V_r —○—

Plan Z = 16,4 mm
La vitesse axiale présente toujours deux pics et au voisinage de l'axe nous trouvons une zone d'écoulement de retour. La vitesse axiale des gouttes augmente, et nous notons une vitesse négative sur l'axe. Sur les distributions de taille, nous avons trouvé dans cette zone des petites gouttes, qui ont été entraînées par la recirculation. Les gouttes ont des vitesse radiales faibles, par contre leur vitesse tangentielle commence à augmenter.

Plan Z = 35,4 mm
Les profils de vitesse pour les deux phases sont très semblables, nous notons un élargissement des pics, ce qui indique une expansion du spray. La vitesse tangentielle des gouttes est très proche de la vitesse tangentielle de la phase continue.

2.3 Conclusion
Cette étude montre quelques caractéristiques d'un spray, produit par un injecteur aérodynamique, obtenues par des méthodes non intrusives (LDA et PDPA).

La présence du spray change la structure de l'écoulement en zone proche de l'injecteur. En aval, pour les trois sections de mesure, nous notons une accélération des gouttes. Il y a donc un échange de quantité de mouvement entre la phase dispersée et la phase continue. Les profils de vitesse dans le dernier plan montrent que l'aérodynamique est reconstituée. La répartition de vitesse des gouttes et le flux volumique sont influencés par la dynamique de l'écoulement tournant.

Afin d'étudier l'influence de la turbulence sur les phénomènes de transport entre phases, une approche simplifiée consiste à étudier l'interaction entre des gouttes monodisperses et un type donné de turbulence (grosses ou petites structures). Ce point constitue la suite de cette présentation.

3. SIMULATION NUMERIQUE
L'approche la mieux adaptée à l'étude du transport des gouttes dans un champ aérodynamique turbulent et réactif est l'approche lagrangienne. La détermination des trajectoires des gouttes injectées dans l'écoulement nécessite la résolution de l'équation de leur mouvement.

3.1 Equation du mouvement d'une particule
L'équation du mouvement d'une particule sphérique repose sur la théorie linéaire de Stokes [7,8] étendue par ODAR et HAMILTON [9]. Les hypothèses qui ont permis d'établir cette équation sont :

- les particules sont sphériques et indéformables,
- les particules ne sont pas en rotation,
- la densité de particules est suffisamment faible pour qu'elles n'agissent ni entre elles, ni sur l'écoulement porteur,
- le diamètre des particules est inférieur à l'échelle de Kolmogorov.

En présence de gradients de vitesse importants, l'équation du mouvement d'une particule sphérique s'écrit de la manière suivante :

$$\rho_p \frac{\pi D_p^3}{6}\frac{d\vec{V}_p}{dt} = \frac{1}{8} C_d \rho \pi D_p^2 \left\|\vec{V}-\vec{V}_p\right\|(\vec{V}-\vec{V}_p) + \rho C_a \frac{\pi D_p^3}{6}\left(\frac{D\vec{V}}{Dt}-\frac{d\vec{V}_p}{dt}\right) + \frac{1}{4} C_h D_p^2 \sqrt{\pi \rho \mu}\int_{-\infty}^{t}\left(\frac{D\vec{V}}{D\tau}-\frac{d\vec{V}_p}{d\tau}\right)\frac{d\tau}{\sqrt{t-\tau}} + \rho \frac{\pi D_p^3}{6}\frac{D\vec{V}}{Dt} + \frac{\pi D_p^3}{6}(\rho_p-\rho)\vec{g} \qquad (3.1)$$

Le premier terme du second membre représente la force de traînée. Le second terme correspond au "terme de masse ajoutée", il traduit le fait qu'une accélération de la particule entraîne une accélération d'une certaine masse de fluide autour d'elle. Le troisième terme représente les effets de gradient de pression à la surface de la particule sphérique. Le quatrième terme est appelé terme "d'histoire" ou de Basset il tient compte de l'évolution du mouvement au cours du temps en prenant en compte les variations de la vitesse relative aux instants antérieurs. Enfin le dernier terme correspond aux forces de volume : poids et poussée d'Archimède.

Si $\rho_p >> \rho$, ce qui est le cas dans nos études, des simulations numériques [7,8,10] ont montré que les termes de masse ajoutée, de gradient de pression et d'histoire peuvent être négligés. Le système d'équations à résoudre pour suivre la particule au cours de son mouvement est donc :

$$\frac{d\vec{V}_p}{dt} = \frac{3}{4}\frac{\rho C_d}{\rho_p D_p}\left\|\vec{V}-\vec{V}_p\right\|(\vec{V}-\vec{V}_p) + (\rho_p-\rho)\vec{g} \qquad (3.2)$$

$$\frac{d\vec{X}_p}{dt} = \vec{V}_p$$

3.2 Approche déterministe
Pour pouvoir intégrer le système d'équations (3.2) et déterminer les trajectoires de particules injectées dans un écoulement turbulent, il est nécessaire de connaître, à chaque pas de temps, les vitesses instantanées du fluide et des particules. Une première méthode, permettant de calculer le champ aérodynamique à tout instant, consiste à utiliser un code de calcul instationnaire [11].

Les trajectoires des particules sont alors calculées en prenant pour valeurs des vitesses instantanées les valeurs des vitesses de la phase gazeuse aux points où se trouvent les particules [10].

3.3 Modèles stochastiques
Une seconde façon de modéliser un champ aérodynamique instantané consiste à reconstruire celui-ci à partir d'un champ moyen obtenu à l'aide d'un modèle de turbulence, en déterminant les fluctuations de vitesse par un tirage aléatoire : un tel modèle est dit *stochastique*.

Après avoir reconstitué le champ aérodynamique instantané, on calcule la trajectoire de la particule dans ce champ pendant un temps T, ou sur une distance L, en conservant les mêmes valeurs de vitesses fluctuantes pour la phase continue. Au bout du temps T, ou lorsque la particule a parcouru la distance L, on effectue une décorrélation, c'est à dire un nouveau tirage des fluctuations de vitesse de la phase gazeuse, puis on réitère le processus.

Modèles "Monte-Carlo"
Ce sont les modèles les plus anciens et les plus répandus, ils ont été utilisés de manière extensive pour l'étude de jets, d'écoulements confinés ou de "swirls" diphasiques. Parmi ceux-ci ont été retenus les trois modèles suivants :

a) Modèle 1 [12]
Le premier modèle que nous avons utilisé recherche seulement une comptabilité temporelle avec la turbulence.

Soit t_0 l'instant d'injection d'une particule. On calcule l'*échelle intégrale temporelle* T_l, puis on génère les vitesses fluctuantes du fluide à la position d'injection par un tirage aléatoire selon une distribution normale. Enfin, en résolvant le système d'équations (3.2), on calcule la position de la particule à l'instant $t = t_0 + \Delta t$. Tant que t reste inférieur à T_l on détermine les positions successives de la particule en conservant les mêmes valeurs pour les fluctuations de vitesse. Quand t devient plus grand que T_l, on génère de nouvelles vitesses fluctuantes.

b) Modèle 2 [12]
Ce modèle relève d'une méthode identique à celle du modèle précédent sauf que le critère de décorrélation temporelle n'est plus basé sur l'échelle intégrale temporelle T_l mais sur le *temps d'interaction de la particule avec le tourbillon* qu'elle traverse T_d

En effet, si la vitesse relative de la particule par rapport à la phase gazeuse est faible, il est possible qu'elle reste dans un tourbillon pendant toute la durée de l'existence de celui-ci alors que, si la vitesse relative de la particule est importante, elle va traverser la structure tourbillonnaire et donc son temps de transit à l'intérieur de celle-ci sera plus court que T_l.

c) Modèle 3 [13]
C'est le modèle utilisé par DIAKOUMAKOS et al, il est tout fait analogue au modèle 2 auquel on ajoute un critère spatial pour les décorrélations. On considère qu'une particule est en interaction avec un tourbillon non seulement si le critère temporel du modèle 2 est respecté, mais aussi si la distance parcourue depuis la décorrélation précédente est inférieure à l'*échelle intégrale spatiale* L_d.

Modèles à deux particules
Dans ces modèles, plus sophistiqués que les approches de type Monte-Carlo, on suit simultanément une *particule discrète* (P) et une *particule fluide* (F) et on détermine la vitesse du fluide au point P en fonction de la vitesse du fluide au point F en respectant les corrélations spatiales eulériennes.

On définit un critère de décorrélation temporelle et un domaine de corrélation spatiale de rayon L_d pour chaque particule fluide. Lorsque la distance FP devient supérieure à L_d, on considère une autre particule fluide dont on simule la trajectoire à partir des coordonnées du point P à l'instant de décorrélation : ce changement de particule fluide est connu sous le nom de "*phénomène de croisement de trajectoires*". Deux modèles à deux particules ont été choisis :

a) Modèle SCOPE [14] (modèle 4)
Le code SCOPE (Simulation du COmportement de Particules dans un Ecoulement bidimensionnel) a été développé par MARMIGNON à l'Ecole Nationale Supérieure des Mines de Paris.

Dans ce modèle on impose aux fluctuations de vitesse de vérifier le tenseur de Reynolds local. Le principe de SCOPE est semblable à celui du modèle 3. A l'instant t_0 on injecte une particule discrète (P) dans l'écoulement à laquelle on associe une particule fluide (F) ayant la même position. On fait un tirage aléatoire des vitesses fluctuantes. Ensuite, on détermine les positions respectives des particules (F) et (P) : si elles sont trop éloignées l'une de l'autre, on effectue une décorrélation spatiale.

De plus, à chaque pas de temps, on vérifie si le critère temporel est respecté, sinon on génère un nouveau vecteur de fluctuation au point F : décorrélation temporelle.

b) Modèle FD [15] (modèle 5)
Ce modèle a été développé par BLUMKE et al. La génération des fluctuations de vitesse se fait ici selon une méthode qui utilise des "Filtres Digitaux" : "filtre temporel" et "filtres spatiaux". De plus, une nouvelle valeur des fluctuations est générée à chaque pas de temps.

Cette modélisation ne fait pas intervenir de décorrélation temporelle, car chaque fluctuation de vitesse respecte la corrélation temporelle représentée par la fonction de transiert du filtre temporel.

4. ETUDE DES PROCESSUS PHYSIQUES FONDAMENTAUX

4.1 Etude de la dispersion et de l'évaporation en turbulence de grille

L'étude de la dispersion des gouttes en turbulence de grille a été réalisée sur le banc présenté sur la figure 9. Ce banc d'essais vertical, de section carrée (150x150 mm^2), est équipé d'une grille en sortie du convergent. La veine d'essais est composée de différents tronçons munis de hublots en quartz pour les visualisations, pour les mesures laser et pour les essais en température. Les variations du niveau de turbulence sont réalisées en modifiant la géométrie de la grille (épaisseur du barreau B, taille de la maille M). L'aérothermique de la veine a été caractérisée par anémométrie laser et par fil chaud. Des exemples de profils de température (moyenne et fluctuations) sont présentés

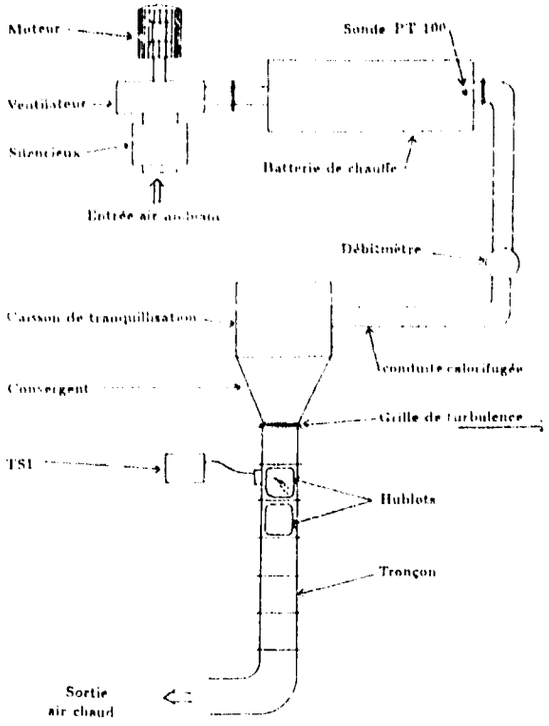

Figure 9 : Vue schématique du banc "Turbulence de grille"

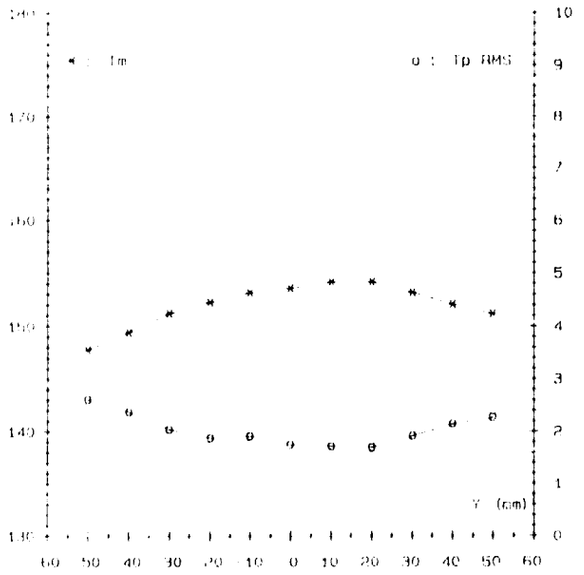

Figure 10 : Profils de température moyenne et fluctuante en aval de la grille

sur la figure 10. La figure 11 montre l'évolution de l'échelle de turbulence en aval de la grille.

a) Dispersion de gouttes monodisperses en isotherme
Un générateur de gouttes (TSI 3450) est employé pour injecter un train de gouttes monodisperses, à partir de la désintégration d'un jet cylindrique [16]. Le mécanisme de rupture est controlé en appliquant une perturbation périodique. Le diamètre des gouttes ainsi générées est compris entre 50 et 300 µm, leur vitesse entre 1 et 4 m/s.

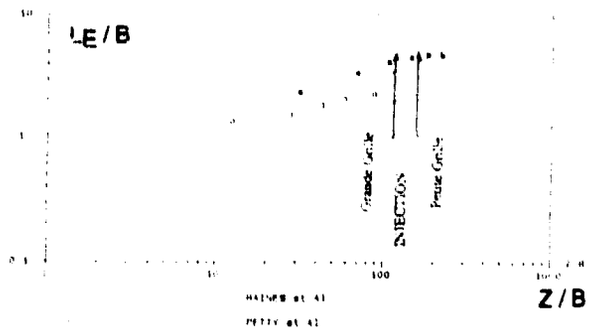

Figure 11 : Evolution de l'echelle de turbulence en aval de la grille

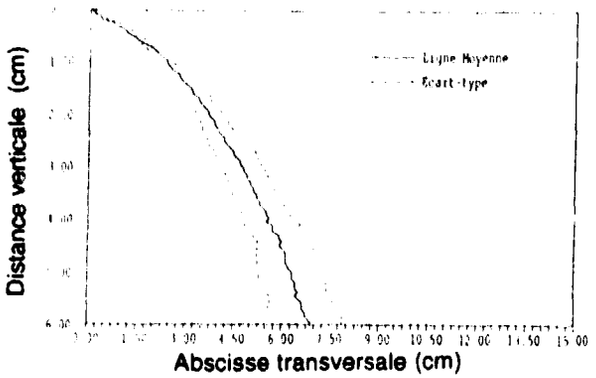

Figure 13 : Trajectoires moyenne des gouttes et écart-type

L'étude de la dispersion de gouttes monodisperses de diamètre 250 µm, injectées avec une vitesse de 3,6 m/s, en paroi et en aval d'une grille de turbulence (mailles carrées de 20 mm et barreaux carrés de 5 mm), est effectuée à partir de visualisations par techniques vidéo rapide et de traitement d'image (figure 12). Cette caméra peut enregistrer, en plein écran, à une cadence d'image allant de quelques images par seconde jusqu'à 1000 images par seconde. Elle a une fréquence maximum de 6000 images par seconde (en 1/6 d'écran). Le point d'injection est situé à 56 mm en aval de la grille, la vitesse moyenne de la phase gazeuse a la même valeur que la vitesse d'injection des gouttes. Au point d'injection l'intensité de la turbulence est de 5 %. La dispersion est caractérisée par la trajectoire moyenne, l'enveloppe et les taux de présence en différentes sections (figures 13 et 14). L'influence du niveau de turbulence sur la dispersion peut être étudiée en modifiant la géométrie de la grille mais aussi en changeant le point d'injection, le niveau de turbulence diminuant en aval de la grille. Ces résultats sont directement comparables à ceux obtenus par simulation numérique à partir de modèles stochastiques (figure 15).

b) Evaporation de gouttes polydisperses

Ce banc d'essais permet aussi l'étude de la dispersion des gouttes en état d'évaporation, la figure 16 présente un exemple d'évolution, en un point de l'écoulement situé à 10 cm en aval de la grille, de l'histogramme des tailles de gouttes entre l'écoulement froid et l'écoulement chaud (Tair = 157 °C). Les gouttes polydisperses sont injectées dans l'axe de la veine à 1,2 m en amont de la grille. Dans ce cas la vitesse moyenne de l'air est de 7 m/s. Les temps d'acquisition de ces deux histogrammes sont identiques. La comparaison des deux histogrammes met en évidence les points suivants .

- disparition des petites gouttes (D_p < 20 µm).
- glissement des tailles moyennes et grandes en plusieurs classes de tailles inférieures.

Une comparaison de ces résultats avec ceux provenant d'une modélisation est en cours au laboratoire.

Figure 12 : Visualisation de la dispersion des gouttes

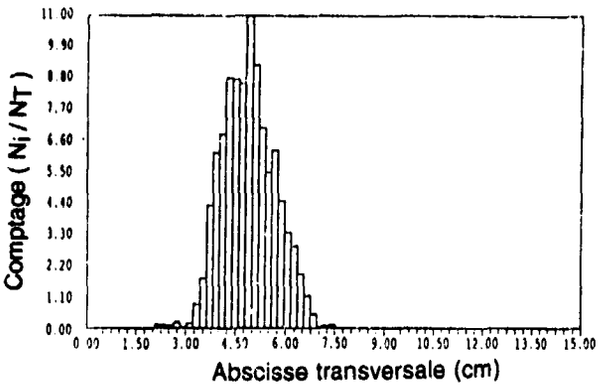

Figure 14 : Histogrammes de taux de présence de gouttes , à 3 cm en aval du point d'injection

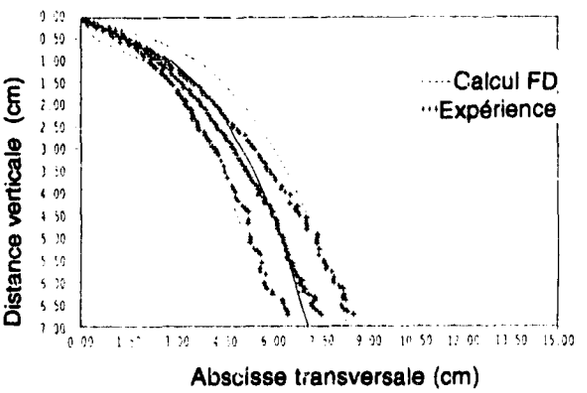

Figure 15 : Comparaison calcul expérience Ligne moyenne, écart- type

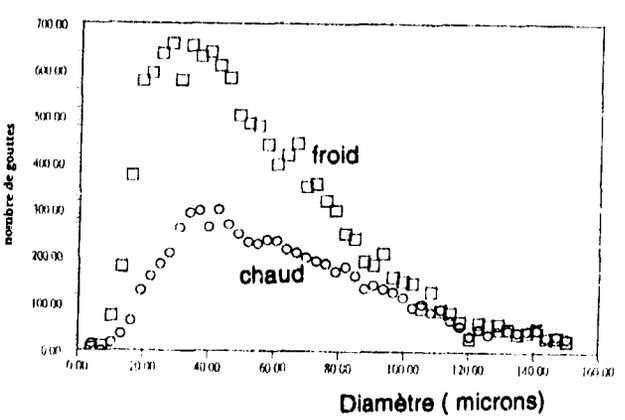

Figure 16 : Comparaison des histogrammes à froid et à chaud (Tair = 157°C)

4.2 Dispersion turbulente en écoulement instationnaire
Les deux configurations de base retenues, pour cette partie de l'étude, sont un écoulement du type zone de mélange et un écoulement en aval d'une marche descendante.

a) ZONE DE MELANGE
La dispersion de gouttes dans une configuration de type zone de mélange a été étudiée dans le but de valider les modèles utilisés pour les simulations.

La veine d'étude est à section carrée 75x75 mm^2. La zone de mélange est créée par deux flux d'air à la température ambiante, cocourants et séparés par une plaque plane horizontale de 5 mm d'épaisseur, présentant en son extrémité un culot rectangulaire. La vitesse débitante de l'écoulement dans la partie supérieure de la veine est de 36 m/s, celle dans la section inférieure est de 9 m/s, soit un rapport de vitesses de 4 (figure 17). A l'aide d'un générateur de gouttes monodisperses, des gouttes de 133 µm sont injectées dans l'écoulement avec une vitesse de 6 m/s.

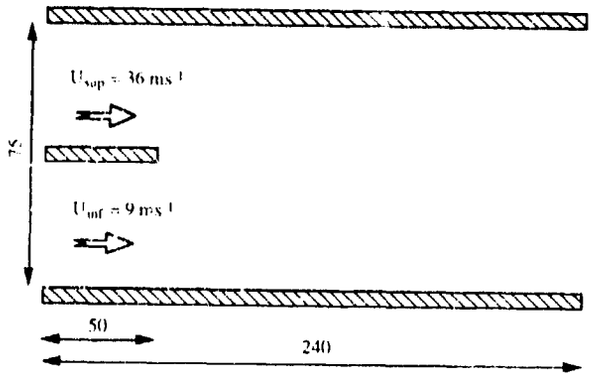

Figure 17 : Géométrie de la zone de mélange

Les instabilités de la zone de mélange ont été visualisées grâce à de la fumée (figure 18). La figure 19 présente les trajectoires moyennes et les enveloppes du panache de gouttes obtenues expérimentalement et celles déterminées par simulation à l'aide du modèle 3. Bien que les trajectoires obtenues par le calcul soient un peu différentes des trajectoires expérimentales, le modèle stochastique utilisé permet bien de retrouver l'allure du panache de gouttes. Cette étude [17] a également permis de mettre en évidence l'importance de l'interaction entre gouttes. En effet, la distance entre gouttes en sortie du générateur étant très faible, le coefficient de trainée doit être modifié pour tenir compte de cet effet d'interaction.

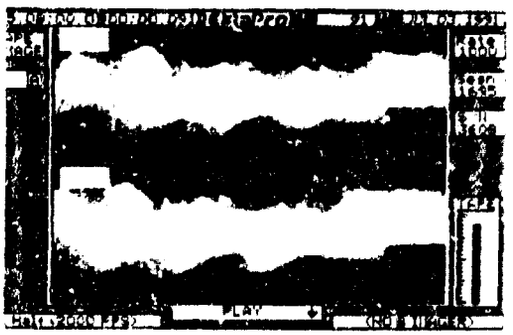

Figure 18 : Visualisation des structures cohérentes

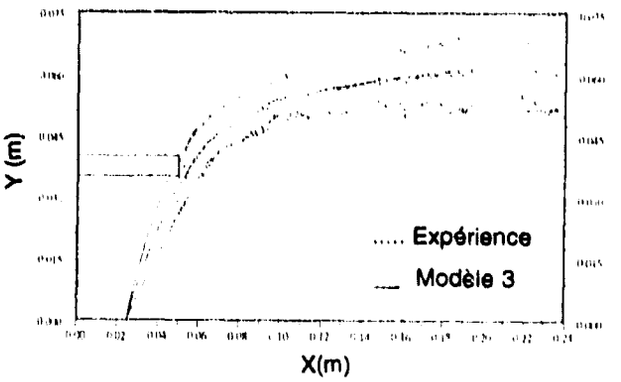

Figure 19 : Dispersion de gouttes (133 µm) dans la zone de mélange

Dans un second temps, des simulations ont été effectuées pour comparer les différents modèles de dispersion. L'étude a porté sur l'injection de gouttelettes de méthanol de 10 µm à l'extrémité du culot et dans l'axe de la veine à une vitesse de 10 m/s. Ces simulations ont montré le rôle majeur des grosses structures de l'écoulement dans la dispersion des gouttes de petite taille. Pour bien mettre en évidence ce phénomène, nous avons comparé la position des tourbillons (figure 20), visualisés grace à un traceur numérique, à celles des gouttelettes (figure 21), calculée par l'approche déterministe, aux mêmes instants. Les gouttes se situent à la périphérie des tourbillons, ce comportement est conforme aux résultats obtenus par d'autres auteurs [18,19,20], compte tenu des temps caractéristiques des deux phases.

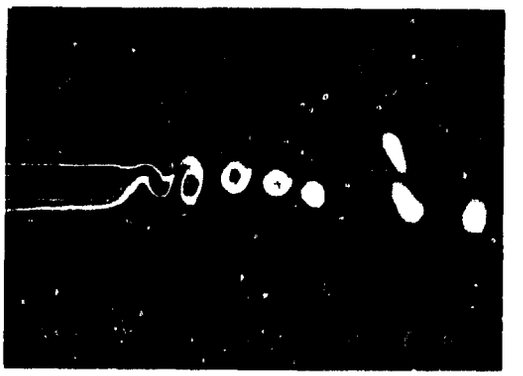

Figure 20 : visualisation des structures à l'aide d'un traceur numérique

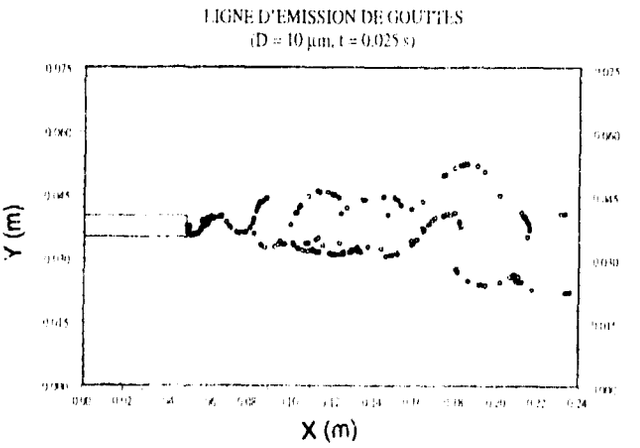

Figure 21 : position des gouttes (approche déterministe)

b) MARCHE DESCENDANTE

Les différentes approches expérimentales et simulations numériques ont aussi été appliquées à une géométrie de marche descendante. La géométrie bidimensionnelle étudiée est présentée sur la figure 22.

Approche numérique

A titre d'exemple des comparaisons entre l'approche instationnaire et différents modèles stochastiques de dispersion sont présentées pour des gouttes de 10 µm injectées au niveau du décrochement de la marche. Les statistiques de la dispersion sont calculées sur un échantillon de 2000 trajectoires (figure 23). Les distributions du taux de présence dans la zone cisaillée et dans la zone de recirculation pour trois sections situées avant le point de recollement présentent deux maxima de concentrations de gouttes (figure 24), la valeur maximale étant dans la zone cisaillée, l'autre correspondant au flux de retour dans la zone recirculée. Pour cette géométrie et pour les conditions d'injection retenues, les modèles SCOPE et FD pour lesquels deux décorrélations (spatiale et temporelle) sont prises en compte, donnent des résultats en bon accord avec l'approche instationnaire prise comme référence en amont du point de recollement. Au point de recollement et en aval de la zone de recirculation, l'approche instationnaire indique une augmentation du taux de présence près de la paroi. Ce phénomène sera vérifié expérimentalement. Ces simulations numériques montrent que les transferts au travers de l'interface de la recirculation, ou au point de recollement, sont provoqués par des mouvements de convection instationnaire des grosses structures beaucoup plus que par de la dispersion turbulente au sens classique du terme. Afin de confirmer ces résultats de simulation, une étude expérimentale a été entreprise sur la même géométrie.

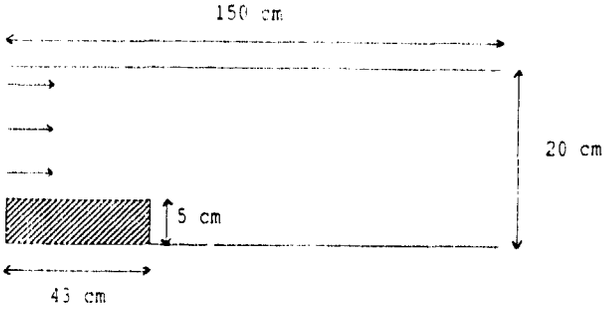

Figure 22 : Géométrie de la marche étudiée

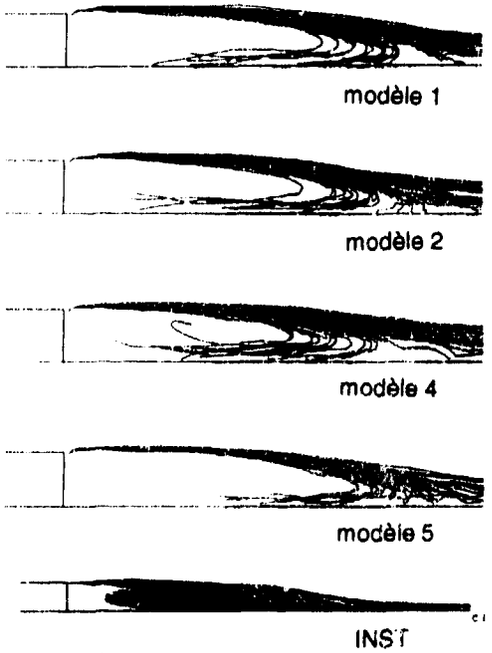

Figure 23 : Dispersion de gouttes (10µm) dans la zone de cisaillement

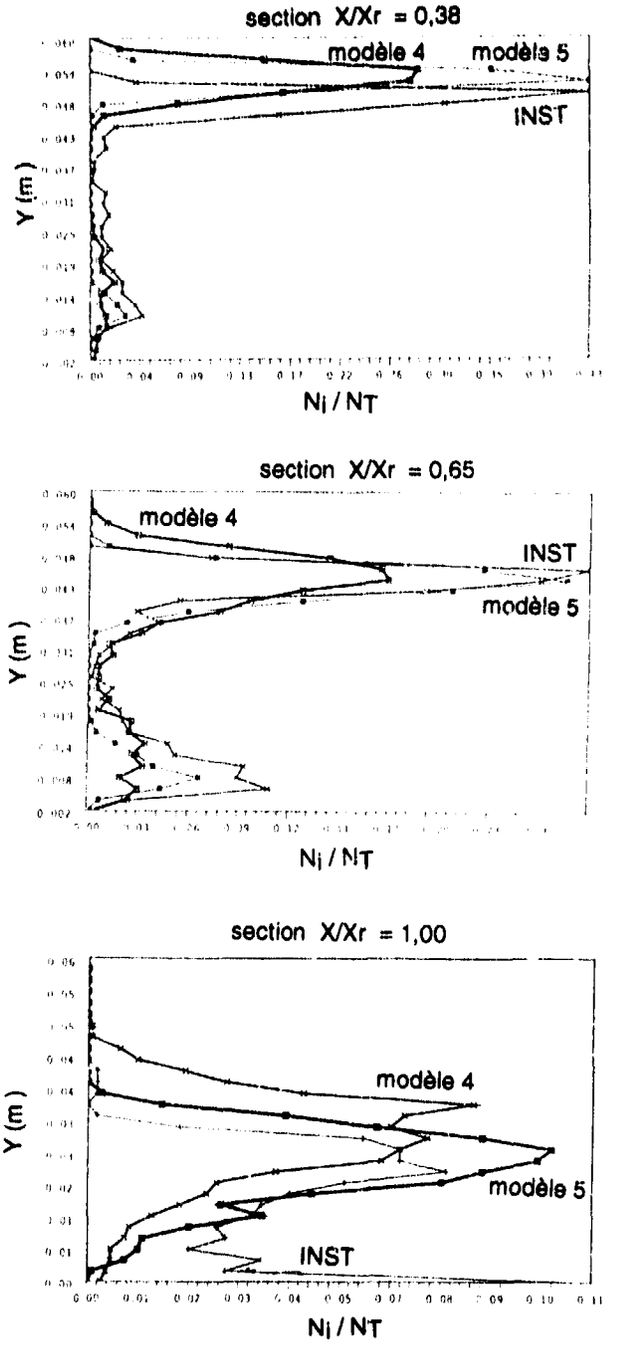

Figure 24 : Taux de présence des gouttes dans trois sections différentes

Approche expérimentale
Au moyen d'un générateur à orifice vibrant, des gouttes monodisperses de diamètre 100 µm ont été injectées en un point de la paroi supérieure, à contre courant, de façon à bien ensemencer l'écoulement au niveau du décrochement de la marche et dans la zone cisaillée. La vitesse des gouttes est de 10 m/s, la vitesse de l'air de 6 m/s. Les visualisations par techniques vidéo rapide du comportement des gouttes dans la zone cisaillée (figure 25) montrent que les gouttes sont bien entraînées par les grosses structures. Les techniques de traitement d'image appliquées à cet écoulement diphasique permettent de suivre l'évolution du taux de présence des gouttes, du point d'injection jusqu'en aval de la zone de recirculation (figure 26). Cette représentation montre bien le changement des distributions en nombre de gouttes dans la zone de recollement et en aval de la zone recirculée. Les simulations numériques pour ce type d'écoulement sont en cours au laboratoire. Les premiers résultats de la comparaison entre les différents modèles et l'expérience confirment les conclusions de l'étude de la zone de mélange : le modèle 3 permet de retrouver, avec une bonne précision, la dispersion observée expérimentalement.

Figure 26 : Evolution du taux de présence de gouttes de 100 µm entre leur point d'injection et l'aval de la zone recirculée

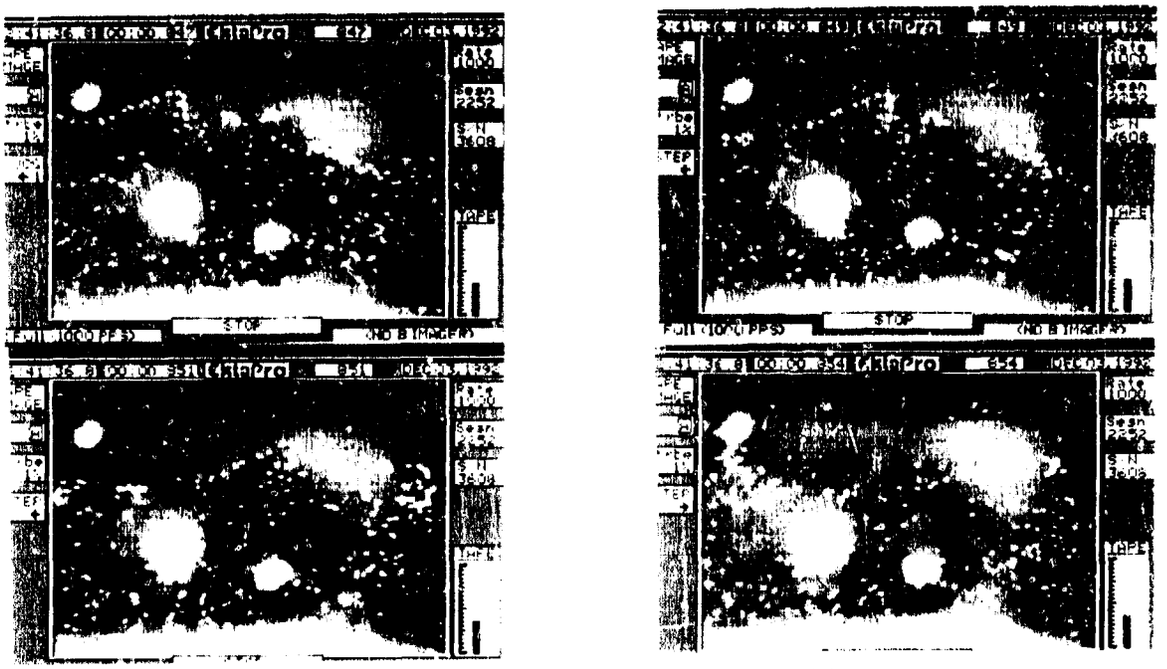

Figure 25 Effet instationnaire des structures cohérentes sur la dispersion des gouttes dans la zone cisaillée

4.3 Interaction goutte-paroi
Dans une chambre de combustion, des systèmes d'injection de carburant génèrent des écoulements diphasiques avec effet de swirl (injecteurs aérodynamiques, injecteurs mécaniques). Par cet effet les grosses gouttes sont centrifugées en périphérie du spray, et certaines peuvent impacter les parois chaudes de la chambre de combustion.

Le transfert de chaleur d'une goutte impactant sur une surface chaude est un phénomène complexe [21]. Les différents comportements d'une goutte sur une paroi chaude sont représentés sur la figure 27. Les conditions pour lesquelles apparaît un film de vapeur entre la goutte et la paroi (phénomène de *Leidenfrost*) doivent être connues. En effet la présence du film de vapeur diminue le transfert thermique entre le liquide et la paroi et est déterminante pour le comportement des gouttes.

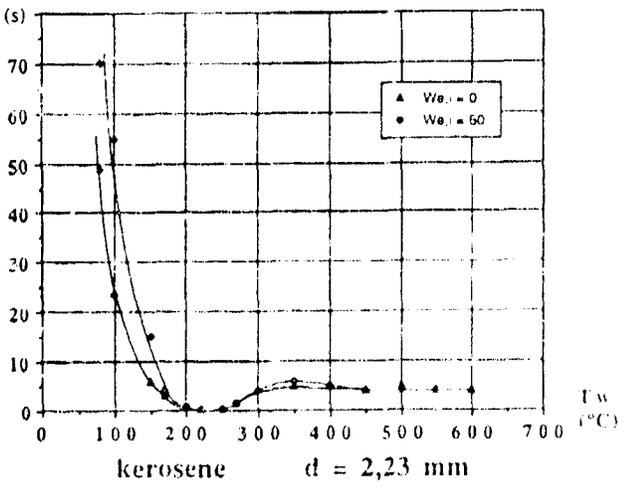

Figure 27 : Influence de la température de paroi sur l'évaporation d'une goutte

Montage expérimental

Une plaque de cuivre (200x150x400 mm^3), comporte cinq cartouches de chauffage. La température (T < 600 °C) est controlée en trois points par des thermocouples. L'uniformité de la température de la plaque est vérifiée par technique infra-rouge.

Les gouttes sont éclairées par ombroscopie et observées au moyen d'une caméra vidéo rapide KODAK EKTAPRO.

Resultats

Un exemple de goutte impactant sur une paroi est donné sur la figure 28. Un logiciel de traitement d'images appliqué à des enregistrements de ce type [22] fournit des informations sur la trajectoire et la vitesse des gouttes avant et après impact. A partir de ces informations nous calculons un nombre de *Weber* :

$$We = \rho_p V_p^2 D_p / \sigma_p$$

L'influence de la température de la plaque sur le phénomène de rebond est représentée sur la figure 29. Ces résultats sont en accord avec ceux de WATCHERS et WESTERLING [23]. Le Weber maximum augmente avec la température de la surface. La condition de non rebond définit un nombre de Weber critique qui est une fonction de la température de la plaque [24,25].

L'influence du diamètre de la goutte sur le phénomène de rebond est représenté sur la figure 30. Dans ce cas nous remarquons que le Weber maximum reste constant. Le Weber critique diminue lorsque la taille des gouttes augmente [26].

Une série d'expériences sur des fluides différents, montre que la vitesse critique et la vitesse maximum de rebond augmentent avec la tension superficielle.

Conclusion

Ces différentes expériences sur l'interaction gouttes-paroi montrent que le rebond d'une goutte est influencé par sa vitesse normale à la paroi (la vitesse tangentielle n'ayant pas d'influence sur le phénomène), par la température de la surface, par le diamètre de la goutte et par la nature du fluide.

Cet ensemble de résultats sur l'interaction gouttes-paroi constitue une première base de données, à utiliser dans les codes de calcul pour les chambres de combustion en tant que "lois de paroi " pour la phase liquide.

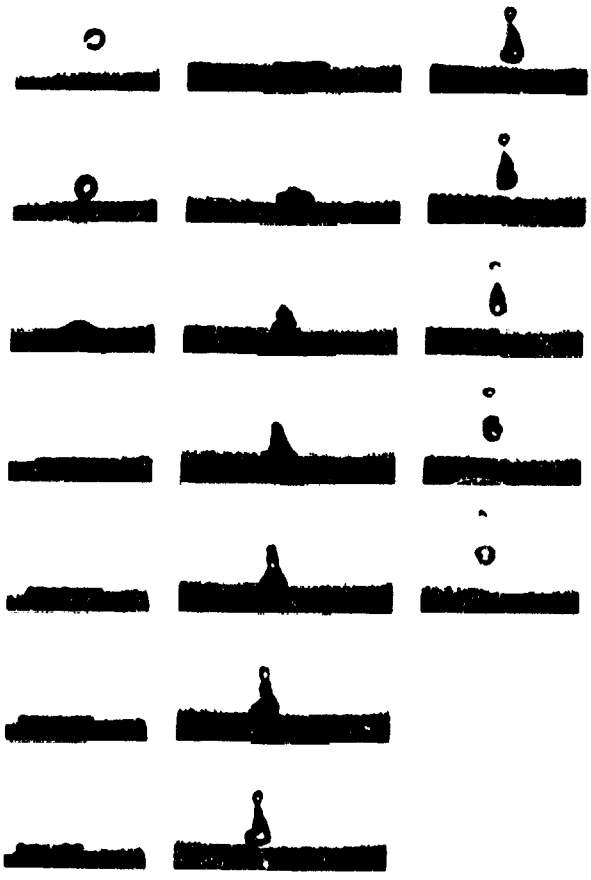

Figure 28 : Exemple d'enregistrement video rapide

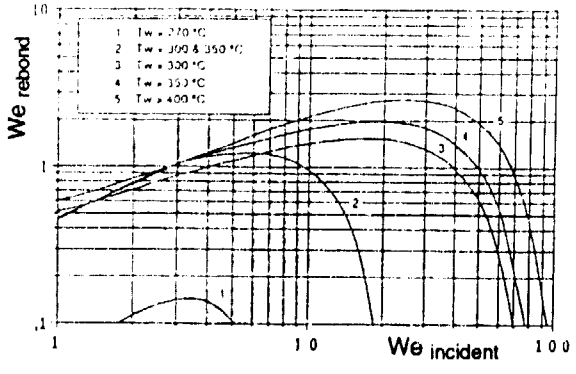

Figure 29 : Influence de la température de paroi sur le rebond

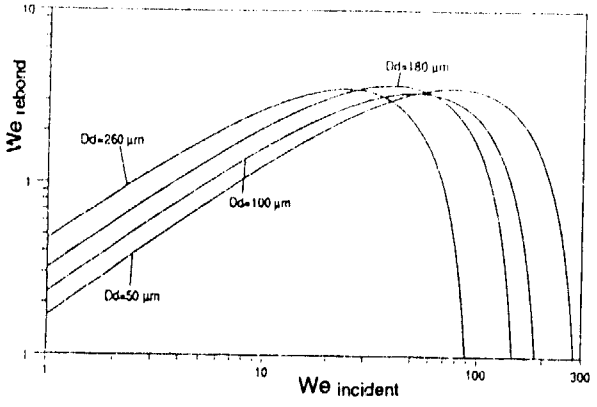

Figure 30 : Influence du diamètre sur le rebond

5. CONCLUSIONS ET PERSPECTIVES

L'objectif de cette recherche est de modéliser la combustion d'un jet de gouttes en présence d'un écoulement gazeux fortement instationnaire. Les techniques optiques récentes permettent des mesures simultanées de différents paramètres de la pulvérisation en aval d'un injecteur réel. Ces mesures doivent être très précises puisque les résultats sont pris comme conditions initiales pour le calcul de la phase liquide dans la simulation numérique. Ces techniques, appliquées à l'étude des phénomènes élémentaires comme l'interaction des gouttes avec les parois, la dispersion et l'évaporation, permettent d'élaborer des modèles qui peuvent être directement introduits dans les codes de calcul ou fournissent des résultats servant à la validation de ces modèles. Ce type d'approche, consistant à mener en parallèle des études expérimentales et numériques, est très bénéfique pour l'amélioration des connaissances de ces divers phénomènes. Il sert aussi à la sélection de modèles stochastiques de dispersion de gouttes, moins couteux en temps de calcul que l'approche instationnaire prise comme référence pour les configurations de base présentées ci-dessus. La comparaison de ces modèles sur ces configurations fait apparaître que le modèle 3 semble être le plus susceptible d'être utilisé dans les logiciels industriels. En effet ce modèle représente le meilleur compromis entre la précision des résultats et la durée, donc le coût, des simulations. Des recherches sont aussi menées en parallèle avec l'ITLR de l'université de Stuttgart sur la combustion des gouttes. Pour rendre ces codes prédictifs, la deuxième étape de ce programme de recherche doit être consacrée dans le futur aux phénomènes d'interaction entre tous ces processus physiques. Par exemple dans les jets denses de gouttes, les interactions entre gouttes ont des effets prépondérants sur leurs trajectoires, sur leur taux d'évaporation et sur leurs régimes de combustion (isolée, par paquet, flamme de diffusion). Les effets de couplage entre les gouttes et l'écoulement gazeux sont aussi très importants (modification du champ aérodynamique et du niveau de turbulence...).

REMERCIEMENTS

Les auteurs expriment leurs remerciements aux services officiels français (DRET groupe 7), à l'ONERA/OE, à la SNECMA et à TURBOMECA pour leur soutien constant dans les recherches sur les phénomènes de base en écoulement diphasique. Ils tiennent aussi à remercier vivement leurs collègues : Y. BISCOS, F. BISMES, G. HEID, B. PLATET pour leur contribution à ces différentes études.

REFERENCES

[1] P. DONNADILLE, A. ROMPTEAUX, G. LAVERGNE, P. HEBRARD
"Turbulent dispersion of two phase flows : experimental and computational approaches"
Int. Symp. of Multiphase Flow, Tsukuba, Japan, 1991

[2] G. LAVERGNE, P. HEBRARD, P. DONNADILLE
"Experimental and computational study of liquid droplets impinging on an afterburner"
ISABE, 91-7108, Nottingham, Great Britain, 1991

[3] W.D. BACHALO, M.J. HOUSER
"Development of the Phase Doppler Spray Analyzer for Liquid Drop Size and Velocity Characterization"
AIAA 20th Joint Propulsion Conference, 1984

[4] V.G. Mc DONNELL, G.S. SAMUELSEN
"Application of the Two Components Phase Doppler Interferometry to the Measurement of Particle Size, Mass Flux and Velocities in Two Phase Flows"
22nd Symposium on Combustion, pp 1961-1971, 1988

[5] A. BRENA DE LA ROSA, W.D. BACHALO, R.C. RUDOFF
"Spray Characterization and Turbulence Properties in an Isothermal Spray with Swirl"
ASME paper 89 GT 273, IGTI Congress, 1989

[6] P. HEBRARD, P. TRICHET, X. BARDEY
"Experimental Investigation of Two Phase Flow in the Near Field of an Airblast Atomizer"
Paper 74, ICLASS 91, 1991

[7] A. BERLEMONT
"Modélisation eulérienne et lagrangienne de la dispersion particulaire en écoulement turbulent"
Thèse de doctorat, Université de Rouen, 1987

[8] M. DADI
"Etude de modèles de comportement de traceurs dans un écoulement et leur validation expérimentale par vélocimétrie holographique à expositions multiples"
Thèse de doctorat, Université de Lille I, 1987

[9] F. ODAR, W.S. HAMILTON
"Forces on a sphere accelerating in a viscous fluid"
Journal of Fluid Mechanics, vol. 18, n°2, pp. 302-314, 1964

[10] P. DONNADILLE
"Comportement de gouttes en écoulement turbulent instationnaire : simulation numérique, modélisation, expérimentation"
Thèse de doctorat, Université de Valenciennes et du Hainaut-Cambrésis, 1992

[11] A. ROMPTEAUX
"Développement d'un code de calcul instationnaire en volumes finis à faible diffusivité numérique"
Thèse de doctorat, ENSAE, 1992

[12] A.D. GOSMAN, E. IOANNIDES
"Aspects of computer simulation of liquid-fuelled combusters"
AIAA 81-0323, 19th Aerospace Sciences Meeting, St-Louis, Missouri, 1981

[13] E. DIAKOUMAKOS, J. ANAGNOSTOPOULOS, G. BERGELES
"A theoretical study of air-solid two-phase flows"
Mathematical Modeling in Combustion and Related Topics, Brauner and Schmidt Lainé Editors, pp. 449-459, 1988

[14] C. MARMIGNON
"Améliorations et extensions d'une méthode de prédiction du comportement de particules en écoulement turbulent"
Rapport technique, ONERA, 1983

[15] E. BLUMKE, H. EICKHOFF, C. HASSA
"Evolution of a spectral dispersion model with experimental results obtained from the dispersion of monosized droplets in a turbulent swirling flow"
5th Workshop on Two-Phase Flow Predictions, Erlangen Germany, 1990

[16] TSI Incorporated
"Model 3450, vibration orifice aerosol generator"
1987

[17] S. HARQUEL
"Etude expérimentale et modélisation de la dispersion de gouttes dans une zone de mélange"
Rapport de DEA, Université de Valenciennes et du Hainaut-Cambrésis, 1992

[18] L. TANG, F. WEN, Y. YANG, C.T. CROWE, J.N. CHUNG, T.R. TROUTT
"Self-organizing particle dispersion mechanism in a plane wake"
Physics of Fluids A, vol. 4, n° 1, pp. 2244-2251, 1992

[19] R. CHEIN, J.N. CHUNG
"Simulation of particle dispersion in a two-dimensionnal mixing layer"
AIChE Journal, vol 34, pp. 946-954, 1988

[20] J.N. CHUNG, T.R. TROUTT
"Simulation of particle dispersion in an axisymetric jet"
Journal of Fluid Mechanics, vol. 186, pp. 199-222, 1988

[21] Z. TAMURA, Y. TANASAWA
"Evaporation and combustion of a drop contacting with a hot surface"
7th Symposium on Combustion, London, 1959

[22] Y. BISCOS, P. BERTHOUMIEU, P. HEBRARD, G. LAVERGNE
"Développement d'une méthode de trajectographie 2D de gouttes par traitement d'images obtenues en vidéo rapide"
Colloque National de l'ANRT, 1991

[23] L.H. WATCHERS, N.A. WESTERLING
"The heat transfer from a hot wall to impinging water drops in the spheroidal state"
Chemical Engineering Science, vol. 21, 1966

[24] P. BEARD
"Etude expérimentale et modélisation du comportement de gouttes au niveau d'une plaque chauffante"
Rapport de DEA, Université de Valenciennes et du Hainaut-Cambrésis, 1990

[25] P. HEBRARD, G. LAVERGNE, P. TRICHET
"Experimental Study of Boundary Conditions for Spray Systems in Combustion Chambers"
6th Annual Conference ILASS Europe, Pise, Italy, 1990
[26] B. REINHARDT
"Etude expérimentale et modélisation du comportement du rebond de gouttes au niveau d'une plaque chauffante"
Rapport de DEA, Université de Valenciennes et du Hainaut-Cambrésis, 1991

Discussion

Question 1. L. de Chanterac
Is there any coalescence model in the code you have developed?

Author's Reply
I studied coalescence effects during my stay in Stuttgart, Germany. I have not yet introduced models which I obtained in Stuttgart into the two phase flow code.

A New Eulerian Model for Turbulent Evaporating Sprays in Recirculating Flows

S. Wittig, M. Hallmann, M. Scheurlen, R. Schmehl
Lehrstuhl und Institut für Thermische Strömungsmaschinen
Universität Karlsruhe (T.H.)
Kaiserstraße 12, D-7500 Karlsruhe, Germany

Summary

A new Eulerian model for the computation of turbulent evaporating sprays in recirculating flows is derived. It comprises droplet heating and evaporation processes by solving separate transport equations for the droplet's temperature and diameter. Full coupling of the droplet and the gaseous phase is achieved by the exchange of source terms due to momentum, heat and mass transfer. The partial differential equations describing the droplet's transport and evaporation in the new method can be solved using the same numerical procedure as for the gas phase equations. The validity of the model is established by comparison with a well known Lagrangian approach and with experimental data. For this purpose calculations of a recirculating droplet charged air flow within a model combustor are presented.

Nomenclature

A, B, C	-	coefficients of the Cox-Antoine vapour pressure equation
C_1, C_2, C_μ	-	constants of the k, ϵ-turbulence model
c_D	-	drag coefficient
$c_{p,p}$	$J/(kg\ K)$	specific heat of droplets
$c_{p,v}$	$J/(mol\ K)$	molar specific heat of vapour
c_{rel}	m/s	relative velocity
c_α	kg/kg	vapour concentration
D	m	diameter
D_x	m	characteristic diameter in the Rosin-Rammler drop size distribution
$\vec{F}$	N/m^3	external forces
Fr	-	Frössling number
h	J/kg	specific enthalpy
Δh_v	J/kg	specific enthalpy of evaporation
k	m^2/s^2	kinetic energy of turbulence
L_x	m	length scale of the k, ϵ-turbulence model
Le	-	Lewis number
M	kg/mol	molecular weight
N	-	parameter in the Rosin-Rammler drop size distribution
Nu	-	Nusselt number
n	mol/m^3	molar concentration
nd	-	number of discrete drop-size classes
Pr	-	Prandtl number
p	N/m^2	pressure
Re	-	Reynolds number
S	$(*)$	source term (equation dependent)
Sc	-	Schmidt number
T	K	temperature
t	s	time
$u, v, w(u_i)$	m/s	velocity components
$\dot{V}$	m^3/s	volume flow rate
$x, y, z(x_i)$	m	cartesian coordinates
v_c	-	volume fraction of the dispersed phase
X	-	mol fraction

Greek symbols

ϵ	m^2/s^3	turbulence energy dissipation rate
Γ	m^2/s	diffusion coefficient
λ	$W/(mK)$	thermal conductivity
μ	Ns/m^2	dynamic viscosity
ν	m^2/s	kinematic viscosity
ω	s^{-1}	particle response frequency
ρ	kg/m^3	density
$\sigma_k, \sigma_\epsilon$	-	constants of the k, ϵ-turbulence model
τ	s	particle response (relaxation) time

Presented at an AGARD Meeting on 'Fuels and Combustion Technology for Advanced Aircraft Engines', May 1993.

Subscripts

air	air
eff	effective
g	gas
l	liquid
p	particle, droplet
ref	reference values (1/3-rule)
s	droplet surface
t	turbulent
v	vapour
∞	ambient

Superscripts

$\vec{\phi}$	vector
$\bar{\phi}$	time average
ϕ'	turbulent fluctuation

Introduction

Liquid fuel combustion processes in gas turbine combustors so far are not well understood and, therefore, object of numerous theoretical and experimental investigations. In particular, the accurate prediction of these processes is extremely difficult due to the combination of complex physical and chemical phenomena. Dispersed phase/turbulence interactions and turbulence effects on chemical reactions are only two examples for the complexity. In addition nonreacting two-phase flows include a variety of unsolved problems, e.g. turbulent droplet dispersion, turbulence effects on heat and mass transfer between the phases, vapour/air mixing etc.. Besides, nonreacting turbulent two phase flows are important by itself. Premixed-prevaporized gas turbine combustors, Diesel engine sprays and rocket plumes are some examples of this type of flow (Mostafa and Elghobashi (1984)).

Approaches for the prediction of droplet transport and evaporation in combustion systems can be classified by two fundamentally different methods. In the Lagrangian approach, the spray is represented by discrete droplets. Each computed droplet represents a number of physical droplets and is observed on its trajectory until it leaves the calculational domain or it evaporates completely. The equations describing the droplet behaviour can be simplified to ordinary differential equations. In turbulent flows, droplet motion and evaporation is simulated by a stochastic or Monte Carlo approach (Gosman and Ioanides (1983), Wittig et al. (1987), Kneer et al. (1990)). In the Eulerian approach, the evaporating spray is treated as an interacting and interpenetrating continuum. The resulting equations are similar to the equations describing the turbulent gas phase. The application of the Eulerian approach for sprays requires the consideration of the continuum assumption (Batchelor (1974)). This assumption is valid, when each computational element contains a large number of droplets in the way that statistically averaged properties can be assigned to the droplets. Crowe (1982) showed that most practical systems satisfy the continuum assumption.

This paper is addressed to the further improvement of a recently developed Eulerian method for the numerical simulation of turbulent evaporating sprays (Hallmann et al. (1993)). Results of the new model are compared with both, experimental data and computations using a Lagrangian approach.

Eulerian methods for the prediction of turbulent two-phase flows have been used by various groups of researchers (e.g. Melville and Bray (1979), Elghobashi et al. (1984), Chen and Wood (1986), Krämer (1988), Abou-Arab and Rocco (1990), Simonin (1990)). They all deal with questions concerning the dispersion of particles in parabolic flows neglecting heat and mass transfer between the two phases. Mostafa and Elghobashi (1985) as well as Mostafa and Mongia (1987) report on Eulerian methods for the computation of turbulent jets with droplet vaporization. However in these papers rather simplified assumptions were used. The authors assumed isothermal flow conditions and a constant droplet (saturation) temperature. In addition, a simplified mass transfer model for the calculation of the droplet diameter was applied. In contrast to these investigations, the present study introduces a new model for the computation of fuel spray characteristics including droplet heating and evaporation by solving separate transport equations for the droplet's temperature and diameter. This model is applicable not only to parabolic flows but also to turbulent recirculating non-isothermal evaporating sprays, which are of major interest within the design process of real gas turbine combustors.

Governing equations

Gas phase equations

For the steady mean flow under consideration, the time averaged continuity equation and the stationary Reynolds equations

$$\frac{\partial}{\partial x_i}(\rho u_i) = S_{m,p} \qquad (1)$$

$$\frac{\partial}{\partial x_i}(\rho u_i u_j) = \frac{\partial}{\partial x_i}(\mu_{eff}(\frac{\partial u_j}{\partial x_i} + \frac{\partial u_i}{\partial x_j} - \frac{2}{3}\frac{\partial u_l}{\partial x_k}\delta_{ij})) - \frac{\partial}{\partial x_j}(p + \frac{2}{3}\rho k) + F_j + S_{u_j,p} \quad (2)$$

in conjunction with the standard k, ϵ-turbulence model

$$\frac{\partial}{\partial x_i}(\rho u_i k) = \frac{\partial}{\partial x_i}(\frac{\mu_{eff}}{\sigma_k}\frac{\partial k}{\partial x_i}) + G_k - \rho\epsilon + S_{k,p} \quad (3)$$

$$\frac{\partial}{\partial x_i}(\rho u_i \epsilon) = \frac{\partial}{\partial x_i}(\frac{\mu_{eff}}{\sigma_\epsilon}\frac{\partial \epsilon}{\partial x_i}) + \frac{\epsilon}{k}(C_1 G_k - C_2\rho\epsilon) + S_{\epsilon,p} \quad (4)$$

$$G_k = \mu_t \frac{\partial u_i}{\partial x_j}(\frac{\partial u_j}{\partial x_i} + \frac{\partial u_i}{\partial x_j}) \quad (5)$$

are solved numerically by a Finite Volume discretization method. In the above equations

$$\mu_{eff} = \mu + \mu_t \quad (6)$$

is the frequently used effective viscosity with the laminar viscosity μ and the eddy viscosity

$$\mu_t = \rho C_\mu \frac{k^2}{\epsilon} \quad (7)$$

External forces acting on the fluid, e.g. gravity are denoted by F_j in the momentum equations (2) and are assumed to be negligible in the present investigations. Turbulent transport of enthalpy and vapour concentration is calculated via additional transport equations:

$$\frac{\partial}{\partial x_i}(\rho u_i h) = \frac{\partial}{\partial x_i}(\frac{\mu_{eff}}{Pr_{eff}}\frac{\partial h}{\partial x_i}) + S_{h,p} \quad (8)$$

$$\frac{\partial}{\partial x_i}(\rho u_i c_\alpha) = \frac{\partial}{\partial x_i}(\frac{\mu_{eff}}{Sc_{eff}}\frac{\partial c_\alpha}{\partial x_i}) + S_{c_\alpha,p} \quad (9)$$

with

$$\frac{\mu_{eff}}{Pr_{eff}} = \frac{\mu}{Pr} + \frac{\mu_t}{Pr_t} \quad (10)$$

$$\frac{\mu_{eff}}{Sc_{eff}} = \frac{\mu}{Sc} + \frac{\mu_t}{Sc_t} \quad (11)$$

The constants of the standard k, ϵ-turbulence model used and the turbulent Prandtl and Schmidt numbers are given in Table 1. Source terms ($S_{\Phi,p}$) due to gas/droplet interactions are described in combination with the new droplet model. The wall function method is used to eliminate the large number of grid points needed to resolve the laminar sublayer (Launder and Spalding (1974)).

C_1	C_2	C_μ	σ_k	σ_ϵ	Pr_t	Sc_t
1.44	1.92	0.09	0.90	1.30	0.9	0.9

Table 1: Constants of the k, ϵ-turbulence model

Droplet equations

The equations describing continuity and momentum exchange of the liquid phase for laminar flow conditions can be derived from a mass- and momentum balance at an infinitesimal small fluid volume:

$$\frac{\partial}{\partial x_i}(v_c \rho_p u_{i,p}) = S_{v_c} \quad (12)$$

$$\frac{\partial}{\partial x_i}(v_c \rho_p u_{i,p} u_{j,p}) = \frac{3}{4} v_c \rho \frac{c_D}{D_p} c_{rel}(u_j - u_{j,p}) + F_{j,p} + S_{v_c} u_{j,p} \quad (13)$$

with

$$c_{rel} = \| \vec{u} - \vec{u_p} \| \quad (14)$$

$$Re_p = \frac{D_p\, c_{rel}}{\nu} \quad (15)$$

$$c_D = 0.36 + 5.48\, Re_p^{-0.573} + \frac{24}{Re_p} \quad (16)$$

The mass source term due to droplet evaporation is obtained by

$$S_{v_c} = v_c \rho_p \frac{3}{D_p}\frac{dD_p}{dt} \quad (17)$$

The term on the l.h.s. of Eq. (13) represents the inertia force per unit volume due to droplet acceleration. The first term on the r.h.s. represents the drag force due to the slip between the two phases, the second contains external forces like gravity and the third takes momentum loss due to droplet evaporation into account. Pressure gradient terms for the dispersed phase are neglected. An expression for the decreasing diameter of a single droplet in Lagrangian coordinates

$$\frac{dD_p}{dt} = -Fr\frac{4 M_v n_{ref} \Gamma_{ref}}{\rho_p D_p} \ln\left(\frac{1 - X_{v,\infty}}{1 - X_{v,p}}\right) \quad (18)$$

with

$$Fr = 1 + 0.276\sqrt{Re_p}\, Sc^{\frac{1}{3}} \quad (19)$$

is given by Faeth (1983) and Wittig et al. (1988) assuming a constant liquid density. The calculation of the reference values and the mol fraction of the vapour is shown in Appendix A.

In order to derive a transport equation for the droplet diameter we first write:

$$\begin{aligned}
&\frac{\partial}{\partial x_i}(v_c \rho_p u_{i,p} D_p) \\
&= D_p \frac{\partial}{\partial x_i}(v_c \rho_p u_{i,p}) + v_c \rho_p u_{i,p} \frac{\partial D_p}{\partial x_i} \\
&= D_p \frac{\partial}{\partial x_i}(v_c \rho_p u_{i,p}) + v_c \rho_p \frac{dD_p}{dt}
\end{aligned}$$

Including Eqs. (12) and (17) yields:

$$\frac{\partial}{\partial x_i}(v_c \rho_p u_{i,p} D_p) = \frac{4}{3} S_{v_c} D_p \qquad (20)$$

A transport equation for the droplet temperature can be derived via an energy balance in the same manner as the momentum equation:

$$\begin{aligned}
\frac{\partial}{\partial x_i}(v_c \rho_p u_{i,p} T_p) &= v_c \frac{6 Nu Fr \lambda_{ref}}{c_{p,p} D_p^2}(T_\infty - T_p) \\
&+ S_{v_c}\left(\frac{\Delta h_v}{c_{p,p}} + T_p\right) \qquad (21)
\end{aligned}$$

with

$$Nu = \frac{2\ Le\ \ln\left(\frac{1-X_{v,\infty}}{1-X_{v,p}}\right)}{\left(\frac{1-X_{v,\infty}}{1-X_{v,p}}\right)^{Le} - 1} \qquad (22)$$

$$Le = \frac{\Gamma_{ref}\ c_{p,v,ref}\ n_{ref}}{\lambda_{ref}} \qquad (23)$$

$$Fr = 1 + 0.276\ \sqrt{Re_p}\ Pr^{\frac{1}{3}} \qquad (24)$$

The model implies a uniform temperature distribution in the droplet assuming an infinite thermal conductivity. In Eq. (21) the first term of the r.h.s. represents droplet heating due to the temperature gradient between the two phases, the second droplet cooling due to droplet evaporation. The specific heat of the liquid $c_{p,p}$ is assumed to be constant. An exact derivation of the expressions describing droplet heating and cooling in the source term of Eq. (21) is given by Faeth (1983) and Wittig et al. (1988).

Turbulence modelling

Turbulence effects are evaluated by introducing fluctuation quantities for the volume fraction and the droplet's velocity, temperature and diameter:

$$\Phi_p = \overline{\Phi}_p + \Phi'_p \qquad (25)$$

$$\overline{\Phi}_p = \frac{1}{\Delta t}\int_t^{t+\Delta t} \Phi_p dt \qquad (26)$$

Inserting Eq. (25) in the l.h.s. of the Eqs. (12), (13), (20) and (21), time averaging and using the following gradient hypothesis for the second order correlations representing the turbulent fluxes of momentum, mass and enthalpy

$$-\rho_p \overline{v'_c u'_{j,p}} = \frac{\mu_{t,p}}{Sc_{t,p}}\left(\frac{\partial v_c}{\partial x_j}\right) \qquad (27)$$

$$-\rho_p v_c \overline{u'_{i,p} u'_{j,p}} = v_c \mu_{t,p}\left(\frac{\partial u_{i,p}}{\partial x_j} + \frac{\partial u_{j,p}}{\partial x_i}\right) \qquad (28)$$

$$-\rho_p v_c \overline{D'_p u'_{j,p}} = v_c \frac{\mu_{t,p}}{Sc_{t,p}}\left(\frac{\partial D_p}{\partial x_j}\right) \qquad (29)$$

$$-\rho_p v_c \overline{T'_p u'_{j,p}} = v_c \frac{\mu_{t,p}}{Sc_{t,p}}\left(\frac{\partial T_p}{\partial x_j}\right) \qquad (30)$$

leads to a set of equations for turbulent evaporating sprays which can easily be casted in a form identical to commonly used gas phase equations:

$$\frac{\partial}{\partial x_i}(v_c \rho_p u_{i,p}) = \frac{\partial}{\partial x_i}\left(\frac{\mu_{t,p}}{Sc_{t,p}}\frac{\partial v_c}{\partial x_i}\right) + S_{v_c} \qquad (31)$$

$$\begin{aligned}
\frac{\partial}{\partial x_i}(v_c \rho_p u_{i,p} u_{j,p}) &= \frac{\partial}{\partial x_i}\left(v_c \mu_{t,p}\left(\frac{\partial u_{j,p}}{\partial x_i} + \frac{\partial u_{i,p}}{\partial x_j}\right)\right) \\
&+ \frac{3}{4} v_c \rho \frac{c_D}{D_p} c_{rel}(u_j - u_{j,p}) \\
&+ F_j + S_{v_c} u_{j,p} \qquad (32)
\end{aligned}$$

$$\begin{aligned}
\frac{\partial}{\partial x_i}(v_c \rho_p u_{i,p} D_p) &= \frac{\partial}{\partial x_i}\left(v_c \frac{\mu_{t,p}}{Sc_{t,p}}\frac{\partial D_p}{\partial x_i}\right) \\
&+ \frac{4}{3} S_{v_c} D_p \qquad (33)
\end{aligned}$$

$$\begin{aligned}
\frac{\partial}{\partial x_i}(v_c \rho_p u_{i,p} T_p) &= \frac{\partial}{\partial x_i}\left(v_c \frac{\mu_{t,p}}{Sc_{t,p}}\frac{\partial T_p}{\partial x_i}\right) \\
&+ v_c \frac{6 Nu Fr \lambda_{ref}}{c_{p,p} D_p^2}(T - T_p) \\
&+ S_{v_c}\left(\frac{\Delta h_v}{c_{p,p}} + T_p\right) \qquad (34)
\end{aligned}$$

Correlations involving fluctuations in the liquid phase density ($\rho_p v_c$) are taken into account only in the continuity equation.

The closure hypothesis (27) and (28) for the turbulent mass flux and momentum transfer have been tested successfully by a lot of researchers (Chen and Wood (1984), Elghobashi et al. (1984), Melville and Bray (1979)) and have been extended by Hallmann et al. (1993) for turbulent heat and mass transfer in evaporating sprays (Eqs. (29), (30)). The turbulent viscosity $\mu_{t,p}$ of the dispersed phase is modeled using the approach of Melville and Bray (1979):

$$\mu_{t,p} = \mu_t \frac{\rho_p}{\rho}\frac{k_p}{k} \qquad (35)$$

with

$$k_p = \frac{1}{2}(\overline{u_p'^2} + \overline{v_p'^2} + \overline{w_p'^2}) \qquad (36)$$

The ratio of the turbulent kinetic energies of the dispersed and the gas phase is calculated following the approach of Krämer (1988):

$$\frac{k_p}{k} = \frac{1}{1+\omega^2\tau^2} \qquad (37)$$

Since in general the droplets do not follow the motion of the surrounding fluid from one point to another it is expected that the ratio k_p/k is different from unity and varies with the particle relaxation time τ and local turbulence quantities (Elghobashi et al. (1984)). Krämer recommends the following equations for the frequency of the particle response

$$\omega = \frac{1}{\tau}\left(\frac{\sqrt{\frac{2}{3}k}}{L_x}\tau\right)^{0.25} \qquad (38)$$

$$\tau = \frac{1}{18}\frac{\rho_p}{\rho}\frac{D_p^2}{\nu}\frac{1}{1+0.133Re_p^{0.687}} \qquad (39)$$

with a characteristic macroscopic length scale of turbulence

$$L_x = C_\mu^{0.75}\frac{k^{1.5}}{\epsilon} \qquad (40)$$

For the turbulent Schmidt number $Sc_{t,p}$ of the dispersed phase Krämer suggests a value of 0.3. In the course of our work we found this value to be particle size dependent. Because more detailed information is not available at the moment we recommend a median value of 2.5 for problems treated in this paper.

Coupling with the gas phase equations

The gaseous phase is affected by the dispersed phase due to momentum, heat and mass exchange. The easy way of coupling the two phases is an evident advantage of the new model. Due to an identical mathematical formulation the same terms appear for both phases, simply with different sign. A drawing up of the coupling terms for the gas phase equations is given in Table 2.

The expressions are added up for all nd discrete drop-size classes. In addition phase coupling is guaranteed by the use of temperature, pressure and vapour concentration dependent properties in the calculations of the gaseous phase.

Source terms ($S_{k,p}$, $S_{\epsilon,p}$) for the equations of the k,ϵ-turbulence model due to the presence of the dispersed phase were modeled following the approach of Chen and Wood (1984, 1986). Because the calculations presented in this paper do not show any significant influence of these terms they are not taken into consideration here.

Φ	$S_{\Phi,p}$
ρ	$-\sum_{k=1}^{nd}(S_{v_c})$
c_α	$-\sum_{k=1}^{nd}(S_{v_c})$
u_j	$-\sum_{k=1}^{nd}\left(\frac{3}{4}v_c\rho\frac{c_D}{D_p}c_{rel}(u_j-u_{j,p})+S_{v_c}u_{j,p}\right)$
h	$-\sum_{k=1}^{nd}\left(c_{p,p}\left(v_c\frac{6NuFr\lambda_{rel}}{c_{p,p}D_p^2}(T-T_p)+S_{v_c}(\frac{\Delta h_v}{c_{p,p}}+T_p)\right)\right)$

Table 2: Coupling terms for the gas phase equations due to droplet transport and evaporation

Solution steps

As mentioned above, the equations of both phases can be solved numerically using the same finite volume discretization method (Noll and Wittig (1991), Noll (1992)). After calculating the droplet field with the preceding values of the gas field properties, the gas field is recalculated with the coupling terms due to droplet transport and evaporation. This procedure is repeated until the coupling terms converge, i.e. both phases have statistically constant values.

Results and discussion

For the verification of the new model, measurements of a recirculating droplet charged air flow (Himmelsbach (1987), Wittig et al. (1987), Wittig et al. (1988)) within a model combustor are compared with. The test section used in our laboratory is shown in Fig. 1. It consists of a rectangular flow channel with a cross sectional area of $100*300\ mm^2$. A prefilming two-dimensional airblast nozzle is incorporated into the test section. The airflow enters the channel through four slots with $60\ m/s$ mean air velocity. Two of these slots are charged with a liquid film. The experimental studies were performed with ethanol at inlet gas temperatures of $320\ K$ and $520\ K$.

The symmetric flow field in the model combustor is characterized by a recirculation zone induced by the centerbody of the nozzle (Fig 2). As reported earlier (Wittig et al. (1987)) it can be predicted with

sufficient accuracy. In the calculations a 68*36 computational grid has been used with the MLU-scheme (Noll (1992)) for the discretization of the convective terms. The convective terms of the droplet equations are discretizised using the well known UPWIND-scheme.

Droplet motion and evaporation were calculated for ten discrete drop-size classes. In Figs. 3 and 4 calculated volume fractions of the liquid phase and characteristic droplet diameters of the spray are plotted against experimental data given by Wittig et al. (1987) for an inlet gas temperature of 320 K. The initial conditions for the droplets were determined from elaborate studies of air-blast atomizers as a function of the operating parameters of the nozzle and the properties of the liquid (Aigner (1986), Sattelmayer (1989)). They can be described with the distribution parameters $D_{63\,2} = 63\ \mu m$ and $N = 2$ in the Rosin Rammler distribution (see Appendix B). Both, measurements and predictions show that in the recirculation zone mainly small droplets are found due to turbulent dispersion, while the forward flowing regions are dominated by large droplets. Highest droplet concentrations occur close to the atomizer's edge decreasing rapidly towards the recirculation zone. Turbulent particle dispersion is slightly underpredicted. Nevertheless measurements and predictions are in good agreement.

Fig. 5 shows the predicted spatial distribution of the decreasing droplet diameter in the upper half of the combustor for an inlet gas temperature of 520 K. For comparison results of a Lagrangian approach are shown. Both computational approaches are based on the same evaporation model, the well known 'Uniform Temperature' law (Faeth(1983), Wittig et al. (1988), Hallmann et al. (1993)). The excellent agreement of the two methods in almost all details is proof that the new Eulerian model yields adequate results for the diameter decrease of the evaporating droplets. It should be noted that the shape of the Eulerian solution in Fig. 5 can be influenced by variations of the turbulent Schmidt number $Sc_{t,p}$. As mentioned before, $Sc_{t,p}$ is not a constant and further investigations in the area of turbulent droplet dispersion are necessary to guarantee a general application of the new model. Fluctuations, which can be seen in the Lagrangian results, are due to the statistical nature of the Monte Carlo sampling method. They could be damped by increasing the number of particles used to evaluate mean droplet diameters.

Figs. 6 and 7 show calculated and measured volume fractions (Himmelsbach (1987)) and characteristic droplet diameters for $T = 520\ K$ (Wittig et al. (1987, 1988)). The larger diameters compared to the cold flow conditions are caused by larger initial diameters ($D_{63\,2} = 78\ \mu m$, $N = 2$) but also by the faster evaporation of small droplets. The computational results are of sufficient agreement with the measurements for both, volume fractions and characteristic diameters of the dispersed phase.

Effects of phase coupling can be seen in Fig. 8 and Fig. 9 for hot flow conditions. The vapour concentration of the gas phase shows a strong increase along the way of the evaporating droplets combined with a decrease of the gas temperature. The recirculating flow transports parts of the cold vapour/air mixture back to the centerbody of the nozzle resulting in very high vapour concentration and temperature gradients near the atomizing edge. At the channels outlet the vapour concentration reaches approximately 10 % resulting in a temperature decrease of more than 100 degrees.

Conclusions

A new Eulerian model for the computation of turbulent evaporating sprays has been developed. In contrast to former Eulerian approaches it comprises transport equations for droplet heating and evaporation and is applicable for recirculating flows. The coupling of the gaseous and the droplet phase is guaranteed by the exchange of source terms due to momentum, heat and mass transfer and by the calculation of temperature, pressure and vapour concentration dependent properties of the gaseous phase. Comparison of the new model with Lagrangian calculations and experiments with respect to diameter distributions and concentrations reveal good agreement.

However, the physical understanding of the turbulent particle dispersion processes need further improvements for a more general application. Nevertheless, the similar structure of the transport equations obtained by the Eulerian approach with the commonly used gas phase equations offers the opportunity for an easy incorporation of our new model in standard CFD-codes. This is a great advantage in contrast to Lagrangian methods which require different numerical procedures for the two phases. In addition, the implementation of Lagrangian methods in codes for boundary fitted non-orthogonal coordinates or unstructured grids is very complicated, but is easily accomplished with the present formulation.

Acknowledgements

This work was supported by the Arbeitsgemeinschaft Hochtemperatur Gasturbine (Turboflam) and by a grant from the SFB 167 (High Intensity Combustors) of the Deutsche Forschungsgemeinschaft.

References

[1] T.W. Abou-Arab, M. C. Roco: Solid Phase Contribution in the Two-Phase Turbulent Kinetic Energie Equation. ASME-Journal of Fluids Engineering, 112, pp. 351-361, 1990.

[2] M. Aigner: Charakterisierung der bestimmenden Einflußgrößen bei der luftgestützten Zerstäubung: Physikalische Grundlagen und meßtechnische Erfassung. Dissertation, Institut für Thermische Strömungsmaschinen, Universität Karlsruhe (T.H.), 1986.

[3] G.K. Batchelor: Transport Properties of Two-Phase Materials with Random Structure. Annual Review of Fluid Mechanics, 6, pp. 227-255, 1974.

[4] C.P. Chen, P.E. Wood: Turbulence Closure Modeling of Two-Phase Flows. Chemical Engineering Communications, 29, pp. 291-310, 1984.

[5] C.P. Chen, P.E. Wood: Turbulence Closure Modeling of the Dilute Gas-Particle Axisymetric Jet. AIChE-Journal, 32, No. 1, pp. 163-166, 1986

[6] C.T. Crowe: Review - Numerical Models for Dilute Gas-Particle Flows. ASME Journal of Fluids Engineering, 104, pp. 297-303, 1982.

[7] S.E. Elgobashi, T.W. Abou-Arab, M. Rizk, A. Mostafa: Prediction of the Particle-Laden Jet with a Two-Equation Turbulence Model. International Journal of Multiphase Flow, 10, No. 6, pp. 697-710, 1984.

[8] G.M. Faeth: Evaporation and Combustion of Sprays. Progress in Energy and Combustion Science, 9, pp. 1-76, 1983.

[9] A.D. Gosman, E. Ioannides: Aspects of Computer Simulation of Liquid-Fueled Combustors. Journal of Energy, 7, No. 6, pp. 482-490, 1983.

[10] M. Hallmann, M. Scheurlen, S. Wittig: Computation of Turbulent Evaporating Sprays: Eulerian Versus Lagrangian Approach. Submitted for presentation: 38th IGTI Conference, Cincinnati, Ohio, USA, May 24-27, 1993

[11] J. Himmelsbach: Experimentelle und numerische Untersuchungen zur Ausbreitung und Verdampfung flüssiger Brennstofftropfen in einer Heißgasströmung. Diplomarbeit, Institut für Thermische Strömungsmaschinen, Universität Karlsruhe (T.H.), 1987.

[12] R. Kneer, E. Benz, S. Wittig: Drop Motion Behind a Prefilming Airblast Atomizer: Comparison of Phase Doppler Measurements with Numerical Predictions. Proceedings of the 5th International Symposium on Applications of Laser Technology to Fluid Mechanics, 1990.

[13] M. Krämer: Untersuchungen zum Bewegungsverhalten von Tropfen in turbulenter Strömung im Hinblick auf Verbrennungsvorgänge. Dissertation, Institut für Feuerungstechnik, Universität Karlsruhe (T.H.), 1988.

[14] B.E. Launder, D.B. Spalding: The Numerical Calculation of Turbulent Flows. Computer Methods in Applied Mechanics and Engineering, 3, pp. 269-289, 1974.

[15] W.K. Melville, K.N.C. Bray: A Model of the Two-Phase Turbulent Jet. International Journal of Heat and Mass Transfer, 22, pp. 647-656, 1979.

[16] A.A. Mostafa, H.C. Mongia: On the Modeling of Turbulent Evaporating Sprays: Eulerian versus Lagrangian Approach. International Journal of Heat and Mass Transfer, 30, No. 12, pp. 2583-2593, 1987.

[17] A.A. Mostafa, S.E. Elghobashi: A Two-Equation Turbulence Model for Jet Flows Laden with Vaporizing Droplets. International Journal of Multiphase Flow, 11, No. 4, pp. 515-533, 1985.

[18] B. Noll: Evaluation of a Bounded High Resolution Scheme for Combustor Flow Computations. AIAA-Journal, 30, No. 1, pp 64-69, 1992.

[19] B. Noll, S. Wittig: A Generalized Conjugate Gradient Method for the Efficient Solution of Three Dimensional Fluid Flow Problems. Numerical Heat Transfer, Part B, 20, No. 2, pp. 207-221, 1991.

[20] T. Sattelmayer, S. Wittig: Performance Characteristics of Prefilming Atomizers in Comparison with Other Airblast Nozzles. Encyclopedia of Fluid Mechanics. 8, pp. 1093-1141, 1989.

[21] O. Simonin: Eulerian Formulation for Particle Dispersion in Turbulent Two-Phase Flows. Proceedings of the 5th Workshop on Two Phase Flow Predictions, Erlangen, March 19-22, pp. 156-166, 1990.

[22] E.M. Sparrow, J.L. Gregg: The Variable Fluid Property Problem in Free Convection. Transactions of ASME 80, pp. 879-886, 1958.

[23] S. Wittig, W. Klausmann, B. Noll: Turbulence Effects on the Droplet Distribution behind Air-blast Atomizers. AGARD-CP-422, 1987.

[24] S. Wittig, W. Klausmann, B. Noll, J. Himmelsbach: Evaporation of Fuel Droplets in Turbulent Combustor Flow. ASME-Paper-88-GT-107, 1988.

Appendix A

The reference values in the models presented are determined according the 1/3-rule of Sparrow and Gregg (1958)

$$T_{ref} = \frac{2}{3}T_p + \frac{1}{3}T_\infty \quad (41)$$

$$X_{v,ref} = \frac{2}{3}X_{v,p} + \frac{1}{3}X_{v,\infty} \quad (42)$$

$$n_{ref} = n(T_{ref}) \quad (43)$$

$$\Gamma_{ref} = \Gamma(T_{ref}) \quad (44)$$

$$c_{p,v,ref} = c_{p,v}(T_{ref}) \quad (45)$$

$$\lambda_{ref} = \lambda(T_{ref}) \quad (46)$$

The mol fraction of vapour at the droplet's surface is given by an exponential law following Cox-Antoine

$$X_{v,p}(p_s) = \frac{p_s}{p} \quad (47)$$

$$p_s(T_p) = \exp\left(A - \frac{B}{T_p + C}\right) \quad (48)$$

where A, B and C are specific values for the droplet liquid under consideration.
The relation between the vapour concentration c_a and the mol fraction of vapour X_v is

$$c_a = \frac{X_v M_v}{X_v M_v + (1 - X_v) M_{air}} \quad (49)$$

Appendix B

In the Rosin Rammler drop-size distribution

$$D_x = D_{63.2} \ln\left(\frac{100}{100 - x}\right)^{\frac{1}{N}} \quad (50)$$

x indicates the volume percentage of all droplets with smaller diameters than D_x. Two characteristic diameters are needed to completely define the distribution. In presenting the results the volumetric mean diameter D_{50} and a characteristic diameter for small droplets D_{10} are used.

Figures

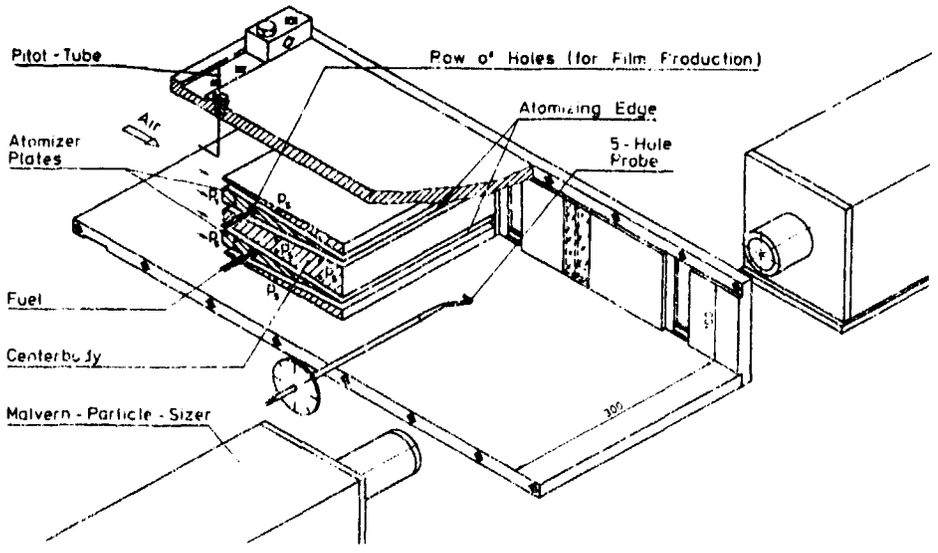

Figure 1: Test section - two dimensional combustor model (Wittig et al. (1987))

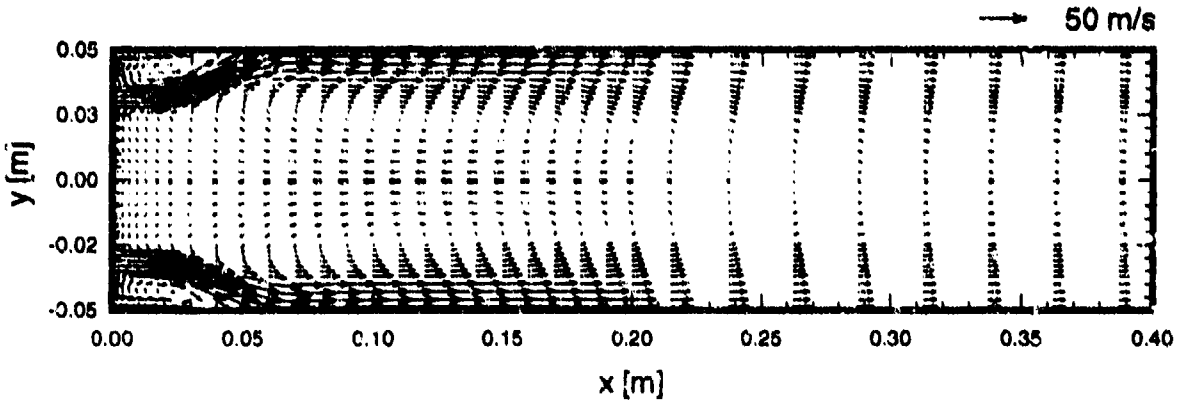

Figure 2: Calculated flow field within the model combustor

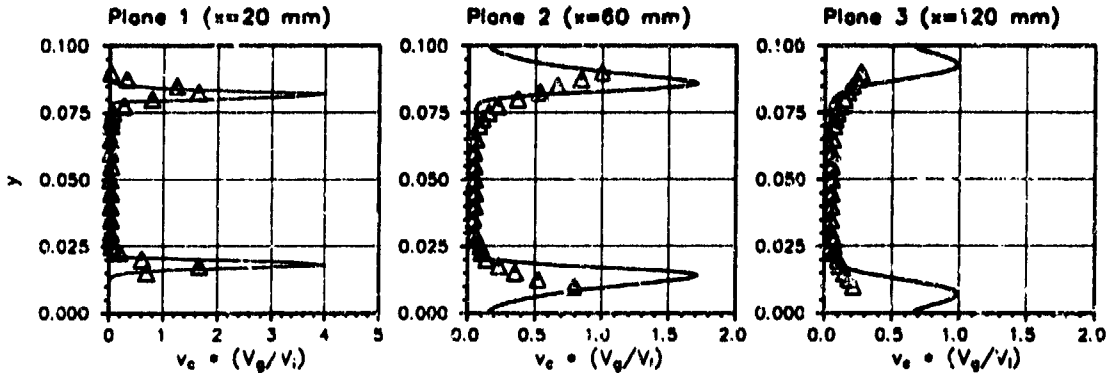

Figure 3: Volume fractions for cold flow conditions; △ measurements, —— calculations

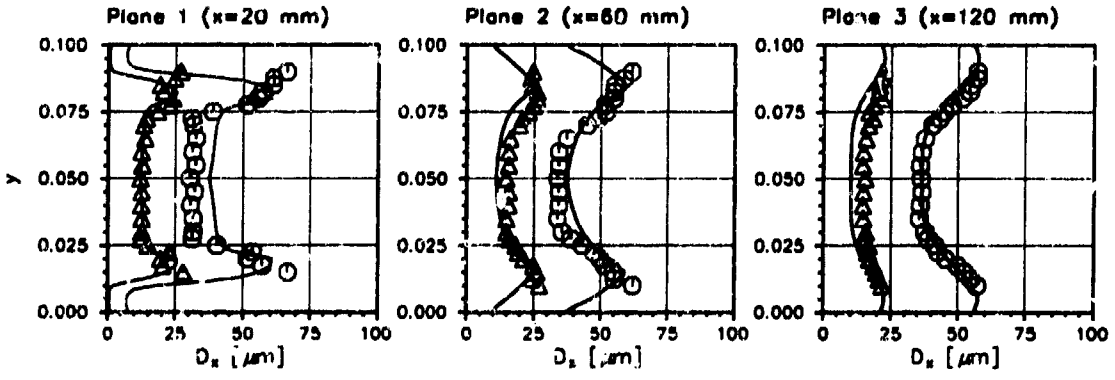

Figure 4: Characteristic diameters for cold flow conditions; measurements: △ D_{10}, ○ D_{50}, —— calculations

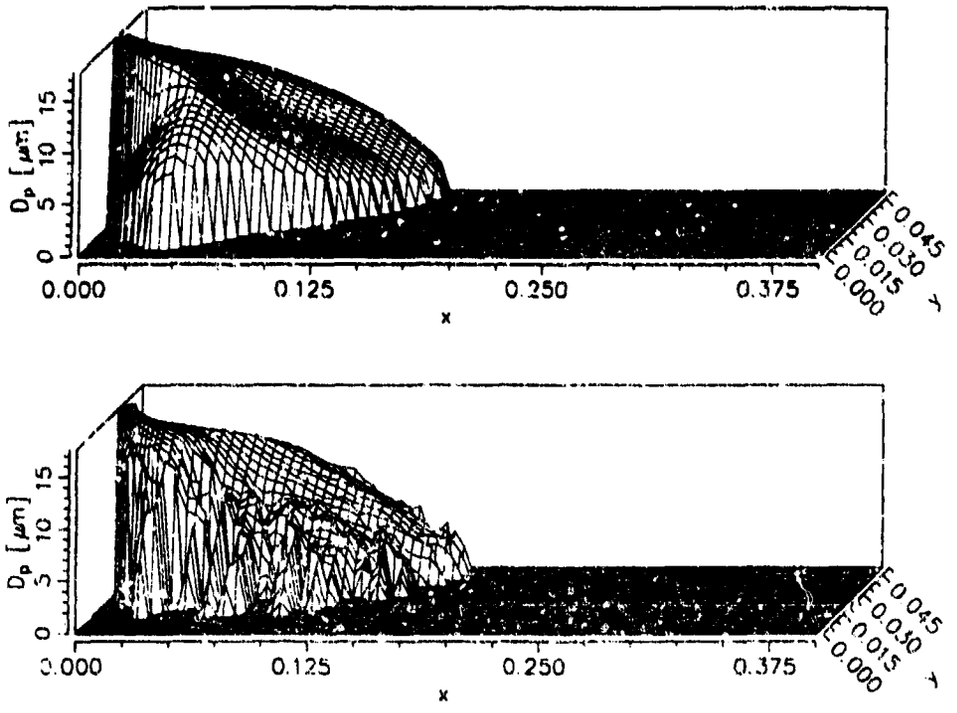

Figure 5: Spatial distribution of the droplet diameter for a starting diameter of 17.67 μm ; upper diagram: Eulerian approach, lower diagram: Lagrangian approach

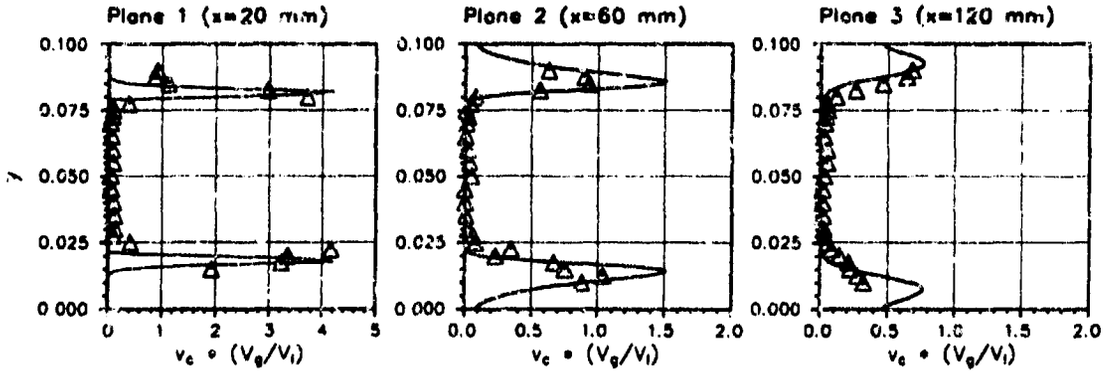

Figure 6: Volume fractions for hot flow conditions ; △ measurements, —— calculations

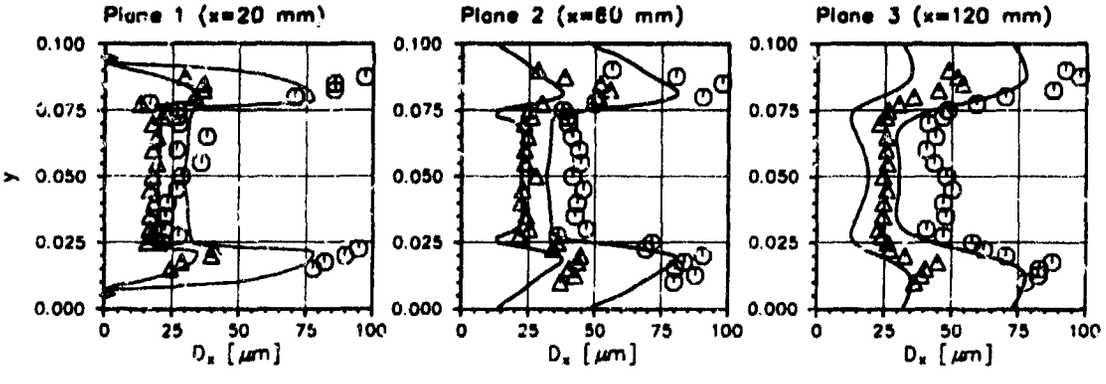

Figure 7. Characteristic diameters for hot flow conditions; measurements: △ D_{10}, ○ D_{50}, —— calculations

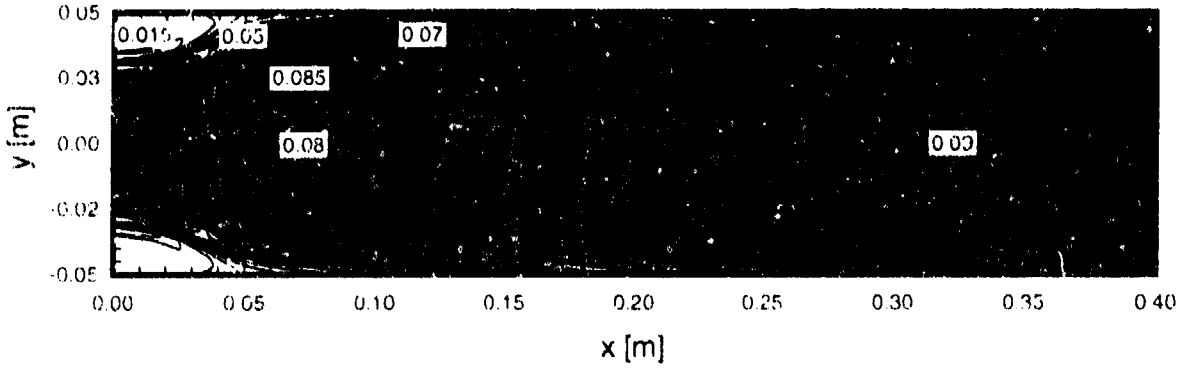

Figure 8: Calculated fuel vapour distribution for hot flow conditions

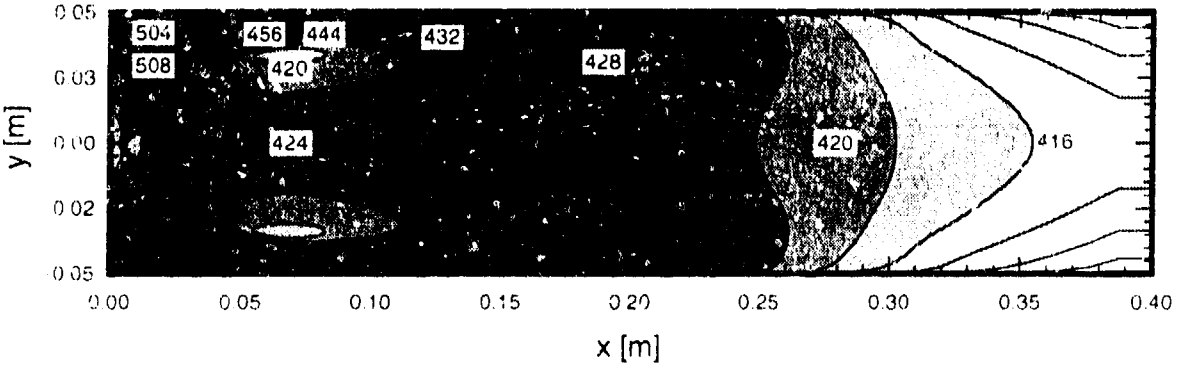

Figure 9: Calculated gas temperature distribution for hot flow conditions

Discussion

Question 1. Dr L. Ivanovski
Why do you not take account of the thermophoresys force in your model for droplets?

Author's Reply
In the flow considered, these forces are of negligible influence.

Question 2. A. Kleitz
In your experimental device, you use a Malvern which doesn't give a "true" local size measurement. What is the size of the measuring volume?

Author's Reply
Knowing that the Malvern Particle Sizer integrates along the laser beam, we have chosen two-dimensional experimental conditions which allows us locally resolved measurements.

Question 3. C. Hassa
Have you compared calculations with experimental investigations giving a liquid flux distribution; for instance, Snyder and Lumley, IEM 1977?

Author's Reply
We compared our predictions with measurements from Hishida et al. which were presented at the "5th Workshop on Two Phase Flow Modelling" in Erlangen. These measurements include particle velocities and volume fluxes for different flow configurations, and these measurements are good.

EXPERIMENTAL STUDIES ON EFFERVESCENT ATOMIZERS WITH WIDE SPRAY ANGLES

by

J.D. Whitlow and A.H. Lefebvre
School of Mechanical Engineering, Purdue University
W. Lafayette, IN 47907, United States

R.J. Rollbuhler
NASA-Lewis,
Cleveland, OH 44135, United States

SUMMARY

An experimental investigation was conducted to examine the operating and spray characteristics of two internal-mixing twin-fluid atomizers that were designed to produce effervescent atomization at low air/liquid mass ratios (ALRs). These two experimental atomizers ejected the two-phase flow so as to produce a wide spray angle. One atomizer was a plain-orifice design that used a 4-hole exit orifice which divided and turned the two-phase flow just prior to ejection. The other atomizer, called the conical-sheet atomizer, ejected the two-phase flow through an annular passage in such a way as to form a hollow cone spray. The atomizer operating parameters varied during this investigation were the air/liquid mass ratio , atomizer operating pressure, and, in the case of the conical-sheet atomizer, the exit gap width. Studies of spray characteristics included measurements of the spray Sauter mean diameter (SMD), drop size distribution, and, for the conical-sheet atomizer, circumferential distribution of the liquid mass within the spray.

For both atomizers it was found that SMD decreases with an increase in either ALR or operating pressure. The effect of ALR on SMD diminishes as the value of ALR increases. For the conical-sheet atomizer, when operating at low values of pressure and ALR, SMD increases with increase in gap width; but the influence of gap width on SMD diminishes with an increase in either pressure or ALR. At the highest operating pressure of the conical-sheet atomizer (552 kPa), SMD is independent of gap width at all ALRs. For both atomizers, changes in operating pressure and ALR have little effect on the distribution of drop sizes in the spray.

1. INTRODUCTION

Internal-mixing, twin-fluid atomizers that produce effervescent atomization show potential for eliminating a number of the problems associated with pressure-swirl and airblast/air-assist atomizers, such as the need for high injection pressures or large quantities of high velocity air. In effervescent atomization, a gas (air in combustion applications) is introduced directly into a flowing liquid at some point upstream of the atomizer exit orifice in such a way as to create a bubbly two-phase flow. When the bubbly flow mixture exits the discharge orifice, the gas bubbles rapidly expand which aids in the breakup of the liquid into drops. Unlike traditional airblast or air-assist atomizers, the gas is not intended to transfer kinetic energy to the liquid upon contact. Instead, the purpose is to create a bubbly two-phase flow that takes advantage of the expansion of the gas after the mixture has been ejected from the atomizer.

Previous studies have shown a number of advantages offered by effervescent atomization [Refs. 1-4]. One advantage is that good atomization can be achieved at low injection pressures and low air/liquid mass ratios. Also, since both the liquid and the atomizing gas are ejected through the same exit, the flow passages can be made larger which greatly reduces the problem of blockage by contaminants in the fuel. Previous work has shown that the quality of atomization is not significantly influenced by changes in orifice diameter [Ref. 3].

All previous studies on effervescent atomization have been confined to atomizers that eject the bubbly two-phase mixture through a single-hole orifice which produced a narrow angle spray. However, combustor designs in gas turbines generally require atomizers that distribute the fuel in the form of a conical spray of approximately 90° cone angle. One objective of the present research is to determine if good atomization can be achieved using effervescent atomizers that turn a two-phase flow through an angle just prior to ejection. If the bubbly flow can be turned at angles and still produce good atomization, then the passages at the exit of the atomizer can be designed to eject the spray at the large angles which are more suitable for combustion applications.

Two atomizers were designed and built to carry out the experimental studies in this investigation. One design was a plain-orifice atomizer that featured a 4-hole exit orifice which divided and turned the bubbly flow through an angle just prior to ejection. The second atomizer, called a conical-sheet atomizer, ejected a bubbly mixture through an annular passage in such a way as to form a hollow cone spray. The conical-sheet atomizer was designed to allow adjustment of the exit gap width.

The experimental studies on both atomizers included measurements of the spray Sauter mean diameter (SMD), drop size distribution and, for the conical-sheet atomizer, the circumferential distribution of the liquid mass within the spray. The operation of the plain-orifice atomizer relative to the internal two-phase flow pattern within the atomizer was also investigated across a wide range of air/liquid mass ratios. The parameters varied during this investigation were the air/liquid mass ratio, atomizer operating pressure, and, in the case of the conical-sheet atomizer, the exit gap width. In this paper, atomizer operating pressure is the static pressure of the air prior to being mixed with the liquid.

2. ATOMIZER DESIGNS

The principal geometrical features of the plain-orifice atomizer and the conical-sheet atomizer are described below.

2.1 Plain-Orifice Atomizer

The 4-hole plain-orifice atomizer shown in Fig. 1 is an internal-mixing twin-fluid atomizer designed to produce effervescent atomization at low air/liquid mass flow ratios (ALRs). The mixing and containment tubes are made from clear acrylic to permit visual observation of the internal two-phase flow. All other components are machined from brass. The mixing tube is enclosed within the containment tube which serves as both the outer wall of the air cavity and to contain the pressure of the atomizer. This allows the pressure difference across any part of the mixing tube to be significantly reduced to only what is necessary to persuade the air to enter the liquid flow.

The overall length of the atomizer is approximately 140 mm. The containment tube has an inside diameter of 51 mm and a wall thickness of 6.4 mm. The mixing tube has an inside diameter of 6.4 mm and a wall thickness of 1.6 mm. Six rows of four holes used for injecting air into the mixing tube are drilled through the wall of the mixing tube perpendicular to its axis. Each row is spaced 6.4 mm apart and rotated 45° from the neighboring row. The last row of these injection holes is located 51 mm upstream of the exit orifice. The size of these injection holes varies somewhat because of difficulties in machining, but the average hole diameter is 0.58 mm.

Liquid enters at the top of the atomizer and flows downward through the mixing tube toward the exit orifice. The mixing tube is surrounded by an air cavity. The static pressure of the air in this cavity is measured through a pressure tap in the top of the

Presented at an AGARD Meeting on 'Fuels and Combustion Technology for Advanced Aircraft Engines', May 1993.

atomizer. Air passes from this cavity through the mixing tube injection holes into the liquid flow. The bubbly two-phase mixture then flows downward to the exit orifice and is ejected through four exit holes drilled at an angle of 40° from the axis of the mixing tube. Each of the four holes has a diameter of 0.8 mm and a length/diameter (l/d) ratio of approximately 5.

2.2 Conical-Sheet Atomizer

The conical-sheet atomizer is shown schematically in Fig. 2. The overall length of the atomizer is approximately 125 mm. The wall of the liquid chamber is made from an acrylic tube with a thickness of 6.4 mm which provides safe containment of the maximum 552 kPa operating pressure of the atomizer. The most critical areas in the design of the conical-sheet atomizer are the annular bubbly flow passage between the stem and the main body, the size and placement of the stem within the main body, and the air injection holes. Since concentric placement of the stem with the main body is essential to provide a uniform annular gap width at the atomizer exit, great care was taken in the fabrication of these two components. The stem screws into the main body with 10-32 UNF threads. The exit gap width is determined by how far the stem is screwed into the main body. In order to eliminate axial thread play, a nylon-tipped, spring-loaded set screw is screwed in the opposite end of the main body to provide a small downward force on the stem. Six rows of eight holes, each 0.51 mm in diameter, are drilled between the air cavity and the annular flow passage. Each row is equally spaced 3.2 mm apart and the last row of holes is located approximately 16 mm upstream from the atomizer exit.

The liquid to be atomized enters the atomizer through the top plate and flows downward through six inlet ports in the main body into the annular flow passage defined by the main body and the stem. The liquid then flows downward through the annular passage toward the atomizer exit. Air flows through a side port into a cavity which surrounds the annular flow passage. It then flows from this cavity through the injection holes into the annular flow passage where it merges with the downward flowing liquid. This two-phase mixture proceeds to the atomizer exit and is ejected into the atmosphere. The static pressure of the liquid is measured at entry to the atomizer and the static pressure of the air is measured just prior to entering the air cavity.

As previously mentioned, the width of the exit gap is adjusted by screwing the stem further into or out of the main body of the atomizer. Since the thread count on the stem is 1.26 threads per millimeter (32 threads per inch), one complete revolution should ideally move the stem 0.79 mm vertically. Numerous checks of the vertical travel of the stem with a depth micrometer showed that angular measurement is, for this setup, a reliable method for determining the vertical distance that the stem moves over a range of movement from the stem being completely closed to one revolution open. The vertical travel was checked every 30° from completely closed to 180° open and every 90° from 180° open to 360° open. Since the conical angle that both the main body and the stem were machined to is known at the exit throat, the annular gap width can be calculated from the angular position of the stem, as measured from completely closed.

3. APPARATUS

3.1 Test Facility

The experimental test facility for the plain-orifice atomizer is shown schematically in Fig. 3. A 1.1 MPa air supply is regulated to 0.93 MPa and provides both atomizing air and air to pressurize the water storage tank. Pressurized air enters the air circuit and is directed to one of two Brooks rotameters connected in parallel by a three-way valve. The smaller rotameter measures a range of flow rates from 0.05 to 0.23 g/s, while the larger rotameter measures flow rates between 0.22 and 1.76 g/s. All pressures in these studies were measured with dial-indicating Bourdon-tube pressure gauges. Air flows from the rotameter to two metering valves of different size connected in parallel. The larger valve is used for coarse adjustment of the flow rate and the smaller valve is used for fine adjustment. The air flow then passes through a ball shut-off valve and flows to the atomizer.

The liquid storage tank is an 83-liter stainless steel sphere. After the tank is filled, a ball valve allows the free surface of the liquid to be pressurized with the regulated air supply. Liquid flows from the storage tank to two metering valves connected in parallel. As in the air circuit, the two metering valves are of a different size to allow coarse and fine adjustment of the flow rate. The liquid flows from the metering valves to one of two Brooks rotameters connected in parallel by a three-way valve. The smaller rotameter is used to measure a range of flow rates from 1.83 to 20.7 g/s. The larger rotameter is capable of measuring flow rates from 11.3 to 91.3 g/s. The liquid then flows from the rotameter through a ball shut-off valve and on to the atomizer.

The plain-orifice atomizer sprayed downward into the atmosphere at normal room conditions. An evacuation system consisting of a conical funnel connected to an industrial vacuum cleaner is mounted below the atomizer. The sole purpose of this evacuation system was to provide a downdraft to reduce the recirculation of drops which could cause errors in the drop size measurements.

The design of the test facility used with the conical-sheet atomizer is nearly identical to the facility shown in Fig. 3. The main differences are that the facility used with the conical-sheet atomizer could supply a greater pressure and larger flow rate of air and liquid and could accommodate a greater quantity of spray and larger spray angles. The rotameters used to measure liquid flow rate shown in Fig. 3 were replaced by a Micro Motion model D40S-SS mass flow meter set to measure flow rates from 20 to 400 g/s. The maximum measurable air flow rate was increased to 4.23 g/s by changes in the air rotameters. The conical-sheet atomizer sprayed downward into a large spray collection box at normal room conditions. A duct at one end of the spray box is connected to the inlet of a large centrifugal fan. Baffles in the spray box provide for a downward flow of air when the fan is operating which prevents spray drops from recirculating and causing errors in the drop size measurements.

3.2 Radial Patternator

A radial patternator is a simple instrument commonly used to measure the radial distribution of liquid within a spray. In this study, a radial patternator was used to give an indication of the angle of the spray emitted from the conical-sheet atomizer. The patternator was constructed by cutting slots which formed sampling tubes into an opaque white plastic sheet over which a clear sheet of acrylic (3.2 mm thick) was glued. There are a total of 29 sampling tubes, spaced 4.5° apart along a radius of 100 mm. All sampling tubes are the same size, and the tube openings are filed to sharp edges. The radial patternator is more completely described in ref. 5.

3.3 Circumferential Patternator

The circumferential distribution of liquid from the conical-sheet atomizer was measured using a circumferential patternator which consists of a clear acrylic cylinder, closed at the bottom and open at the top, and divided into 16 equal pie-shaped cavities. Equal-spaced lines are scribed into the outer wall of the cylinder from the bottom of the cavities to the top. These lines provide a convenient means for measuring the relative liquid volume in each cavity. During data collection, the patternator is mounted under the atomizer with the axis of the patternator on the spray axis. The circumferential patternator is more completely described in ref. 5.

3.4 Drop Sizing Instrumentation

Drop size measurements of the sprays were made using a Malvern Particle Size Analyzer, model 2600D, manufactured by Malvern Instruments Ltd. This well-known instrument provides a nonintrusive line-of-sight measurement based on Fraunhofer diffraction theory. The receiver of the Malvern system is fitted

with a 300 mm focal length lens which allows measurement of a drop size range from 5.8 to 564 μm.

The drop size distributions of the sprays produced in atomization can be represented by the Rosin-Rammler [Ref.6] q parameter. The q parameter provides a measure of the range of drop sizes in a spray. The higher the value of q, the more equal are the drop sizes and the more narrow is the drop size distribution. If $q = \infty$, all the drops in the spray are the same size. For most fuel sprays the value of q is between 2 and 4 [Ref. 7].

The two-parameter Rosin-Rammler data reduction routine resident in the Malvern system was used to obtain "measured" drop size data from the light intensities directly measured by the Malvern system. All the "measured" values of Sauter mean diameter (SMD) and the Rosin-Rammler drop size distribution parameter, q, were corrected for the effects of multiple scattering. The method of correction suggested by Dodge [Ref.8] was used when the obscuration of the incident light beam was between 40 and 65 percent, and the method suggested by Felton et al. [Ref. 9] was employed when the obscuration was 65 percent or greater. The correction method suggested by Felton et al. is based on a theoretical model and is preferred, when applicable, to the empirical solution provided by Dodge. However, Felton et al. cautioned against the use of their correction method for obscurations less than 65 percent. The method presented by Dodge allows correction of the results when obscuration is between 40 and 65 percent and reduces the sudden change in SMD that occurs at an obscuration of 65 percent if the Felton et al. correction is used alone.

4. RESULTS

4.1 Plain-Orifice Atomizer

In all experiments with the plain-orifice atomizer, the liquid employed was water. Atomizer operation was investigated along lines of constant pressure with increasing ALR. The operating pressures ranged from 138 to 689 kPa, and atomizer operation was investigated across a range of ALR from zero to over 0.4. Several operating characteristics were observed and noted across the full range of nozzle operation. These characteristics include the steadiness of the spray, visual observation of the internal two-phase flow, steadiness of the air cavity and water inlet pressures, and any other visual or audible signs that might indicate a change in the spray. The operational parameters and characteristics, along with the information furnished by the Malvern particle size analyzer, provide a good basis for describing the performance of the atomizer.

At the low pressures employed in this investigation, operation of the plain-orifice atomizer with no atomizing air produced only solid jets of water. With the addition of only a very small amount of air, the water jets were broken into a coarse spray. As the ALR was increased with the operating pressure held constant, three regimes of atomizer operation, as defined by changes in the spray behavior, were identified. These differences in spray behavior were the result of changes in the internal two-phase flow. The three regimes are designated as follows: bubbly flow regime, transition regime, and annular flow regime.

Effervescent atomization occurs only in the bubbly flow regime, but investigation of atomizer operation across a wide range of ALRs provides some insight into how the atomizer functions. The bubbly flow regime occurred at low ALRs. The sprays produced during operation in the bubbly flow regime were steady. In the bubbly flow regime the internal two-phase flow appeared, by visual observation, to be well mixed and uniformly distributed within the mixing tube. The exact flow pattern present across the full range of ALR in the bubbly flow regime could not be determined with certainty, but all indications suggest that the internal flow pattern that occurred in this regime could be classified as a bubbly flow pattern. As the ALR was increased across the bubbly flow regime, a point was reached where the atomizer operation and spray became unstable. This point marks the onset of the transition regime which is so-named because it signifies the transition between a stable bubbly flow regime and a stable annular flow regime. The transition regime may consist of several commonly observed internal two-phase flow patterns, including slug flow, plug flow, and churn flow. The annular flow regime occurred at high ALRs where the instabilities observed during operation in the transition regime were no longer present. Although the exact flow pattern present at the onset of the annular flow regime could not be determined with certainty, an annular flow pattern was observed at slightly higher values of ALR.

Drop size measurements for the plain-orifice atomizer were made at operating pressures of 138, 276, 414, 552, and 689 kPa. All drop size measurements reported in this paper for the plain-orifice atomizer were made in the bubbly flow regime, where effervescent atomization occurs. The light beam was positioned to take measurements across the axis of the spray emitted from one orifice at a distance of 152 mm downstream from the nozzle, as measured along the length of the spray axis. The flow rate of water from each orifice was measured to select a single orifice that was representative of all orifices. Since the liquid in a spray is much more difficult to collect than a jet of liquid, the flow rate check was performed with no atomizing air. The results of this check for two water flow rates showed that each of the four orifices flowed within 1 per cent of one quarter of the total flow. Thus, all four orifices were regarded as acceptable and one was chosen at random.

The effect of ALR and pressure on SMD while operating in the bubbly flow regime is illustrated in Fig. 4. The highest ALR shown for each pressure represents the end of the bubbly flow regime for that operating pressure. Figure 4, as expected, shows that SMD decreases as ALR increases. Changes in operating pressure have only a small effect on SMD, with an increase in pressure resulting in a decrease in SMD. Figure 4 contains all the SMD data taken with the 4-hole orifice in the bubbly flow regime. The validity of the SMD data presented for the lower ALRs in Fig. 4 is questionable because the light intensity distribution recorded by the Malvern Particle Size Analyzer had a bimodal shape that suggested the increased presence of large drops. The Rosin-Rammler data reduction routine, which was used in this study, is not suitable for a bimodal-shaped distribution. The value of ALR below which a bimodal-shaped light intensity distribution was recorded varied somewhat depending on operating pressure. As an example, the bimodal-shaped distribution occurred for ALRs lower than 0.011 at 689 kPa and for ALRs lower than 0.017 at 276 kPa. The SMD data at these lower ALRs is shown in Fig. 4 only to indicate approximate trends in SMD at these lower ALRs.

Figure 5 presents q as a function of ALR at four different pressures for the plain-orifice atomizer with the 4-hole orifice operating in the bubbly flow regime. All q values shown in Fig. 5 are from measurements with a monomodal-shaped light intensity distribution. Figure 5 shows that changes in operating pressure and ALR have little effect on q with all values ranging between 1.5 and 1.8.

As previously stated, one objective of this study is to determine if good atomization can be achieved using effervescent atomizers that turn the two-phase flow through an angle just prior to ejection. The plain-orifice atomizer fitted with the 4-hole orifice described in this study has also been fitted with a single-hole orifice [Ref. 5] for similar experiments. The atomizer showed the same general operating characteristics with the single-hole orifice and the 4-hole orifice; but, for the same ALR and operating pressure, the single-hole orifice produced a spray with lower SMD values in the bubbly flow regime (down to approximately 25 μm) and operated at lower ALRs without the greatly increased presence of large drops identified by the bimodal-shaped light intensity distribution as described above. The 4-hole orifice was the first attempt to achieve a wide spray angle with the effervescent atomizer and the exit holes were not optimized. The l/d ratio of 5 that the 4-hole orifice has is

considerably larger than the single-hole orifice's l/d of 0.5. A smaller l/d may improve atomization quality or increase the range of ALRs that gives good atomization in the bubbly flow regime.

4.2 Conical-Sheet Atomizer

The liquid employed in all experiments with the conical-sheet atomizer was water. Operation of the conical-sheet atomizer was investigated along lines of constant pressure with increasing ALR at several discharge gap widths. Observations of the operating and spray characteristics were made during the collection of drop size data. These observations, along with the information furnished by the Malvern system, provide a good basis for describing the operation of the atomizer. Atomizer operation is described below for a range of parameters, including operating pressures from 69 to 552 kPa, gap widths from 0.10 to 0.37 mm, and ALRs from zero to as high as 0.12 at some pressures.

Atomizer operation with no air injection (ALR = 0), at the low pressures examined in this investigation, showed that the liquid exited the atomizer in the form of a conical sheet which subsequently broke up into large drops several centimeters downstream. With the addition of only a very small amount of air, the continuous liquid sheet was sporadically disrupted at the atomizer exit by the expanding gas bubbles. As the ALR was increased, the greater quantity of air in the internal two-phase flow caused more thorough breakup of the liquid sheet and eventually produced a finely atomized spray with liquid breakup occurring at the atomizer exit.

The conical-sheet atomizer exhibited smooth and continuous changes in spray properties across all pressures, gap widths, and ALRs investigated, with no regions of unstable operation. This continuously stable atomizer operation was unlike the plain-orifice atomizer where changes in the internal two-phase flow caused the spray to become unsteady. The range of ALRs over which atomizer operation was investigated was smaller with the conical-sheet atomizer than with the plain-orifice atomizer because of flow limitations of the experimental apparatus, but the conical-sheet atomizer operated steadily at ALRs where the plain-orifice atomizer operation was unsteady and classified as being in the transition regime. Since the two-phase flow passage in the conical-sheet atomizer was machined from brass, no observations of the internal two-phase flow were possible. No previous work was found on the classification of flow patterns in downward cocurrent two-phase flow in an annular flow passage. The nature of the two-phase flow pattern present in the atomizer across its range of operation is thus unknown. Based on previous work with circular flow passages, a bubbly flow pattern most likely exists at the lower ALRs. At the higher ALRs however, a bubbly flow pattern is unlikely because of the higher void fractions. For example, an operating point with an ALR of 0.05 and a pressure of 138 kPa has an average void fraction of 0.946 which is considerably higher than previously reported for a bubbly flow pattern. One possible explanation for the absence of any region of unstable operation is that the annular flow passage and exit throat may moderate the effects of detrimental flow patterns that might be formed, such as slug flow, by providing an area around the annulus for the large air voids to spread out and possibly break up. The air and liquid may also distribute themselves differently in an annular flow passage and never form flow patterns which cause noticeable unsteadiness in the spray. Another possibility is that the exit slot spreads out large liquid slugs which are then broken up by the atomizing air. In any case, the flow instabilities that occurred with the plain-orifice atomizer were outside the range of effervescent atomization.

Liquid is discharged from the exit throat of the conical-sheet atomizer to form a hollow cone spray where most of the droplets are concentrated around the outer edge of a conical spray pattern. One of the advantages of this atomizer is that the angle of the internal flow passage may be designed to give virtually any desired spray angle. The radial patternator described above was used to give an approximation of the angle of the spray emitted from the conical-sheet atomizer. All measurements were taken with no atomizing air because of the difficulty of obtaining reliable measurements from the sprays produced with air injection. With no atomizing air the liquid was concentrated in the form of a conical sheet, and spray angles were measured by observing which patternator sampling tube and the location within that tube that the liquid entered (ref. 5 gives a more complete description of the procedure). Measurements were made at five gap widths from 0.10 to 0.29 mm, with operating pressures varying from 138 to 552 kPa at some gap widths. The measured spray angle increased with increasing gap width from 78.5° at 0.10 mm to 86.5° at 0.29 mm. Variations in pressure had no effect on the spray angle. The measured spray angles were within the range expected since the exit of the atomizer body was machined to an angle of 70° and the atomizer stem had an angle of 90°. When air was added to the liquid upstream of the exit throat, the spray dispersed about the conical path defined by the liquid sheet with no air addition.

The circumferential distribution of liquid emitted from the conical-sheet atomizer was measured using the circumferential patternator. All measurements were taken without atomizing air to eliminate the problem of drops recirculating out of the patternator that occurred when air injection was used. Figure 6 shows the volume flow rate measured by the circumferential patternator as a function of patternator section at three gap widths. The volume flows were normalized by the average flow collected in all sections. The data shown in Fig. 6 were taken at an operating pressure of 276 kPa. Measurements at 138 and 552 kPa showed similar results. This plot illustrates that a fairly even distribution of liquid was discharged from the annular exit throat with the only discrepancy occurring at sections 11 through 13. This even distribution of liquid indicates proper alignment of the stem within the atomizer body giving a constant gap width around the annulus of the exit throat.

Measurements of SMD were made across a range of parameters which included four gap widths from 0.10 mm to 0.37 mm and four operating pressures from 69 kPa to 552 kPa. The range of ALRs investigated at each pressure varied because of flow limitations of the experimental apparatus, but all measurements were within a range of ALRs from 0.001 to 0.12. The light beam was positioned to take measurements along a horizontal path passing through the axis of the spray 152 mm below the atomizer exit. To assure an accurate representation of the spray, drop size measurements were taken with the atomizer rotated about the spray axis to several positions, as described below. The width of the spray cone at 152 mm below the atomizer exit required that a light guide be used to keep the length of the sampling volume within 300 mm of the Malvern receiver lens. The light guide was a steel tube mounted horizontally that shielded the laser beam from half of the spray so that the sampling volume started at the axis of the spray cone.

The dependence of SMD on ALR and operating pressure is illustrated in Figs. 7 through 10 where SMD is plotted as a function of ALR for four pressures. Each figure presents a different gap width with the atomizer body held at a fixed position termed Position A. These plots show that SMD decreases as ALR increases at low values of ALR, but tends to level off at the higher ALRs. At some pressures, measurements were made at ALRs up to 0.12. Data at these higher values of ALR continued to show the trend of leveling off and are not presented here to avoid compressing the graphs. The data also show that the general effect of an increase in operating pressure is to decrease the SMD.

Drop size measurements were made at several ALRs lower than those shown in Figs. 7 through 10, but the light intensity distribution recorded by the Malvern system had a bimodal shape which indicated a substantial increase in the number of large drops. The bimodal shape at these lower ALRs indicates that the spray was not fully developed. The Rosin-Rammler data reduction routine is not suitable for a bimodal-shaped

distribution, and SMD values calculated for these points are not shown.

Drop size measurements were also taken with the atomizer rotated 100° about the spray axis from Position A so that the Malvern system was sampling data at a different location in the spray. This alternative position is designated as Position B. The trends in SMD shown at Position B were generally the same as those shown at Position A. This may be observed by comparing Figs 8 and 11.

The effect of gap width on SMD is illustrated in Fig. 12 where SMD is plotted as a function of ALR for four gap widths. This plot presents spray data for a constant operating pressure of 276 kPa with the atomizer located in Position B. Inspection of all the SMD data obtained over a range of pressures from 69 to 552 kPa shows that the influence of gap width on SMD decreases as pressure or ALR increases. At the lowest pressure examined, 69 kPa, data at ALRs less than 0.04 show that the larger gap widths produce sprays with larger SMDs; but at ALRs greater than 0.04, gap width appears to have no effect on SMD. At pressures of 138 and 276 kPa, the influence of gap width on SMD progressively decreases until, at a pressure of 552 kPa, gap width has no noticeable effect on SMD.

The Rosin-Rammler q parameter calculated from measurements made with the Malvern particle size analyzer is used to represent the drop size distribution of the spray produced by the conical-sheet atomizer. Figure 13 is typical of the results obtained. For pressures from 69 to 552 kPa and gap widths from 0.10 to 0.37 mm, most q values lie between 1.5 and 2.0, although some values at 69 kPa are as high as 2.3. Air/liquid mass ratio has only a small effect on q, with all values at a given pressure and gap width falling within a range of approximately 0.3. In general, q decreases with increases in pressure.

The influence of gap width on q is illustrated in Fig. 14 where q is plotted as a function of ALR for four gap widths. Examination of these and other data show that, in general, an increase in gap width reduces q.

5. CONCLUSIONS

Experimental results for the 4-hole plain-orifice atomizer operating in the bubbly flow regime show that SMD decreases with an increase in either ALR or operating pressure. The effect of ALR on SMD decreases as the value of ALR is increased. The q values in the bubbly flow regime are almost independent of ALR and operating pressure. The most significant result with this atomizer is that good atomization can be achieved with an orifice that turns the two-phase flow through an angle just prior to ejection.

The conical-sheet atomizer was investigated over a range of operating pressures from 69 to 552 kPa, gap widths from 0.10 to 0.37 mm, and ALRs from zero to as high as 0.12 at some pressures. No major changes in spray behavior were identified across this range of ALR. This result was somewhat surprising considering that the experiments included some values of ALR where the expected internal two-phase flow patterns should have caused unstable atomizer operation similar to that which occurred during the transition regime identified with the plain-orifice atomizer. This lack of unstable atomizer operation indicates that the two-phase flow in the conical-sheet atomizer is inherently more stable for atomization purposes than that in the plain-orifice atomizer. One possible explanation for the absence of any region of unstable atomizer operation is that the annular flow passage and annular exit throat may moderate the effects of detrimental flow patterns that might be formed, such as slug flow, by providing an area around the annulus for the large air voids to spread out and possibly break up. The air and liquid may also distribute themselves differently in an annular flow passage and never form flow patterns which cause noticeable unsteadiness in the spray. Another possibility is that the annular exit throat spreads out large liquid slugs which are then broken up by the atomizing air.

Drop size measurements on the conical-sheet atomizer showed the following trends. Sauter mean diameter decreases with an increase in either ALR or operating pressure. As with the plain-orifice atomizer, the effect of ALR on SMD decreases as the value of ALR increases. At low values of both pressure and ALR, SMD increases with increases in gap width. The influence of gap width on SMD decreases with an increase in either pressure or ALR. Above an ALR of 0.04, gap width has no effect on SMD regardless of pressure. At the highest pressure investigated (552 kPa), SMD was independent of gap width for all ALRs. Air/liquid mass ratio has only a small effect on the Rosin-Rammler q parameter. Operating pressure also has a weak influence on the value of q, with an increase in pressure producing a small decrease in q. In general, an increase in gap width results in a small decrease in q.

6. REFERENCES

1. Lefebvre, A. H., Wang, X. F., and Martin, C. A., "Spray Characteristics of Aerated-Liquid Pressure Atomizers", *AIAA Journal of Propulsion and Power*, Vol. 4, No. 4, July-August 1988, pp. 293-298.

2. Wang, X. F., Chin, J. S., and Lefebvre, A. H., "Influence of Gas-Injector Geometry on Atomization Performance of Aerated-Liquid Nozzles", *International Journal of Turbo and Jet-Engines*, Vol. 6, Nos. 3 and 4, 1989, pp. 271-279.

3. Roesler, T. C., and Lefebvre, A. H., "Studies on Aerated-Liquid Atomization", *International Journal of Turbo and Jet-Engines*, Vol. 6, Nos. 3 and 4, 1989, pp. 221-229.

4. Lefebvre, A. H., *Atomization and Sprays*, Hemisphere, Washington D.C., 1989.

5. Whitlow, J. D., "An Experimental Investigation of Internal-Mixing, Twin-Fluid Atomization", MSME Thesis, Purdue University, 1990.

6. Rosin, P., and Rammler, E., "The Laws Governing the Fineness of Powdered Coal", *Journal of the Institute of Fuel*, Vol. 7, No. 31, 1933, pp. 29-36.

7. Lefebvre, A. H., *Gas Turbine Combustion*, Hemisphere, New York, 1983.

8. Dodge, L. G., "Change of Calibration of Diffraction-Based Particle Sizers in Dense Sprays", *Optical Engineering*, Vol. 23, No. 5, September-October 1984, pp. 626-630.

9. Felton, P. G., Hamidi, A. A., and Aigal, A. K., "Measurement of Drop Size Distribution in Dense Sprays by Laser Diffraction", *Proceedings 3rd International Conference on Liquid Atomisation and Spray Systems* (ICLASS-85), London, 1985, IVA/4/1-11.

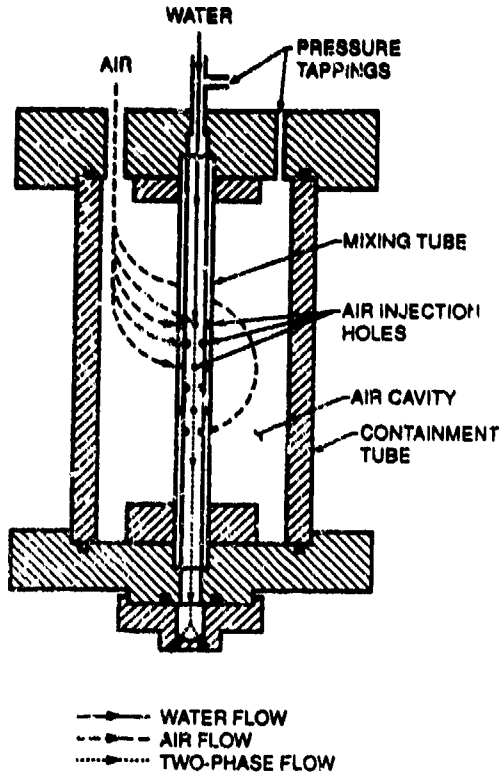

Fig. 1 4-hole plain-orifice atomizer.

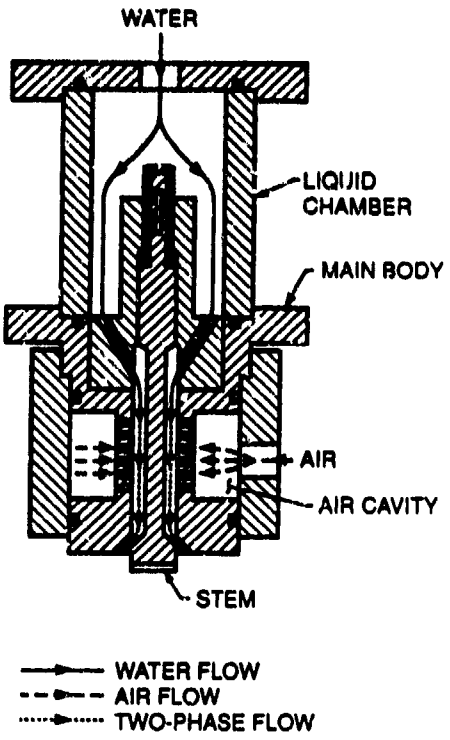

Fig. 2 Conical-sheet atomizer

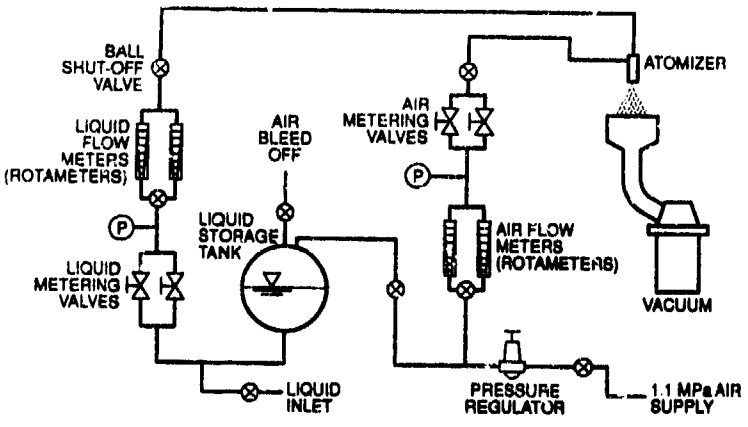

Fig. 3 Schematic diagram of test facility

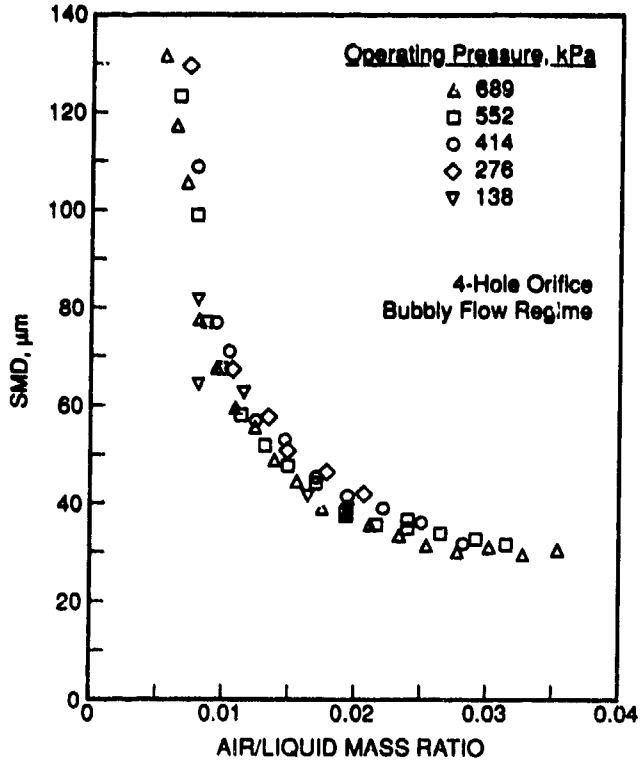

Fig. 4 SMD versus air/liquid mass ratio for the plain-orifice atomizer

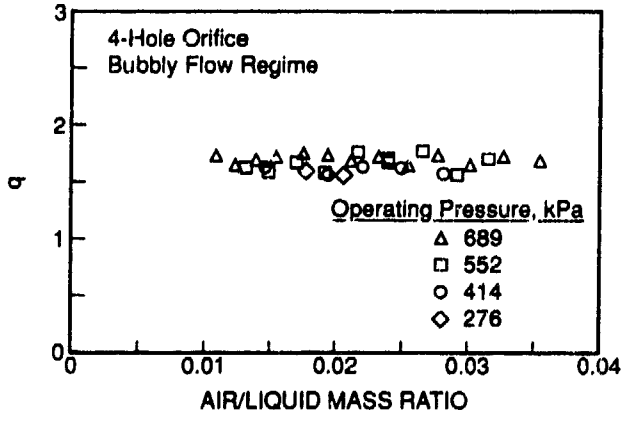

Fig. 5 Effect of air/liquid mass ratio and operating pressure on drop size distribution

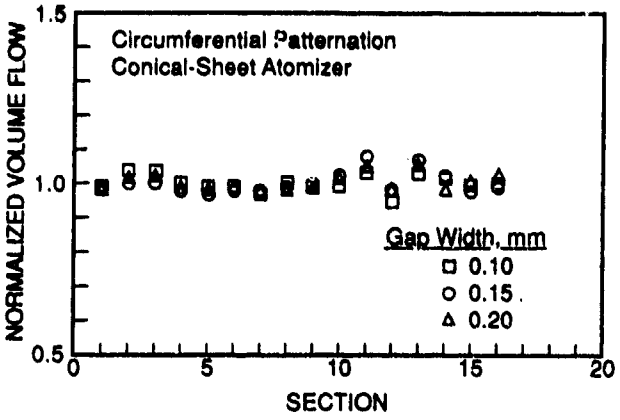

Fig. 6 Circumferential liquid distribution of conical-sheet atomizer

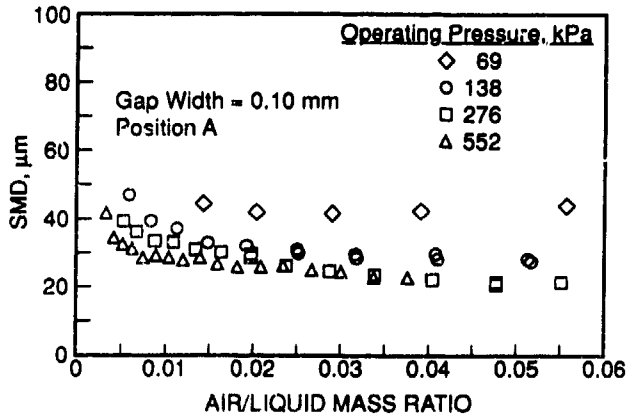

Fig. 7 SMD data for conical-sheet atomizer with a gap width of 0.10 mm

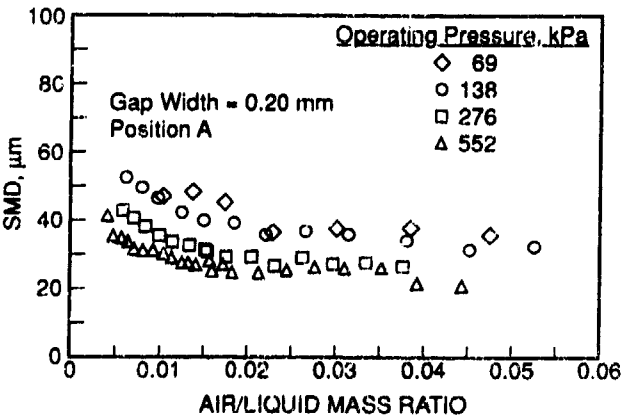

Fig. 8 SMD data for conical-sheet atomizer with a gap width of 0.20 mm

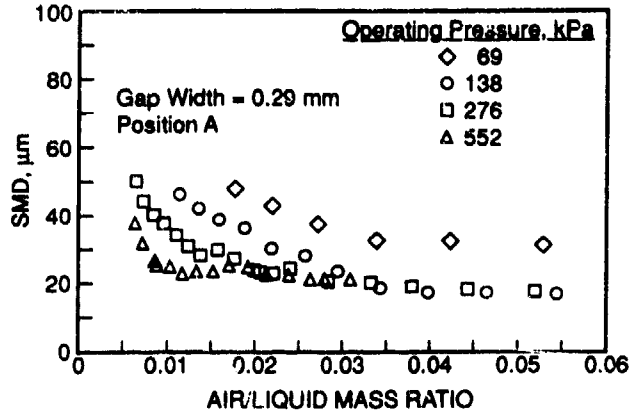

Fig. 9 SMD data for conical-sheet atomizer with a gap width of 0.29 mm

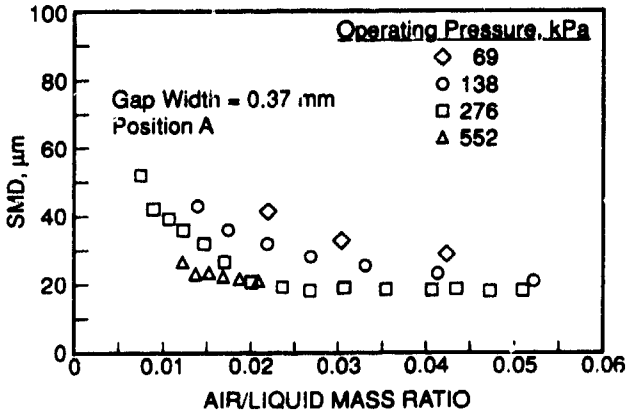

Fig. 10 SMD data for conical-sheet atomizer with a gap width of 0.37 mm

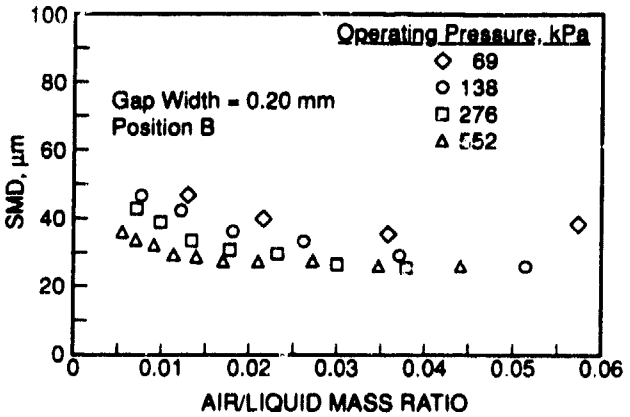

Fig. 11 SMD data for conical-sheet atomizer at position B

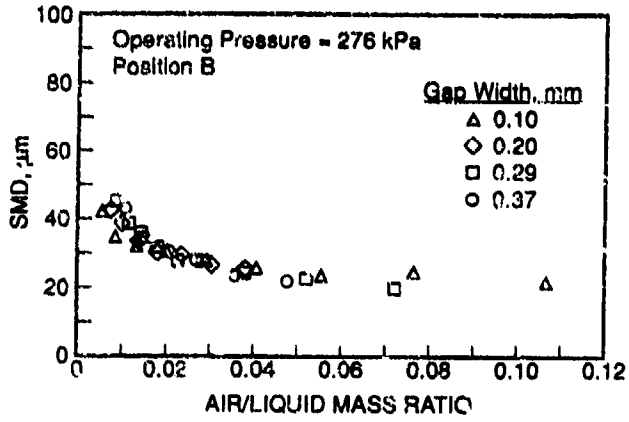

Fig. 12 Effect of gap width on SMD for conical-sheet atomizer

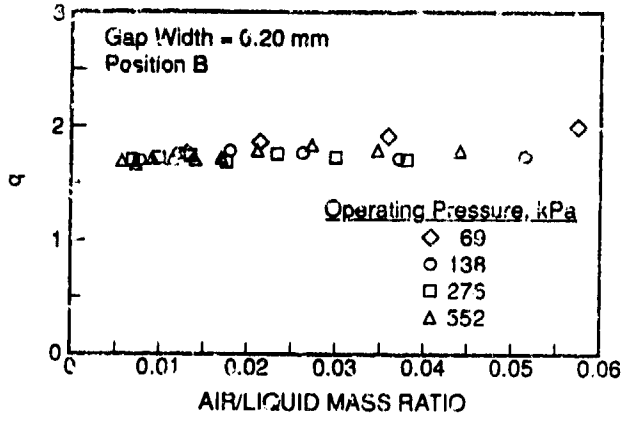

Fig. 13 Effect of operating pressure on drop size distribution for conical-sheet atomizer

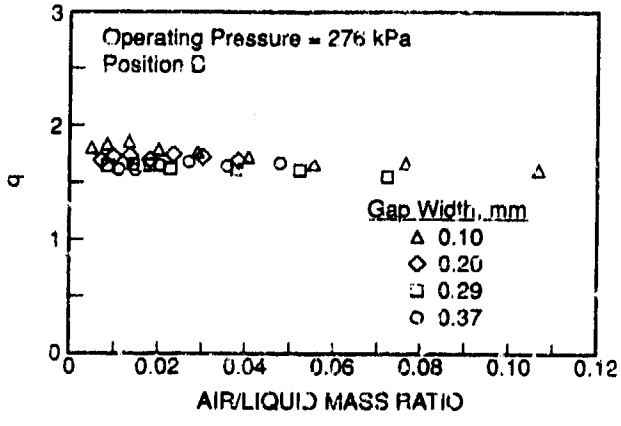

Fig. 14 Effect of gap width on drop size distribution for conical-sheet atomizer

Discussion

Question 1. K. Jeckel
In what range can the fuel mass flow be varied without strongly affecting the dropsize? What is the advantage of this system compared to pressure and airblast atomizers?

Author's Reply
Unlike pressure atomizers which lack the ability to achieve good atomization over a wide range of fuel flows, the quality of atomization from an effervescent atomizer is a function of air/liquid mass ratio as well as injection pressure. Also, the injection pressure in an effervescent atomizer is a function of the rates of both the liquid and the atomizing gas. These factors provide the opportunity to achieve good atomization over a wider range of fuel flow rates. The range over which good atomization can be produced is dependent on the design and operating characteristics of the particular atomizer.

Effervescent atomizers have the ability to achieve good atomization at lower pressures than pressure atomizers, and, since both the liquid and the atomizing gas are ejected through the same exit, the flow passages in the atomizer can be made larger which reduces the problem of blockage by fuel contaminents.

Advantages of effervescent atomizers over airblast atomizers include the ability to achieve good atomization at relatively low air/liquid mass ratios, plus larger flow passages which reduce blockage problems.

Question 2. S. Sivasegaram
The SMD values obtained with the Malvern instrument are subject to some uncertainty relating to the assumed droplet size distribution. Were any of your results compared with measurements using the Phase-Doppler method?

Author's Reply
No spray measurements of either of the two experimental atomizers used in these studies were taken with a Phase Doppler Particle Analyzer. Except where noted in the paper, the light intensity distribution recorded by the Malvern Particle Size Analyzer indicated that the Rosin-Rammler distribution model was appropriate for all data presented in this paper. The data reduction routine resident on the Malvern system calculates and presents an error term for the data fit to the assumed distribution model. Except for the data points noted in the paper as having questionable validity, the error term for all presented data is low with the Rosin-Rammler distribution model. These low values of the error term are further indication that the Rosin-Rammler distribution model is appropriate. For the experimental atomizers employed in these studies, the general level of the SMD achieved and the trends in atomization quality are more important than the exact value of the data points.

THE MIXING PROCESS IN THE QUENCHING ZONE OF THE RICH-LEAN-COMBUSTION CONCEPT

by

Th. Doerr and D.K. Hennecke
of Flight Propulsion
Technical University Darmstadt
Petersenstrasse 30
6100 Darmstadt
Germany

Abstract

The RQL-combustion system is a potential concept to reduce both NO_x and CO, UHC emissions. In view of the concept's crucial mixing process, an experimental investigation of a non-reacting multiple jet mixing with a confined crossflow has been conducted. Temperature distributions, mixing rate and standard deviation were determined for measurements with round jet orifices by parametric variation of flow and geometric conditions. The results show that best mixing strongly depends on an optimum momentum flux ratio. Too high ratios yield a deterioration of mixing process, due to the mutual impact of opposed entraining jets. Furthermore, over a wide range of geometries investigated, inline and staggered configurations provide similar mixing rates. An appreciable enhancement of mixing with staggered orifice configurations only occurs for high momentum flux ratios and large spacings.

Nomenclature

A_j	jet orifice area
A_∞	mainstream area
c_D	discharge coefficient
d	jet diameter
h	height of duct
J	momentum flux ratio $= (\rho_j/\rho_\infty)\cdot(v_j/v_\infty)^2$
s	spacing of jet centerlines
$\dot{m}_j$	jet massflow
$\dot{m}_\infty$	mainstream massflow, before mixing
n	number of data points in y-z-plane
T_i	local temperature
T_j	jet temperature
T_{adb}	adiabatic, ideal mixing temperature

$$T_{adb} = \frac{m_\infty \cdot T_\infty + \dot{m}_j \cdot T_j}{\dot{m}_\infty + \dot{m}_j}$$

T_∞	mainstream temperature, before mixing
v_j	jet velocity
v_∞	mainstream velocity, before mixing
w	width of duct
x	downstream location from jet centerline
y	lateral distance from middle of channel
z	vertical distance from middle of channel
ε_i	local mixing rate
ε	overall mixing rate
ρ_j	jet flow density
ρ_∞	mainstream density
σ	standard deviation from ideal mixing temperature
Θ_i	dimensionless, local temperature

Introduction

Alteration of the high tropospheric and stratospheric chemistry combined with the depletion of the Earth's protective ozone layer require the scrutiny of emissions from aircraft engines. Conventional aviation releases pollutants at altitudes where the chemical balance of the atmosphere is extremely sensitive [1]. Continuously improving the efficiency of gas turbines by increasing turbine inlet temperatures along with higher pressure ratios raised the levels of emitted NO_x while diminishing the rate of CO and UHC. New combustion systems must be developed to reduce both NO_x and CO / UHC pollutants. This holds true not only for high speed civil transport (HSCT) [2,3]. The stoichiometric operation of the primary zone has to be avoided due to the strong temperature dependance of thermal NO_x formation (Zeldovich mechanism). The most promising combustor approaches to reduce NO_x emittance up to 10% of common levels are the lean premixed/prevaporized (LPP) and the rich burn/quick quench/lean burn (RQL) -combustion systems [4]. Significant drawbacks of the LPP- combustor include flame stability, altitude relight and flashback problems. This recently led to increasing emphasis on the RQL-research, which originally was conceived for burning high fuel-bound-nitrogen fuels in stationary gas turbines [5,6].

The RQL-combustion initially takes place under fuel-rich conditions with equivalence ratios above 1.3 in order to lower primary zone temperature and the formation of thermal NO_x. The primary zone is followed by the quick mixing with additional air in the quenching sec-

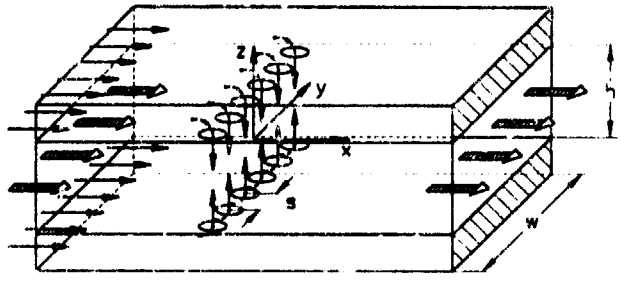

Fig. 1 Schematic of multiple jet mixing

Presented at an AGARD Meeting on 'Fuels and Combustion Technology for Advanced Aircraft Engines', May 1993.

tion to achieve lean conditions in the secondary zone.
The combustion is completed operating at an equivalence ratio of 0.5 to 0.7. Thus, pollutants are reduced formed by partial burning.
Besides difficulties in cooling the liner of the primary zone without film cooling, the predominant problem consists in the rapid and intense mixing of air injected between the stages.
Therefore, an investigation of a multiple jet injection into a crossflow without chemical reaction is presented, in order to examine favourable parameters for mixing.

Basic Considerations

A considerable amount of effort has been devoted in the past to jet mixing, e.g. [7,8,9]. The major distinction in previous investigations has been, that injected massflow to mainstream ratio is about 2, which can hardly be realized by one row of opposing jets. At least 3 opposing rows of circular jets are required in the mixing module. In the present paper, basic studies with corresponding massflow of one row of opposing jets are presented. Keeping mainstream conditions constant, orifice size and spacing are varied.
In comparison to the concentration difference of the streams in the RQL-combustor the mainstream is heated up, using temperature as an indicator of mixing. It enters the test section with a temperature of 325K and a velocity of 19 m/s ($Re_\infty = 10^5$), while jets are injected with a temperature of 300 K.
The density ratio ρ_j/ρ_∞ is about 1. In so far as momentum flux ratio is unaffected, the influence of density ratio on mixing is neglected [7]. Combustion-caused pressure drops across the liner (≈3%) and density ratios of 3 provide high momentum flux ratios, especially for the first row of jets in the mixing zone. Hence, main effort was concentrated on geometries for high momentum flux ratios up to 180, according to the application. The measurements in the mixing zone are carried out by traversing a temperature probe in the y-z-plane at different locations x/h (fig. 1).
The dimensionless temperature distributions are expressed in terms of

$$\Theta = \frac{1}{n} \sum_{i=1}^{n} \frac{T_i - T_j}{T_\infty - T_j}$$

To get a criterion for the degree of mixing in the y-z-plane the local ε_i and overall mixing rate ε are defined with

$$\varepsilon_i = \begin{cases} \dfrac{T_i - T_j}{T_{adb} - T_j} & \text{for } T_j < T_i < T_{adb} \\ \dfrac{T_i - T_\infty}{T_{adb} - T_\infty} & \text{for } T_{adb} < T_i < T_\infty \end{cases}$$

and

$$\varepsilon = \frac{1}{n} \sum_{i=1}^{n} \varepsilon_i$$

In addition more comparisons to published results [2,11] can be achieved introducing the standard deviation from ideal mixing temperature

$$\sigma = \frac{\sqrt{\dfrac{1}{n} \sum_{i=1}^{n} (T_i - T_{adb})^2}}{T_\infty - T_j}$$

Experimental Facility

The experiments were carried out in the institute's mixing chamber test rig (fig. 2). The airflow is supplied by a radial compressor (max. 2.6 kg/s at 4 bars). By means of throttles, the flow is divided into the jetstream and the mainstream, which is subsequently heated. Upper and lower jetstream and the mainstream pass settling chambers, flow straighteners with nozzles and enter the mixing section (fig. 1).
The atmospheric mixing chamber consists of 3 parallel ducts of constant rectangular cross sections. The test section itself is 300 mm in width and 100 mm in height. The mixing configurations are 2 mm thick plates, which can be exchanged. A 3 axis traversing mechanism can

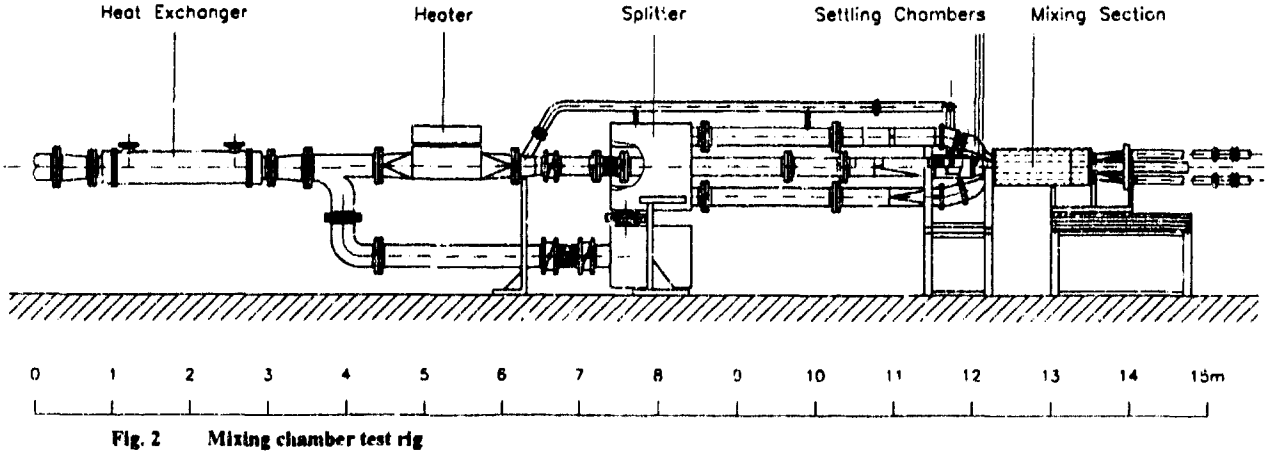

Fig. 2 Mixing chamber test rig

reach y-z-planes over 600 mm in the streamwise direction.
Traversing of the probe, the data acquisition and the operation of the test rig is controlled by a PC 386. For temperature measurements, iron-constantan thermocouples were used. The massflow of each stream was measured by orifice flow meters. Conventional pressure transducers in combination with scanivalve devices provide the pressure acquisition.
The turbulence level of the mainstream was kept constant at 1%. For further investigations the turbulence intensity can be varied up to 10% by a turbulence generator. Moreover it is possible to pass jet massflow around the test section without mixing, to simulate the dilution air supply.

Mixing Configurations

Fig. 3 shows the configurations investigated. Each of the circular orifice planes was analysed with opposing jets inline and staggered. Thus, 12 different configurations were mounted in the test section. The discharge coefficients c_D for all geometries was about 0.63 without - and 0.68 with - crossflow, slightly depending on momentum flux ratio.
Two different test series originally with constant spacing (s/d = 2) and then with constant mass flow (ΣA_j = const.) were conducted.

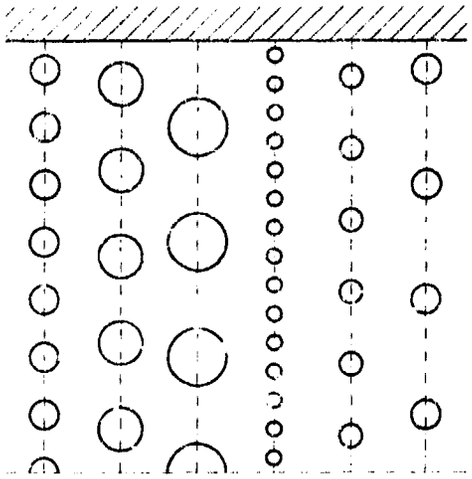

Conf.	1	2	3	4	5	6
h/d	10	6.67	5	20	12.5	10
s/d	2	2	2	2	3.12	4
$\Sigma A_j/A_\omega$	0.078	0.118	0.147	0.039	0.040	0.042

Fig. 3 Mixing configurations

Results and Discussion

For each configuration the momentum flux ratio J was varied to look for optimum ratios and mixing (maximum range investigated J= 5 - 180). Mixing rates and standard deviation were determined over several pitches in the middle of the test section taking a periodical flowfield into account.

A Variation of Momentum Flux Ratio

The mixing rate and standard deviation versus x/h are shown in fig. 4 and fig. 5, respectively with h/d = 6.67 and parametric variation of J.

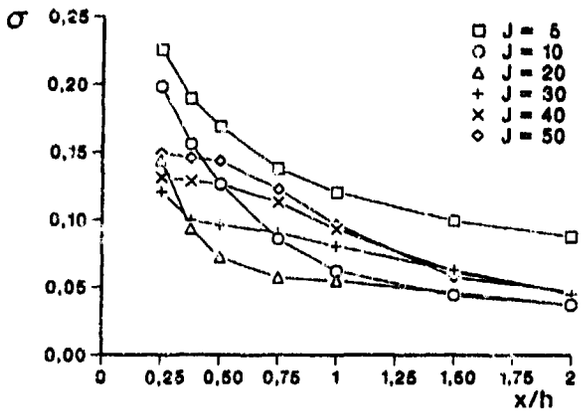

Fig. 4 Standard deviation, configuration 2

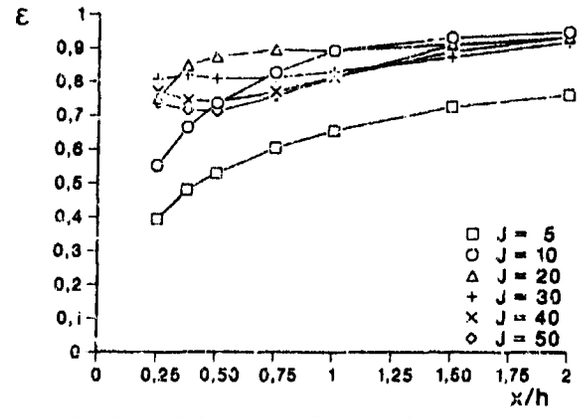

Fig. 5 Mixing rate, configuration 2

In this particular case an optimum J of 20 was observed. In contrast to previous jet mixing investigations [10,11], optimum values of momentum flux ratio occurred for all configurations tested. Exceeding the optimum ratio leads to an impairment of mixing quality. Beyond that, ε and σ show good agreement for all configurations in respect of tendency and optimum values of J. Thus, further results are restricted to presentation of mixing rates.
Fig. 6 shows the Θ-distributions in the y-z-plane for three different momentum flux ratios at several downstream locations x/h. Θ = 0 corresponds to unmixed jet flow; Θ = 1 to mainstream. In the optimum case of J = 20 the cores of the jets are maintained, offering maximum transfer surface between jet and mainstream for thermal equalization. For low ratios of J = 10, the crossflow in the middle of the duct remains unaffected by the entraining jets. At higher momentum flux ratios (J = 40) the jets coalesce and an accumulation of jet flow in the mid axis of the duct is observed. The mainstream passes the mixing section at the sidewalls of the channel. Underpenetration ($J < J_{opt.}$) and overpenetration (J >

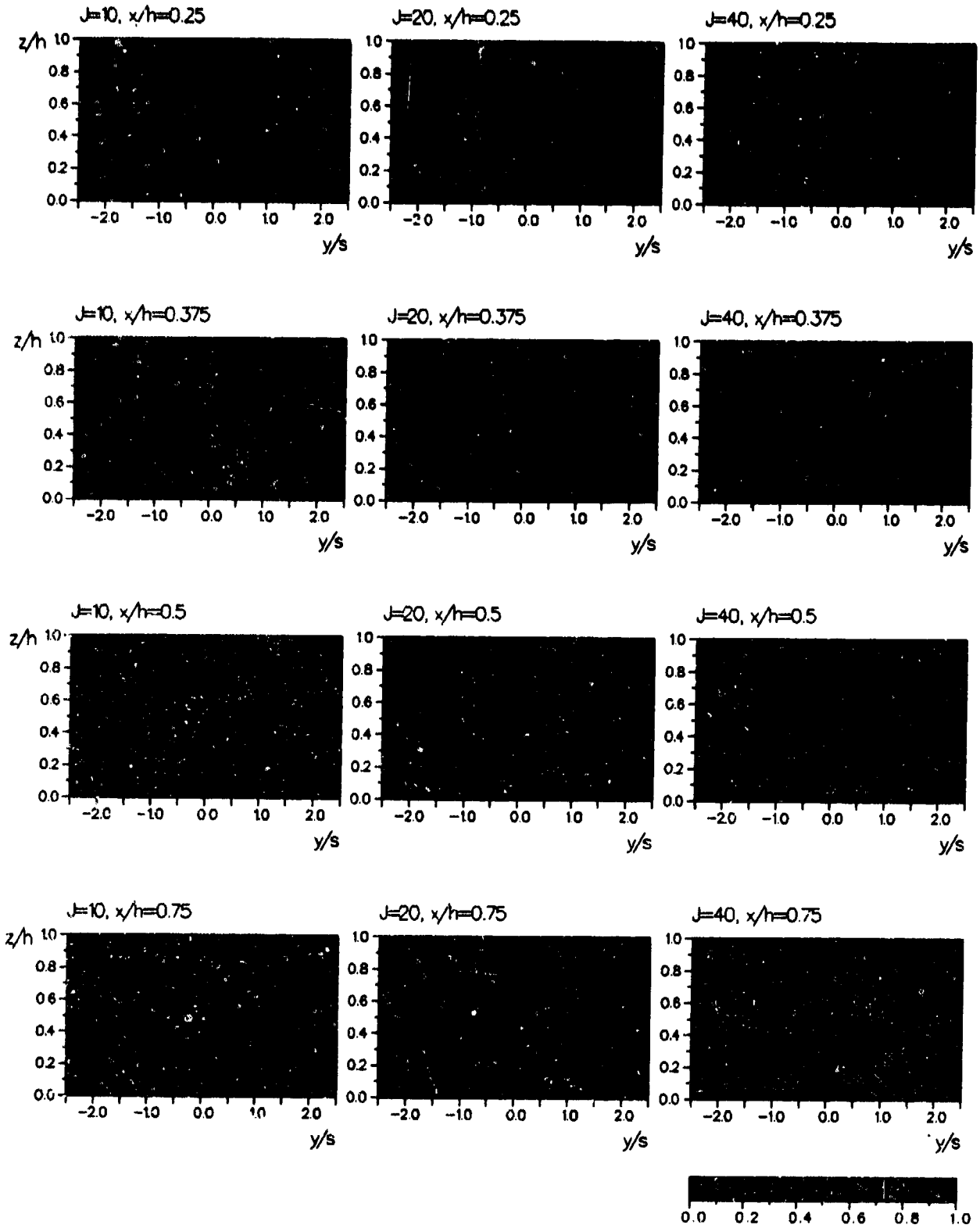

Fig. 6 Θ-distributions, conf. 2, s/d=2, h/d=6.67

$J_{opt.}$) of the jets yield to a thermal stratification of the flowfield. Therefore, this thermal transfer surface between jets and mainstream decreases and the mixing process deteriorates. The three-dimensional jet-injection into the crossflow becomes a two-dimensional mixing layer problem with slow thermal equalization.

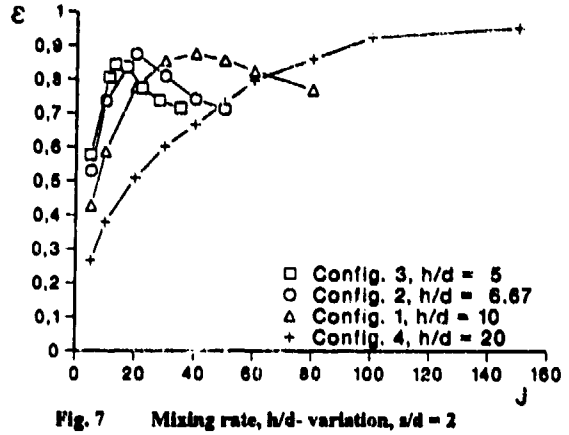

Fig. 7 Mixing rate, h/d- variation, s/d = 2

Fig. 7 shows the mixing rate as a function of J for different geometries h/d, keeping the spacing constant s/d = 2. A characteristic downstream distance of x/h = 0.5 is chosen. The optimum value for J is steadily increasing at high h/d ratios, i.e. smaller jet orifices. A satisfactory mixing rate at high momentum flux ratios of J = 120 - 180 can only be achieved with a geometry of h/d = 20 (fig. 8). For this configuration it is not possible to merge the jets in the midaxis, even for high values of J. The test configurations concentrated on relatively low s/d ratios of 2, because of the high required jet-to-mainstream massflow ratio of the prospective application.

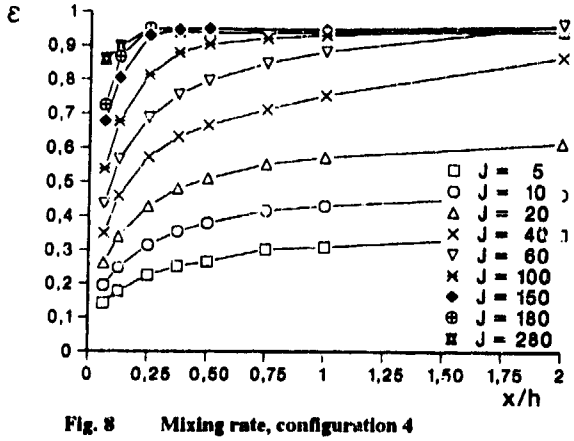

Fig. 8 Mixing rate, configuration 4

B Variation of Discharge Area Distribution

Comparing mixing configurations with different total orifice areas implies different jet-to-mainstream massflow ratios if the momentum flux ratio is kept constant. Therefore, it is difficult to comment on mixing efficiencies while changing massflow ratios. For this reason, a variation of orifice distribution with the configurations 4, 5 and 6 (fig.3) was carried out.

The total discharge area ΣA_j was kept constant [2]. Fig.9 shows the mixing rate vs. x/h for s/d = 4 and h/d = 10.

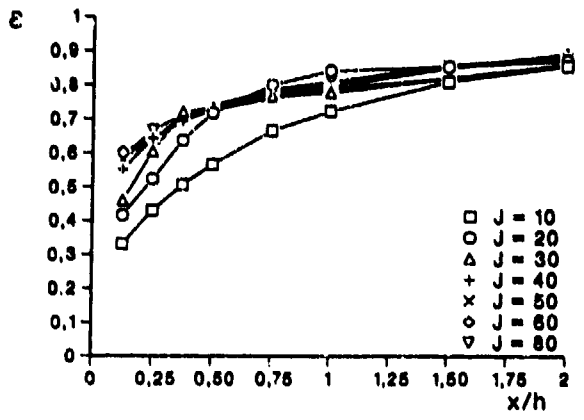

Fig. 9 Mixing rate, configuration 6

Increasing the momentum flux ratio above J = 40 does not change the tendency for ε. The optimum value of J is lower than similar geometry with s/d = 2 (fig.7), due to a smaller blockage effect on the mainstream. For J = 80, jet backflow is observed. In spite of enlarging the mixing region in the upstream direction during jet backflow, mixing efficiency diminishes. Backflow involves local stoichiometric regions in the primary zone with inevitable high NO_x emissions.

Fig. 10 presents a comparison of the configurations 4,5 and 6 with a momentum flux ratio of J = 5 and 50. For low values of J, mixing rate is augmented with high s/d and low h/d ratios, respectively.

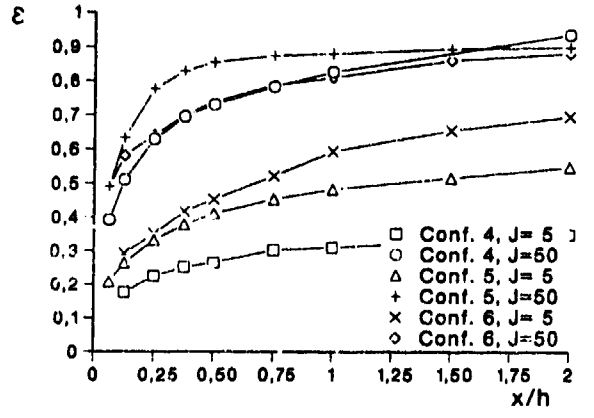

Fig. 10 Mixing rate, variation of area distribution

Increasing the momentum flux ratio (J = 50), best mixing is shifted towards s/d = 3.125 and h/d = 12.5. Mixing for values of J higher than 80 without stratification of the flowfield and jet backflow is only feasible for h/d = 20, s/d = 2 (fig. 8).

In Fig. 11, the case of J = 50 is shown for different geometries at discrete downstream locations. As mentioned for that particular momentum flux ratio, good mixing rates occur at s/d = 3.125 and h/d = 12.5. Smaller orifices (s/d = 2, h/d = 20) lead to underpenetration of the jets and larger hole diameters (s/d = 4, h/d = 10) provide a stratification of the streams, a lower thermal transfer surface and a worse mixing rate.

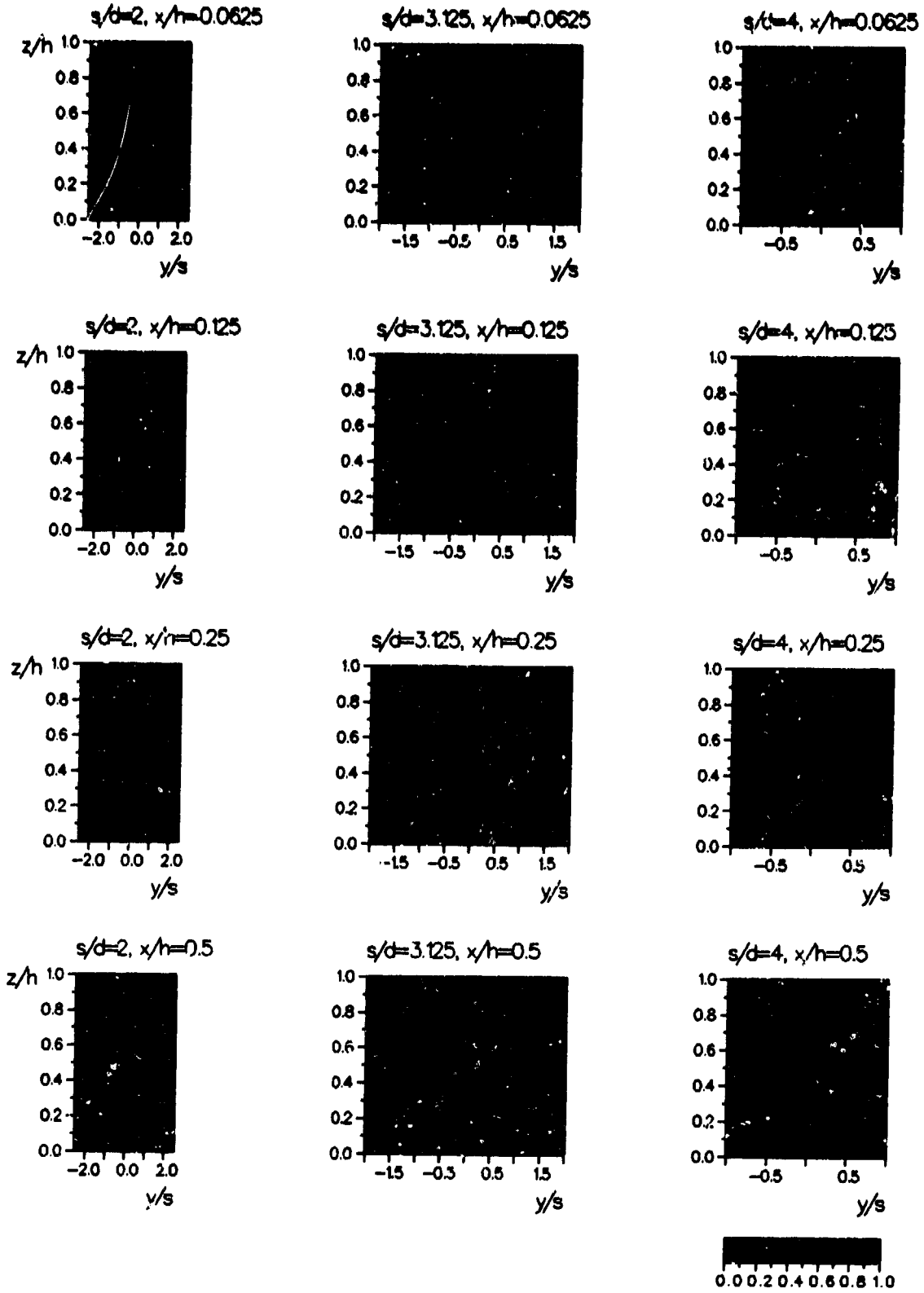

Fig. 11 Θ- distributions, conf. 4,5 and 6, J = 50

C Staggered Configurations

The preceeding results confirm that mixing quality and downstream mixing development basically depend upon maximizing the contact and transfer surface between jets and the mainstream - not upon enlarging of momentum flux ratio. One possibility to enhance this transfer surface is a staggered arrangement of the jets in the rows. Thus, all geometries shown in fig. 3 were tested with inline and staggered configurations.
Fig. 12 compares the mixing rates for both configurations with s/d = 2 and h/d = 20. In the case of underpenetration, the jets do not merge in the mid-axis and no difference in mixing rate between inline and staggered configuration occurs.

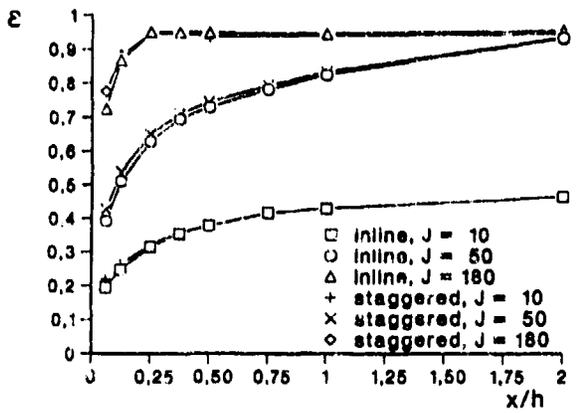

Fig. 12 Mixing rate, conf. 4, inline and staggered

Even for high momentum flux and high h/d ratios with an impact of opposing jets, it is not possible to force the jets to pass one another, due to small spacing and the spread of the entraining jets. By enlarging the spacing between the orifices, jets can cross the opposite row and the mid-plane of the channel.
In Fig. 13, Θ-distributions are illustrated for configuration 6 (s/d = 4) with inline and staggered arrangement. As far as the cores of the opposing jets do not meet in the mid of the channel (J = 40), inline and staggered geometry provide similar results. However, for J = 120 the jets

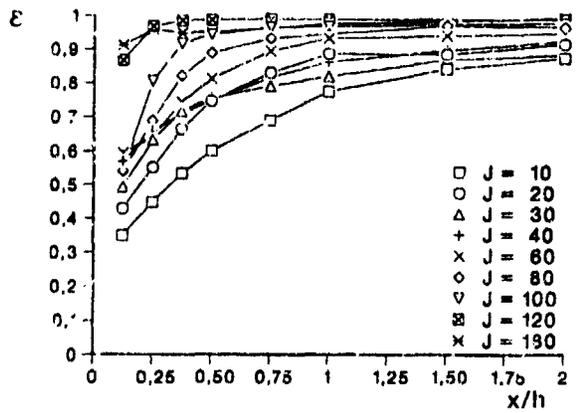

Fig. 14 Mixing rate, configuration 6, staggered

pass the opposing row. As a result of an increase of contact surface between the streams, staggered mixing is intensified, in comparison to the inline configuration.

The mixing rate for the spacing of s/d = 4 is shown in fig. 14. In contrast to fig. 9, it is remarkable that similar tendency, up to momentum flux ratios of J = 40, are observed. For this value of J, the spreading jets meet in the middle of the duct. But, unlike inline geometry, a further increase in J does not leed to a stratification of the flowfield. For high momentum flux ratios, the cores of the jets cross the mid-plane of the channel and mix with the mainstream. Thus, if mixing rates must be optimized, the cores of jets must be well distributed over the y-z-plane, in accordance with the results of chapter A.

Conclusions

This investigation has pointed out that mixing quality strongly depends on the momentum flux ratio and the geometry of the mixing zone. The results show that:

- Standard deviation and mixing rate as defined match in respect of their information about tendency and optimum momentum flux ratios.

- For all configurations investigated an optimum momentum flux ratio is observed. Exceeding this limit yields to a deterioration of mixing process.

- Optimum mixing precludes the mergence of the opposing jets. The distribution of the jet cores over the flowfield should be as homogeneous as possible, in order to increase the thermal transfer surface between jets and crossflow.

- For all inline and staggered configurations with low ratios of s/d, an impact of opposing jets must be avoided to achieve best mixing. In this range, comparable inline and staggered geometries provide similar mixing rates.

- Staggered configurations require high values of s/d to allow mutual passing of opposing jets.

- Small s/d ratios and/or staggered configurations are preferred to meet the application's requirements of high momentum flux ratios and intense mixing.

Acknowledgements

The authors are indebted to the Deutsche Forschungsgemeinschaft DFG for the financial support, which made this research project possible.

References

[1] Simon, B.,"Entwicklung neuer Brennkammerkonzepte für schadstoffarme Flugzeugantriebe", MTU Focus, 2/1990

[2] Talpallikar, M.V., Smith, C.E., Lai, M.C., Holdeman, J.D., "CFD Analysis of Jet Mixing in the Low NO_x Flametube Combustors", Trans. ASME, J. Eng. f. Gas Turbines and Power , p. 416, Vol. 114, (1992)

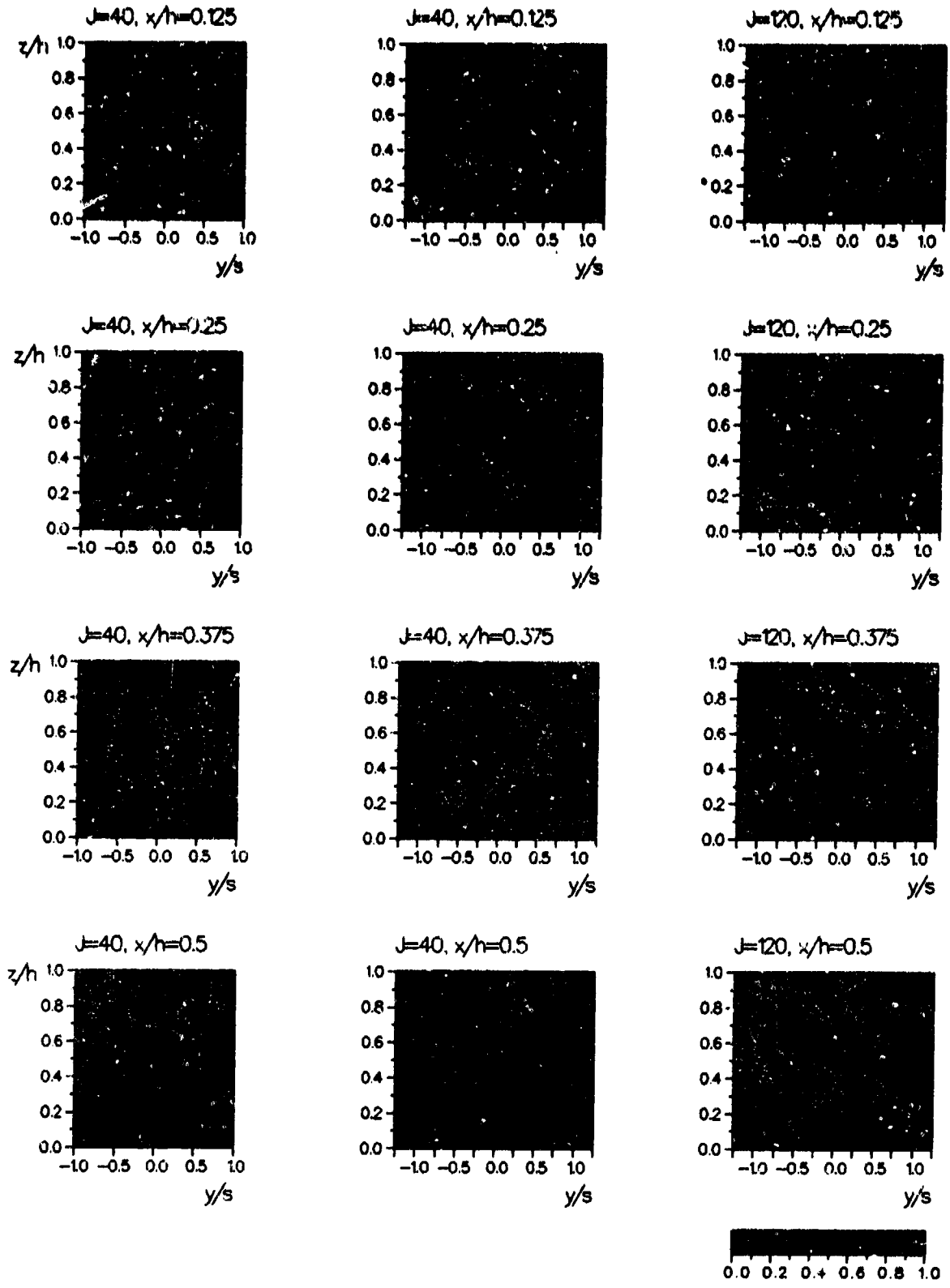

Fig. 13 Θ- distributions, config. 6, staggered

[3] Nguyen, H., Bittker, D., Niedzwiecki, R., "Investigation of Low NO_x Staged Combustor Concept in High Speed Civil Transport Engines", AIAA 89-2942, 25th Joint Propulsion Conf., Monterey, (1989)

[4] Peters, J.E., "Current Gas Turbine Combustion and Fuels Research and Development", AIAA, J. Propulsion and Power, p. 193, Vol. 4, No. 3 , (1988)

[5] White, D.J., Batakis, A., LeCren, R.T., Yacobucci, H.G., "Low NO_x Combustion Systems for Burning Heavy Residual Fuels and High-Fuel-Bound Nitrogen Fuels", Trans. ASME, J. Eng. f. Gas Turbines and Power, p. 377, Vol. 104, (1982)

[6] Russell, P.L., Beal, G.W., Sederquist, R.A., Schultz, D., "Evaluation of Concepts for Controlling Exhaust Emissions from Minimally Processed Petroleum and Synthetic Fuels", ASME, 81-GT-157, (1981)

[7] Holdeman J.D., Walker, R.E., "Mixing of a Row of Jets with a Confined Crossflow", AIAA Journal, p. 243, Vol. 15, No. 2, (1977)

[8] Holdeman, J.D., Srinivasan, R., Coleman, E.B., Meyers, G.D., White, C.D., "Effects of Multiple Rows and Noncircular Orifices on Dilution Jet Mixing",AIAA, J. Propulsion and Power, p. 219, Vol. 3, No. 3 , (1987)

[9] Norgren, C.T., Humenik, F.M., "Dilution- Jet Mixing Study for Gas- Turbine Combustors", NASA TN D-4695, (1968)

[10] Oechsle, V.L., Mongia, H.C., Holdeman, J.D., "A Parametric Numerical Study of Mixing in a Cylindrical Duct", AIAA -92-3088, 28th Joint Propulsion Conf., Nashville, (1992)

[11] Liscinsky, D.S., True, B., Vranos, A., Holdeman, J.D., "Experimental Study of Cross-Stream Mixing in a Rectangular Duct", AIAA -92-3090, 28th Joint Propulsion Conf., Nashville, (1992)

Discussion

Question 1. Dr L. Ianovski
Are you planning to measure the mixing of non perpendicular jets?

Author's Reply
Firstly, we investigated the basic parameters on jet mixing, so the jet axis was perpendicular to the gas flow. In the future we plan to pass the jet mass flow around the test section without mixing to simulate the dilution air supply, so the jet axis will be inclined in that investigation.

Question 2. J. Tilston
Have you measured the mainstream pressure drop that occurs across the mixing section?

Author's Reply
Yes, we measured pressure drop. However, in contrast to the usual jet mixing problems, momentum flux ratio and pressure drop are fixed because of the RQL application. Therefore, momentum flux ratio is chosen to match the application and pressure drop is not of primary interest.

Question 3. Mario Nina
The multiple jet configuration can be affected by low frequency oscillations depending on jet diameter and spacing. Have you found evidence of this phenomenon in your measurements?

Author's Reply
We measured average quantities, because of conventional thermocouple measurements. However, no oscillation could be observed with hot wire measurements in cold flow, other than turbulent fluctuations.

Investigation of the Two-Phase Flow in a Research Combustor under Reacting and Non-Reacting Conditions

C. Hassa, A. Delck, H.Eickhoff
DLR Institute for Propulsion Technology
Linder Höhe
W-5000 Köln 90
Germany

SUMMARY

The flow resulting from an airblast atomizer with prefilmer and corotating swirl was investigated in a cylindrical combustion chamber. Gas- and droplet velocities were measured by a Phase Doppler Anemometer and species and gas temperature by gas sampling probes respectively thermoelements at atmospheric conditions and without fuel and air preheat. Because of interference with the liquid phase, the species measurements were restricted to a minimum distance of 40 mm from the atomizer lip. The temperature measurements showed the dominating influence of the external recirculation zone on flame stabilization for the investigated nozzle configuration with a small expansion angle of the swirling flow. The species concentration fields exhibit homogeneous radial profiles at an axial distance of 100 mm behind the atomizer, although droplets are observed up to 140 mm. Integrating the measured liquid volume flux density profiles it was found, that the fuel flux at 45 mm behind the atomizer had diminished to 14% of the maximum measured value. The axial profile of the liquid flux weighted Sauter mean diameter is almost linearly increasing from 22 to 31 µm. Systematic experimental errors and losses of the system sensitivity, which enter the results partly with opposite signs, have an influence on the measured flux densities and moments of the particle size distribution. The measurement of individual flux density profiles was reproducible to within 45 %. A comparison between the gasflow in the nearfield of the atomizer under reacting and nonreacting conditions showed a partial suppression of the expansion of the velocity profiles by the hot corner vortex. Together with the combustion induced axial acceleration the thus effected reduction of the effective swirl number leads to the breakdown of the recirculation at 29 mm.

1. INTRODUCTION

The fuel preparation system is seen as a key element of combustors for advanced aircraft engines. Since the advent of exhaust emissions regulations, airblast atomizers have demonstrated superiority over other types of atomizers for the simultaneous atomization and mixing of fuel and air [1]. They are thus the element of the combustor, that controls primary zone homogeneity, which is in turn the key to all pollution reduction methods presently considered. Hence, the spray dynamics of airblast atomizers have received a great deal of attention, especially since the introduction of nonintrusive instrumentation for the investigation of single and two phase flows. The concurrent development and increased use of numerical models for the design of gas turbine combustors has created an additional demand for more dimensional data of combustor flows for the validation of the computer codes. Investigations have been made of the gas flow from atomizers [2] and the influence of various design parameters with Laser Doppler Anemometry [3]. A wide body of literature exists on the relation of mean dropsizes to the main physical parameters of atomization [4], mostly using the Laser light diffraction particle sizing method.

The Phase Doppler Anemometer allows to extend the experimental analysis to the characterization of the dispersed phase flow with increasing similarity to the real operating conditions. Investigations have been reported for the cold flow with and without confinement [5], with low and high particle loading [6], with and without reaction at atmospheric pressure [7], under high pressures without reaction [8], and with combustion at medium pressures [9]. A recent cross correlation, exercised with a practical nozzle, strengthened the confidence in the technique with respect to mean diameters and velocities measured in cold flows [10]. However, the measurement of liquid volume fluxes remains uncertain and the interpretation of results in the harsher environments is difficult.

The present contribution represents a step in a succession of experiments with a research atomizer-combustion chamber configuration, that has been designed for ease of experimental investigation, but tries to retain some essential features of primary zone flows relevant to the two phase flow. Furthermore, some aspects easing the validation of two phase flow model predictions [11], could be taken into account. The aim of the experimental effort is therefore to use the advantage of the geometrical freedom inherent in a research atomizer to provide data especially in its near field to further the general understanding of such two phase flows.

2. EXPERIMENT

Airblast Atomizer-Combustion Chamber Configuration

A cross section of the airblast atomizer is shown below in Fig. 1. A prefilming atomizer with corotating radial swirlers

1 a,b prechambers
2 swirler
3 inner swirl channel
4 outer swirl channel
5 Cone
6 Atomizing-lip
7 Fuel-line
8 nozzle back-wall (window optional)
9 nozzle front-wall (window optional)

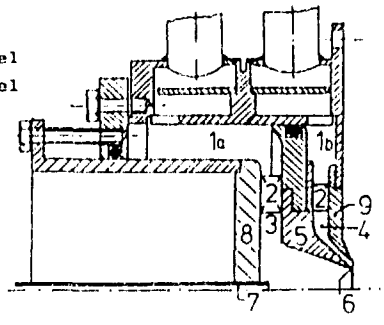

Fig. 1: Airblast atomiser with housing

Presented at an AGARD Meeting on 'Fuels and Combustion Technology for Advanced Aircraft Engines', May 1993.

was chosen. The fuel is sprayed from the fuel line (7) onto the atomizer cone (5). Near the end of the line two tangential air entry slots and a conical diffusor provide good axial symmetry of the fuel film, which can be visually observed through the window in the back wall (8). A symmetry assessment of the spray has been made with the Phase Doppler Anemometer of the unconfined nozzle and water as the test fluid. A pattern index of 11 and a Min/Max ratio of 75% was found. On the atomizer cone, the fuel is driven by the air flow in the inner swirl channel (3) to the atomizing lip (6), where it is atomized in the shear layer between the inner and outer (4) swirl channel flow, respectively. The two swirler flows (2) can be observed through windows in the nozzle front (9) and back wall and were measured with the Laser Dual Focus technique [12]. The midsection of the inner swirl channel together with a vector plot of the measured velocities is shown in Fig. 2. It

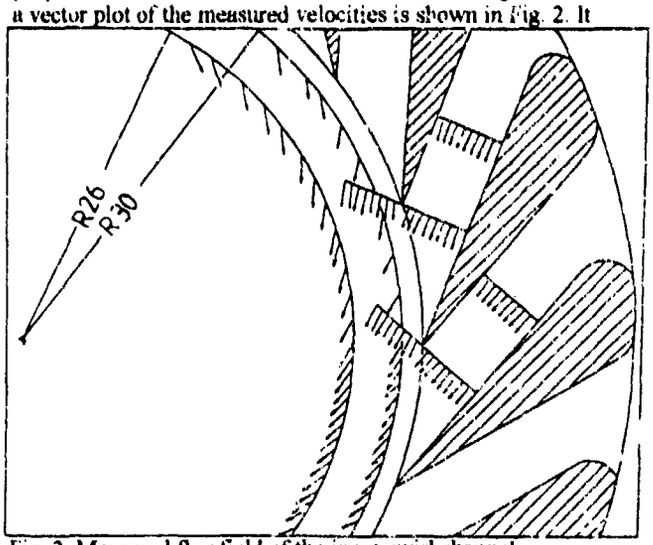

Fig. 2: Measured flowfield of the inner swirl channel

can be seen, that the wakes behind the blades are evened out at the 26 mm radius and cylindrical symmetry exists in the nozzle. The mass flows into the prechambers, (1a, b) on Fig. 1, are separately controlled by critical nozzles for easy manipulation of the outlet velocity profiles, which are shown in

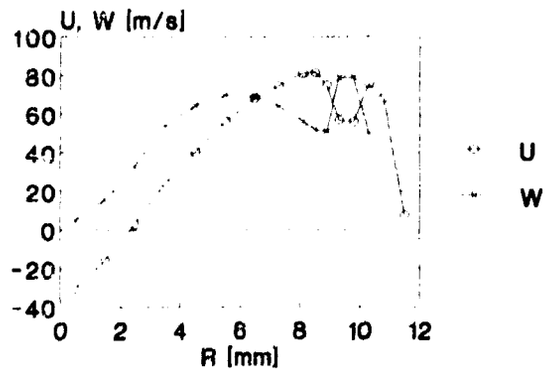

Fig. 3: Measured axial and tangential velocity at z = 1 mm

Fig. 3. The aim, though not fully reached, was to avoid steep gradients of the profiles of the axial and tangential velocity in the vicinity of the atomizing lip. The swirl number, as computed from the velocity at the swirler outlets and nondimensionalized with the nozzle diameter, was 0.95, giving approximately the same amount of axial and tangential velocity at the outlet, as can be seen in Fig. 3. For the present investigation, the air mass flow was 22 g/s and the AFR 25.6 ; the fuel used was Jet A.

The cylindrical flame tube with the main dimensions and the construction of the windows are shown in Fig. 4.

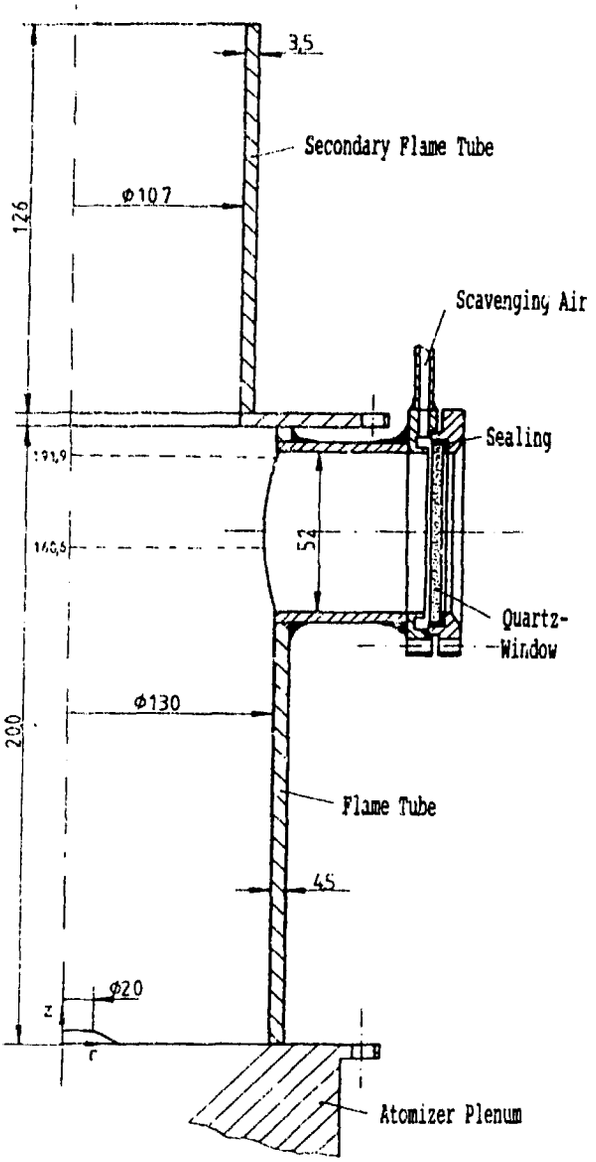

Fig. 4: Cross section of the combustion chamber

The expansion ratio from the nozzle to the flame tube diameter is 1: 6.5. For better optical access, the nozzle protrudes a little bit into the combustor. Ignition is effected with a hydrogen pilot flame emerging from a 5 mm hole in the flame tube at z = 25 mm. The hydrogen in turn is ignited with a spark plug. After 200 mm, the cross sectional area of the tube is reduced by one third to prevent back flow from the downstream end of the combustor. The lower part of the flame tube was sectored into three equally long rings, one of them having three cooled windows. By changing the position of the windowed sector, most of the combustor volume was accessible for the PDA. 5% of the total air were used for scavenging the windows. A topview of the windowed sector is shown in Fig. 5. With the angular position of the windows at 136° and 120°, PDA measurements of one side of the combustor at scattering angles of 70° and 30° were rendered possible.

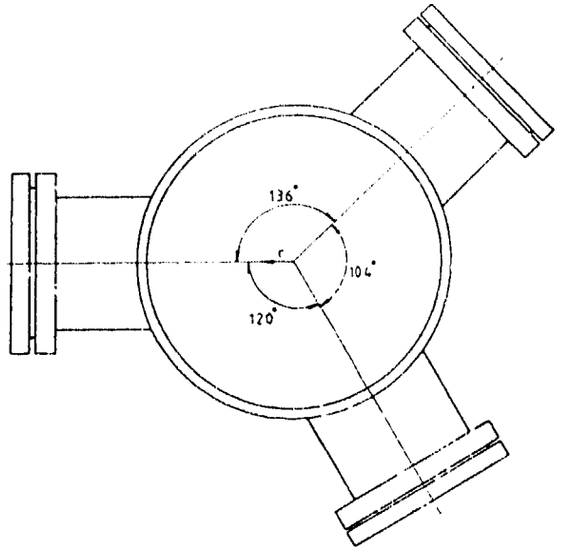

Fig. 5: Topview of the windowed flame tube sector

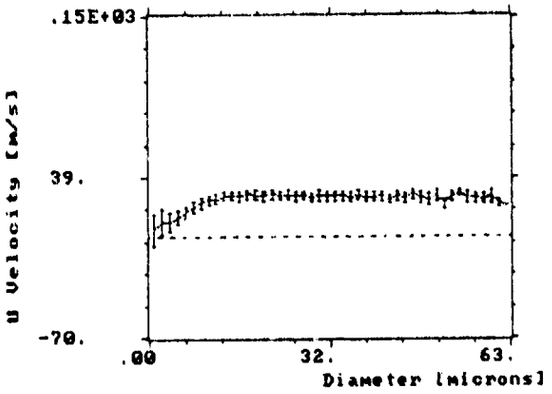

Fig. 6: Size-velocity correlation of the axial velocity at Z = 7 mm, R = 13 mm

Diagnostics

Liquid phase flow properties and the gas phase velocities in the combustor were measured by a two component Phase Doppler Anemometer [13] powered by a 5 W Argon Ion Laser. The laser light was transmitted to the front lens of the sending optics by monomode optical fibers. The dimensions of the measurement volume were 70 x 70 x 200 µm, the axial width being limited by the projection of the 100 µm receiving optics slit. The nominal maximum particle concentration is then calculated at 750 particles per cubic millimeter. The refractive index of kerosene was set to 1.46, and measurements of the liquid phase were performed at 69°, the Brewsters angle for that medium. The photomultiplier voltage was set by controlling the modulation depth of the biggest dc signals with a digital oscilloscope to avoid cutoff. The upper limit of the size range was 176 µm, resulting from a lowered maximum phase angle of 190°, set to enable a software rejection of reflected signals [14]. An exploratory measurement of the cold spray with a Malvern particle sizer showed a 99 % diameter of 98 µm and a 99,9 % diameter of 176 µm using the model independent algorithm, with a beam obscuration of 36 %, giving a minimal secondary scattering bias towards size reduction of big particles.

A separate run of PDA measurements with optimum system sensitivity was performed for the measurement of gas velocities. For the first profiles up to 30 mm behind the atomizer, only the first size bin below 0.9 µm was used. Thereafter, a decision had to be made between a statistically valid sample size and a low diameter cutoff by inspecting the size-velocity correlation. In regions of high streamwise velocity gradients, clear size-velocity correlations occur at the small size range below 10 µm. As an example, the size-velocity correlation of the axial velocity at Z = 7 mm, R = 13 mm, a point both near the nozzle, and near the corner vortex is shown in Fig. 6. The line represents the mean velocity of the size bin and the bars depict its rms value. Quite large differences especially for the turbulent velocity are discernible even below 4 µm. Therefore the conclusion can be drawn, that for the exact mapping of e.g. reverse flow boundaries as small particles as possible should be used. For the cold flow velocity measurements glycerine alcohol tracer particles were used and a comparison of measurements with and without sizing option showed equivalence of the pure velocity measurement to a combined size and velocity measurement with a 1.5 µm cutoff.

The measurement of liquid volume flux densities was influenced by the following main sources of error:
- A relatively small number of big drops in the samples, nevertheless carrying a nonnegligeable amount of mass, did not suffice to create a stable burst length distribution for the measurement volume correction [15] to work correctly. The cross section of the respective size bins is underestimated, and consequently the volume flux overestimated.
- Larger velocity components in the direction orthogonal to the receiving optics- and the combustor axis cause the burst length to be limited by the receiving optics slit width, again causing too low burst lenghts and an overestimation of the volume flux.
- A high number density of drops causes more than one particle to be present in the measuring volume and because of the stochastic distribution of particles, this is due to happen even if the measured concentration is one order of magnitude below the nominal maximum concentration, [16] as it was the case in the present investigation. This contributes to a reduction of the measured flux.
- The turbidity induced by the spray between sending and receiving optics can reduce the sensitivity of the system and lower the data rate. In an investigation of a highly laden spray [17], it was found, that the effect is much bigger if the spray is between the measurement volume and the receiving optics side, and the PDA was set up accordingly.
- For a confined spray with temperature gradients, the optical losses of the windows, reduction of the aperture at off axis positions and beam steering will further reduce the system sensitivity.
- Multicomponent fuels and temperature gradients within the droplets during the heat up phase influence the sizing in an unpredictable manner.

The foregoing enumeration of problems shows systematic errors with positive and negative signs, so that an agreement between integrated and litered fluxes is not necessarily a measure of the quality of the measurement. Nevertheless such a comparison has been made in the cold and the comousting flow at Z = 10.5 mm. In the cold flow the increase of the measured flux in the axial direction came to a standstill at that distance, believed to be caused by the end of atomization and rounding of drops. The flame luminescence was visible at

15 mm from the nozzle for the combusting case, so that the spray was considered to be not much altered by evaporation at 10.5 mm. In Fig. 7 the comparison of flux density- and Sauter diameter profiles is shown for the cold free flowing and the confined combusting case.

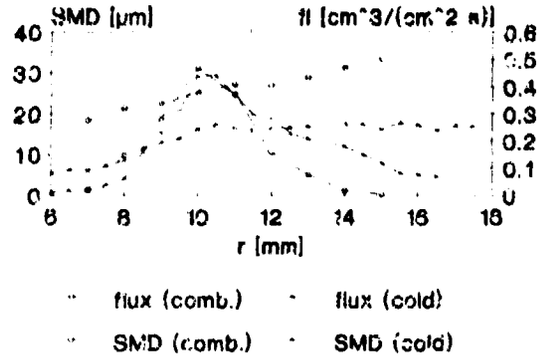

Fig. 7. Liquid flux density and Sauter diameter profile for unconfined, cold and confined, combusting case, $z = 10.5$ mm

The Sauter diameter of the cold flow is markedly smaller as in the combusting case, which can be attributed to the reduced system sensitivity as well as to the prevaporization of small particles. To get a rough idea of the relative influence of both causes, the size distributions were reevaluated at the point of maximum flux density. The cold size distribution will have the same Sauter diameter as the one measured during combustion, if all droplets below 12 µm are neglected. Since it is not expected that a 12 µm drop can be completely vaporized without preheat at a 10 mm distance, it is concluded, that the deterioration of optical conditions plays a major role for the differences seen in the Sauter diameters.

The integration of the flux density profiles gives a difference to the litered flux of +40% for the cold and -3% for the combusting case. For the latter a reduction from 90 to 70% of accepted measurements was noted, and to prevent excessive loss of data, the signal to noise ratio validation criterion for the particle size measurement was relaxed. That is the assumed reason for the slightly higher maximum flux density in the combusting case. Consequently, its smaller flux difference is mostly attributed to a cancellation of errors and the reproducibility of the flux density profiles is not better than 45%.

Temperature measurements were performed with an uncoated NICR-NI thermoelement. The maximum measured temperature was below 1500K, and the lean equivalence ratio prevented excessive corrosion hence no durability problems were encountered during the measurement. The radiation correction was performed with measured velocity values whereever possible. Below $z = 24.4$ mm, cooling by droplet impingement was considered to be too strong, so that the temperature measurement was limited to the area downstream of that position.

The species measurements of CO_2, CO, O_2, NO_x, and UHC were confined to the area above 40.6 mm, because of the clogging of the sampling probes. Because of the lean equivalence ratio and the entirely blue flame luminescence, no soot measurement was made. The gas analysis instruments operated on the dry gases, for the evaluation of the wet concentrations, the NO_x concentrations were neglected. The H/C ratio used for the evaluation was 2; at the exhaust, values between 1.89 and 2.08 were computed from the measurements.

3. Results

Temperature and Concentration Fields

The measured temperature distribution is shown in Fig. 8.

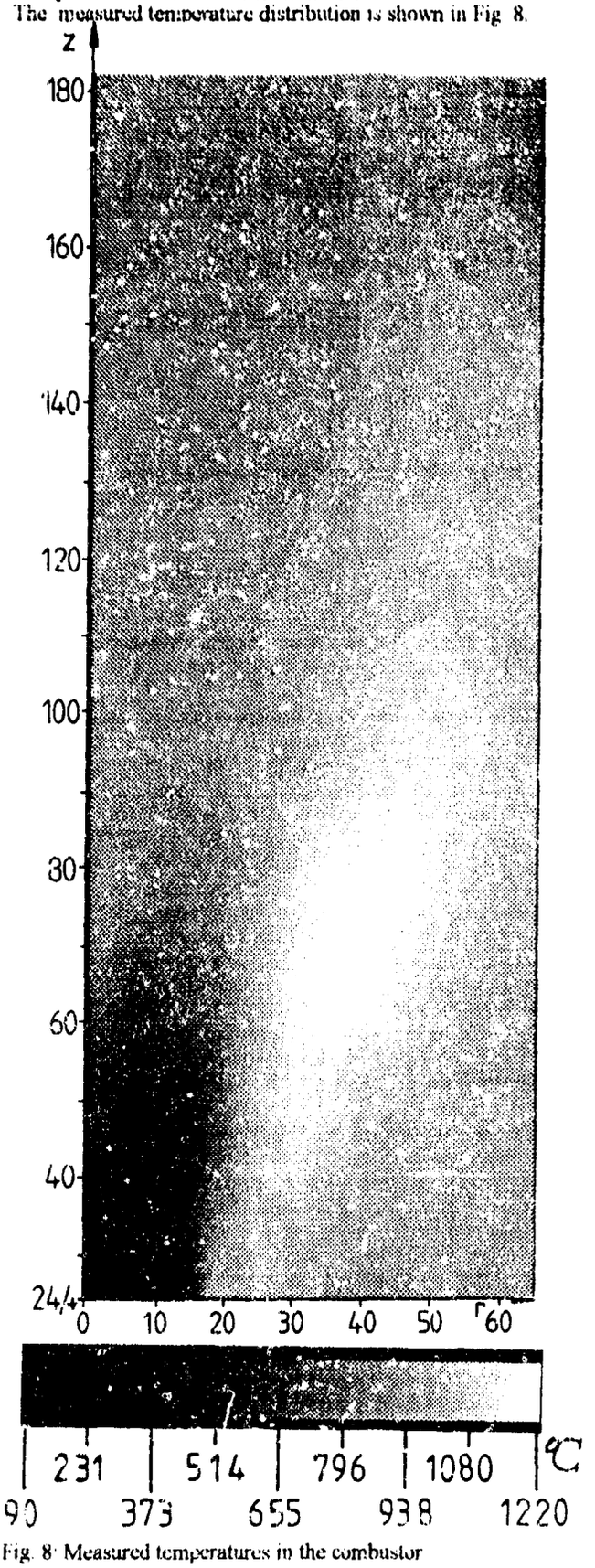

Fig. 8. Measured temperatures in the combustor

The temperature field can be subdivided into three zones: a cold central core up to 20 mm, a hot outer zone with isocontours following the spray dispersion, and an area with small temperature gradients above 120 mm. The hot combustion gases reach the wall at $z \approx 80$ mm, the corner recirculation ends at about $z \approx 100$ mm, c.f. Fig. 8. Because of the heat loss to the walls, the exit temperatures are about 150 °K lower than the adiabatic temperature of 1555 °K.

Spray angle and flame luminescence

In a preparatory step, a quartz glass flame tube of the same diameter without wall cooling replaced the aforementioned sectored flametube, and photographs of the flame luminescence were made to extract the expansion of the outer flame contour. It is marked by the line on the left side of Fig. 9. The expansion angle was 58° and the luminescence ended at $z = 110$ mm. The light of an Argon Ion laser beam, shining centrally through the tube at successive z positions, was scattered by the droplets and the extent of the bright lines at both sides of the center gave a first impression of the spray contour, which is marked with points. The line on the right side in Fig 9 gives its mean expansion angle of 64°. Hence, the flame nearly surrounds the outer spray contour.

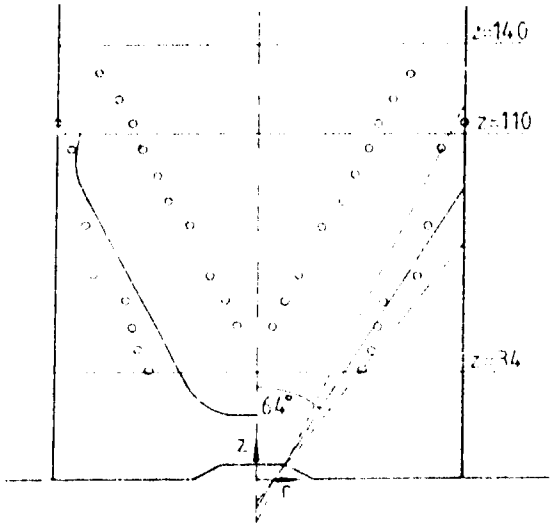

Fig. 9: Contour and expansion angle of the spray

Droplets are seen to hit the wall at $z = 110$ mm and to prevail up to 140 mm. The long droplet lifetime could be partly caused by the wide size distribution of the spray. A Rosin-Rammler fit of the aforementioned laser light diffraction measurement produced a q-parameter value of 1.26, while 2-4 being a normal value for airblast atomizers according to [4]. Fuel being transported from the fuel line out of the nozzle without hitting the atomizer cone could be one reason for this high q-value.

Gas analysis

The distribution of the equivalence ratio is given in Fig. 10. It compleats the temperature field of Fig. 8 as the lowest value for the equivalence ratio is found in the low temperature core and the highest values in the corner recirculation. It is therefore recognized as the primary flame stabilization mechanism, the internal recirculation zone being a byproduct of the swirling spray expansion. Homogeneous radial profiles are reached at 100 mm, with a small excursion at the combustor wall due to the corner recirculation. As the highest measured equivalence ratio was 0.815, no fat spots could be detected througout the measured volume

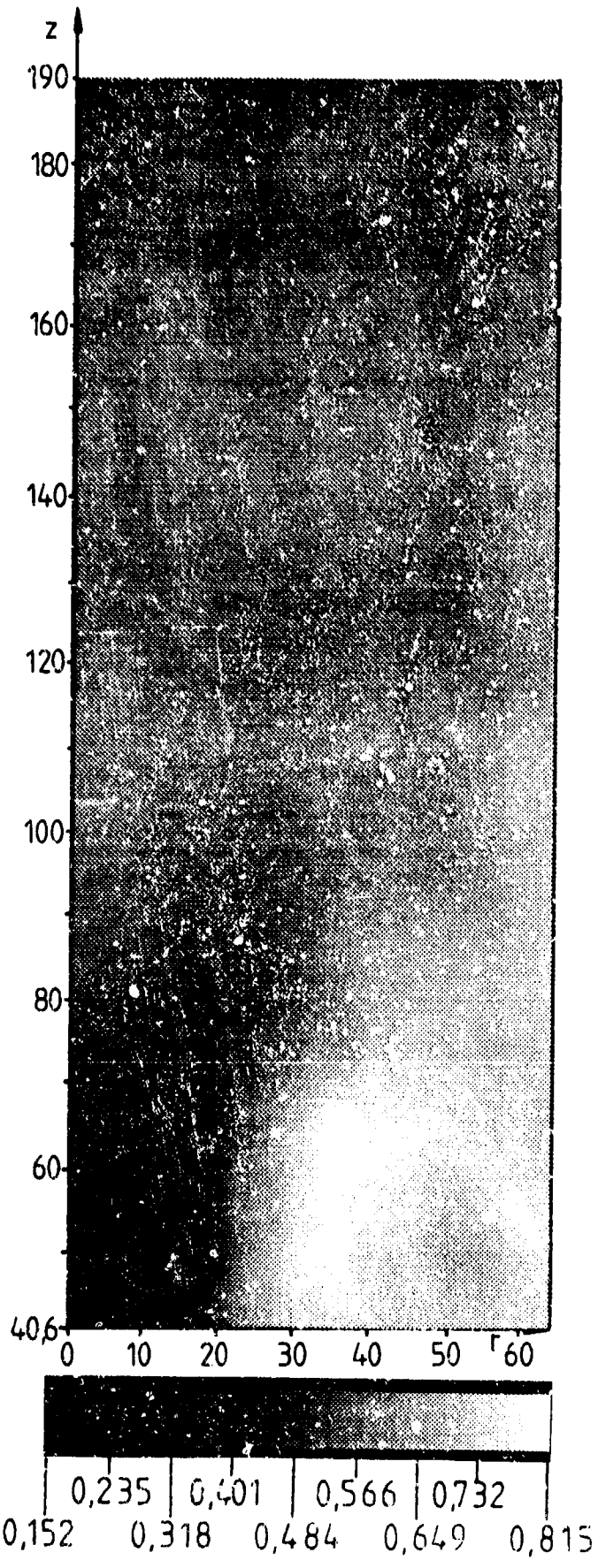

Fig. 10: Equivalence ratio

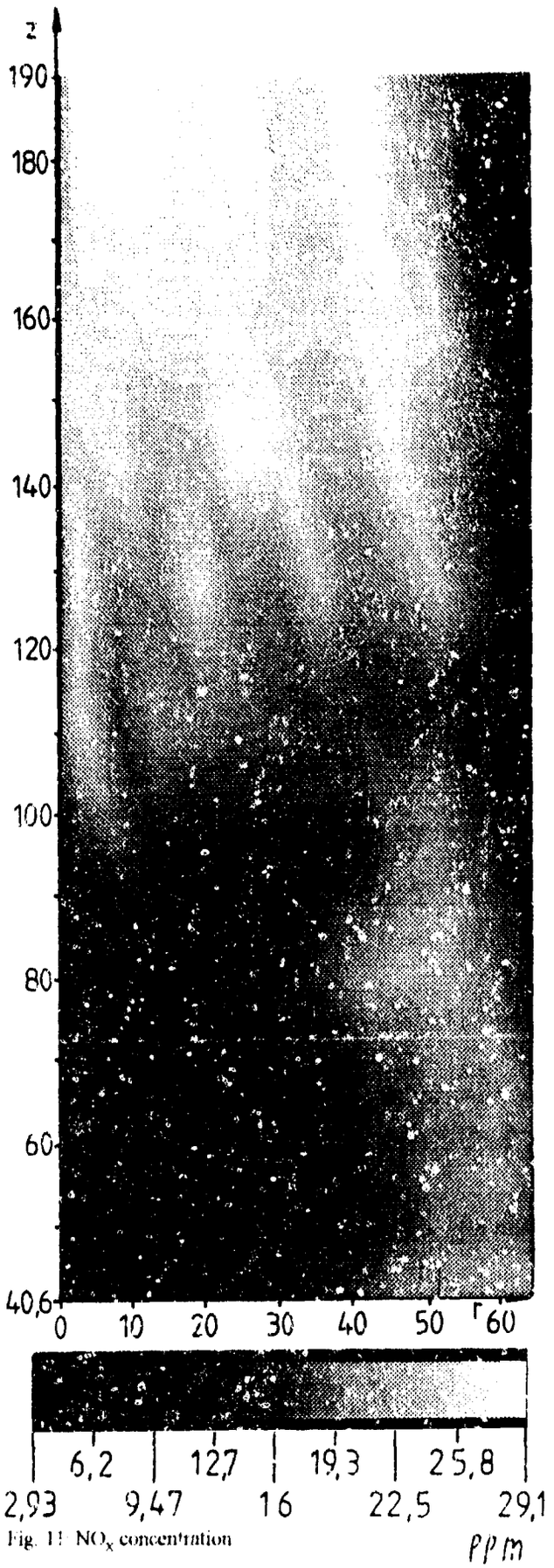

Fig. 11: NO_x concentration

The measured NO_x concentrations are displayed on Fig. 11. As it is to be expected from the low temperatures, the NO_x concentrations are also quite low. The exhaust emission indices at the end of the secondary flame tube at 300 mm from the nozzle were: EI NO_x = 1.2 g/Kg, EI CO = 0.23 g/Kg, above 103 mm no UHC could be measured. There is a step in the NO_x concentrations at 120 mm. Below that height, the level remains below 20 ppm, with the exeption of one spot just about the reattachment point of the corner vortex at z = 90 and r = 50 mm. Above, the concentrations increase by 10 ppm with a transition region with vertical "fingers". The maximum concentration fluctuations registrated amounted to 8 ppm, which explains the bumpy radial profile in the transition at 130 mm, however a clear explanation for the increase could not be found.

Gas Flow

Fig. 12 a and b show a comparison of the axial velocities for the cold and combusting case.

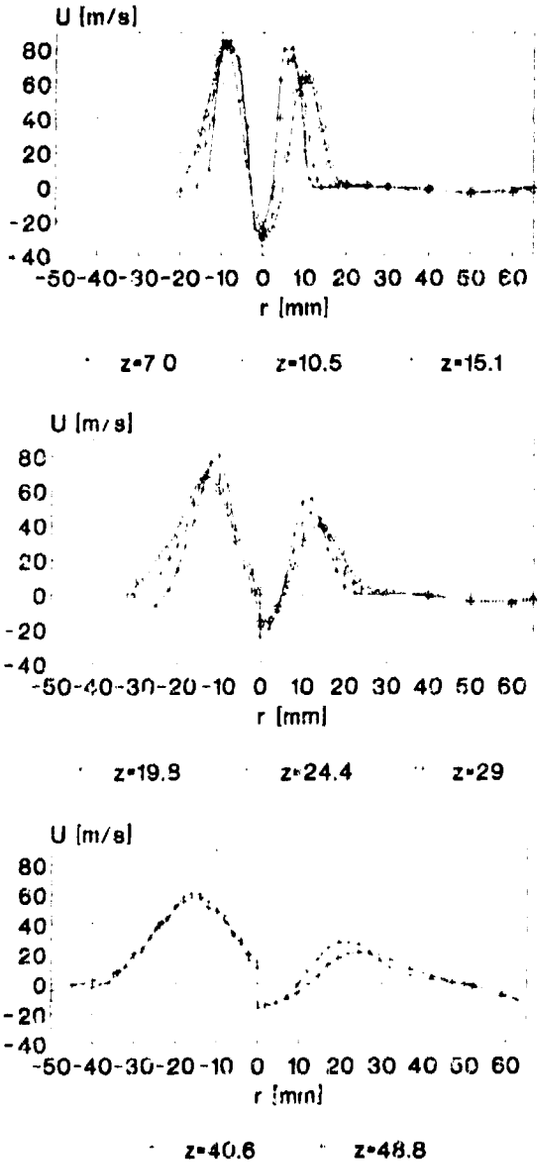

Fig. 12: Comparison of axial gas velocities, cold velocities on the right, with combustion on the left side

The combustion leads to constant axial velocity maxima, at the same radial position up to z = 24.4 mm, whereas the cold velocity profiles move outward right from the start. Together with the reduction of the effective swirl number by the combustion induced axial acceleration, the suppression of the expansion of the swirling flow leads to the breakdown of the recirculation at z = 29 mm. The interaction of the corner vortex with the forward flow is demonstrated in Fig. 13, where the profiles of the radial velocity at cold and hot conditions are shown together with the temperature.

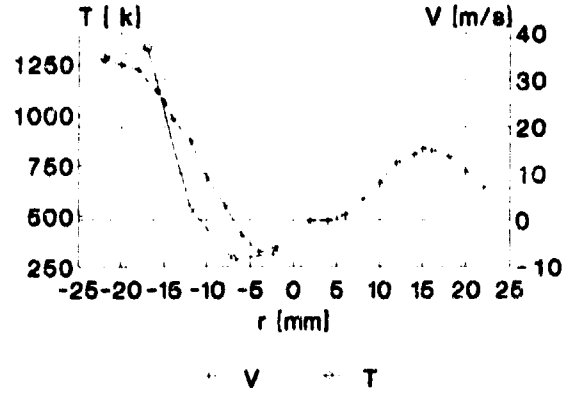

Fig. 13: Radial velocity and temperature at z = 24.4 mm
cold flow on the right, with combustion on the left

The combusting flow moves faster outside than the isothermal flow for radii above 10 mm, and that is the boudary between the cold core and the hot corner flow. Inside that boundary, the combusting profile has a negative loop, which is not existant in the isothermal flow. The profiles of the tangential velocity remain virtually unchanged by combustion up to 30 mm, the acceleration is first seen at 40 mm.

The profiles of the fluctuating velocities follow the mean velocity gradients up to 15 mm distance from the nozzle. As an example, the mean and fluctuating axial velocity at z = 10.5 are shown together in Fig. 14.

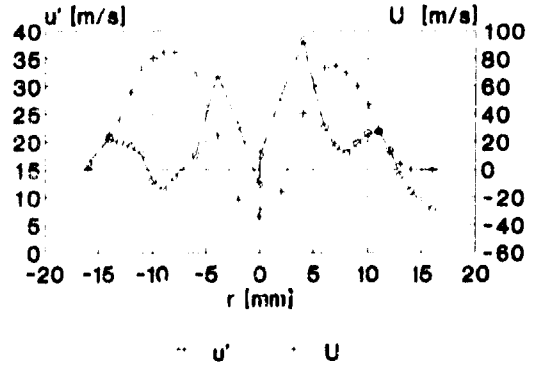

Fig. 14: Mean and fluctuating axial velocities at z=10.5mm,
cold flow on the right, with combustion on the left

At this position, the small velocity difference from inner to outer swirl channel seen in Fig. 3 has disappeared, and consequently, a region of lower turbulence exists in the middle of the forward flow. The other components of the fluctuating velocity exhibit the same structure. This is believed to be beneficial for atomization, since the liquid is less likely to escape the high velocity region, that provides the shear force necessary for atomization. Since the measurement of the isothermal flow was performed without fuel, the comparison of the cold and combusting gas flow combines the effects of heat release and dispersed phase feedback. Inspection of Fig. 8 suggests, that the density change only becomes important outside of r = 10 mm, and the reduction of the fluctuating velocity at r = 9 mm is attributed to the presence of the spray, which had a number concentration of 17 /mm³ with high relative velocities for all particle sizes, c.f. Fig. 19a., so that a reduction of the turbulent energy in the large scale fluctuations can be expected.

At the maximum of the fluctuating velocity at r = 4 mm, near the zero crossing of the mean velocity a bimodal velocity distribution exists, which is shown in Fig. 15.

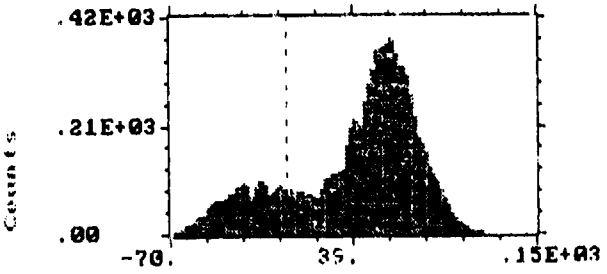

Fig. 15: Distribution of the axial velocity at z = 10.5,
r = 4 mm, isothermal flow

As a whizzle can be heard from the nozzle during the isothermal operation, the bimodal distribution is interpreted as a manifestation of a precessing vortex core, a phenomenon often observed in swirling flows and described e.g. in [18]. The extend of the bimodality is not so strong for the combustion, cf. the height of the two maxima on Fig. 15, hence it appears, that the precessing vortex core is damped by the combustion in this configuration.

Above z = 15 mm, the dip in the profiles of the fluctuating velocity disappears. For z = 29 mm, the profiles for the axial and radial mean and fluctuating velocities are shown in Fig. 16. Due to the increased radial velocity gradient, the

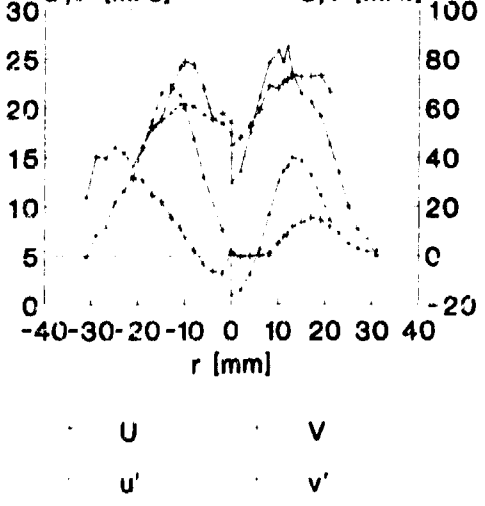

Fig. 16: Axial and radial mean and fluctuating velocities at
z = 29 mm, cold flow on the right, combusting flow
on the left

fluctuating velocity is higher than the axial in the combusting case. At the outer boundary of the measured radial profile, which was limited by the diameter of the cylindrical window, cf. Fig.5., a marked difference is apparent: the cold fluctuation intensity is very high, surpassing the mean velocity, and leading to an anisotropy of the normal stresses. This means, that the outer boundary of the swirling jet is unstable and changes from suction to ejection of turbulent fluid. A time record of the axial and radial velocity at that position is shown in Fig. 17. A periodic, burstlike structure is seen in

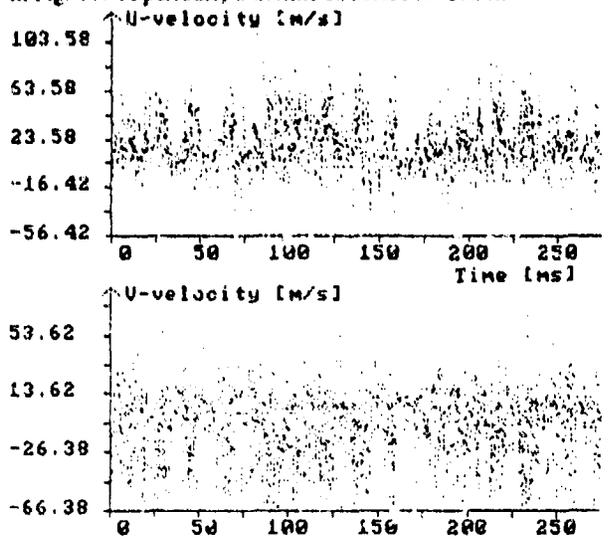

Fig. 17: Time record of the axial and radial velocity at Z = 29 mm, r = 21 mm, isothermal flow

both components, with burst periods between 1 and 2 ms, corresponding roughly to the period of rotation computed with the local perimeter and tangential velocity. The relaxation time of a 19 µm drop, the Sauter diameter measured by laser-light diffraction would be 1.1 ms, so it can be assumed, that the particles react to the bursts. It has been shown, that this anisotropy can have an effect on the turbulent dispersion [19], and since the liquid flux density is high at that point, it can alter the character of the two phase flow.

In contrast to the isothermal behaviour, the normal stresses in the axial and radial direction are of the same size at the boundary of the swirling jet in the combusting case. An explanation of the difference is suggestet with reference to Fig. 12 b: In the isothermal case, there is a rather wide region of near zero axial velocity, so that the swirling flow has the character of a free swirling jet before it reaches the combustor wall, whereas in the combusting case, the zero crossing of the axial velocity has a high gradient, resulting from the expansion of the hot corner vortex, which stabilizes the swirling flow.

Further downstream, the normal stresses remain smaller for the combusting case.

Dispersed Phase flow

The axial development of the measured and integrated hot mass flow is depicted in Fig. 18 together with the mass weighted Sauter mean diameter integrated over the measuring plane. At z = 10.5 mm, the Sauter diameter of the isothermal free nozzle flow is additionaly given. The difference between the isothermal and combusting value is largely attributed to the reduced sensitivity of the size measurement, cf. the

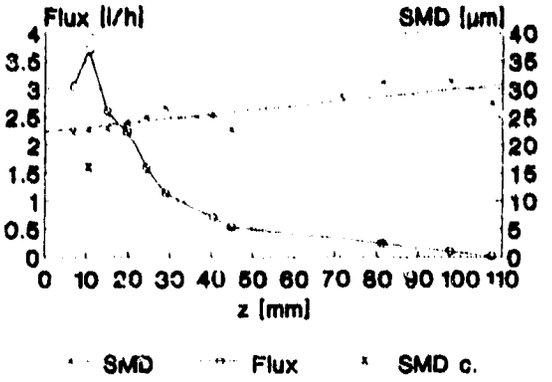

Fig. 18: Axial development of hot liquid volume flux and flux weighted , integrated Sauter mean diameter, with a straight line showing the trend
SMD c.:Sauter mean diameter of isothermal free flow

discussion on Fig. 7. The Sauter diameter profile is not monotonic, however the straight line throug the measured points shows an increase with axial distance. This is a tendency, that has been observed in other investigations too, cf. [20], and results from the fast disappearence of small drops, which is not compensated by the size reduction of the big drops. As the spray is much thinner in the downstream regions, errors due to turbidity no longer exist, and the measured diameter is probably nearer to the true value. Hence it is conjectured, that the true gradient of the SMD profile is more like a line between the 16 µm cold measurement and the 31 µm at the end.

The liquid volume flux curve has a near hyperbolic character, which is consistent with the trend of the Sauter diameter profile, the increase of which gives an indication of a reduced evaporation rate, characterized by the surface mean diameter, in relation to the relative droplet mass, characterized by the volumetric mean diameter. The measured flux value at z = 7 mm is shown for completeness, high droplet density and unroundness of the big highly accelerated droplets exclude a correct result at that point. At z = 45 mm, the measured flux is reduced to 14 % of its peak value. It is also the point, where most of the droplets have reached the gas velocity, Fig.19 a, and the reduction of the evaporation rate from 29 to 40 mm is probably mostly due to the reduced relative velocity of the droplets. At the higher measuring planes above 80 mm, Fig. 19 b, the droplets are faster than the gas flow, and single droplet burning with blue streaks can be observed. Fig.

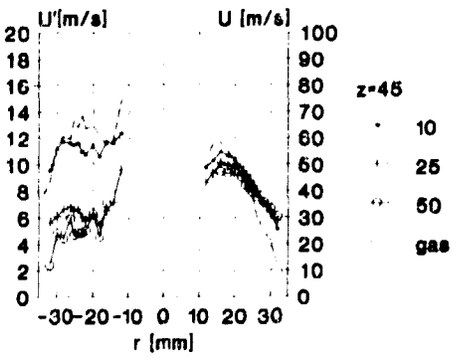

Fig 19 a: Mean and turbulent axial velocities of 10, 25 and 50µm droplets with the gas flow, width of the size bins equals 10 % of the diameter

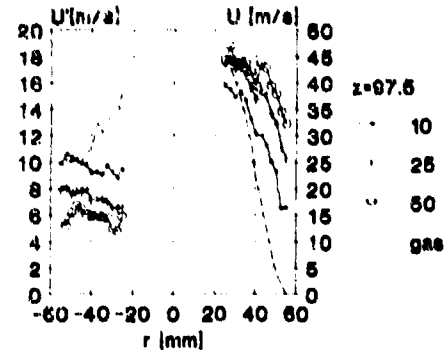

Fig. 19 b: As Fig. 19 a, z = 97.5 mm

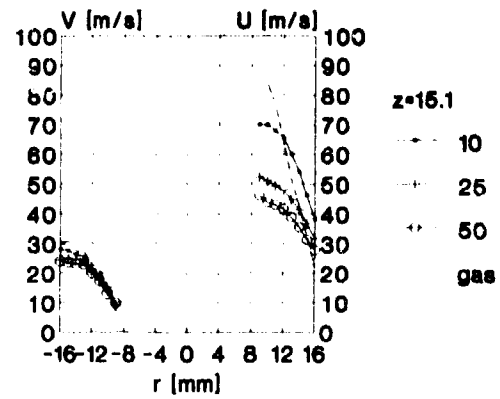

Fig. 19 c: Axial and radial droplet velocities and gas velocity at z = 15.1 mm, same size classes as in Fig 19 b

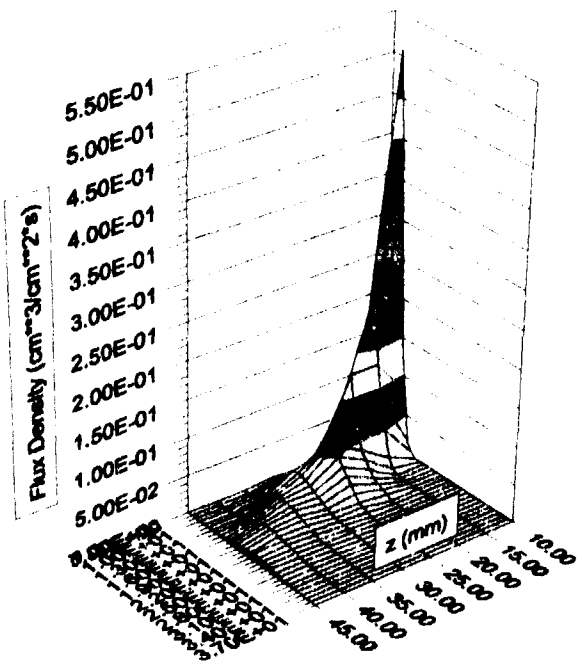

Fig. 20 Surface plot of the liquid flux density field

19 c will be referred to later. In Fig.20 a surface plot shows the measured flux density field. The range of the sector extends between 7 mm < r < 37 mm and 10 mm < z < 45 mm, the view is with a 30° angle to the z axis in the axial-radial plane onto the nozzle. Due to the radial dispersion of the droplets, the peak flux density reduces much quicker than the flux itself. At z = 24.4 mm it is reduced by one order of magnitude. Up to a distance of 29 mm, the radial shift of the maxima is slow. In Fig. 19 c, where the radial and axial droplet velocities are shown together with the gas velocity at z = 15 mm, the spray is seen to accelerate axially, but keeping track of the radial gas velocity by virtue of the centrifugal force and thus slowly crossing the streamlines of the gas flow in the outward direction. Downstream of the 29 mm profile, the centrifugal force becomes dominant, and Fig 20 shows the remaining part of the droplet stream to move out faster.

Since the evaporation is coupled most directly to the surrounding temperature, a succession of flux density profiles together with the respective temperature profiles are shown in Fig. 21. As the spray moves radially outward, it dives

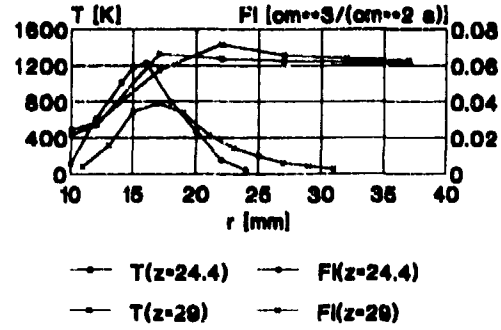

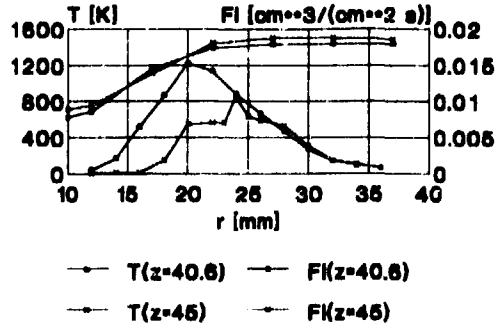

Fig. 21: Temperature and flux density profiles at z = 24,4 and 29 mm , and z = 40,6 and 45 mm, note the scale change for the flux density

into the high temperature zone, finally at z = 45 mm, the mean temperature around the spray is nearly homogeneous. It is therefore to expect, that evaporation starts at the outer part of the spray. Fig. 22 therfore gives a comparison of an isothermal and hot flux density profile at 29 mm. The isothermal values are taken from [5], in contrast to Fig. 7 the liquid was water with an SMD of 30 µm, but the same mass flux as in the present investigation. For convenience the profile was normalized with the present liquid flow rate. The expansion ratio was 1:9 instead of 1:6.5, but it was shown, that for a distance of 29 mm, the dispersion characteristics are quite the same for the free and confined flow, so they are used here

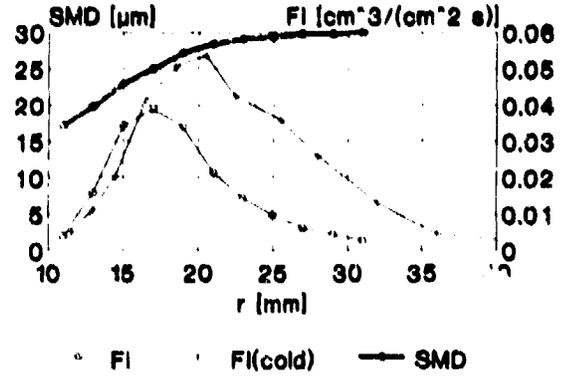

Fig. 22: Cold and combusting flux density and Sauter diameter at z = 29 mm

too. With the exception of the inner boudary of the evaporating flux density profile shifted slightly inward, following the modified gas velocity, cf. Fig 12 b, the fuel placement hasn't changed, but evaporation on the high temperature side has diminished the flux density. The form of the outer wing is similar to that of the axial profile, Fig.18, perhaps reflecting in the same way the changing Sauter diameter, increasing in the radial direction by the centrifugal forces and evaporation. With these features in mind, Fig. 7 can be reexamined. The comparison of the isothermal and combusting flux density profile shows the same trends as in Fig. 22, and since the peak of the flux density profile is probably in a low temperature region where not much evaporation has happenend, the coincidence of the two peak values suggests the difference at the outer wing to be due to evaporation. The different character of the SMD profiles, with the hot SMD increasing at the region, where differences of the flux density profiles exist, whereas the cold SMD profile doesn't, would also be ascribed to evaporation. It then would follow, that at the outer part of the spray a region with substantial prevaporization exists before the appearence of the flame luminescence.

Apart from the increase of the Sauter diameter by evaporation, the width of the size distribution is also reduced. As an example, the 10%, 50% and 90% undersize diameters are shown at z = 29 mm. It can be clearly seen, that both the

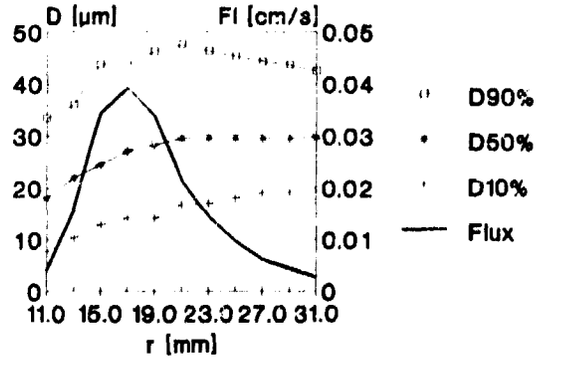

Fig. 23: Profile of representative diameters and flux density at z = 29 mm

D10% and the D90% profile move toward the D50% profile. The effect is not visible before the onset of the flame luminescence at 15 mm, but becomes more pronounced in the downstream direction.

The last results to be shown for the liquid phase are a comparison between the flux density profiles and those of the unburnt Hydrocarbons in Fig. 24 a and b. On the first picture,

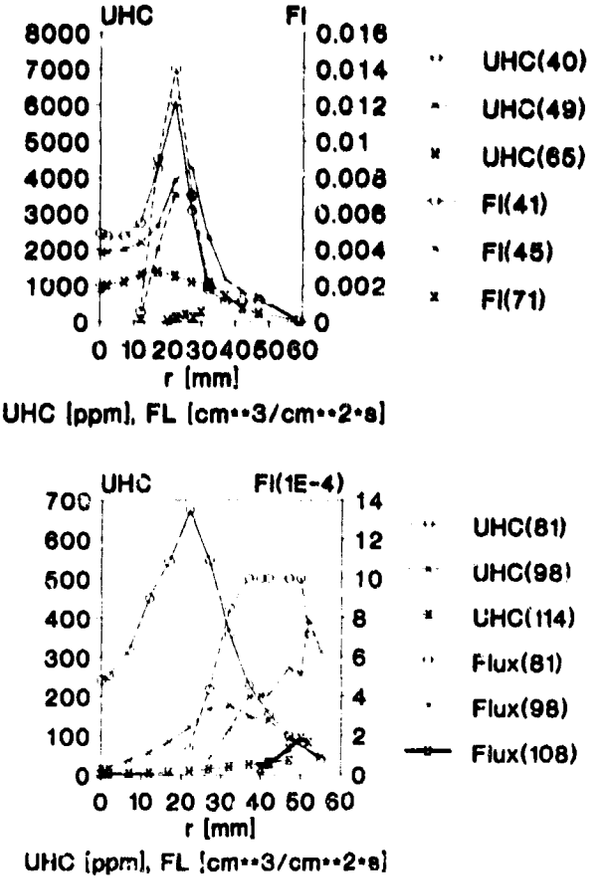

Fig. 24: Unburned Hydrocarbons and liquid flux density

the two quantities are similar, with the exeption of a sizeable quantity of UHC in the inner core of the flow. Between z = 41 and z = 81 mm the proportionality of the respective profiles also stays the same, so that the depletion of gaseous fuel and the supply by evaporation progress at approximately the same rate. From z = 81 mm onwards, the profiles separate, because the centrifugal force drives the droplets outward, and the UHC profile decreases faster, with no more gaseous fuel added on the inside, and it being rapidely consumed on the outside. The crossing of the gasstreamlines by the centrifugal motion of he liquid fuel seen in Fig. 24 b works towards a more homogeneous gaseous fuel distribution, since the evaporative flux is deposited away from the maximum of the gaseous fuel profile.

4. DISCUSSION

The geometry of the present nozzle and combustion chamber and equivalence ratio were chosen for good optical access to the spray, respectively in the interest of a thin spray without optical interference from soot. This resulted in a specific flowfield with a swirl flow, that expands with a small angle and a spray, that remains in the high velocity regime and is accelerated for an extended period, before the droplets fly outward, and in the isothermal case, to the wall. Although a combustor primary zone flowfield has been described [21], that is similar to the present investigation, the dominating role of the corner recirculation for the flame stabilization is not as common in aeroengine combustors as the flame

stabilization by an internal recirculation zone. Hence the role of that difference will be specifiely discussed. However, prior to that, some conclusions concerning the measurement technique will be drawn.

The profiles of the gas velocity and flux density at z = 10.5 mm show a reduction of the gas turbulence even for atmospheric conditions and a very light particle loading. The reduction of the turbulence intensity in comparison to the noncombusting case is conserved, so that an influence on the mixing is probable. It follows, that there is probably no such thing as a thin spray and for small liquid to air ratios and good atomization a precise mathematical description of the flow has to take into account the feedback of the dispersed phase onto the gas turbulence.

The foregoing and the observed modification of the flux density profile for the combusting case at that position show, that important developments in the liquid phase flow have started before they are accessible to the Phase Doppler Anemometer, either because of high particle density or unroundness of drops. Therefore measuring techniques, that allow for smaller measuring volumina [22], or coupled use of flow visualization and Phase Doppler Anemometry will be necessary in the very important range in the immediate vicinity of the nozzle.

On the other hand, the development of the evaporation with the bulk of the fluid evaporated at 45mm even without preheat, suggests that for the practical case with air preheat and high pressures, the region behind 50 mm is probably not important for the two phase flow, exept for the ballistics of the big droplets.

The size measurements show an influence of the overall system sensitivity on the measured mean diameters, as well as some influence on the measured flux. Thus it has to be kept in mind, that Phase Doppler Anemometry is a relative measuring technique only with respect to the single particle measurement, and worsening optical conditions, caused by high particle densities or dirty windows can overshadow other trends. Especially, for a constant liquid flowrate spray which is successively finer atomized, there will be a minimum in the measured diameters, at the point, where the turbidity produced by the increased number of particles outweights the lowered mean diameter.

Concerning the classification of spray flames, [23] have given a parameter, which caracterizes the extent, to which a spray flame is either on the diffusion flame or the single droplet burning side. It is the ratio of an evaporation length V to an entrainment length E. The evaporation length is given by a reference velocity, e g. in the present case the mass weighted mean droplet velocity at the z = 10.5 mm plane, times a evaporation time, which scales with the square of the surface mean diameter and an evaporation rate constant.

$$E = U_{ref} D_{20}^2 / K_{vap}$$

The entrainment length is defined for an axisymmetric nozzle flow as the length in the direction of the path of the center of gravity of the droplets in the axial radial plane, which is needed to entrain enough air to reach a stoichiometric mixture. It is again the product of the reference velocity and an entrainment time scale. Here the time scale is defined as the ratio of the standard deviation of the droplets in the plane perpendicular to the movement of the center of gravity needed to fulfill the stoichiometric requirement and a dispersion velocity.

$$L = U_{ref} L_{sd} / U_{disp}$$

The parameter is then

$$P = D_{20}^2 U_{disp} / K_{vap} L_{sd}$$

A high very high value of P would signify single droplet burning and a very low value a diffusion flame. Neither of the two extremes is fully desirable, since both are coupled to high burning temperatures and accompanying thermal NO_x formation. For a high degree of prevaporization *and* good mixing prior to reaction, the parameter would have a medium value

The present configuration with a mostly axial droplet movement, and a swirling gas flow with a small expansion results in especially high droplet reference velocities, where a longer evaporation and thus combustor length is tolerated for the benefit of better mixing by keeping the droplets in a highly turbulent zone while they evaporate. This can lead to a leaner local equivalence ratio because the fuel vapour is given a chance to distribute by turbulent diffusion before more vapour is added by evaporation. However for the practical case of combustion with high inlet temperatures and pressures, the parameter changes towards the diffusion burning side. The increased pressure head decreases the droplet diameters, and the vaporization rate increases by the elevated inlet temperatures. Furthermore, the dispersion length L_{sd} is a function of the nozzle AFR, and the AFR of the present investigation was especially low, since all the air was put through the nozzle. Thus the parameter will be much lower and hence the evaporation length smaller. The turbulence created by the slowly expanding swirling shear layer would be not effective, if most of it is comes to bear after the reaction. Hence, the effectiveness of the geometry can only be shown in a realistic environment.

5. Acknowledgements

The financial support from the TECHLAM research initiative is gratefully acknowledged. Thanks are due to A. Fuchs and K. Kallergis for assistance in preparation of the figures.

6. References

1. Lefebvre, A. H., "Gas Turbine Combustion" , New York, USA, Hemisphere Publishing Corp., 1983, ISBN 0-07-037029-x, pp 413-448

2. Blümcke, E., Eickhoff, H., Hassa, C., Koopman, J., "Analysis Of The Flow Through Double Swirl Airblast Atomizers", in " Combustion and Fuels in Gasturbine Engines", AGARD CPP 422, June 1988, Paper 40

3. Cohen, J. M., Rosfjord, T.J., "Influences on the Sprays formed by High-Shear Fuel Nozzle/Swirler Assemblies", J. of Propulsion and Power, 9,1, Jan 1993, 99 16-27

4. Lefebvre, A. H., "Atomization and Sprays", New York, USA, Hemisphere Publishing Corp., 1989, ISBN 0-89116-603-3, pp 238-261

5. Hassa, C., Blümcke, E., Brandt, M., Eickhoff, H., "Experimental and Theoretical Investigation of a Research Atomizer/Combustion Chamber Configuration", ASME GT-137, June 1992

6. Mc Vey, J.B., Kennedy, J.B., and Russell, S., "Application of Advanced Diagnostics to Airblast Injector Flows", J. of

Engineering for Gas Turbines and Power, 111, 1, Jan 1989, pp 53-67

7. Mc Donnell, V. G. and Samuelson, G. S., "Evolution of the Two-Phase Flow in the Near Field of an Air Blast Atomizer Under Reacting and Non Reacting Conditions", in 4th. Int. Symp. on Appl. of Laser Anemometry to Fluid. Mech., July 1988, Paper 15.1

8. Jasuja, A. K., Tam, C. K.,"Measurements in Dense Sprays" Brite/Euram Contract AERO 1019, Task 4.2.1. May 1992

9. Cormack, G. "Phase Doppler Anemometry in a Twin-Sector Rectangular Combustor at 1 to 5 bar", Brite/Euram Contract AERO 1019, Task 4.2.2., May 1992

10. Hassa, C. et al., "Cross Correlation of Drop Sizing Techniques on an Airspray Fuel Injector", in 6th. Int. Symp. on Appl. of Laser Techniques to Fluid Mech., July 1992, Paper 18.3

11. Blümcke, E., Eickhoff, H., Hassa, C., "Evaluation of a Spectral Dispersion Model with Experimental Results Obtained from the Dispersion of Monosized Droplets in a Turbulent Swirling Flow", in 5th. Workshop on Two Phase Flow Predictions, 1991, pp 109-121

12. Schodl, R., "Laser-Two-Focus Velocimetry", AGARD-CP-399, Paper 7, 1986

13. PDA User's Manual, Dantec Measurement Technology, 1992

14. Taylor, A.M.K.P., "Phase-Doppler anemometry", in "Experimental & Computational Techniques For Dispersed Two Phase Flows", Imperial College of Science & Technology, September 1989, Part 2

15. Saffman, M., "Automatic Calibration of LDA Measurement Volume Size", Applied Optics, 26, 13, 1987, pp 2592-2597

16. Edwards, C. F. and Marx, K.D., "Application of Poisson Statistics to Size and Volume Flux Measurement by Phase-Doppler Anemometry" in ICLASS, July 1991, Paper 72

17. Brandt, M., Hassa, C. Eickhoff, H., "An Experimental Study of Spray - Gasphase Interaction for a Co - Swirling Airblast Atomizer", in ILASS-Europe, October 1992, pp 115-122

18. Gupta, A. K., Lilley, D.G., Syred, N., "Swirl Flows", Tunbridge Wells, UK, Abacus Press, 1984, ISBN 0-85626-175-0, pp 187-218

19. Blümcke, E., Brandt, M., Eickhoff, H., Hassa, C., "Particle Dispersion in Highly Swirling Turbulent Flows", submitted to Part. Part. Syst. Charact

20. Edwards, C.F., Rudoff, R.C., Bachalo, W.D., " Measurement of Correlated Droplet Size and Velocity Statistics, Size Distribution and Volume Flux Characteristics in a Steady Spray Flame", in 5th. Int. Symp. on Appl of Laser Tech. to Fluid Mech., July 1990, Paper 31.5

21. Sturgess, G.J. et al., "Lean Blowout in a Research Combustor at Simulated Low Pressures", J.Eng. Gas Turbines and Power, V114, pp 13-19, 1992

22. Pavlovskij, B., Semidetnov, N., "Simultaneous Velocity, Size and Concentration Measurement for Particles moving in two-phase flows. Technique of Measurements, ISSN 0368-1025, 9, 1991, pp 40-42 from russian

23. Bolado, R., Yule, A.J.," The Relationship Between Atomization Characteristics and Spray Flame Structures", ICLASS, 1982, Paper 9-1

Discussion

Question 1. Dr G. Andrews

You have produced good spray measurement results in a lean burning fuel injector in the near burner region. Unfortunately, with no air preheat, you were unable to study combustion in this region. Do you have any plans to add air preheat to this system? Also, the very large flow expansion downstream of the swirl atomiser produced unrealistically low velocities and high residence times. How did this influence your results and could it have contributed to the flame fluctuations.

Author's Reply

In our laboratory, experiments are performed on RQL combustors with preheat and with nozzles similar to the one presented. In those tests, the flame also does not sit on the burner mouth, but has its root at some distance from the nozzle, so I am not sure that the situation shown is not representative of preheated combustion. It would be most interesting to see the influence of preheat on the behaviour but it is not planned in the near future, unfortunately.

As to the second question, the nozzle-combustor expansion ratio was adopted to stay with the ratios chosen for an earlier investigation of the cold flow field (see Ref. 5). The resulting large combustor volume helps to investigate a lean flame with optical instrumentation without the additional expense of preheat, but the residence times are in fact not typical of an aeroengine combustor, and the emissions measurements might well be influenced by that. I have no data to make an informed guess on the possible influence of a greater than usual combustor volume on the intermittent nature of the flame.

Time-resolved Measurements in a Three Dimensional Model Combustor

R. Jeckel, S. Wittig
Lehrstuhl und Institut für Thermische Strömungsmaschinen
Universität Karlsruhe (T.H.)
Kaiserstr. 12, D-7500 Karlsruhe (Germany)

Abstract

Locally and time-resolved measurements of the velocity, temperature and species concentration in a three dimensional jet-stabilized combustor are presented. The combustor was developed at the Institute for Thermal Turbomachinery, University of Karlsruhe, for extended benchmark experiments. For the present investigation, the combustor was fired by propane. The profiles of the velocity, temperature and species distribution were determined at 7 planes along the combustor axis. For a better understanding, also a comparison between the cold flow and the reacting hot gas conditions is given.

The time-resolved velocity and temperature measurements were performed by a two component LDA-system as well as specially designed and optimized thermocouple probes. The time-dependent analysis demonstrates that the velocity and turbulence and/or the temperature fluctuations are dramatically increased under hot combusting conditions.

Finally, the locally determined species distributions are compared with the global concentrations at the exit of the combustor providing an excellent data base for numerical tests.

1 Introduction

The development of modern aircraft gasturbines is guided by the demand of high efficiency together with low emissions. In this context, one of the major topics is the optimization of the combustion chamber, because of its keyrole for both development goals. However, the high complexity of real combustors makes experimental as well as numerical investigations extremely difficult. As a consequence, predominantly simplified geometries have been used for scientific combustor studies. These model combustors can be subdivided into different groups according to the flame stabilization method.

Numerous studies are concerned with the analysis of bluff body stabilized flames (e. g. Sislian et al. [13], Roquemore et al. [12]) and swirl stabilized flames (e. g. Kutz [9], Edwards and Rudoff [3], Jones and Wilhemi [7]). Extensive research has also been done on flames combining different methods of flame stabilization. Ferrao and Heitor [4] examined a flame stabilized by a bluff body surrounded by a swirler. Richards and Samuelsen [11] investigated a combustor where radial injecting air jets interact with the recirculation region induced by a swirler at the combustor inlet. Despite the interaction of the jets with the recirculation zone, the flow in this combustor remains mainly 2-dimensional, like in all other studies, where the recirculation was induced by swirlers or bluff bodies.

However, no investigations of combustors with a strongly three-dimensional flow field have been published yet, even though there is general need for such studies, serving as bench marks for the evaluation and testing of modern computer codes for three-dimensional reacting flows. The intention of this paper is, to provide detailed data of a propane fired, reacting combustor with a strongly three-dimensional and also fluctuating velocity and temperature distribution.

The extended data base provides an advanced understanding of this type of flame and can be used as benchmark for the verification of the results of numerical calculations as presented in our parallel studies (Kurreck at al. [8]).

Presented at an AGARD Meeting on 'Fuels and Combustion Technology for Advanced Aircraft Engines', May 1993.

2 Experimental Configuration

The jet-stabilized combustor is designed in a way, that various geometrical configurations can be investigated using the same test facility. In addition, easy access for probe as well as optical measurement techniques is provided at each location inside the combustor .

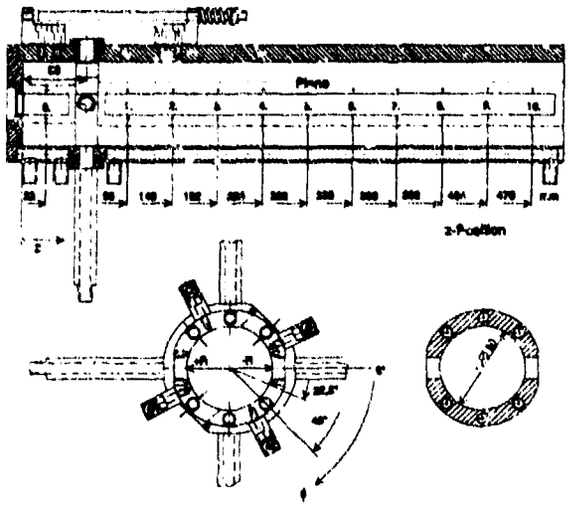

Fig. 1: Geometry of the combustor

The combustion chamber has a modular concept providing ready exchange of several components. Thus, the fuel-specie and fuel-injection systems can easily be changed by mounting different bottom plane sections with integrated atomizers. Also various air injecting tubes with different diameters can be mounted. The main features of the combustor are shown in Fig. 1.

The flame tube radius r_{FT} is 40 mm. The four jets are located 60 mm downstream from the bottom. The jet diameter is $d_{Jet} = 8\ mm$. The entire air mass flow is provided by these jets. The combustor entrance at the bottom plane is connected to the fuel supply. For the present measurements propane (C_3H_8) was used as fuel. But it is also possible to use liquid fuels like JP-4 or DF-2. The wall of the combustor is cooled by water, fed through six axial 0.5 m long channels (Fig. 1), enabling long time runs, which is a basic demand for the time consuming measurements.

The access for probe measurement techniques and optical diagnostics is provided by two axial slots, each of them covered by eleven metallic bricks. Instead of these bricks also glass windows or probe supports can be mounted. The ring with the four jets can be rotated about 65°. The angle of symmetry of the combustor is 45°. Hence it is possible to observe the relevant angle of 45° without moving the combustor.

3 Measurement Techniques

The inlet conditions and the wall-temperatures and -pressures as well as the overall emissions are monitored by standard equipment employing an IEC-Bus system for the data transfer. This guarantees constant conditions without a drift during the time consuming field measurements.

3.1 LDA – Setup

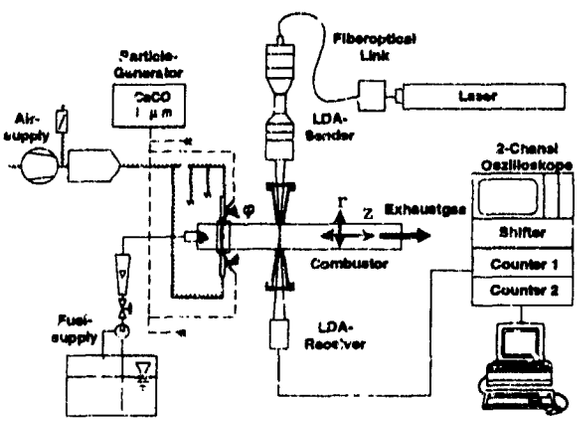

Fig. 2: LDA setup at the jet-stabilized combustor

The mean velocities and their fluctuations are measured by a Dantec two channel dual beam LDA. The LDA setup is shown in Fig. 2. The Ar-Ion laser (Coherent Inova 90) is connected via a fiberoptical link to the optical modules. The system is used in forward scattering mode for maximum scattering light power. The angle between the two measurement planes of the different colors is 90°. The angle between the measurement plane and the r, z - plane of the combustor (Fig. 1) is +/ – 45°.

The signals are converted by counters (Dantec) and processed via a Zech acquistion interface on a PC

'386. For the time dependent analysis a new LDA controlling software was developed. Performance comparisons with a Dantec burst spectrum analyser show excellent agreement of the velocities detected even in zones of very low data rates.

The optical access to the combustor is achieved by window modules. These windows are kept clean and cold by an air flow, which provides a swirling air film over the combustor side of the quartz glass window. The flow of the window cooling air is adjusted such, that the main flow within the combustor is not affected.

The air of each jet is seeded with calzium carbonate particles with a D_{50} of 1 μm. A Polytec particle generator (RGB 1000) is used for dispersing the particles in the flow.

3.2 Temperature – Measurements

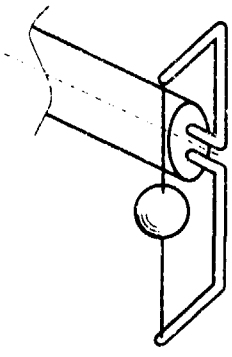

Fig. 3: Thermocouple probe

With respect to the requirements of locally resolved combustor measurements platinum / platinum rhodium – thermocouples are most convenient. The fundamentals of the thermocouple measuring technique in highly tubulent flames are given in various references (e.g. Heitor [5], Sislian et al. [13]). However, preliminary studies using simple thermocouple probes demonstrated, that the conduction losses of the probe are strongly affected by the design of the sensor. Even thermocouple probes of the design proposed by Bradley and Matthews [1] showed significant thermal losses, which was easily demonstrated, whenever the probe was inserted from both sides in radial direction into the combustor at locations with temperature gradients leading to different temperatures. Consequently, an improved probe design was developed starting from a rigorous analysis of the governing heat transfer processes inside the probe. The small diameter of the bare wires of 65 μm reduces the heat conduction, that can influence the temperature sensitive spot of the probe significantly. On the other hand, the sphere with a diameter of 2.5 mm offers a large area for the convective heat transfer from the flow.

The remaining problem of radiation losses could not yet be solved sufficiently. However, it is expected to have a relatively strong influence in such a combustor, where a high intensive reacting flame and watercooled walls interact with the probe. Various approaches are found to account for radiation losses in the literature. They all suffer from the problem, that neither the emissivities of the probe, the gas and the combustor walls nor the heat transfer coefficient of convection governed by the flows velocity and viscosity are known in detail. Therefor in this paper all temperatures are presented without any correction of the radiative losses.

However, the new probe design gives identical temperature profiles independently from the traversing direction. This is an important step towards exact measurements of local temperatures. Because of the probes integrating nature, only time average measurements are possible, which however are best suited for comparison with results of the numerical analysis.

3.3 Gasanalysis – System

For the determination of the species concentration a new gas analysis system is set up. The flow diagram of the sample gas is shown in Figure 4. The unburned hydrocarbons (C_xH_y) are measured by a hot, wet sampling system using a flame ionisation detector. On the cold side of the system, the water is quenched off with a sample gas cooler. Non dispersive infrared analysers detect carbon monoxide, carbon dioxide and nitrogen oxide. An electrochemical sensor is used for measuring the oxygen contents of the sample

With respect to the well known problems of isokinetic gas sampling a constant mass flow rate of 160 l/h is adjusted, according to the requirements of the analysis system. Unwanted reactions of the gas sample inside the probe are avoided due to high velocities inside the probe. Several investigations on the design of the sampling probe demonstrated, that the

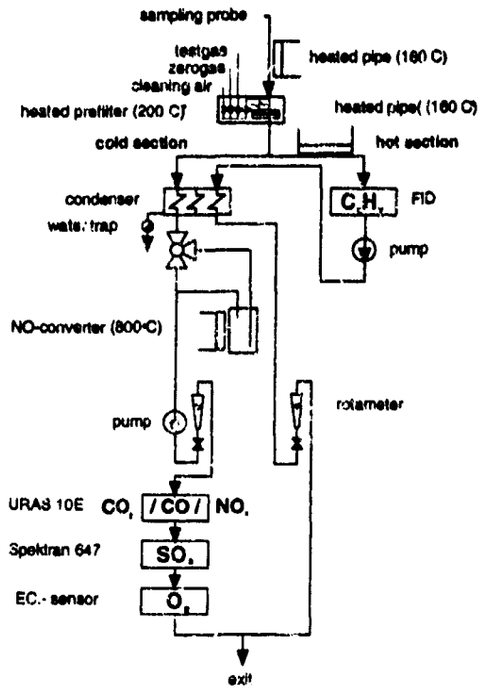

Fig. 4: Gasanalysis rack

shaft diameter of the probe has strong influence on the measured gas composition. It is estimated that probes with larger diameter act as flame holders. In consequence, a probe with a very small diameter is used.

4 Results

The results are presented with the intention to describe the isothermal and the reacting - propane fired - flow completely in detail. The figures provided in this chapter are selected to illustrate the discussion of major effects. However, the entire datasets are presented in overview diagrams in the appendix providing a database for numerical calculations.

For a complete analysis of the flow in this atmospheric combustor all ambient and inlet conditions were recorded (see Table 1).

4.1 Jet Profiles

The four jets, which provide the total air mass flow, induce a recirculation zone between the bottom plate and the air injection plane. A correct symmetry of the recirculation zone requires a uniform distribution of the air over the four jets. For verification of the uniformity, the velocity and turbulence level profiles of the four jets have been checked by a hot wire anemometer (Fig. 5)

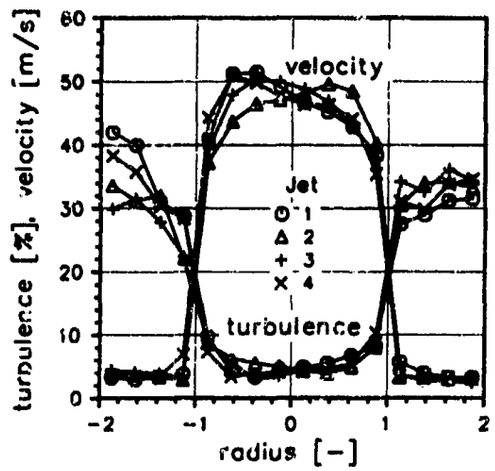

Fig. 5: Comparison of the four jets: velocity and turbulence profiles

In contrast to the fully developed turbulent flow profile expected, a not completely axissymmetric profile is observed. The orientation of these profiles relative to the axis depends on the location of the tubes, which connect the air supply to the jets. This instabilitiy is of dominant influence on the resulting velocities in the planes analysed (Fig. 1). Therefore, the orientation of the four tubes is kept constant during all following measurements to obtain reproducible inlet conditions.

4.2 Velocity

The velocity distribution of the cold flow in the combustor has been discussed earlier in detail by Jeckel et al. [6]. In addition, the axial velocities of the $\varphi = 0°$ - plane are presented in the appendix of this paper (Fig. 17). It has to be noted, that no dependence of the velocity distribution on the injection angle φ can be observed under nonreacting conditions, because of the high turbulence levels.

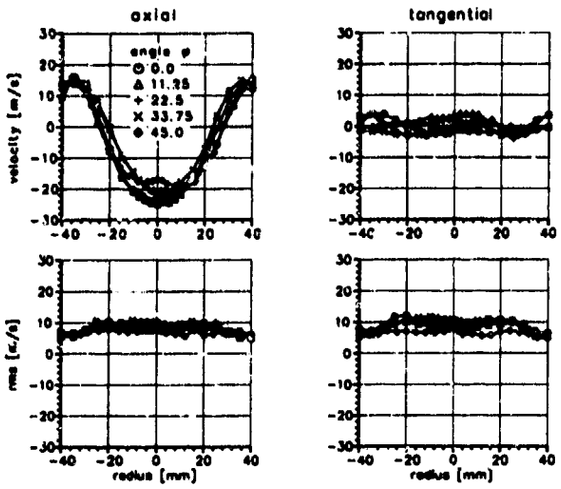

Fig. 6: Velocity profiles in plane 0
z = 22 *mm*; $\dot{m}_{air,total}$ = 33,5 *kg/h*;
$\dot{m}_{propane,total}$ = 1,0 *kg/h*;

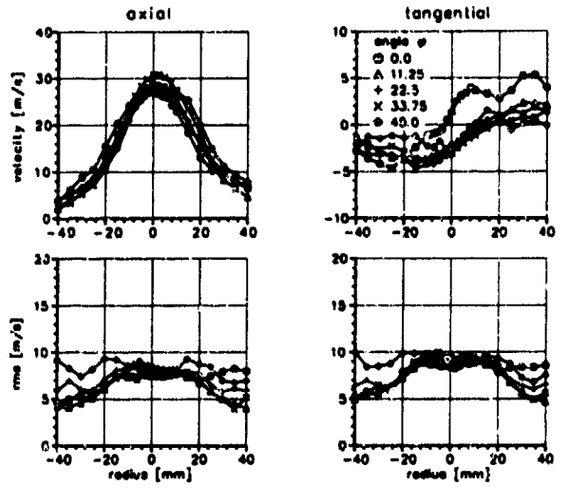

Fig. 7: Velocity profiles in plane 1
z = 98 *mm*; $\dot{m}_{air,total}$ = 33,5 *kg/h*;
$\dot{m}_{propane,total}$ = 1,0 *kg/h*;

In the following the reacting flow is considered. Figure 6 shows the flow in plane 0 (z = 22 *mm*) inbetween the dome of the combustor and the air jets. Obviously, a recirculation zone is established, which stabilizes the flame. The distribution of the tangential velocity component indicates, that no predominant direction of rotation is established in the flow. In addition, the extremly high fluctuations, shown as rms-values for each component in Figure 6, are also found under reacting conditions.

The velocity profiles of the plane 1 (z = 98 *mm*; downstream of the air injecting plane) are presented in Figure 7. The flow has a Gaussian velocity distribution with its maximum values on the axis of symmetry (r = 0). In this plane the highest axial velocity is found compared to all planes downstream of air injection. The tangential velocity profiles indicate that the interaction of the four jets induces a rotation of the flow. It decreases rapidly downstream, because of strong turbulent mixing, which is caused by the combustor configuration and enhanced by chemical reaction of the fuel with the air. Therefore, turbulent mixing induces a homogenisation of the velocity profiles further downstream. As consequence, a piston profile was found in plane 9 (z = 434 *mm*) close to the combustor exit (Figure 18).

4.3 Temperature

Detailed measurements of the temperature were performed at all seven axial positions for three different air injection angles. The temperature distribution in plane 0 (z= 22 *mm*) (Fig. 8) shows two maxima, each located around the center of the recirculation zone, with highest temperatures of about 1600 *K* and minimum temperatures of about 900 *K* on the combustors axis. The very lean fuel to air ratio

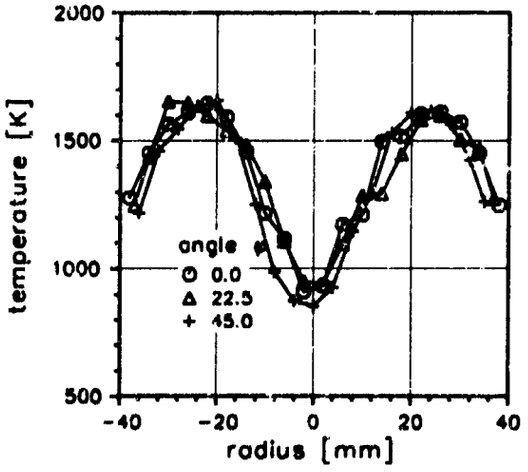

Fig. 8: Temperature distribution at various jet angles φ
z = 22 *mm*; $\dot{m}_{air,total}$ = 33,5 *kg/h*;
$\dot{m}_{propane,total}$ = 1,0 *kg/h*,

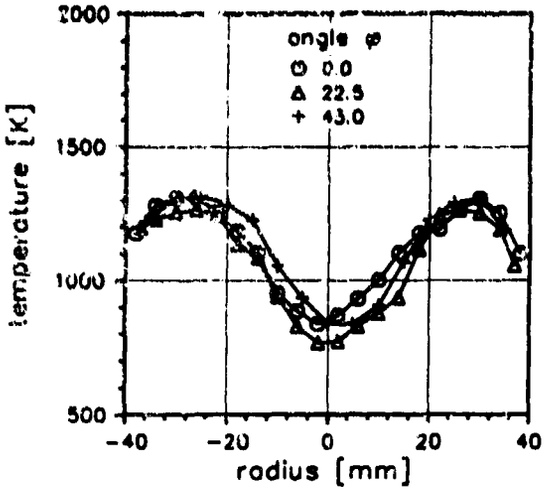

Fig. 9: Temperature distribution at various jet angles φ
$z = 98\ mm$; $\dot{m}_{air,total} = 33{,}5\ kg/h$; $\dot{m}_{propane,total} = 1{,}0\ kg/h$;

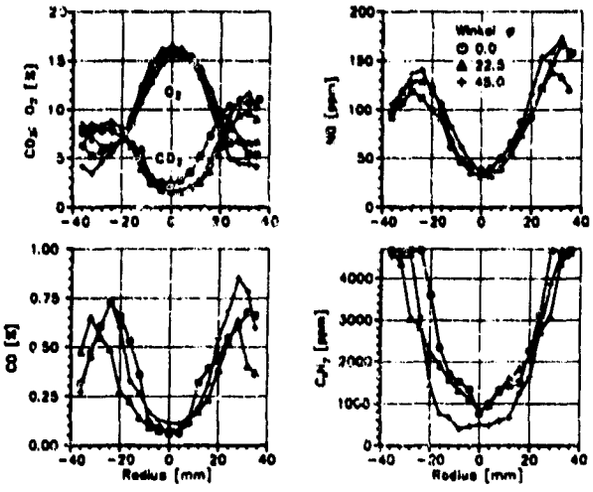

Fig. 10: Comparison of the emission profiles in plane 0 ($z = 22\ mm$)
$\varphi = 0°$; $\dot{m}_{air,total} = 33{,}5\ kg/h$; $\dot{m}_{propane,total} = 1{,}0\ kg/h$;

(compare Table 1) and also the watercooled walls of the combustor are responsible for the relatively low temperature maxima of 1600 K. The minimum values of 900 K on the axis are caused by recirculating fresh air. Also, no dependence on the air injection angle could be detected in the temperature profiles (Fig. 9).

This was also found in the plane directly behind the air injection (Fig. 9). The minimum value on the axis of 900 K is caused by the fresh air flowing directly downstream. The maxima of the temperature at radial positions of $\pm$ 25 mm are with 1300 K not as high as in plane 0, due to enhanced turbulent mixing.

4.4 Species Concentration

The gas composition was analysed at identical positions as the temperatures. The sampling system gave the possibility of analysing O_2, CO_2, CO, C_xH_y and NO_x. The results of the sampling in the first two planes are shown in Figure 10 and 11 for all five species. The species distributions are directly correlated with the temperature distributions (see Chapter 4.3). The high oxygen concentrations on the combustor axis are due to the jet induced fresh air flow on the axis. Consequently, the carbon dioxide concentrations have their minimum in this region. The unburned hydrocarbons are found mainly at large radial positions, indicating that the entire fuel mass flow is shifted to the outer regions of the combustor. This is due to the recirculating fresh air on the axis, which transports the fuel to the regions, where the recirculation zone allows the stabilization of the flame. Here, the major advantage of this type of flame stabilization becomes obvious, as only fluiddynamic effects are responsible for the flame stabilization. No additional hardware is required to act as flame holder.

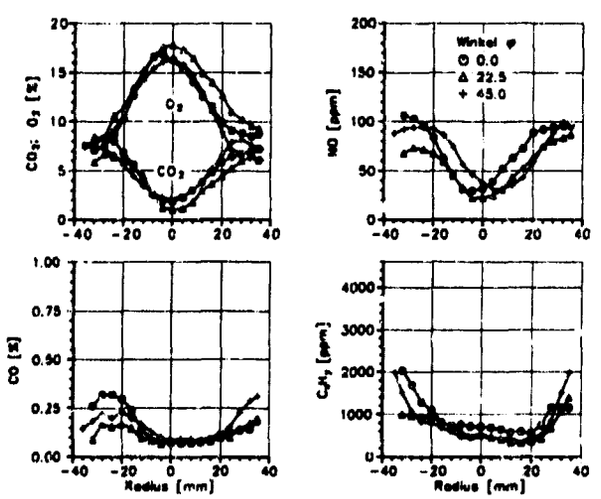

Fig. 11: Comparison of the emission profiles in plane 1 ($z = 98\ mm$)
$\varphi = 0°$; $\dot{m}_{air,total} = 33{,}5\ kg/h$; $\dot{m}_{propane,total} = 1{,}0\ kg/h$;

The concentration of the unburned hydrocarbons downstream of the air injection plane ($z = 98\ mm$, Fig. 11) indicate, that the reaction is almost completed. This statement is also confirmed by visual observation. The gradients of the concentration profiles are relatively high at the outer radii, but the turbulent mixing homogenizes the radial distributions of the species concentrations further downstream (Fig. 20 and 21).

4.5 Time Resolved Analysis

All measurements presented so far, indicate no dependence of the flow on the angle φ of air injection. In order to analyse the reasons for this unexpected behaviour, a detailed time dependent analysis of the velocity and temperature fluctuations was performed.

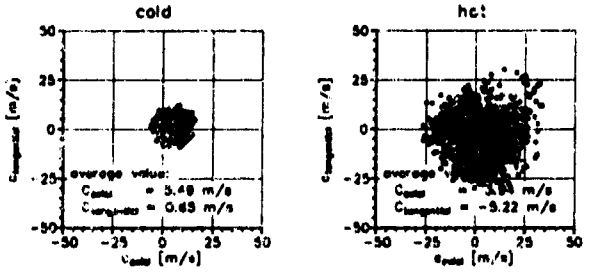

Fig. 12: Comparison of the local velocity at position z = 22 mm, $\varphi = 0°$, r = -25; $\dot{m}_{air,total}$ = 33,5 kg/h; $\dot{m}_{propane\ total}$ = 1,0 kg/h;

The axial and tangential velocity fluctuations were analysed on basis of LDA-samples containing 10'000 single measurements (sampling rate 1 kHz). Figure 12 visualizes the difference between the cold and hot flow case. The distribution of the cold velocity around the average value is very broad, but in the reacting case, there is still an enormous increase in the broadness of the distribution. The plots of the axial velocity versus the tangential velocity of both flow conditions (Fig. 12) show a stochastic distribution but no bi-modality or other effects indicating a flapping between different flow patterns. Due to the enhanced turbulence level of the reacting flow the velocity distribution is also broadened.

This is confirmed by plotting the axial velocity versus time, as shown in Figs. 13 and 14. Here, the velocity distribution is nearly stochastic for both flow situations, but the intensity of the fluctuations is

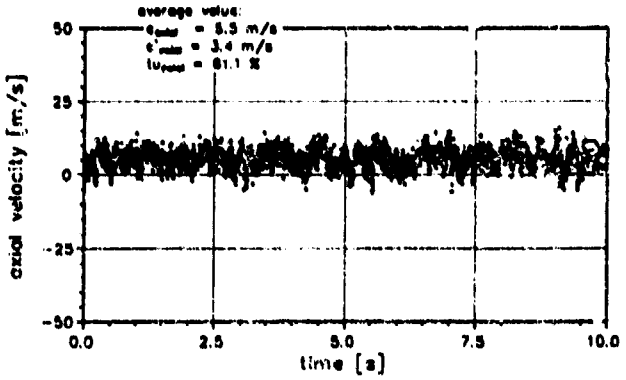

Fig. 13. Cold flow: timedependence of the axial velocity at position z = 22 mm, $\varphi = 0°$, r = -25; $\dot{m}_{air,total}$ = 33,5 kg/h;

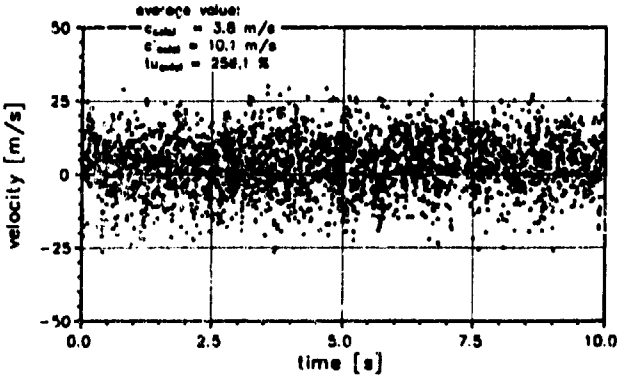

Fig. 14: Hot flow: timedependence of the axial velocity at position z = 22 mm, $\varphi = 0°$, r = -25; $\dot{m}_{air,total}$ = 33,5 kg/h; $\dot{m}_{propane,total}$ = 1,0 kg/h;

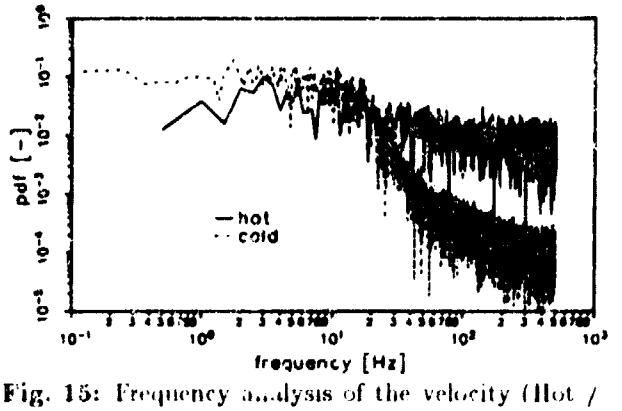

Fig. 15: Frequency analysis of the velocity (Hot / Cold) in the point z = 22 mm, $\varphi = 0°$, r = -25; $\dot{m}_{air,total}$ = 33.5 kg/h; $\dot{m}_{propane,total}$ = 1.0 kg/h.

much higher for the reacting flow.

In order to get a deeper insight whether the velocity fluctuations are really stochastic or whether dominant frequencies are detectable, the recorded velocities were transformed in power spectra by means of the FFT-method.

The FFT-method allows an analysis in a frequency range depending on the sampling rate $f_{sampling}$ and the sampling depth n_{sample}.

$$f_{min} = \frac{f_{sampling}}{n_{sample}}$$

$$f_{max} = \frac{f_{sampling}}{2}$$

For the sampling rate chosen of 1 kHz, a detectable frequency is in range from 0.1 Hz to 500 Hz.

The two spectra of the cold and the reacting flow (Fig. 15) show similar characteristics with a couple of high intensity, low frequent shares and a decrease of the intensity for increasing frequencies. But it is important to note, that at higher frequencies ($f \geq 20$ Hz) the intensity of the velocity fluctuations of the cold flow is about one order of magnitude below that of the reacting flow. For the cold flow a pronounced decrease of the fluctuations is obtained above 20 Hz , whereas for the reacting flow only a slight decrease is observed.

The extremly high level of the turbulent fluctuations is also detectable in the plot of the temperature versus time, measured with a time response optimized thermocouple with a sampling rate of 2500 Hz. Knowing that thermocouples are not able to follow fluctuations of high frequency , this figure gives only an impression of the range of the temperature fluctuations in the reaction zone.

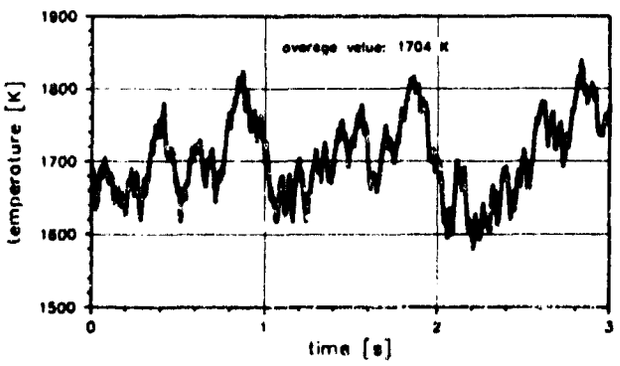

Fig. 16: Temperature time serie.
$z = 22\ mm$, $\varphi = 0°$, $r = -25$;
$m_{air,total} = 33.5\ kg/h$; $m_{propane\ total} = 1.0\ kg/h$;

5 Conclusions

The flow field, temperature distribution and species concentration and their fluctuations have been studied in a jet-stabilized combustor under burning and nonburning conditions. The measurements provide an extensive data base for verification and testing of numerical codes.

For high accuracy measurements under operating combustor conditions improved thermocouple and species sampling probes have beeen developed.

The measurements of time averaged velocity, temperature and species distributions reveal, that threedimensional effects induced by the highly turbulent flow in this type of combustor are of major significance.

Therefor, special emphasis has been put on the study of the effects by time resolved measurements of the velocity and temperature, using an advanced LDA sampling technique and optimized thermocouple probes. The results show that turbulence is strongly enhanced under reacting conditions.

Acknowledgement

The present study was supported by a grant from the AG TURBO (Arbeitsgemeinschaft Hochtemperatur-Gasturbine) sponsored by the Federal Minister of Research and Technology.

References

[1] Bradley D., Matthews K.J.: Measurement of High Gas Temperatures with Fine Wire Thermocouples. Journal Mechanical Engineering Science; Vol.10; No.4; p.299-305; (1968)

[2] Brum R.D., Seiler E.T., Larue J C., Samuelsen G.S.: Instantaneous Two-Component Laser Anemometry and Temperature Measurements in a Complex Flow Model Combustor. AIAA 21^{st} aerospace science meetings. Reno, Nevada; paper 83 - 0334, (10 - 13 Aug.1983)

[3] Edwards C.F., Rudoff R.C.: Structure of a Swirl-Stabilized Spray Flame by Imaging, Laser Doppler Velocimetry, and Phase Doppler Anemometry. 23^{rd} (Int.) Symposium on Combustion, p. 1353 - 1359, (1990)

[4] Ferrao P., Heitor M. V.: Simultaneous Measurements of Velocity and Scalar Characteristics for the Analysis of Turbulent Heat Transfer in Recirculating Flames. 6^{th} int. Symposium on the Application of Laser Techniques to Fluid Mechanics, Lissabon, (20 - 23 July 1992)

[5] Heitor, M. V.: Experiments in turbulent reacting flows. Thesis of the University of London, Imperial college, (August 1985)

[6] Jeckel R., Noll B., Wittig S.: Three Dimensional Time-resolved Velocity Measurements in a Gas Turbine Model Combustor. 6^{th} Int. Symposium on the Application of Laser Techniques to Fluid Mechanics, Lisbon, (20 - 23 July 1992)

[7] Jones W.P., Wilhelmi F.: Velocity, Temperature and Composition Measurements in a confined Swirl-Driven Recirculating Flow. Combustion Science and Technology, Vol. 63, p. 13 - 31, (1989)

[8] Kurreck M., Scheurlen M., Wittig S.: Vergleich der numerischen Simulation von 3-dimensionalen jet-stabilisierten Brennkammerströmungen mit einem Vektorrechner und einem Workstationcluster. to be published: VDI-Berichte, 16. Deutscher Flammentag, (1993)

[9] Kurz R. H.: Bestimmung der Abgasemissionen aus Brennräumen: Möglichkeiten und Grenzen von Modellansätzen bei Brennstoffzerstäubung. Dissertation, Institut für Thermische Strömungsmaschinen, Universität Karlsruhe, (1985)

[10] Pfeiffer, A.; Schultz, A.; Wittig, S.: Design and Development of the ITS Ceramic Research Combustor. Proceedings of the 1991 Yokohama International Gas Turbine Congress, Japan, 91-Yokahama-IGTC-45, (1991).

[11] Richards C.D., Samuelsen G.S.: The Role of Primary Jets in the Dome Region Aerodynamics of a Model Can Combustor. ASME-Paper 90-GT-142; Int. Gas Turbine and Aeroengine Congress and Exposition; Brussels, Belgium; (June 11-14 1990)

[12] Roquemore W.M., Bradley R.P., Stutrud J.S., Reeves C.M., Obringer C.A.: Utilization of Laser Diagnostics to evaluate Combustor Models. AGARD - CP - 353, pp. 36, (Oct.1983)

[13] Sislian J. P., Jiang L. Y., Cusworth R. A.: Laser Doppler Velocimetry Investigations of the Turbulence Structure of Axisymmetric Diffusion Flames. Prog. Energy Combust. Sci., Vol 14, p. 99 - 146 (1988)

Nomenclature

Symbol	Unit	Physical Property
AFR	-	air to fuel ratio
D_{50}	μm	mean diameter of seeding particles
c	m/s	velocity
$\bar{c}_{ax}$	m/s	axial mean velocity
$\bar{c}_{tan}$	m/s	tangential mean velocity
c'_{ax}	m/s	axial velocity fluctuations
c'_{tan}	m/s	tangential velocity fluctuations
d	mm	diameter
f_{min}	Hz	lowest detectable frequency
f_{max}	Hz	highest detectable frequency
f_{sample}	Hz	sampling frequency
n_{sample}	-	number of samples
$\dot{m}$	kg/h	mass flow
r	mm	radius
r_{FT}	mm	radius of the combustor flame tube
ϕ	-	equivalence ratio
φ	[-]	angle between injection and measurement plane
EIX	gr/kg	emission index of specie x
P	KW	power
T	$^{\circ}K$	temperature
Tu	%	turbulence level
z	mm	axial distance from bottom plane

Appendix

d_{FL}	80.0	mm
z_{total}	1220.0	mm
$z_{watercooledTube}$	520.0	mm
$z_{Bottom/Jet}$	60.0	mm
d_{Jet}	8.0	mm
$\dot{m}_{Air}$	33.5	kg/h
T_{Air}	292.0	K
$\bar{c}_{Jet,in}$	38.5	m/s
$Fuel$	C_3H_8	$Propane$
$\dot{m}_{Fuel}$	1.0	kg/h
T_{Fuel}	292.0	K
$c_{Fuel,in}$	20.0	m/s
λ	2.28	
AFR	33.5	
$P_{thermal}$	12.1	kW
$P_{specific}$	40.1	MW/m^3
$\dot{m}_{CW}$	400.0	kg/h
$T_{CW,in}$	279	K
$T_{CW,out}$	289	K
$\bar{T}_{Wall}$	350	K
$T_{exhaust}$	750	K
$VK(O_2)$	12.5	%
$VK(CO_2)$	5.5	%
$VK(CO)$	784	ppm
$VK(NO_x)$	63	ppm
$VK(C_xH_y)$	121	ppm

Table 1: Characteristics of the Jet-stabilized Combustor

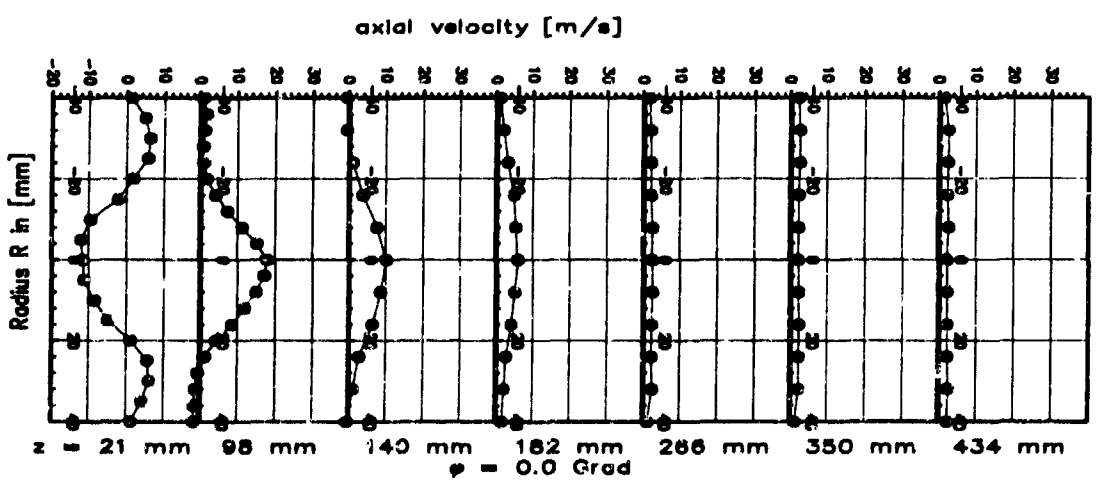

Fig. 17: Axial - velocity - profiles in the combustor: cold flow; 0° - degree - plane; $\dot{m}_{air} = 33.5\ kg/h$

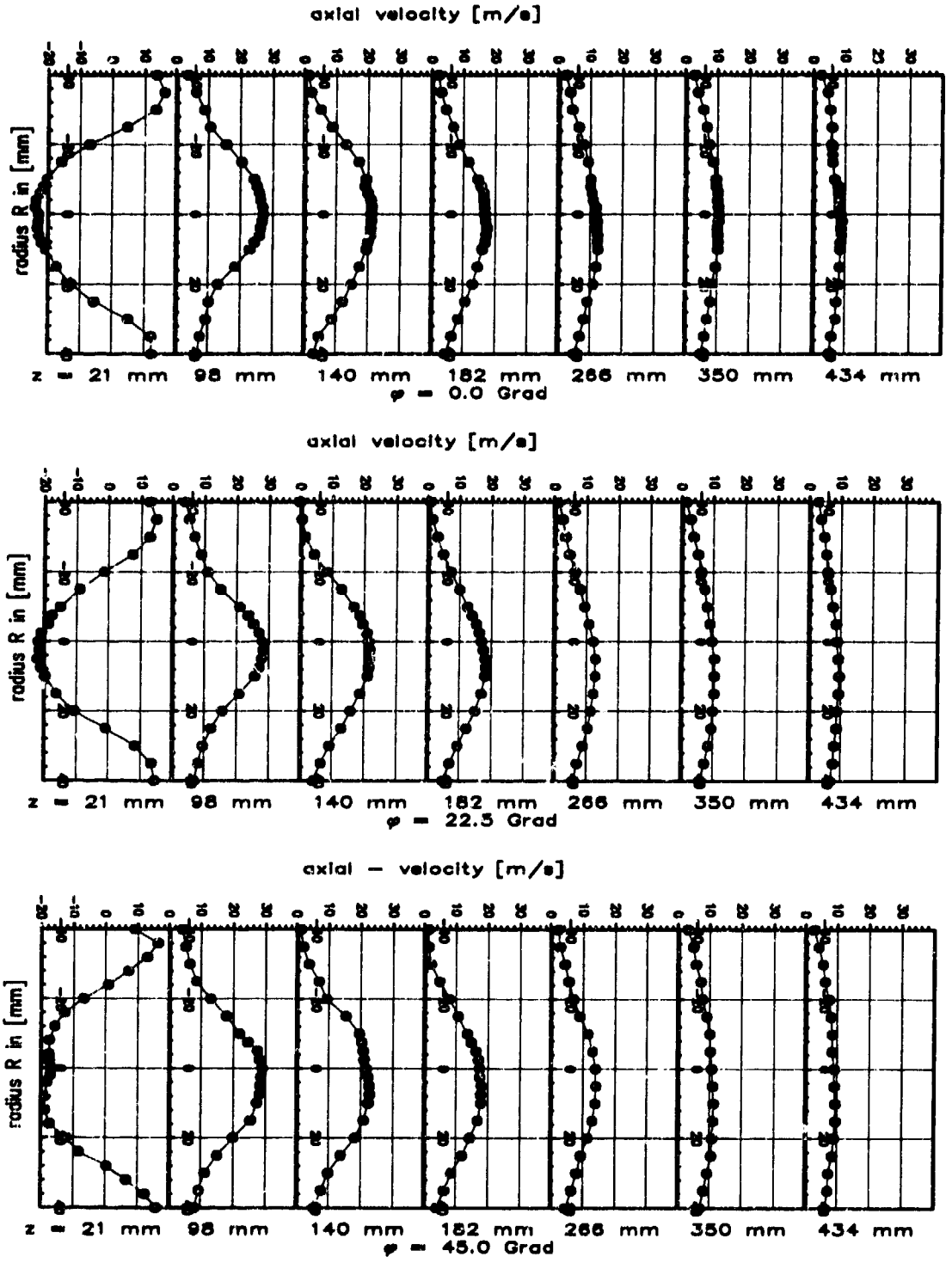

Fig. 18: Axial velocity profiles in the combustor: $\dot{m}_{air,total} = 33{,}5\ kg/h$; $\dot{m}_{propane,total} = 1{,}0\ kg/h$;

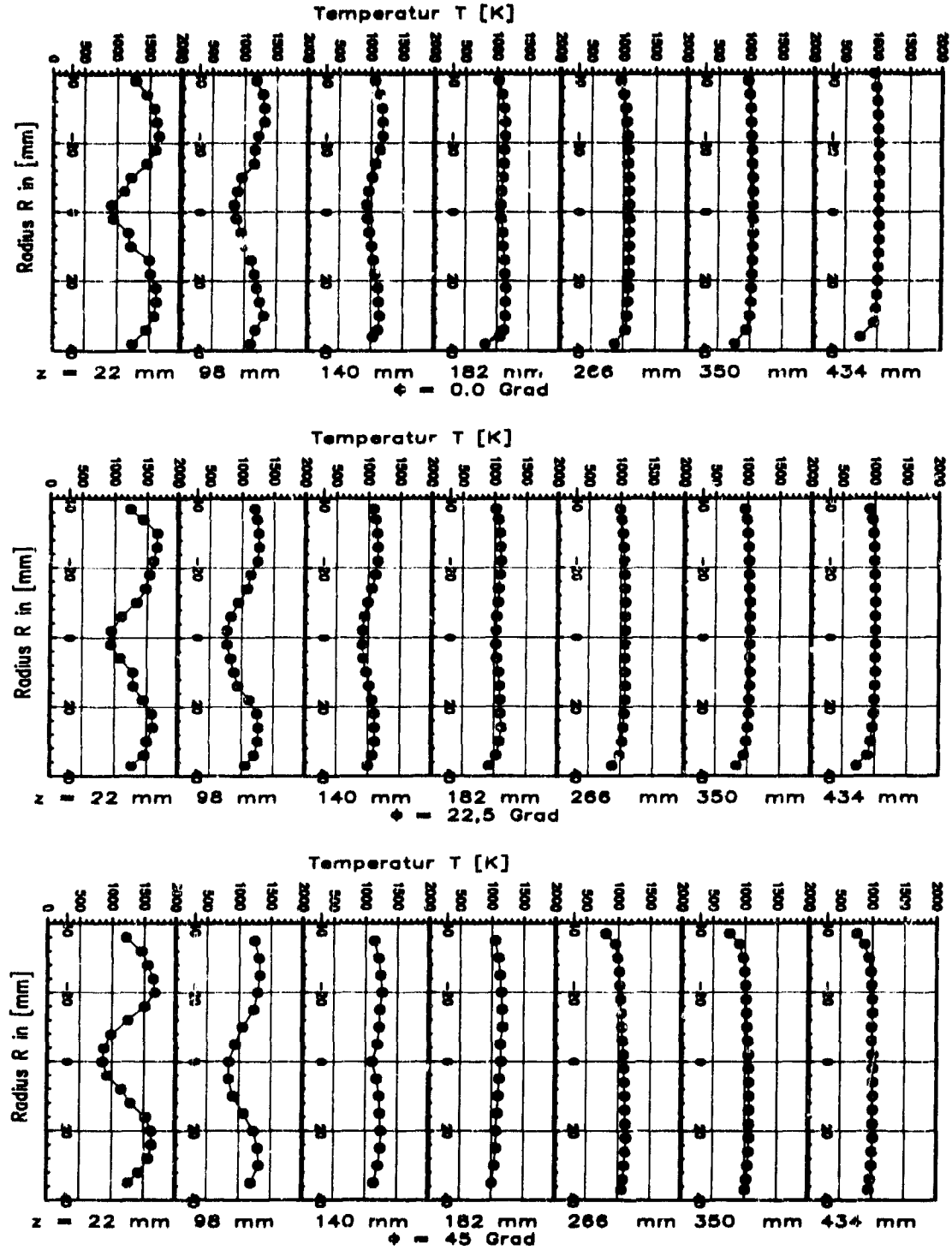

Fig. 19: Temperature profiles in the combustor: $\dot{m}_{air,total} = 33{,}5\ kg/h$; $\dot{m}_{propane,total} = 1{,}0\ kg/h$;

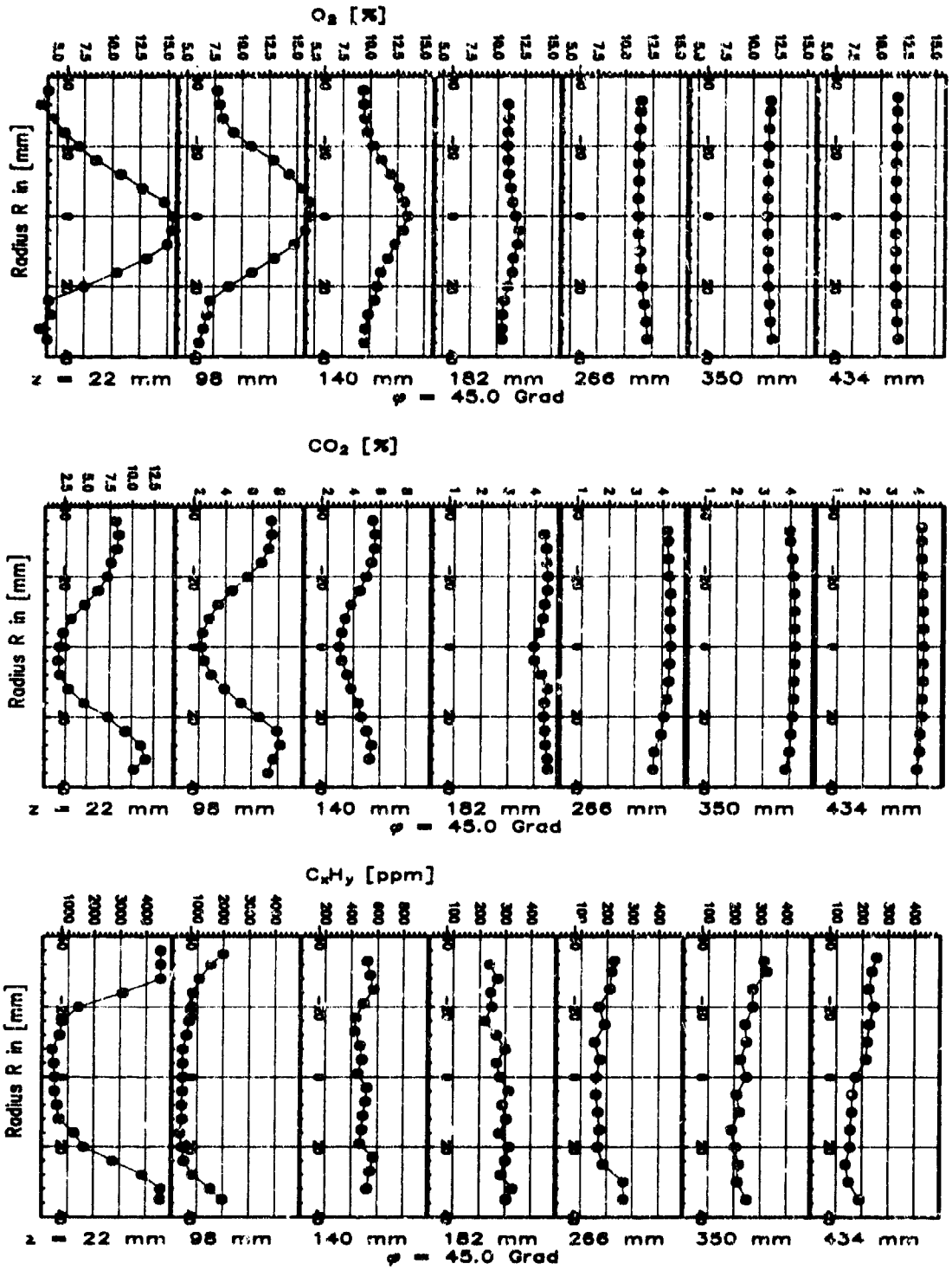

Fig. 20: Emission profiles in the combustor: $\varphi = 0°$; $\dot{m}_{air,total} = 33{,}5\ kg/h$; $\dot{m}_{propane,total} = 1{,}0\ kg/h$;

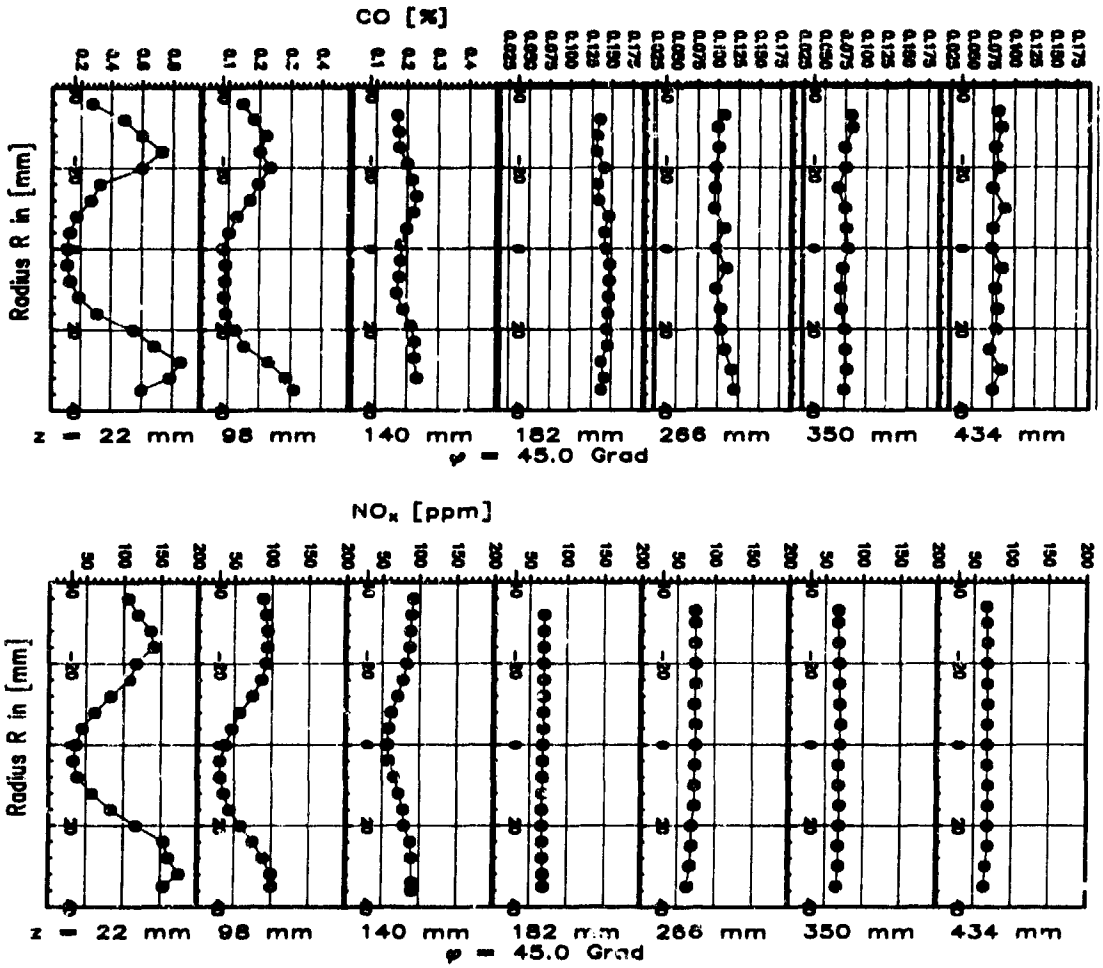

Fig. 21: Emission profiles in the combustor: $\varphi = 0°$; $\dot{m}_{air,total} = 33{,}5\ kg/h$; $\dot{m}_{propane,total} = 1{,}0\ kg/h$;

Discussion

Question 1. M. Nina
The configuration you showed for your thermocouple seems to be prone to large errors due to the large surface area of the sphere at the weld. The errors would be mainly from radiation and catalytic effects of platinum and platinum rhodium. Would you comment on these aspects?

Author's Reply
Our intention for recommending this probe design was the reduction of the temperature error due to conduction losses, which are extreme in a flame with high gradients, like the one in the combustor investigated. This probe design provides symmetric results, even in a flame with two maxima. Also the results are independent of the traverse direction. This proves the advantage of this new probe design, compared to various probe designs proposed in the literature. Of course there are errors due to radiation and catalytic effects. According to the literature the catalytic error is estimated to be relatively small. This was confirmed by our experiments using coated and uncoated probes. The radiation errors are not negligible, of course. However, we developed a program which compares the most important radiation corrections available in the literature. These different approaches result in a correction in the sampled temperature data over a range from 20 to 400K at every high temperature point. In our opinion, however, the presentation of the raw sampled data is the best way to present the measured thermocouple temperatures.

Question 2. S. Maidhof
Can you give an estimate of the extension of the measuring volumes for the various measuring techniques? Can the independence of the measurements of the tangential position be partly caused by the tangential size of the measuring volume?

Author's Reply
For the LDA measurements, the measurement volume had a diameter of 200 microns and a length of 600 microns. The thermocouple sphere diameter was 2.5 millimetres. A suction probe was used for gas sampling with an inner diameter of 1mm and an outer diameter of 1.6mm. Therefore, the local resolution is much better than the distance between the different angular positions at the outer radii where the differences would be expected.

Question 3. J. Tilston
The time resolved temperature measurements seem to show a one second sawtooth profile period. Is this real or is it just a visual illusion on this illustration?

Author's Reply
The temperature fluctuations in the combustor primary zone are very extreme at every point. At some locations the time resolved temperatures indicate a sawtooth profile, but it is not reproducible. Considering all the data available, it can be concluded that the temperature fluctuations are more or less stochastic.

Question 4. S. Sivasegaram
Have you carried out measurements of the fluctuating temperatures with the flow rate and fuel/air ratio as variables, in order to identify the source of the very low frequency fluctuation?

Author's Reply
No, we have not examined that in detail until recently, since our intention was to collect a complete local resolved dataset. However, a variation of the fuel/air ratio influenced the sound emission.

Question 5. S. Alizadeh
Do you think it is surprising that the time resolved measurements, taken at a location within the combustor primary zone, indicate isotropic turbulence?

Author's Reply
Yes, it is surprising. However, even the angle independence of the measured profiles indicate there is strong mixing which is direction independent. A detailed examination of the data revealed that the fluctuations are extreme and that they are isotropic. The level of the fluctuations decreases with increasing z-positions, but the isotropy was found throughout the combustor. This statement is emphasized by the excellent agreement of the measured results with the calculated data using the kappa, epsilon model.

TEMPERATURE AND COMBUSTION ANALYSIS OF COMBUSTOR WITH ACOUSTICALLY CONTROLLED PRIMARY ZONE AIR-JET MIXING

P.J. Vermeulen*, V. Ramesh**, B. Sanders***
Department of Mechanical Engineering
The University of Calgary
Calgary, Alberta, Canada. T2N 1N4

and

J. Odgers
Professor Titulaire (Retired)
Département de Génie Mécanique
Université Laval
Québec, P.Q., Canada. G1K 7P4

SUMMARY

A small tubular combustor of normal design and behaviour, employing acoustically controlled primary zone air-jet mixing processes, has been successfully tested at scaled ¼ load operating conditions, and some data was obtained at ½, ⅝ and ¾ loads. The acoustic control produced a distinct richening effect, measured just downstream of the primary zone, which produced a decrease in combustion efficiency and a somewhat increased and flatter combustion gas temperature distribution. The prime cause of richening was due to combustor flow blockage caused by acoustically enhanced jet penetration. This, and the secondary effect of acoustically shed jet toroidal vortices, resulted in up to 35% increase in mixing, relative to "no-drive" measured just downstream of the primary zone.

The acoustic drive produced a more uniform exit plane temperature pattern, resulting in up to 35% improvement in mixing relative to "no-drive" and in up to 20% relative improvement in the temperature pattern quality. The effects depended on air/fuel ratio and in general improved relative to "no-drive" with richening. At ¼ load, 150W single driver power, the acoustic driving effectiveness was reduced by about 80% with correspondingly reduced improvements in mixing and quality. The effects of acoustic drive were favourably controllable by means of the driving power, and the exit plane data showed increased flow blockage caused by increased jet penetration by the acoustic drive was the major control mechanism.

NOMENCLATURE

A/F	overall air/fuel ratio (by mass flow rate)
D	jet orifice diameter
EI	local emission index
f	driving frequency
$\dot{M}_a$	total air mass flow rate
$\dot{M}_{ae}$	equivalent mean air mass flow rate at entrance to secondary zone
$\dot{M}_f$	fuel mass flow rate
M_r	reference Mach number based on maximum I.DIA. of casing
n	number of data points
ND	"no-drive"
P_2	inlet static pressure
P_3	exit static pressure
P_{02}	inlet stagnation pressure
P_{03}	exit stagnation pressure
Q	exit temperature pattern quality
R	residual temperature standard deviation
S_m	mixing standard deviation calculated for all exit plane temperature data
S_{ms}	mixing standard deviation based on combustion gas temperatures
S_{mt}	mixing standard deviation calculated for truncated exit plane temperature data
S_p	temperature profile acoustic driving standard deviation calculated for all data of set
S_{pt}	temperature profile acoustic driving standard deviation calculated for truncated data set
T	local average stagnation temperature ≅ local average static temperature
T_d	dilution zone wall temperature
T_f	fuel temperature
T_g	local combustion gas temperature
T_{gm}	mean combustion gas temperature
T_p	primary zone wall temperature
T_2	inlet temperature
T_3	exit plane local average temperature
T_{3m}	exit plane mean temperature
T_{3max}	exit plane local average maximum temperature
T_{3ND}	exit plane local average temperature "no-drive"
T_{3WD}	exit plane local average temperature "with-drive"
$\bar{T}_{3m}$	average value of T_{3m} "no-drive" and T_{3m} "with-drive"
$(T_3)_0$	exit plane local average temperature at 0° thermocouple array position.

*Professor, **Research Associate, ***Research Technician

Presented at an AGARD Meeting on 'Fuels and Combustion Technology for Advanced Aircraft Engines', May 1993

$(T_3)_{360}$ exit plane local average temperature at 360° thermocouple array position

U_e jet velocity excitation pulsation amplitude, at the orifice exit plane centre (unsteady flow)

U_j steady mean jet velocity at the orifice exit plane

$\dot{W}$ power at acoustic driver

$\overline{\dot{W}}$ average total power, all tests, for three acoustic drivers

WD "with-drive"

η_c local combustion efficiency

θ_m local average dimensionless relative temperature

ρ_j density of the jet flow at orifice exit plane

ϕ local equivalence ratio, stoic. A/F/local actual A/F

ϕ_{ND} local equivalence ratio "no-drive"

ϕ_o overall equivalence ratio due

ϕ_{WD} local equivalence ratio "with-drive"

$\overline{\Delta\phi}$ average change in equivalence ratio due to acoustic drive

1. INTRODUCTION

Previous studies (1),(2) showed that the mixing processes of the dilution-air jets of a small tubular combustor of normal design could be beneficially acoustically controlled. This demonstrated that acoustic modulation of the dilution-air jet flows allowed progressive and selective control of the exit-plane temperature distribution. Specifically, for a good temperature traverse quality, it was possible to trim the temperature profile. Accordingly, a desired exit-plane temperature distribution may be achieved. From these results it was inferred that the entrainment rate and mixing of the dilution-air jets was increased by the acoustic pulsations. This promoted detailed investigations into acoustically pulsed free-jet mixing (3),(4),(5), and showed that the entrainment and entrainment coefficient of the jet could be considerably increased, by up to 6 times. Since jet entrainment is responsible for the mixing produced by a jet, jet mixing would also be improved.

Gas turbine combustor performance depends on jet flow mixing and in particular on the mixing of air jets with a confined hot crossflow. Therefore, experimental studies were done on an acoustically pulsed air jet mixing with a confined crossflow (6),(7), and showed that mixing was significantly increased and penetration at least 100% increased. The response of the acoustically pulsed jet, as determined from penetration and mixing, was found to be optimum at a Strouhal number of about 0.27.

Acoustic excitation pulses the jet at its orifice exit plane causing the jet flow to develop a train of toroidal vortices (3),(6),(8). The entraining action of the travelling toroidal vortices is the primary mechanism of the acoustically augmented mixing and penetration processes. The success of these activities has now resulted in the technique being applied to the air jets of the combustor primary zone of Ref. 1, also Fig. 1 because of the potential for control and improvement in combustor performance. These novel experiments were designed to examine the effectiveness and control by the acoustic drive, by means of combustion products measurements across a mid-plane diameter of the combustor secondary zone, Fig. 1, ie., just downstream of the primary zone, and by temperature profile measurements in the combustor exit plane. Tests were made over representative ranges of overall air/fuel ratio A/F, reference Mach number M_r (load) and acoustic driver power $\dot{W}$.

2. EXPERIMENTAL

Combustor with Acoustically Pulsed Primary Zone Air Jets

The apparatus is essentially the same as that described in Refs. 1 and 2, except that the combustor exit plane temperature distribution is now measured by 18 shielded thermocouples in a 3 spoked array which was rotated in 15° steps to produce a polar data array of 432 temperature measurements. Reference 1 shows a cross-section of the combustor, unmodified for acoustic control, giving its air-distribution and important features. Provision was made for the measurement of air and fuel mass flow rates and the combustor inlet and exit conditions. Thermocouples attached to the outside wall of the flame tube measured wall temperatures in the primary and dilution zones. Combustion products distributions were measured by a water cooled probe traversed diametrally through a secondary zone air hole, at approximately the 3:30 o'clock position looking upstream. Gas samples were then passed to instruments for the measurement of concentrations of CH_4, CO, CO_2 and O_2. The pressure and temperature data obtained was processed by a Personal Computer controlled data logging system, and exit plane temperature distributions were analysed by a Sun mainframe computer.

Figure 1 illustrates the method for acoustic control of the normal tubular combustor primary zone. The usual liquid fuel atomizer has been replaced by a conical gas injector for the burning of commercial natural gas. The method channels air from upstream of the combustor inlet via 6 by-pass tubes connecting to a split manifold of 3 separate segments which feeds the 20 primary zone air jet holes in the flame tube. Ten pairs of radial tubes cross the combustor annulus to connect the air holes of the flame tube to the manifold segments surrounding the combustor casing. Each manifold segment is connected by a driver tube to a 300 W loudspeaker which provides the acoustic driving and control. The strongest acoustic driving mode of the system was established by means of an HP 5423A two channel analyzer, using as an input signal a voltage proportional to the loudspeaker current, and as an output signal the voltage from a microphone measuring sound pressure near the exit of a primary zone air jet hole in the flame tube. These measurements were made without airflow through the combustor. However, to check that the measurements were meaningful, a hot film anemometer was used to measure the air jet velocity through a primary zone hole for a modest air flow through the combustor. Under acoustic drive conditions, the anemometer detected the strongest pulsating flow at the strongest acoustic mode of the system, thereby confirming that the no flow analysis was meaningful, and that the optimum acoustic test frequency was 227 Hz. Because of limited funding, a single two channel amplifier powered the 3 loudspeakers, thereby necessitating a parallel connection for two speakers when all three speakers were being used simultaneously. Power at a loudspeaker driver was measured by an a.c. voltmeter

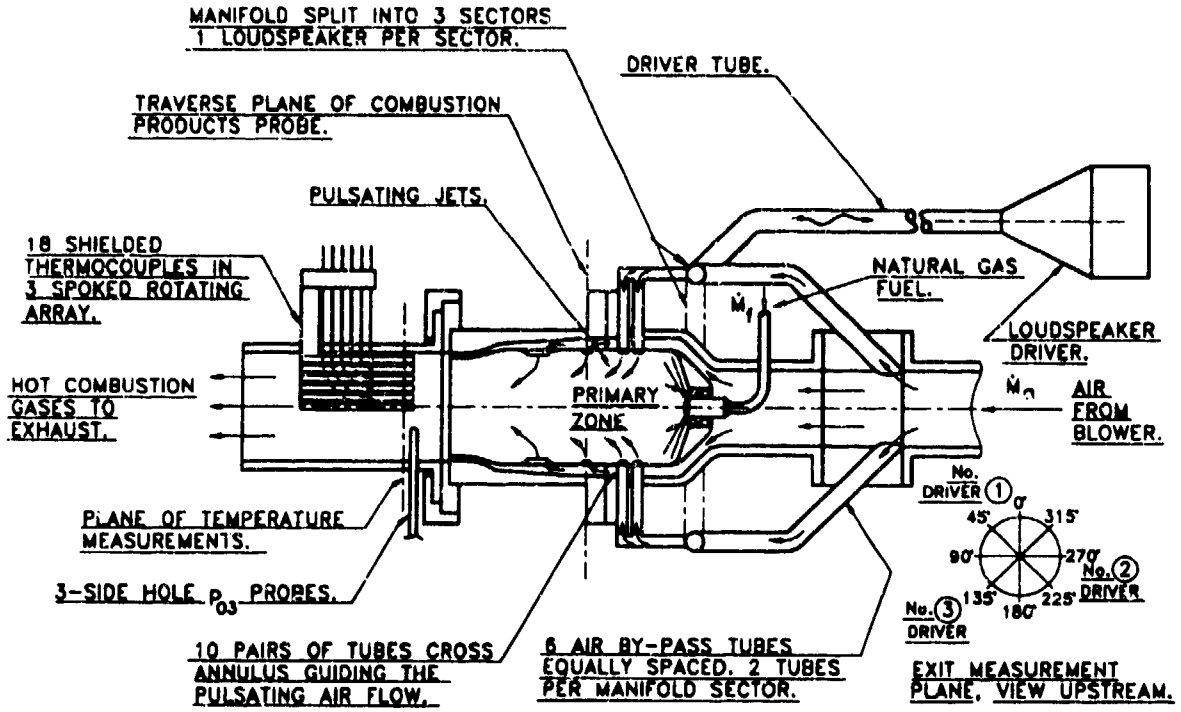

Fig. 1 Method for Acoustic Control of Combustor Primary Zone Air-Jet Mixing.

and ammeter, ignoring the power factor since previous work had shown it to be close to unity (4).

Table I summarises the range of test conditions used and indicates that up to scaled "¾ load" operation, based upon the reference Mach number aerodynamic scaling factor, was achieved. As is usual for this type of combustor, M_r was calculated at the maximum inside diameter of the casing (142.9 mm dia.).

TABLE I
SAMPLE TEST CONDITIONS

TEST No	LOAD	$\dot{M}_a$ kg/s	A/F	M_r	P_2 kPa	T_2 C	T_{3m} C	$\frac{P_{02}-P_{03}}{P_{02}}$	f = 227 Hz DRIVER No ① W	② W	③ W
6	0.23	0.0698	117.4	0.015	88.9	68.5	COMBUSTION PRODUCTS TESTS		34	29	34
7	0.21	0.0665	67.5	0.012	88.9	67.8			34	28	34
4	0.19	0.0598	50.4	0.011	89.1	69.8			33	29	33
5	0.39	0.1245	59.7	0.022	89.8	60.0			37	29	37
8	0.54	0.1879	62.6	0.031	92.8	58.5			37	27	37
27	1/4	0.0789	99.5	0.0143	89.5	57.3	ND 458 WD 480	0.80	-		150
25/150	1/4	0.0781	70.4	0.0143	88.9	57.4	ND 616 WD 618	0.75			150
31	1/4	0.0784	56.1	0.0142	89.5	56.6	ND 733 WD 735	0.72		-	150
35	1/4	0.0785	71.2	0.0144	88.7	57.6	ND 474 WD 619	0.66	-	147	153
42	1/4	0.0783	100.4	0.0141	88.9	58.7	ND 450 WD 453	0.81	149	149	156
36	1/4	0.0777	70.5	0.0142	88.8	57.2	ND 618 WD 620	0.67	147	147	156
37	1/4	0.0790	56.2	0.0141	90.7	55.7	ND 735 WD 736	0.72	148	148	157
32	1/2	0.1566	70.6	0.0278	91.1	53.8	ND 623 WD 626	2.19			150
34	1/4	0.2485	70.7	0.0420	93.9	53.2	ND 528 WD 531	4.71	-	-	150
THEORETICAL FULL-LOAD NOMINAL		1.1657	60.4	0.0570	395.4	203		6.05	STANDARD COMBUSTOR		
STOICHIOMETRIC			17.16								

Combustor Measurements and Accuracy

Combustion gas samples were measured to within ±2% or better.

The thermocouples measuring the exit plane temperature distribution were arranged so that 7 thermocouples measured the temperature of seven equal area zones. The 11 remaining thermocouples were then arranged so that well defined diametral temperature profiles would be measured, all thermocouples being positioned at different fixed radii, as shown in Fig. 10. Each local temperature measurement T_3 was the average of 11 samples, and the whole array of 432 measurements was averaged to define the exit plane mean temperature T_{3m}. The chromel-alumel thermocouples were accurate to ±2%, including random uncertainty, over the experimental range. The flame tube wall thermocouples were similar.

The air and fuel mass flow rates were accurate to ±2½%, and ±1½% respectively.

Individual static and stagnation pressure measurements were accurate to ±0.2%, whilst the hot pressure loss $P_{02} - P_{03}$ was measured to within ±4%; P_{02} and P_{03} are inlet and exit stagnation pressures respectively.

Combustion Products Measurements and Results

These measurements were made in order to determine for the measurement plane:

(a) the diametral distributions of pollutants, CO and CH_4.

(b) the diametral distributions of equivalence ratio ϕ, combustion efficiency η_c and combustion gas temperature T_g.

From the gas analysis data for a particular test and the standard combustion equation for methane, the number of mols of products were calculated and hence the equivalence ratio determined. With all the coefficients in the combustion equation now known the combustion efficiency η_c was calculated using standard net calorific values for CH_4 and CO, and since some unburnt CH_4 and

CO was measured $\eta_c < 1$. Then from the First Law of Thermodynamics and assuming the combustor was adiabatic, T_g was calculated using standard enthalpy values for the reactants and products.

Typical diametral distributions of ϕ, pollutants, combustion efficiency loss $(1 - \eta_c)$ and T_g are presented in Figs. 2-5. Approximately symmetrical equal driving of all primary zone air jets was assured by powering the three acoustic drivers at an average power of 31.3W each. The driving power for all tests was approximately constant at an average of 33W per driver, whilst the load (air mass flow rate) was varied from 0.2 to 0.5 with selected variation of A/F from 50 to 117. All the combustion products measurements were made before the combustor exit plane temperature profile measurement assembly was manufactured. Hence the combustion products data and exit plane temperature profile data are completely independent, and since the combustion products were measured on one diameter for mostly single tests they should be considered as preliminary data only.

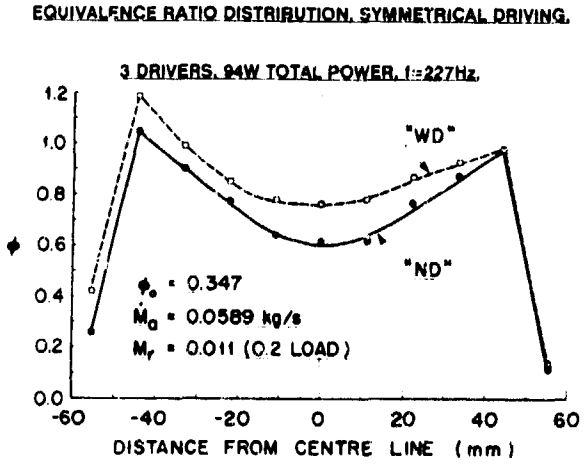

Fig. 2 Typical Combustion Zone Diametral Equivalence Ratio Distribution, Symmetrical Driving at Constant Power, Test No.4, 0.2 Load, See Table I also.

Test Results-Combustion Products "No Acoustic Drive"

Figures 2 to 5 typically show concave distributions about the combustor centre-line for the "no-drive" condition. Thus ϕ is lean in the combustor centre becoming approximately stoichiometric close to the flame tube wall. The emission index *EI* for CH_4 has a minimum value at the centre-line raising to a maximum near the flame tube wall, and *EI* for *CO* behaves similarly except the maximum occurs at about one half radius from the centre-line, subsequently decreasing as the flame tube wall is approached. The efficiency loss distribution reflects that of the emission indices as would be expected. The maximum in *CO* corresponds to about 70% in combustion efficiency and must decrease in proximity to the wall since η_c is very low and CH_4 must dominate. The temperature distribution follows that of ϕ, as determined by the ϕ, T_g plot of Fig. 6 with some low temperature data conspicuously in error.

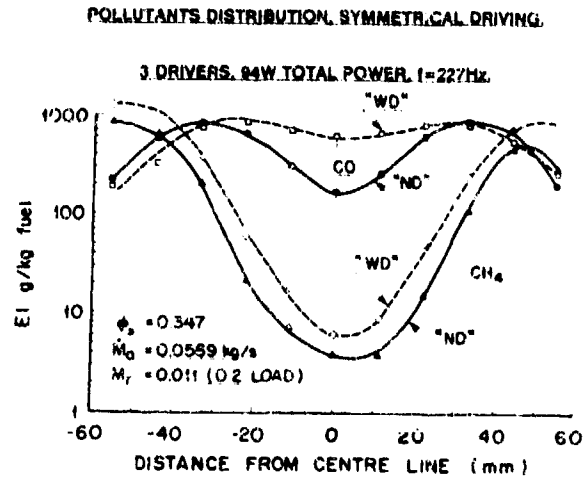

Fig. 3 Typical Combustion Zone Diametral Pollutants Distribution, Symmetrical Driving at Constant Power, Test No.4, 0.2 Load, See Table I also.

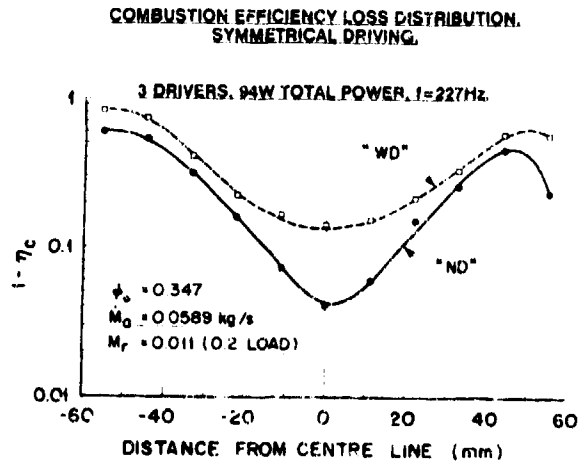

Fig. 4 Typical Combustion Zone Diametral Combustion Efficiency Loss Distribution, Symmetrical Driving at Constant Power, Test No.4, 0.2 Load, See Table I also.

All the data are conveniently summarised in Fig. 6 and by plotting ϕ, η_c (Fig. 7) and *EI* for CH_4 and *CO* against $(1 - \eta_c)$, Figs. 8 and 9. Figure 7 shows combustion efficiency peaking at about $\phi = 0.45$ (ie., about $\phi = 0.9$ in the primary zone) which agrees with that of most combustors. The emission index for CH_4, Fig. 8, exhibits similar behaviour to that of the data from other combustors (9), (10), (11) as does *EI CO*, Fig. 9. The maximum in *EI CO* as the combustion efficiency becomes very low is clearly shown in Fig. 9. Unfortunately there is a fair amount of scatter in the data, Fig. 7, perhaps due to measurement limitations, and some data at low η_c is obviously suspect.

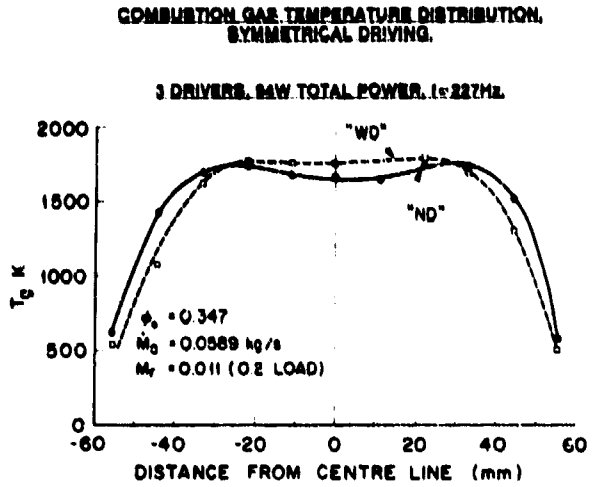

Fig. 5 Typical Combustion Zone Diametral Gas Temperature Distribution, Symmetrical Driving at Constant Power, Test No.4, 0.2 Load, See Table I also.

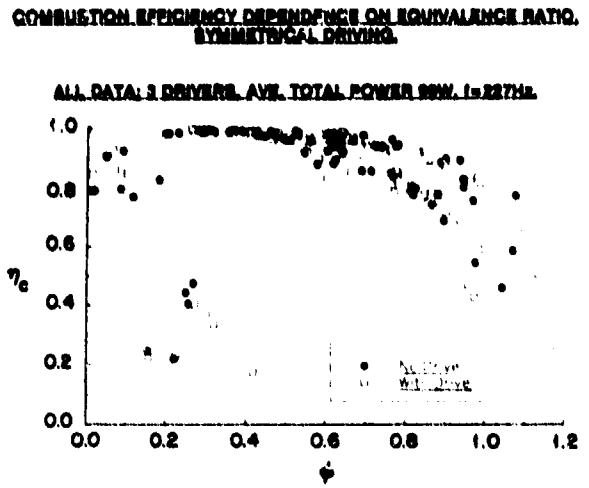

Fig. 7 Downstream of Primary Zone Combustion Efficiency Versus Equivalence Ratio, All Data, Symmetrical Driving at approximate Constant Power.

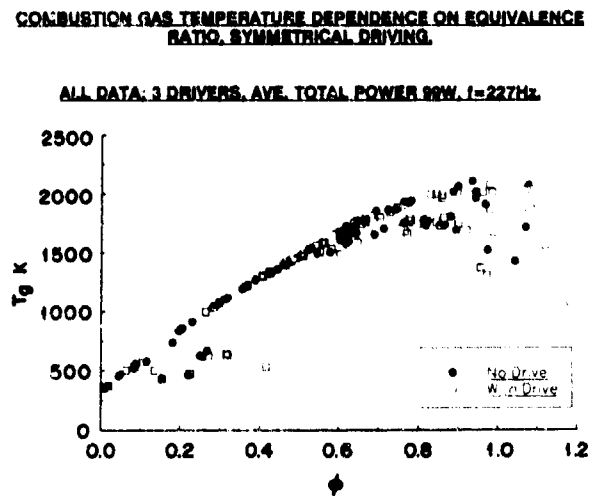

Fig. 6 Combustion Zone Gas Temperature Versus Equivalence Ratio, All Data, Symmetrical Driving at approximate Constant Power.

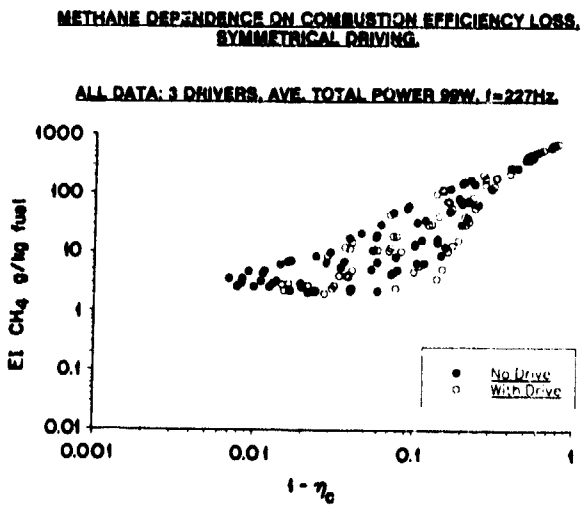

Fig. 8 Combustion Zone Methane Concentration Versus Combustion Efficiency Loss, All Data, Symmetrical Driving at approximate Constant Power.

Test Results-Combustion Products "With Acoustic Drive"

Figures 2 to 5 show the general effect of acoustic drive on the distributions across the combustor diameter of ϕ, pollutants, $(1-\eta_c)$ and T_g, and in general all parameters tend to increase, and become more uniform under the acoustic augmentation of penetration, entrainment and mixing, thereby carrying more material towards the centre-line. At first sight there is little discernable separation of the data by acoustic drive in Figs. 6,7,8 and 9, indicating that the richening by acoustic drive simply produces corresponding changes in η_c, and therefore in the pollutants, according to the "no-drive relationship of η_c with ϕ.

Exit Plane Temperature Profile Measurements and Results

The objective of these measurements was to establish:

(a) that the temperature pattern was satisfactory, and typical, without acoustic drive,

(b) that the temperature pattern was stable and repeatable for the selected conditions,

(c) the magnitude of changes in the temperature pattern caused by acoustic drive.

For comparative purposes, the data are presented in terms of the local average dimensionless relative temperature

$$\theta_m = \frac{T_3 - T_{3m}}{T_{3m} - T_2} \qquad (1)$$

where T_2 is the combustor average inlet temperature. The data may also be summarised in terms of the single mixing parameter

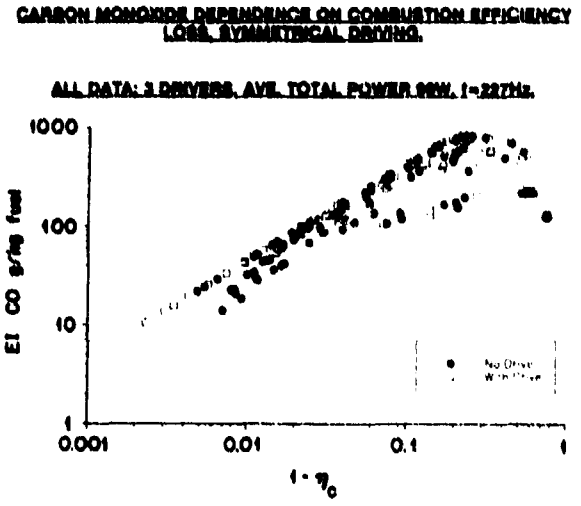

Fig. 9 Combustion Zone Carbon Monoxide Concentration Versus Combustion Efficiency Loss, All Data, Symmetrical Driving at approximate Constant Power.

$$S_m = \left[\frac{\sum_1^n (T_3 - T_{3m})^2}{n-1} \right]^{\frac{1}{2}}, \qquad (2)$$

and the temperature profile acoustic driving effectiveness parameter

$$S_p = \left[\frac{\sum_1^n (T_{3WD} - T_{3ND})^2}{n} \right]^{\frac{1}{2}}, \qquad (3)$$

where "*ND*" means "no-drive" and "*WD*" means "with-drive". Both θ_m and S_m tend to zero as mixing is increased by the acoustic drive, whilst S_p maximises. The "peakiness" of the temperature pattern was evaluated by the temperature pattern quality parameter

$$Q = \frac{T_{3max} - T_{3m}}{T_{3m} - T_2}, \qquad (4)$$

where T_{3max} is the exit plane local average maximum temperature.

In order that differences between "no-drive" and "with-drive" conditions would not be masked by small-changes in running conditions, these values for a particular angular setting of the thermocouple array were obtained in pairs. That is, after obtaining a set of particular "no-drive" values, the acoustic drive was turned on, conditions allowed to stabilise and then "with-drive" values recorded. The drive was then turned off and the array rotated to the next position followed by stabilisation before the measurement procedure was repeated. As a check on steady operation, data at the 360° setting were obtained for comparison with the initial set at 0°.

When the data were analyzed, it was realised that the acoustic drive had little affect on the wall boundary layer flows, and therefore to avoid masking effects calculations of S_m and S_p were made on truncated data to eliminate the temperature boundary layer in the exit plane. To

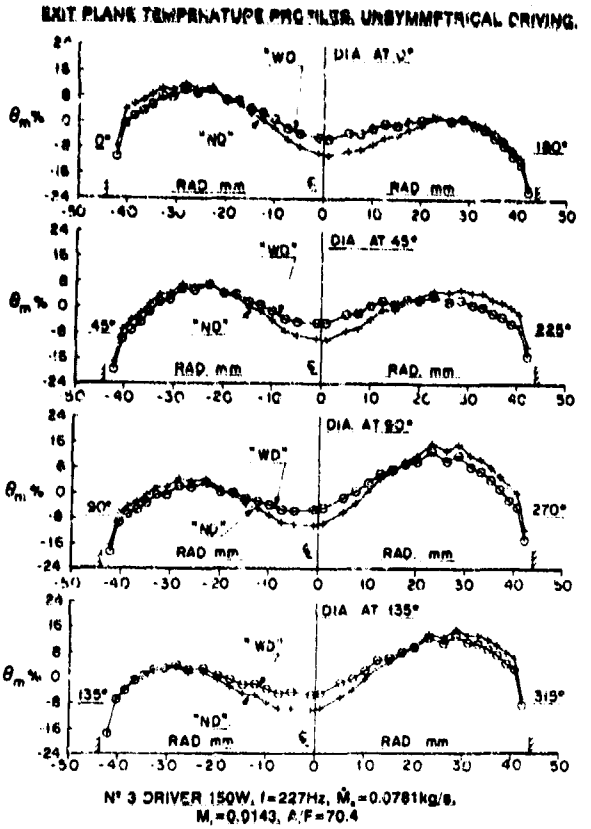

Fig. 10 Typical Combustor Exit Plane Diametral Dimensionless Temperature Profiles, Unsymmetrical Driving, ¼ Load, "No-Drive" Q = 16.4%, "With-Drive" Q = 13.3%, Test No. 25/150, See Fig. 1 and Table I also.

indicate this, these parameters have been designated as S_{pm} and S_{pt}.

Figure 10 presents typical exit plane diametral local average dimensionless temperature profiles for unsymmetrical driving by No.3 driver at 7:30 o'clock position. The 8 primary zone air jets from the approximate 5 o'clock to 9 o'clock positions were strongly pulsed by the single driver at 150 W. Figure 11 shows similar plots for symmetrical equal driving of all primary zone air jets by the three drivers at an average power of 150 W each. Table I shows a slight difference in individual driver powers caused by small differences in driver impedance which is considered to be insignificant. The influence of driver power, air/fuel ratio and air mass flow rate (load) were also investigated.

Test Results - Temperature Measurements "No Acoustic Drive"

Visual comparison between Figs. 10 and 11 "no-drive" reveals very good repeatability between the tests. This is quantified by the mixing parameter, which has been plotted against A/F in Fig. 12 for all the data, and demonstrates that repeatability was within ±2% of the best fit line. Good similarity of temperature pattern was observed for all tests at $M_r \cong 0.0143$ (¼ load) over the range of A/F values. But, as the load was increased to M_r=0.0420 (¾

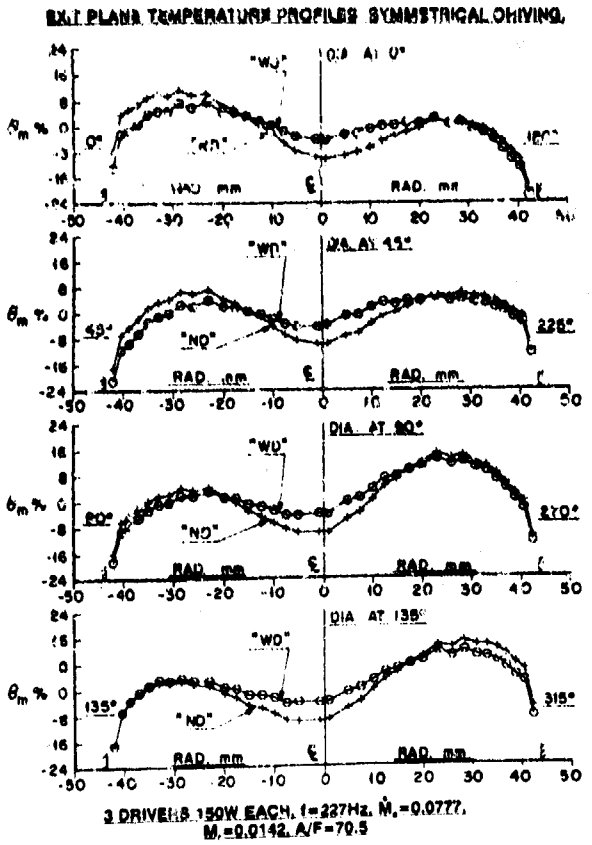

Fig. 11 Typical Combustor Exit Plane Diametral Dimensionless Temperature Profiles, Symmetrical Driving, ¼ Load, "No-Drive" Q = 15.1%, "With-Drive" Q = 12.8%, Test No. 36, See Fig. 1 and Table I also.

load) the "cool" central core in the pattern was flattened out. To check that the temperature pattern was stable

$$R = \left[\frac{\sum_{1}^{n} \{(T_3)_{360} - (T_3)_0\}^2}{n} \right]^{\frac{1}{2}} \qquad (5)$$

was calculated, where $(T_3)_0$ and $(T_3)_{360}$ are exit plane local temperature measurements at the 0° and 360° settings of the thermocouple array. This showed that the temperature pattern was stable to within ±¼% in terms of $R/(T_{3m} - T_2)$%. A similar calculation for the "with-drive" data showed the same stability tolerance. Stability of fuel mass flow rate, air mass flow rate, M_r, A/F and the hot pressure loss ratio $(p_{02} - p_{03})/p_{02}$ during a test was on average within about ±2½%. Individual values, $\dot{M}_f$ for instance, could be as good as ±0.2%.

Figure 14 gives the mixing S_{mt} for "no-drive" for truncated data versus A/F, and shows appreciable improvement in mixing for A/F >70 as compared with the total data S_m calculations of Fig. 12. Mixing S_{mt} for "no-drive" improves with air mass flow rate or M_r as shown in Fig. 16, presumably due to flow turbulence increase.

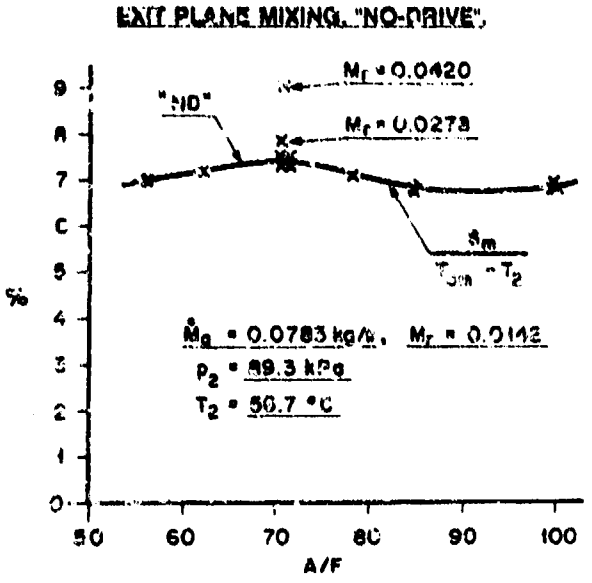

Fig. 12 Exit Plane "No-Drive" Dimensionless Mixing Parameter Versus Air/Fuel Ratio, Untruncated Data, ¼ Load, Data at ½ and ¾ Loads Shown for Reference.

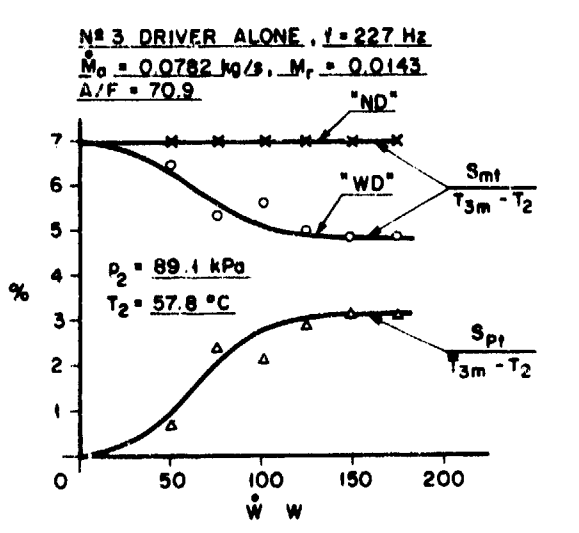

Fig. 13 Exit Plane Dimensionless Mixing and Driving Effectiveness Parameters Versus Driving Power, Unsymmetrical Driving, ¼ Load, Truncated Data.

The temperature pattern quality Q peaks at about 15.8% at A/F = 70 for "no-drive", ¼ load, and improves with loading to about 14% at ¾ load. This is consistent with a full load design value of $Q \cong 15\%$ at A/F = 60.4.

Test Results - Temperature Measurements "With Acoustic Drive"

Figures 10 and 11 show typical temperature changes due to strong acoustic drive, and despite the different driving arrangements, the temperature patterns were similar. The

overall effect was to produce a more uniform temperature pattern. The affect of varying acoustic power was assessed for the unsymmetrical case of driving No.3 driver alone, at ¼ load and A/F = 70.9, as for Fig. 10. Figure 13 shows the results in terms of S_{mt} and S_{pt}, which clearly shows a significant 31% improvement in mixing (S_{mt}) although this saturated because the acoustic driving effectiveness (S_{pt}) saturated at 3.1% for powers greater than 150 W. The rogue data point at 101 W appeared to be caused by combustor instability at this power; several tests were run producing inconsistent results.

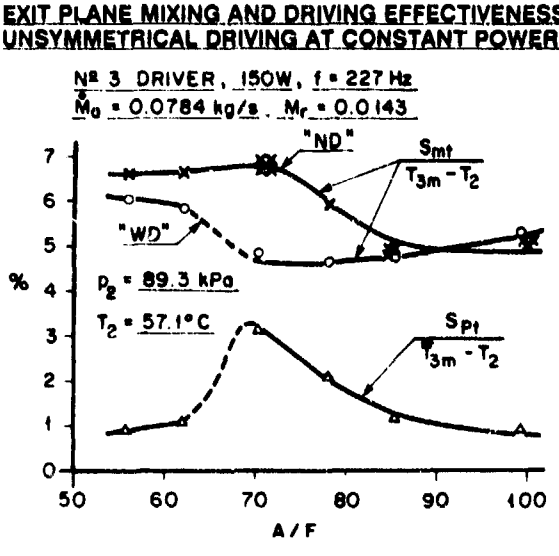

Fig. 14 Exit Plane Dimensionless Mixing and Driving Effectiveness Parameters Versus Air/Fuel Ratio, Unsymmetrical Driving at Constant Power, ¼ Load, Truncated Data.

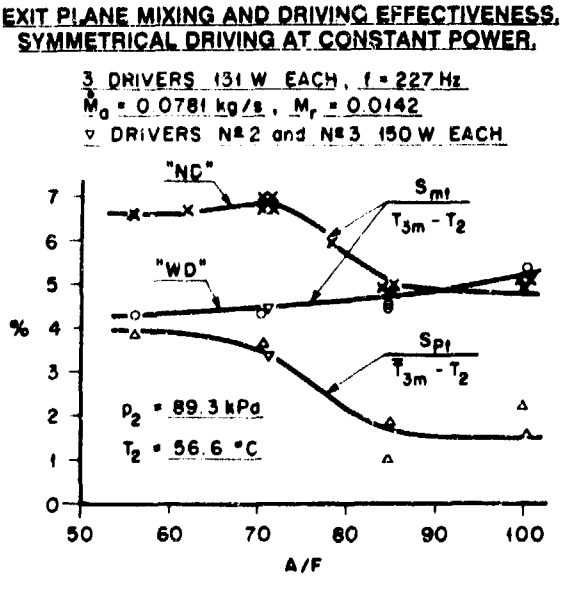

Fig. 15 Exit Plane Dimensionless Mixing and Driving Effectiveness Parameters Versus Air/Fuel Ratio, Symmetrical Driving at Constant Power, ¼ Load, Truncated Data.

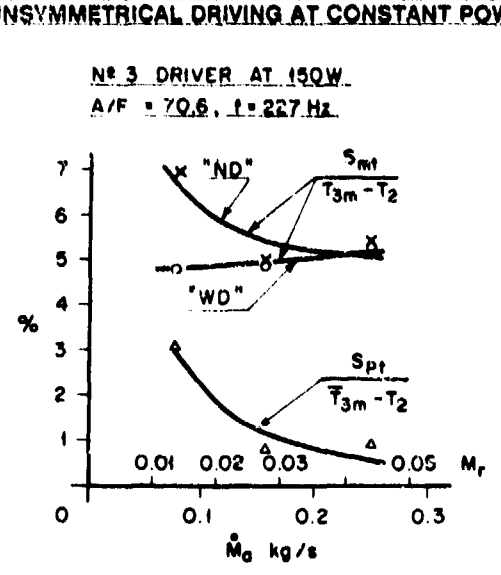

Fig. 16 Exit Plane Dimensionless Mixing and Driving Effectiveness Parameters Versus Total Air Mass Flow Rate (Load), Unsymmetrical Driving at Constant Power, Truncated Data.

Varying the air/fuel ratio at ¼ load with No. 3 driver at 150W produced the data shown in Fig. 14, where comparison shows that mixing improves by 32% "with-drive" up to A/F = 70. Further richening resulted in poorer mixing, although still 9% better than "no-drive", due to a sharp decline from 3.2% to 0.9% in acoustic driving effectiveness. Repeating these tests for all drivers at 151W yielded the results of Fig. 15. In this case, the mixing "with-drive" improved steadily over that for "no-drive" up to 35% as A/F was decreased. Effectively acoustic control maintained approximately the same mixing at all A/F values, which was brought about by acoustic driving effectiveness increasing with richening to 3.9%. Surprisingly S_{pt} for three drivers at 151W is only slightly greater than S_{pt} for one driver at 150W for richening up to A/F = 70, and S_{mt} "with-drive" is almost identical. A single test, for drivers No. 2 and 3 at 150W average each, therefore is not surprisingly in close agreement as shown on Fig. 15.

As the loading was decreased (from ¾ to ¼ load) Fig. 16 shows that acoustic driving effectiveness increased in a manner sufficient to maintain approximately the same mixing "with-drive" at all loads tested. This was for No. 3 driver constant at 150W and A/F constant at 70.6. The curve fitted to the S_{pt} data has been constructed to vary inversely with $(\dot{M}_a)^{\frac{3}{2}}$ as will be discussed later.

The corresponding behaviour of the temperature pattern quality Q "with-drive" parallels that of the mixing parameter (S_{mt}). At ¼ load, and A/F = 70.9, condition of greatest change, increasing driver power improved Q by up to 19% (150W) for unsymmetrical driving by No. 3 driver alone. For ¼ load, 151W symmetrical driving, a 20%

maximum improvement in Q with A/F richening was found at A/F = 70. And as driving effectiveness reduced with load increased up to ¼ load, so did the improvement in Q, being only 5% for 150W unsymmetrical driving at A/F = 70.6.

Table I shows a small consistent increase in the exit plane mean temperature T_{3m} "with-drive", a maximum increase of 1.3% was found for Test No. 37 at ¼ load and A/F = 56.2. This suggests that acoustic drive produced a slight richening in A/F.

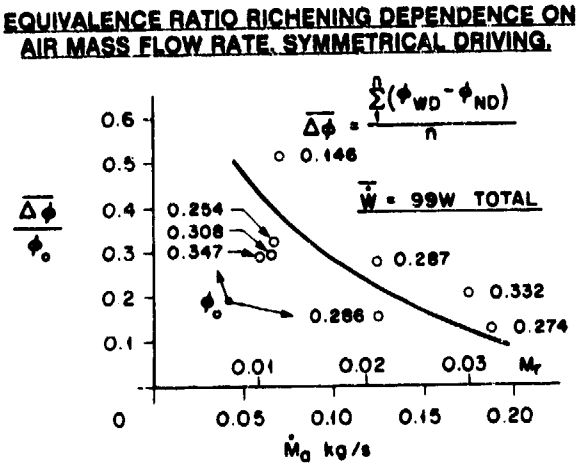

Fig. 17 Combustion Zone Normalised Average change in Equivalence Ratio by Acoustic Drive Versus Total Air Mass Flow Rate, All Tests, Symmetrical Driving at approximately Constant Power, f = *227 Hz.*

3. DISCUSSION

Combustion Analysis

The richening by acoustic drive for all the data is summarised in Fig. 17 where the average change in equivalence ratio

$$\overline{\Delta\phi} = \frac{\sum_1^n (\phi_{WD} - \phi_{ND})}{n} \qquad (6)$$

for each test, normalised by the overall equivalence ratio ϕ_o, has been plotted against the total air mass flow rate. There is a distinct richening effect with perhaps an indication of dependence on ϕ_o, and the effect decreased with increase of $\dot{M}_a$ (or M_r). The jet velocity U_j increases with $\dot{M}_a$, and since the acoustic driver power is constant, equation (8) shows the excitation or pulsation strength U_e/U_j decreases (U_e is the excitation pulsation velocity amplitude of the jet), which decreases the acoustically enhanced jet entrainment and mixing (4),(5). References (6) and (7) also show that reducing U_e/U_j diminishes the jet penetration. Thus the acoustically controlled jet mixing factors and hence the richening effect decrease with $\dot{M}_a$ increase for $\dot{W}$ constant. The most likely cause of richening, change of entrainment or penetration, can be established by calculating the ratio of the equivalent mean air mass flow rate at the combustion probe traverse plane $\dot{M}_{as}$ to the total air mass flow rate, from the ratio of ϕ_o and the mean equivalence ratio measured at the traverse diameter. The results are shown in Fig. 18 where $\dot{M}_{as}/\dot{M}_a$ has been plotted against $\dot{M}_a$ for "no-drive" and "with-drive" conditions. Despite the undue scatter there is a distinct decrease of $\dot{M}_{as}$ "with-drive", and the magnitude of decrease diminishes as $\dot{M}_a$ increases as just explained. All tests showed this decrease which can be clearly seen in Fig. 18 by examining "no-drive" and "with-drive" data pairs. Thus since the fuel mass rate was constant for each test (choked flow) $\dot{M}_{as}$ decrease caused the richening, and is most probably due to increased penetration (6), (7) of the primary zone air jets by the acoustic drive thereby increasing combustor flow blockage. This seems convincing but it should be borne in mind that the data is for one traverse diameter only and for mostly single tests.

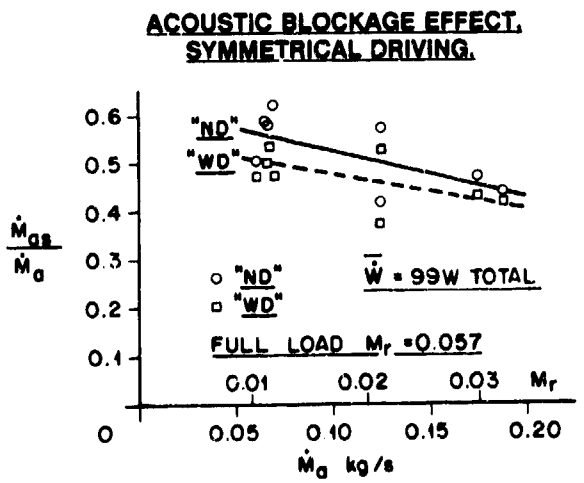

Fig. 18 Combustion Zone Air Split Ratio Versus Total Air Mass Flow Rate. All Tests, Symmetrical Driving at approximately Constant Power, f = *227 Hz.*

The acoustically augmented jet entrainment and mixing (4), (5) should be reflected in the distributions of the various parameters as shown by the central flattenings in Figs. 2 to 5. However, according to Fig. 7 there is no distinction between "no-drive and "with-drive" so far as combustion efficiency and equivalence ratio behaviour are concerned. But at a given efficiency more thorough mixing should produce proportionately more carbon monoxide, and close examination of Fig. 9 seems to show this. Methane ought to be reduced therefore by acoustically improved mixing, and careful scrutiny of Fig. 8 supports this by indicating some diffusion to lower EI values of the "with-drive" data through the "no-drive" data. An overall evaluation of mixing may be made by calculating the mixing standard deviation S_{mg}, based on the measured combustion gas temperature distributions for each test

$$S_{mg} = \left[\frac{\sum_{1}^{n} (T_g - T_{gm})^2}{n-1} \right]^{\frac{1}{2}} , \qquad (7)$$

where T_{gm} is the mean combustion gas temperature. Figure 19 presents the normalised results showing up to 35% improvement in mixing "with-drive", ie. S_{mg} tends to zero as mixing improves. Except for one data pair acoustic drive always improved the mixing. However the importance of blockage versus entrainment by Toroidal vortices cannot be decided by these data. As the mass flow rate was increased the acoustic improvement in mixing decreased as explained previously.

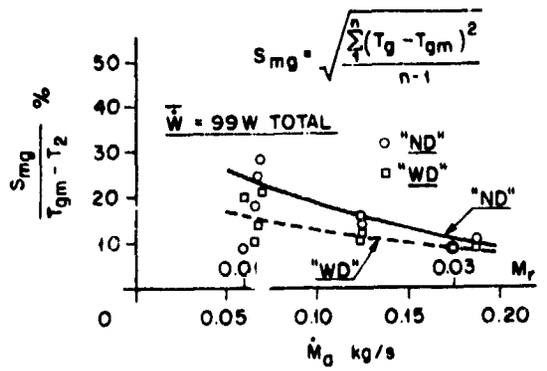

Fig. 19 Combustion Zone Dimensionless Mixing Parameter Versus Total Air Mass Flow Rate, All Tests, Symmetrical Driving at approximately Constant Power, $f = 227$ Hz.

The Temperature Pattern Measurements

The "no-drive" temperature pattern typified by Figs. 10 and 11, and those at other loads (not shown), compare favourably with those shown in Ref. 1 and are satisfactory and typical for this kind of combustor without acoustic drive. The "no-drive" mixing behaviour of Fig. 12 is about 7% on average whereas that for Ref. 1 is somewhat better at an average value of about 5%. The "no-drive" mixing for untruncated data worsens as load is increased for these tests and those of Ref. 1, but the Ref. 1 mixing is again better (about 6% versus 8% at ½ load). The reason for somewhat worse mixing may be due to the facts that a more powerful blower and a new flame tube (our best copy) are now used with respect to Ref. 1.

Figs. 12 and 14 for "no-drive" clearly show the effect of removal of the thermal boundary layer by truncating the data, and reveals a stronger dependence by mixing (S_{mt} compare S_m) on A/F. This appears to be quite reasonable since as the mixture richens combustion is more vigorous, temperature changes are more pronounced, and mixing worsens until A/F = 70 is reached. Furthermore, Fig. 16, indicates "no-drive" mixing (S_{mt}) improves with increase in loading whereas plotting untruncated data shows the opposite behaviour in that mixing (S_m) worsens due to boundary layer thickening by increased turbulence.

Masking also has a strong effect on the "with-drive" data, halving the change in mixing (S_{mt} to S_m) shown in Fig. 13, and totally obscuring the trend in S_{mt} of Fig. 14 for instance. In Figs. 13 to 16, the variation of S_p is closely identical to S_{pt}, as it should be since the thermal boundary layer is subtracted out when calculating S_p for the total data, and this also confirms that the truncation radius chosen for the S_{pt} calculation was correctly selected.

Comparing the temperature profiles shown in Figs. 10 and 11, for the same "no-drive" conditions, reveals closely similar "with-drive" patterns despite unsymmetrical versus symmetrical, 150W per driver, action. This surprising behaviour can be explained by referring to Figs. 14 & 15 where it will be observed that mixing "with-drive" (S_{mt}), for richening to A/F = 70, is nearly constant and identical for the different driving conditions. In contrast, the "no-drive" mixing worsens strongly with richening to A/F = 70. Thus it appears that the acoustic drive offsets the effect of increasing combustion intensity on the mixing level S_{mt}, and since the driving pattern has no effect, it is most likely that increased jet penetration by the acoustic drive, causing increased blockage, is the cause. This general blockage effect supports the explanation for acoustically promoted richening in the combustion probe measurement diameter, and shows other traverse diameters would have given similar results. Careful inspection of the "with-drive" data shows that all the "with-drive" temperature patterns are very similar, ie., the acoustic drive is strong enough to maintain the lean "no-drive" temperature pattern over the richening effect. Richening beyond A/F = 70, for unsymmetrical driving, Fig. 14, breaks the "with-drive" blockage and the mixing (S_{mt}) worsens to nearly "no-drive" rich values. For symmetrical driving, Fig. 15, this does not occur and indicates that the aerodynamics of the combustor primary zone are being maintained in their lean state, whereas the unbalanced effects of a single driver can only achieve this with richening to A/F = 70. Furthermore, the basic temperature pattern is not affected by the driving arrangements or by A/F effects showing that major changes in the primary zone aerodynamics do not occur. Paradoxically, it is the "no-drive" mixing (S_{mt}) behaviour with A/F richening which appears to control the acoustic driving effectiveness S_{pt}, since this is effectively the difference between "with-drive" and "no-drive" S_{mt} as Figs. 14 & 15 demonstrate. However, Fig. 13 shows that S_{mt} and S_{pt} depend on acoustic driving power, demonstrating that there is progressive acoustic control between the "no-drive" and "with-drive" mixing curves of Figs. 14 & 15 until full blockage or saturation occurs at about 150W per driver. Figures 14 & 15 show that symmetrical driving produces slightly stronger effects than one driver alone, also despite blockage being the dominant factor, the slightly improving "with-drive" mixing curves with richening suggest that the improved mixing by the modulated air jets has some effect.

Turning now to Fig. 16 and the effects of loading. As the air mass flow rate is increased, the velocity of the primary zone air jets increase proportionately. Also, according to Ref. 6

$$\frac{U_a}{U_j} \propto \left[\frac{\dot{W}}{\rho_j D^2 U_j^3}\right]^{\frac{1}{2}}, \qquad (8)$$

that is, for a given jet of orifice diameter D and constant acoustic driver power the excitation or pulsation strength U_a/U_j is inversely proportional to $(U_j)^{\frac{3}{2}}$. Therefore the acoustic driving effectiveness S_{pt} should vary in a similar way with load, which is demonstrated by Fig. 16 where the S_{pt} curve was constructed in this manner. However, the "no-drive" S_{mt} curve (A/F = 70.6) has also reduced with load increase, and if the lean S_{mt} values did not correspondingly reduce with load, then this would contribute to the reduction in S_{pt}. Thus the agreement of S_{pt} reduction with decrease in acoustic excitation with load increase is perhaps fortuitous. Clearly, considerably more data is required before a full understanding is possible, and particularly for increased driving power.

The temperature pattern quality behaviour parallels that of mixing S_{mt} of Figs. 13 to 16, and for similar reasons. In general, acoustic drive improves the quality, which, depending on conditions, can be as much as 20% improvement.

Overall the combustion and temperature pattern measurements established a distinct improvement in mixing by acoustic drive, up to 35% relative to "no-drive". This was due primarily to flow blockage caused by acoustically enhanced jet penetration, and a secondary cause was enhanced mixing by acoustically shed jet toroidal vortices Furthermore, the improvement was brought about by acoustically pulsing only 11% of the combustor total air mass flow rate. Also the combustion gas temperature patterns, for one combustion products probe traverse diameter, were similar to the exit plane temperature patterns for the complete flow, giving confidence that the single traverse diameter results were typical of the total flow in the combustion probe traverse cross-sectional plane.

The affect on NO_x production by the acoustically augmented blockage and mixing is of important interest. Unfortunately, NO_x measurements by the combustion products probe and by gas samples in the combustor exit plane have not yet been made because of instrumentation difficulties and insufficient funds.

Exit Plane Mean Temperature Measurements

Table I gives the exit plane mean temperature values for "no-drive" and "with-drive" conditions. This allows the "no-drive" mean temperature rise values $(T_{3m} - T_2)$ to be compared with those given in Refs. 1 and 2; the agreement is very good and shows that the combustor behaved normally. Inspection of Table I will reveal that there is always a small increase in T_{3m} "with-drive", on average about 0.5% at ¼ load. This is equivalent to an average change in A/F of -0.7% which agrees with -0.5% measured at ¼ load, and also there was an average change "with-drive" in air mass flow rate $\dot{M}_a$ of -0.5%. Since the fuel mass flow rate on average was constant to within 0.1%, then the change in A/F was due to that in $\dot{M}_a$, and is evidence of flow blockage by the acoustic drive.

Hot Pressure Loss Measurements

Small changes between "no-drive" and "with-drive" hot pressure loss measurements were apparent, but these were always smaller than the estimated uncertainty in the difference and therefore were not significant. Table I therefore gives the average of the "no-drive" and "with-drive" hot pressure loss measurements for a particular test. These values are in good agreement with the "no-drive" hot pressure loss measurements of Refs. 1 and 2 and are normal for this type of combustor.

Driving Power Requirements

The energy conversion rate of the combustor at ¼ load rich conditions is about 75 kW, therefore the 0.45 kW driving power used for effective acoustic control is insignificant. No meaningful estimate of driving power required for significant acoustic control at full load conditions can be made because of the lack of data at ½ and ¾ load conditions.

4. CONCLUSIONS

A small tubular combustor of normal design and behaviour employing acoustically controlled primary zone air-jet mixing processes has been successfully tested at scaled ¼ load operating conditions, and some data was obtained at ½, ⅜ and ¾ loads. The acoustic control produced a distinct richening effect, measured just downstream of the primary zone, which produced a decrease in combustion efficiency and a somewhat increased and flatter combustion gas temperature distribution. There was a central flattening, in the diametral distributions of equivalence ratio and emission indices for CO and CH_4, indicating improved mixing by acoustically shed jet toroidal vortices, albeit a somewhat secondary effect. At a given combustion efficiency more CO and less CH_4 was indicated as a consequence of acoustically augmented mixing. The prime cause of richening was due to increased penetration of the primary zone air jets by the acoustic drive thereby increasing combustor flow blockage. This and the secondary effect of jet toroidal vortices, resulted in up to 35% increase in mixing, relative to "no-drive", as shown by a single combustion probe diametral traverse.

The acoustic drive produced a more uniform exit plane temperature pattern, resulting in up to 35% improvement in mixing relative to "no-drive" and in up to 20% relative improvement in the temperature pattern quality. The effects depended on air/fuel ratio and in general improved relative to "no-drive" with richening. The acoustic driving effectiveness also improved with richening for a maximum value of 3.9% (28°C) of the mean temperature rise. Increasing the loading to ¾ load, 150W single driver power, reduced the acoustic driving effectiveness by about 80% with correspondingly reduced improvements in mixing and quality. Whether driving effectiveness could be regained by increased driving power was not resolved.

The effects of acoustic drive, as determined by exit plane temperature measurements, were controllable by means of the driving power, but saturated at about 150W when a single acoustic driver was used. Increased flow blockage, caused by increased jet penetration by the acoustic drive,

appeared to be the control mechanism, in agreement with the combustion measurements results, and did not depend on the driving pattern. However, symmetrical driving produced slightly stronger effects than one driver alone, and despite blockage being the dominant factor, there was evidence of slightly improved mixing due to acoustically shed jet toroidal vortices. Effectively acoustic control maintained the aerodynamics of the combustor primary zone in the lean state. Overall, acoustic control improved mixing and produced favourable general progressive control over the combustor exit plane temperature pattern.

Changes in the hot pressure loss were not significant. Also, the maximum driving power used for effective acoustic control was insignificant in comparison with the energy conversion rate of the combustor.

ACKNOWLEDGEMENTS

The authors are indebted to Mr. R. Bechtold, Chief Technical Supervisor, and particularly to Technicians Mr. W. Crews, Mr. C. Imer, Mr. G. East and Mr. P. Halkett, for their expert work in the building of the test rig. We are also grateful to Research Technicians Mr. A. Moehrle and Mr. R.W. Gustafson for their invaluable assistance with instrumentation and operational requirements. Special thanks are due to project students Mr. P. Ivers, Miss L. Sharp, Mr. T. Wagner and Mr. S. Giacomin for their careful work with the combustion analysis. The work was supported financially by the Natural Sciences and Engineering Research Council of Canada, under Grant No A7801. Canadian Western Natural Gas Co. Ltd., generously supplied the natural gas for operation of the test rig.

REFERENCES

1. Vermeulen, P.J., Odgers, J. and Ramesh, V., "Acoustic Control of Dilution-Air Mixing in a Gas Turbine Combustor", *Trans. ASME, Journal of Engineering for Power*, Vol. 104, No. 4, Oct. 1982, pp. 844-852.

2. Vermeulen, P.J., Odgers, J. and Ramesh, V., "Full Load Operation of Gas Turbine Combustor with Acoustically Controlled Dilution-Air Mixing", *International Journal of Turbo & Jet-Engines*, Vol. 4, Nos. 1-2, 1987, pp. 139-147.

3. Vermeulen, P.J. and Yu, Wai Keung, "An Experimental Study of the Mixing by an Acoustically Pulsed Axisymmetrical Air-Jet", *International Journal of Turbo and Jet Engines*, Vol. 4, Nos. 3-4, 1987, pp. 225-237.

4. Vermeulen, P.J., Ramesh, V. and Yu, Wai Keung, "Measurements of Entrainment by Acoustically Pulsed Axisymmetric Air Jets", *Trans. ASME, Journal of Engineering for Gas Turbines and Power*, Vol. 108, No. 3, July 1986, pp. 479-484.

5. Vermeulen, P.J., Rainville, P. and Ramesh, V., "Measurements of the Entrainment Coefficient of Acoustically Pulsed Axisymmetric Free Air Jets", *Trans. ASME, Journal of Engineering for Gas Turbines and Power*, Vol. 114, No. 2, April 1992, pp. 409-415.

6. Vermeulen, P.J., Chin, Ching-Fatt and Yu, Wai Keung, "Mixing of an Acoustically Pulsed Air Jet with a Confined Crossflow", *AIAA Journal of Propulsion & Power*, Vol. 6, No. 6, 1990, pp. 777-783.

7. Vermeulen, P.J., Grabinski, P. and Ramesh, V., "Mixing of an Acoustically Excited Air Jet with a Confined Hot Crossflow", *Trans. ASME, Journal of Engineering for Gas Turbines and Power*, Vol. 114, No. 1, January 1992, pp. 46-54.

8. Ho, Chih-Ming, and Huerre, P., "Perturbed Free Shear Layers", *Annual Reviews of Fluid Mechanics*, Vol. 16, 1984, pp. 365-424.

9. Gleason, C.G., Oller, T.L., Shayerson, M.W. and Bahr, D.W., "Evaluation of Fuel Character Effects on J79 Engine Combustion System", *Report No. AFAPL-TR-79-2015, CEEDO-TR-79-06, G.E. Company, Aircraft Group*, Cincinnati, Ohio, June 1979.

10. Gleason, C.G., Oller, T.L., Shayerson, M.W. and Bahr, D.W., "Evaluation of Fuel Character Effects on F101 Engine Combustion System", *Report No. AFAPL-TR-79-2018, CEEDO-TR-79-07, G.E. Company, Aircraft Group*, Cincinnati, Ohio, June 1979.

11. Gleason, C.C., Oller, T.L., Shayerson, M.W. and Kenworthy, M.J., "Evaluation of Fuel Character Effects on J79 Smokeless Combustor", *Report No. AFAPL-TR-80-2092, G.E. Company, Aircraft Group*, Cincinnati, Ohio, June 1980.

Discussion

Question 1. C. Moses
If this concept improves the mixing, then why is efficiency reduced?

Author's Reply
Since the blockage effect causes richening, and since most data lies to the right of the peak efficiency in the curve shown in Figure 7, the efficiency drop follows the normal behaviour.

Question 2. S. Sivasegaram
What was the basis on which the driving frequency was chosen, and what effect did a variation of this frequency have on combustor performance?

Author's Reply
The driving frequency was the strongest resonance mode of the system, chosen by two channel analysis using an input and output signal for the system. Small variations of frequency had a negligible effect. However, variations of the resonance mode produced weak driving which in turn caused smaller measured effects.

Question 3. Dr G. Andrews
You mentioned that there were more practical ways of generating the pulsations. Can you expand on this?

Author's Reply
Self oscillating systems are possible, but would involve ingenious design. Rotating and oscillating valves may be more reliable, but our experience shows that frequencies greater than 100 Hz are hard to achieve. The electromechanical piston (loudspeaker) is the most flexible, but it is limited by flexure design and poor cooling. It ought to be possible to overcome these deficiencies by better design, i.e., a good linear motor.

ENDOTHERMIC FUELS FOR HYPERSONIC AVIATION

by

Dr Leonid S. Ianovski
Laboratory Head
Central Institute of Aviation Motors (CIAM)
Moscow, Russia

Edited by[1]

Dr Clifford Moses
Chairman, Program Committee and Institute Engineer
Southwest Research Institute
San Antonio, Texas

The creation of hypersonic vehicles and the use of jet engines with higher temperature cycles has resulted in a significant increase in the thermal stresses of the engine elements. In order to use the fuel as the coolant for these elements, it is necessary to increase the heat capacity of hydrocarbon fuels.

This problem can be solved by taking advantage of such high temperature chemical processes as [1-3]:

- catalytic dehydrogenation of the hydrocarbon fuels;
- thermal cracking or pyrolysis of hydrocarbon fuels, including the addition of the initiators and catalysts.

The chemical heat capacity of hydrocarbon fuels can be used for the direct cooling such elements as combustion chambers, nozzles, and front wing edges; indirect cooling these elements can be accomplished by using a heat-transport medium in the fuel/air or fuel/gas heat exchangers. The gaseous products of the decomposed fuels can be used as a working medium for the drive of the equipment of a fuel/feeding system of the engines.

It appears that the efficiency of the engine can be improved by taking advantage of the added cooling capacity which results in a higher heat of combustion and a higher specific gas constant. The application of endothermic fuels in the hypersonic vehicles requires a solution of a number problems, especially the following:

1. an evaluation of endothermic fuel compositions to determine chemical reactions at the given temperature ranges, and the effects of catalysts, initiators, and materials or covers to increase heat absorption, to decrease the temperature threshold of fuel decomposition, and to reduce the formation of coke deposits;
2. a determination of the chemical reaction rates for the different endothermic fuels;
3. a determination of the heat and mass transfer rates in the fuel channels in both the liquid and vapour phases including supercritical states, and also under conditions of chemical reactions of decomposition;
4. a development of the compact heat exchangers and cooling systems which can utilize the chemical heat capacity of the endothermic fuels, and the estimation of the efficiency of these endothermic fuels to cool high speed aircraft.
5. to achieve effective combustion of products of the endothermic reactions in subsonic and supersonic flows.

Investigations are being conducted at CIAM to address these questions. This report is a brief review of some of the results.

Experimental Installations and Methods

The experimental investigations of the chemical fuel decomposition processes have been carried out by laboratory installations at one atmospheric and elevated (to 8.0 MPa) pressures. A schematic of the flow apparatus is shown in Figure 1. Two different types of reactors are used: One type is made of either hollow or coaxial round tubes made of quartz and filled with catalytic material. Figure 2 illustrates the second type of reactor which is made from flat plates with internal turbulence generators; in this type, the walls are coated with catalytic material.

The fuel decomposition takes place in the reactors with the formation of hydrogen (H_2) and light hydrocarbon gases; also, there is the formation of coke deposits. The gas compositions are determined by chromatography. The quantities and composition of coke deposits are determined by carbon burnoff at temperatures 800-900°C and by other methods. The heats of reaction and average molecular masses of the decomposition products are determined by using the composition of these products. In the channels, all fuels made the coke deposits while still in the liquid phase; these deposits affected the heat transfer to the fluid over the course of the experiment, sometimes resulting in higher wall temperatures while other times lower. To reduce the formation of deposits, the dissolved oxygen and other contaminants and additives are removed from the fuels.

[1]. At the request of the PEP Executive, I have endeavoured to edit the original text so that a reader not familiar with the subject matter of this paper would be more able to understand the presentation and its significance. I have tried to maintain the original content without interpretation or change. In the interest of time, this was unfortunately carried out without the knowledge or consent of Dr Ianovski. For a copy of the original text, please contact Dr Moses or the PEP Executive.

Presented at an AGARD Meeting on 'Fuels and Combustion Technology for Advanced Aircraft Engines', May 1993.

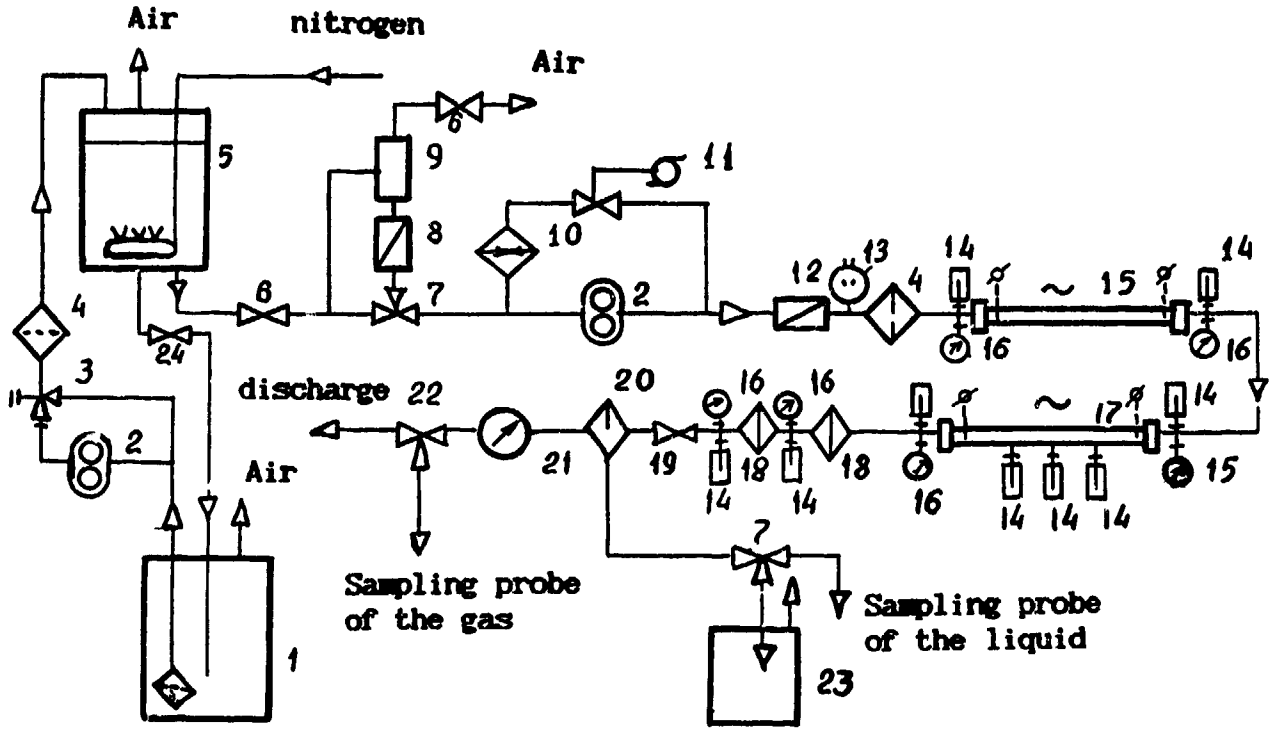

Figure 1 Schematic of the experimental plant U-404: 1 — inlet fuel tank; 2 — pump; 3 — relief valve; 4 — filter; 5 — flowmeter tank; 6 — valve; 7 — 3-ways valve; 8 — volumeter; 9 — equalazer tank; 10 — heat exchanger; 11 — electro-contact valve; 12 — fuel flow rate controller; 13 — electro-contact manometer; 14 — thermocouple; 15 — electro-heater; 16 — manometer; 17 — reactor; 18 — refrigerator; 19 — regulation valve; 20 — fuel-air separation; 21 — gas flow-meter; 22 — conrol valve; 23 — drain tank; 24 – closed valve.

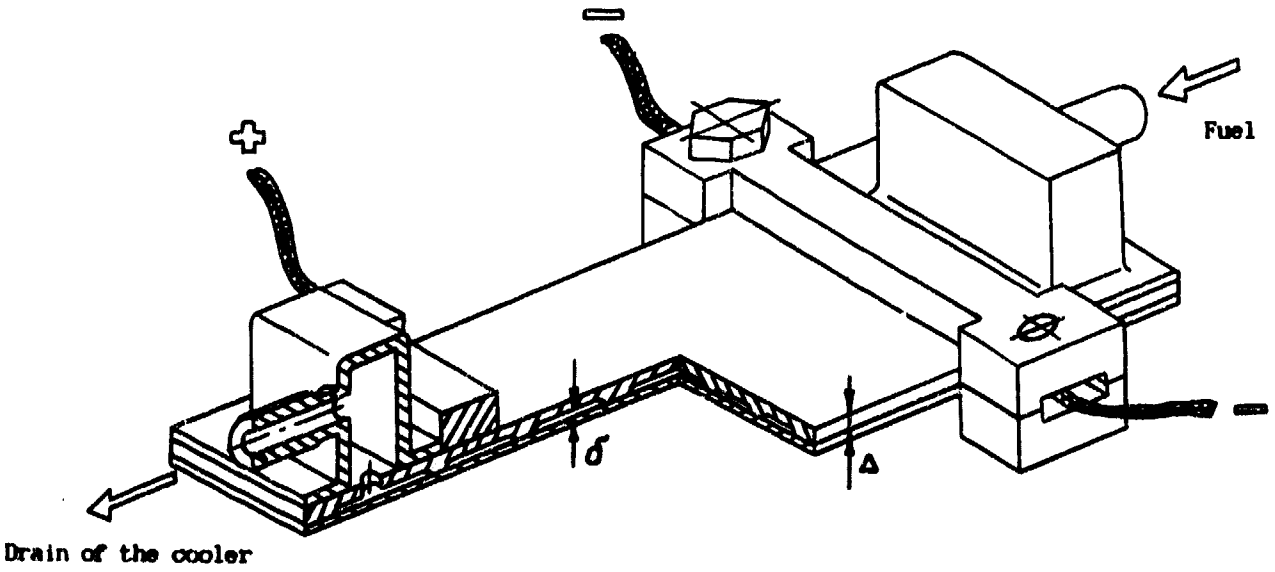

Figure 2 The general look of the flat wall with internal microchannels.

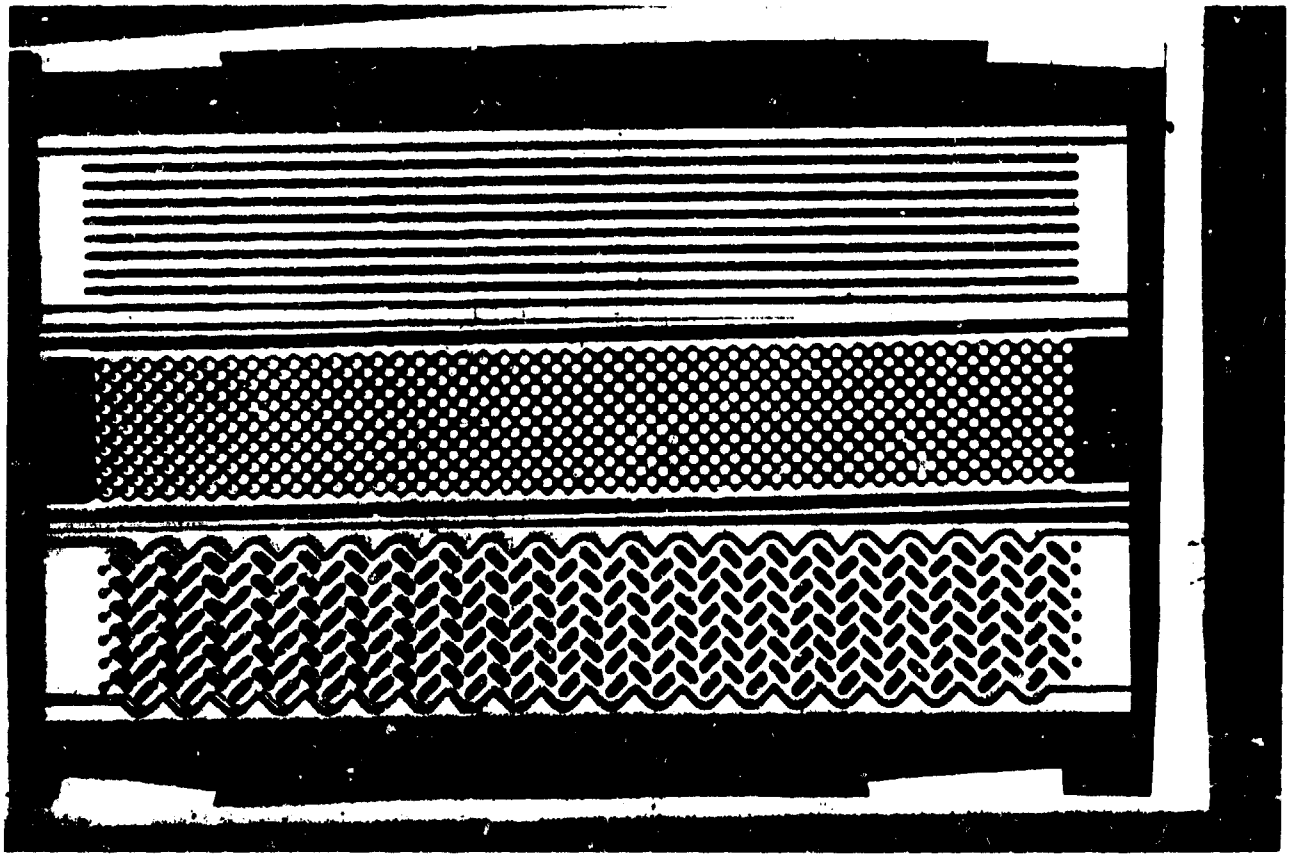

Fig. 3 Scheme of channels with turbulentors.

Results of Experiments

The most interesting endothermic processes are the catalytic dehydrogenization of hydrocarbons. Cyclohexane, methyl cyclohexane, and several special fuel compositions were investigated. Table 1 lists several examples of dehydrogenation reactions that have been addressed in the literature, but unfortunately experimental data are not sufficient for the design and construction of hardware.

Table 1

nn	Reaction	H, kkal/mol
1	$C_6H_{12} \rightarrow C_6H_6 + H_2$	33.73
2	$C_4H_{10} \rightarrow C_4H_8 + H_2$	27.50
3	$C_6H_{12} \rightarrow C_6H_6 + 3H_2$	49.25
4	$C_7H_{14} \rightarrow C_7H_8 + 3H_2$	48.94
5	$C_nH_m \rightarrow C_nH_{m-2} + 2H_2$	—

The kinetic parameters of cyclohexane and other fuels dehydrogenization at various catalysts were investigated and reaction rate constants and activation energy were determined. Dehydrogenization of C_6H_{12} and C_7H_{14} and related fuel compositions were studied with various kinds of catalysts at pressures of 0.1–1.0 MPA and temperatures of 360–620°C.

Catalyst temperature was found to be an important parameter to catalyst performance. This is illustrated in Figure 4 for the dehydrogenation of C_6H_{12} over two different catalysts. The temperature dependence varied with the catalyst; some could be increased by only a factor of 2, while others could be increased by a factor of 10.

During some experiments it was observed that under the conditions of the experiments, the catalyst activity decreased during the first 30 minutes of the test. Examination of the catalyst surfaces before and after the experiments using electron microscopy showed that this decrease in activity was caused by an agglomeration of Pt and Pd particles on the surface of catalysts. It was suggested that creating binary metallic

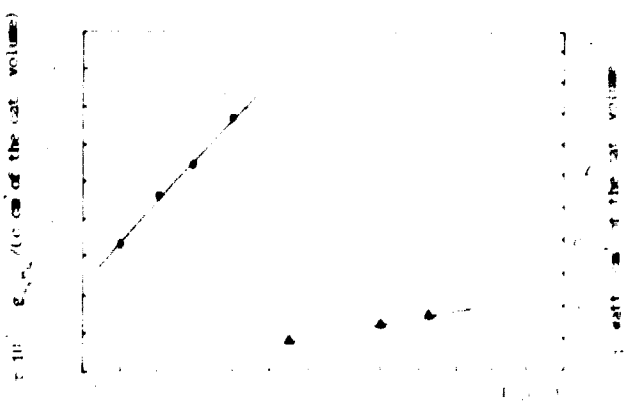

Figure 4 Dependence of the maximal specific rate of decomposition C_6H_{12} and the energetic catalyzer productivity from the catalyzer layer temperature (P=1.03 MPa): 1 — Pd/C; 2 — Ni,SnC.

catalysts would stabilize the activity. In CIAM a new technology was then used to prepare the catalysts by mixing the metal powders and then baking the system at high temperature. This technology of catalysts preparation guaranteed a firm coupling of the catalyst with the thermoconductive surfaces and the activity was much more stable.

Figure 5 illustrates this improved stability for C_7H_{14} over two different catalysts. During the first 80 minutes of the work the energetic productivity of the catalysts decreased about 17% and during the following 4 hours, only about 11%. The coke formation was not large for these experiments. Strain energy at a temperature of 375°C was 14 W/cm³, and the heat transfer rate from wall to the catalyst was 40 kW/m². The dehydrogenization of cyclohexane, methylcyclohexane and other related fuel compositions at 450°C provide a maximum catalyst power intensity 18 w/cm³ and a heat flow intensity q = 35 kW/m². The nature of the coke deposits was not observed in these experiments. The rate of formation of coke deposits was decreased and catalysts lifetime was increased as the pressure was increased from 0.1 to 1.0 MPa. The optimum compositions of fuel mixtures were selected and the catalysts which provide with least falling of the activity were identified; also the ways of increasing the catalysts stability were projected.

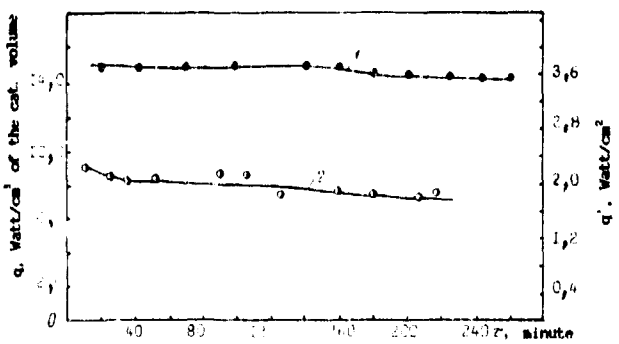

Figure 5 Change of the energetic catalyzer productivity and the heat transfer rate to the layer at C_7H_{14} dehydrogenisation: 1 — catalyzer N 1, 2 — catalyzer N 2, m = 2 g; G = 2 cm³/min; τ_{in} = 1350 h⁻¹; τ_{out} = 3500 h⁻¹; t = 375°.

At higher fuel temperatures, above 500°C, it is necessary to employ the processes of thermal cracking or pyrolysis of jet fuels. CIAM created the first samples of the Russian endothermic fuel T-15 which is stable to thermooxidation processes and have not corrosive activity to the constructional materials and rubber and not toxic. The fractional composition and the saturated vapour pressure for T-15 are not distinguished from the standard jet fuels such as Russian T-6 or American JP-7.

The mass heat of combustion of T-15 on 14% is larger than for fuels T-6 or JP-7, (is 14% larger, ed.?) and has better burning characteristics. The decomposition products of fuel T-15 have a specific gas constant: R = 0.22 kJ/(kg-K), that allows to maintain the drive of the fuel feeding systems of engines by the pyrogas. The total heat capacity of the T-15 sample at temperatures <800°C is over 4600 kJ/kg as shown in Figure 6. The T-15 heat capacity is 8-10% from the mass heat combustion at the temperature range from 20°C to 760°C. To compare the liquid hydrogen has heat capacity per unit mass heat combus-

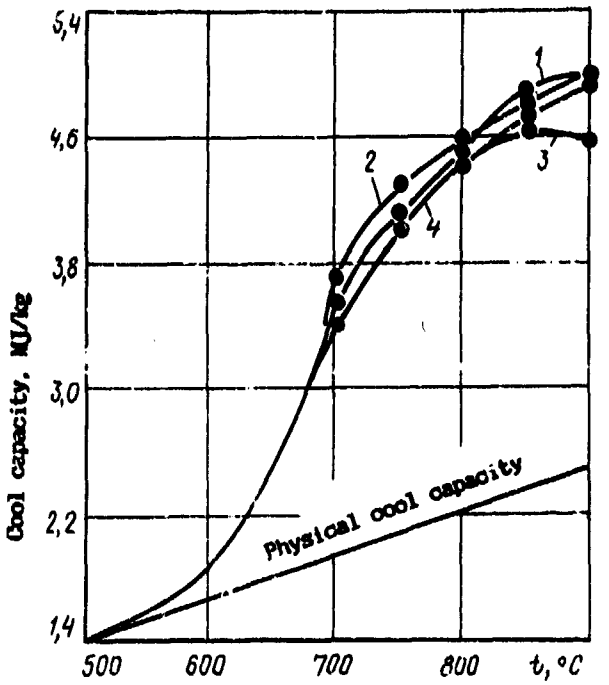

Figure 6 The cool capacity as a function of temperature for endothermic fuel different samples.

tion near 11%. That is very close to endothermic fuels. This result shows that the heat capacity of endothermic fuels will be comparable with liquid hydrogen heat capacity with due account of increasing the hydrocarbon flow rate 3 times much as hydrogen flow rate.

In order to intensify the process of fuel cracking and also to decrease the temperature of beginning fuel decomposition, homogeneous initiators and heterogeneous catalysts were selected. The following considerations formed the basis of the choice of homogeneous initiators:

- first, initiators must generate active radicals (H, CH_3, C_2H_5) which attach to the fuel hydrocarbons;
- secondly, the initiator must have high efficiency so only small concentrations are necessary to force the fuel cracking;
- further, the radical generation rate by means of the initiators must be more than the cracking fuel rate;
- finally, all initiators must react during the cracking time because otherwise all the radicals will simply react between themselves.

The bond brake energy of initiators must be lower than C-C bond brake energy.

We found effective liquid initiators which in concentrations of less than 0.8% accelerate the fuel cracking from 2 to 7 times in the temperature range 500-630°C and also decrease the beginning cracking temperature nearly at 100°. This is illustrated in Figure 7. All the more, the binary initiator mixtures are created which give a synergetic effect equal 2. One of their initiators generates radicals at decomposition and accelerates the decomposition of second initiator and the fuel at all.

Coke deposits are one of the important factors defining the limits of application of the fuel cracking processes in cooling

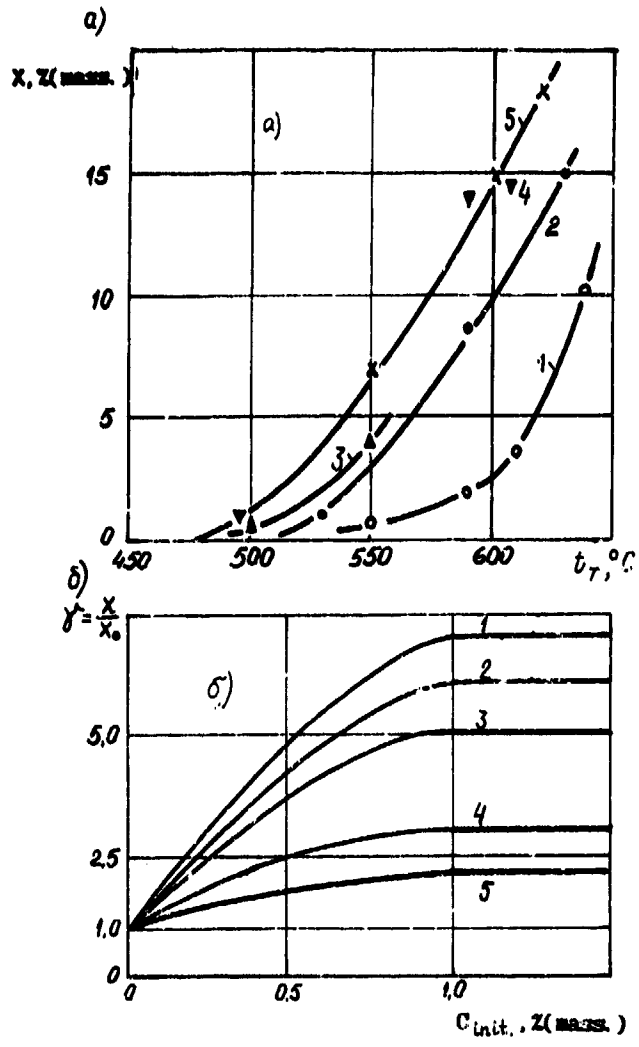

Figure 7 Influence of the initiator concentration of the fuel gacification. P=5,0 MPa; a) C,%: 1 — 0; 2 — 0,4; 3 — 0,7; 4 — 0,8; 5 — 1,5; b) T, C: 1 — 560°; 2 — 580°C; 3 — 600°C; 4 — 620°C; 5 — 630°.

Table 2

Technology of processing	Coking, % mass
Without processing (6 cleanliness)	0.039
Mechanical processing (7 clean.)	0.036
Mechanical processing (10 clean.)	0.028
Chemical processing	0.032
Mechanical processing (10 clean.) + gaseous processing	0.026
Mechanical processing + electrolytical-plasmous processing	0.002

Temperature 820 C; τ = 1s; τ_w = 5h; Ø 6 × 0.5 × 180; Gas, %, 88

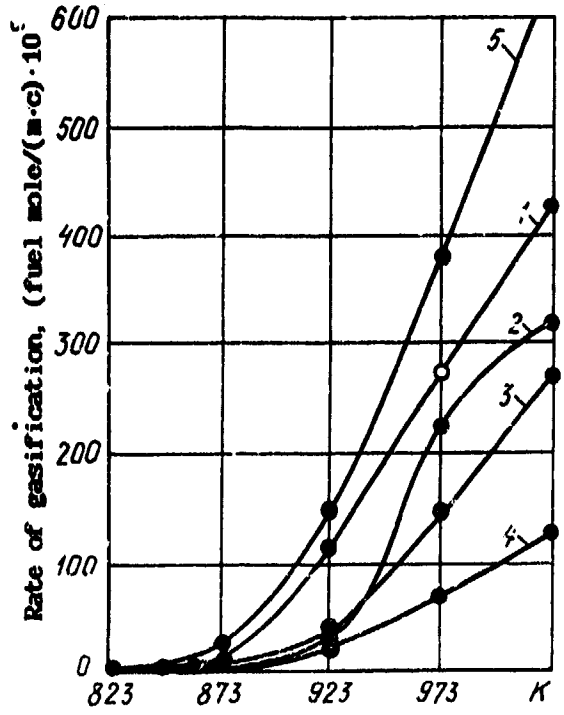

Figure 8 The rate of gasification as a function of temperature at the contact with different metals. 1 — X18H10T, 2 — NiCr, 3 — Fe, 4 — Ni, 5 — Ti.

systems. Various technologies of suppressing the coke deposit formation in the channels were investigated including the selection of materials and coatings which are catalytically inert to coking. Materials were identified which decreased the coke deposit by 40-50 times as compared to the steel surface under equal conditions. Table 2 compares the results of investigations of various technologies of material surface processing in order to decrease the coke deposits. These technologies were tested for five hours under extreme conditions, at temperatures to 820°C. The combination of mechanical processing of the material surfaces to high level of cleanliness combined with electrolytic-plasmous processing gave the highest effect — practically no coking.

In order to intensify of cracking process a metal packing was placed in the reaction zone. Different metals were investigated. Figure 8 shows that the metal catalytic effect on the fuel decomposition was different for the metals tested. If is of interest to note that metals influences the beginning temperature of fuel decomposition and displaces it in the range to 50-60°. The temperature dependence of the reaction heat effect also influenced the kind of the metals.

Kinetic parameters of gas and coke formations at the fuel cracking in the contact with various metals were determined. Connection between catalytic properties of metals and its internal properties (for example, the atomic radius) permitted the prediction of the catalytic properties. Thus our investigation allowed the selection of optimum compositions of endothermic fuels, construction materials and coatings and the technologies of their processing, which provide with possibility of using this fuels for cooling of the scramjet engines.

In order to provide design data for cooling systems on endothermic fuels, a series of heat transfer experiments were carried out in which fuels were decomposed at different temperatures, pressures, and contact times. The generalized dependences of heat transfer were obtained. The critical specific heat flows which leads to the phenomenon analogous to "heat explosion" in the diffusive field proceeding the decomposition process were determined.

The regularities of coke deposits formation at fuel cracking were obtained. The calculating methods of gas formation intensity at fuel cracking and the wall temperatures considering the rates of coke formation in the approach of boundary layer and also in single-measured approach were elaborated. The results of modelling of the fuel cracking process in reactors and their comparison with experimental data were presented on Figures 9-13, including the modelling of a fuel/air heat exchanger shown in Figure 13.

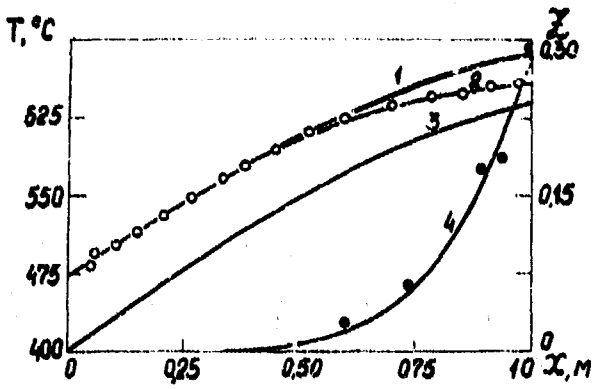

Figure 9 Wall bulk temperature distributions and conversion degree along the length of the canal at the PT fuel thermodestruction. ϕ 4×1000; T_{in} = 400°C; G = 1,2·10^{-3} kg/s; q_w = 5·10^5 Watt/m^2.
Solid linis — computed values, plots — experimental data: 1 — with chemical reaction, 2 — without chemical reaction.

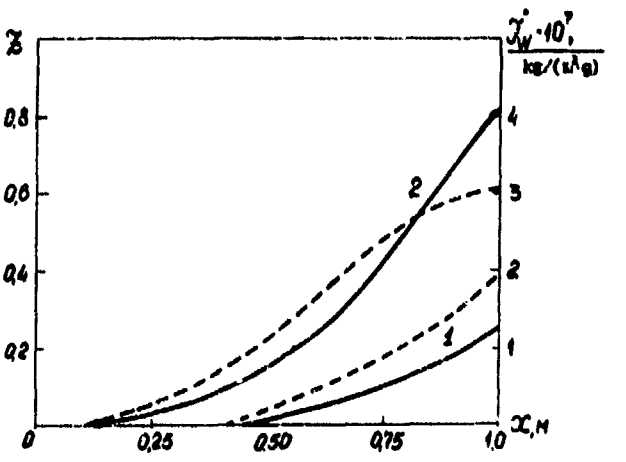

Figure 11 Influence of the mass flow rate on the change of the degree conversion (solid lines) and the coke deposit rate along the length of the canal ϕ4×1000. N — octan, T_{in} = 573 K; q_w = 5·10^5 Watt/m^2; G,kg/s: 1 — 4·10^{-3}; 2 — 8·10^{-3}

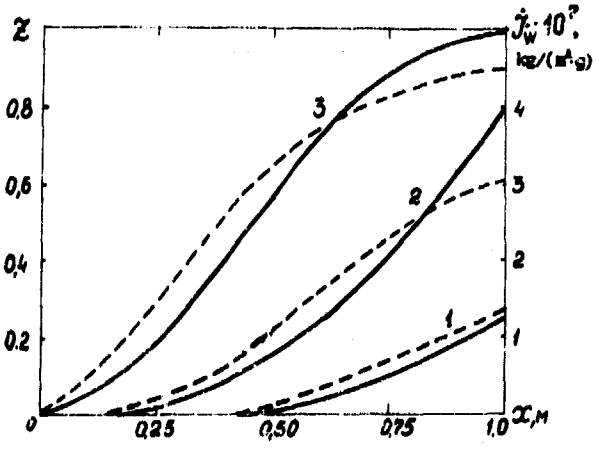

Figure 10 Influence of the heat flux on degree of the fuel conversion (solid lines) and the coke deposits rate (dashed lines) along the length of the canal ϕ 4×1000. N-octan; T_{in} = 573 K; G = 4,1·10^{-3} kg/s; q_w Watt/m^2: 1 — 0,3·10^6; 2 — 0,5·10^6; 3 — 1,1·10^6

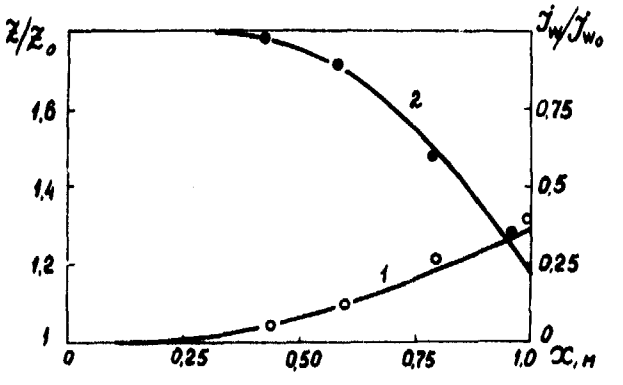

Figure 12 Influence of the initiator of the gasification (1) and the coke deposit rate (2) at n-octan thermodestruction. T_{in} = 573 K; q_w = 5·10^5 Watt/m^2; G = 4,1·10^{-3} kg/s. The index "0" — without initiator. Lines — computed values, plots — experiment.

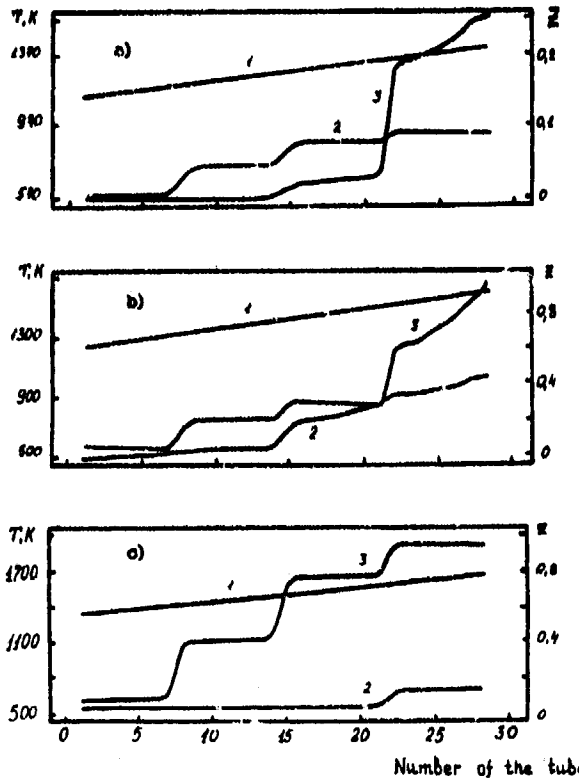

Figure 13 The calculation of exchanger-reactor on endothermic fuel. The temperature of covered air flow, K: a) 1400, b) 1600, c) 1700, 1 — air temperature, 2 — fuel temperature, 3 — degree of the fuel conversion.

The experimental installation for studying the burning characteristics of cracked fuel products in subsonic air flow is shown on Figure 14. It includes the combustion chamber fuel and air systems, the reactor-gasifier, the refrigerators, the fuel and inert gas delivery systems.

The results of the burning investigations are presented in Figure 15. The calculation of the coefficient of heat emission η_h had been made with considering the spended heat on the decomposition. It is clear that combustor had more high values η_h over the total range of the charge V_{air} and α at pregasified fuel introduction.

The stability characteristics of combustor at the lean fuel/air mixtures was improved by the feeding of fuel decomposition products at the fuel transformation degree $z = 0.25$, $\alpha_{mean} = 26.7$; while at the initial fuel $\alpha_{mean} = 14.6$. The obtained regularity of the character change of the dependence η on the mixture composition in the feeding the fuel decomposition products may be explained first by increasing of the rate owing to hydrogen formation and secondly, by the increase of the volumetric fuel rate at the expense of the gaseous fuels decomposition products (for $z = 0.25$ $V_{prod} = 4V_0$).

Thus the comparative investigations of some characteristics of the combustion at the endothermic fuel decomposition products qualitatively confirmed the possibility of the improvement of working process in the combustor by fuel pregasification. Further investigations are necessary for the determination of the quantitative regularities, and also in supersonic air flows. A special installation has been created at CIAM to obtain the characteristics of burning the fuel decomposition products in supersonic flows.

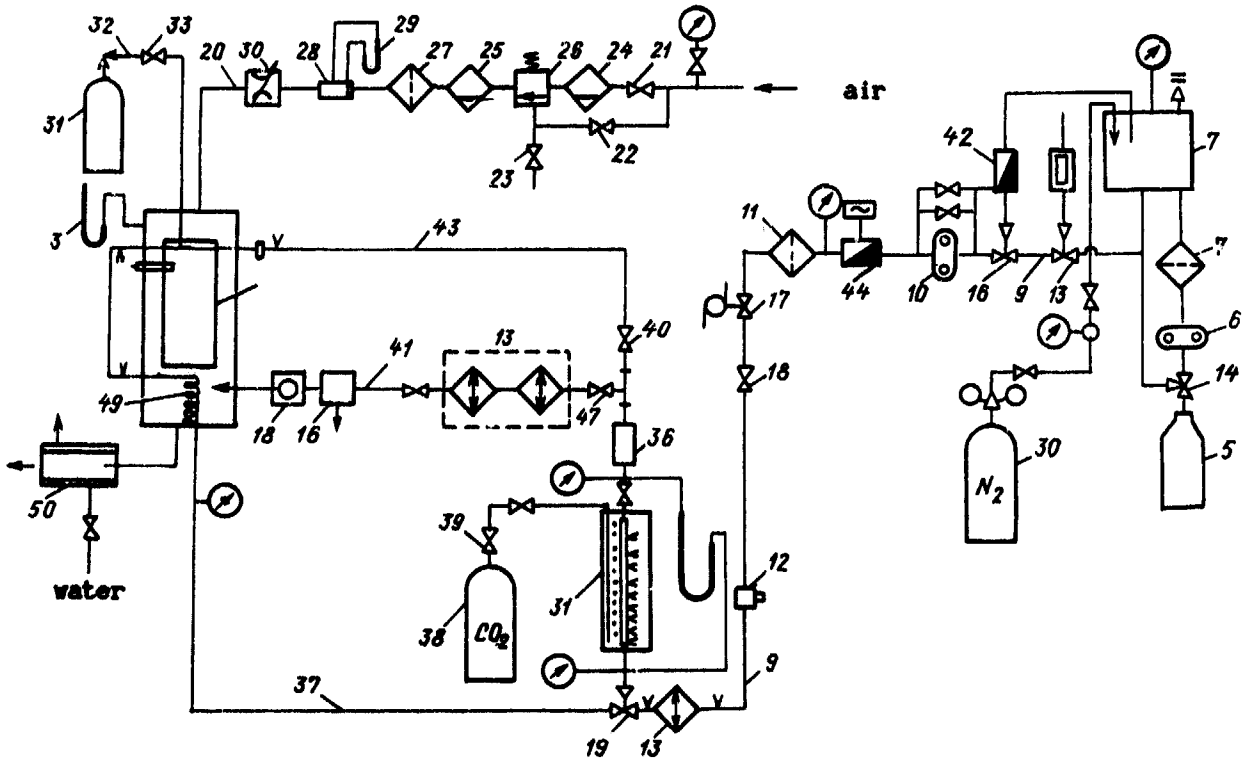

Figure 14 The plant for determination of burning characteristics of endothermic aircraft fuels.

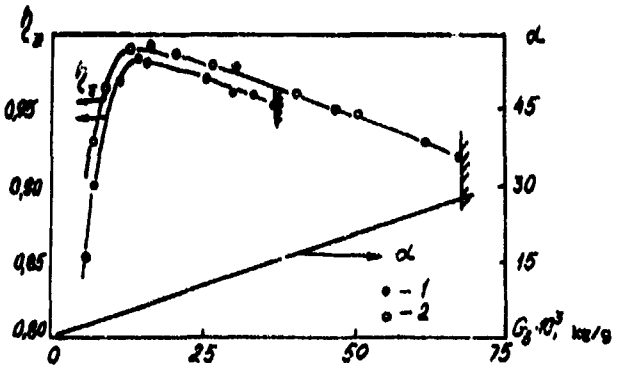

Figure 15 Combustion characteristics against air mass flow for the different conversion degree Z. Fuel — PT. Z: 1 — 0; 2 — 0,25.

Literature

1. Hausman J and Voeks G
   Steam Reforming of Methyl Fuel, Proc. of the III Inter. Conf. on Hydrogen Energetics, Miami FL, USA, 1982.

2. Doolan KR and Mackie JC
   Kinetics of Pyrolysis in Argon-Hydrogen Mixtures, Combustion and Flame, Vol. 50, p29, 1983.

3. Anikeev Vi, Bayev VK, Kundo NN, Kirillov VA and Ramazanova TF
   Possibilities of Applying Heterogeneous Catalysts in Energy Devices, Proc. of the 7th World Hydrogen Energy Conf., pp. 1693-1709, Moscow, 1988.

Discussion

Question 1. C. Moses
I am interested in the nature of the initiators that you used.

Author's Reply
The initiators are the homogeneous substances dissolved in fuels. These initiators are the inorganic substances generating the active radicals (H, CH_3, C_2H_5) which when heated attach to the hydrocarbon molecules sooner than the cracking of the hydrocarbon molecules take place. The concentration of initiators in fuels is less than 0.8% by mass, but they accelerate fuel cracking from 2 to 7 times in the temperature range of 500 to 630 degrees C.

REPORT DOCUMENTATION PAGE

1. Recipient's Reference	2. Originator's Reference	3. Further Reference	4. Security Classification of Document
	AGARD-CP-536	ISBN 92-835-0719-3	UNCLASSIFIED/ UNLIMITED

5. Originator Advisory Group for Aerospace Research and Development
North Atlantic Treaty Organization
7 Rue Ancelle, 92200 Neuilly sur Seine, France

6. Title FUELS AND COMBUSTION TECHNOLOGY FOR ADVANCED AIRCRAFT ENGINES

7. Presented at the Propulsion and Energetics Panel 81st Symposium held in Fiuggi, Italy, 10th—14th May 1993.

8. Author(s)/Editor(s)	9. Date
Various	September 1993
10. Author's/Editor's Address	**11. Pages**
Various	512

12. Distribution Statement There are no restrictions on the distribution of this document. Information about the availability of this and other AGARD unclassified publications is given on the back cover.

13. Keywords/Descriptors

Fuels for aircraft	Fuel injection	Mixing in combustors
Combustion	High temperature fuels	Supersonic transport
Modeling	Emission	Hydrocarbons
Pollution	Atomization of fuels	NOx
Smoke production	Soot formation	

14. Abstract

The Conference Proceedings contains the 38 papers presented at the Propulsion and Energetics Panel 81st Symposium on "Fuels and Combustion Technology for Advanced Aircraft Engines" which was held from 10th—14th May 1993, in Fiuggi, Italy. The Technical Evaluation Report and the Keynote Address are included at the beginning, and discussions follow most papers.

The Symposium was arranged in the following Sessions: Technology Overview Papers (2); Modelling: Pollutant Formation (4); Modelling: Combustor Design (5); High Temperature Fuels and Fuel Systems (6); Combustion Research: Performance (6); Combustion Research: Emissions (5); Fuel Atomization: Diagnostics and Modelling (5); and Combustion Research: Flowfield and Mixing (4). The last paper is a contribution from Russia not allocated to a session.

New technologies for low NOx combustors and advanced high-pressure/high temperature cycle engines result in unique problems in design and performance. There have been significant advances in modelling and diagnostics to aid the development of these technologies. The purpose of the Symposium was to bring together experts from industry, research establishments and universities to discuss fundamental and applied research in these areas as relevant to the development of advanced gas turbine engines, to exchange practical experience and to discuss the state of the art.

AGARD Conference Proceedings 536
Advisory Group for Aerospace Research and Development, NATO
FUELS AND COMBUSTION TECHNOLOGY FOR ADVANCED AIRCRAFT ENGINES
Published September 1993
512 pages

The Conference Proceedings contains the 38 papers presented at the Propulsion and Energetics Panel 81st Symposium on "Fuels and Combustion Technology for Advanced Aircraft Engines" which was held from 10th–14th May 1993, in Fiuggi, Italy. The Technical Evaluation Report and the Keynote Address are included at the beginning, and discussions follow most papers.

The Symposium was arranged in the following Sessions: Technology Overview Papers (2); Modelling: Pollutant

P.T.O.

AGARD-CP-536

Fuels for aircraft
Combustion
Modeling
Pollution
Smoke production
Fuel injection
High temperature fuels
Emission
Atomization of fuels
Soot formation
Mixing in combustors
Supersonic transport
Hydrocarbons
NOx

AGARD Conference Proceedings 536
Advisory Group for Aerospace Research and Development, NATO
FUELS AND COMBUSTION TECHNOLOGY FOR ADVANCED AIRCRAFT ENGINES
Published September 1993
512 pages

The Conference Proceedings contains the 38 papers presented at the Propulsion and Energetics Panel 81st Symposium on "Fuels and Combustion Technology for Advanced Aircraft Engines" which was held from 10th–14th May 1993, in Fiuggi, Italy. The Technical Evaluation Report and the Keynote Address are included at the beginning, and discussions follow most papers.

The Symposium was arranged in the following Sessions: Technology Overview Papers (2); Modelling: Pollutant

P.T.O.

AGARD-CP-536

Fuels for aircraft
Combustion
Modeling
Pollution
Smoke production
Fuel injection
High temperature fuels
Emission
Atomization of fuels
Soot formation
Mixing in combustors
Supersonic transport
Hydrocarbons
NOx

AGARD Conference Proceedings 536
Advisory Group for Aerospace Research and Development, NATO
FUELS AND COMBUSTION TECHNOLOGY FOR ADVANCED AIRCRAFT ENGINES
Published September 1993
512 pages

The Conference Proceedings contains the 38 papers presented at the Propulsion and Energetics Panel 81st Symposium on "Fuels and Combustion Technology for Advanced Aircraft Engines" which was held from 10th–14th May 1993, in Fiuggi, Italy. The Technical Evaluation Report and the Keynote Address are included at the beginning, and discussions follow most papers.

The Symposium was arranged in the following Sessions: Technology Overview Papers (2); Modelling: Pollutant

P.T.O.

AGARD-CP-536

Fuels for aircraft
Combustion
Modeling
Pollution
Smoke production
Fuel injection
High temperature fuels
Emission
Atomization of fuels
Soot formation
Mixing in combustors
Supersonic transport
Hydrocarbons
NOx

AGARD Conference Proceedings 536
Advisory Group for Aerospace Research and Development, NATO
FUELS AND COMBUSTION TECHNOLOGY FOR ADVANCED AIRCRAFT ENGINES
Published September 1993
512 pages

The Conference Proceedings contains the 38 papers presented at the Propulsion and Energetics Panel 81st Symposium on "Fuels and Combustion Technology for Advanced Aircraft Engines" which was held from 10th–14th May 1993, in Fiuggi, Italy. The Technical Evaluation Report and the Keynote Address are included at the beginning, and discussions follow most papers.

The Symposium was arranged in the following Sessions: Technology Overview Papers (2); Modelling: Pollutant

P.T.O.

AGARD-CP-536

Fuels for aircraft
Combustion
Modeling
Pollution
Smoke production
Fuel injection
High temperature fuels
Emission
Atomization of fuels
Soot formation
Mixing in combustors
Supersonic transport
Hydrocarbons
NOx

Formation (4); Modelling: Combustor Design (5); High Temperature Fuels and Fuel Systems (6); Combustion Research: Performance (6); Combustion Research: Emissions (5); Fuel Atomization: Diagnostics and Modelling (5); and Combustion Research: Flowfield and Mixing (4). The last paper is a contribution from Russia not allocated to a session.

New technologies for low NOx combustors and advanced high-pressure/high temperature cycle engines result in unique problems in design and performance. There have been significant advances in modelling and diagnostics to aid the development of these technologies. The purpose of the Symposium was to bring together experts from industry, research establishments and universities to discuss fundamental and applied research in these areas as relevant to the development of advanced gas turbine engines, to exchange practical experience and to discuss the state of the art.

ISBN 92-835-0719-3

Formation (4); Modelling: Combustor Design (5); High Temperature Fuels and Fuel Systems (6); Combustion Research: Performance (6); Combustion Research: Emissions (5); Fuel Atomization: Diagnostics and Modelling (5); and Combustion Research: Flowfield and Mixing (4). The last paper is a contribution from Russia not allocated to a session.

New technologies for low NOx combustors and advanced high-pressure/high temperature cycle engines result in unique problems in design and performance. There have been significant advances in modelling and diagnostics to aid the development of these technologies. The purpose of the Symposium was to bring together experts from industry, research establishments and universities to discuss fundamental and applied research in these areas as relevant to the development of advanced gas turbine engines, to exchange practical experience and to discuss the state of the art.

ISBN 92-835-0719-3

Formation (4); Modelling: Combustor Design (5); High Temperature Fuels and Fuel Systems (6); Combustion Research: Performance (6); Combustion Research: Emissions (5); Fuel Atomization: Diagnostics and Modelling (5); and Combustion Research: Flowfield and Mixing (4). The last paper is a contribution from Russia not allocated to a session.

New technologies for low NOx combustors and advanced high-pressure/high temperature cycle engines result in unique problems in design and performance. There have been significant advances in modelling and diagnostics to aid the development of these technologies. The purpose of the Symposium was to bring together experts from industry, research establishments and universities to discuss fundamental and applied research in these areas as relevant to the development of advanced gas turbine engines, to exchange practical experience and to discuss the state of the art.

ISBN 92-835-0719-3

Formation (4); Modelling: Combustor Design (5); High Temperature Fuels and Fuel Systems (6); Combustion Research: Performance (6); Combustion Research: Emissions (5); Fuel Atomization: Diagnostics and Modelling (5); and Combustion Research: Flowfield and Mixing (4). The last paper is a contribution from Russia not allocated to a session.

New technologies for low NOx combustors and advanced high-pressure/high temperature cycle engines result in unique problems in design and performance. There have been significant advances in modelling and diagnostics to aid the development of these technologies. The purpose of the Symposium was to bring together experts from industry, research establishments and universities to discuss fundamental and applied research in these areas as relevant to the development of advanced gas turbine engines, to exchange practical experience and to discuss the state of the art.

ISBN 92-835-0719-3

AGARD
NATO OTAN
7 RUE ANCELLE · 92200 NEUILLY-SUR-SEINE
FRANCE
Télécopie (1)47.38.57.99 · Télex 610 176

DIFFUSION DES PUBLICATIONS AGARD NON CLASSIFIEES

Aucun stock de publications n'a existé à AGARD. A partir de 1993, AGARD détiendra un stock limité des publications associées aux cycles de conférences et cours spéciaux ainsi que les AGARDographies et les rapports des groupes de travail, organisés et publiés à partir de 1993 inclus. Les demandes de renseignements doivent être adressées à AGARD par lettre ou par fax à l'adresse indiquée ci-dessus. *Veuillez ne pas téléphoner.* La diffusion initiale de toutes les publications de l'AGARD est effectuée auprès des pays membres de l'OTAN par l'intermédiaire des centres de distribution nationaux indiqués ci-dessous. Des exemplaires supplémentaires peuvent parfois être obtenus auprès de ces centres (à l'exception des Etats-Unis). Si vous souhaitez recevoir toutes les publications de l'AGARD, ou simplement celles qui concernent certains Panels, vous pouvez demander à être inclu sur la liste d'envoi de l'un de ces centres. Les publications de l'AGARD sont en vente auprès des agences indiquées ci-dessous, sous forme de photocopie ou de microfiche.

CENTRES DE DIFFUSION NATIONAUX

ALLEMAGNE
Fachinformationszentrum,
Karlsruhe
D-7514 Eggenstein-Leopoldshafen 2

BELGIQUE
Coordonnateur AGARD-VSL
Etat-Major de la Force Aérienne
Quartier Reine Elisabeth
Rue d'Evere, 1140 Bruxelles

CANADA
Directeur du Service des Renseignements Scientifiques
Ministère de la Défense Nationale
Ottawa, Ontario K1A 0K2

DANEMARK
Danish Defence Research Establishment
Ryvangs Allé 1
P.O. Box 2715
DK-2100 Copenhagen Ø

ESPAGNE
INTA (AGARD Publications)
Pintor Rosales 34
28008 Madrid

ETATS-UNIS
National Aeronautics and Space Administration
Langley Research Center
M/S 180
Hampton, Virginia 23665

FRANCE
O.N.E.R.A. (Direction)
29, Avenue de la Division Leclerc
92322 Châtillon Cedex

GRECE
Hellenic Air Force
Air War College
Scientific and Technical Library
Dekelia Air Force Base
Dekelia, Athens TGA 1010

ISLANDE
Director of Aviation
c/o Flugrad
Reykjavik

ITALIE
Aeronautica Militare
Ufficio del Delegato Nazionale all'AGARD
Aeroporto Pratica di Mare
00040 Pomezia (Roma)

LUXEMBOURG
Voir Belgique

NORVEGE
Norwegian Defence Research Establishment
Attn: Biblioteket
P.O. Box 25
N-2007 Kjeller

PAYS-BAS
Netherlands Delegation to AGARD
National Aerospace Laboratory NLR
P.O. Box 90502
1006 BM Amsterdam

PORTUGAL
Força Aérea Portuguesa
Centro de Documentação e Informação
Alfragide
2700 Amadora

ROYAUME UNI
Defence Research Information Centre
Kentigern House
65 Brown Street
Glasgow G2 8EX

TURQUIE
Milli Savunma Başkanlığı (MSB)
ARGE Daire Başkanlığı (ARGE)
Ankara

Le centre de distribution national des Etats-Unis (NASA/Langley) ne détient PAS de stocks des publications de l'AGARD. D'éventuelles demandes de photocopies doivent être formulées directement auprès du NASA Center for Aerospace Information (CASI) à l'adresse suivante:

AGENCES DE VENTE

NASA Center for
Aerospace Information (CASI)
800 Elkridge Landing Road
Linthicum Heights, MD 21090-2934
United States

ESA/Information Retrieval Service
European Space Agency
10, rue Mario Nikis
75015 Paris
France

The British Library
Document Supply Division
Boston Spa, Wetherby
West Yorkshire LS23 7BQ
Royaume Uni

Les demandes de microfiches ou de photocopies de documents AGARD (y compris les demandes faites auprès du CASI) doivent comporter la dénomination AGARD, ainsi que le numéro de série d'AGARD (par exemple AGARD-AG-315). Des informations analogues, telles que le titre et la date de publication sont souhaitables. Veuiller noter qu'il y a lieu de spécifier AGARD-R-nnn et AGARD-AR-nnn lors de la commande des rapports AGARD et des rapports consultatifs AGARD respectivement. Des références bibliographiques complètes ainsi que des résumés des publications AGARD figurent dans les journaux suivants:

Scientifique and Technical Aerospace Reports (STAR)
publié par la NASA Scientific and Technical
Information Program
NASA Headquarters (JTT)
Washington D.C. 20546
Etats-Unis

Government Reports Announcements and Index (GRA&I)
publié par le National Technical Information Service
Springfield
Virginia 22161
Etats-Unis

(accessible également en mode interactif dans la base de données bibliographiques en ligne du NTIS, et sur CD-ROM)

Imprimé par Specialised Printing Services Limited
40 Chigwell Lane, Loughton, Essex IG10 3TZ

AGARD

NATO OTAN

7 RUE ANCELLE · 92200 NEUILLY-SUR-SEINE

FRANCE

Telefax (1)47.38.57.99 · Telex 610 176

DISTRIBUTION OF UNCLASSIFIED AGARD PUBLICATIONS

AGARD holds limited quantities of the publications that accompanied Lecture Series and Special Courses held in 1993 or later, and of AGARDographs and Working Group reports published from 1993 onward. For details, write or send a telefax to the address given above. *Please do not telephone.*

AGARD does not hold stocks of publications that accompanied earlier Lecture Series or Courses or of any other publications. Initial distribution of all AGARD publications is made to NATO nations through the National Distribution Centres listed below. Further copies are sometimes available from these centres (except in the United States). If you have a need to receive all AGARD publications, or just those relating to one or more specific AGARD Panels, they may be willing to include you (or your organisation) on their distribution list. AGARD publications may be purchased from the Sales Agencies listed below, in photocopy or microfiche form.

NATIONAL DISTRIBUTION CENTRES

BELGIUM
Coordonnateur AGARD — VSL
Etat-Major de la Force Aérienne
Quartier Reine Elisabeth
Rue d'Evere, 1140 Bruxelles

CANADA
Director Scientific Information Services
Dept of National Defence
Ottawa, Ontario K1A 0K2

DENMARK
Danish Defence Research Establishment
Ryvangs Allé 1
P.O. Box 2715
DK-2100 Copenhagen Ø

FRANCE
O.N.E.R.A. (Direction)
29 Avenue de la Division Leclerc
92322 Châtillon Cedex

GERMANY
Fachinformationszentrum
Karlsruhe
D-7514 Eggenstein-Leopoldshafen 2

GREECE
Hellenic Air Force
Air War College
Scientific and Technical Library
Dekelia Air Force Base
Dekelia Athens TGA 1010

ICELAND
Director of Aviation
c/o Flugrad
Reykjavik

ITALY
Aeronautica Militare
Ufficio del Delegato Nazionale all'AGARD
Aeroporto Pratica di Mare
00040 Pomezia (Roma)

LUXEMBOURG
See Belgium

NETHERLANDS
Netherlands Delegation to AGARD
National Aerospace Laboratory, NLR
P.O. Box 90502
1006 BM Amsterdam

NORWAY
Norwegian Defence Research Establishment
Attn: Biblioteket
P.O. Box 25
N-2007 Kjeller

PORTUGAL
Força Aérea Portuguesa
Centro de Documentação e Informação
Alfragide
2700 Amadora

SPAIN
INTA (AGARD Publications)
Pintor Rosales 34
28008 Madrid

TURKEY
Milli Savunma Başkanlığı (MSB)
ARGE Daire Başkanlığı (ARGE)
Ankara

UNITED KINGDOM
Defence Research Information Centre
Kentigern House
65 Brown Street
Glasgow G2 8EX

UNITED STATES
National Aeronautics and Space Administration (NASA)
Langley Research Center
M/S 180
Hampton, Virginia 23665

The United States National Distribution Centre (NASA/Langley) does NOT hold stocks of AGARD publications.
Applications for copies should be made direct to the NASA Center for Aerospace Information (CASI) at the address below.

SALES AGENCIES

NASA Center for
Aerospace Information (CASI)
800 Elkridge Landing Road
Linthicum Heights, MD 21090-2934
United States

ESA/Information Retrieval Service
European Space Agency
10, rue Mario Nikis
75015 Paris
France

The British Library
Document Supply Centre
Boston Spa, Wetherby
West Yorkshire LS23 7BQ
United Kingdom

Requests for microfiches or photocopies of AGARD documents (including requests to CASI) should include the word 'AGARD' and the AGARD serial number (for example AGARD-AG-315). Collateral information such as title and publication date is desirable. Note that AGARD Reports and Advisory Reports should be specified as AGARD-R-nnn and AGARD-AR-nnn, respectively. Full bibliographical references and abstracts of AGARD publications are given in the following journals:

Scientific and Technical Aerospace Reports (STAR)
published by NASA Scientific and Technical
Information Program
NASA Headquarters (JTT)
Washington D.C. 20546
United States

Government Reports Announcements and Index (GRA&I)
published by the National Technical Information Service
Springfield
Virginia 22161
United States
(also available online in the NTIS Bibliographic
Database or on CD-ROM)

Printed by Specialised Printing Services Limited
40 Chigwell Lane, Loughton, Essex IG10 3TZ

ISBN 92-835-0719-3